STAGED CONSTRUCTION MODELING OF LARGE DIAMETER STEEL PIPES USING 3-D NONLINEAR FINITE ELEMENT ANALYSIS

by

MOJTABA SALEHI DEZFOOLI

Presented to the Faculty of the Graduate School of

The University of Texas at Arlington in Partial Fulfillment

of the Requirements

for the Degree of

DOCTOR OF PHILOSOPHY

THE UNIVERSITY OF TEXAS AT ARLINGTON

DECEMBER 2013

Acknowledgements

I would like to express my sincere gratitude to my doctoral advisor, Professor Ali Abolmaali, for his consistent support, guidance, and wisdom during the course of my Ph.D. studies. Without him, this research work would not have been possible. It has been my great pleasure and honor to have the opportunity to work with him. In addition, my warm appreciation is extended to my doctoral committee members, Professors John H. Matthys, Pranesh Aswath, and Shih-Ho Chao for their time, guidance, and helpful suggestions.

The research for the present dissertation was sponsored by the Integrated Pipeline Project and Tarrant Regional Water District. The guidance and support of David Marshall, Shelly Hattan, and Matt Gaughan are appreciated. The pipes which were used in the field test were donated by Hanson Pipe and Precast and American Spiral Weld (ASW).

I am also very grateful to my wife, Leila, for her endless love, support, and encouragement. Thanks to my colleagues and friends Dr. Mohammad Razavi and Dr. Yeonho Park, who donated their time and energy to this research.

Last, but not least, I would like to extend my utmost heartfelt appreciation to my family for their endless love, encouragement, and support. They have always been the great source of inspiration to me.

November 15, 2013

Abstract

STAGED CONSTRUCTION MODELING OF LARGE DIAMATER
STEEL PIPES USING 3-D NONLINEAR
FINITE ELEMENT ANALYSIS

Mojtaba Salehi Dezfooli, PhD

The University of Texas at Arlington, 2013

Supervising Professor: Ali Abolmaali

This study investigates the performance of large diameter steel pipes during stage construction. Using this study, metal pipes are designed utilizing existing native soil for embedment around the pipe rather than imported materials. This indeed, translates into a considerable amount of cost saving and advances in designing pipeline. This model is used for peer review/ designing of a 242 km (150 miles) pipeline project, Integrated Pipeline (IPL), that transports approximately hundreds of millions of gallons from Lake Palestine, 137 km (85 miles) southeast of Dallas, to Lake Benbrook, Tarrant County, Texas. The IPL project supplies water to more than1.8 million people living in 11 counties of North Texas. The results of this study not only benefits the Tarrant Regional Water District but also can be used in other projects.

A comprehensive robust nonlinear finite element analysis model was developed and verified by four experimental tests which were conducted at the University of Texas at Arlington. The developed FEM model considered all three nonlinear algorithms including geometric, material, and contact nonlinearities. The developed FEM model considered the soil compaction which is an important force in staged construction modeling of the steel pipes. Also the geometric change of pipe during construction was

modeled accurately for the first time to accurately obtain the behavior of the buried steel pipes. Four instrumented large diameter steel pipes, with the diameter of 1.83 m (72 in.), were placed in a 6.1 m (20 ft) wide rigid trench with different backfilling configurations. The promising results of the study indicated that the developed model successfully predicted the experimental tests. The developed FEM model was further modified then by incorporating flexible trench wall and other unique tools to be capable of modeling different pipeline designs. Moreover, the modified FEM model was used to verify three field tests which were conducted in Rolling Hills Booster Pump Station, in Fort Worth, Texas. The comparison of the results showed that the modified FEM model also successfully predicted the real field condition.

Finally, a comprehensive parametric study was conducted by identifying the most common geometric and force related parameters for large diameter pipe-soil interaction systems. These parameters include but not limited to pipe geometric parameters, backfilling properties and type and level of compaction, and in-situ soil condition. The parametric study models were generated by using a Design Program (DP) which was developed specifically in this study to support the main FEM model analysis. The DP allows the designer to feed the developed FEM model with the required design parameters which will generate the FEM model in a fraction of time compared to conventional manual model development. The results of the parametric study then were used to develop series of design equations for moment, thrust, shear, and horizontal and vertical deflection of buried steel pipes as a function of independent variables which were comprehensively identified in parametric study. The developed equation will be a platform to be used in the steel pipe design manuals.

Table of Contents

List of Illustrations

List of Tables

Chapter 1

Introduction

The Integrated Pipeline Project (IPL) is designed allowing multiple pipe material options capable of incorporating short-term and long-term soil performance. Steel and pre-stressed concrete cylinder pipes (PCCP) are among the pipe material options under considerations by the IPL Team. Generally, steel pipes are categorized as flexible pipe systems, which depend on their surrounding soil envelop to form a soil-structure interaction composite system to develop adequate stiffness and strength to carry the specified loads. Thus, carefully controlled backfilling of the trench width through proper compaction of selected soil material is an important factor in achieving optimum pipe performance. Studying the pipe behavior during backfilling is one of the priorities before designing and installing pipelines. Design limitations are introduced by the American Water Works Association (AWWA) for flexible and rigid pipes. These limitations are for both service and ultimate conditions. Several backfill and embedment materials are used in different conditions. Estimating pipe behavior in different backfill conditions during installation and considering the soil properties along the project route and path are important factors.

A part of this study was conducted at the Center for Underground Infrastructure Research and Education (CUIRE) at UT Arlington. Four (4) steel pipes were instrumented and installed in the soil box (rigid trench) to evaluate the pipe behavior. Then a 3-D Finite Element Method (FEM) model was developed using the data obtained from the soil box tests. Based on the results, three (3) field tests (flexible trench) were designed with different trench widths and backfill materials. The developed FEM model successfully predicted the field test results. Ultimately, the essential design parameters were selected for sensitivity study, and the developed FEM model was used to generate

different trench and backfilling conditions to evaluate buried steel pipes performance. The results of the sensitivity study were then used to develop the design equations for different conditions and configurations.

The intellectual merit of this project was to develop a high fidelity, highly robust nonlinear three-dimensional (3-D) FEM model for steel pipe. This model would be used to predict pipe performance under varying backfill and loading conditions. The FEM model contains an algorithm for shape distortion control for the pipe and surrounding soil during stage construction, which is done for the first time. This research establishes a relationship between the essential design parameters for pipe installation and the buried pipe performance (deflections and forces). The FEM model and the unique developed "Design Program," were used for verification of a pipe design. The field instrumentation and tests were conducted for model verification. This study will be a significant contribution toward informed design of large diameter flexible pipe systems. Results of this project will become a platform for further studies related to pipe design and installation.

1.1. Needs

The need to develop a Finite Element algorithm and technique to model and predict the pipe behavior during stage construction is one of the priorities in design and installation of pipelines.

Deflection control has always been a significant concern in designing buried flexible pipes. Indeed, American Water Works Association (AWWA) has limited pipe deflection between 2 to 5 percent of the pipe diameter for different lining systems. AWWA manual M11 does not recommend designing steel pipe in the elastic-plastic range when the deflections are not controlled. The accepted design stress for the water steel pipes is 50% of the minimum yield strength (AWWA M11, 2004). The stiffness of a flexible pipe

structure highly depends on the soil stiffness provided by the pipe's bedding and backfill materials to form a soil-structure interaction composite system. During staged construction installation of a buried pipe, as different lifts of the soil are poured, the shape, stiffness, boundary conditions, and loadings exerted on the pipe will change. As a consequence, the deflection of a pipe during its service life is not only a function of service loads, such as surcharge and live load, but it is also sensitive to the sequences of the construction, material, thickness, and compaction level of each lift.

Although several studies have been conducted on the analysis of buried pipes using soil-pipe interaction theories (Duncan, 1976; Duncan, 1979; Katona, 1976), limited investigations have explored the behavior of the flexible pipes during staged construction.

Zarghamee (1986) developed a 2-D finite element analysis program, FLEXPIPE, and showed in steel pipes significant flexural stresses are developed at the invert of the pipe after installation. The deflection history of the pipe, during installation was not reported in this study. The interface contact between soil-soil was not considered in this study.

Suleiman et al. (2003) investigated the effects of large deflection behavior on buried plastic pipes. This study compared the small deflection analysis theory results by using Culvert ANalysis and DEsign (CANDE) software with the large deflection analysis theory using ANSYS. The authors reported that for the deflections above 4 percent the difference between the small and the large deformation theory is 10 percent.

Katona et al. (1976) developed a 2-D finite element program, CANDE, for analysis and design of buried culverts. This FEM program is also using stage construction modeling for pipe-soil system. The beam element is used for the pipe sections. The program was developed and calibrated based on the experimental results. The squeeze layer method was defined to model the soil compaction.

McGrath (1998) conducted a study on the pipe-soil interaction during backfilling. Different backfilling materials were used in different compaction levels. This study conducted several soil box tests and field tests on steel, concrete, and plastic pipes to compare the results for different backfilling material, trench conditions, trench widths, and bedding material. The point load was applied onto the pipe in the FEM program, CANDE, to model the horizontal effects of compaction on the pipe.

The Integrated Pipeline Project (IPL), will connect Lake Palestine to Lake Benbrook. This Pipeline will be 242 km (150 miles) in length. One of the scopes of this project is to use the in-situ material as backfilling and embedment material. Since the geology and the soil properties are different in 242 km (150 miles) of the project, Tarrant Regional Water District (TRWD) decided to conduct research to evaluate the performance of several pipes under different conditions of backfilling and installation. Since testing all the possible scenarios was not feasible, it was decided to conduct four soil box tests (rigid trench wall). Therefore, 4 soil box tests were conducted at the Center for Underground Infrastructure Research and Education (CUIRE) at UT Arlington. Although the soil box test were successfully completed and the FEM program developed based on that, but the rigid wall condition and fixed trench width in the soil box tests, resulted in designing three (3) field tests (flexible trench wall) with narrower trench and different backfilling materials including Controlled Low Strength Material (CLSM).

Then the verified FEM model was used to develop different configurations of the pipe installation. After analyzing all the possible cases for the project, the design equations were developed to predict and estimate the pipe behavior in different conditions.

Figure 1-1 presents the framework of the conducted study.

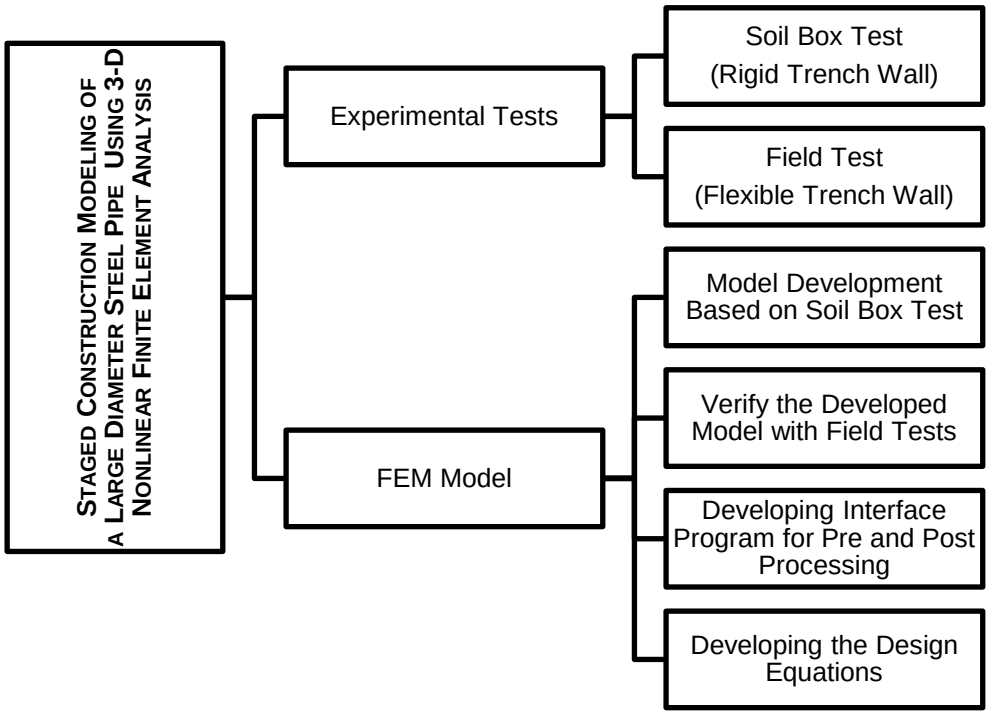

Figure 1-1 Framework of the conducted research

1.2 Goals

The primary goal of this study was to develop a benchmark for designing buried steel pipes in different backfill material. To accomplish this goal, several experimental tests were conducted and the results of the conducted tests were then verified with the developed finite element model. Moreover, different trench configurations with various backfilling conditions were modeled in the parametric study. The results of the parametric study were used to develop design equations for steel pipes.

1.3 Objectives

This study presents computational benchmarks on numerical modeling and associated algorithms for staged construction of flexible buried pipes using 3-D nonlinear finite element analysis. The proposed model was presented to accurately predict pipe

performance under varying backfill and loading conditions. The FEM analysis algorithm considered material, geometric, and contact nonlinearities. The material nonlinearity consists of elasto-plastic and Mohr-Coulomb plasticity for steel and soil, respectively. The geometric nonlinearity includes the large deformation analysis for soil and steel pipe materials. Finally, the contact nonlinearity includes the contact elements used at the interface between the pipe and soil and different soil layers during sequential layered construction. The FEM modeling of this study was initially developed by using test deflection results from four (4) 1.83 m (72 in.) steel pipe tests reported by Najafi (2012).

The developed model then was used to verify three (3) field tests results which were conducted at Rolling Hills Booster Pump Station, Fort Worth, Texas. After verification of the FEM model, the essential parameters for the pipe design were identified comprehensively to conduct the sensitivity study. The results of sensitivity models then were used to develop design equations to predict the deflections and the stresses of the pipe.

The need to use the in-situ material as backfill material in pipe installation was one of the objectives of the current study. Thus, the developed finite element model and algorithm should be capable of modeling different pipe installation situations. Using the ordinary material (native material) as backfill material is beneficial to the design and cost of the project. Moreover, the design criteria, deflection limit and stress limit, should be considered during backfill selection. Therefore, the native material will be treated with other materials like cement, fly ash, or lime to satisfy the design criteria and have the benefits of using native material. Finally, in the worst case of native soil material, in which no treatment would be helpful, a select fill material of sand or crushed limestone would be used for pipe backfilling.

1.4 Research Contribution

The staged construction model for large diameter buried steel pipes was developed and verified using soil box and field tests. The lateral effect of soil compaction was simulated using uniform thermal loading for the first time. The developed design equations of this study will be presented to different committees in AWWA (M11) and ASCE (MOP-119) for adoption as the basis for designing buried steel pipes. The required parameters for the presented design equations in this study are obtained from laboratory tests and there is no need to use traditional hybrid or fictitious soil parameters like E'.

1.5 Outline for Dissertation

Chapter 2 presents a review of current pipe design manuals. Some theoretical background on finite element modeling is presented in this chapter. Also the background on finite element modeling of steel pipes is discussed in Chapter 2.

The algorithms and techniques which were used in the development of the 3-D model are presented in Chapter 3. The details of the soil box tests and the comparison of the results of the finite element model and the experiments are also included in this chapter.

Chapter 4 of this dissertation presents the details of the field tests and the deflection results of the field tests were compared with the results of the developed FEM model. Also the required modifications, which were needed to model various trench configurations, were explained in Chapter 4.

The parametric study models and the developed equations for buried steel pipe design are discussed and presented in Chapter 5.

In Chapter 6 the findings of this study are summarized, the conclusions are presented, and the issues that need further investigations are introduced.

Chapter 2

Literature Review

2.1 Mechanics of Material of Pipe

Chapter 2 of this report presents the current advances of pipe design and installation. While the behavior of large diameter steel pipes during stage construction was studied in this report, knowing the design concept of pipe and different installation types is a key to have a better understanding of the pipe behavior. Different pipe design manuals are presented and introduced in this chapter. Moreover, as the finite element analysis was used as a tool to study the behavior of the pipe in different stages of construction, some theoretical background on the finite element method is presented in this chapter. Lastly, different material and plasticity models are discussed in the present chapter.

Figure 2-1 and Figure 2-2 presents a typical pipe and trench, respectively, showing the terminologies which are used in this study.

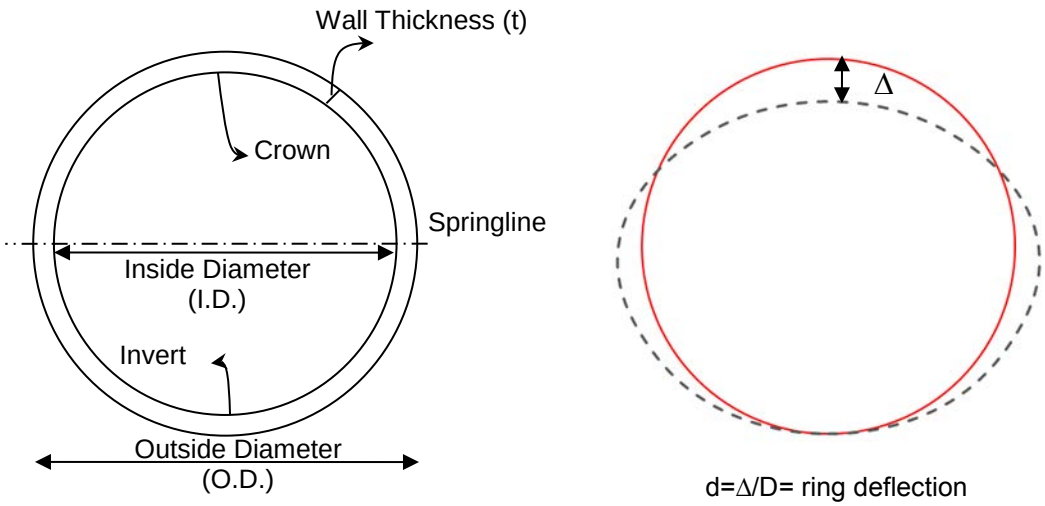

Figure 2-1 Typical definitions in pipe (Card 2012, MOP 119)

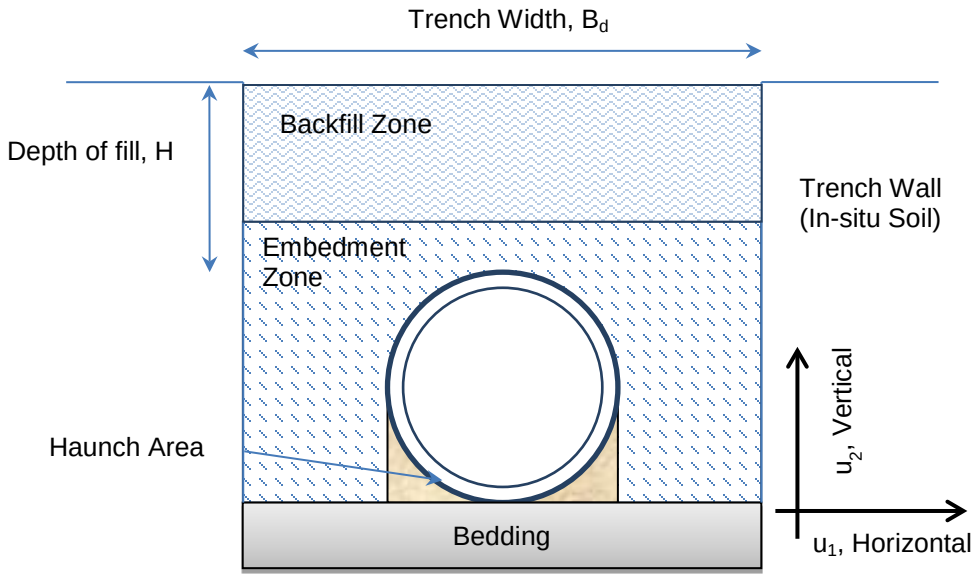

Figure 2-2 Typical nomenclature of trench (Card 2012, MOP 119)

2.1.1. Strength of Material; Flexible and Rigid Pipes

A pipe should be strong enough to carry the applied stresses. These stresses are due to different loading such as soil compaction, soil weight, transient live loads, and internal pressure. The pipe's stiffness is a function of pipe's material modulus of elasticity and it is the capability of the pipe to resist the deflection. Moreover, the pipe should be durable to tolerate the attack and changes in the environment.

There are several pipe materials available. However, pipes are categorized due to their behavior into two major groups; flexible and rigid (Moser A., 2013). The examples are concrete and clay pipes for rigid category and steel and thermal plastic pipes for flexible pipes. American Water Works Association (AWWA) has limited steel pipe (flexible pipe) deflections between 2 to 5 percent of the pipe diameter for different lining systems. Moreover the stresses in the allowable deflection should be in the acceptable range. For example the accepted design stress for the water transmission steel pipes is 50% of the

minimum yield strength (AWWA M11, 2004). For the rigid pipes, the criterion is the strength of the pipe to withstand the stresses caused by external soil loads and internal pressure (Moser A. 2013).

A semi-rigid pipe is a pipe which is not flexible or rigid. The current pipe design manuals are based on either flexible theory or rigid pipe design theory.

The pipe's stiffness is important in the design of flexible pipes. The stiffness of flexible pipes is critical for cases with buckling and also to resist the ring deflection, as shown in Figure 2-3 (Moser 2013).

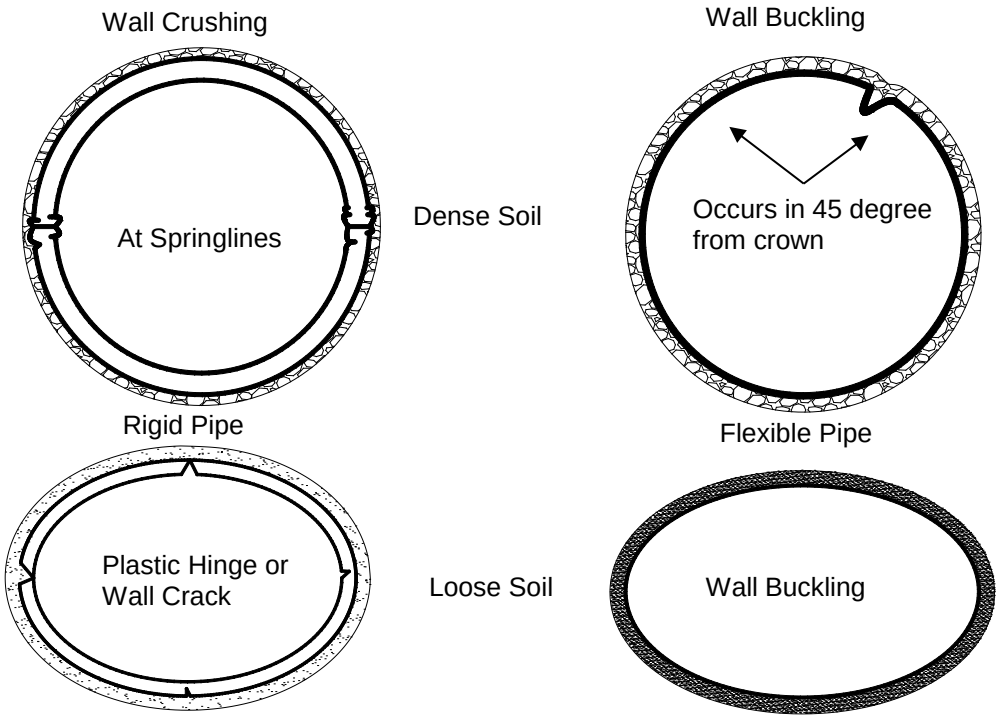

Figure 2-3 Typical performance limits of buried pipe rings due to external soil pressure (Watkins 2000)

The American Water Works Association (AWWA) and the ASCE have published several manuals to design and predict pipe behaviors for different pipe material. Since

this study concentrates on flexible pipes, two current manuals for designing steel pipes are introduced in this chapter.

2.2 Designing Steel Pipes

The M11 standard, which is published by AWWA has been used for design and performance of the steel pipes. Also the ASCE buried flexible steel pipe design and structural analysis (MOP-119, 2009) was introduced to ease the design of steel pipes.

Any pipe design has certain steps. The diameter and size of the pipe will be identified by using hydraulics equations and needs. The Hazen-Williams formula, Scobey formula , and Manning formula (Lamont, 1981) for designing and calculating the flow in pipes were introduced by M11 to determine the pipe size. However, pipe thickness depends on several factors which are discussed in M11. External loads including soil compaction, soil at-rest lateral pressure, and live load and internal load including design pressure and water-hammer pressure are among those which affect the design of pipe wall thickness.

The M11 and MOP-119 presented Equation 2-1 to calculate the pipe thickness based on the internal pressure. The hoop stresses are the basis for design of pipe wall thickness in Equation 2-1.

$$t = \frac{pO.D.}{2s} \qquad 2\text{-}1$$

Where:

t = minimum pipe wall thickness for the specified internal design pressure, mm (in.)

p = internal design pressure, kPa (psi)

O.D. = outside diameter of steel pipe (not including coating), mm (in.)

s = allowable stress design, kPs (psi)

Parmakian (1982) recommended the minimum wall thickness. Equations 2-2 through 2-4 present the minimum pipe wall thicknesses for different pipes.

$t = \frac{I.D.}{288}$ for pipes up to 1,350 mm (54 in.) 2-2

$t = \frac{I.D.+20}{400}$ for pipes greater than 1,350 mm (54 in.) 2-3

$t = \frac{I.D.}{240}$ for steel pipes coated with flexible and mortar-lined coating 2-4

There are several external loads acting on the buried pipe including weight of backfilling material, soil lateral pressure i.e. at-rest lateral soil pressure and horizontal effect of compaction, and transient live loads (Katona, 1976 and 2008). Figure 2-4 illustrates the definition of different stresses in the pipe wall.

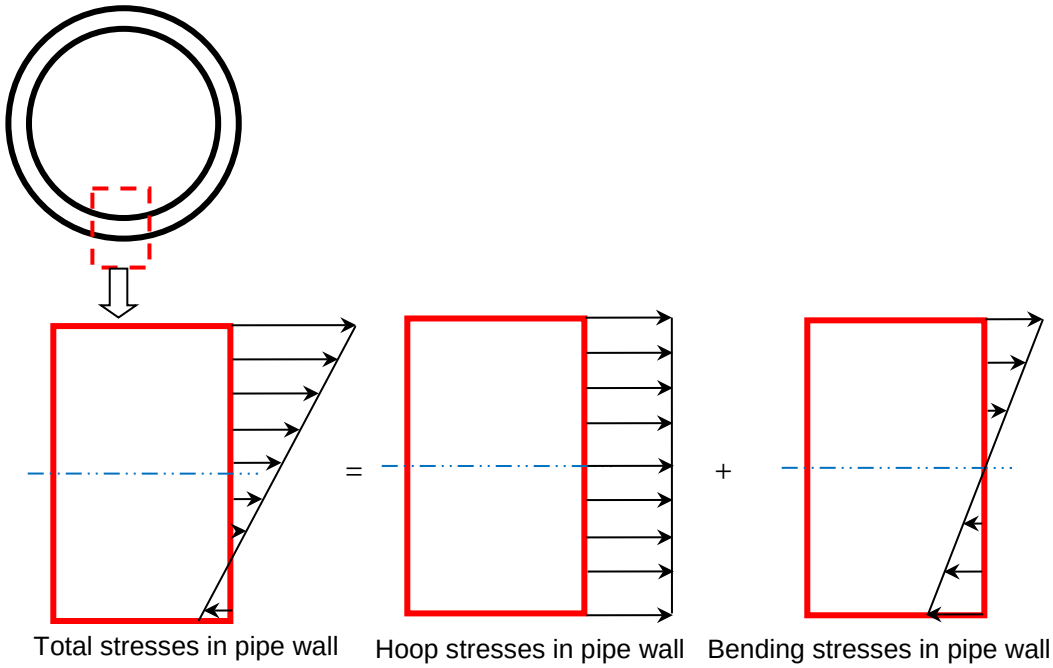

Figure 2-4 Hoop and bending stresses in pipe wall thickness

To determine the soil prism weight and external loads due to weight of the soil, the Marston theory (1929) is considered. As M11 indicated, for the design of steel pipes a simplified method is suggested to calculate the external loads. If the trench width is less

than twice the diameter of the pipe, Equation 2-5 is appropriate. Moreover, for wide trench and embankment conditions, Equation 2-6 used to calculate the external soil load.

$$W_C = C_d w {B_d}^2 \left(\frac{B_c}{B_d}\right) \quad 2\text{-}5$$

$$W_C = C_c w {B_c}^2 \quad 2\text{-}6$$

Where:

W_C = external soil load on pipe, kg/m (lb/ linear ft) of pipe

B_d = width of trench at top of pipe, m (ft)

C_d = load coefficient based on $\left(\frac{H_c}{B_d}\right)$ where H_c is the height of fill above conduit

w = unit weight of fill, kg/m^3 (lb/ft^3)

B_c = diameter of pipe, m (ft)

C_c = coefficient for embankment conditions which is a function of soil properties

Equation 2-7 defines the coefficient for embankment conditions, C_c, for flexible pipes.

$$C_c = \frac{H_c}{B_c} \quad 2\text{-}7$$

Where:

H_C = Height of fill above the top of the pipe, m (ft)

The AWWA steel pipe manual (M11, 2004) and the ASCE buried flexible steel pipe design and structural analysis (MOP-119, 2009) introduced the modified Iowa deflection equation (Watkinson and Spangler, 1958). Modified Iowa deflection formulation, Equation 2-8, predicts the pipe's deflection by using pipe wall and soil stiffness.

$$\Delta x = D_l \left(\frac{KWr^3}{EI + 0.061E'r^3}\right) \quad 2\text{-}8$$

Where:

Δx = horizontal deflection of pipe, mm (in.)

D_l = deflection lag factor (1.0- 1.5)

K = Bedding constant (0.1)

W = load per unit of pipe length, kg/mm (lb/ linear in)

r = radius, mm (in.)

EI = pipe wall stiffness

E = modulus of elasticity, kPa (psi)

I = transverse moment of inertia per unit length of individual pipe wall components = $t^3/12$, t is in mm (in.)

E' = modulus of soil reaction, kPa (lbf/in^2)

In order to calculate the stiffness of backfilling soil, a hybrid soil module, E', was defined. Howard (1977, 1996) conducted 113 tests on different flexible pipes in different backfilling materials to determine the soil-pipe hybrid modulus for different soils. Most of the steel pipes were small diameter pipes and there were a limited number of large diameter steel pipes in the tests matrix. Moreover, there are different parameters affecting E' and subsequently pipe deflection, which were not accounted for in the above specifications. For example trench width, different soil type, the thickness of compaction layer, and other important variables were not considered. Also, new trench configurations such as sloped trench wall and gap filler were not addressed in the current table of E'. Furthermore, for the new materials like Controlled Low Strength Material (CLSM) a series of full scale tests should be conducted to estimate soil hybrid modulus. Also, as explained by M11, back calculation of E', which is common among engineers for pipe design, caused severe problems. Krizek et al. (1971) defined a constrained soil modulus, M_s, which could be calculated directly from elastic modulus of soil. Another study by Hartley and Duncan (1987) illustrated that the soil E' modulus and M_s varies along the depth of

the soil. While, a verified FEM model with different tests, would easily estimate the pipe deflection without any need to evaluate E' or M_s. Moreover, the pipe buckling or collapse which is introduced in M11 is also a function of E' which has the same problems as deflection. This manual summarized the value for E' for certain soil types at different compaction levels.

MOP-119 introduced a simple method to calculate the pipe deflection during construction (ASCE, MOP-119, 2009). A rod with a specified length, L, should touch the pipes interior wall at two points, as shown in Figure 2-5 (a). Then the distance between the center of the rod and pipe, e, will be obtained. The radius of the curvature of the deflected pipe at different locations is calculated by using Equation 2-9. Furthermore, the graph in Figure 2-5 (b) will be used to calculate the maximum deflection in the pipe.

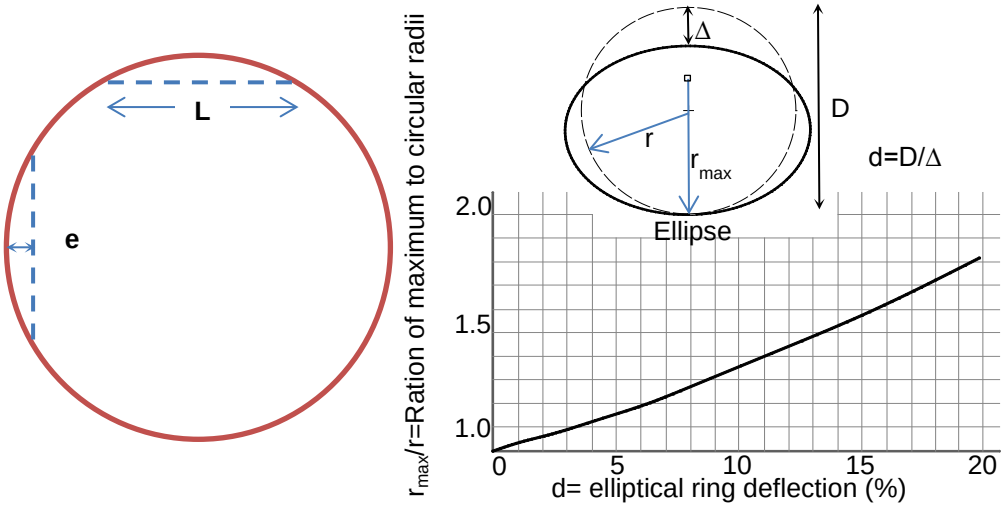

(a) (b)

Figure 2-5 (a) Method for calculating the curvature based on MOP-119; (b) Measuring pipe deflection based on the maximum radius of curvature (MOP-119)

$$r = \frac{4e^2 + L^2}{8e} \qquad 2\text{-}9$$

M11 has limited pipe deflection to certain values for different systems of lining and coating. The allowable deflection for pipes with mortar-lining and coating is two (2) percent of the pipe diameter. This value is three (3) percent when the pipe is coated mortar lining and flexible coating. The five (5) percent limitation is applicable to the pipes which are coated with flexible coating and lining.

Live load and transient load should be calculated and evaluated for pipe design.

M11 is introduced a table which has summarized the effect of live load for two (2) different loads, i.e. AASHTO HS-20 truck load or Cooper E-80 railroad, applied at different height of soil cover. As the soil cover is increasing the effect of live load is decreasing on the pipes. M11 states that for soil cover above 2.44 m (8 ft) and 9.14 m (30 ft), the effects of live load should be neglected for ASSHTO HS-20 and Cooper E-80, respectively.

Design manuals also introduced the information for designing joints and fittings. Designing coating and lining for the pipes, which are protecting the pipes against corrosion, are also discussed in the manuals.

In conclusion, different parameters including hydraulic needs, internal pressure and pipe wall stiffness (thickness), transportation issues due to thin wall of the pipe, capability of carrying different external loads, and corrosion should be considered while designing a pipe. (Watkins, 2000)

Figure 2-6 illustrates the installed stulls in a pipe to prevent excessive deformation and impact on the pipe wall during transportation and installation.

Figure 2-6 Stulls were installed in the manufacturer's plant to prevent excessive deformation

Moreover in the design procedure of the pipe, a designer should be aware of the importance of the backfilling material. The pipe and its surrounding soil are acting as one system. Especially for flexible pipe the pipe stiffness is negligible in comparison to backfill material. Thus, it is very important to pick and select a proper backfill material. There are several backfilling options available for a designer including compacted native soil, treated native soil, select fill, and Controlled Low Strength Material (CLSM). The native soil is a soil which is available in the area where the pipe will be installed (in-situ). Thus, in order to get a stiff backfill for the pipe a proper compaction is needed for the native soil. If the native soil is not stiff enough, other options are available. Native soil may be treated with different materials including lime, fly ash, or cement. However, if the native soil is not proper for treatment, other options should be considered. Importing material from outside of the working area is one option. This material is called select fill and there are some disadvantages to import material to the site including cost and also recycling native soil. Therefore researchers (Green, 2004) introduced a new material which is called CLSM. The CLSM is a flowable material which is composed of shredded (if needed) native soil, water, and cement. The CLSM will flow below the pipe and will fill the small gaps.

Moreover use of the combination of the abovementioned material is also beneficial to a designer. A designer may select the CLSM material for the haunch zone of the pipe in which the compaction is not feasible. Also for the narrow trenches (I.D.+12 in. to I.D.+24 in.) the compaction of lower part of the trench is not feasible (below 70% of the I.D.) so the CLSM material is one of the best options for those situations.

2.3 Material Modeling and FEM Modeling

The relation between stress and strain in a material is defined by certain equations. In this equation which is the material model the rate of stress are related to strain rate.

Equations 2-10 and 2-11 illustrate the stress and strain tensor in matrix form.

$$\sigma = \begin{bmatrix} \sigma_{xx} & \sigma_{xy} & \sigma_{xz} \\ \sigma_{yx} & \sigma_{yy} & \sigma_{yz} \\ \sigma_{zx} & \sigma_{zy} & \sigma_{zz} \end{bmatrix} \quad \text{2-10}$$

$$\epsilon = \begin{bmatrix} \epsilon_{xx} & \epsilon_{xy} & \epsilon_{xz} \\ \epsilon_{yx} & \epsilon_{yy} & \epsilon_{yz} \\ \epsilon_{zx} & \epsilon_{zy} & \epsilon_{zz} \end{bmatrix} \quad \text{2-11}$$

Finally, Figure 2-7 illustrates the general stress state in a 3-D system.

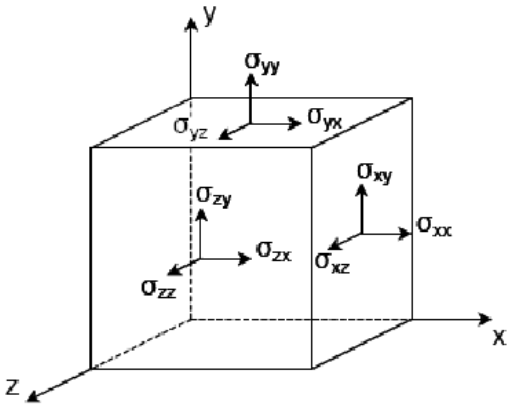

Figure 2-7 General three-dimensional coordinate system for stresses

2.3.1 Nonlinear Algorithms

The structural mechanics problems always have a type of nonlinearities in the analysis. The possible three (3) general types of nonlinearities in each problem are material, geometric, and contact nonlinearities.

In the material nonlinearities, the constitutive equation which relates stress and strain rates is nonlinear. Materials behave linearly until they reach to a certain point, which is called elastic limit, after this point the behavior is nonlinear. There are different nonlinear material models for different types of material.

The second possible nonlinearity is geometric nonlinearity. In geometrical nonlinear analysis, the relationship between strain and displacement is not linear. Large rotation, large strain, and large displacement are different types of geometric nonlinearities. Lagrangian and Eulerian techniques should be applied to solve the geometric nonlinearity.

In Lagrangian point of view, material and mesh points are attached so they deform and translate together. However, in Eulerian mesh, points will stay in their initial position during the analysis and material nodes will move independent of the mesh nodes. The later formulation is suitable for liquid materials.

Contact nonlinearity is the last possible type of nonlinearity in any structural mechanics analysis. This nonlinearity happens when the boundary conditions of the problem are changing. Also when the load path is going through the contact of two surfaces this type of nonlinearity will occur. Two (2) constraints are applied to contact nonlinearity; no penetration should occur between the two (2) surfaces of the contact which is known as displacement constraint, and no load or force should keep the two surfaces together, which is called force constraint.

2.3.1.1 Material Nonlinearities

For each plasticity models, different parameters including yield criteria, hardening rule, and flow rule should be defined

2.3.1.1.1 Yield criteria: The behavior of the materials is different when they are subjected to multi axial loading condition. The materials are either pressure dependent or pressure independent. For pressure independent materials yield criteria defined in terms of second deviatoric stress invariant (J_2) and they are independent of first stress invariant (J_1). The hydrostatic pressure would affect the yielding in some material models like Rankin, Mohr-Coulomb, and Drucker-Prager in which the material behavior depends on the pressure. The materials which are independent of J_1 are sensitive to deviatoric stress. The yielding criteria which are independent of J_1 are Tresca criterion and the Von Mises criterion. When the octahedral shear stress reaches a critical value the yielding will happen in Von Mises criterion.

Equation 2-12 defines the Von Mises yield criterion.

$$f(\sigma_{ij}) = 3J_2 - k^2(\epsilon_p) = 0 \qquad 2\text{-}12$$

Where:

ϵ_p= the effective plastic strain

J_2 =the second invariant of the reduced deviatoric stress which is defined in Equation 2.13.

$$J_2 = \frac{1}{2}\bar{S}_{ij}\bar{S}_{ji} \qquad 2\text{-}13$$

Where:

$\bar{S}_{ij}$ = the reduced deviatoric stress which is defined by Equation 2-14.

$$\bar{S}_{ij} = S_{ij} - \alpha_{ij} \qquad 2\text{-}14$$

Where:

α_{ij} is the back stress (center of yield surface) which is zero for isotropic hardening and S_{ij} is defined by Equation 2-15.

$$S_{ij} = \sigma_{ij} - \frac{1}{3}\sigma_{kk}\delta_{ij} \qquad 2\text{-}15$$

Where:

σ_{ij} = stress

S_{ij} = deviatoric stress

δ_{ij} = Kronecker delta

2.3.1.1.2 Hardening: The elastic-perfectly plastic material yields the same in loading, unloading, and reloading cycles. However, in a material which has hardening properties, yield strength will be different in various load cycles. Thus, the behavior of the material and the elastic region of it depend on its previous loading cycles. There are three (3) major hardening theories for materials including isotropic hardening, kinematic hardening, and mixed hardening.

The isotropic hardening theory assumes that the hardening is the same in all directions. As shown in Figure 2-8 the yield surface will expand symmetrically about its origin. Figure 2-9 shows the effect of isotropic hardening on stress-strain curve.

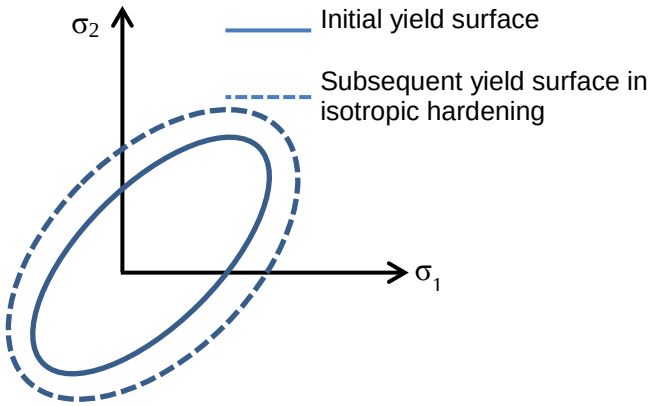

Figure 2-8 Effect of isotropic hardening model on yield surface

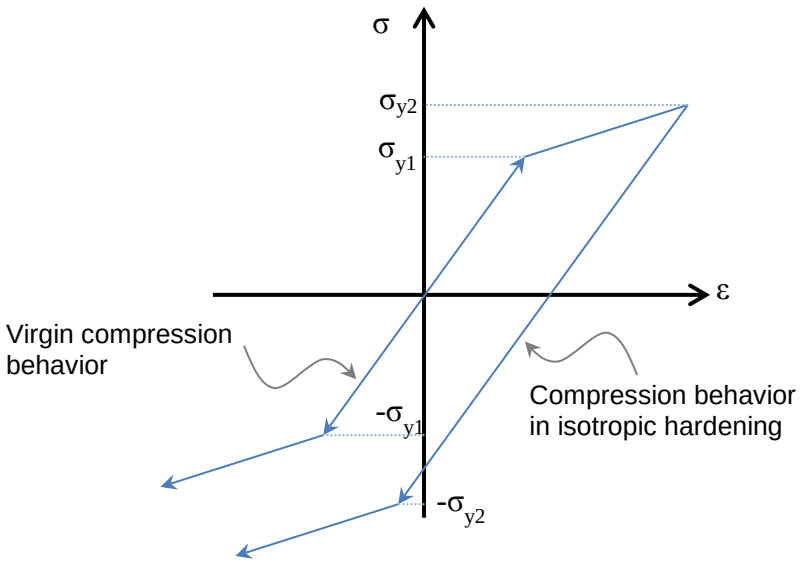

Figure 2-9 Effect of isotropic hardening on stress-strain curve

To include the Bauschinger effect which occurs in cyclic loading of metals, another hardening theory was defined, which is kinematic hardening. In kinematic hardening theory, the hardening in one direction will decrease while the hardening in other directions equally increases. Figure 2-10 shows the effect of kinematic hardening model on yield surface. Figure 2-11 illustrates the effect of kinematic hardening on stress-strain curve.

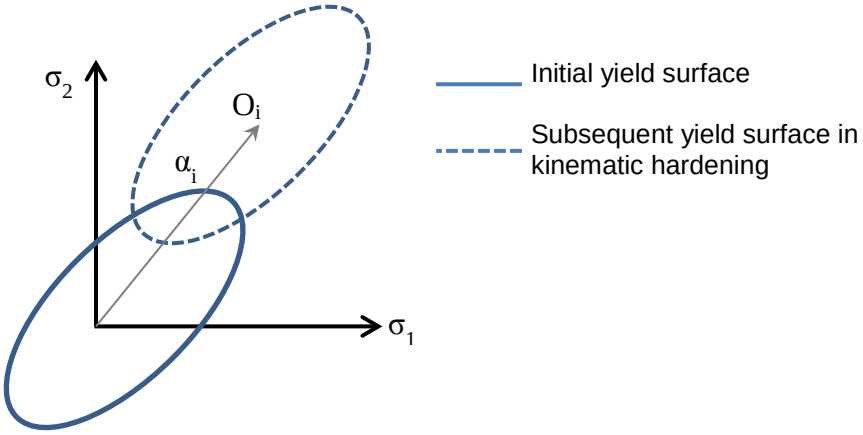

Figure 2-10 Effect of kinematic hardening model on yield surface

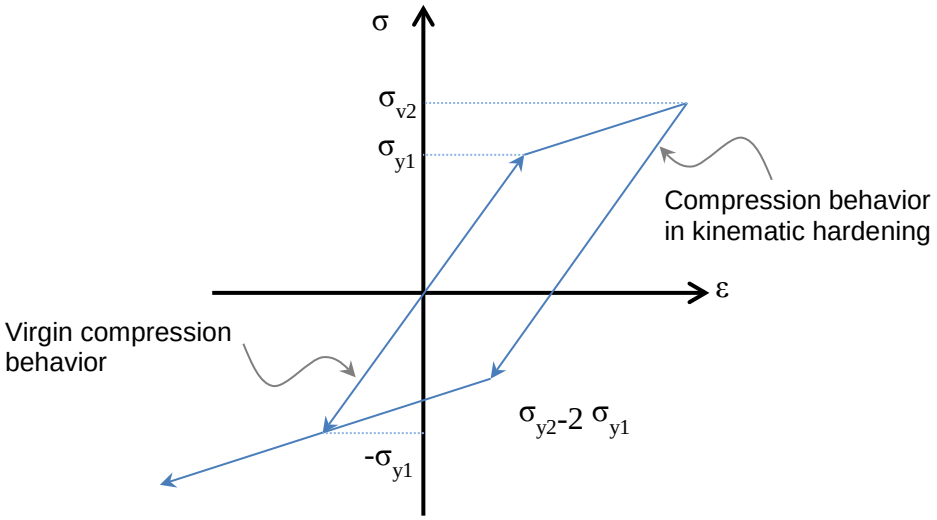

Figure 2-11 Effect of kinematic hardening theory on stress-strain curve

The mixed formulation model is a combination of the previous hardening models. A weighted average of plastic strain increment of the either models will be calculated.

2.3.1.1.3 Flow rule: The direction of the plastic strain increments due to the loading beyond the yield surface is defined by flow rule. For the flow rule the plastic potential function is adopted to find the direction of plastic strain increments.

Flow rule specifies the ratio of the component of the plastic strain increment tensor, de^P, or the direction of de^P in the strain space, e_{ij}. It should be noted that the plastic strain vector corresponding to a given stress tensor, σ_{ij}, is a vector normal to the potential function. If the potential function, G, is the same as the function for yield criteria, F, then the flow rule is associated otherwise the flow rule is non-associated. For most cases the associated flow rule is adopted. Hence for some geotechnical problems the associated flow rule overestimates the plastic volume expansion, it is suggested to use non-associated flow rule. It should be noted that the application of non-associated flow rule will cause the stiffness matrix to be an asymmetric matrix.

2.3.1.2 Geometric Nonlinearity and Large Deformation

Either small strains with large rotation (Figure 2-12) or large strain with large rotation (Figure 2-13) are considered as large deformation.

The total Lagrangian and updated Lagrangian formulation was used to taking the large deformation in to account.

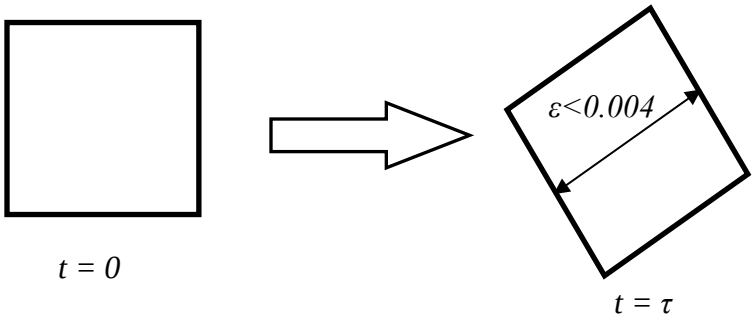

Figure 2-12 Large displacement: small strain + large rotation

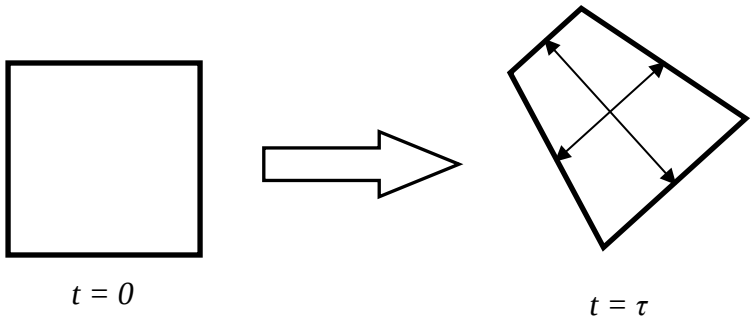

Figure 2-13 Large displacement: large strain + large rotation

Figure 2-14 illustrates an object location in three (3) different times: *0, t*, and ***t+Δt.***

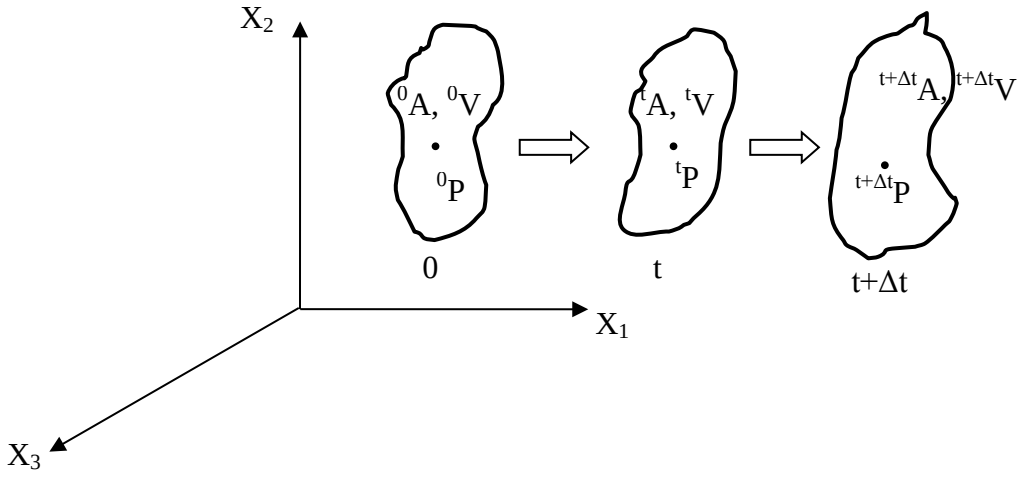

Figure 2-14 Location of an object in different times

For each time the location of the object could be written as Equations 2-16 (a), (b), and (c):

at time 0: ${}^0X_1,\ {}^0X_2,\ {}^0X_3 = {}^0\vec{X}_P$ 2-16 (a)

at time t: ${}^tX_1,\ {}^tX_2,\ {}^tX_3 = {}^t\vec{X}_P$ 2-16 (b)

at time t + Δt: ${}^{t+\Delta t}X_1, {}^{t+\Delta t}X_2, {}^{t+\Delta t}X_3 = {}^{t+\Delta t}\vec{X}_P$ 2-16 (c)

Where:

${}^0\vec{X}_P$ is the material point position vector at time *0*

${}^{t}\vec{X}_P$ is the material point position vector at time *t*

${}^{t+\Delta t}\vec{X}_P$ is the material point position vector at time *t*+Δ*t*

Figure 2-15 and Equations 2-17 (a) and (b) illustrate the definition of the ${}^{t}X_i$.

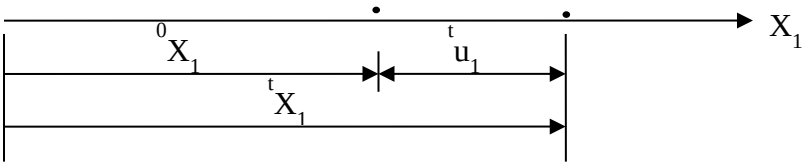

Figure 2-15 Definition of ${}^{t}X_i$ and ${}^{t}u_i$

$${}^{t}X_i = {}^{0}X_i + {}^{t}u_i \qquad \text{2-17 (a)}$$

$${}^{t+\Delta t}X_i = {}^{0}X_i + {}^{t+\Delta t}u_i \qquad \text{2-17 (b)}$$

So the increment is written as Equation 2-18.

$$u_i = {}^{t+\Delta t}u_i - {}^{t}u_i \qquad \text{2-18}$$

To perform large deformation analysis, the derivation should be started with principle of virtual work at *t*+*Δt* which presented as Equation 2-19.

$$\int_{t+\Delta t_V} {}^{t}\tau_{ij}\delta_{t+\Delta t}e_{ij}\,{}^{t+\Delta t}dV = \int_{t+\Delta t_V} {}^{t+\Delta t}f_i^B\delta u_i\,{}^{t+\Delta t}dV + \int_{t+\Delta t_S} {}^{t+\Delta t}f_i^S\delta u_i^{S\,t+\Delta t}dS \qquad \text{2-19}$$

where

$${}^{t}\tau_{ij} = Cauchy\ Stress = \left(\frac{Force}{{}^{t+\Delta t}A}\right)$$

$$\delta_{t+\Delta t}e_{ij} = \frac{1}{2}\left(\frac{\partial\delta u_i}{\partial x_j} + \frac{\partial\delta u_j}{\partial x_i}\right)$$

Since the volume at time = *t*+*Δt* is unknown, from above, the integration cannot done over an unknown volume and the calculation cannot perform directly with increment in Cauchy stress.

For large deformation, a measure for large strain is needed which is known as "Green-Lagrange" strain tensor. Thus, the virtual work equation (variational formulation) needs to be re-write to incorporate the large strain.

A stress tensor also should be defined to be energy conjugate to Green Lagrange strain in order to form the condition in Equation 2-20.

$$\int_{t+\Delta t_V} {}^{t+\Delta t}\tau_{ij}\delta\ {}_{t}e_{ij}\ {}^{t}dV = \int_{{}_0V} {}^{t}_{0}S_{ij}\delta\,{}^{t}_{0}\epsilon_{ij}\ {}^{0}dV \qquad \forall t \qquad \text{2-20}$$

Where:

${}^{t}_{0}\underline{\epsilon} = Green\ Lagrange\ Strain\ Tensor$

Thus, the 2nd Piola-Kirchhoff stress tensor, ${}^{t}_{0}S_{ij}$, is introduced above to act on $\delta\,{}^{t}_{0}\epsilon_{ij}$ in order to the above equation to hold and to be true.

The 2nd Piola-Kirchhoff stress tensor relates forces in the reference configuration to areas in the reference configuration.

To develop the incremental finite element equations, Equation 2-21 should be used, which is now integrated over a known volume, ${}^{0}V$.

$$\int_{{}_0V} {}^{t+\Delta t}_{0}S_{ij}\delta\,{}^{t+\Delta t}_{0}\epsilon_{ij}\ {}^{0}dV = \int_{t+\Delta t_V} {}^{t+\Delta t}f_i^B\delta u_i{}^{t+\Delta t}dV + \int_{t+\Delta t_S} {}^{t+\Delta t}f_i^S\delta u_i^{S\,t+\Delta t}dS \qquad \text{2-21}$$

Both S_{ij} and ϵ_{ij} should be incrementally decomposed as Equations 2-22 (a) and (b), respectively.

$${}^{t+\Delta t}S_{ij} = {}^{t}_{0}S_{ij} + {}_{0}S_{ij} \qquad \text{2-22 (a)}$$

$${}^{t+\Delta t}\epsilon_{ij} = {}^{t}_{0}\epsilon_{ij} + {}_{0}\epsilon_{ij} \qquad \text{2-22 (b)}$$

where ${}_{0}S_{ij}$ and ${}_{0}\epsilon_{ij}$ are the increments on 2nd Piola-Kirchhoff stress and Green-Lagrange strain tensor, respectively. The Green-Lagrange strain tensor is defined by Equation 2-23.

$$\epsilon_{ij} \text{ or } \underline{\epsilon} = \frac{1}{2}\left({}^{t}_{0}\underline{C} - \underline{I}\right) \quad \text{2-23}$$

where

$\underline{C} = {}^{t}_{0}\underline{X}^{T}\,{}^{t}_{0}\underline{X}$ (deformation tensor)

${}^{t}_{0}\underline{X}$ is the deformation gradient matrix and can be written as Equation 2-24.

$${}^{t}_{0}\underline{X} = \frac{\partial\ {}^{t}X_i}{\partial\ {}^{0}X_j} = {}^{t}_{0}X_{i,j} \quad \text{2-24}$$

In Equation 2-24, ${}^{t}_{0}\underline{X}$ contains both stretch part of the deformation and the rotations. Also, ${}^{t}_{0}\underline{X}$ may not be symmetric, however, $\underline{C}$ is symmetric and thus, $\underline{\epsilon}$ is also symmetric. For rigid body motion between t and *t+Δt,* ${}^{t+\Delta t}_{0}\underline{\epsilon} = {}^{t}_{0}\underline{\epsilon}$, and ${}^{t}_{0}\underline{\epsilon} = 0$ for motion between *0* and *t*

Equation 2-24 can be re-written as Equation 2-25.

$${}^{t+\Delta t}_{0}\underline{X} = \underline{R}\,{}^{t}_{0}\underline{u} \quad \text{2-25}$$

where $\underline{R}$ is plane rotation matrix. Equation 2-26 simplifies the definition of deformation tensor.

$${}^{t}_{0}\underline{C} = {}^{t}_{0}\underline{X}^{T}\,{}^{t}_{0}\underline{X} = \left({}^{t}_{0}\underline{R}\,{}^{t}_{0}\underline{u}\right)^{T}\left({}^{t}_{0}\underline{R}\,{}^{t}_{0}\underline{u}\right) = {}^{t}_{0}\underline{u}^{T}\,\underbrace{{}^{t}_{0}\underline{R}^{T}\,{}^{t}_{0}\underline{R}}_{\underline{I}}\,{}^{t}_{0}\underline{u} = \left({}^{t}_{0}\underline{u}\right)^{2} \quad \text{2-26}$$

Thus, ${}^{t}_{0}\underline{C}$ is invariant under a rigid body rotation.

Since the ${}^{t}_{0}\underline{C}$ is symmetric, ${}^{t}_{0}\underline{\epsilon}$ is symmetric. Thus as Equation 2-27 presents, the Green-Lagrange strain tensor is written as two (2) parts of linear and nonlinear in displacement.

$${}^{t}_{0}\epsilon_{ij} = \frac{1}{2}\left(\underbrace{{}^{t}_{0}u_{i,j} + {}^{t}_{0}u_{j,i}}_{\substack{Linear\ in \\ displacement}} + \underbrace{{}^{t}_{0}u_{k,i}\,{}^{t}_{0}u_{k,i}}_{\substack{Non\ linear\ in \\ displacement}}\right) \quad \text{2-27}$$

Where ${}^{t}_{0}u_{i,j} = \frac{\partial\ {}^{t}u_i}{\partial\ {}^{0}X_j}$

The Green-Lagrange strain tensor, ${}_0^t\epsilon_{ij}$, is exact and valid for any amount of stretching. The 2nd Piola-Kirchhoff stress is defined as Equation 2-27.

$${}_0^tS_{ij} = \frac{{}^0\rho}{{}^t\rho}\,{}_t^0X_{i,m}\tau_{mn}\,{}_t^0X_{j,n} \quad \text{(Indicial format)} \qquad \text{2-27 (a)}$$

$${}_0^t\underline{S} = \frac{{}^0\rho}{{}^t\rho}\,{}_t^0\underline{X}\;{}^t\tau\,{}_t^0\underline{X} \quad \text{(Matrix format)} \qquad \text{2-27 (b)}$$

Given the solution at time *t*, a displacement increment, u_i, is sought to obtain the displacement at time *t+Δt*.

$${}_0^{t+\Delta t}u_i = {}_0^tu_i + u_i$$

The Cauchy stress can then be obtained at time *t+Δt*, which satisfy the principle of virtual work at time *t+Δt*. The goal is to linearize the equation of the principle virtual work by using the finite element solution so an equation can be obtained in the form of Equation 2-28.

$$\underbrace{{}^t\underline{K}}_{\substack{Tangant\\ Stiffness}}\ \underbrace{\underline{\Delta}^{(1)}}_{\substack{Displacement\\ increment}} = \underbrace{{}^{t+\Delta t}\underline{R}}_{\substack{Externally\\ Applied\ Load}} - \underbrace{\underline{{}^tF}}_{\substack{Noadl\ Force\ Vector\\ Corresponding\ to\ the\\ Element\ Internal\\ Stresses\ at\ Time\ t}} \qquad \text{2-28 (a)}$$

In Equation 2.28 (a), $\underline{\Delta}^{(1)}$ gives an approximation to the displacement increment.

Thus Equation 2-28 can be re-write as following equation.

$$\left[\,{}^tK\right]_{n\times n}\left\{\Delta u^{(1)}\right\}_{n\times 1} = \left\{{}^{t+\Delta t}R\right\}_{n\times 1} - \left\{\,{}^tF\right\}_{n\times 1} \qquad \text{2-28 (b)}$$

To linearize a known reference configuration and use 2nd Piola-Kirchhoff stresses and Green-Lagrange strain tensor can be used. Two choices of linearization are available;

With respect to time, *time=0*, which is called “Total Lagrangian” formulation

With respect to time, *time=t*, which is called “Updated Lagrangian” formulation

Equation 2-28 (b) can be linearized either with Total Lagrangian (TL) formulation or Updated Lagrangian (UL) formulation.

2.3.1.2.1 Total Lagrangian formulation: In Total Lagrangian view of point, at each step the initial location of the object is considered as the reference point at each increment of solution. The final linearization of Equation 2-28 (b) for Total Lagrangian formulation is shown by Equation 2-29.

$$\underbrace{\int_{{}_0V} {}_0C_{ijrs}\ {}_0e_{rs}\delta\ {}_0e_{ij}\ {}^0dV + \int_{{}_0V} {}^t_0S_{ij}\delta\ {}_0\eta_{ij}\ {}^0dV}_{\delta\underline{u}^T\,{}^t_0\underline{K}\Delta\underline{u}} = \underbrace{{}^{t+\Delta t}R - \int_{{}_0V} {}^t_0S_{ij}\delta\ {}_0e_{ij}\ {}^0dV}_{\delta\underline{u}^T({}^{t+\Delta t}\underline{R} - {}^t\underline{F})} \qquad 2\text{-}29$$

Where;

${}_0C_{ijrs}$ is the fourth order material tensor

${}_0e_{ij} = {}^t_0u_{i,j} + {}^t_0u_{j,i} = \text{linear part of } {}^t_0\epsilon_{ij}$

${}_0\eta_{ij} = {}^t_0u_{k,i}\,{}^t_0u_{k,i} = \text{nonlinear part of } {}^t_0\epsilon_{ij}$

The presented flow chart in Figure 2-16 summarizes the Total Lagrangian formulation for solving the Equation 2-29.

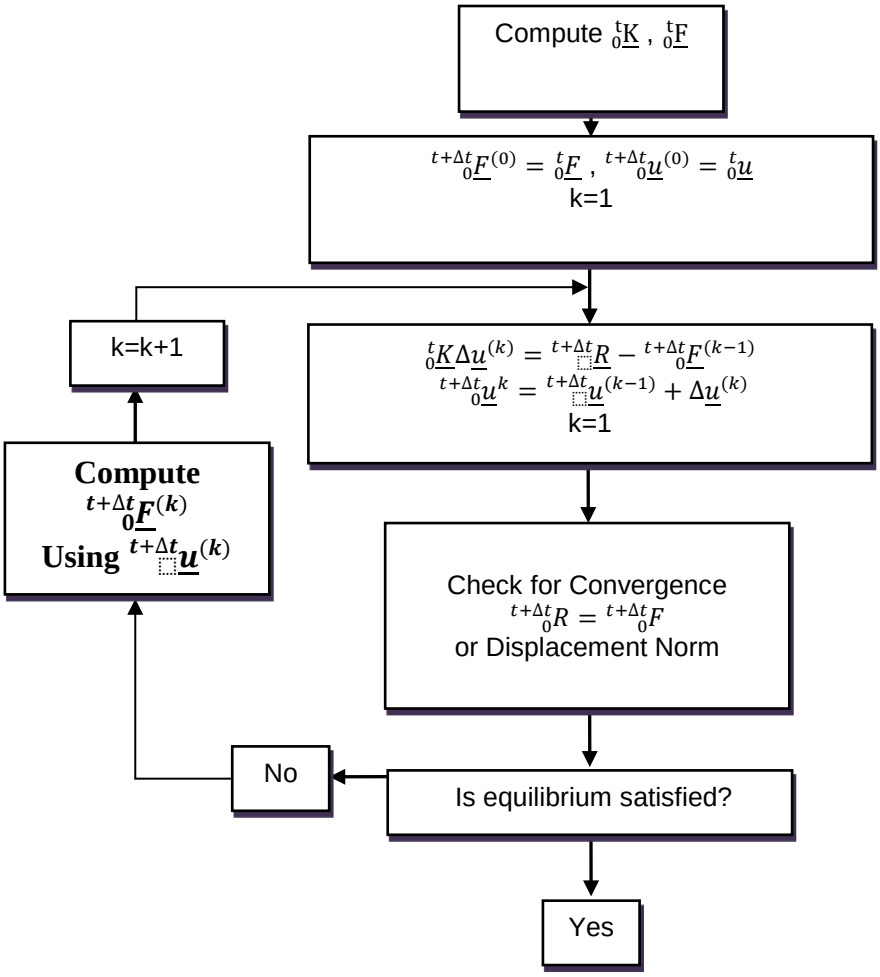

Figure 2-16 Total Lagrangian flow chart

2.3.1.2.2 Updated Lagrangian formulation: In Updated Lagrangian view of point, at each step the initial location of the object is considered as the time= t at each increment of solution. The final linearization of Equation 2-28 (b) for Updated Lagrangian formulation is presented by Equation 2-30.

$$\int_{{}^{t}V} {}_{t}C_{ijrs}\ {}_{t}e_{rs}\delta\ {}_{t}e_{ij}\ {}^{t}dV + \int_{{}^{t}V} {}^{t}\tau_{ij}\delta\ {}_{t}\eta_{ij}\ {}^{t}dV = {}^{t+\Delta t}R - \int_{{}^{t}V} {}^{t}\tau_{ij}\delta\ {}_{t}e_{ij}\ {}^{t}dV \qquad 2\text{-}30$$

The illustrated flow chart in Figure 2-17 summarizes the Updated Lagrangian formulation for solving Equation 2-30.

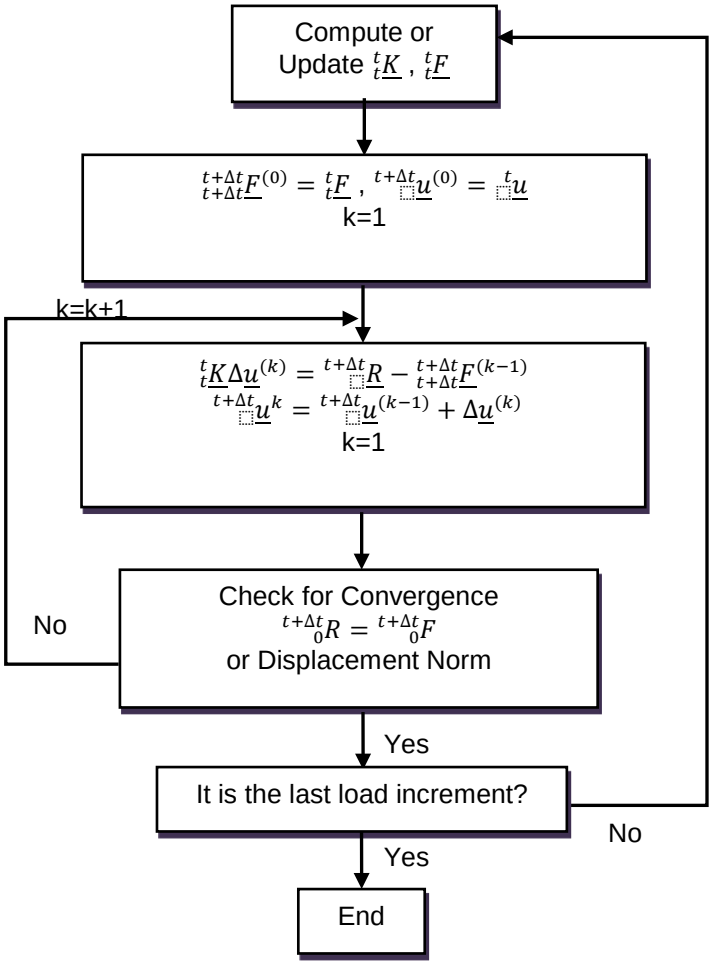

Figure 2-17 Updated Lagrangian flow chart

2.3.1.2.3 Newton Raphson and modified Newton Raphson iterations: To linearize any nonlinear problem, different numerical approaches and methods could be adopted. Newton Raphson and modified Newton Raphson iterations are two available solutions.

Newton Raphson method is updating the stiffness matrix after each increment as shown in Figure 2-18 while in modified Newton Raphson the stiffness is kept the same in all increment as shown in Figure 2-19.

Equation 2-31 presents the Total Lagrangian equation for modified Newton Raphson iteration.

$$\int_{{}_0V} {}_0C_{ijrs}\Delta e_{rs}^{(k)}\delta\ {}_0e_{ij}\ {}^0dV + \int_{{}_0V} {}_0^tS_{ij}\delta\eta_{ij}^{(k)}\ {}^0dV$$

$$= {}^{t+\Delta t}R - \int_{{}_0V} {}^{t+\Delta t}S^{(k-1)}\delta\,{}_0^{t+\Delta t}\epsilon_{ij}{}^{(k-1)}\ {}^0dV \qquad \text{2-31}$$

where:

$${}^{t+\Delta t}u_i^{(k)} = {}^{t+\Delta t}u_i^{(k-1)} + \Delta u_i^{(k)}$$

$${}^{t+\Delta t}u_i^{(0)} = {}^tu_i$$

$${}^{t+\Delta t}S_{ij}^{(0)} = {}_0^tS_{ij}$$

$${}^{t+\Delta t}\epsilon_{ij}^{(0)} = {}_0^t\epsilon_{ij}$$

Equation 2-32 is applied for the Updated Lagrangian equation for modified Newton Raphson iteration.

$$\int_{{}_tV} {}_tC_{ijrs}\Delta\ {}_te_{rs}^{(k)}\delta\ {}_te_{ij}\ {}^tdV + \int_{{}_tV} {}^t\tau_{ij}\delta\eta_{ij}^{(k)}\ {}^tdV$$

$$= {}^{t+\Delta t}R - \int_{{}^{t+\Delta t}V^{(k-1)}} {}^{t+\Delta t}\tau^{(k-1)}\delta_{t+\Delta t}e_{ij}{}^{(k-1)\,t+\Delta t}dV \qquad \text{2-32}$$

where:

$${}^{t+\Delta t}u_i^{(k)} = {}^{t+\Delta t}u_i^{(k-1)} + \Delta u_i^{(k)}$$

$${}^{t+\Delta t}u_i^{(0)} = {}^tu_i$$

$${}^{t+\Delta t}\tau_{ij}^{(0)} = {}^t\tau_{ij}$$

$${}^{t+\Delta t}e_{ij}^{(0)} = {}_te_{ij}$$

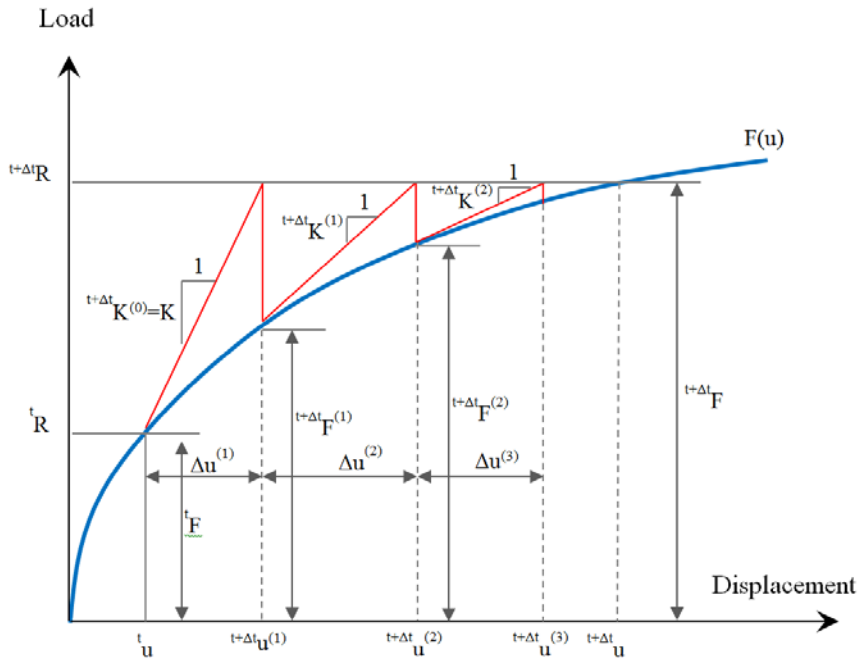

Figure 2-18 Newton Raphson iteration

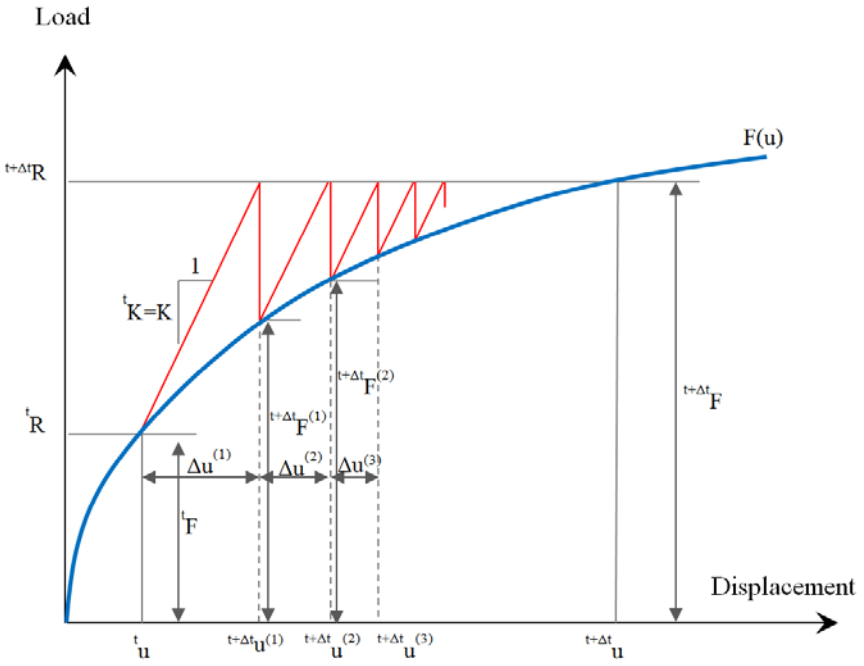

Figure 2-19 Modified Newton Raphson iteration

2.3.1.3 Contact Nonlinearity

For defining contacts, two algorithms are available; node-to-surface, and surface-to-surface. For both algorithms, two surfaces should be defined including slave and master surface. Generally, if a smaller surface contacts a larger surface, it is best to choose the smaller surface as the slave surface. If that distinction cannot be made, the master surface should be chosen as the surface of the stiffer body or as the surface with the coarser mesh if the two surfaces are on structures with comparable stiffnesses. The stiffness of the structure and not just the material should be considered when choosing the master and slave surface. For example, a thin sheet of metal may be less stiff than a larger block of rubber even though the steel has a larger modulus than the rubber material. If the stiffness and mesh density are the same on both surfaces, the preferred choice is not always obvious.

The choice of master and slave roles typically has much less effect on the results with a surface-to-surface contact formulation than with a node-to-surface contact formulation. However, the assignment of master and slave would have a significant effect on performance with surface-to-surface contact if the two surfaces have dissimilar mesh refinement; the solution can become quite expensive if the slave surface is much coarser than the master surface.

Also for each algorithm, the tracking approach should be selected. There are two different tracking approaches available. The first one is finite sliding which is the most general and allows separation and sliding of finite amplitude and arbitrary rotation of the surfaces.

The second approach is small sliding, which assumes that although two bodies may undergo large motions, there will be relatively little sliding of one surface along the other one.

2.3.1.3.1 Node-to-surface: For the node-to-surface algorithm, each contact involves a single node on slave surface and a group of nearby nodes on master surface from which values are interpolated to the projection point. Figure 2-20 illustrates the schematic of node-to-surface contact algorithm.

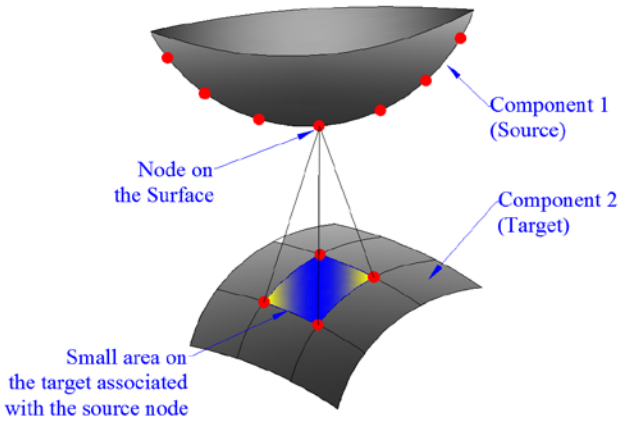

Figure 2-20 Schematic of node-to-surface contact algorithm

2.3.1.3.2 Surface-to-surface: The surface-to-surface formulation enforces contact conditions in an average sense over regions nearby slave nodes rather than only at individual slave nodes. Figure 2-21 shows the schematic of surface-to-surface contact algorithm.

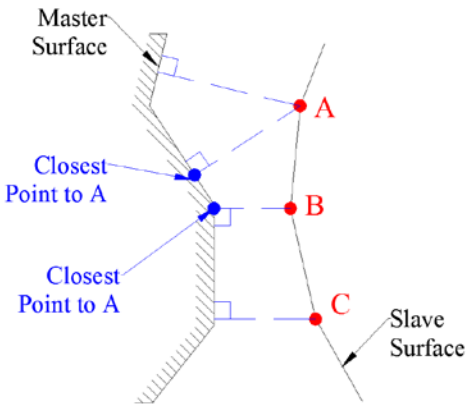

Figure 2-21 Schematic of surface-to-surface contact algorithm

2.3.2 Soil Model

There are different soil constitutive models available for different purposes and the more sophisticated the soil models, more information and parameters are needed for creating the model. Thus picking a proper soil constitutive model will be beneficial for the study. Some of the available constitutive models for soil are Hooke's law (linear), the Mohr-Coulomb, the Drucker-Prager, the Duncan-Chang (Hyperbolic model), Cam-Clay (Modified Cam-Clay), Plaxis Soft Soil, and Plaxis Hardening Soil model. (Brinkgreve, 2005).

The Mohr-Coulomb model was used in this study which is an elastic- perfectly plastic model. Five (5) input parameters were needed for this model including; soil Young's elastic modulus (E), Poisson's ratio (v), the angle of friction (φ), cohesion (c), and the dilatancy angle (ψ) which come from the non-associated flow rule discussed in this chapter. The change in volume of the soil in shear is not reversible in shear loading and due to this reason the non-associate flow rule parameter, dilatancy angle, is introduced to Mohr-Coulomb soil model. (Lade, 2005). This model assumes that the failure of the material is a function of maximum shear stress and it depends on the applied normal stress. The Mohr's circles for different states of stresses should be drawn as showed in Figure 2-22. The best tangential line to all of the Mohr's circles is the failure line (Figure 2-22). Moreover; Equation 2-33 should be used as the equation of failure line.

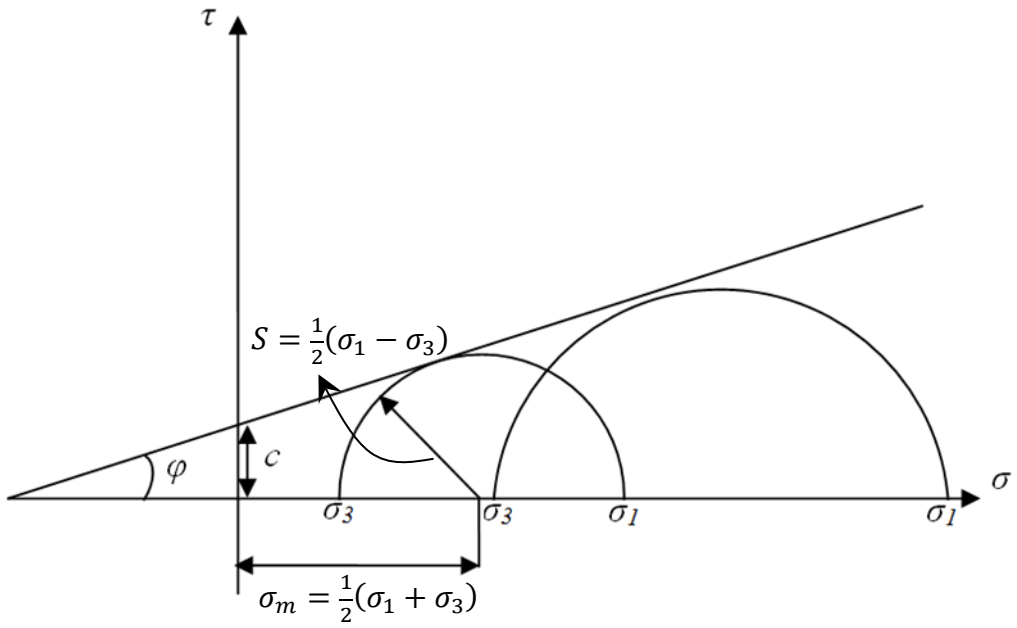

Figure 2-22 Mohr's circles and failure line for Mohr-Coulomb model

$$\tau = c - \sigma \tan \varphi \qquad 2\text{-}33$$

Where:

σ = normal stress which is negative in compression

τ = shear stress

From Figure 2-22, Equation 2-34 and 2-35 can be derived.

$$\tau = s \cos \varphi \qquad 2\text{-}34$$

$$\sigma = \sigma_m + s \sin \varphi \qquad 2\text{-}35$$

Thus, Equation 2-33 can be re-written as the following equation by substituting τ and σ from Equations 2-34 and 2-35.

$$s + \sigma_m \sin \varphi - c \cos \varphi = 0 \qquad 2\text{-}33$$

Where

$\sigma_m = \frac{1}{2}(\sigma_1 + \sigma_3)$ (Average of maximum stress and minimum stress)

$s = \frac{1}{2}(\sigma_1 - \sigma_3)$ (Average of the difference between maximum and minimum stresses)

The failure surface of this model is often written in Haigh–Westergaad coordinates. Thus, Equation 2-33 can be expressed in terms of invariants, *p*, *q*, and *r*. The following is the derivation of failure surface in terms of stress invariants.

Expanding Equation 2-33, we will have Equation 2-36.

$$\frac{1}{2}(\sigma_1 - \sigma_3) + \frac{1}{2}(\sigma_1 + \sigma_3)\sin\varphi - c\cos\varphi = 0$$

$$\sigma_1 \frac{(1+\sin\varphi)}{2c\cos\varphi} - \sigma_3 \frac{(1+\sin\varphi)}{2c\cos\varphi} = 1 \qquad \text{2-36}$$

The stress invariants are related to the principle stresses by using Equation 2-37 (a) and (b).

$$\sigma_1 = \frac{1}{\sqrt{3}}\xi + \sqrt{\frac{2}{3}}\rho\cos\theta \qquad \text{2-37 (a)}$$

$$\sigma_3 = \frac{1}{\sqrt{3}}\xi + \sqrt{\frac{2}{3}}\rho\cos\left(\theta + \frac{2\pi}{3}\right) \qquad \text{2-37 (b)}$$

By substituting Equations 2-37 (a) and (b) in Equation 2-36, Equation 2-38 will be obtained.

$$\left(\frac{1}{\sqrt{3}}\xi + \sqrt{\frac{2}{3}}\rho\cos\theta\right)\frac{(1+\sin\varphi)}{2c\cos\varphi} - \left(\frac{1}{\sqrt{3}}\xi + \sqrt{\frac{2}{3}}\rho\cos\left(\theta + \frac{2\pi}{3}\right)\right)\frac{(1+\sin\varphi)}{2c\cos\varphi} = 1$$

$$-\sqrt{2}\xi\sin\varphi + \rho\left(\cos\theta - \cos\left[\theta + \frac{2\pi}{3}\right]\right) - \rho\sin\varphi\left(\cos\theta + \cos\left[\theta + \frac{2\pi}{3}\right]\right) = \sqrt{6}c\cos\varphi \qquad \text{2-38}$$

Where:

$$\xi = \sqrt{3}p$$

$$\rho = \sqrt{\frac{2}{3}}q$$

$p = -\frac{1}{3}tr(\sigma)$ in which $tr(\sigma)$ is the trace of the stress matrix.

q = Mises equivalent stress

r = 3rd invariant of deviatoric stress

$\theta = \frac{1}{3}\arccos\left(\left[\frac{r}{q}\right]^3\right)$ which is the deviatoric polar angle

If we plug ξ and ρ in Equation 2-38, another form of failure surface will be derived which is presented by Equation 2-39.

$$\left(\frac{1}{\sqrt{3}\cos\varphi}\sin\left[\theta+\frac{\pi}{3}\right]-\frac{1}{3}\tan\varphi\cos\left[\theta+\frac{\pi}{3}\right]\right)q - p\tan\varphi = c \qquad 2\text{-}39$$

The coefficient of q, is a function of φ and θ and it can be defined as Equation 2-40. Thus, φ is the slope of Mohr-Coulomb model when the stress plane is p-$R_{mc}(\theta,\varphi)q$, as shown in Figure 2-233.

$$R_{mc}(\theta,\varphi) = \frac{1}{\sqrt{3}\cos\varphi}\sin\left[\theta+\frac{\pi}{3}\right]-\frac{1}{3}\tan\varphi\cos\left[\theta+\frac{\pi}{3}\right] \qquad 2\text{-}40$$

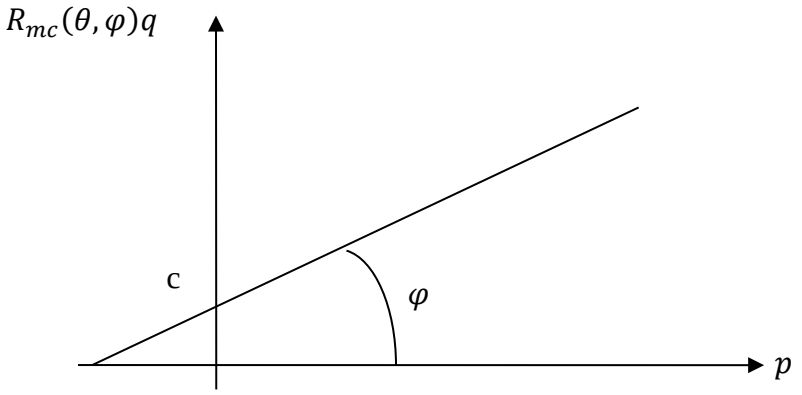

Figure 2-23 Mohr-Coulomb failure surface in is p-$R_{mc}(\theta,\varphi)q$ plane

The shape of the failure surface in the deviatoric plane is controlled by the friction angle (φ). This angle will vary in the range of 0^o to 90^o. Figure 2-24 illustrates the failure

surface for Mohr-Coulomb model in deviatoric plane and compares Mohr-Coulomb model with Tresca and Rankine model at φ = 0^o and φ = 90^o, respectively.

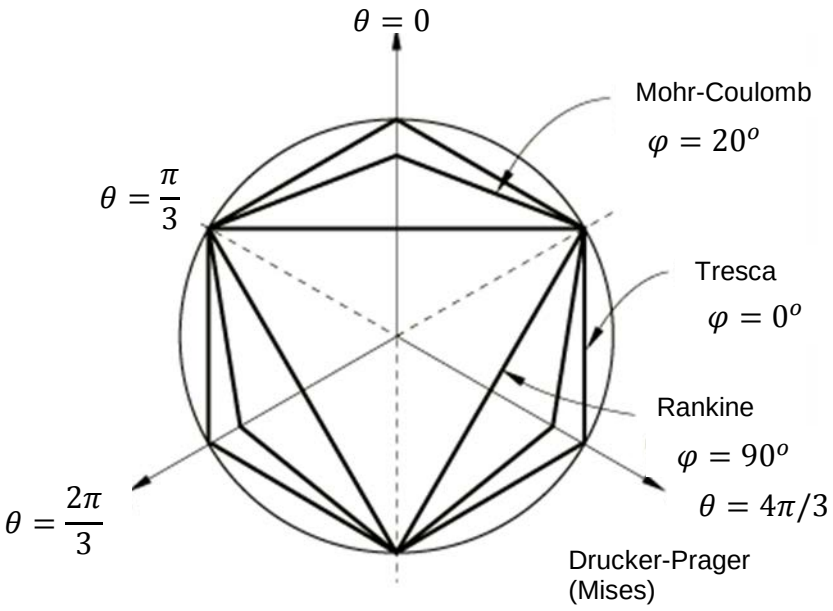

Figure 2-24 Mohr-Coulomb failure surface in deviatoric plane

2.3.3 Element Types

Solid elements were picked to be the infinitesimal blocks in different components of the model. Obviously the elements are 3-D elements. Also the reduced integration (lower-order integration of the stiffness matrix) was used to alleviate the intrinsic model stiffness due to finite element approximation. A direct integration static method using full newton solution technique was selected for the analysis. Eight (8)-nodded linear brick element and six (6)-nodded wedge element with reduced integration and hourglass control was used for both soil and steel materials. Moreover, hourglass control was also used to improve mesh distortion due to large deformation and to enhance the nonlinear response. Figure 2-25 illustrates the elements which were used in this study.

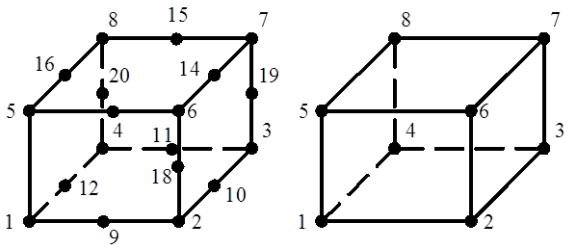

Figure 2-25 Eight (8) -nodded and 20-nodded brick elements

Furthermore, continuum or soil elements include triangles, tetrahedral, and wedge elements. Figure 2-26 illustrates different types of continuum elements.

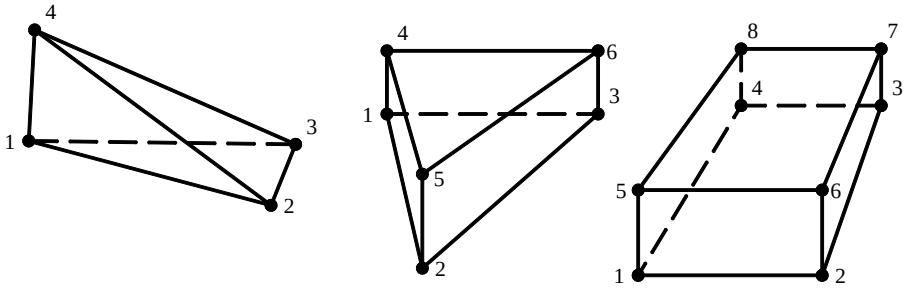

Figure 2-26 Different continuum elements; triangle, wedge, and tetrahedral

2.4 Application of Finite Element Analysis in Pipe Design

Development of a finite element algorithm and technique to model and predict the large diameter pipe behavior during stage construction is an essential tool to determine the changes in the pipe geometry and stresses due to the compaction forces during installation prior to application of the surcharge load. As explained earlier in this chapter, deflection control and stress limit has always been a significant concern in designing buried flexible pipes. Also as mentioned, American Water Works Association (AWWA) has limited pipe deflections between 2 to 5 percent of the pipe diameter for different lining systems. AWWA manual M11 (2004) does not recommend designing steel pipe in the elastic-plastic range when the deflections are not controlled. The accepted

design stress for the water transmission steel pipes is 50% of the minimum yield strength. The stiffness of a flexible pipe structure highly depends on the soil stiffness provided by the pipe's bedding and backfill materials to form a soil-structure interaction composite system. During staged construction installation of a buried pipe, as different layers of soil are applied, the shape, stiffness, boundary conditions, and loadings exerted on the pipe will change. As a consequence, the deflection of a pipe during its service life is not only a function of service loads, such as surcharge and live load, but it is also sensitive to the sequences of the construction, material, and the thickness of each layer.

Although several studies were conducted on the analysis of buried pipes using soil-pipe interaction theories (Duncan, 1976; Duncan, 1979; Katona, 1976; Katona, 1982; Leonards et al., 1982; Sharp et al. 1984; Sharp et al., 1985; Zarghamee 1986; Spitzley, 1987; Abdel-motaleb, 1995; McGrath, 1998; J. Zhang, 2002; Suleiman, 2003; Evans, 2004; Y. Tian, 2008; A.Srivastave, 2013), limited investigations have explored the behavior of flexible pipes during staged construction by using 3-D nonlinear FEM.

Zhang et al. (2002) developed a kinematic hardening model for pipeline-soil interaction under various loading conditions and they conducted experimental tests on the beam centrifuge by using calcareous sand soil. The developed hardening model required 13 parameters.

Tian et al. (2008) modified the model which was developed by Zhang (2002) and they introduced three plasticity models which could be used to simulate pipe–soil interaction numerically. The beam element was used for structural members in the FEM model. The developed model was used to model the pipe in ocean environments on sand material as the bedding. Further study should be conducted to show the efficiency of the developed model by Tian (2008) on buried steel pipes in trench condition in which there are more loads acting on the buried pipe.

Srivastava (2013) conducted several laboratory tests on a buried PVC pipe to investigate the response of soil-pipe system in term of load-settlement. Then the conducted tests were compared with a 2-D finite element model. However, the conducted tests were performed on small diameter PVC pipes (110 mm) and the 2-D FEM model was used to evaluate the conducted tests.

Zarghamee (1986) developed a 2-D finite element analysis program, FLEXPIPE, and showed in steel pipes significant flexural stresses are developed at the invert of the pipe after installation. The deflection history of the pipe, during installation was not reported in this study.

Suleiman et al. (2003) investigated the effects of large deflection behavior on buried plastic pipes. This study compared the small deflection analysis theory results by using Culvert ANalysis and DEsign (CANDE) software with the large deflection analysis theory using ANSYS. The authors reported that for the deflections above 4 percent the difference between the small and the large deformation theory is 10 percent.

McGrath (1998) conducted a study on the pipe-soil interaction during backfilling. Fourteen (14) different tests with two (2) pipe diameters of 900 mm (36 in.) and 1500 mm (60 in.) were designed and backfilled with different materials which compacted in different compaction level. Several soil box tests and field tests on steel, concrete, and plastic pipes were conducted to compare the results for different backfilling material, trench conditions, trench widths, and bedding material. This study used CANDE to simulate the stages of the construction. Three (3) different approaches were adopted; applying the soil weight and vertical loads (no compaction), applying and adopting CANDE's "squeeze method", and finally applying horizontal point loads on pipe nodes. As explained by McGrath, modeling the soil-pipe interaction without considering the effect of compaction was not adequate and the FEM model which doesn't consider the effect of compaction is

incomplete. Thus McGrath adopted the squeeze method which was introduced by CANDE (2007). Figure 2-27 illustrates the squeeze layer method. As shown in Figure 2-27, in squeeze layer method, upon applying each soil layer, a distributed vertical pressure will apply on top of the soil layer (Step 2, distributed load 1). Then in the next stage of the construction another distributed pressure will apply on top of the next layer (Step 3, distributed load 2). However, at the same time another distributed load (Step 3, distributed load 1) with the same magnitude as the first compaction load (Step 2, distributed 1) but in opposite direction will apply on the bottom surface of that soil layer to remove the previous pressure applied on the soil layer. This method was called squeeze layer method and introduced by Katona et al. (1976) and adopted in CANDE. The soil layer will expand horizontally because of Poisson's ration effect.

Moreover, the deflection effect of compaction load is about 2% of pipe diameter for some steel cases. (CANDE, 2007)

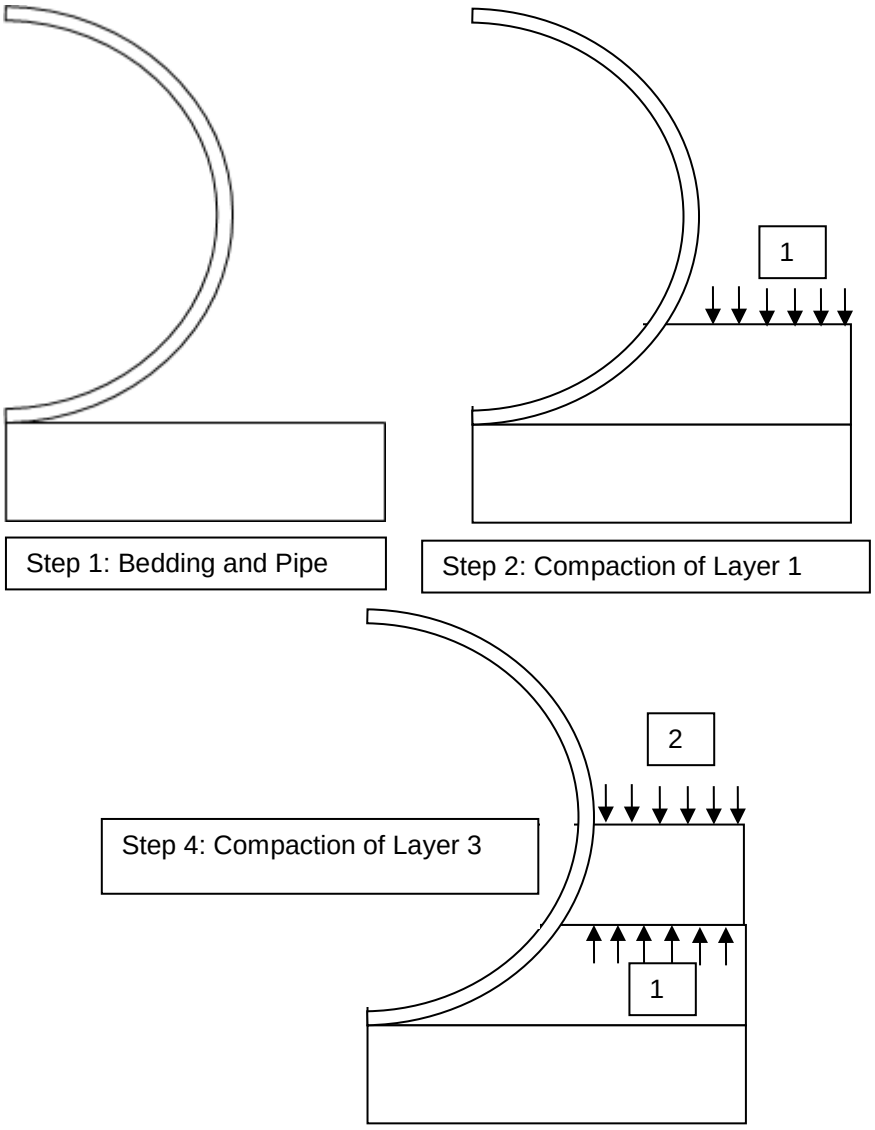

Figure 2-27 Squeeze layer method

As McGrath (1999) explained, the squeeze layer method was insufficient and was not modeling the soil-pipe interaction properly since the pipe behaves elastic in the most of the cases, and the effect of compaction will fade away by applying the same load on the same surface but in opposite direction. As he explained, using the first and second methods was unsuccessful. Thus he decided to apply a point load on the pipe's nodes. A

point load was applied on pipe in FEM program, CANDE, to model the horizontal effect of compaction on pipe. This approach has limitations and does not take into account the distributive effects of the compaction force on the pipe. This method also did not consider the interaction of soil-pipe.

McGrath (1999) suggested certain values for horizontal stresses which induced by compaction. As explained in that study, this value depends on several variables including pipe material, pipe size, backfilling material, type of compactor, compactor frequency, and trench wall stiffness. Also this study explained that this value will be higher for the case of 3-D modeling. Figure 2-28 illustrates the technique to apply point load on the pipe nodes versus the distributed technique which is adopted in the current study.

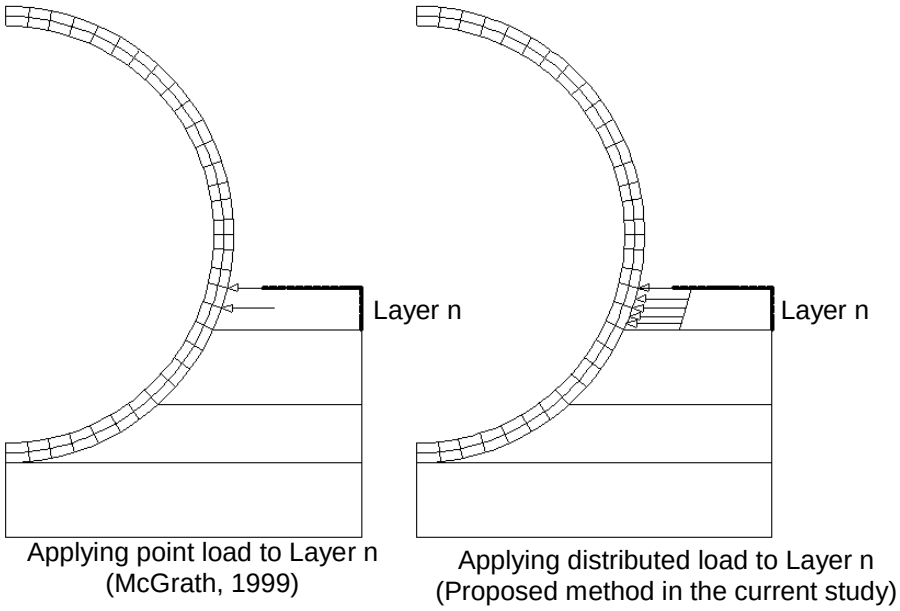

Figure 2-28 Application of point load as horizontal load induced by compaction versus distributed pressure exerted on pipe due to soil compaction

The lateral effect of soil compaction force was modeled in detail in the current study. Moreover, the contacts between different parts of the model were identified and modeled in detail. Also an algorithm was developed in the finite element to accommodate the changes in geometry of the model in different stages of the construction. Since the developed FEM model was verified with different experimental tests and successfully predicted the tests' results, the developed design equations are unique tool to predict and estimate pipe behavior in different conditions.

Chapter 3

Development of Three-Dimensional Finite Element Model

The initial 3-D finite element model was developed by using the soil box tests conducted (Najafi, 2012). Four (4) soil box tests were designed and installed in the Center for Underground Infrastructure Research and Education (CUIRE) by Najafi (2012). The results and data of the soil box tests were obtained in order to provide initial simulation for the development of the finite element model. This chapter presents the algorithms, techniques, and different modules which were used in the model development. Moreover, the information about the soil box tests are summarized in this chapter. Finally, the results of the finite element analysis were compared with the results of the experimental tests. Figure 3-1 illustrates the frame work for the conducted study for soil box tests.

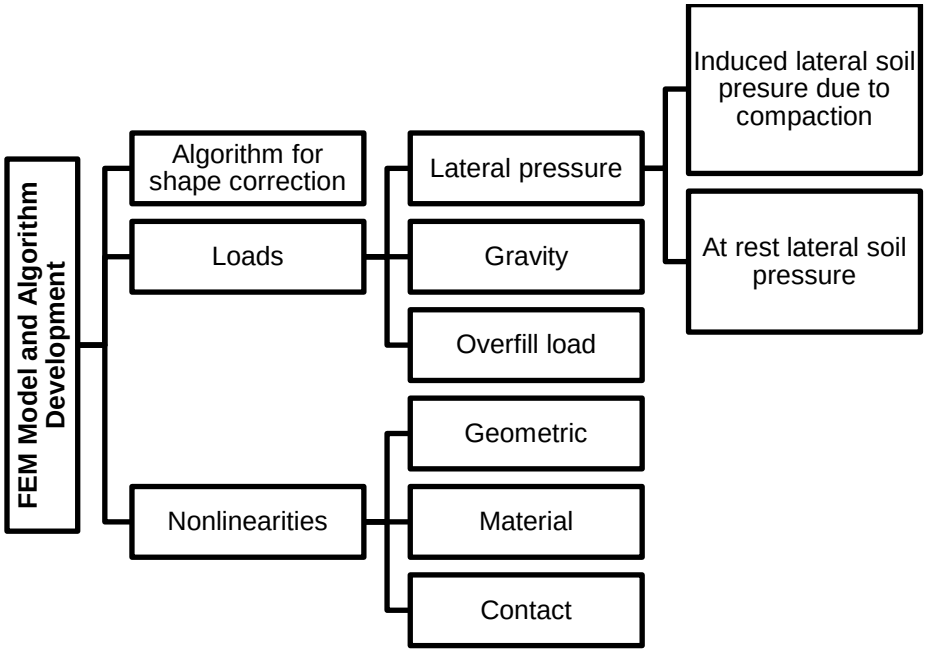

Figure 3-1 Framework of the conducted research works for the soil box test

3.1 Modeling and Analysis Algorithms

A 3-D finite element analysis algorithm was developed to predict the soil-steel pipe behavior during staged construction. The details of different modulus of modeling are described comprehensively in this section.

The effects of trench wall were taken into account by considering proper boundary conditions which mimics the same behavior. Different layers of the backfill were modeled separately to account for different soil properties and enable the implementation of contact algorithm between each soil layer. The layers' geometries were defined according to the installation configuration. The surcharge was modeled by using an equivalent surface distributed pressure and applied as a surcharge on top of the last soil layer. Taking advantage of the symmetric nature of the trench configuration, one half of the pipe and backfill geometry was modeled. The degrees of freedom perpendicular to the plane of symmetry were restrained to take advantage of plane of symmetry. Typical FEM models with different length are shown in Figure 3-2.

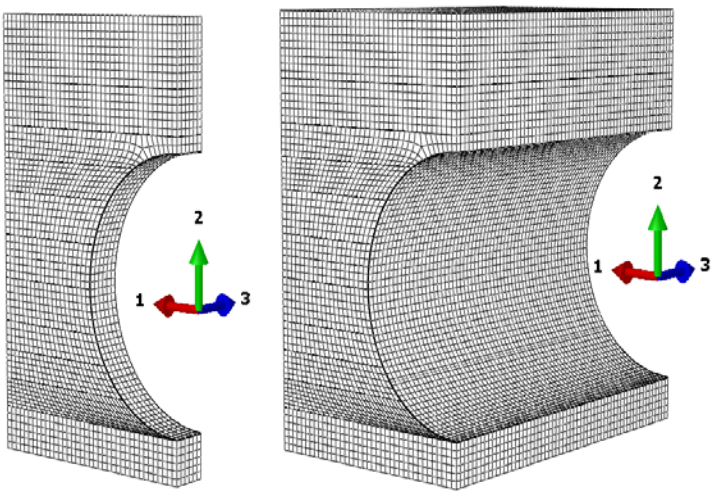

Figure 3-2 Typical FEM models

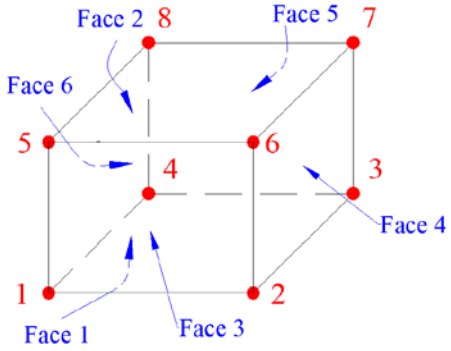

Figure 3-3 Schematic of eight-nodded linear brick element

A direct integration static method using full newton solution technique was selected for the analysis. Eight (8)-nodded linear brick element and six (6)-nodded wedge element with reduced integration and hourglass control was used for both soil and steel materials. Figure 3-3 shows typical elements which were used in the analysis. Moreover, reduced integration (lower-order integration of the stiffness matrix) was used to alleviate the intrinsic model stiffness due to finite element approximation. Hourglass control was also used to improve mesh distortion due to large deformation and to enhance the nonlinear response. The large deformation theory, as shown in Figure 3-4, is applied to either small strains with large rotation or large strain with large rotation.

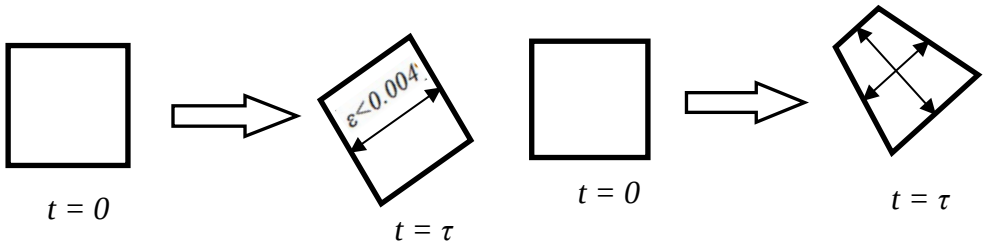

Figure 3-4 Large deformation theory; (a) small strain with large rotation, (b) large strain with large rotation

3.1.1 Staged Construction Modeling

A staged construction was modeled identical to the installation procedure. The first analysis step was the placement of the pipe on the bedding in which the pipe weight and the bedding weight were the only loads acting on the pipe model. Each of the soil layers were added to the system in separate analysis steps. In each step, gravity and compaction loads due to the placing of a new layer were applied to the model. The equivalent distributed surcharge due to the soil cover was applied to the system in the final step.

All the parts were introduced and assembled in the initial stage of the modeling when the parts were in their un-deformed shape. Thus, when the n^{th} layer was activated, its geometry was corrected to fit and accommodate the pipe geometrical change due to the compactive force of Layers 1 through n-1. This assumption was made in order to simplify the definition of layers' geometry. On the other hand, in each step of the construction, the geometry of new layer should be redefined based on the deformed shape of the pipe and the previous soil layer due to the gravity and compaction loads. To overcome this challenge, the deactivation and activation algorithms were employed to capture the geometry of each layer in different stages. The stiffness matrices of the deactivated parts, i.e. Layer $n+1^{th}$ and the layers after that when Layers 1 through n were active, were not assembled in the total stiffness matrix of the system, so their effects were eliminated from the model.

These algorithms were introduced to the FEM model such that each deactivated part was able to map its new geometry after activation based on the deformation of the pipe caused by the compaction of the previous layers. To resolve this problem, in the activation and deactivation algorithms, the deactivated soil elements shared certain nodes with the activated soil and pipe elements. It should be noted that the activated

elements could be either as of soil or pipe. The activated soil elements considered for the Layer n were the compacted soil elements of the Layer 1 through n-1, while the elements of the soil elements adjacent to the pipe were always activated. (Figure 3-6)

Figure 3-5 illustrates bedding and two layers in contact with the pipe in the step that only pipe and bedding were activated in the model. As shown, the elements of the soil layers adjacent to the pipe were always kept activated to capture the updated geometry of the soil layers. The shared nodes as shown in the figure were located inside the soil layers, and they were not on the contact surface of the pipe and the soil layer.

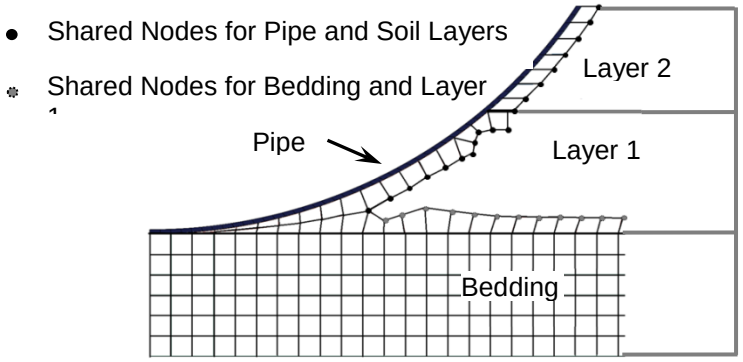

Figure 3-5 Share nodes between active and deactivated parts

Additionally, Layer n has 3 interface neighbors: pipe, Layer n-1, and Layer n+1. The shared nodes allow each part to capture and track the modified geometry according to the deformed shape of its neighboring part (Figure 3-6). For the aforementioned example, the shared nodes with the pipe will deform and track the modified geometry. Also, the shared nodes with Layer n-1 capture the modified geometry for the bottom of Layer n. The shared nodes with Layer n+1 causes Layer n+1 to see its modified geometry. Figure 3-6 illustrates the algorithms for Layer n before and after activation.

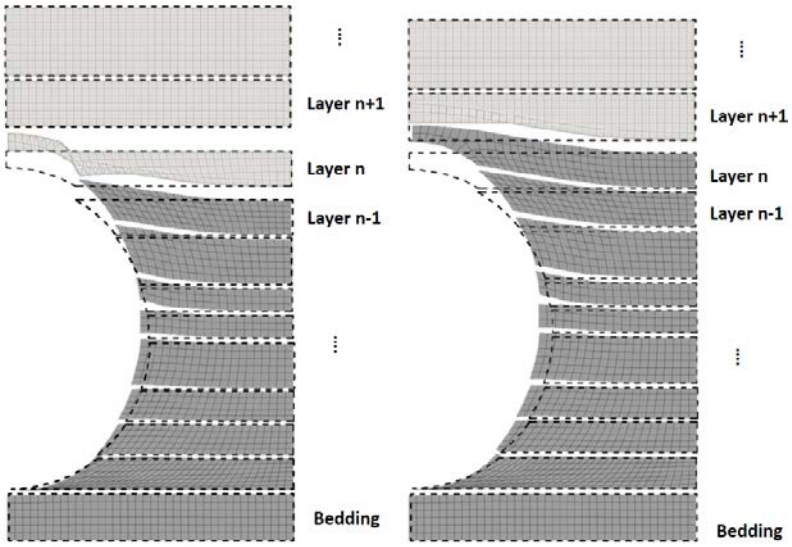

Figure 3-6 Activation and deactivation algorithms on Layer n

Figure 3-7 shows the initial geometry of Layer n, as well as the deformed geometry before and after the activation process. It is important to note that the soil layers were activated in a stress free environment.

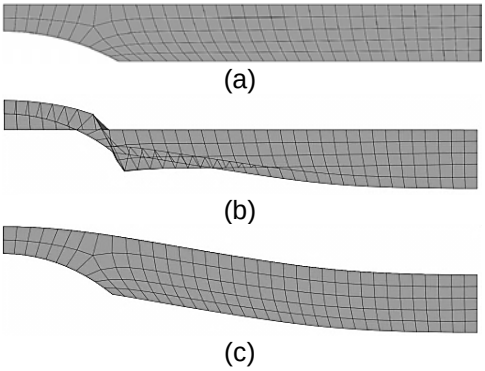

Figure 3-7 Geometry of Layer n in; (a) initial stage, (b) deformed shape before activation, and (c) deformed shape after activation

Shaded areas in Figure 3-8 demonstrate the shared nodes for different layers. The shared elements of Layer n are shaded in black and other parts are shaded in gray.

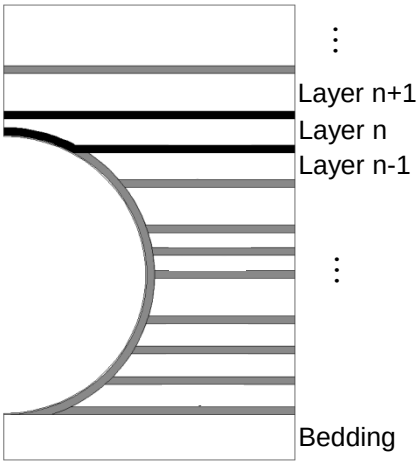

Figure 3-8 Shared nodes (elements) for different layers

3.1.2 Contact Definition

The interfaces between two different parts of the model were simulated using contact algorithm. Two types of contact were defined in this study, the contact between the steel pipe and the soil, and the contact between different soil layers.

Figure 3-9 presents different contact algorithms which were used in the developed model. For a node-to-surface contact, each contact involves a single slave node (Ω_A surface) and a group of nearby master nodes (Ω_B surface) from which values was interpolated to the projection point. The surface-to-surface contact discretization enforces contact conditions in an average sense over regions nearby slave nodes (Ω_A surface), rather than only at individual slave nodes. (Bathe, 1996)

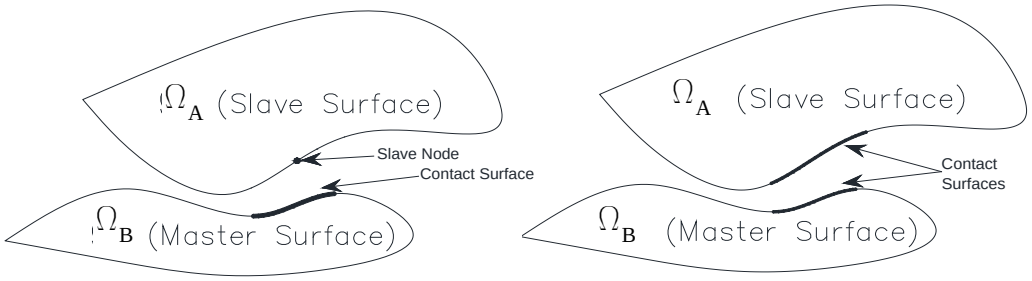

Figure 3-9 Contact discretization

The contact properties were defined in two (2) perpendicular directions of tangential and normal. The tangential behavior was defined by a friction coefficient which was selected according to El-Chazli et al. (2005). This study suggested considering the coefficient between 0.2 and 0.5. Coefficient of friction of 0.3 was selected according to this study. The normal contact was assumed to be a “hard contact.” The hard contact dictates that two contacting parts cannot penetrate into each other.

3.1.3 Boundary Conditions and Applied Loads

The boundary conditions of the FEM model were defined to simulate the real behavior of the trench wall. Figure 3-10 demonstrates the applied boundary conditions, which were replacing the trench wall in the FEM model. The sides of the backfill as shown by the hatched lines were constrained in the x-direction and the bottom of the bedding, shown by dotted line was constrained in all translational directions.

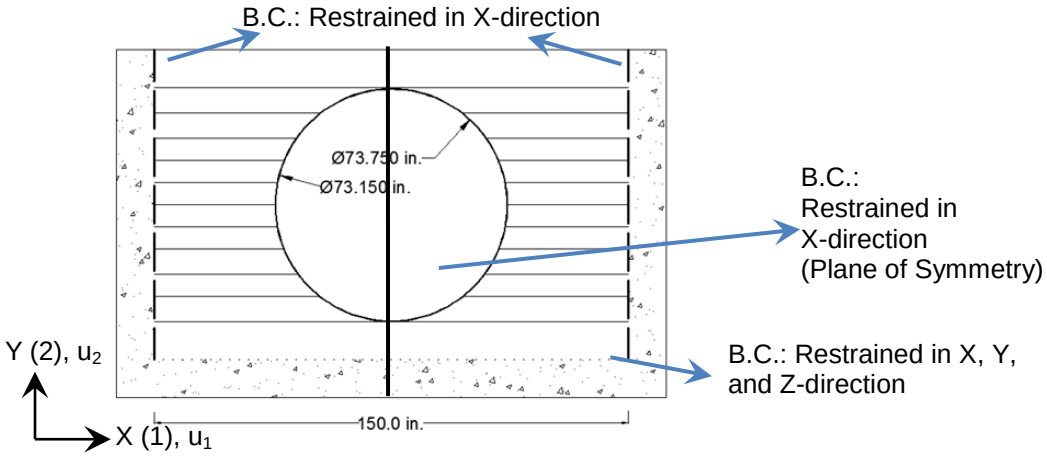

Figure 3-10 Applied boundary condition in the FEM model

The plane of symmetry is shown by a dark line in Figure 3-10. The nodes on the plane of symmetry were constrained in the x-direction, but they were able to freely move along the y and z directions.

There were several loads acting on the soil-pipe interaction including the weight of pipe and the soil layers; the soil compaction load; the soil horizontal load due to compaction and due to the lateral at rest pressure; and the surcharge. The weight of each part was activated upon its introduction to the model by applying the gradually increasing gravitational constant from zero to 9.81 m/s^2 (386.22 in/s^2). For the surcharge, a uniform distributed pressure load was applied on top of the last soil layer.

The induced lateral pressure due to the compaction was studied by several researchers (Pettibone, 1976; Potter, 1985; Sargand, 1998; Shumulevich, 1985). Duncan et al. (1986) proposed models to evaluate the residual and maximum horizontal pressure induced by compaction on the rigid walls and also free to move fields. This study presented certain loading, unloading, and reloading curves, including the related parameters for obtaining the curves. According to Clayton et al. (1992), the horizontal induced load due to the compaction of cohesive soils depends on the plasticity index of the soil. The higher the plasticity index, the higher the stresses are exerted on the soil. In this study, the horizontal stress due to compaction is related to the un-drained shear strength, C_u of the cohesive soils. This study suggested the horizontal stress of 0.8 C_u for higher plasticity indices and 0.2 C_u for lower amount of the plasticity index. Selig (1988) showed that the grain size has effect on the stiffness of compacted backfill soil. This study illustrated that the increase in fine grains increases the effort needed to achieve to a certain stiffness of backfill material. Furthermore, McGrath (1990) presented the required energy to obtain a required E' value in different soil types.

Katona et al. (1979) noted that the compaction load is difficult to address and calculate because of its variability and dependency on several parameters like the compactor frequency, the operator, the layer thickness, and the soil properties. This study suggested a method which is called "squeeze layer." In the "squeeze layer" method

the lateral compaction effects were modeled by applying a vertical pressure. This vertical stress then induces a lateral stress due to the Poisson's effects. Vertical stresses were induced due to the vertical pressure in the soil elements which are not realistic. Therefore, the stresses in soil layers could not be evaluated with this method. The horizontal stress is related to vertical stress by Poisson's ratio. This ratio has a range of 0.3-0.4 for different soil types. Thus, if a higher compaction level needed, a higher vertical pressure should be applied. In reality, the ratio of horizontal to vertical stresses in soil can be higher than 0.5 which is not covered by the Poisson's ratio range. The constant vertical pressure load, i.e. 35 kPa (5 psi) which is proposed by CANDE, is not applicable to all the compaction cases with different soil types. Therefore, this pressure magnitude should be calibrated for different soil types, trench width, installation type, and layer thicknesses. Also as the next soil layer is applied on top of the previous layer, the applied pressure should be removed and since the flexible pipe remains elastic in most of the cases, the effects of the squeeze layer method will dissipate from the model.

On the other hand, the proposed technique in the current study, which is applying uniform thermal loading, eliminates the abovementioned limitations because the horizontal pressure was applied to the soil independent of the vertical pressure. Furthermore, the effect of soil compaction isolated or coupled with the at-rest lateral soil pressure was not well documented in the literature. Considering only the effect of the at-rest lateral soil pressure would be inadequate and not representing the true behavior based on the test results. Obviously, any FEM model that neglects the effect of backfill compaction isolated or coupled with the at-rest lateral soil pressure would not simulate the actual behavior. Thus, current study identified the effect of soil compaction coupled with the at-rest lateral soil pressure. The one possible alternative was to develop the FEM model with the controlled experimental testing which was done in this study in which soil-

pipe interaction load-deformation results were used as an elegant tool to calibrate the frequency and subsequently compaction load exerted on soil in developed FEM model.

Subsequently, the coupled effect of compaction and the at-rest lateral soil pressure was related to the un-drained shear strength, C_u, for different soil materials such as native and treated native soil used in this study. To apply the horizontal load, the stresses due to the at-rest lateral soil pressure and the soil compaction were calculated. Then, the calculated stresses were applied to each soil layer using the equivalent temperature loading.

The calculated fictitious temperature for each soil layer was applied upon activation of that layer. The thermal load was determined for all layers in x-direction and "zero" for the other two (2) directions (y and z).

3.1.4 Material Models

Mohr-Coulomb model and isotropic plasticity model were implemented to the FEM model for the soil and the steel materials, respectively.

Since the loading condition in the pipe installation practice was so rapid and the soil did not have the chance to drain, the un-drained properties of the soil were selected for the model development. Brinkgreve (2005) suggested considering adequate care when the drained condition were assumed for the embedment conditions.

Mohr-Coulomb model is an elastic perfectly plastic model and five parameters were needed for this model. This model is suitable for the analysis of geotechnical structures. The Mohr-Coulomb soil plasticity model is commonly used in designing soil structures. The Drucker-Prager model (Drucker and Prager, 1952) is a modified Mohr-Coulomb model. The failure surface in Mohr-Coulomb model is a hexagonal shape as shown in Figure 3-11. This surface is a cone in Drucker-Prager model as shown in Figure 3-11.

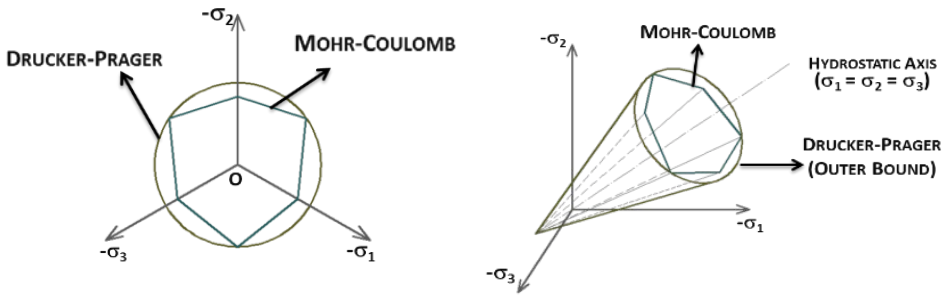

Figure 3-11 Failure surface for Mohr-Coulomb and Drucker-Prager soil models

3.2 Experimental Soil Box Test

The test procedure was a staged construction. At the first stage the steel pipe was placed on the compacted bedding. Then the soil layers, in different lift thicknesses, were applied until the embedment reached at least 30.5 cm (12 in.) above the pipe crown.

Four (4) soil box tests were conducted by Najafi (2012) using similar 1.83 m (72 in.) diameter, 6.1 m (20 ft) long steel pipes. A photograph of the conducted soil box tests is shown in Figure 3-12. Figure 3-13 illustrates the definition and terminologies in soil box test. Table 3-1 presents different parts in the soil box tests and their associated material. Material properties for steel pipe are presented in **Error! Reference source not found.**. The embedment profile section, test setup plan view, backfill and bedding material properties for Tests 1 through 4 are shown in **Error! Reference source not found.** through **Error! Reference source not found.**, respectively.

In Test 1, pea gravel (**Error! Reference source not found.**) was used for the bedding material and the backfill material was native soil (Table 3-2). The layers were applied and compacted in eleven (11) layers with variable heights (**Error! Reference source not found.** and Table 3-3). The pipe was instrumented in different sections as shown in Figure 3-18.

Figure 3-12 Photograph of conducted test by Najafi (2012)

Table 3-1 Material assigned to each part

Part	Material
Soil Box (Load-Cell)	Concrete
Bedding	Pea Gravel/Treated Native Soil
Backfill Soil	Native soil/ Treated Native Soil/Crushed Limestone
Surcharge	Pea Gravel
Pipe	Steel

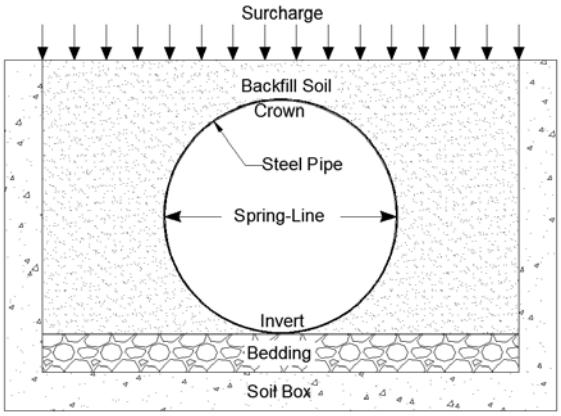

Figure 3-13 Definition of terms in the soil box test set-up

The pipe in Test 1 was instrumented with 36 strain gauges in three (3) sections as shown in Figure 3-18. Each section was instrumented with twelve (12) strain gauges; eight (8) of them were inside in circumference of the pipe, one (1) in interior wall in crown and in longitudinal direction, and three (3) of them were attached to the springlines and

crown of the pipe on exterior side of the pipe. The pipe was also enhanced with ten (10) load pressure cells to obtain the induced horizontal and vertical pressures and also vertical pressure on bedding and on pipe crown. Two (2) earth pressure cells were attached to the concrete box close to either ends of the pipe to study the effect of installation parallel to the direction of the pipe. Six (6) convergence meters were used to obtain the vertical and horizontal deflection for every test.

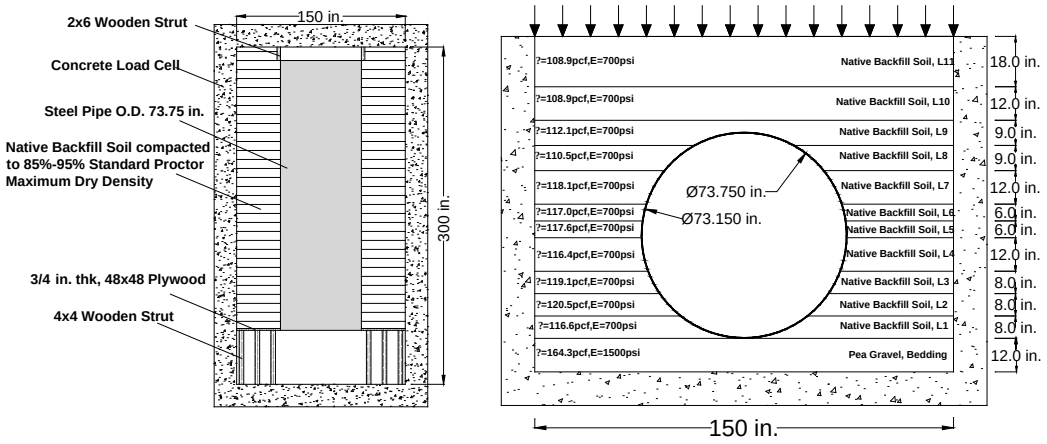

Figure 3-14 Details of Soil Box Test 1

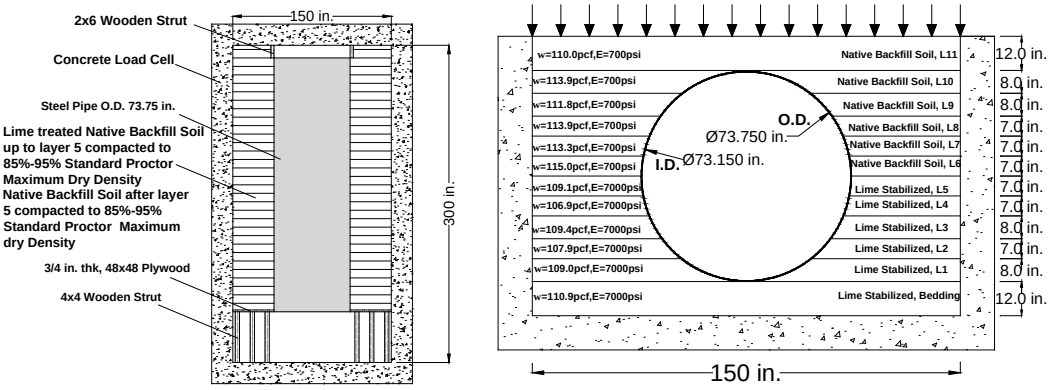

Figure 3-15 Details of Soil Box Test 2

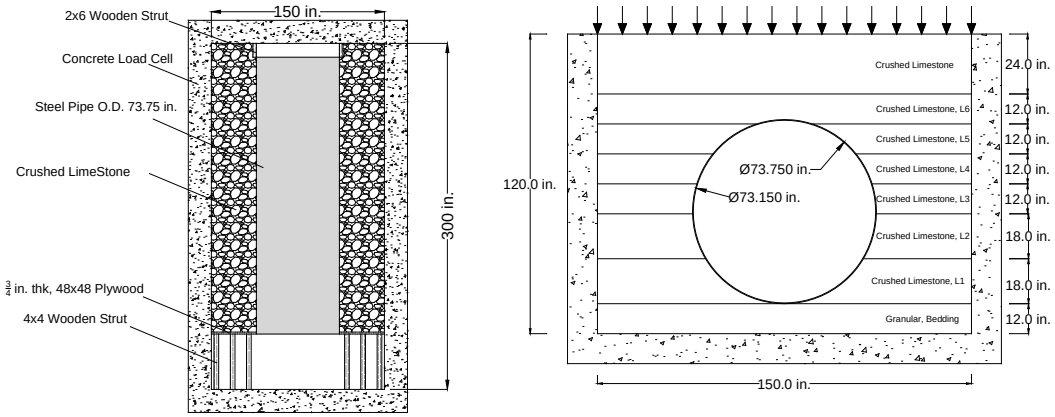

Figure 3-16 Details of Soil Box Test 3

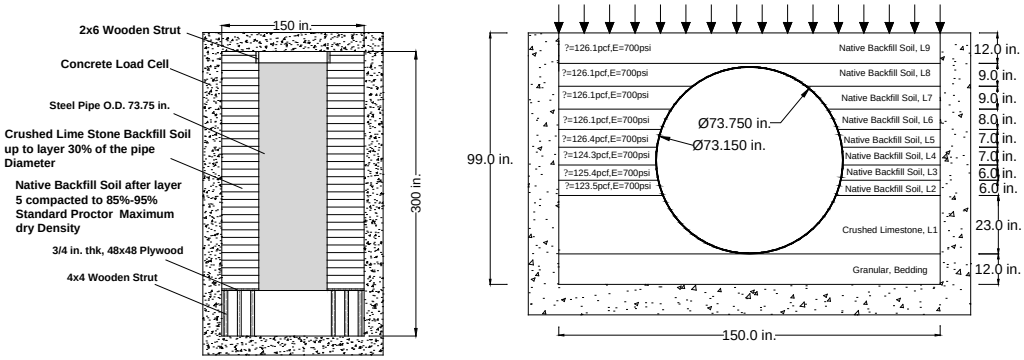

Figure 3-17 Details of Soil Box Test 4

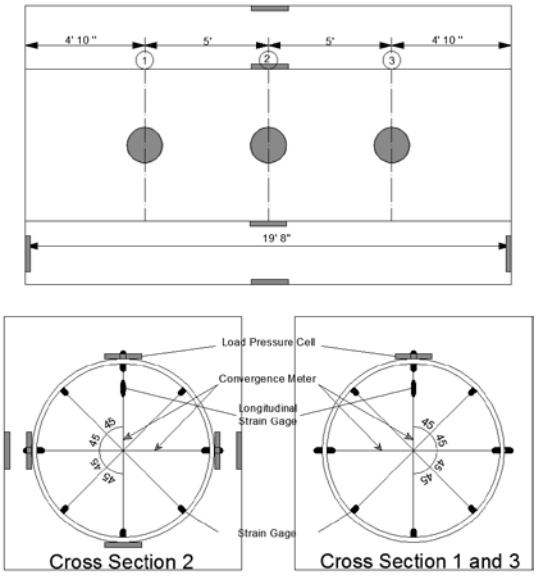

Figure 3-18 Instrumentations for Test 1

Table 3-2 Native and treated native soil properties

	Native Soil	Treated Native Soil
Soil Plasticity	Mohr Coulomb	Mohr Coulomb
Maximum dry density	17 kN/m^3 (108.1 pcf)	15.5 kN/m^3 (98.6 pcf)
Optimum moisture content	16.2 %	19 %
Un-drained cohesion, C_u	100 kPa (14.5 psi)	160 kPa (23.2 psi)
Angle of friction, φ	8.1 ^{o}	25.8^o
Unconfined compression Strength	156.5 kPa (22.7 psi)	425.5 kPa (61.7 psi)
Poisson's ratio	0.3	0.3
Elastic Modulus **Confining pressure=7.5 psi**	4 MPa (565.6 psi)	24.5 MPa (3552.4 psi)
Elastic modulus **Confining pressure=15 psi**	4.35 MPa (630.9 psi)	54 MPa (7826.9 psi)
Elastic modulus **Confining pressure=22.5 psi**	4.5 MPa (657.03 psi)	53.1 MPa (7701.8 psi)

Table 3-3 Details of Test 1

Soil Layer Name	Layer Thickness (in)	Material used	Compaction
Bedding	12	Pea gravel	
Layer 1	7	Native backfill soil	92%
Layer 2	8	Native backfill soil	91.3%
Layer 3	9	Native backfill soil	91.6%
Layer 4	9	Native backfill soil	92.7%
Layer 5	7	Native backfill soil	92.2%
Layer 6	8	Native backfill soil	93.2%
Layer 7	10	Native backfill soil	92.3%
Layer 8	9	Native backfill soil	92.4%
Layer 9	11	Native backfill soil	91.3%
Layer 10	12	Native backfill soil	90.1%
Layer 11	18	Native backfill soil	
Surcharge	84	Pea gravel	

In Test 2, the bedding material was lime treated native soil (Table 3-2). The backfill material was also compacted lime treated native soil up to springline and then native soil was compacted for the remaining of the depth. Finally, pea gravel was used as an additional surcharge above the embankment to represent the cover placed on the top which is equivalent to 2.4 m (8 ft) of native soil cover with an average density of 17.3 kN/m^3 (110 pcf). The profile of the soil layers for Test 2 is shown in Figure 3-15. Table 3-4 presents the thickness and other properties of the soil layers in Test 2. Figure 3-19 illustrates the instrumentation for Test 2.

Ten (10) earth pressure cells were used to obtain the pressure magnitude in different locations for Test 2, as shown in Figure 3-19. For this test, 24 strain gauges were attached to the interior wall of the pipe. All of the strain gauges were in circumferential direction for this test, as illustrated in Figure 3-19.

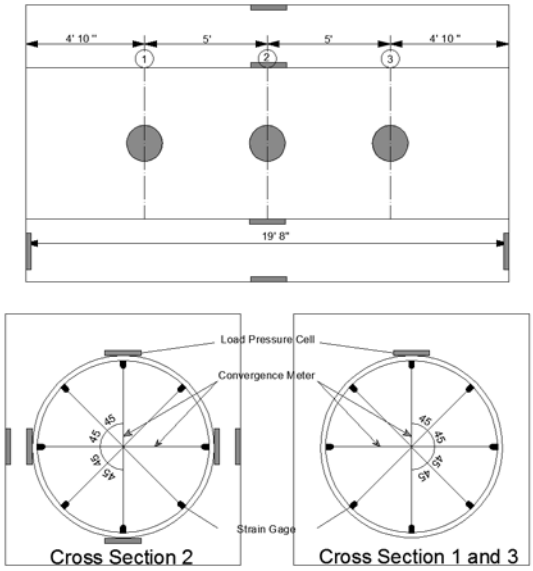

Figure 3-19 Instrumentations for Test 2

Table 3-4 Details of Test 2

Soil Layer Name	Layer Thickness (in)	Material used	Compaction
Bedding	6	Lime Stabilized	92.5%
Bedding	6	Lime Stabilized	92.5%
Layer 1	8	Lime Stabilized	91.8%
Layer 2	7	Lime Stabilized	91.6%
Layer 3	8	Lime Stabilized	91.6%
Layer 4	7	Lime Stabilized	90.9%
Layer 5	7	Lime Stabilized	91.0%
Layer 6	7	Native backfill soil	90.7%
Layer 7	7	Native backfill soil	90.3%
Layer 8	7	Native backfill soil	89.6%
Layer 9	8	Native backfill soil	89.5%
Layer 10	8	Native backfill soil	89.8%
Layer 11	12	Native backfill soil	
Surcharge	96	Pea gravel	

The bedding material for Test 3 was crushed limestone and crushed limestone was also constructed and compacted in six (6) layers for backfilling the steel pipe. Table 3-5 presents the material properties for crushed limestone. The soil profile for Test 3 is presented in Figure 3-16. Table 3-6 also summarizes the properties of each soil layer for this test.

Table 3-5 Crushed lime-stone

Unit Weight (Dry Rodded)	15.6 kN/m^3 (99 pcf)
Unit Weight (Dry Loose)	14.2 kN/m^3 (90 pcf)
Modulus of Elasticity	138 MPa (20000 psi)
Poisson's ratio	0.35
Angle of friction, φ	48 ^{o}

Figure 3-20 illustrates the instrumentation for this test. As shown in Figure 3-20, eight (8) earth pressure cells and thirty-six (36) strain gauges were employed in Test 3. The location and explanation of the strain gauges is similar to Test 1.

Table 3-6 Details of Test 3

Soil Layer Name	Layer Thickness (in)	Material used	Compaction
Bedding	12	Pea gravel	
Layer 1	18	Crushed limestone	92%
Layer 2	18	Crushed limestone	91.3%
Layer 3	12	Crushed limestone	91.6%
Layer 4	12	Crushed limestone	92.7%
Layer 5	12	Crushed limestone	92.2%
Layer 6	12	Crushed limestone	93.2%
Surcharge	24	Crushed limestone	
	84	Pea gravel	

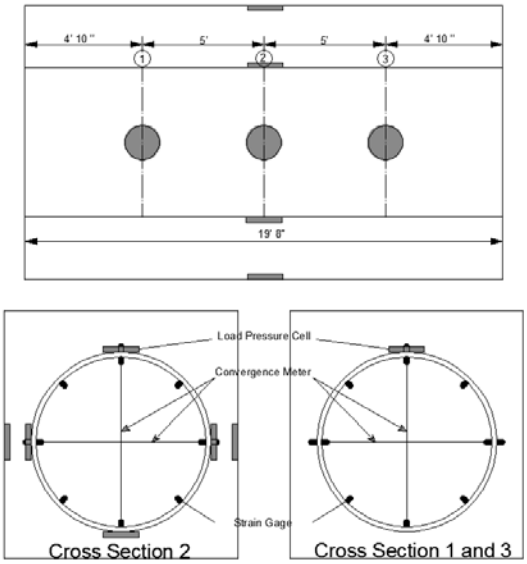

Figure 3-20 Instrumentations for Test 3

The pipe was backfilled with crushed limestone up to 30% of its diameter in Test 4. Then the native soil was compacted and applied on top of the crushed limestone as shown in Figure 3-17. The 30.5 cm (12 in.) thick granular lift was used as the bedding material for this test.

The pea gravel is used to simulate the surcharge load. This test was instrumented similar to Test 1.

3.3 Results

For each soil box test, a model was created and verified with the test results. The initial deflection of pipe due to its self-weight was not reported in the test data, so in the graphs for the verified models, the initial deflection due to the pipe self-weight was reduced from the data. The verified model of Test 1 was then used for the sensitivity study on the effects of different modeling parameters including compaction, mesh density, contact properties, and length of the model. It should be noted that the initial deflection of pipe due to its self-weight was considered in the graphs for sensitivity study.

3.3.1 Deflection Results

The initial models were verified based on the deflection graph. For each test, three (3) sections in pipe were instrumented in order to obtain vertical and horizontal deflection. Then the analysis results of the models were compared with the horizontal and vertical deflections obtained from the full-scale test data in each stage of construction. Figure 3-21 through Figure 3-24 illustrate the horizontal and vertical deflection for the simulated model versus test results for soil box Tests 1, 2, 3, and 4, respectively. As shown in these figures, the analysis results were closely simulating the test data curve.

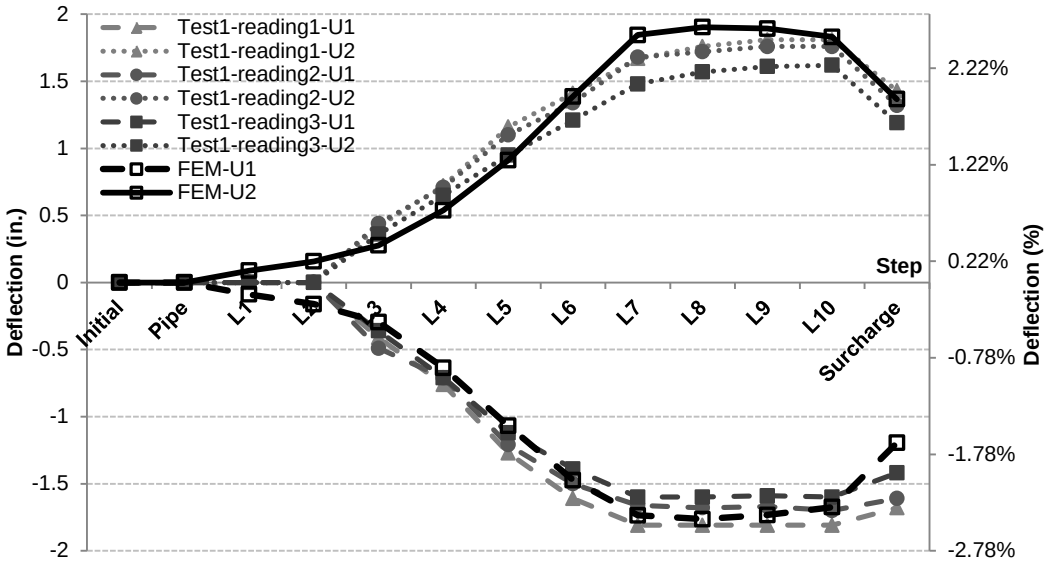

(a)

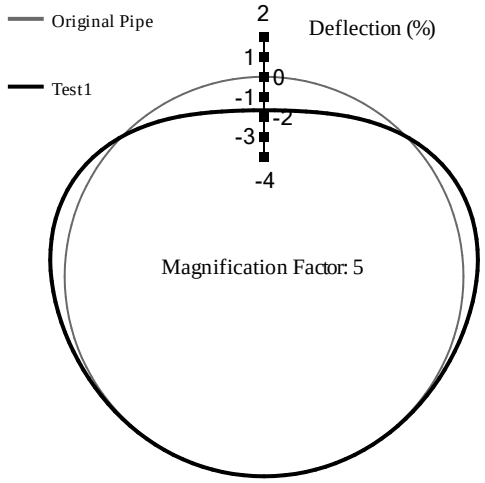

(b)

Figure 3-21 (a) Horizontal and vertical deflections of the pipe, FEM vs. Test 1 results; (b) deflected shape of the pipe at the end of Test 1 (FEM)

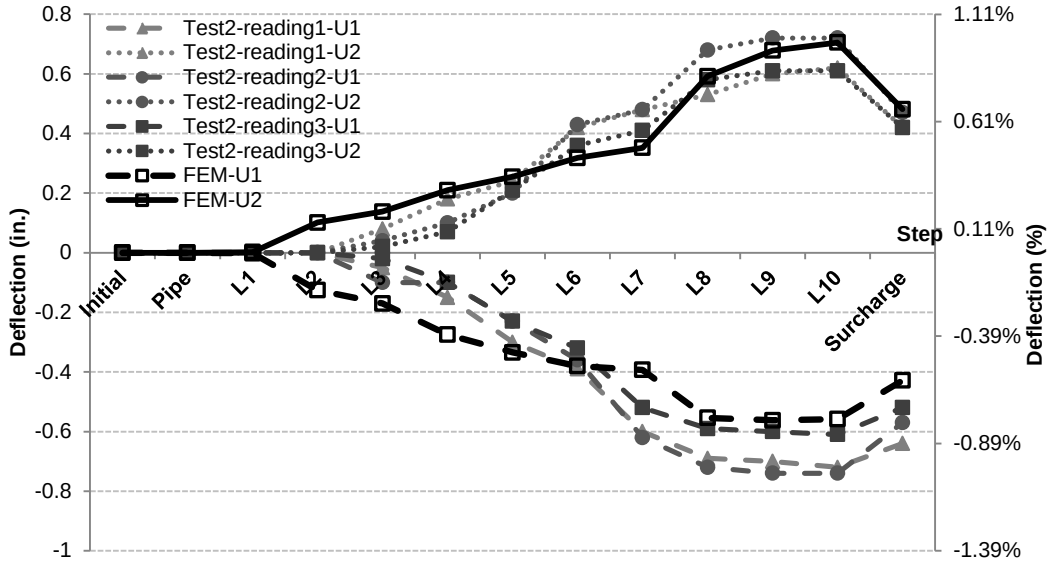

(a)

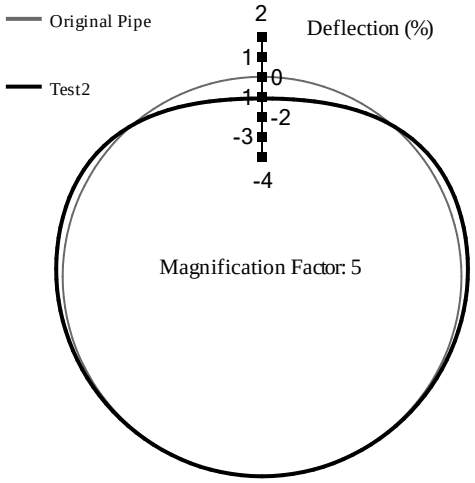

(b)

Figure 3-22 (a) Horizontal and vertical deflections of the pipe, FEM vs. Test 2 results; (b) deflected shape of the pipe at the end of Test 2 (FEM)

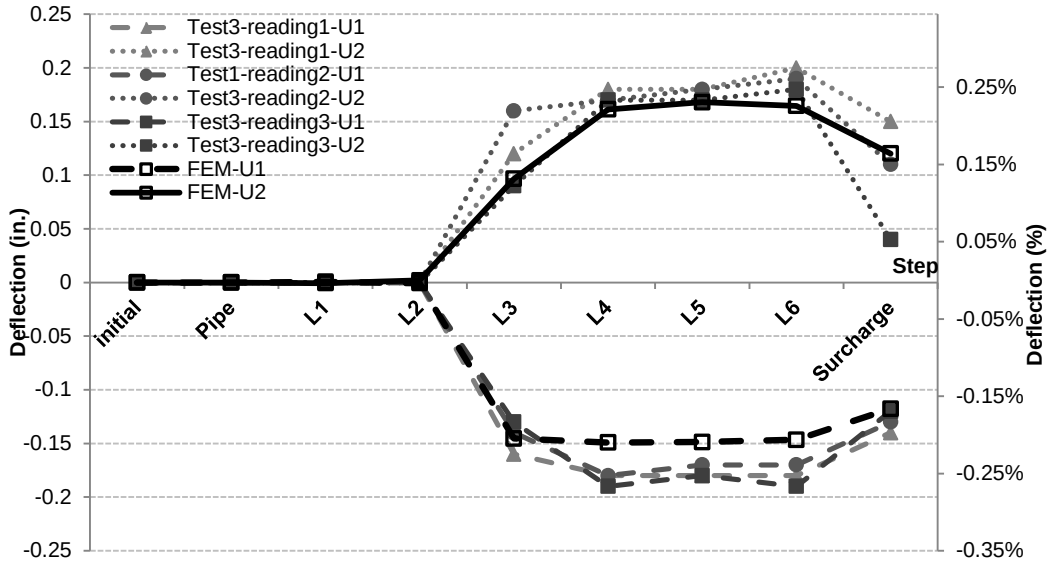

(a)

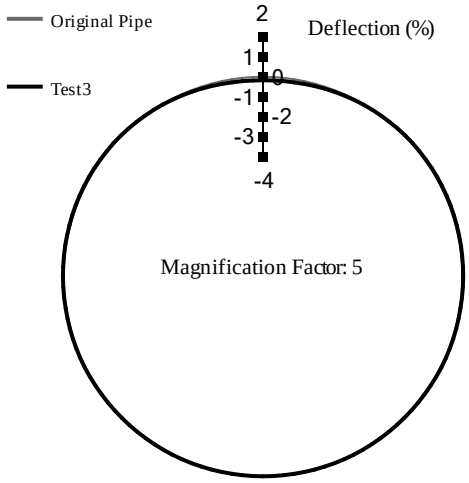

(b)

Figure 3-23 (a) Horizontal and vertical deflections of the pipe, FEM vs. Test 3 results; (b) deflected shape of the pipe at the end of Test 3 (FEM)

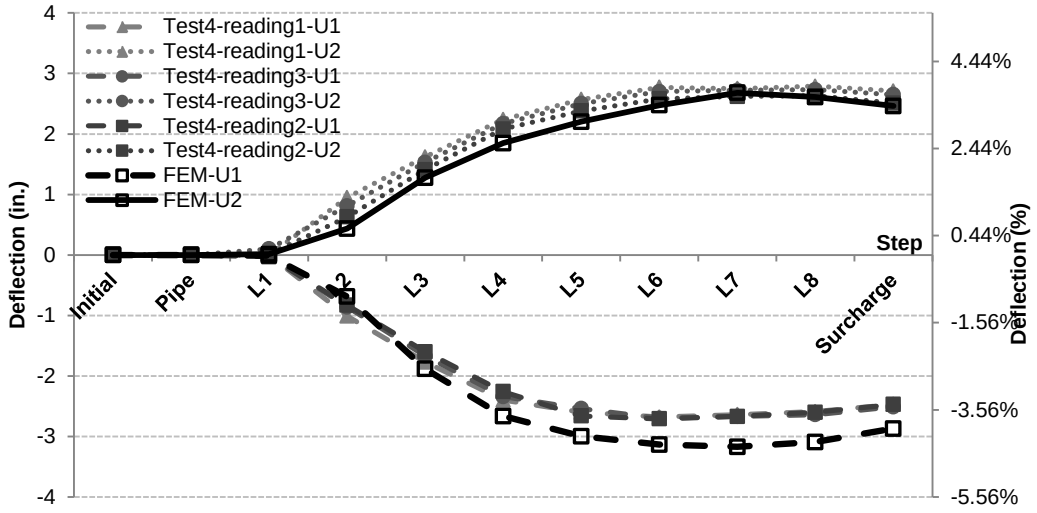

(a)

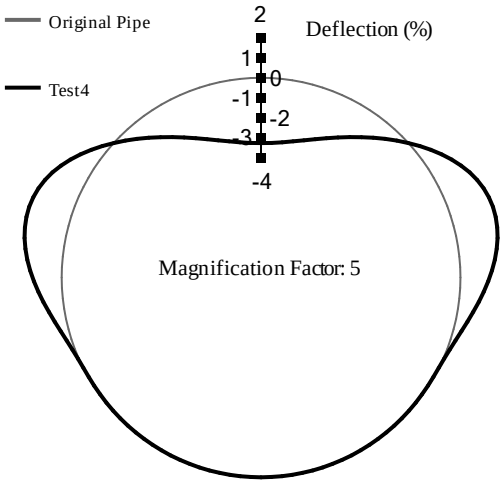

(b)

Figure 3-24 (a) Horizontal and vertical deflections of the pipe, FEM vs. Test 4 results; (b) deflected shape of the pipe at the end of Test 4 (FEM)

3.3.3 Moment, Thrust, and Shear Results

Figure 3-25 through Figure 3-43 illustrate the stress results of the soil box test versus the FEM for Tests 1 through 4, respectively. Moreover, the results of FEM were

used to calculate the moment, thrust force, and shear force in the pipe wall thickness, which are presented in Figure 3-25 through Figure 3-43.

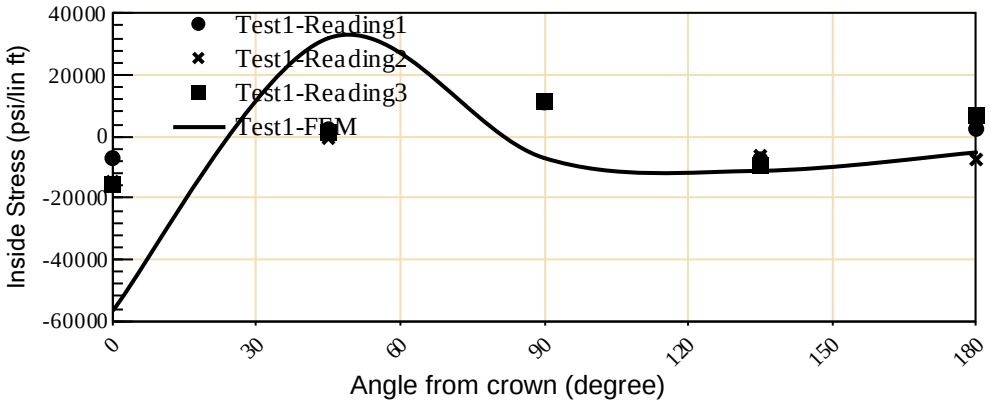

Figure 3-25 Circumferential stresses for the pipe interior wall in Test 1, FEM vs. Test

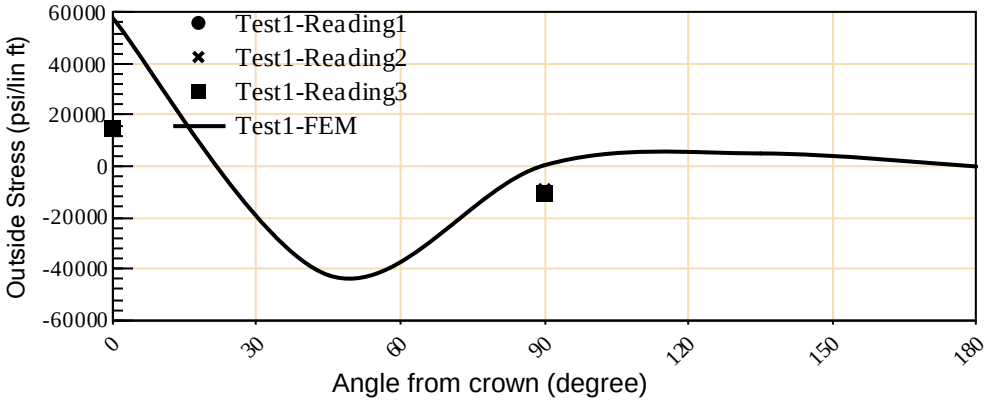

Figure 3-26 Circumferential stresses for the pipe exterior wall in Test 1, FEM vs. Test

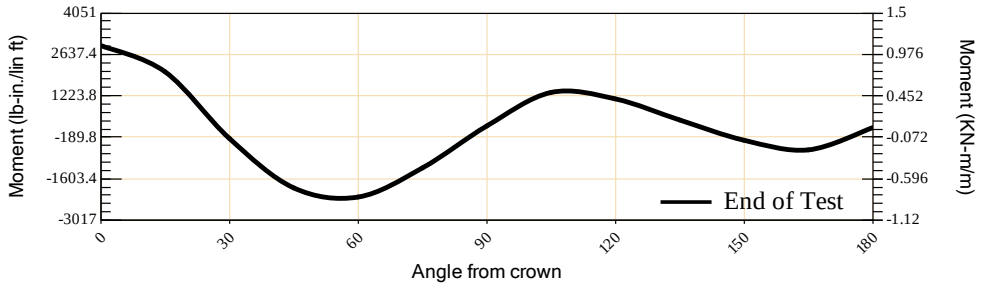

Figure 3-27 FEM moment graph in Test 1

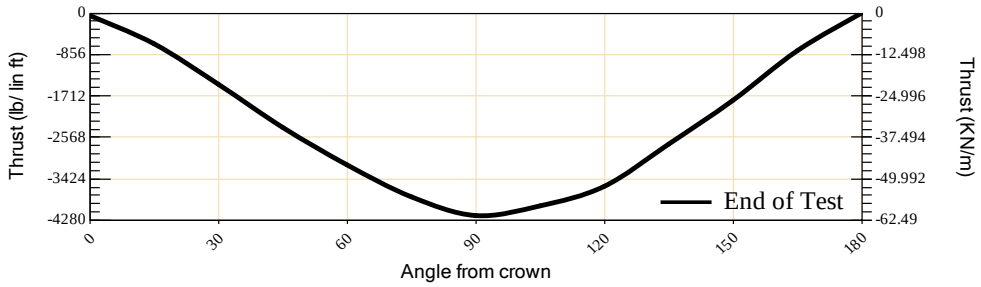

Figure 3-28 FEM thrust force in Test 1

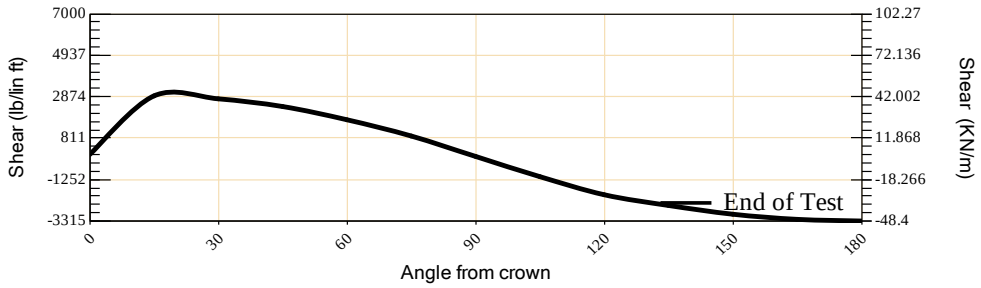

Figure 3-29 FEM shear force in Test 1

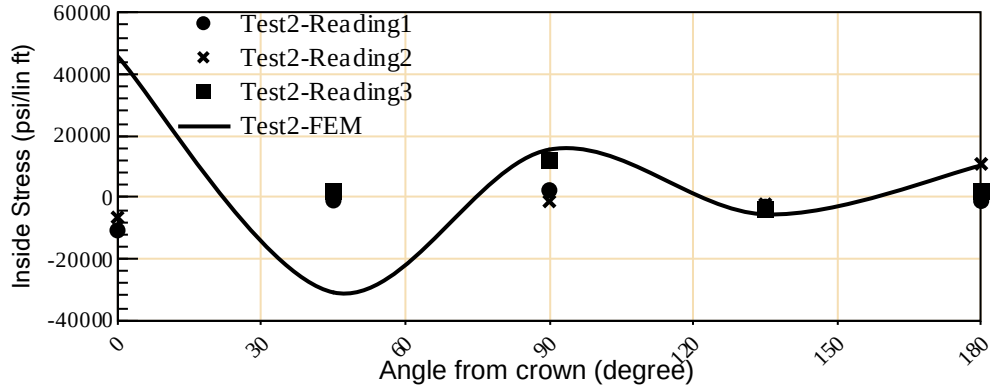

Figure 3-30 Circumferential stresses for the pipe in Test 2, FEM vs. Test

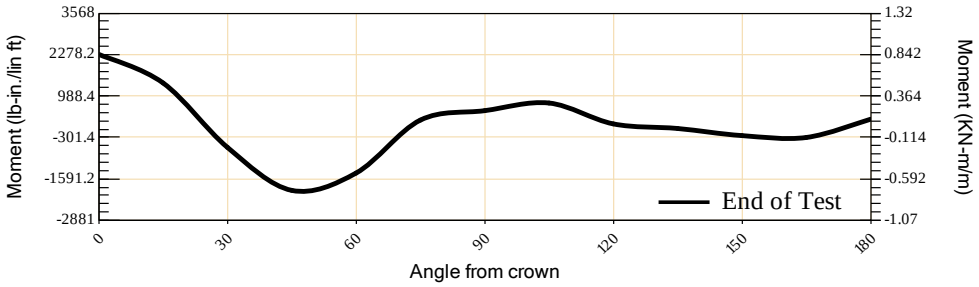

Figure 3-31 FEM moment graph in Test 2

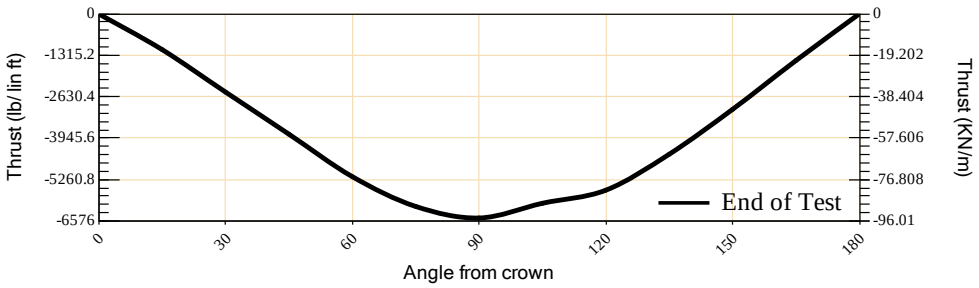

Figure 3-32 FEM thrust force in Test 2

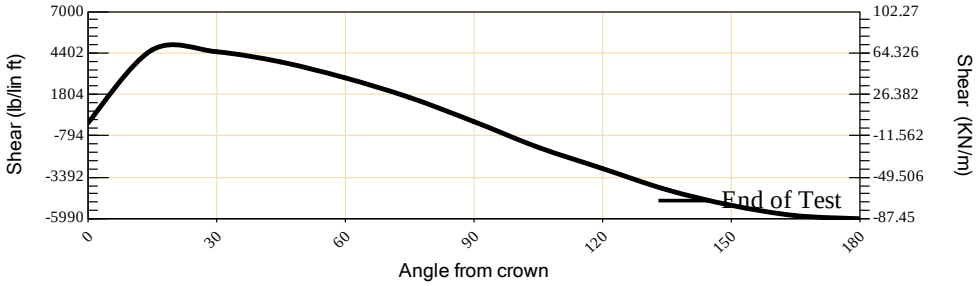

Figure 3-33 FEM shear force in Test 2

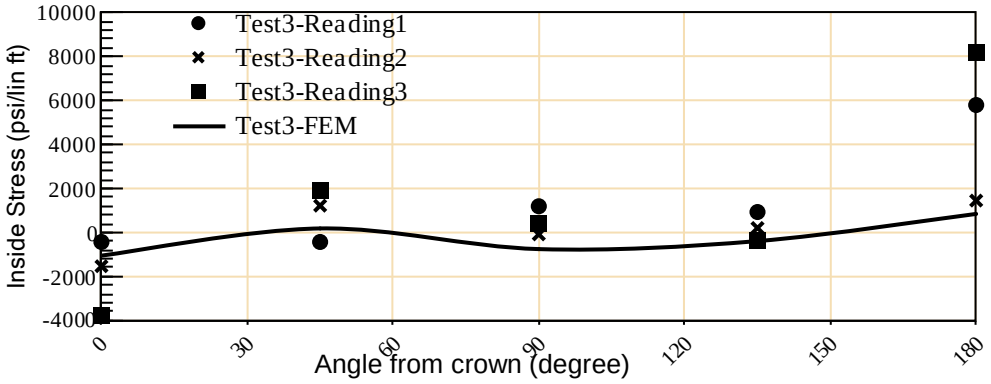

Figure 3-34 Circumferential stresses for the pipe interior wall in Test 3, FEM vs. Test

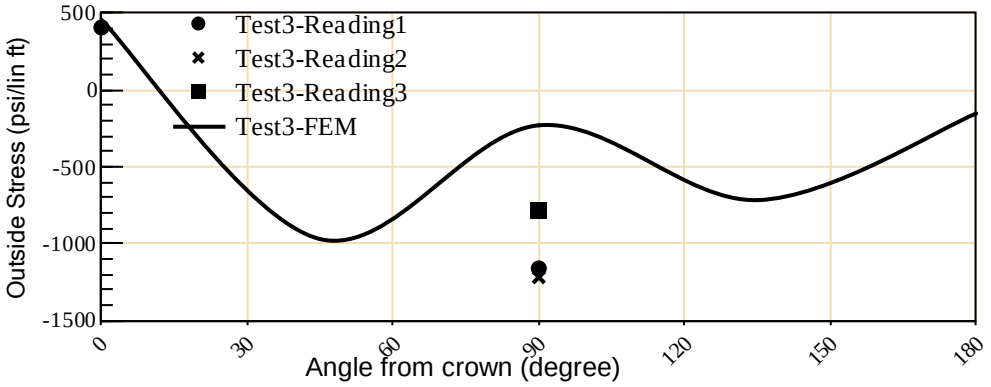

Figure 3-35 Circumferential stresses for the pipe exterior wall in Test 3

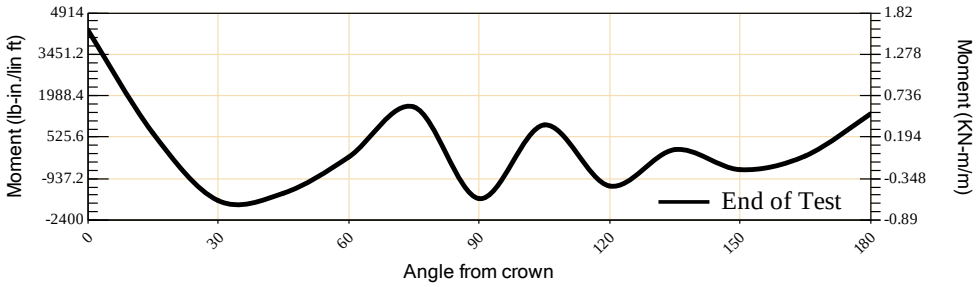

Figure 3-36 FEM moment graph in Test 3

Figure 3-37 FEM thrust force in Test 3

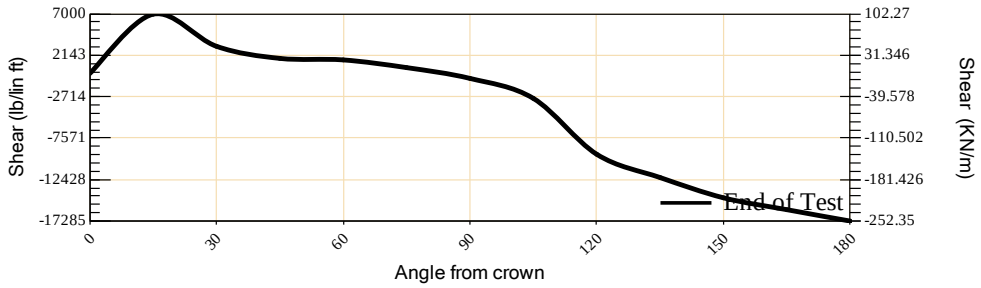

Figure 3-38 FEM shear force in Test 3

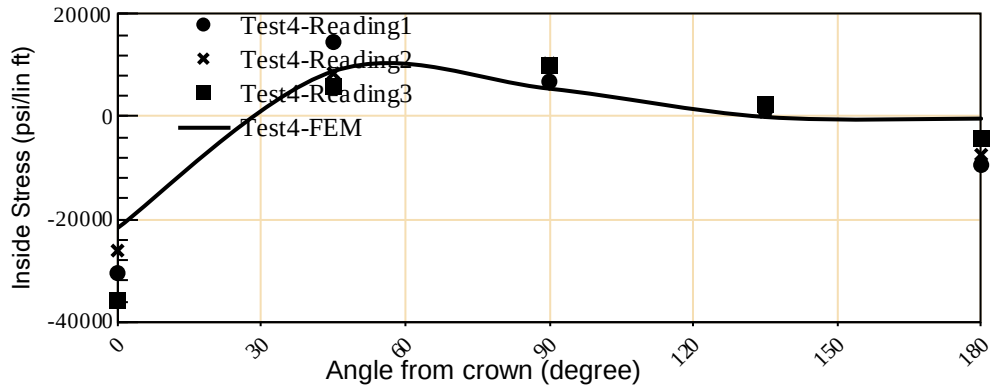

Figure 3-39 Circumferential stresses for the pipe interior wall in Test 4, FEM vs. Test

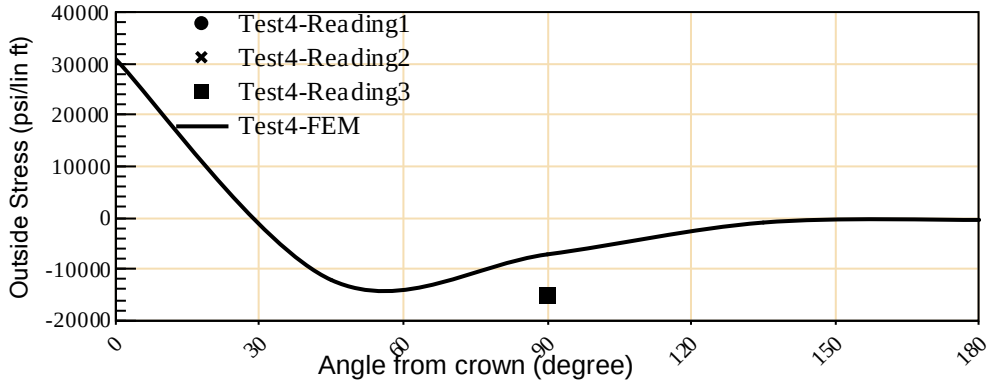

Figure 3-40 Circumferential stresses for the pipe exterior wall in Test 4

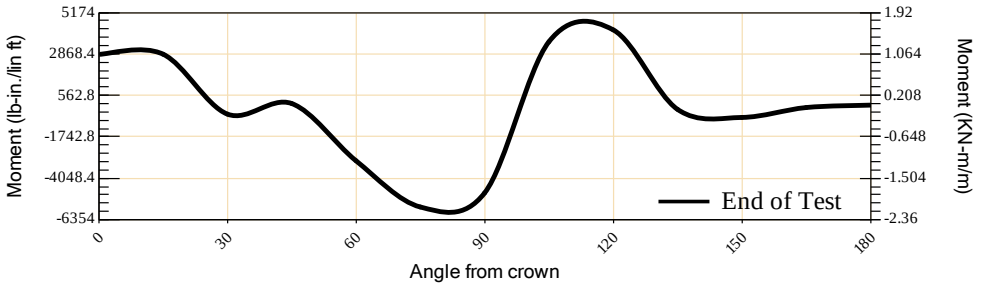

Figure 3-41 FEM moment graph in Test 4

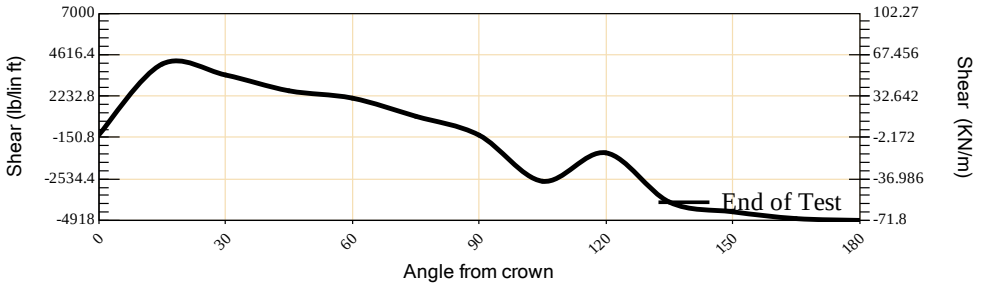

Figure 3-42 FEM thrust force in Test 4

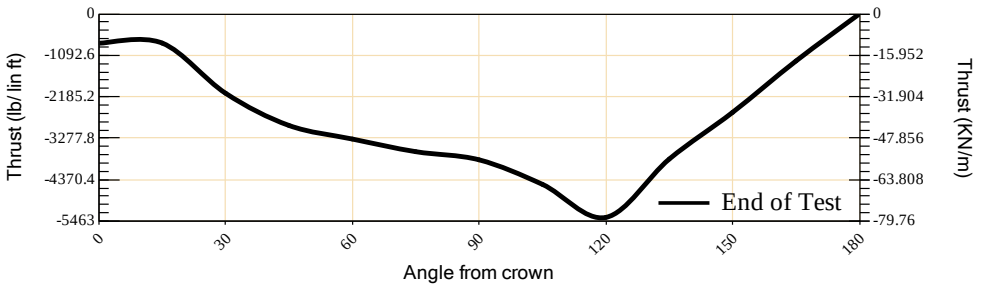

Figure 3-43 FEM shear force in Test 4

The strain gauges in the tests could not show the initial strain in the pipe due to its self-weight. However, this initial strain is considered in the FEM analysis. Thus the data from strain gauges are different from FEM results at crown and springline. It also should be noted that some the strain gauges were damaged during experiments so in some graphs those strain gauges data were missing.

3.3.3 Sensitivity Study

The essential variable for sensitivity study was identified. Then a study conducted on the identified parameters including compaction, model length, contact properties, and mesh density. The parametric study on essential modeling parameters was conducted on Test 1.

3.3.3.1 Compaction

Compaction load was applied to the model in a range of 0.2 C_u to 0.7 C_u to study the sensitivity of the computational results to the amount of compaction load. As shown in Figure 3-44, the results indicate that for the lower layers (haunch area), the compaction was not effective. Thus, the stress value of $0.2C_u$ was used in the hunch zone, but as the compaction was performed for higher soil layers, compaction stress values between $0.3C_u$ and $0.5C_u$ simulate the behavior more accurately.

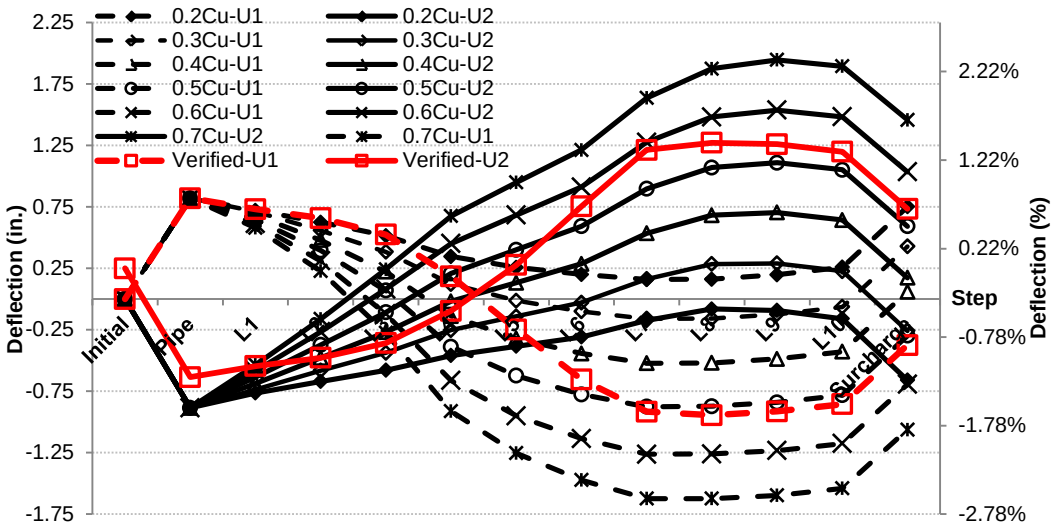

Figure 3-44 Results of compaction study for Test 1

There was a transition distance between the step Layer 3 and the step Layer 7. Before adding the Layer 3, haunch area, due to difficulties in compaction of that area, the value of $0.2C_u$ would be picked. Between the step Layer 3 and the step Layer 7 the value was transmitted from $0.2C_u$ to $0.5C_u$. Furthermore, after the step Layer 6, the $0.5C_u$ was a proper representative for compaction stress.

Per Clayton et al. (1992) for plasticity index of 48% the value of $0.8C_u$ can be assumed and this study proposed the value of $0.25C_u$ for plastic index of 22%. The plasticity index of the applied soils in current study was 26%. Thus verified range of $0.35C_u$-$0.4C_u$ in this study is in agreement with Clayton's suggested range.

3.3.3.2 Length

Figure 3-45 shows the deflection comparison between different models with variable length of 30.5 cm (1 ft), 61 cm (2ft), 152.4 cm (5 ft), 304.8 cm (10 ft) and 609.6 cm (20 ft). The variation of the model length for Test 1 indicates that the difference between 30.5 cm (1 ft) model and 609.6 cm (20 ft) model was in a range of 1-2%. However, since the longer model requires more analysis time, the 30.5 cm (1 ft) model

was used for the parametric study. However, a study was conducted to compare the results of 2D and 3D model. The results showed that the difference for 2D and 3D model is in range of 10-20%.

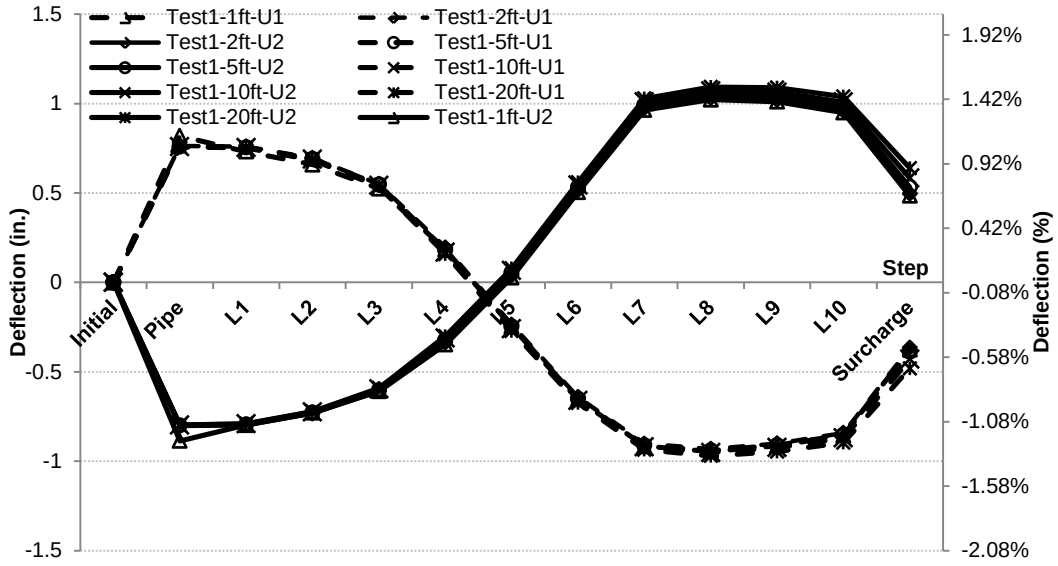

Figure 3-45 Parametric study on different mode length for Test 1

3.3.3.3 Contact

A range of coefficient of friction of 0.2 to 0.5 was reported by El-Chazli et al. (2005) for the friction between soil and pipe materials. Therefore, a parametric study was performed on the friction coefficient between soil-pipe and soil-soil to study the sensitivity of analysis to variation of this parameter. Figure 3-46 shows the results of deflection for different contact properties.

The deflection variation between the model which has μ=0.2 and the model with μ=0.5 was 5-20%. Thus, the value of μ=0.3 was recommended in this study.

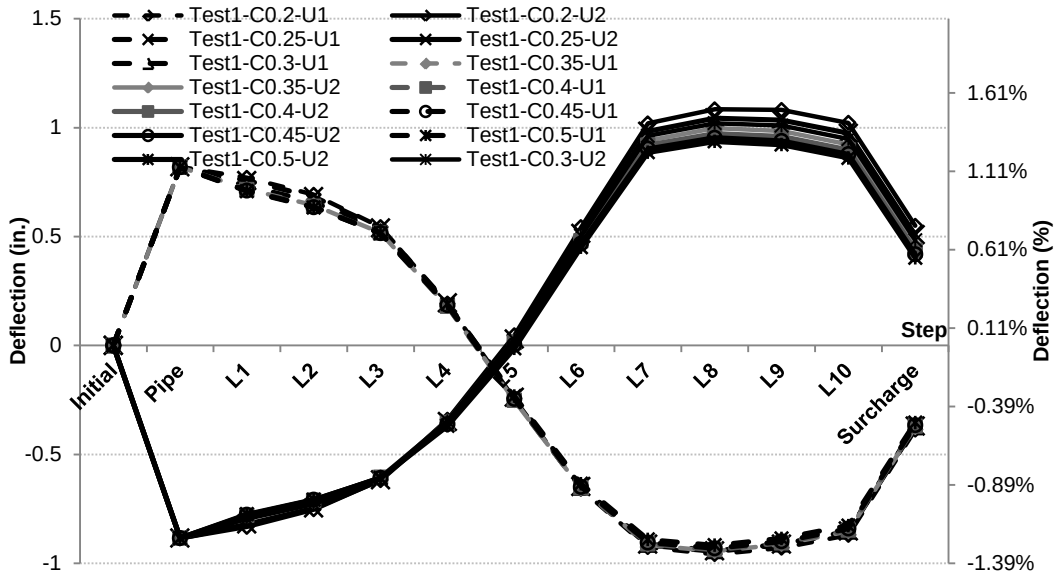

Figure 3-46 Parametric study results for different contact properties conducted for Test 1 results

3.3.3.4 Mesh Density

Four (4) different mesh sizes of 38.1 mm (1.5 in.), 44.45 mm (1.75 in.), 50.8 mm (2 in.), and 69.85 mm (2.75 in.) were selected for this parametric study. The denser meshes were more expensive in calculation time. Thus, a convergence study on the optimum mesh size would be beneficial for time efficiency. The lifts thicknesses were varying between 15.24 cm (6 in.) to 45.72 cm (18 in.) So the value of 50.8 mm (2 in.) was initially selected for the mesh sizes. Then several mesh densities chosen to check the convergence. As shown in Figure 3-47, the deflection difference between the denser mesh, 38.1 mm (1.5 in.), and the less dense mesh, 69.85 mm (2.75 in.), was 15-30%.

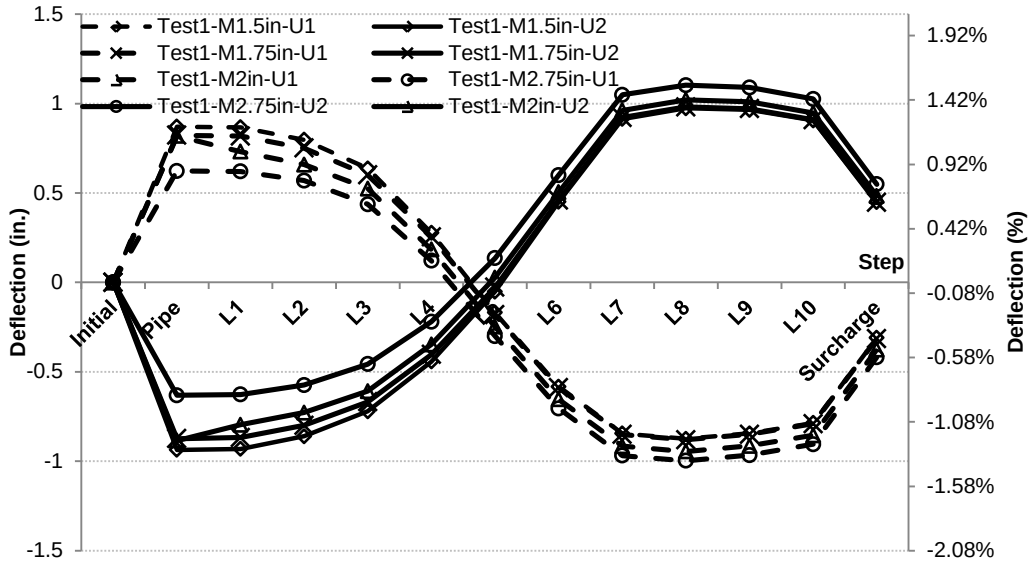

Figure 3-47 A graph of results for conducted mesh density study for the results of Test 1

3.4 Conclusion

The presented 3-D nonlinear finite element model was successfully predicted the vertical and horizontal deflections of the flexible buried steel pipe during a staged construction. The stress data of the soil box tests then were compared with the results of the FEM analyses. The graphs are indicating that the FEM analyses were successfully predicted the soil box tests. Furthermore, the strain gauges in the soil box tests were not able to show the strain due to pipe self-weight since the pipe was instrumented after those deflections due to the pipe self-weight. However, the FEM is capable of detecting the strains due to the pipe self-weight. The moment, the shear, and the thrust force in the pipe wall thickness along the circumference of the pipe were calculated and presented in this chapter.

The compaction force, for the first time, was accurately simulated using uniform thermal forces. The staged construction was properly modeled by using mesh activation and de-activation algorithms technique. The change in geometry of the pipe during

backfilling was modeled precisely for the first time using the aforementioned unique algorithm. Sensitivity studies were conducted on the model length, contact properties, mesh size, and compaction which suggested that proper values for the above critical parameters were utilized during modeling process. The FEM developed accurately simulated the load–deformation results from the full-scale experimental tests.

Chapter 4

Field Test and The Development of Long-Term FEM Model

The developed FEM model was successfully predicted the results of soil box tests. As discussed in previous chapter, the tests utilized a rigid concrete box and a 1.83 m (72 in.) pipe. Various backfill materials, including ordinary soil, lime-treated soil, and crushed limestone were used in the tests. However, the soil box tests were conducted in a rigid trench wall condition as explained in Chapter 3 of this dissertation. Moreover, the backfilling and embedment materials were limited to certain types of soil material. Also the pipe diameter and the pipe wall thickness was the same for all the tests. Additionally, the trench wall was vertical in the soil box tests. Consequently, three field tests were designed to further verify the developed FEM model for different trench configurations and different pipes.

As explained in the previous chapter, the developed three-dimensional nonlinear finite element model consisted of different steps, which are summarized in Figure 4-1.

This chapter presents the information and procedure for conducted field tests. The required modifications for different steps in the FEM model (Figure 4-1) to analyze different configurations are discussed in this chapter. Lastly, the results of the field tests and the FEM are compared in this chapter. Figure 4-2 illustrates the frame work of the conducted research works for the field tests and the associated developed long-term FEM model which is incorporated the real steel pipe-interaction condition to the developed FEM model in Chapter 3.

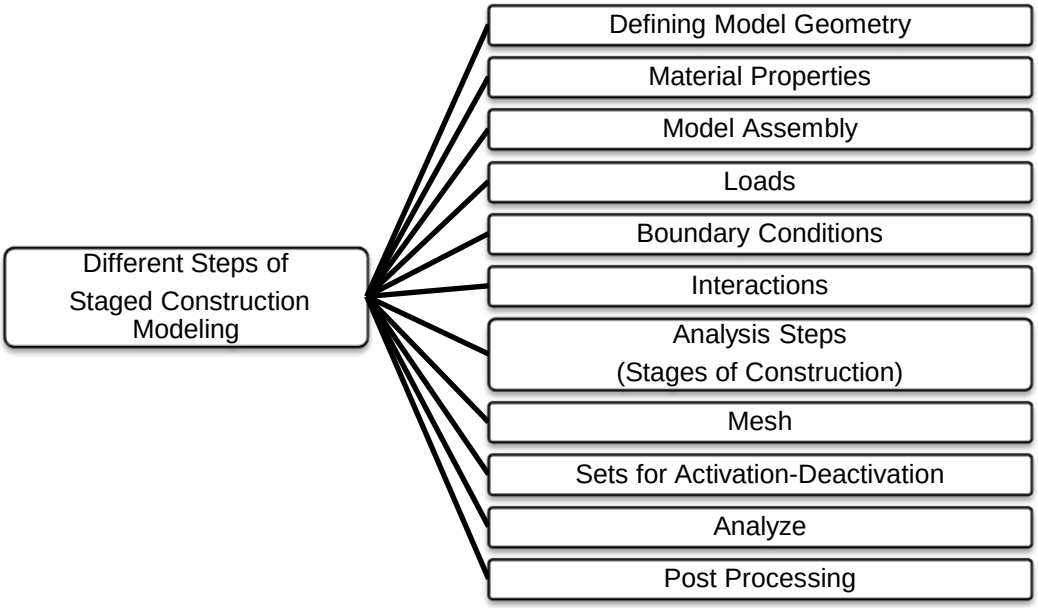

Figure 4-1 Different Steps of the staged construction modeling of steel pipes using 3-D FEM

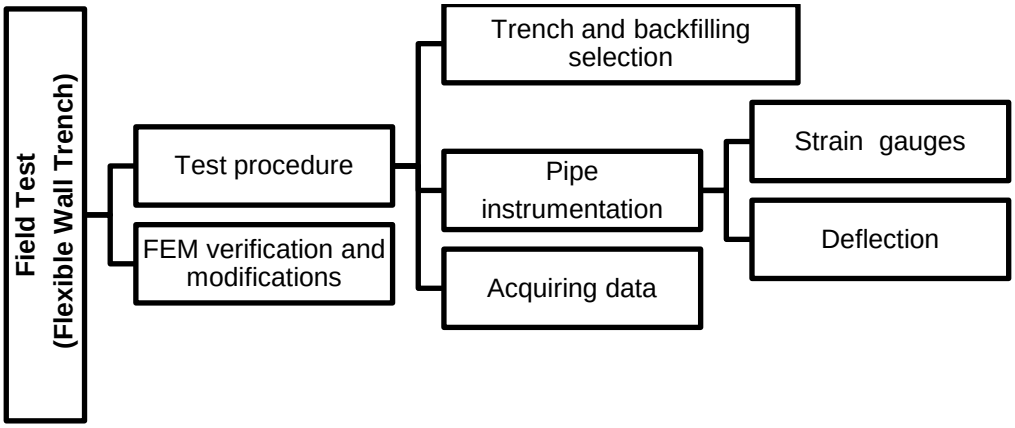

Figure 4-2 Framework of the conducted research works for the field test

4.1 Conducted Field Tests

Three (3) 2.13-m (84-in.) diameter, 7.62 m (25 ft) long steel pipes were instrumented as shown in Figure 4-3. Each pipe was instrumented in two sections. As

shown in Figure 4-3, the sections were placed at the one-third and two-third of the pipe length.

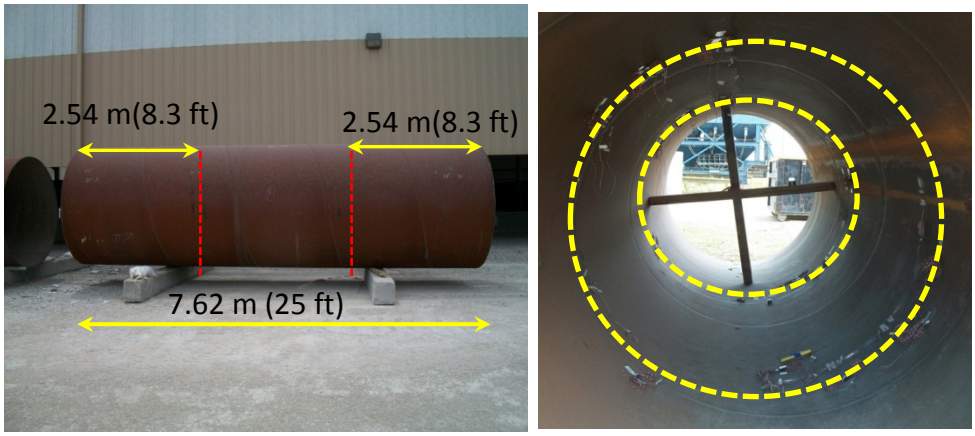

Figure 4-3 The instrumented 2.13-m (84-in.) steel pipes

Each section had ten instrumentations including eight (8) strain gauges and two (2) Cable Displacement Sensors (CDS). Figure 4-4 illustrates the location of the strain gauges and the CDSs.

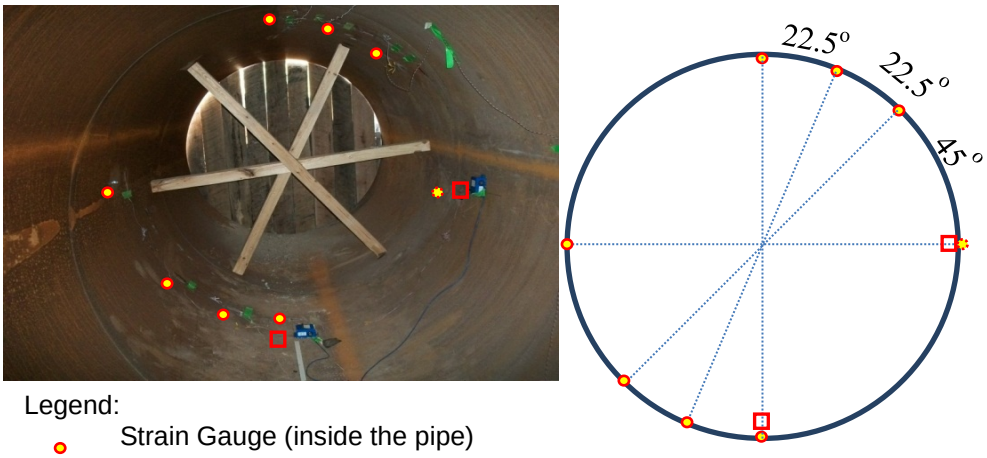

Legend:

- Strain Gauge (inside the pipe)
- Strain Gauge (outside the pipe)
- CDS

Figure 4-4 Typical instrumented section for each steel pipe

The field tests were conducted at Rolling Hills Buster Pump Station, Fort Worth, Texas. Three (3) trench configurations with different backfilling materials were designed to obtain the adequate data to verify the developed FEM model. It should be noted that the trench wall in the field tests was in-situ soil which is commonly applicable to the real installation practices. Thus, in the field tests the effect of rigid trench walls were removed and the actual effects of the trench wall were studied on the behavior of the buried steel pipes. The material properties and the log profile for trench wall soil are shown in Figure 4-5. The soil tests and log profile were conducted and prepared by Fugro Consultant Company.

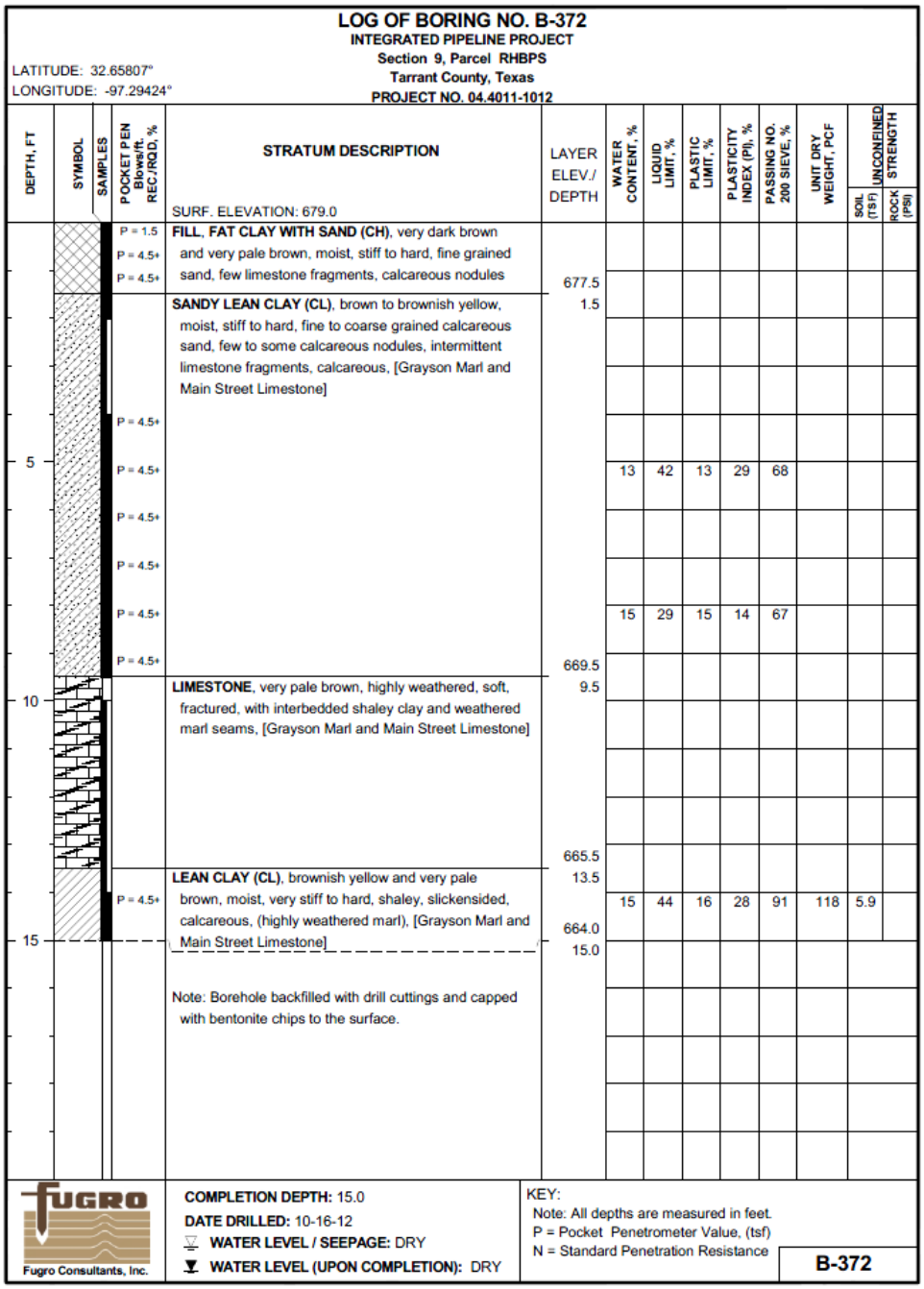

Figure 4-5 Soil log profile for the trench wall in the conducted field tests

Moreover, the Controlled Low Strength Material (CLSM) was used as the embedment material for the field tests. As mentioned in Chapter 2, the compaction of the

haunch zone is difficult due to the geometry of the pipe and the trench. Additionally, for the narrow trench conditions the compaction of the pipes is not feasible below the springline. Consequently, the application of CLSM, which is a flowable material, is desirable for the designers. Three (3) different trench configurations are presented in Figure 4-6 in detail.

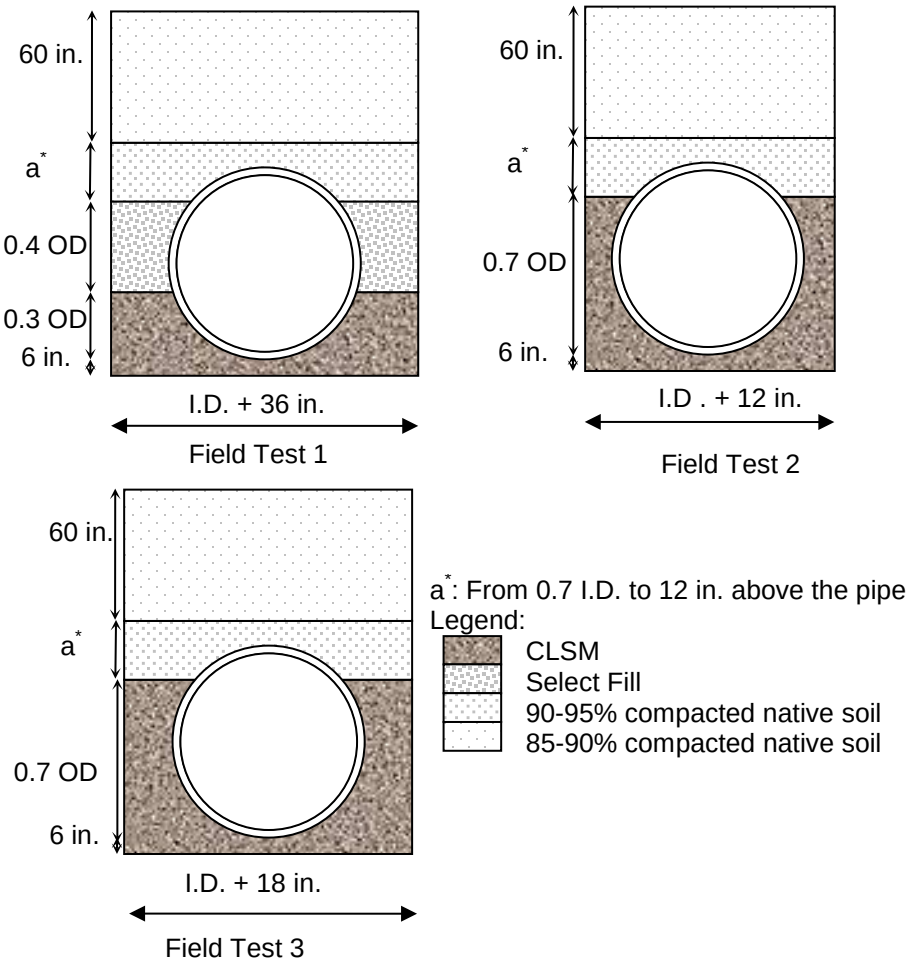

Figure 4-6 Three different trench configurations for the field test

Two (2) manholes were designed accurately by Hanson Pipe and Precast, Grand Prairie, Texas to be installed in between the pipes in order to have access to the pipes

and the instrumentation. The pipes were not connected through manholes and they were deformed decoupled from each other under the process of backfilling. Figure 4-7 shows a photograph of installed pipes and the manholes between them.

Figure 4-7 The excavated trench, installed pipes, and manholes

The end of Pipes 1 and 3 and also the intersection of pipes and manholes were sealed and waterproofed to prevent the flow of CLSM or water inside the pipes, as shown in Figure 4-8. The surveying and measurements of the trench dimensions, the location of the pipes, and height of backfill at different stages were conducted as shown in Figure 4-9.

Figure 4-8 Capping and sealing the end of the pipes to prevent the flow of water or CLSM inside the pipes

Figure 4-9 Surveying was conducted in order to obtain the exact trench configuration

After placing the pipes in the excavated trench, the strain gauges and the CDSs were then connected to the data acquisition system (DAQ) which was placed in the DAQ head quarter. As mentioned earlier, each pipe had two instrumented sections and each section had ten instrumentations. Thus, the cables were organized and labeled accurately inside and outside the pipes as shown in Figure 4-10 to ease the control and access to them. It should be noted that the cables were passed through channels to protect them against the environmental damages.

Figure 4-10 Protection of cables against environment

The backfilling started upon checking and controlling the initial data which was obtained from the instrumentations. All the pipes were initially backfilled with CLSM up to 30% of their diameter. Figure 4-11 illustrates the machine which was prepared and cast the CLSM inside the trench.

Figure 4-11 Preparation and casting of CLSM (panorama view)

The next lift of backfill was started next day when the first lift of CLSM was hardened. Select fill material (sand), as shown in Figure 4-12, was compacted and placed up to 70% of the diameter of the pipe (from 30% of I.D. to 70% of I.D.) as the backfilling for the first pipe.

Figure 4-12 Select fill was compacted by jumping jack compactor for the first pipe

The procedure of backfilling of this layer for the first pipe is show in Figure 4-13.

Figure 4-13 Compaction and backfilling of the select fill for the first pipe

Then the first pipe was backfilled with ordinary soil (the in-situ soil of the field). The soil cover was 1.52 m (5 ft) as this value is a common value in pipe design.

It should be noted that the soil properties including density, the moisture, and the level of compaction were tested after compaction of each soil lift. The nuclear densometer apparatus was used to determine the soil properties for each layer at four (4) points which were located above the two (2) sections of each pipe (two (2) readings per section in north side and south side of the pipe). The process and the densometer apparatus is shown in Figure 4-14.

Figure 4-14 Measurement of density, compaction level, and water content of the compacted soil by using nuclear densometer

The second and third pipes were backfilled with CLSM up to 70% of their outside diameter. The CLSM was cast from 30% of I.D. to 70% of I.D. one day after the cast of the first CLSM lift. Figure 4-15 illustrates the process of casting the second lift of CLSM for the second and third pipe.

Figure 4-15CLSM was cast for the second and third pipes up to 70% of their outside diameter

The ordinary (native) soil material then was poured and compacted for the remaining of the backfill. Figure 4-16 presents the photograph of ordinary soil. The pipes were then backfilled 1.52 m (5 ft) above their crown.

Figure 4-16 Ordinary (native) soil was compacted as backfill material with the jumping compaction and sheep feet compactor

Figure 4-17 shows the final surface of the trench after completion of the backfilling and compaction of the soil material.

Figure 4-17 Final surface of the trench after completion of the backfilling

In order to model the trench and steel pipe-soil interaction properly, the material properties and the trench configuration dimensions and conditions were obtained during the experiment. The properties of the CLSM were obtained by collecting cylinder and beam samples. Figure 4-18 illustrates a typical CLSM cylinder and the test beam specimen obtained for compressive and tensile strength of the CLSM, respectively.

Figure 4-18 Photograph of typical CLSM specimen for compressive strength test

The properties of the CLSM are reported in Table 4-1.

Table 4-1 Compressive strength of the cast CLSM

Cure Time (days)	1	3	7
Cylinder 1	11.7 kPa (1.7 psi)	377.8 kPa (54.8 psi)	266 kPa (38.6 psi)
Cylinder 2	23.4 kPa (3.4 psi)	387.5 kPa (56.2 psi)	474 kPa (68.7 psi)
Cylinder 3	270 kPa (39.1 psi)	384 kPa (55.7 psi)	451 kPa (65.4 psi)

Also the air content of the CLSM was measured during the experiment, as shown in Figure 4-19.

Figure 4-19 Air content test was conducted on the CLSM material

It should also be noted that the flowability of the CLSM was tested by using the spread test. This test is similar to the slump test for concrete. Figure 4-20 presents a photograph of a typical conducted spread test for the CLSM.

Figure 4-20 Spread test conducted on the CLSM to quantify the flowability of the CLSM

4.2 Finite Element Analysis of the Field Test

As mentioned earlier in this chapter, the field tests were conducted to verify the initial FEM model which was developed by using the soil box test. Moreover, the field tests were used to further modify and complete the developed FEM model to incorporate the long-term effects in addition to implementing as build boundary conditions in the field. This was accomplished by adding backfill materials and in-situ trench wall which are necessary to simulate the real field conditions. The analysis algorithm accommodated the nonlinear material constitutive relationship for soil. The element types and the interface or contact elements between the soil-pipe and soil-soil closely followed those identified in the initial developed FEM. However, the number of iterations needed to obtain the converged solution and the solution path were different due to the changes in the boundary conditions. This section contains the information about the utilized modification for developed FEM model.

4.1.1 Introduction

The soil box tests which were conducted in the CUIRE's facility at UT Arlington were successfully modeled in this study. The finite element model was developed to mimic the exact conditions in the tests. The tests utilized a rigid concrete box and a 1.83 m (72 in.) pipe. Various backfill materials, including ordinary soil, lime-treated soil, and crushed limestone were used in the tests. However, every pipeline will be designed and installed under different conditions: different pipe diameter, trench wall stiffness, trench width, embedment and backfill materials, cover, live load, and trench wall slope. Moreover, the CLSM that will be used as embedment material in different pipelines was not used in the conducted soil box tests. Thus, the modifications were needed to enhance the FEM model with the capability of modeling and analyzing different pipelines in different situations.

To develop the long-term 3-D FEM, some changes were made in the FEM model. The aforementioned changes will be explained and addressed in the current section. Moreover, the developed long-term 3-D nonlinear FEM model will be used to analyze different trench configuration scenarios to conduct the parametric study on the essential pipe design parameters, which will be presented and discussed in Chapter 5.

4.1.2 Required Modifications for the Developed FEM Model

Several modeling modules including loads, boundary conditions, geometry of parts, and materials were modified for the long-term 3-D FEM model. These changes enhancing the finite element model for future analysis of common pipe installation and design. The design program (DP) was developed (Chapter 5) by the researchers in the Center for Structural Engineering Research/ Simulation (CSER), at UT Arlington and was prepared based on the required changes for the long-term 3-D nonlinear model. Thus, the DP requires the parameters to generate the model to be similar to field conditions.

The boundary conditions, including the trench stiffness, were different from the applied boundary conditions in the soil box test. Thus, the trench wall and its stiffness were modeled in the long-term model to simulate the regular field installation. Moreover, the in-situ soil was modeled below the bedding layer. The trench wall and the in-situ soil below the bedding layer were extended so that the stresses due to the pipe installation were dissipated along the extended length. Figure 4-21 shows the new part, which is called “In-situ” soil, in the long-term FEM model and the applied mesh pattern. This part has finer mesh near the trench and coarser mesh in farthest region from the trench.

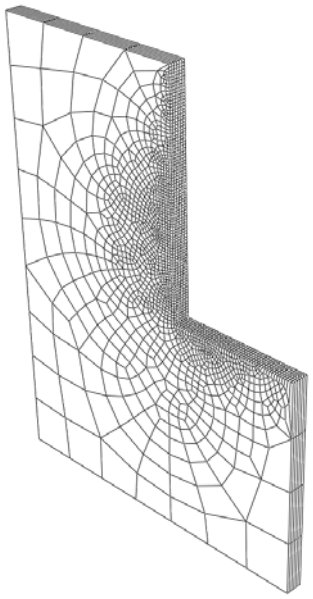

Figure 4-21 In-Situ part is introduced to the long-term FEM model

The interaction between soil layers and the in-situ soil, which was not simulated in the soil box test models, was modeled in the long-term FEM. Thus, the boundary conditions were different from the ones of the soil box test models. The boundary conditions for the soil box test and long-term FEM are shown in Figure 4-22.

The soil box tests were conducted on 1.83 m (72 in.) pipes; however, different pipe diameters will be considered in different projects, including 2.13 m (84 in.), 2.44 m (96 in.), and 2.74 m (108 in.) pipes. Thus, the developed FEM model should be capable of modeling different pipe sizes and different pipe wall thicknesses. Therefore, the model was modified in this task to evaluate different pipe sizes.

The trench width was 3.8 m (150 in.) for the conducted soil box test. However, the trench width is a variable parameter in the pipe design and depends on the in-situ soil, the embedment and the backfill materials, the pipe's diameter, and the height of soil

cover above the crown. Thus, the FEM model was modified to analyze different trench widths.

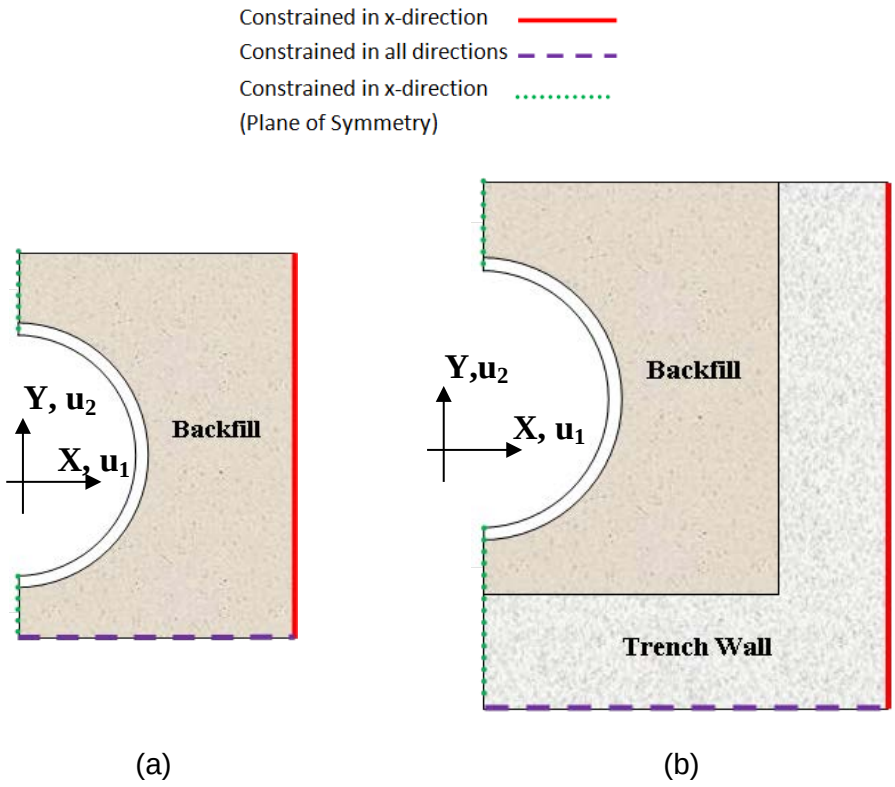

Figure 4-22 Boundary conditions in: (a) soil box test, (b) long-term model

The long-term model developed in this task is capable of modeling different configurations. Furthermore, the capability of modeling gap-filler configuration was added to the DP. Figure 4-23 presents a typical gap-filler configuration. Gap-filler configuration is another trench installation type which is used by designers.

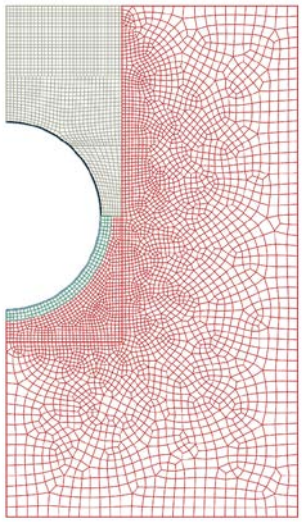

Figure 4-23 Typical gap filler configuration

The walls for the soil box test were vertical; however, the trench wall can be sloped. The FEM model developed in this task was utilized with the ability to model the sloped trench wall, as illustrated in Figure 4-24.

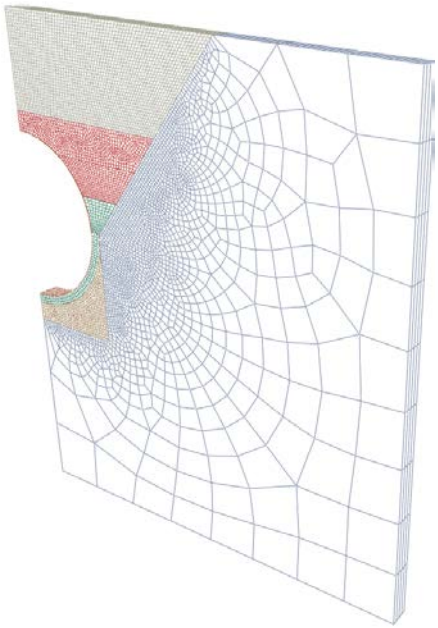

Figure 4-24 The sloped wall trench configuration

The induced lateral effect of compaction also depends on the trench configuration and soil properties. The current modified FEM model, for the first time, considered various effective parameters in the induced lateral effect of compaction. The aforementioned load was applied to the system (pipe and soil) by converting it to the corresponding uniform thermal loading as explained in earlier chapters. The long-term developed FEM model considered different parameters to calculate a proper thermal load to apply on a specific soil layer.

The soil box tests were modeled in the FEM and the pipe's horizontal and vertical deflection were used to verify the model. The FEM model accurately simulated the results of experiments, as explained in Chapter 3. Since the induced lateral effect of the compaction was applied to the system by using uniform thermal load, the amount of thermal load should be calculated for different soil types and trench configurations. To calculate the modified thermal load for different trench configurations, the stiffness of pipe, backfill, and trench was simplified as a system shown in Figure 4-25.

Figure 4-25 Simplified model to derive the thermal load equation

The mechanics of material formulations for springs was used to calculate the temperature required for simulation of the compaction force. It was assumed that there were three (3) springs in series formation in the system to simulate the interaction between the stiffness of the pipe wall, the soil mass, and the trench wall. The total strain of the soil is equal to the strain in the soil due to the thermal loading plus the strain in the soil due to the other two boundary components; pipe and wall, as shown in Equation 4-1.

$$\epsilon_{Soil} = \epsilon_{Thermal\ loading} - \epsilon_{(pipe+Wall)} \quad 4\text{-}1$$

where:

ϵ_{Soil} = Soil strain = $\frac{\sigma_{Soil}}{E_{Soil}}$;

$\epsilon_{Thermal\ loading}$ = Strain in soil due to thermal loading = $\alpha\Delta T$;

$\epsilon_{(pipe+Wall)}$= Strain in the soil due to the pipe and the wall stiffness = $\frac{\Delta_{Pipe}+\Delta_{Wall}}{L_{Soil}}$;

σ_{Soil} = Induced lateral stress in the soil due to compaction;

E_{Soil} = Tangent modulus of elasticity of soil;

α = Coefficient of expansion for soil;

ΔT = Applied thermal load;

Δ_{Pipe} = Pipe's horizontal displacement due to $\sigma_{Soil} = \frac{F_{Pipe}}{K_{Pipe}}$;

Δ_{Wall} = Trench wall's horizontal displacement due to $\sigma_{Soil} = \frac{F_{Wall}}{K_{Wall}}$;

L_{Soil}= Length of the soil layer;

For series springs, the force in all the springs is equal. Therefore,

$F_{Pipe} = F_{Wall} = F_{Soil} = A_{Soil}\sigma_{Soil}$;

A_{Soil} = The surface area of the soil layer (in pipe length direction);

K_{Pipe}, K_{Wall} = Stiffness of the pipe wall thickness and trench wall, respectively.

Substituting aforementioned variables in Equation 4-1, Equations 4-2 through 4-4 were derived.

$$\epsilon_{Soil} = \alpha\Delta T - \frac{\Delta_{Pipe} + \Delta_{Wall}}{L_{Soil}} \quad 4\text{-}2$$

$$\frac{\sigma_{Soil}}{E_{Soil}} = \alpha\Delta T - \frac{1}{L_{Soil}}\left(\frac{A_{Soil}\sigma_{Soil}}{K_{Pipe}} + \frac{A_{Soil}\sigma_{Soil}}{K_{PWall}}\right) \quad 4\text{-}3$$

$$\alpha\Delta T = \sigma_{Soil}\left(\frac{A_{Soil}}{L_{Soil}K_{Pipe}} + \frac{A_{Soil}}{L_{Soil}K_{PWall}} + \frac{1}{E_{Soil}}\right) \quad 4\text{-}4$$

Equation 4-4 was implemented in the developed long-term FEM model, and the thermal loading for any trench configuration and soil material was identified in the model as described above.

Pea gravel was used in the soil box test to represent the surcharge load on the top of the pipe crown. However, the developed program in this task was capable of accommodating different trench heights, trench wall stiffness, and all variables needed during modeling actual field test.

4.3 Results

The developed FEM model in this task was used to simulate the conducted field tests at the Rolling Hills Booster Pump Station, Fort Worth, Texas. Three (3) 2.13 m (84 in.) pipes were instrumented and loaded in different trench configurations. The first and the second pipes were placed in a trench with a trench width of 'inside pipe diameter (I.D.) plus 91.4 cm (36 in.). The trench width for the third pipe was I.D. plus 45.7 cm (18 in.). The backfill material for the first pipe was CLSM up to 30% of I.D. and compacted sand from 30% of I.D. to 70% of I.D. Native soil was compacted up to 30.5 cm (12 in.) above the pipe crown. The second and third pipes were backfilled with CLSM up to 70% of their I.D. Native soil was compacted up to 30.5 cm (12 in.) above the pipe crown. Five (5) feet (1.524 m) of native soil was applied on top of the backfill material to simulate the surcharge load. The field tests were then simulated using the developed FEM model that explained comprehensively in Chapter 3. Figure 4-26 and Figure 4-27 illustrate the comparison of typical results of the field test and the FEM results. The results of the field tests were not presented and explained comprehensively in this dissertation report since it was a part of another thesis (Bellaver, 2013). However, the developed model in Chapter 3 was used to evaluate and verify the developed FEM model in the flexible trench condition. Furthermore, as presented in Figure 4-26 and Figure 4-27 promising

results were obtained during analyzing the field tests. The comparison of the results of the field test and the FEM indicates that the FEM model was successfully predicted the field test configurations.

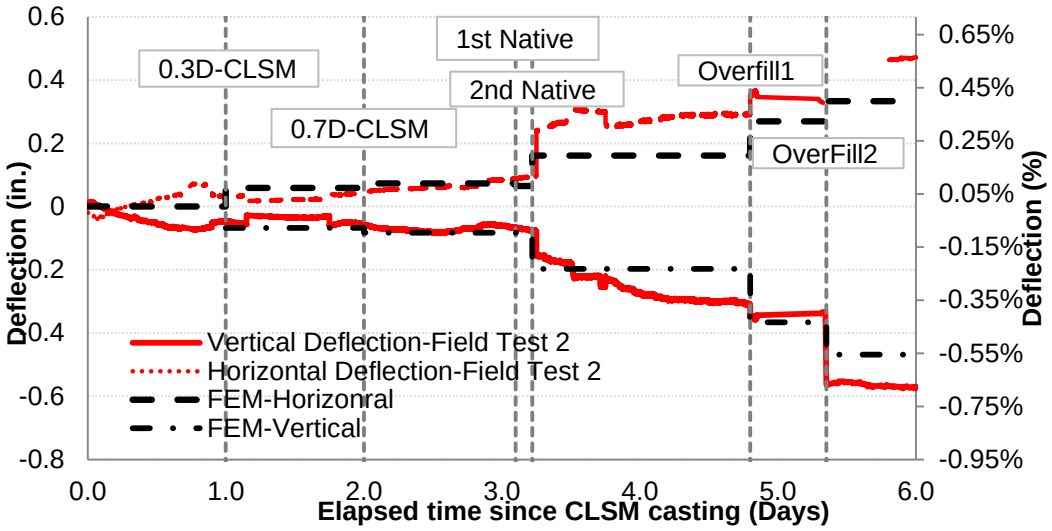

Figure 4-26 Comparison of results of developed FEM in Chapter 3 and results of Field Test 2

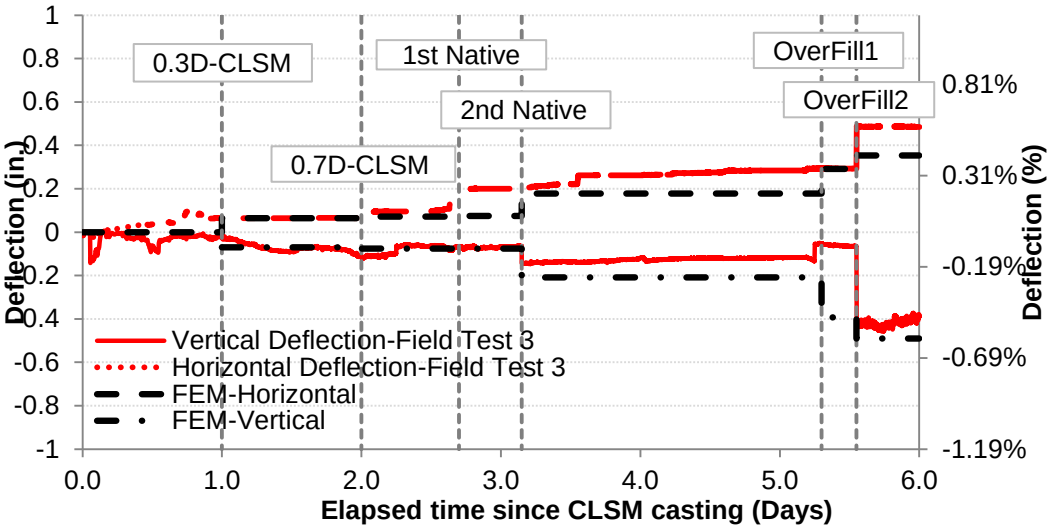

Figure 4-27 Comparison of results of developed FEM in Chapter 3 and results of Field Test 3

Figure 4-28, Figure 4-29, and Figure 4-30 present the FEM results for the moment, the shear force, and the thrust force in the Field Tests 1, 2, and 3, respectively.

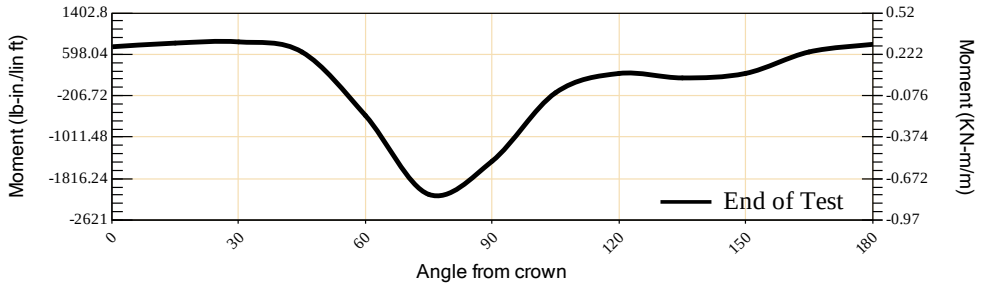

(a)

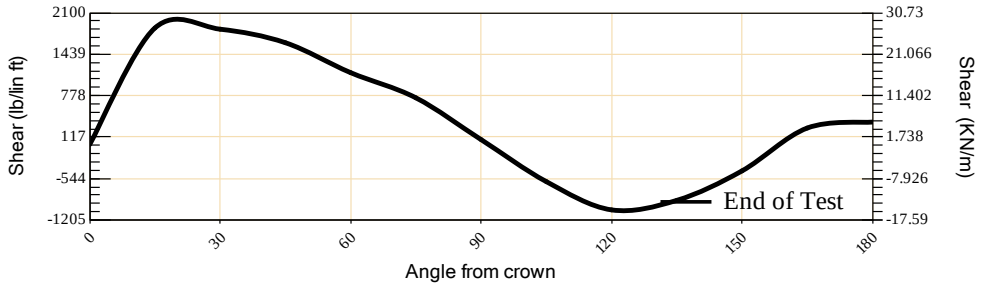

(b)

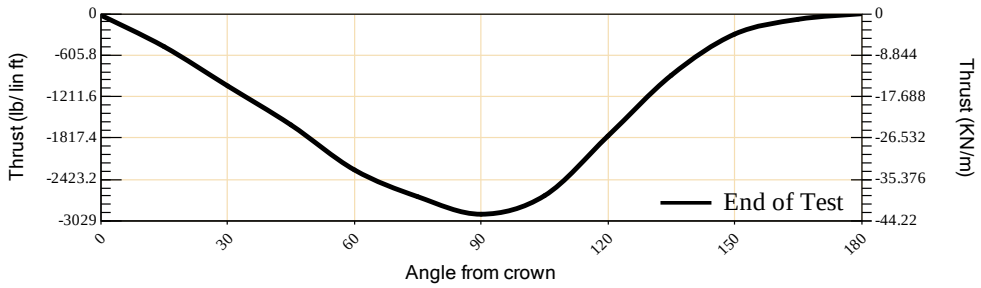

(c)

Figure 4-28 Results from FEM analysis for (a) Moment; (b) shear force in pipe wall; (c) thrust force of the Field Test 1

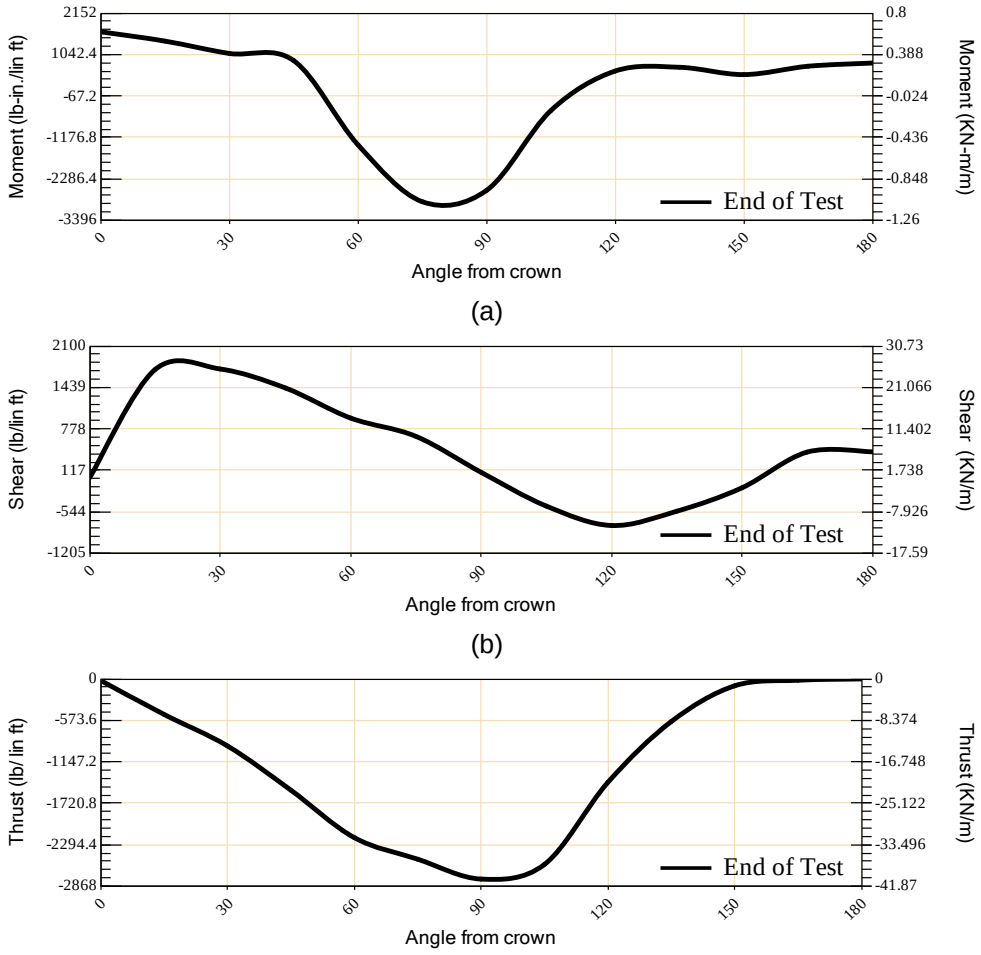

Figure 4-29 Results from FEM analysis for (a) Moment; (b) shear force in pipe wall; (c) thrust force of the Field Test 2

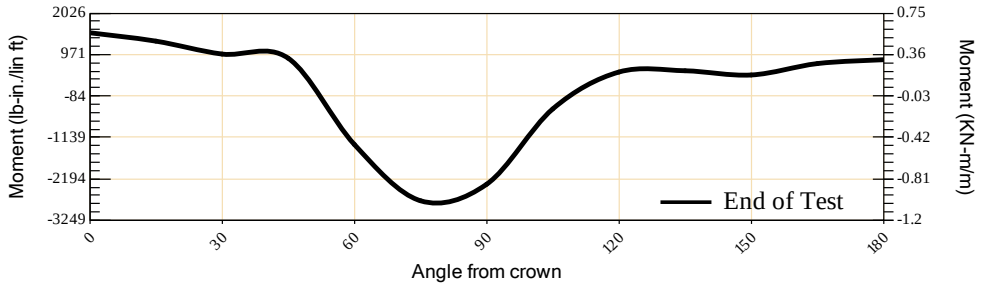

(a)

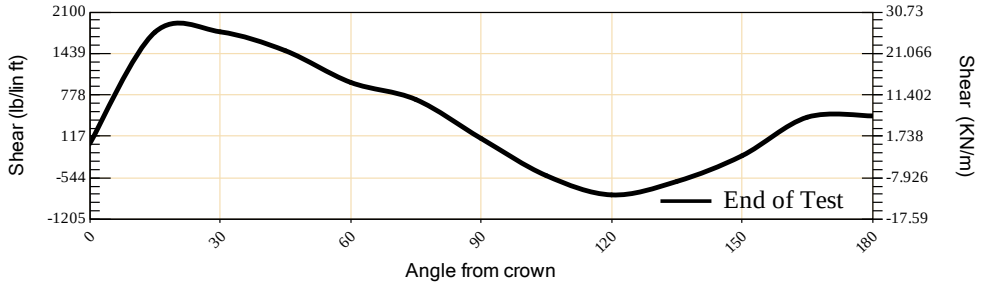

(b)

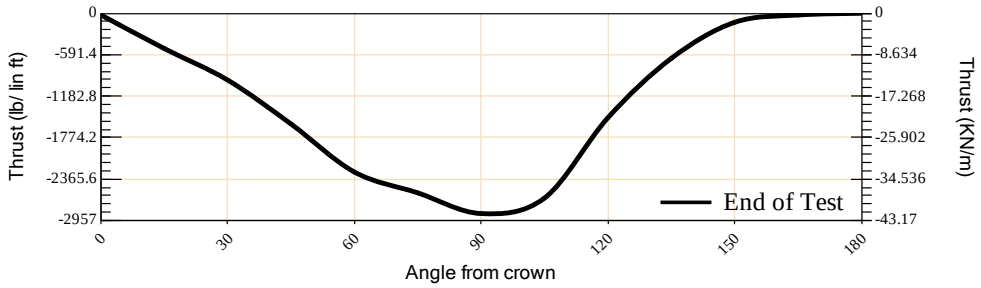

(c)

Figure 4-30 Results from FEM analysis for (a) Moment; (b) shear force in pipe wall; (c) thrust force of the Field Test 3

As illustrated in Figure 4-28 through Figure 4-30 the moment magnitude is high when the trench width is narrower, i.e. the moment results for Field Test 2 is maximum since the trench width was minimum for this field test while Field Test 3 has the second highest moment and the Field Test 1 has the lowest moment value. However, since the

backfilling stiffness for Field Test 1 was the lowest among the conducted tests, the thrust force value is the maximum for this test.

4.4 Conclusion

Three (3) field tests were designed and conducted with different backfilling configurations. Three (3) 2.13 m (84 in.) pipes were used to study the effect of stage construction. The developed FEM model was further modified to utilize the model with the real condition of the pipeline. The flexible trench wall was added to the developed FEM model. Furthermore, the compaction equation was derived to accommodate different backfilling configuration along with various trench widths, trench wall stiffness and different pipe wall stiffness. The CLSM material was used to backfill some portion of pipe in different field tests cases. Then the deflection results of the field tests were compared with the results of developed FEM model. The comparison of the results indicates that the modified FEM model in this chapter is capable of predicting the deflection of the buried steel pipes in different backfilling and trench configuration. The results and the modification of Chapter 4 were used to automate the creation of the FEM model for different steel pipeline configurations. The developed FEM model also was used to develop a unique design program to generate different pipe-soil interaction system models in a fraction of time when compared to conventional manual method of generating models.

Chapter 5

Parametric Study

The essential modeling parameters for designing a steel pipe were identified. The pipe diameter and wall thickness, trench wall stiffness, backfill material, soil cover above the pipe, and trench width are among the essential parameters which are included in this study. The parametric study of this research is concentrated on the native, treated soil, and select fill backfill material. CLSM was not considered as a part of parametric study. Figure 5-1 presents the flow chart for the conducted study for sensitivity study on essential design parameters.

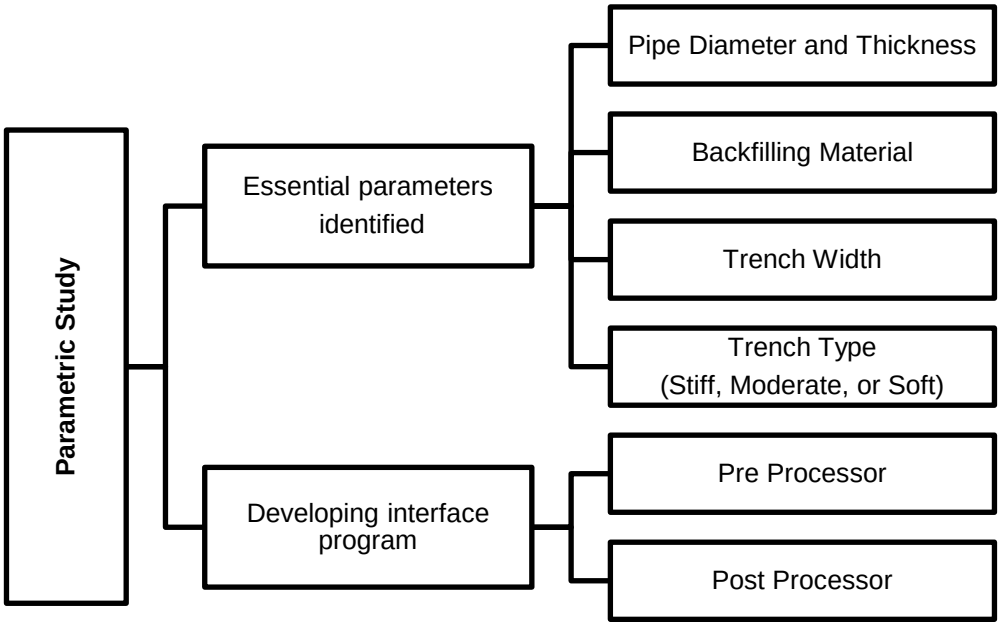

Figure 5-1 Framework of the conducted parametric study

Thus, the parametric study was designed based on the essential designing parameters. However, as shown in Figure 5-2, approximately 800 models were considered among the cases for parametric study which is not included the CLSM or gap filler backfilling.

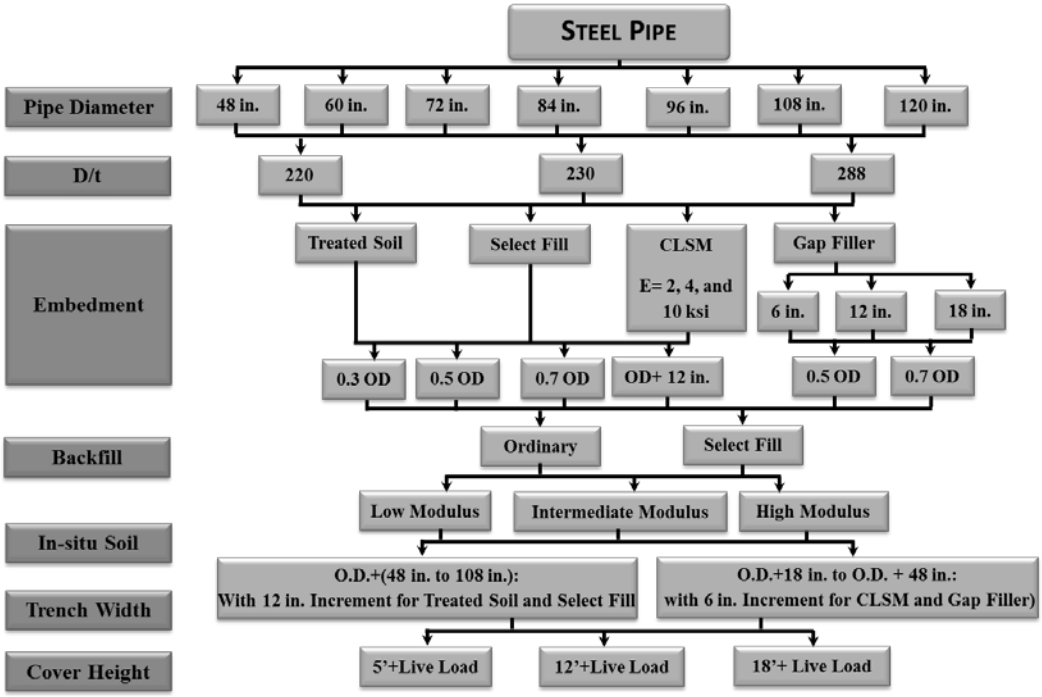

Figure 5-2 Flow chart of the essential parameters

Generating the mesh for these models is a time-consuming procedure and also errors may happen during creating and generating each mode. Thus, a pre-processor program which is called Design Program (DP) in this research was developed. Furthermore, analyzing the generated mesh was conducted automatically by a python program which was prepared for this purpose. Moreover, preparing the desired graphs for design for each parametric case is also very critical and needs a significant amount of time. A designer would need a moment, shear, thrust, and deflection graph for designing a pipe. Thus, a post-processor was developed to extract the data from analyzed FEM models required to generate the graphs at different stages of construction. Figure 5-3 illustrates the diagram of interaction between a designer and the DP and the post-processor.

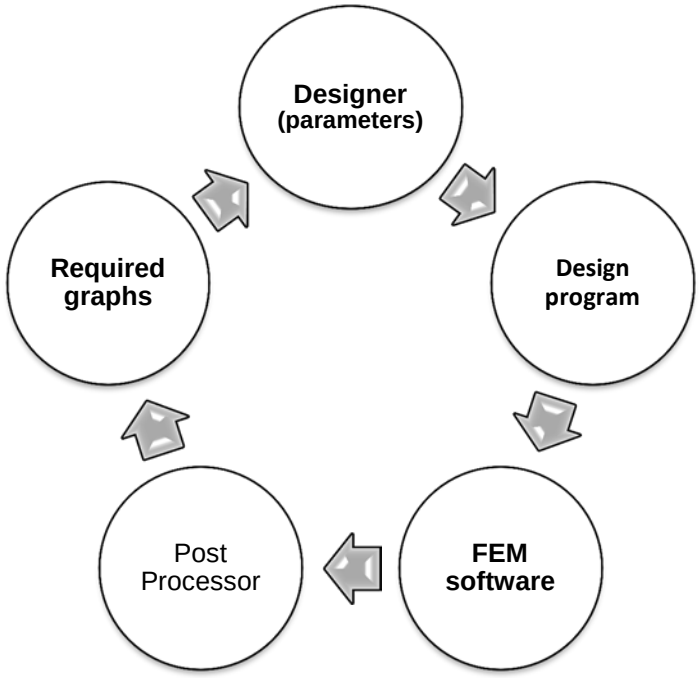

Figure 5-3 Diagram of interaction between a designer, developed Design Program, and 3D-FEM model

5.1 Pre-Processor

The Design Program (DP) was developed using a C# programming language that produces Python scripts for different trench configurations. The Python script was imported into the finite element software for the analysis purpose. Figure 5-4 shows the interface of the DP.

Table 5-1 presented some of the important properties that should be provided by a user for the DP.

Table 5-1 The required input parameter sheet

Input Parameter		Input Value
Pipe Diameter (in.)		
Pipe Diameter/Pipe Wall Thickness		
Trench Width (in.)		
Bedding	Material	
	Thickness	
	Modulus of Elasticity (psi)	
	γ (pcf)	
	Poisson's Ratio	
	Compressive Strength (For CLSM)	
	C (psi) (For Soil)	
	φ (For Soil)	
Embedment Material	Height Material Gap Filler Configuration? Modulus of Elasticity (psi) γ (pcf) Poisson's Ratio Compressive Strength (For CLSM) C (psi) (For Soil) φ (For Soil) Thickness of Gap Filler (in.)	
Backfill Material	Height Material Modulus of Elasticity (psi) γ (pcf) Poisson's Ratio C (psi) φ	
In-situ Material	Material Modulus of Elasticity (psi) γ (pcf) Poisson's Ratio C (psi) φ	
Trench Wall Slope	Slope Starting Point of Sloped Face	
Cover Height	Material γ (pcf) Height Live Load	

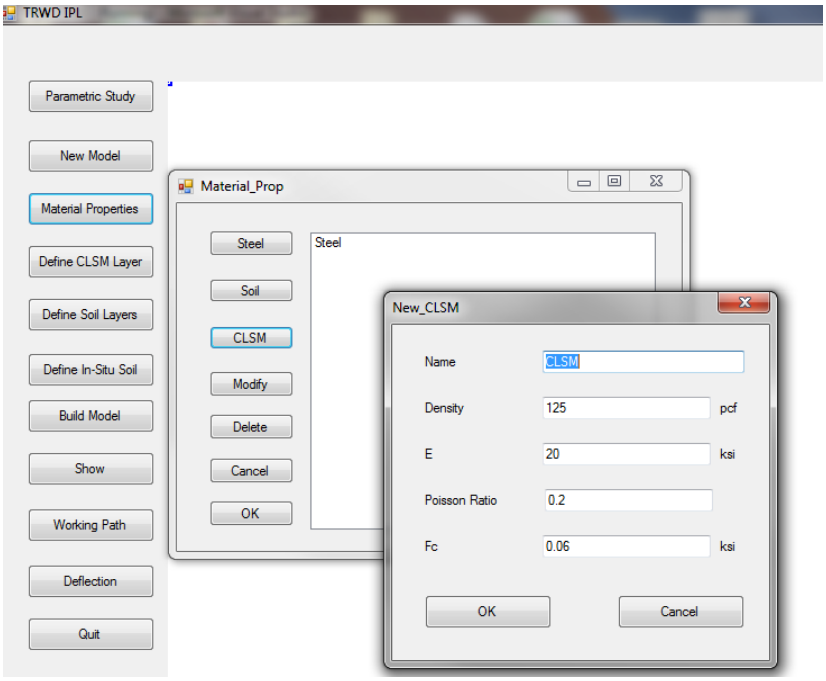

Figure 5-4 Interface of the Design Program

Moreover, in order to create the models for the parametric study, an option was added to the DP to prevent some of the repeating procedures. Thus, some of the parameters were pre-defined in the DP to ease the process of creating the models. Figure 5-5 illustrates the interface of the DP in order to create the parametric study models. It should be noted that the prepared Python code will then feed to the finite element software.

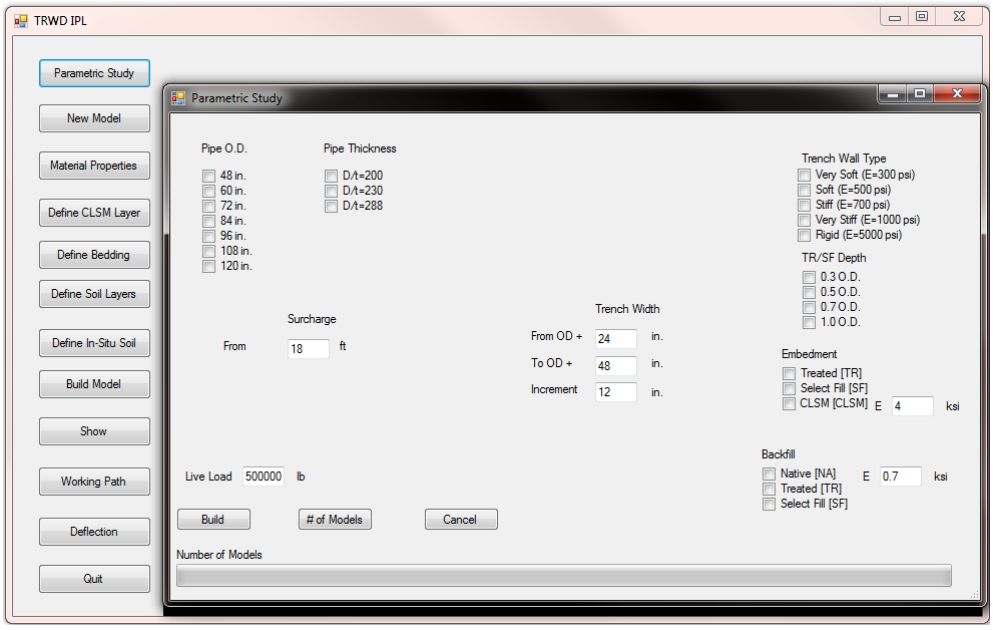

Figure 5-5 Interface of the Design Program for parametric study

Another Python code was prepared to make a queue of the generated models to analyze them. The DP will designate a proper name to each generated mesh which is an indicative of the properties of the trench configuration and pipe. A typical designated name for each configuration is shown below:

“Param-48-PW200-SF3OR-OD+48-EW3-H5-LiveLoad”

The designated name has eight parts. The first part shows that the model belongs to parametric study analysis. The second part which is a number showing the inside diameter of the pipe in inches. The next part determines the pipe wall thickness. This part shows the ratio of the pipe diameter over the pipe wall thickness. For example PW200 means that the pipe diameter/pipe wall thickness is 200. The fourth element in the designated model name determines the embedment and backfilling material and their depth. For example, as shown above, select fill (SF) was used up to 30 percent of the pipe diameter as the embedment material and then the pipe was backfilled with the

native soil (OR) up to 1 ft above its crown. For the case of treated soil, TR is used as the abbreviation. If we have treated soil or select fill to the top of the pipe, the designated name would be TR10TR and SF10SF, respectively. In the parametric study the native soil was not used as the embedment material as the native soil was not stiff enough. The next term in the designated name is the trench width, i.e. OD+48 means that the trench width equals to OD plus 48 inches. The sixth part in the model name is the type and stiffness of the trench wall soil. In the abovementioned example, EW3 means that the trench wall is flexible and its modulus of elasticity is E_w = 300 psi. The next part in the name determines the height of the ordinary soil above the pipe crown. Thus in this example five feet of the ordinary soil was modeled on top of the crown. The last part of the name shows that whether the live load is applied on top of the soil cover or not. Here in this study a load of a 136-ton (150-ton in US unit) crane was applied on the live load foot print of the crane. Figure 5-6 shows the 136-ton (150-ton in US unit) crane.

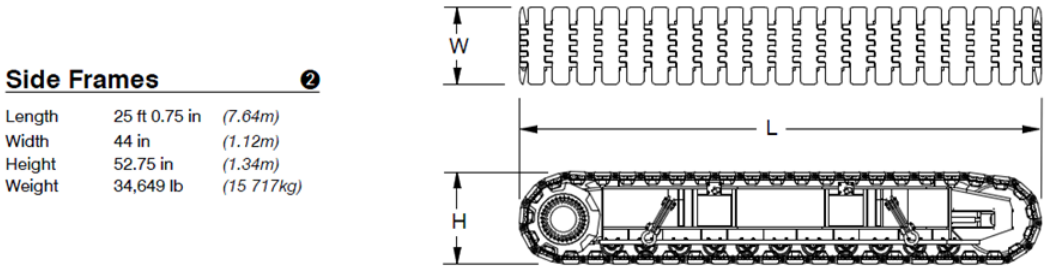

Figure 5-6 The load and weight of a 136-ton (150-ton in US unit) crane was applied on its foot print as live load (Technical data for 238 crawler crane)

A study was conducted to determine the critical location of applied live load. The results of the conducted study, which is shown in Figure 5-7, indicated that the center line of the pipe is the critical location. Furthermore, Figure 5-7 shows that for the higher soil cover the effect of live load is less than those of for smaller soil cover. For example for 3.66 m (12 ft) soil cover applying load in different location from center line has almost the

same effect. Thus, as shown in Figure 5-8, the live load was applied on the center line of the pipe.

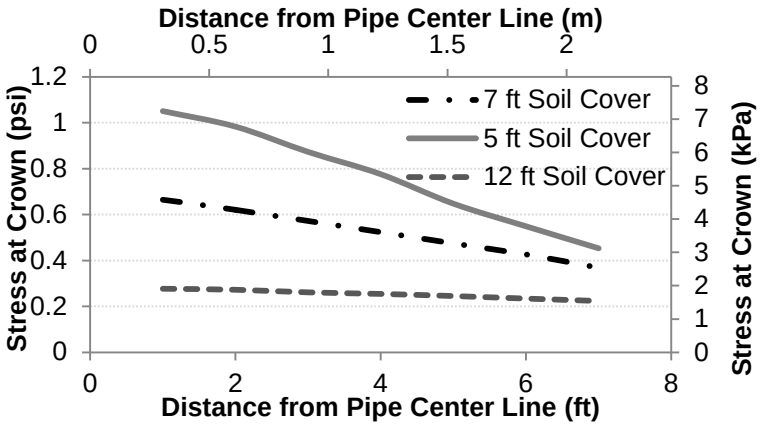

Figure 5-7 The results of conducted study on the effect of location of applying live load

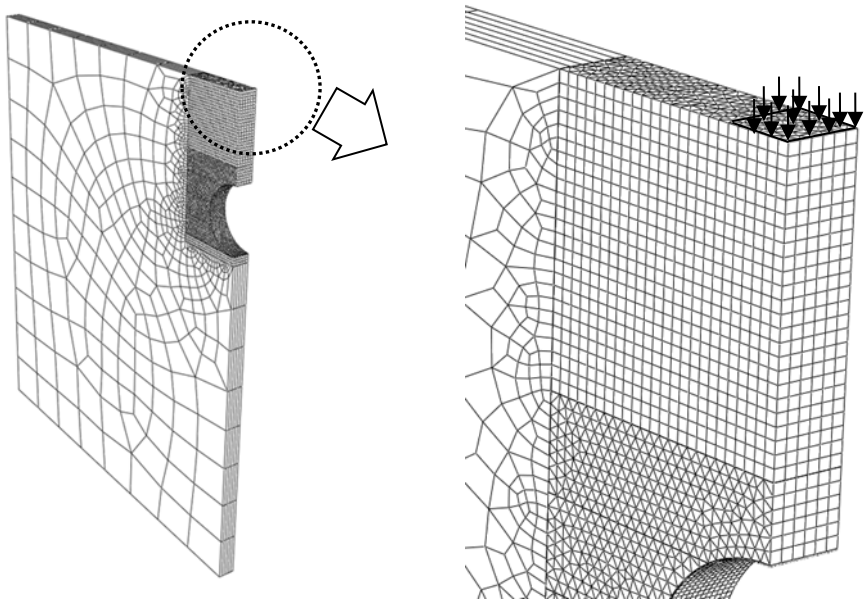

Figure 5-8 Live load was applied on the center line of the pipes

5.2 Post-Processor

A Python code was prepared to extract the required data once the analysis is completed. In order to find and calculate pipe deflected shape and the moment, thrust, and shear forces in the pipe, two circular paths were defined along the pipe circumference; one path on the inner wall and the other one on the exterior wall, as shown in Figure 5-9. The information of every 61 points on the half of the pipe (every 3 degrees) then is obtained along each of the paths which are shown by dots in Figure 5-9

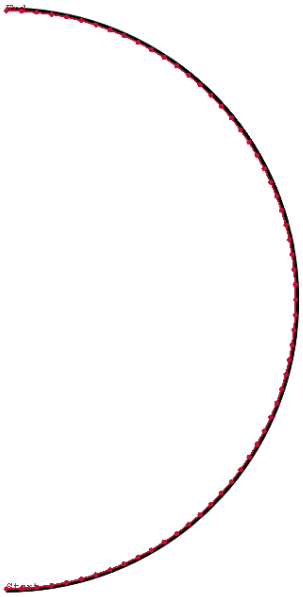

Figure 5-9 Two circular paths were defined to extract the pipe data by using post-processor

In order to calculate the moment at each section, three global stresses were obtained at each point; including σ_{xx}, σ_{yy} , and σ_{xy}. Then by using Equation 5-1 the tangential and normal stresses at each point were calculated (local stresses).

$$\begin{bmatrix}\sigma_{XX}\\ \sigma_{YY}\\ \sigma_{XY}\end{bmatrix} = \begin{bmatrix}\cos^2\theta & \sin^2\theta & 2\sin\theta\cos\theta\\ \sin^2\theta & \cos^2\theta & -2\sin\theta\cos\theta\\ -\sin\theta\cos\theta & \sin\theta\cos\theta & (\cos^2\theta-\sin^2\theta)\end{bmatrix}\begin{bmatrix}\sigma_{xx}\\ \sigma_{yy}\\ \sigma_{xy}\end{bmatrix} \quad 5\text{-}1$$

Figure 5-10 illustrates the definition of different terms in Equation 5-1.

Also five linear paths were defined two obtain the soil stress including vertical pressure below and above the pipe; and horizontal pressure near the pipe, near the trench wall, and between the pipe and the trench wall.

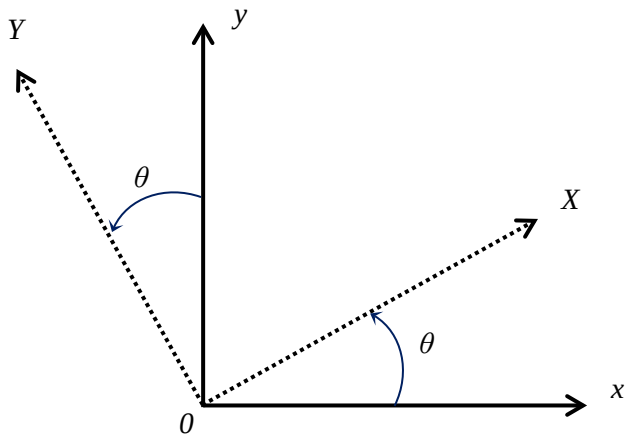

Figure 5-10 Definition of global (x-y)axis, local (X-Y) axis, and θ

The exterior stress is called σ_{top} and the interior normal stress is called σ_{bottom}. As explained in Chapter 2 (Figure 2-4), the total stress can be divided into two different stresses; thrust (ring compression or hoop) and bending stress. In order to calculate the moment in each section, Equation 5-2 will be used. The unit for the calculated moment is kN-m/linear m (Kip-in./linear ft).

$$M = \underbrace{12}_{model\ length} \times \underbrace{\sigma_{bottom-bending} \times \frac{t}{4}}_{area\ under\ stress\ graph} \times \underbrace{\frac{2t}{3}}_{moment\ arm}$$

$$M = 2\sigma_{bottom-bending} \times t^2 \qquad 5\text{-}2$$

Where:

t= pipe wall thickness

$\sigma_{bottom-bending}$= the bending part of the σ_{bottom}

Equation 5-3 will be used to calculate thrust at each location. The unit of calculated thrust is kN/linear m (Kip/linear ft).

$$Thrust = \underbrace{12 \times t}_{area} \times \underbrace{\sigma_{hoop}}_{hoop\ stress} \quad 5\text{-}3$$

Finally, Equation 5-4 will be used to calculate the shear at each location with the unit of kN/linear m (Kip/linear ft).

$$Shear = \underbrace{12 \times t}_{area} \times \sigma_{shear} \quad 5\text{-}4$$

Where:

σ_{shear} = local (X-Y coordinate system) shear stress in pipe interior wall

Figure 5-11 illustrates a typical output result from finite element analysis software for moment, shear, and thrust for different predefined sections along the pipe, which is another method of obtaining the desired results along the pipe.

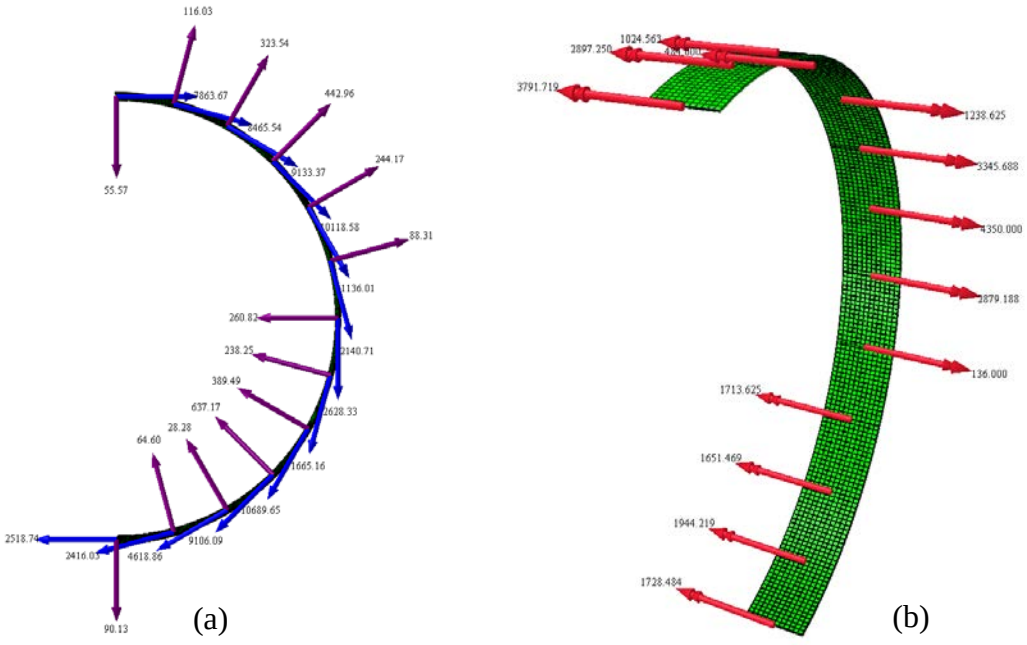

Figure 5-11 A typical results for (a) shear and thrust; (b) moment obtained from FEM a different predefined sections

5.3 Development of the Design Equations

5.3.1 Basis of Regression Analysis

Regression equations were developed from sample data obtained from numerous FEM analyses conducted, to determine the values of the response parameters for predetermined values of independent parameters. However, the finite element analysis is not a physical experiment in true sense; it is an analytical process for experiments. This is because the results for each case are completely deterministic and reproducible.

To perform the regression analysis, it is common procedure to represent the response of dependent or response variable as a function of the independent variables. In this study, the five dependent parameters of the pipe were measured as functions of the independent parameters. These independent parameters for the 682 cases selected, as presented in Table 5-2, were the input data to the developed design program, which eventually were analyzed and the response variables including horizontal and vertical deflections, shear force, thrust, and moment were obtained. Thus, the objective of the regression analysis was to develop equations for the response variables in two different stages of loading; after applying the final soil cover, and after applying live load on pipe-soil system. For example, Equation 5-5 would be the form of the equation which is a function of certain parameters:

$$f = f(OD, t, \alpha, E_{embed}, \beta, E_{back}, \sigma_{soil}, W_{trench}, E_{wall}, p) \qquad 5\text{-}5$$

Equation 5-6 would be assumed as the general function for the regression analysis.

$$y = f(X_1, X_2, X_3, \ldots\ldots\ldots\ldots X_n) \qquad 5\text{-}6$$

In Equation 5-6, y is a function of n independent or response variables intended to fit data collected from a study. A linear (or summation) regression model for the function is written as Equation 5-7 (Draper, 1966).

$$y = C_0 + C_1X_1 + C_2\ X_2 + C_3X_3 + ... + C_nX_n + C_{12}X_1X_2 + C_{23}X_2X_3 + ... + C_{n1}X_nX_1 + C_{123}X_1X_2X_3 + ... + C_{123...n}(X_1X_2X_3...X_n) \quad 5\text{-}7$$

Table 5-2 Independent variables for the conducted regression analysis

Independent variable	Description
OD	Pipe diameter, ft
t	Pipe wall thickness, in.
α	Ration of embedment material to pipe diameter
E_{embed}	Modulus of elasticity of embedment material, ksi
β	Ration of backfilling material to pipe diameter (if $\alpha = 1$ the value for β should assume to be 1)
E_{back}	Modulus of elasticity of backfilling material, ksi (if $\alpha = 1$ the value for E_{back} should assume to be E_{embed})
W_{trench}	Width of trench, ft
E_{wall}	Modulus of elasticity of in-situ soil, ksi
p	Pressure due to soil cover, pcf

These techniques yield information on the relative significance of not only the main parameters X_1, X_2,…, X_3 but also the interactions between the same parameters X_1X_2, $X_1X_2X_3$,…, ($X_1X_2…X_n$). However, in most practical problems, such as the one

studied, many of the higher-order interactions may be eliminated on the basis of physical and intuitive considerations. Probable interactions must, however, be included in the model. There are many parameters that can be considered in an analytical study and regression analysis. For example, pipe diameter, pipe wall thickness, backfilling properties, trench width, in-situ soil (trench wall), surcharge load, transient load, and applied compaction load for backfilling can be factors contributing to the pipe responses. This possibility makes this type of an analytical study and regression analysis a complex and interesting study, but does not facilitate the complete defining of all the interactions.

If a linear regression model is not found satisfactory, an alternative method is the product regression model as presented in Equation 5-8.

$$y = C_0 X_1^{C_1} X_2^{C_2} \cdots X_n^{C_n} \quad \text{5-8}$$

This nonlinear regression method was used in this project because of the complexity of the interactions involved. This may be reduced to a linear regression model if the logarithms are taken off from both sides as shown in Equation 5-9:

$$\ln y = \ln C_0 + C_1 \ln X_1 + C_2 X_2 + ... + C_n \ln X_n \quad \text{5-9}$$

Equation 5-9 would be re-written as Equation 5-10 by denoting the logarithms of the various parameters by prime superscripts.

$$y' = C_0' + C_1 X_1' + C_2 X_2' + ... + C_n X_n' \quad \text{5-10}$$

Equation 5-10 is similar to the linear terms in Equation 5-7. It should be noted that in Equation 5-10, product terms of the form X_1', X_2', X_3' etc., do not occur, so no interactions are present.

In this study, the coefficient C_0' and the exponents $C_1, C_2, \cdots, C_n$ in Equation 5-10 are determined by multiple regression analysis, so as to obtain the best least square fit to the data. With this method, the best fit regression equation is taken as the one which

minimizes the sum of the squares of the deviations of the data points from the equation fit to the data. However, another series of regression equations were developed by assuming not intercept for Equation 5-10 which indicated that the $C_0 = 1$. This part was conducted because the powers in the equations with intercept were small. Moreover, the goodness of fit for equations without intercept were not as good as the ones for the equations with intercept. To demonstrate the basic principles, say that the value of the response variable predicted from the best fit equation is y_i', for any particular set of values, $X_{1i}', X_{2i}', X_{3i}', \cdots, X_{ni}'$, while it is measured (or directly determined) that the value is $\overline{y}_i{}'$. Deviation of the predicted value from the measured value is given by Equation 5-11.

$$\overline{y}_i{}' - y_i' = \overline{y}_i{}' - (C_0' + C_1 x_{1i}' + C_2 x_{2i}' + \cdots + C_n x_{ni}') \quad 5\text{-}11$$

The sum of the squares, ∑ for n number of data is presented in Equation 5-12.

$$\Sigma = \sum_{i=1}^{n} \left(\overline{y}_i{}' - y_i'\right)^2 \quad 5\text{-}12$$

The unknown coefficients $C_0', C_1, C_2, \cdots, C_n$ are determined by minimizing the quality ∑ with respect to each coefficient; in other words, by setting it equal to zero, as shown in Equation 5-13.

$$\frac{\partial \Sigma}{\partial C_0'} = \frac{\partial \Sigma}{\partial C_1} = \frac{\partial \Sigma}{\partial C_2} = \cdots = \frac{\partial \Sigma}{\partial C_n} = 0 \quad 5\text{-}13$$

This will result in (n+1) linear simultaneous equations from which the coefficients $C_0', C_1, C_2, \cdots, C_n$ would be determined. To determineC_0, the anti-logarithm of C_0' must be found.

There are several methods to show a “goodness of fit” of the prediction equation including the coefficient of determination (R^2) and Pearson's chi-squared test (Chernoff, 1954). The coefficient of determination (R^2) is a useful statistic to show a goodness of a fit. In regression analysis, the response variables, $\overline{y}_i{}'$, are directly obtained while the

regression equation will predict the value of the response variable, y_i'. Equation 5-14 presented the average of the obtained value for n observations.

$$\overline{y} = \frac{\sum_{i=1}^{n} \overline{y}_i{}'}{n} \qquad 5\text{-}14$$

Where;

n= number of observations

$\overline{y}_i{}'$= obtained value for i^{th} observation

$\overline{y}$= average of n observations

Different sums of squares (SS) are defined to measure variability of the data set. If the independent variables are ignored, the total variability of the $\overline{y}_i{}'$ observations is called the total sum of squares (SS_{Tot}) as shown by Equation 5-15.

$$SS_{Tot} = \sum_{i=1}^{n} \left(\overline{y}_i{}' - \overline{y}\right)^2 \qquad 5\text{-}15$$

The regression sum of squares (SS_{Reg}) is the variability that is explained by the regression model and is presented in Equation 5-16. (Neter, 1996)

$$SS_{Reg} = \sum_{i=1}^{n} (y_i' - \overline{y})^2 \qquad 5\text{-}16$$

The unexplained variability is defined as error some of squares (SS_{Res}). Equation 5-17 presents the formula to calculate SS_{Res}.

$$SS_{Res} = \sum_{i=1}^{n} \left(\overline{y}_i{}' - y_i'\right)^2 \qquad 5\text{-}17$$

The coefficient of multiple determination, R^2 is defined by the Equation 5-18.

$$R^2 = 1 - \frac{SS_{Res}}{SS_{Tot}} \qquad 5\text{-}18$$

A value of R^2=1 implies that the regression prediction equation passes through all the data points. A value of R^2=0.95 means that 95 % of the sum of squares of the

deviations of the observed (or directly determined) $\overline{y}_i{}'$ values about their y_i' can be explained by the prediction equation obtained.

In the parametric study conducted, all the cases considered had the independent parameters inputted into the developed finite element model, and the output was the response of the dependent parameters. The coefficient of multiple determination, R^2 was the unique criterion used to measure the accuracy of the prediction equations to characterize the behavior of the buried pipe.

Pearson's chi-squared test is another method to test a goodness of a fit. This method establishes if an observed dependent variable, $\overline{y}_i{}'$, defers from the value which is predicted by regression equation, y_i'. For this method, a value of chi-squared tests statistic, χ^2, is calculated by using Equation 5-19.

$$\chi^2_{cal} = \sum_{i=1}^{n} \frac{\left(\overline{y}_i{}' - y_i'\right)^2}{y_i'} \qquad 5\text{-}19$$

Then χ^2_{cal} value should be compared with the χ^2_{table} for the desired α and the degree of freedom (df) of the regression (Peaeson et al., 1976). The tables for χ^2 do not include the df above 100. For df>100 the Wilson-Hilferty formula as shown in Equation 5-20 should be used (Wilson et al., 1931).

$$\chi^2 = n\left(1 - \frac{2}{9n} + z\left[\frac{2}{9n}\right]^{\frac{1}{2}}\right)^3 \qquad 5\text{-}20$$

In Equation 5-20, z is the appropriate normal deviate for the required tail area (α). The value for z at different level of probability is shown in Table 5-3.

Table 5-3 Value of z for Equation 5-20

Tail (α)	0.1	0.05	0.025	0.01	0.005	0.001
z	1.2816	1.6449	1.9600	2.3263	2.5758	3.0902

Moreover, if the calculated value for chi-squared, χ^2_{cal} is less than the value of chi-squared from table for the specified number of data points and confidence level, the hypothesis of goodness of fit is accepted otherwise the fit is not good.

Therefore, in this study both methods were utilized to verify the goodness of developed equations.

5.3.2 Design Equations for Buried Steel Pipe

Ten (10) empirical equations are obtained for the horizontal and vertical deflection, moment, thrust, and shear stress in pipe in two (2) different stages of construction; after completion of backfilling, and after applying a transient load by conducting regression analyses. This is accomplished by multiplication of the undetermined powers for all the independent parameters described in Table 5-2. It simply implies that the changes in these geometric parameters are independent to each other (independent variables), thus, they are independent variables. The aforementioned empirical equations as well as the coefficients of determination (R^2) and chi-squared test are presented in this section.

5.3.2.1 Design Equations with Intercept

As mentioned earlier in this chapter, two (2) sets of equations were developed by using regression analysis. The first sets of equations which have the intercept are presented in this part. Equations 5-21 through 5-25 are the equations for the stage of completion of backfilling and soil cover and Equations 5-26 through 5-30 for the stage in which the live load was applied.

It should be noted that the outlier data were removed for each set of equation by using statistical methods including cook's distance, studentized residuals, hat diagonals, Dffits, and DFbetas. Also the F- and t- tests were conducted to examine the significance of the regression and the significance of each independent variable, respectively.

The prediction equations with intercept for soil cover stage are:

Horizontal deflection, soil cover stage (Δx_{SC}):

- Criteria for Goodness of fit

1) R^2=0.9439

2) Chi-squared test: $\chi^2_{cal} = 67.32 < \chi^2_{table}(n = 608, \alpha = 0.05) = 666.466$

Table 5-4 ANOVA table for the Δx_{SC} with intercept

Source	DF	Sum of Squares	Mean Square	F Value	$P_r > F$
Model	8	746.23919	93.27990	1260.37	<.0001
Error	599	44.33178	0.07401		
Corrected Total	607	790.57097			

Root MSE	0.27205	**R^2**	0.9439
Dependent Mean	-0.05105	**R_a^2**	0.9432
Coeff Var	-532.95259		

Table 5-4 presents the ANOVA table for the developed equation. The conducted F-test indicates that the regression is significant.

Table 5-5 presents the estimate value for each independent parameter. Also the F-test was conducted for each parameter estimate, as shown in

Table 5-5. Two variables (α and β) are not significant according to this test but since the variance inflation value for these two parameters is less than 5 (last column in Table 5-5) the parameters were not removed from the equation.

The Pearson correlation coefficient for this equation is presented in Table 5-6. This coefficient indicates the correlation between different parameters. The values above 0.7 (not on the diagonal of the matrix) should be considered as high correlation. In this equation two parameters (T_{width}/OD and OD×t) has the absolute value of 0.741 which is above 0.7. Thus, these two parameters should be considered as highly correlated.

Table 5-5 The values for the coefficient of the estimators for the Δx_{SC} with intercept

Variable	DF	Parameter Estimate	Standard Error	t Value	$P_r > \|t\|$	Variance Inflation
Intercept	**1**	-0.49316	0.08563	-5.76	<.0001	0
OD×t	**1**	1.39655	0.02303	60.63	<.0001	2.68051
α	**1**	-0.04091	0.02890	-1.42	0.1575	1.11556
E_{embed}	**1**	-0.16791	0.02027	-8.28	<.0001	1.01788
β	**1**	-0.03042	0.02783	-1.09	0.2748	1.11417
E_{back}	**1**	-0.11648	0.00892	-13.05	<.0001	1.13425
T_{width}/OD	**1**	-0.92239	0.06677	-13.81	<.0001	2.22248
E_{wall}	**1**	-0.29308	0.02315	-12.66	<.0001	1.00934
p/OD	**1**	0.68246	0.02137	31.94	<.0001	1.50146

Table 5-6 Pearson correlation coefficient for the Δx_{SC} with intercept

	OD×t	α	E_{embed}	β	E_{back}	T_{width}/OD	E_{wall}	p/OD
OD×t	1.000	-0.059	0.016	0.011	-0.032	-0.741	-0.000	-0.572
α	-0.059	1.000	-0.001	-0.196	0.203	0.040	-0.016	0.021
E_{embed}	0.016	-0.001	1.000	0.009	-0.120	-0.022	0.024	-0.011
β	0.011	-0.196	0.009	1.000	0.202	0.005	0.008	0.029
E_{back}	-0.032	0.203	-0.120	0.202	1.000	0.027	-0.030	0.041
T_{width}/OD	-0.741	0.040	-0.022	0.005	0.027	1.000	0.012	0.438
E_{wall}	-0.000	-0.016	0.024	0.008	-0.030	0.012	1.000	0.071
p/OD	-0.572	0.021	-0.011	0.029	0.041	0.438	0.071	1.000

$$\Delta x_{SC}(in.) = e^{-0.49}\,(OD \times t)^{1.4}(\alpha)^{-0.17}(E_{embed})^{-0.03}(\beta)^{0.02}(E_{back})^{-0.12}\left(\frac{W_T}{OD}\right)^{-0.92}(E_w)^{-0.29}\left(\frac{p}{OD}\right)^{0.68} \quad \text{5-21}$$

Vertical deflection, soil cover stage (Δy_{SC}):

- Criteria for Goodness of fit

1) R^2=0.9300

2) Chi-squared test: $\chi^2_{cal} = 77.04288 < \chi^2_{table}(n = 615, \alpha = 0.05) = 673.7921$

Table 5-7 ANOVA table for the Δy_{SC} with intercept

Source	DF	Sum of Squares	Mean Square	F Value	$P_r > F$
Model	8	796.33033	99.54129	1006.73	<.0001
Error	606	59.91888	0.09888		
Corrected Total	614	856.2492			

Root MSE	0.31445	**R^2**	0.93
Dependent Mean	-0.0797	**R_a^2**	0.9291
Coeff Var	-394.57		

Table 5-7 presents the ANOVA table for the developed equation. The conducted F-test indicates that the regression is significant. Table 5-8 presents the estimate value for each independent parameter. Also the F-test was conducted for each parameter estimate, as shown in Table 5-8. One variable (α) is not significant according to this test but since the variance inflation value for this parameter is less than 5 (last column in Table 5-8) the parameter was not removed from the equation.

The Pearson correlation coefficient for this equation is presented in

Table 5-9. This coefficient indicates the correlation between different parameters. The values above 0.7 (not on the diagonal of the matrix) should be considered as high correlation. In this equation two parameters (T_{width}/OD and OD×t) has the absolute value of 0.738 which is above 0.7. Thus, these two parameters should be considered as highly correlated.

Table 5-8 The values for the coefficient of the estimators for the Δy_{SC} with intercept

Variable	DF	Parameter Estimate	Standard Error	t Value	$P_r > \|t\|$	Variance Inflation
Intercept	**1**	-1.0524	0.09625	-10.93	<.0001	0
OD×t	**1**	1.55287	0.0267	58.16	<.0001	2.71304
α	**1**	-0.0094	0.03296	-0.28	0.7764	1.11668
E_{embed}	**1**	-0.1051	0.02326	-4.52	<.0001	1.01439
β	**1**	-0.0649	0.03178	-2.04	0.0417	1.10635
E_{back}	**1**	-0.0907	0.01029	-8.82	<.0001	1.13823
T_{width}/OD	**1**	-0.7752	0.07642	-10.14	<.0001	2.20087
E_{wall}	**1**	-0.4327	0.02655	-16.3	<.0001	1.01167
p/OD	**1**	0.91028	0.0247	36.85	<.0001	1.55842

Table 5-9 Pearson correlation coefficient for the Δy_{SC} with intercept

	OD×t	α	E_{embed}	β	E_{back}	T_{width}/OD	E_{wall}	p/OD
OD×t	1.000	-0.056	0.020	-0.001	-0.019	-0.738	0.003	-0.593
α	-0.056	1.000	-0.007	-0.182	0.218	0.032	-0.025	0.011
E_{embed}	0.020	-0.007	1.000	0.006	-0.110	-0.014	0.022	-0.010
β	-0.001	-0.182	0.006	1.000	0.200	0.015	0.029	0.023
E_{back}	-0.019	0.218	-0.110	0.200	1.000	0.019	-0.042	0.029
T_{width}/OD	-0.738	0.032	-0.014	0.015	0.019	1.000	-0.006	0.452
E_{wall}	0.003	-0.025	0.022	0.029	-0.042	-0.006	1.000	0.070
p/OD	-0.593	0.011	-0.010	0.023	0.029	0.452	0.070	1.000

$$\Delta y_{SC}(in.) = -e^{-1.05}(OD \times t)^{1.55}(\alpha)^{-0.01}(E_{embed})^{-0.1}(\beta)^{-0.06}(E_{back})^{-0.09}\left(\frac{W_T}{OD}\right)^{-0.8}(E_w)^{-0.43}\left(\frac{p}{OD}\right)^{0.9} \quad 5\text{-}22$$

Maximum moment in pipe wall, soil cover stage (M_{SC}):

- Criteria for Goodness of fit

1) R^2=0.9744

2) Chi-squared test: $\chi^2_{cal} = 58.062963 < \chi^2_{table}(n = 592, \alpha = 0.05) = 649.7057$

Table 5-10 ANOVA table for the M_{SC} with intercept

Source	DF	Sum of Squares	Mean Square	F Value	$P_r > F$
Model	8	821.174	102.647	2769.56	<.0001
Error	583	21.6074	0.03706		
Corrected Total	591	842.781			

Root MSE	0.19252	**R^2**	0.9744
Dependent Mean	7.56023	**R_a^2**	0.974
Coeff Var	2.54643		

Table 5-10 presents the ANOVA table for the developed equation. The conducted F-test indicates that the regression is significant. Table 5-11 presents the estimate value for each independent parameter. Also the F-test was conducted for each parameter estimate, as shown in Table 5-11. One variable (E_{embed}) is not significant

according to this test but since the variance inflation value for this parameter is less than 5 (last column in Table 5-11) the parameter was not removed from the equation.

The Pearson correlation coefficient for this equation is presented in Table 5-12. This coefficient indicates the correlation between different parameters. The values above 0.7 (not on the diagonal of the matrix) should be considered as high correlation. In this equation two parameters (T_{width}/OD and OD×t) has the absolute value of 0.744 which is above 0.7. Thus, these two parameters should be considered as highly correlated.

Table 5-11 The values for the coefficient of the estimators for the M_{SC} with intercept

Variable	DF	Parameter Estimate	Standard Error	t Value	$P_r > \|t\|$	Variance Inflation
Intercept	**1**	5.90386	0.06371	92.67	<.0001	0
OD×t	**1**	1.72672	0.01731	99.76	<.0001	2.73627
α	**1**	-0.1528	0.02067	-7.39	<.0001	1.12728
E_{embed}	**1**	-0.0084	0.01459	-0.58	0.5631	1.0263
β	**1**	0.07006	0.02025	3.46	0.0006	1.12937
E_{back}	**1**	-0.1419	0.00645	-22	<.0001	1.13661
T_{width}/OD	**1**	-0.0913	0.04932	-1.85	0.0647	2.24223
E_{wall}	**1**	-0.3084	0.01664	-18.54	<.0001	1.00546
p/OD	**1**	0.57043	0.01522	37.49	<.0001	1.50303

Table 5-12 Pearson correlation coefficient for the M_{SC} with intercept

	OD×t	α	E_{embed}	β	E_{back}	T_{width}/OD	E_{wall}	p/OD
OD×t	1.000	-0.006	-0.016	0.039	-0.029	-0.744	0.057	-0.576
α	-0.006	1.000	-0.012	-0.226	0.198	0.003	0.007	0.006
E_{embed}	-0.016	-0.012	1.000	0.003	-0.137	-0.015	0.019	-0.035
β	0.039	-0.226	0.003	1.000	0.195	-0.027	0.025	-0.021
E_{back}	-0.029	0.198	-0.137	0.195	1.000	0.038	0.009	0.003
T_{width}/OD	-0.744	0.003	-0.015	-0.027	0.038	1.000	-0.041	0.434
E_{wall}	0.057	0.007	0.019	0.025	0.009	-0.041	1.000	-0.006
p/OD	-0.576	0.006	-0.035	-0.021	0.003	0.434	-0.006	1.000

$$M_{SC}\left(\frac{kip-in.}{lin\,ft}\right)$$

$$= \frac{e^{5.90}}{1000}(OD \qquad \text{5-23}$$

$$\times t)^{1.73}(\alpha)^{-0.15}(E_{embed})^{-0.01}(\beta)^{0.07}(E_{back})^{-0.14}\left(\frac{W_T}{OD}\right)^{-0.09}(E_w)^{-0.31}\left(\frac{p}{OD}\right)^{0.57}$$

Maximum Thrust in pipe wall, soil cover stage (T_{SC}):

- Criteria for Goodness of fit

1) R^2=0.9453

2) Chi-squared test: $\chi^2_{cal} = 61.56336 < \chi^2_{table}(n = 630, \alpha = 0.05) = 689.4902$

Table 5-13 presents the ANOVA table for the developed equation. The conducted F-test indicates that the regression is significant.

Table 5-13 ANOVA table for the T_{SC} with intercept

Source	DF	Sum of Squares	Mean Square	F Value	$P_r > F$
Model	8	207.417	25.9271	1342.48	<.0001
Error	621	11.9933	0.01931		
Corrected Total	629	219.41			

Root MSE	0.13897	**R^2**	0.9453
Dependent Mean	8.40003	**R_a^2**	0.9446
Coeff Var	1.65441		

Table 5-14 presents the estimate value for each independent parameter. Also the F-test was conducted for each parameter estimate, as shown in Table 5-14. One variable (T_{width}/OD) is not significant according to this test but since the variance inflation value for this parameter is less than 5 (last column in Table 5-14) the parameter was not removed from the equation.

The Pearson correlation coefficient for this equation is presented in Table 5-15. This coefficient indicates the correlation between different parameters. The values above 0.7 (not on the diagonal of the matrix) should be considered as high correlation. In this

equation two parameters (T_{width}/OD and OD×t) has the absolute value of 0.751 which is above 0.7. Thus, these two parameters should be considered as highly correlated.

Table 5-14 The values for the coefficient of the estimators for the T_{SC} with intercept

Variable	DF	Parameter Estimate	Standard Error	t Value	$P_r > \|t\|$	Variance Inflation
Intercept	**1**	7.85076	0.04297	182.7	<.0001	0
OD×t	**1**	0.8329	0.01148	72.54	<.0001	2.80039
α	**1**	-0.0342	0.01414	-2.42	0.0157	1.12169
E_{embed}	**1**	-0.0325	0.01018	-3.19	0.0015	1.02036
β	**1**	0.08589	0.01415	6.07	<.0001	1.11852
E_{back}	**1**	-0.0839	0.00451	-18.6	<.0001	1.13478
T_{width}/OD	**1**	-0.0358	0.03242	-1.1	0.2703	2.29556
E_{wall}	**1**	0.03949	0.01146	3.45	0.0006	1.00431
p/OD	**1**	0.71875	0.01045	68.81	<.0001	1.49174

Table 5-15 Pearson correlation coefficient for the T_{SC} with intercept

	OD×t	α	E_{embed}	β	E_{back}	T_{width}/OD	E_{wall}	p/OD
OD×t	1.000	0.024	-0.016	0.011	0.006	-0.751	0.062	-0.573
α	0.024	1.000	-0.014	-0.208	0.206	-0.010	-0.003	0.003
E_{embed}	-0.016	-0.014	1.000	-0.007	-0.129	-0.008	0.006	-0.022
β	0.011	-0.208	-0.007	1.000	0.199	0.010	-0.016	-0.007
E_{back}	0.006	0.206	-0.129	0.199	1.000	0.005	-0.003	-0.001
T_{width}/OD	-0.751	-0.010	-0.008	0.010	0.005	1.000	-0.052	0.428
E_{wall}	0.062	-0.003	0.006	-0.016	-0.003	-0.052	1.000	-0.039
p/OD	-0.573	0.003	-0.022	-0.007	-0.001	0.428	-0.039	1.000

$$T_{SC}\left(\frac{kip}{lin\ ft}\right) = -\frac{e^{7.85}}{1000}(OD \times t)^{0.83}(\alpha)^{-0.03}(E_{embed})^{-0.03}(\beta)^{0.08}(E_{back})^{-0.08}\left(\frac{W_T}{OD}\right)^{-0.036}(E_w)^{0.04}\left(\frac{p}{OD}\right)^{0.72} \quad 5\text{-}24$$

Maximum Shear in pipe wall, soil cover stage (V_{SC}):

- Criteria for Goodness of fit

1) R^2=0.9249

2) Chi-squared test: $\chi^2_{cal} = 44.6339 < \chi^2_{table}(n = 651, \alpha = 0.05) = 711.461$

Table 5-16Table 5-13 presents the ANOVA table for the developed equation. The conducted F-test indicates that the regression is significant.

Table 5-16 ANOVA table for the V_{SC} with intercept

Source	DF	Sum of Squares	Mean Square	F Value	$P_r > F$
Model	8	192.632	24.079	988.68	<.0001
Error	642	15.6358	0.02435		
Corrected Total	650	208.268			

Root MSE	0.15606	**R^2**	0.9249
Dependent Mean	7.94824	**R_a^2**	0.924
Coeff Var	1.96345		

Table 5-17 presents the estimate value for each independent parameter. Also the F-test was conducted for each parameter estimate, as shown in Table 5-17. Three variables (α, E_{embed}, and β) are not significant according to this test but since the variance inflation value for these parameters is less than 5 (last column inTable 5-17) the parameters were not removed from the equation.

The Pearson correlation coefficient for this equation is presented in Table 5-18. This coefficient indicates the correlation between different parameters. The values above 0.7 (not on the diagonal of the matrix) should be considered as high correlation. In this equation two parameters (T_{width}/OD and OD×t) has the absolute value of 0.743 which is above 0.7. Thus, these two parameters should be considered as highly correlated.

Table 5-17 The values for the coefficient of the estimators for the V_{SC} with intercept

Variable	DF	Parameter Estimate	Standard Error	t Value	$P_r > \|t\|$	Variance Inflation
Intercept	**1**	7.40424	0.04571	161.97	<.0001	0
OD×t	**1**	0.7872	0.01238	63.61	<.0001	2.69561
α	**1**	-0.0022	0.0153	-0.14	0.8854	1.10051
E_{embed}	**1**	-0.0097	0.01124	-0.87	0.3865	1.0181
β	**1**	0.0264	0.01534	1.72	0.0857	1.11056
E_{back}	**1**	-0.1217	0.00499	-24.37	<.0001	1.14401
T_{width}/OD	**1**	0.09063	0.03552	2.55	0.011	2.23631
E_{wall}	**1**	0.13044	0.01258	10.37	<.0001	1.00647
p/OD	**1**	0.65557	0.01145	57.25	<.0001	1.48774

Table 5-18 Pearson correlation coefficient for the V_{SC} with intercept

	OD×t	α	E_{embed}	β	E_{back}	T_{width}/OD	E_{wall}	p/OD
OD×t	1.000	0.012	-0.006	0.001	0.014	-0.743	0.073	-0.572
α	0.012	1.000	0.001	-0.170	0.203	-0.014	-0.007	-0.002
E_{embed}	-0.006	0.001	1.000	-0.005	-0.125	0.000	-0.005	-0.012
β	0.001	-0.170	-0.005	1.000	0.224	0.001	-0.011	-0.011
E_{back}	0.014	0.203	-0.125	0.224	1.000	-0.005	-0.024	-0.009
T_{width}/OD	-0.743	-0.014	0.000	0.001	-0.005	1.000	-0.060	0.436
E_{wall}	0.073	-0.007	-0.005	-0.011	-0.024	-0.060	1.000	-0.055
p/OD	-0.572	-0.002	-0.012	-0.011	-0.009	0.436	-0.055	1.000

$$V_{SC}\left(\frac{kip}{lin\ ft}\right) = \frac{e^{7.40}}{1000}(OD \times t)^{0.79}(\alpha)^{-0.002}(E_{embed})^{-0.01}(\beta)^{0.03}(E_{back})^{-0.12}\left(\frac{W_T}{OD}\right)^{0.09}(E_w)^{0.13}\left(\frac{p}{OD}\right)^{0.66} \quad 5\text{-}25$$

Horizontal deflection, live load stage (Δx_{LL}):

- Criteria for Goodness of fit

1) R^2=0.9519

2) Chi-squared test: $\chi^2_{cal} = 32.6086 < \chi^2_{table}(n = 590, \alpha = 0.05) = 647.6086$

Table 5-19Table 5-13 presents the ANOVA table for the developed equation. The conducted F-test indicates that the regression is significant.

Table 5-19 ANOVA table for the Δx_{LL} with intercept

Source	DF	Sum of Squares	Mean Square	F Value	$P_r > F$
Model	8	412.389	51.5486	1477.2	<.0001
Error	597	20.833	0.0349		
Corrected Total	605	433.222			

Root MSE	0.18681	**R^2**	0.9519
Dependent Mean	0.4343	**R_a^2**	0.9513
Coeff Var	43.0127		

Table 5-20 presents the estimate value for each independent parameter. Also the F-test was conducted for each parameter estimate, as shown in Table 5-20. One variable

(β) is not significant according to this test but since the variance inflation value for this parameter is less than 5 (last column in Table 5-20) the parameter was not removed from the equation.

Table 5-20 The values for the coefficient of the estimators for the Δx_{LL} with intercept

Variable	DF	Parameter Estimate	Standard Error	t Value	$P_r > \|t\|$	Variance Inflation
Intercept	**1**	0.3106	0.05877	5.29	<.0001	0
OD×t	**1**	0.85157	0.01597	53.33	<.0001	2.77278
α	**1**	-0.1018	0.01989	-5.12	<.0001	1.13862
E_{embed}	**1**	-0.1034	0.01394	-7.42	<.0001	1.01732
β	**1**	-0.0202	0.01973	-1.03	0.3054	1.14402
E_{back}	**1**	-0.1321	0.00614	-21.52	<.0001	1.12936
T_{width}/OD	**1**	-0.8706	0.04536	-19.19	<.0001	2.31525
E_{wall}	**1**	-0.3716	0.01588	-23.41	<.0001	1.00714
p/OD	**1**	0.22469	0.01449	15.51	<.0001	1.49775

The Pearson correlation coefficient for this equation is presented in Table 5-21. This coefficient indicates the correlation between different parameters. The values above 0.7 (not on the diagonal of the matrix) should be considered as high correlation. In this equation two parameters (T_{width}/OD and OD×t) has the absolute value of 0.753 which is above 0.7. Thus, these two parameters should be considered as highly correlated.

Table 5-21 Pearson correlation coefficient for the Δx_{LL} with intercept

	OD×t	α	E_{embed}	β	E_{back}	T_{width}/OD	E_{wall}	p/OD
OD×t	1.000	-0.006	0.000	0.004	-0.011	-0.753	-0.024	-0.573
α	-0.006	1.000	-0.017	-0.251	0.188	0.007	-0.011	0.027
E_{embed}	0.000	-0.017	1.000	0.009	-0.124	-0.004	0.016	0.005
β	0.004	-0.251	0.009	1.000	0.192	0.014	0.026	-0.014
E_{back}	-0.011	0.188	-0.124	0.192	1.000	0.017	-0.042	0.034
T_{width}/OD	-0.753	0.007	-0.004	0.014	0.017	1.000	0.012	0.442
E_{wall}	-0.024	-0.011	0.016	0.026	-0.042	0.012	1.000	0.060
p/OD	-0.573	0.027	0.005	-0.014	0.034	0.442	0.060	1.000

$$\Delta x_{LL}(in.) = e^{0.31}(OD \times t)^{0.85}(\alpha)^{-0.10}(E_{embed})^{-0.10}(\beta)^{-0.02}(E_{back})^{-0.13}\left(\frac{W_T}{OD}\right)^{-0.87}(E_w)^{-0.4}\left(\frac{p}{OD}\right)^{0.22} \quad 5\text{-}26$$

Vertical deflection, live load stage (Δy_{LL}):

- Criteria for Goodness of fit

1) R^2=0.9589

2) Chi-squared test: $\chi^2_{cal} = 46.503 < \chi^2_{table}(n = 606, \alpha = 0.05) = 664.3732$

Table 5-22Table 5-13 presents the ANOVA table for the developed equation. The conducted F-test indicates that the regression is significant.

Table 5-22 ANOVA table for the Δy_{LL} with intercept

Source	DF	Sum of Squares	Mean Square	F Value	$P_r > F$
Model	8	362.989	45.3737	1694.8	<.0001
Error	581	15.5547	0.02677		
Corrected Total	589	378.544			

Root MSE	0.16362	**R^2**	0.9589
Dependent Mean	0.525	**R_a^2**	0.9583
Coeff Var	31.1663		

Table 5-23 presents the estimate value for each independent parameter. Also the F-test was conducted for each parameter estimate, as shown in Table 5-23. One variable (α) is not significant according to this test but since the variance inflation value for this parameter is less than 5 (last column in Table 5-23) the parameter was not removed from the equation.

Table 5-23 The values for the coefficient of the estimators for the Δy_{LL} with intercept

Variable	DF	Parameter Estimate	Standard Error	t Value	$P_r > \|t\|$	Variance Inflation
Intercept	**1**	0.13614	0.05334	2.55	0.0109	0
OD×t	**1**	0.84392	0.01455	58.02	<.0001	2.85064
α	**1**	-0.0044	0.01803	-0.25	0.806	1.16098
E_{embed}	**1**	-0.0463	0.01235	-3.75	0.0002	1.01479
β	**1**	-0.0737	0.01766	-4.17	<.0001	1.15029
E_{back}	**1**	-0.1047	0.0055	-19.04	<.0001	1.1453
T_{width}/OD	**1**	-0.7628	0.04093	-18.64	<.0001	2.38513
E_{wall}	**1**	-0.4532	0.0142	-31.92	<.0001	1.0086
p/OD	**1**	0.24436	0.01297	18.84	<.0001	1.50398

The Pearson correlation coefficient for this equation is presented in Table 5-24. This coefficient indicates the correlation between different parameters. The values above 0.7 (not on the diagonal of the matrix) should be considered as high correlation. In this equation two parameters (T_{width}/OD and OD×t) has the absolute value of 0.762 which is above 0.7. Thus, these two parameters should be considered as highly correlated.

Table 5-24 Pearson correlation coefficient for the Δy_{LL} with intercept

	OD×t	α	E_{embed}	β	E_{back}	T_{width}/OD	E_{wall}	p/OD
OD×t	1.000	-0.002	-0.011	0.004	0.012	-0.762	-0.028	-0.574
α	-0.002	1.000	-0.020	-0.258	0.215	0.015	-0.015	0.007
E_{embed}	-0.011	-0.020	1.000	0.027	-0.106	-0.005	0.023	0.002
β	0.004	-0.258	0.027	1.000	0.181	0.005	0.045	0.004
E_{back}	0.012	0.215	-0.106	0.181	1.000	0.002	-0.053	0.055
T_{width}/OD	-0.762	0.015	-0.005	0.005	0.002	1.000	0.023	0.448
E_{wall}	-0.028	-0.015	0.023	0.045	-0.053	0.023	1.000	0.044
p/OD	-0.574	0.007	0.002	0.004	0.055	0.448	0.044	1.000

$$\Delta y_{LL}(in.) = -e^{0.14}(OD \times t)^{0.84}(\alpha)^{-0.004}(E_{embed})^{-0.05}(\beta)^{-0.07}(E_{back})^{-0.1}\left(\frac{W_T}{OD}\right)^{-0.76}(E_w)^{-0.45}\left(\frac{p}{OD}\right)^{0.2} \quad 5\text{-}27$$

Maximum moment in pipe wall, live load stage (M_{LL}):

- Criteria for Goodness of fit

1) R^2=0.9543

2) Chi-squared test: $\chi^2_{cal} = 146.928 < \chi^2_{table}(n = 601, \alpha = 0.05) = 659.1405$

Table 5-25Table 5-13 presents the ANOVA table for the developed equation. The conducted F-test indicates that the regression is significant.

Table 5-25 ANOVA table for the M_{LL} with intercept

Source	DF	Sum of Squares	Mean Square	F Value	$P_r > F$
Model	8	655.358	81.9198	1543.6	<.0001
Error	592	31.4179	0.05307		
Corrected Total	600	686.776			

Root MSE	0.23037	**R^2**	0.9543
Dependent Mean	8.00039	**R_a^2**	0.9536
Coeff Var	2.8795		

Table 5-26 presents the estimate value for each independent parameter. Also the F-test was conducted for each parameter estimate, as shown in Table 5-26. Two variables (E_{embed} and β) are not significant according to this test but since the variance inflation value for these parameters is less than 5 (last column in Table 5-26) the parameters were not removed from the equation.

Table 5-26 The values for the coefficient of the estimators for the M_{LL} with intercept

Variable	DF	Parameter Estimate	Standard Error	t Value	$P_r > \|t\|$	Variance Inflation
Intercept	**1**	6.74954	0.07447	90.63	<.0001	0
OD×t	**1**	1.38955	0.02027	68.54	<.0001	2.75099
α	**1**	-0.1458	0.02475	-5.89	<.0001	1.14388
E_{embed}	**1**	-0.0311	0.01724	-1.8	0.072	1.01538
β	**1**	0.00675	0.02428	0.28	0.7812	1.12893
E_{back}	**1**	-0.1399	0.00764	-18.31	<.0001	1.13225
T_{width}/OD	**1**	-0.2233	0.05773	-3.87	0.0001	2.32815
E_{wall}	**1**	-0.3913	0.01972	-19.84	<.0001	1.00994
p/OD	**1**	0.25502	0.01782	14.31	<.0001	1.46883

The Pearson correlation coefficient for this equation is presented in Table 5-27. This coefficient indicates the correlation between different parameters. The values above 0.7 (not on the diagonal of the matrix) should be considered as high correlation. In this equation two parameters (T_{width}/OD and OD×t) has the absolute value of 0.755 which is above 0.7. Thus, these two parameters should be considered as highly correlated.

Table 5-27 Pearson correlation coefficient for the M_{LL} with intercept

	OD×t	**α**	**E_{embed}**	**β**	**E_{back}**	**T_{width}/OD**	**E_{wall}**	**p/OD**
OD×t	1.000	0.002	-0.020	-0.007	0.015	-0.755	0.086	-0.564
α	0.002	1.000	-0.024	-0.237	0.216	0.003	-0.010	0.017
E_{embed}	-0.020	-0.024	1.000	0.010	-0.113	-0.004	0.001	-0.003
β	-0.007	-0.237	0.010	1.000	0.180	0.013	0.025	0.000
E_{back}	0.015	0.216	-0.113	0.180	1.000	-0.009	-0.033	0.002
T_{width}/OD	-0.755	0.003	-0.004	0.013	-0.009	1.000	-0.057	0.445
E_{wall}	0.086	-0.010	0.001	0.025	-0.033	-0.057	1.000	-0.041
p/OD	-0.564	0.017	-0.003	0.000	0.002	0.445	-0.041	1.000

$$M_{LL}\left(\frac{kip-in.}{lin\ ft}\right) = \frac{e^{6.75}}{1000}(OD \times t)^{1.2}(\alpha)^{-0.14}(E_{embed})^{-0.03}(\beta)^{0.01}(E_{back})^{-0.14}\left(\frac{W_T}{OD}\right)^{-0.2}(E_w)^{-0.4}\left(\frac{p}{OD}\right)^{0.3} \quad 5\text{-}28$$

Maximum Thrust in pipe wall, live load stage (T_{LL}):

- Criteria for Goodness of fit

1) R^2=0.9212

2) Chi-squared test: $\chi^2_{cal} = 58.794 < \chi^2_{table}(n = 641, \alpha = 0.05) = 701.002$

Table 5-28 presents the ANOVA table for the developed equation. The conducted F-test indicates that the regression is significant.

Table 5-28 ANOVA table for the T_{LL} with intercept

Source	DF	Sum of Squares	Mean Square	F Value	$P_r > F$
Model	8	95.7885	11.9736	923.1	<.0001
Error	632	8.19767	0.01297		
Corrected Total	640	103.986			

Root MSE	0.11389	**R^2**	0.9212
Dependent Mean	8.78782	**R_a^2**	0.9202
Coeff Var	1.296		

Table 5-29 presents the estimate value for each independent parameter. Also the F-test was conducted for each parameter estimate, as shown in Table 5-29. One variable (α) is not significant according to this test but since the variance inflation value for this parameter is less than 5 (last column in Table 5-29) the parameter was not removed from the equation.

Table 5-29 The values for the coefficient of the estimators for the T_{LL} with intercept

Variable	DF	Parameter Estimate	Standard Error	t Value	$P_r > \|t\|$	Variance Inflation
Intercept	**1**	8.77173	0.03373	260.02	<.0001	0
OD×t	**1**	0.49879	0.00916	54.46	<.0001	2.69582
α	**1**	-0.0152	0.01148	-1.32	0.1866	1.11432
E_{embed}	**1**	-0.046	0.00829	-5.55	<.0001	1.02296
β	**1**	0.10264	0.01148	8.94	<.0001	1.11549
E_{back}	**1**	-0.0984	0.00365	-26.97	<.0001	1.12063
T_{width}/OD	**1**	-0.1984	0.02636	-7.52	<.0001	2.25083
E_{wall}	**1**	0.08235	0.00926	8.89	<.0001	1.00303
p/OD	**1**	0.37488	0.00844	44.4	<.0001	1.47905

The Pearson correlation coefficient for this equation is presented in Table 5-30. This coefficient indicates the correlation between different parameters. The values above 0.7 (not on the diagonal of the matrix) should be considered as high correlation. In this equation two parameters (T_{width}/OD and OD×t) has the absolute value of 0.745 which is above 0.7. Thus, these two parameters should be considered as highly correlated.

Table 5-30 Pearson correlation coefficient for the T_{LL} with intercept

	OD×t	α	E_{embed}	β	E_{back}	T_{width}/OD	E_{wall}	p/OD
OD×t	1.000	0.045	0.011	0.033	0.026	-0.745	0.052	-0.569
α	0.045	1.000	-0.033	-0.217	0.185	-0.038	0.010	-0.016
E_{embed}	0.011	-0.033	1.000	-0.033	-0.148	-0.018	0.006	-0.010
β	0.033	-0.217	-0.033	1.000	0.190	-0.018	-0.003	-0.031
E_{back}	0.026	0.185	-0.148	0.190	1.000	-0.014	0.004	-0.017
T_{width}/OD	-0.745	-0.038	-0.018	-0.018	-0.014	1.000	-0.046	0.437
E_{wall}	0.052	0.010	0.006	-0.003	0.004	-0.046	1.000	-0.039
p/OD	-0.569	-0.016	-0.010	-0.031	-0.017	0.437	-0.039	1.000

$$T_{LL}\left(\frac{kip}{lin\ ft}\right) = -\frac{e^{8.77}}{1000}(OD \times t)^{0.50}(\alpha)^{-0.02}(E_{embed})^{-0.046}(\beta)^{0.1}(E_{back})^{-0.1}\left(\frac{W_T}{OD}\right)^{-0.2}(E_w)^{0.08}\left(\frac{p}{OD}\right)^{0.37} \quad 5\text{-}29$$

Maximum Shear in pipe wall, live load stage (V_{LL}):

- Criteria for Goodness of fit

1) R^2=0.9076

2) Chi-squared test: $\chi^2_{cal} = 48.47 < \chi^2_{table}(n = 652, \alpha = 0.05) = 712.501$

Table 5-31Table 5-13 presents the ANOVA table for the developed equation. The conducted F-test indicates that the regression is significant.

Table 5-31 ANOVA table for the T_{LL} with intercept

Source	DF	Sum of Squares	Mean Square	F Value	$P_r > F$
Model	8	120.477	15.0596	789.85	<.0001
Error	643	12.2597	0.01907		
Corrected Total	651	132.736			

Root MSE	0.13808	**R^2**	0.9076
Dependent Mean	8.32296	**R_a^2**	0.9065
Coeff Var	1.65904		

Table 5-32 presents the estimate value for each independent parameter. Also the F-test was conducted for each parameter estimate, as shown in Table 5-32. Two

variables (α and β) are not significant according to this test but since the variance inflation value for these parameters is less than 5 (last column inTable 5-32) the parameters were not removed from the equation.

Table 5-32 The values for the coefficient of the estimators for the T_{LL} with intercept

Variable	DF	Parameter Estimate	Standard Error	t Value	$P_r > \|t\|$	Variance Inflation
Intercept	**1**	8.2732	0.04034	205.09	<.0001	0
OD×t	**1**	0.51661	0.01089	47.42	<.0001	2.67657
α	**1**	-0.0258	0.01354	-1.9	0.0575	1.1002
E_{embed}	**1**	-0.029	0.00994	-2.92	0.0037	1.01853
β	**1**	0.02202	0.01357	1.62	0.1051	1.11018
E_{back}	**1**	-0.157	0.00441	-35.59	<.0001	1.14371
T_{width}/OD	**1**	-0.1209	0.03137	-3.85	0.0001	2.22802
E_{wall}	**1**	0.16128	0.01112	14.51	<.0001	1.00614
p/OD	**1**	0.33186	0.01012	32.8	<.0001	1.48362

The Pearson correlation coefficient for this equation is presented in Table 5-33. This coefficient indicates the correlation between different parameters. The values above 0.7 (not on the diagonal of the matrix) should be considered as high correlation. In this equation two parameters (T_{width}/OD and OD×t) has the absolute value of 0.742 which is above 0.7. Thus, these two parameters should be considered as highly correlated.

Table 5-33 Pearson correlation coefficient for the T_{LL} with intercept

	OD×t	α	E_{embed}	β	E_{back}	T_{width}/OD	E_{wall}	p/OD
OD×t	1.000	0.013	-0.004	0.002	0.011	-0.742	0.070	-0.570
α	0.013	1.000	0.002	-0.170	0.202	-0.014	-0.008	-0.002
E_{embed}	-0.004	0.002	1.000	-0.005	-0.127	0.000	-0.007	-0.011
β	0.002	-0.170	-0.005	1.000	0.223	0.001	-0.012	-0.010
E_{back}	0.011	0.202	-0.127	0.223	1.000	-0.005	-0.022	-0.010
T_{width}/OD	-0.742	-0.014	0.000	0.001	-0.005	1.000	-0.060	0.436
E_{wall}	0.070	-0.008	-0.007	-0.012	-0.022	-0.060	1.000	-0.056
p/OD	-0.570	-0.002	-0.011	-0.010	-0.010	0.436	-0.056	1.000

$$V_{LL}\left(\frac{kip}{lin\ ft}\right)$$

$$= \frac{e^{8.27}}{1000}(OD \qquad \text{5-30}$$

$$\times t)^{0.52}(\alpha)^{-0.03}(E_{embed})^{-0.03}(\beta)^{0.02}(E_{back})^{-0.16}\left(\frac{W_T}{OD}\right)^{-0.12}(E_w)^{0.16}\left(\frac{p}{OD}\right)^{0.33}$$

The independent variables are defined in Table 5-2.

5.3.2.2 Comparison between predicted (with intercept) and finite element results

The developed equations (Equations 5-21 through 5-30) for the horizontal deflection, vertical deflection, moment, thrust, and shear of the buried steel pipe in stage of soil cover and live load were compared to those obtained from the finite element analyses. The plots for comparing obtained response value from FEM and predicted value based on developed equations are presented in Figure 5-12 through Figure 5-21. Different limiting bounds in Figure 5-12 through Figure 5-21 indicate that the developed equations show a close correlation. The developed equations were accurately predicted the behavior of the buried steel pipe.

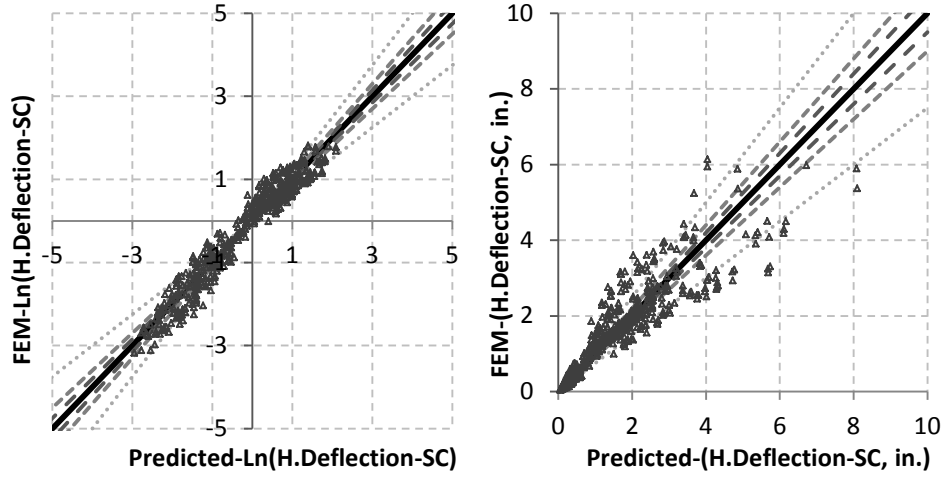

Figure 5-12 Comparison of observed and the predicted horizontal deflection at stage of soil cover (with intercept)

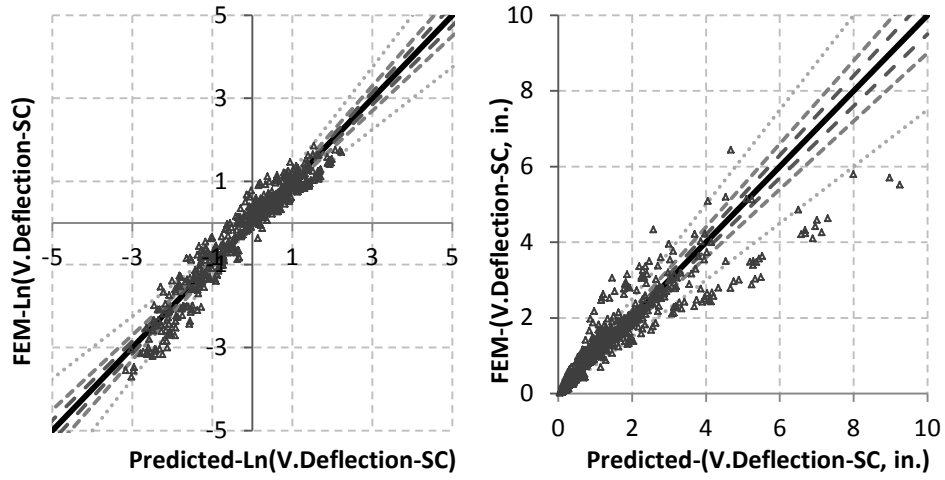

Figure 5-13 Comparison of observed and the predicted vertical deflection at stage of soil cover (with intercept)

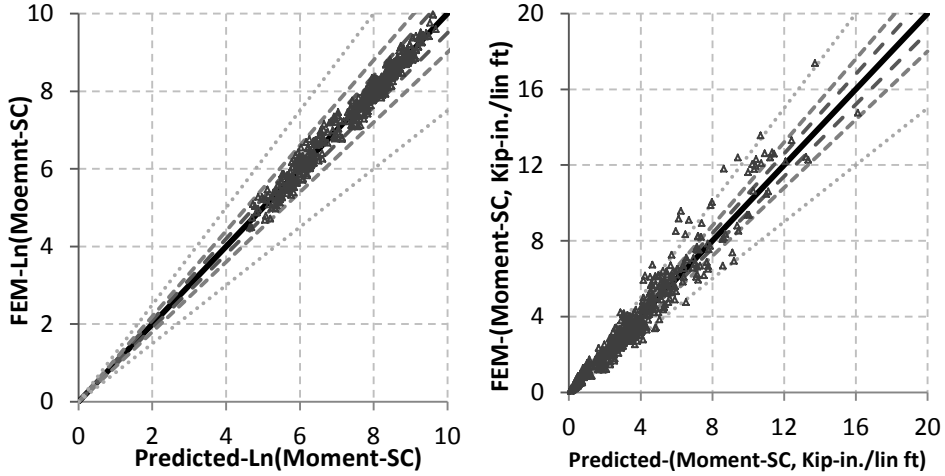

Figure 5-14 Comparison of observed and the predicted maximum moment at stage of soil cover (with intercept)

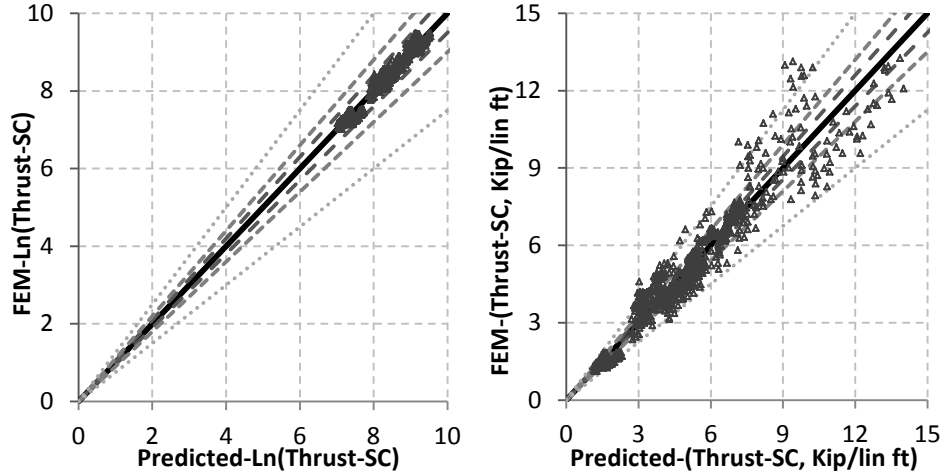

Figure 5-15 Comparison of observed and the predicted maximum thrust at stage of soil cover (with intercept)

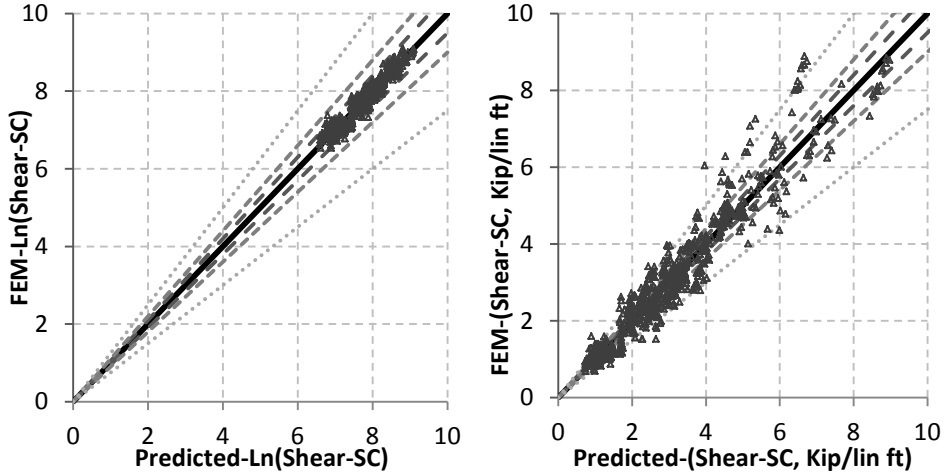

Figure 5-16 Comparison of observed and the predicted maximum shear at stage of soil cover (with intercept)

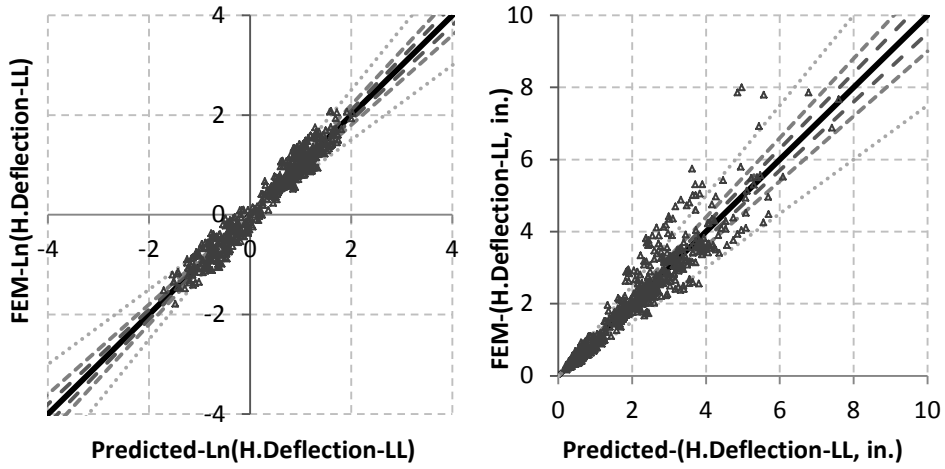

Figure 5-17 Comparison of observed and the predicted horizontal deflection at stage of live load (with intercept)

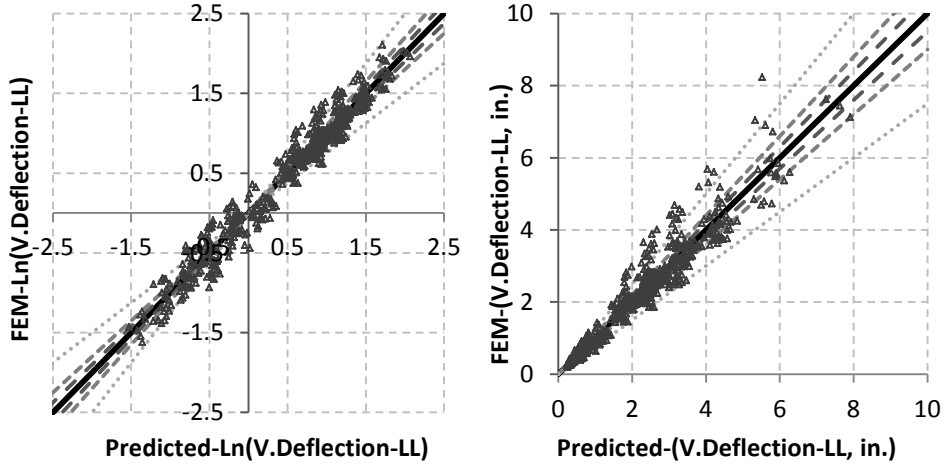

Figure 5-18 Comparison of observed and the predicted vertical deflection at stage of live load (with intercept)

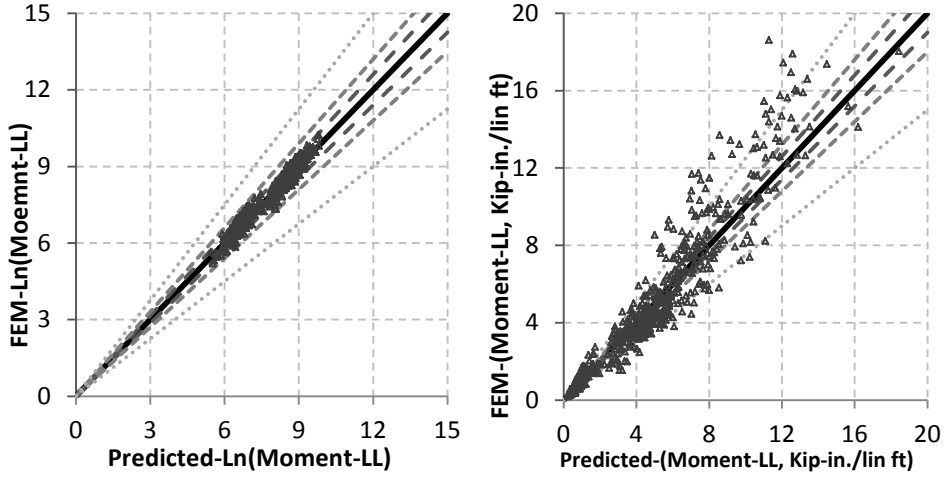

Figure 5-19 Comparison of observed and the predicted maximum moment at stage of live load (with intercept)

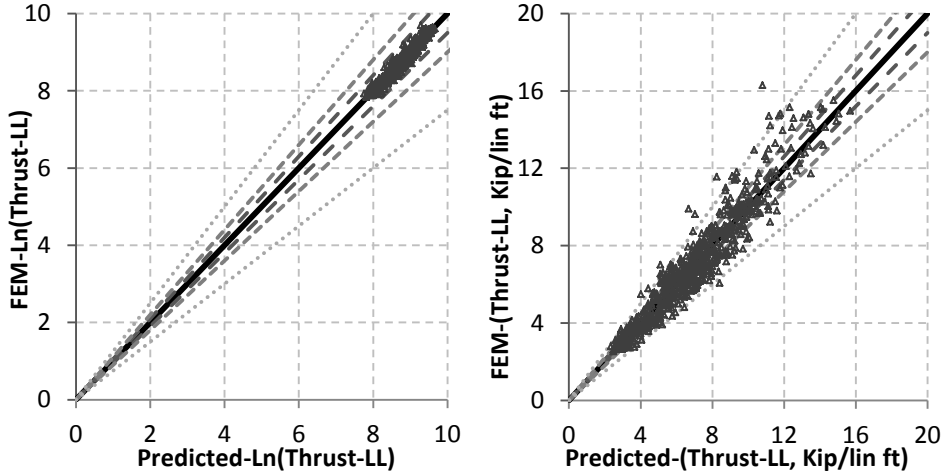

Figure 5-20 Comparison of observed and the predicted maximum thrust at stage of live load (with intercept)

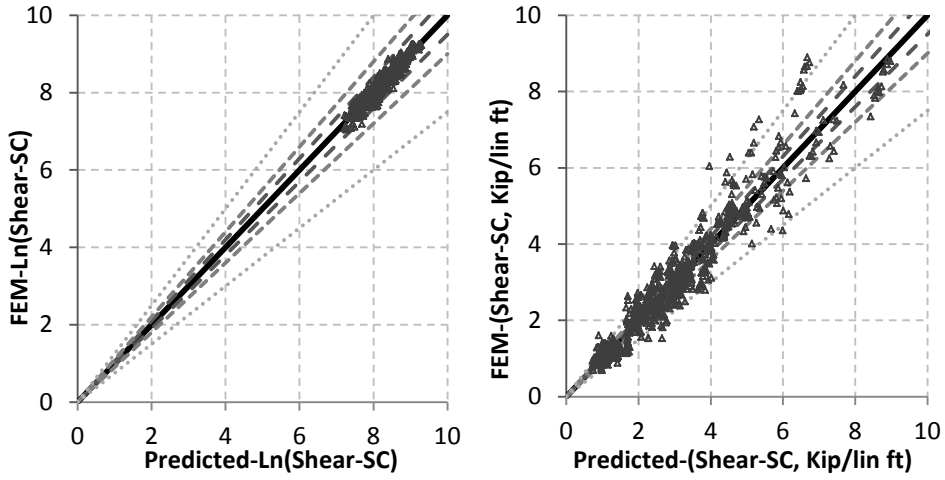

Figure 5-21 Comparison of observed and the predicted maximum shear at stage of live load (with intercept)

5.3.2.3 Design Equations without Intercept

As mentioned earlier in this chapter, the powers of the parameters in the developed equations with intercept are small. However the effects of the different parameters were considered in the intercept. To increase the magnitude the powers of the dependent parameters, another sets of equations were developed by removing the intercept value. However, the calculated R^2 value for the equations is not a good representative of the goodness of fit since this value is not unbiased anymore. Moreover, the developed equations without intercept are presented in this section. Equations 5-31 through 5-35 are the equations for the stage of completion of backfilling and soil cover and Equations 5-36 through 5-40 for the stage in which the live load was applied.

The prediction equations without intercept for soil cover stage are:

Horizontal deflection, soil cover stage (Δx_{SC}):

- Criteria for Goodness of fit

1) R^2=0.9409
2) Chi-squared test: $\chi^2_{\text{cal}} = 67.2676 < \chi^2_{\text{table}}(\text{n} = 608, \alpha = 0.05) = 666.466$

$$\Delta x_{SC}(in.) = (OD \times t)^{1.32}(\alpha)^{0.01}(E_{embed})^{-0.23}(\beta)^{0.02}(E_{back})^{-0.13}\left(\frac{W_T}{OD}\right)^{-1.19}(E_w)^{-0.27}\left(\frac{p}{OD}\right)^{0.66} \quad 5\text{-}31$$

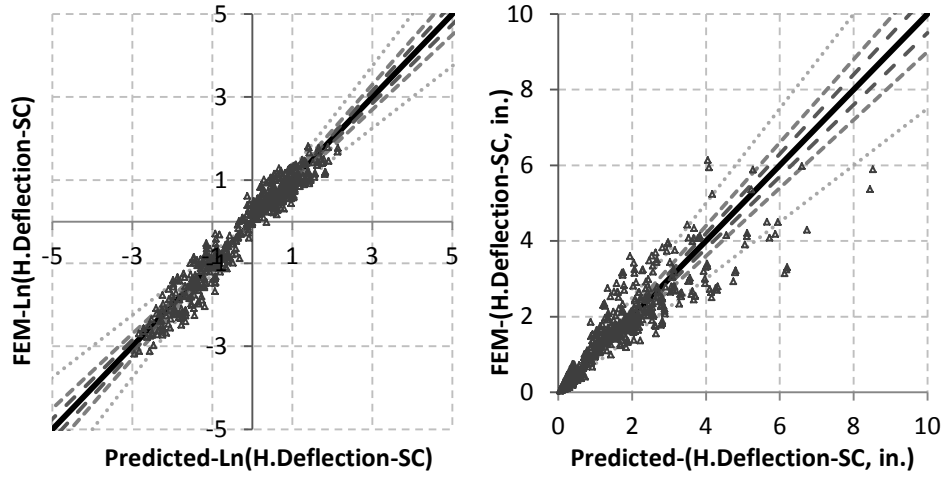

Figure 5-22 Comparison of observed and the predicted horizontal deflection at stage of soil cover (without intercept)

Figure 5-22 illustrates the comparison of predicted and observed values for horizontal deflection in the stage of soil cover for the equations without intercept. Comparing Figure 5-22 and Figure 5-12 it can be concluded that either equation with intercept or without intercept would predict the horizontal deflection in the stage of soil cover precisely.

Vertical deflection, soil cover stage (Δy_{SC}):

- Criteria for Goodness of fit

1) R^2=0.9166
2) Chi-squared test: $\chi^2_{\text{cal}} = 82.146 < \chi^2_{\text{table}}(\text{n} = 615, \alpha = 0.05) = 673.7921$

$$\Delta y_{SC}(in.) = (OD \times t)^{1.38}(\alpha)^{0.09}(E_{embed})^{-0.24}(\beta)^{0.05}(E_{back})^{-0.12}\left(\frac{W_T}{OD}\right)^{-1.34}(E_w)^{-0.38}\left(\frac{p}{OD}\right)^{0.87} \quad 5\text{-}32$$

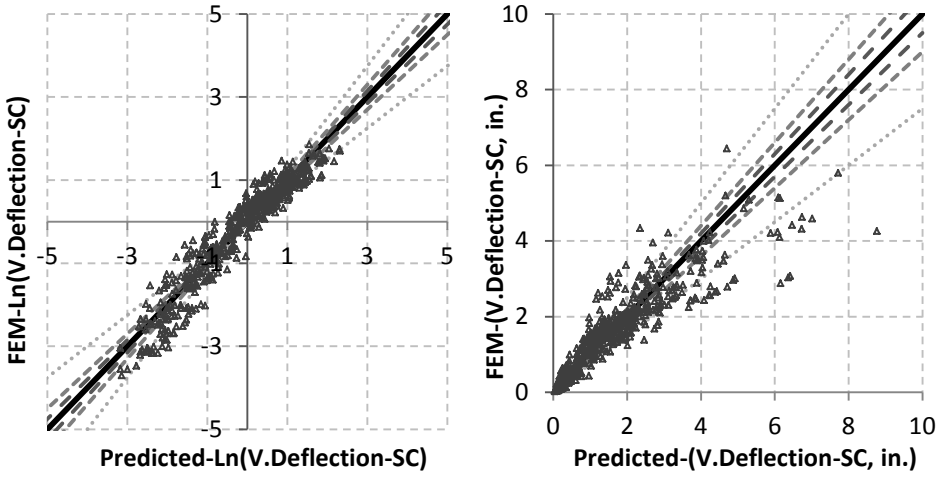

Figure 5-23 Comparison of observed and the predicted vertical deflection at stage of soil cover (without intercept)

Figure 5-23 illustrates the comparison of predicted and observed values for horizontal deflection in the stage of soil cover for the equations without intercept. Comparing Figure 5-23 and Figure 5-13 it can be concluded that equation with intercept would predict the vertical deflection in the stage of soil cover more precisely than the equation without intercept term.

Moment, soil cover stage (M_{SC}):

- Criteria for Goodness of fit

1) R^2=0.9902
2) Chi-squared test: $\chi^2_{\text{cal}} = 1145.417 > \chi^2_{\text{table}}(\text{n} = 592, \alpha = 0.05) = 649.7057$

$$M\left(\frac{Kip-in.}{lin\ ft}\right)$$

$$= \frac{1}{1000}(OD \qquad \text{5-33}$$

$$\times t)^{2.77}(\alpha)^{-0.73}(E_{embed})^{0.75}(\beta)^{-0.52}(E_{back})^{0.03}\left(\frac{W_T}{OD}\right)^{3.05}(E_w)^{-0.59}\left(\frac{p}{OD}\right)^{0.81}$$

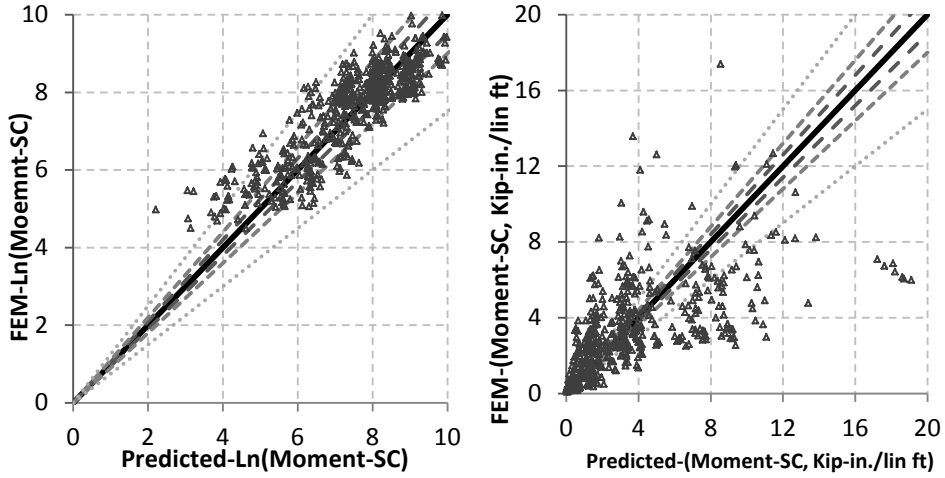

Figure 5-24 Comparison of observed and the predicted moment at stage of soil cover (without intercept)

Comparing the R^2 for Equation 5-33 (R^2=0.9902) and Equation 5-23 (R^2=0.9744), Equation 5.33 has a larger R^2 but comparison of the χ^2_{cal}, Figure 5-24 and Figure 5-14 indicates that the equation with intercept would predict the moment in stage of soil cover more precisely.

Thrust, soil cover stage (T_{SC}):

- Criteria for Goodness of fit

1) R^2=0.9853
2) Chi-squared test: $\chi^2_{\text{cal}} = 3946.162 > \chi^2_{\text{table}}(\text{n} = 630, \alpha = 0.05) = 689.4902$

$$T\left(\frac{Kip}{lin\ ft}\right) = \frac{1}{1000}(OD \times t)^{2.15}(\alpha)^{-0.88}(E_{embed})^{1.02}(\beta)^{-0.78}(E_{back})^{0.15}\left(\frac{W_T}{OD}\right)^{4.03}(E_w)^{-0.31}\left(\frac{p}{OD}\right)^{1.03} \quad 5\text{-}34$$

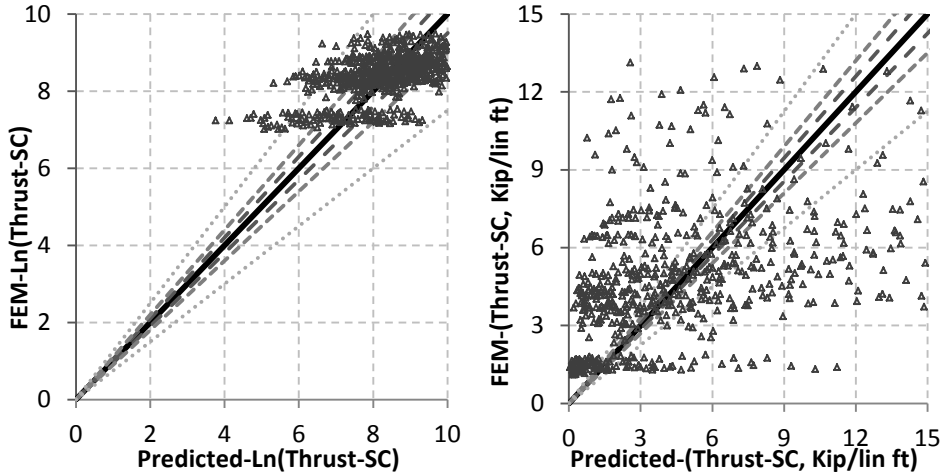

Figure 5-25 Comparison of observed and the predicted thrust at stage of soil cover (without intercept)

Comparing the R^2 for Equation 5-34 (R^2=0.9853) and Equation 5-24 (R^2=0. 0.9453), Equation 5.34 has a larger R^2 but comparison of the χ^2_{cal}, Figure 5-25 and Figure 5-15 indicates that the equation with intercept would predict the thrust in stage of soil cover more precisely.

Shear, soil cover stage (V_{SC}):

- Criteria for Goodness of fit

1) R^2=0.9842
2) Chi-squared test: $\chi^2_{\text{cal}} = 2517.133 > \chi^2_{\text{table}}(\text{n} = 651, \alpha = 0.05) = 711.461$

$$V\left(\frac{Kip}{lin\ ft}\right)$$

$$= \frac{1}{1000}(OD \qquad \text{5-35}$$

$$\times t)^{1.98}(\alpha)^{-0.76}(E_{embed})^{1.02}(\beta)^{-0.74}(E_{back})^{0.11}\left(\frac{W_T}{OD}\right)^{3.96}(E_w)^{-0.19}\left(\frac{p}{OD}\right)^{0.89}$$

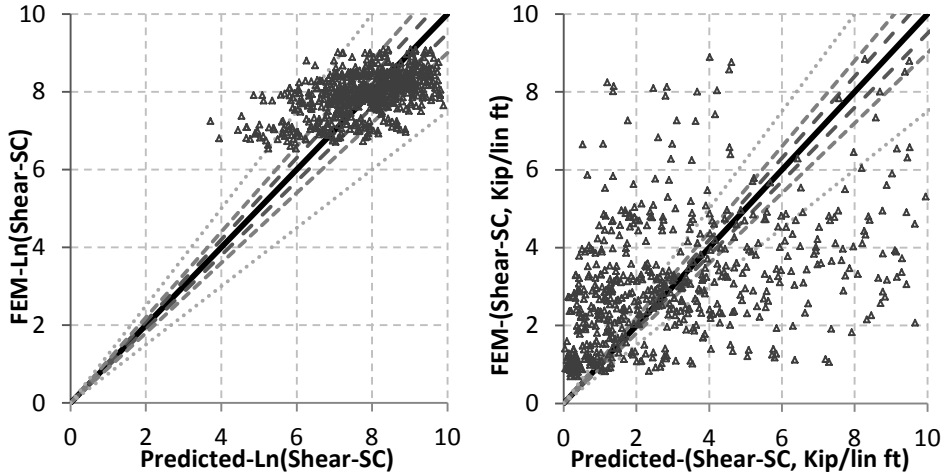

Figure 5-26 Comparison of observed and the predicted shear at stage of soil cover (without intercept)

Comparing the R^2 for Equation 5-35 (R^2=0.9842) and Equation 5-25 (R^2=0. 0.9249), Equation 5.35 has a larger R^2 but comparison of the χ^2_{cal}, Figure 5-25 and Figure 5-16indicates that the equation with intercept would predict the shear in stage of soil cover more precisely.

Horizontal deflection, live load stage (Δx_{LL}):

- Criteria for Goodness of fit

1) R^2=0.9602

2) Chi-squared test: $\chi^2_{\text{cal}} = 49.8705 < \chi^2_{\text{table}}(\text{n} = 606, \alpha = 0.05) = 664.3732$

$$\Delta x_{LL}(in.) = (OD \times t)^{0.90}(\alpha)^{-0.14}(E_{embed})^{-0.06}(\beta)^{-0.06}(E_{back})^{-0.12}\left(\frac{W_T}{OD}\right)^{-0.71}(E_w)^{-0.38}\left(\frac{p}{OD}\right)^{0.23} \quad \text{5-36}$$

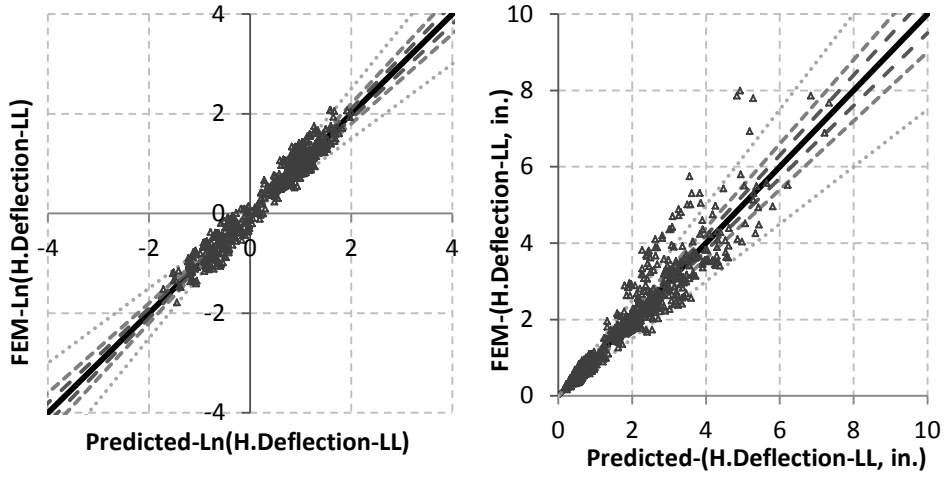

Figure 5-27 Comparison of observed and the predicted horizontal deflection at stage of live load (without intercept)

Figure 5-27 illustrates the comparison of predicted and observed values for horizontal deflection in the stage of live load for the equations without intercept. Comparing Figure 5-27 and Figure 5-17 it can be concluded that either equation with intercept or without intercept would predict the horizontal deflection in the stage of live load precisely.

Vertical deflection, live load stage (Δy_{LL}):

- Criteria for Goodness of fit

1) R^2=0.9709
2) Chi-squared test: $\chi^2_{\text{cal}} = 82.146 < \chi^2_{\text{table}}(\text{n} = 615, \alpha = 0.05) = 673.7921$

$$\Delta y_{LL}(in.) = (OD \times t)^{0.87}(\alpha)^{-0.02}(E_{embed})^{-0.03}(\beta)^{-0.09}(E_{back})^{-0.10}\left(\frac{W_T}{OD}\right)^{-0.69}(E_w)^{-0.46}\left(\frac{p}{OD}\right)^{0.25} \quad 5\text{-}37$$

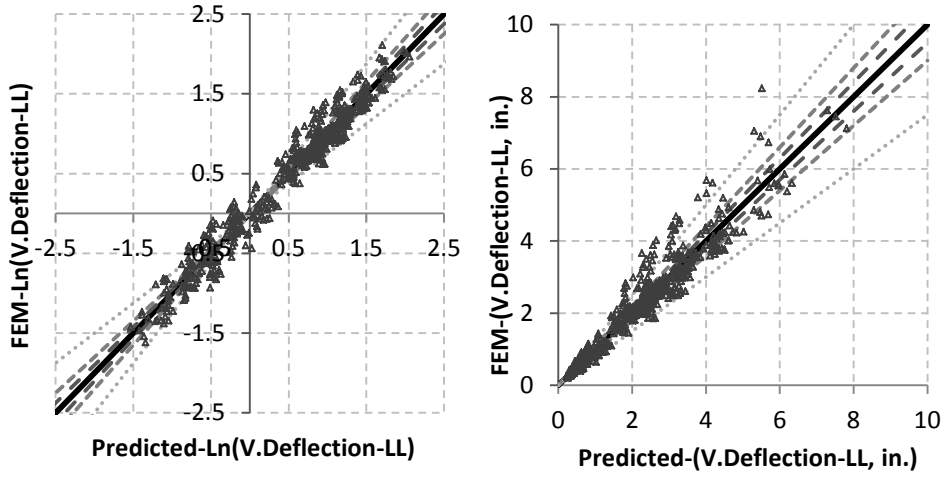

Figure 5-28 Comparison of observed and the predicted vertical deflection at stage of live load (without intercept)

Figure 5-28 illustrates the comparison of predicted and observed values for horizontal deflection in the stage of soil cover for the equations without intercept. Comparing Figure 5-28 and Figure 5-18 it can be concluded that both equations with or without intercept would predict the vertical deflection in the stage of live load precisely.

Moment, live load stage (M_{LL}):

- Criteria for Goodness of fit

1) R^2=0.9881
2) Chi-squared test: $\chi^2_{\text{cal}} = 2270.462 > \chi^2_{\text{table}}(\text{n} = 601, \alpha = 0.05) = 659.1405$

$$M\left(\frac{Kip-in.}{lin\ ft}\right)$$

$$= \frac{1}{1000}(OD \qquad \text{5-38}$$

$$\times t)^{2.55}(\alpha)^{-0.86}(E_{embed})^{0.82}(\beta)^{-0.70}(E_{back})^{0.04}\left(\frac{W_T}{OD}\right)^{3.44}(E_w)^{-0.71}\left(\frac{p}{OD}\right)^{0.44}$$

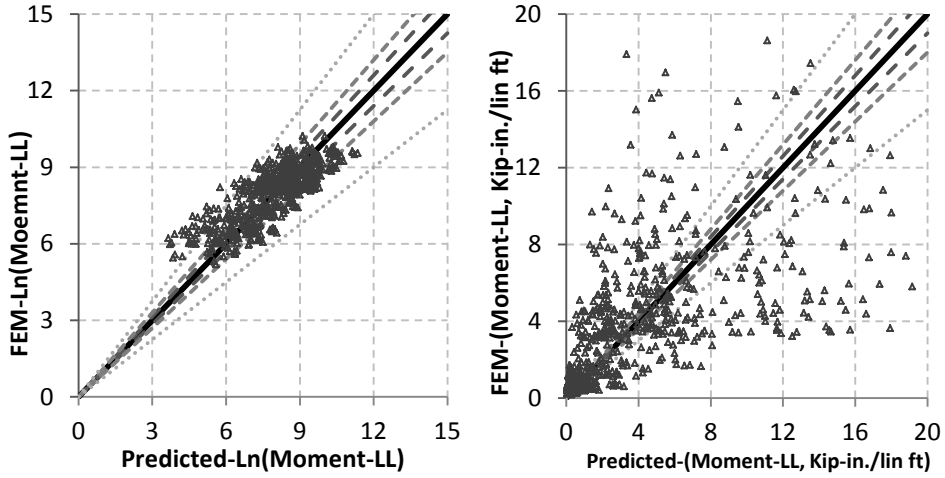

Figure 5-29 Comparison of observed and the predicted moment at stage of live load (without intercept)

Comparing the R^2 for Equation 5-38 (R^2=0.9881) and Equation 5-28 (R^2=0.9543), Equation 5.38 has a larger R^2 but comparison of the χ^2_{cal}, Figure 5-29 and Figure 5-19 indicates that the equation with intercept would predict the moment in stage of live load more precisely.

Thrust, live load stage (T_{LL}):

- Criteria for Goodness of fit

1) R^2=0.9822
2) Chi-squared test: $\chi^2_{\text{cal}} = 8061.665 > \chi^2_{\text{table}}(\text{n} = 641, \alpha = 0.05) = 701.0021$

$$T\left(\frac{Kip}{lin\ ft}\right) = \frac{1}{1000}(OD \times t)^{1.94}(\alpha)^{-0.92}(E_{embed})^{1.13}(\beta)^{-0.83}(E_{back})^{0.17}\left(\frac{W_T}{OD}\right)^{4.48}(E_w)^{-0.30}\left(\frac{p}{OD}\right)^{0.63} \quad 5\text{-}39$$

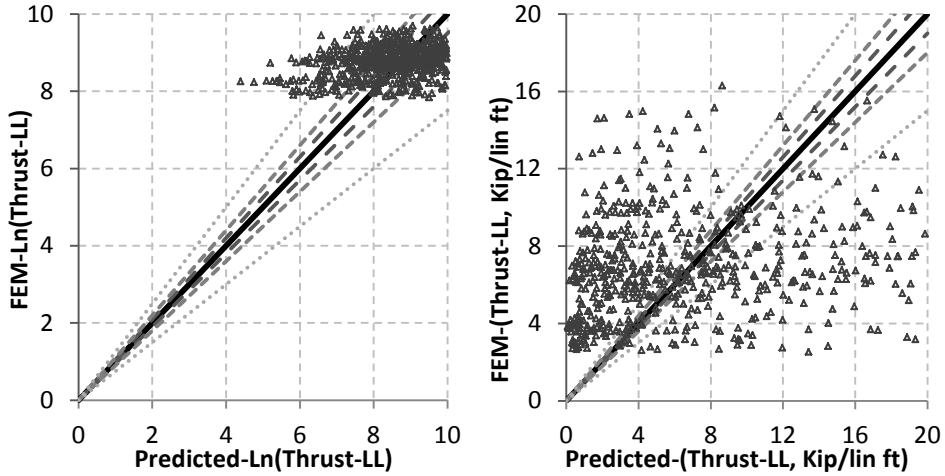

Figure 5-30 Comparison of observed and the predicted thrust at stage of live load (without intercept)

Comparing the R^2 for Equation 5-39 (R^2=0.9822) and Equation 5-29 (R^2=0. 0.9212), Equation 5.39 has a larger R^2 but comparison of the χ^2_{cal}, Figure 5-30 and Figure 5-20 indicates that the equation with intercept would predict the thrust in stage of soil cover more precisely.

Shear, live load stage (V_{LL}):

- Criteria for Goodness of fit

1) R^2=0.982
2) Chi-squared test: $\chi^2_{\text{cal}} = 4696.489 > \chi^2_{\text{table}}(\text{n} = 652, \alpha = 0.05) = 712.501$

$$V\left(\frac{Kip}{lin\ ft}\right) = \frac{1}{1000}(OD \times t)^{1.84}(\alpha)^{-0.88}(E_{embed})^{1.12}(\beta)^{-0.85}(E_{back})^{0.11}\left(\frac{W_T}{OD}\right)^{4.19}(E_w)^{-0.19}\left(\frac{p}{OD}\right)^{0.59} \quad 5\text{-}40$$

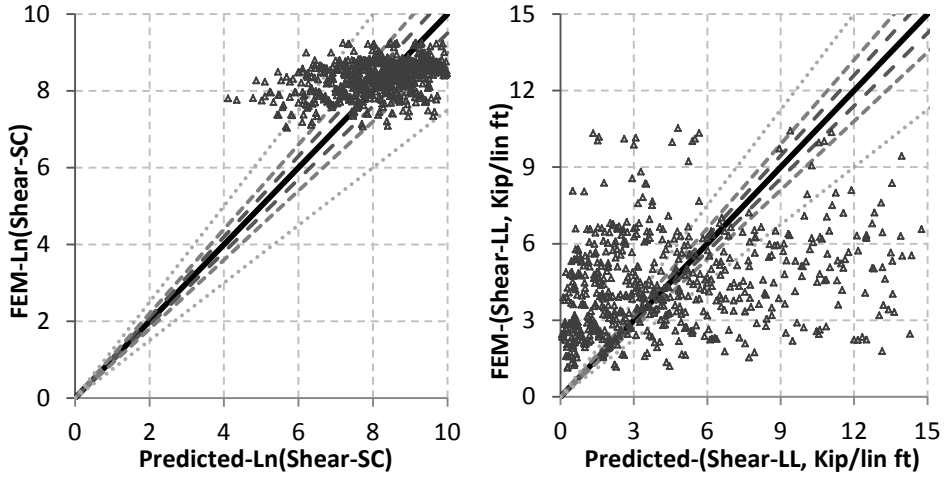

Figure 5-31 Comparison of observed and the predicted shear at stage of live load (without intercept)

Comparing the R^2 for Equation 5-40 (R^2=0.982) and Equation 5-30 (R^2=0. 0.9076), Equation 5.40 has a larger R^2 but comparison of the χ^2_{cal}, Figure 5-31 and Figure 5-21 indicates that the equation with intercept would predict the shear in stage of soil cover more precisely.

5.5. Conclusion

A design program was developed to automate the process of model creation using visual C# programming language. Different parameters for designing a pipeline, including trench properties and configuration, backfilling properties, and also pipe geometry and properties were required to be defined in the developed design program. Then the design program generates a Python code which is analyzed in the FEM

software. Moreover, the developed post-processor extracts the required data and creates the desired graph.

Using the developed design program and the post-processor a parametric study was developed based on different essential design parameters which were identified in this study. Then the results of the parametric study were used to develop design equations for buried steel pipes. Five (5) design equations were successfully developed for horizontal and vertical deflection, moment, thrust, and shear stress for buried steel pipe in two different stages of construction; stage of completion of backfilling (soil cover), and stage of applying live load (live load). It should also be noted that two sets of equation were developed; in the first set, the intercept was included in the equations hence in the second set the intercept was removed from the equations. The results of both cases were compared for each equation in detail.

Different statistical methods were adopted to verify the goodness of fit for each set of equation. The predicted values for different dependent variables were then compared with the observed values from FEM. The comparison of the observed and predicted values and also different means to verify the goodness of fit indicated that developed equations were well fitted and also they predicted the pipe behavior.

Chapter 6

Summary and Conclusion

6.1 Summary

The Integrated Pipeline Project (IPL) is designed allowing multiple pipe material options capable of incorporating short-term and long-term soil performance. Steel and pre-stressed concrete cylinder pipes (PCCP) are among the pipe material options under considerations by the IPL Team. Generally, steel pipes are categorized as flexible pipe systems, which depend on their surrounding soil envelop to form a soil-structure interaction composite system to develop adequate stiffness and strength to carry the specified loads. Thus, carefully controlled backfilling of the trench width through proper compaction of selected soil material is an important factor in achieving optimum pipe performance. Studying the pipe behavior during backfilling is one of the priorities before designing and installing pipelines. Design limitations are introduced by the American Water Works Association (AWWA) for flexible and rigid pipes. These limitations are for both in service and ultimate conditions. Several backfill and embedment materials are used in different conditions. Estimating pipe behavior in different backfill conditions during installation and considering the soil properties along the project route and path are important factors.

A robust 3-D nonlinear finite element model was developed to predict the pipe behavior in various backfilling and loading conditions. Three (3) possible nonlinearities including geometric, material, and contact nonlinearities were considered in the developed FEM model. A unique algorithm was implemented in the FEM model for the first time to track the changes in the pipe geometry and correct the model geometry, accordingly. Also, for the first time, the induced lateral effect of soil compaction was modeled and applied on the backfilling material as a uniform thermal loading. Then, the

developed FEM model was used to predict the behavior of four (4) soil box tests which were conducted at University of Texas at Arlington. It should be noted that the soil box tests of this study were conducted at the Center for Underground Infrastructure Research and Education (CUIRE) at UT Arlington. The results were indicated that the developed FEM model successfully predicted the soil box tests. It should be noted that the soil box tests were conducted in a rigid concrete box. Thus, the effects of flexible trench wall were not considered in the conducted tests and also developed FEM model in this stage. Therefore the developed FEM model required more modifications to be capable of modeling a real conditions. Consequently, the developed model was further modified to enhance the model with the capability of analyzing different pipe diameters, different trench widths, various backfilling materials, different loading condition, and various trench wall materials. Moreover, three (3) field tests were designed and conducted at Rolling Hills Booster Pump Station, in Fort Worth, Texas. Then the modified model was used to evaluate the pipe behavior in the field test. The FEM model successfully predicted the pipe behavior in the field tests which represented the real conditions. This study was comprehensively discussed in another thesis (Bellaver, 2013) and a brief discussion of the field tests was presented in this dissertation.

Ultimately, a comprehensive parametric study was preformed based on the essential design parameters which were identified accurately in this study. Furthermore, a program using C# programming language was developed specifically for this research to generate the FEM model for the buried steel pipes. The Design Program was used to generate the parametric study cases in a fraction of time in comparison to conventional manual model generation. Then the results of the parametric study models were obtained from the finite element software using the post-processor program. The results for horizontal and vertical deflection, moment, thrust, and shear were obtained in this stage.

Then multi-linear regression analysis was used to develop design equations for the aforementioned results. The equations were developed as a function of the material and geometric properties of backfilling materials, trench wall materials, and steel pipe. It should be noted that the developed design equation could be implemented in the steel pipe design manuals including AWWA-M11 and ASCE-MOP119 as a benchmark for designing buried steel pipes.

6.2. Conclusion Remarks

- A unique comprehensive 3-D nonlinear FEM model was developed to predict the behavior of the buried steel pipes in a staged construction process. All the three (3) possible nonlinearities including material, geometric, and contact nonlinearities were included in the developed FEM model. The results of 4 soil box tests which were conducted at University of Texas at Arlington were predicted by developed FEM. It is concluded that the developed FEM model is capable of modeling the geometries and boundary conditions similar to the soil box tests. The difference between the predicted results and the test results is less than 1% for the conducted soil box tests.

- The induced lateral effect of compaction was modeled using thermal loading, for the first time. This method allows the user to exert a uniform stress as the lateral result of compaction force to the backfilling soil. The required induced lateral soil pressure for different soil material were recommended by verifying the FEM model with 4 soil box tests which were conducted at University of Texas at Arlington. The induced lateral stress due to compaction is related to un-drained shear strength for cohesive soils. This induced lateral stress varies between 6.9 to 27.6 kPa (1 to 4 psi) for different soil types.

- The changes in geometry of the steel pipe during staged construction were modeled in the developed FEM model precisely by defining required algorithms to

track the geometry of the pipes' nodes. This study is a pioneer in identifying and addressing these changes during stage construction. The changes in geometry of the pipe affect the pipe performance and behavior during backfilling and stage construction. It is concluded that the introduced algorithm for shape correction is capable of modeling different pipes in different configurations.

- The developed FEM model was further modified to enhance the model with the capability of modeling different trench and pipe configuration. These configurations include but are not limited to gap filler condition, CLSM backfilling, sloped trench wall, different pipe diameter, different trench width, different backfilling material, and different in-situ material. The results of 3 field tests conducted at Rolling Hills Booster Pump Station in Fort Worth, Texas were accurately predicted by the modified developed FEM model. It is concluded that the introduced modifications to the model utilized the model to simulate different configuration in real trench practices.

- The modified developed FEM model was used to prepare a design program using C# programming language. The developed design program generates the model in a fraction of time in comparison with the conventional manual model generation. The Design Program includes a pre- and post-processor. The essential parameters for steel pipe-soil interaction system design will fed in the pre-processor part of the Design Program. Then the Design Program will generate a FEM model based on the inputted design parameters. Moreover, the FEM software will be used to analyze the generated model. Then the post-processor will extract the required and desired graphs after completion of the analysis. The pre and post processor would be used to automate the process of simulation and analysis of different pipes in a fraction of time in compare to the conventional manual methods.

- The essential design parameters for a steel pipe-soil interaction system were identified in this study. Then a comprehensive parametric study was designed and conducted by changing the design parameters. The design parameters include but are not limited to pipe geometric properties, backfilling soil geometry and properties, level of compaction of backfilling material, and properties of in-situ soil.

- The results of parametric study models were used to develop design equations for buried steel pipes in different backfilling material. The design equations were developed for moment, shear, thrust, and horizontal and vertical deflection of steel pipe in two different stages of loading; after completion of soil cover, and after applying live load. The design equations are developed as a function of independent variables which include but not limited to: geometry and material properties of trench wall, material properties and geometrical information of backfilling material, and pipe diameter and its wall thickness. As shown in Figure 5-12 through Figure 5-21 the predicted value for deflection, moment, shear, and thrust using developed equations and FEM are within the band width of 75%. The R^2 values for the developed equations are greater than 90%.

- The design equations are recommended to use for preliminary design of buried steel pipes and different designing manuals including AWWA-M11 and ASCE-MOP119 could adopt the design equations for the benchmark of designing steel pipes in the applicable backfilling condition.

6.3 Suggested Future Studies

Some aspects of the research work presented herein needs to be further studied. Some suggestions for future studies on these topics are:

- Further investigation on the effect of adding different lining material including concrete lining is needed. Since the conducted tests in this study were used the steel pipes without lining, no lining was modeled. However, for this purpose, a new part

should be introduced to the developed FEM and the modified model should be verified with experimental tests on steel pipes with lining.

- The controlled low strength material (CLSM) is a popular backfilling material in designing pipes. Since the focus of this study was on soil material as backfilling, the development of design equations for configurations with CLSM is needed.
- More experimental and analytical investigations should be conducted to explore the material behavior and constitutive law for the CLSM.
- Although the developed FEM model incorporated the sloped wall trenches, this configuration needs further verification through full scale tests. A study would be beneficial to investigate the effect of sloped trench wall and verify the developed FEM model.
- The effect of pressurizing the pipe internally should be investigated in the future work.
- This study investigates the behavior of steel pipes. However, performance of different flexible pipes and also rigid and semi-rigid pipes in different backfilling configurations is not addressed in the current study. Evaluation of different pipe material behavior is suggested in future studies.
- The developed FEM model should be adopted to evaluate other methods of quality control such as laser profiling measurements of the pipe diameter and the recommended method by MOP-199.

Appendix A

Results of Conducted FEM Analysis for Parametric Study

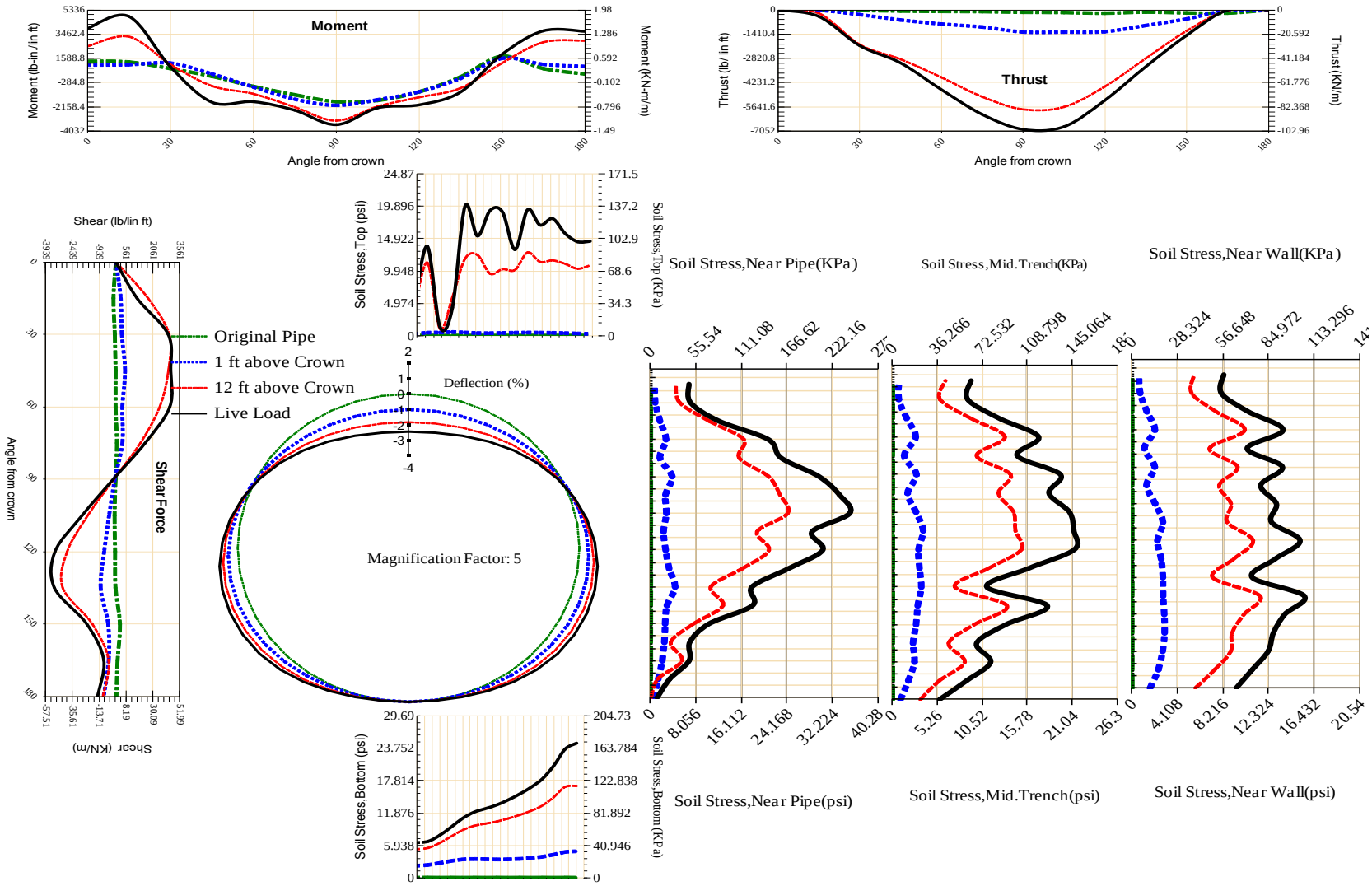

Figure A-1 Param-108-PW230-SF10SF-OD+72-EW5-H12-LiveLoad

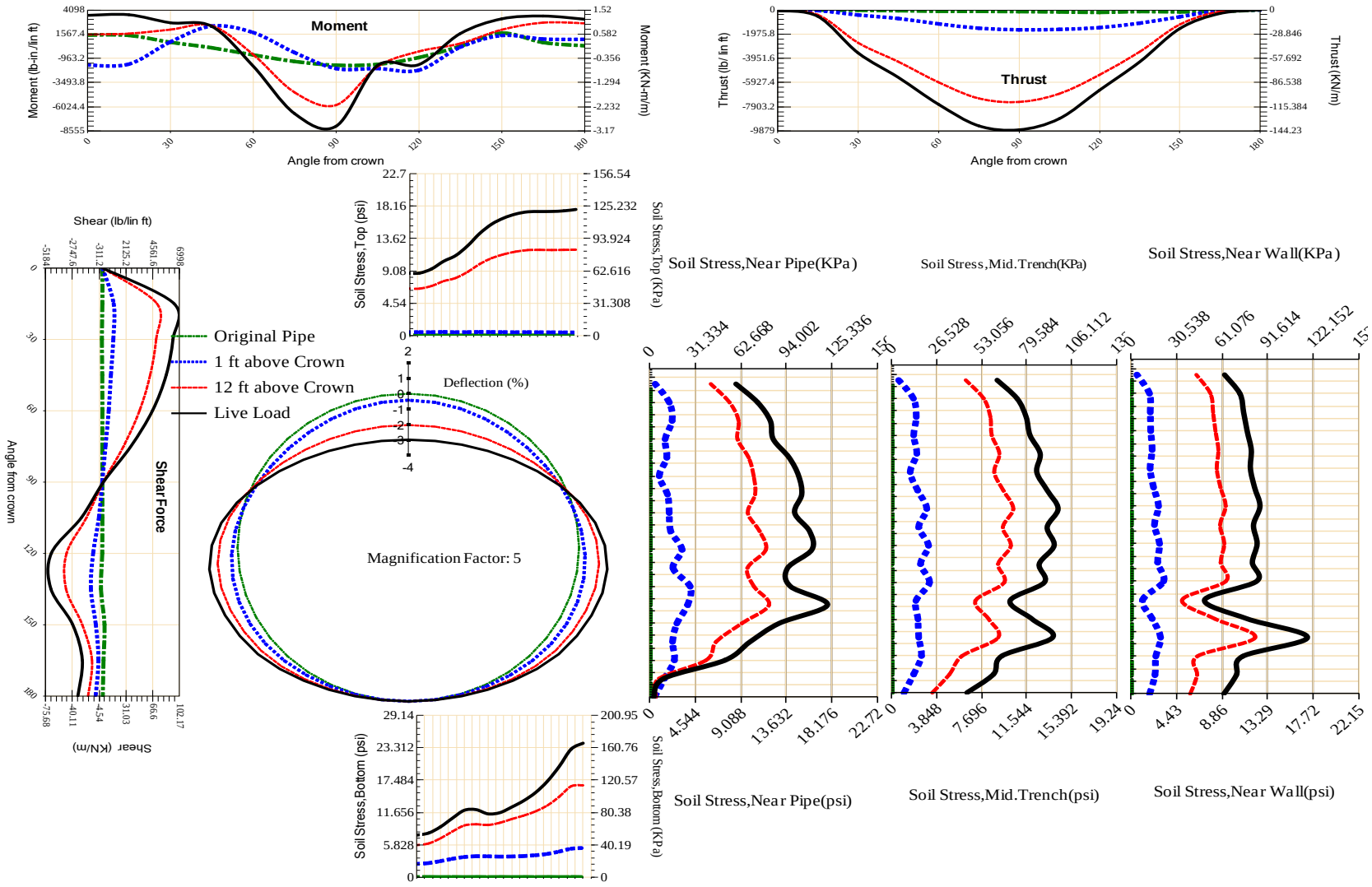

Figure A-2 Param-108-PW230-SF3OR-OD+72-EW5-H12-LiveLoad

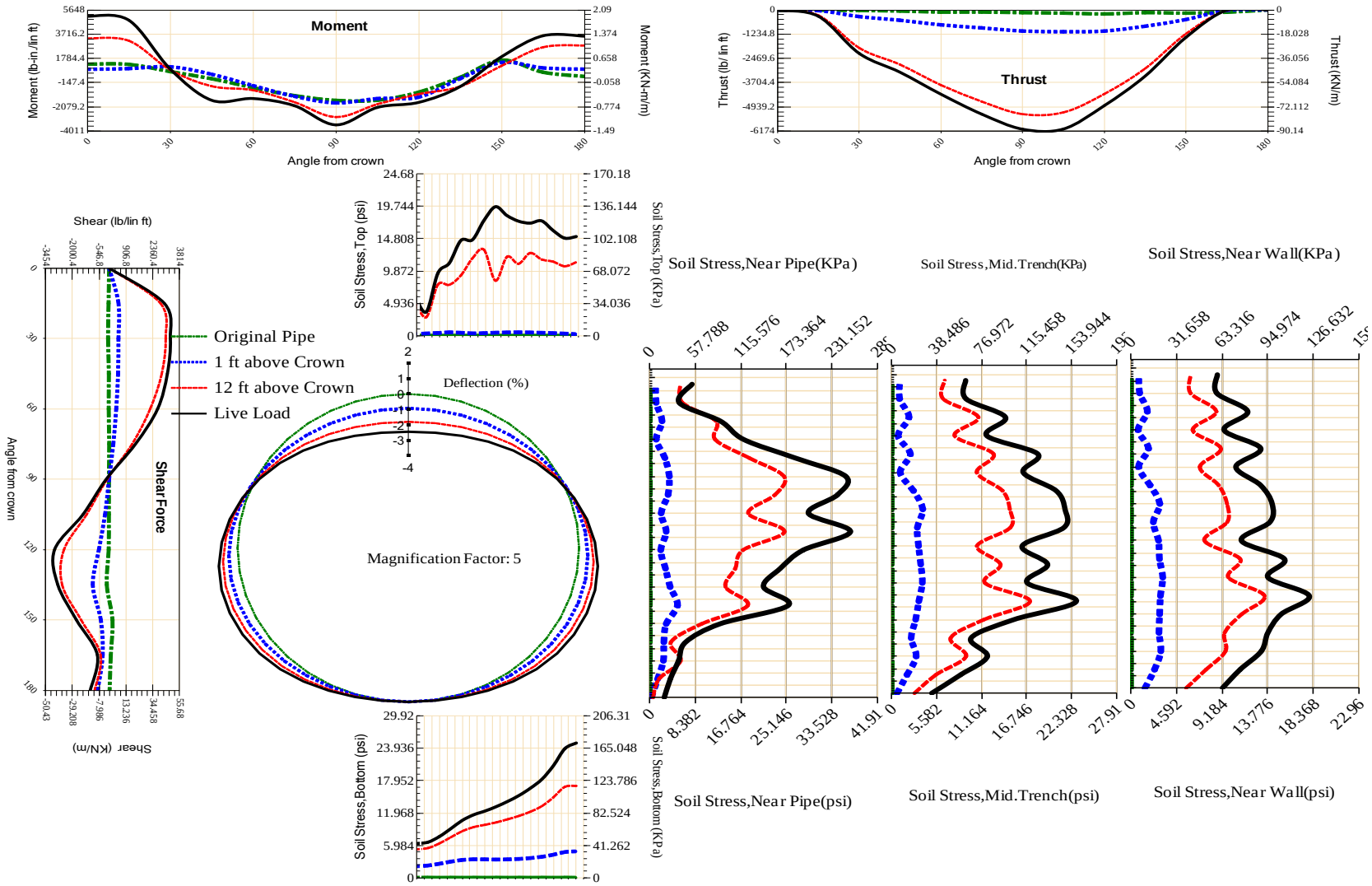

Figure A-3 Param-108-PW230-SF3TR-OD+72-EW5-H12-LiveLoad

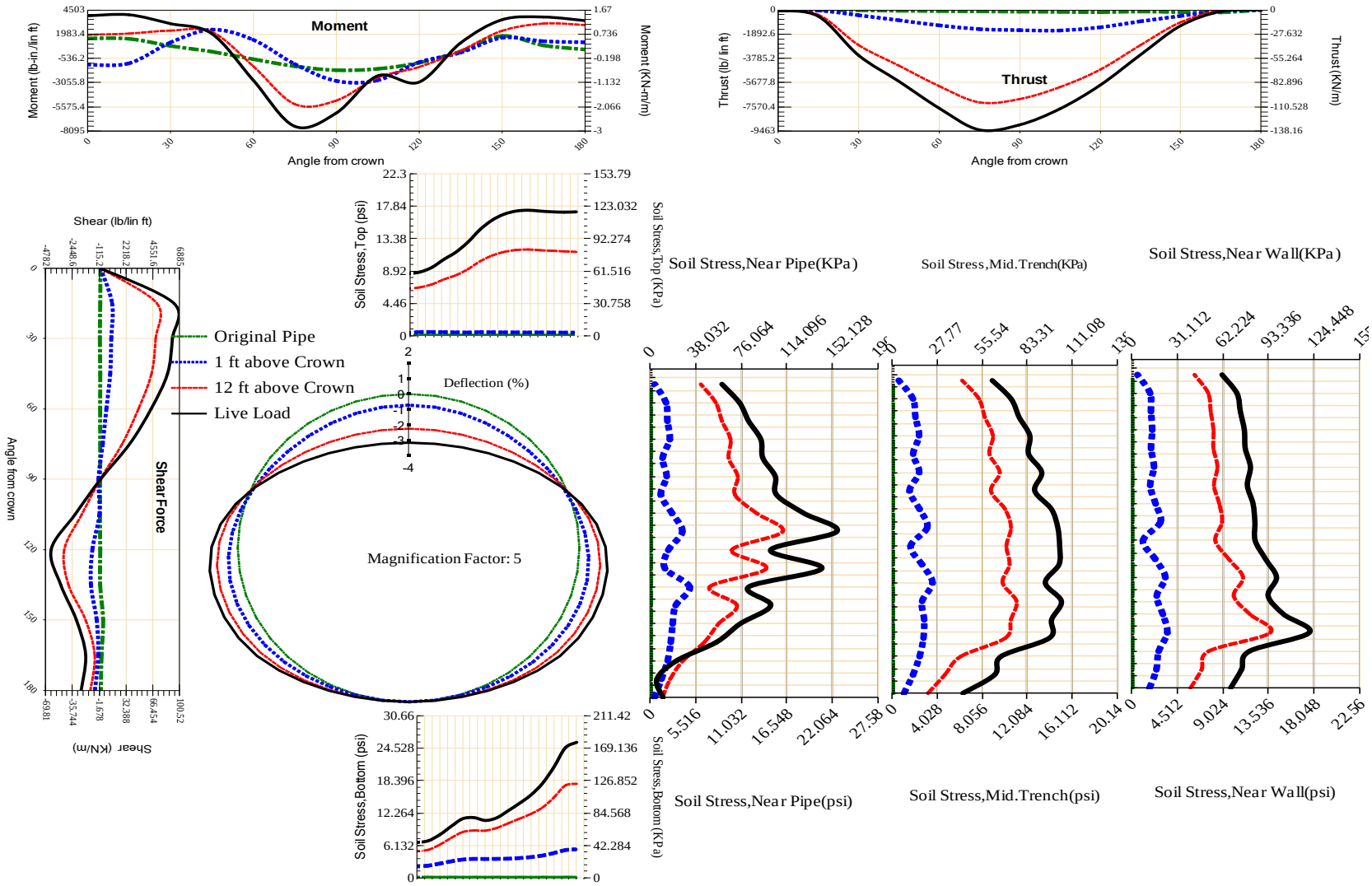

Figure A-4 Param-108-PW230-SF5OR-OD+72-EW5-H12-LiveLoad

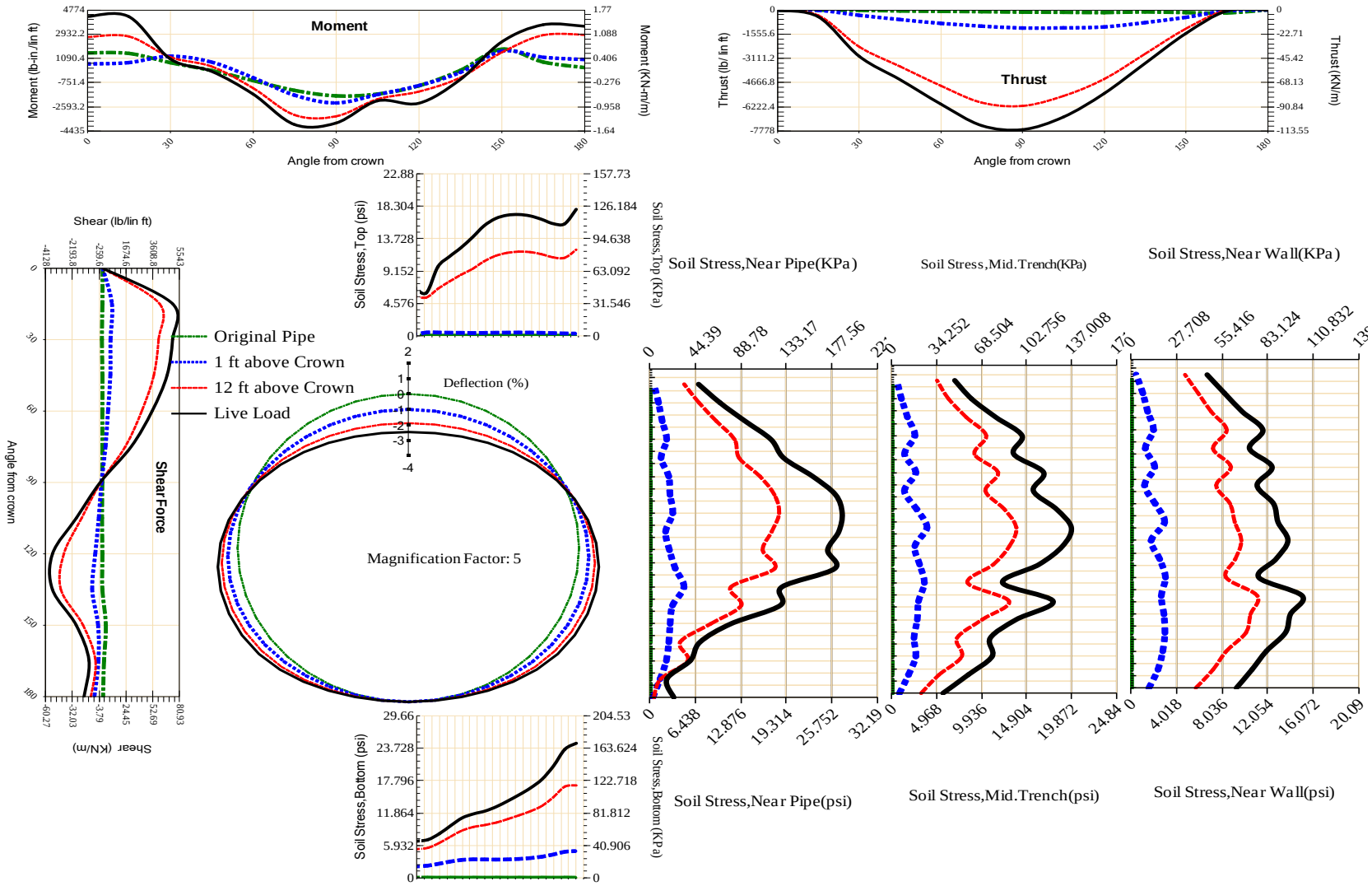

Figure A-5 Param-108-PW230-SF5TR-OD+72-EW5-H12-LiveLoad

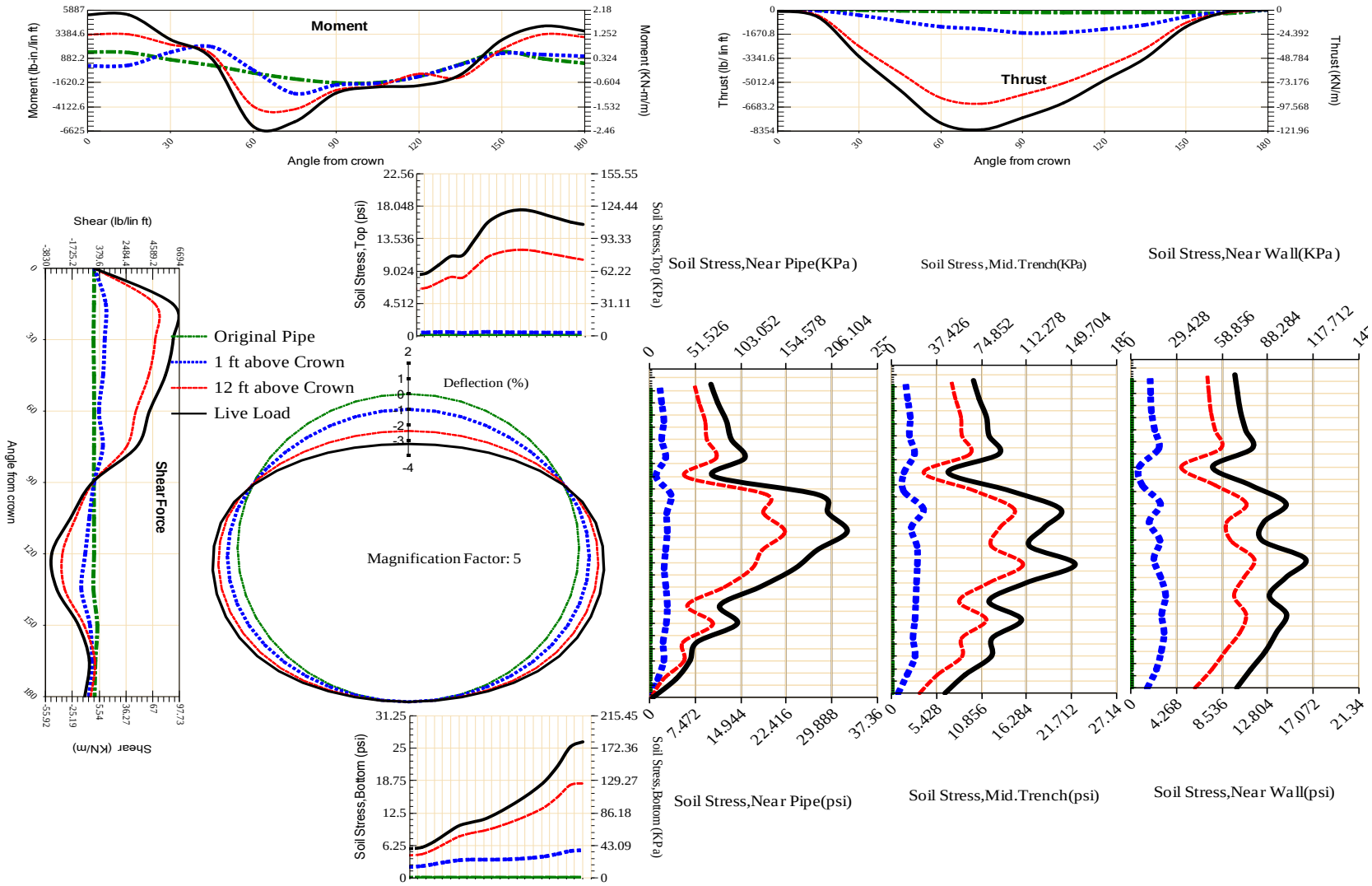

Figure A-6 Param-108-PW230-SF7OR-OD+72-EW5-H12-LiveLoad

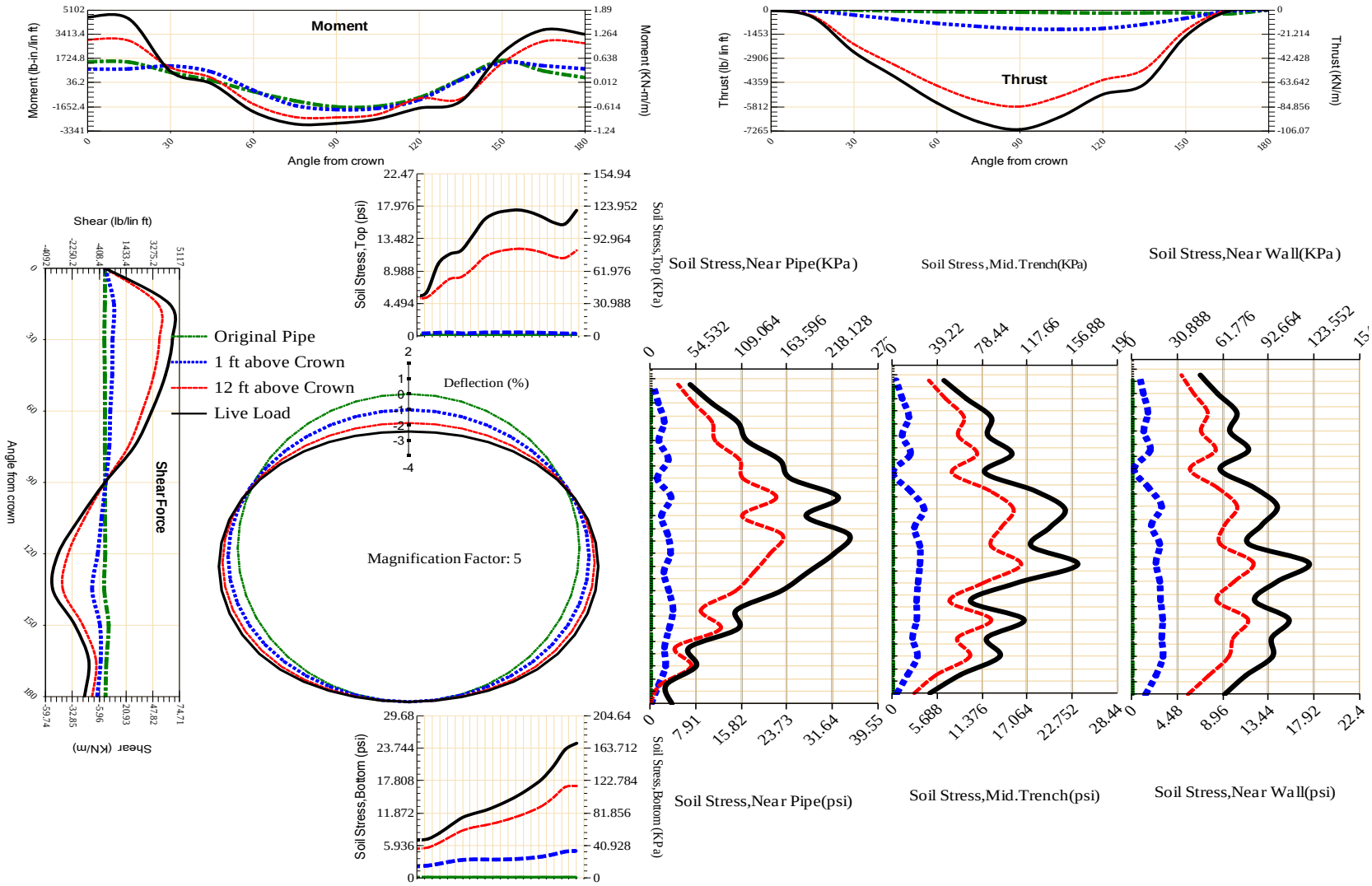

Figure A-7 Param-108-PW230-SF7TR-OD+72-EW5-H12-LiveLoad

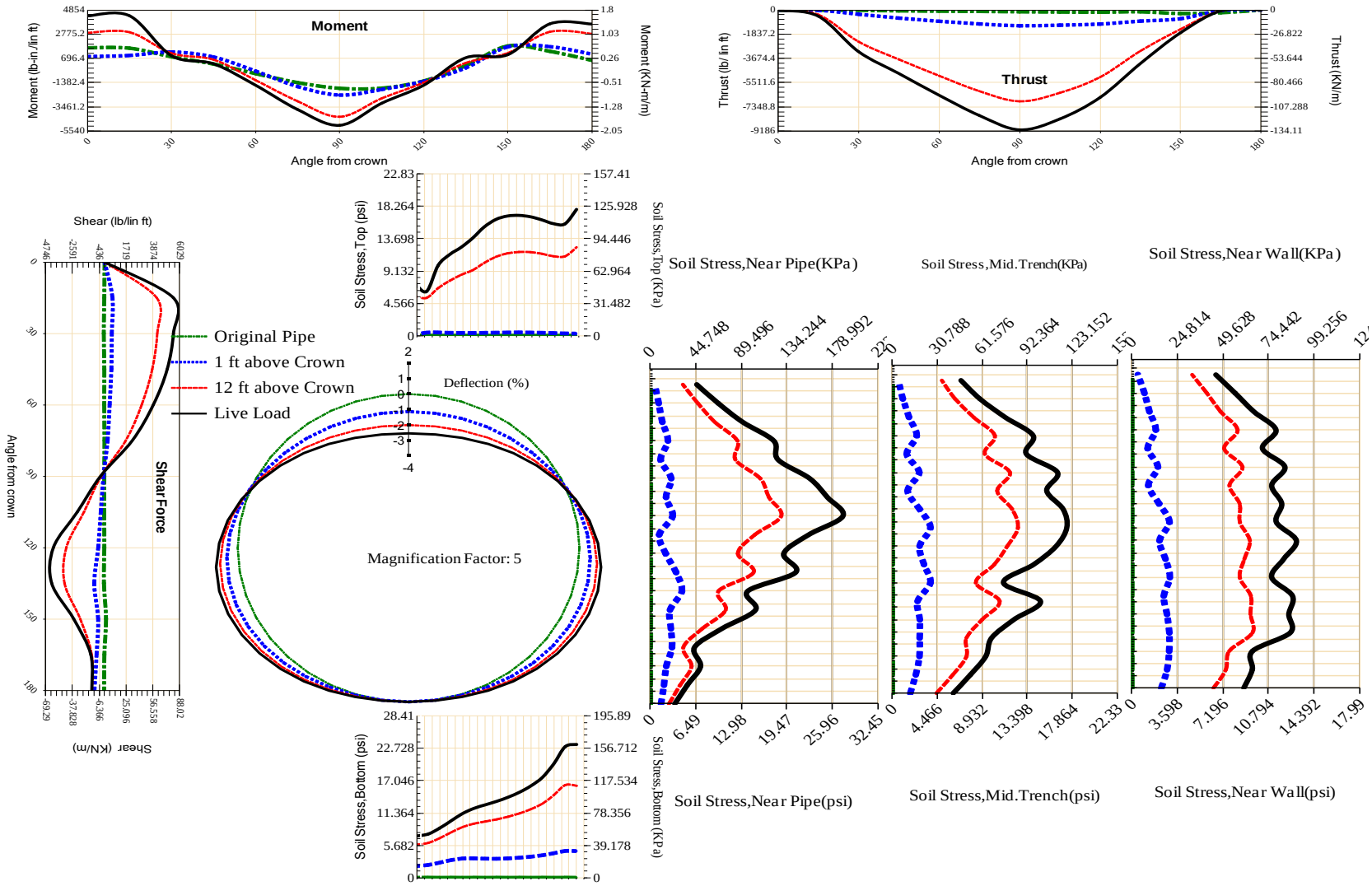

Figure A-8 Param-108-PW230-TR10TR-OD+72-EW5-H12-LiveLoad

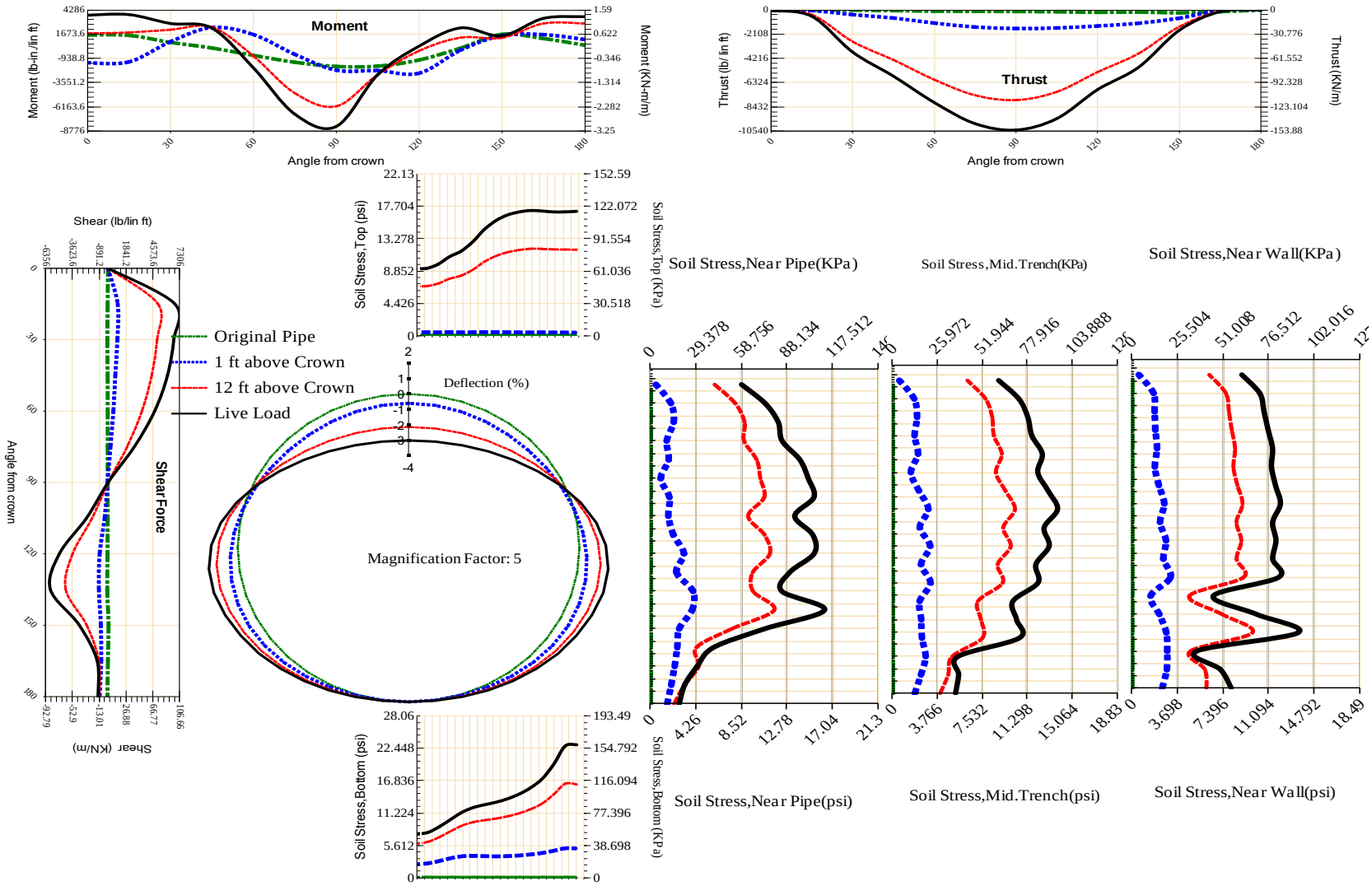

Figure A-9 Param-108-PW230-TR3OR-OD+72-EW5-H12-LiveLoad

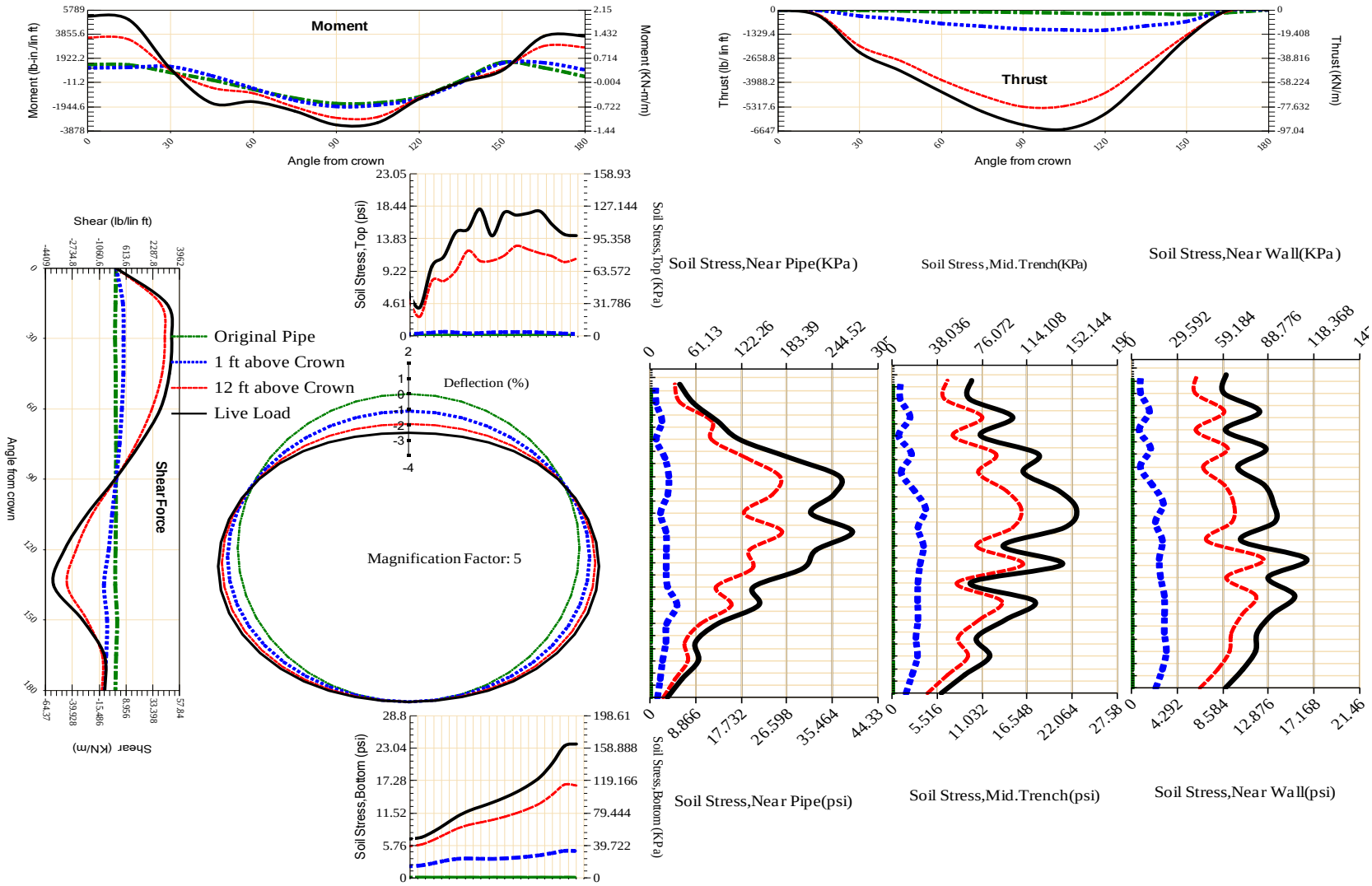

Figure A-10 Param-108-PW230-TR3SF-OD+72-EW5-H12-LiveLoad

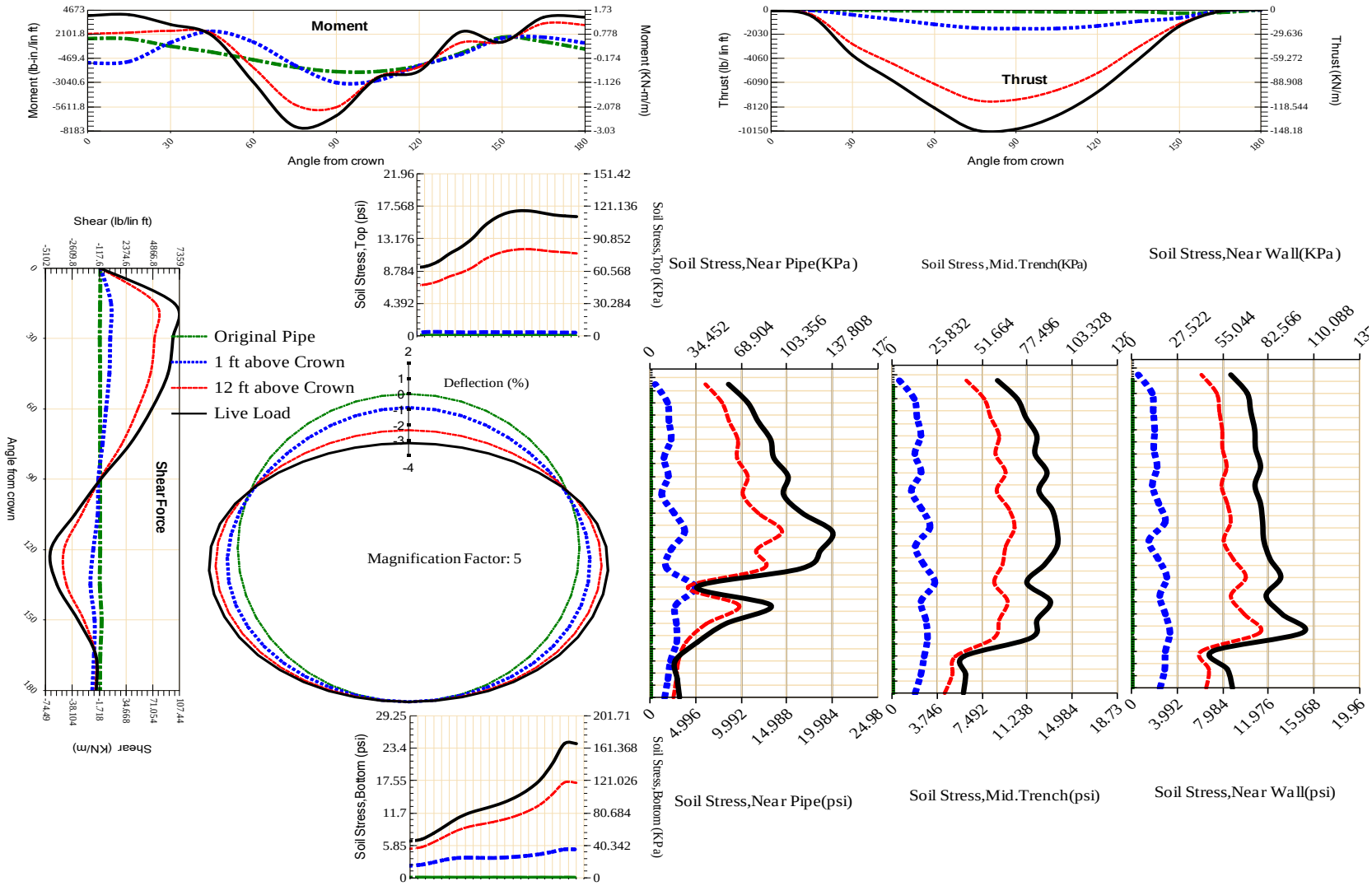

Figure A-11 Param-108-PW230-TR5OR-OD+72-EW5-H12-LiveLoad

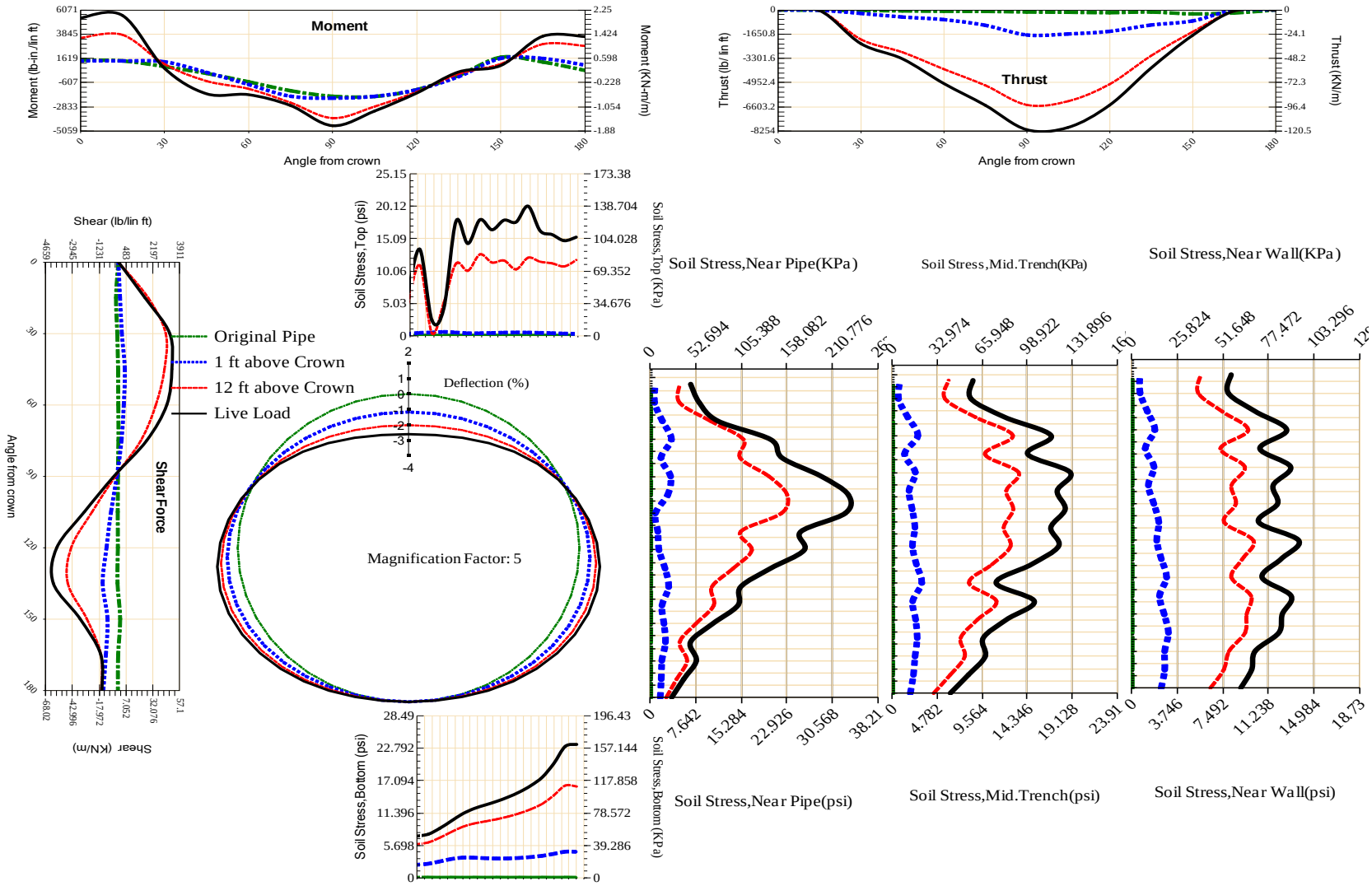

Figure A-12 Param-108-PW230-TR5SF-OD+72-EW5-H12-LiveLoad

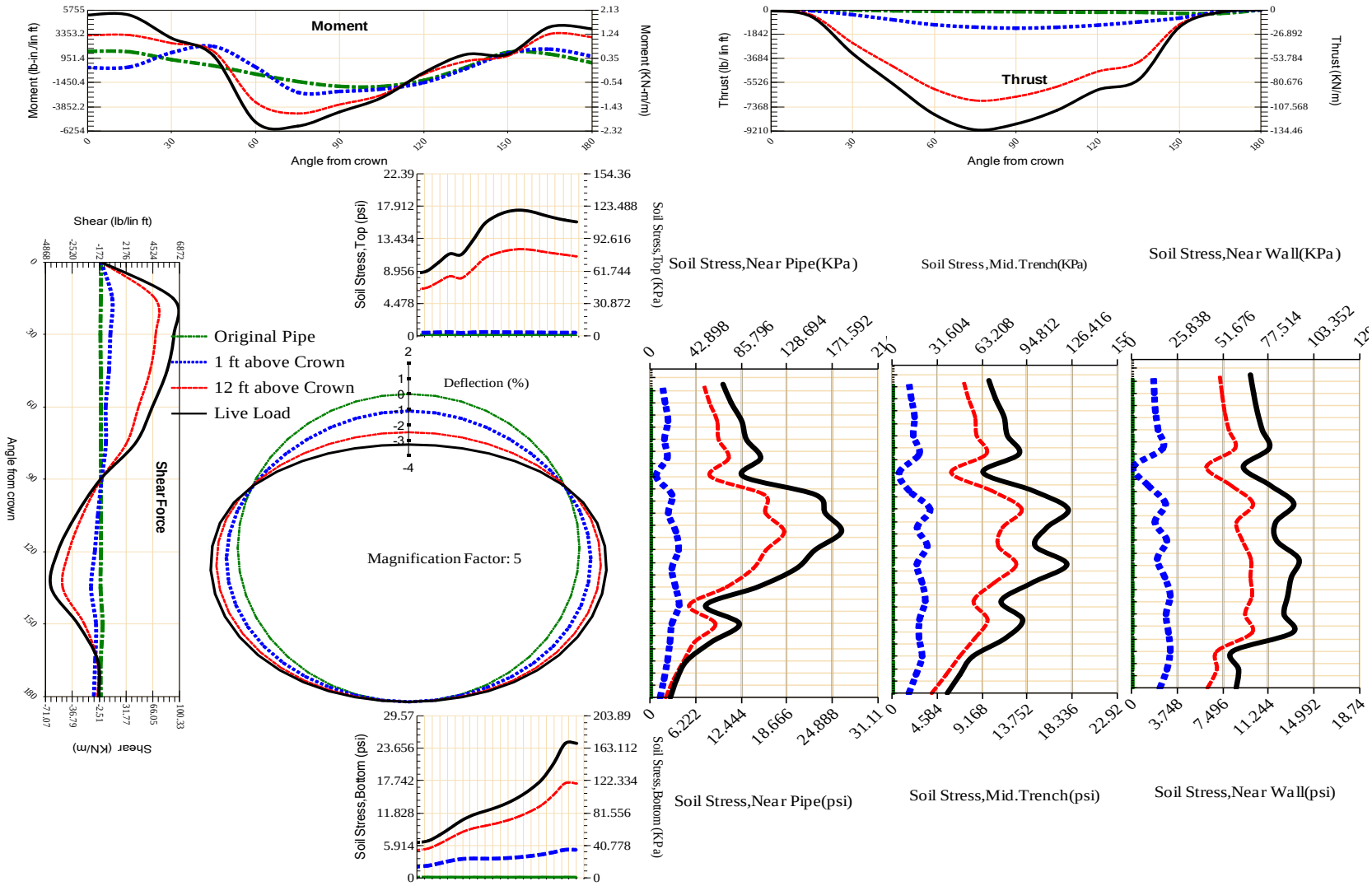

Figure A-13 Param-108-PW230-TR7OR-OD+72-EW5-H12-LiveLoad

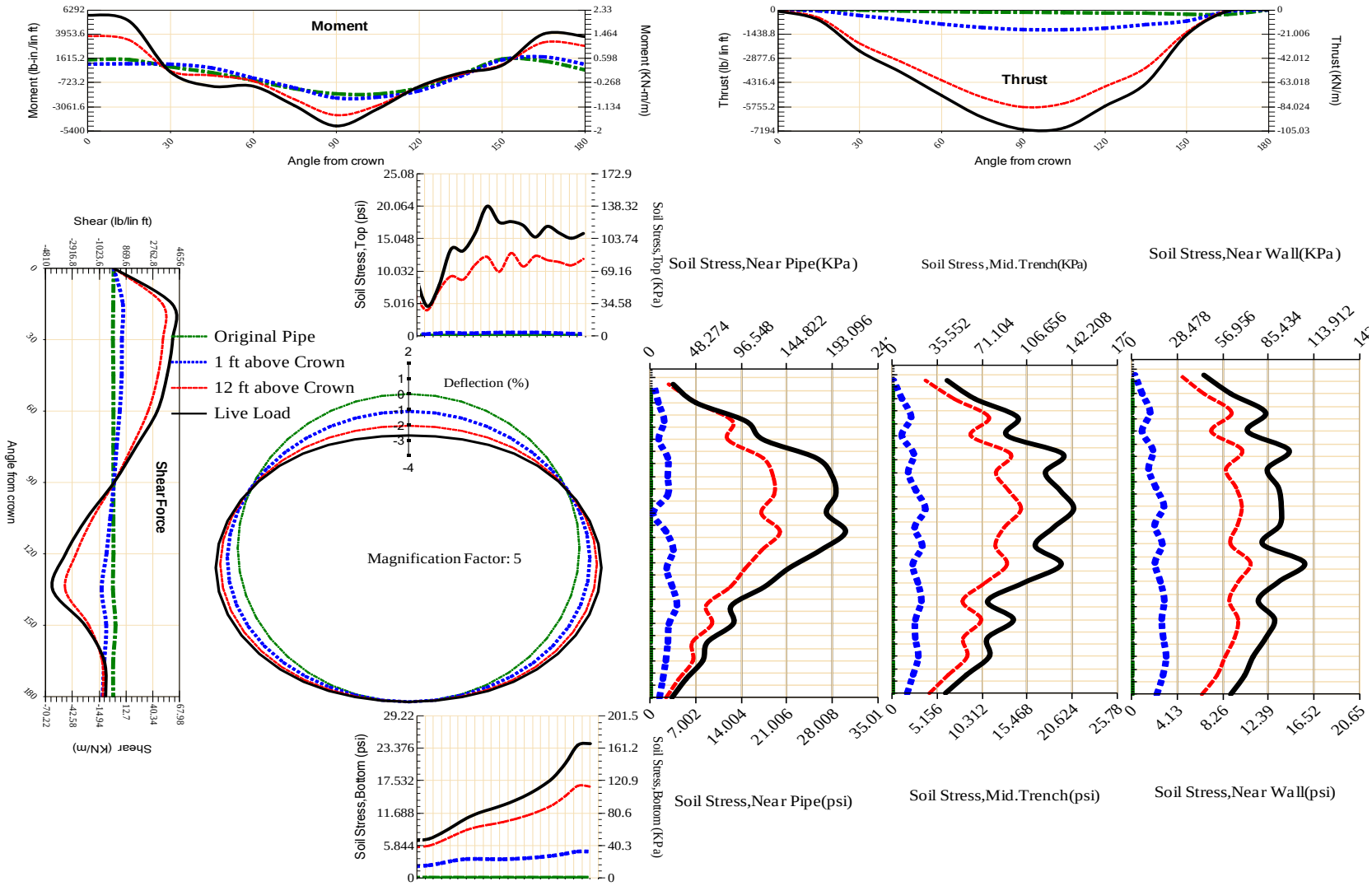

Figure A-14 Param-108-PW230-TR7SF-OD+72-EW5-H12-LiveLoad

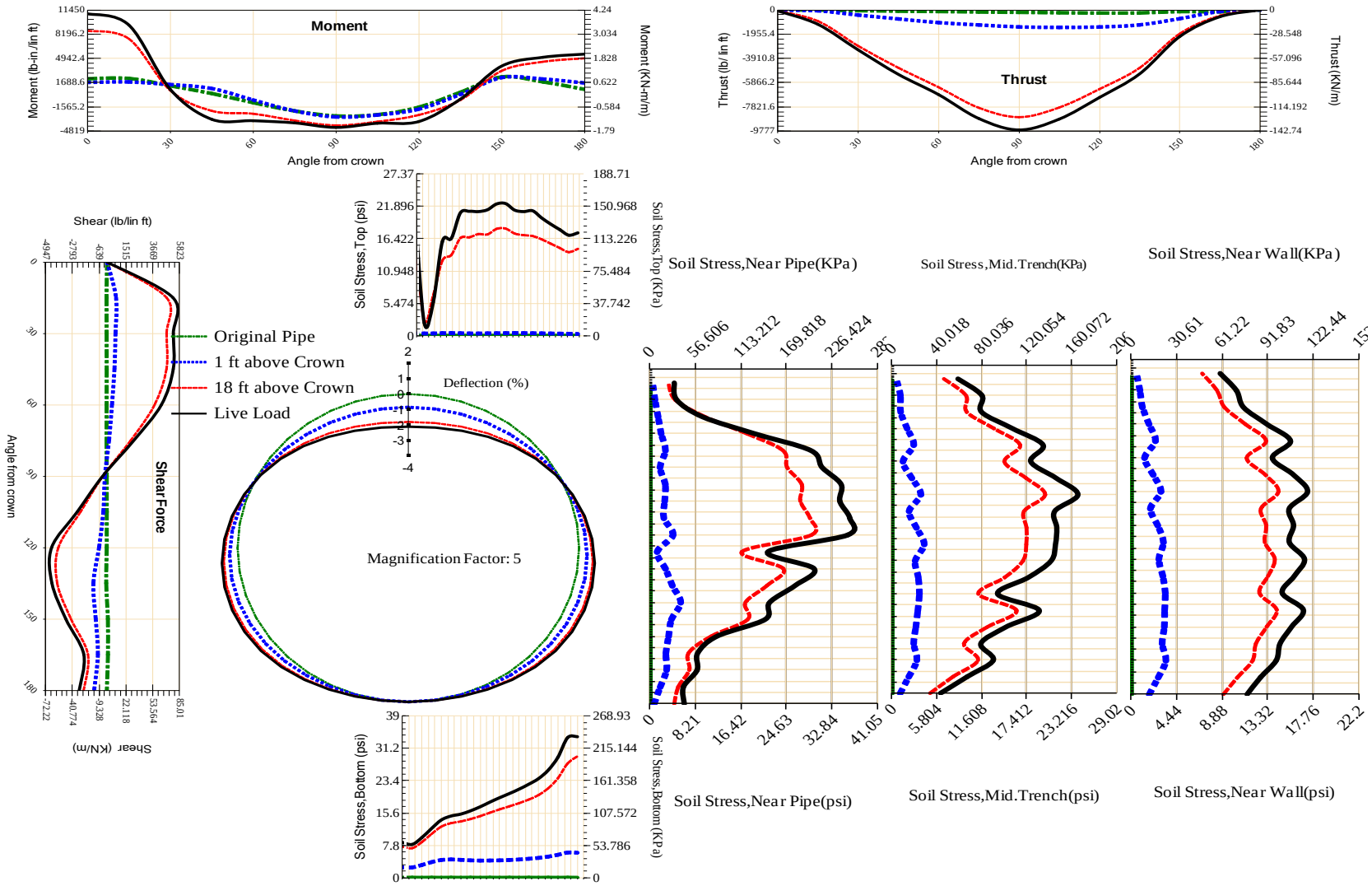

Figure A-15 Param-120-PW200-SF10SF-OD+108-EW10-H18-LiveLoad

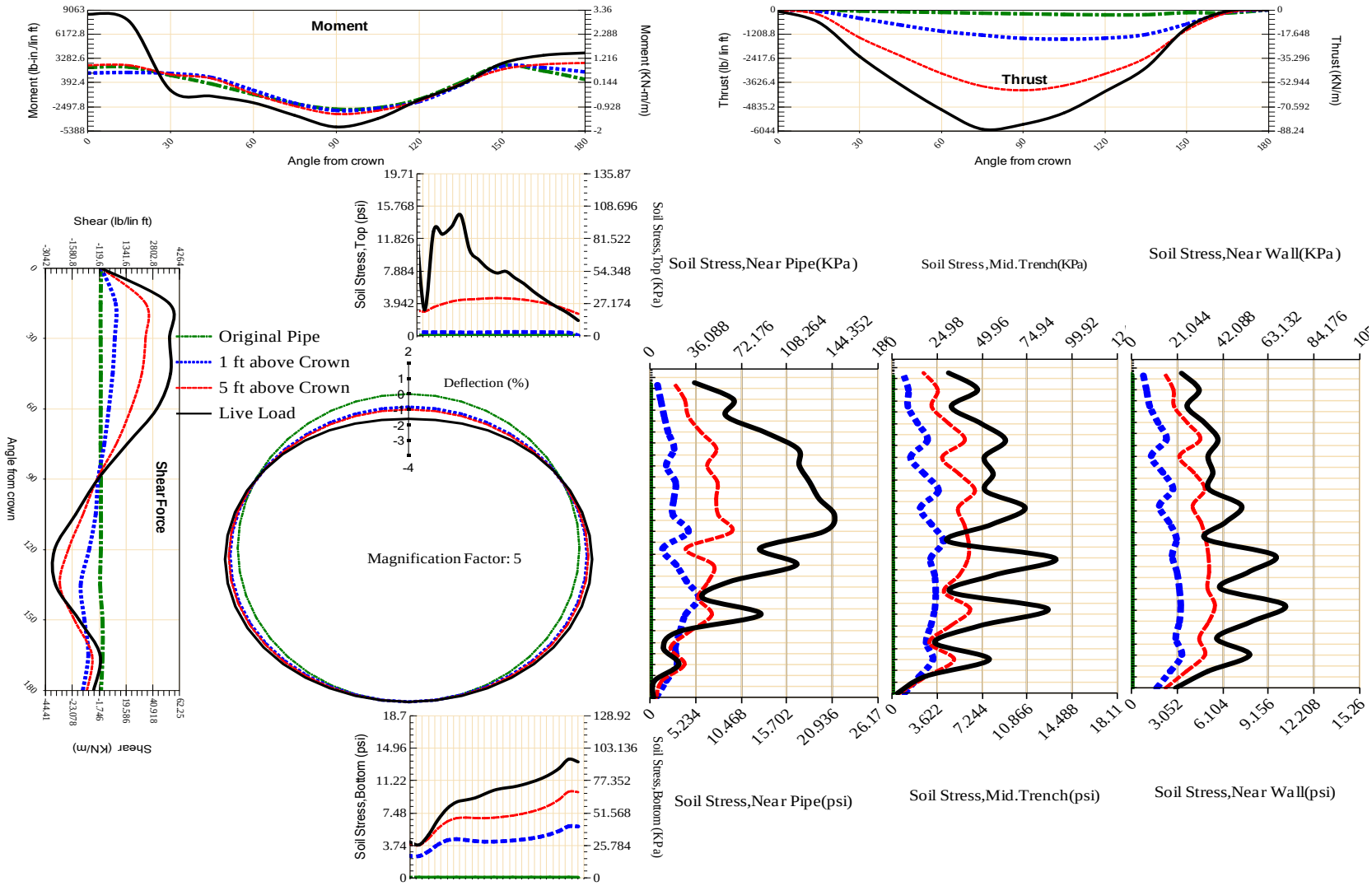

Figure A-16 Param-120-PW200-SF10SF-OD+108-EW10-H5-LiveLoad

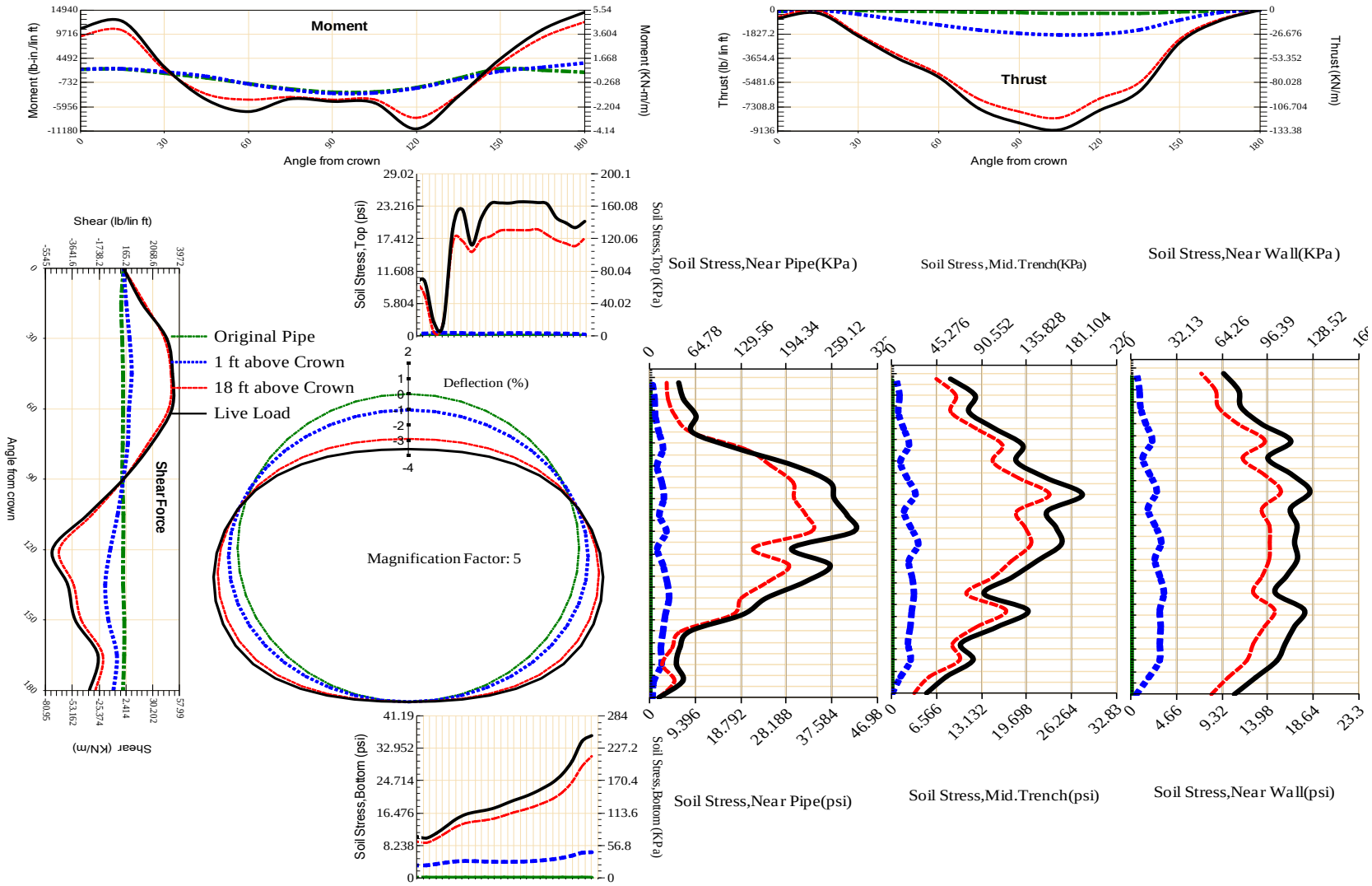

Figure A-17 Param-120-PW200-SF10SF-OD+108-EW3-H18-LiveLoad

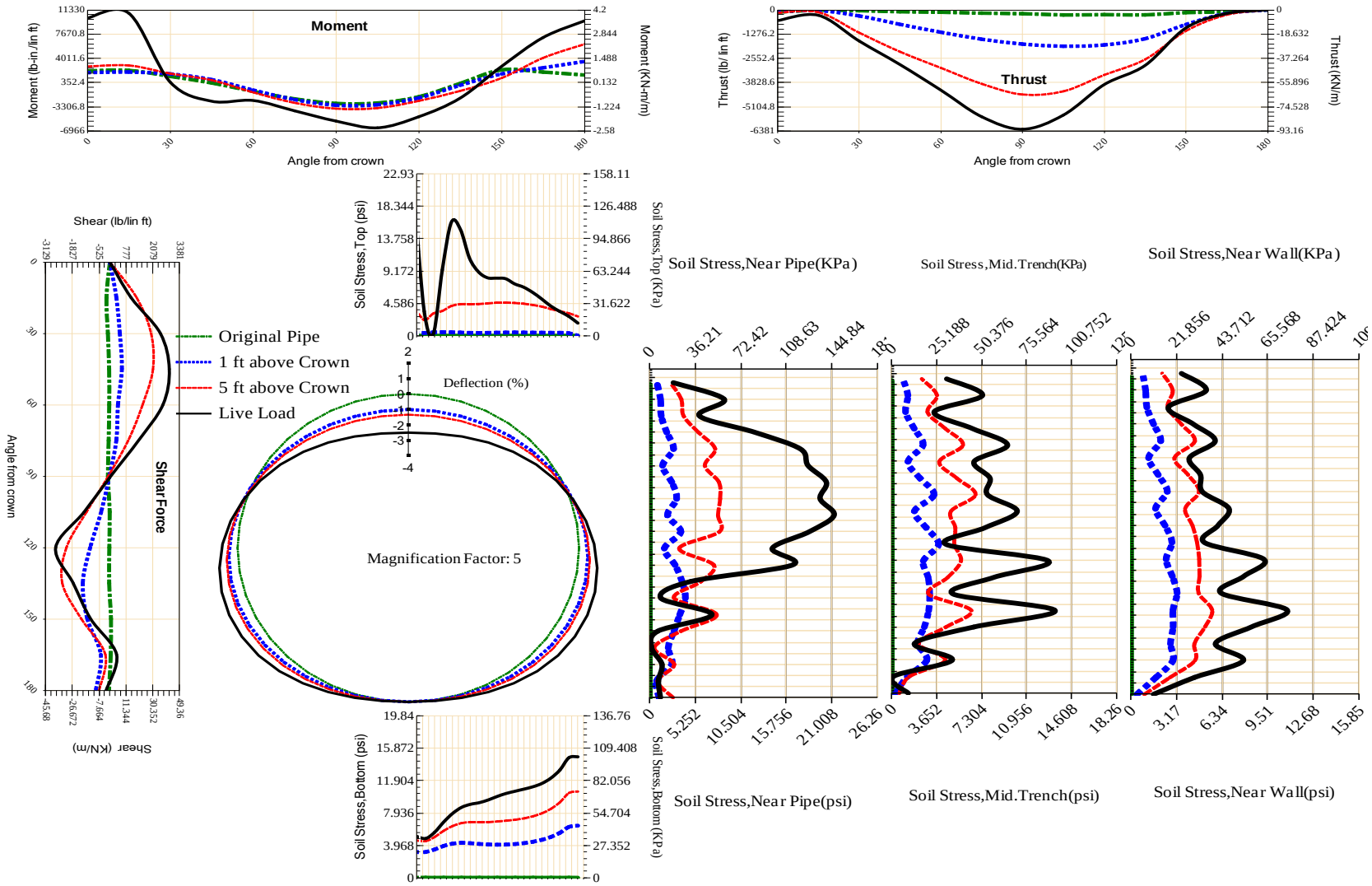

Figure A-18 Param-120-PW200-SF10SF-OD+108-EW3-H5-LiveLoad

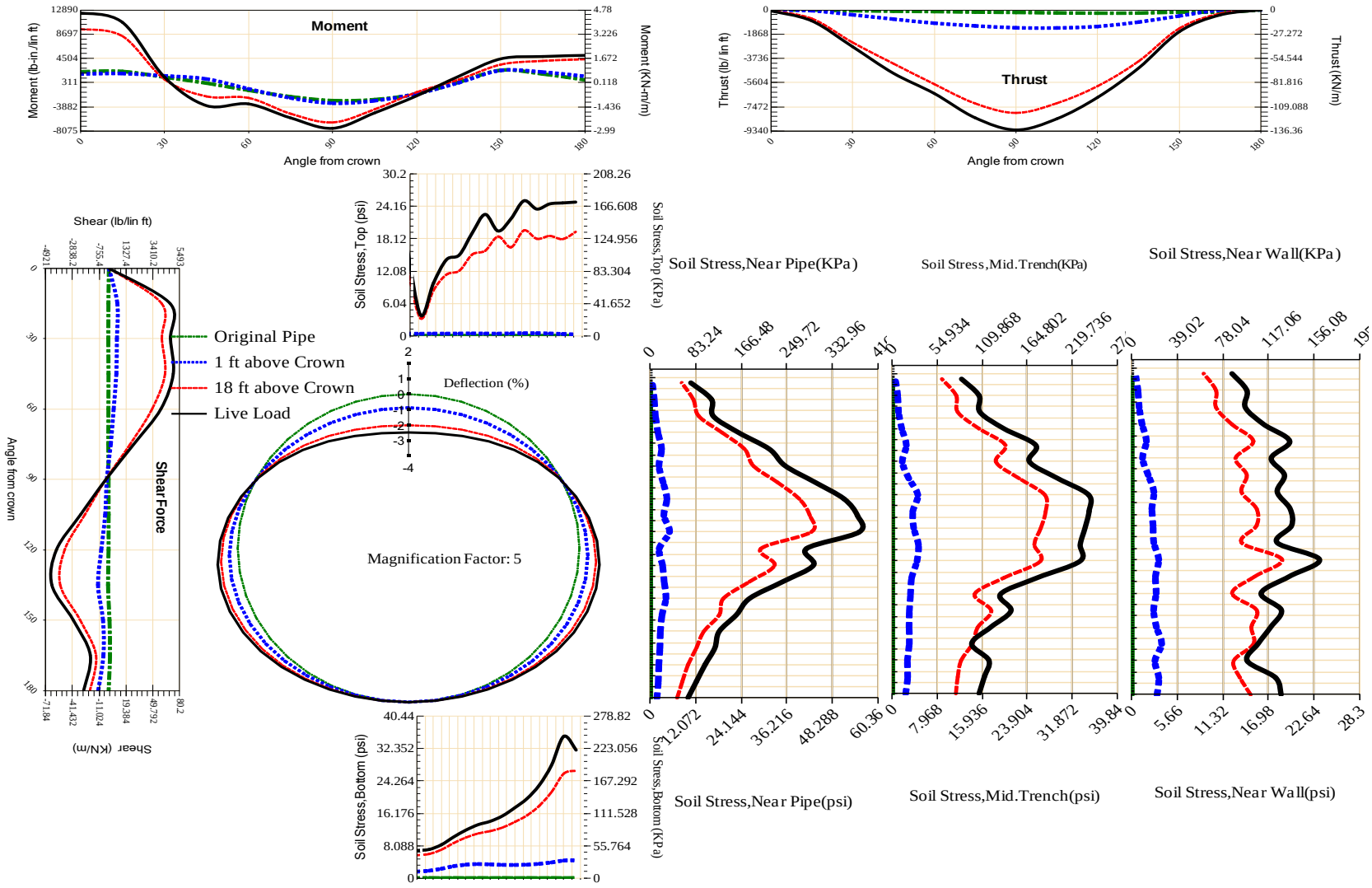

Figure A-19 Param-120-PW200-SF10SF-OD+48-EW10-H18-LiveLoad

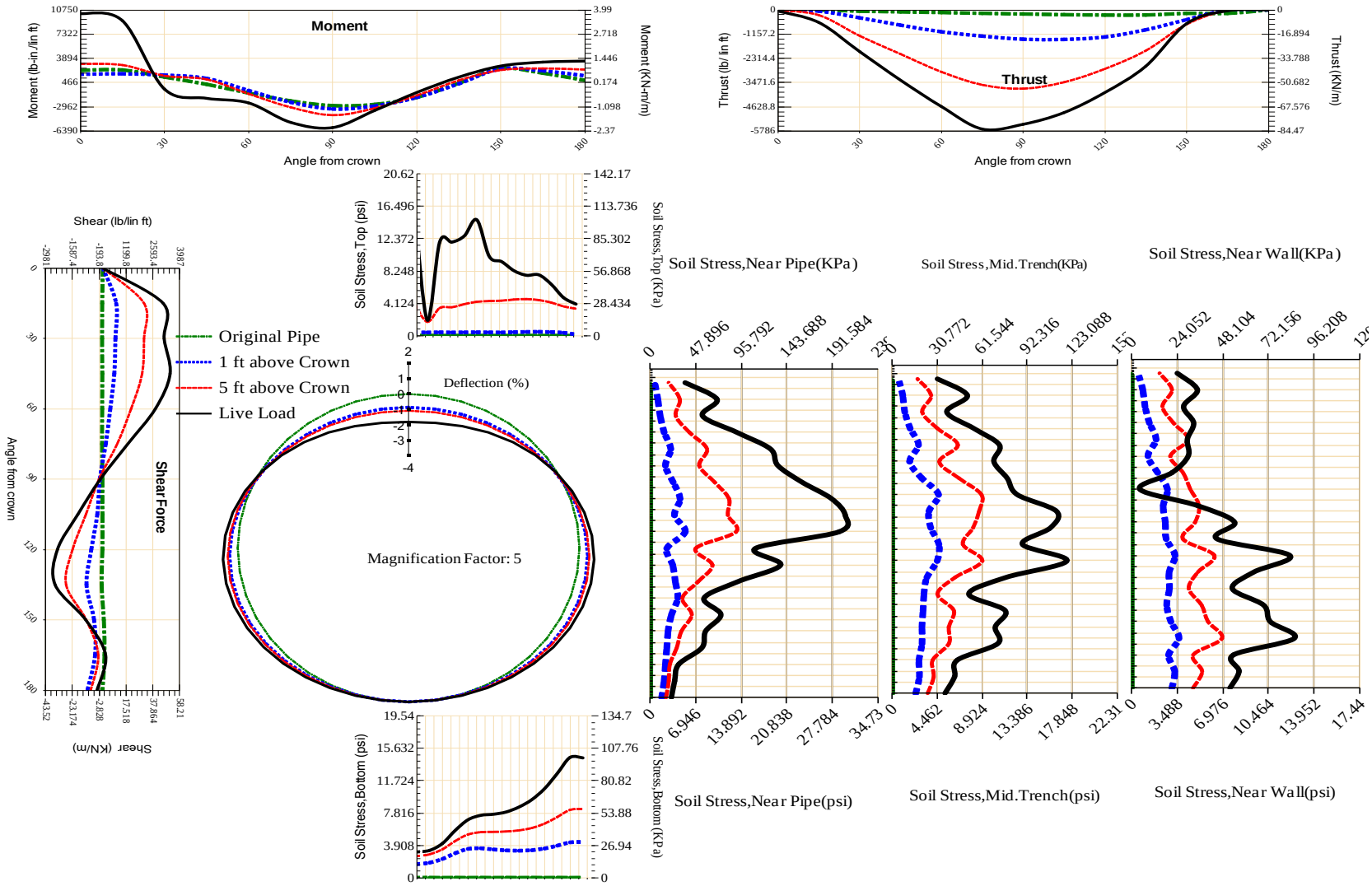

Figure A-20 Param-120-PW200-SF10SF-OD+48-EW10-H5-LiveLoad

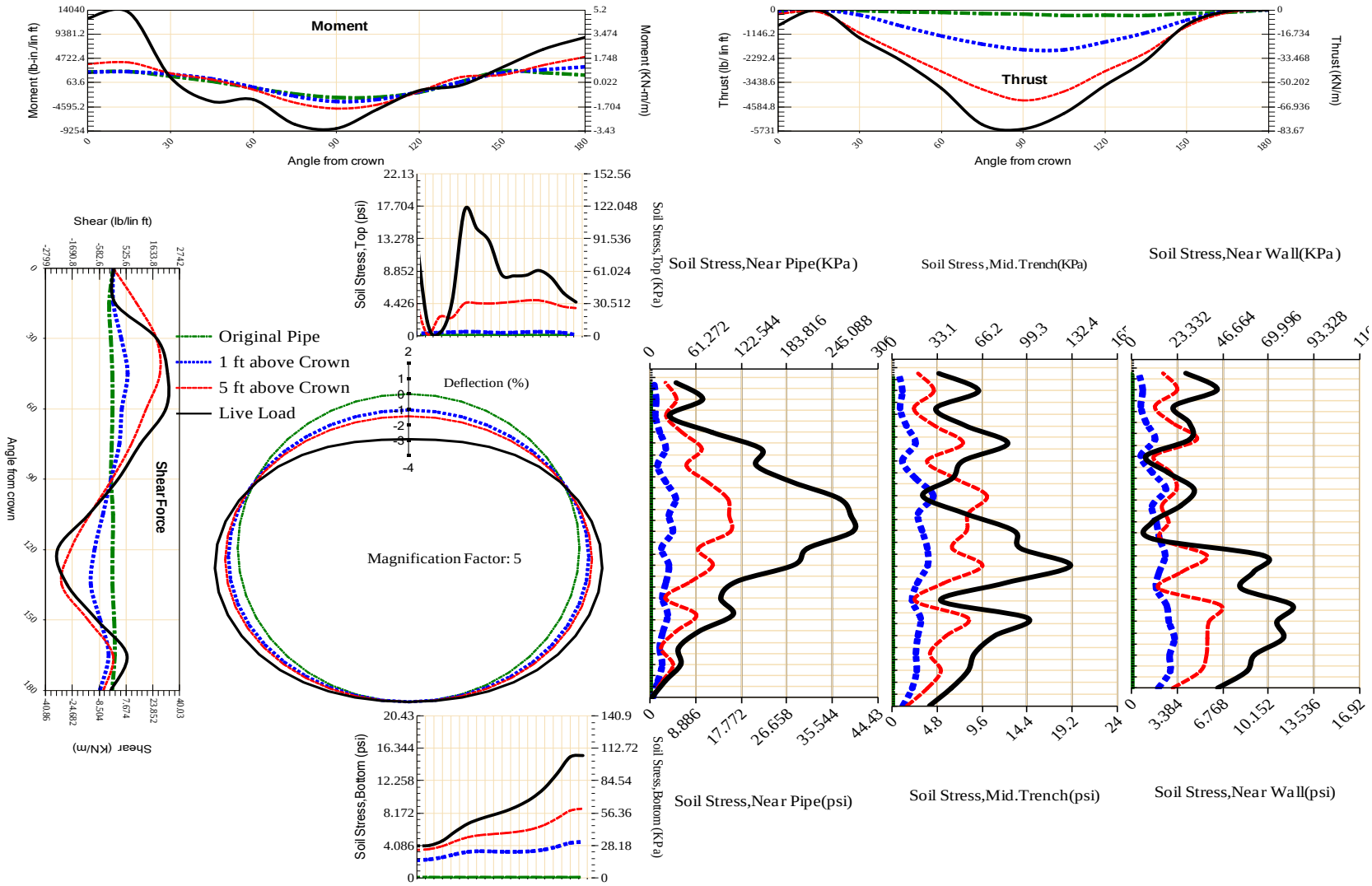

Figure A-21 Param-120-PW200-SF10SF-OD+48-EW3-H5-LiveLoad

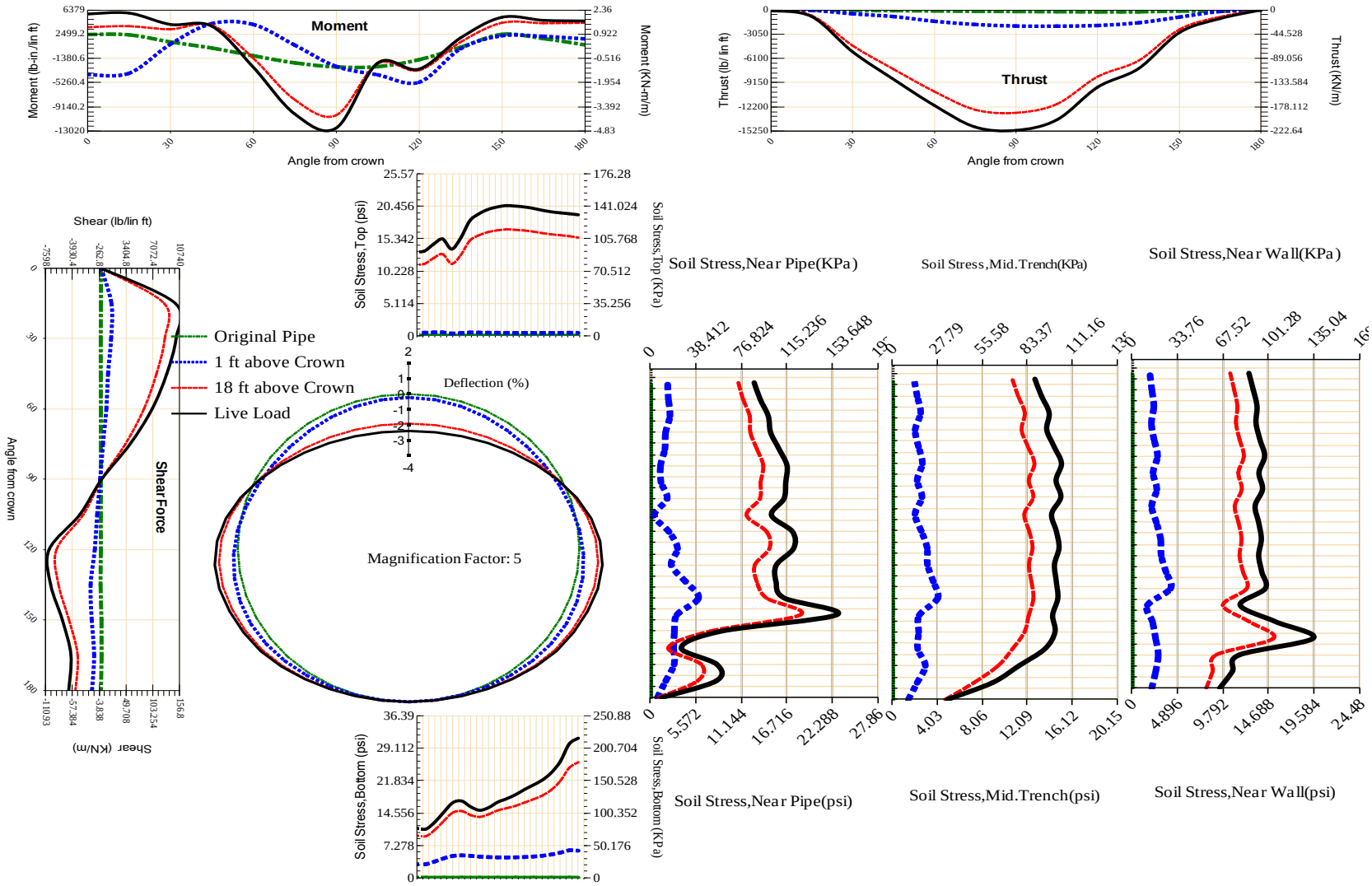

Figure A-22 Param-120-PW200-SF3OR-OD+108-EW10-H18-LiveLoad

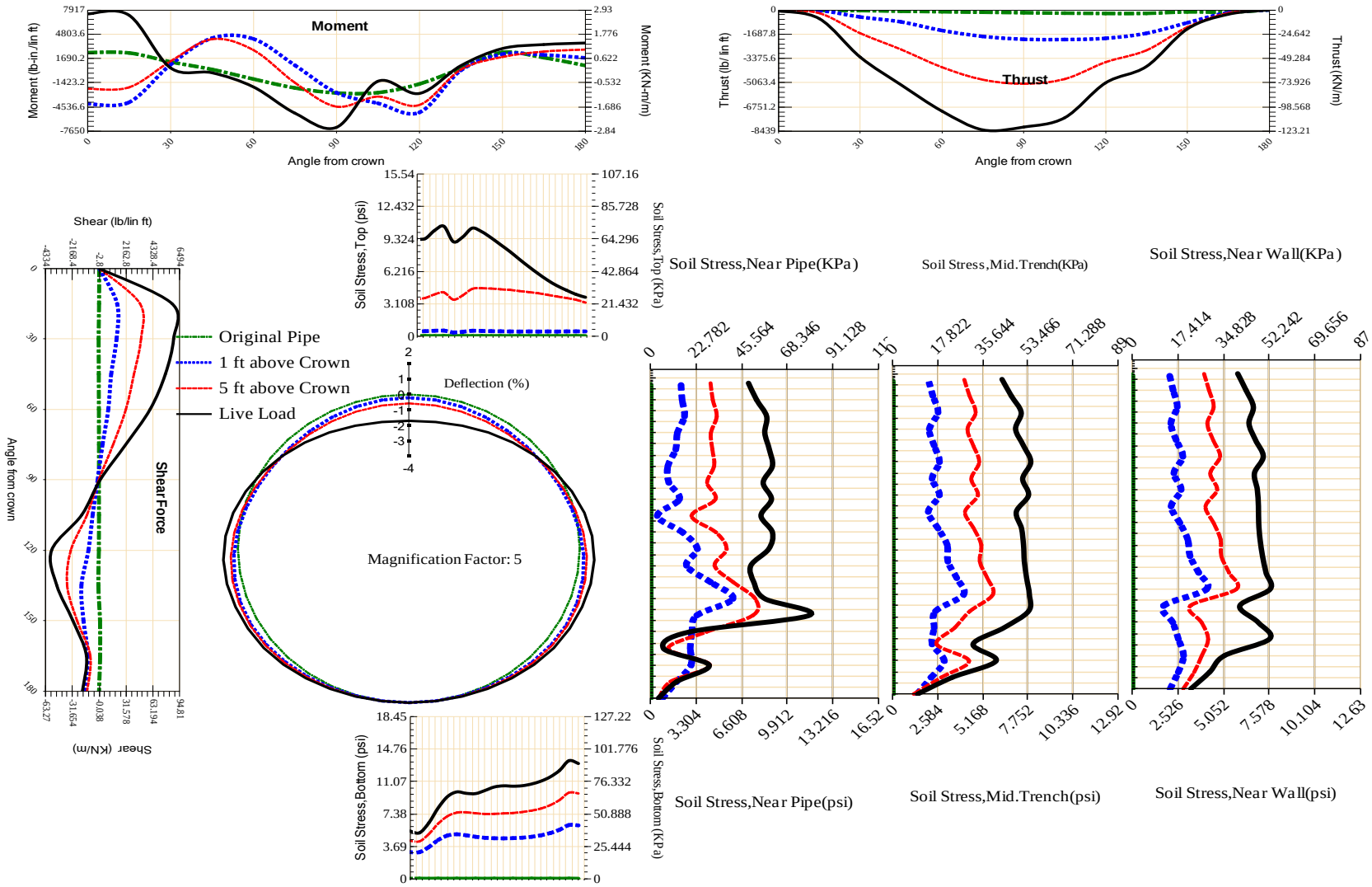

Figure A-23 Param-120-PW200-SF3OR-OD+108-EW10-H5-LiveLoad

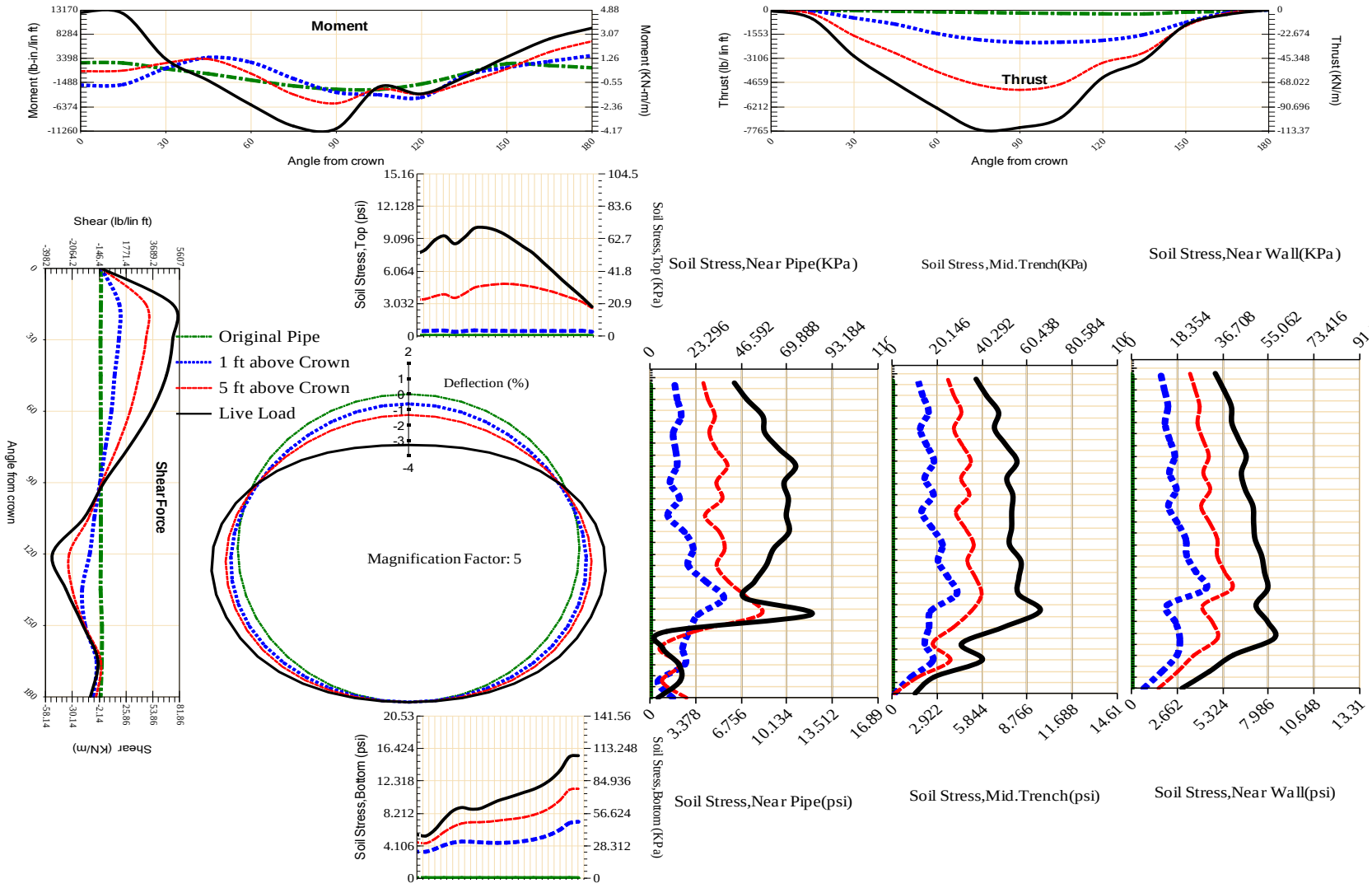

Figure A-24 Param-120-PW200-SF3OR-OD+108-EW3-H5-LiveLoad

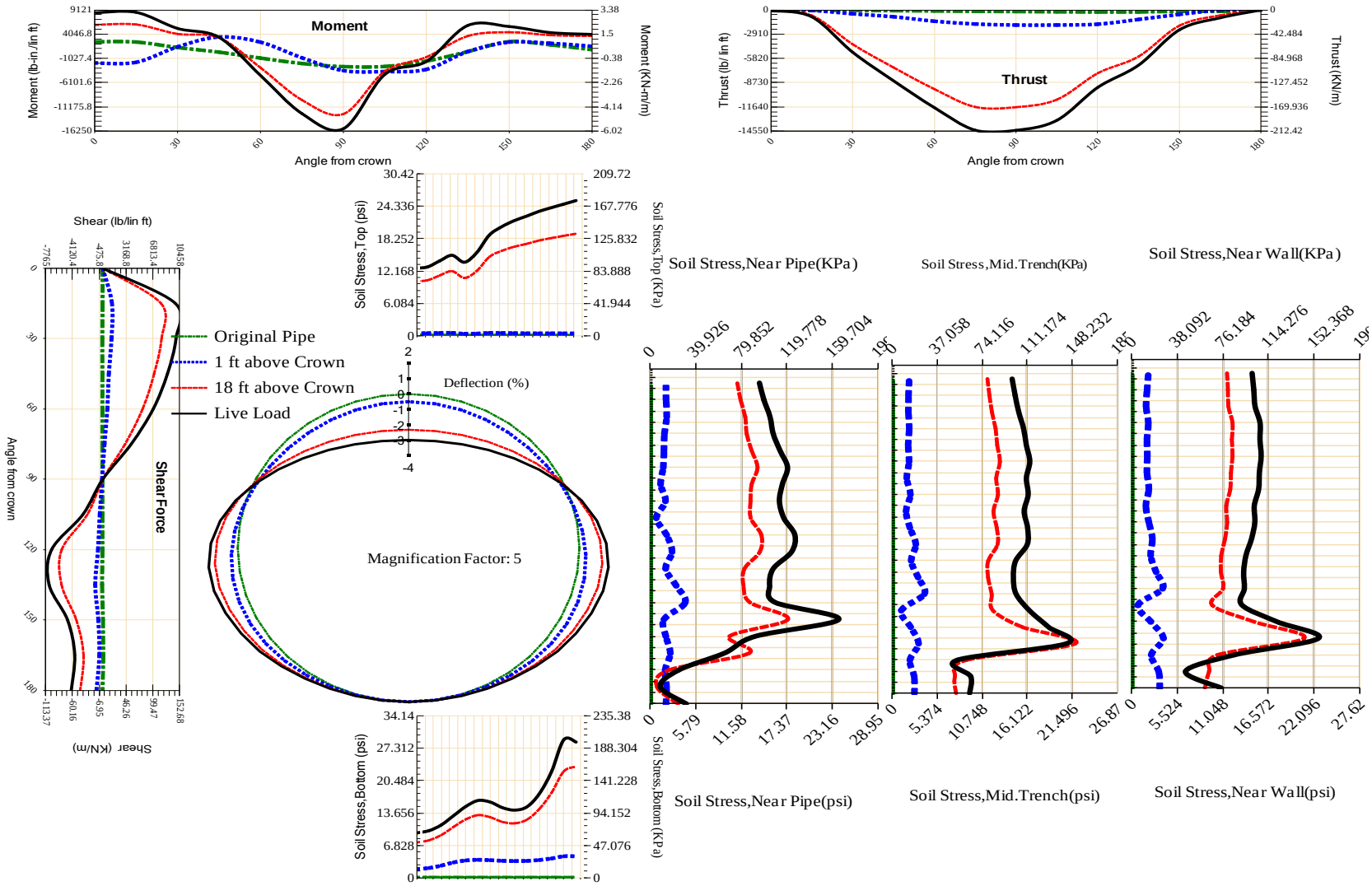

Figure A-25 Param-120-PW200-SF3OR-OD+48-EW10-H18-LiveLoad

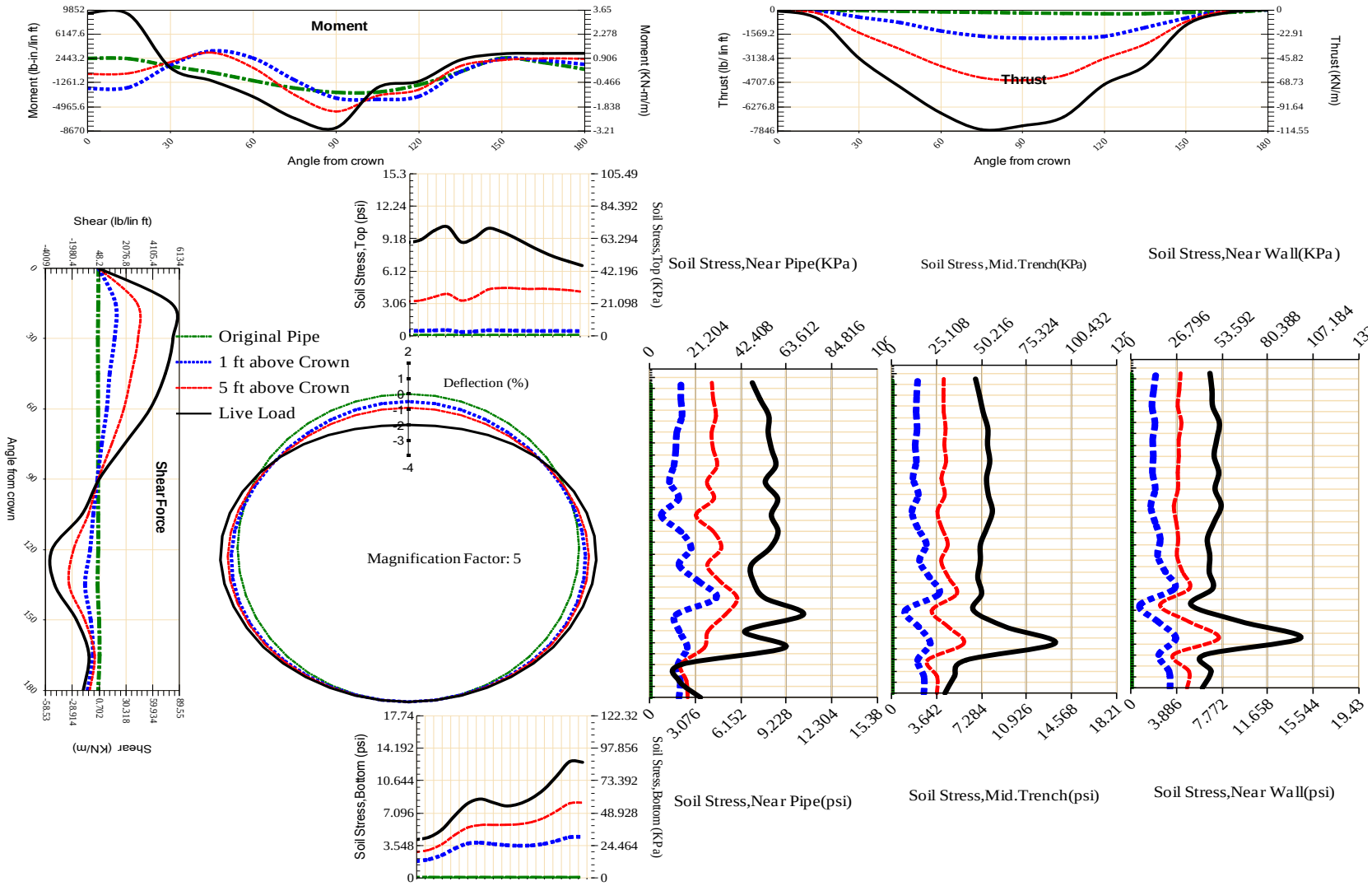

Figure A-26 Param-120-PW200-SF3OR-OD+48-EW10-H5-LiveLoad

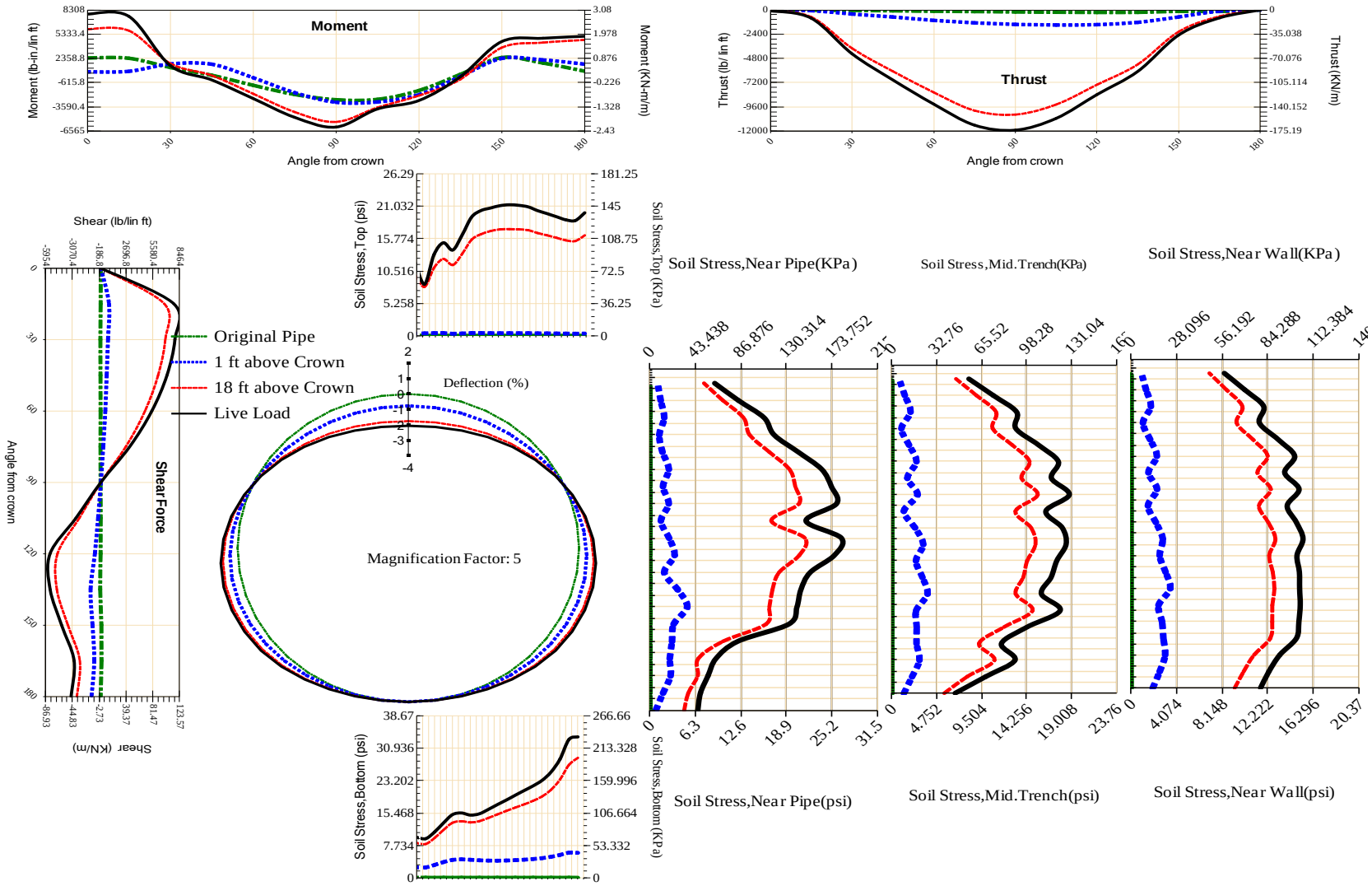

Figure A-27 Param-120-PW200-SF3TR-OD+108-EW10-H18-LiveLoad

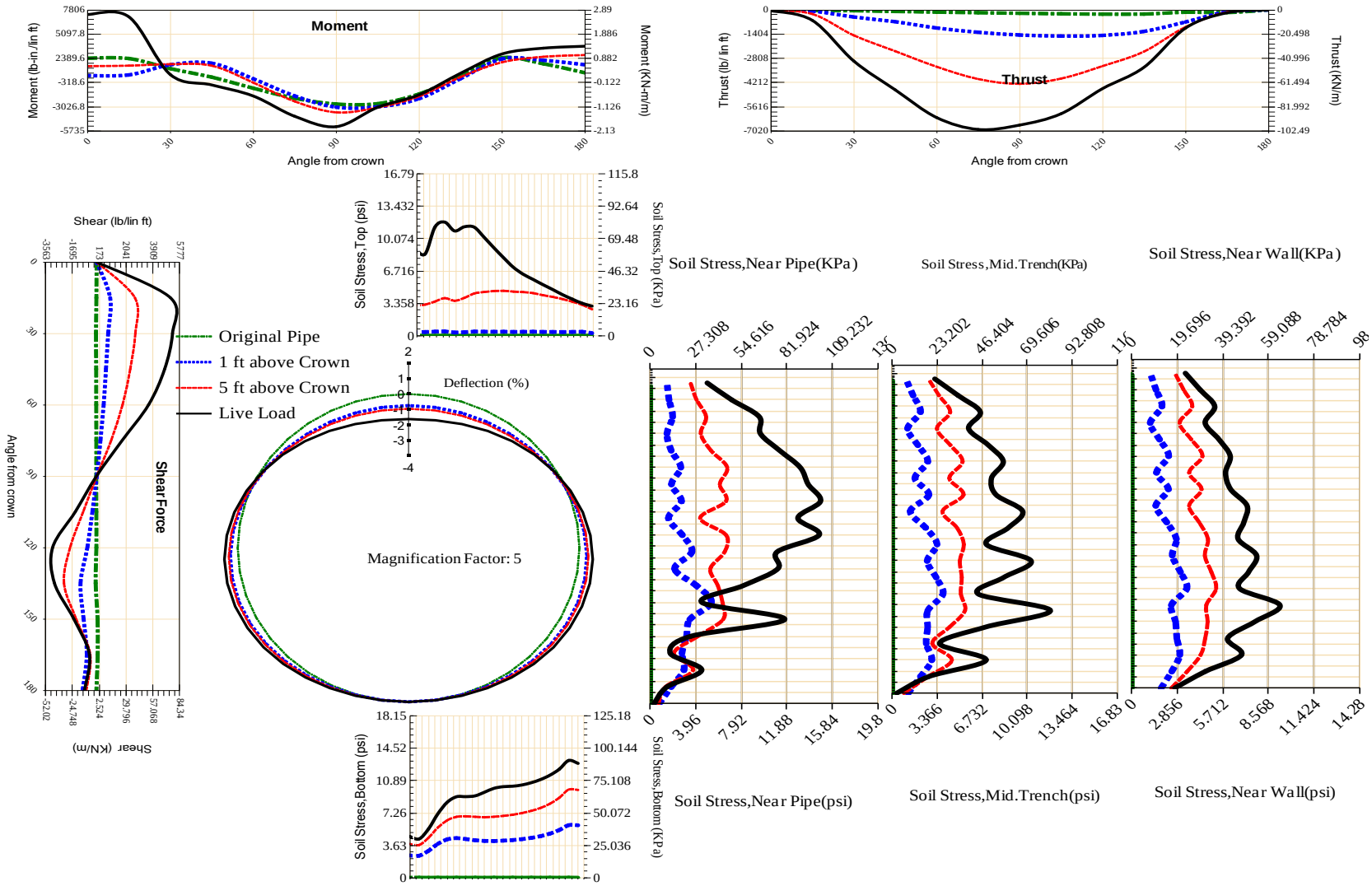

Figure A-28 Param-120-PW200-SF3TR-OD+108-EW10-H5-LiveLoad

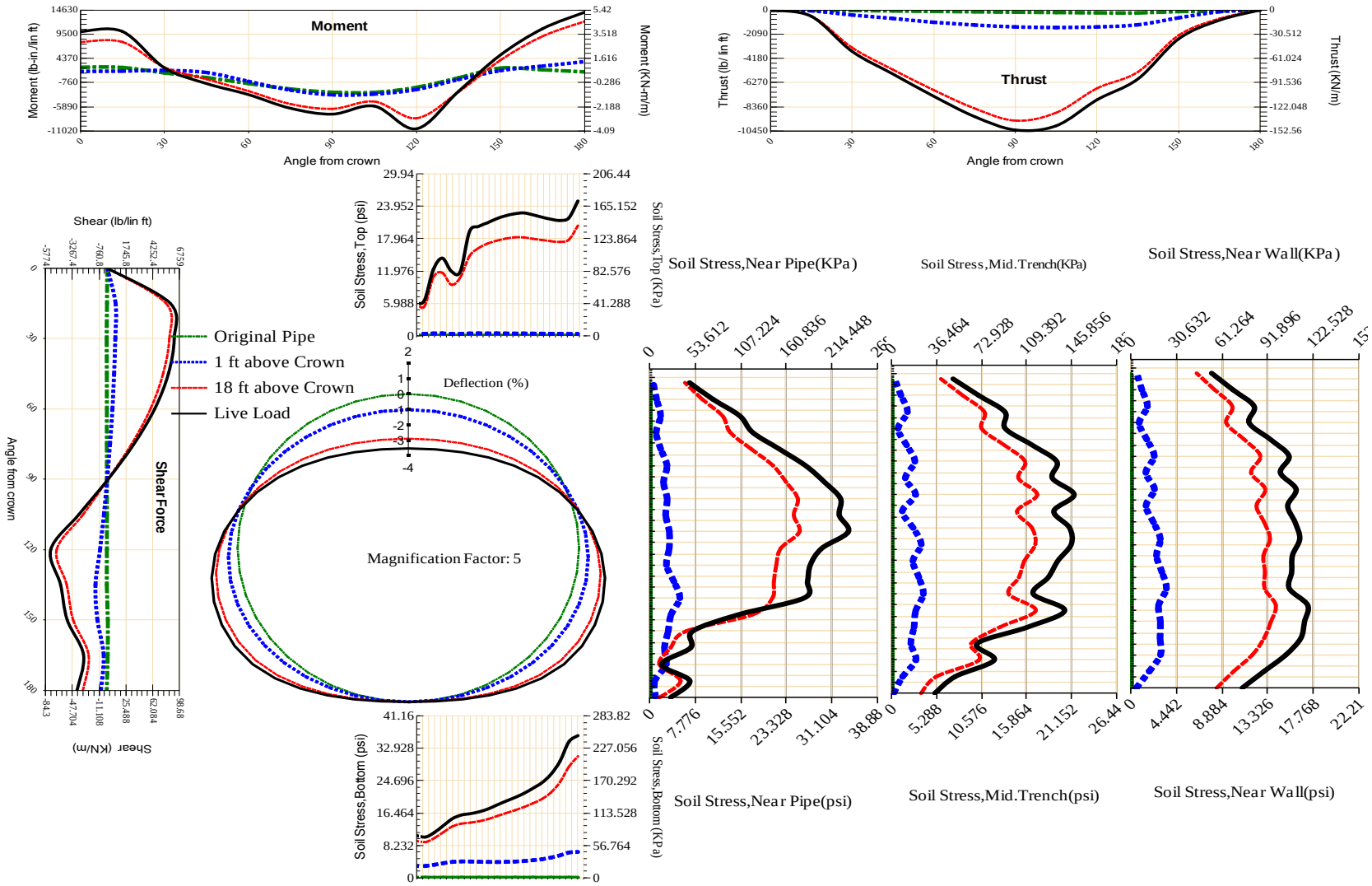

Figure A-29 Param-120-PW200-SF3TR-OD+108-EW3-H18-LiveLoad

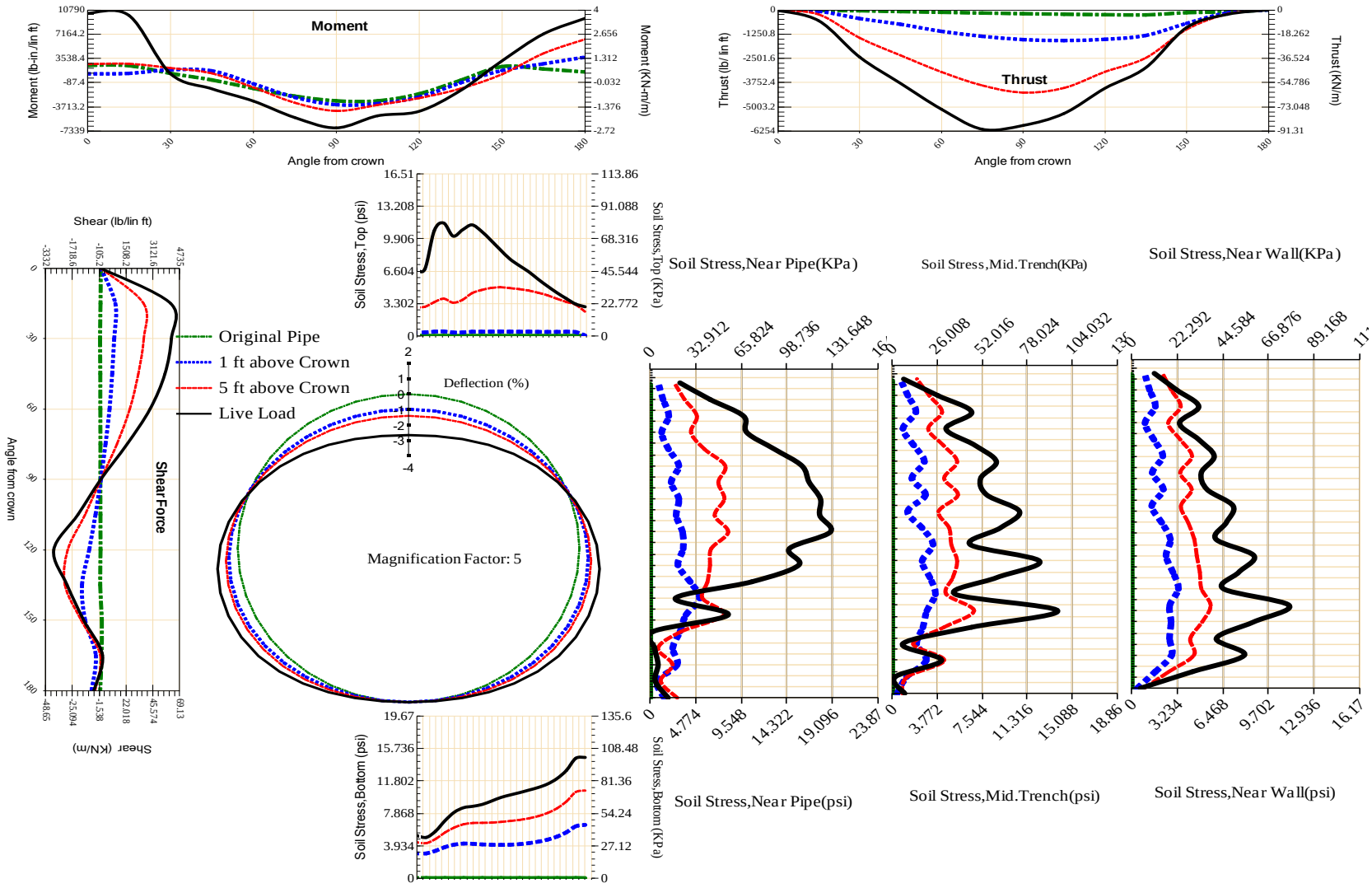

Figure A-30 Param-120-PW200-SF3TR-OD+108-EW3-H5-LiveLoad

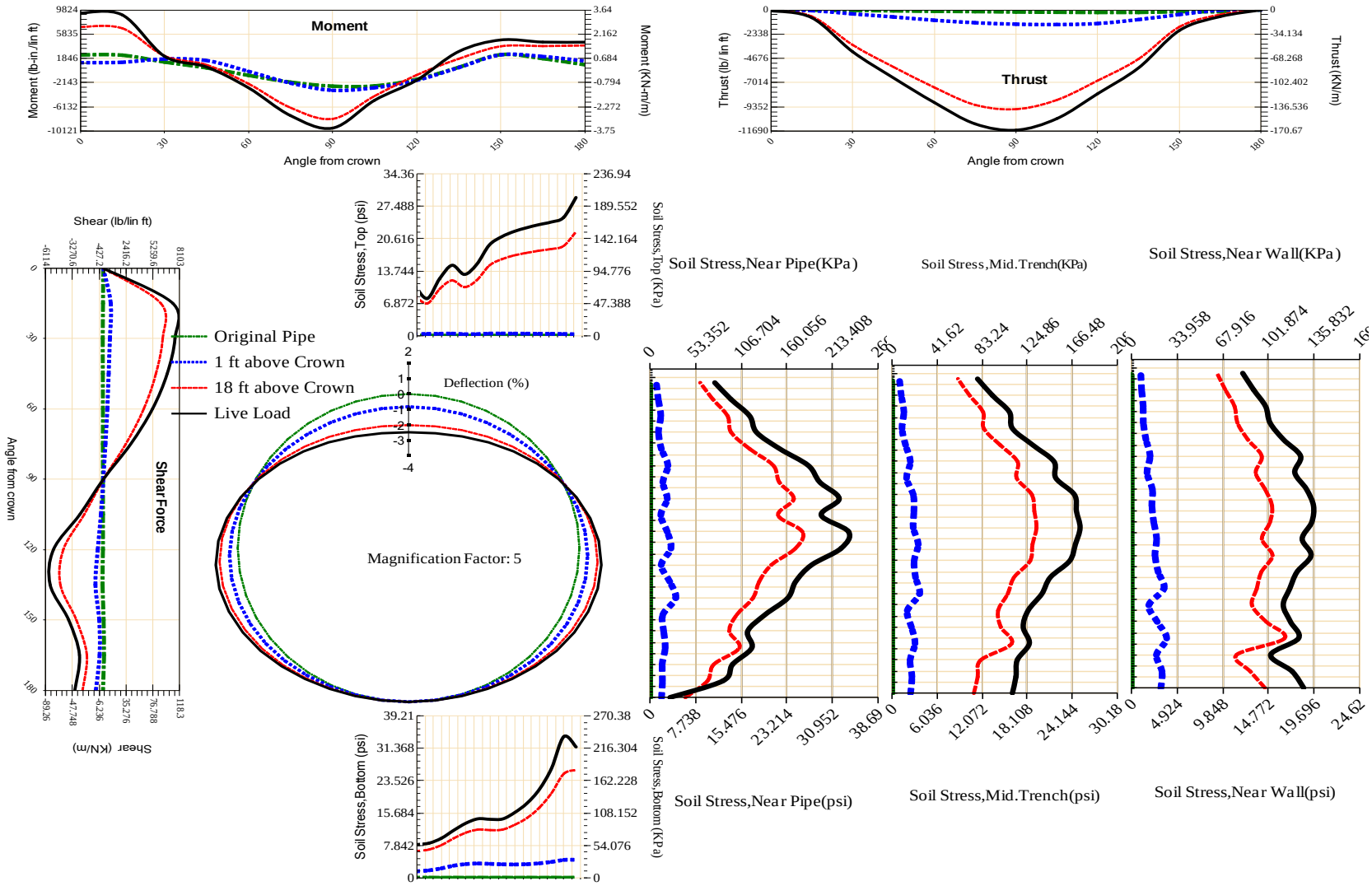

Figure A-31 Param-120-PW200-SF3TR-OD+48-EW10-H18-LiveLoad

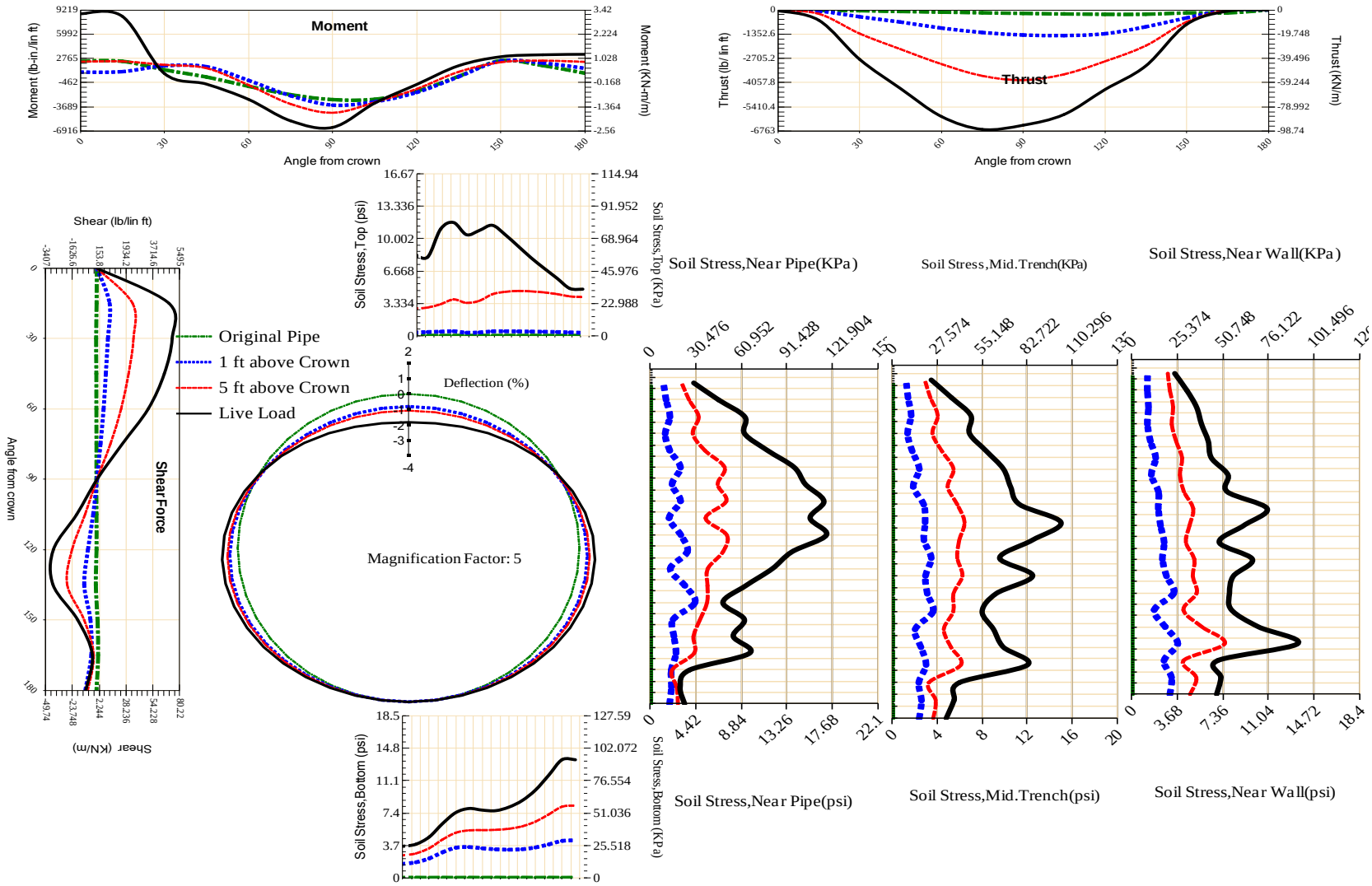

Figure A-32 Param-120-PW200-SF3TR-OD+48-EW10-H5-LiveLoad

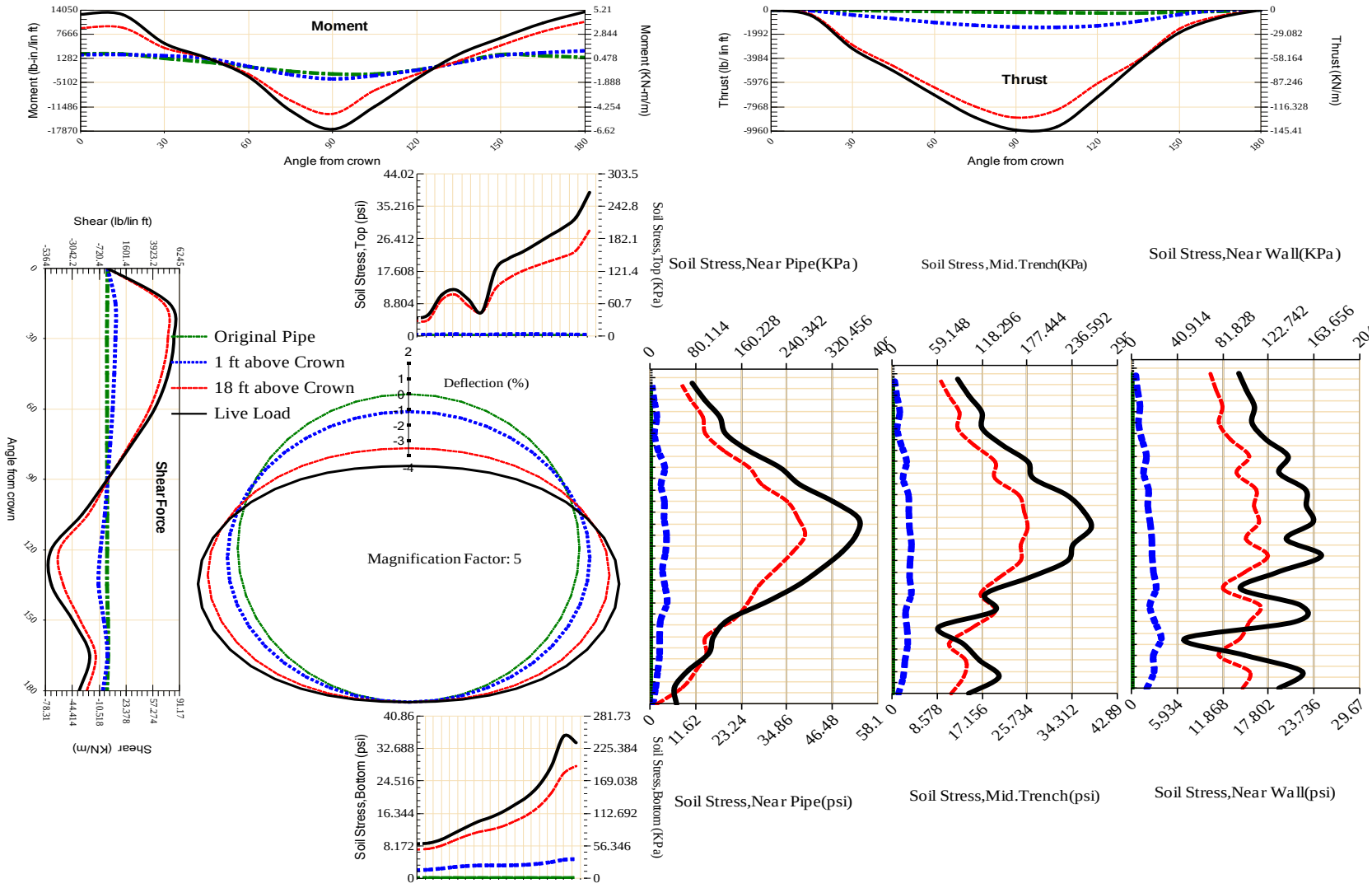

Figure A-33 Param-120-PW200-SF3TR-OD+48-EW3-H18-LiveLoad

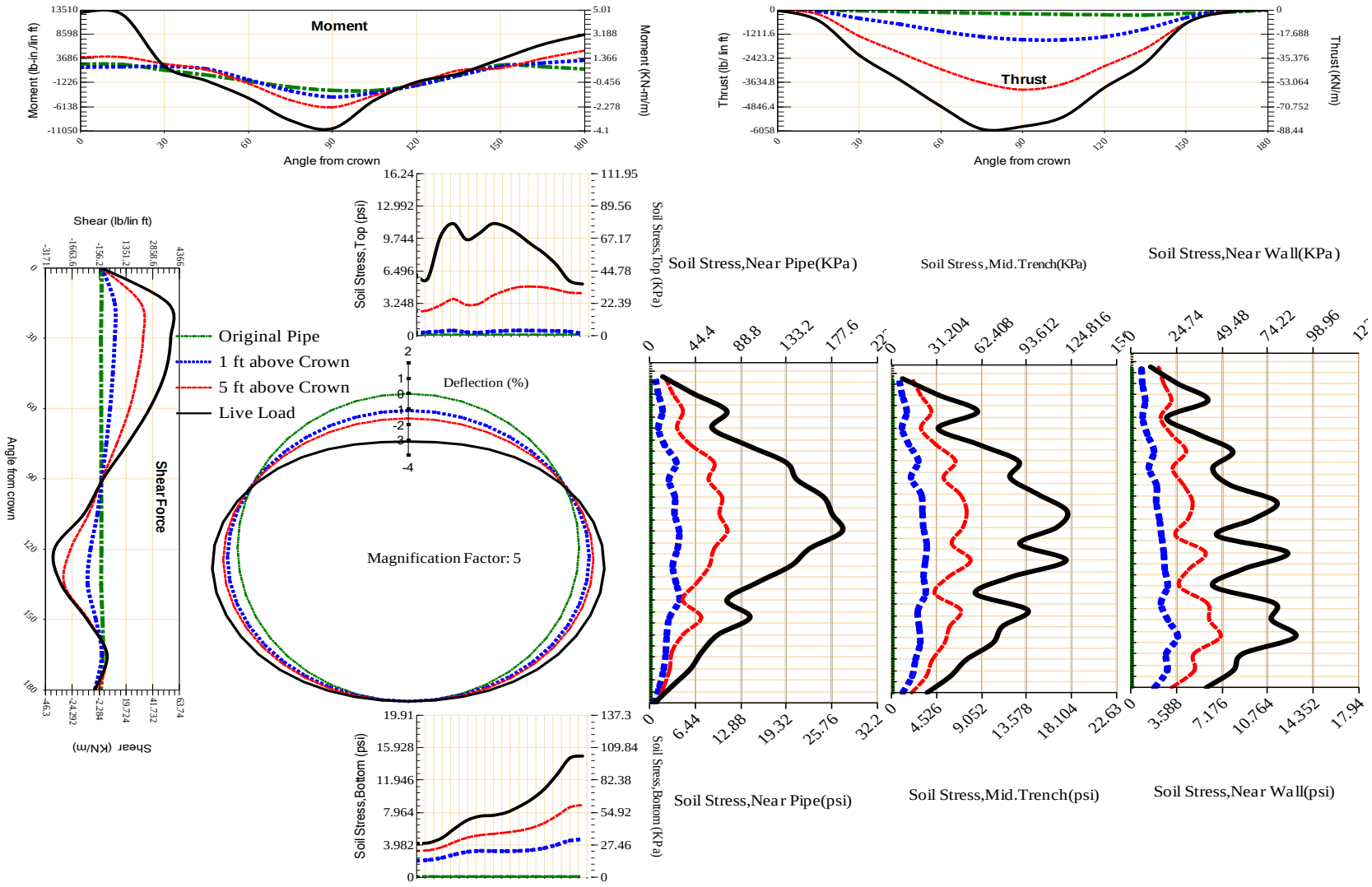

Figure A-34 Param-120-PW200-SF3TR-OD+48-EW3-H5-LiveLoad

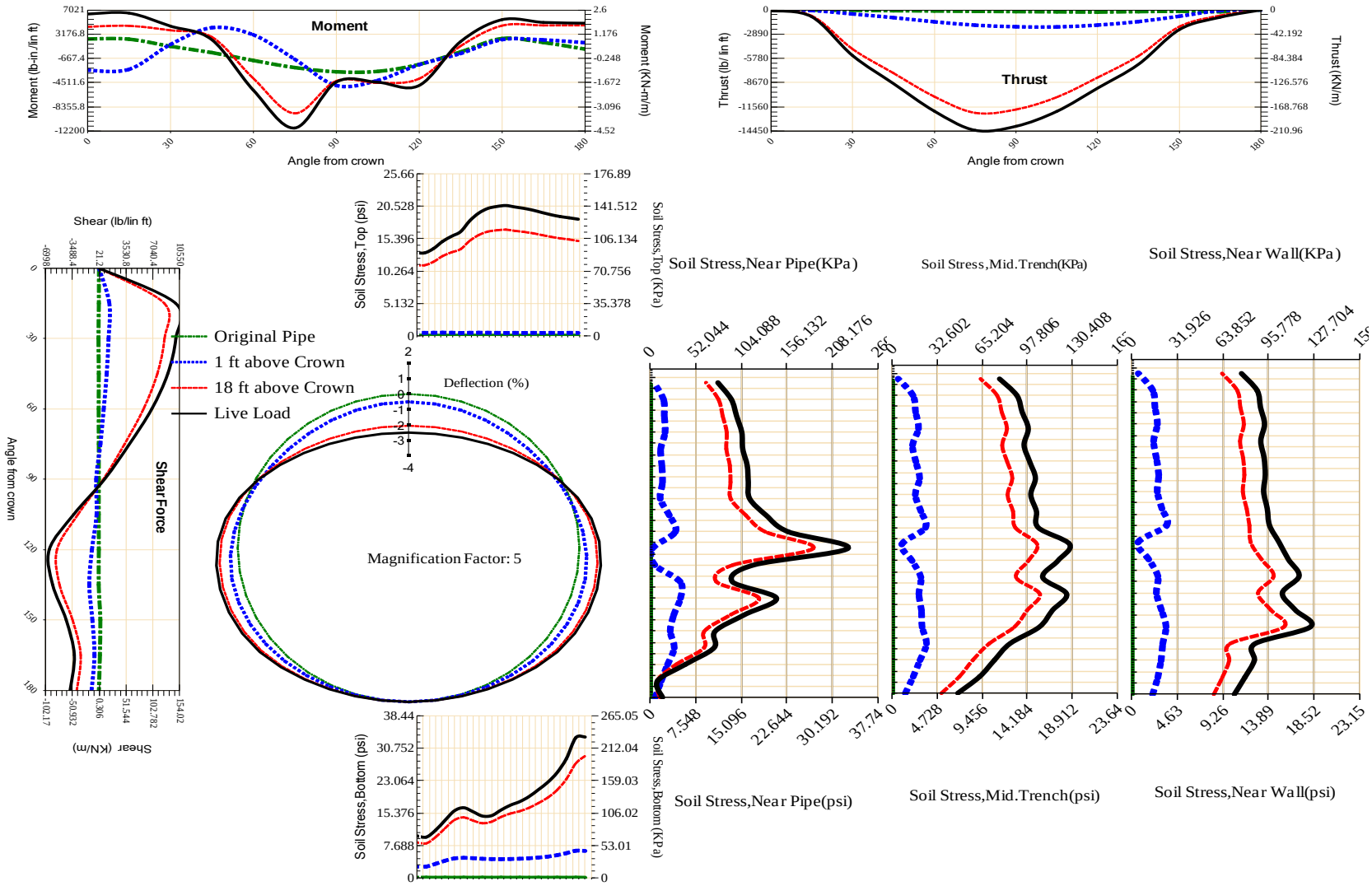

Figure A-35 Param-120-PW200-SF5OR-OD+108-EW10-H18-LiveLoad

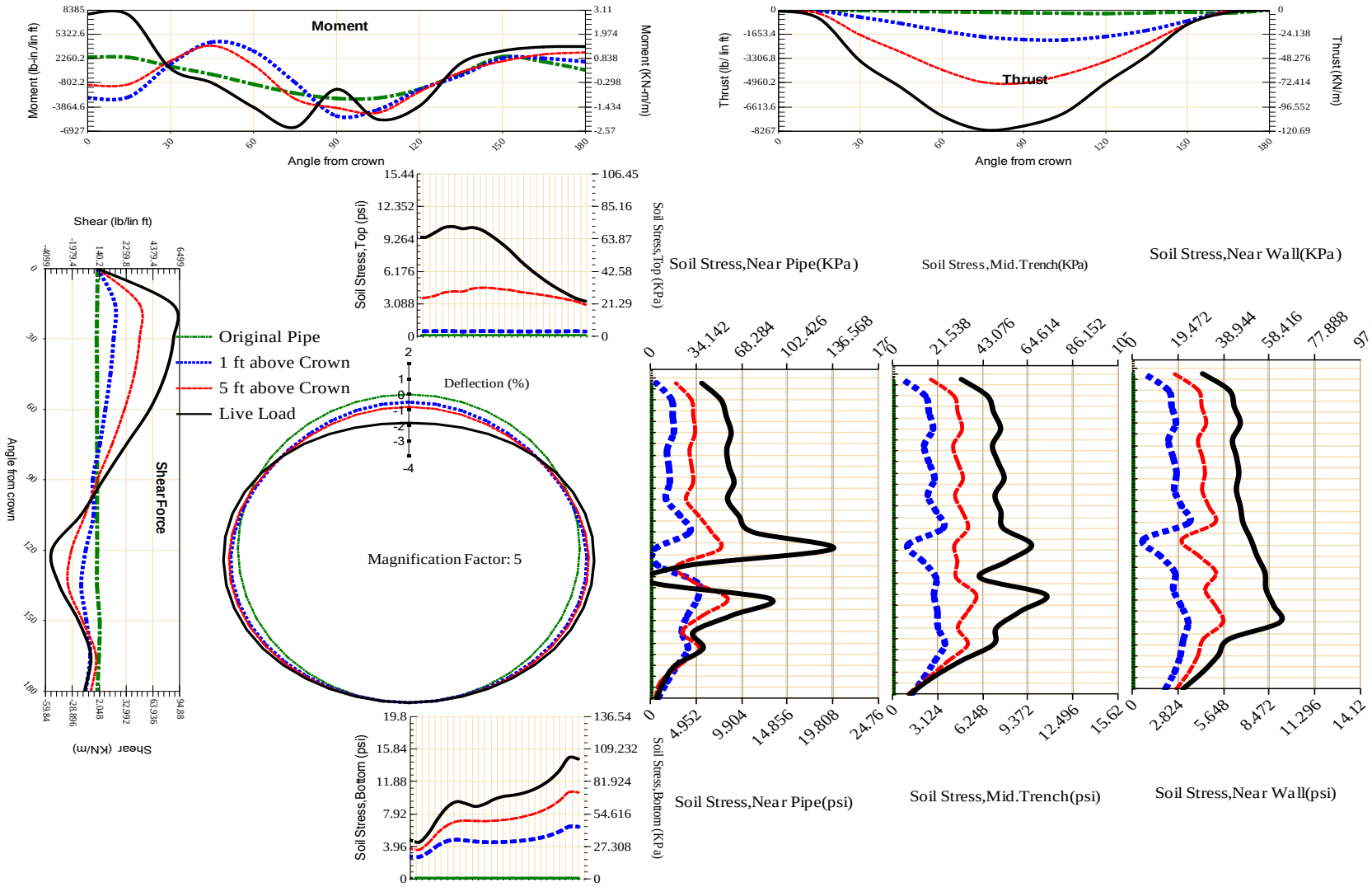

Figure A-36 Param-120-PW200-SF5OR-OD+108-EW10-H5-LiveLoad

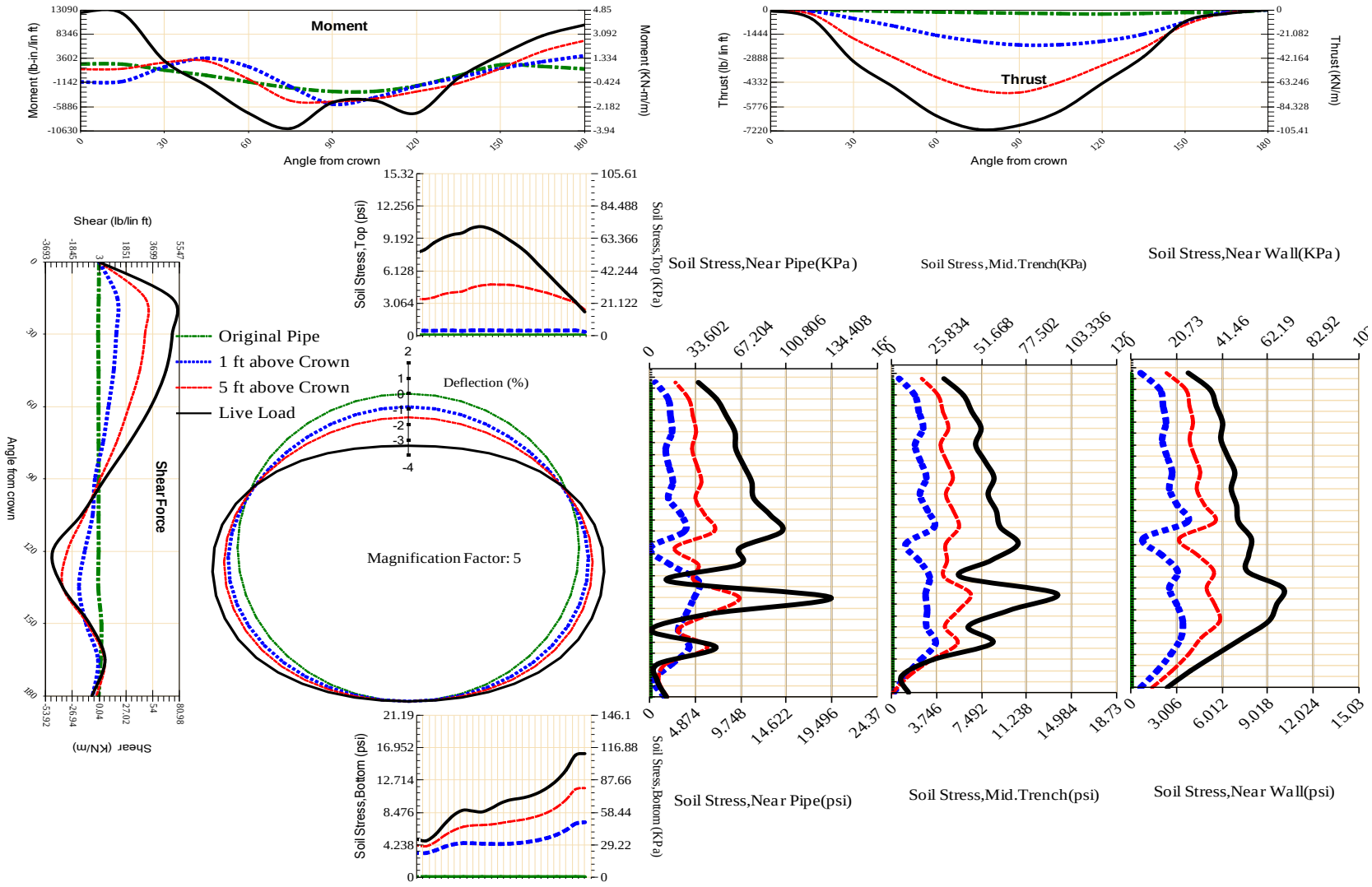

Figure A-37 Param-120-PW200-SF5OR-OD+108-EW3-H5-LiveLoad

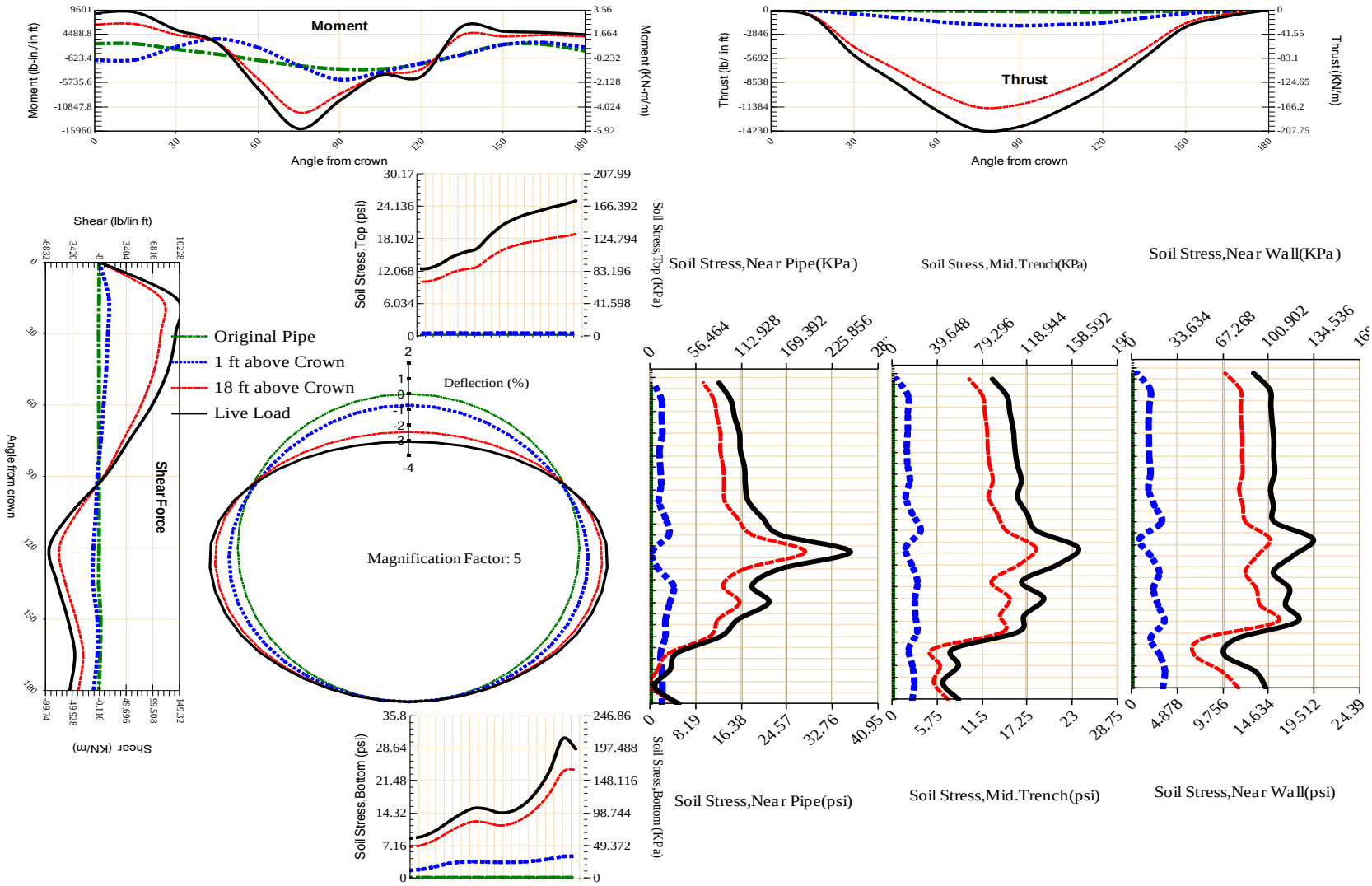

Figure A-38 Param-120-PW200-SF5OR-OD+48-EW10-H18-LiveLoad

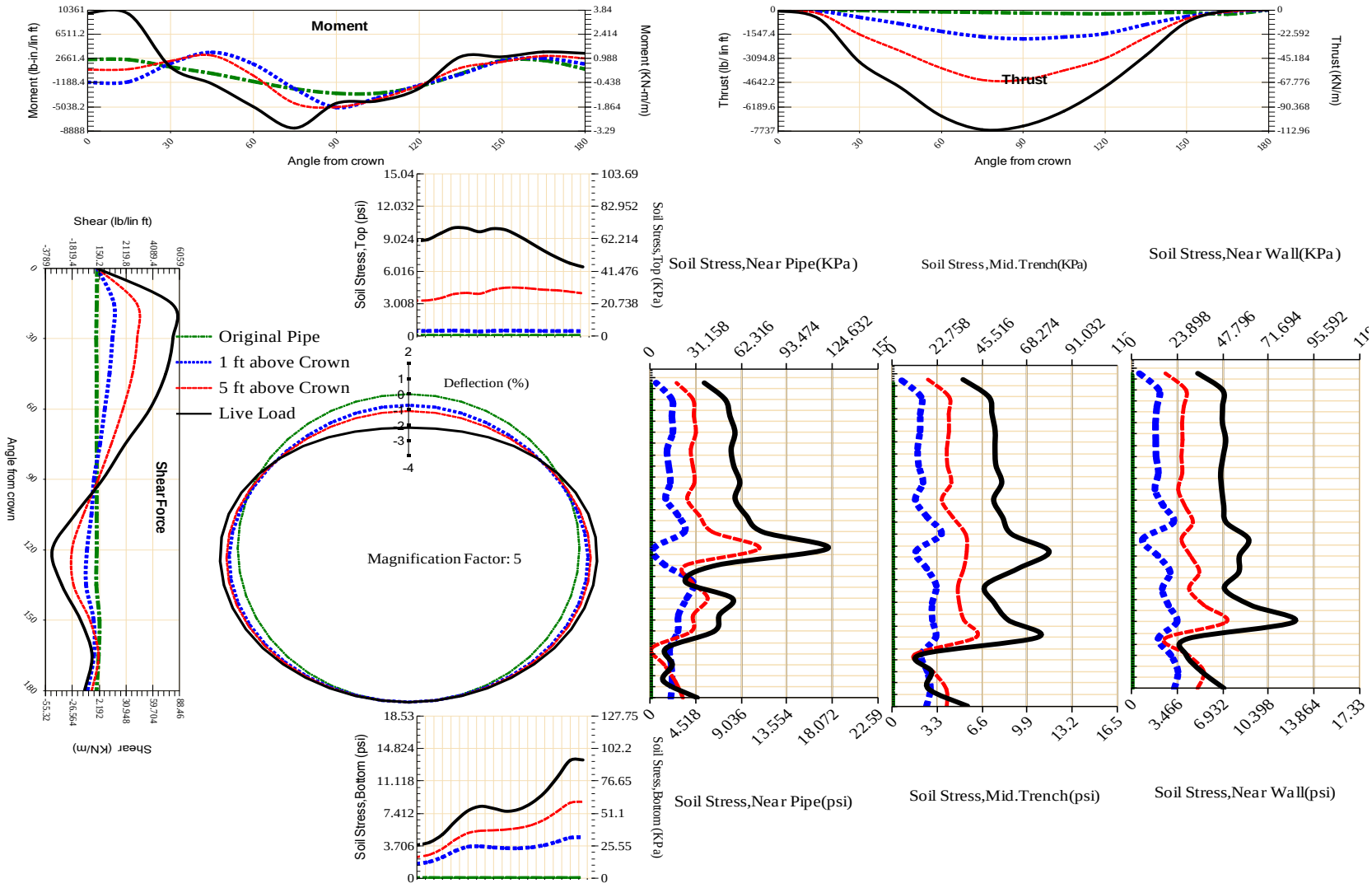

Figure A-39 Param-120-PW200-SF5OR-OD+48-EW10-H5-LiveLoad

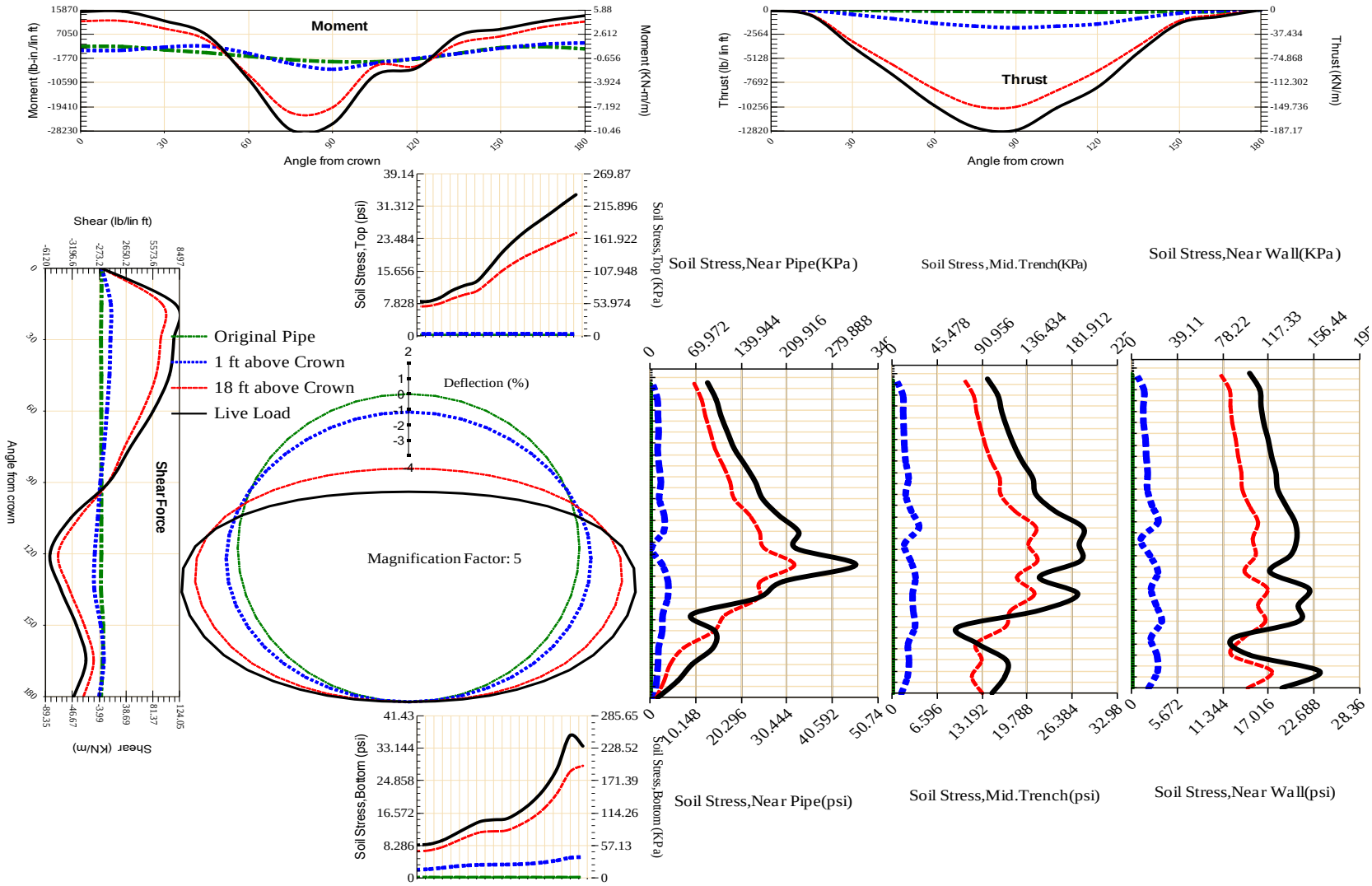

Figure A-40 Param-120-PW200-SF5OR-OD+48-EW3-H18-LiveLoad

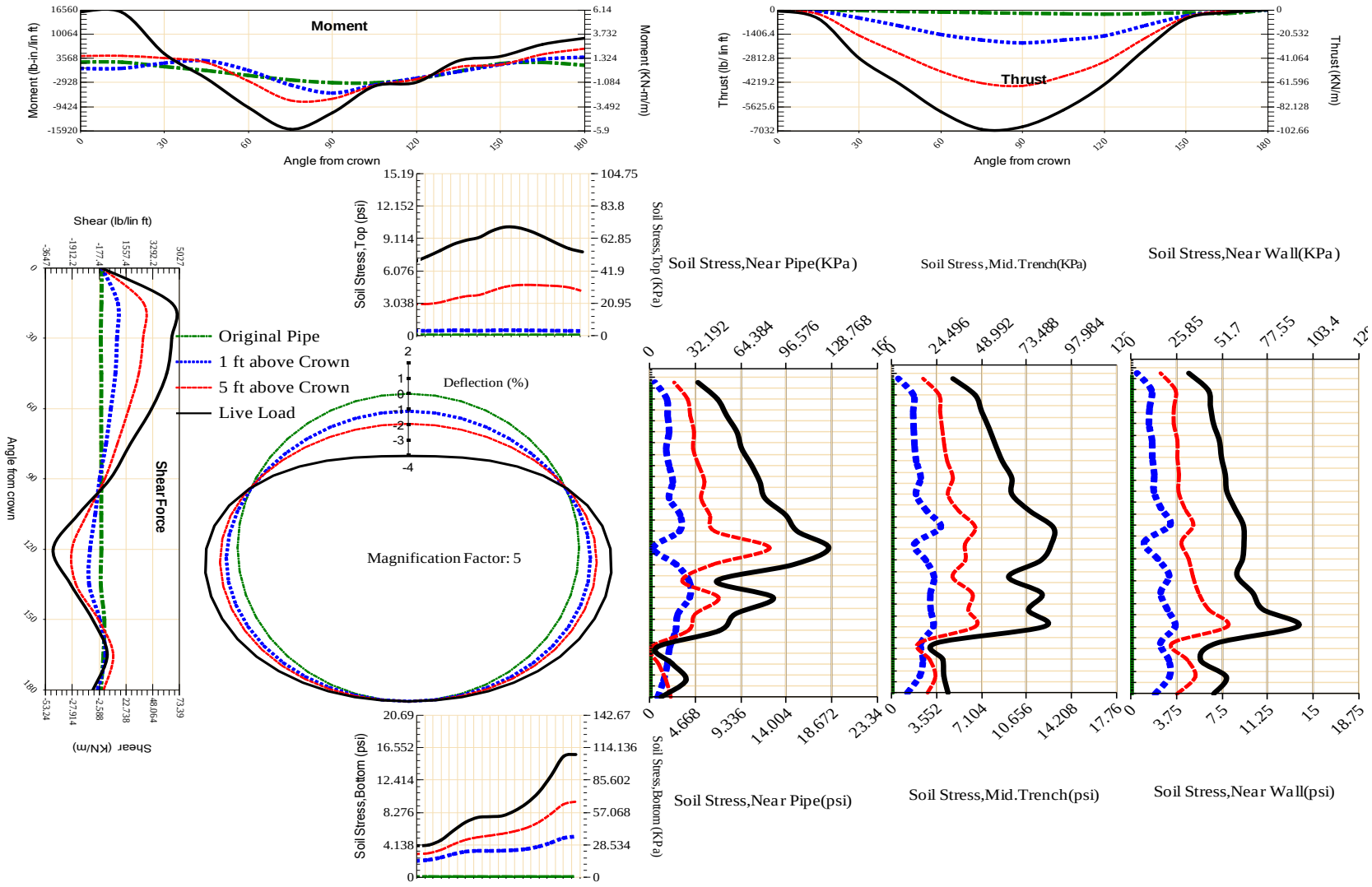

Figure A-41 Param-120-PW200-SF5OR-OD+48-EW3-H5-LiveLoad

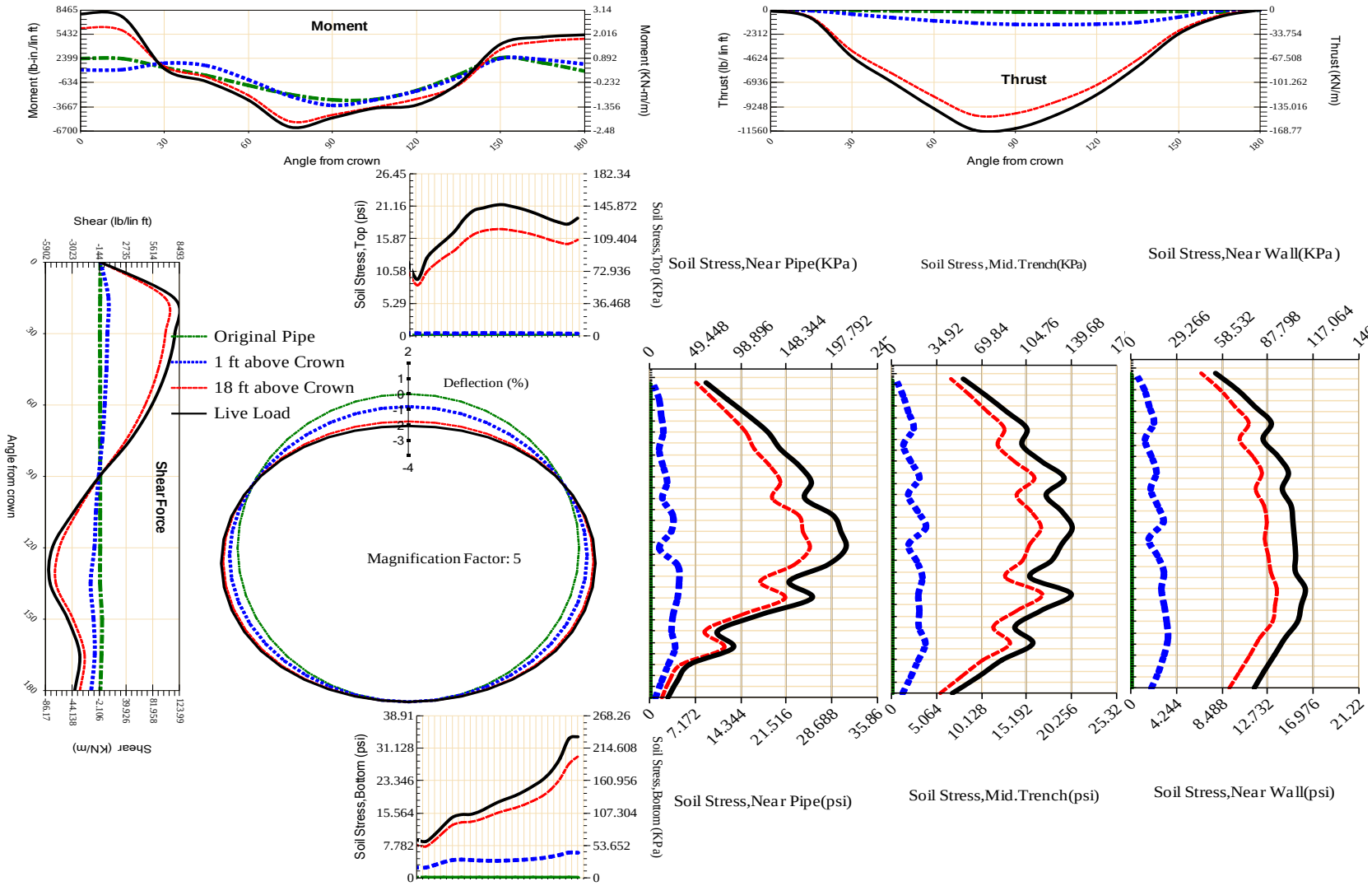

Figure A-42 Param-120-PW200-SF5TR-OD+108-EW10-H18-LiveLoad

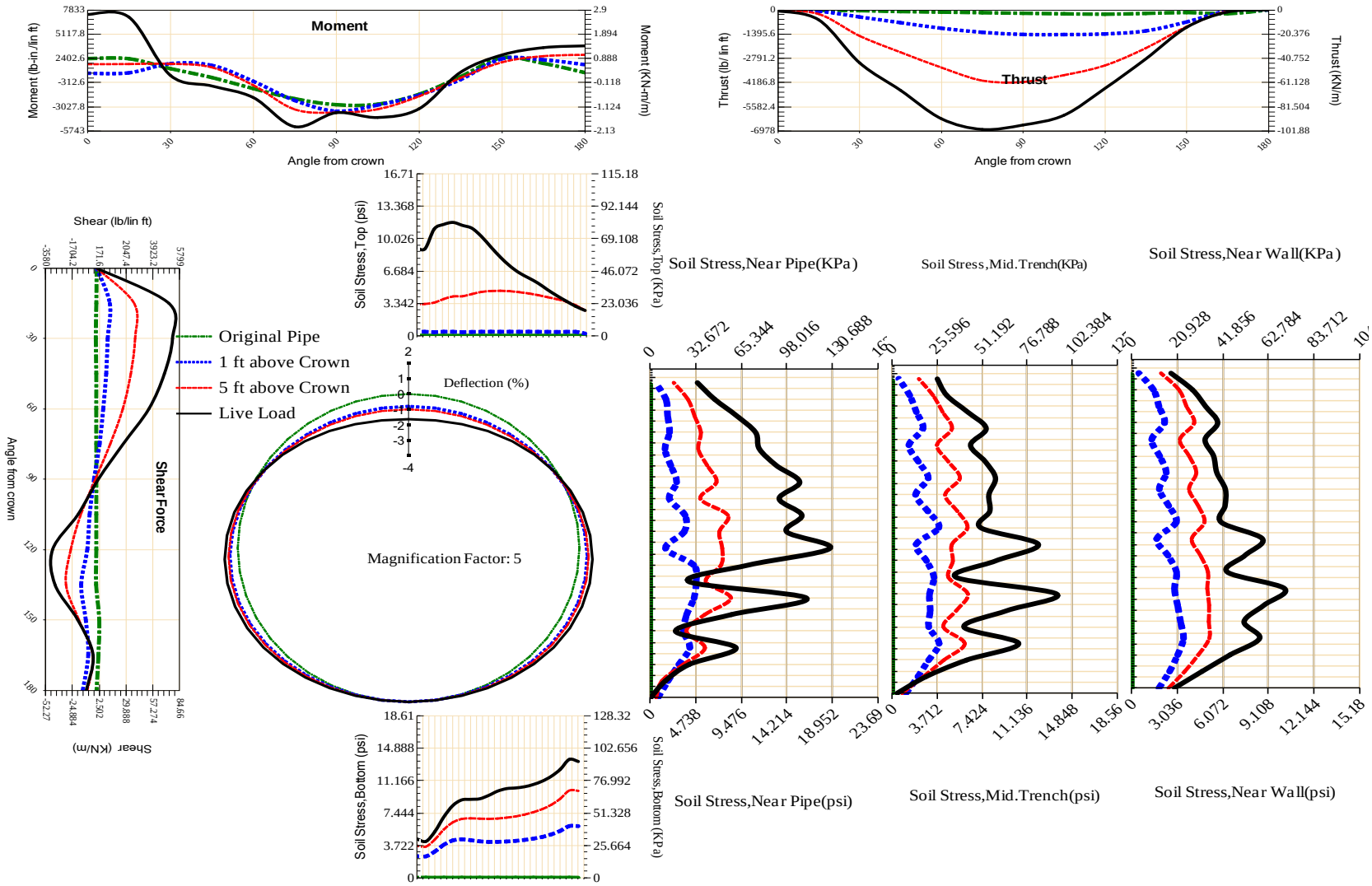

Figure A-43 Param-120-PW200-SF5TR-OD+108-EW10-H5-LiveLoad

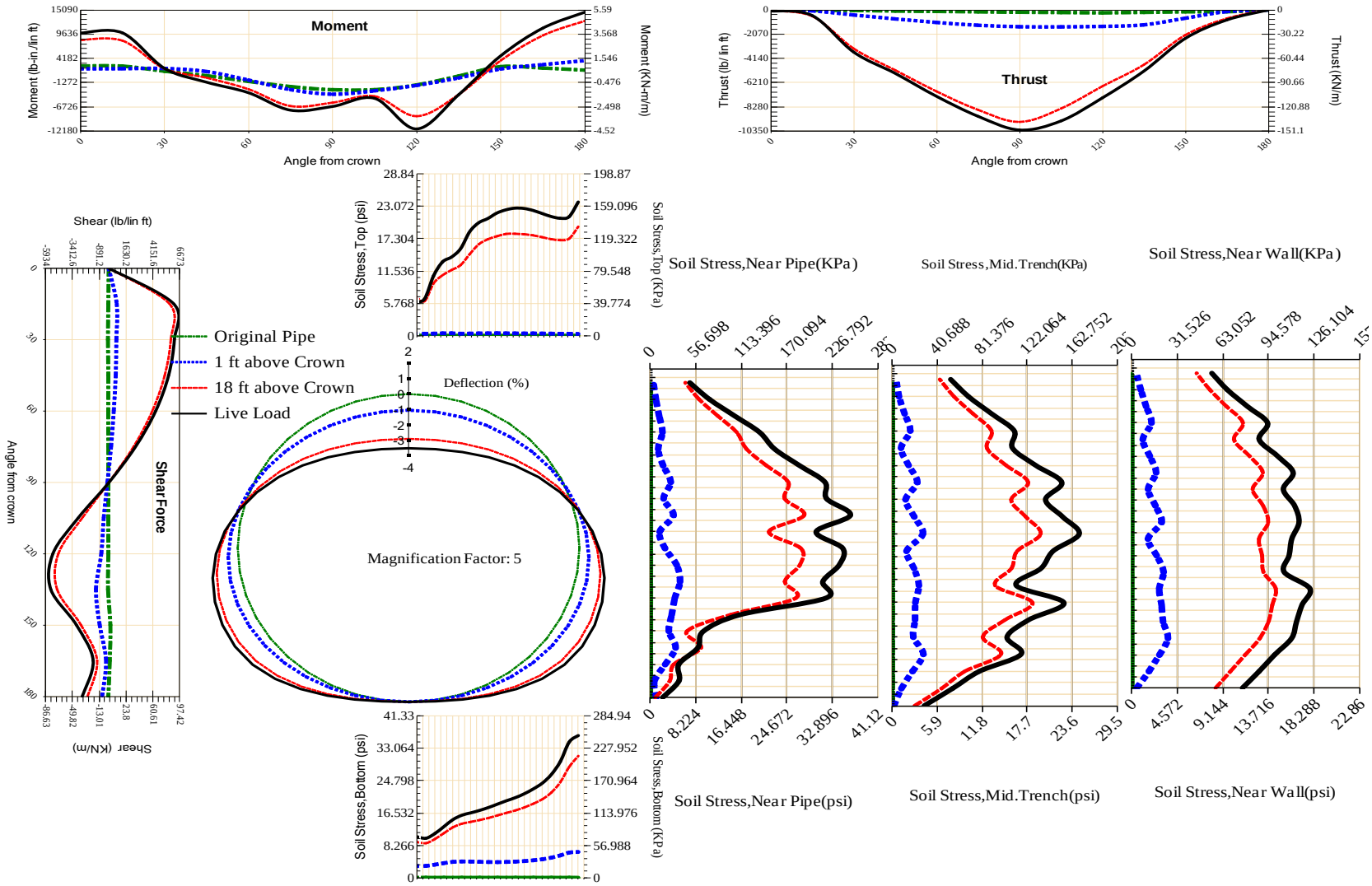

Figure A-44 Param-120-PW200-SF5TR-OD+108-EW3-H18-LiveLoad

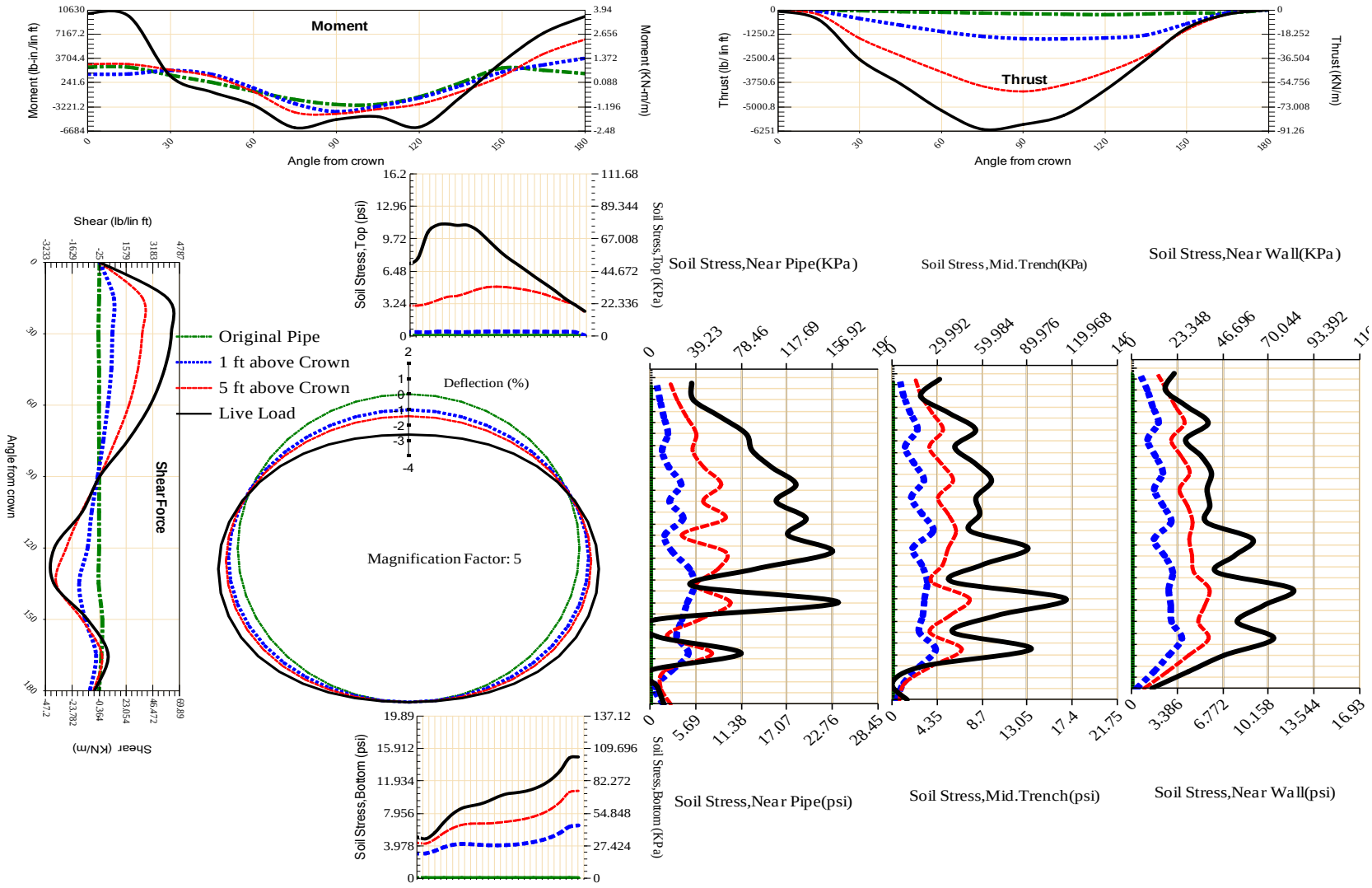

Figure A-45 Param-120-PW200-SF5TR-OD+108-EW3-H5-LiveLoad

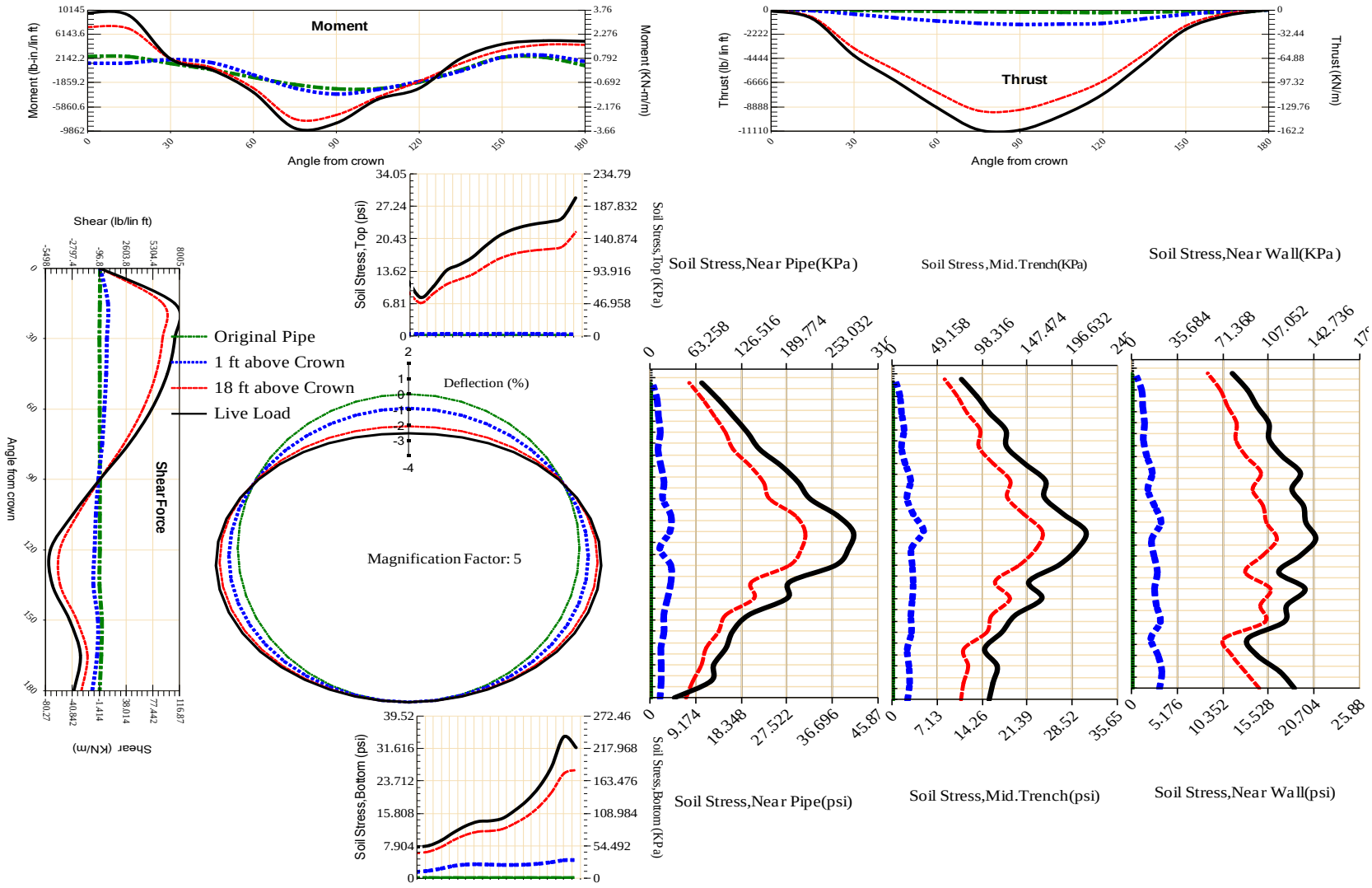

Figure A-46 Param-120-PW200-SF5TR-OD+48-EW10-H18-LiveLoad

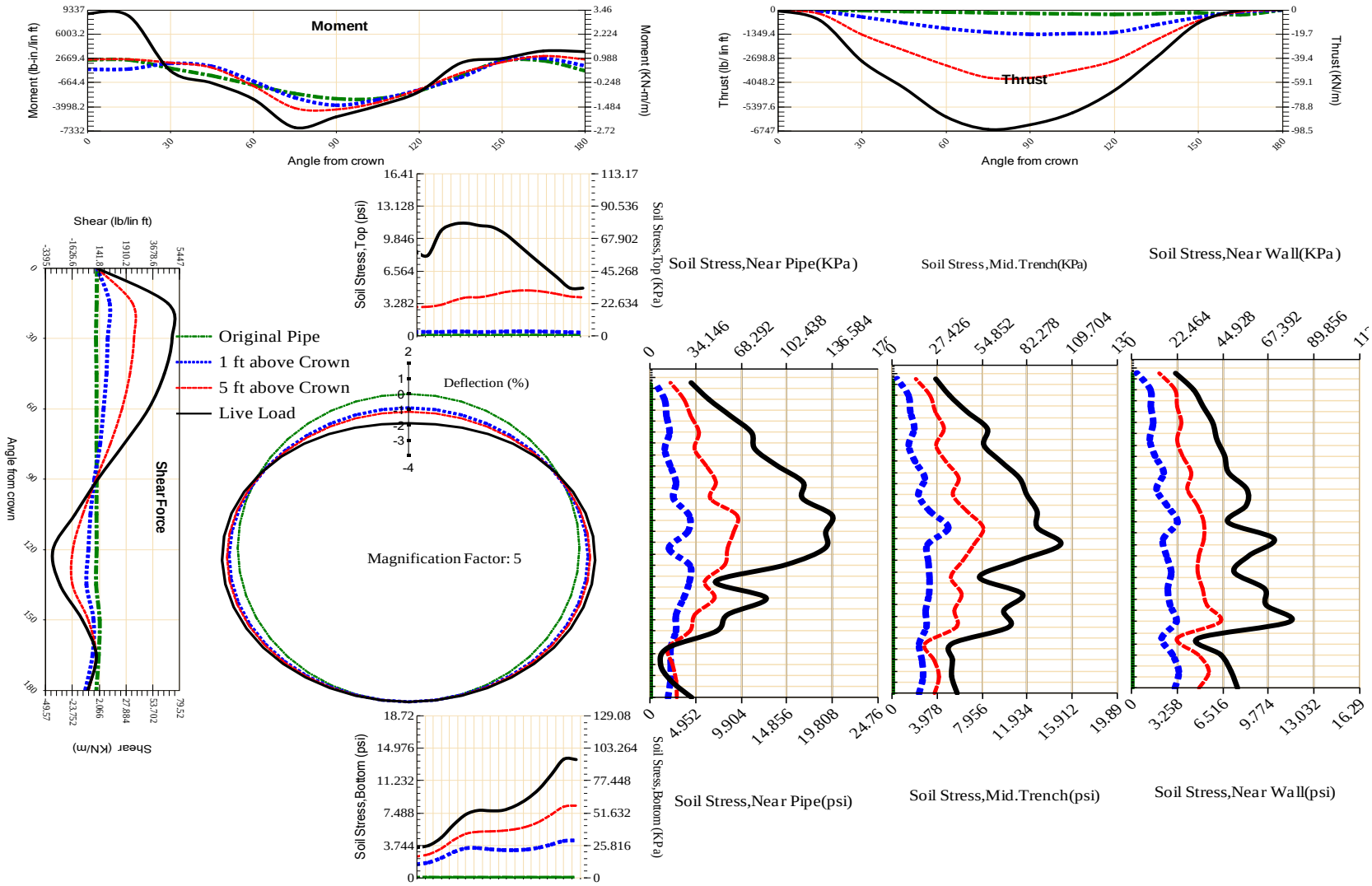

Figure A-47 Param-120-PW200-SF5TR-OD+48-EW10-H5-LiveLoad

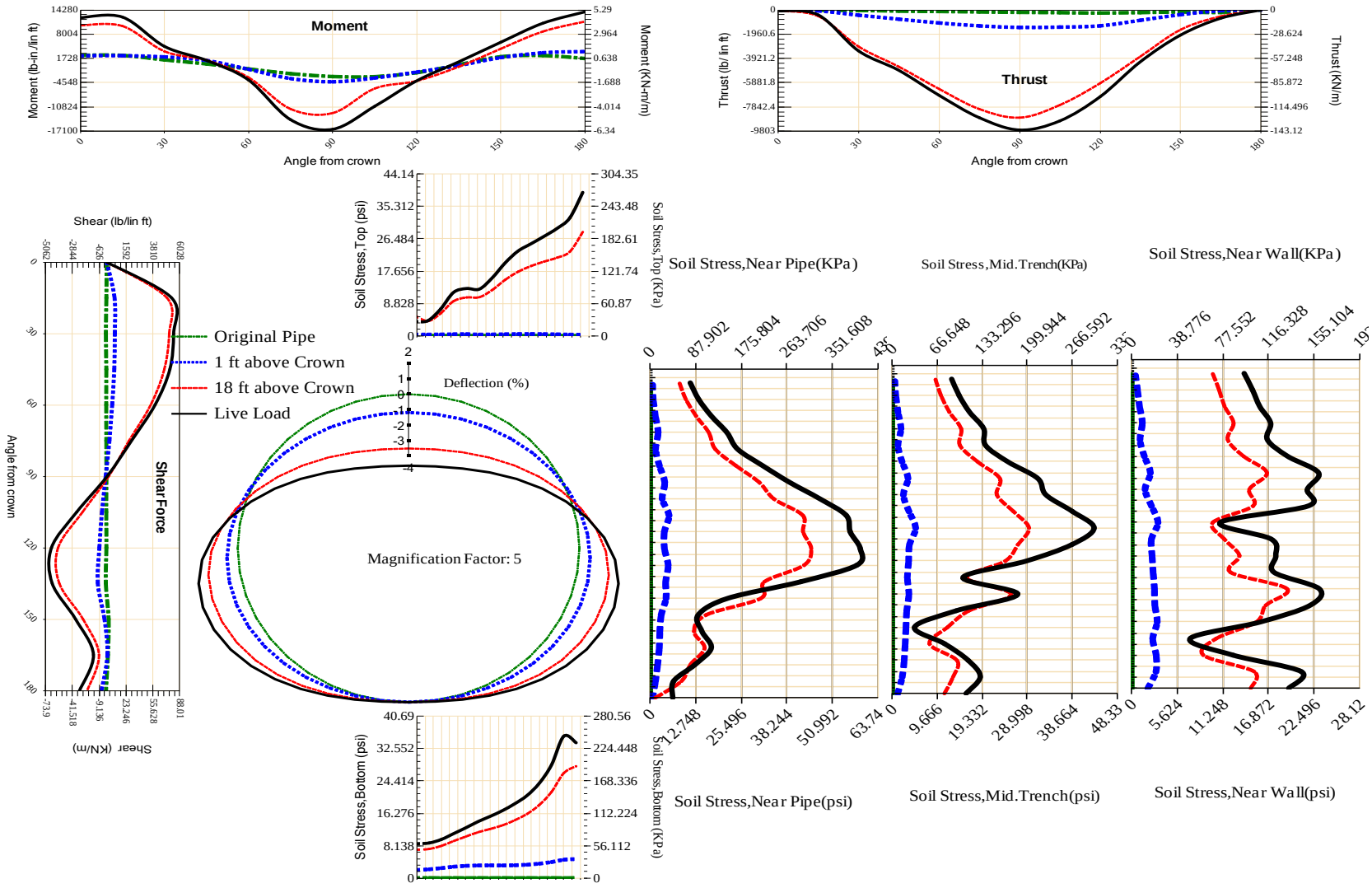

Figure A-48 Param-120-PW200-SF5TR-OD+48-EW3-H18-LiveLoad

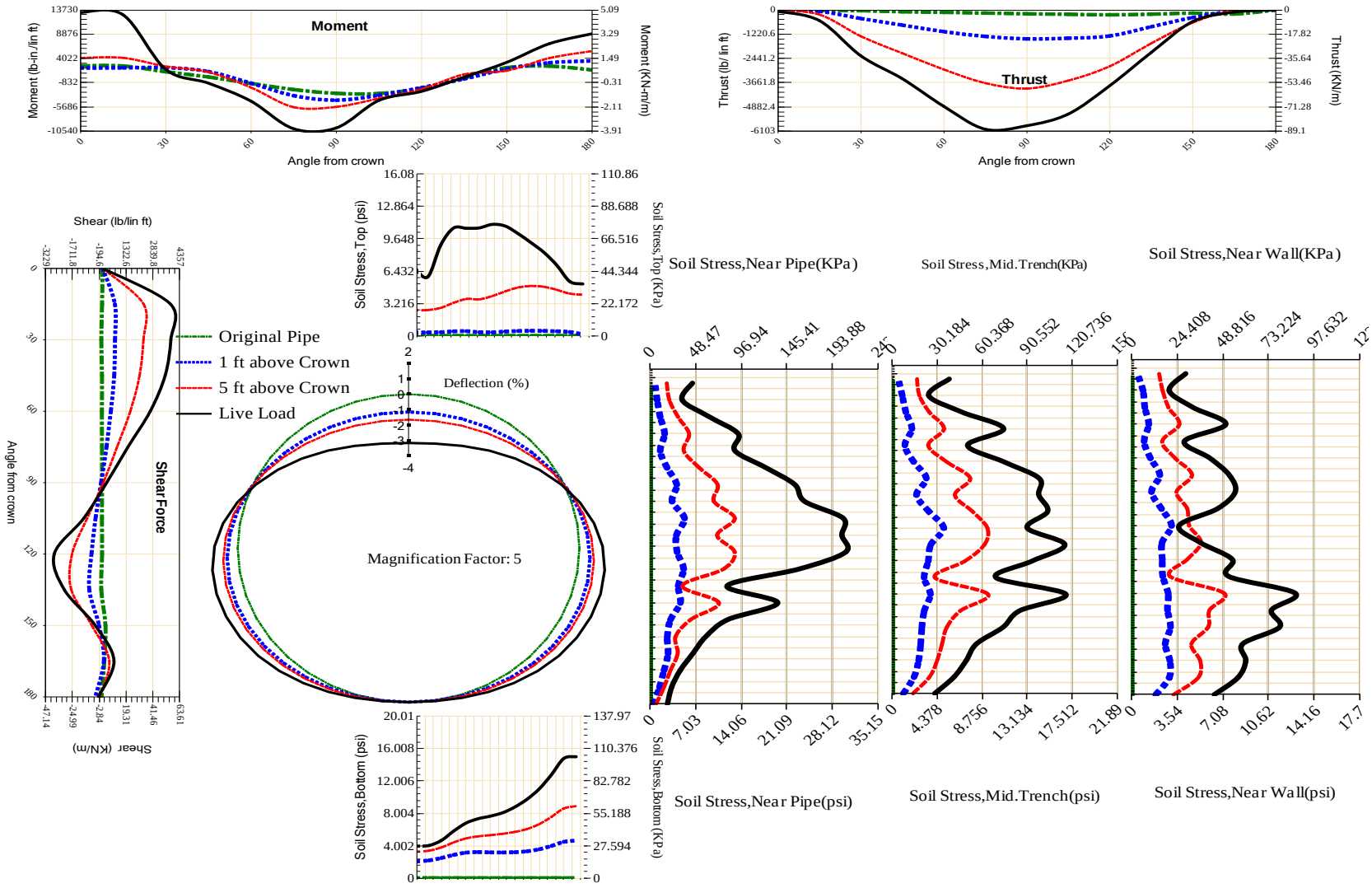

Figure A-49 Param-120-PW200-SF5TR-OD+48-EW3-H5-LiveLoad

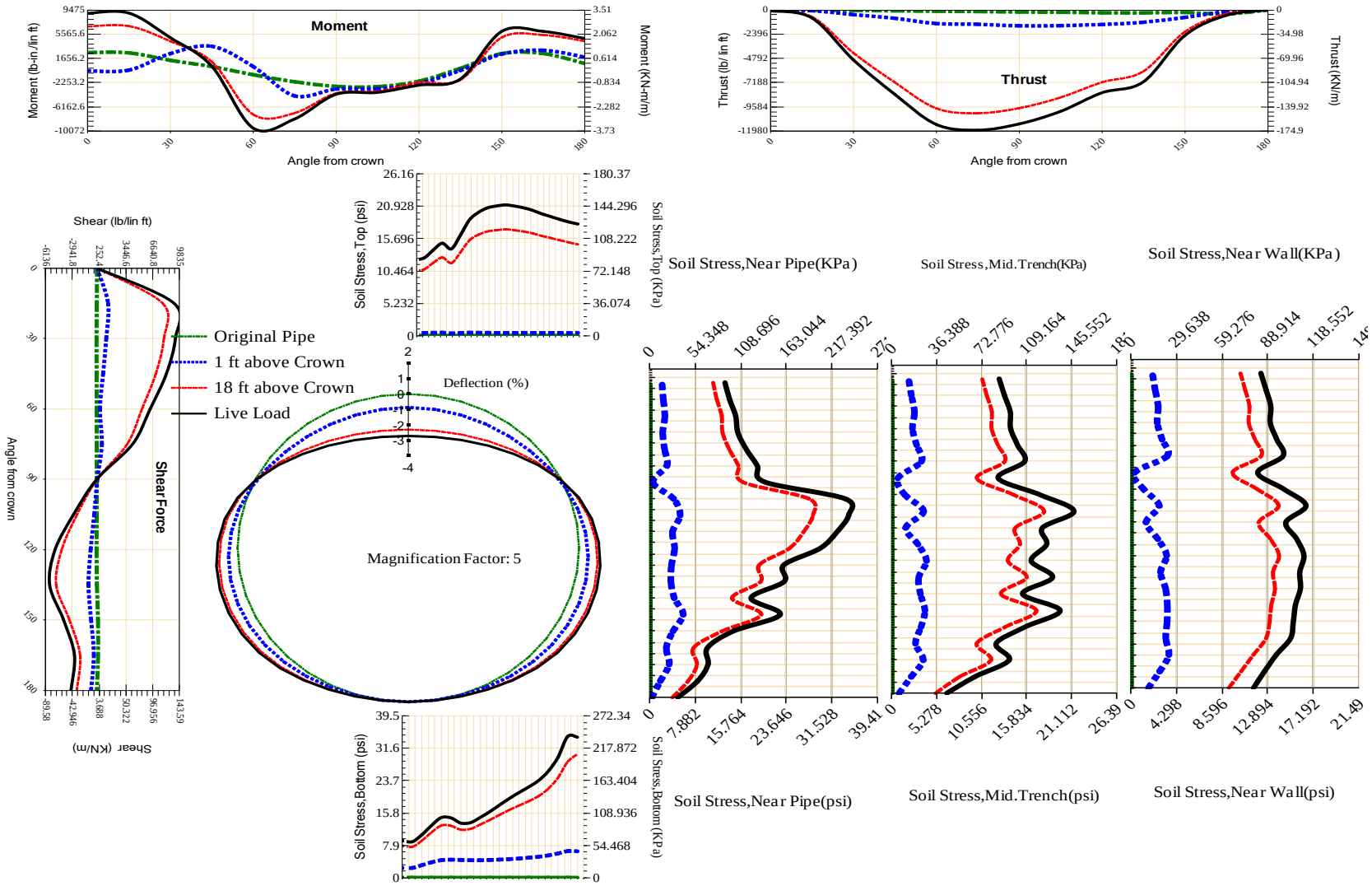

Figure A-50 Param-120-PW200-SF7OR-OD+108-EW10-H18-LiveLoad

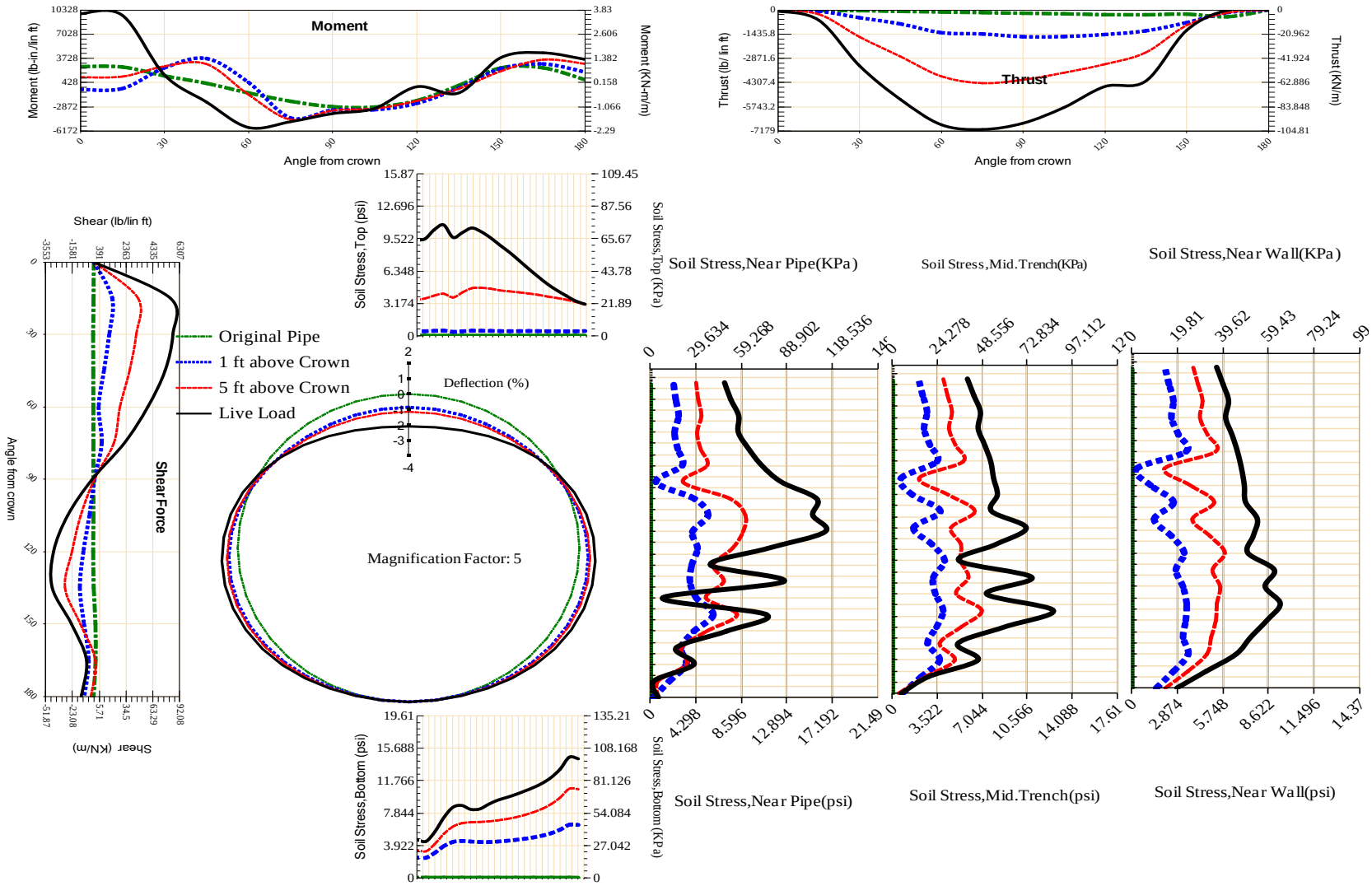

Figure A-51 Param-120-PW200-SF7OR-OD+108-EW10-H5-LiveLoad

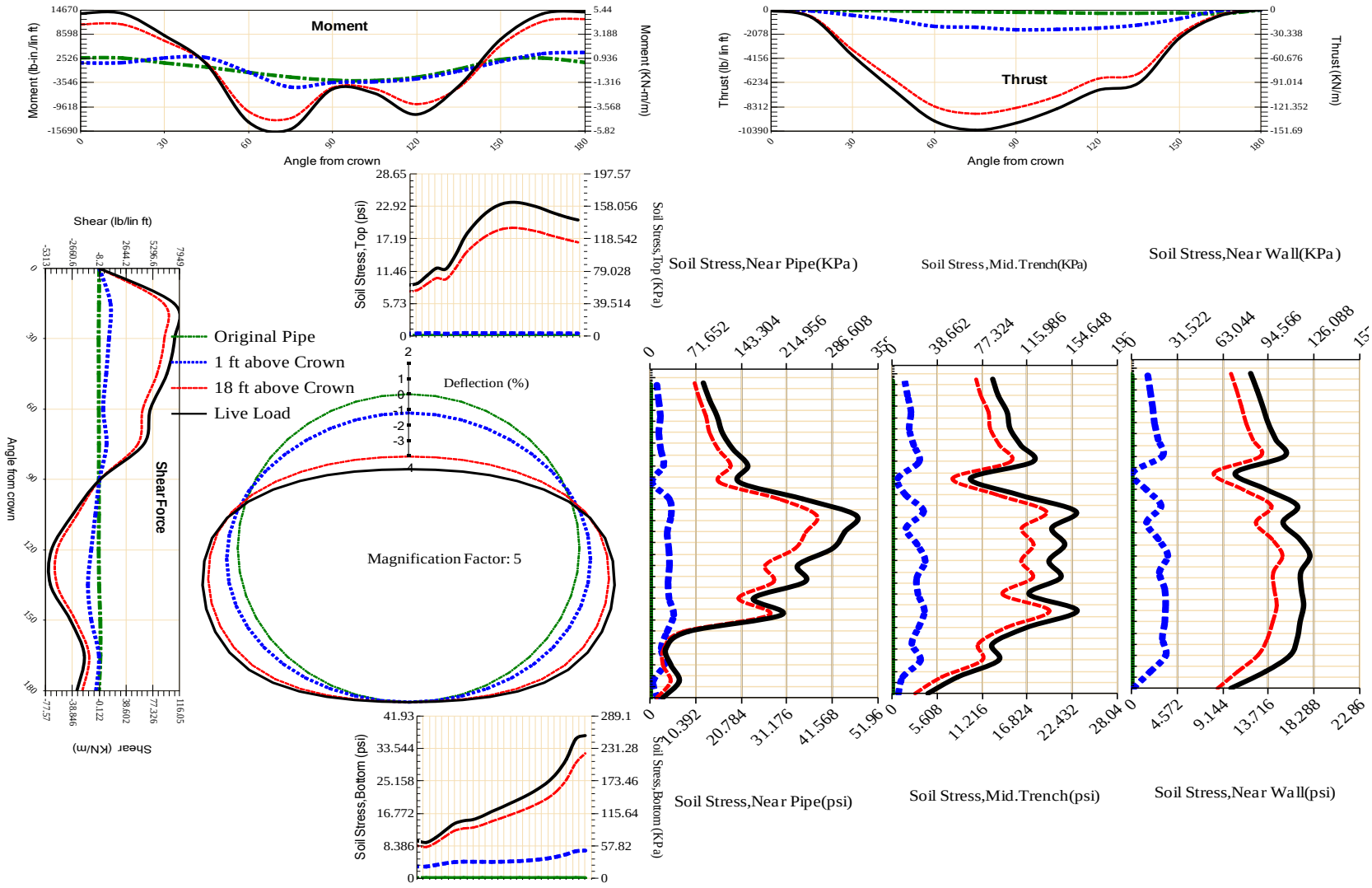

Figure A-52 Param-120-PW200-SF7OR-OD+108-EW3-H18-LiveLoad

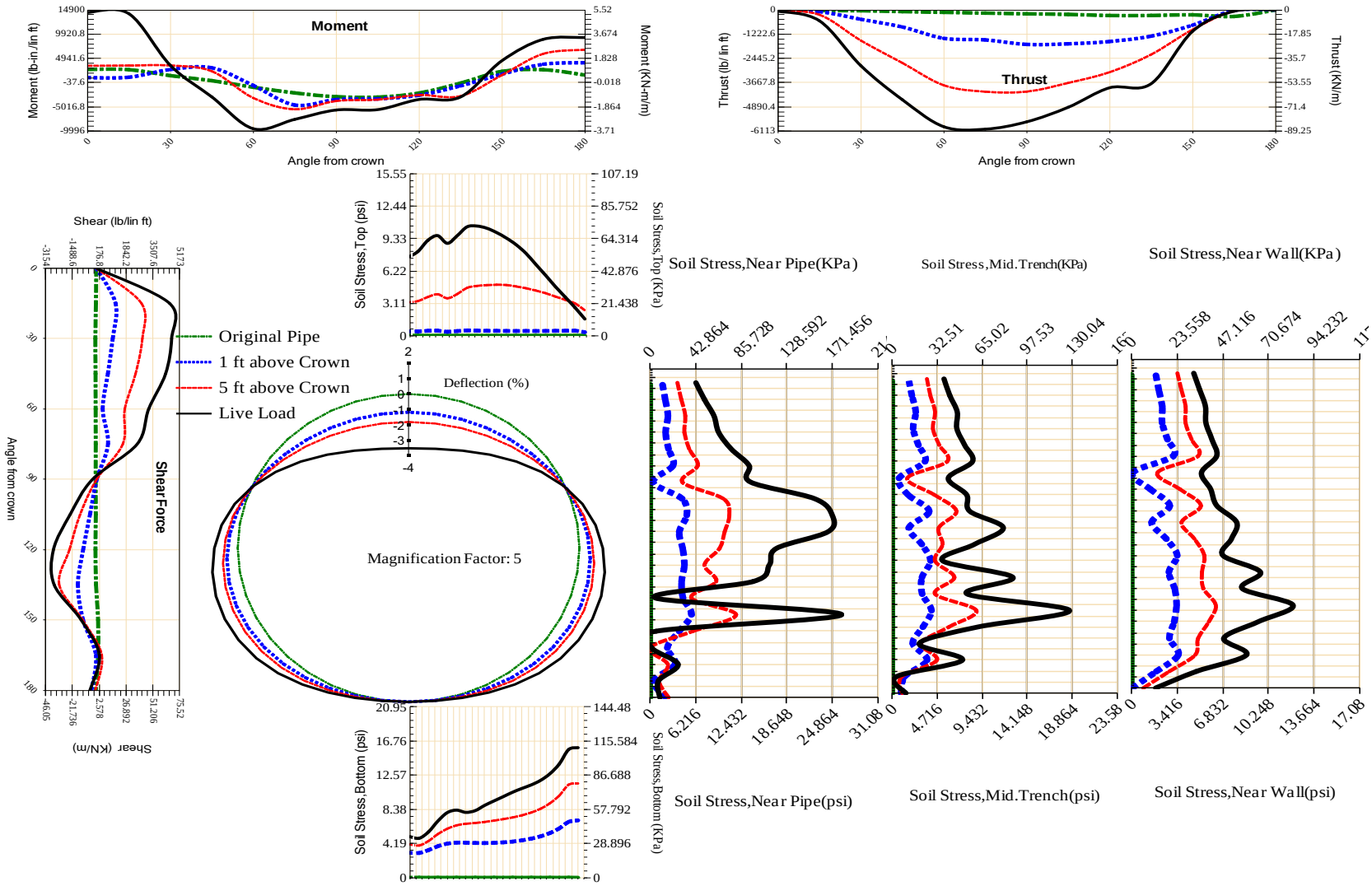

Figure A-53 Param-120-PW200-SF7OR-OD+108-EW3-H5-LiveLoad

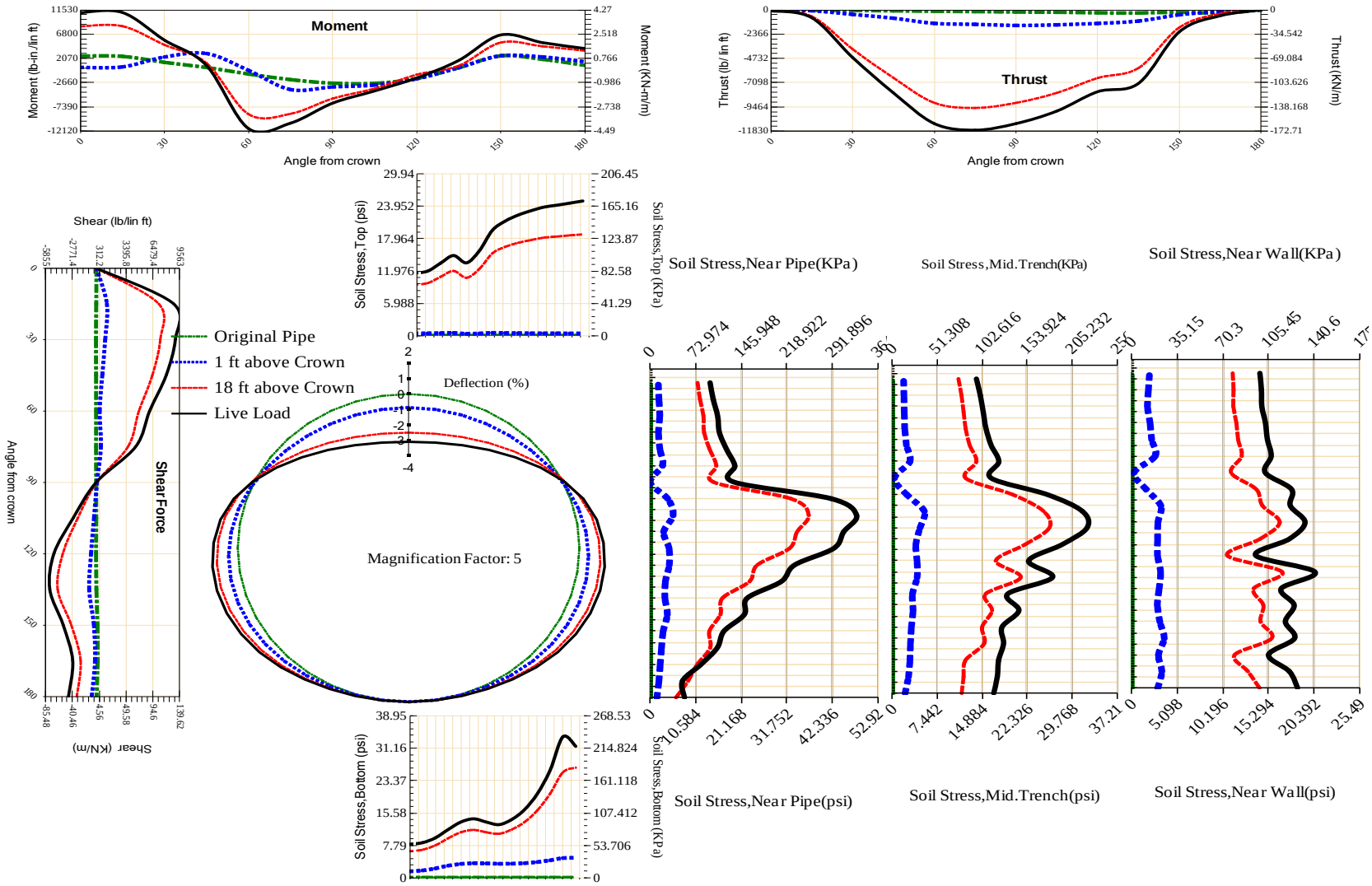

Figure A-54 Param-120-PW200-SF7OR-OD+48-EW10-H18-LiveLoad

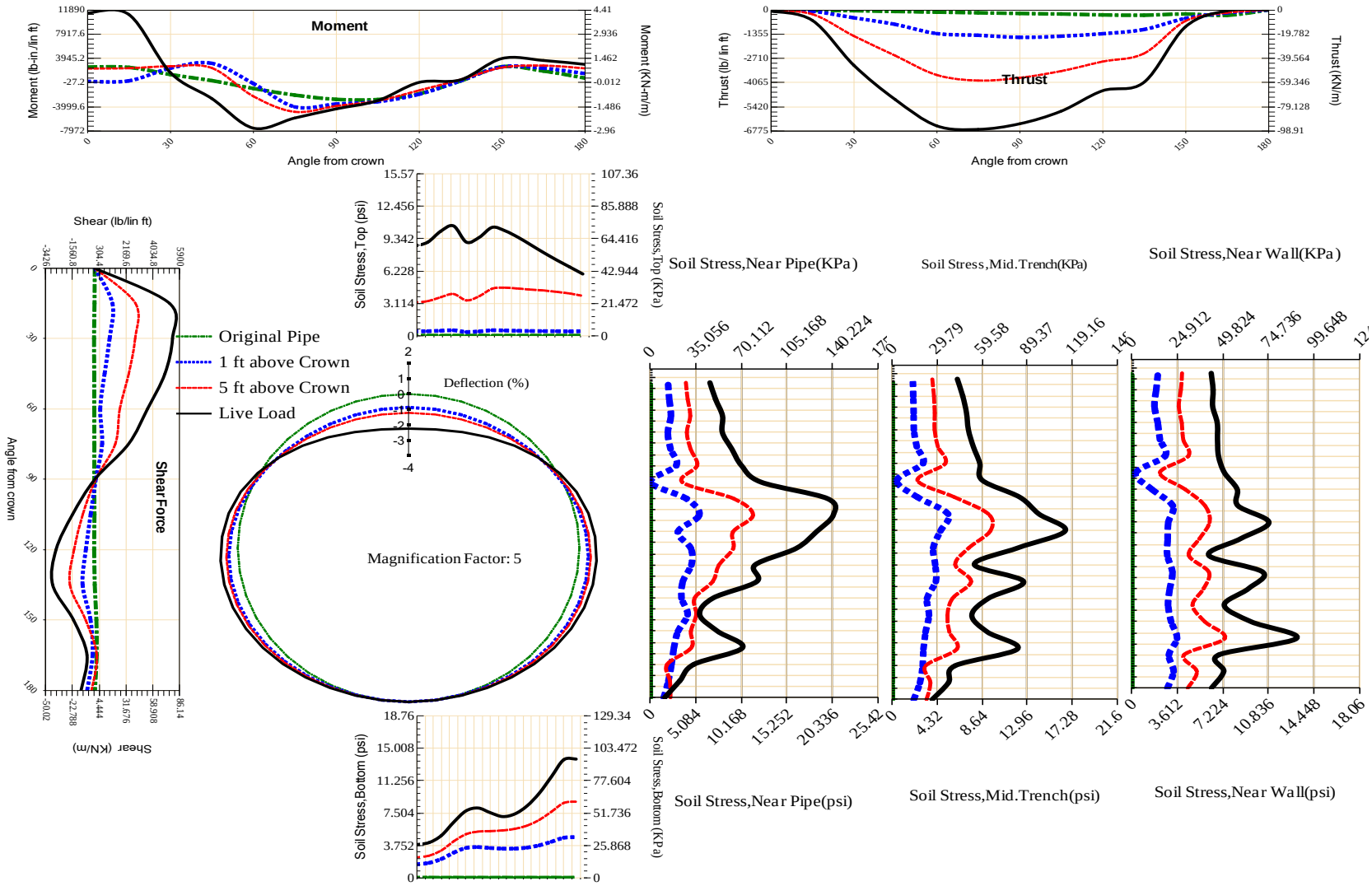

Figure A-55 Param-120-PW200-SF7OR-OD+48-EW10-H5-LiveLoad

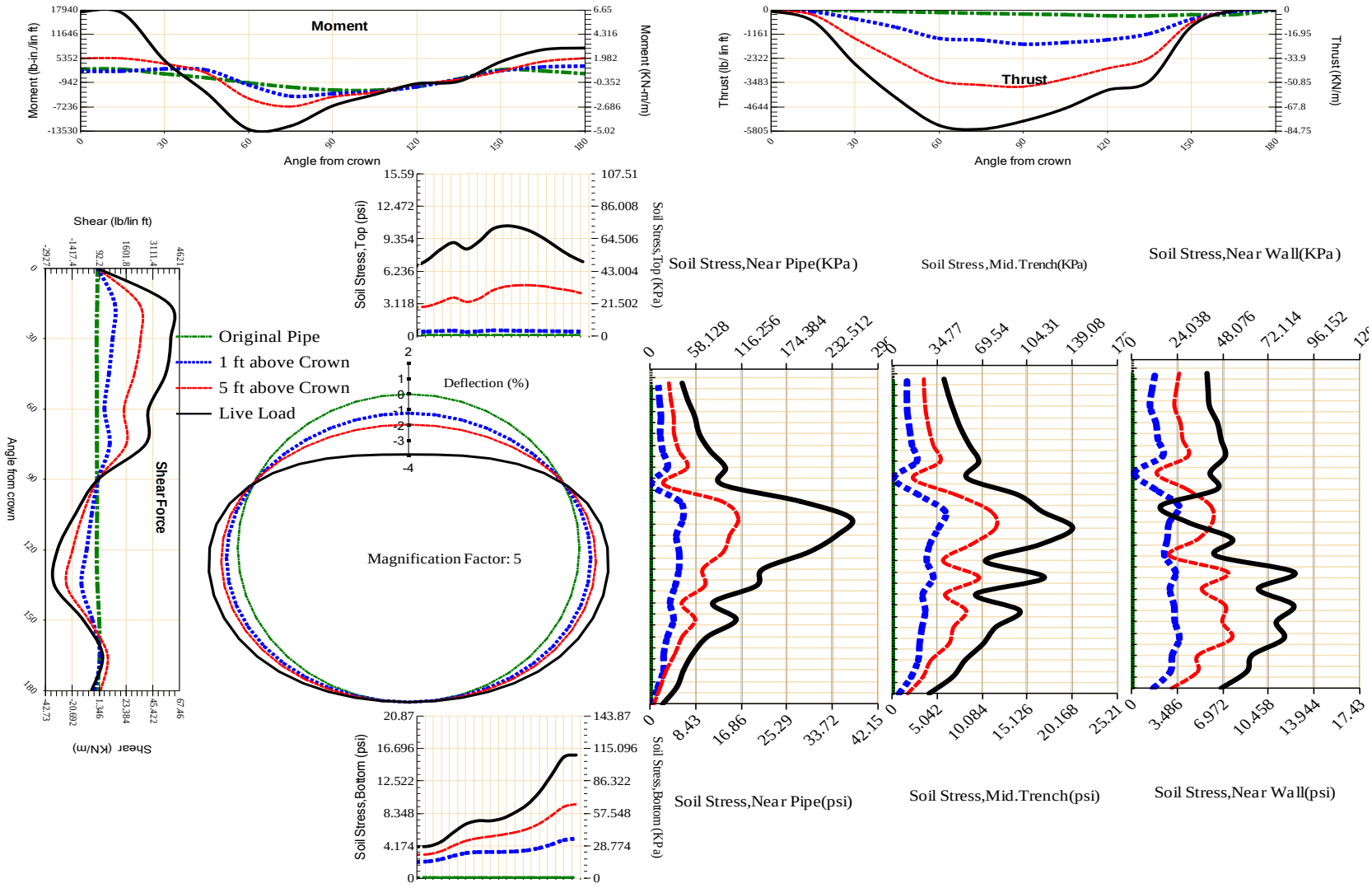

Figure A-56 Param-120-PW200-SF7OR-OD+48-EW3-H5-LiveLoad

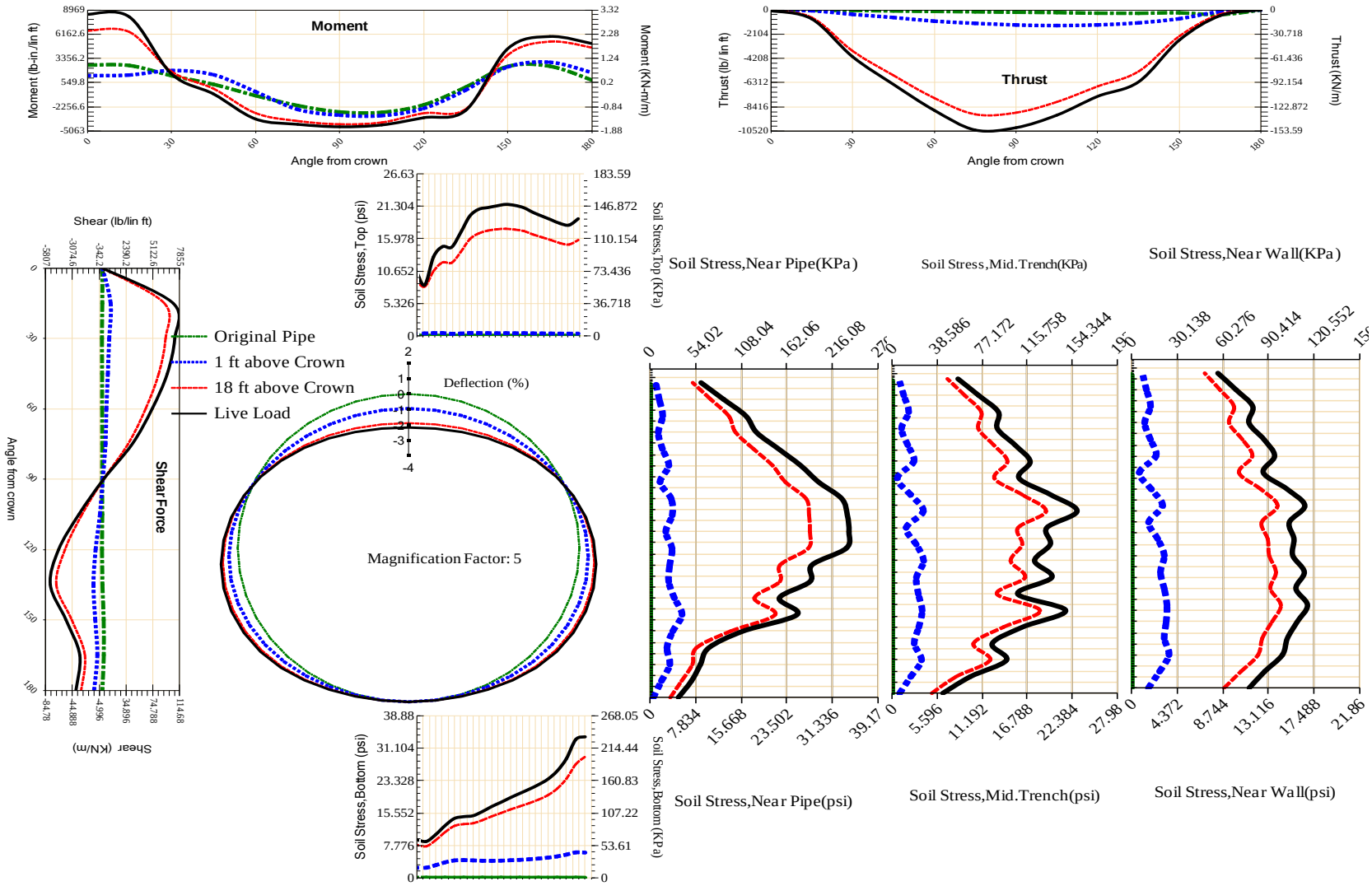

Figure A-57 Param-120-PW200-SF7TR-OD+108-EW10-H18-LiveLoad

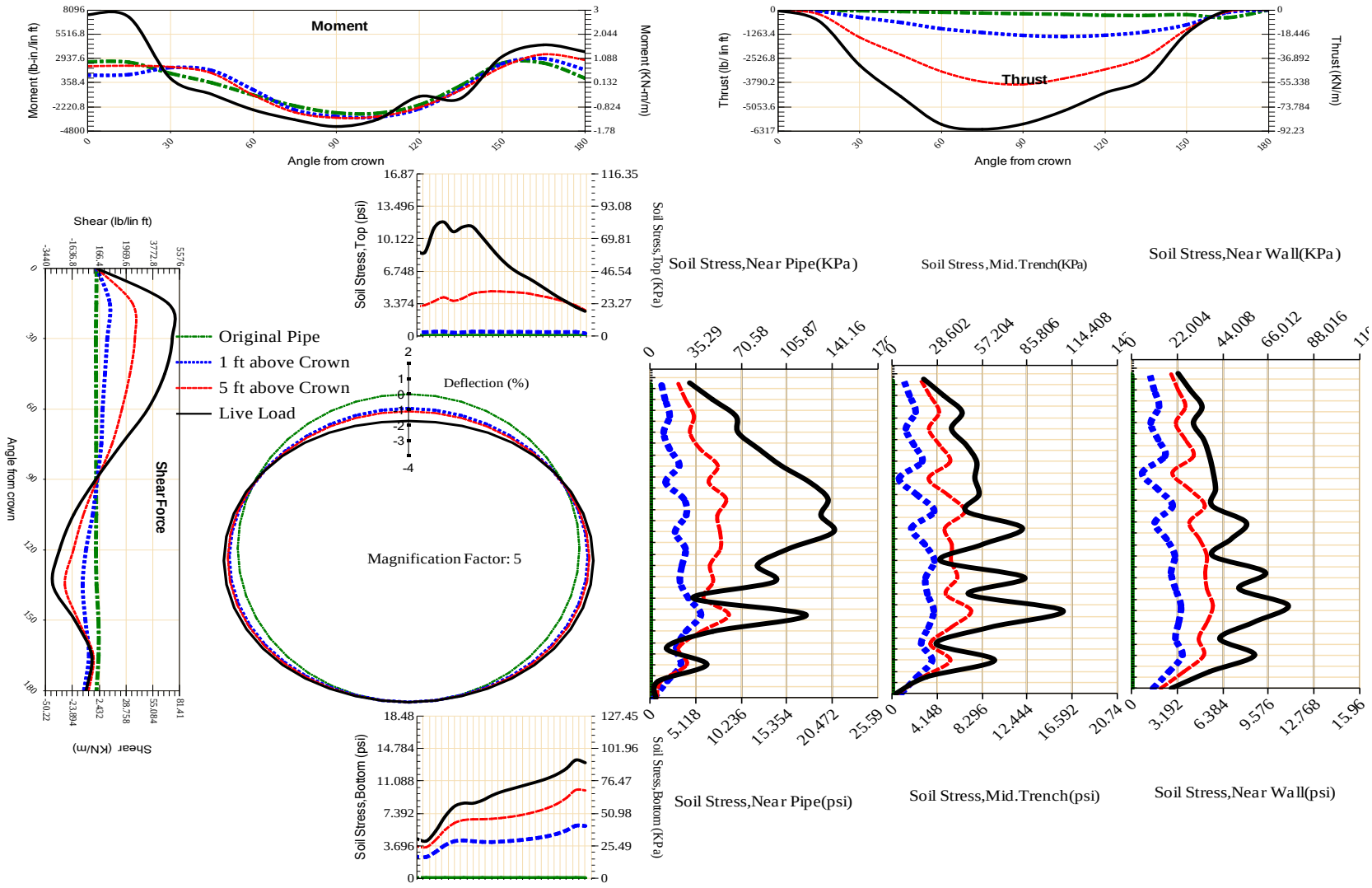

Figure A-58 Param-120-PW200-SF7TR-OD+108-EW10-H5-LiveLoad

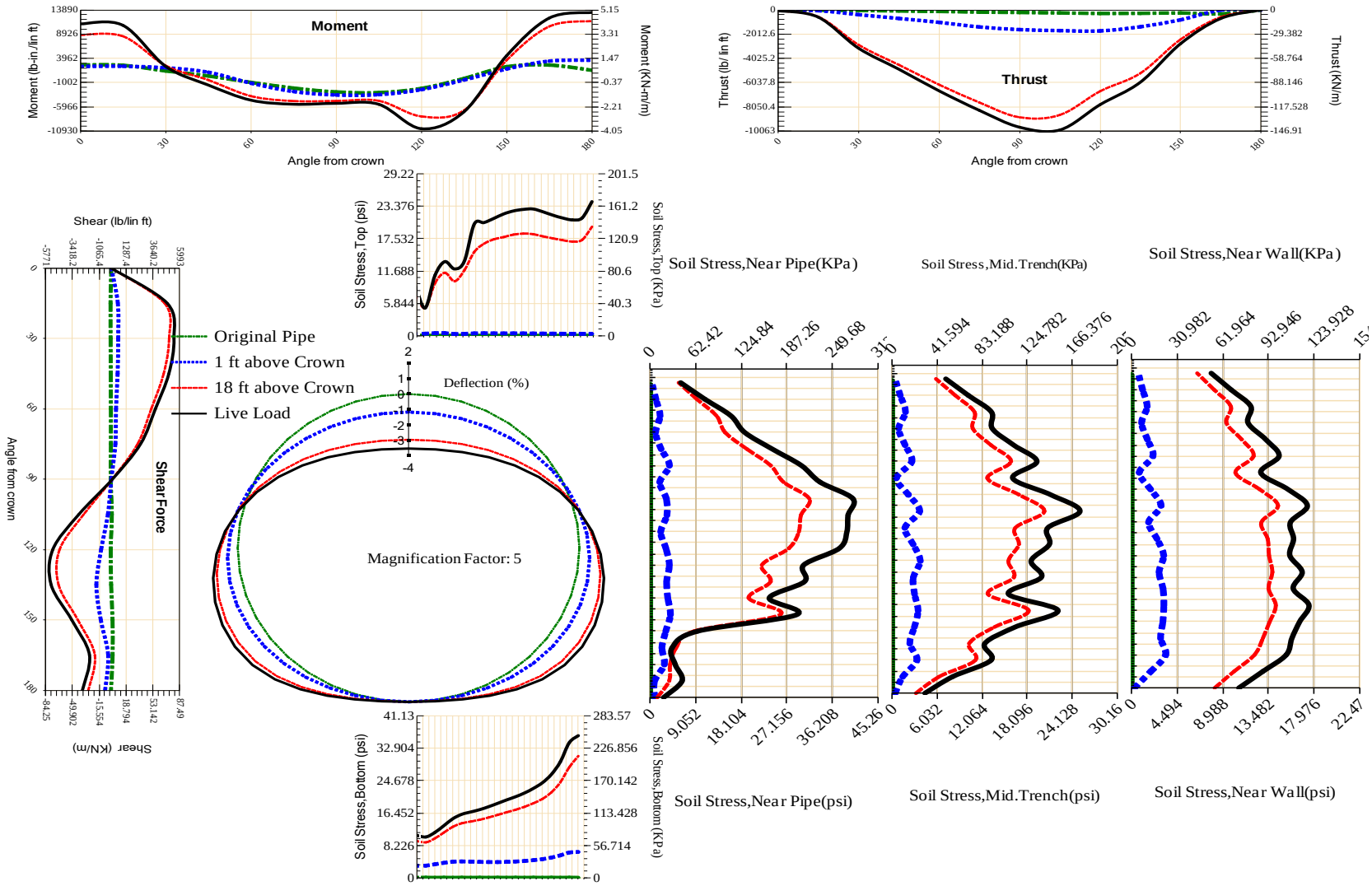

Figure A-59 Param-120-PW200-SF7TR-OD+108-EW3-H18-LiveLoad

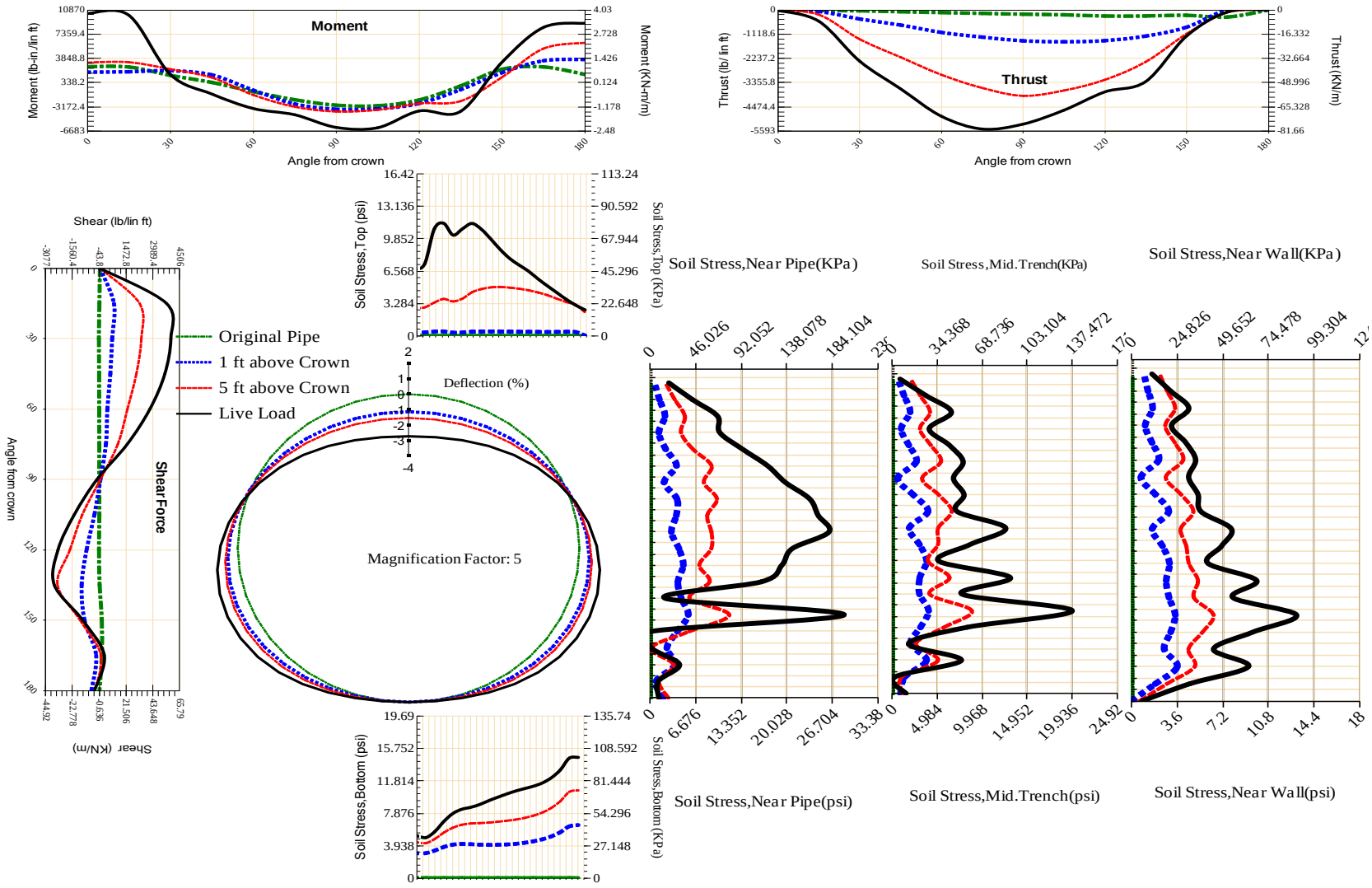

Figure A-60 Param-120-PW200-SF7TR-OD+108-EW3-H5-LiveLoad

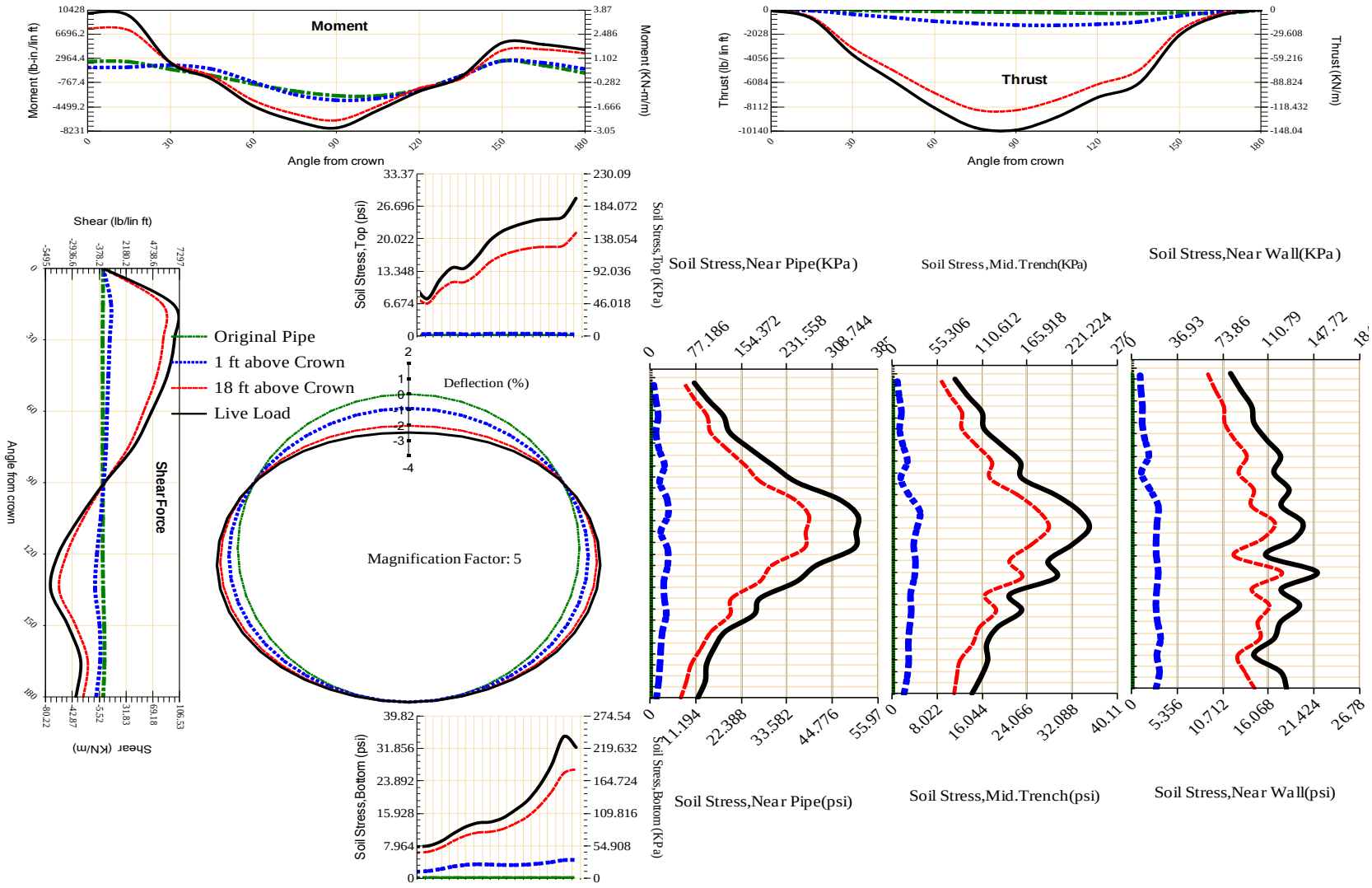

Figure A-61 Param-120-PW200-SF7TR-OD+48-EW10-H18-LiveLoad

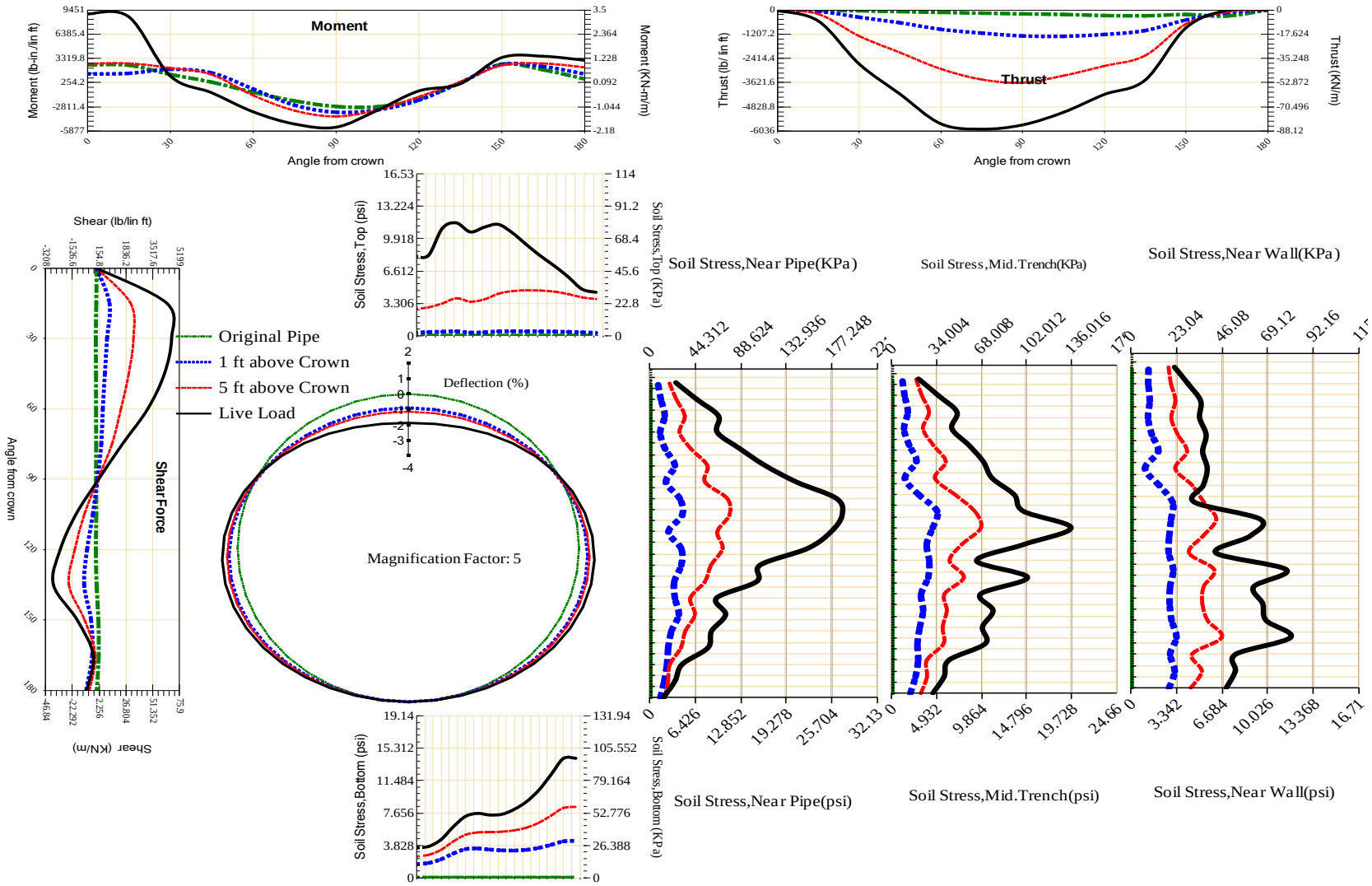

Figure A-62 Param-120-PW200-SF7TR-OD+48-EW10-H5-LiveLoad

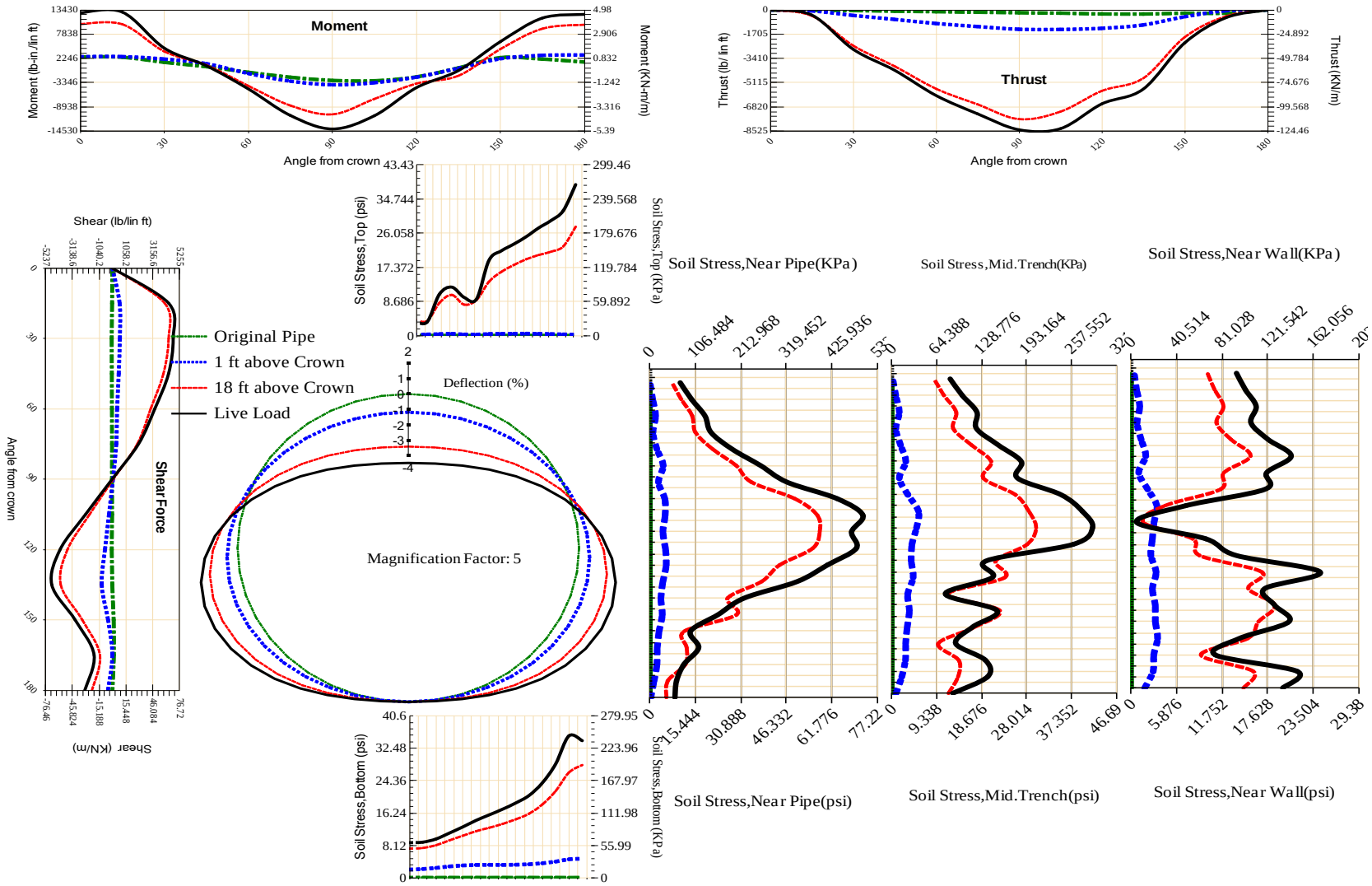

Figure A-63 Param-120-PW200-SF7TR-OD+48-EW3-H18-LiveLoad

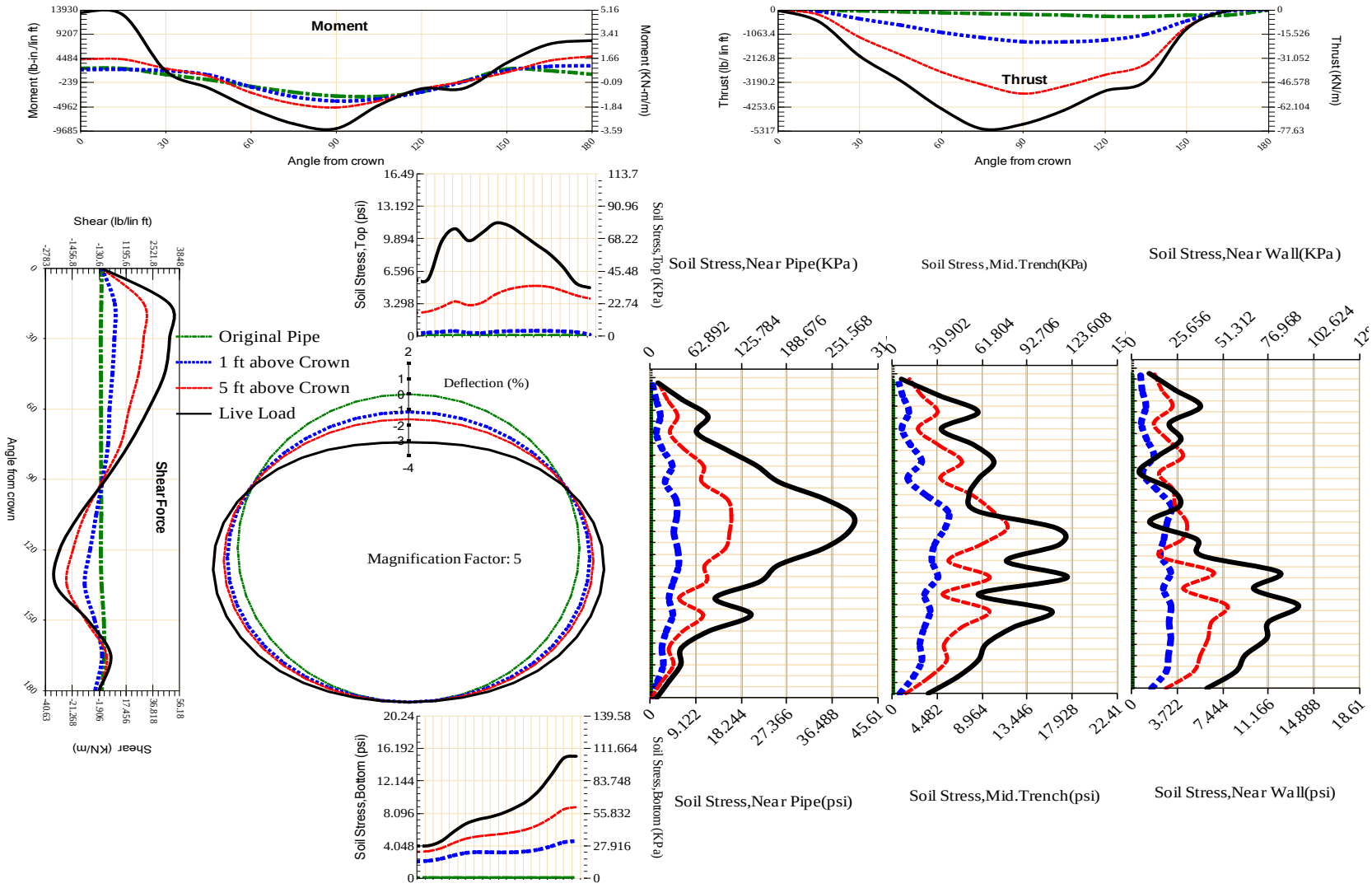

Figure A-64 Param-120-PW200-SF7TR-OD+48-EW3-H5-LiveLoad

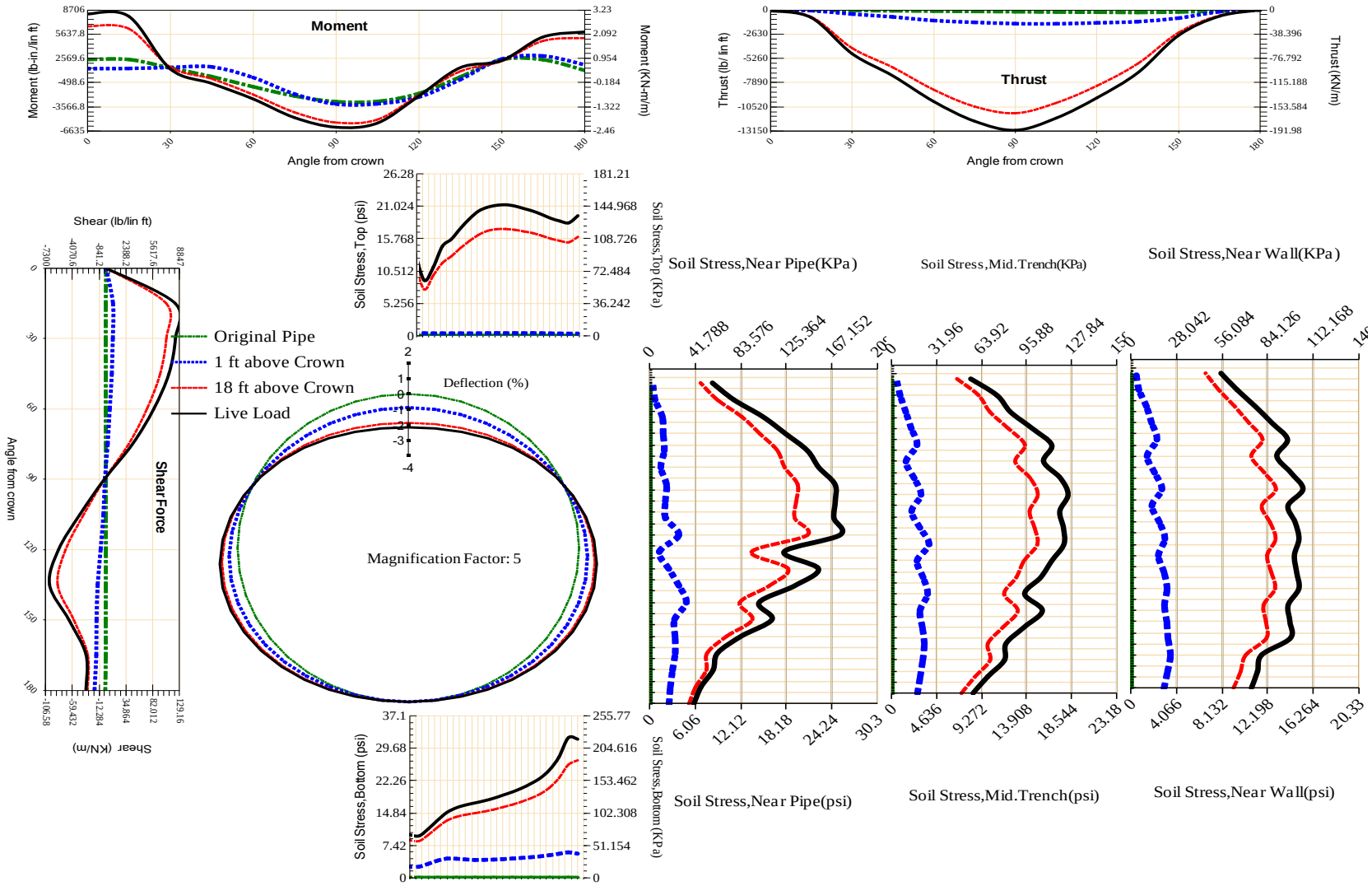

Figure A-65 Param-120-PW200-TR10TR-OD+108-EW10-H18-LiveLoad

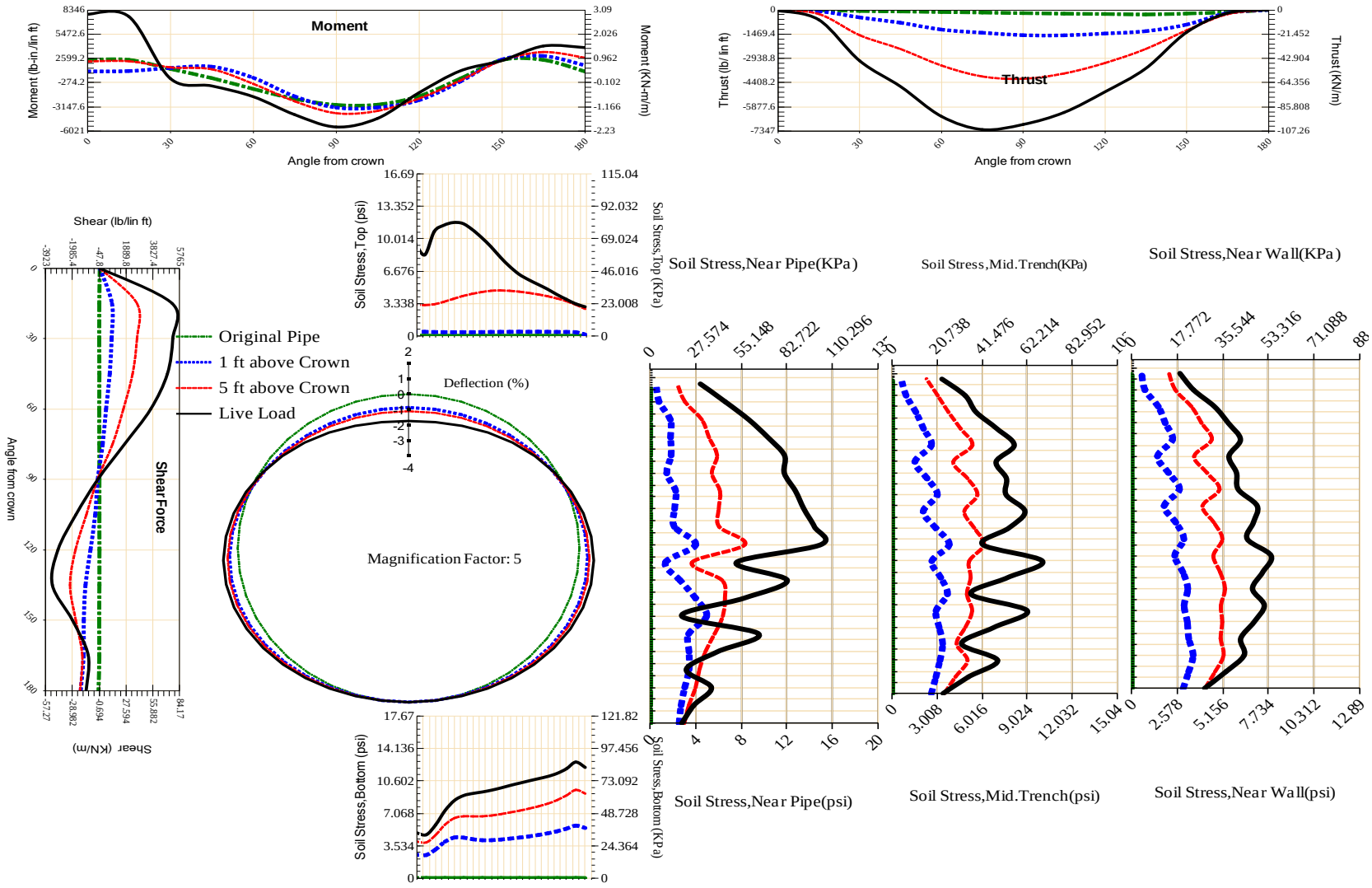

Figure A-66 Param-120-PW200-TR10TR-OD+108-EW10-H5-LiveLoad

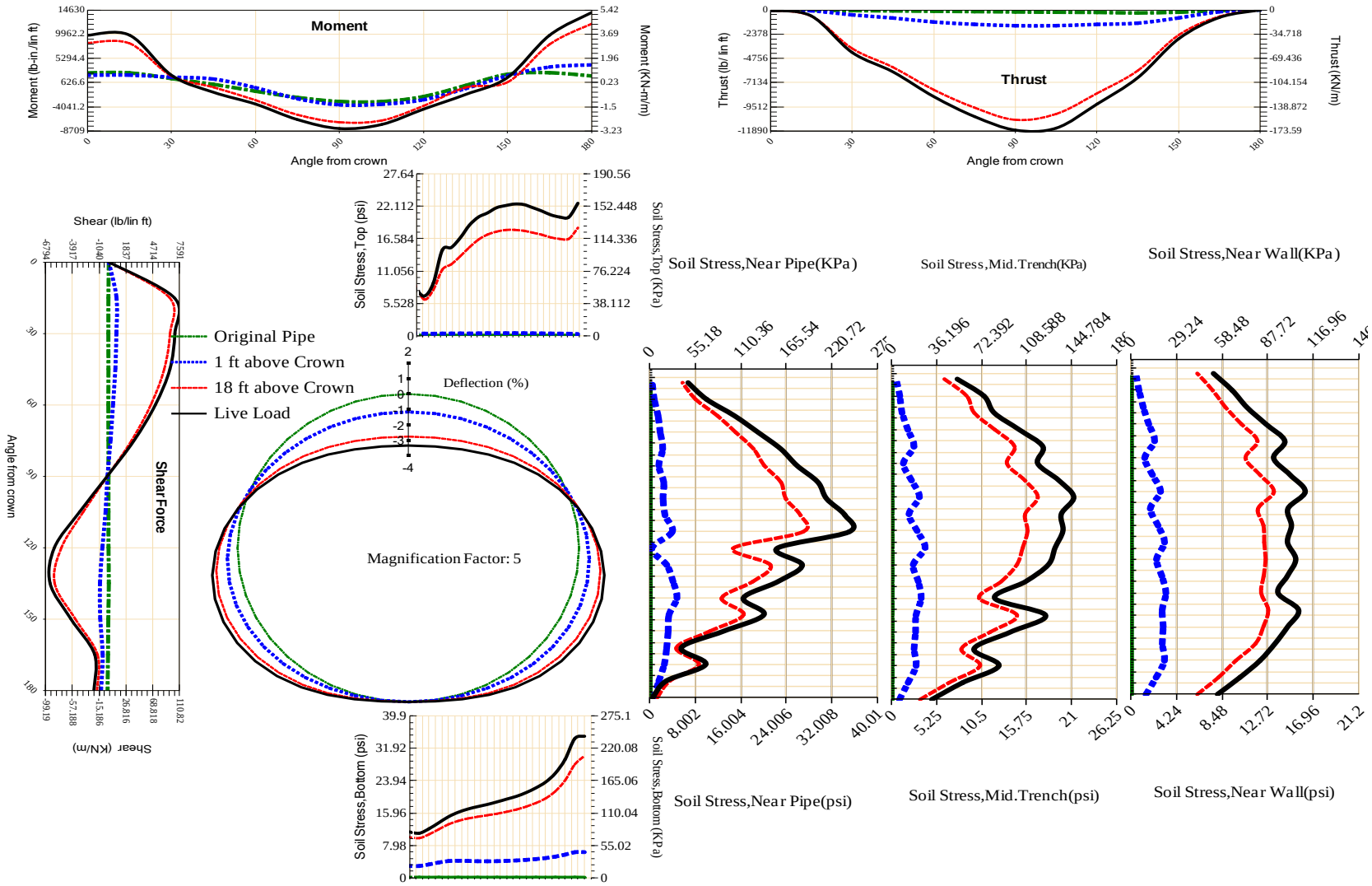

Figure A-67 Param-120-PW200-TR10TR-OD+108-EW3-H18-LiveLoad

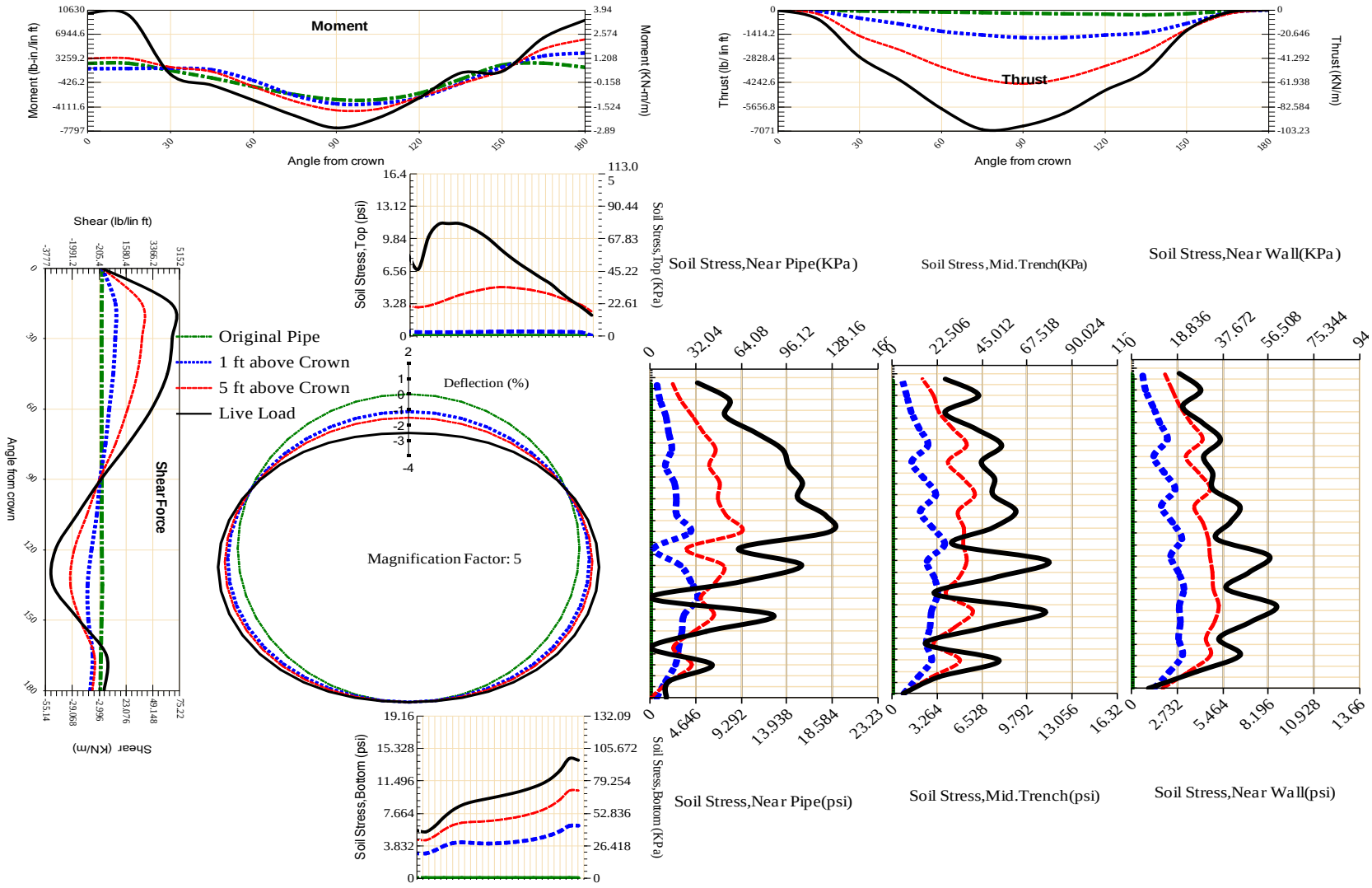

Figure A-68 Param-120-PW200-TR10TR-OD+108-EW3-H5-LiveLoad

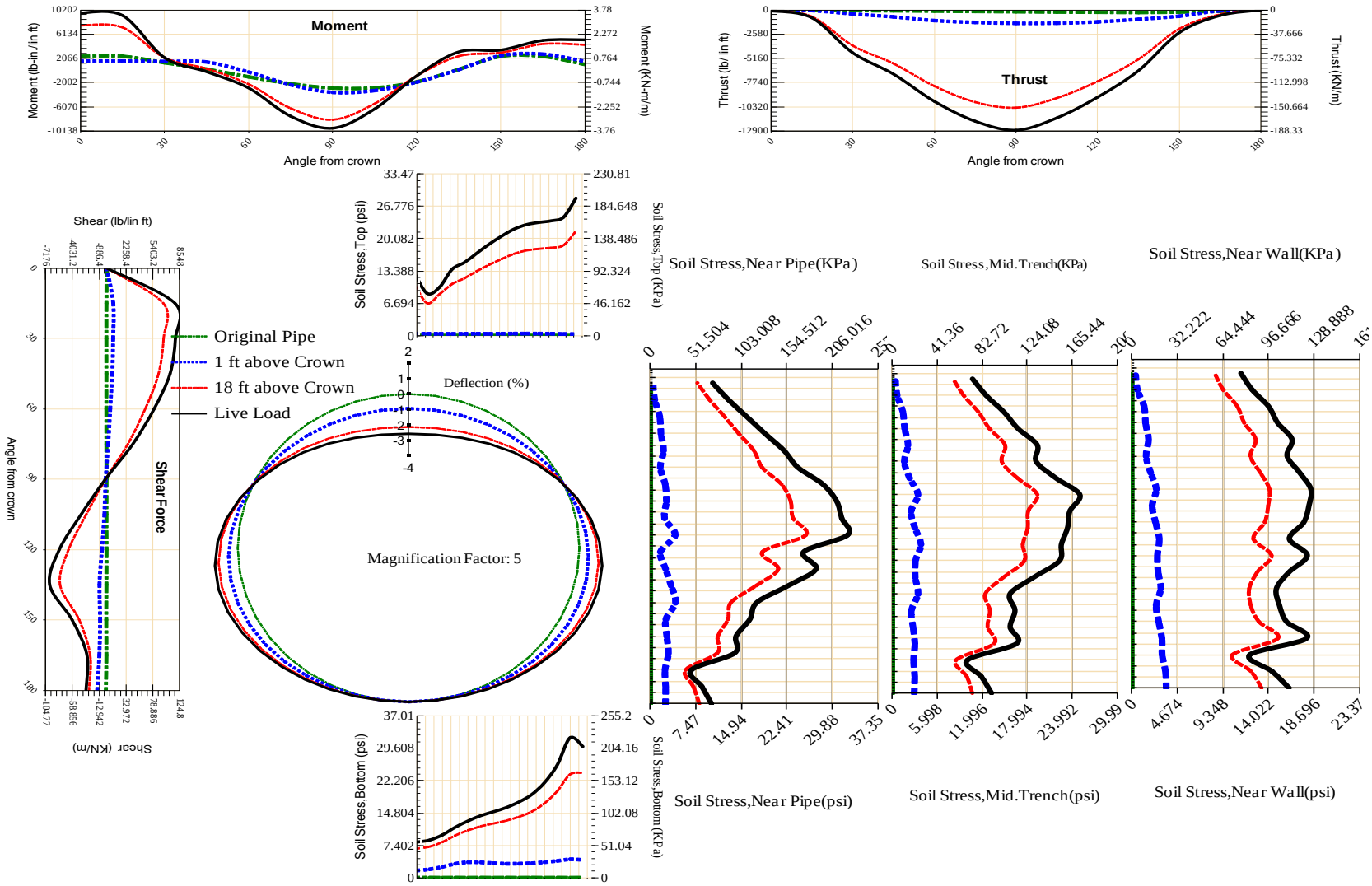

Figure A-69 Param-120-PW200-TR10TR-OD+48-EW10-H18-LiveLoad

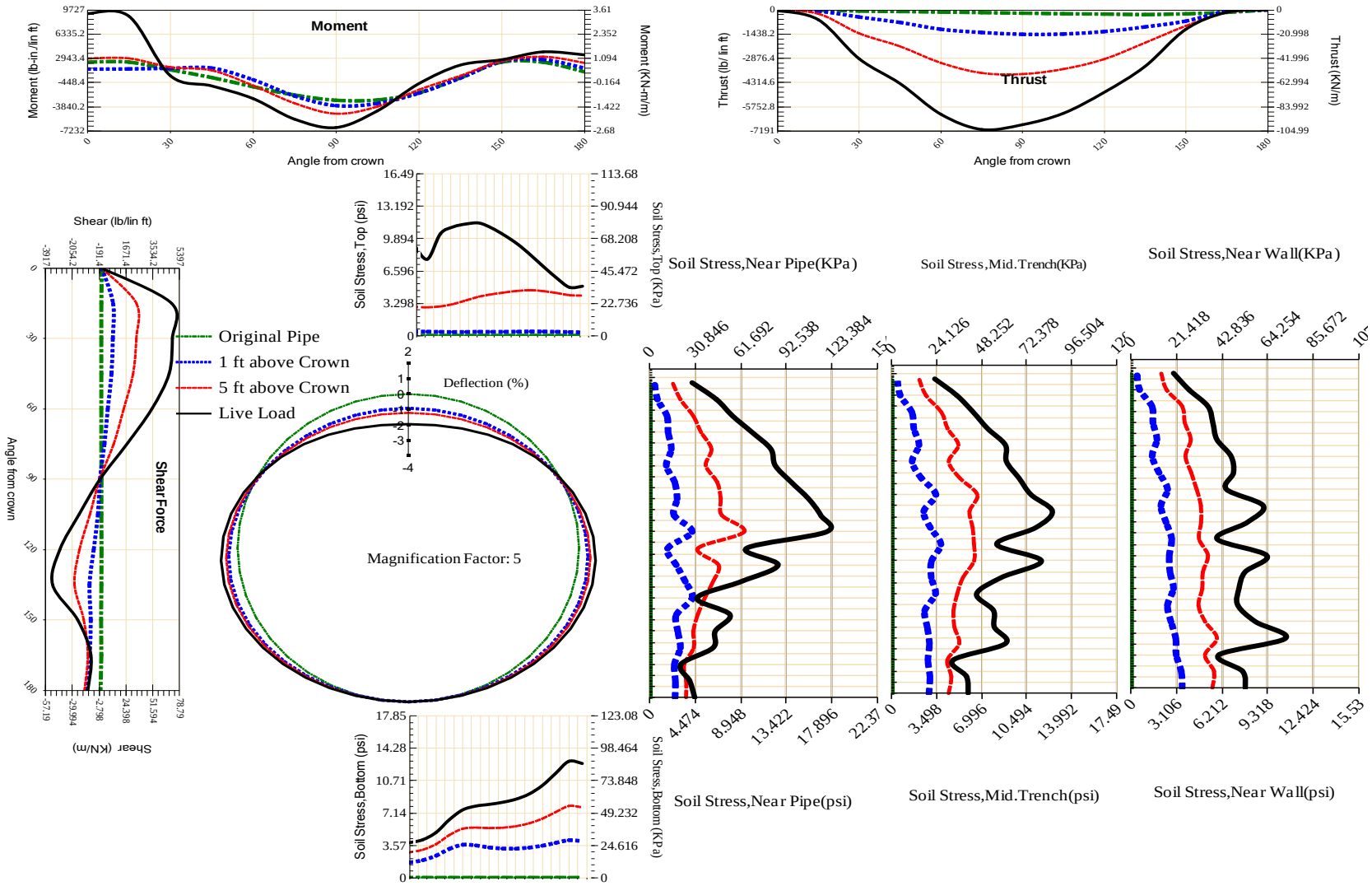

Figure A-70 Param-120-PW200-TR10TR-OD+48-EW10-H5-LiveLoad

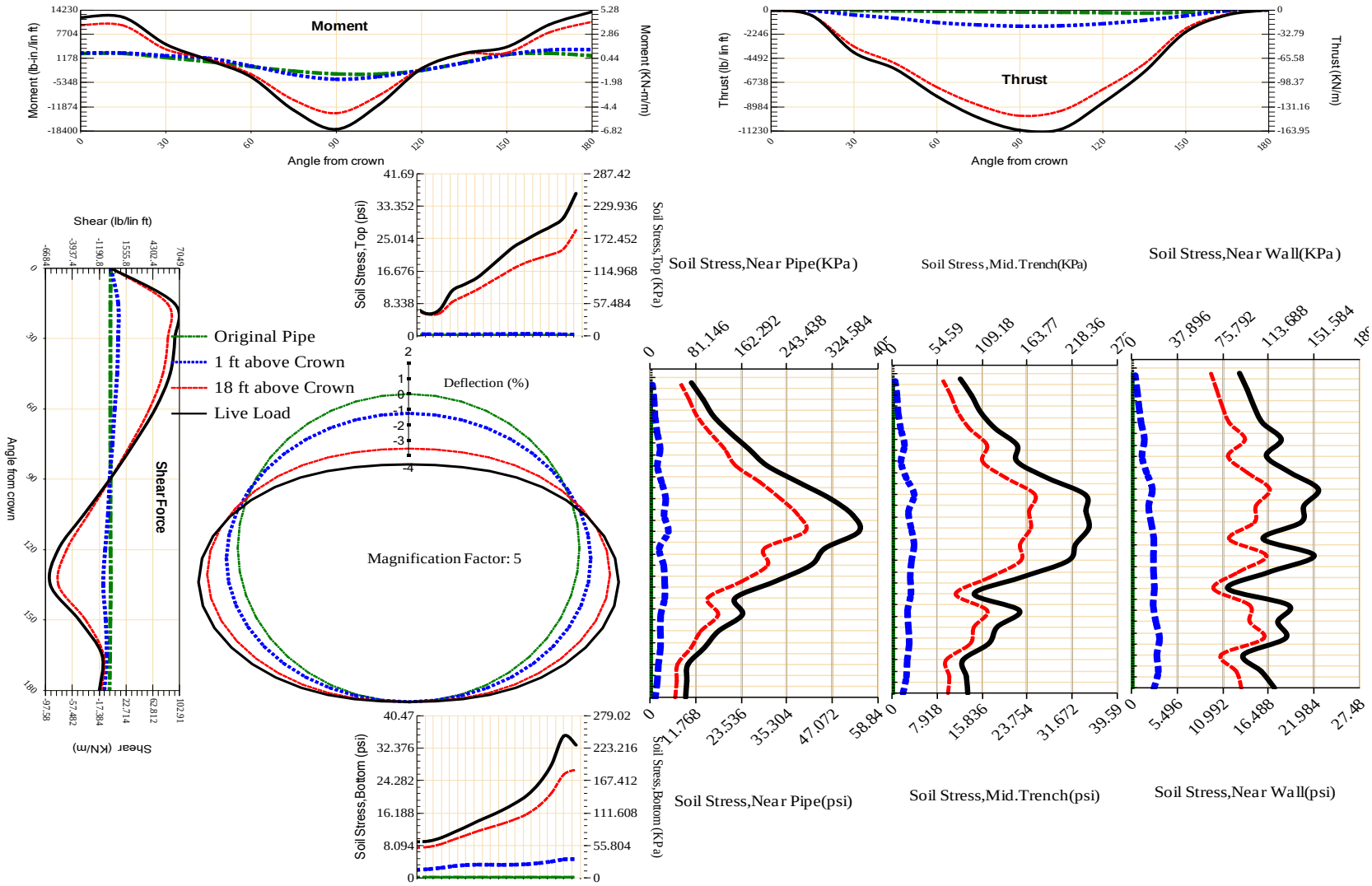

Figure A-71 Param-120-PW200-TR10TR-OD+48-EW3-H18-LiveLoad

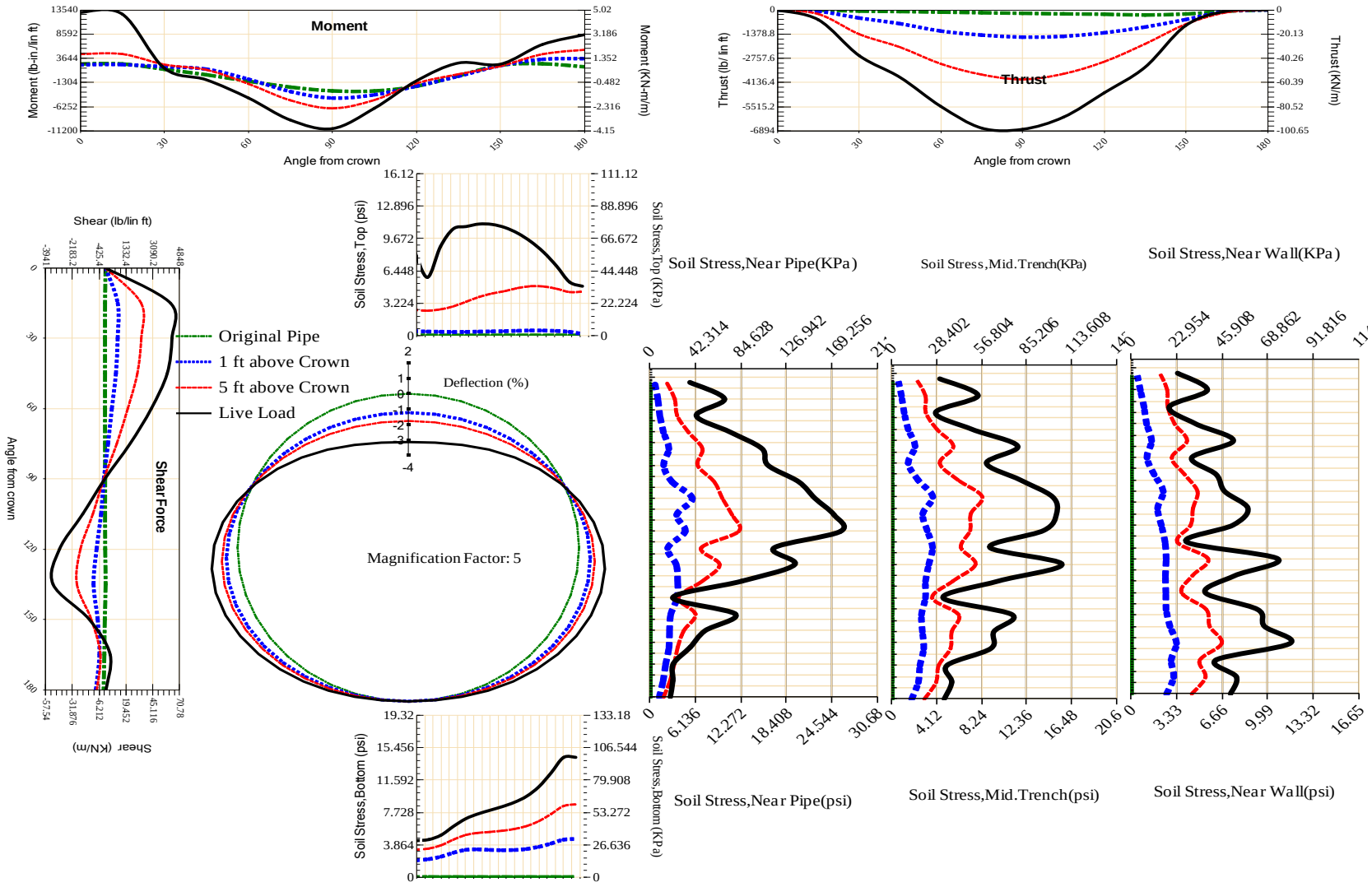

Figure A-72 Param-120-PW200-TR10TR-OD+48-EW3-H5-LiveLoad

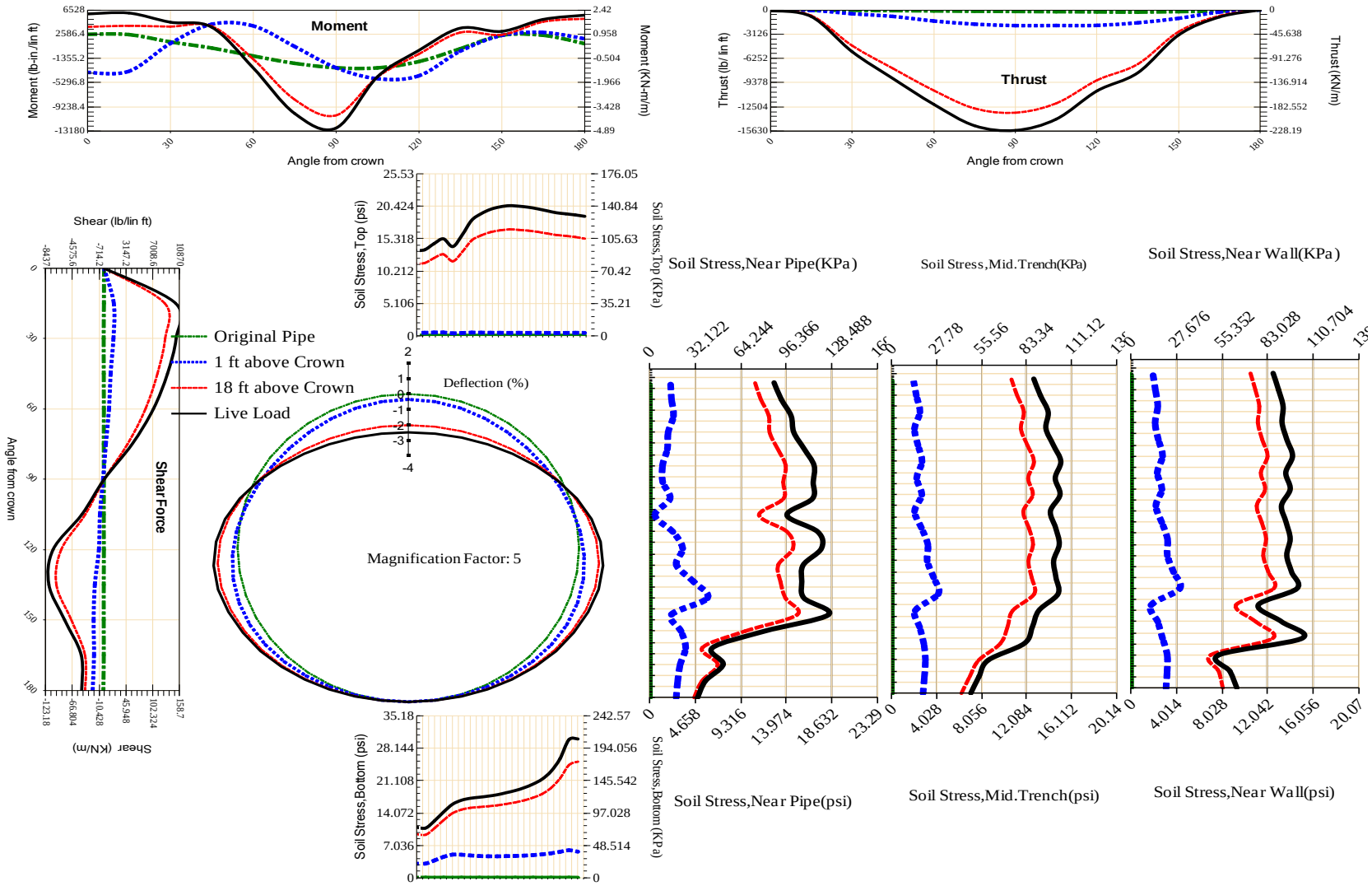

Figure A-73 Param-120-PW200-TR3OR-OD+108-EW10-H18-LiveLoad

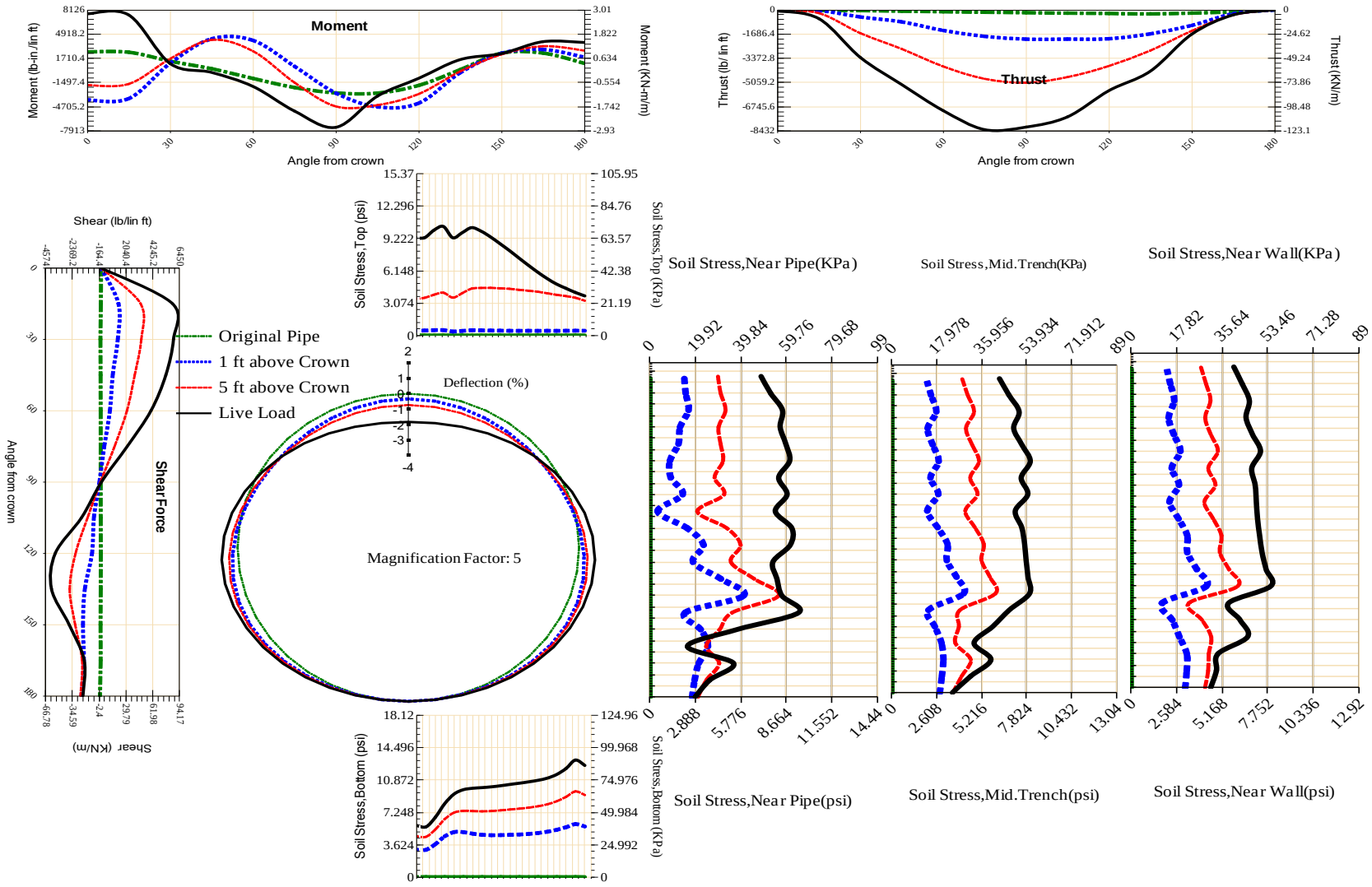

Figure A-74 Param-120-PW200-TR3OR-OD+108-EW10-H5-LiveLoad

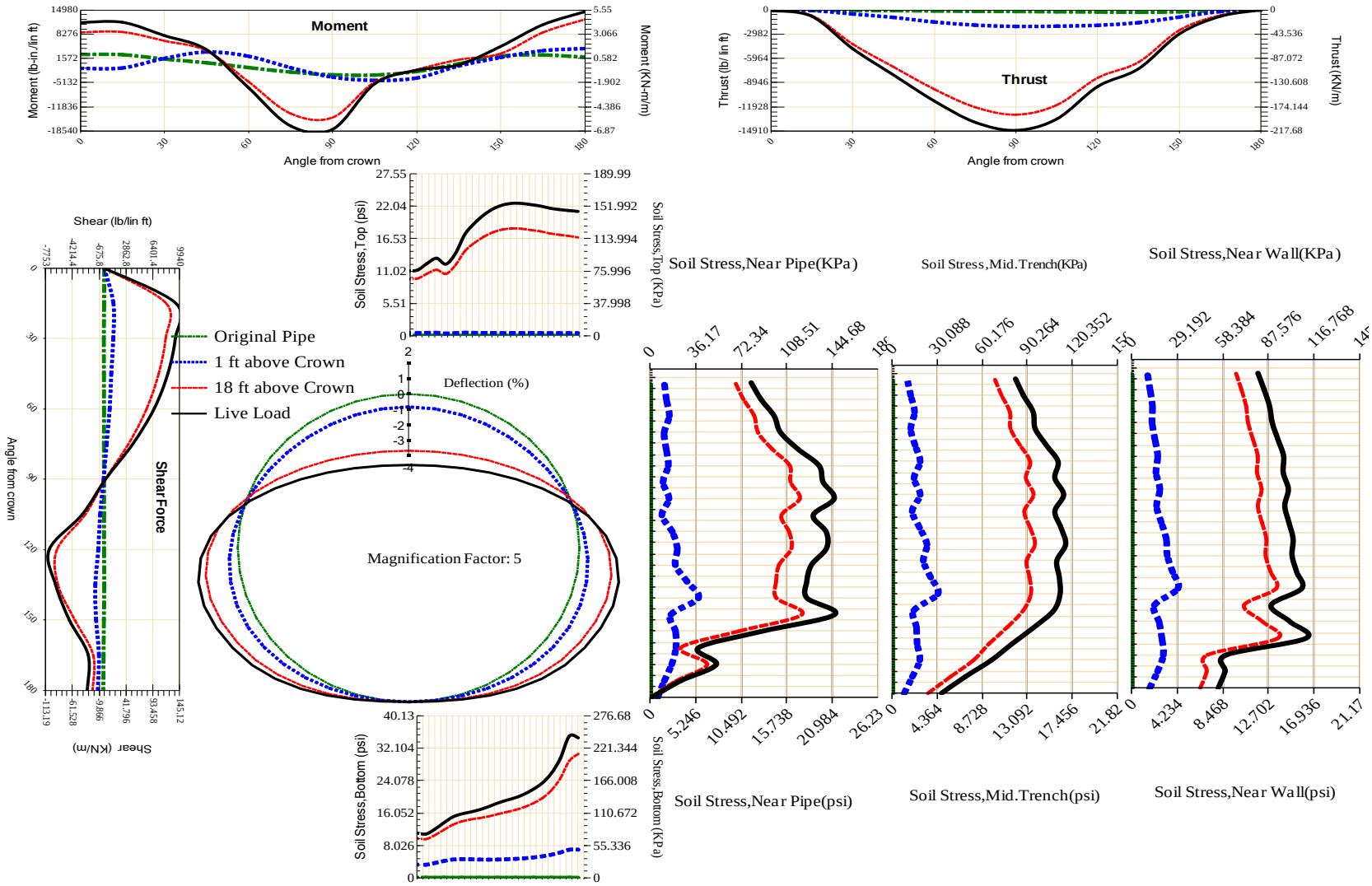

Figure A-75 Param-120-PW200-TR3OR-OD+108-EW3-H18-LiveLoad

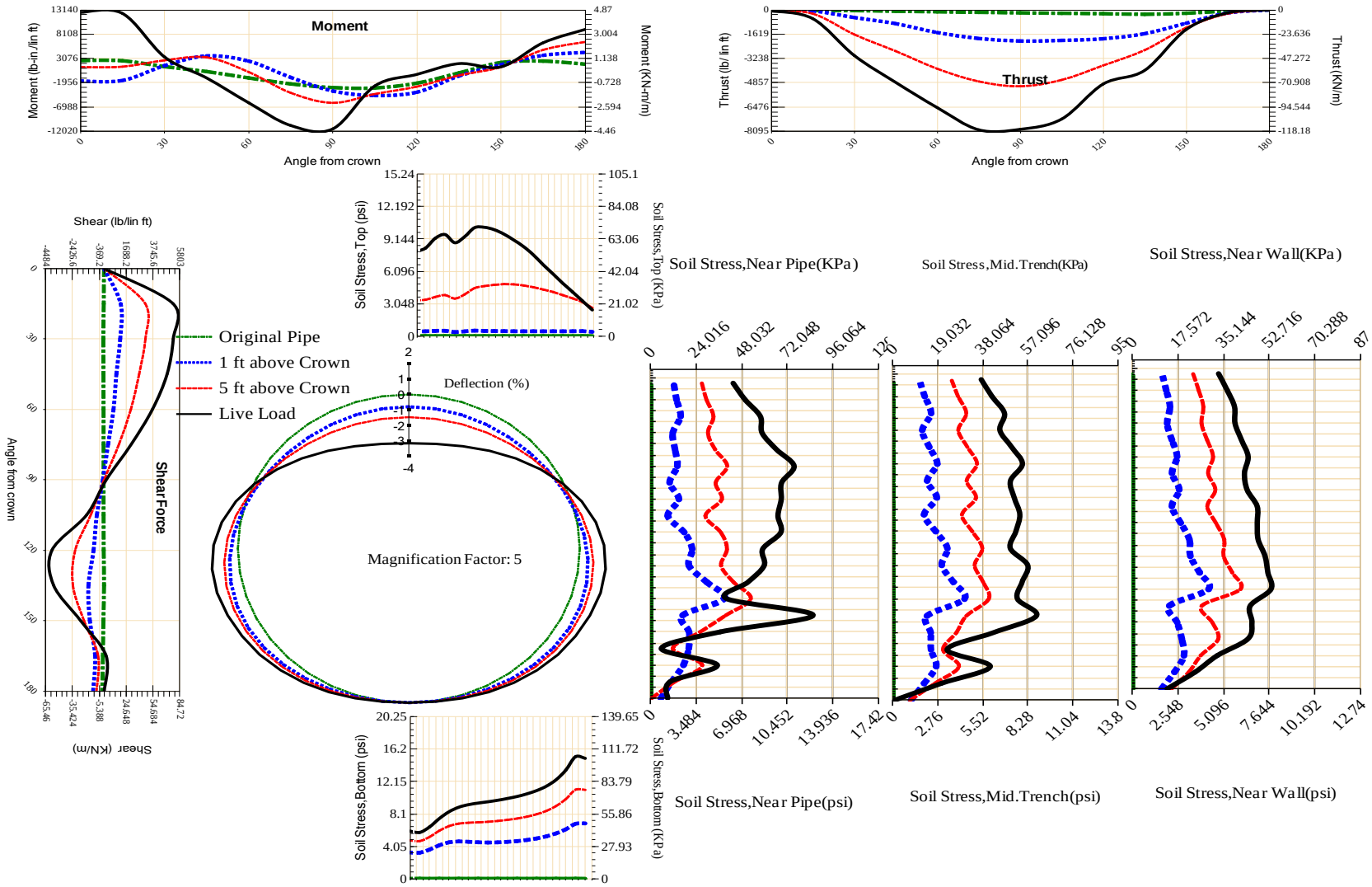

Figure A-76 Param-120-PW200-TR3OR-OD+108-EW3-H5-LiveLoad

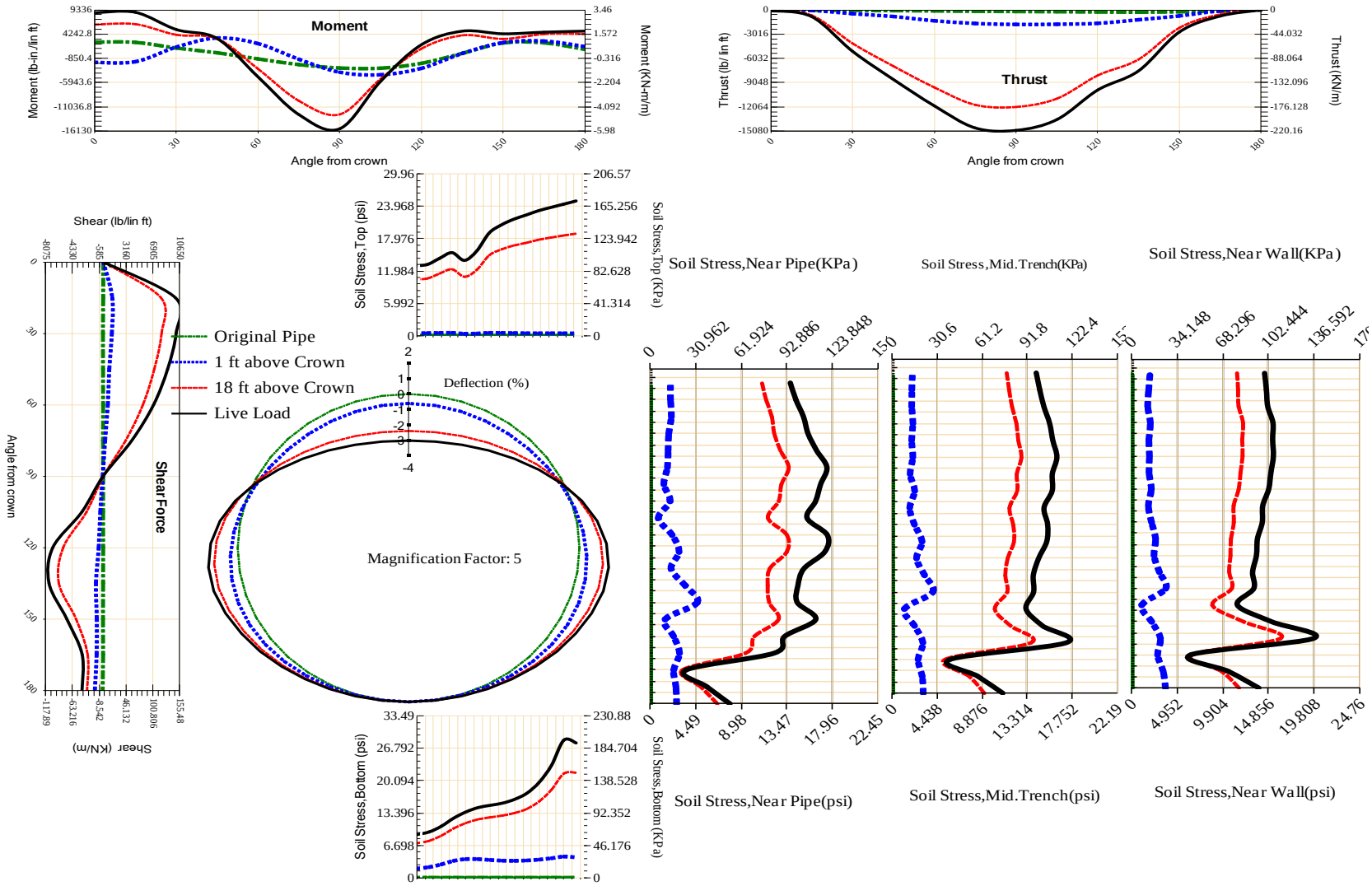

Figure A-77 Param-120-PW200-TR3OR-OD+48-EW10-H18-LiveLoad

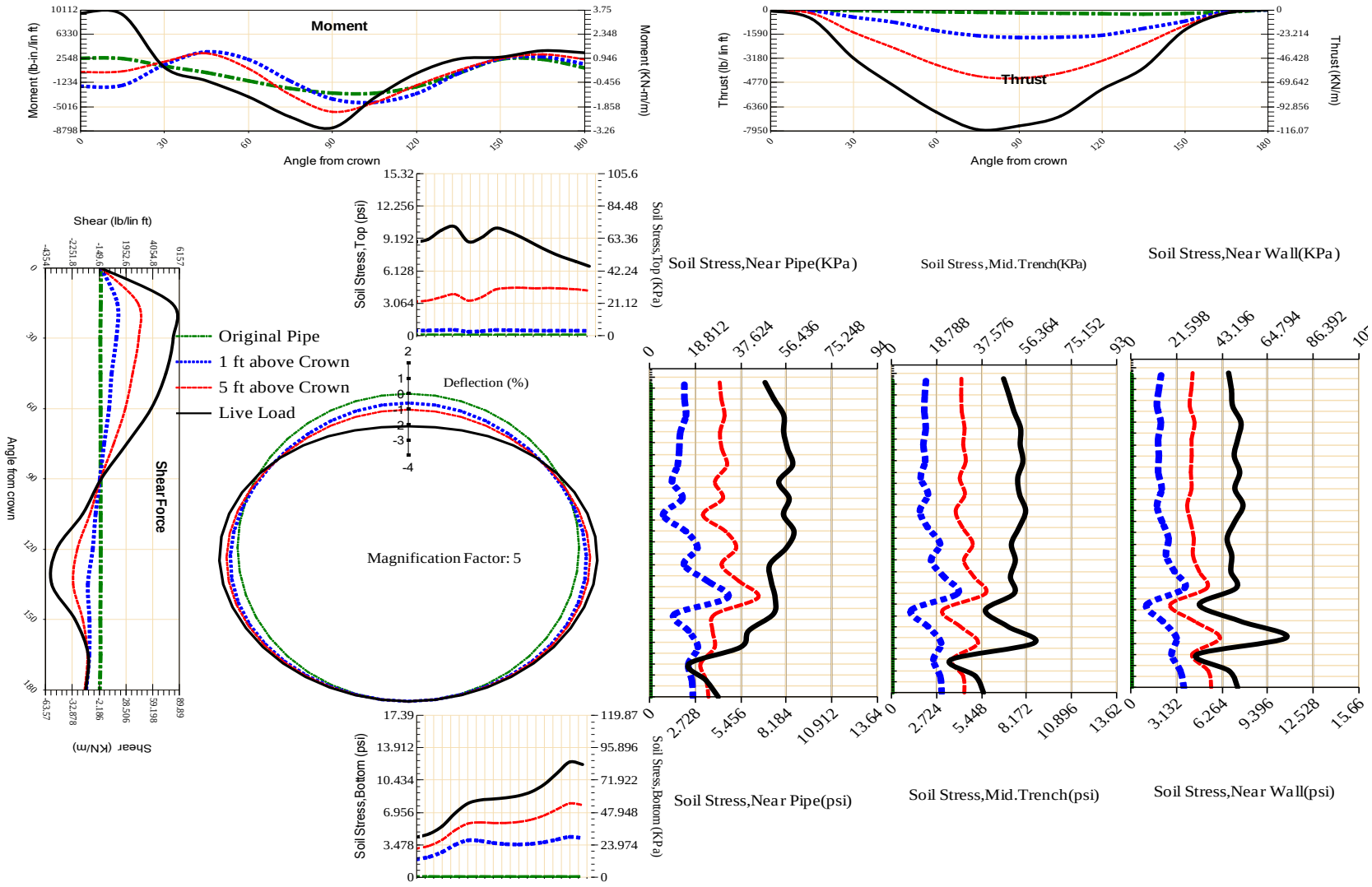

Figure A-78 Param-120-PW200-TR3OR-OD+48-EW10-H5-LiveLoad

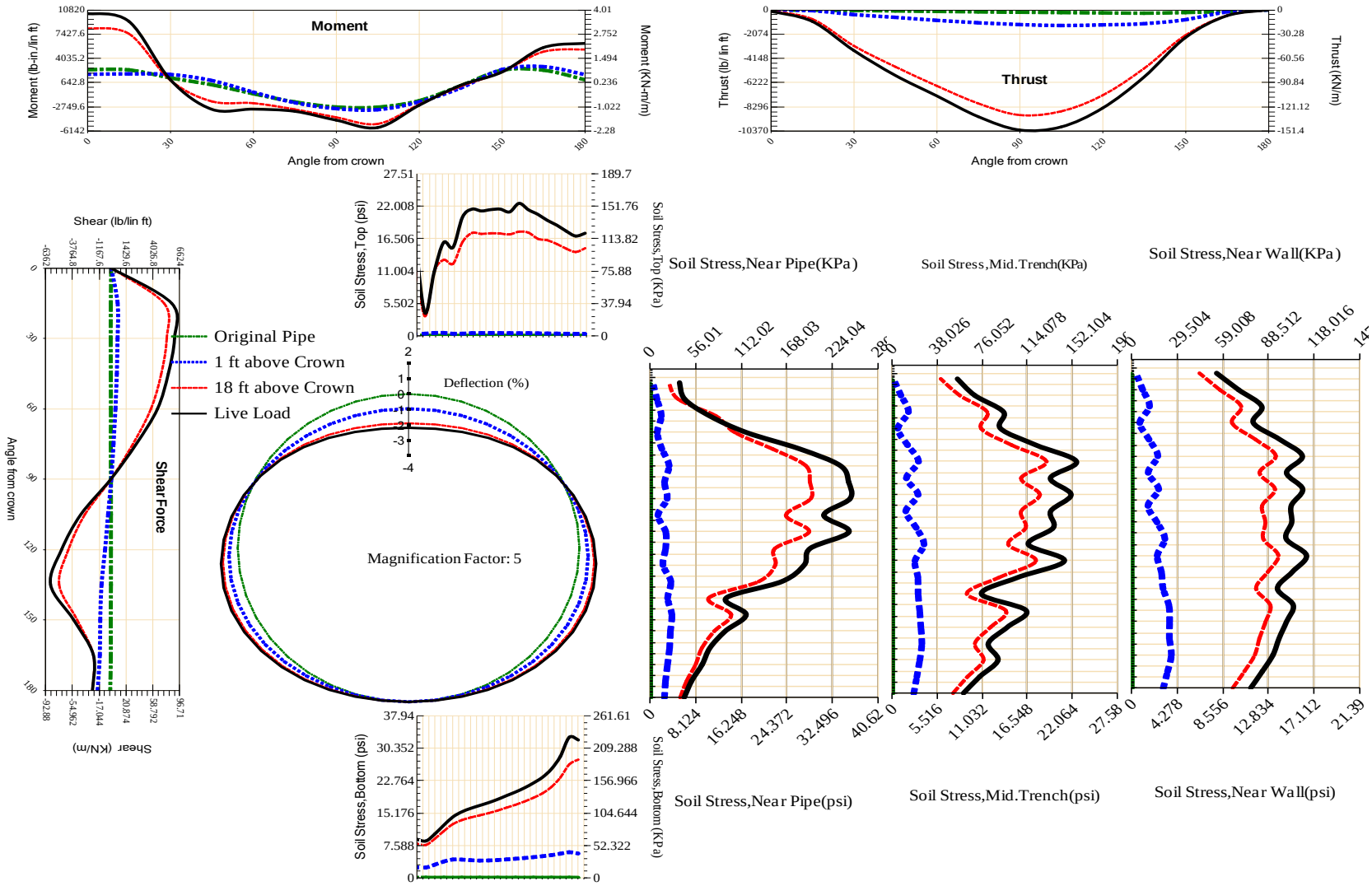

Figure A-79 Param-120-PW200-TR3SF-OD+108-EW10-H18-LiveLoad

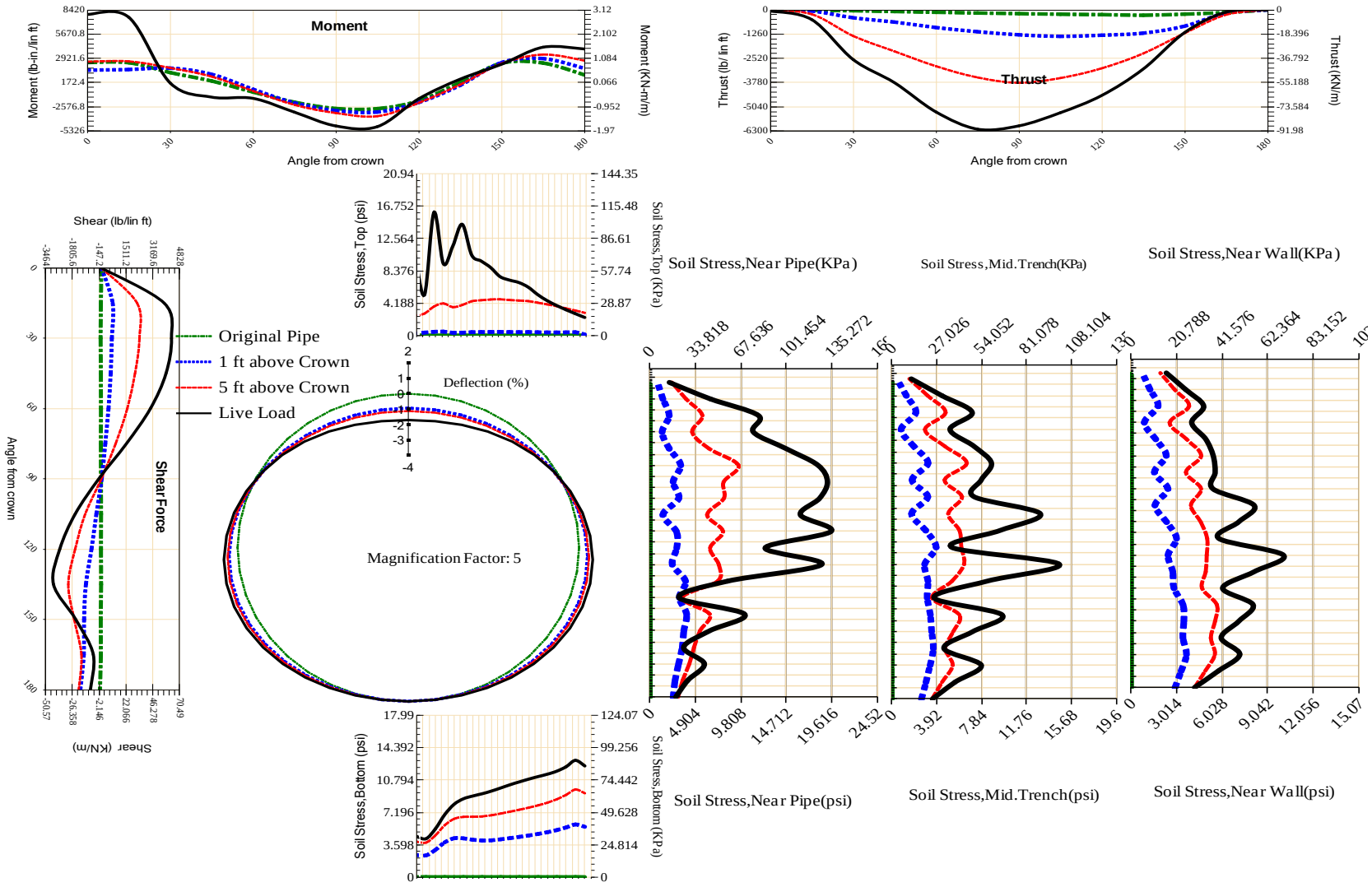

Figure A-80 Param-120-PW200-TR3SF-OD+108-EW10-H5-LiveLoad

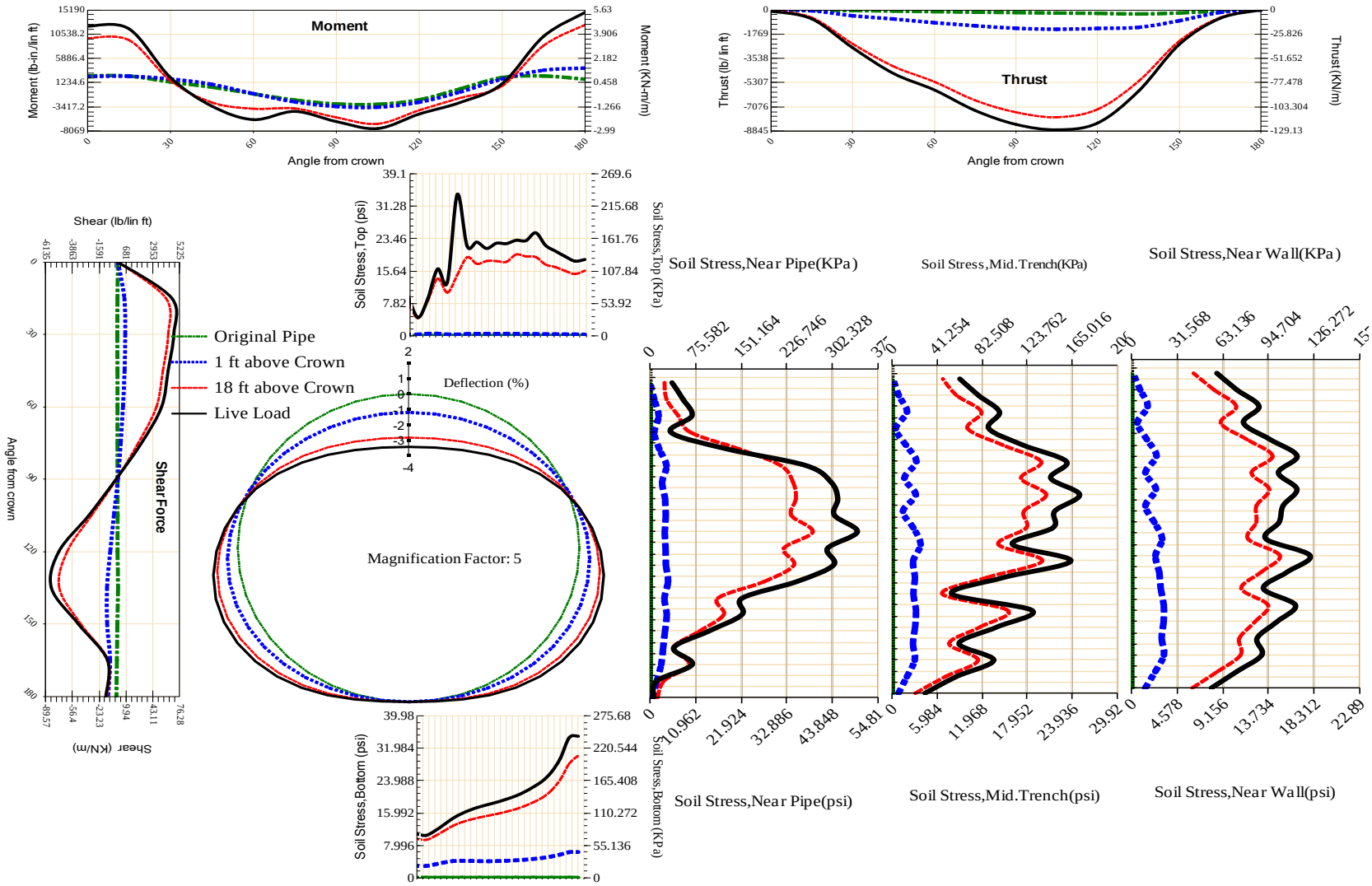

Figure A-81 Param-120-PW200-TR3SF-OD+108-EW3-H18-LiveLoad

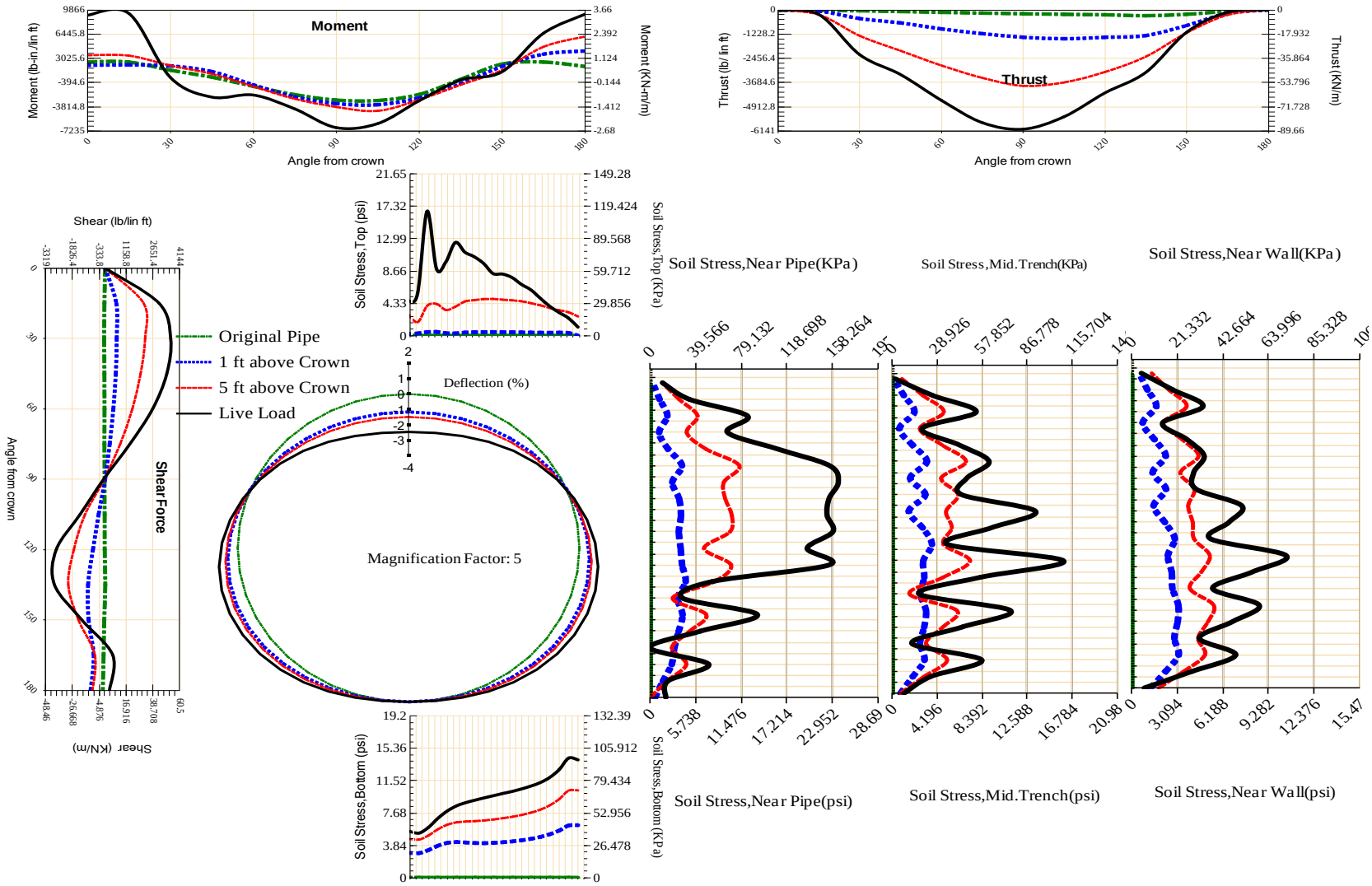

Figure A-82 Param-120-PW200-TR3SF-OD+108-EW3-H5-LiveLoad

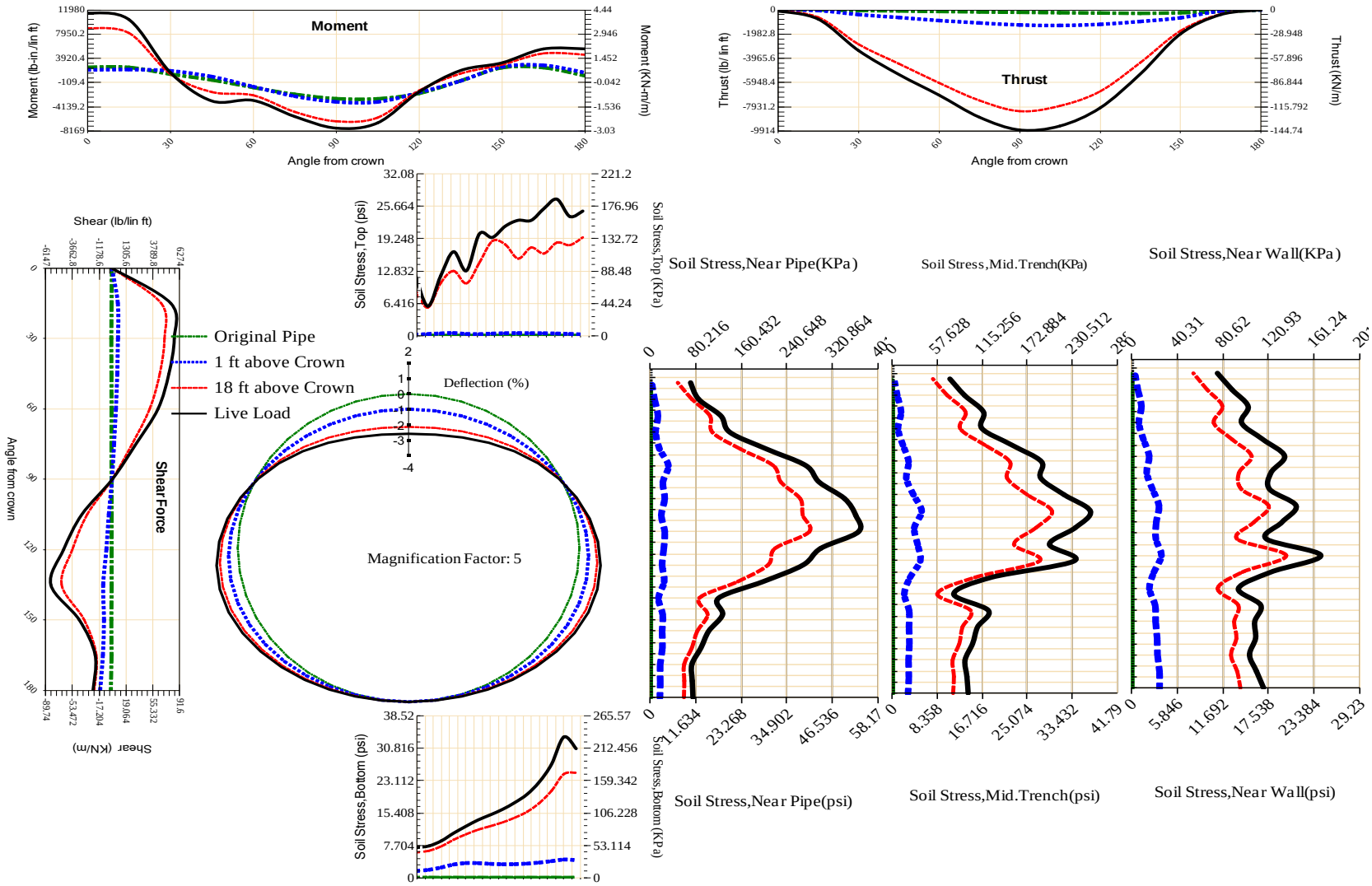

Figure A-83 Param-120-PW200-TR3SF-OD+48-EW10-H18-LiveLoad

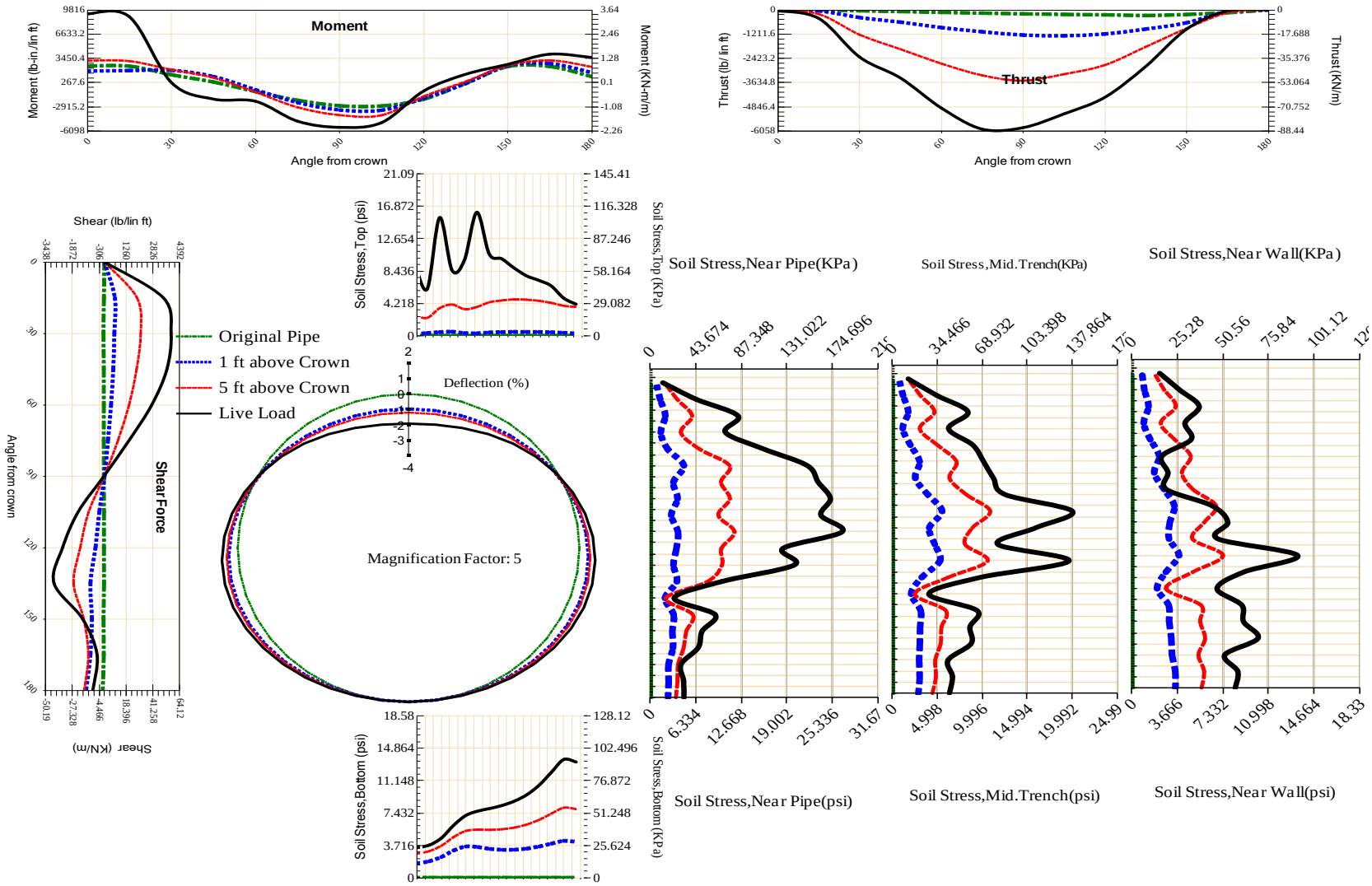

Figure A-84 Param-120-PW200-TR3SF-OD+48-EW10-H5-LiveLoad

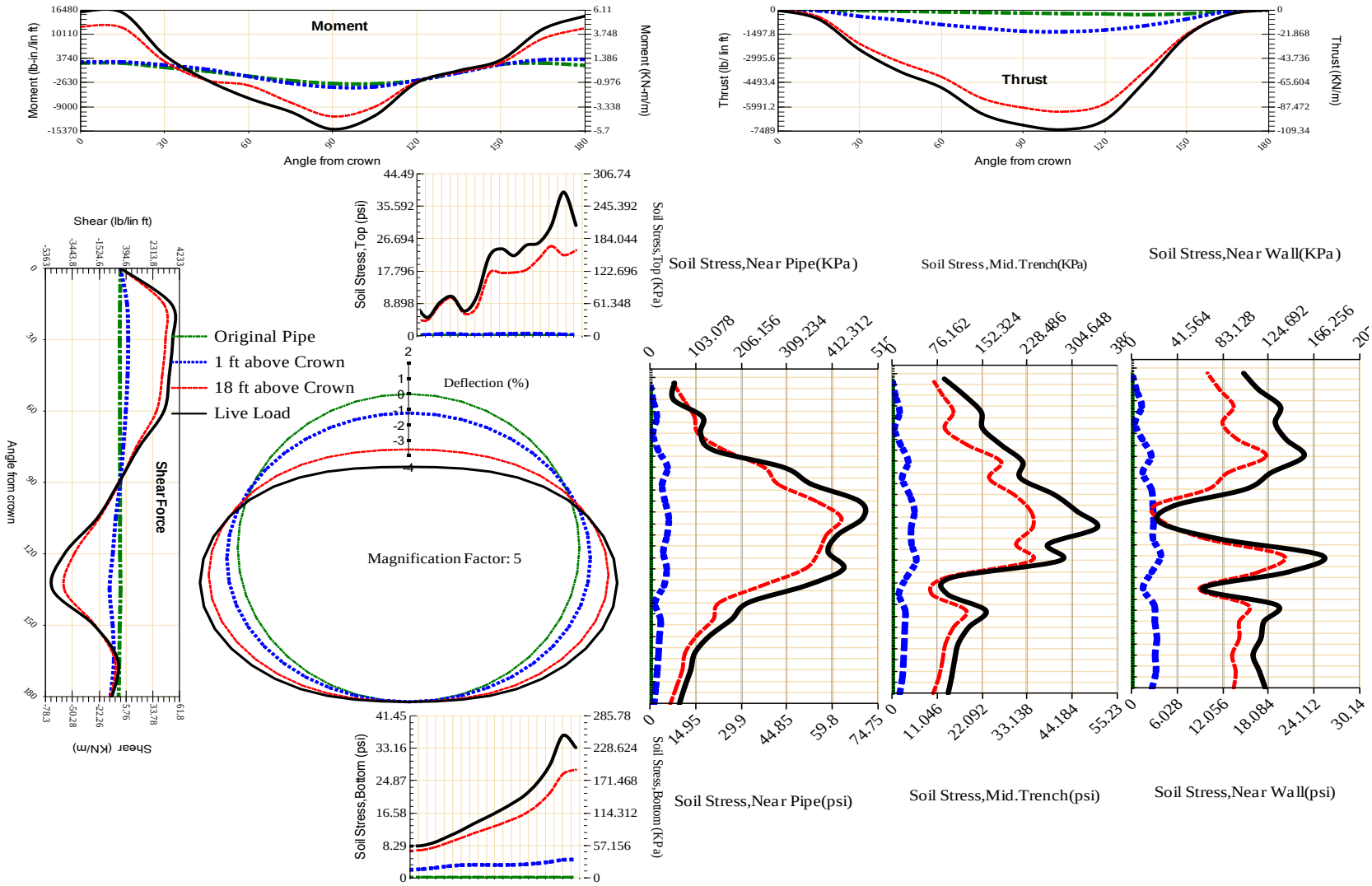

Figure A-85 Param-120-PW200-TR3SF-OD+48-EW3-H18-LiveLoad

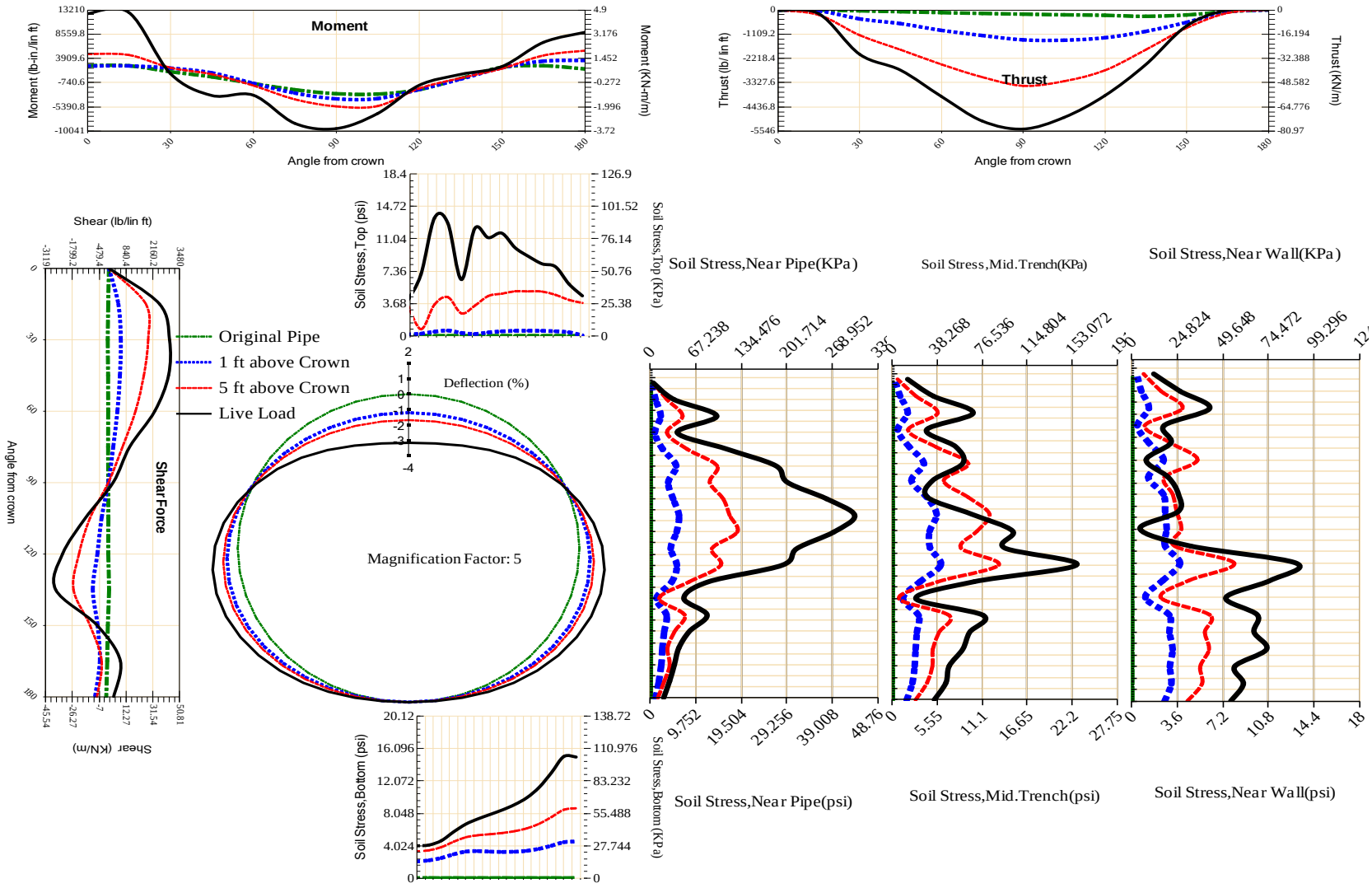

Figure A-86 Param-120-PW200-TR3SF-OD+48-EW3-H5-LiveLoad

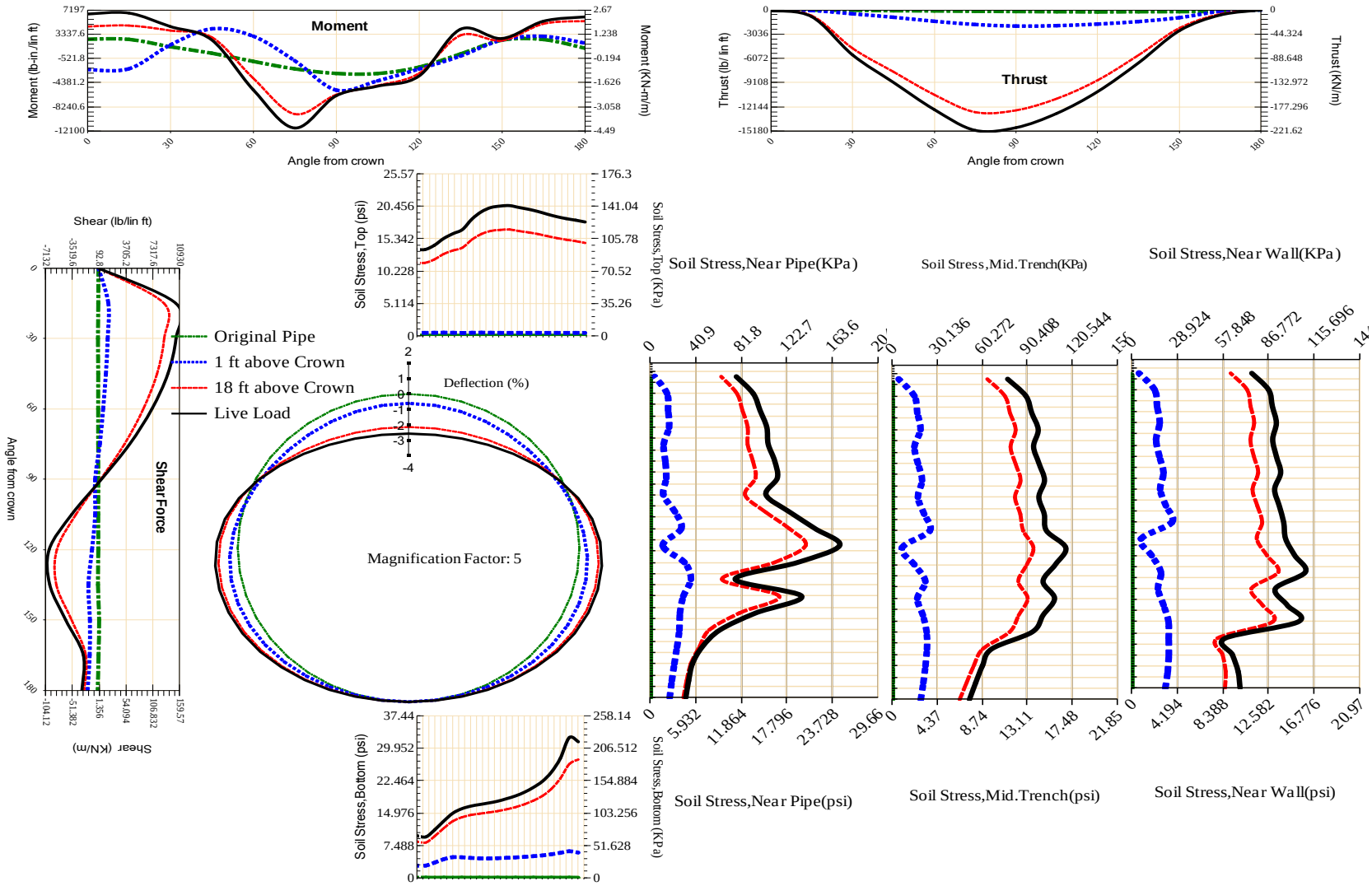

Figure A-87 Param-120-PW200-TR5OR-OD+108-EW10-H18-LiveLoad

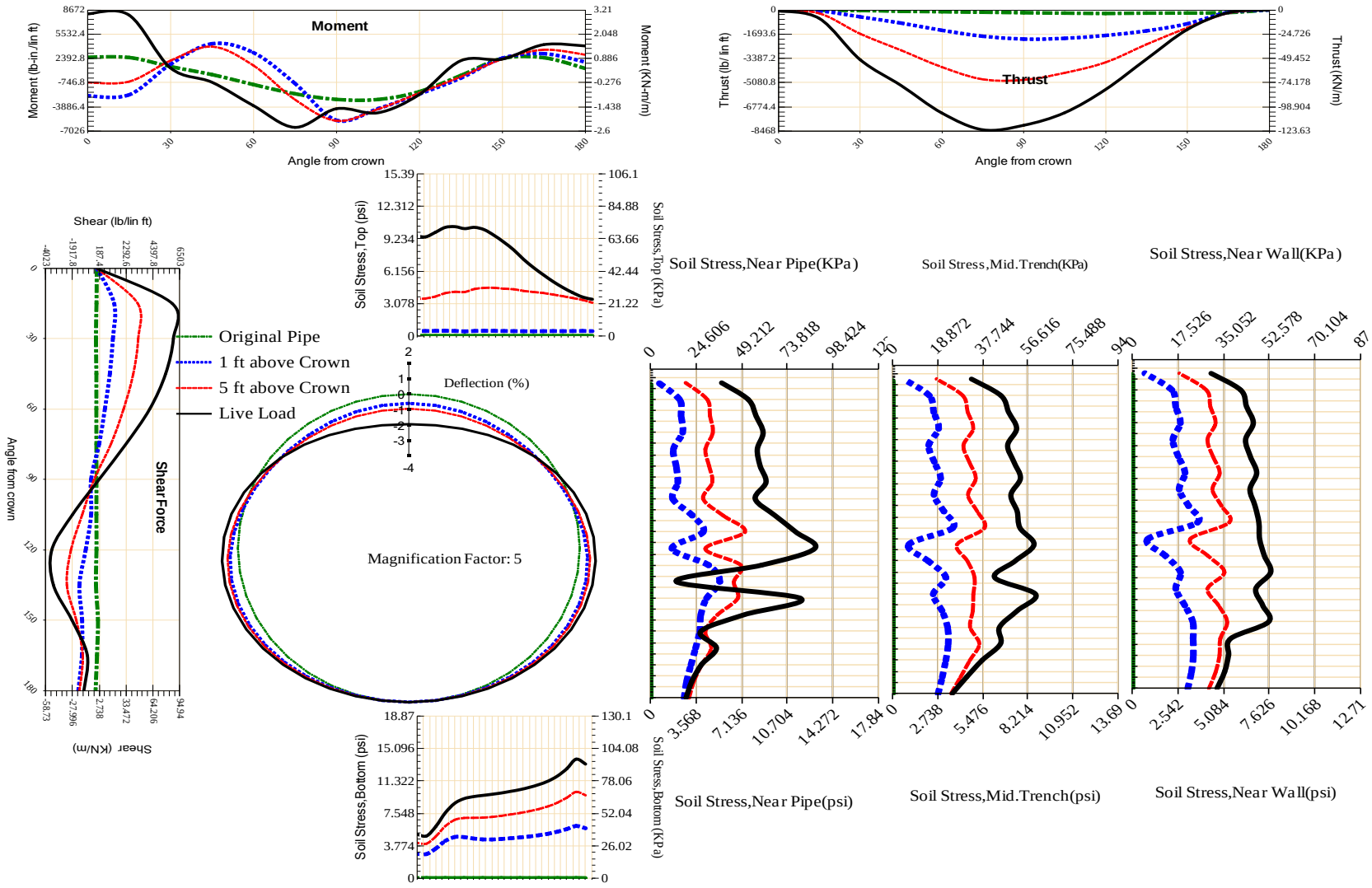

Figure A-88 Param-120-PW200-TR5OR-OD+108-EW10-H5-LiveLoad

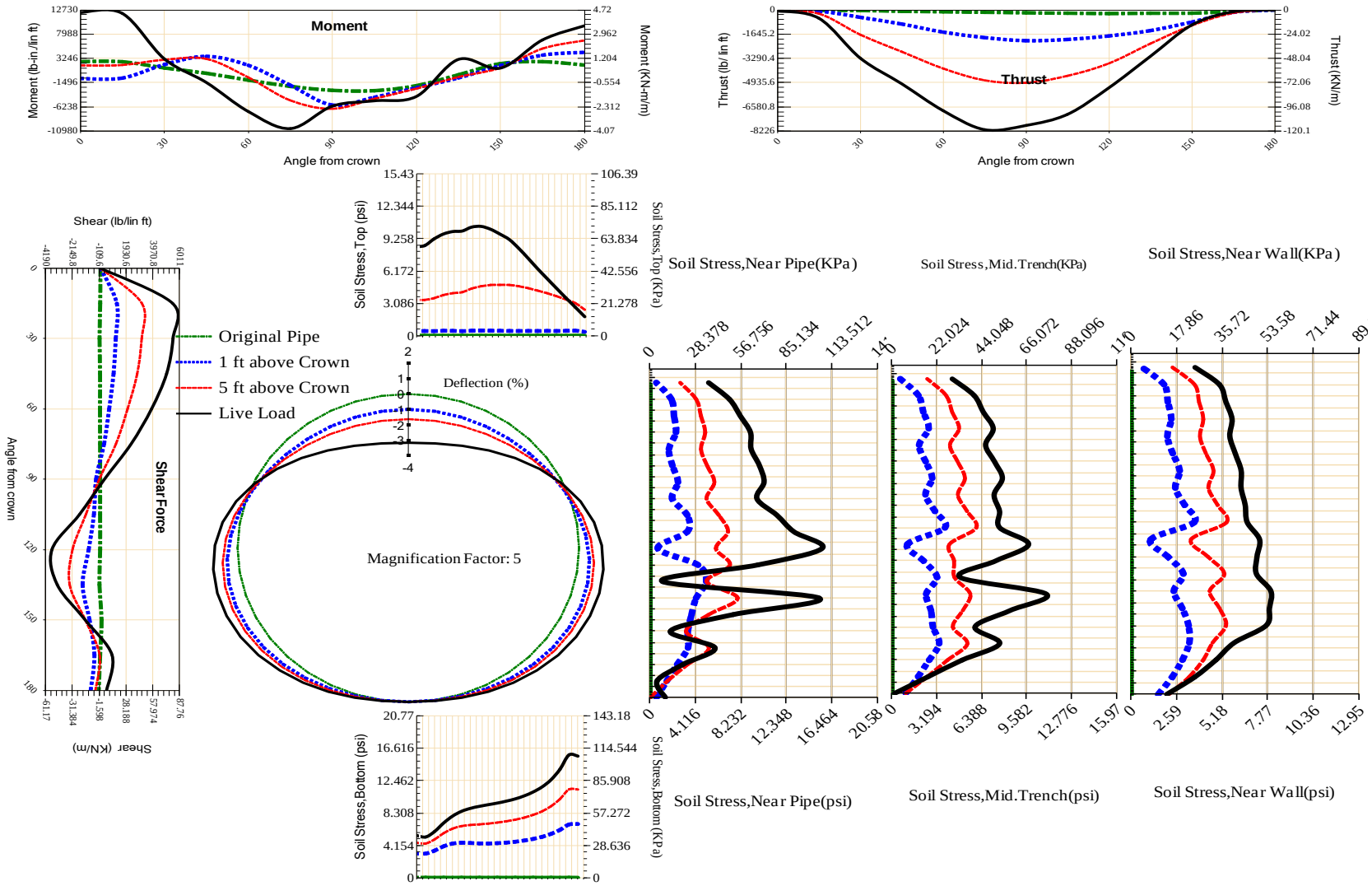

Figure A-89 Param-120-PW200-TR5OR-OD+108-EW3-H5-LiveLoad

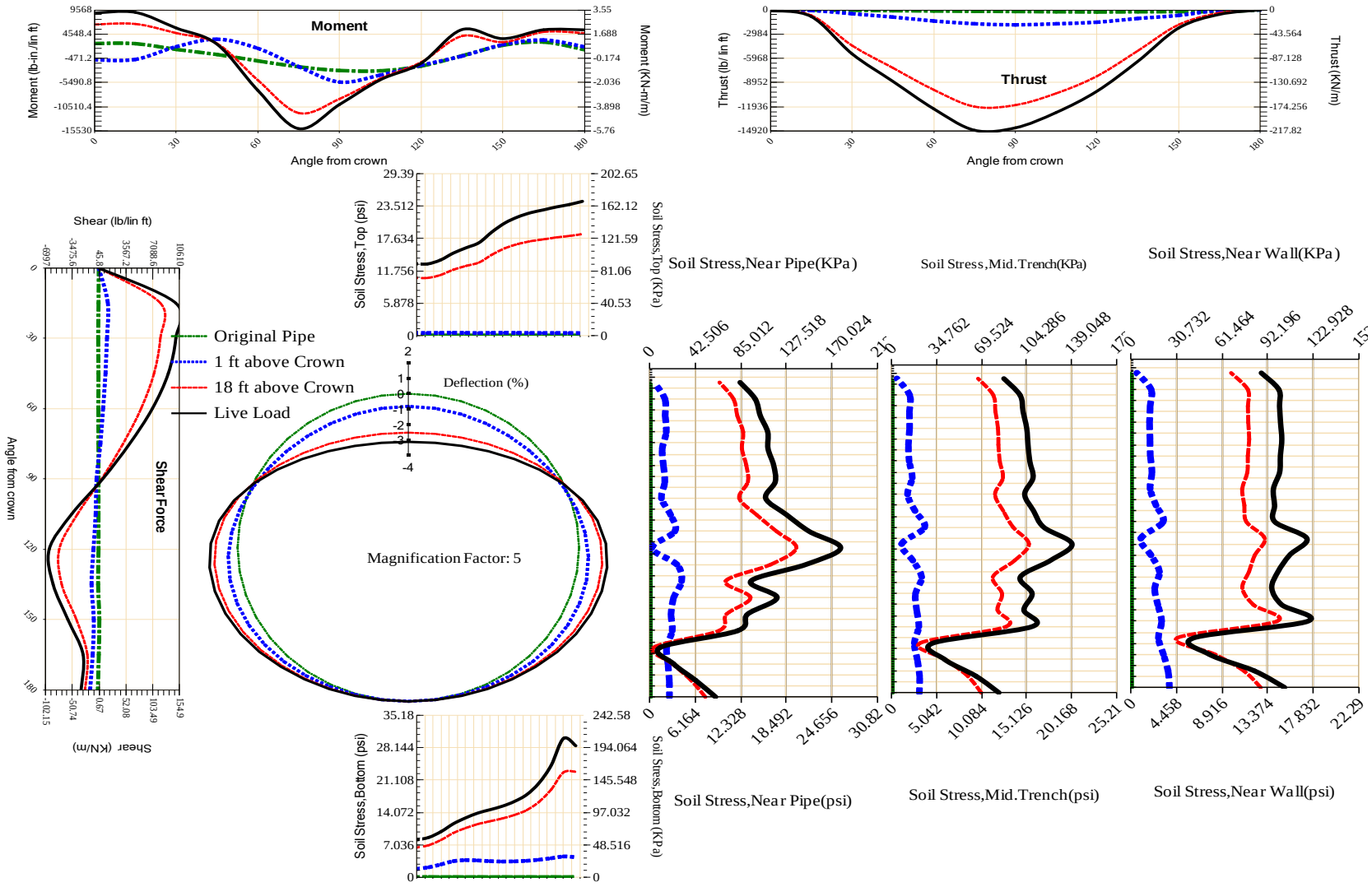

Figure A-90 Param-120-PW200-TR5OR-OD+48-EW10-H18-LiveLoad

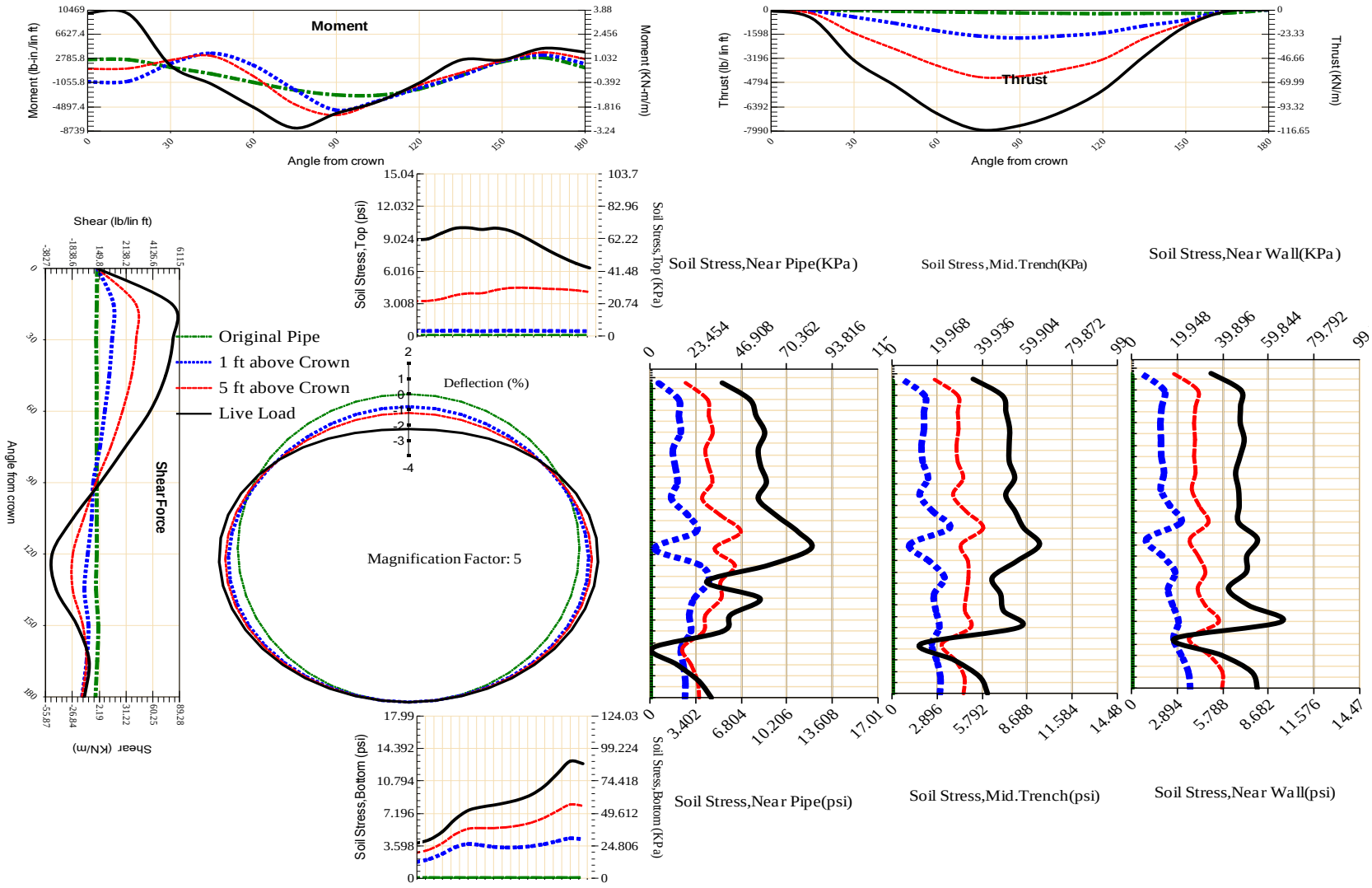

Figure A-91 Param-120-PW200-TR5OR-OD+48-EW10-H5-LiveLoad

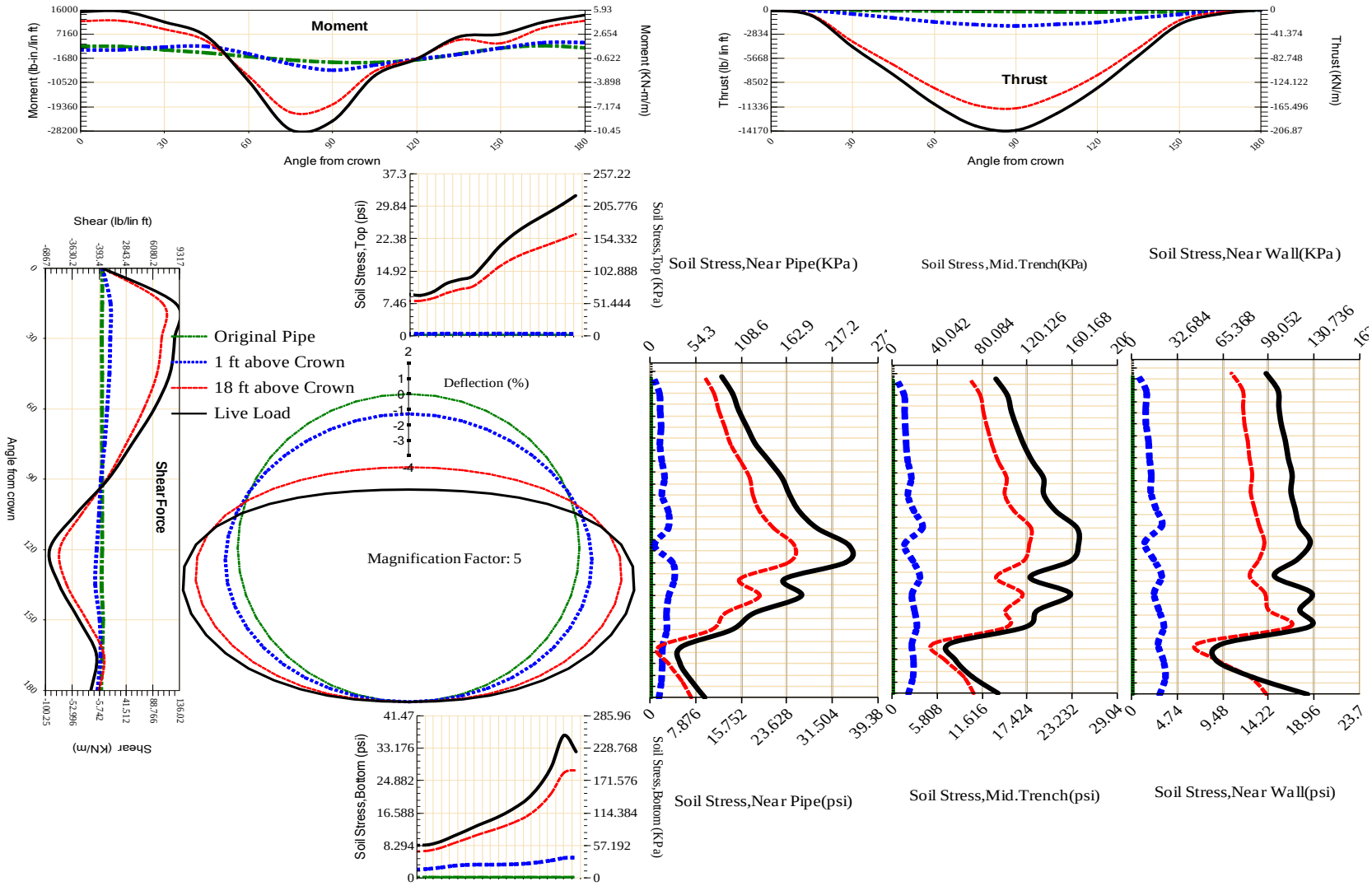

Figure A-92 Param-120-PW200-TR5OR-OD+48-EW3-H18-LiveLoad

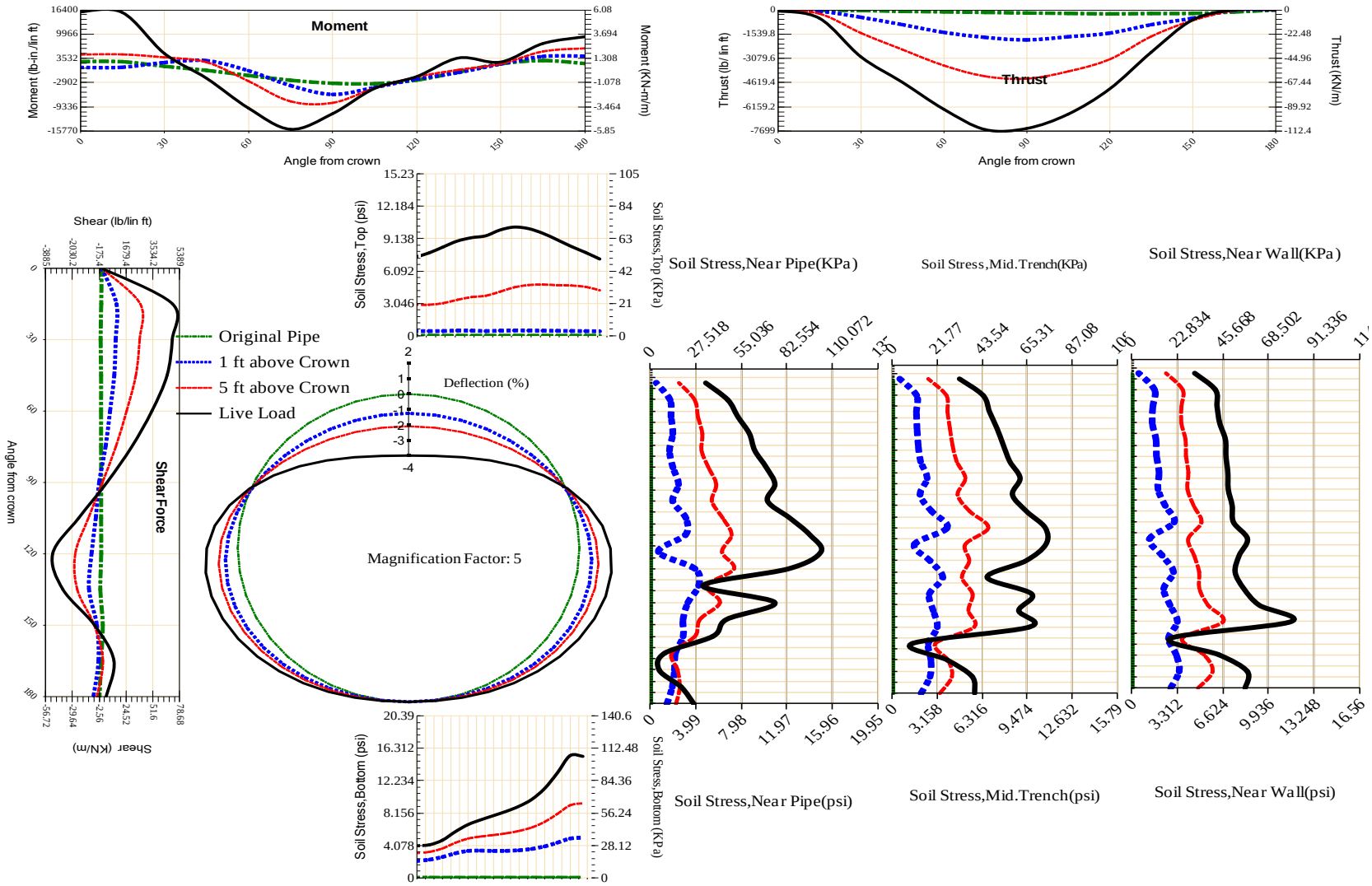

Figure A-93 Param-120-PW200-TR5OR-OD+48-EW3-H5-LiveLoad

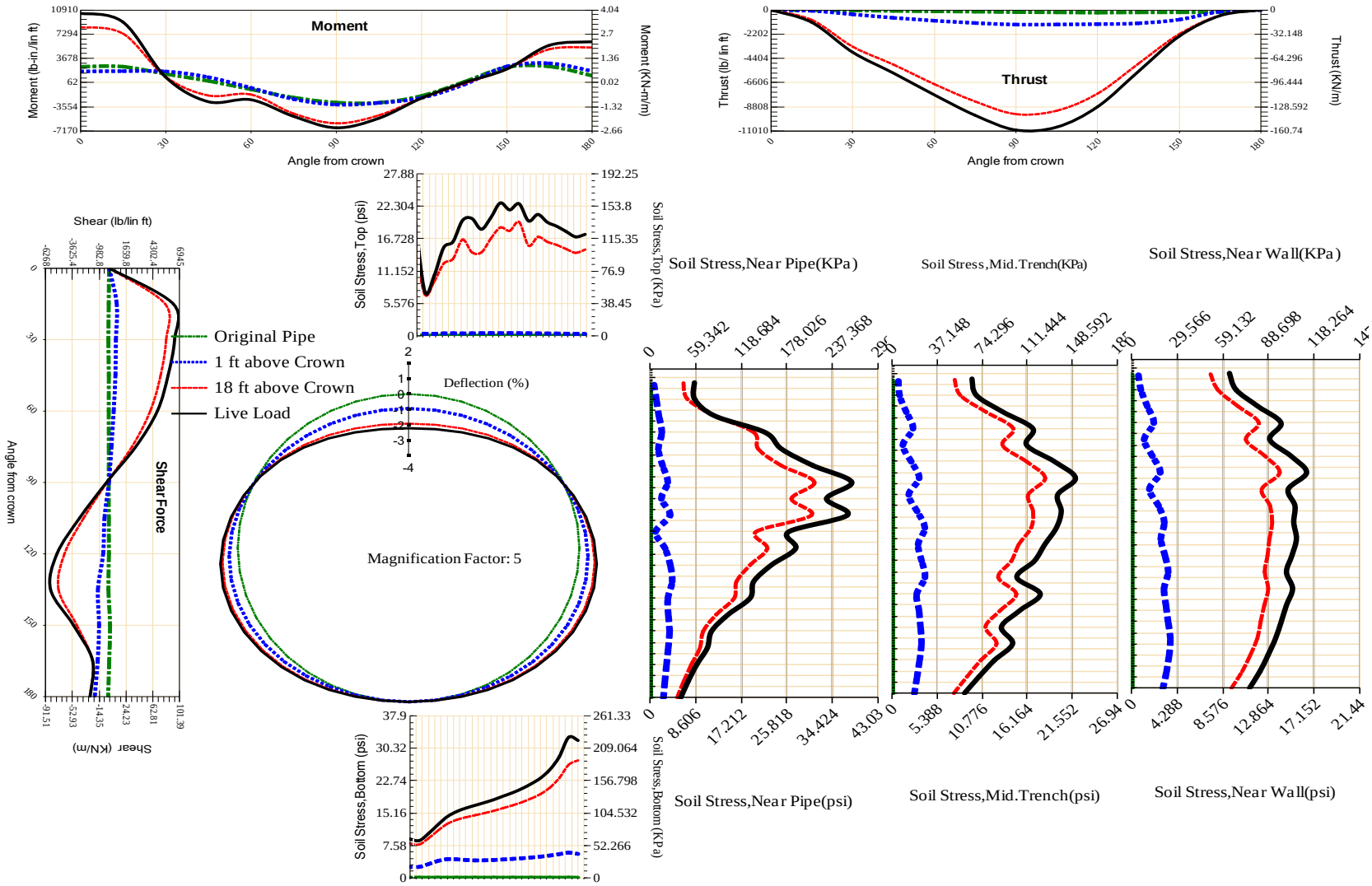

Figure A-94 Param-120-PW200-TR5SF-OD+108-EW10-H18-LiveLoad

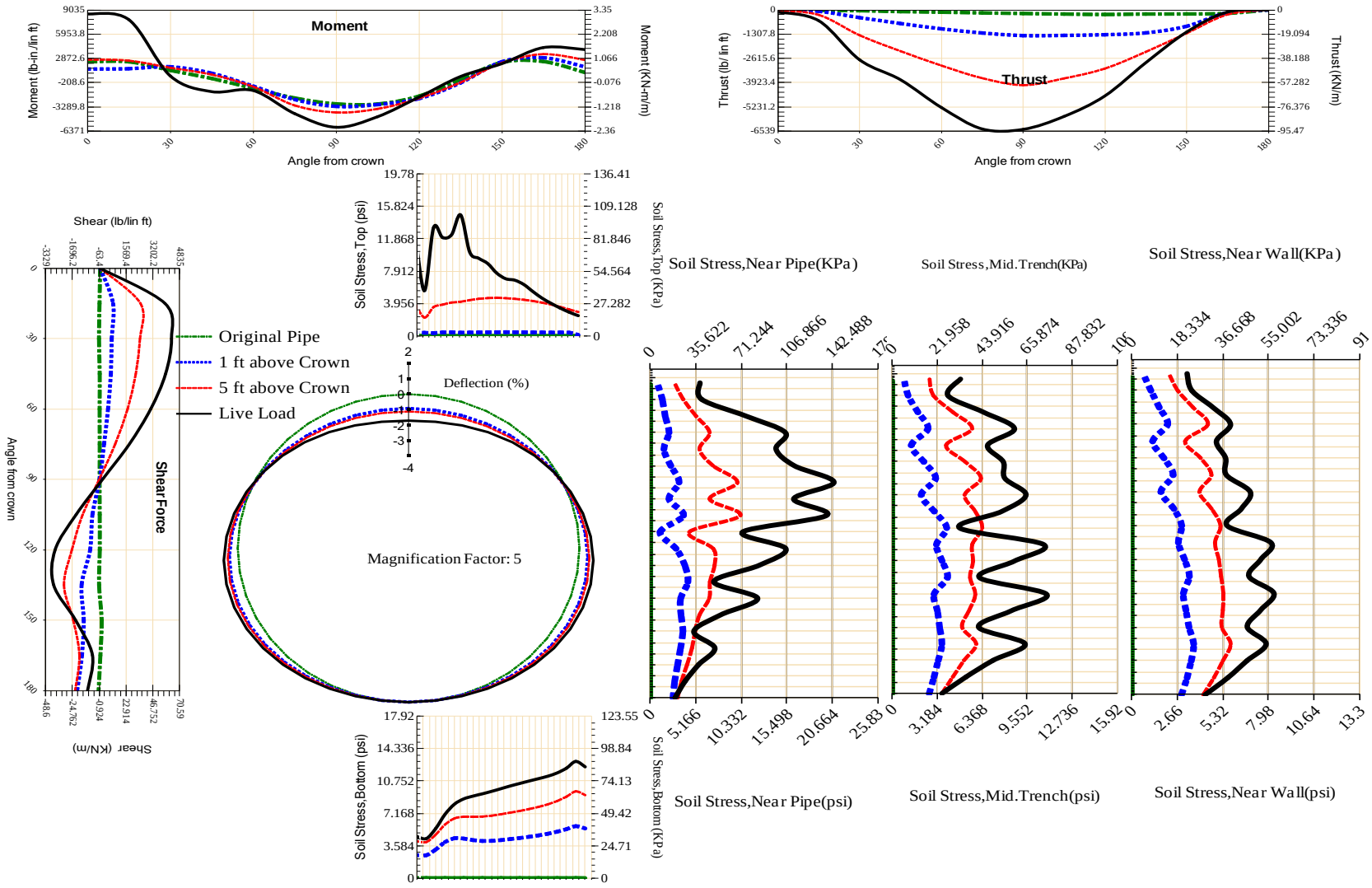

Figure A-95 Param-120-PW200-TR5SF-OD+108-EW10-H5-LiveLoad

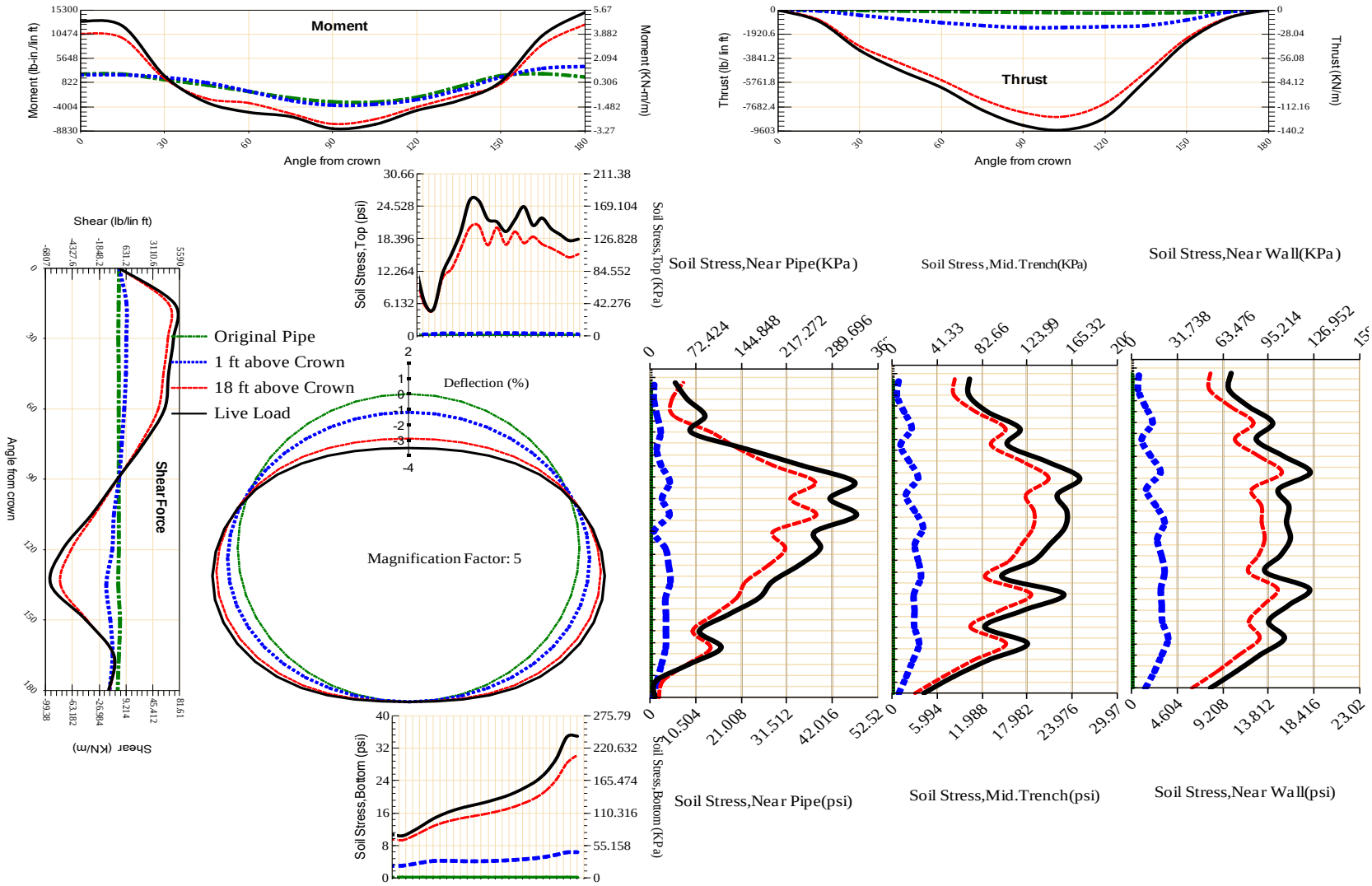

Figure A-96 Param-120-PW200-TR5SF-OD+108-EW3-H18-LiveLoad

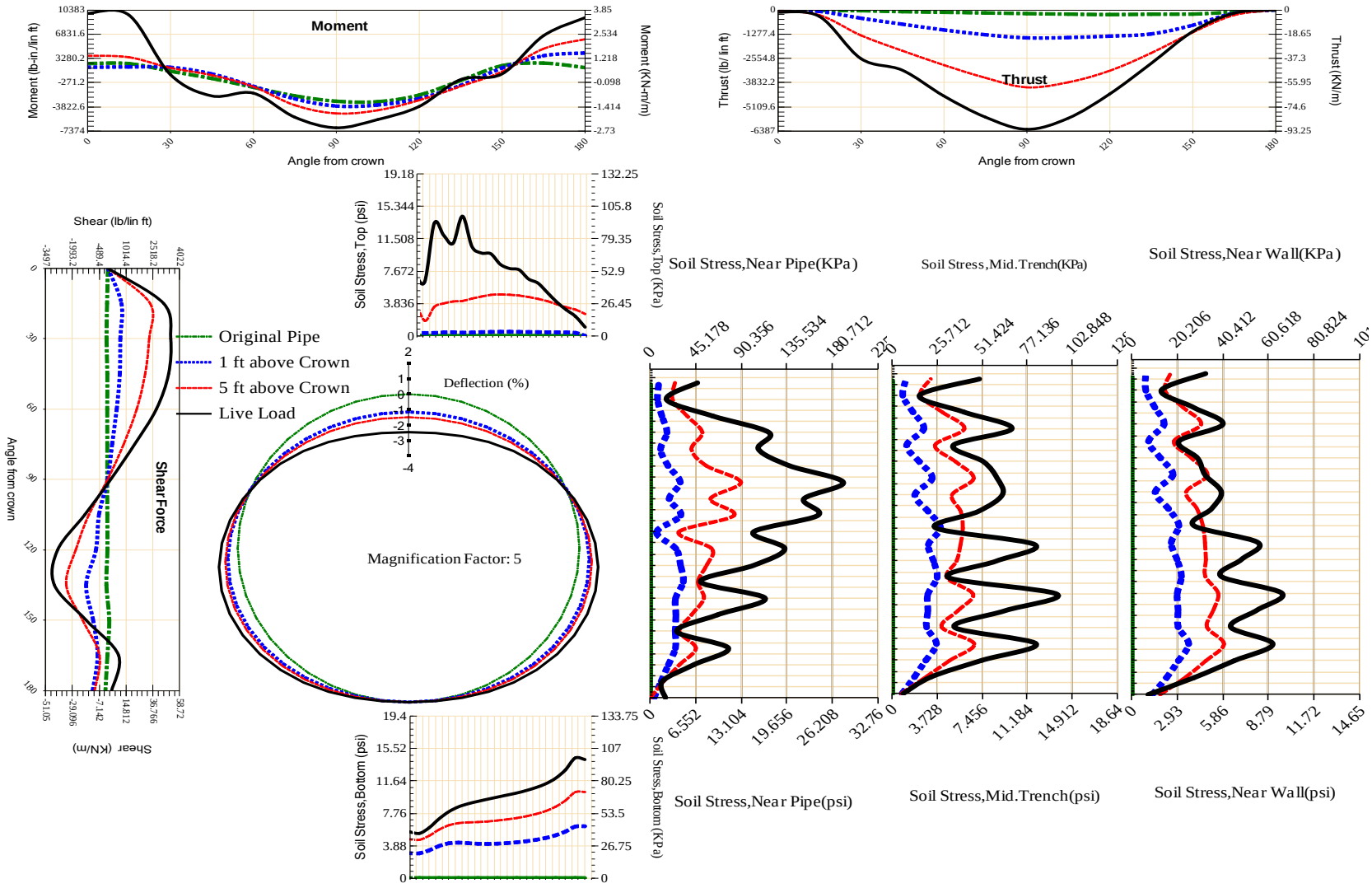

Figure A-97 Param-120-PW200-TR5SF-OD+108-EW3-H5-LiveLoad

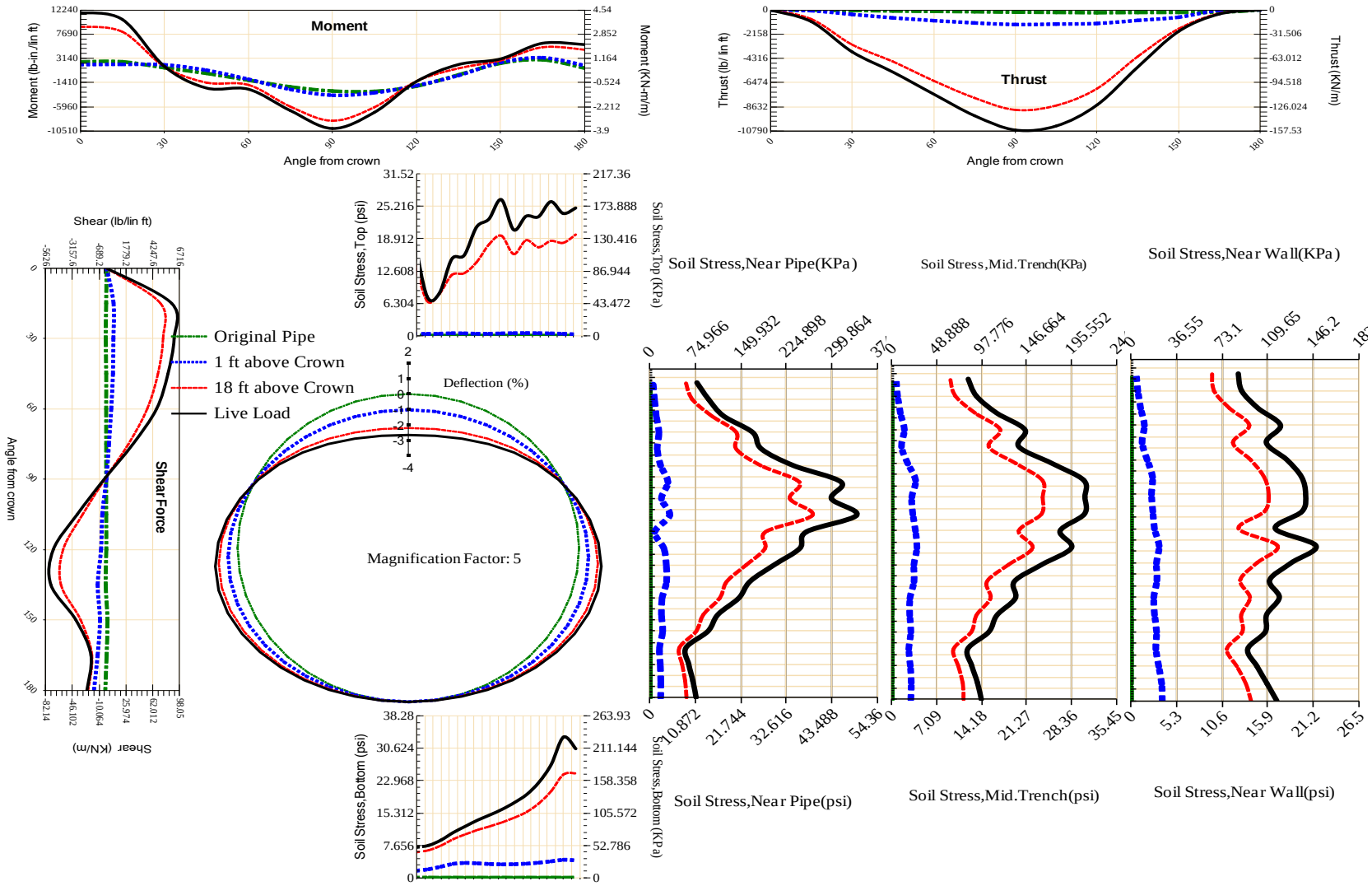

Figure A-98 Param-120-PW200-TR5SF-OD+48-EW10-H18-LiveLoad

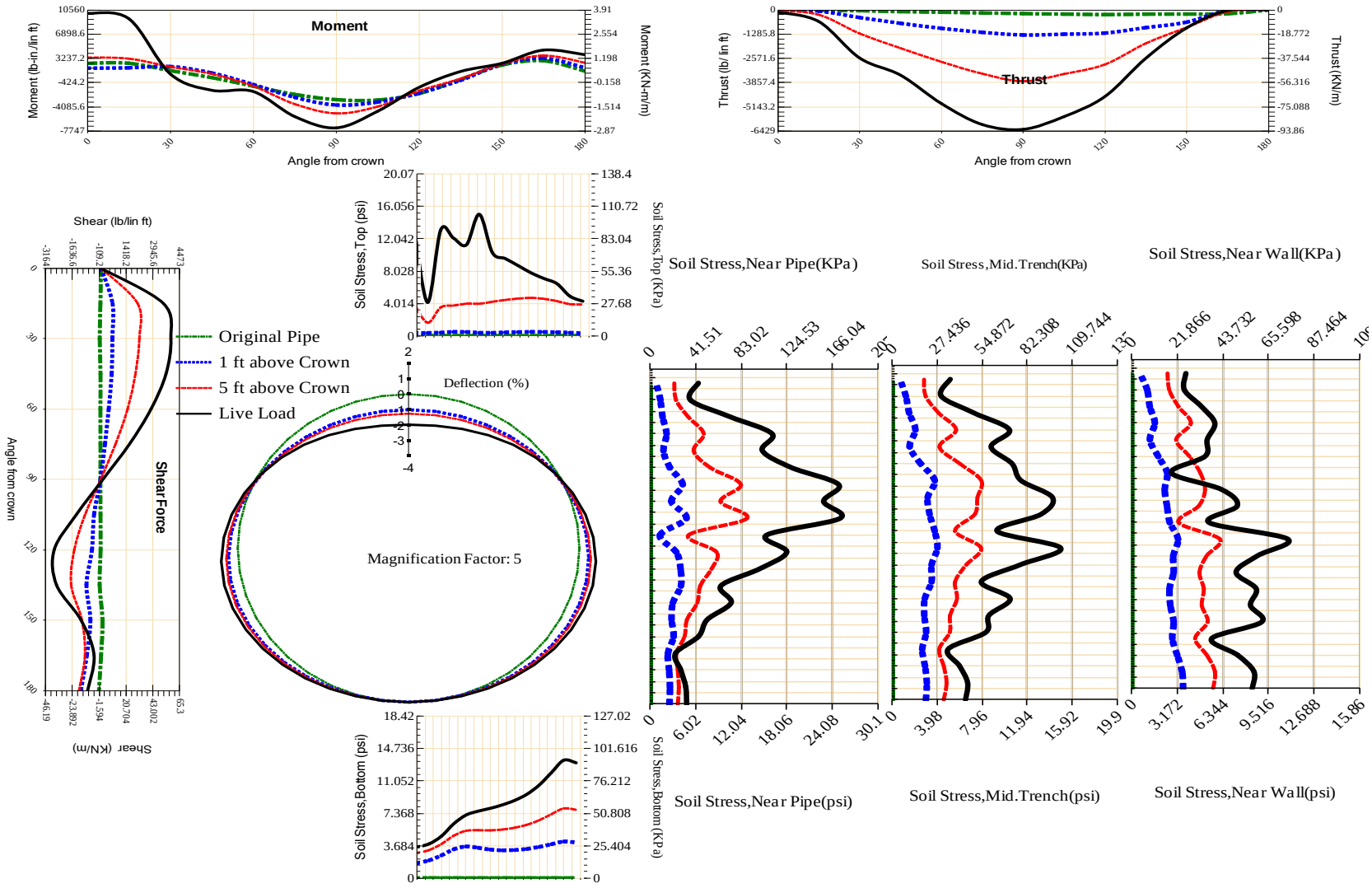

Figure A-99 Param-120-PW200-TR5SF-OD+48-EW10-H5-LiveLoad

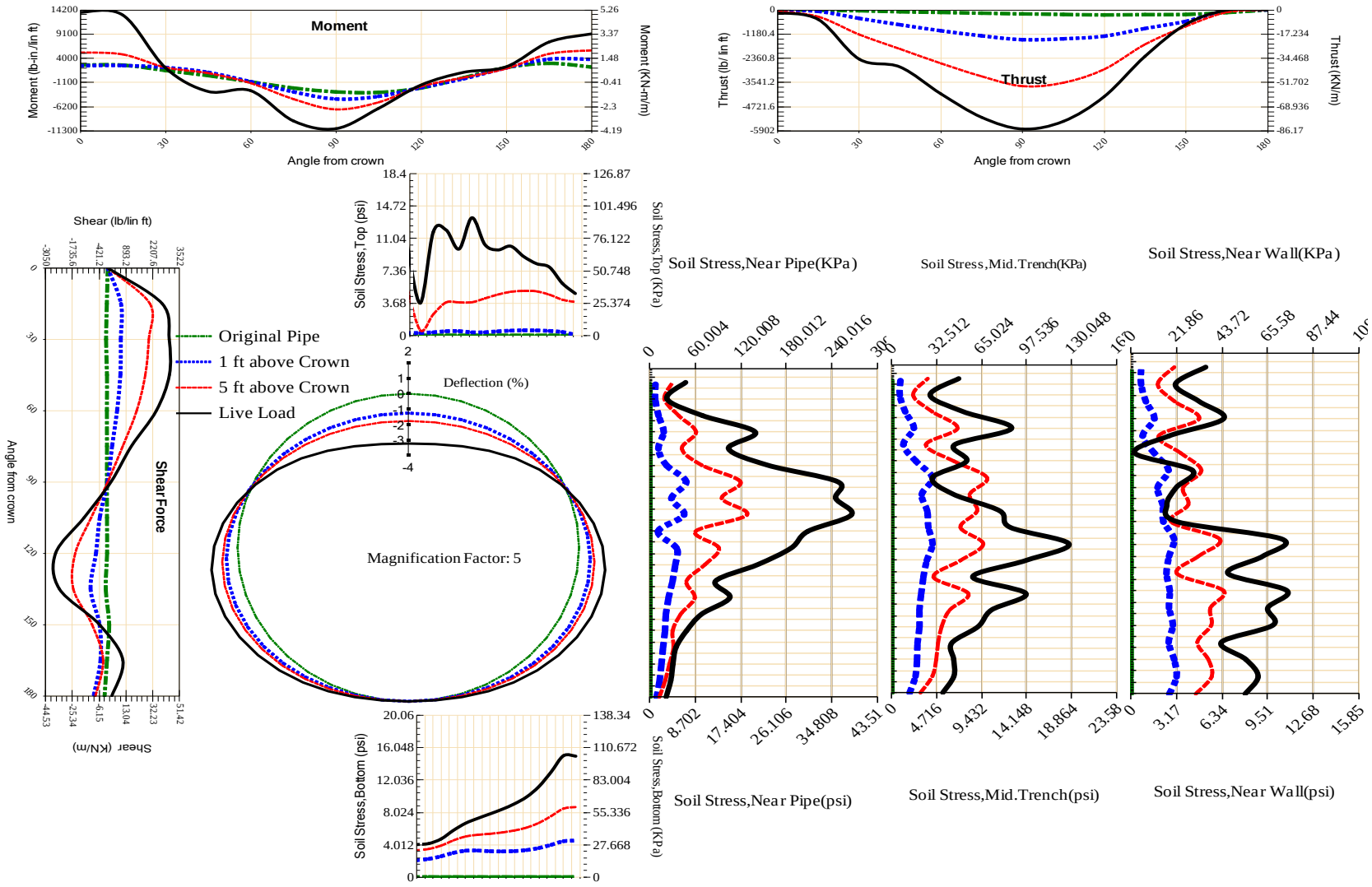

Figure A-100 Param-120-PW200-TR5SF-OD+48-EW3-H5-LiveLoad

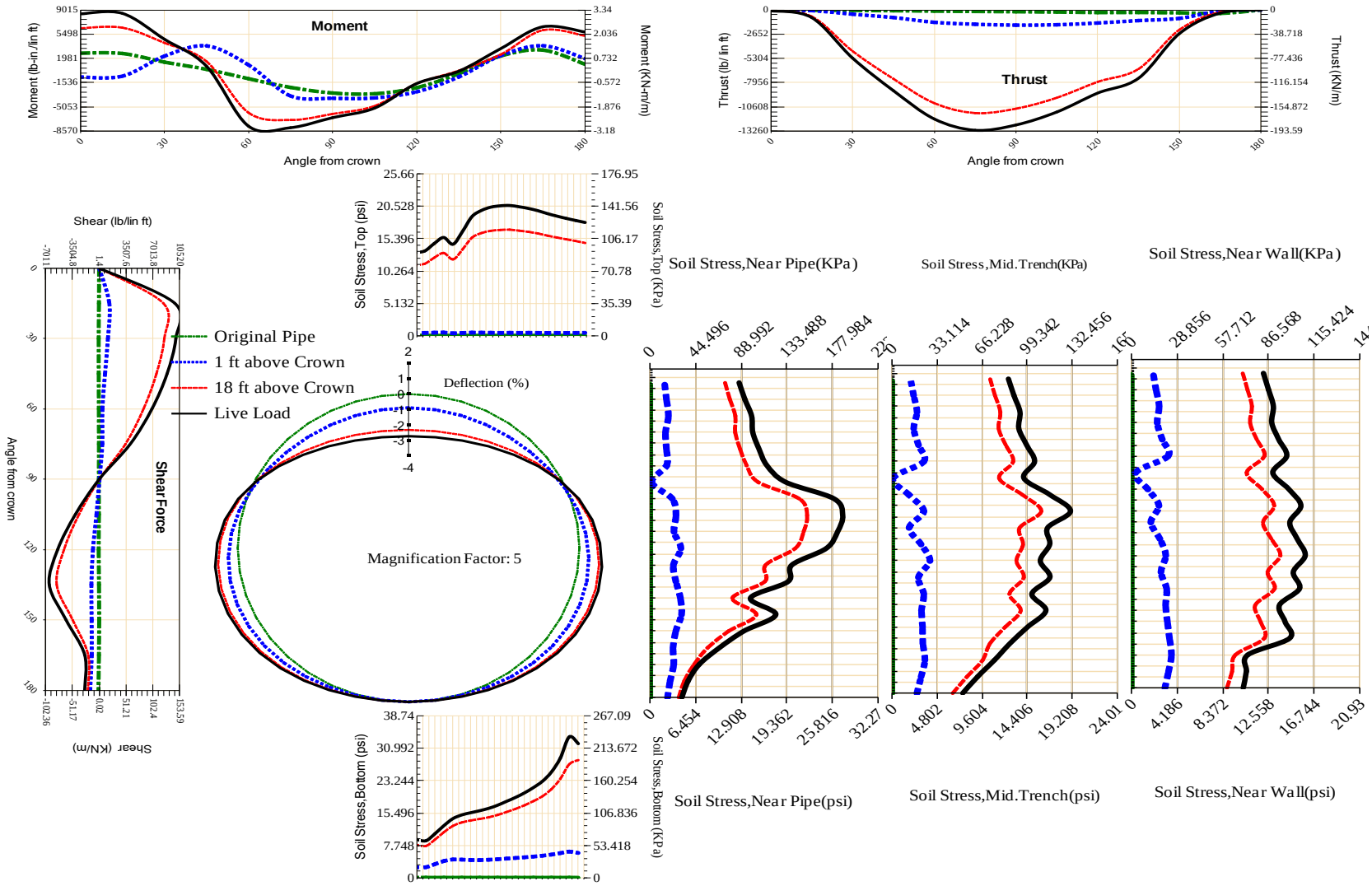

Figure A-101 Param-120-PW200-TR7OR-OD+108-EW10-H18-LiveLoad

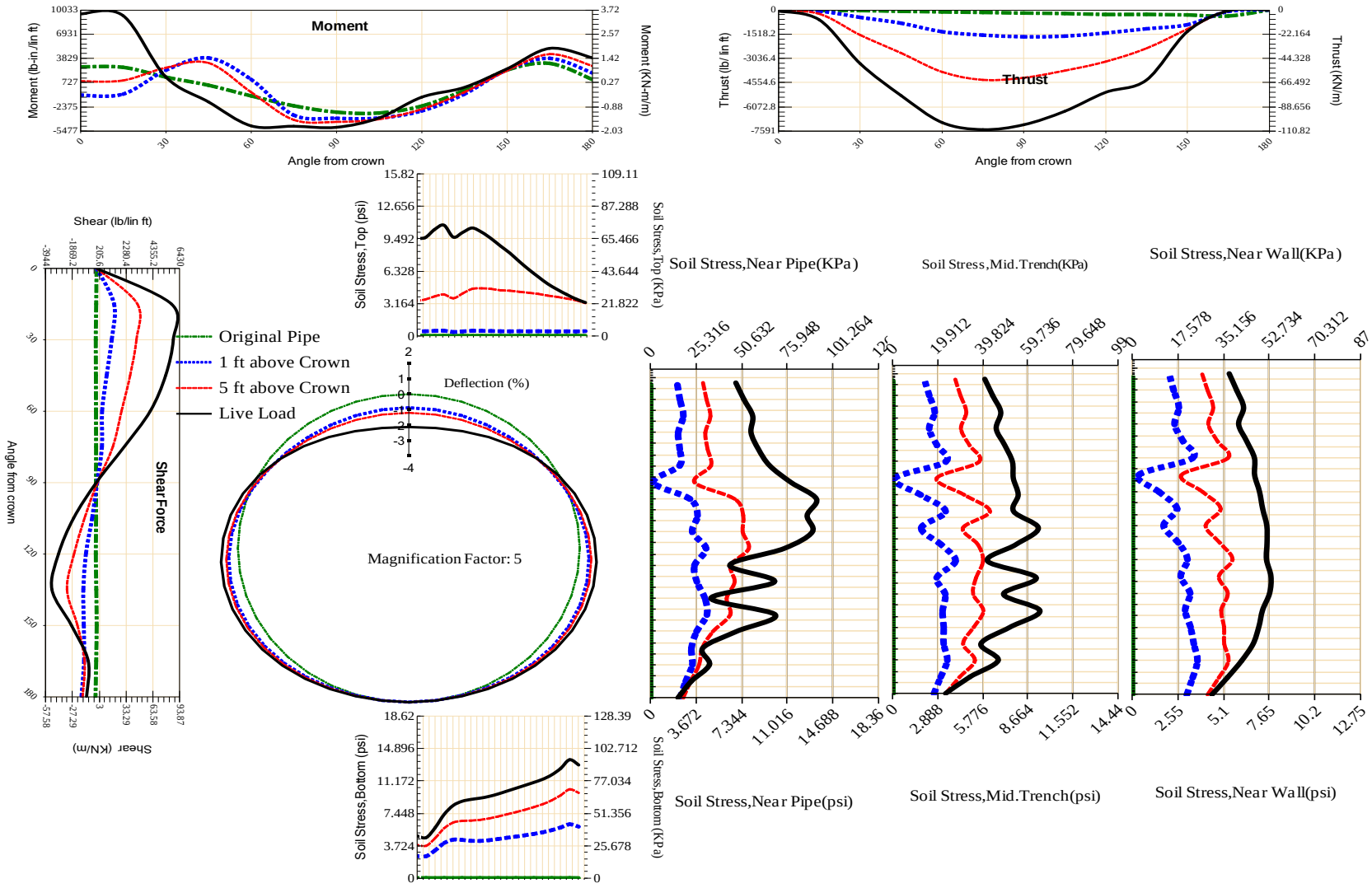

Figure A-102 Param-120-PW200-TR7OR-OD+108-EW10-H5-LiveLoad

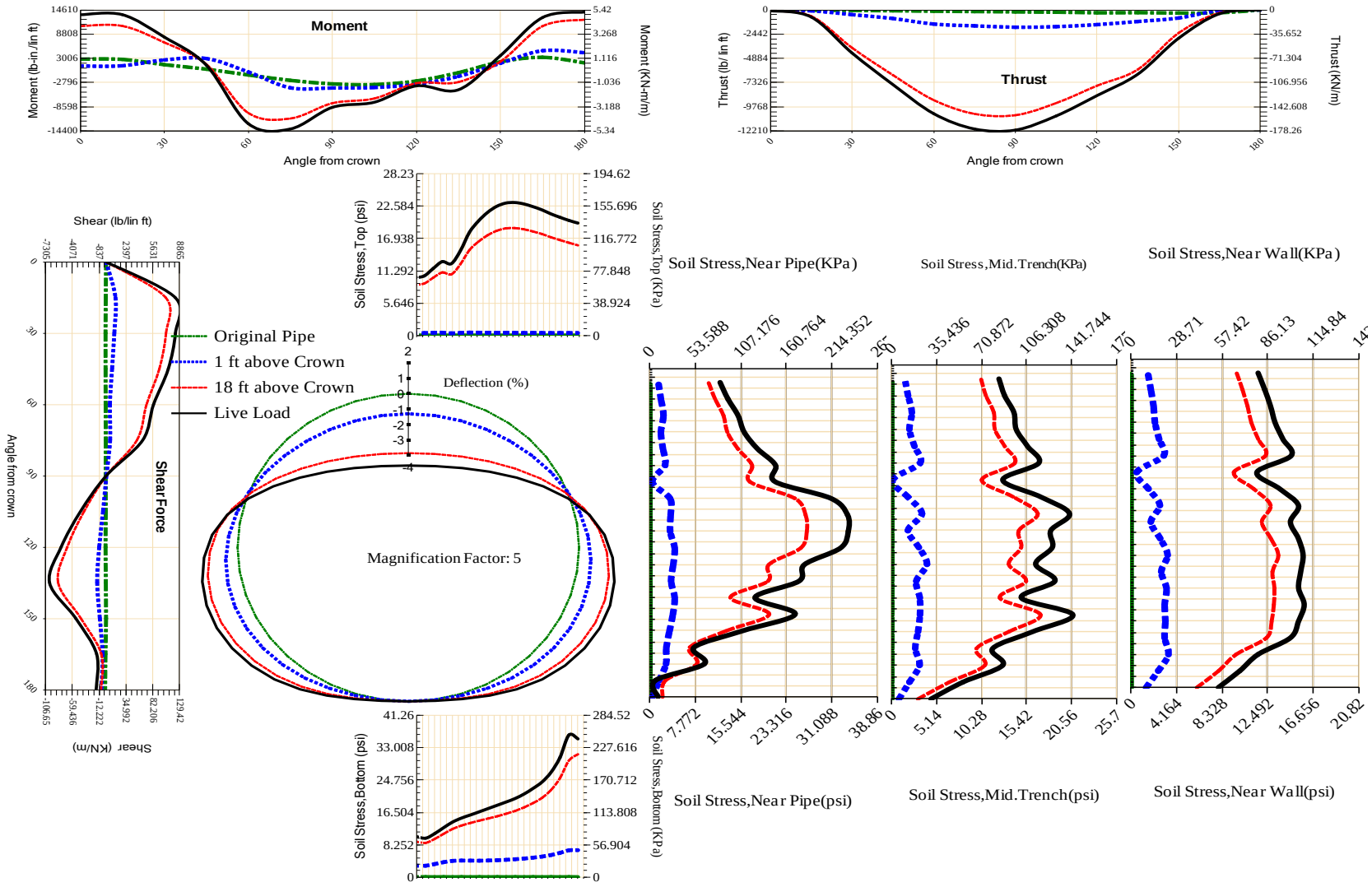

Figure A-103 Param-120-PW200-TR7OR-OD+108-EW3-H18-LiveLoad

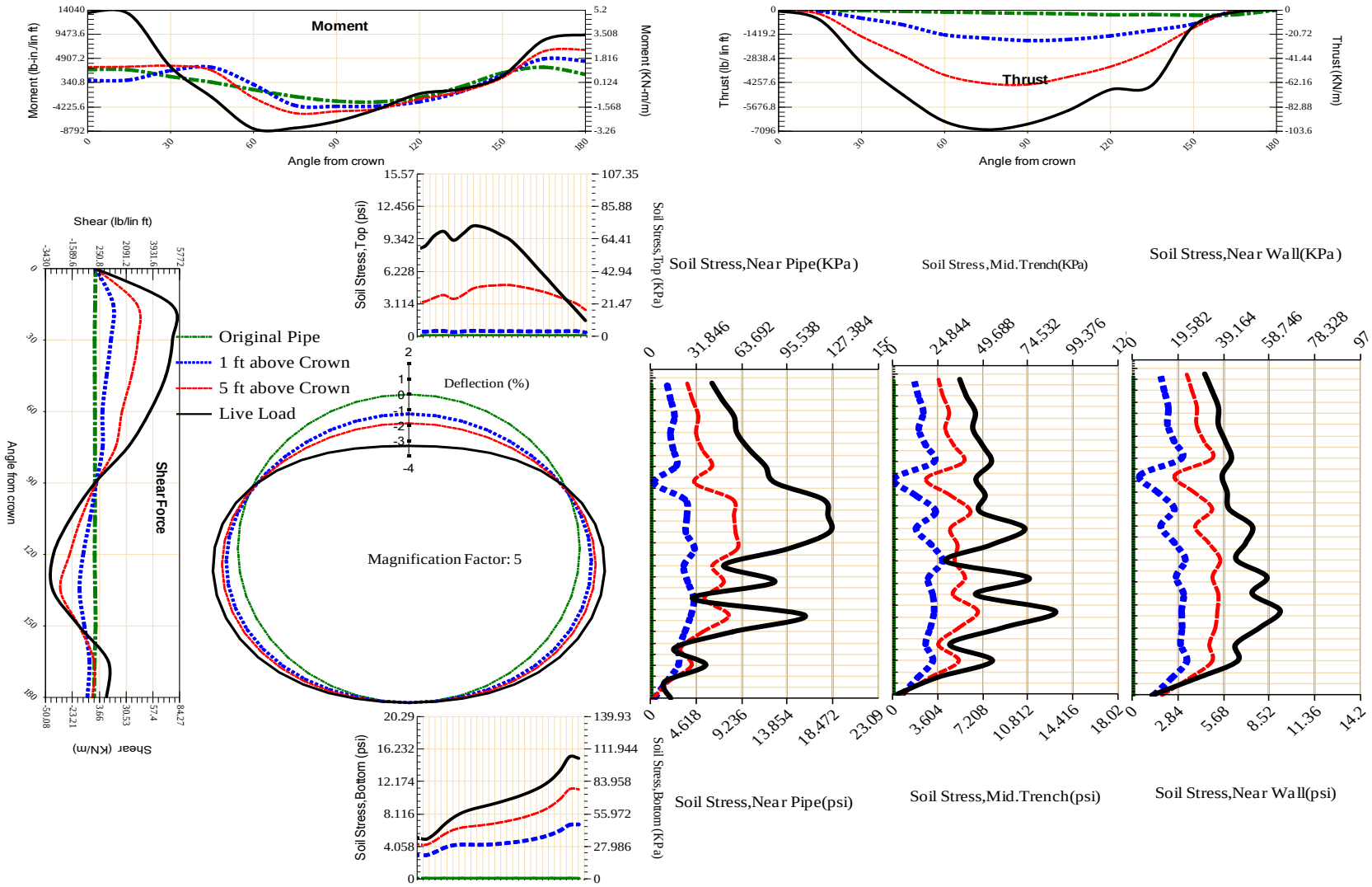

Figure A-104 Param-120-PW200-TR7OR-OD+108-EW3-H5-LiveLoad

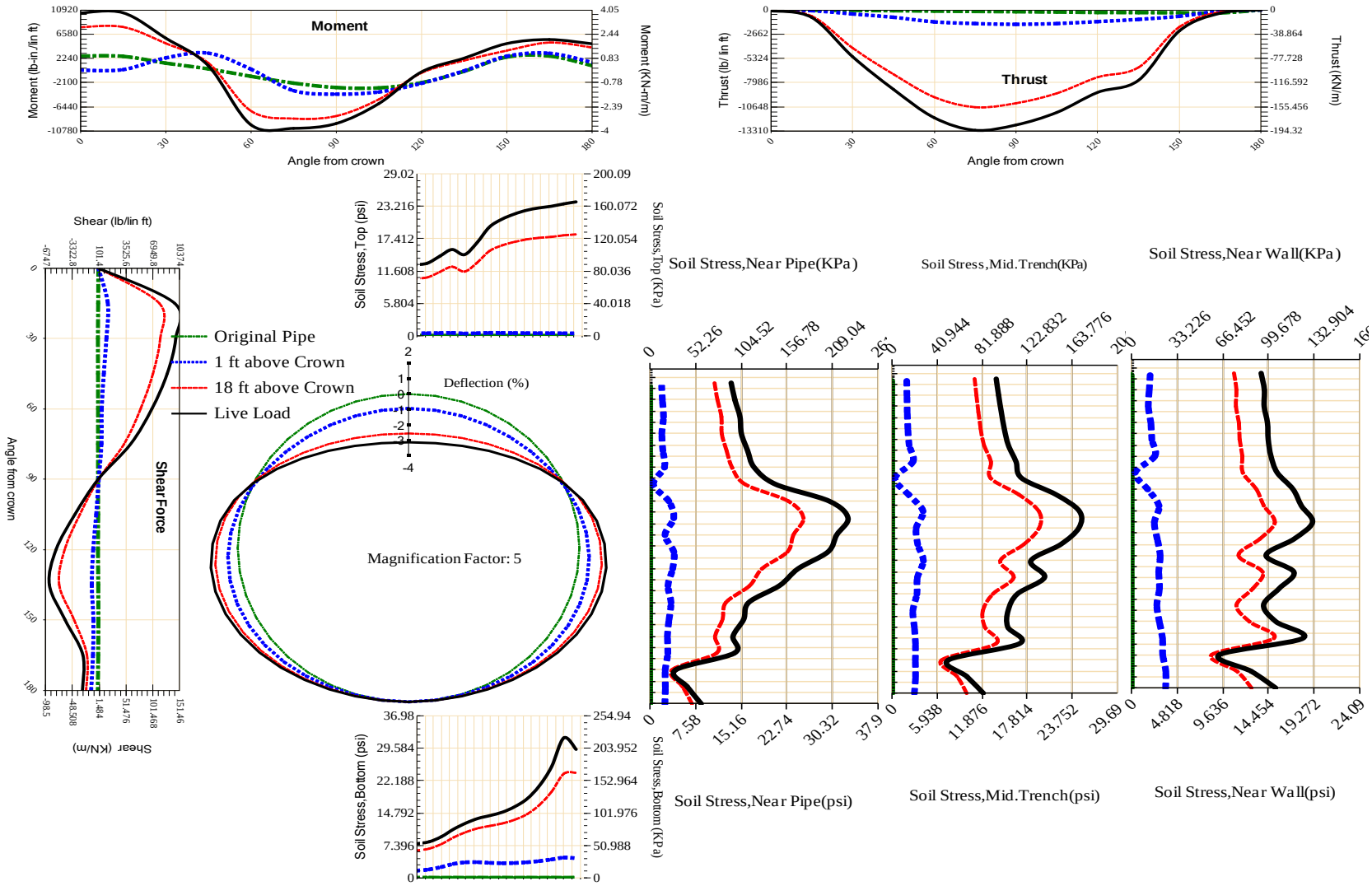

Figure A-105 Param-120-PW200-TR7OR-OD+48-EW10-H18-LiveLoad

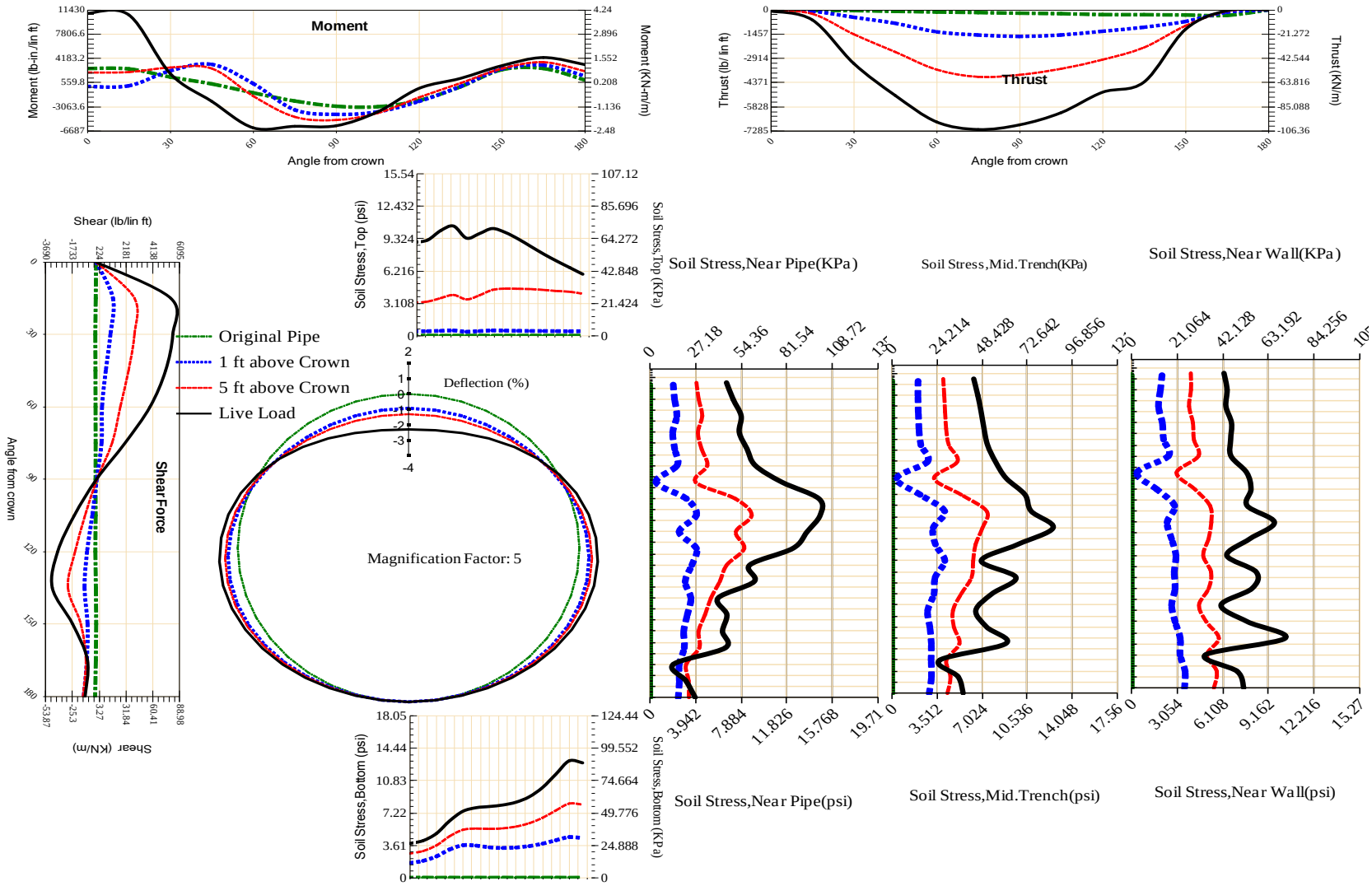

Figure A-106 Param-120-PW200-TR7OR-OD+48-EW10-H5-LiveLoad

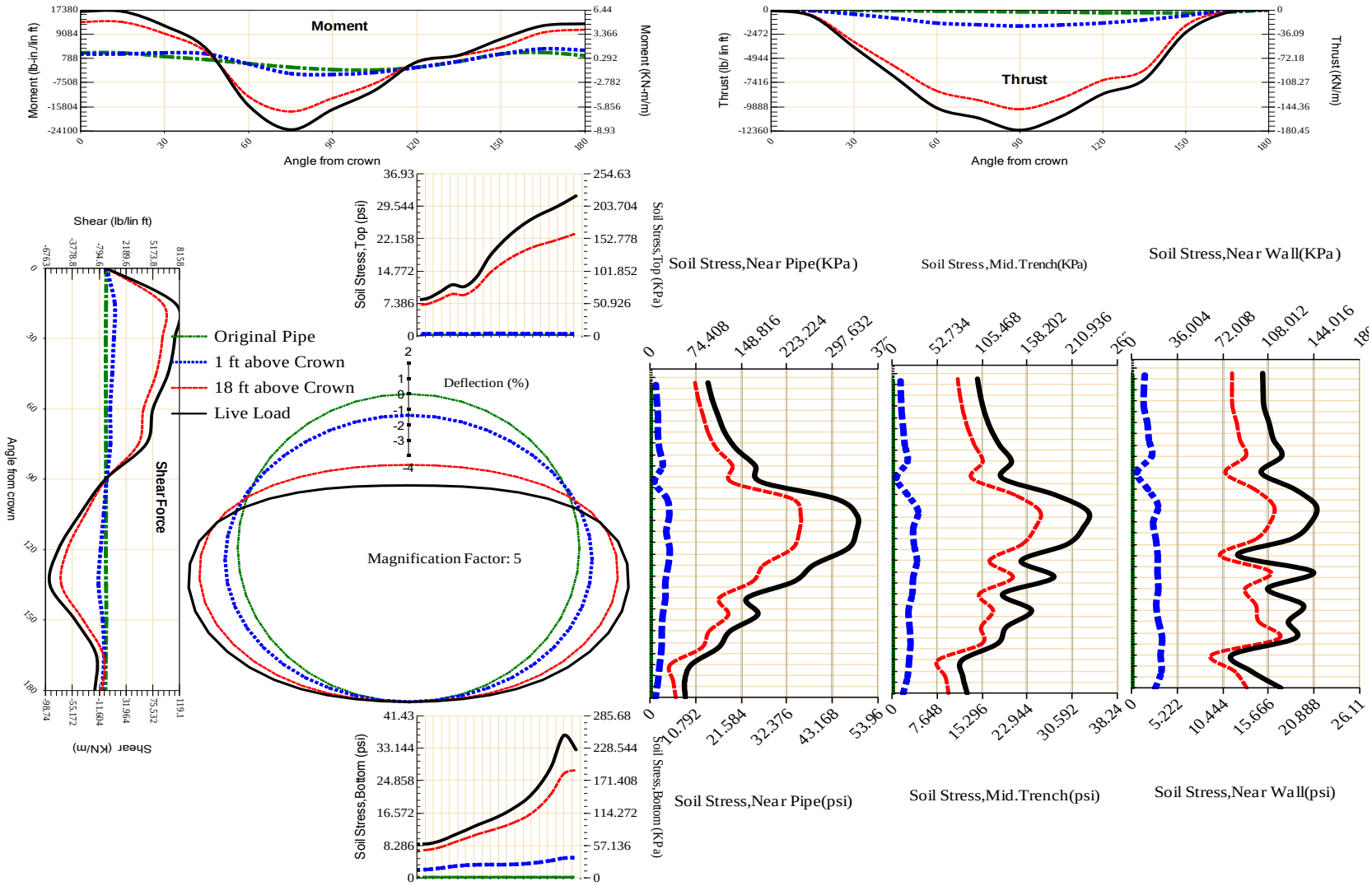

Figure A-107 Param-120-PW200-TR7OR-OD+48-EW3-H18-LiveLoad

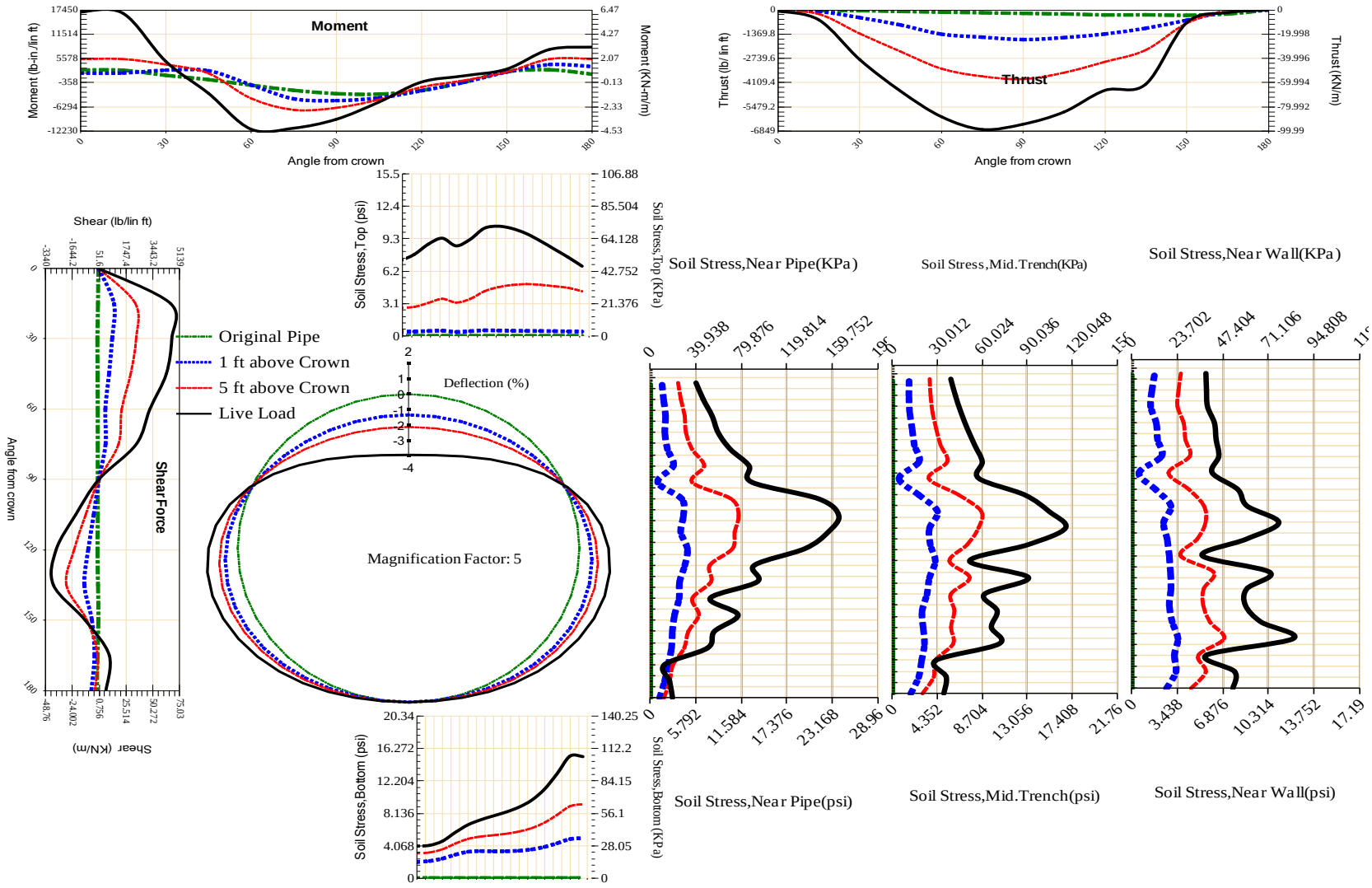

Figure A-108 Param-120-PW200-TR7OR-OD+48-EW3-H5-LiveLoad

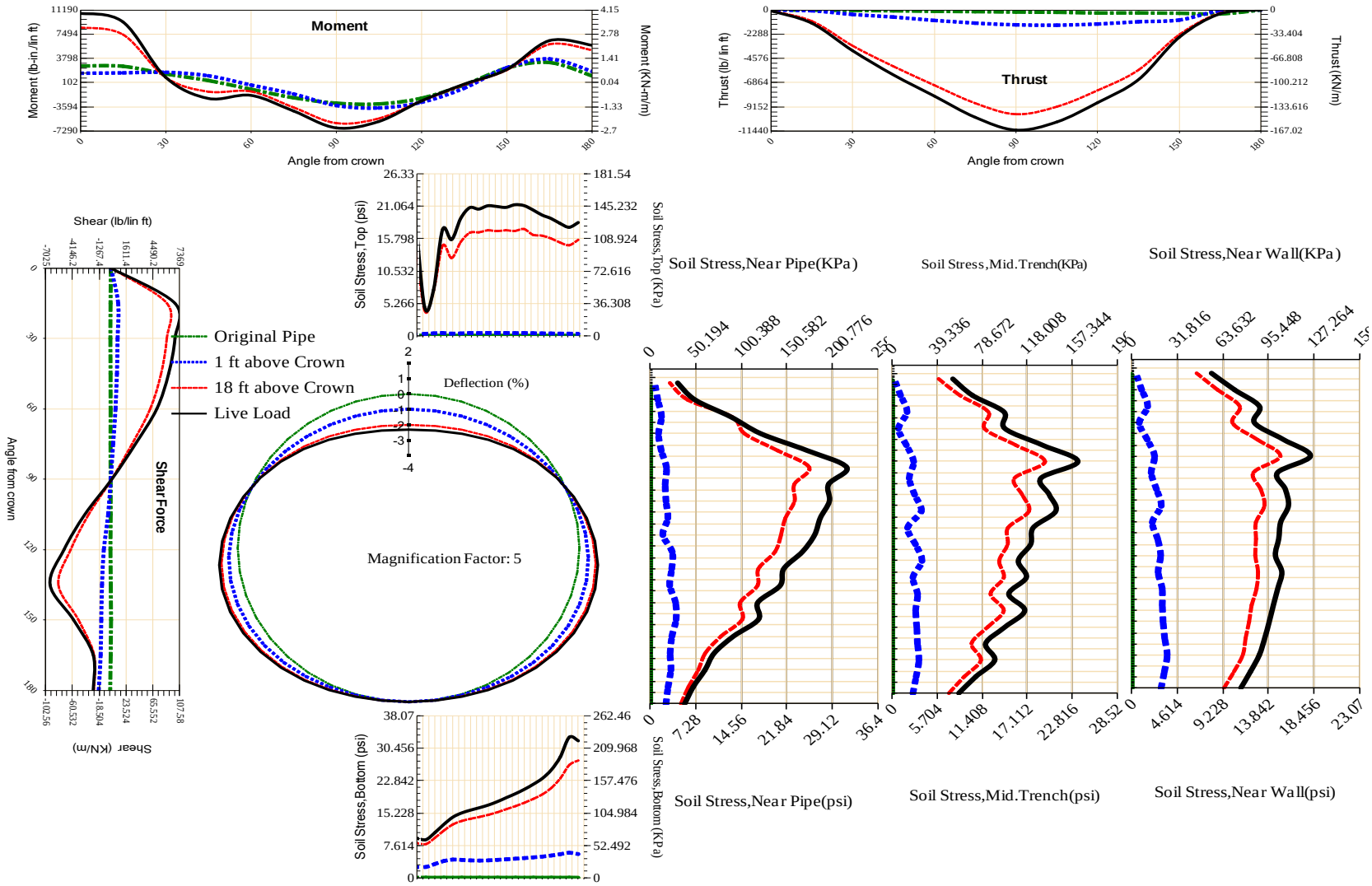

Figure A-109 Param-120-PW200-TR7SF-OD+108-EW10-H18-LiveLoad

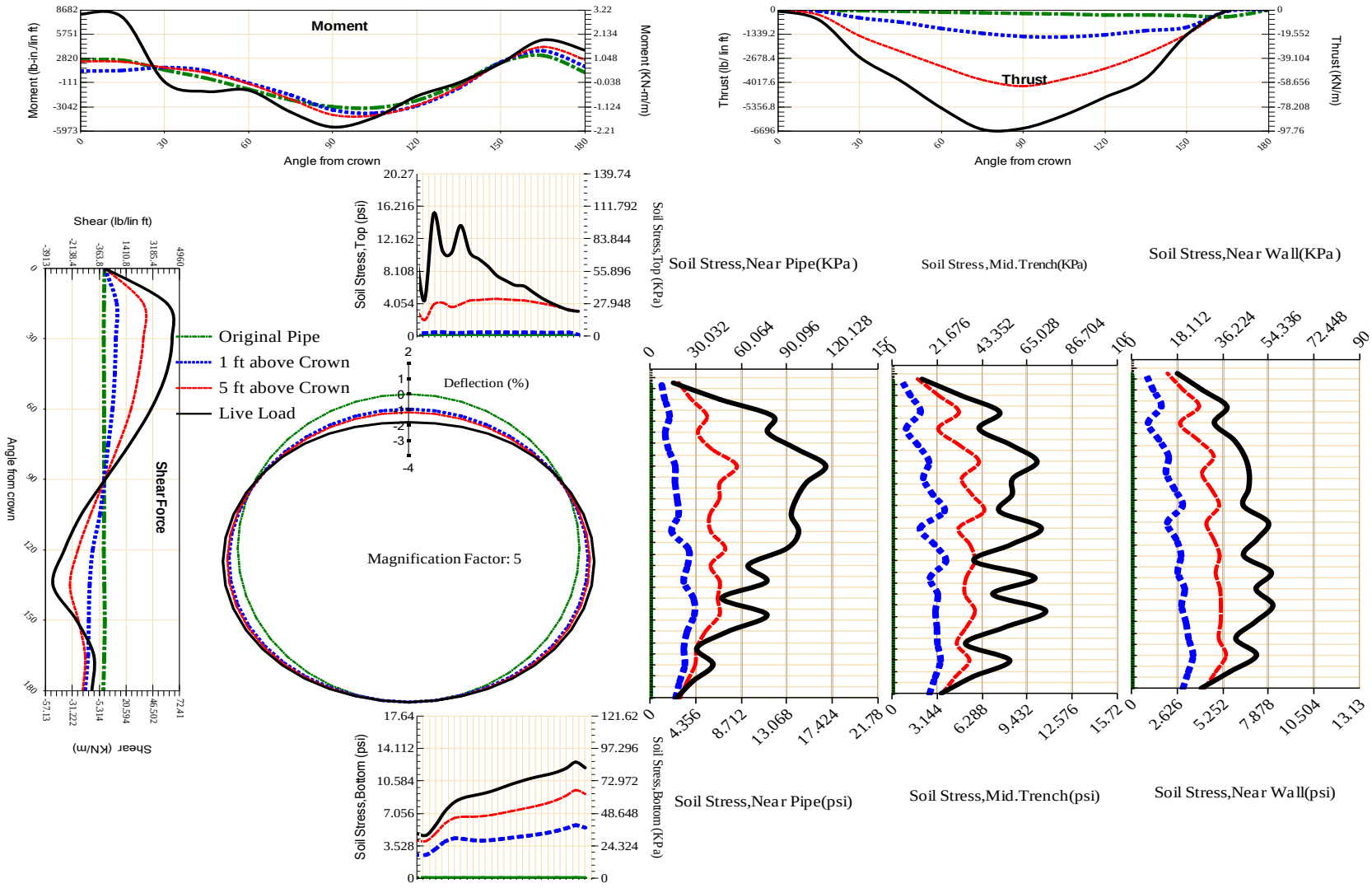

Figure A-110 Param-120-PW200-TR7SF-OD+108-EW10-H5-LiveLoad

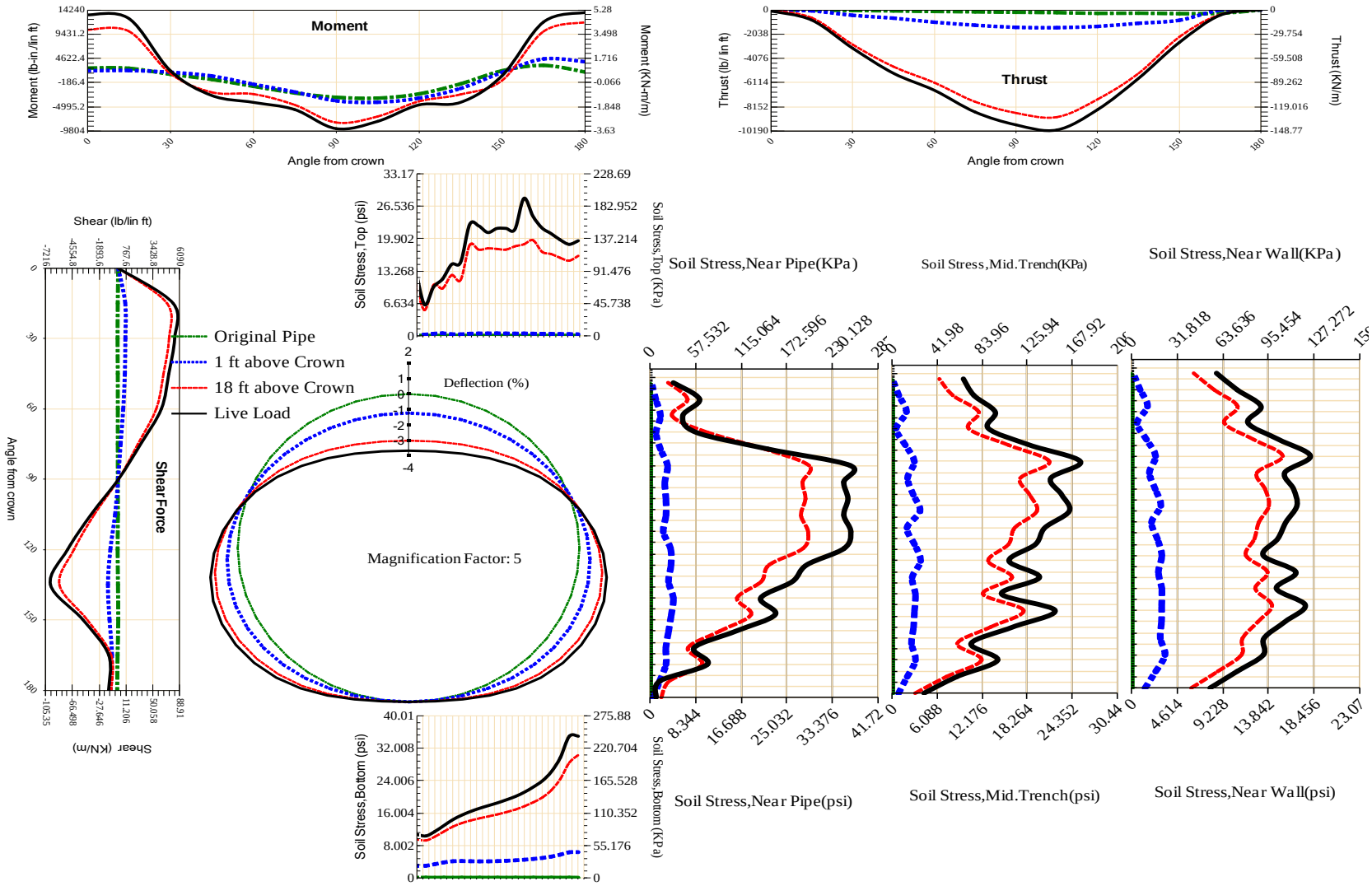

Figure A-111 Param-120-PW200-TR7SF-OD+108-EW3-H18-LiveLoad

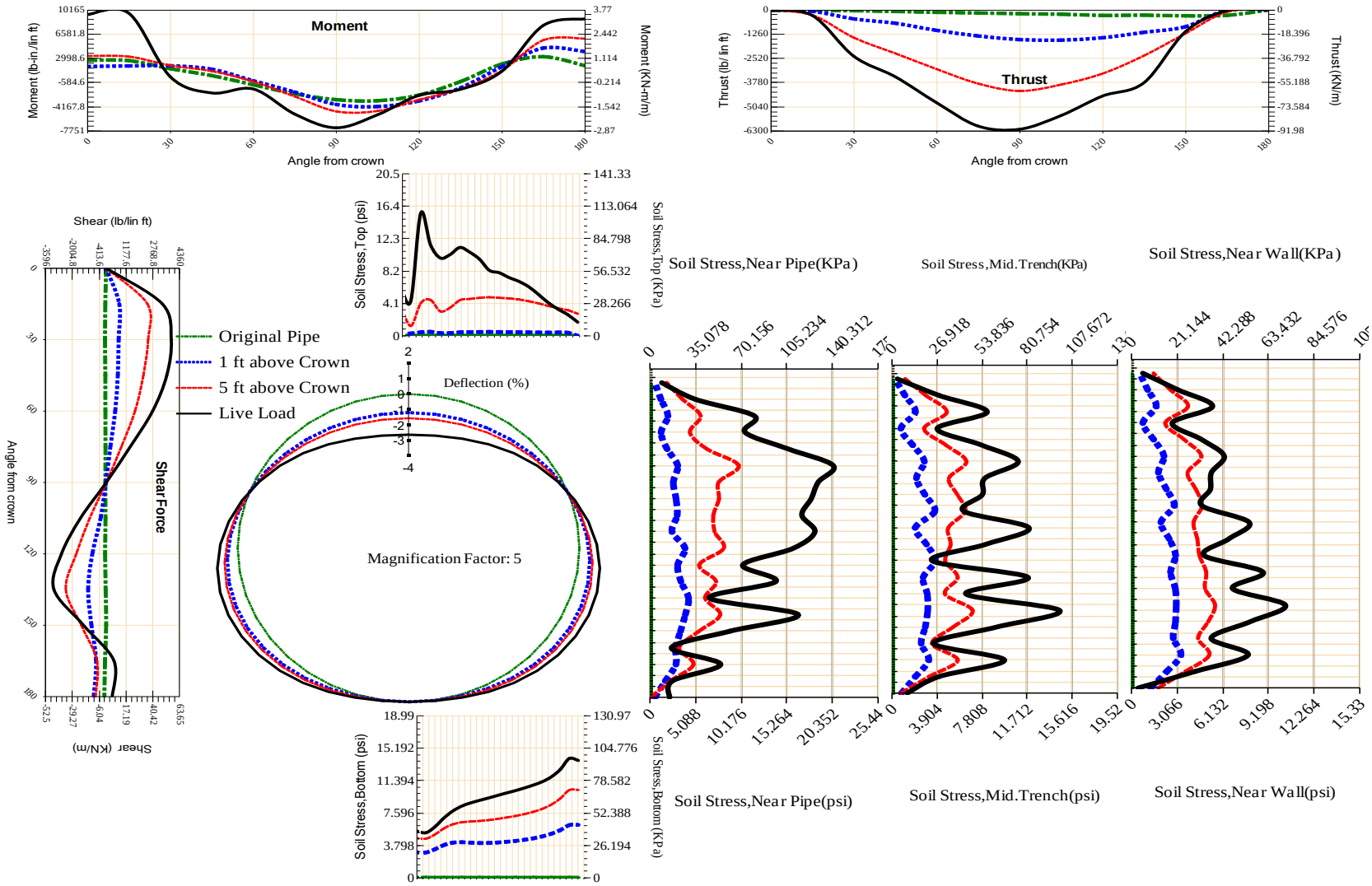

Figure A-112 Param-120-PW200-TR7SF-OD+108-EW3-H5-LiveLoad

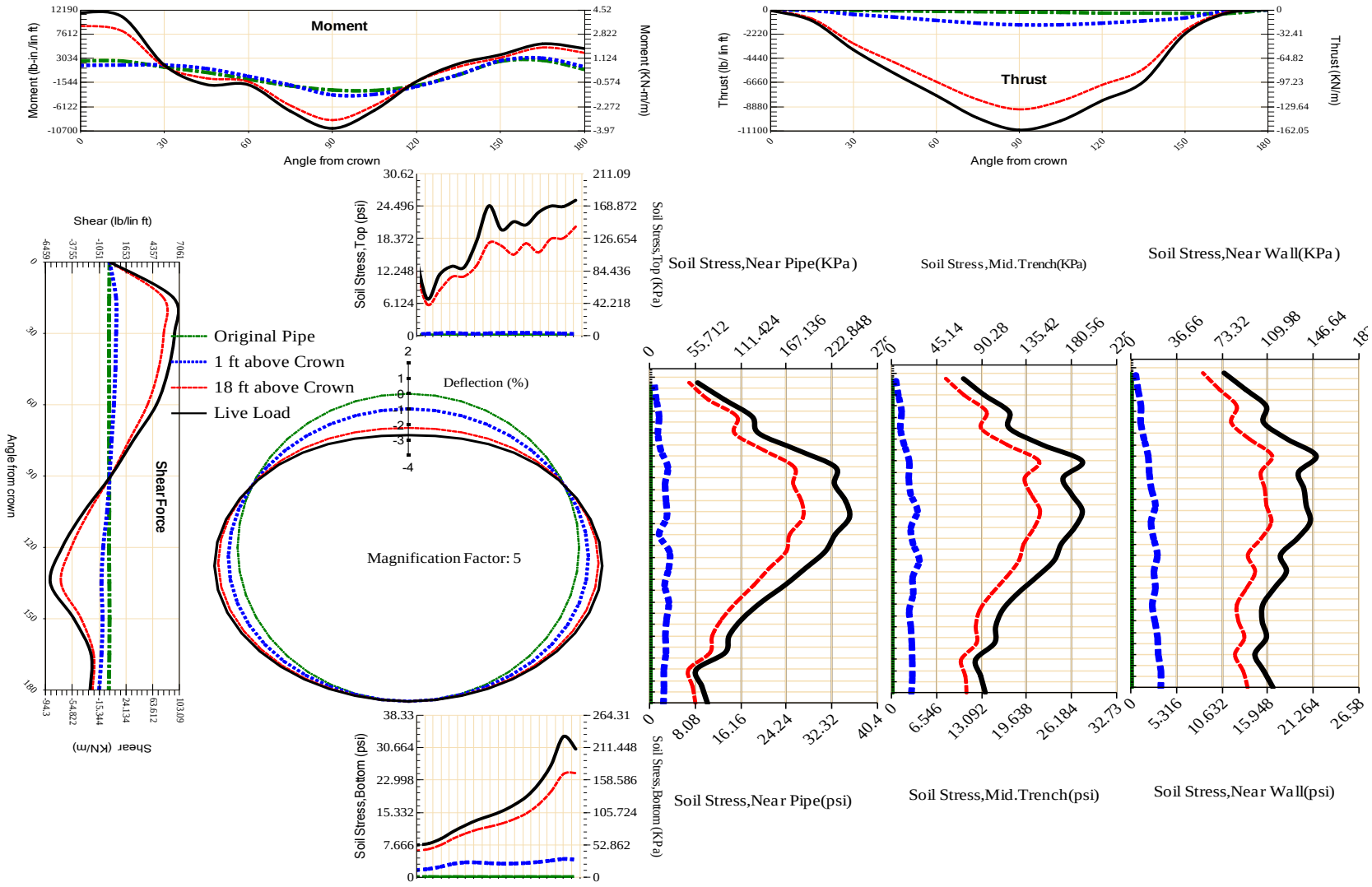

Figure A-113 Param-120-PW200-TR7SF-OD+48-EW10-H18-LiveLoad

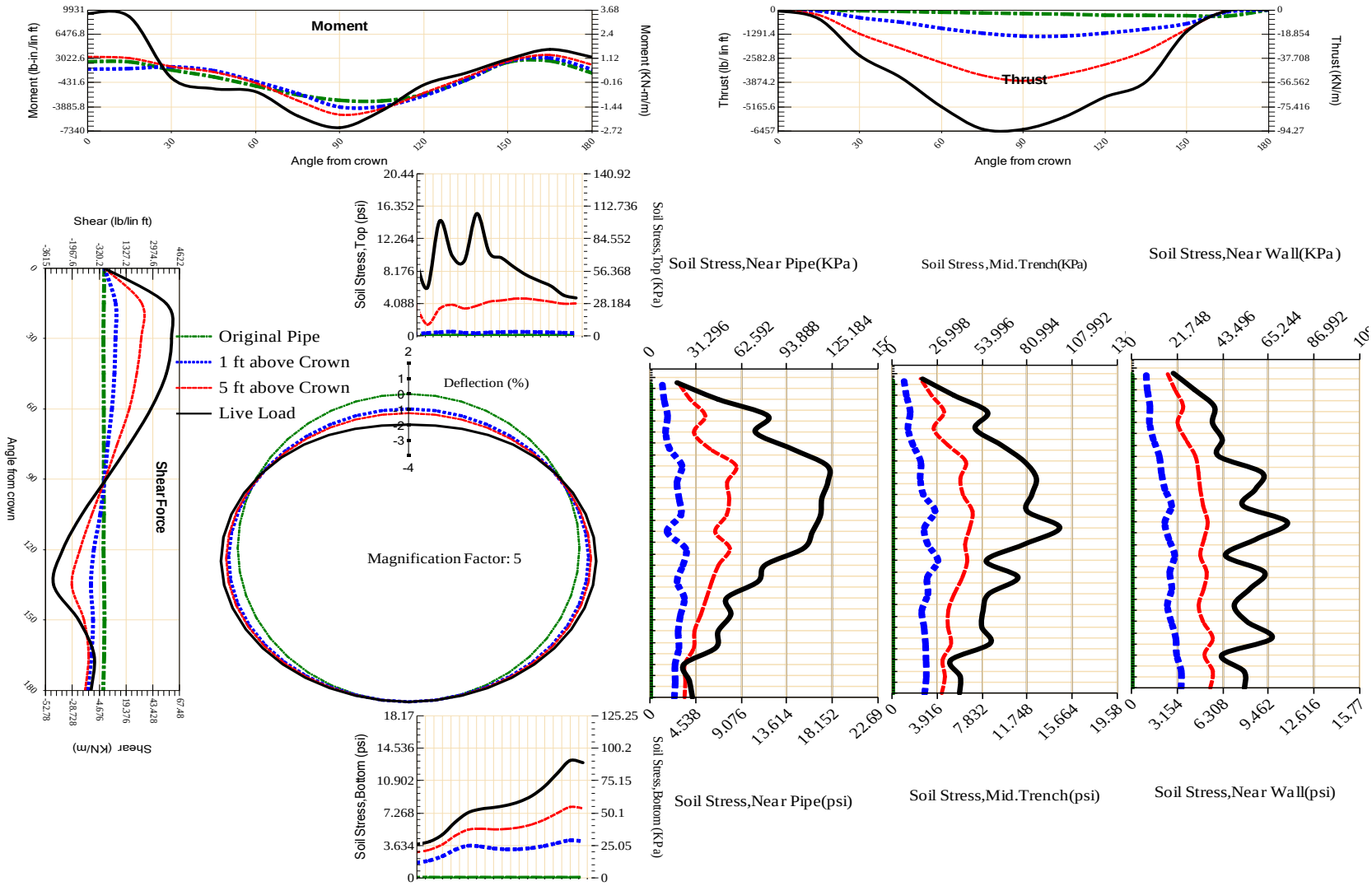

Figure A-114 Param-120-PW200-TR7SF-OD+48-EW10-H5-LiveLoad

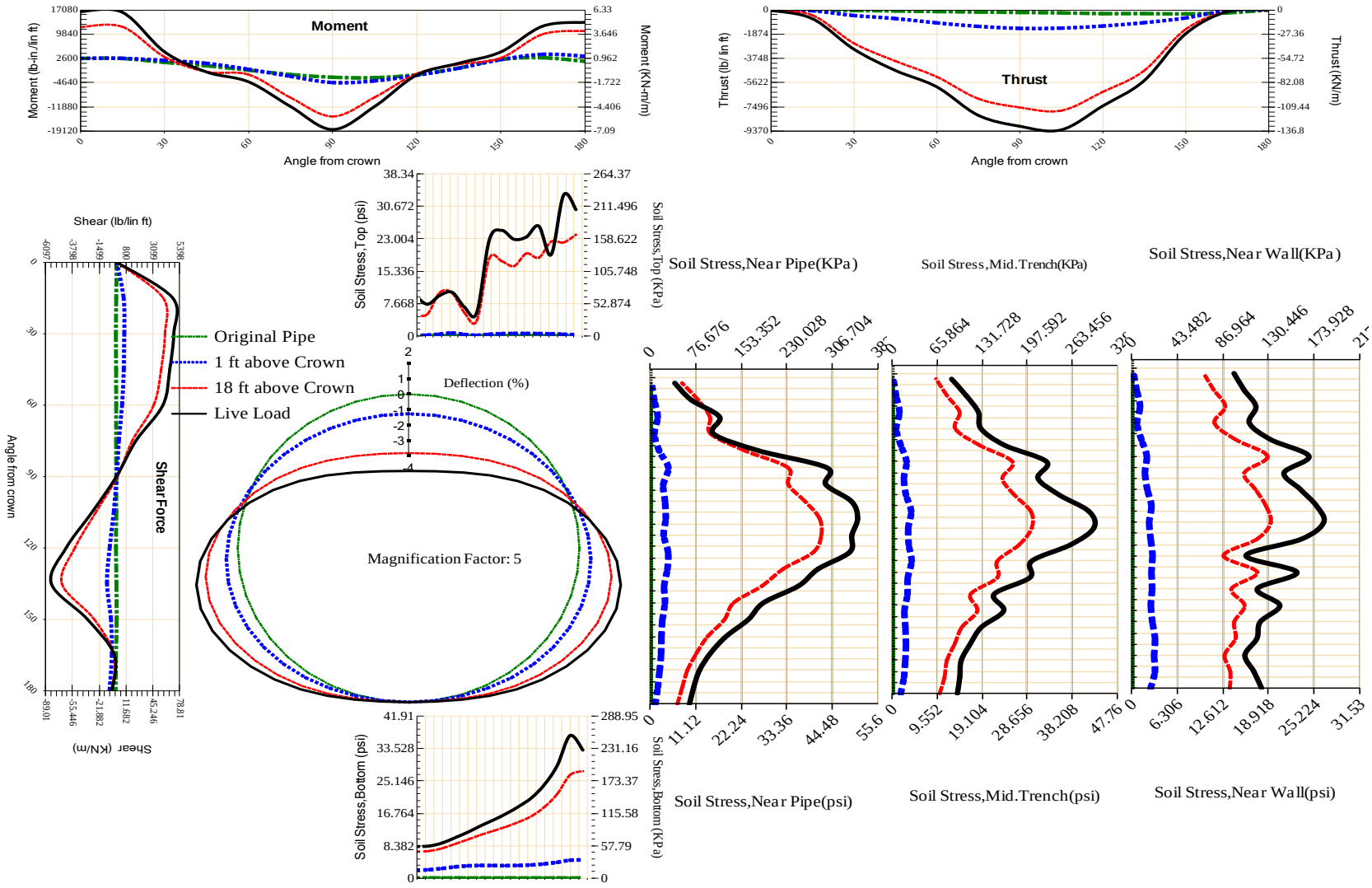

Figure A-115 Param-120-PW200-TR7SF-OD+48-EW3-H18-LiveLoad

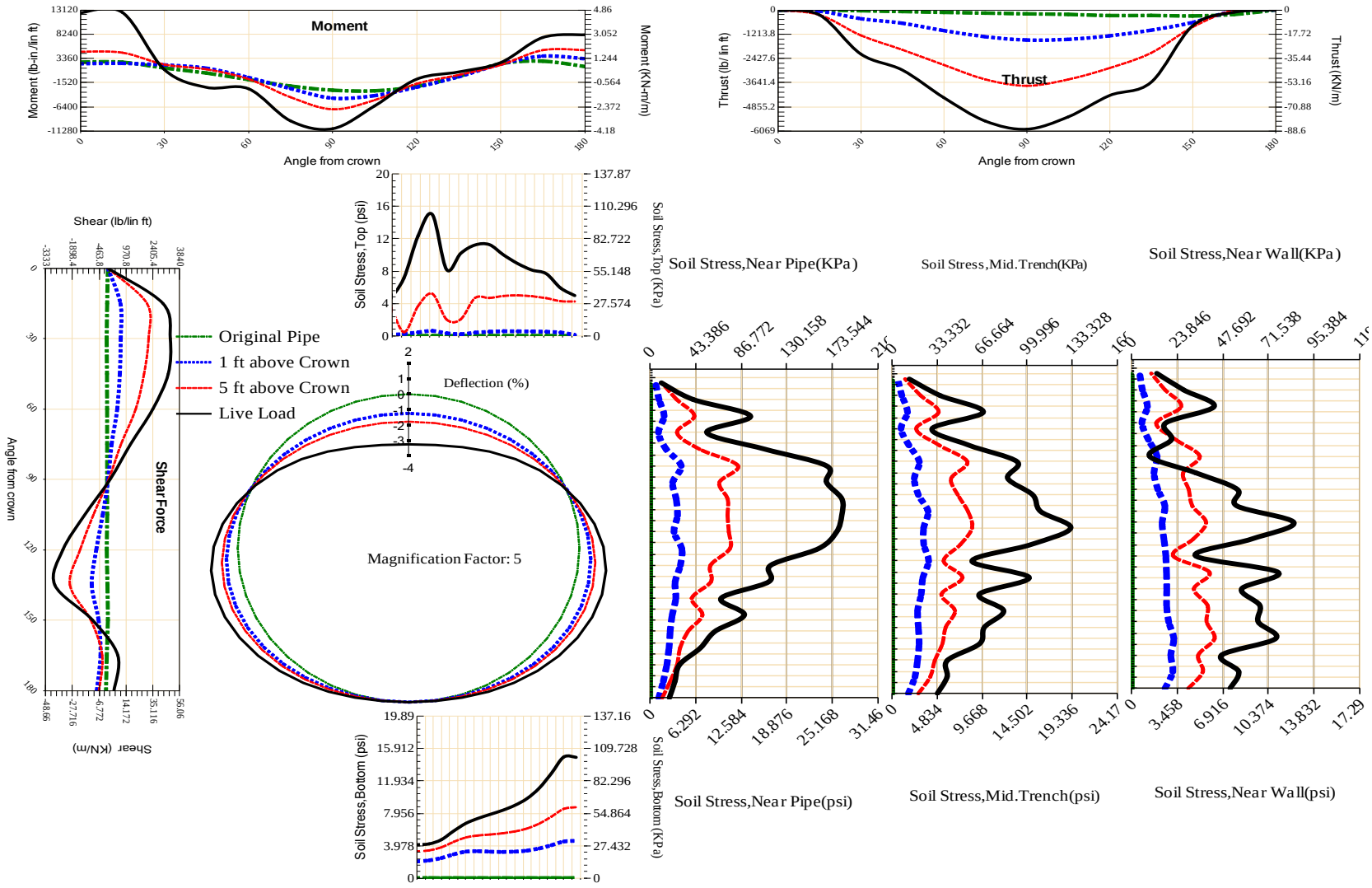

Figure A-116 Param-120-PW200-TR7SF-OD+48-EW3-H5-LiveLoad

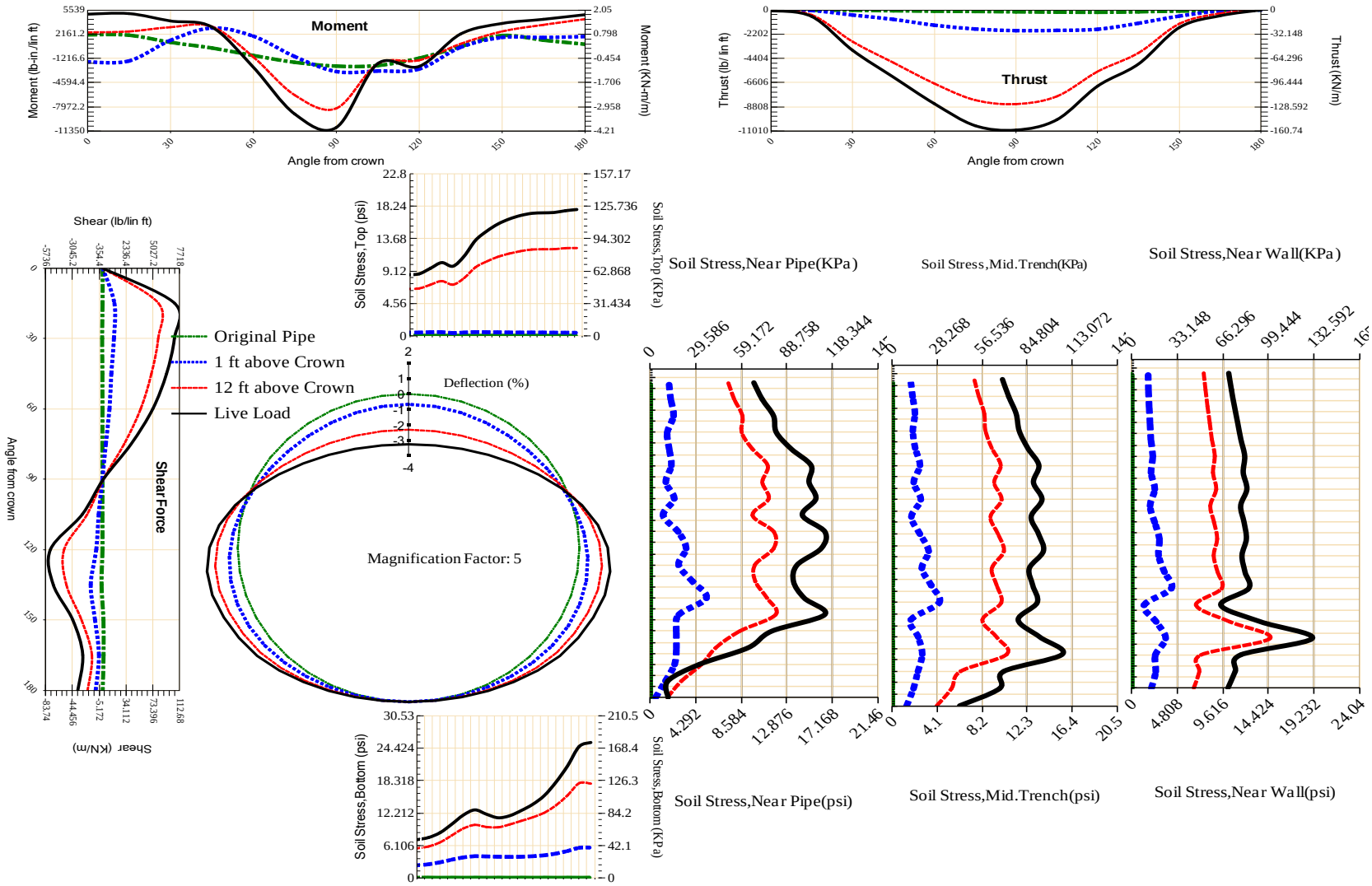

Figure A-117 Param-120-PW230-SF3OR-OD+72-EW5-H12-LiveLoad

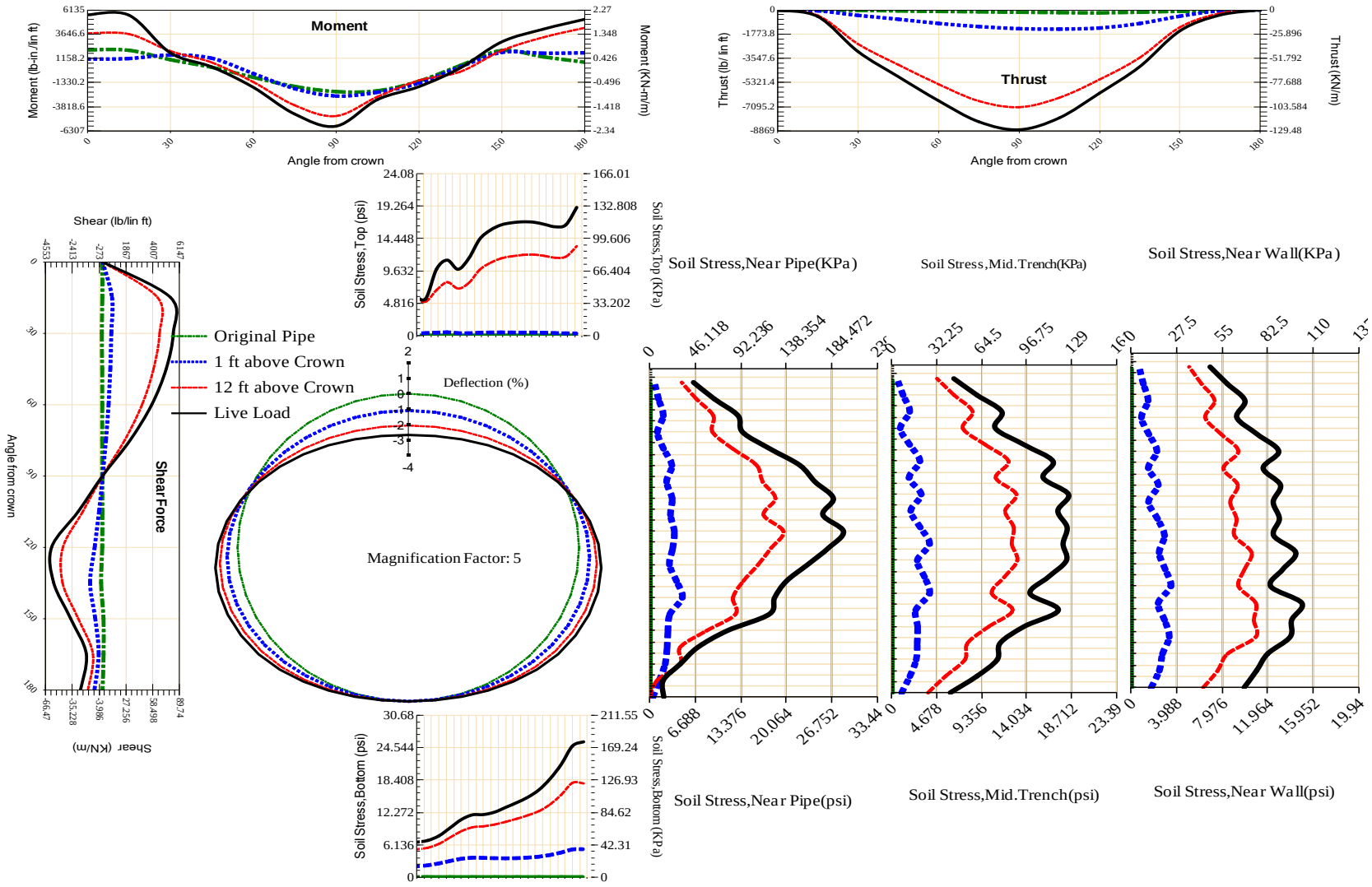

Figure A-118 Param-120-PW230-SF3TR-OD+72-EW5-H12-LiveLoad

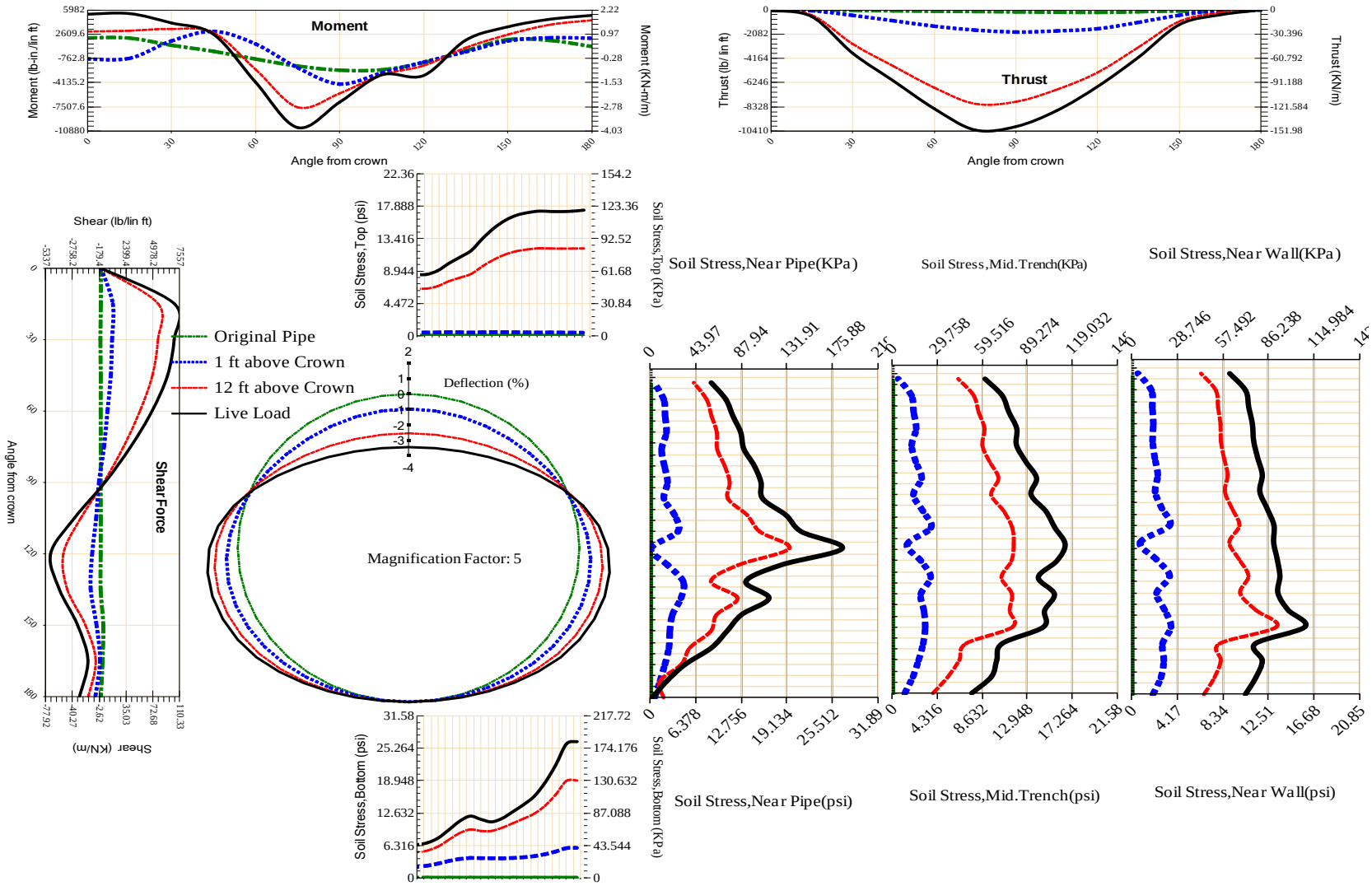

Figure A-119 Param-120-PW230-SF5OR-OD+72-EW5-H12-LiveLoad

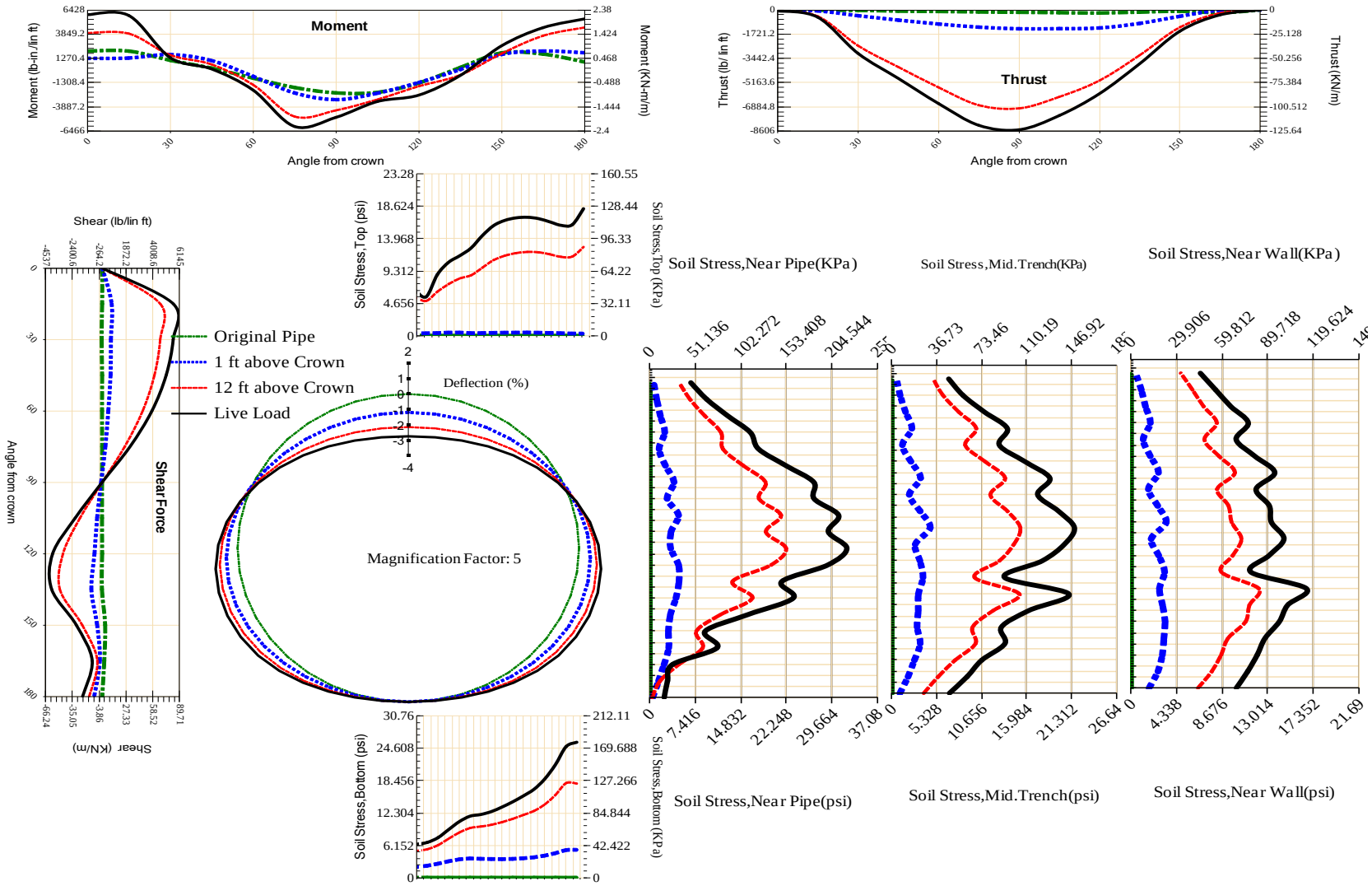

Figure A-120 Param-120-PW230-SF5TR-OD+72-EW5-H12-LiveLoad

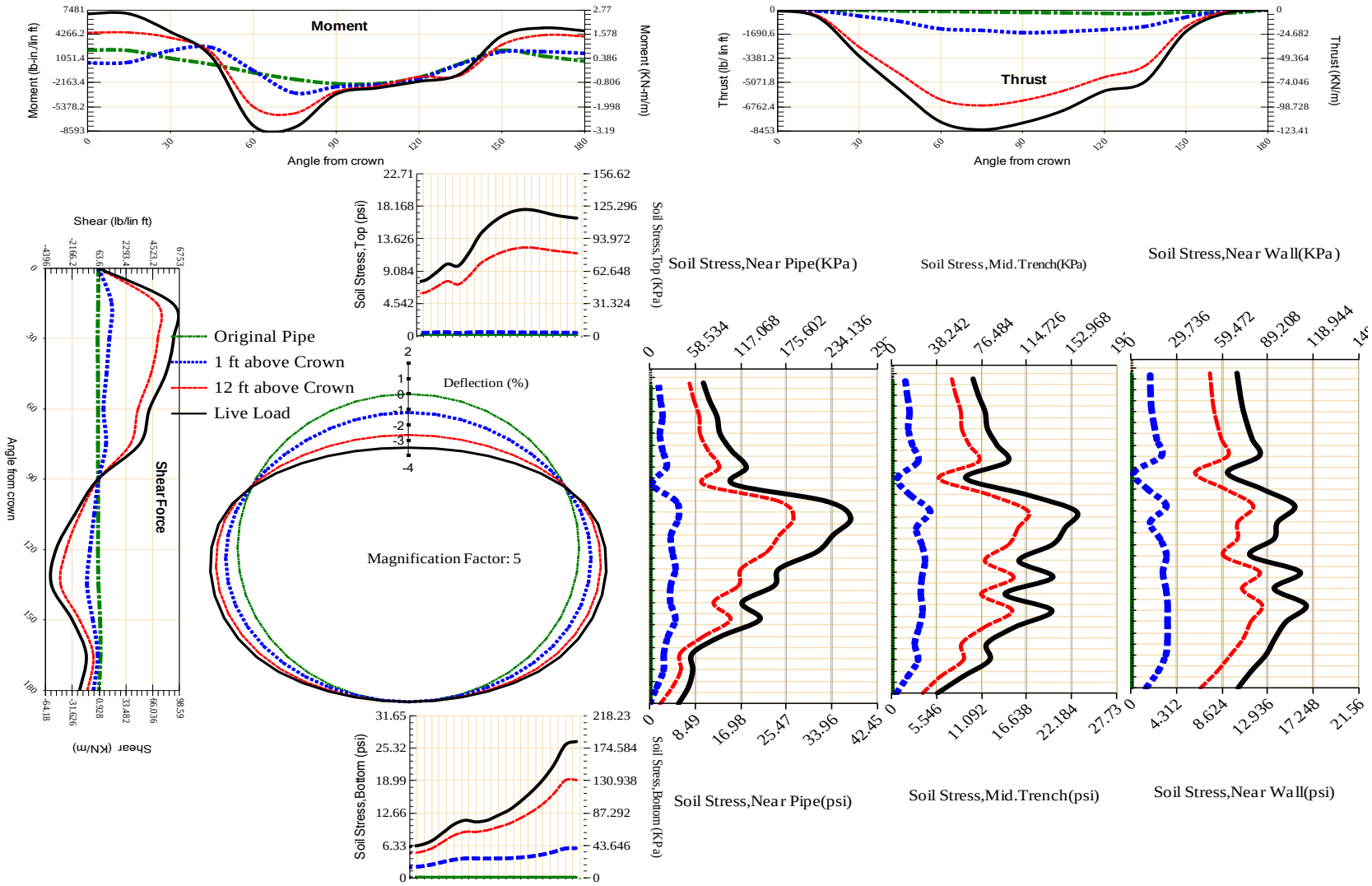

Figure A-121 Param-120-PW230-SF7OR-OD+72-EW5-H12-LiveLoad

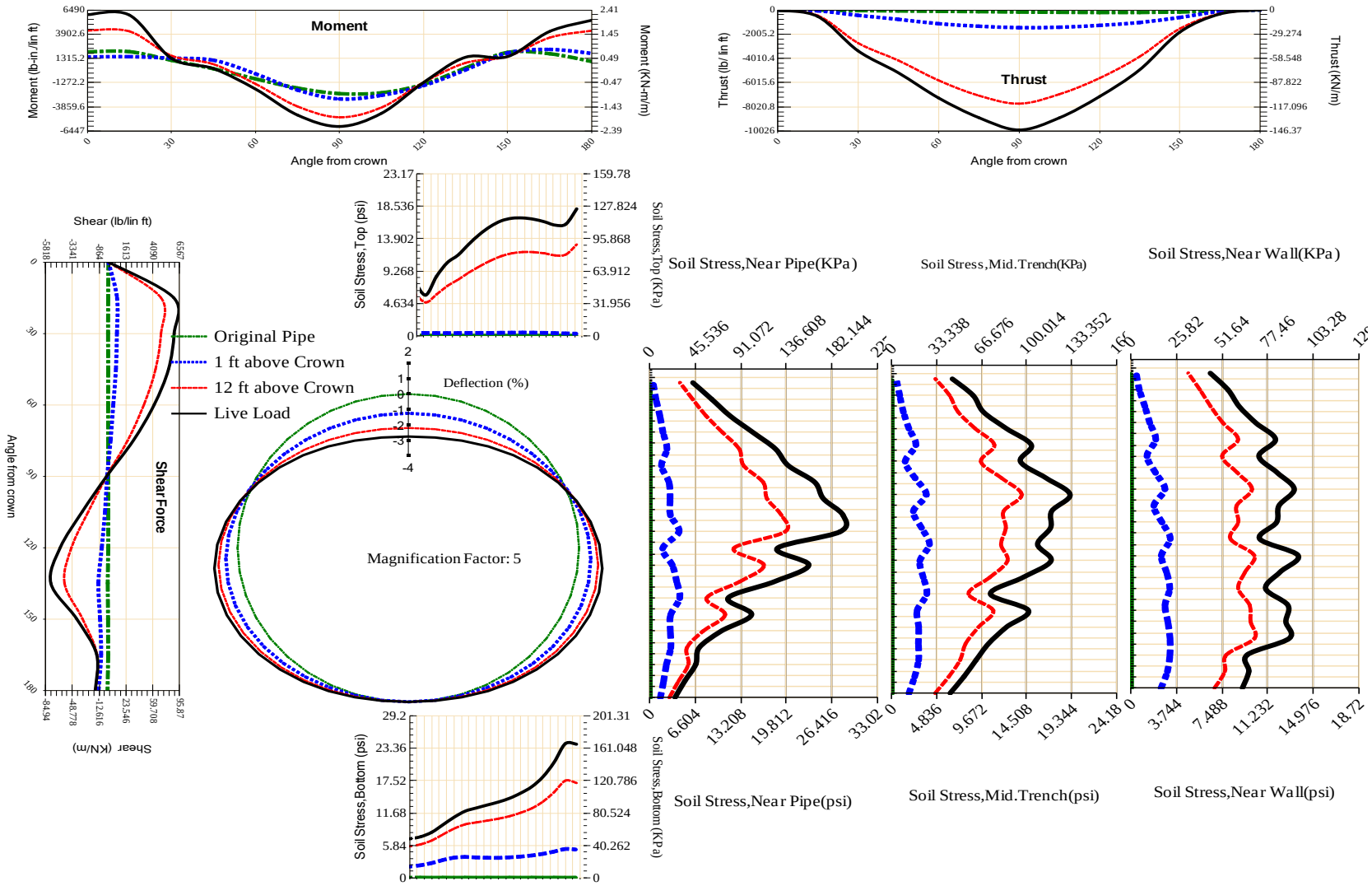

Figure A-122 Param-120-PW230-TR10TR-OD+72-EW5-H12-LiveLoad

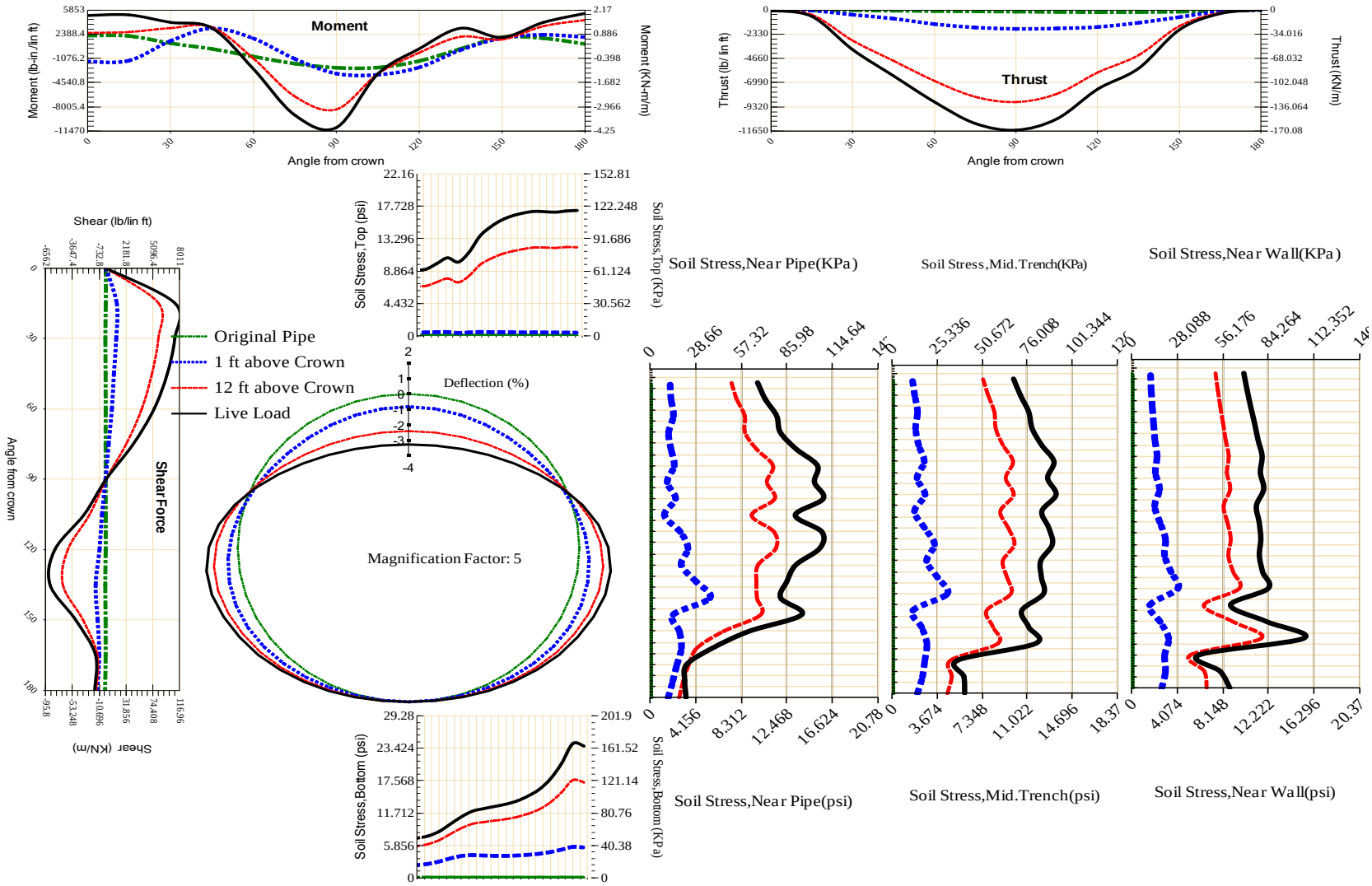

Figure A-123 Param-120-PW230-TR3OR-OD+72-EW5-H12-LiveLoad

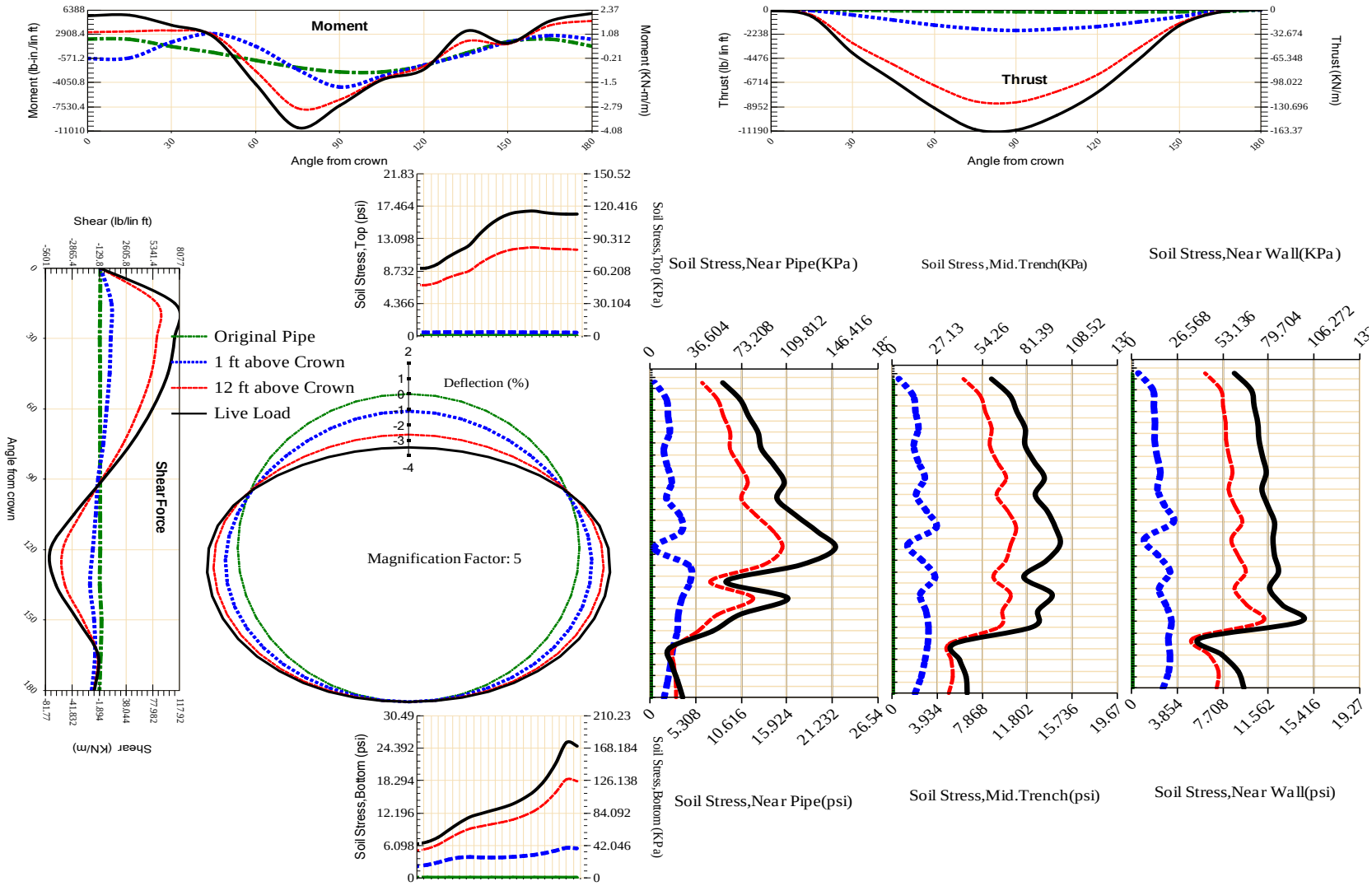

Figure A-124 Param-120-PW230-TR5OR-OD+72-EW5-H12-LiveLoad

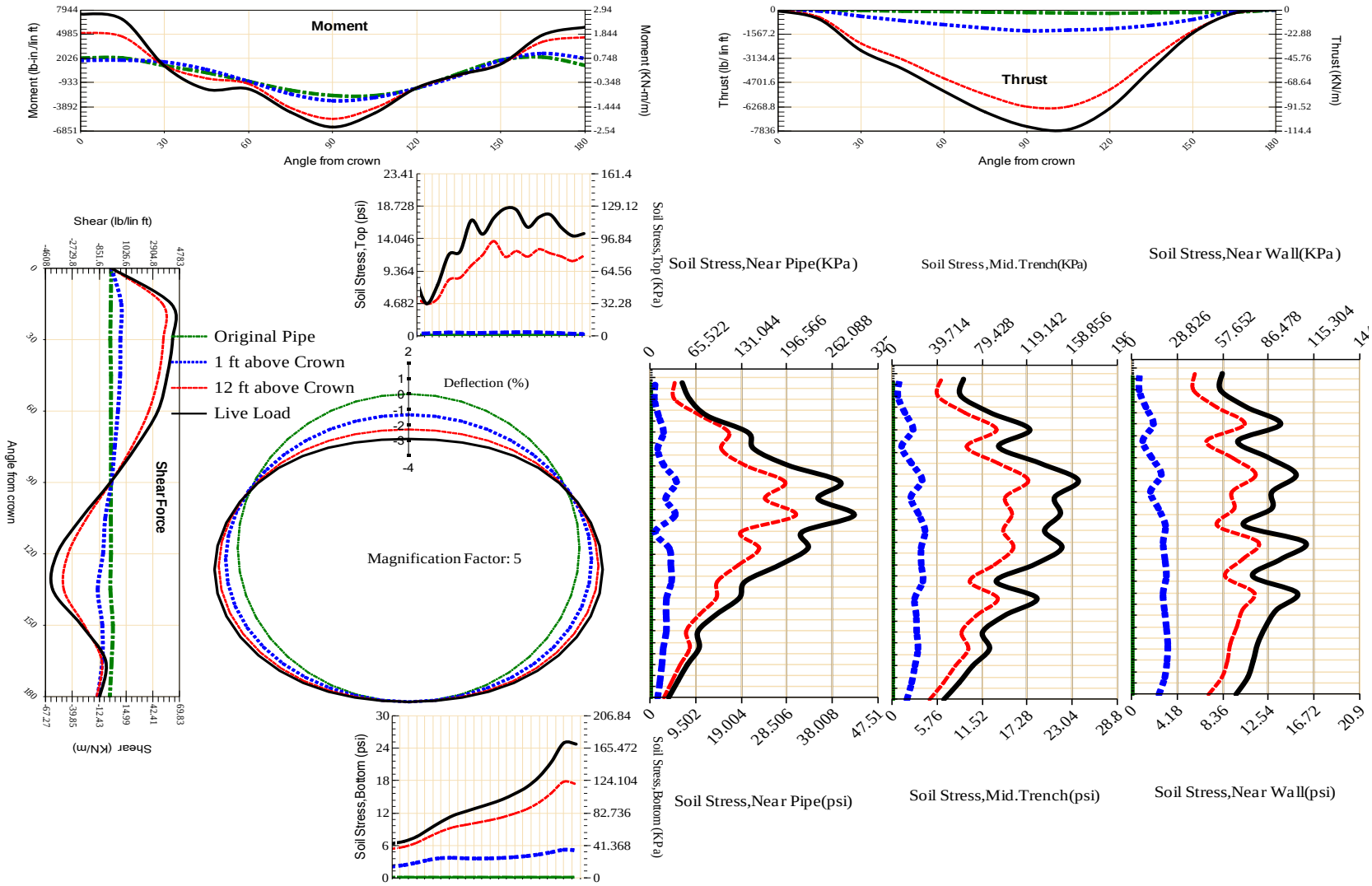

Figure A-125 Param-120-PW230-TR5SF-OD+72-EW5-H12-LiveLoad

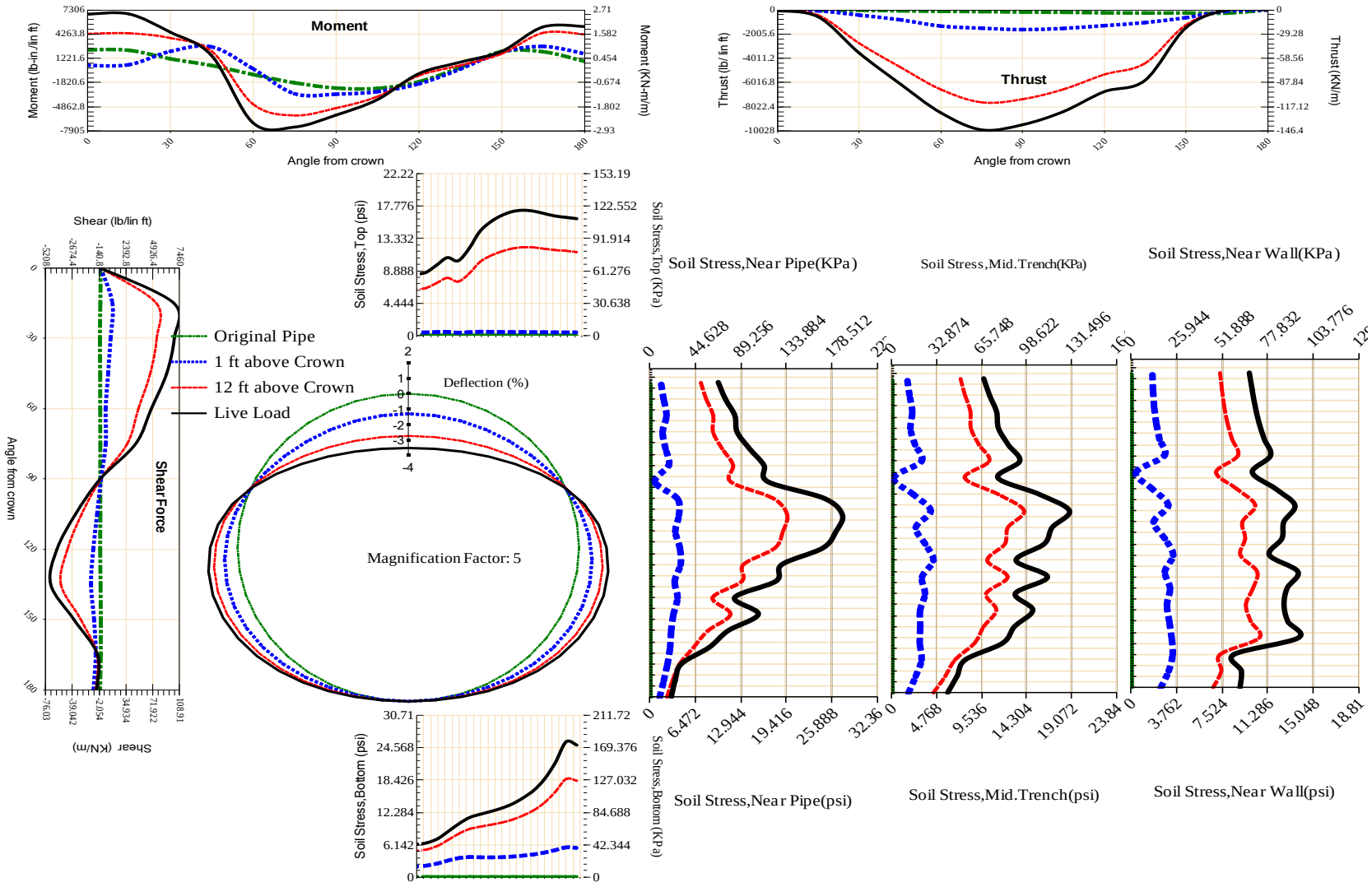

Figure A-126 Param-120-PW230-TR7OR-OD+72-EW5-H12-LiveLoad

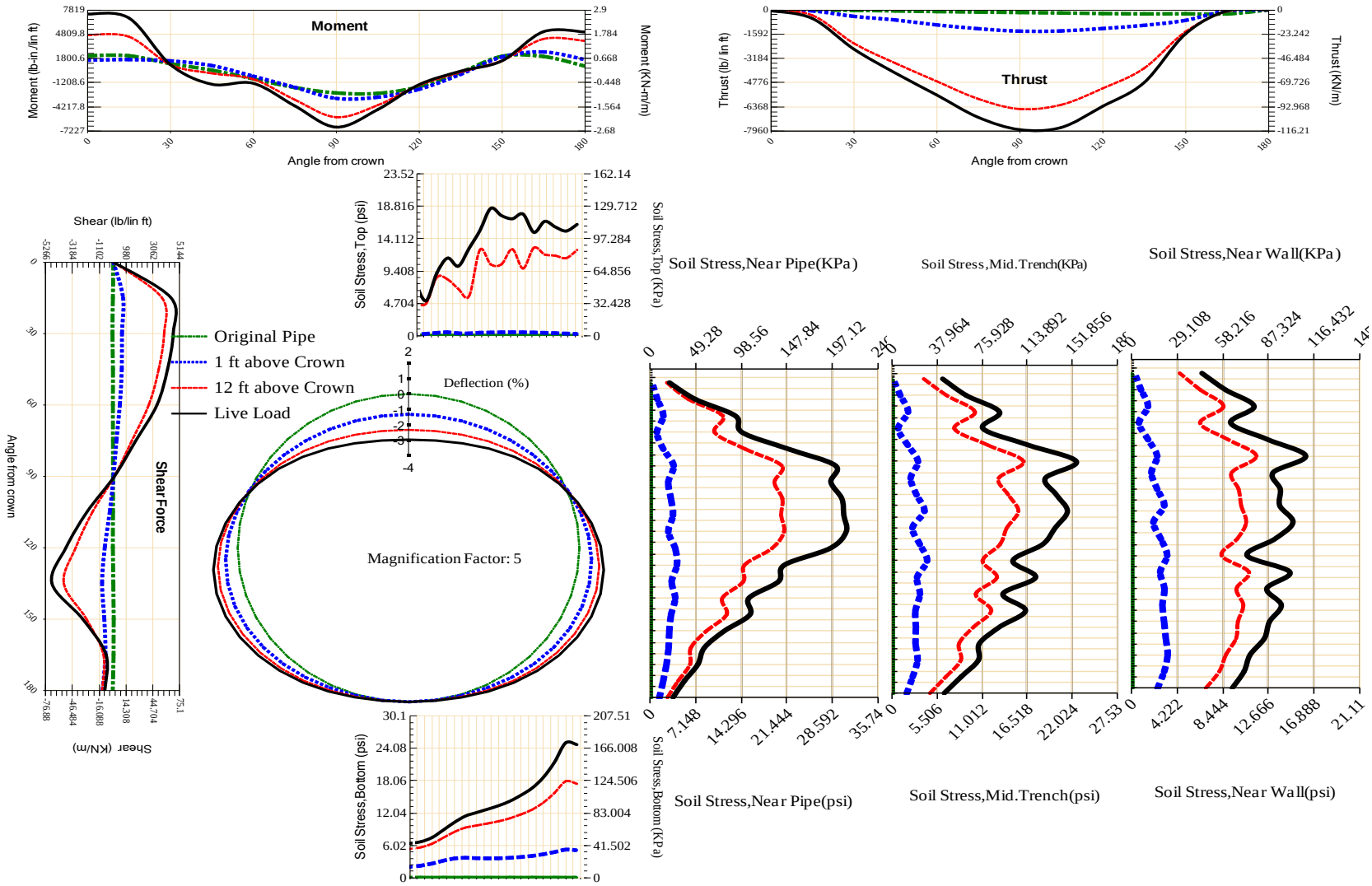

Figure A-127 Param-120-PW230-TR7SF-OD+72-EW5-H12-LiveLoad

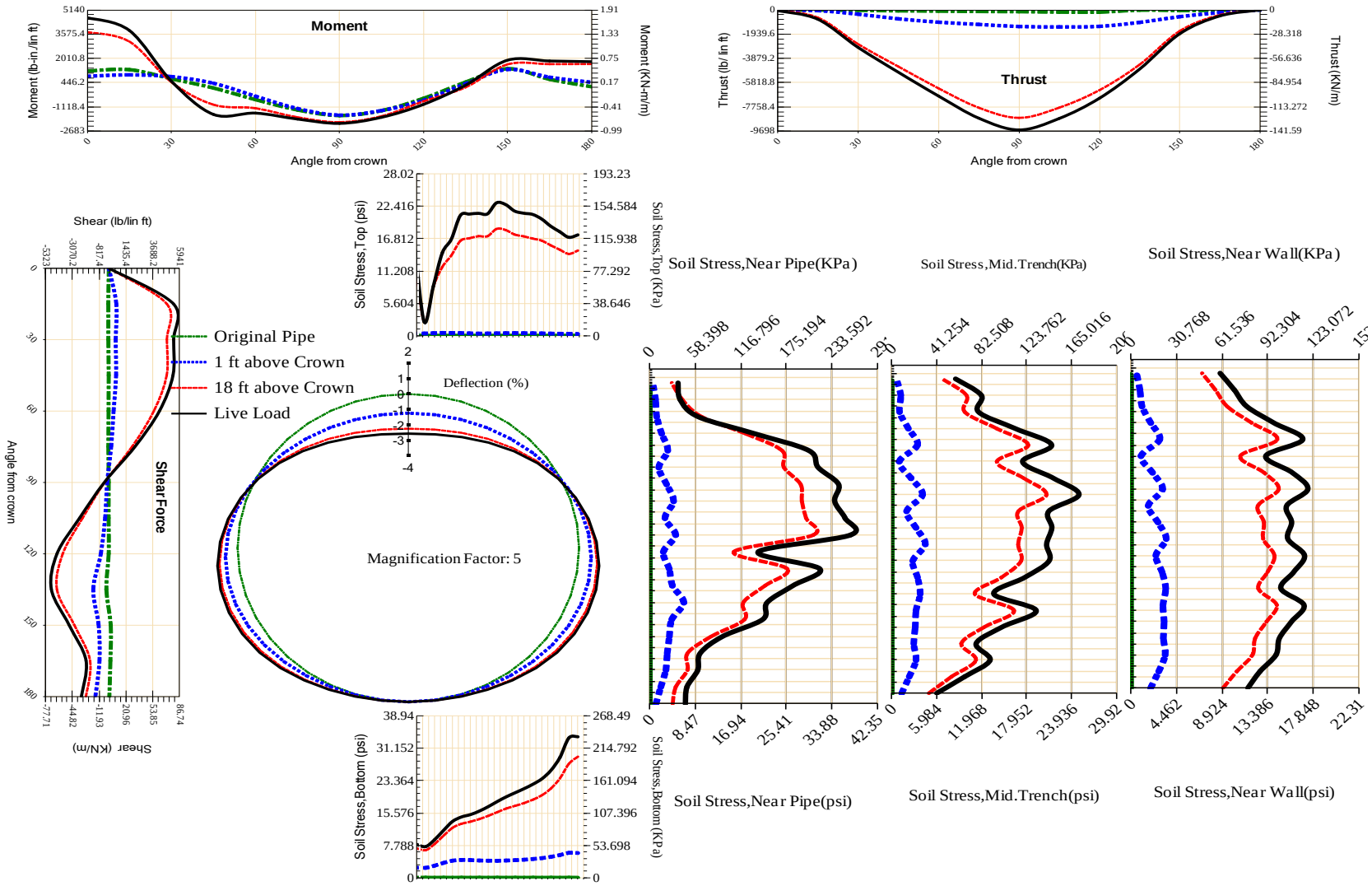

Figure A-128 Param-120-PW288-SF10SF-OD+108-EW10-H18-LiveLoad

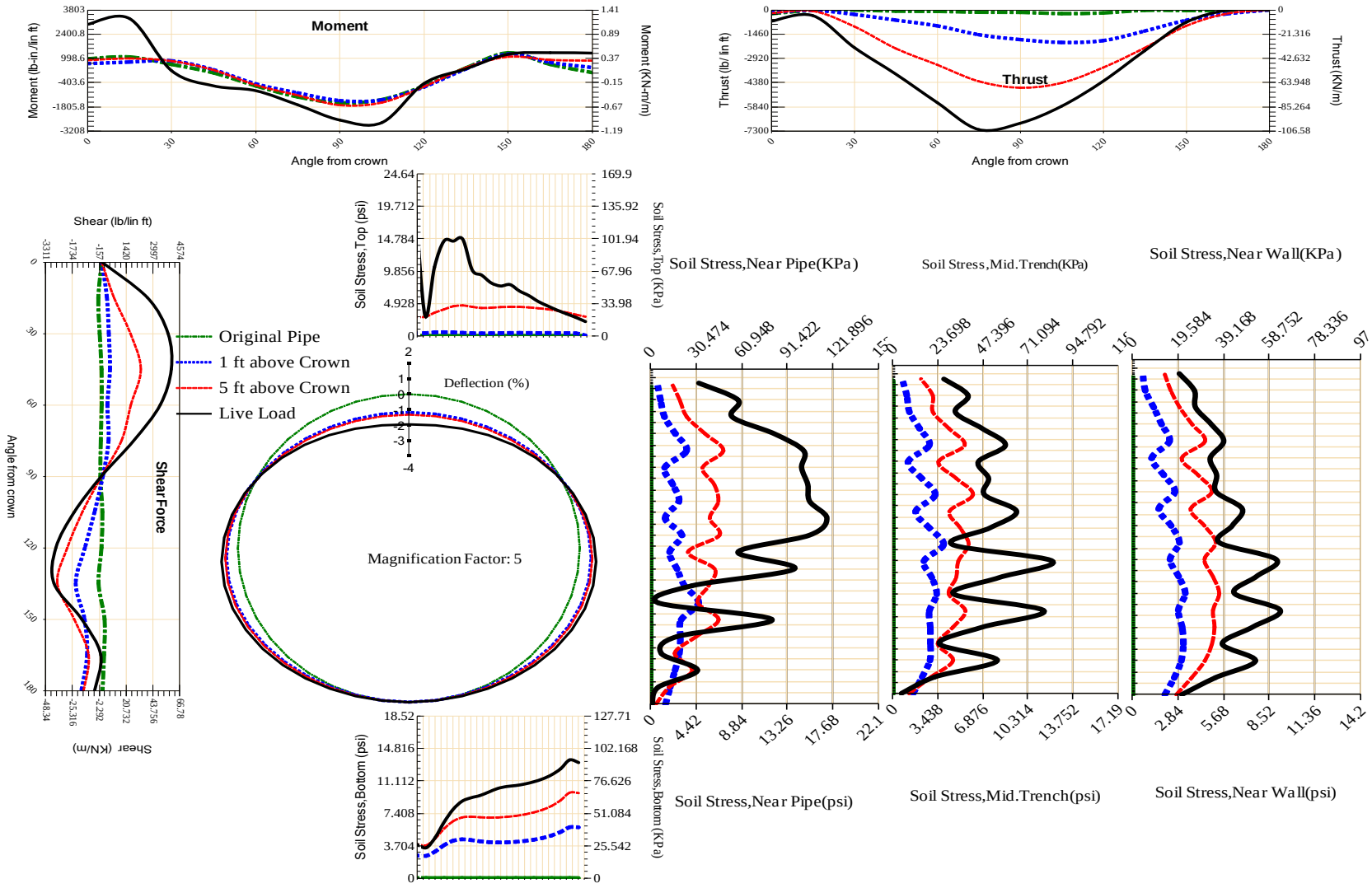

Figure A-129 Param-120-PW288-SF10SF-OD+108-EW10-H5-LiveLoad

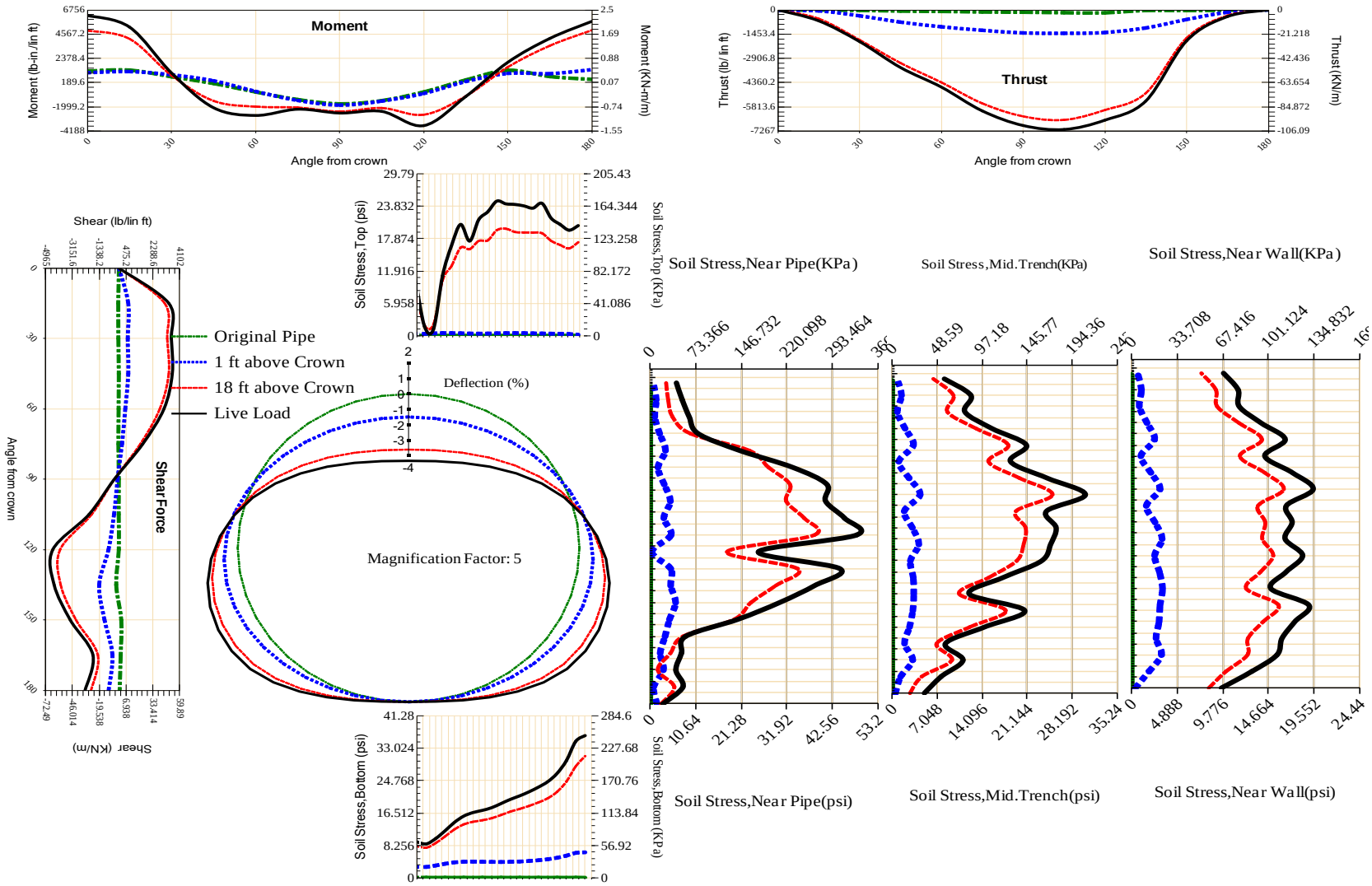

Figure A-130 Param-120-PW288-SF10SF-OD+108-EW3-H18-LiveLoad

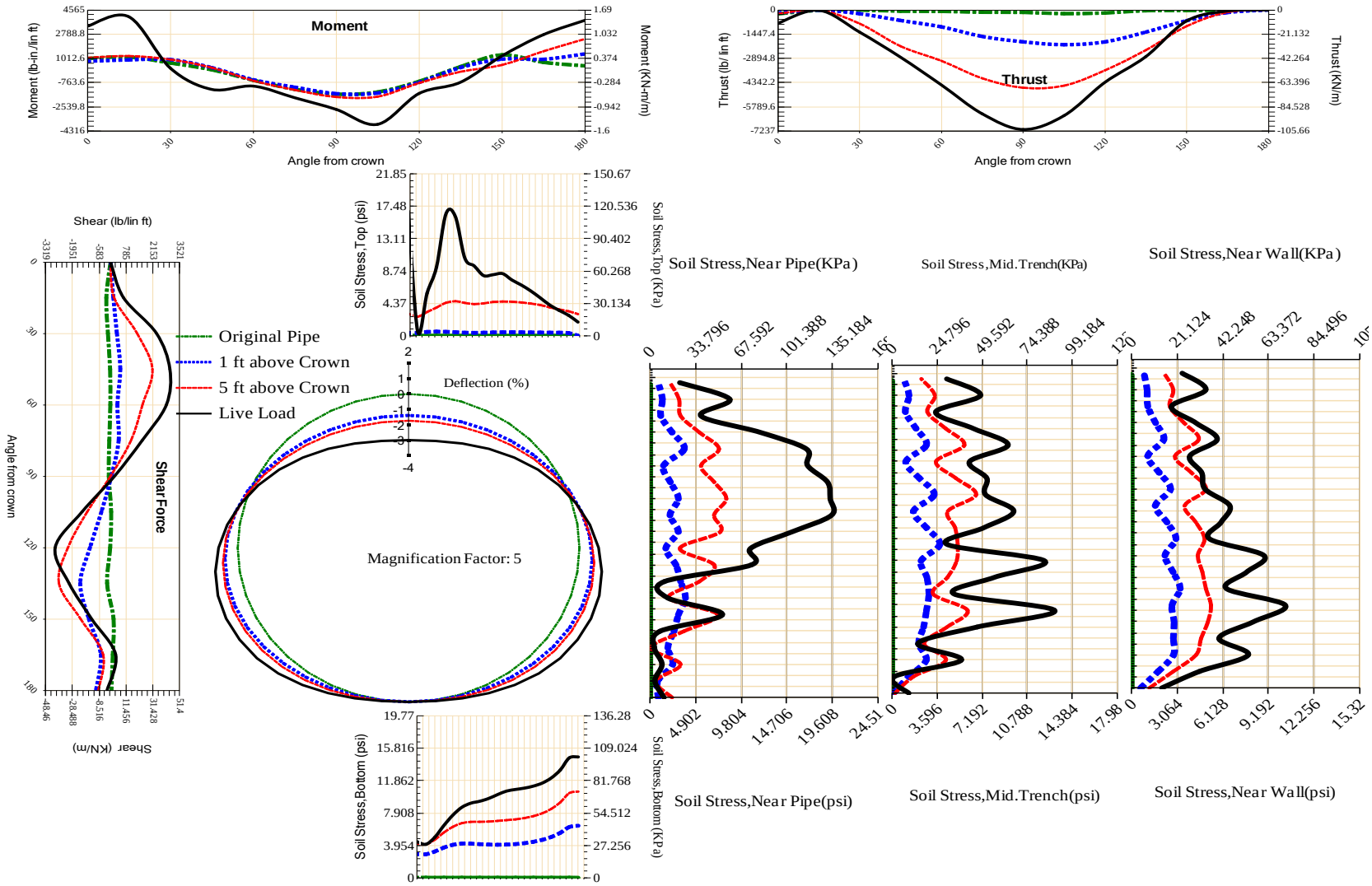

Figure A-131 Param-120-PW288-SF10SF-OD+108-EW3-H5-LiveLoad

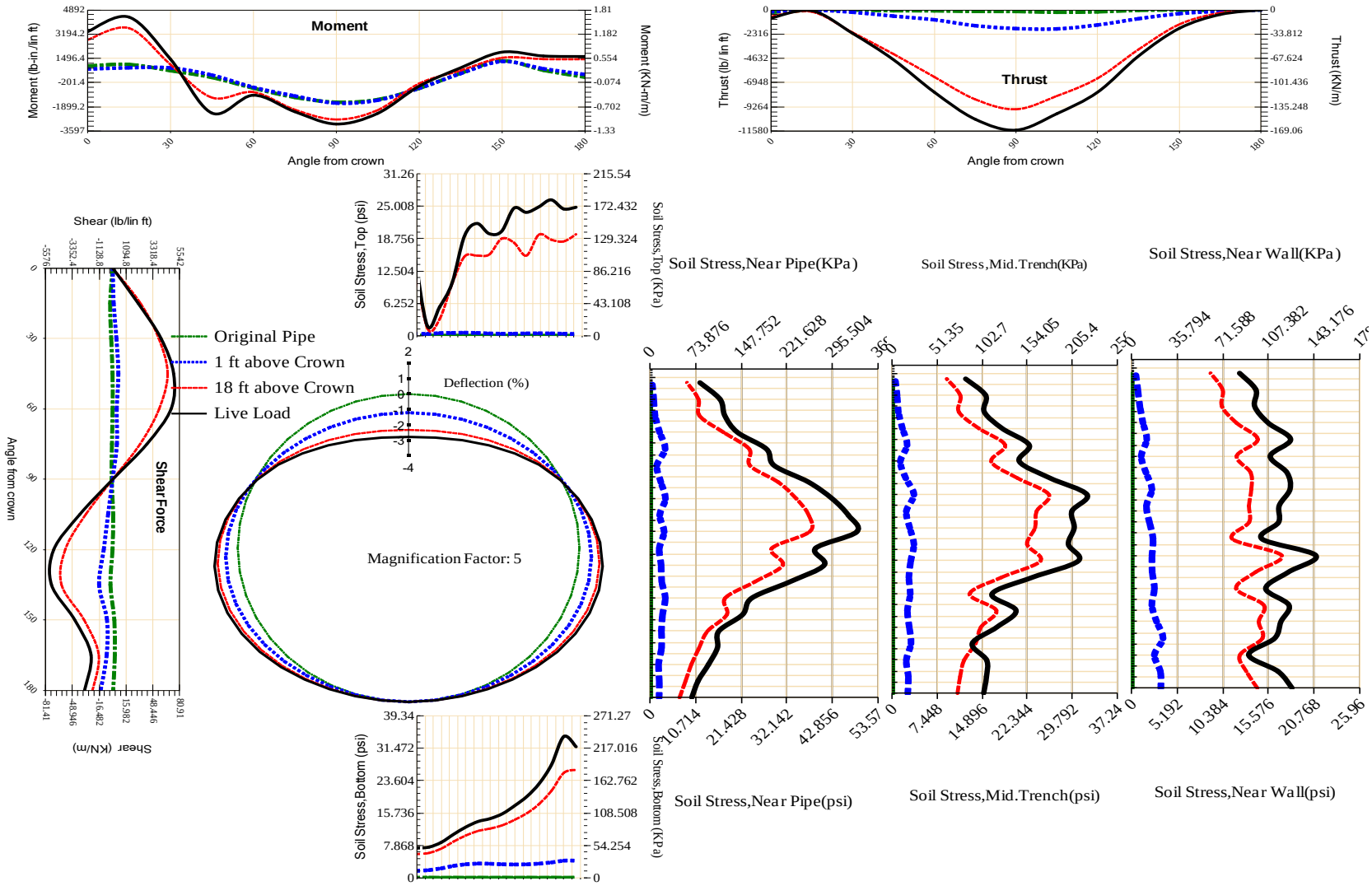

Figure A-132 Param-120-PW288-SF10SF-OD+48-EW10-H18-LiveLoad

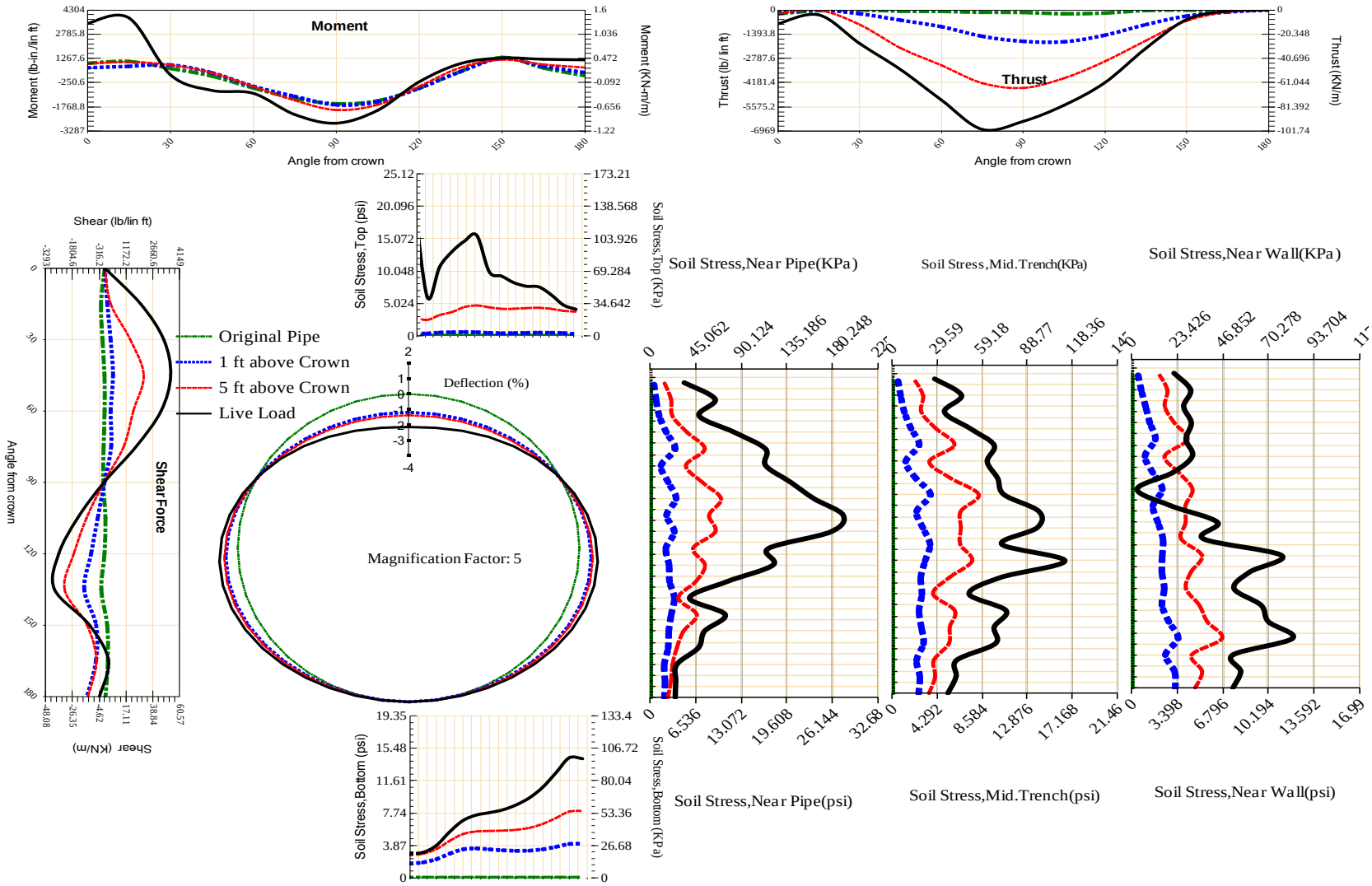

Figure A-133 Param-120-PW288-SF10SF-OD+48-EW10-H5-LiveLoad

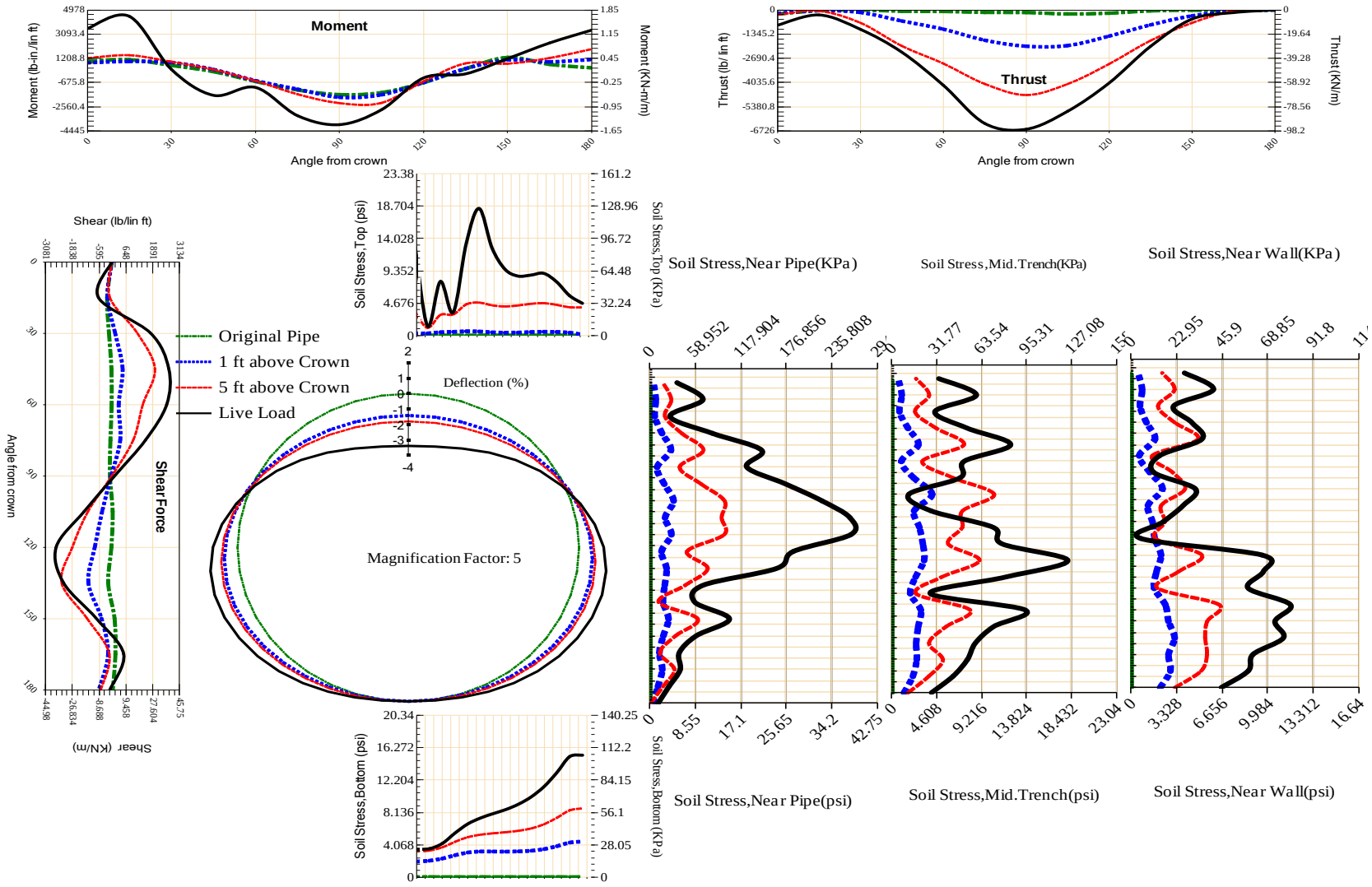

Figure A-134 Param-120-PW288-SF10SF-OD+48-EW3-H5-LiveLoad

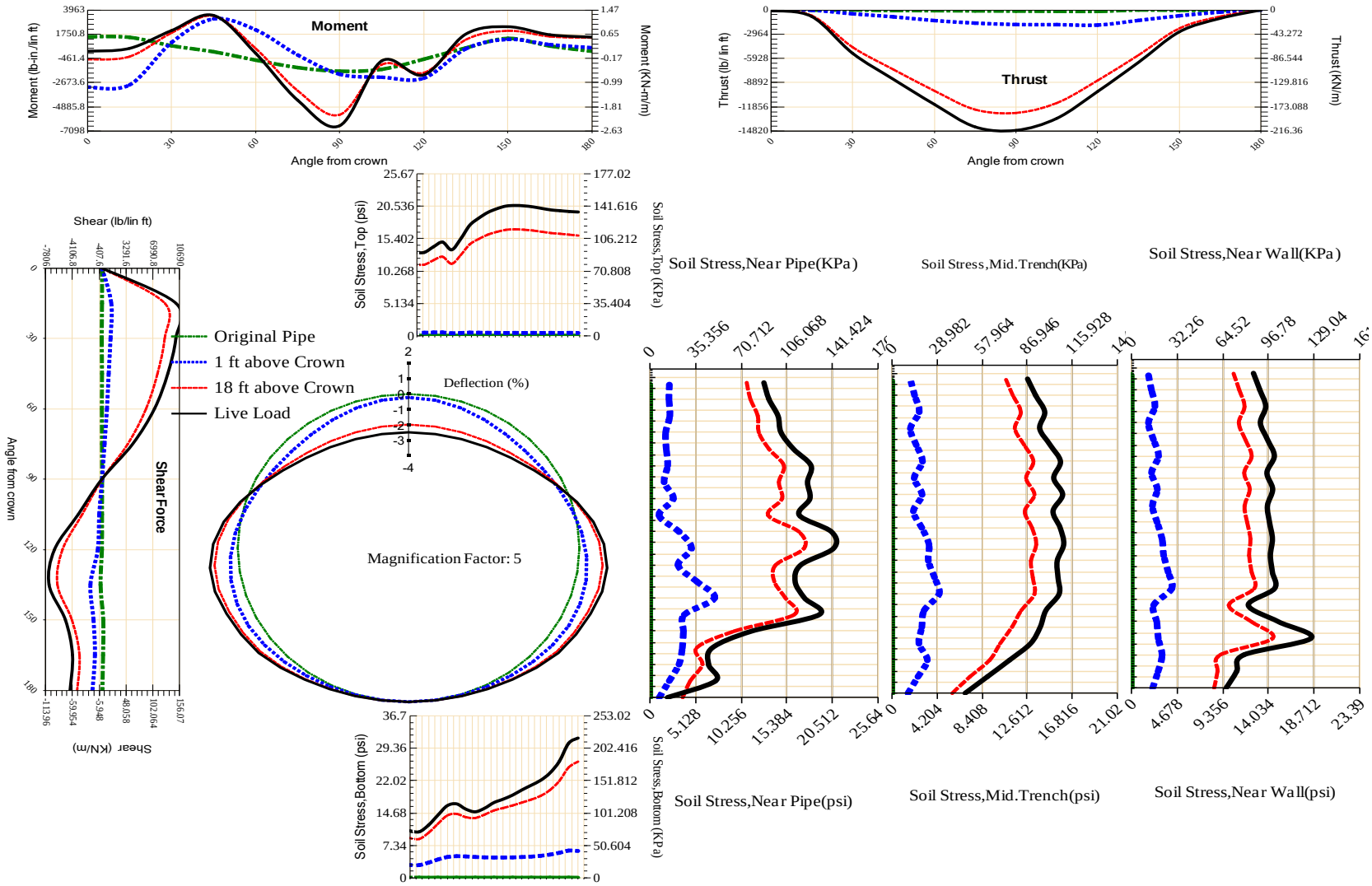

Figure A-135 Param-120-PW288-SF3OR-OD+108-EW10-H18-LiveLoad

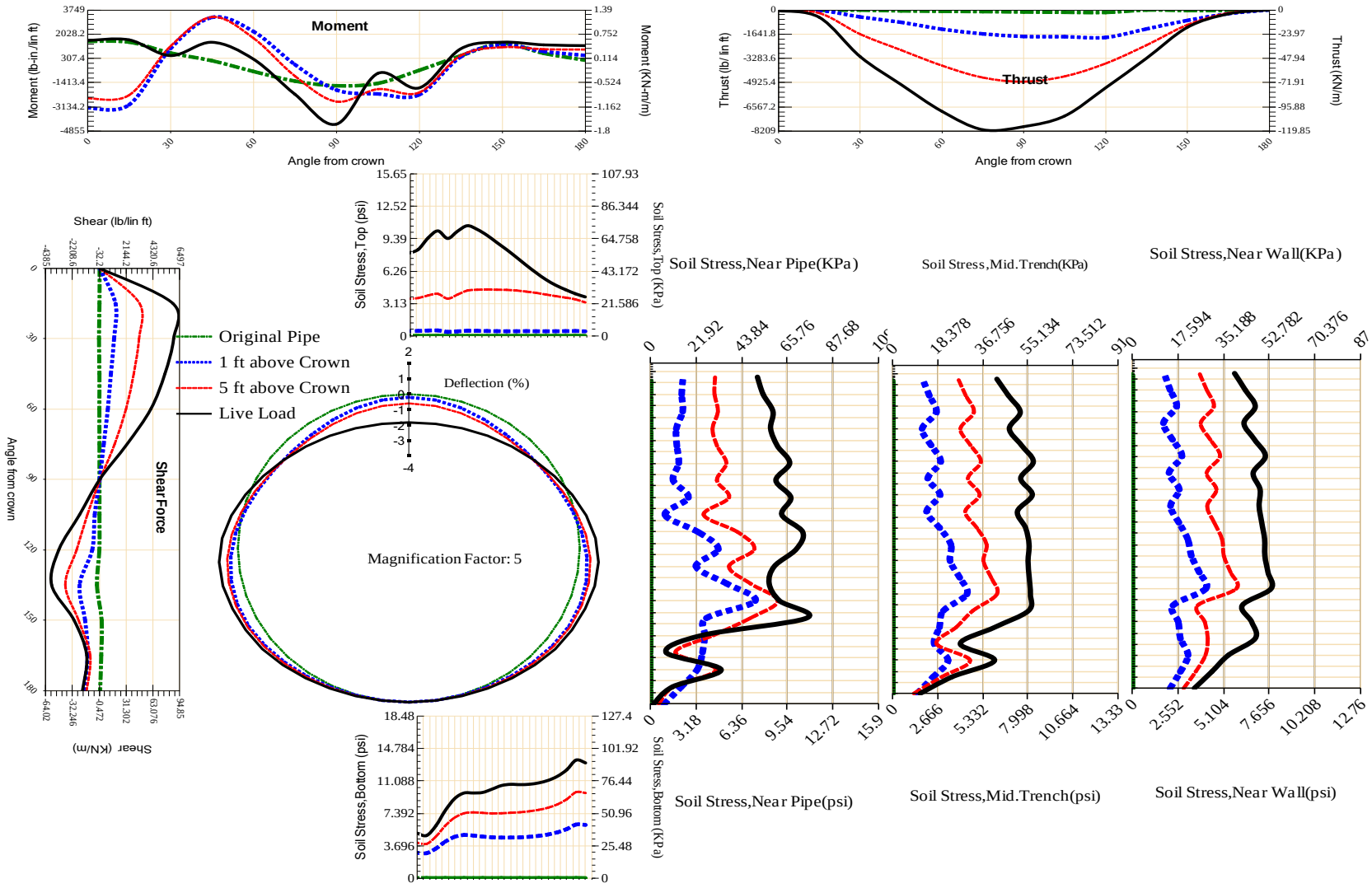

Figure A-136 Param-120-PW288-SF3OR-OD+108-EW10-H5-LiveLoad

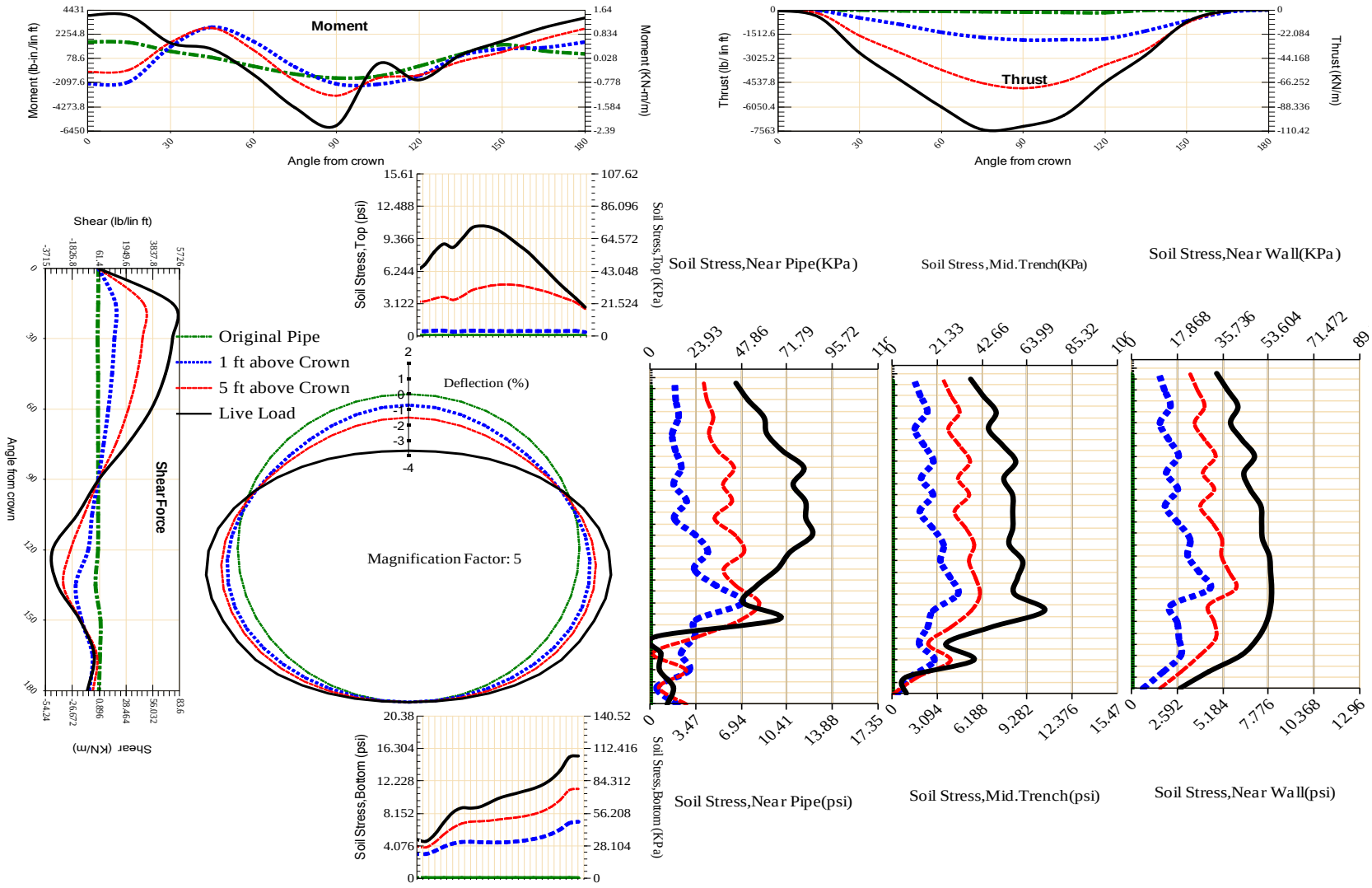

Figure A-137 Param-120-PW288-SF3OR-OD+108-EW3-H5-LiveLoad

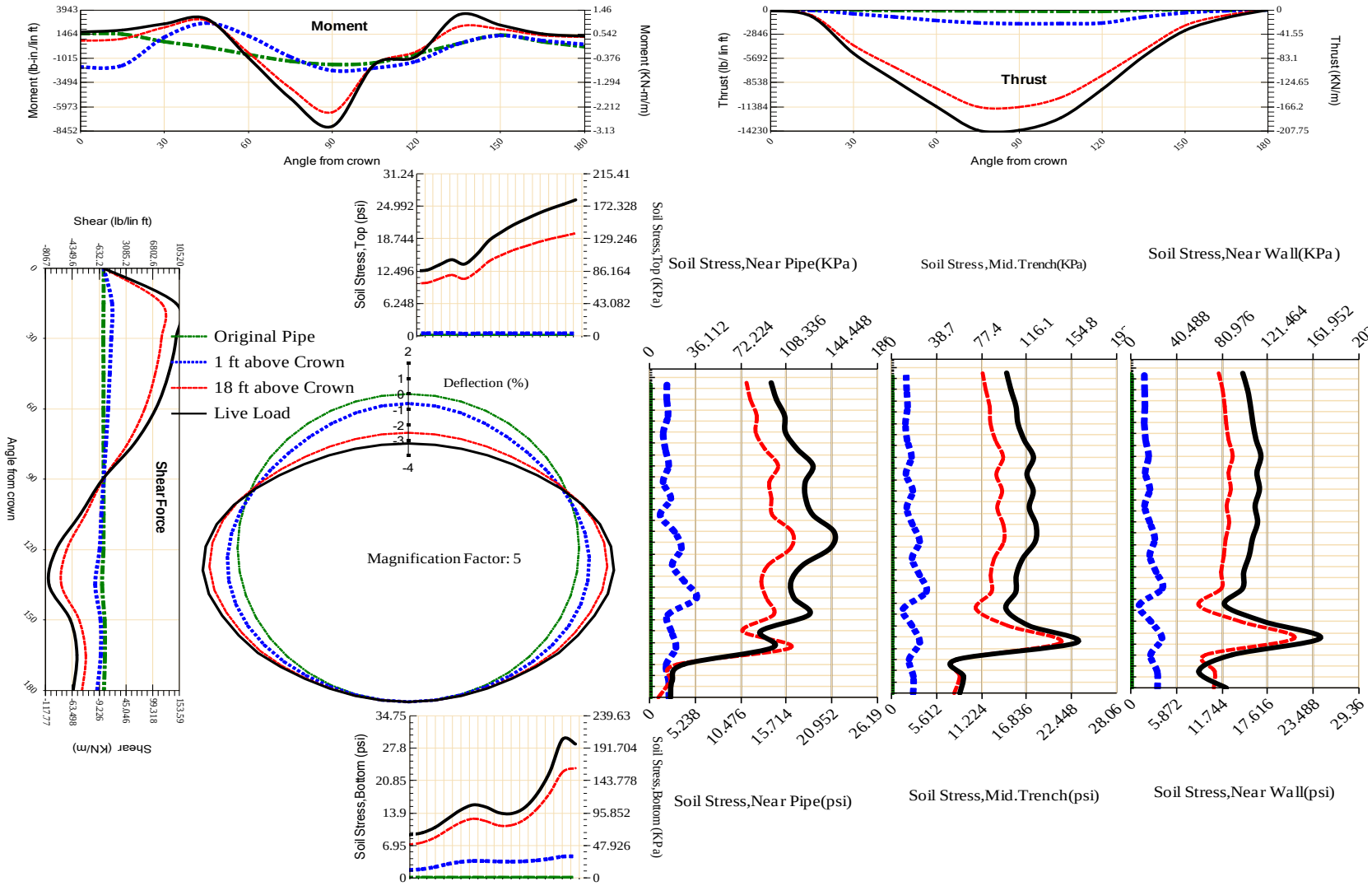

Figure A-138 Param-120-PW288-SF3OR-OD+48-EW10-H18-LiveLoad

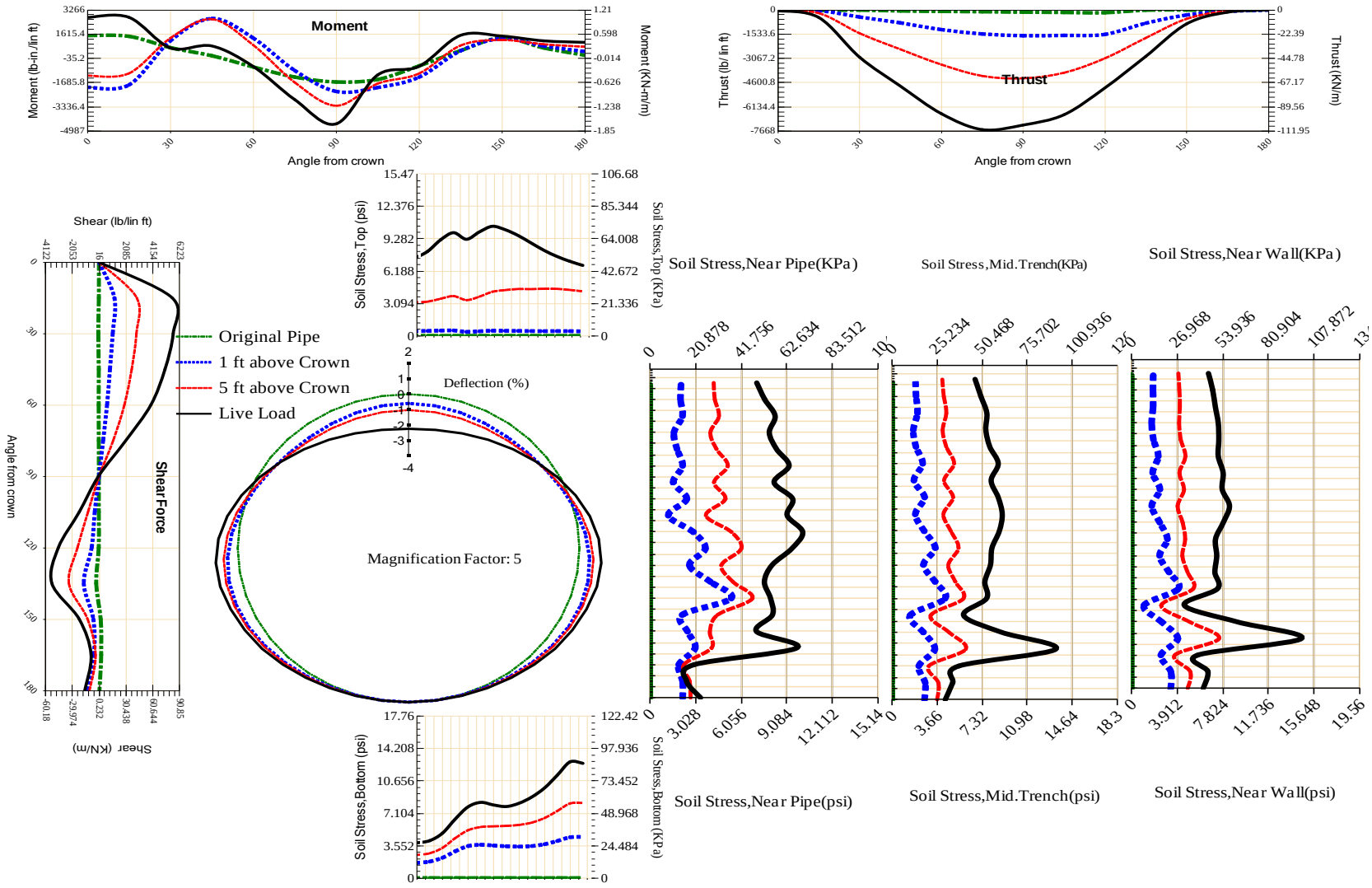

Figure A-139 Param-120-PW288-SF3OR-OD+48-EW10-H5-LiveLoad

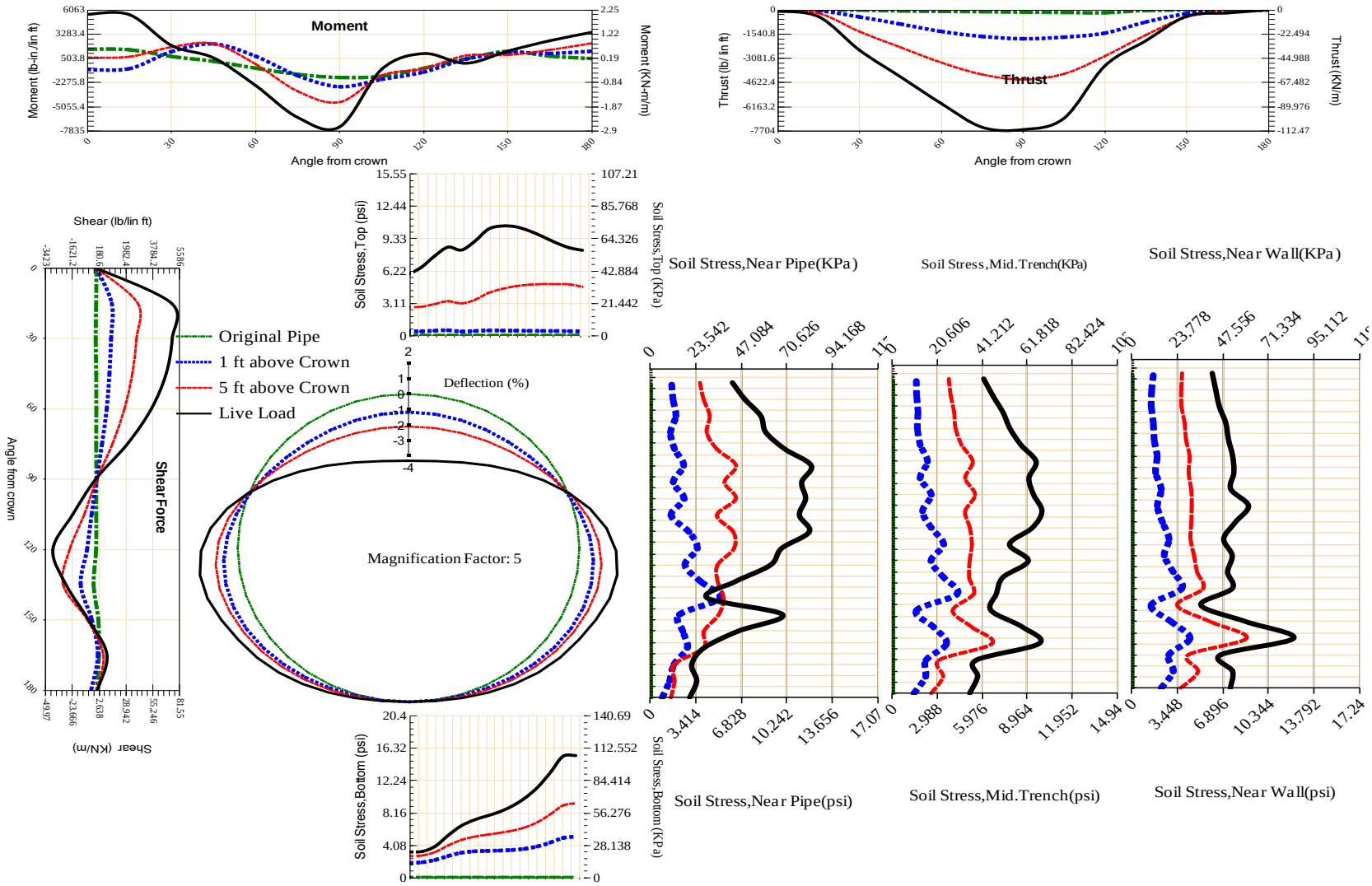

Figure A-140 Param-120-PW288-SF3OR-OD+48-EW3-H5-LiveLoad

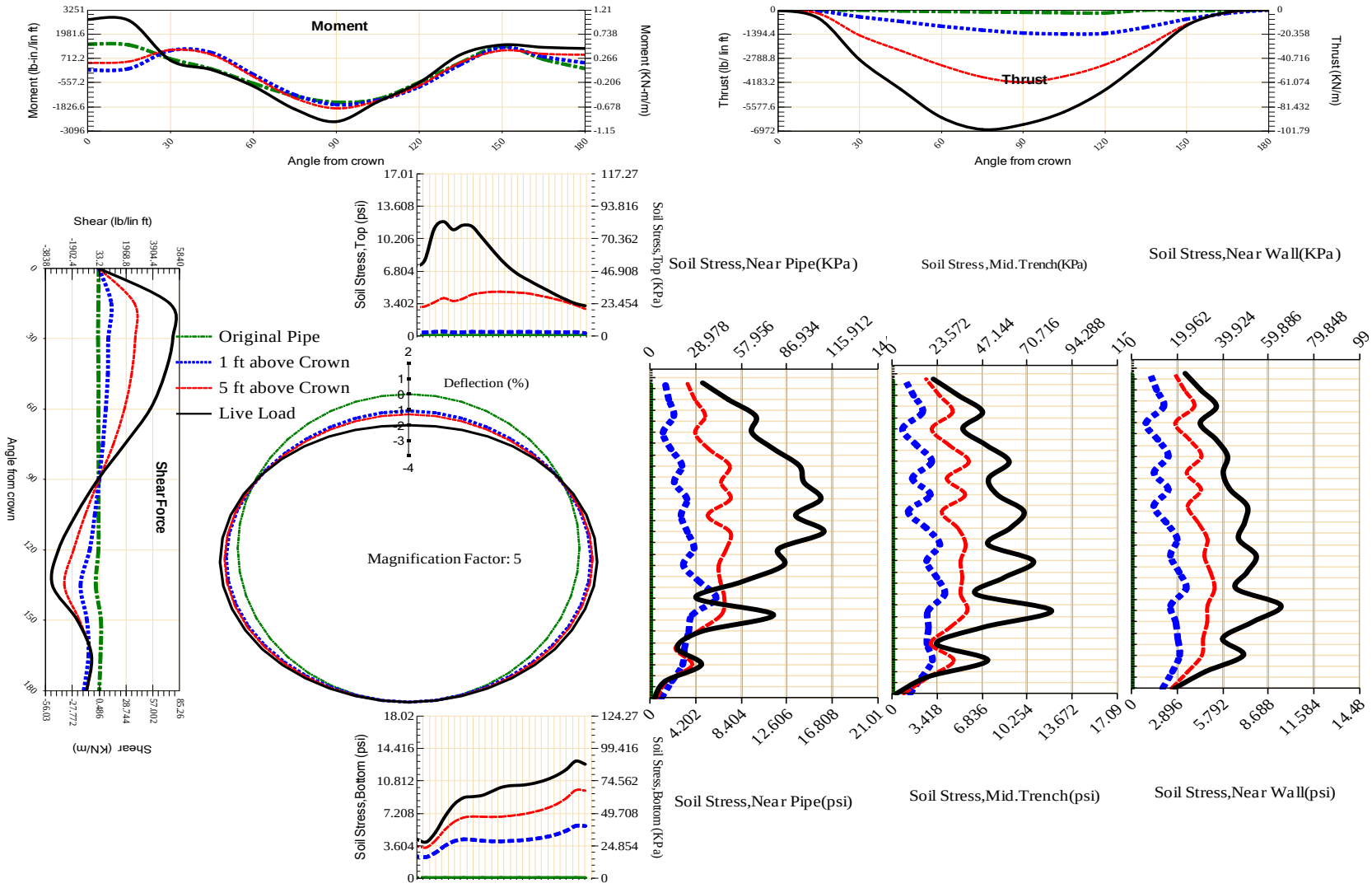

Figure A-141 Param-120-PW288-SF3TR-OD+108-EW10-H5-LiveLoad

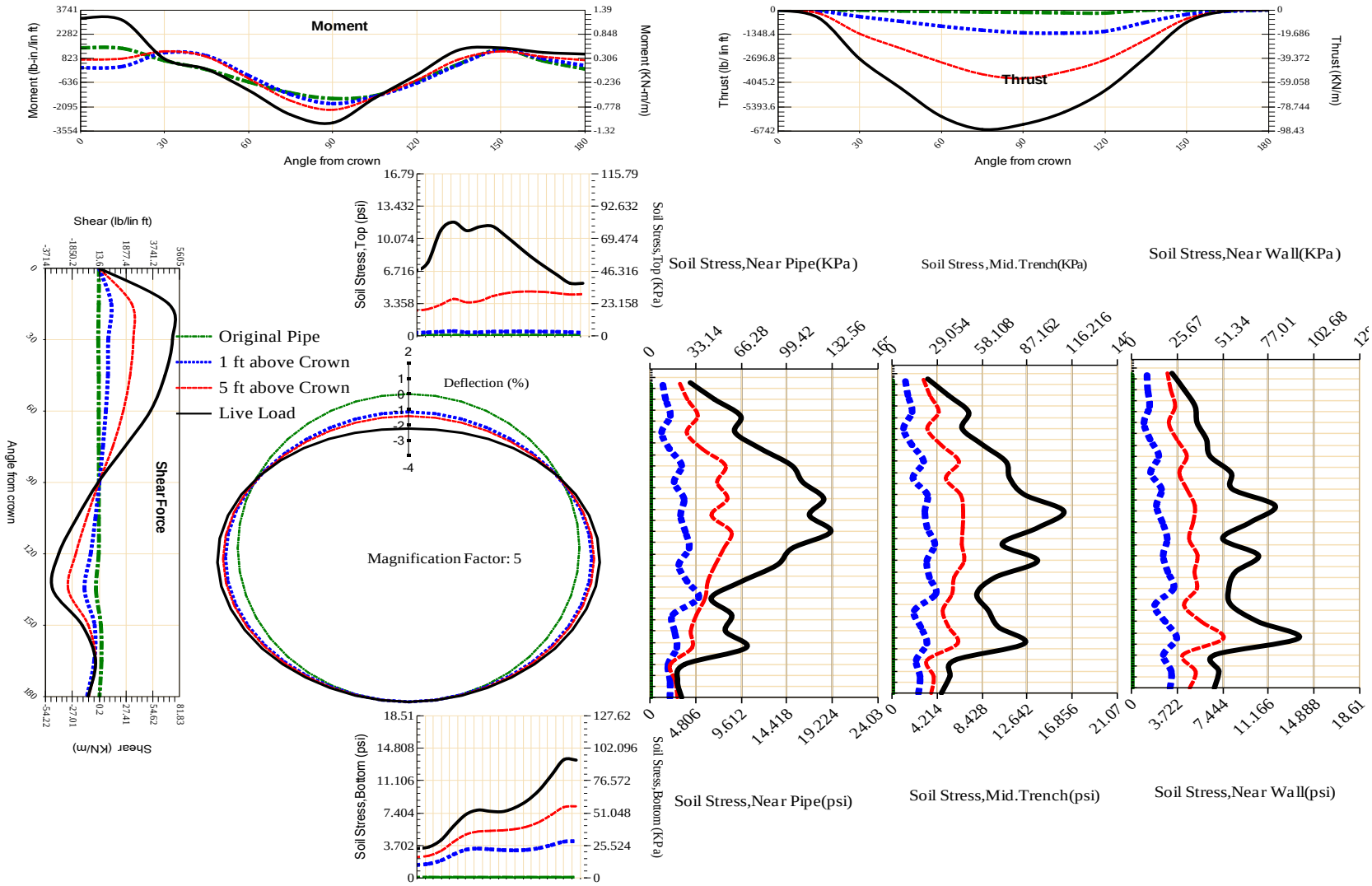

Figure A-142 Param-120-PW288-SF3TR-OD+48-EW10-H5-LiveLoad

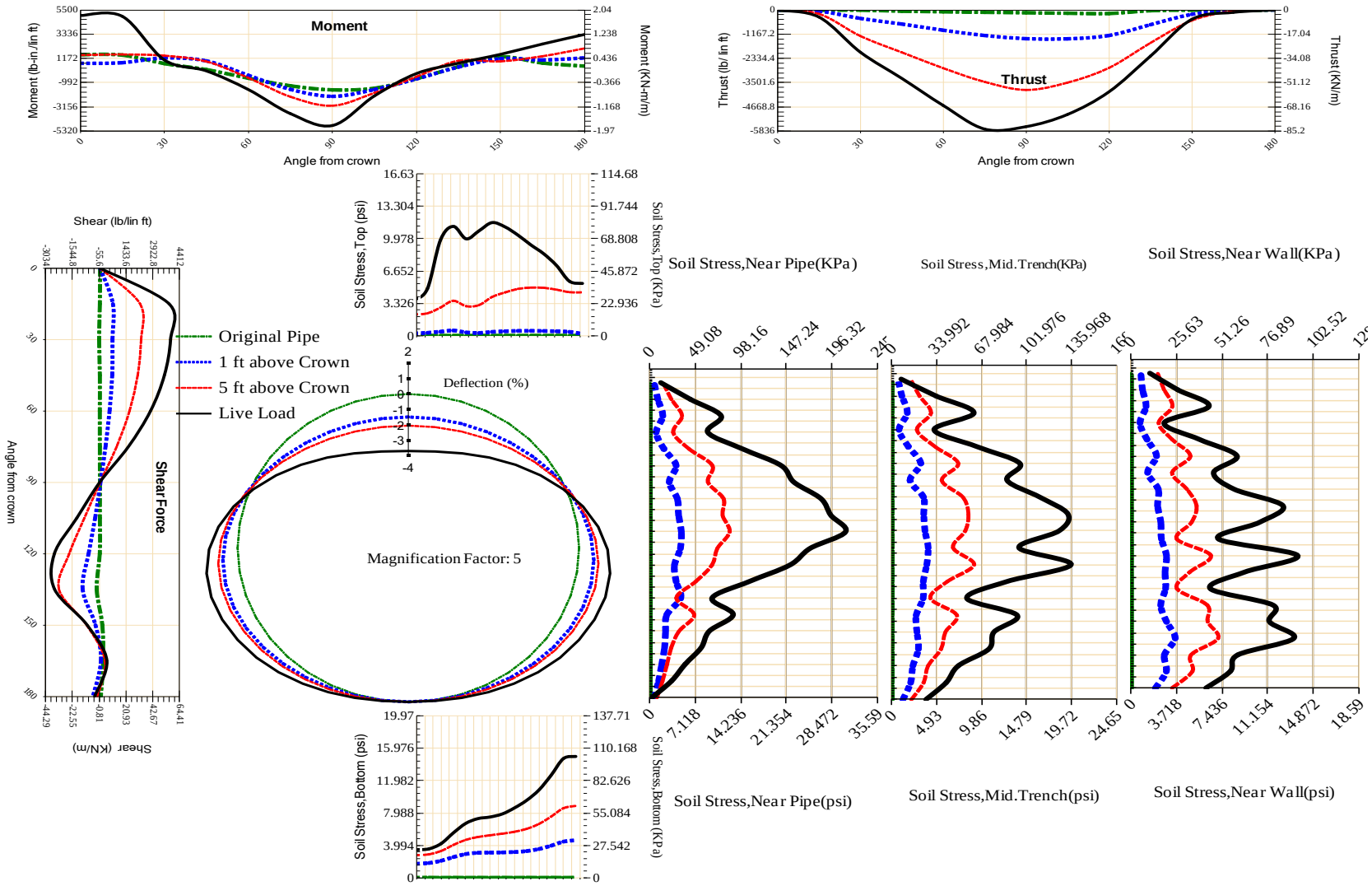

Figure A-143 Param-120-PW288-SF3TR-OD+48-EW3-H5-LiveLoad

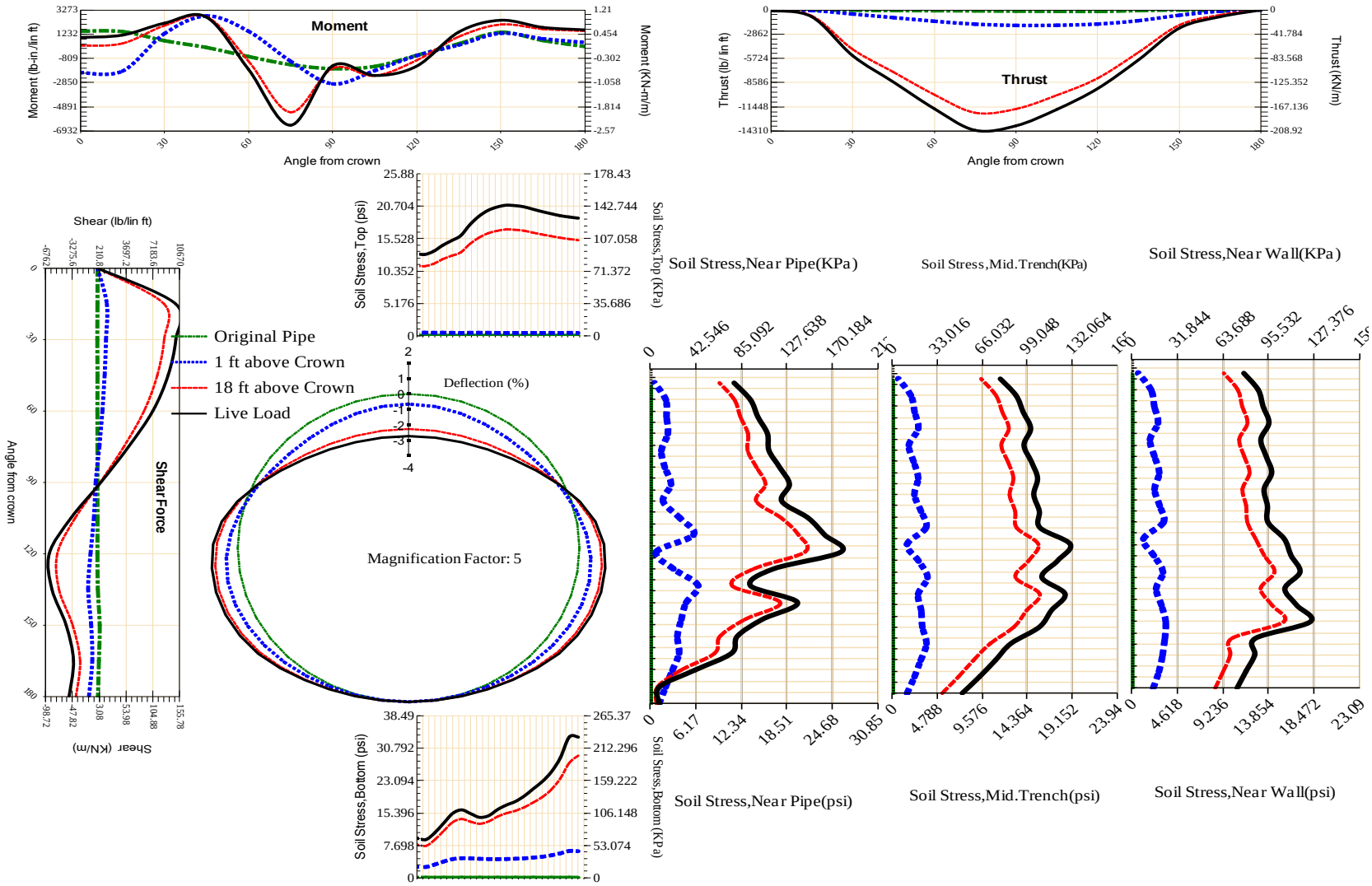

Figure A-144 Param-120-PW288-SF5OR-OD+108-EW10-H18-LiveLoad

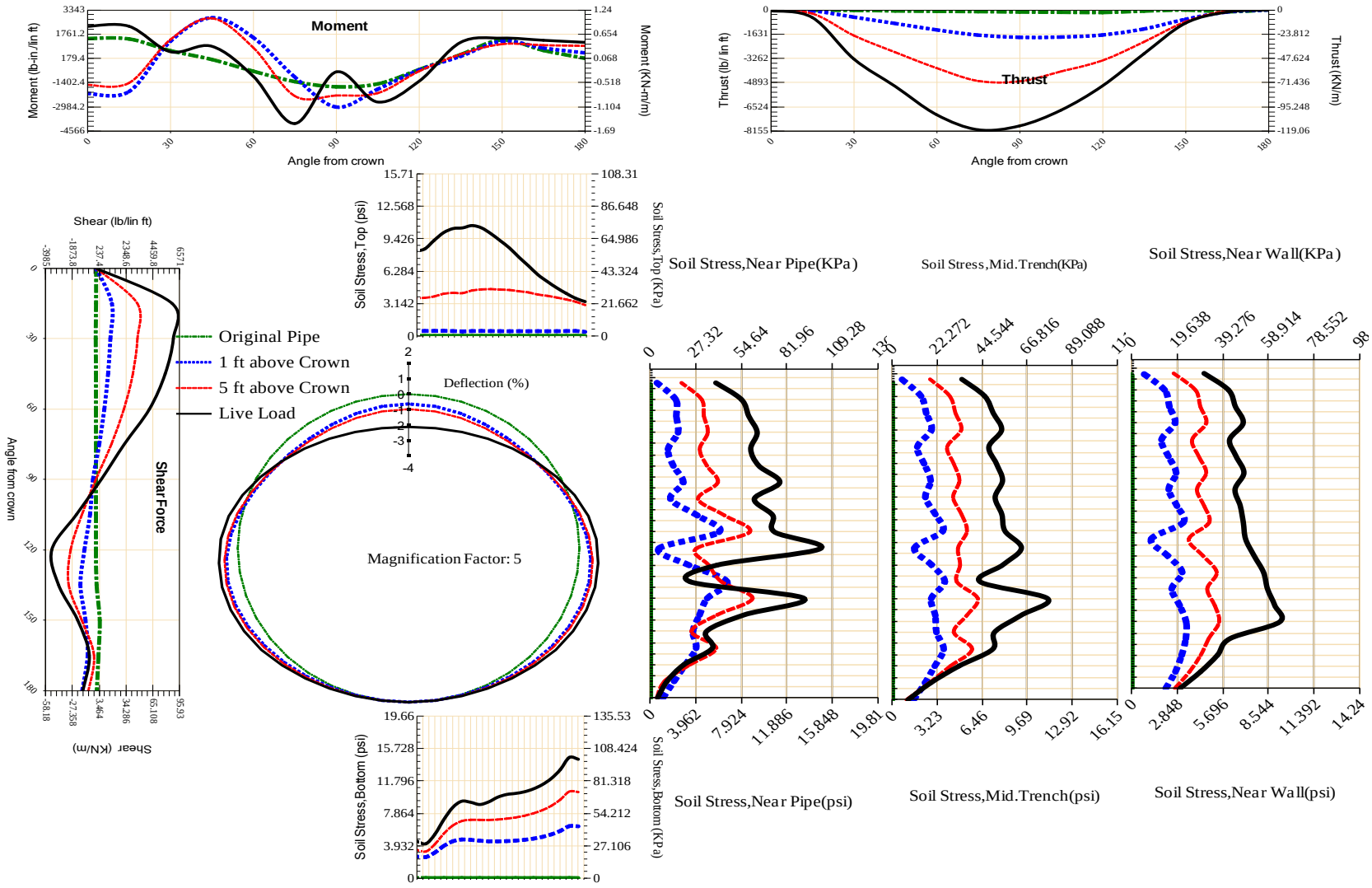

Figure A-145 Param-120-PW288-SF5OR-OD+108-EW10-H5-LiveLoad

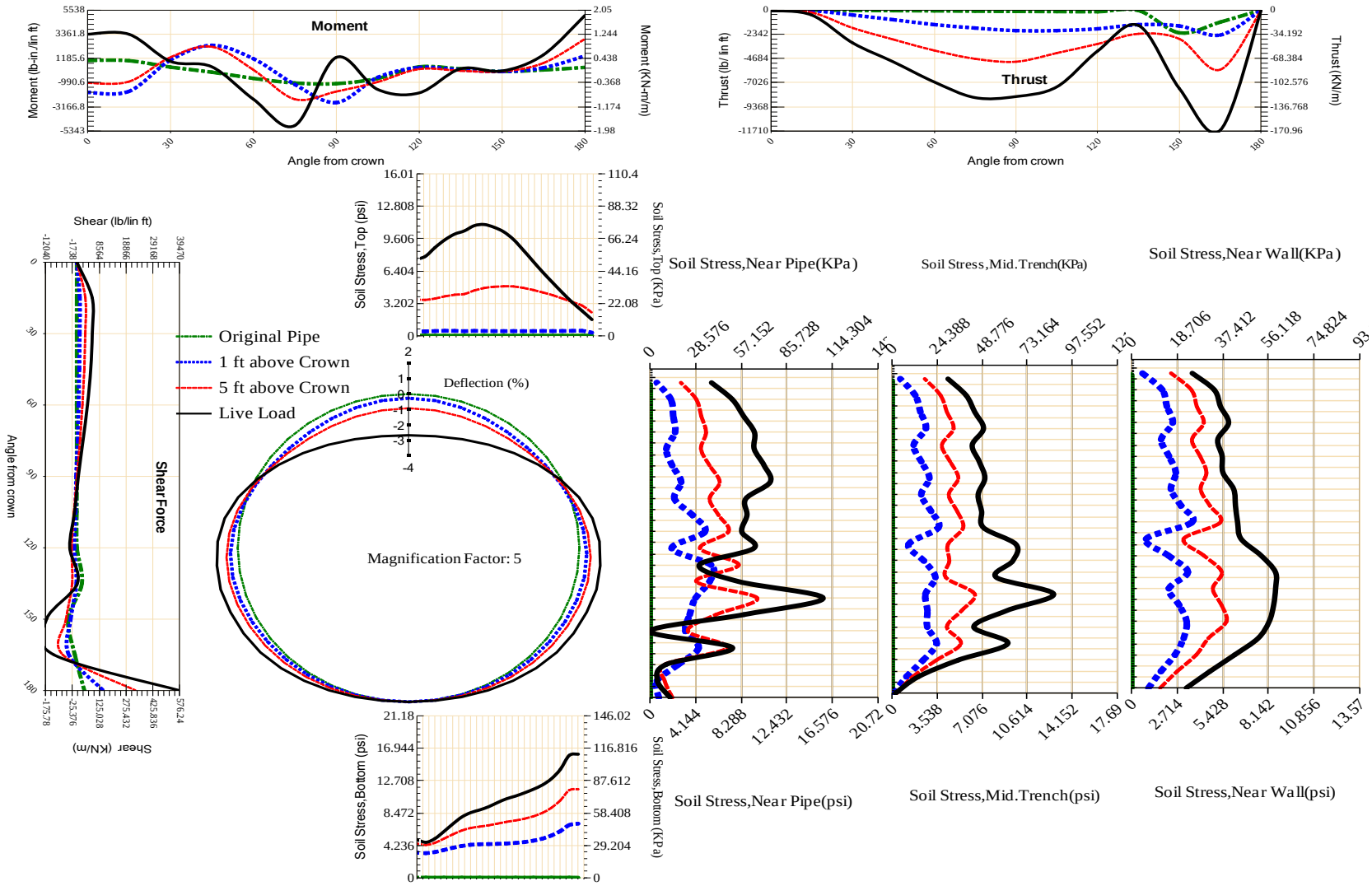

Figure A-146 Param-120-PW288-SF5OR-OD+108-EW3-H5-LiveLoad

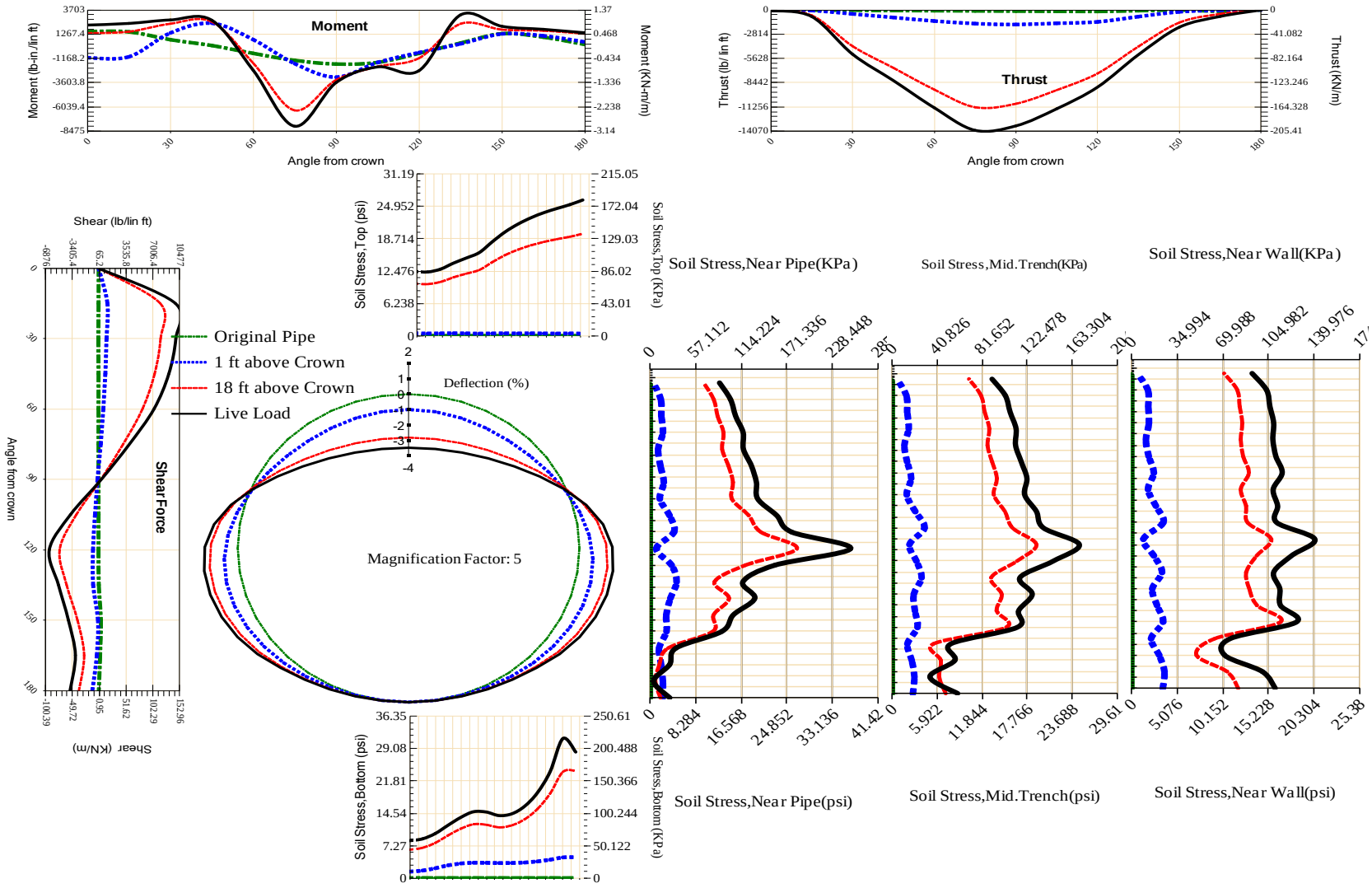

Figure A-147 Param-120-PW288-SF5OR-OD+48-EW10-H18-LiveLoad

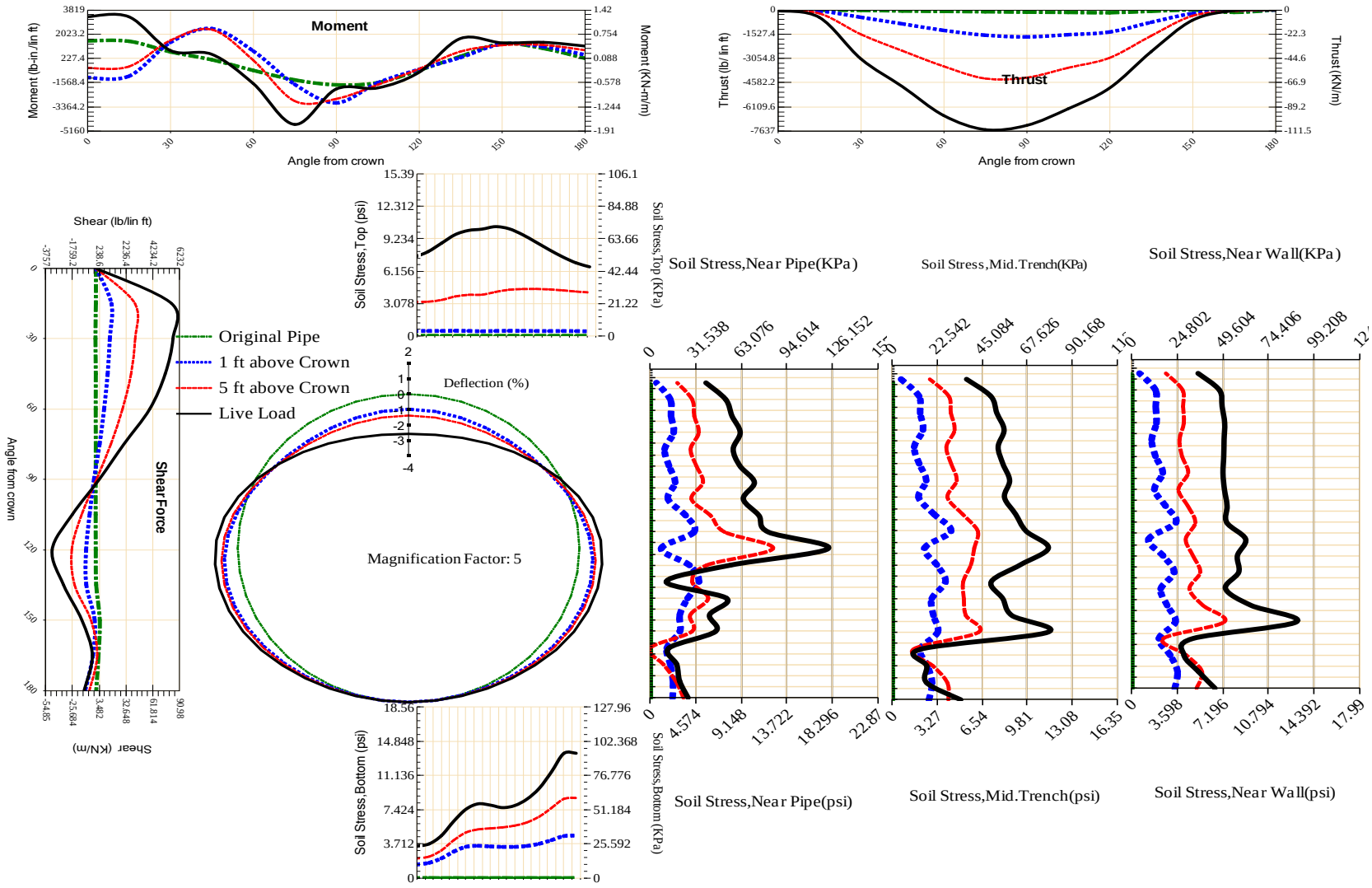

Figure A-148 Param-120-PW288-SF5OR-OD+48-EW10-H5-LiveLoad

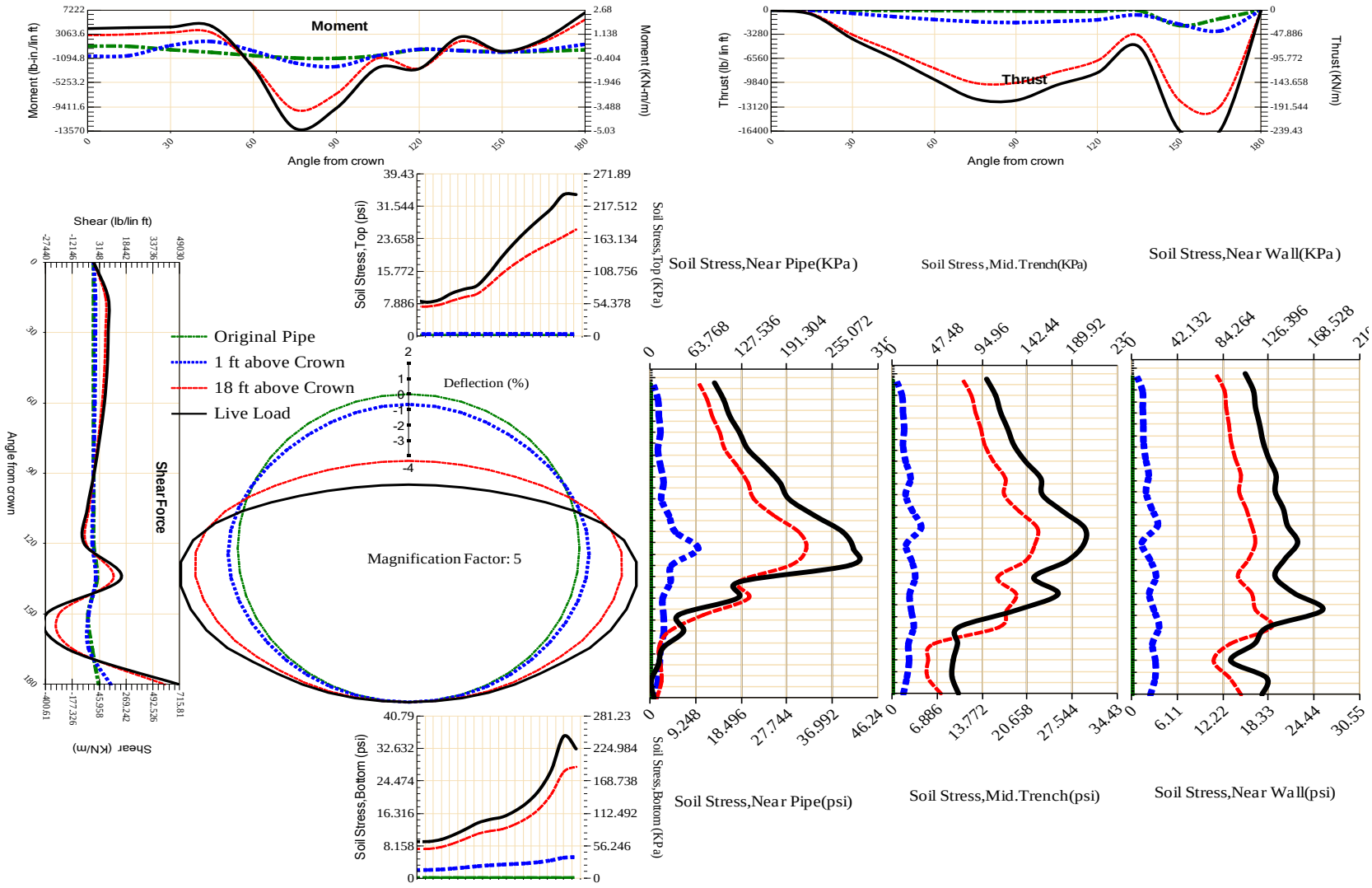

Figure A-149 Param-120-PW288-SF5OR-OD+48-EW3-H18-LiveLoad

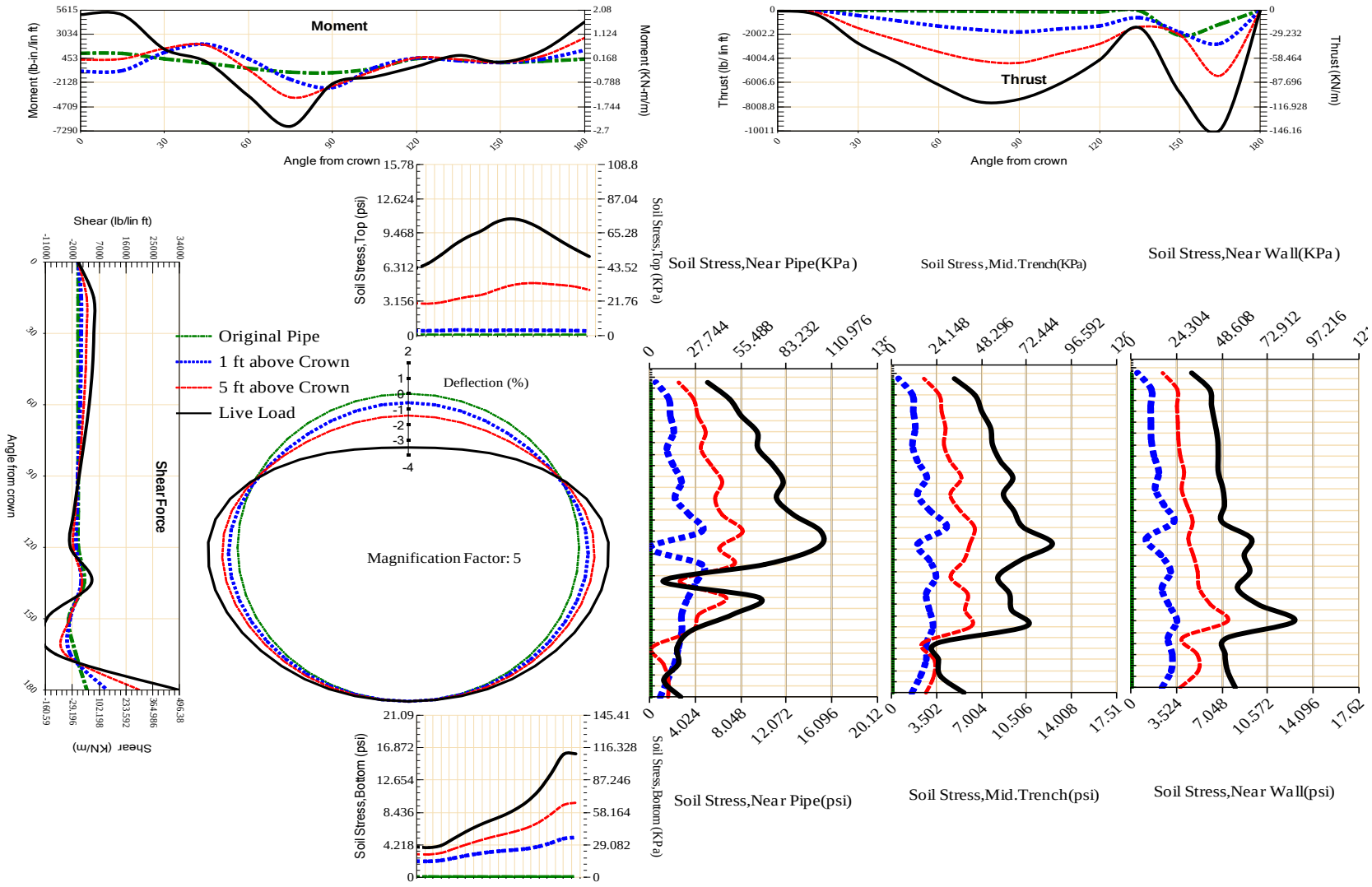

Figure A-150 Param-120-PW288-SF5OR-OD+48-EW3-H5-LiveLoad

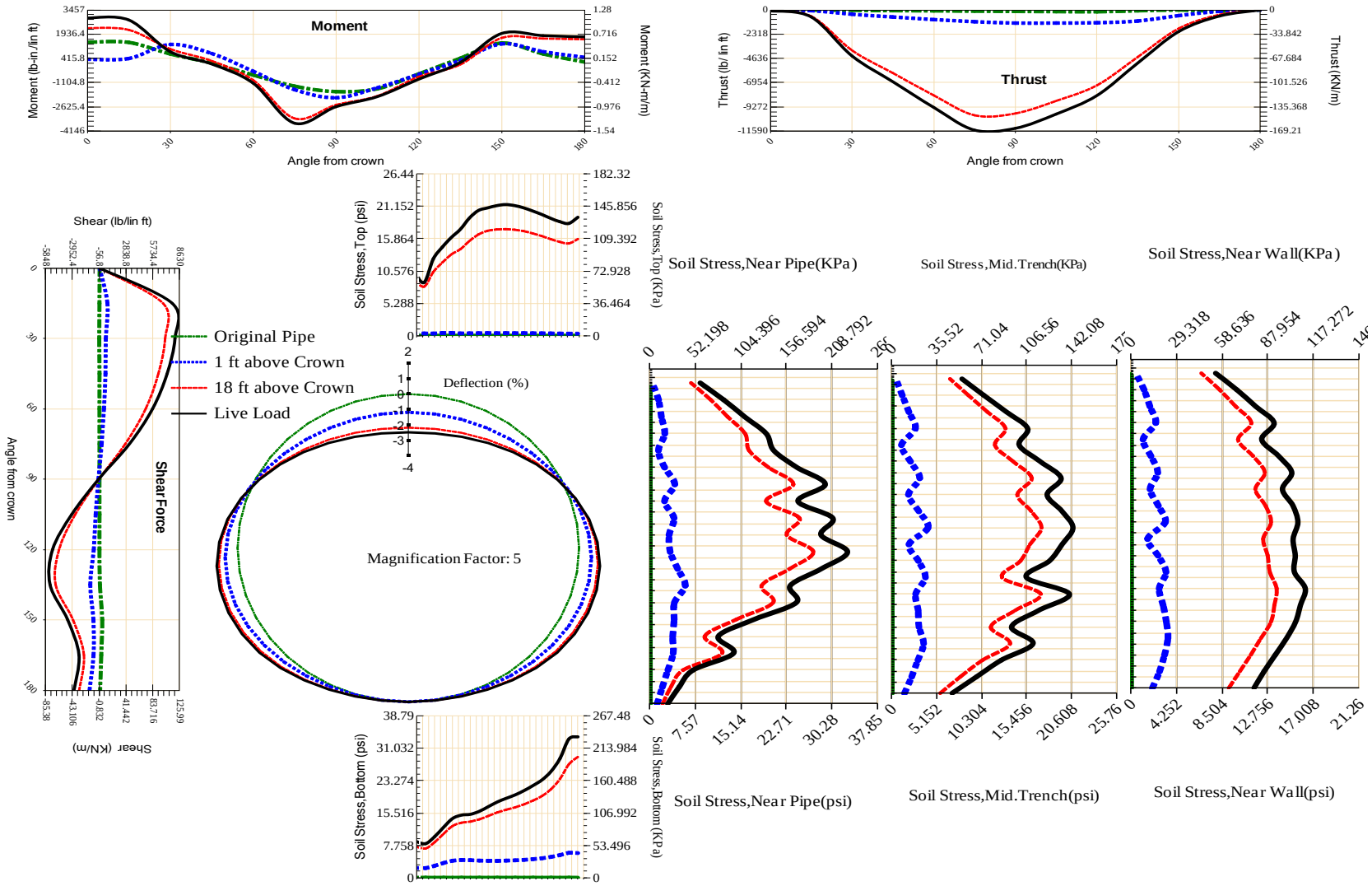

Figure A-151 Param-120-PW288-SF5TR-OD+108-EW10-H18-LiveLoad

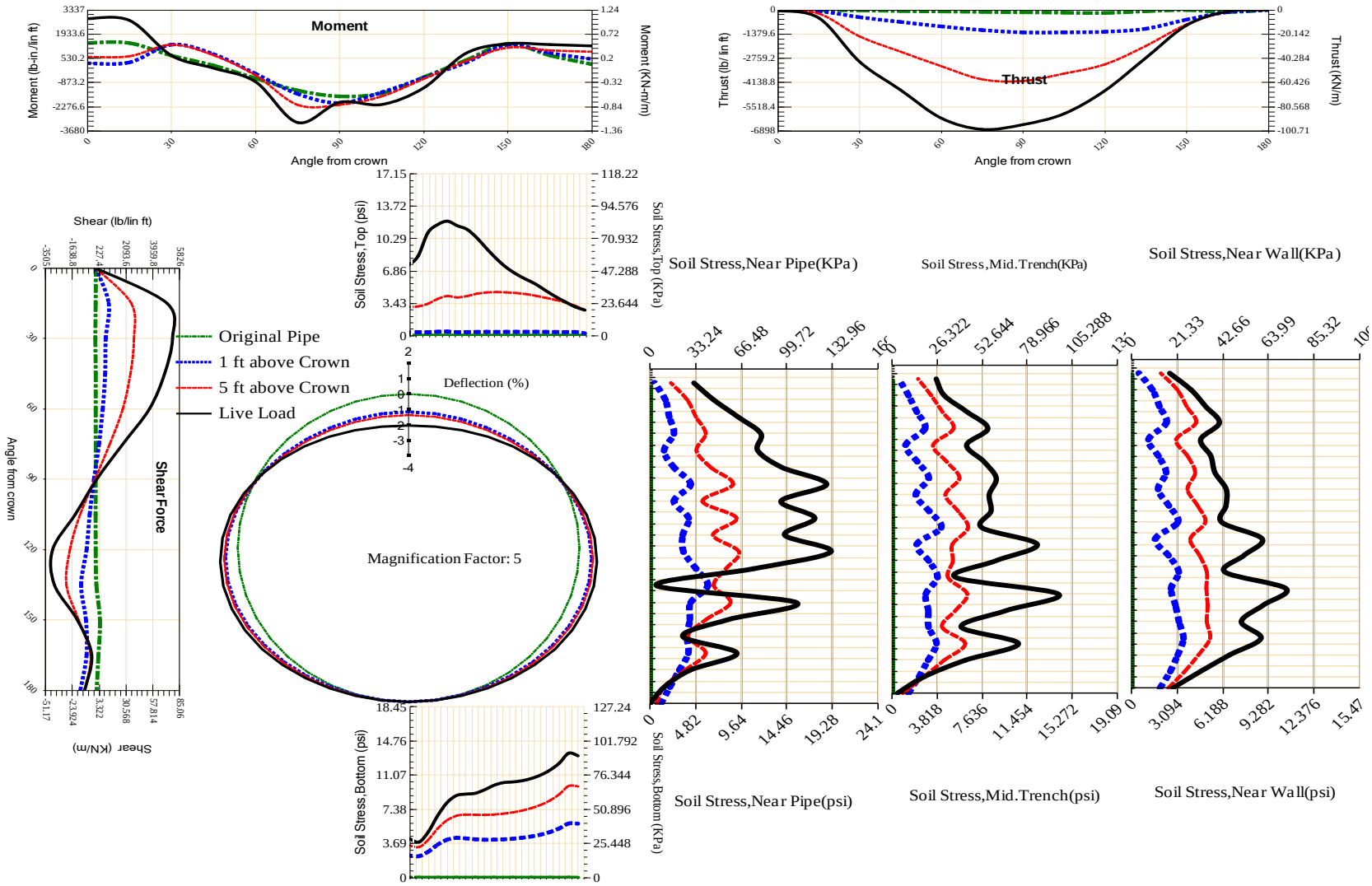

Figure A-152 Param-120-PW288-SF5TR-OD+108-EW10-H5-LiveLoad

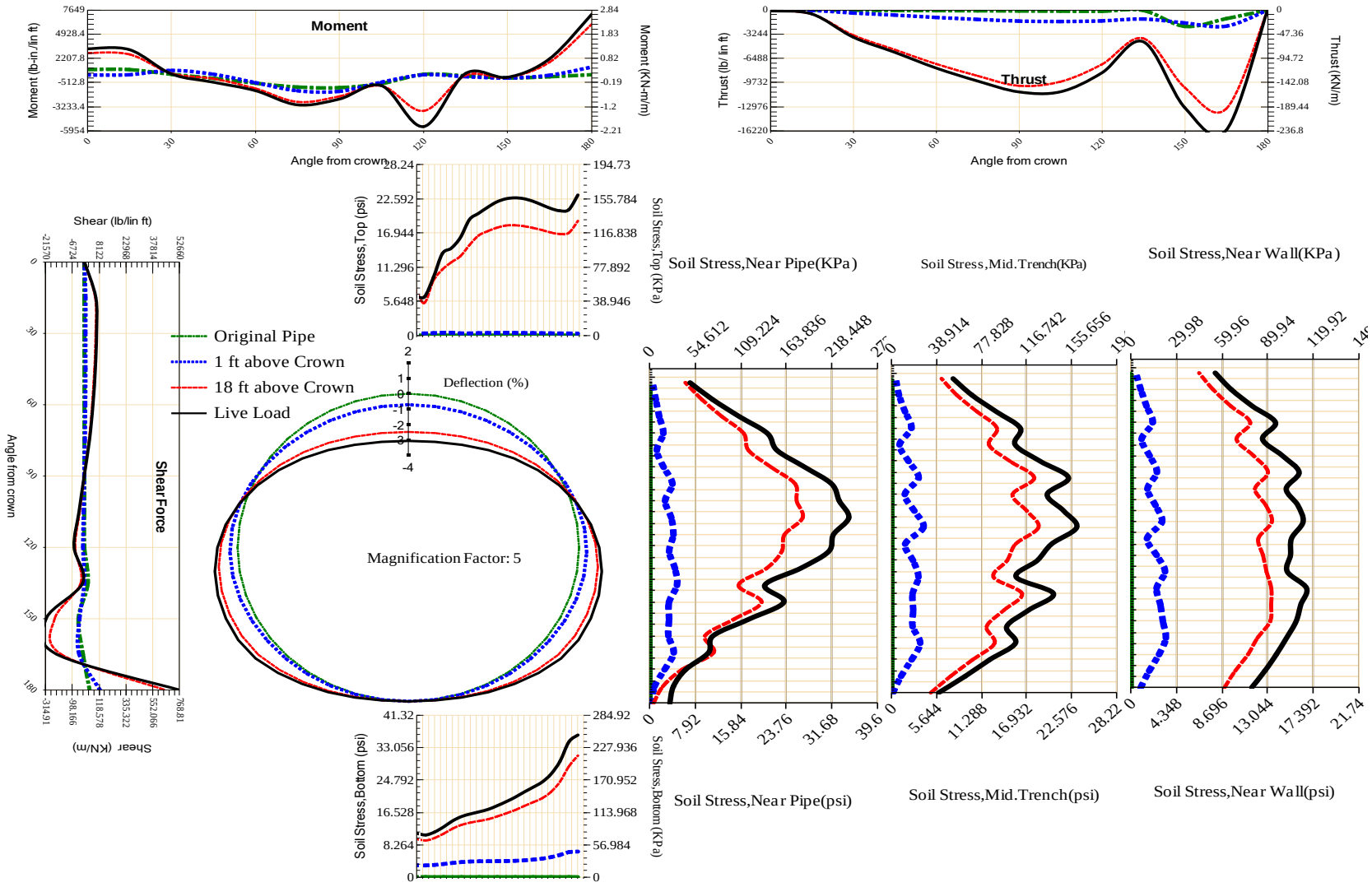

Figure A-153 Param-120-PW288-SF5TR-OD+108-EW3-H18-LiveLoad

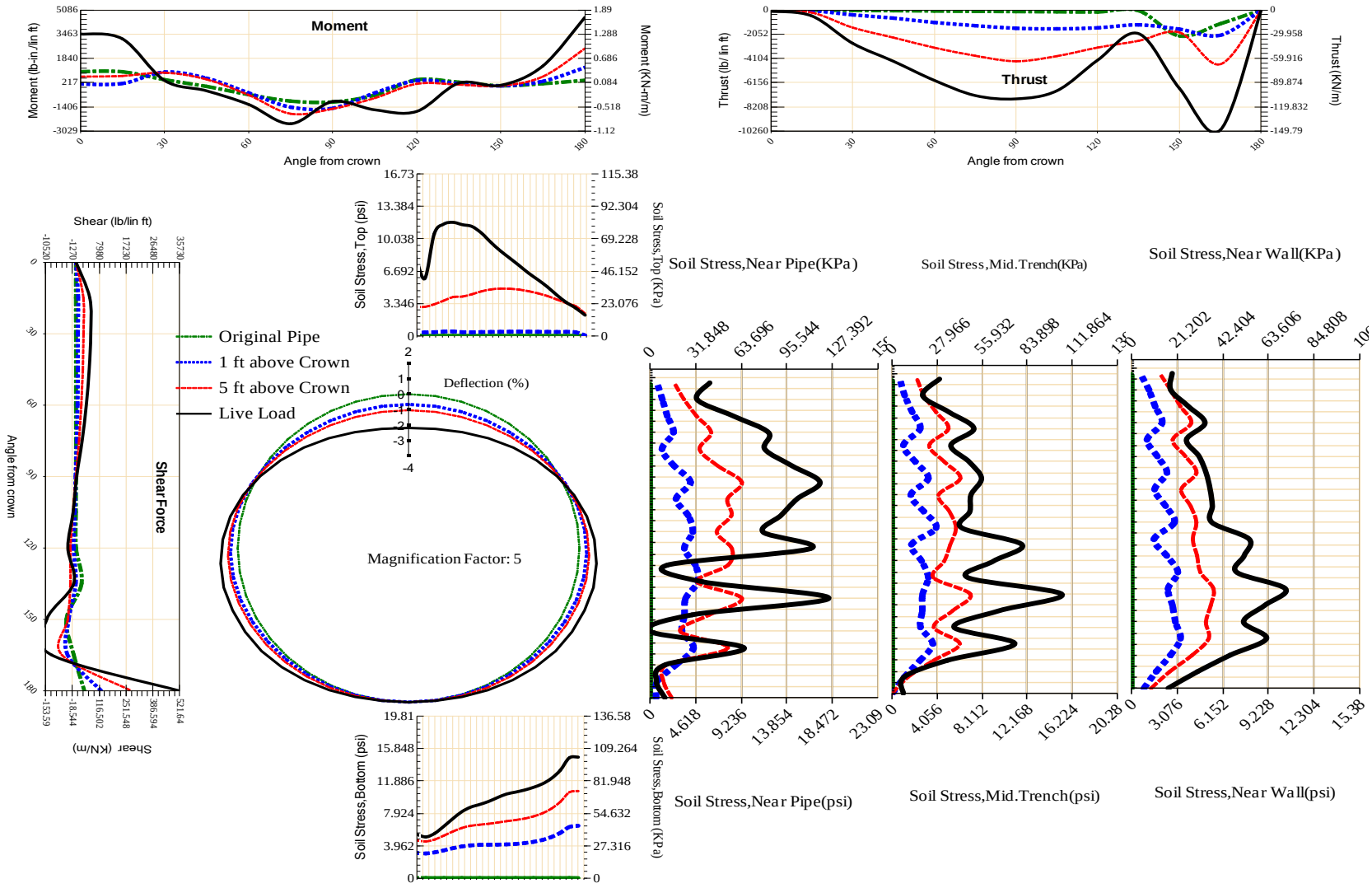

Figure A-154 Param-120-PW288-SF5TR-OD+108-EW3-H5-LiveLoad

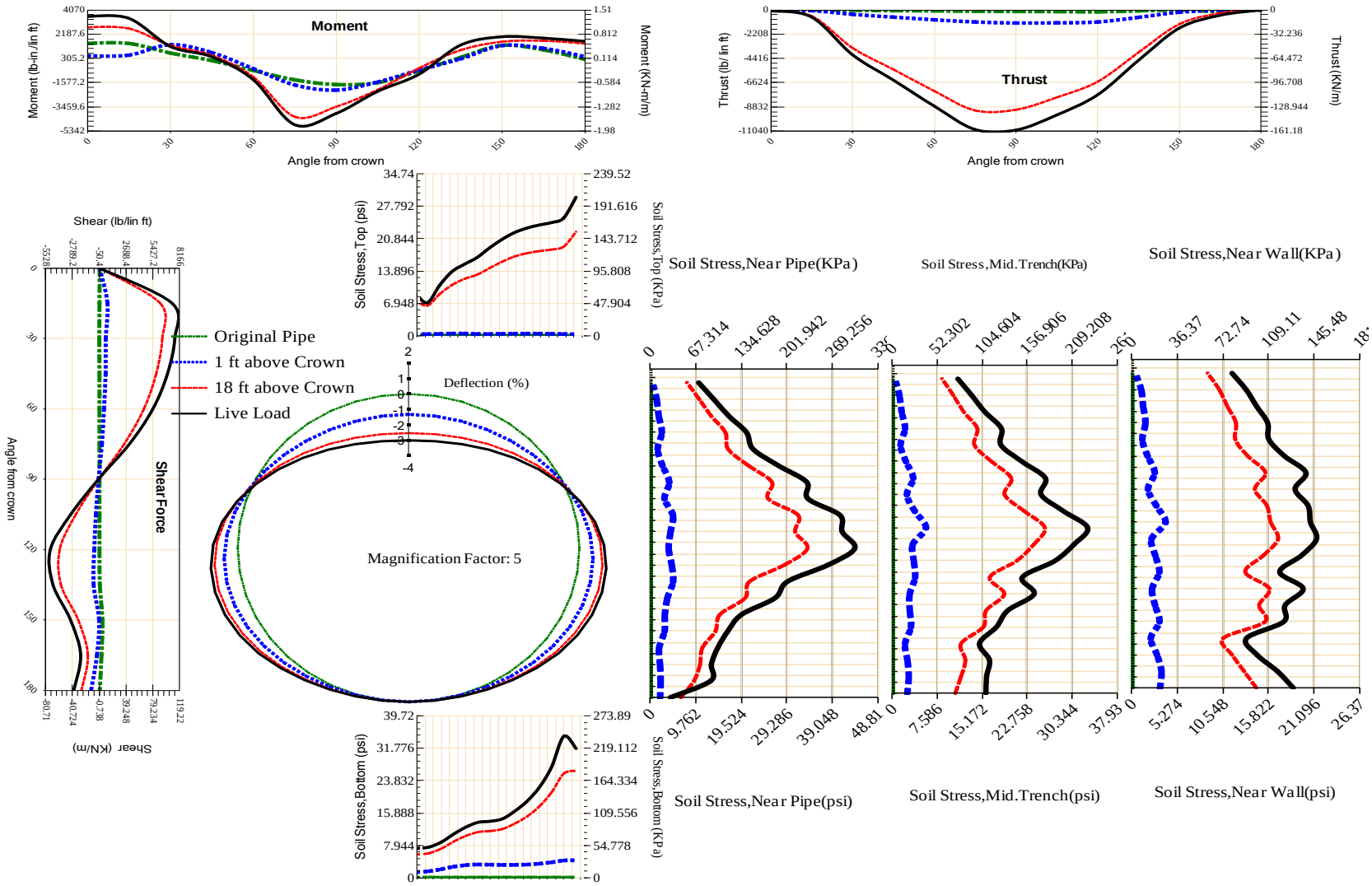

Figure A-155 Param-120-PW288-SF5TR-OD+48-EW10-H18-LiveLoad

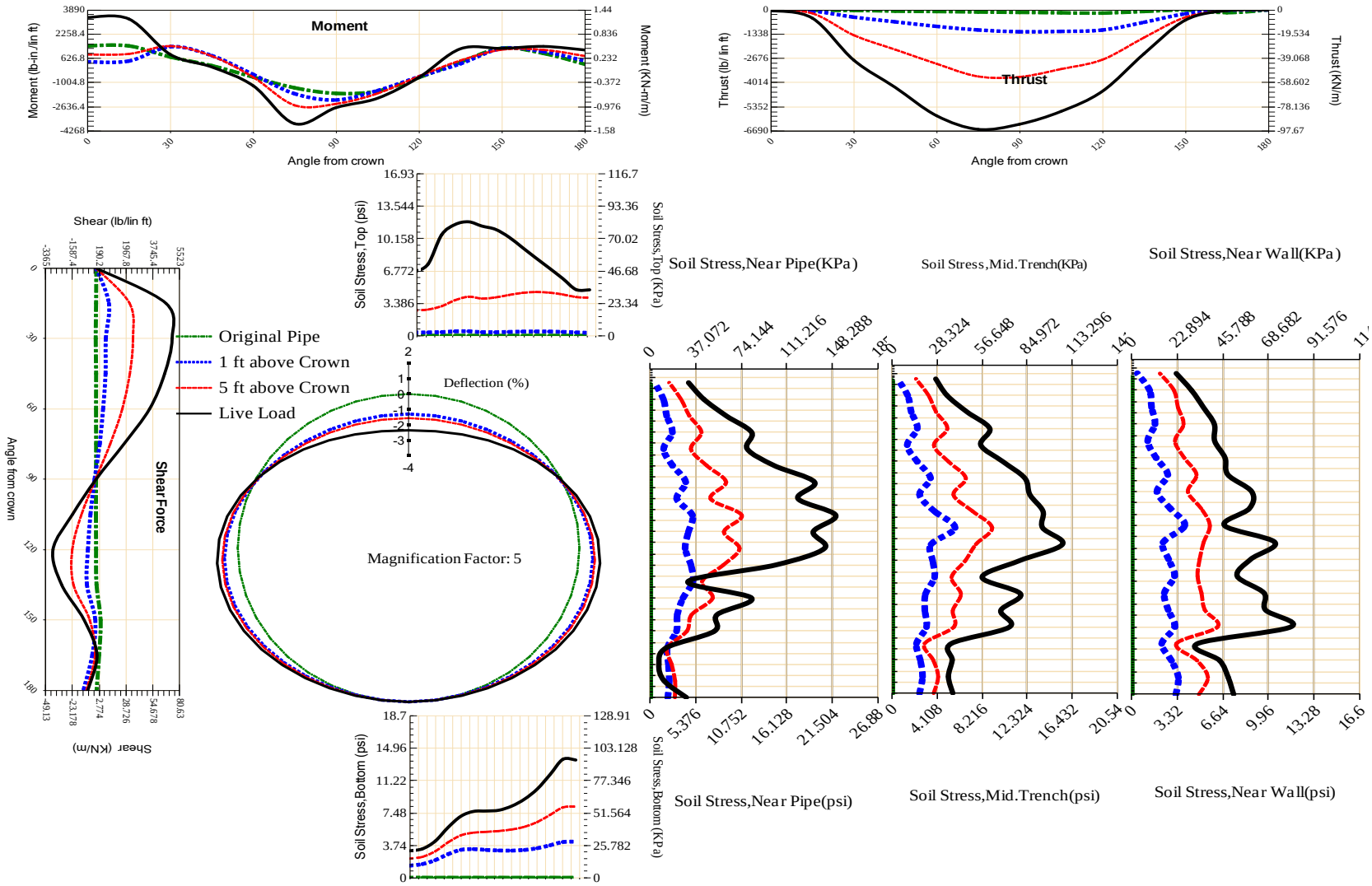

Figure A-156 Param-120-PW288-SF5TR-OD+48-EW10-H5-LiveLoad

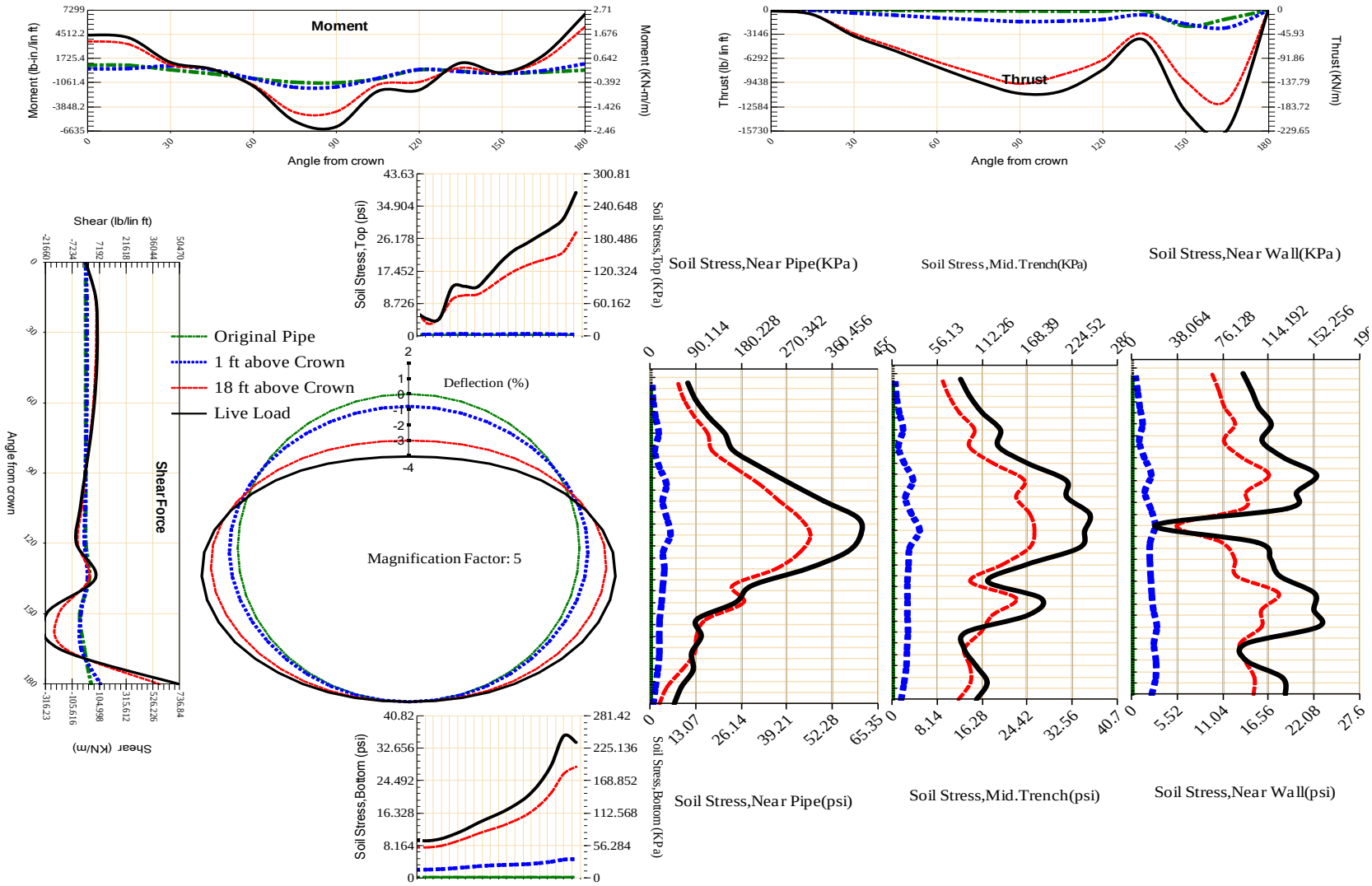

Figure A-157 Param-120-PW288-SF5TR-OD+48-EW3-H18-LiveLoad

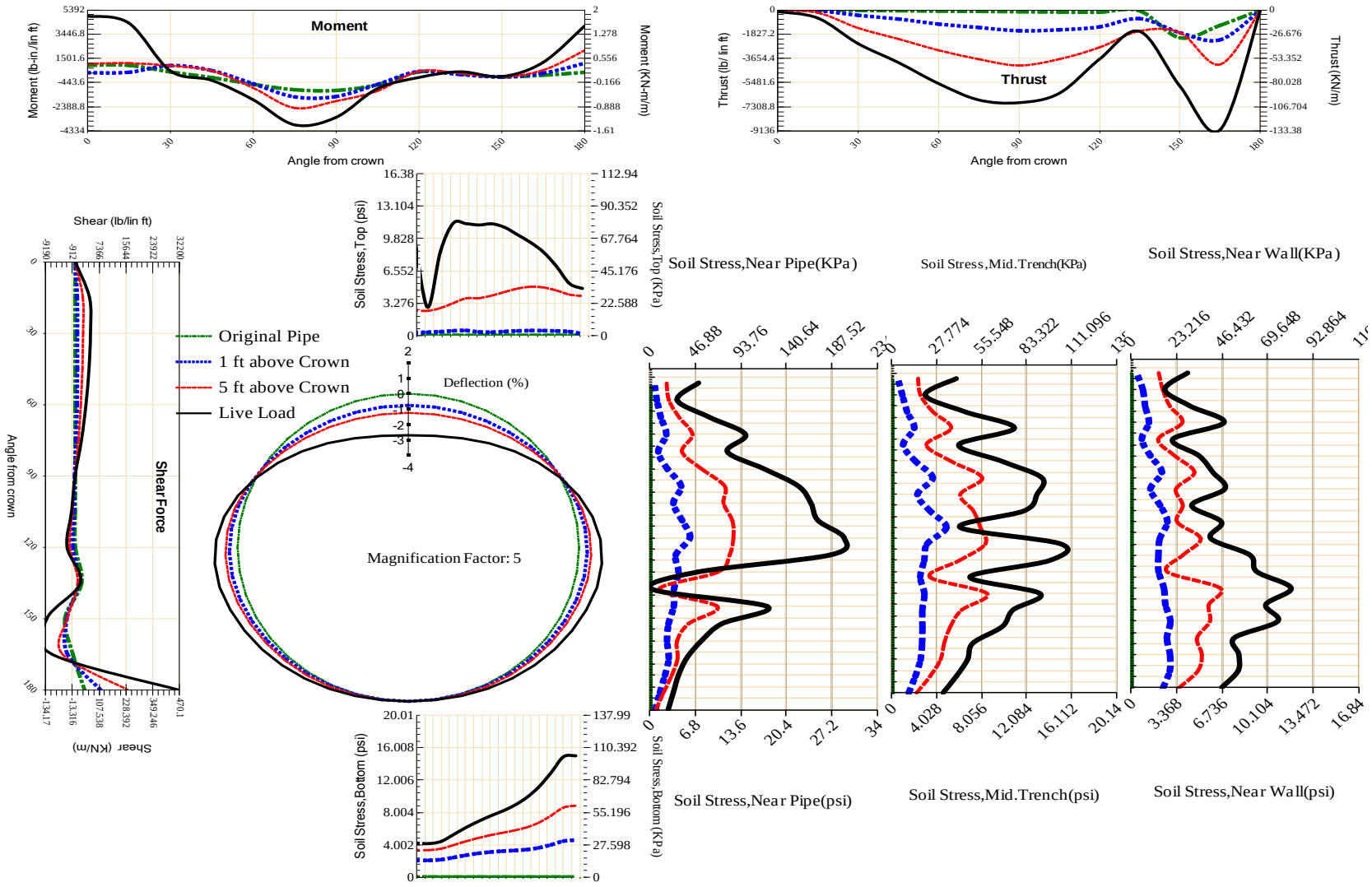

Figure A-158 Param-120-PW288-SF5TR-OD+48-EW3-H5-LiveLoad

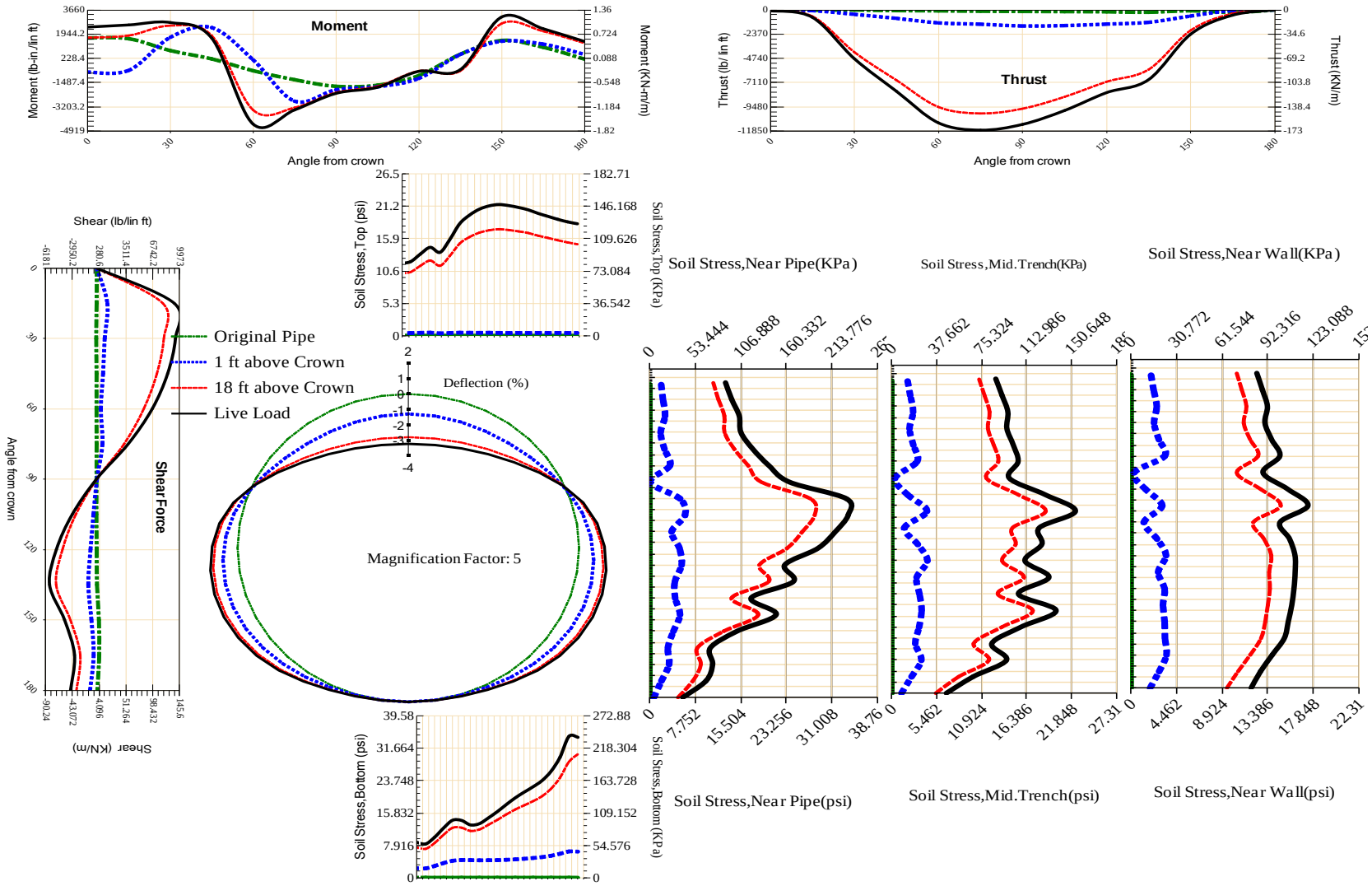

Figure A-159 Param-120-PW288-SF7OR-OD+108-EW10-H18-LiveLoad

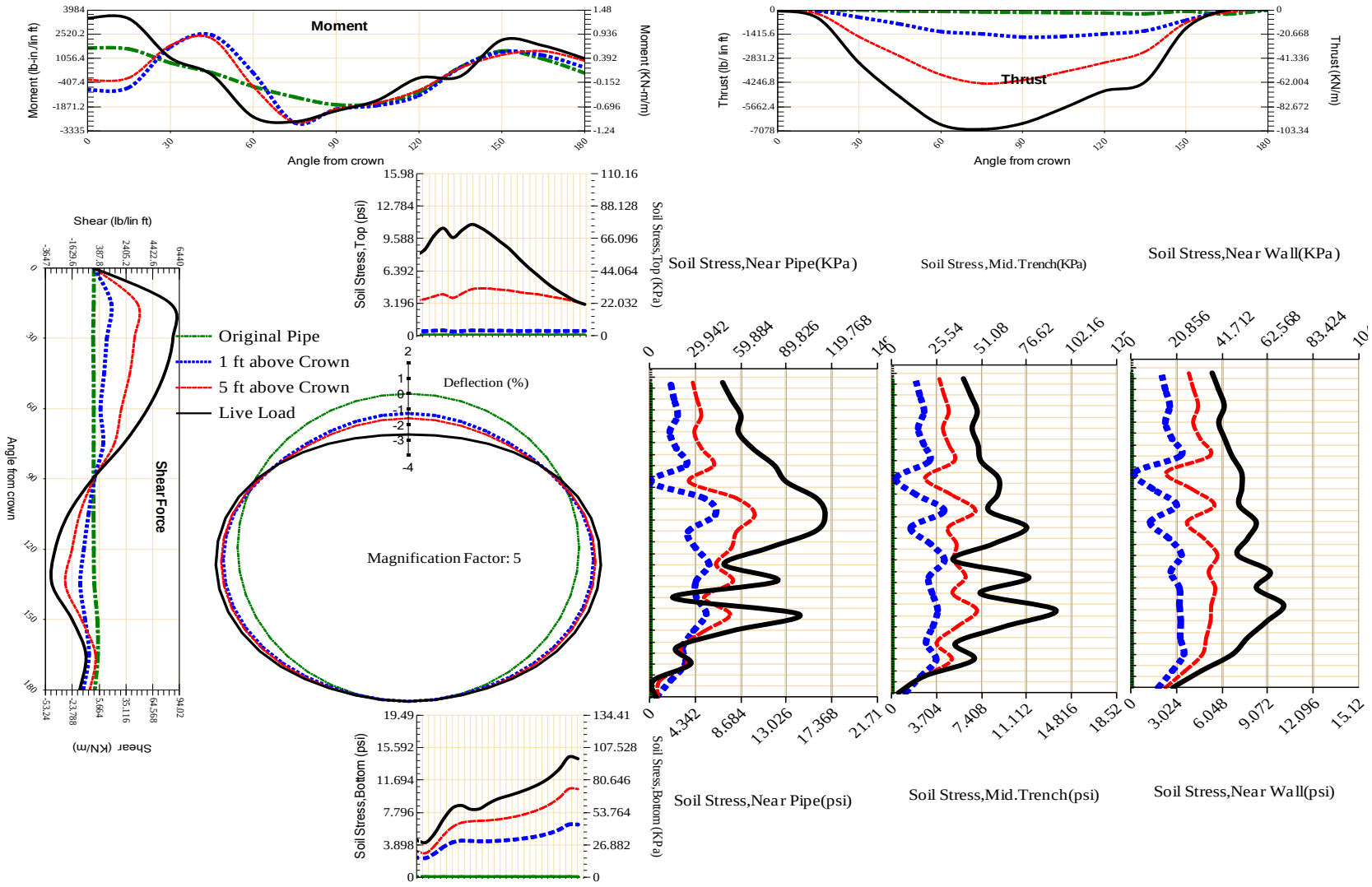

Figure A-160 Param-120-PW288-SF7OR-OD+108-EW10-H5-LiveLoad

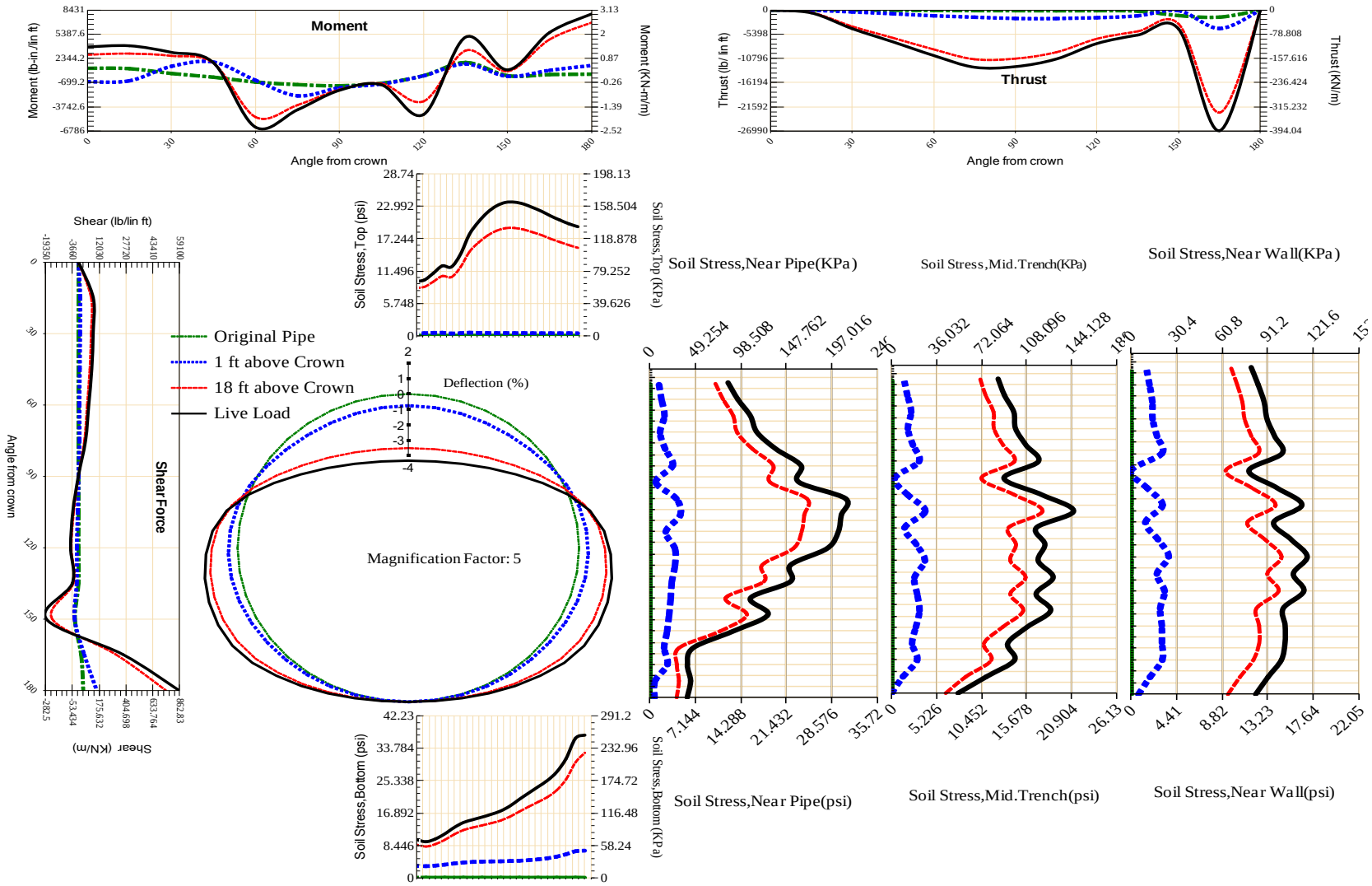

Figure A-161 Param-120-PW288-SF7OR-OD+108-EW3-H18-LiveLoad

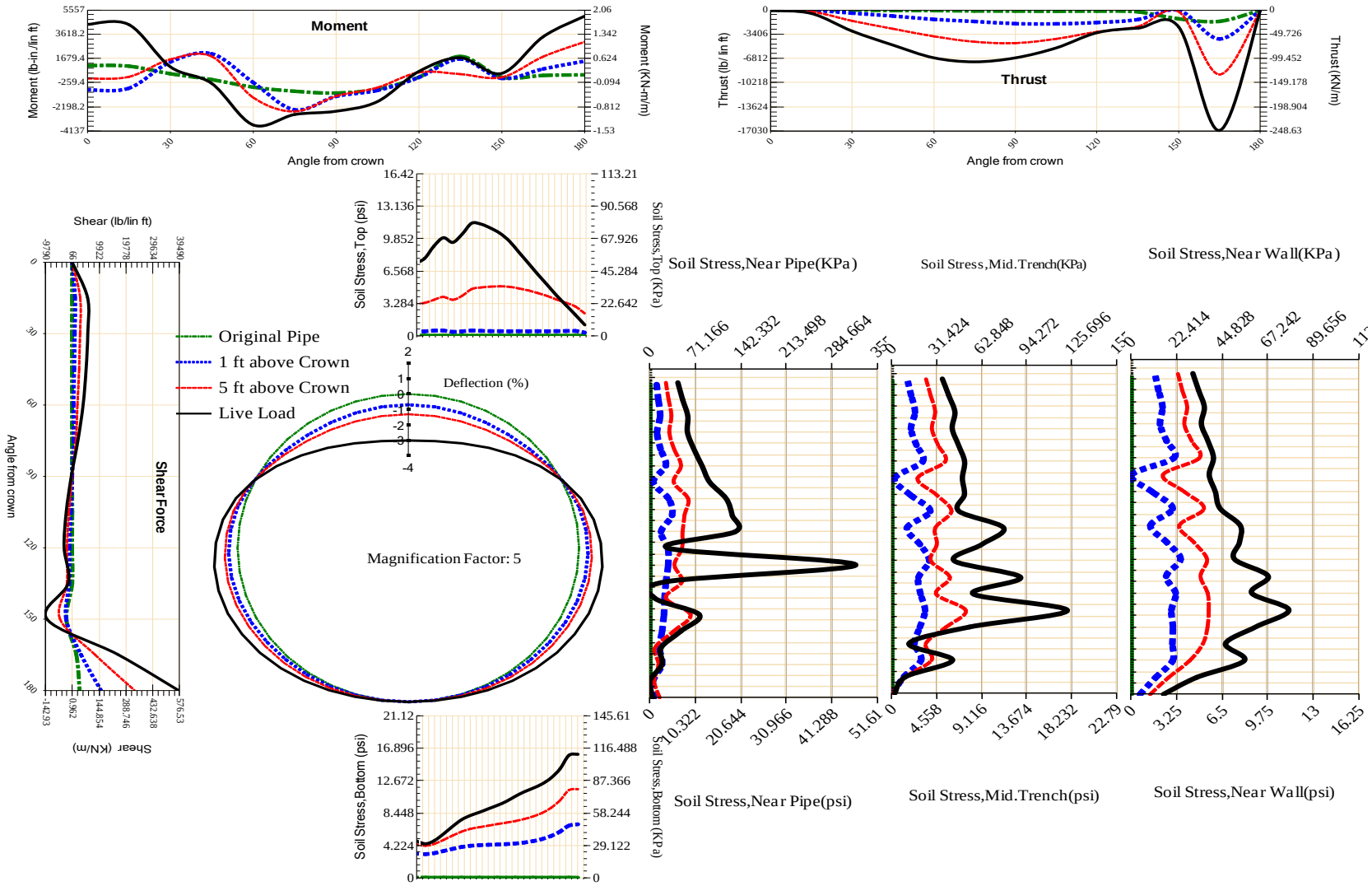

Figure A-162 Param-120-PW288-SF7OR-OD+108-EW3-H5-LiveLoad

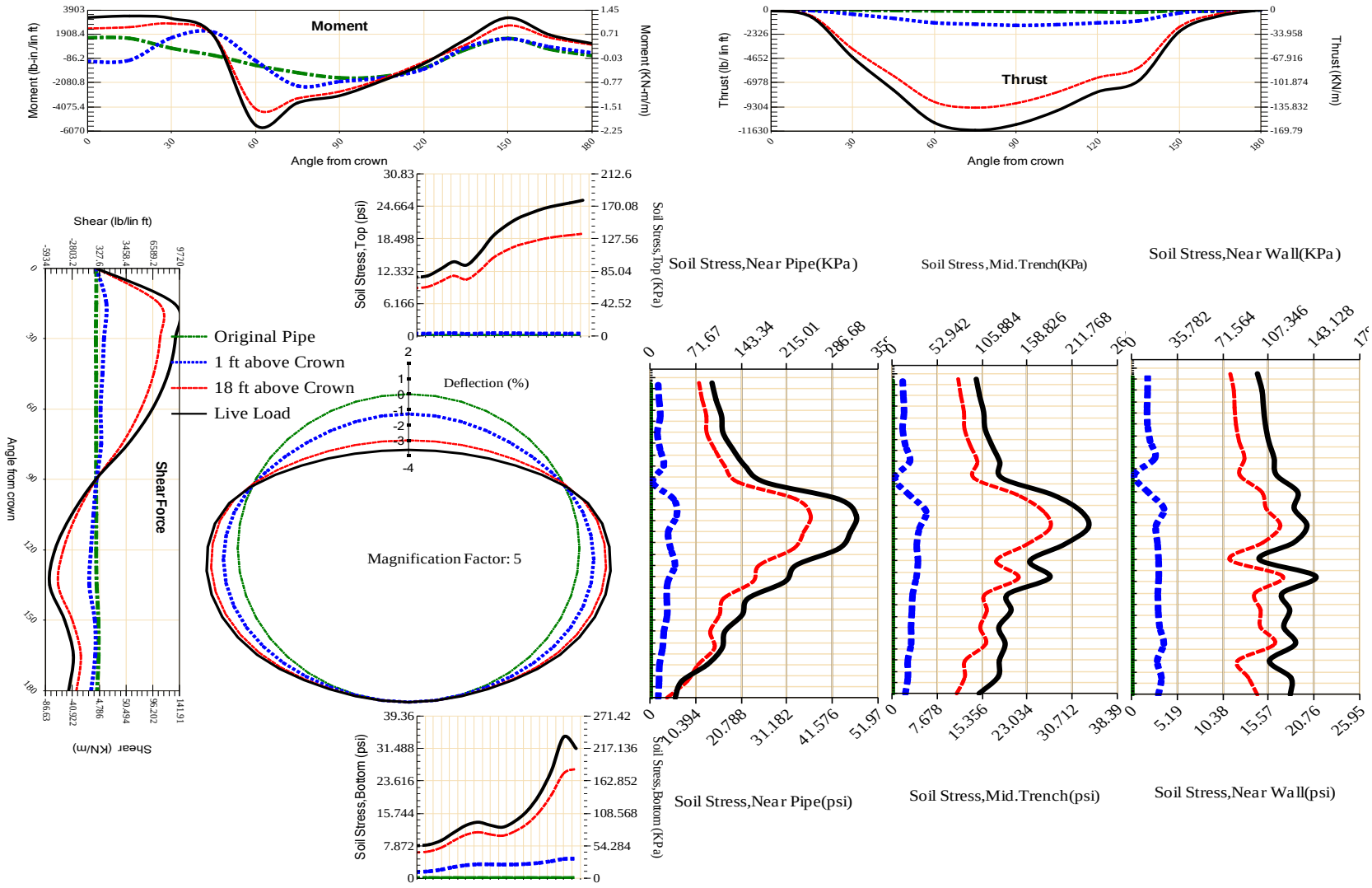

Figure A-163 Param-120-PW288-SF7OR-OD+48-EW10-H18-LiveLoad

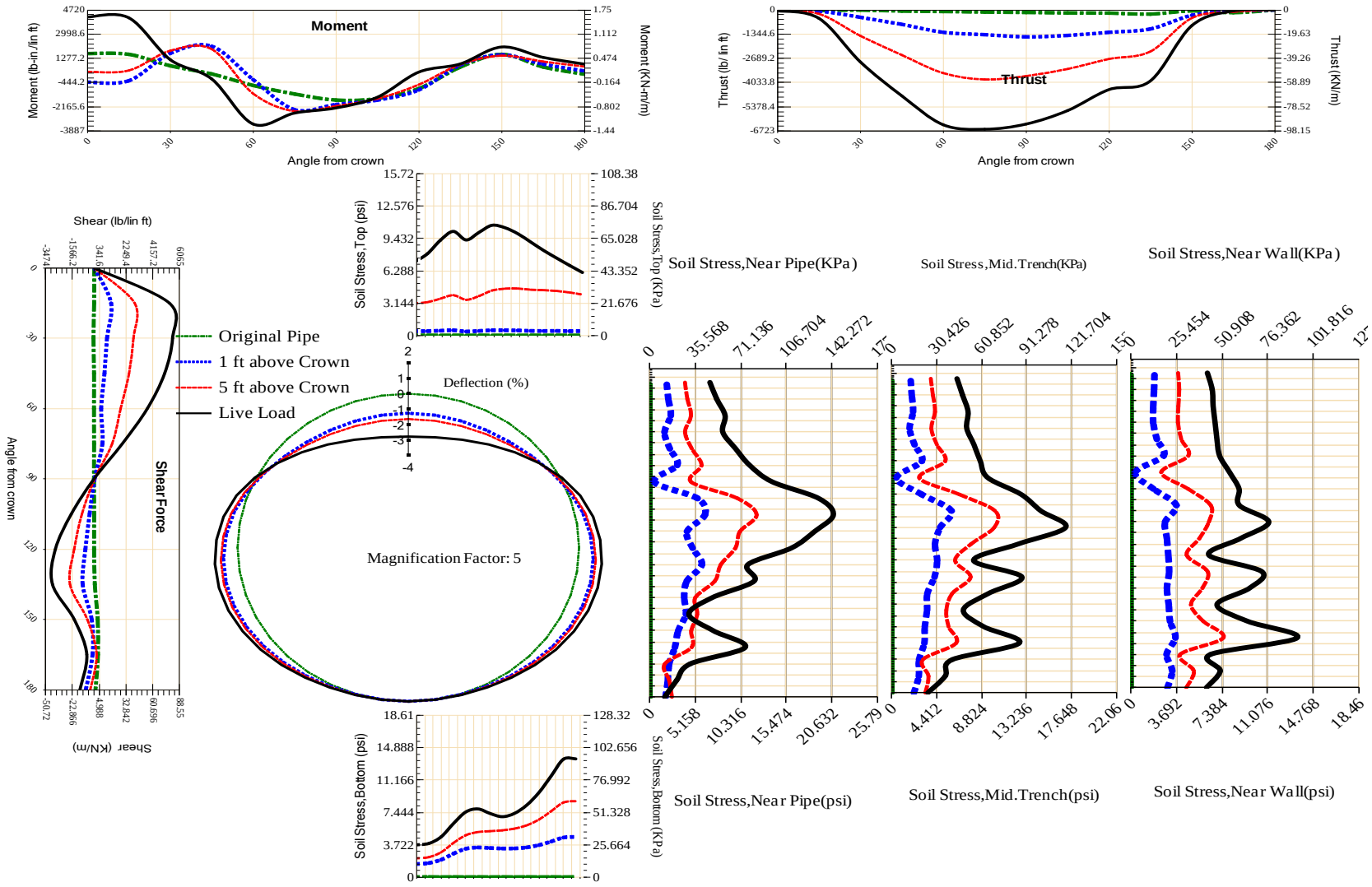

Figure A-164 Param-120-PW288-SF7OR-OD+48-EW10-H5-LiveLoad

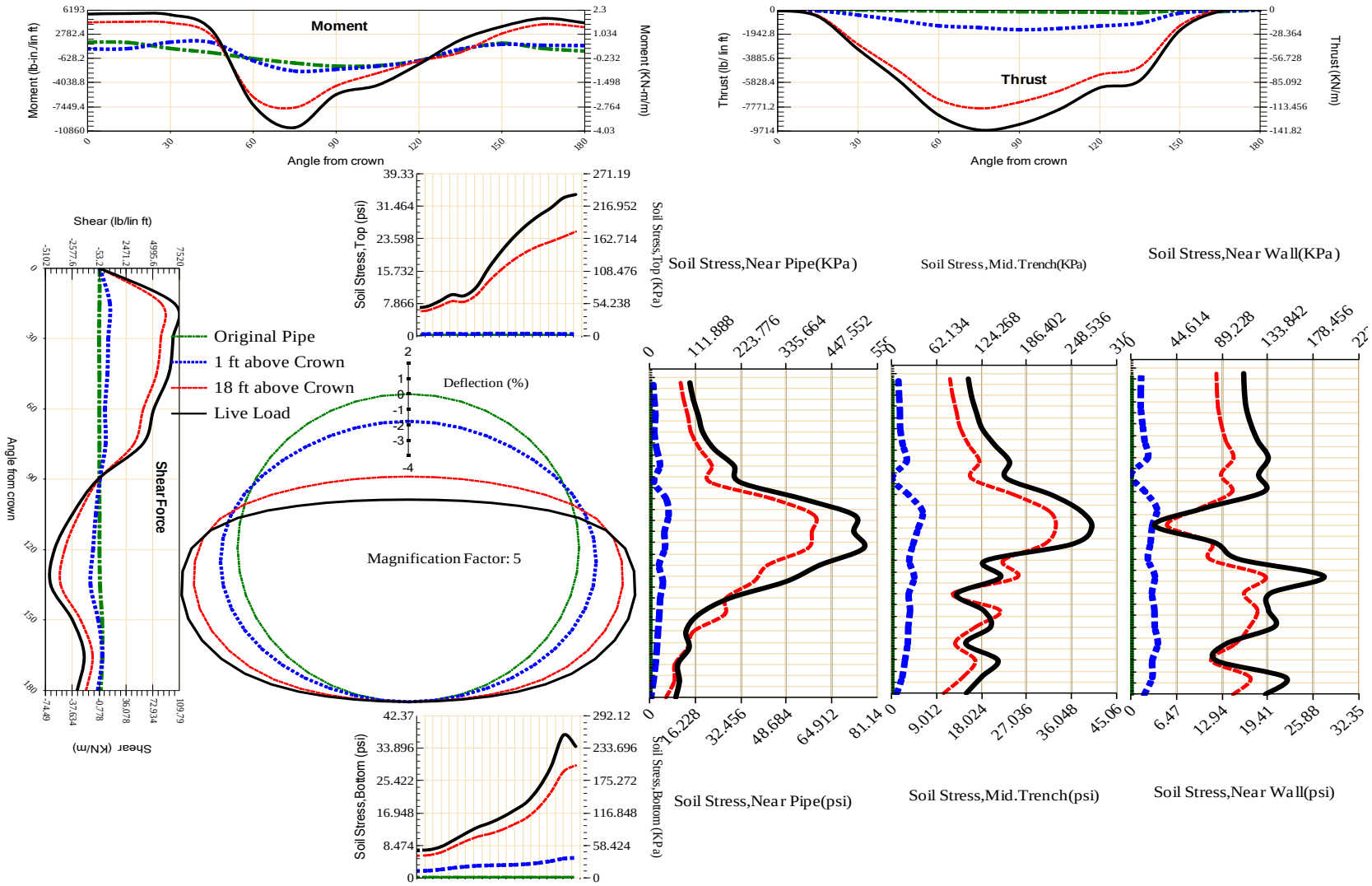

Figure A-165 Param-120-PW288-SF7OR-OD+48-EW3-H18-LiveLoad

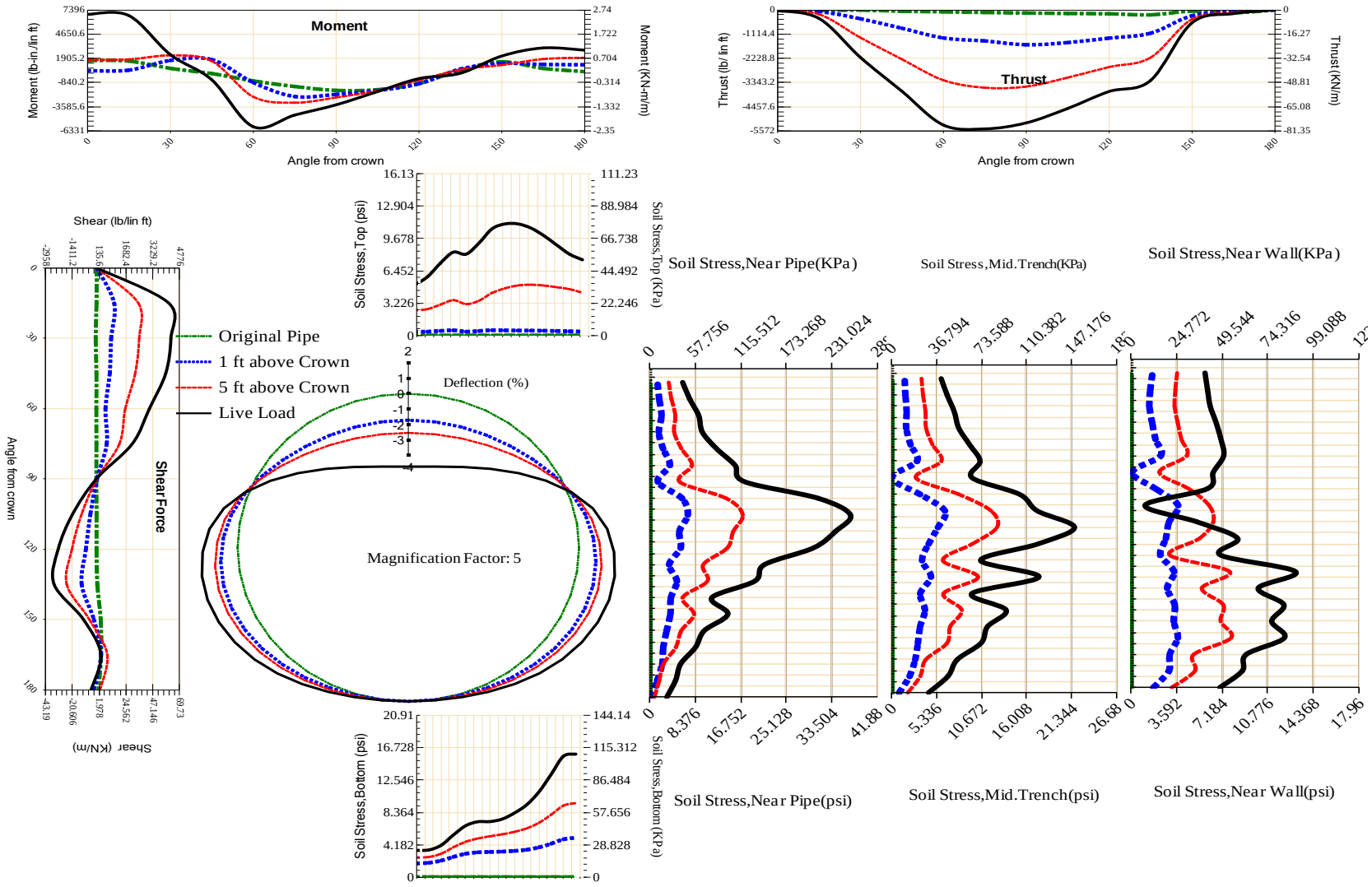

Figure A-166 Param-120-PW288-SF7OR-OD+48-EW3-H5-LiveLoad

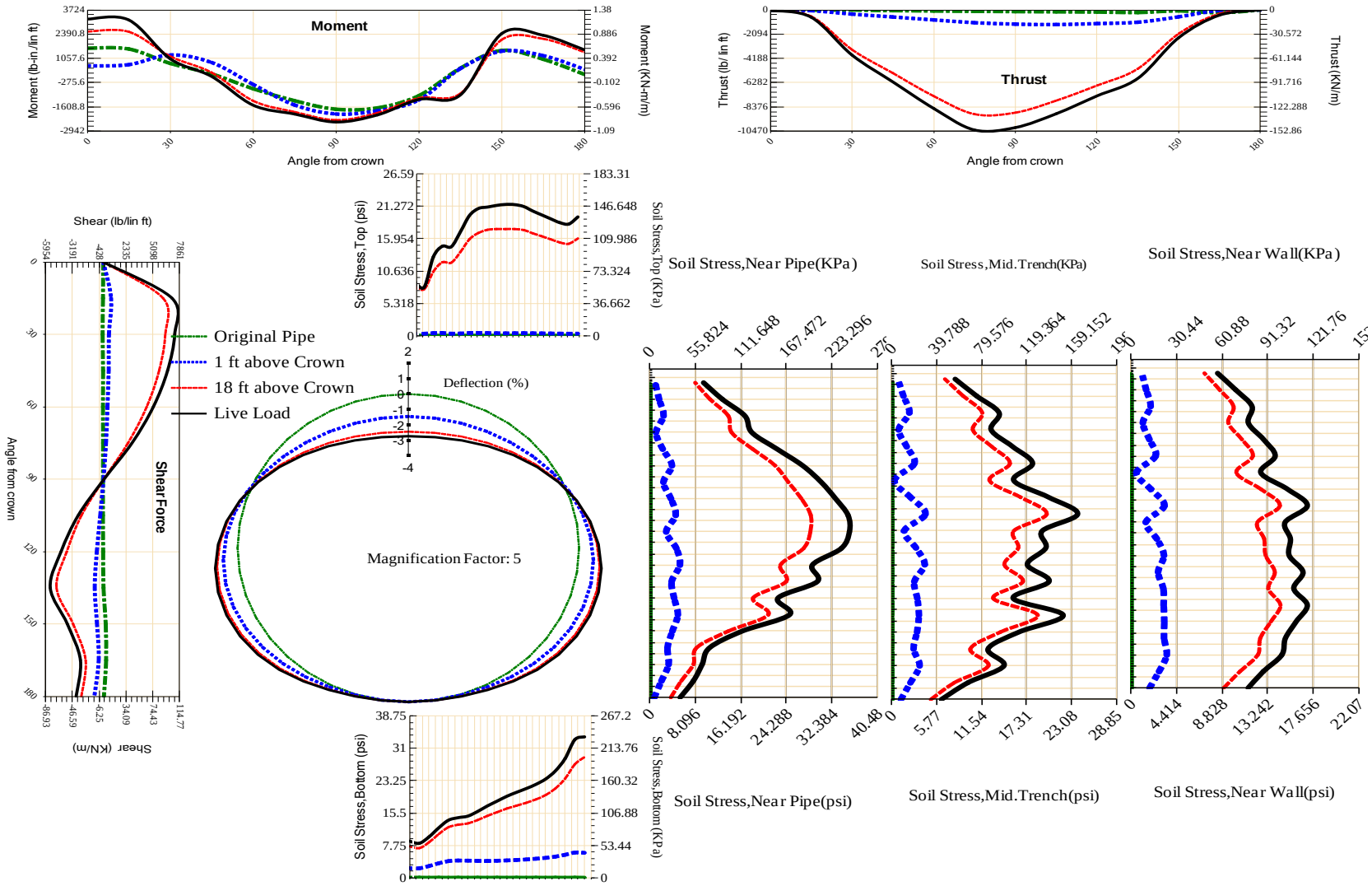

Figure A-167 Param-120-PW288-SF7TR-OD+108-EW10-H18-LiveLoad

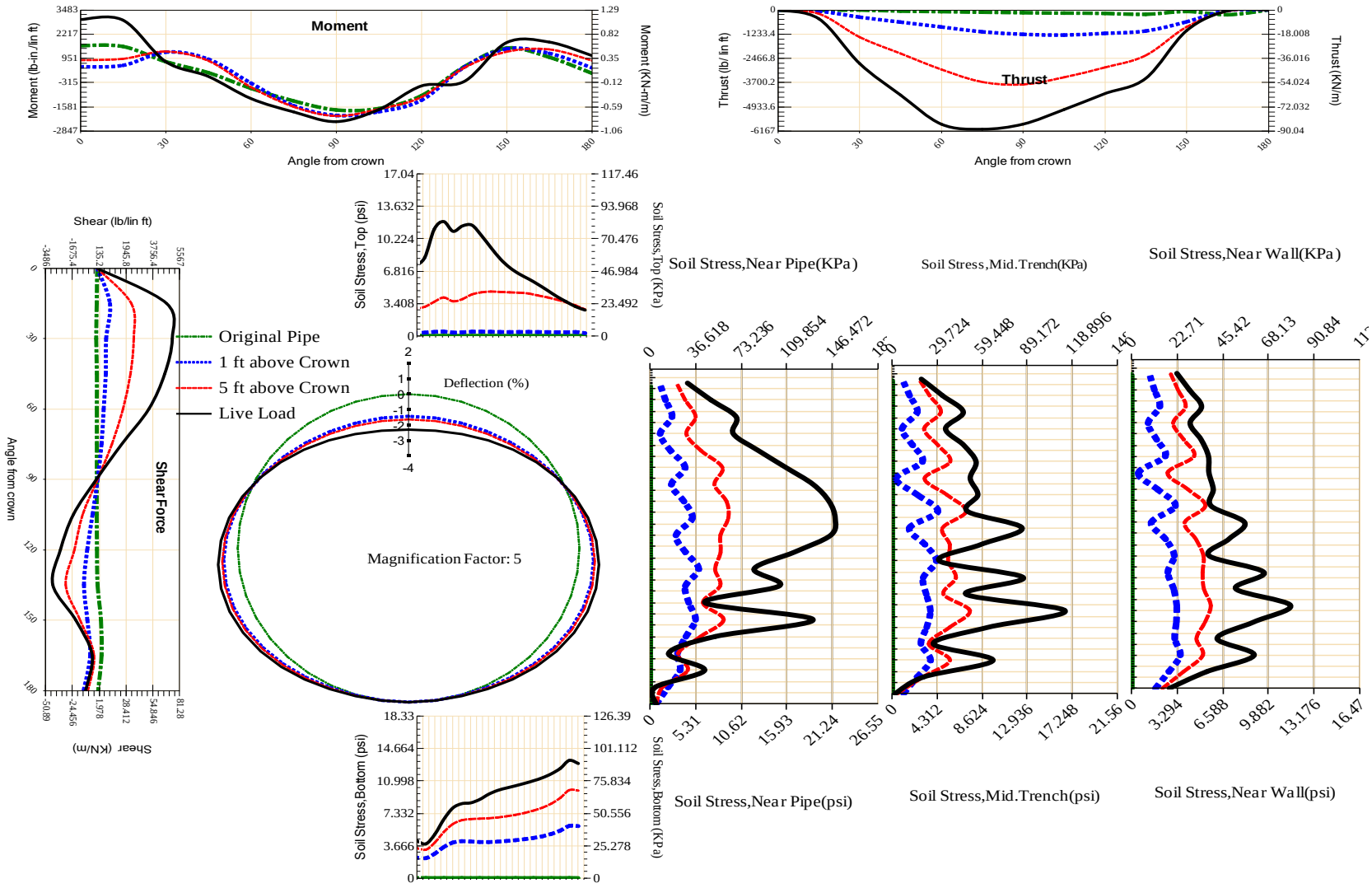

Figure A-168 Param-120-PW288-SF7TR-OD+108-EW10-H5-LiveLoad

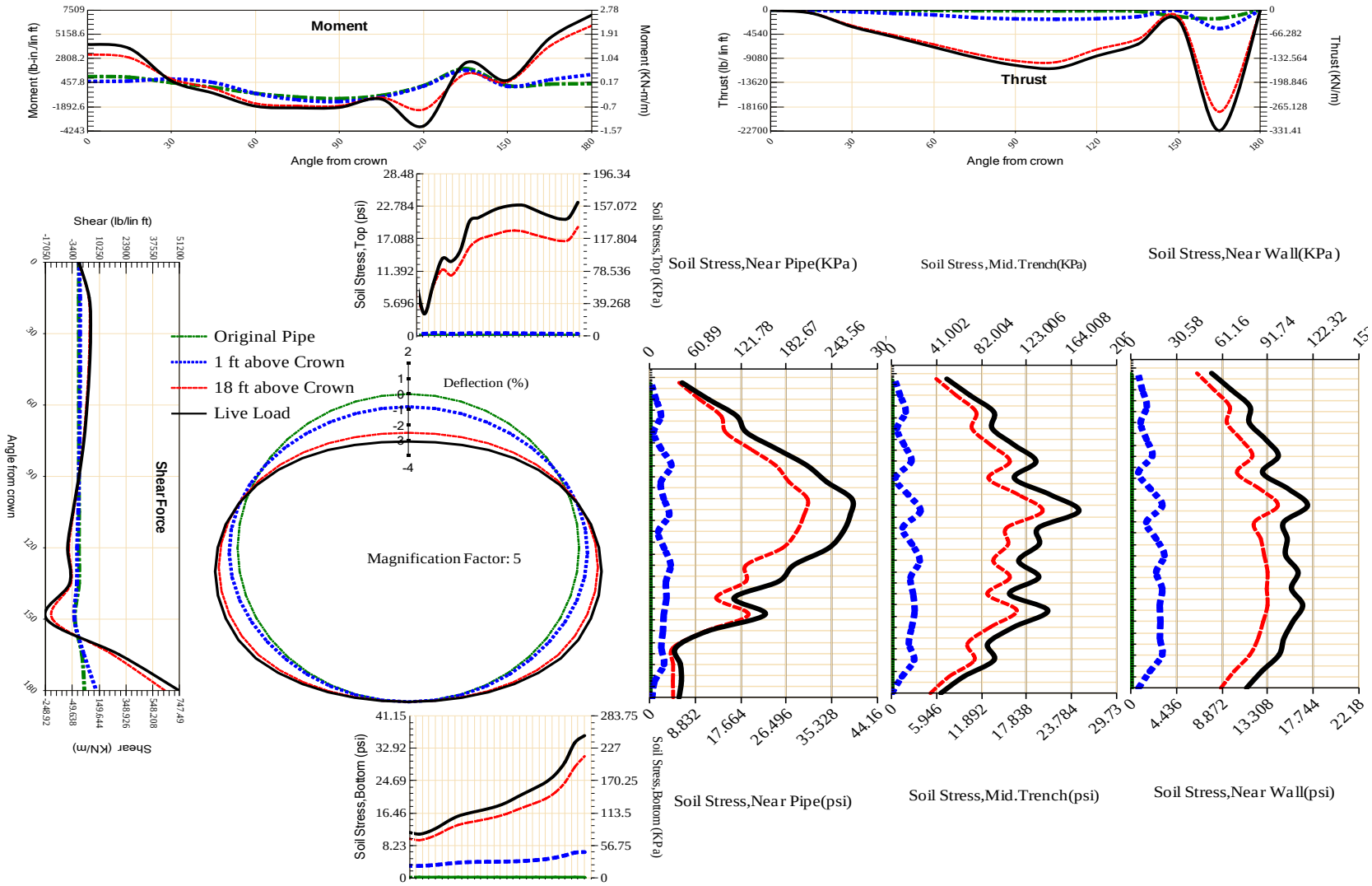

Figure A-169 Param-120-PW288-SF7TR-OD+108-EW3-H18-LiveLoad

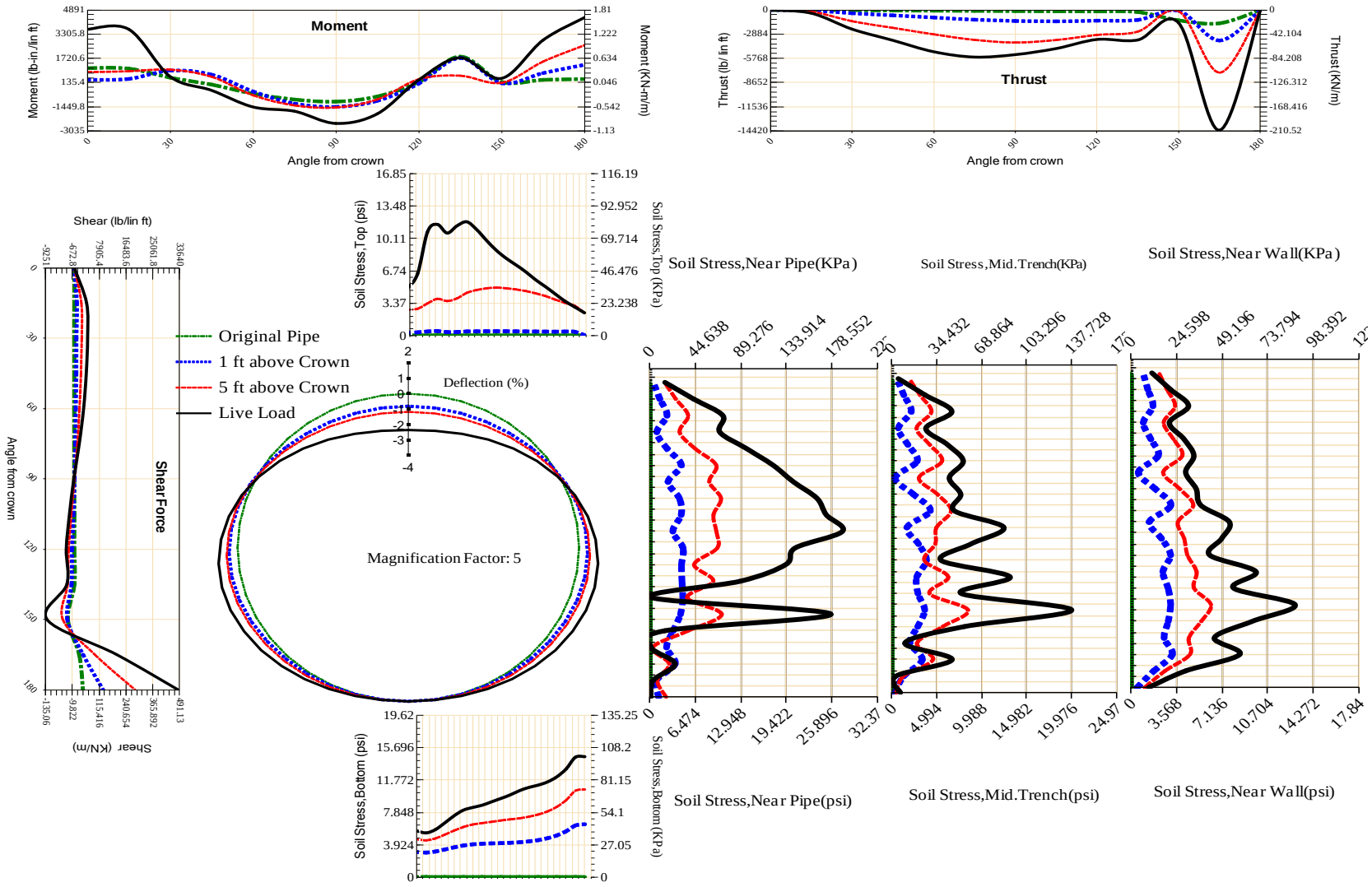

Figure A-170 Param-120-PW288-SF7TR-OD+108-EW3-H5-LiveLoad

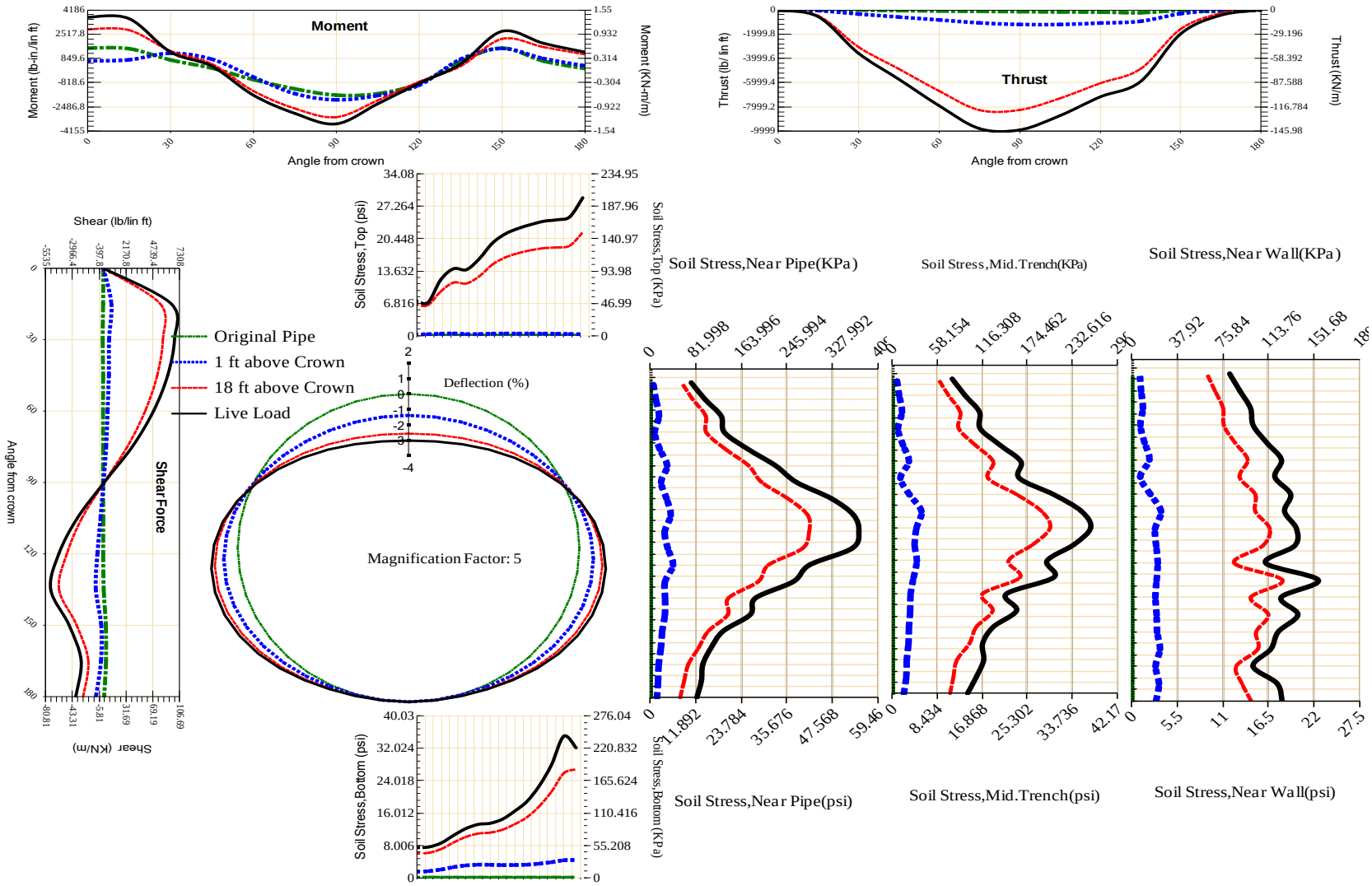

Figure A-171 Param-120-PW288-SF7TR-OD+48-EW10-H18-LiveLoad

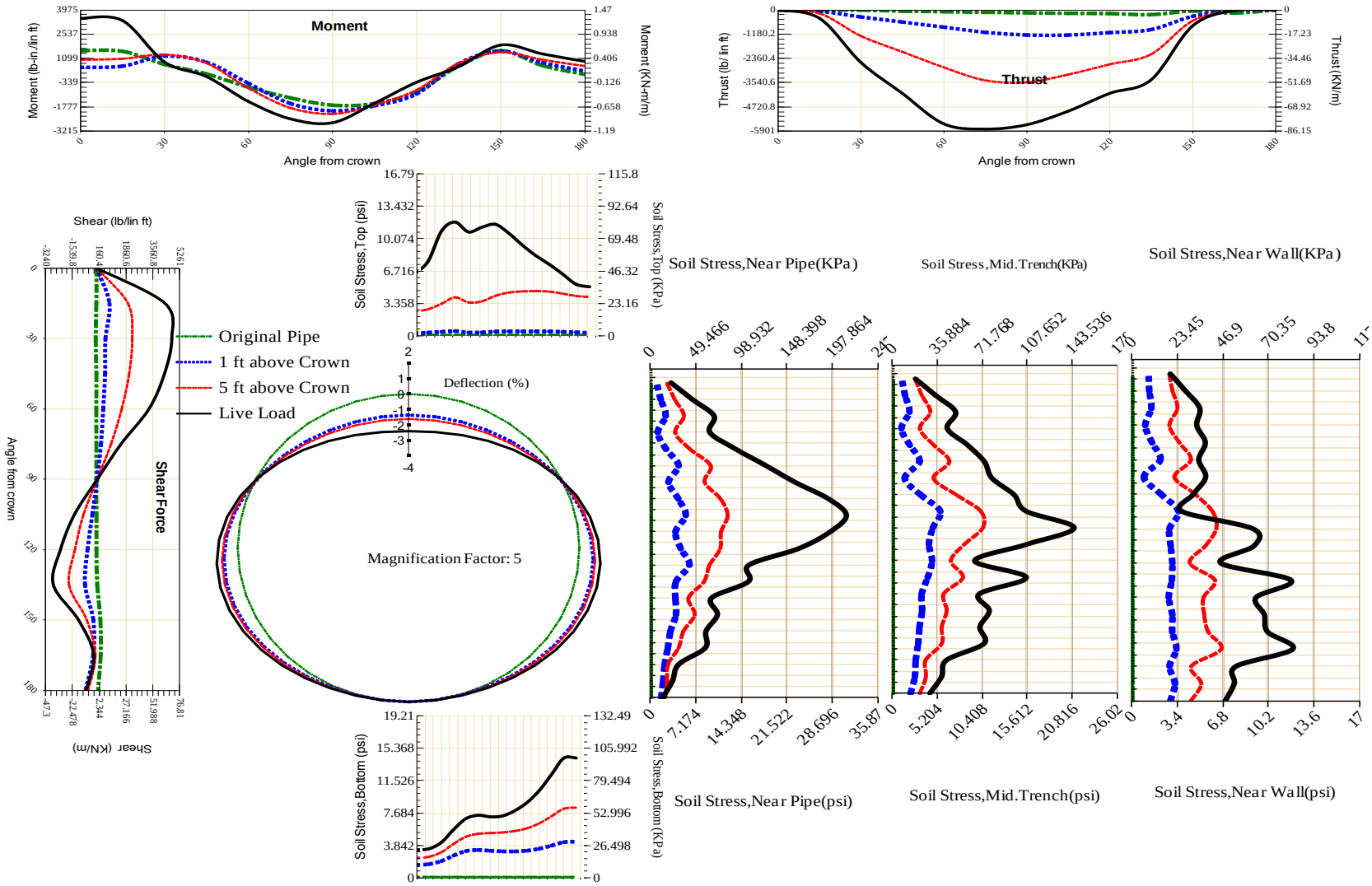

Figure A-172 Param-120-PW288-SF7TR-OD+48-EW10-H5-LiveLoad

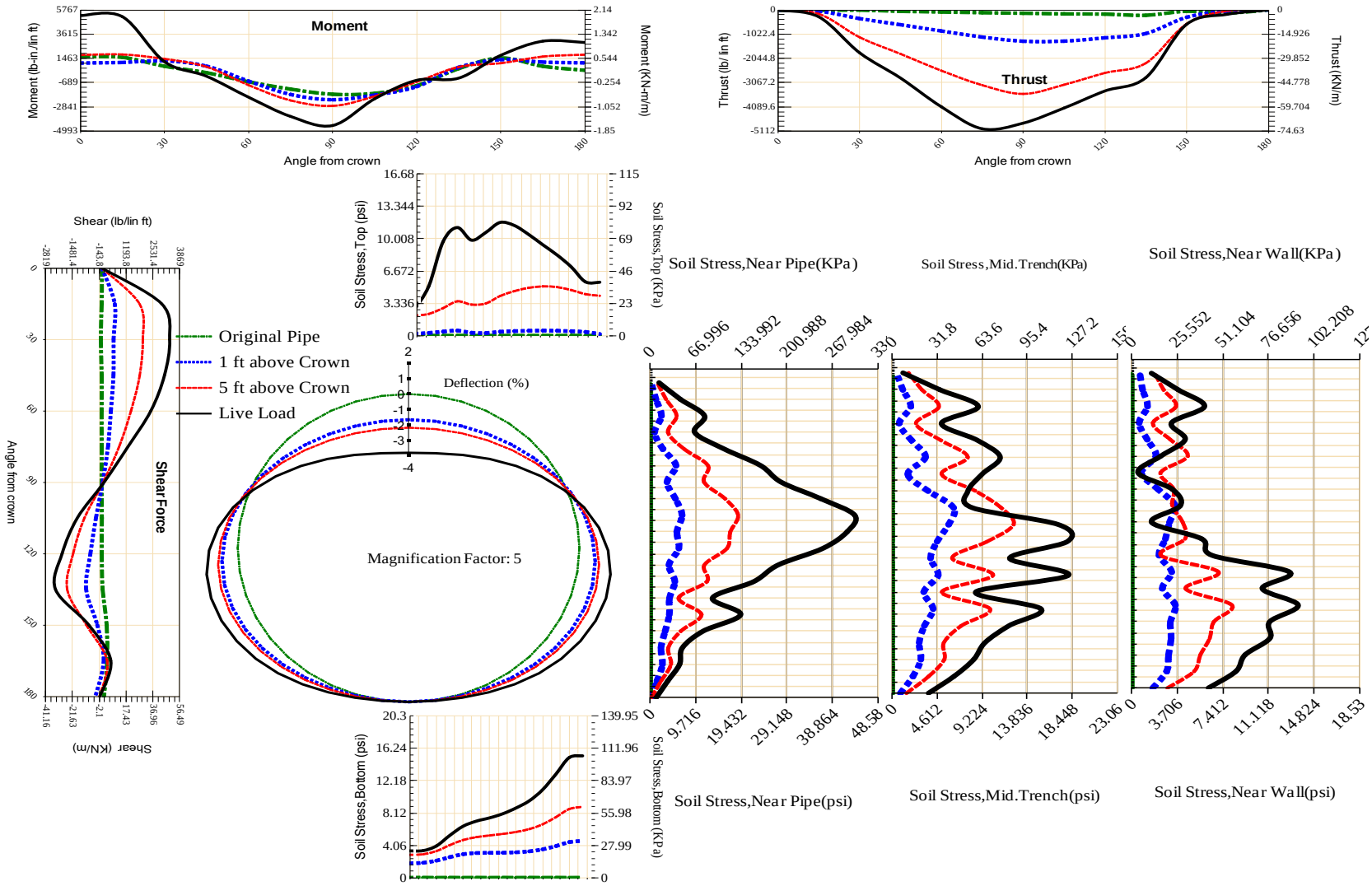

Figure A-173 Param-120-PW288-SF7TR-OD+48-EW3-H5-LiveLoad

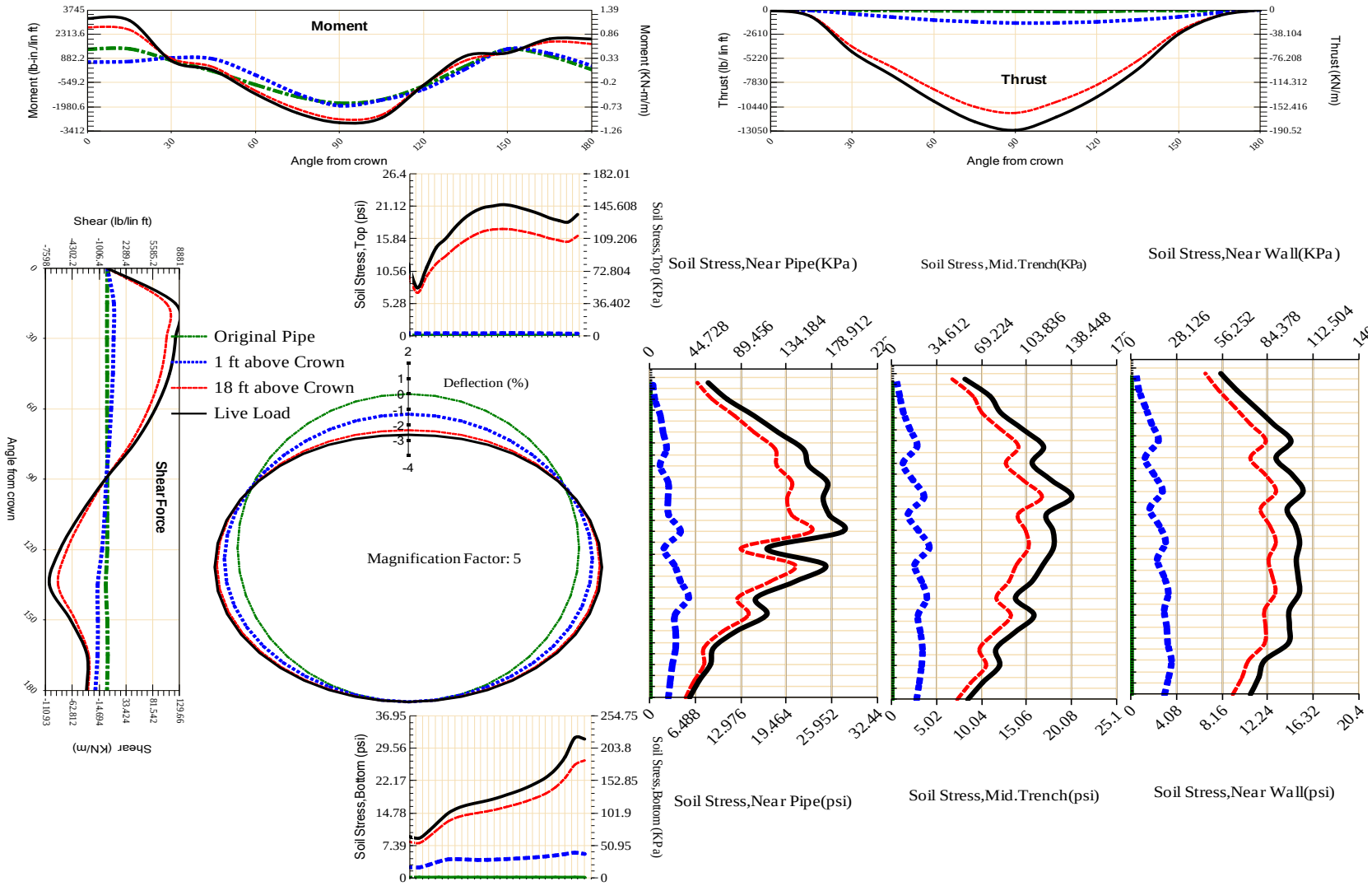

Figure A-174 Param-120-PW288-TR10TR-OD+108-EW10-H18-LiveLoad

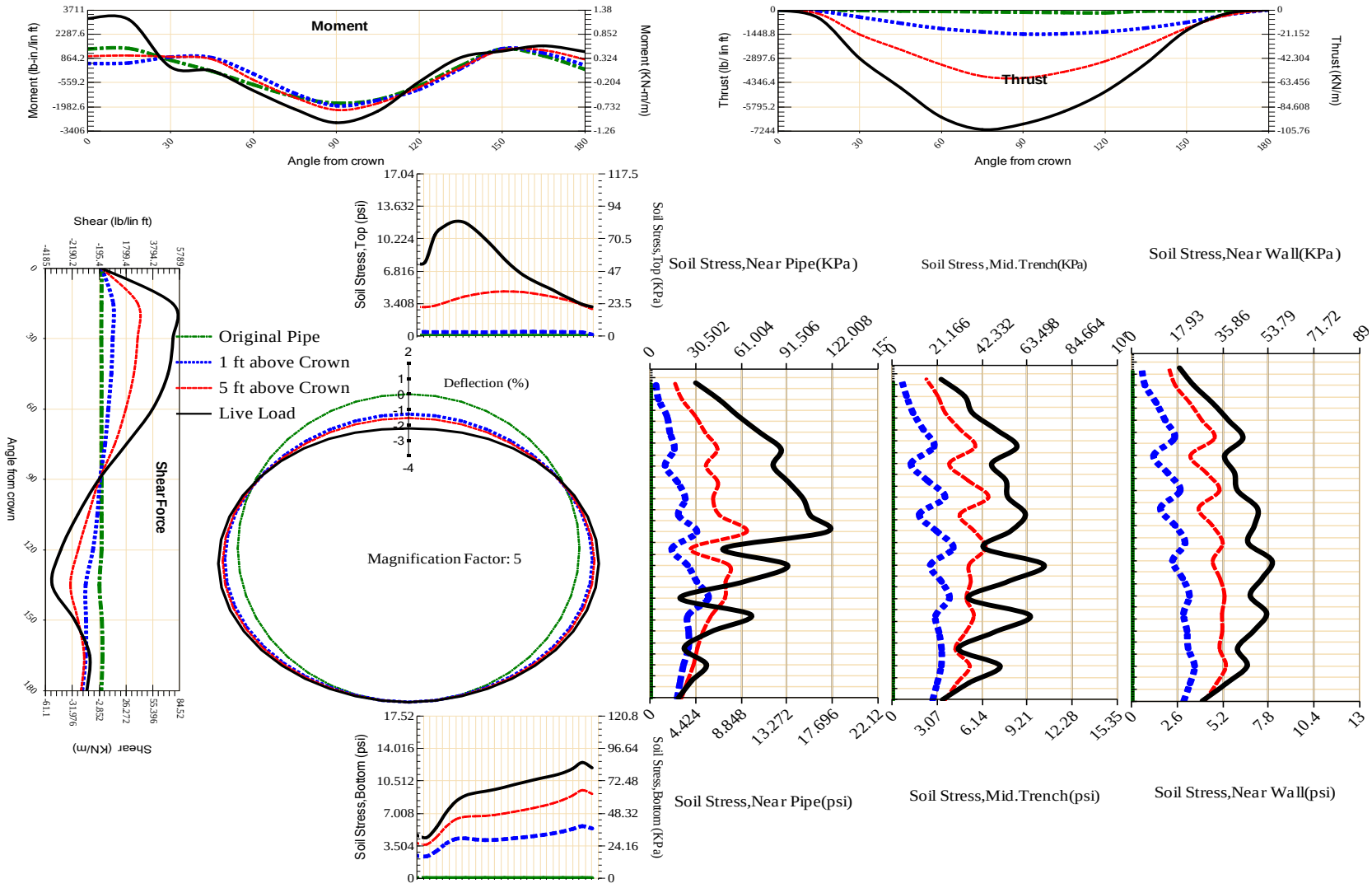

Figure A-175 Param-120-PW288-TR10TR-OD+108-EW10-H5-LiveLoad

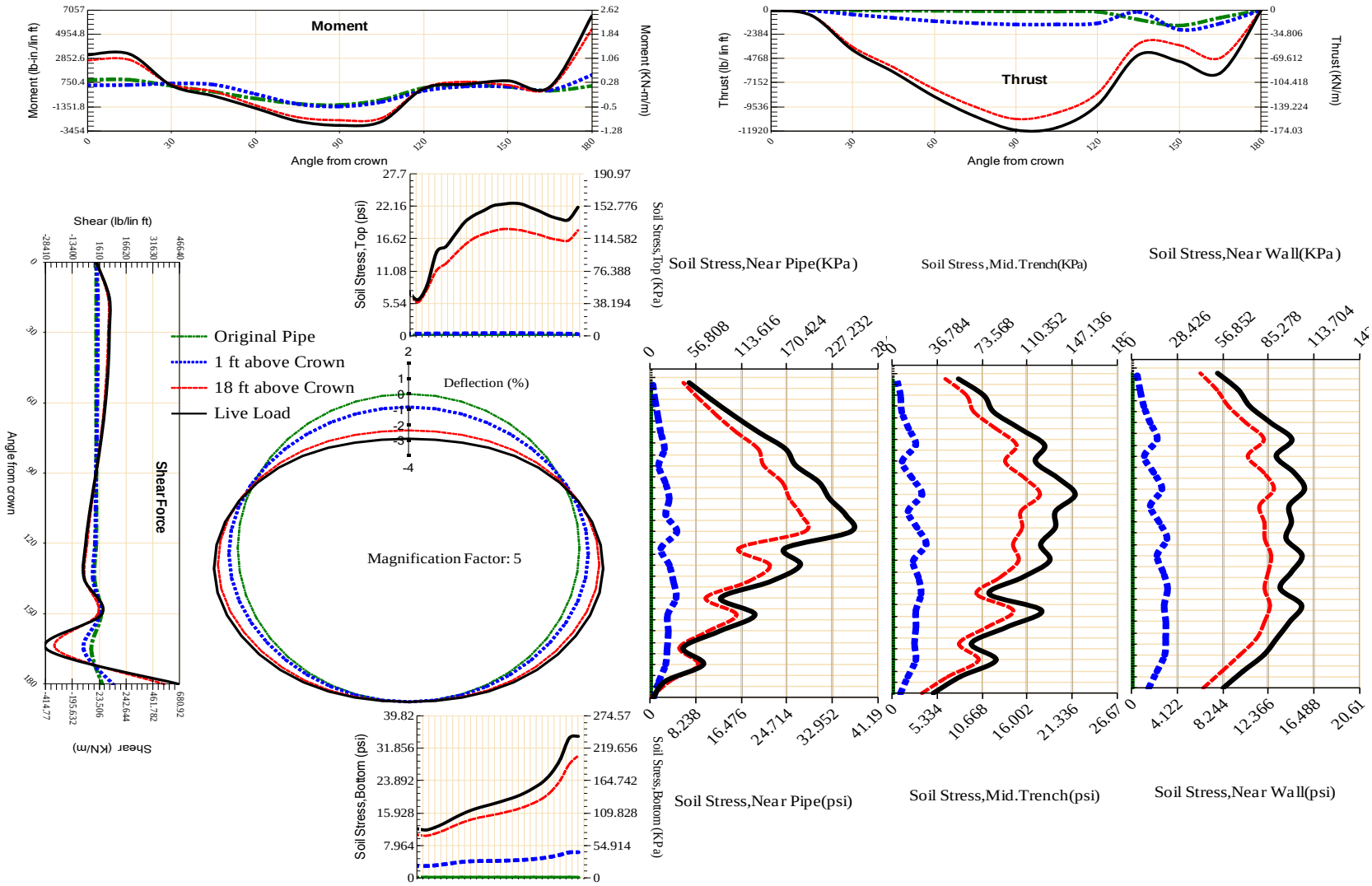

Figure A-176 Param-120-PW288-TR10TR-OD+108-EW3-H18-LiveLoad

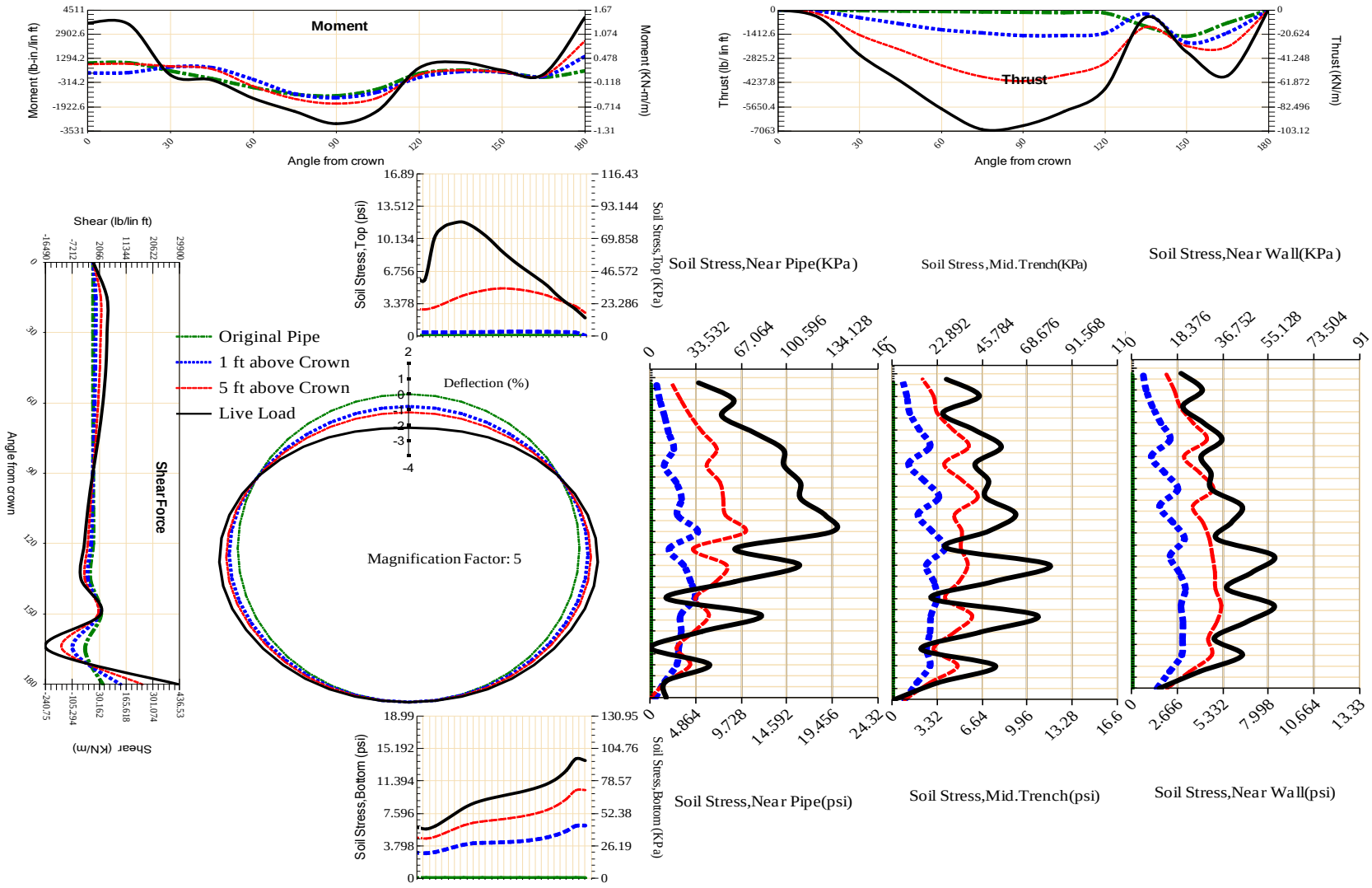

Figure A-177 Param-120-PW288-TR10TR-OD+108-EW3-H5-LiveLoad

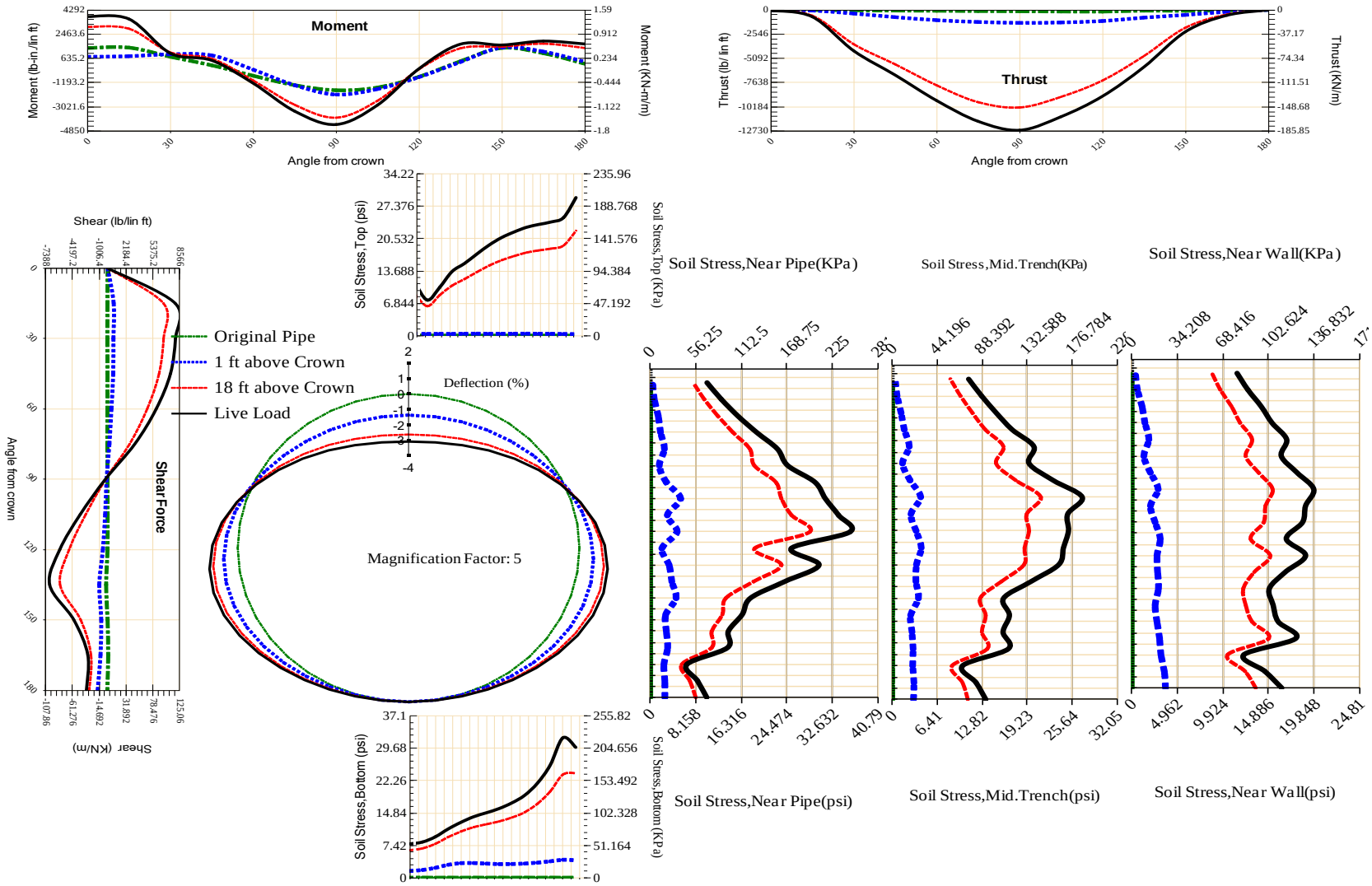

Figure A-178 Param-120-PW288-TR10TR-OD+48-EW10-H18-LiveLoad

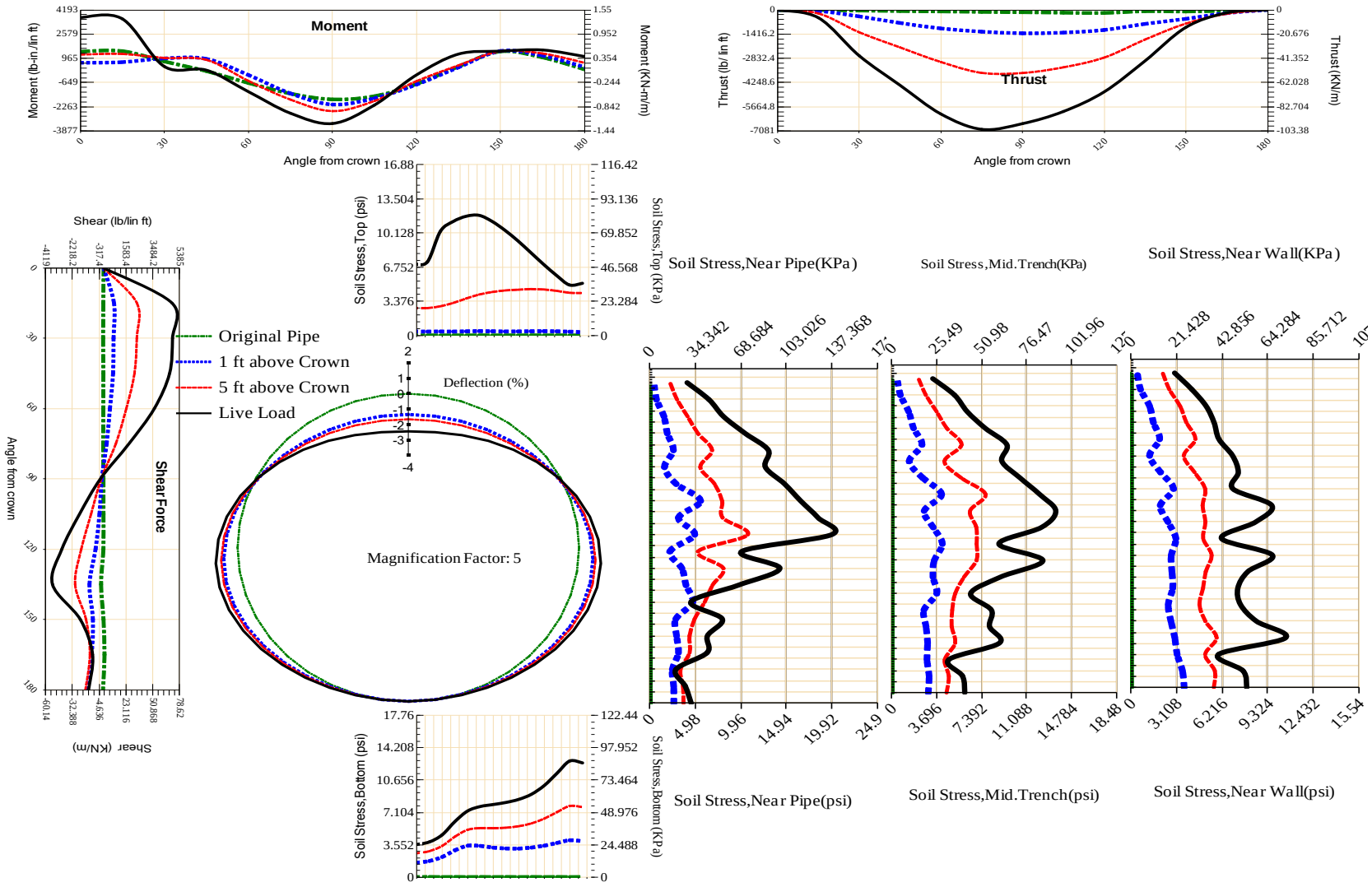

Figure A-179 Param-120-PW288-TR10TR-OD+48-EW10-H5-LiveLoad

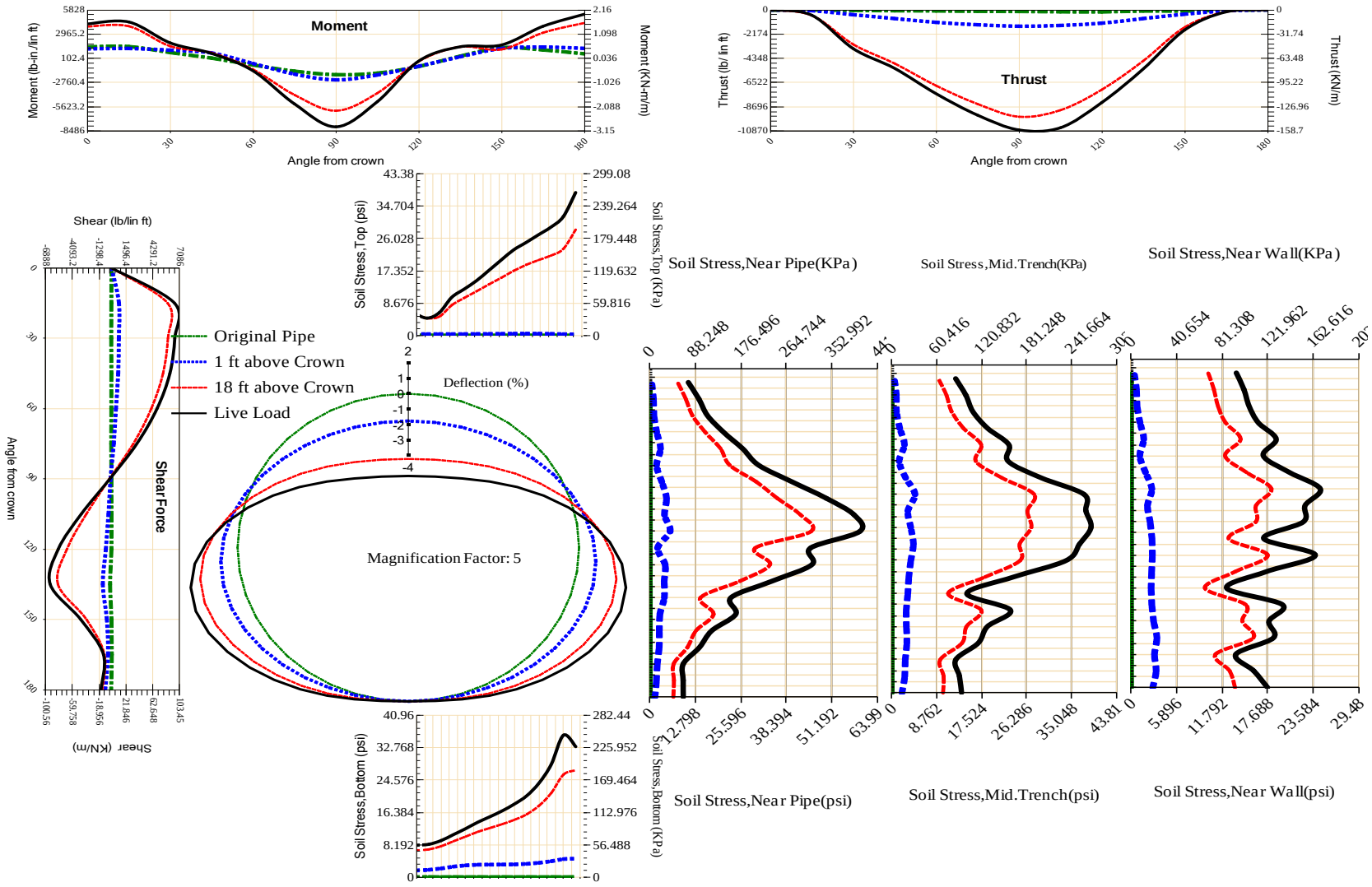

Figure A-180 Param-120-PW288-TR10TR-OD+48-EW3-H18-LiveLoad

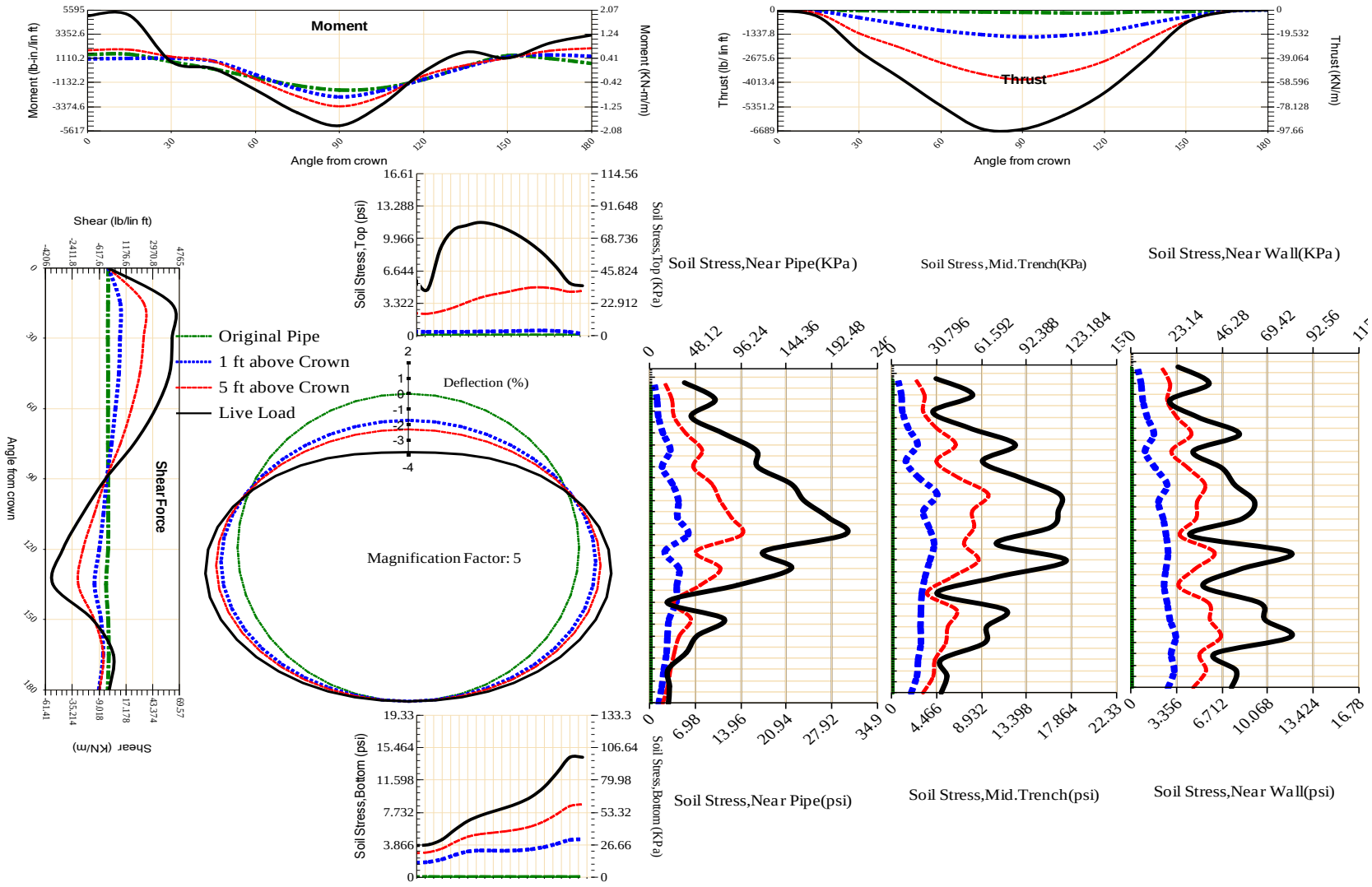

Figure A-181 Param-120-PW288-TR10TR-OD+48-EW3-H5-LiveLoad

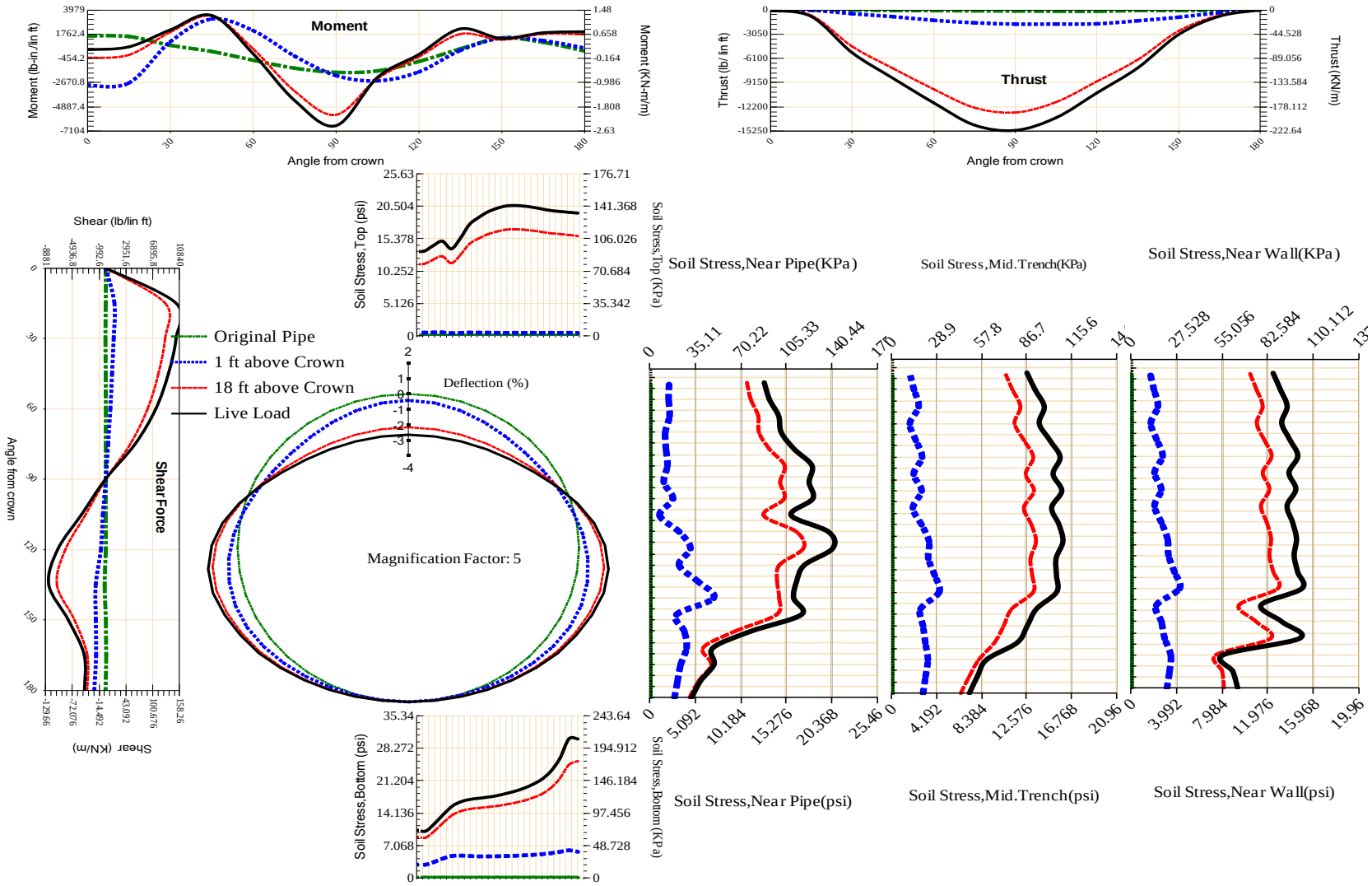

Figure A-182 Param-120-PW288-TR3OR-OD+108-EW10-H18-LiveLoad

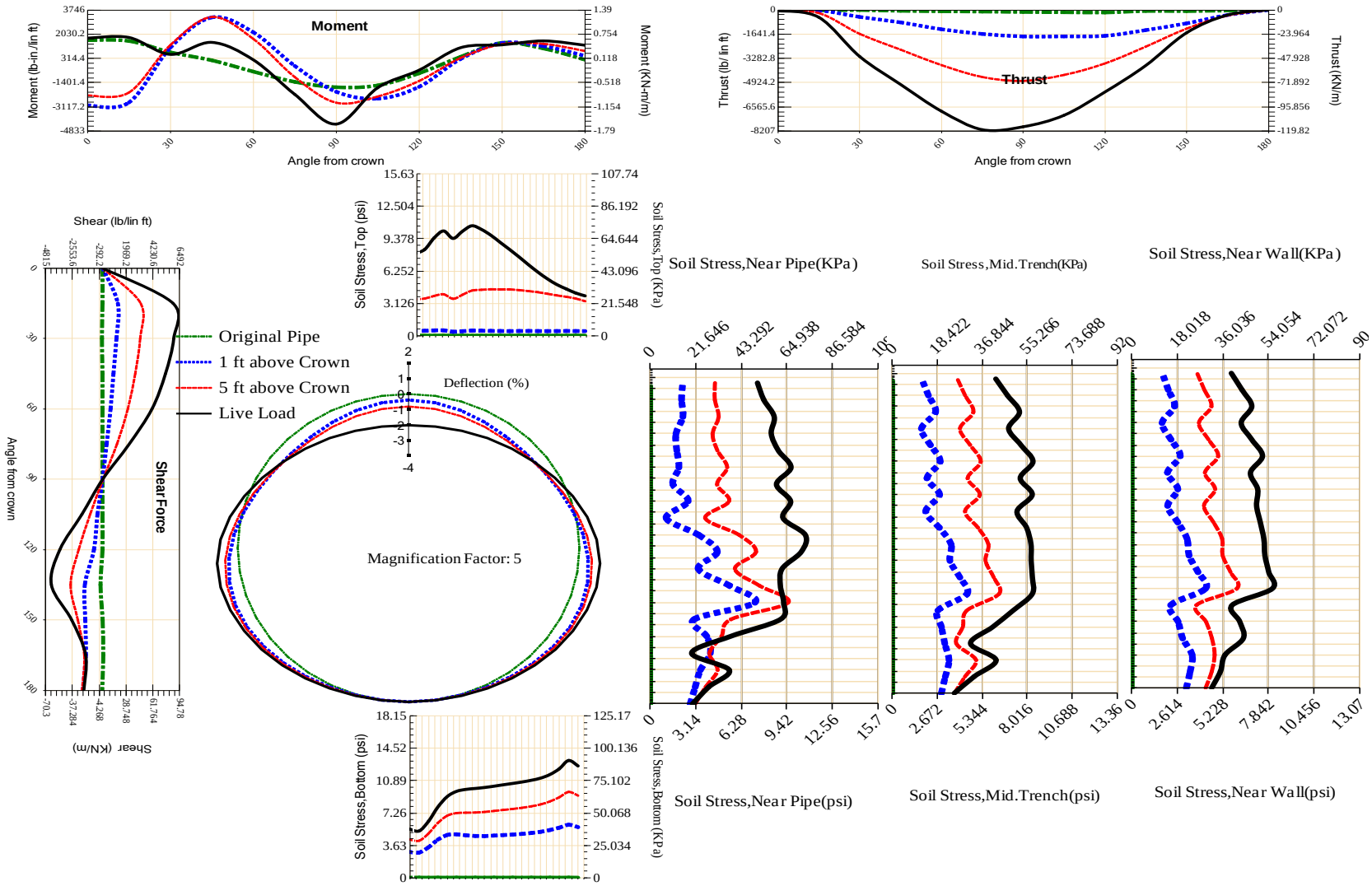

Figure A-183 Param-120-PW288-TR3OR-OD+108-EW10-H5-LiveLoad

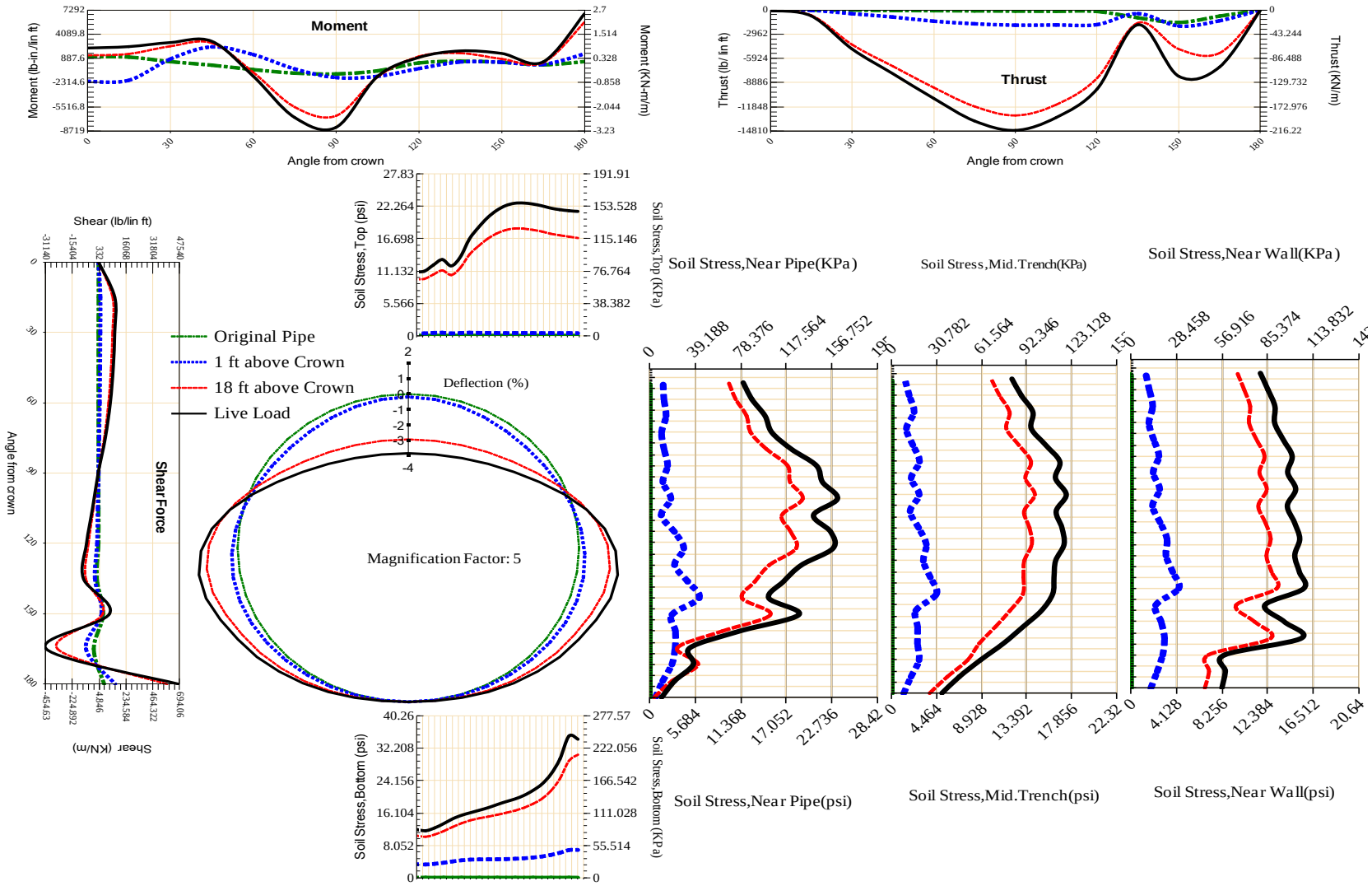

Figure A-184 Param-120-PW288-TR3OR-OD+108-EW3-H18-LiveLoad

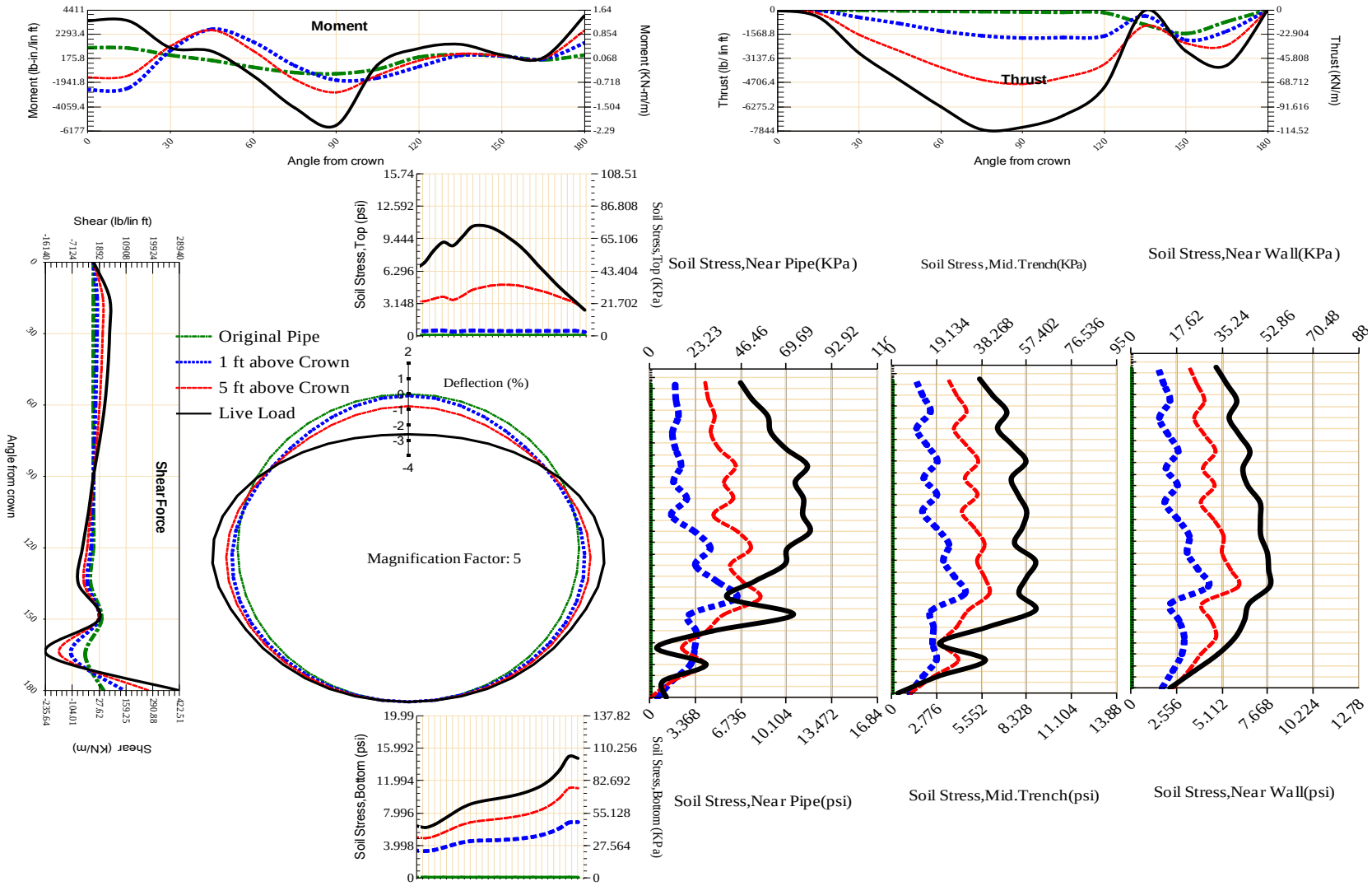

Figure A-185 Param-120-PW288-TR3OR-OD+108-EW3-H5-LiveLoad

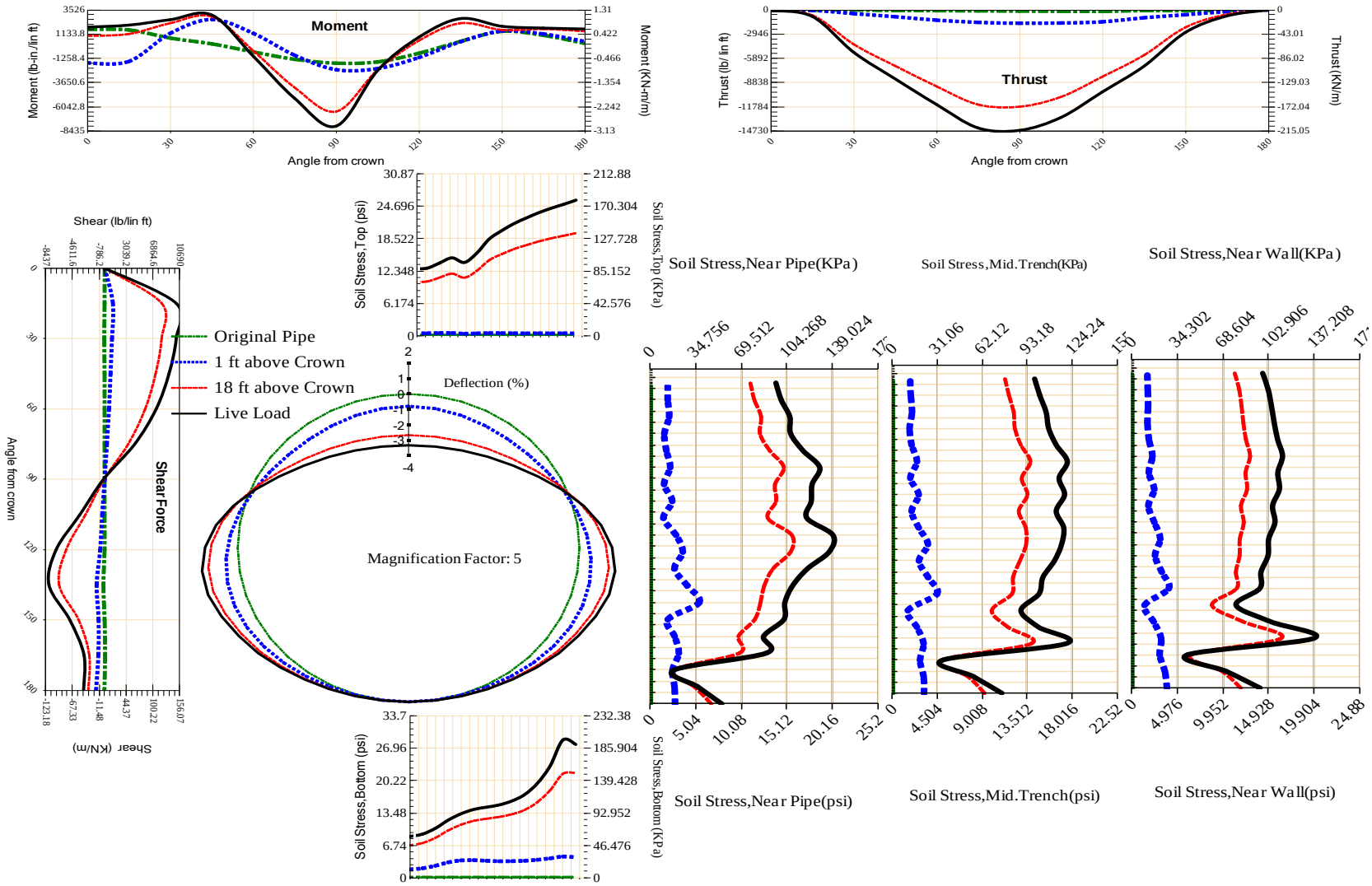

Figure A-186 Param-120-PW288-TR3OR-OD+48-EW10-H18-LiveLoad

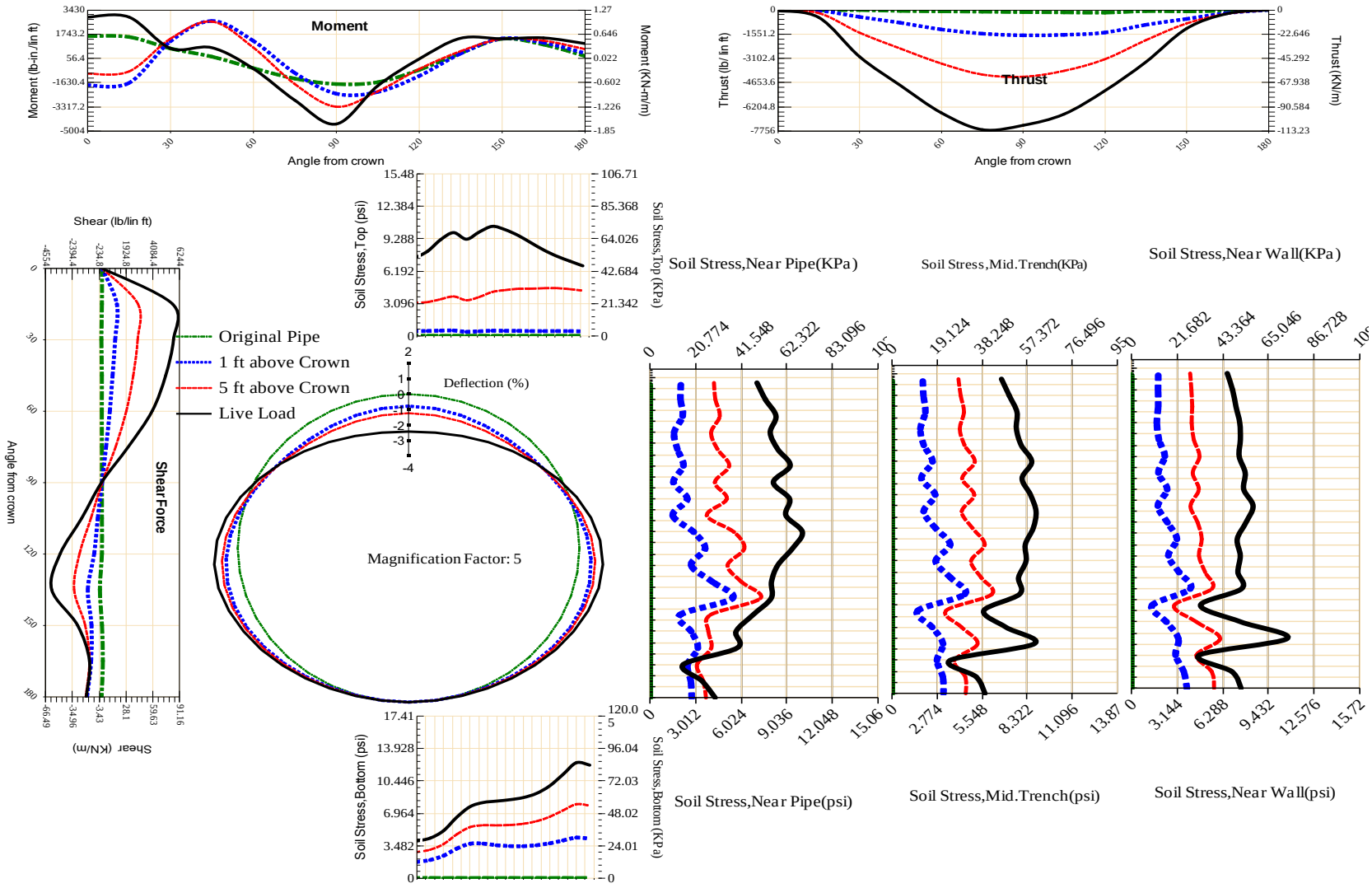

Figure A-187 Param-120-PW288-TR3OR-OD+48-EW10-H5-LiveLoad

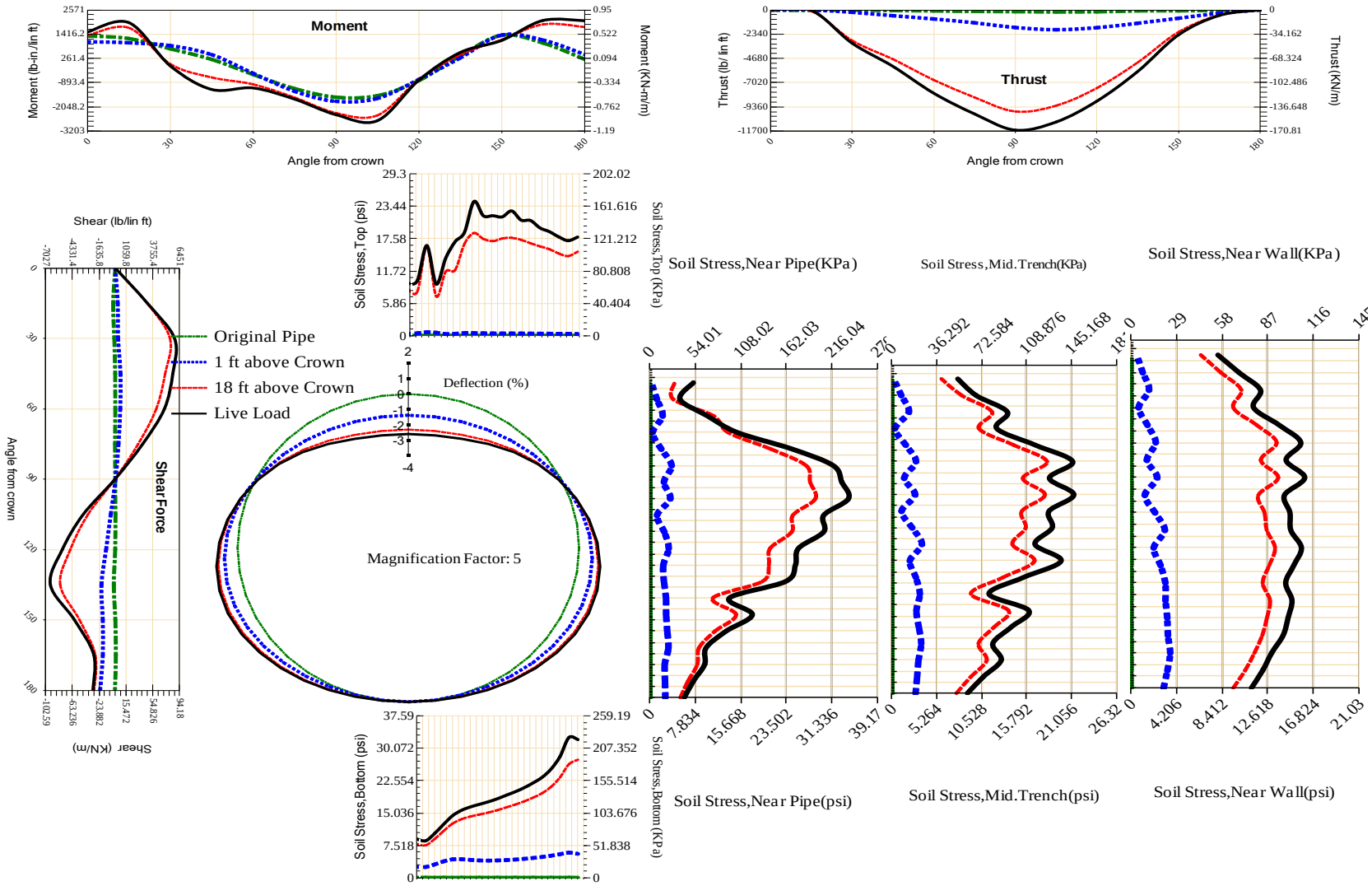

Figure A-188 Param-120-PW288-TR3SF-OD+108-EW10-H18-LiveLoad

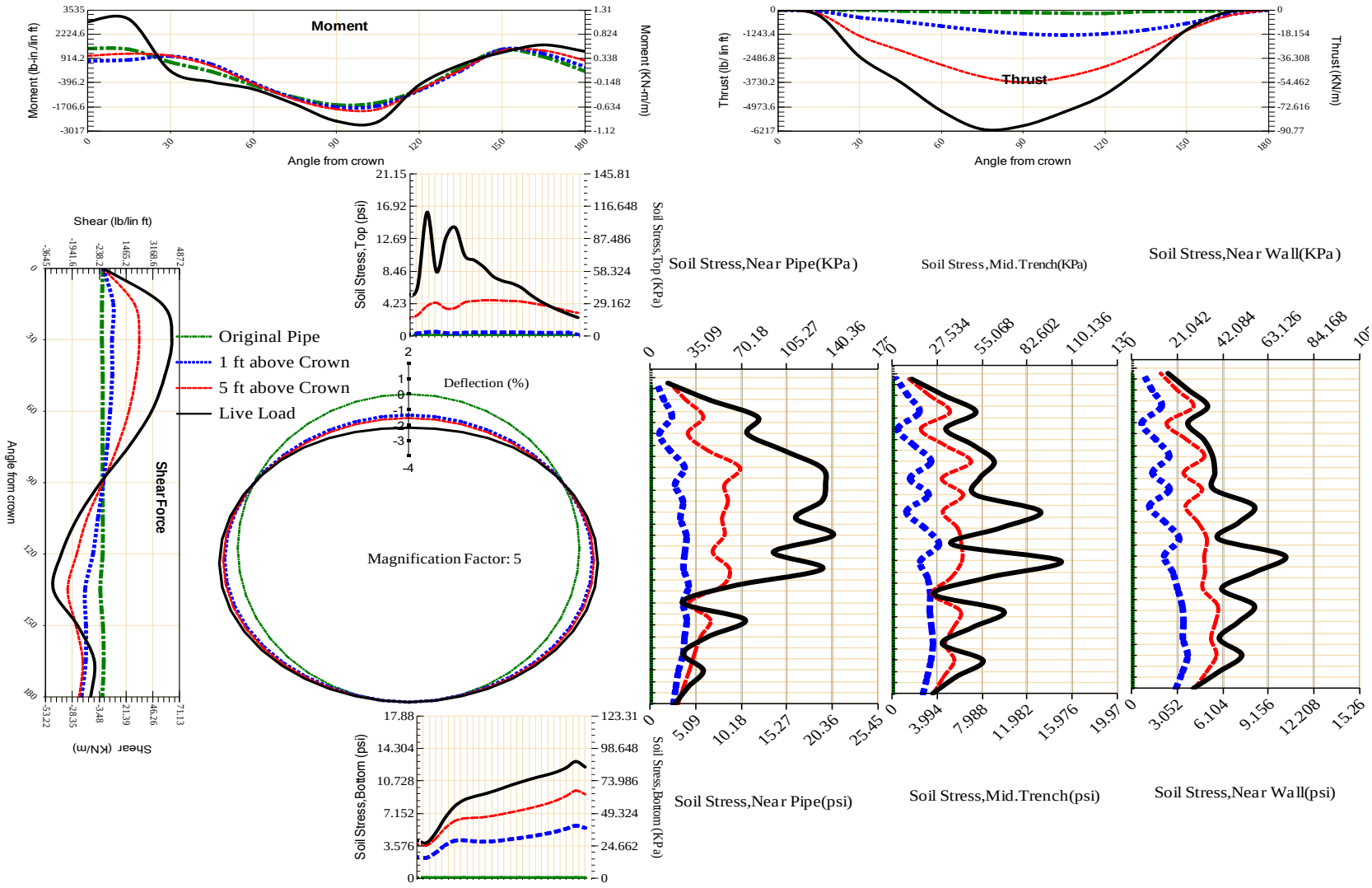

Figure A-189 Param-120-PW288-TR3SF-OD+108-EW10-H5-LiveLoad

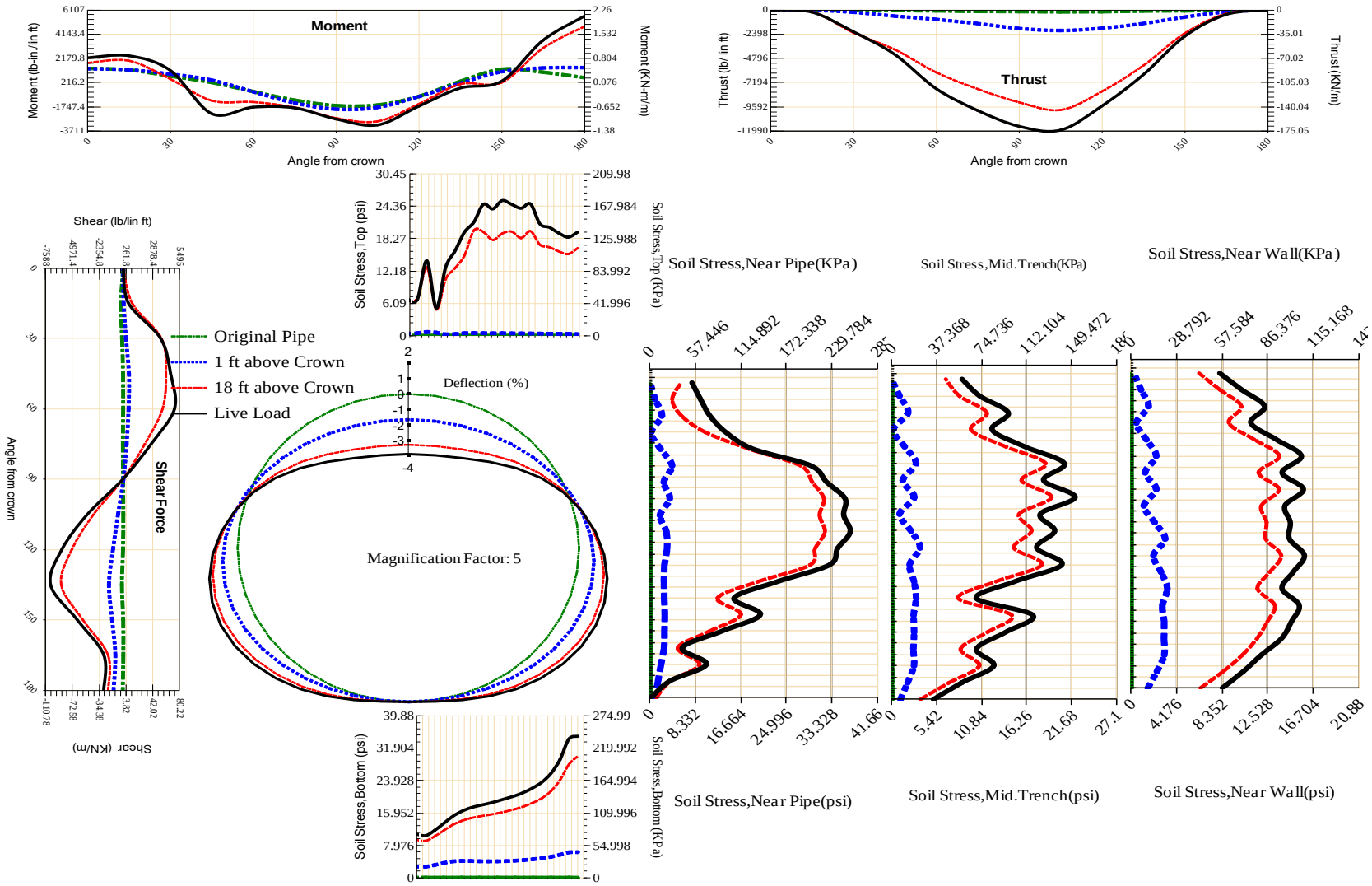

Figure A-190 Param-120-PW288-TR3SF-OD+108-EW3-H18-LiveLoad

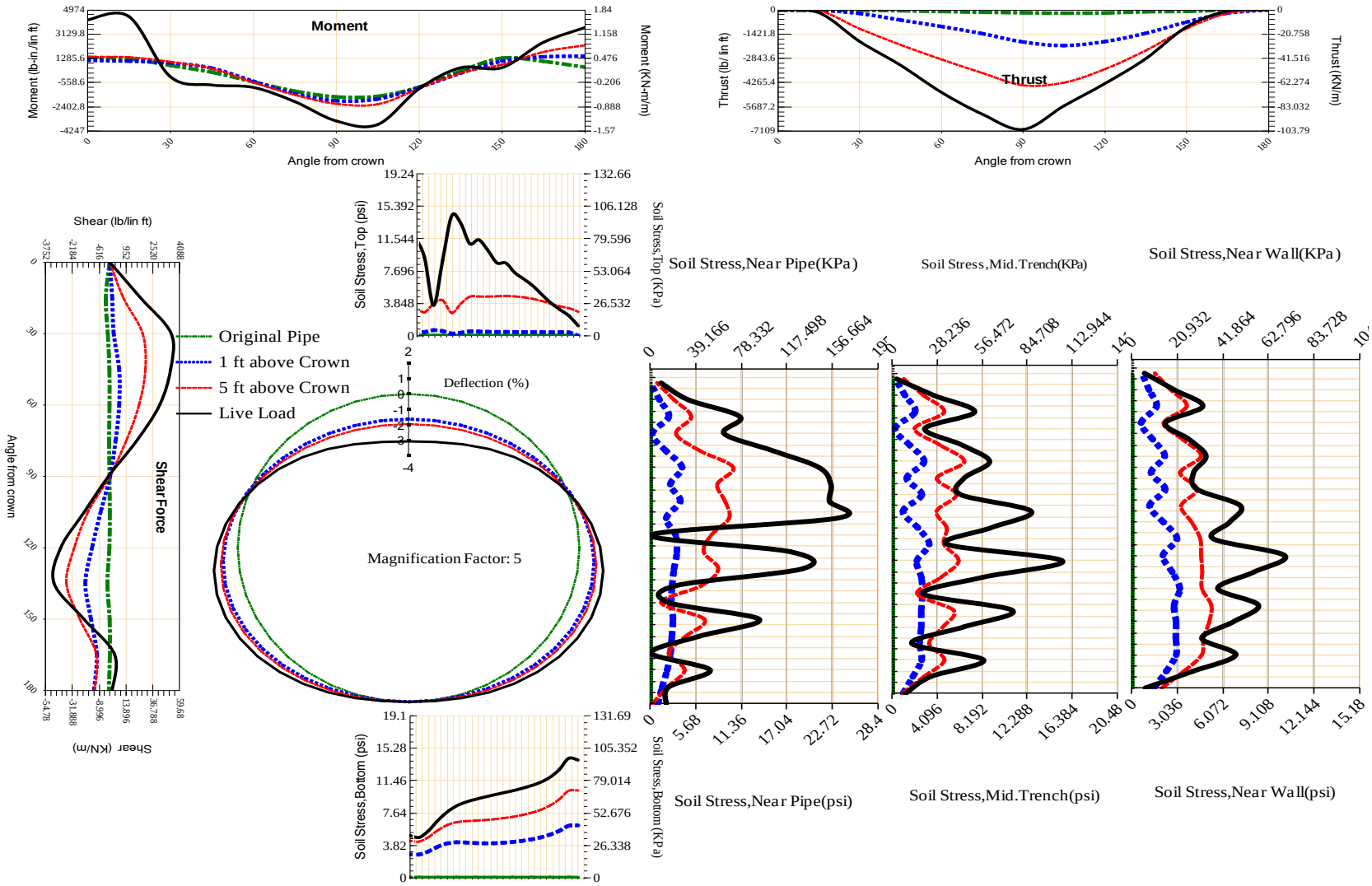

Figure A-191 Param-120-PW288-TR3SF-OD+108-EW3-H5-LiveLoad

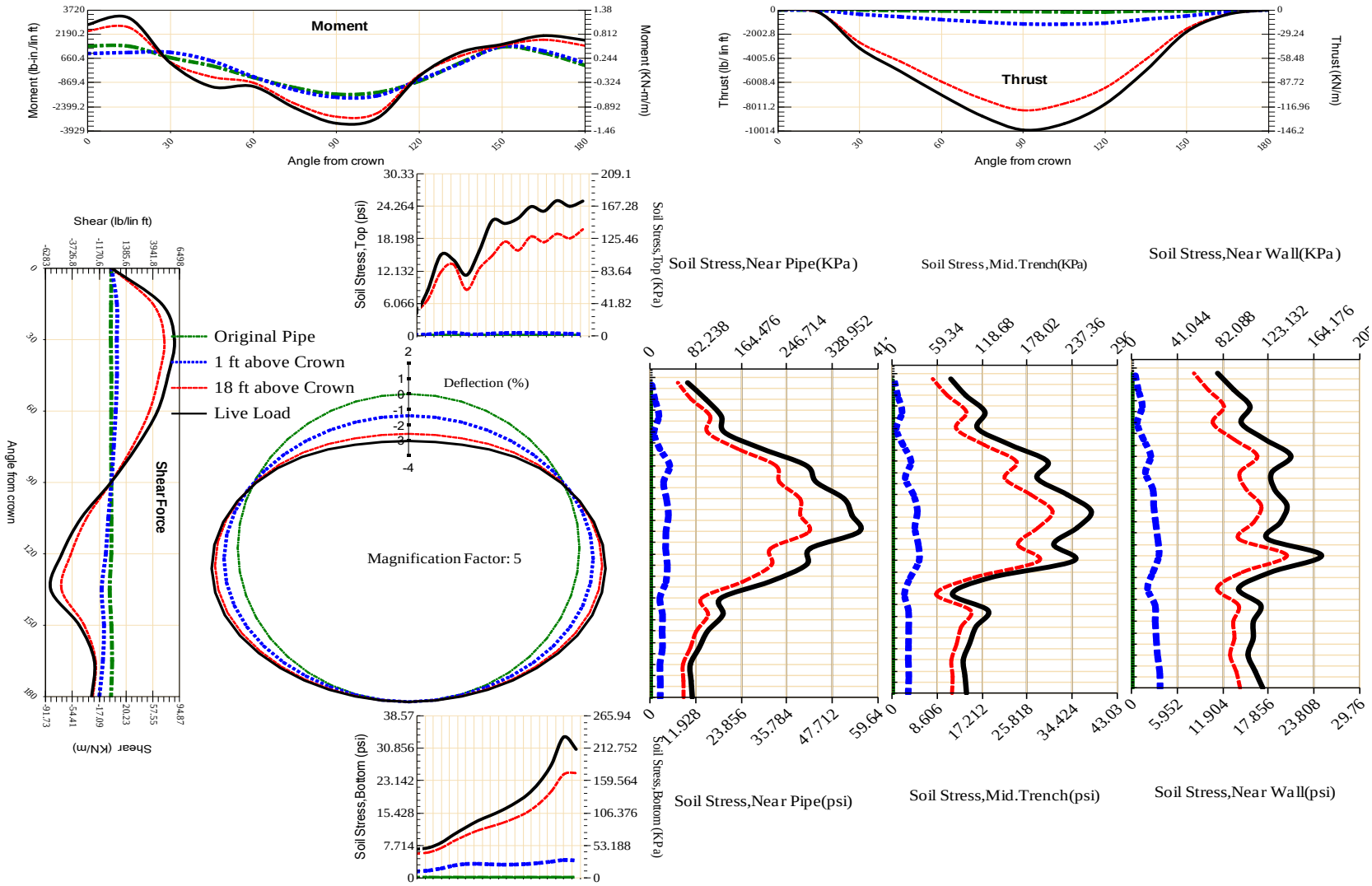

Figure A-192 Param-120-PW288-TR3SF-OD+48-EW10-H18-LiveLoad

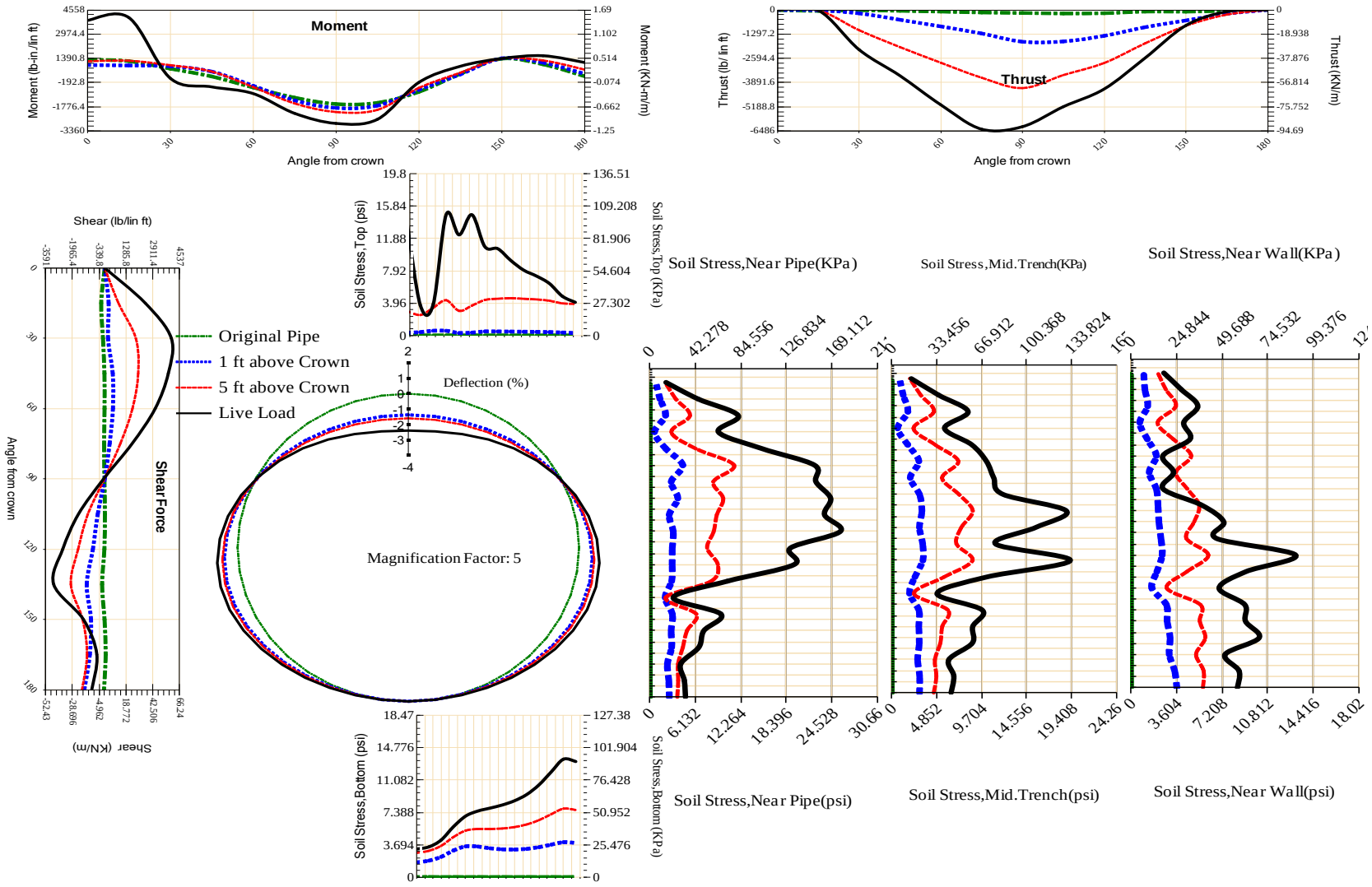

Figure A-193 Param-120-PW288-TR3SF-OD+48-EW10-H5-LiveLoad

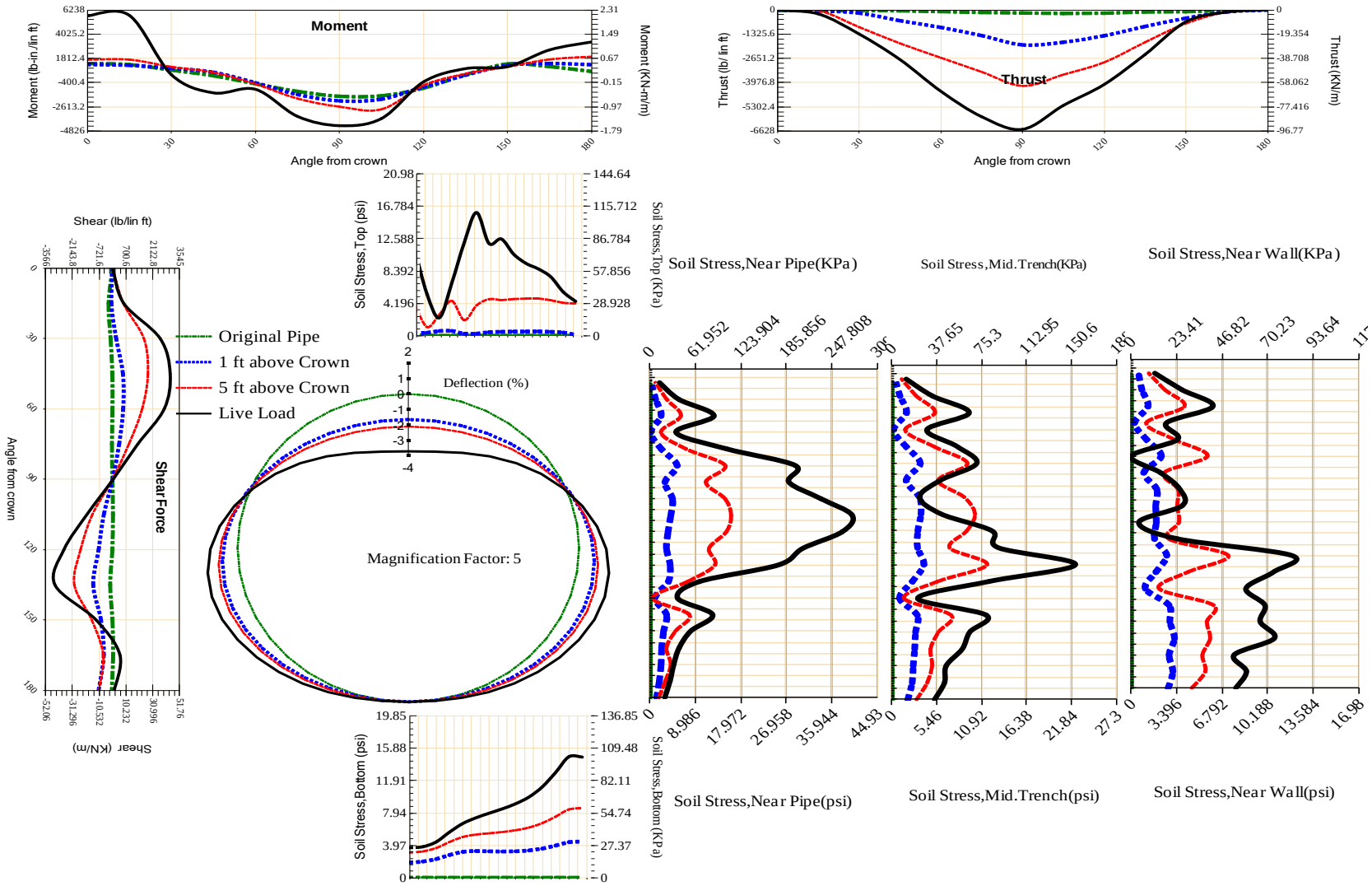

Figure A-194 Param-120-PW288-TR3SF-OD+48-EW3-H5-LiveLoad

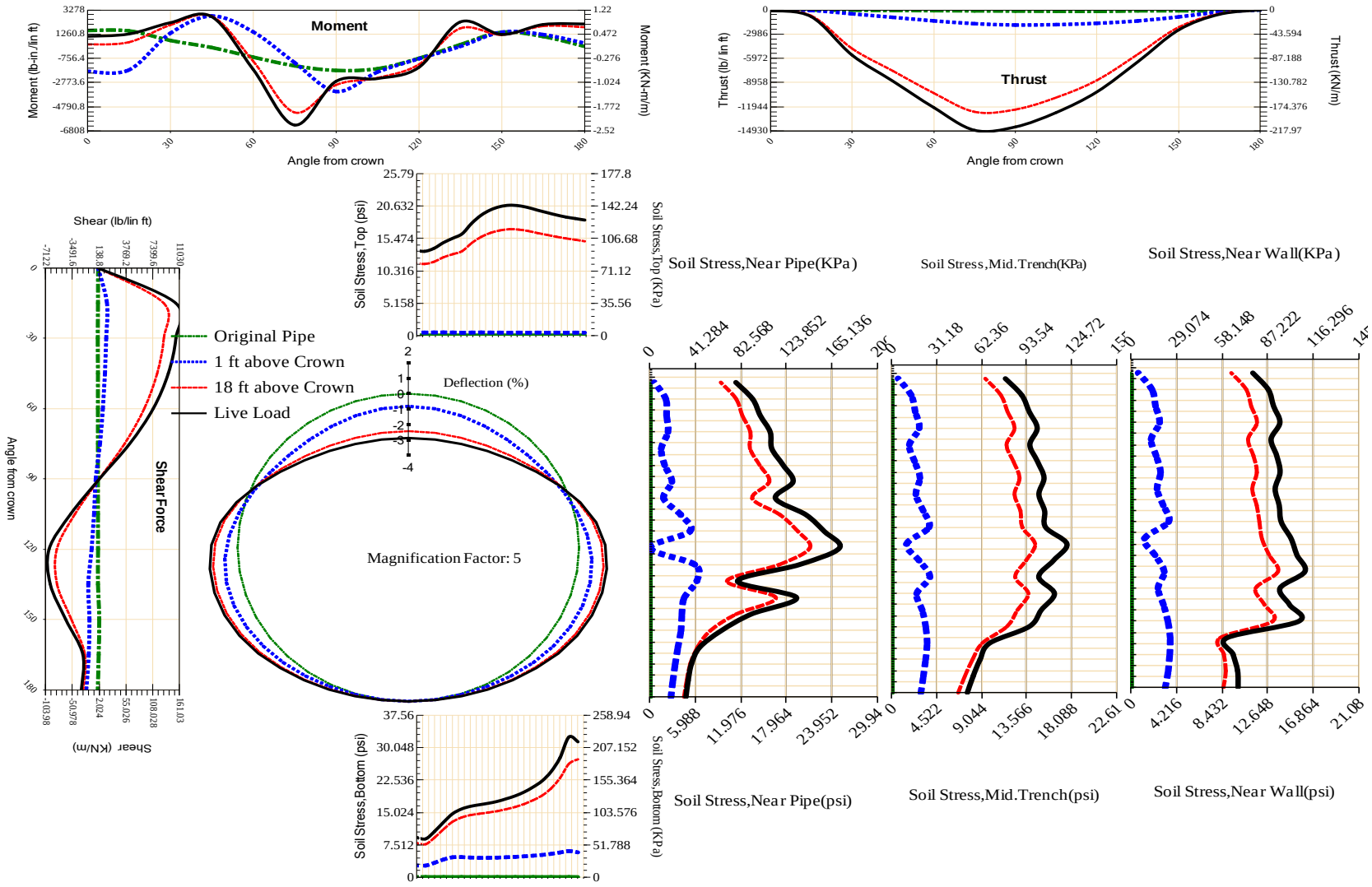

Figure A-195 Param-120-PW288-TR5OR-OD+108-EW10-H18-LiveLoad

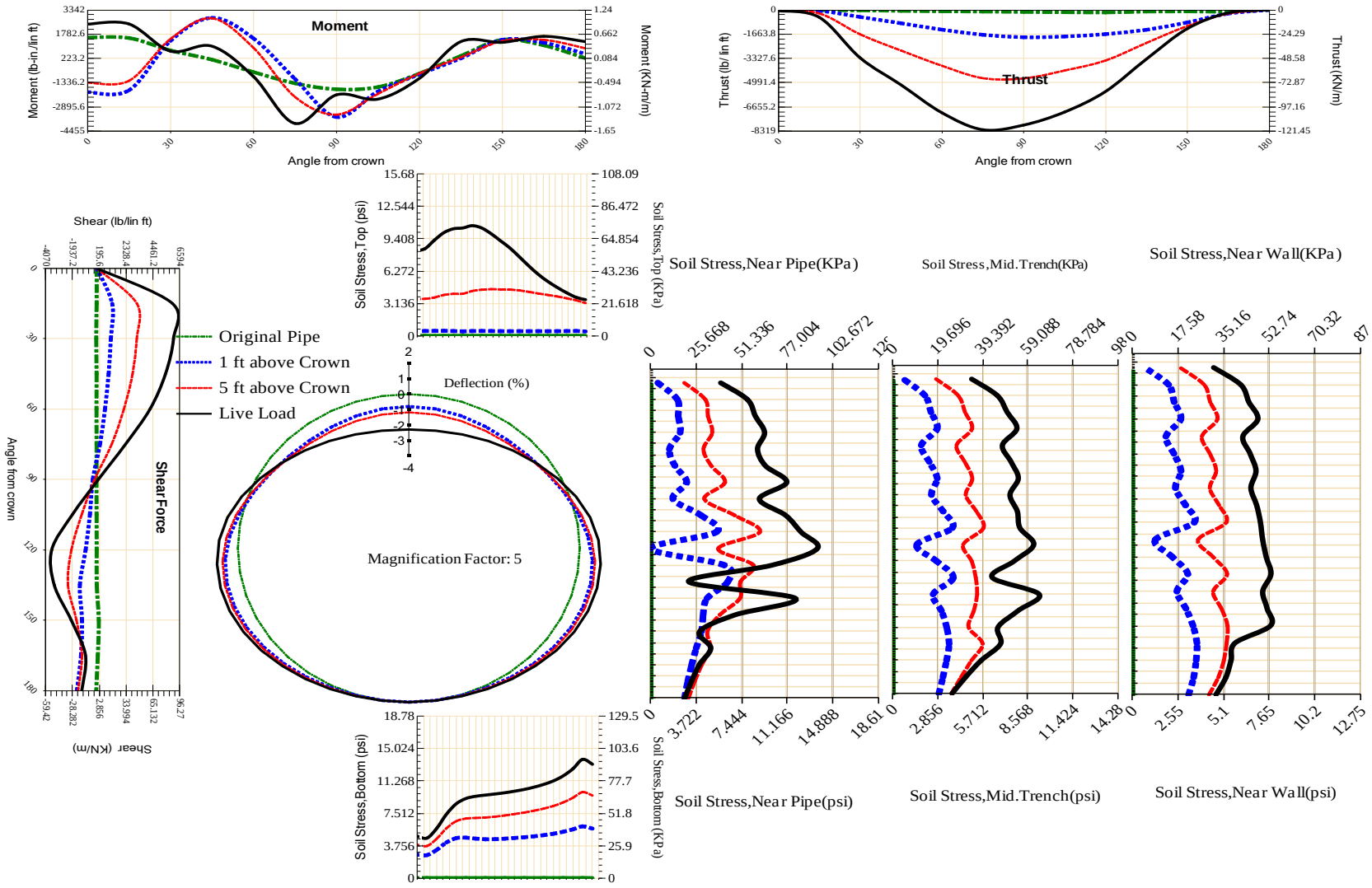

Figure A-196 Param-120-PW288-TR5OR-OD+108-EW10-H5-LiveLoad

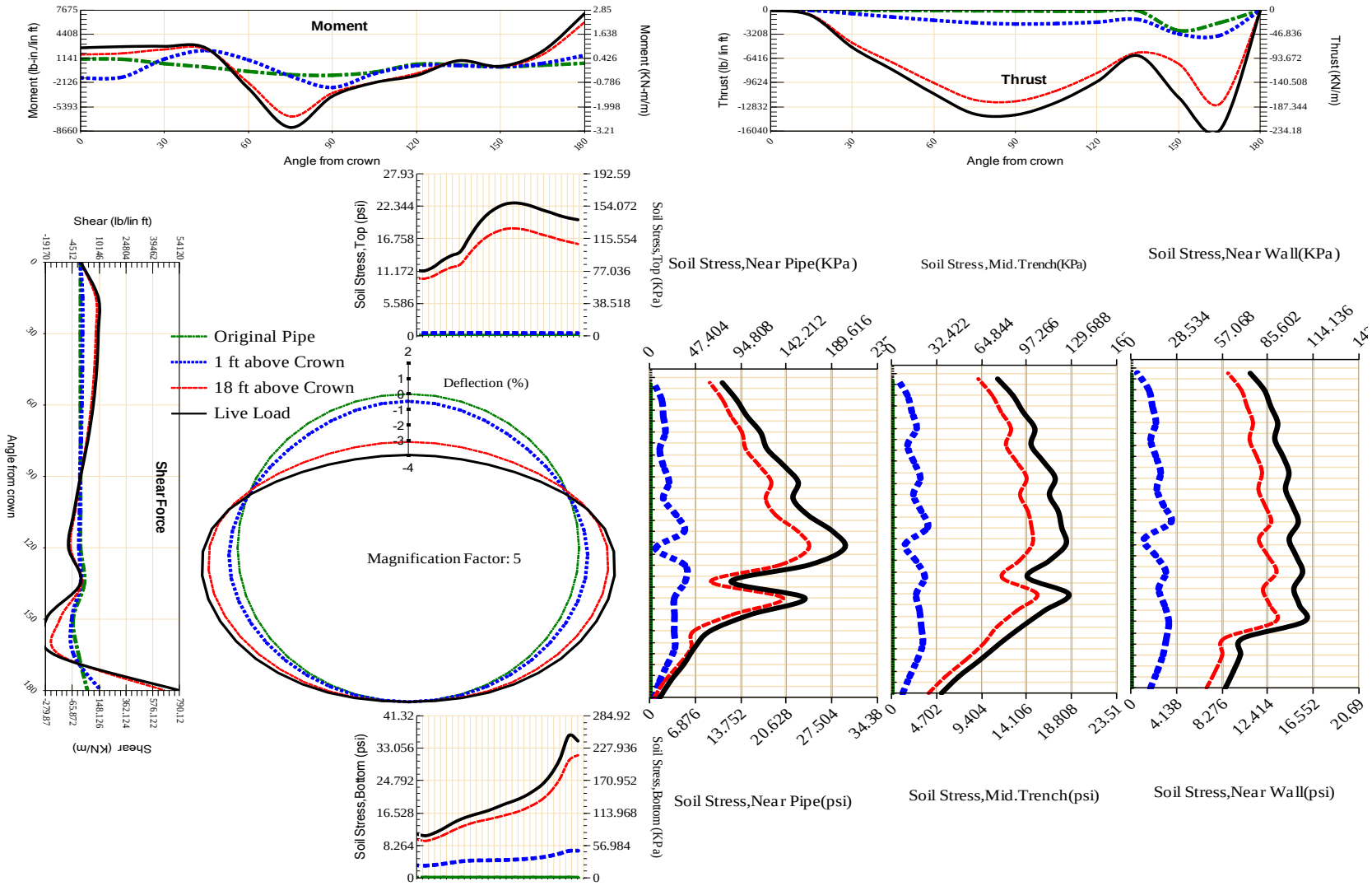

Figure A-197 Param-120-PW288-TR5OR-OD+108-EW3-H18-LiveLoad

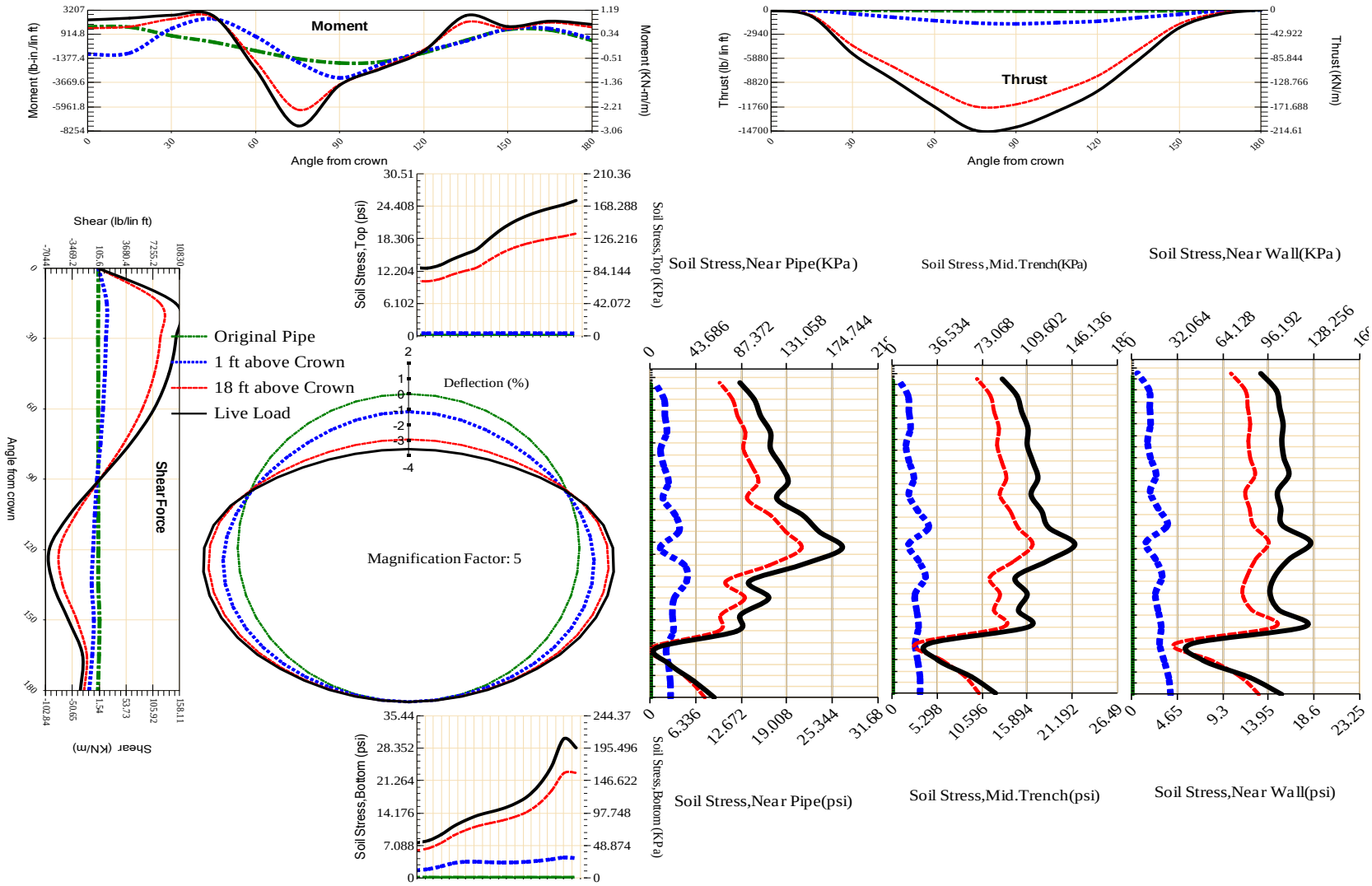

Figure A-198 Param-120-PW288-TR5OR-OD+48-EW10-H18-LiveLoad

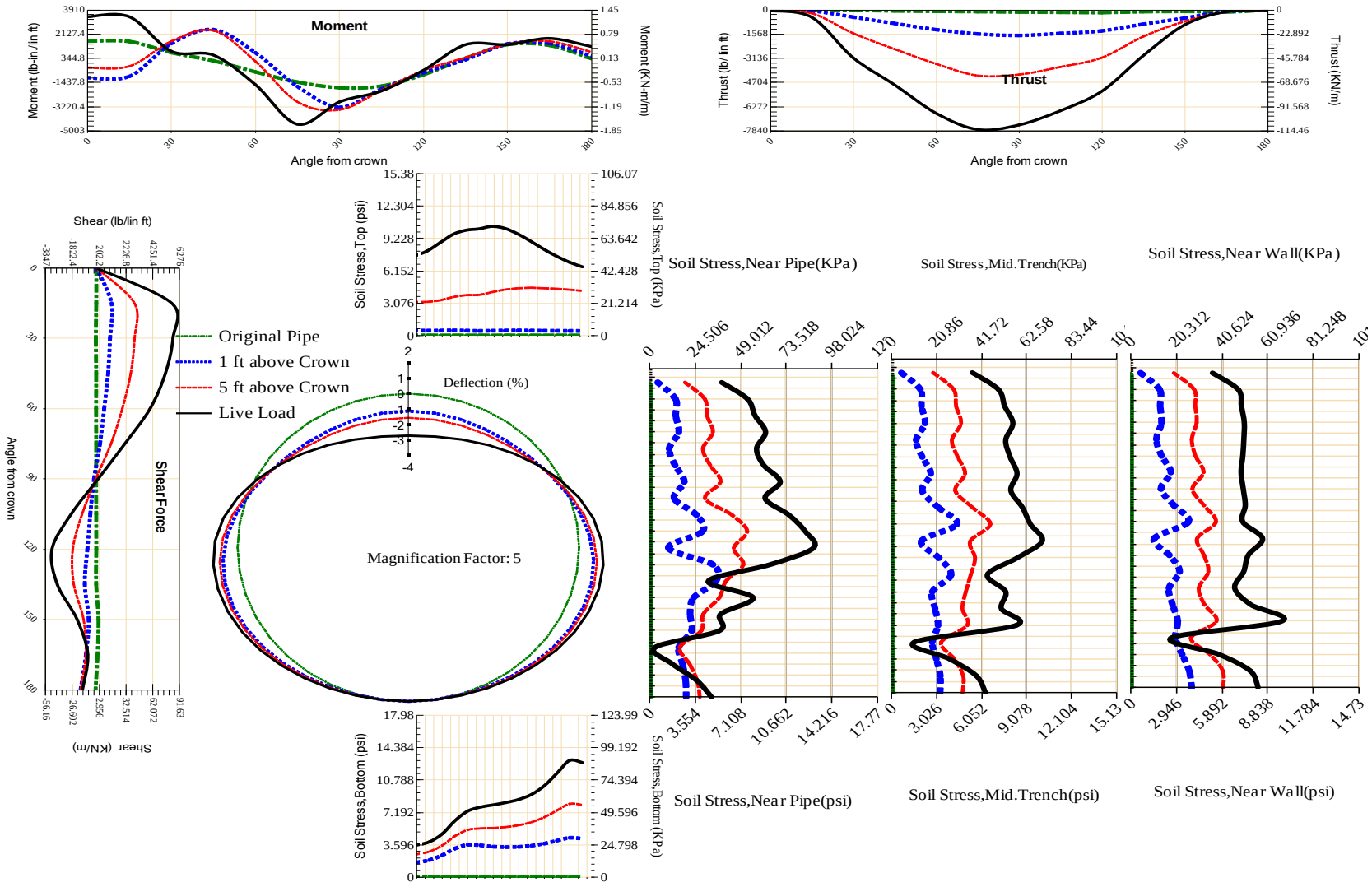

Figure A-199 Param-120-PW288-TR5OR-OD+48-EW10-H5-LiveLoad

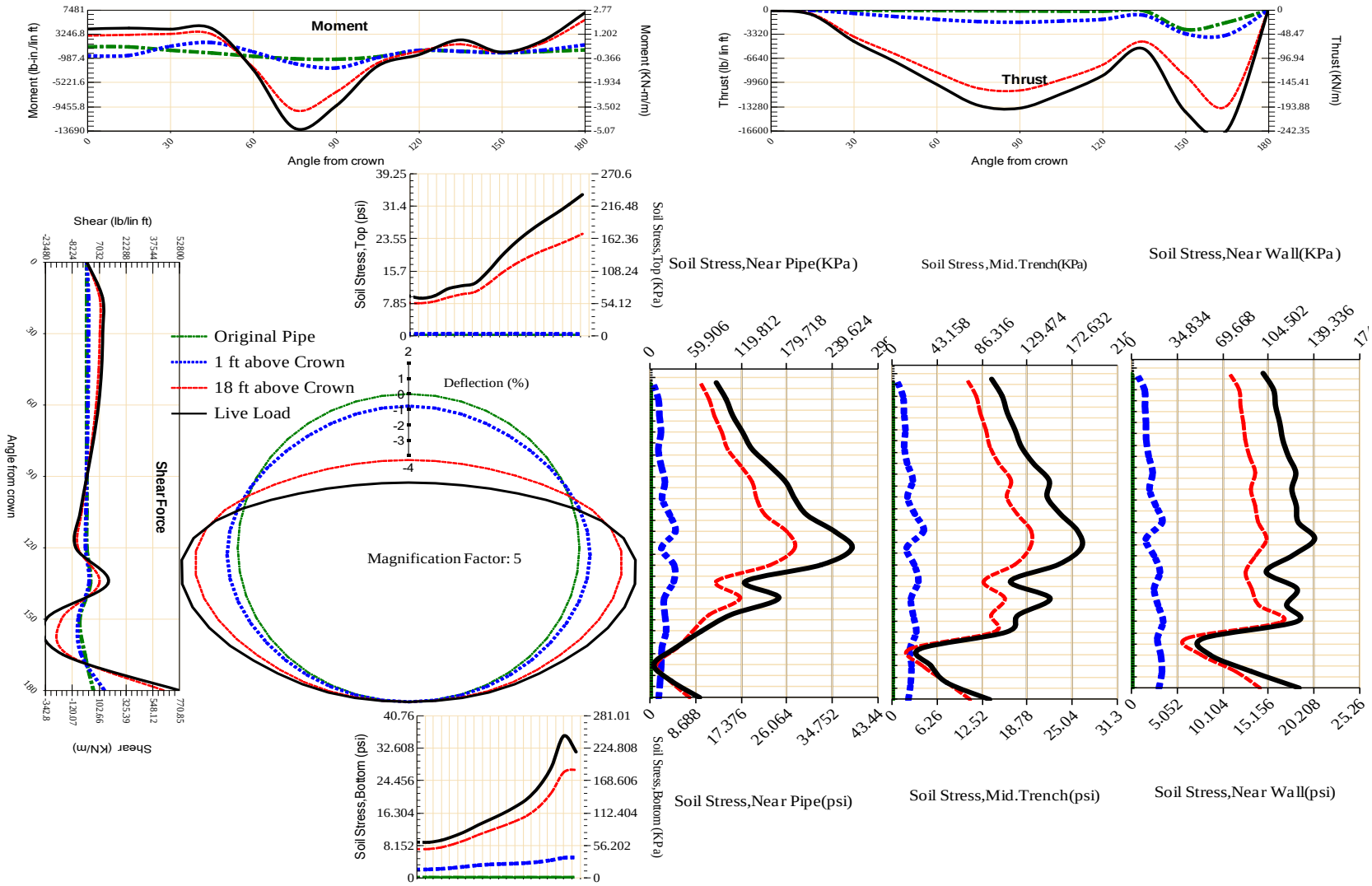

Figure A-200 Param-120-PW288-TR5OR-OD+48-EW3-H18-LiveLoad

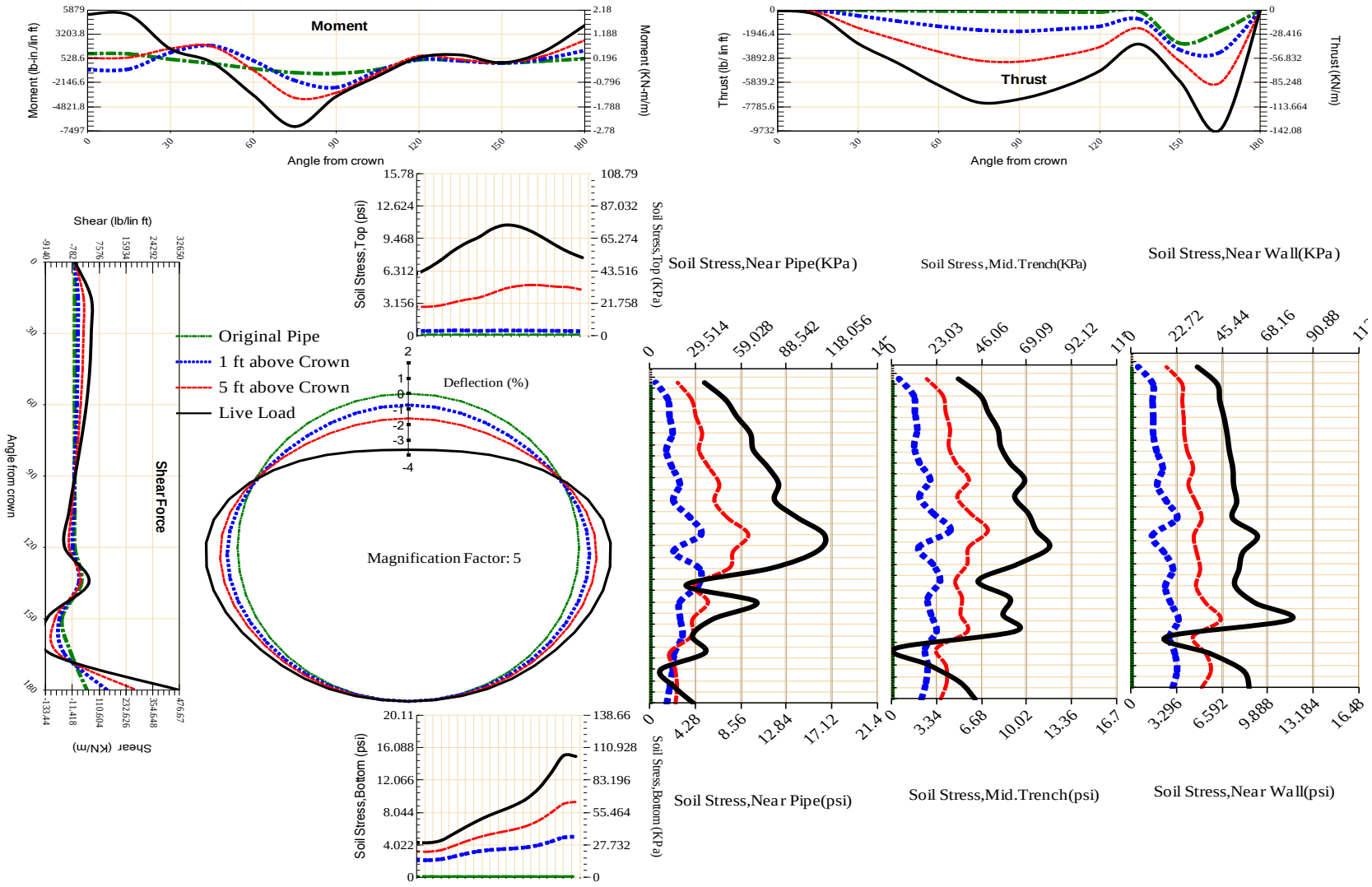

Figure A-201 Param-120-PW288-TR5OR-OD+48-EW3-H5-LiveLoad

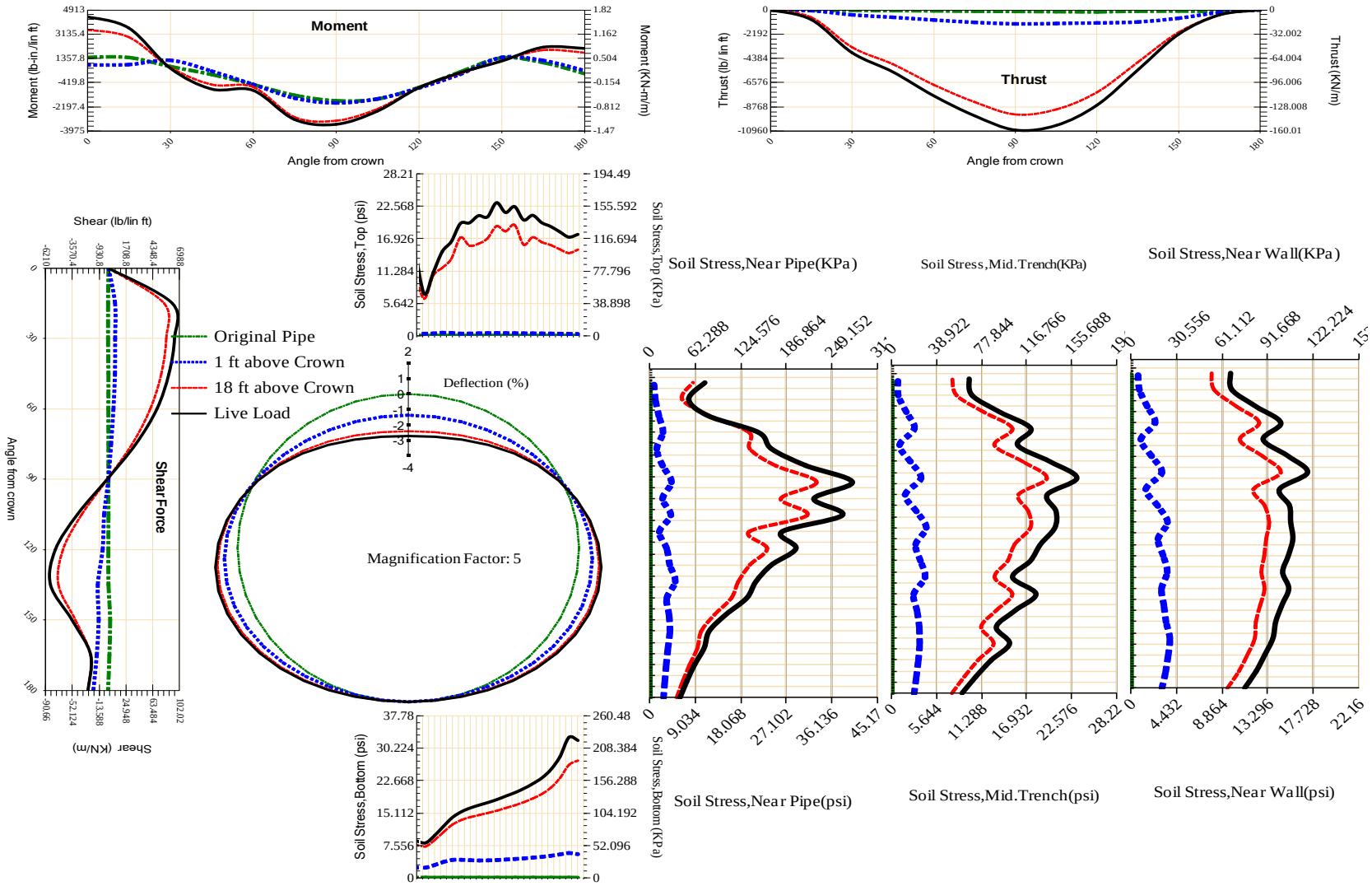

Figure A-202 Param-120-PW288-TR5SF-OD+108-EW10-H18-LiveLoad

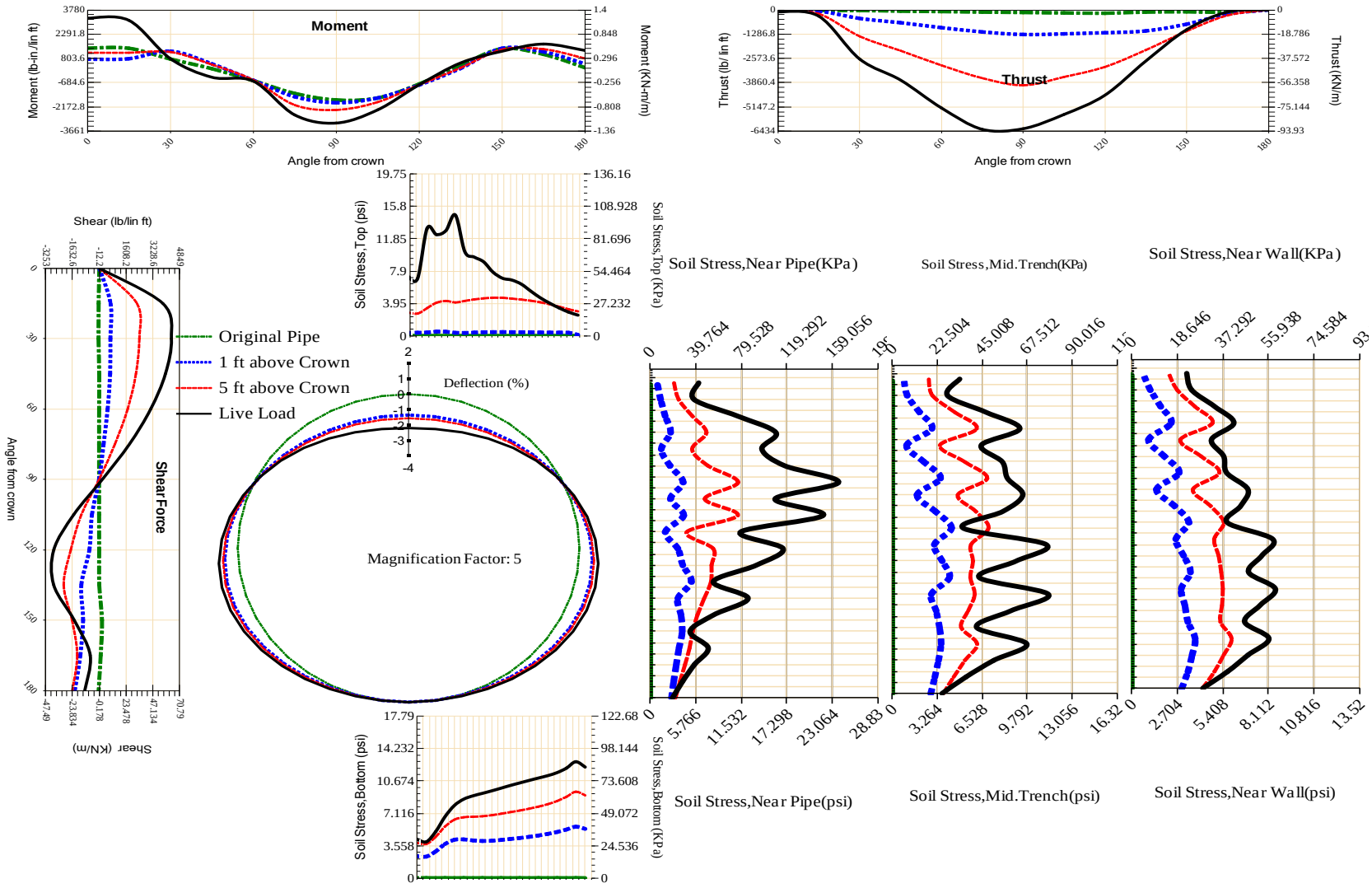

Figure A-203 Param-120-PW288-TR5SF-OD+108-EW10-H5-LiveLoad

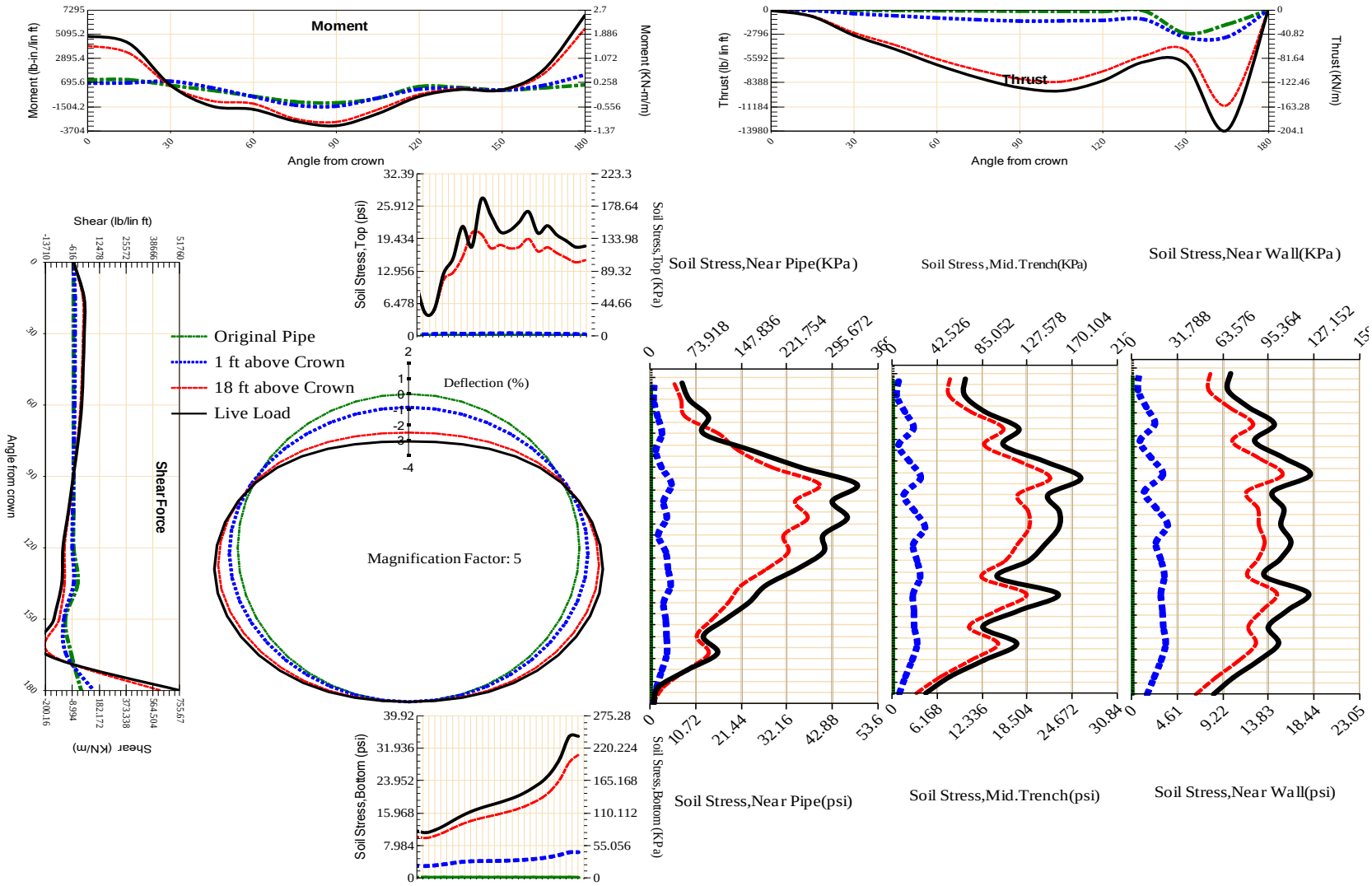

Figure A-204 Param-120-PW288-TR5SF-OD+108-EW3-H18-LiveLoad

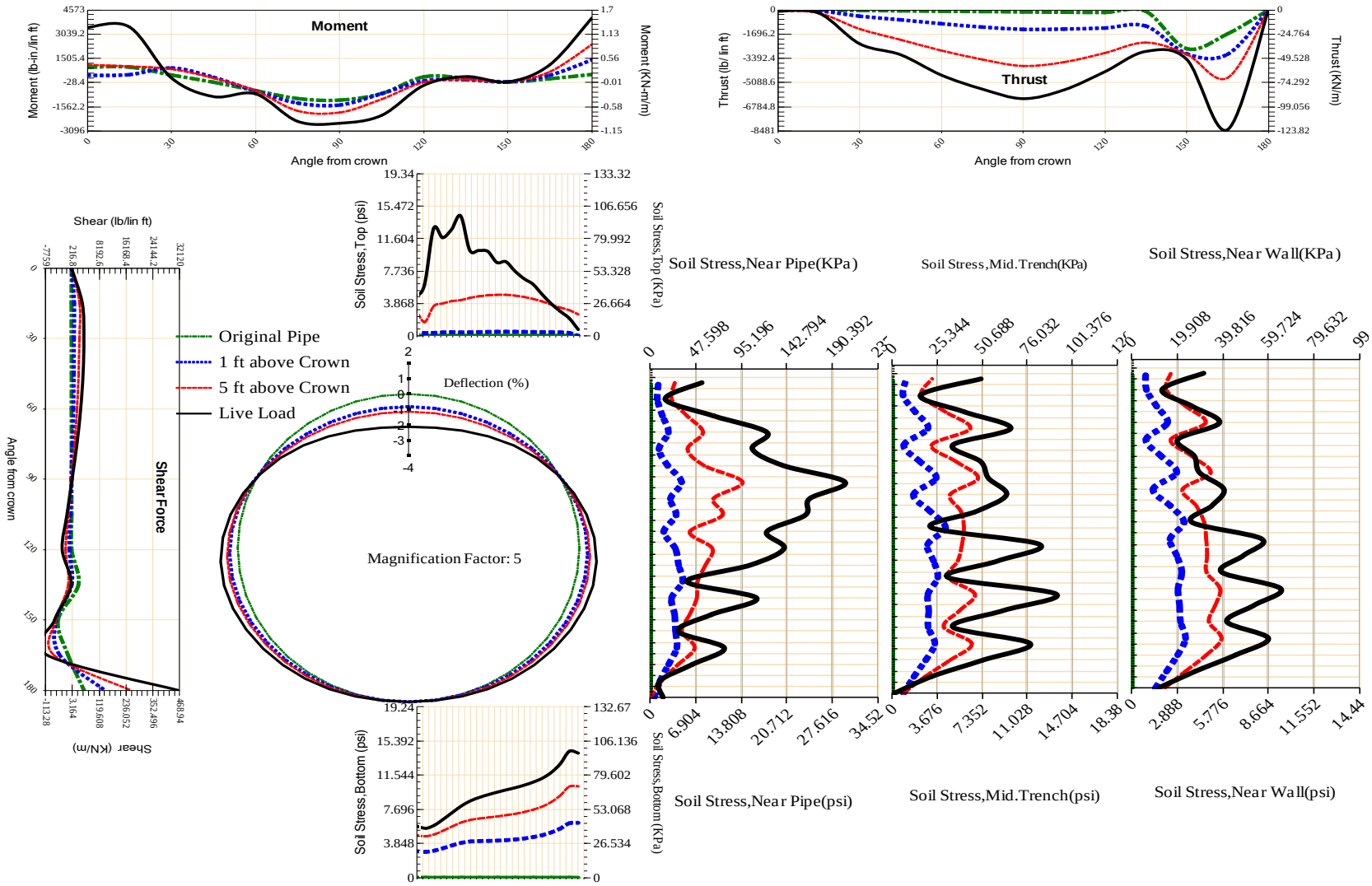

Figure A-205 Param-120-PW288-TR5SF-OD+108-EW3-H5-LiveLoad

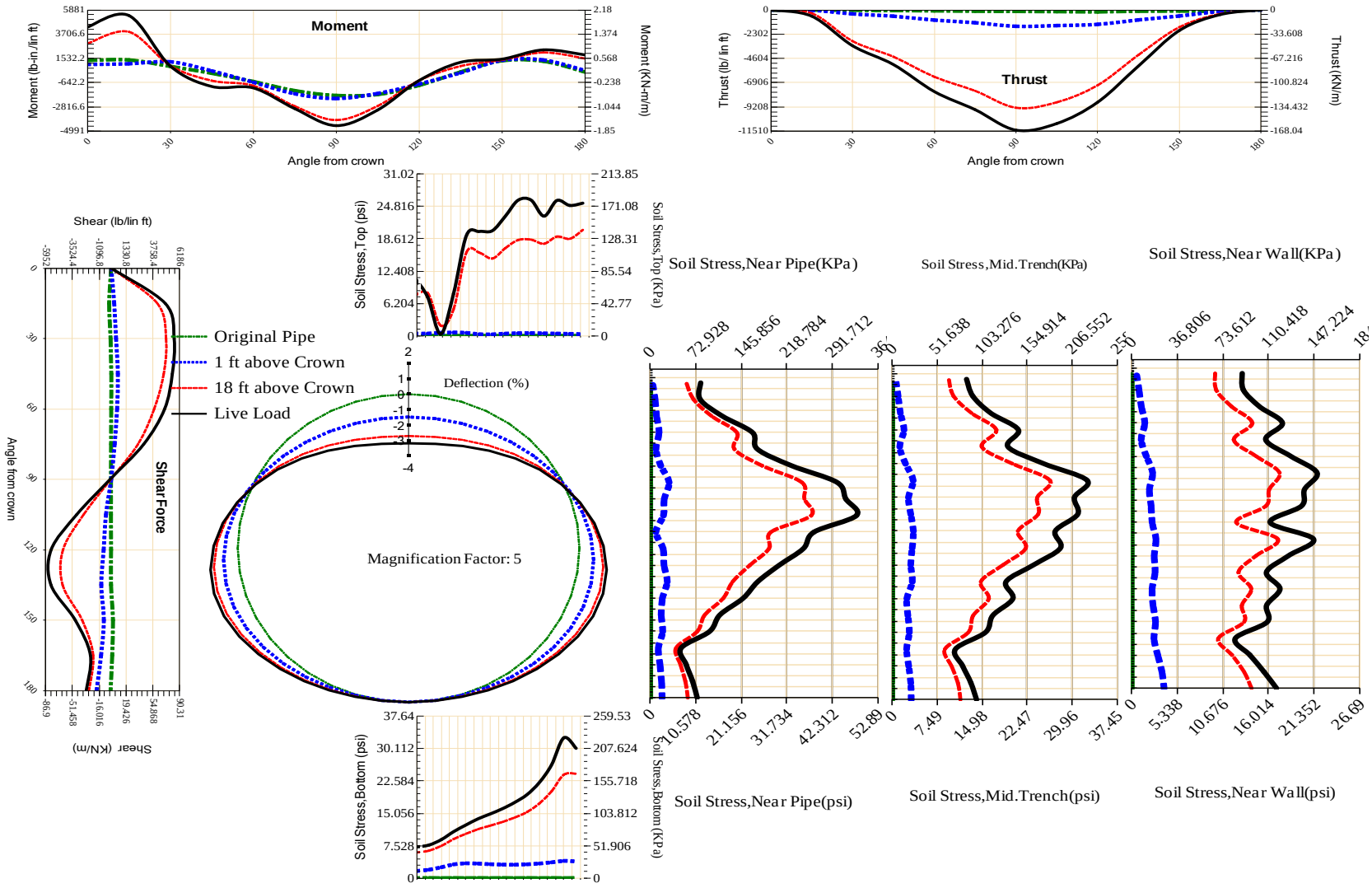

Figure A-206 Param-120-PW288-TR5SF-OD+48-EW10-H18-LiveLoad

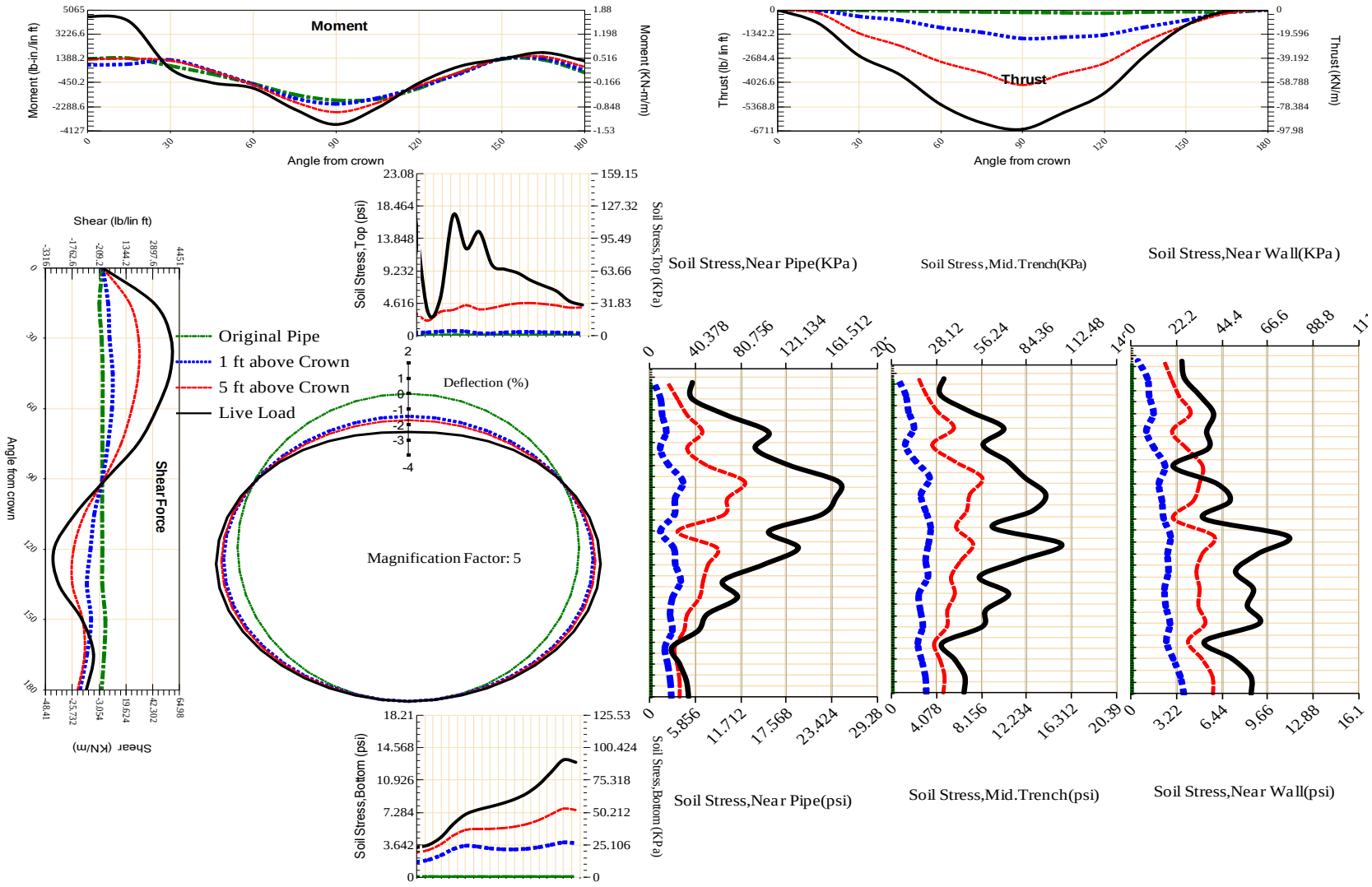

Figure A-207 Param-120-PW288-TR5SF-OD+48-EW10-H5-LiveLoad

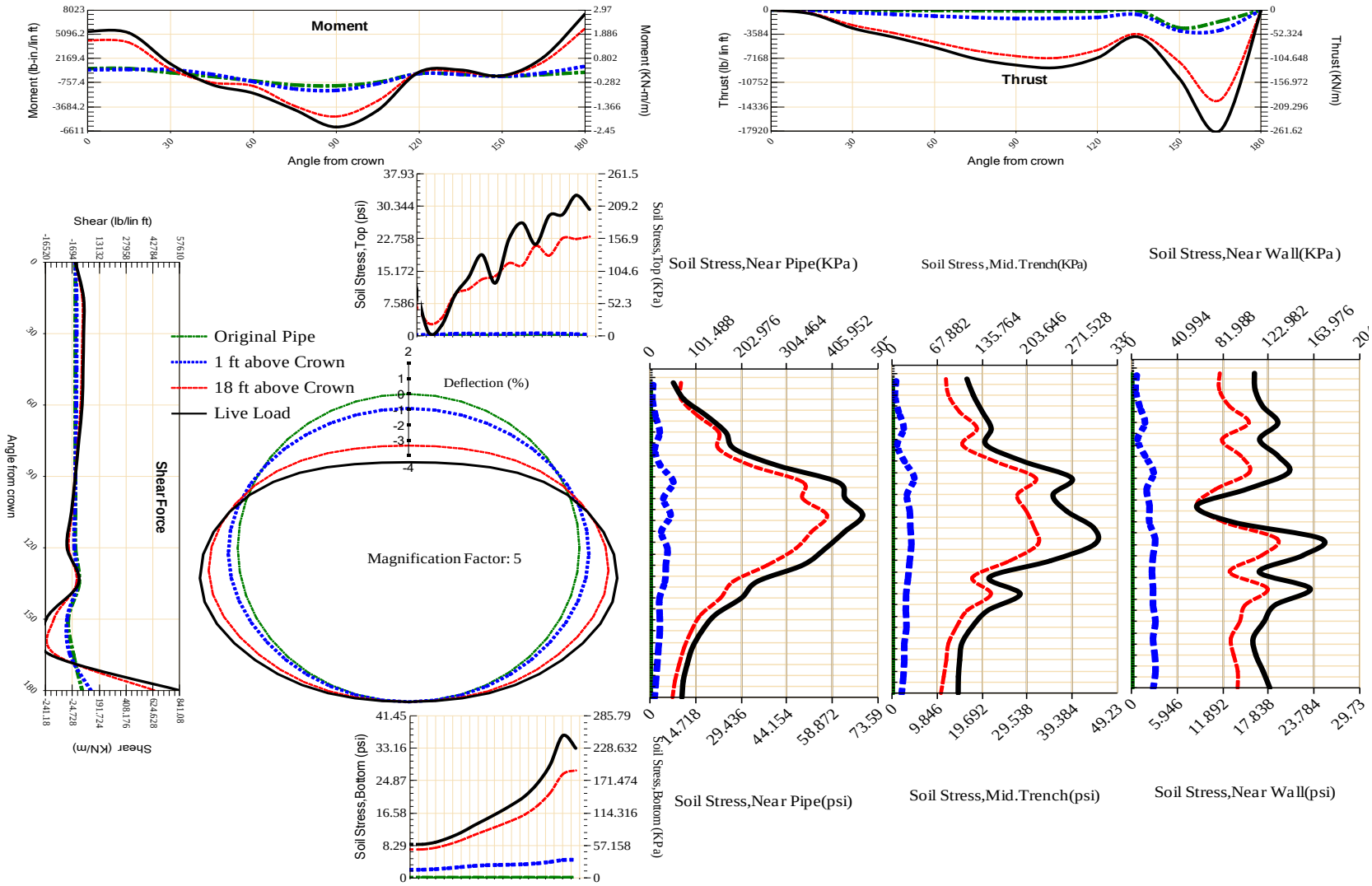

Figure A-208 Param-120-PW288-TR5SF-OD+48-EW3-H18-LiveLoad

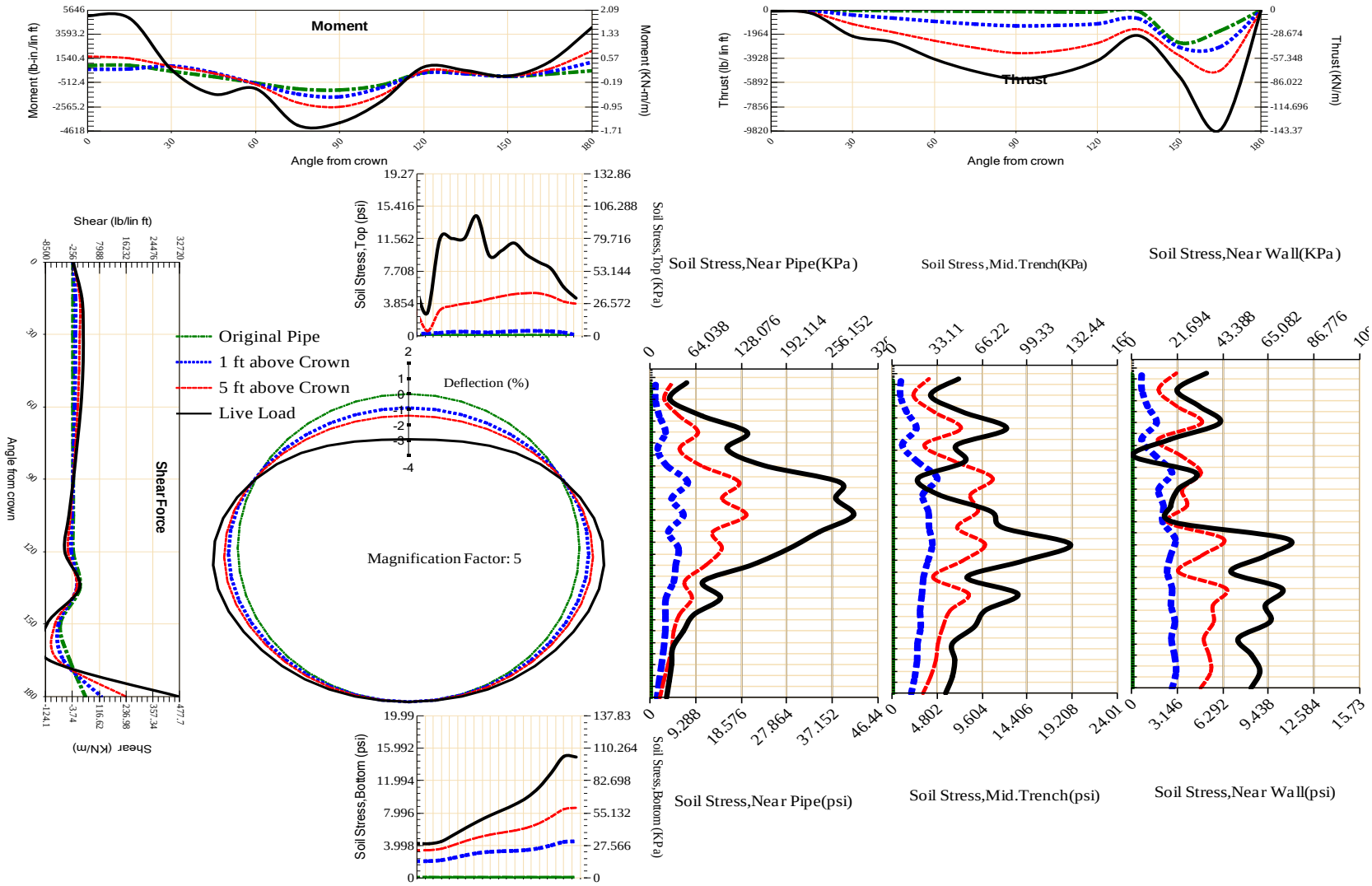

Figure A-209 Param-120-PW288-TR5SF-OD+48-EW3-H5-LiveLoad

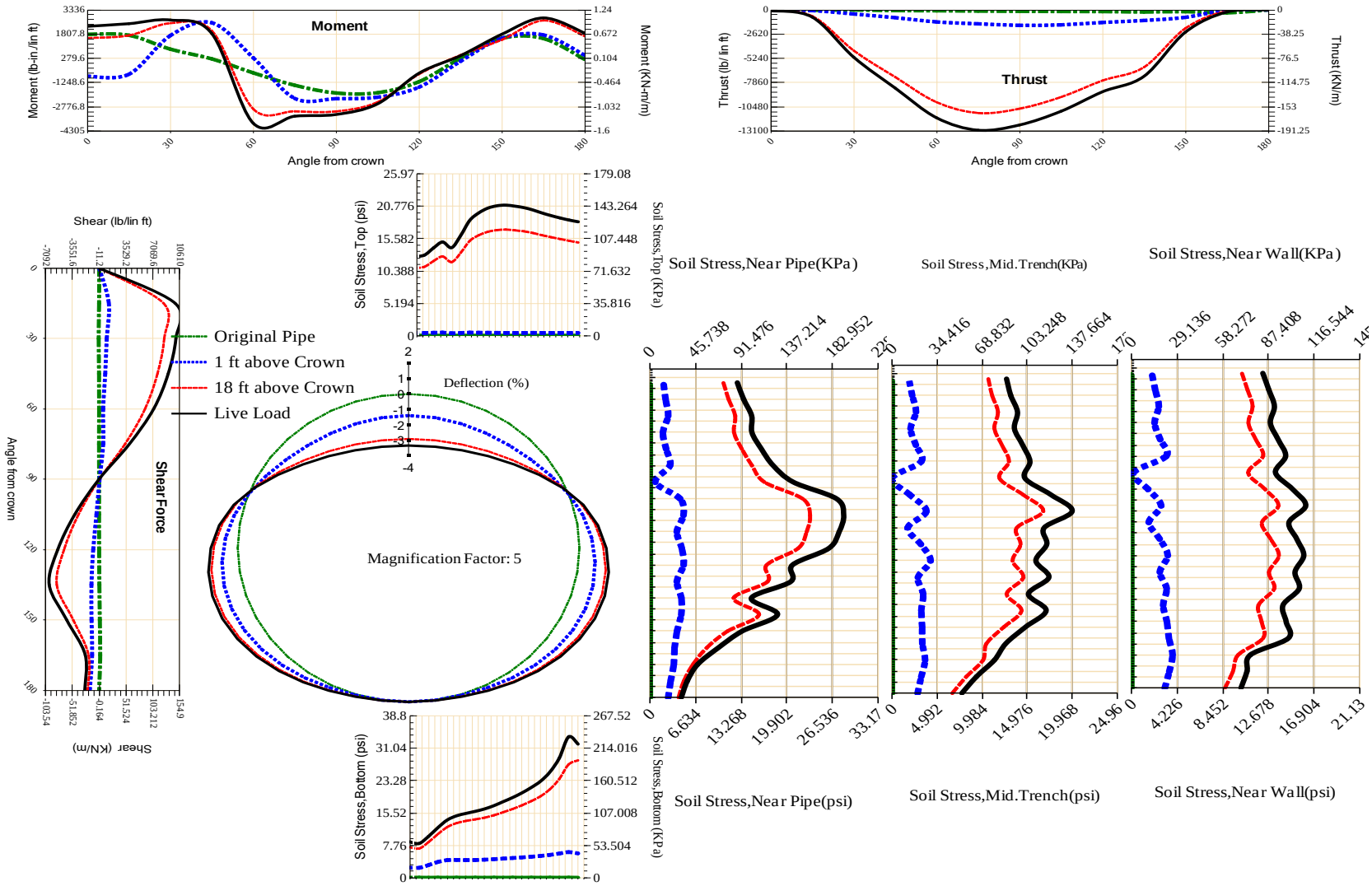

Figure A-210 Param-120-PW288-TR7OR-OD+108-EW10-H18-LiveLoad

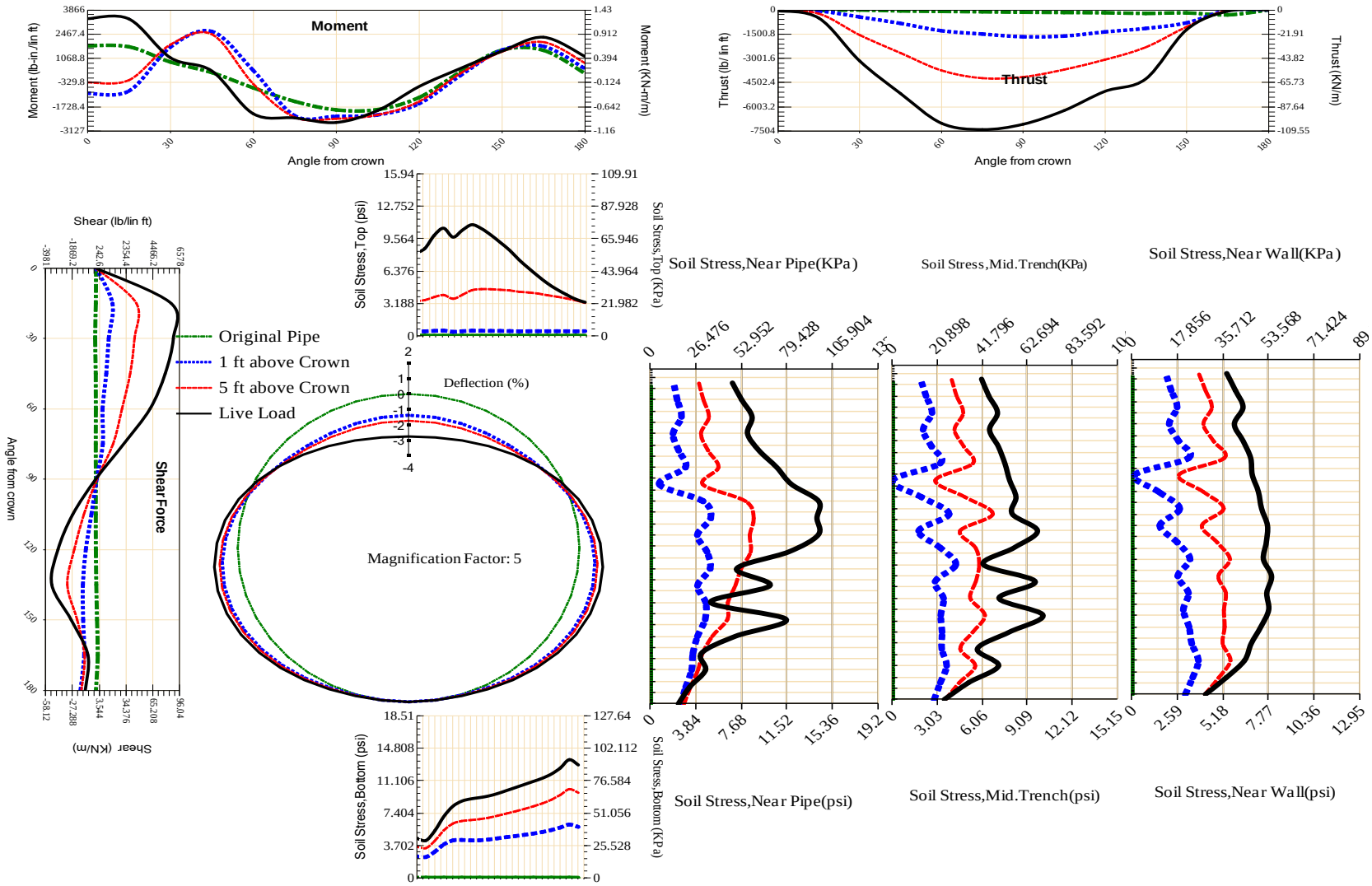

Figure A-211 Param-120-PW288-TR7OR-OD+108-EW10-H5-LiveLoad

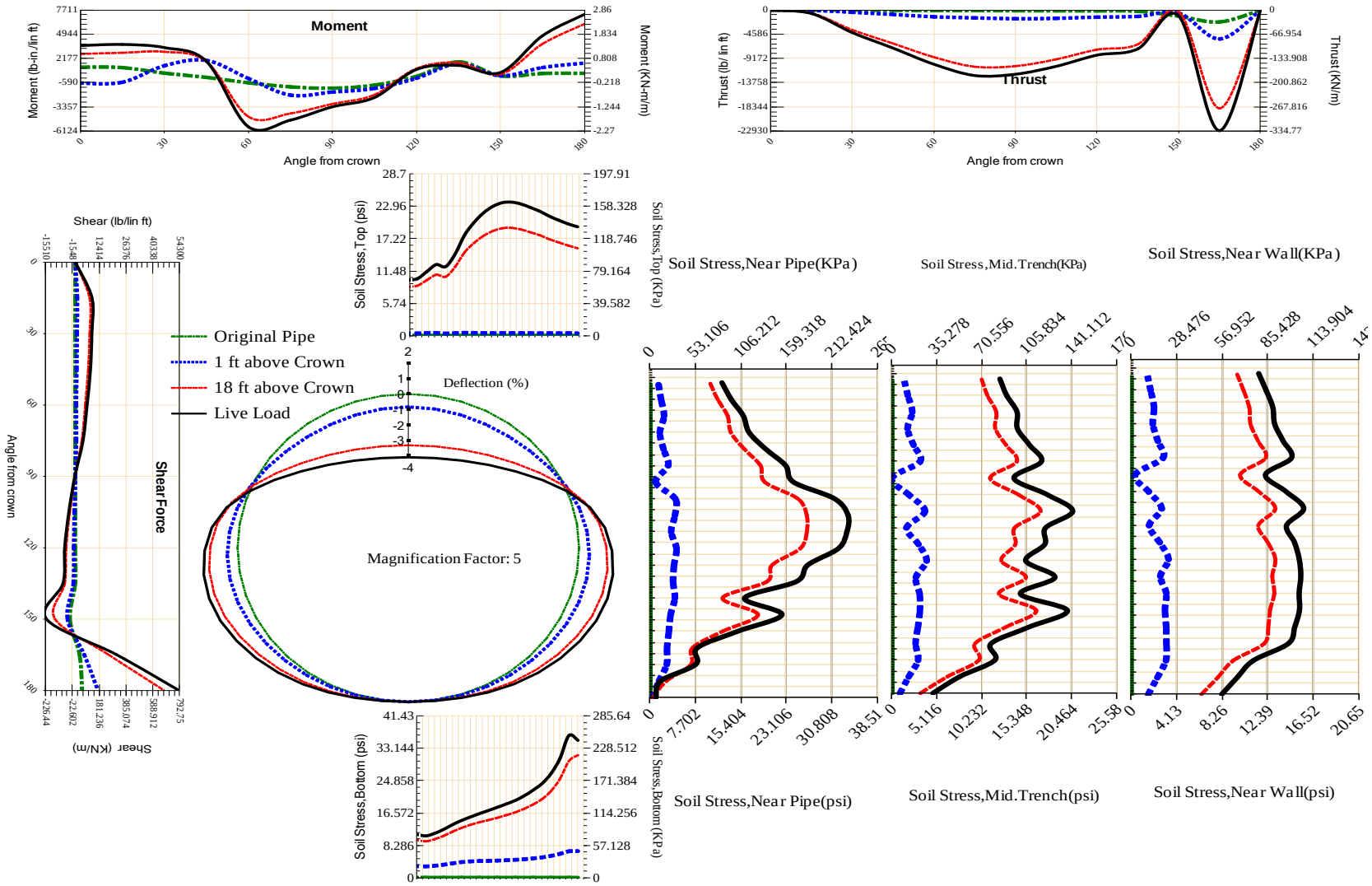

Figure A-212 Param-120-PW288-TR7OR-OD+108-EW3-H18-LiveLoad

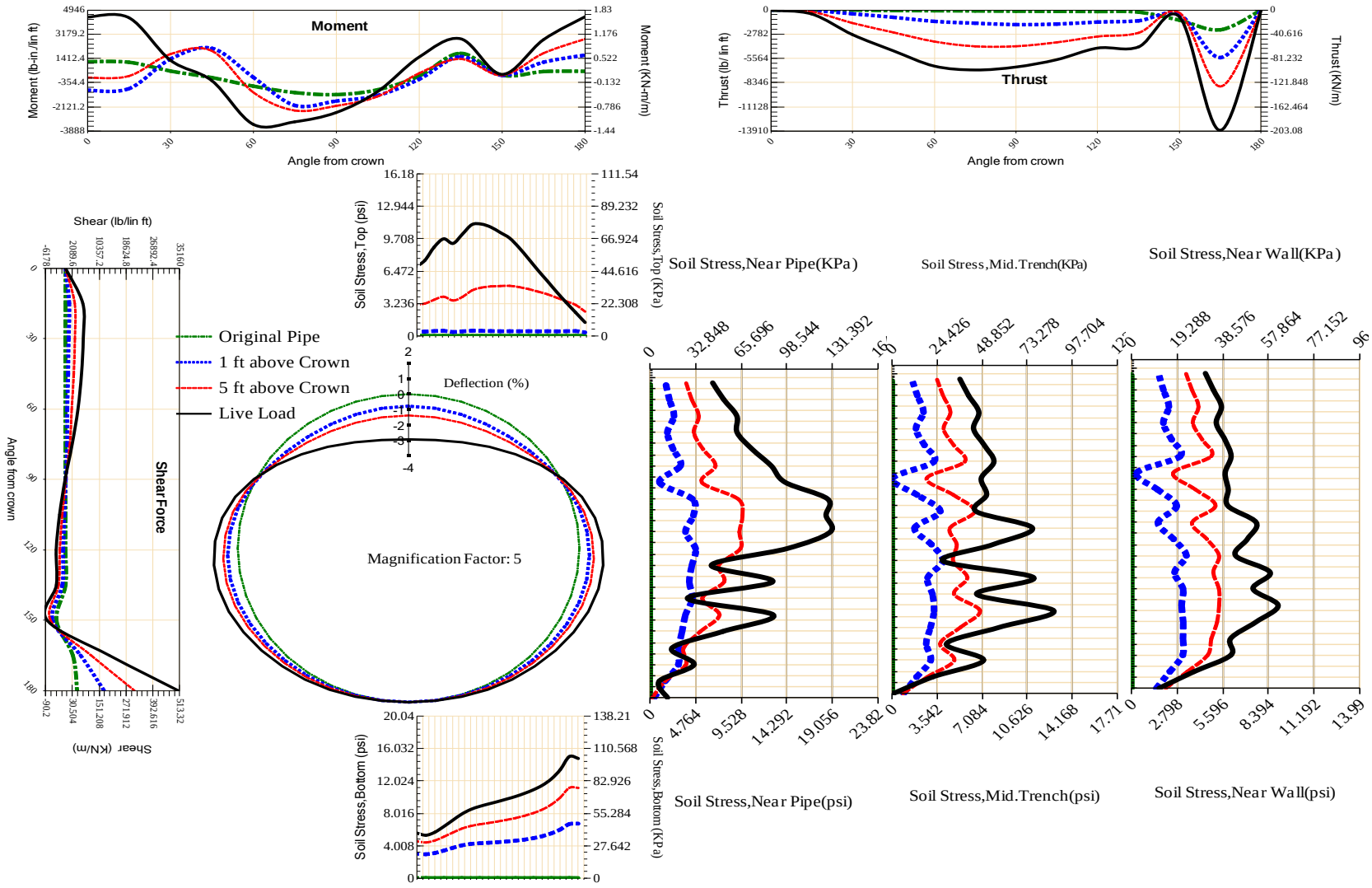

Figure A-213 Param-120-PW288-TR7OR-OD+108-EW3-H5-LiveLoad

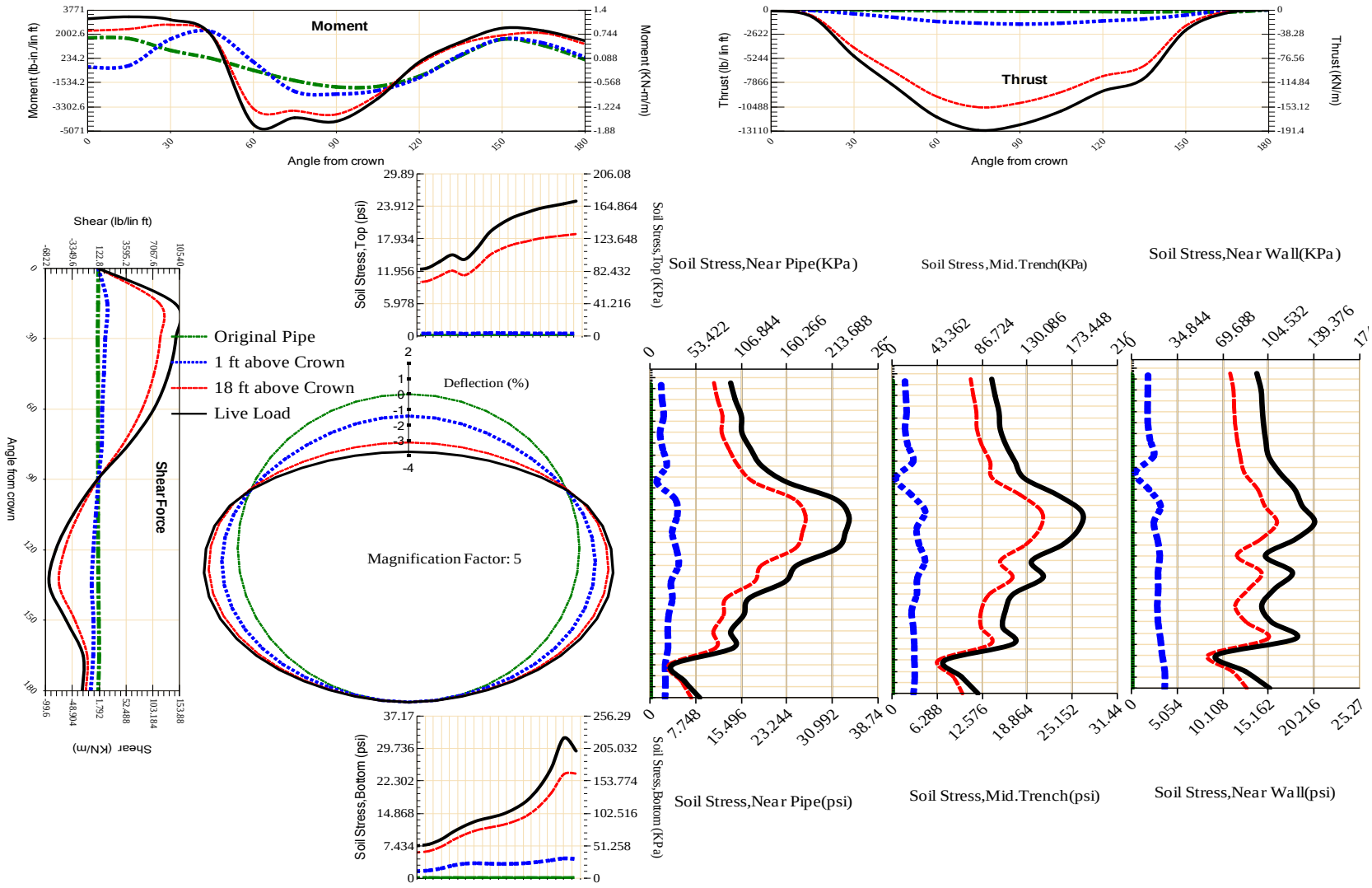

Figure A-214 Param-120-PW288-TR7OR-OD+48-EW10-H18-LiveLoad

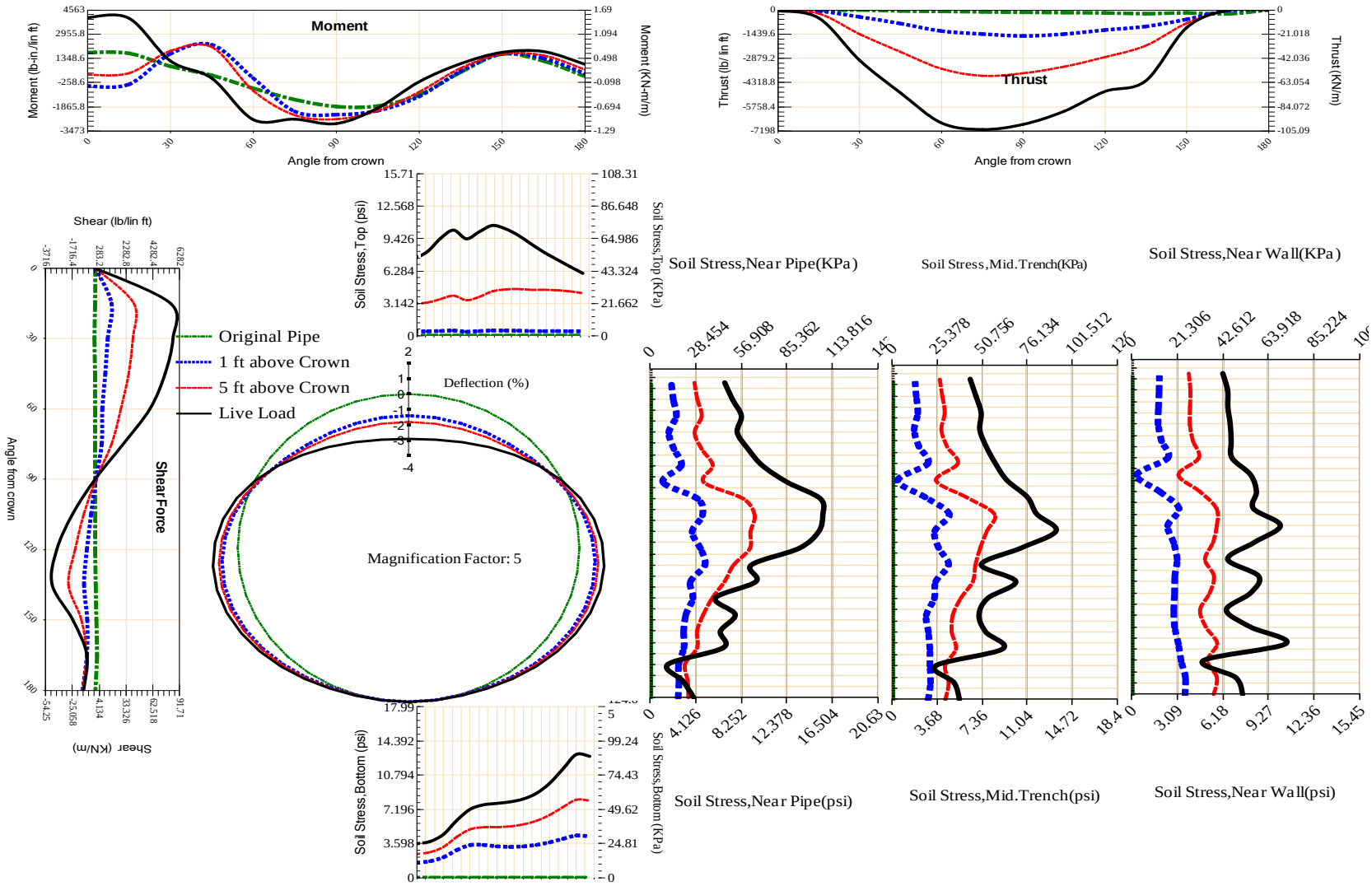

Figure A-215 Param-120-PW288-TR7OR-OD+48-EW10-H5-LiveLoad

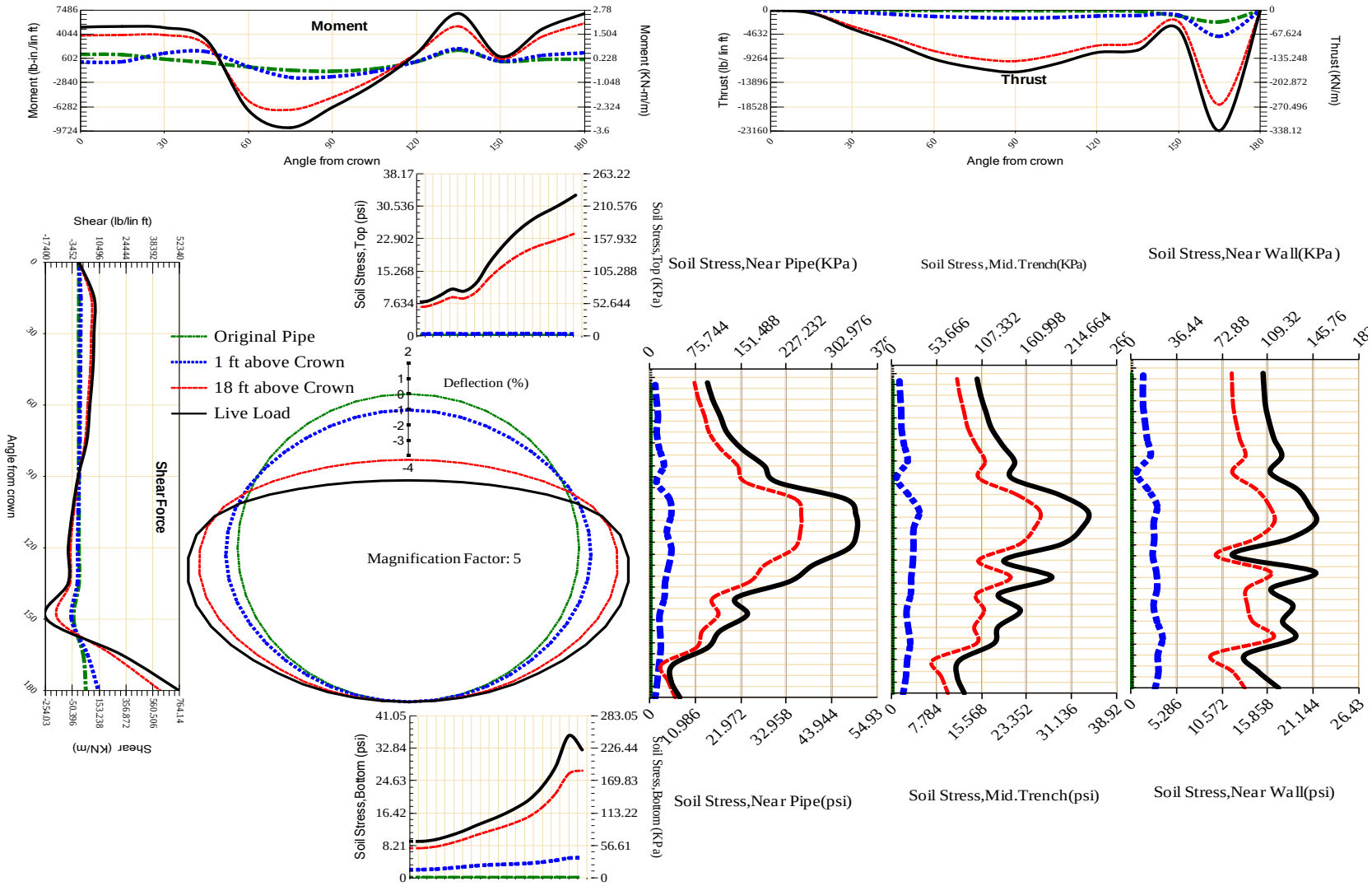

Figure A-216 Param-120-PW288-TR7OR-OD+48-EW3-H18-LiveLoad

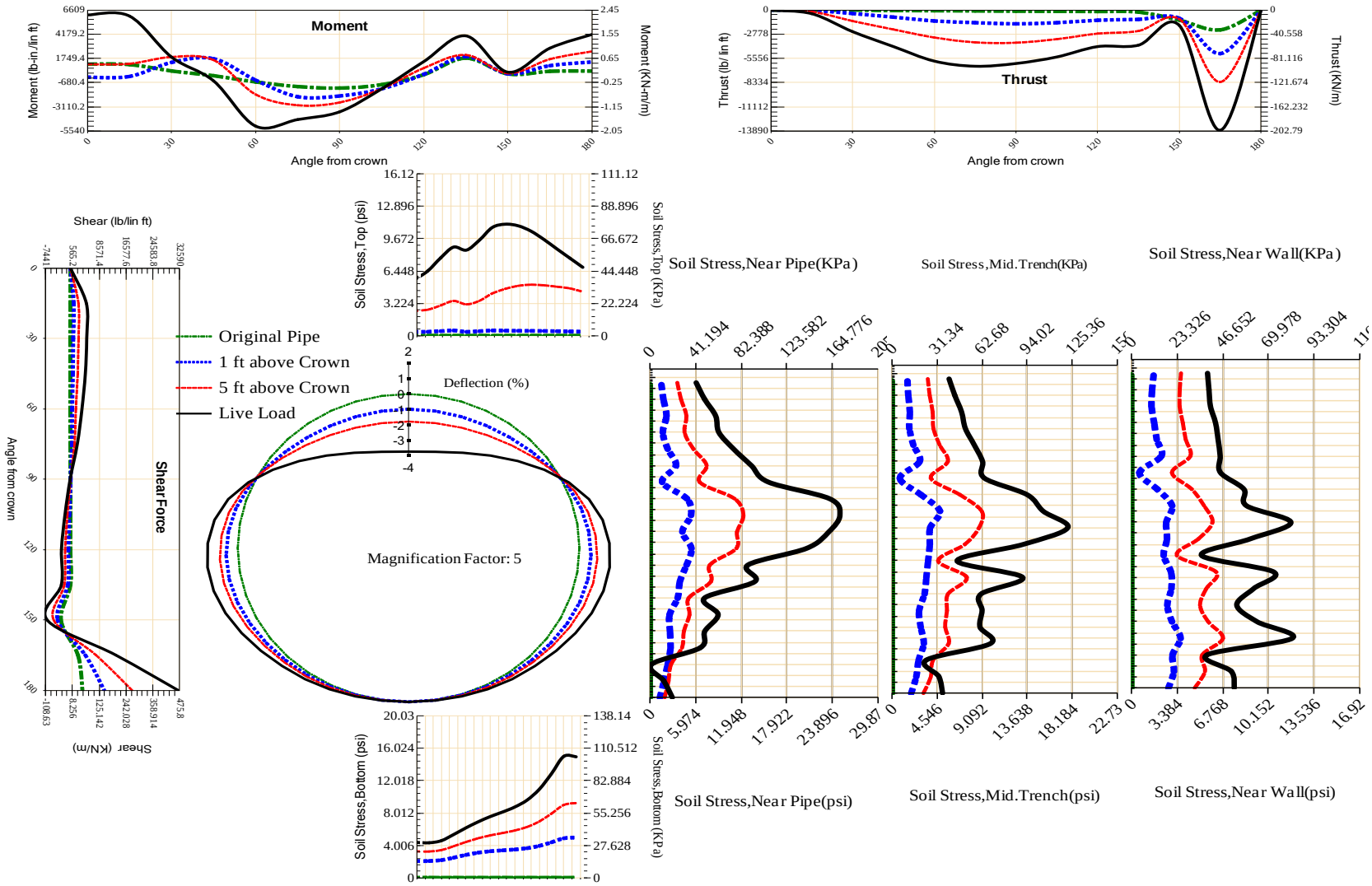

Figure A-217 Param-120-PW288-TR7OR-OD+48-EW3-H5-LiveLoad

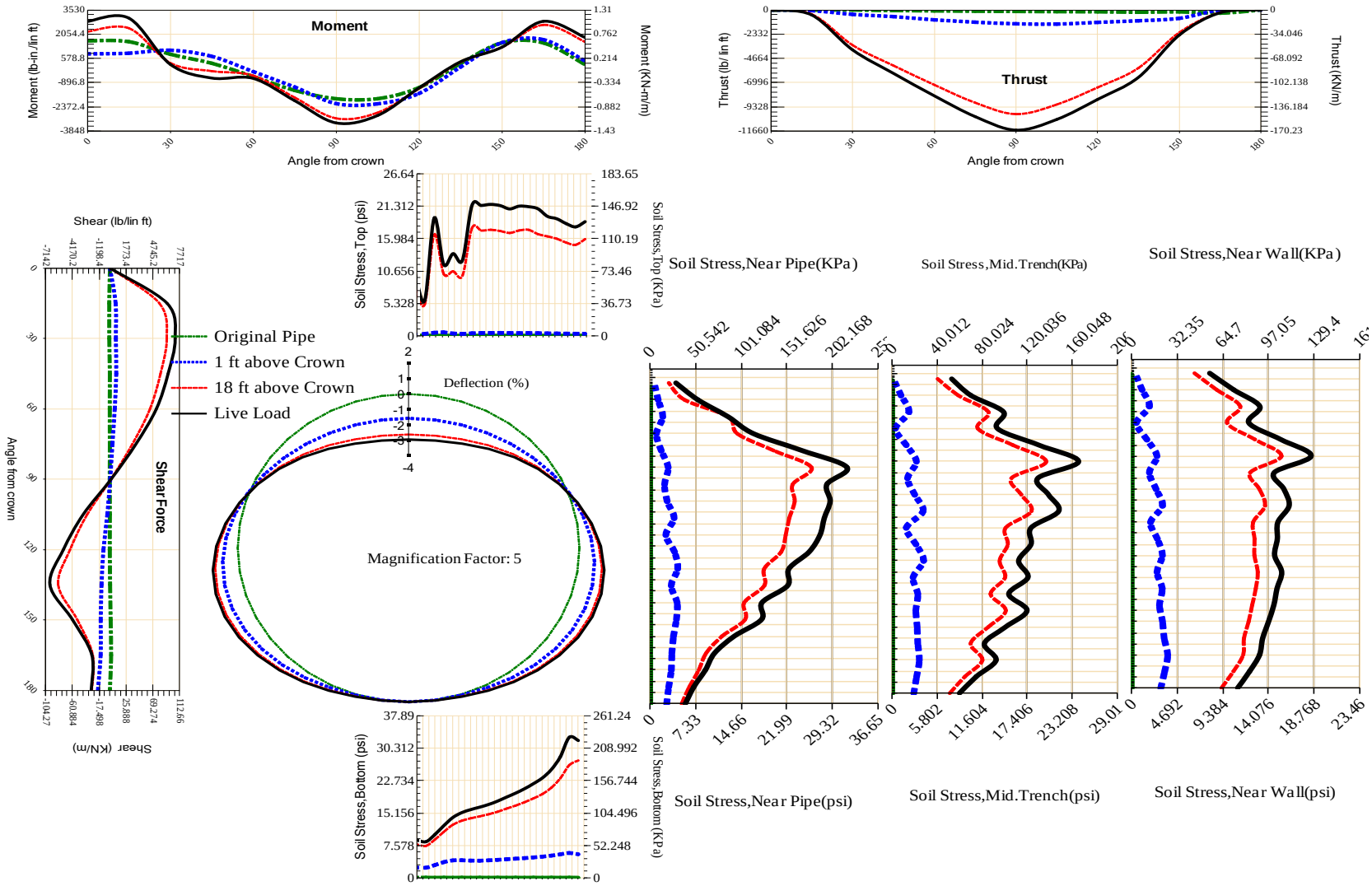

Figure A-218 Param-120-PW288-TR7SF-OD+108-EW10-H18-LiveLoad

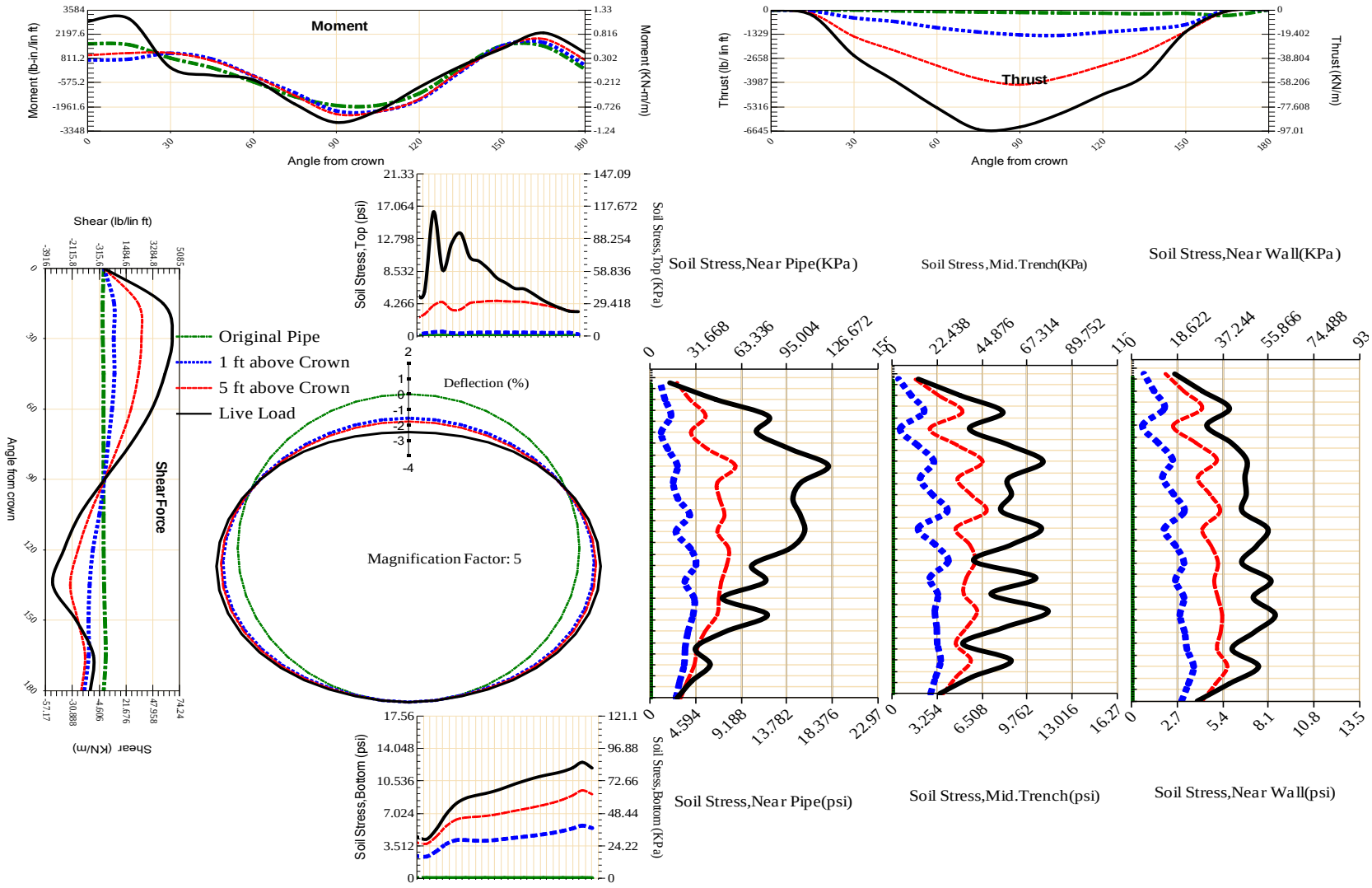

Figure A-219 Param-120-PW288-TR7SF-OD+108-EW10-H5-LiveLoad

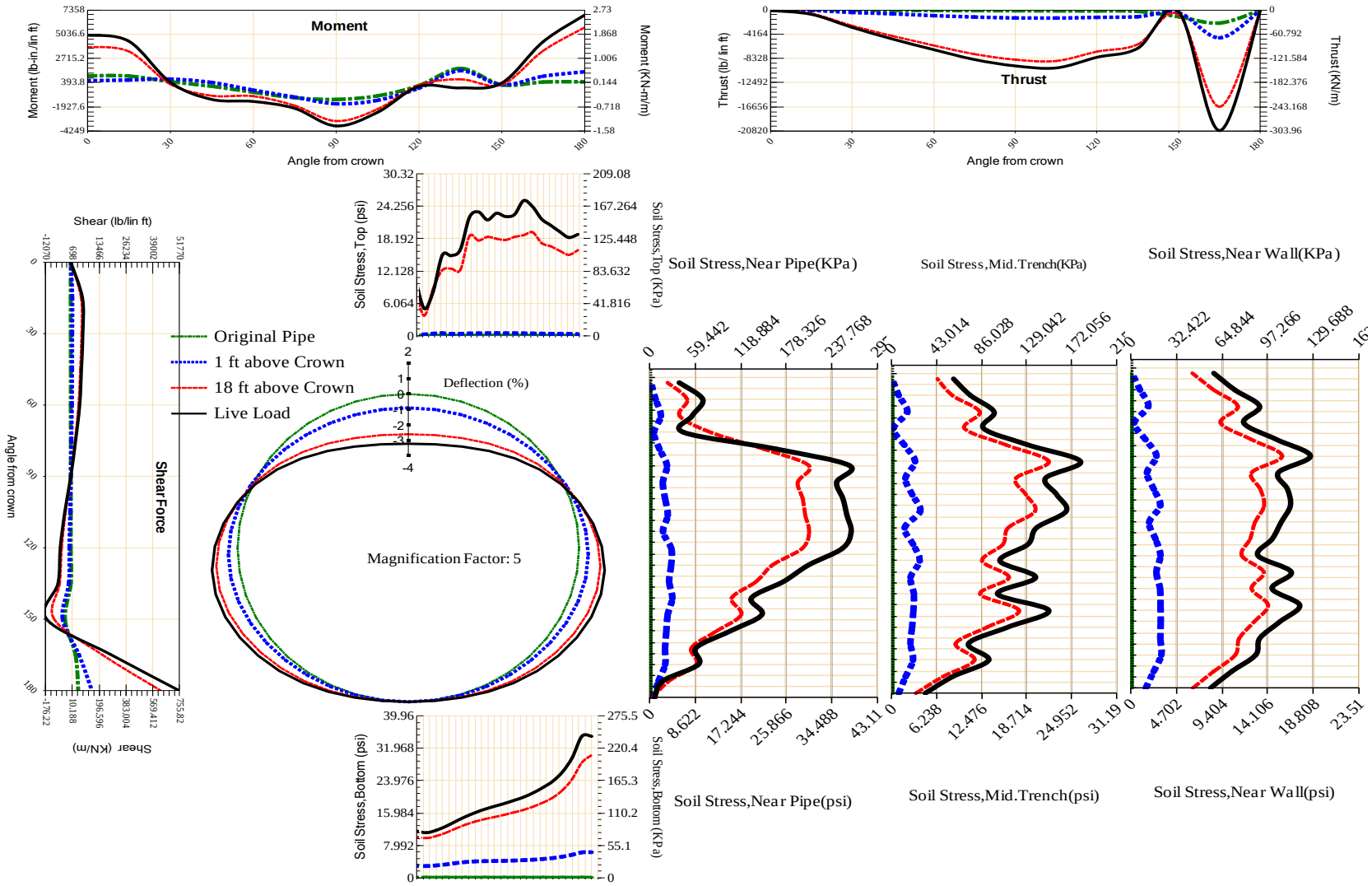

Figure A-220 Param-120-PW288-TR7SF-OD+108-EW3-H18-LiveLoad

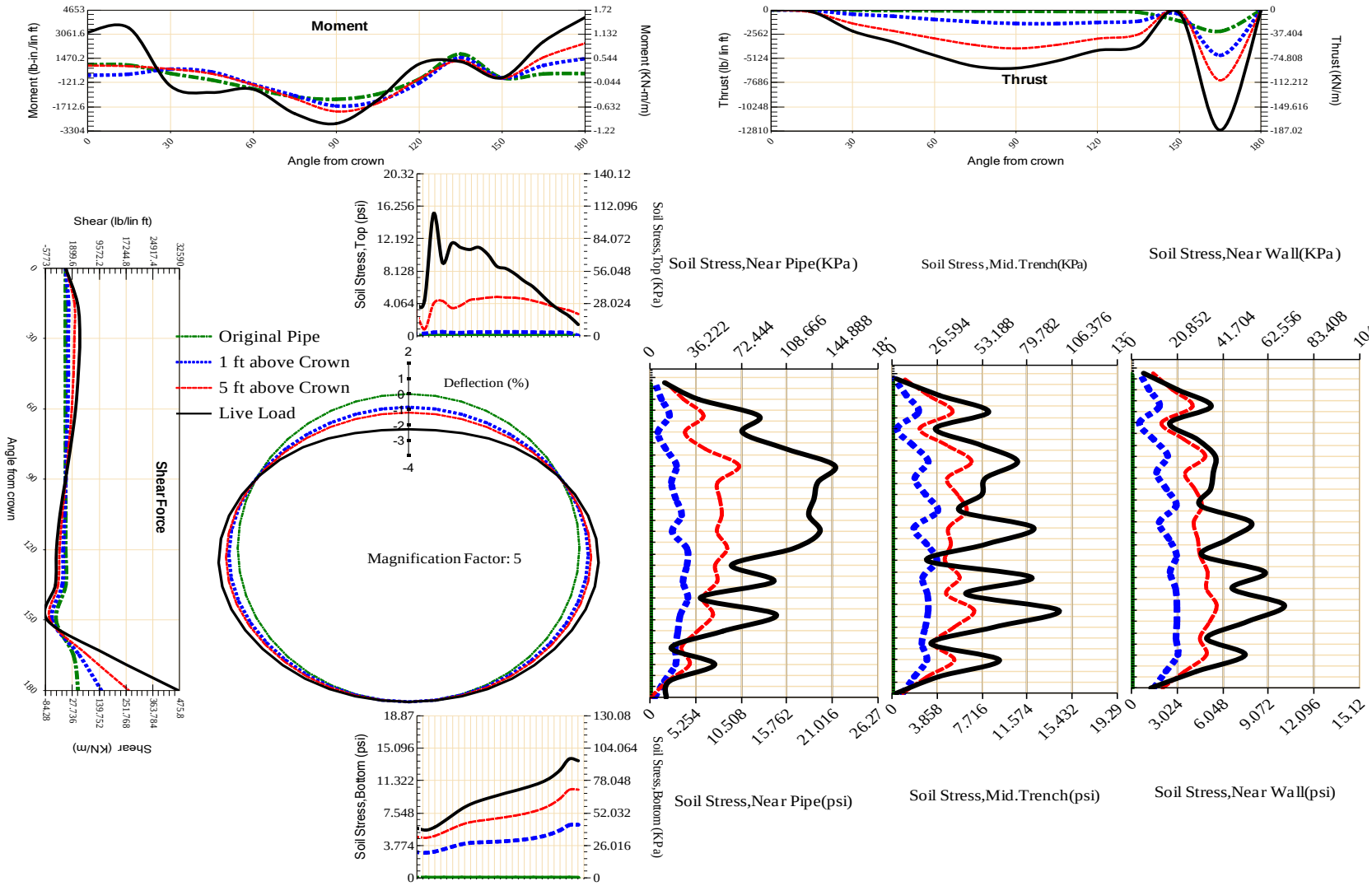

Figure A-221 Param-120-PW288-TR7SF-OD+108-EW3-H5-LiveLoad

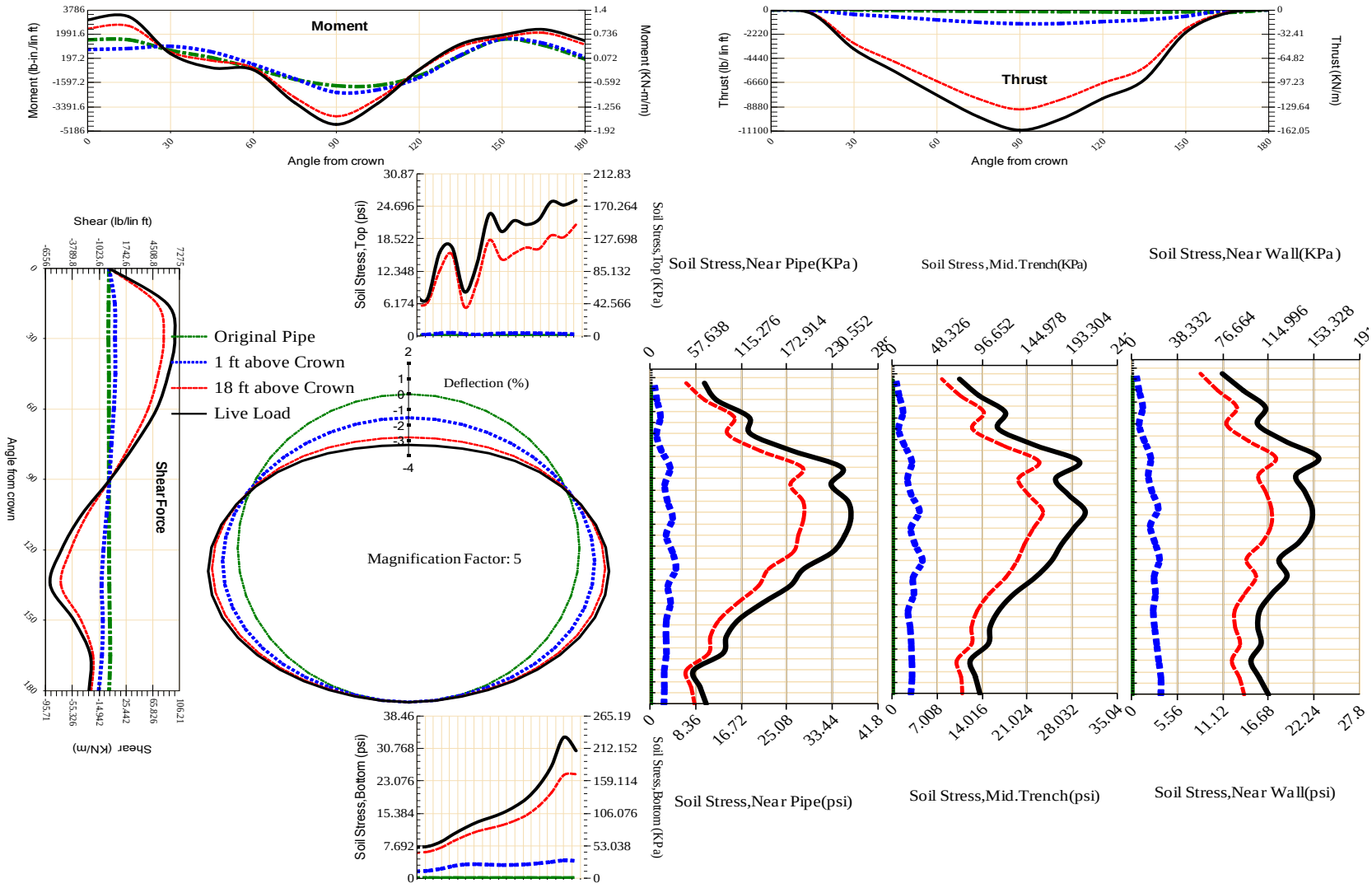

Figure A-222 Param-120-PW288-TR7SF-OD+48-EW10-H18-LiveLoad

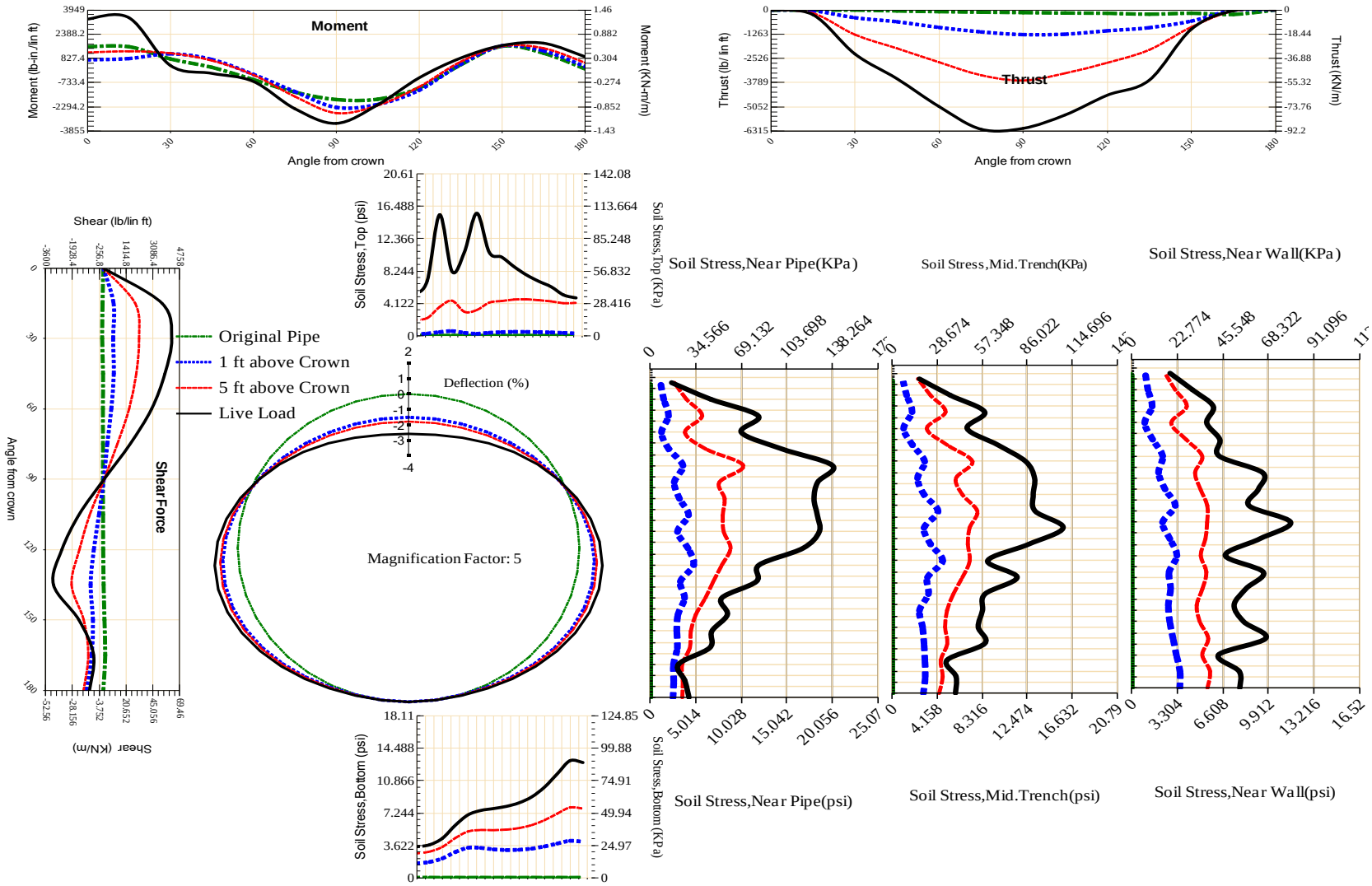

Figure A-223 Param-120-PW288-TR7SF-OD+48-EW10-H5-LiveLoad

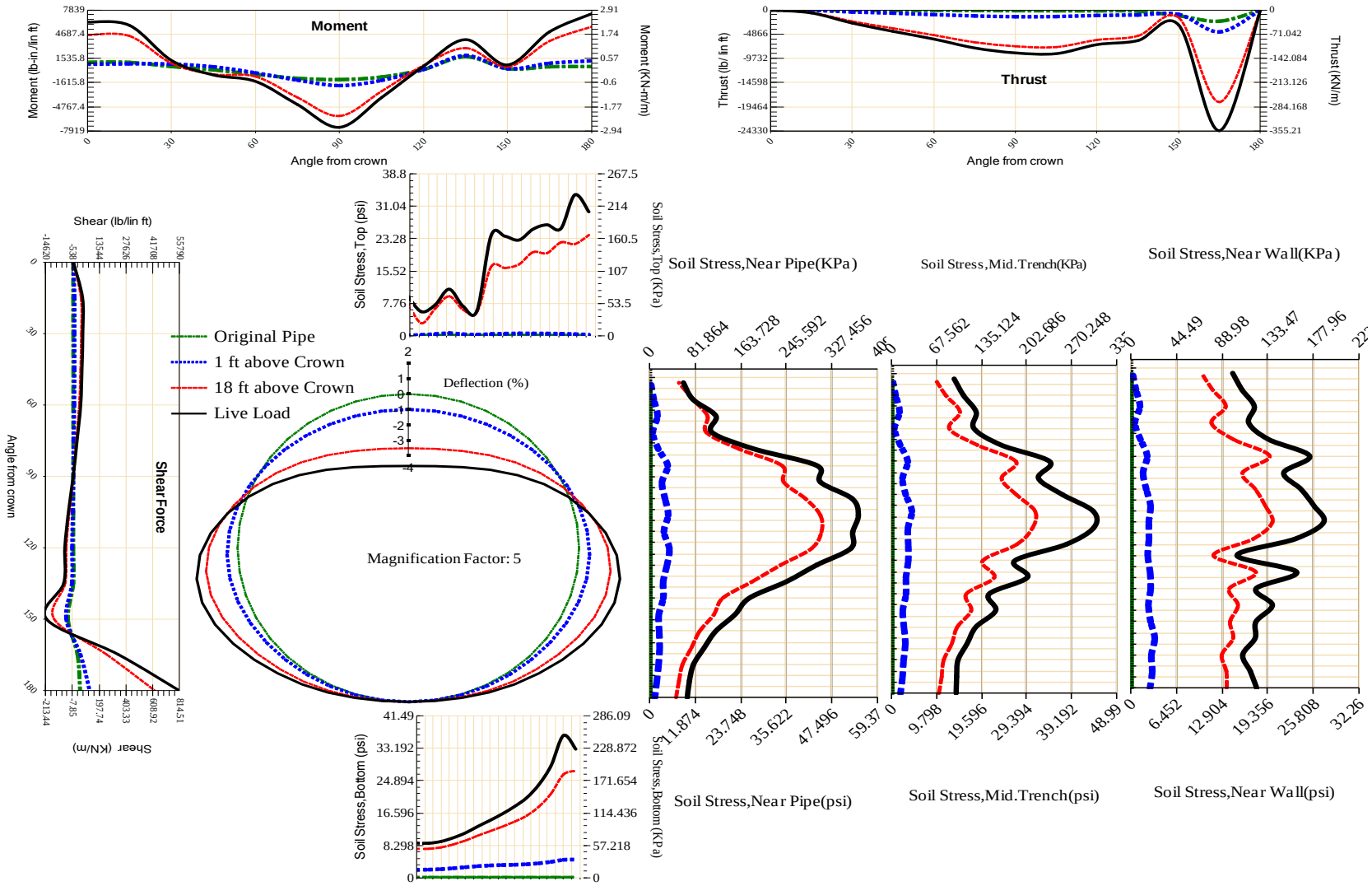

Figure A-224 Param-120-PW288-TR7SF-OD+48-EW3-H18-LiveLoad

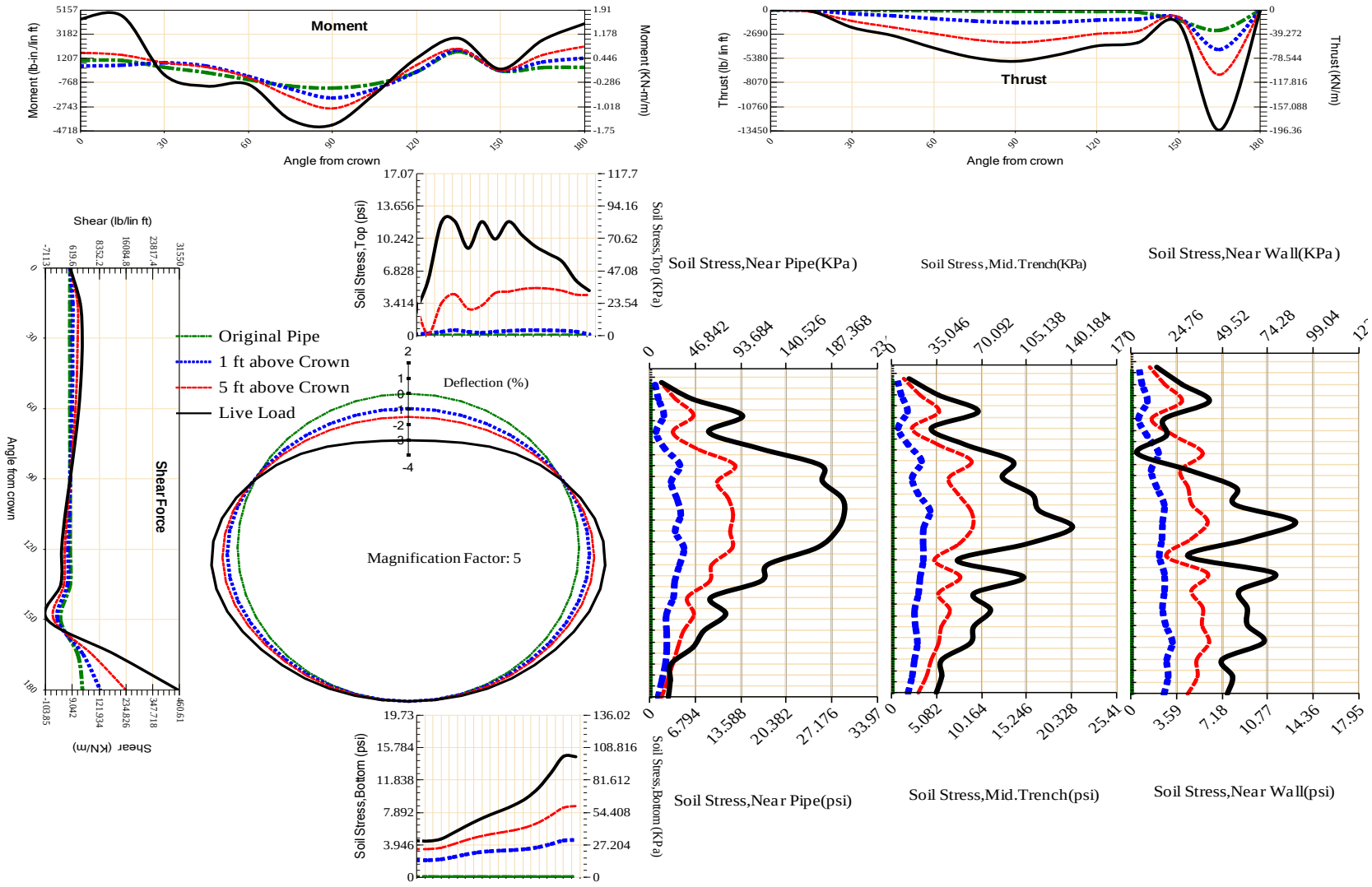

Figure A-225 Param-120-PW288-TR7SF-OD+48-EW3-H5-LiveLoad

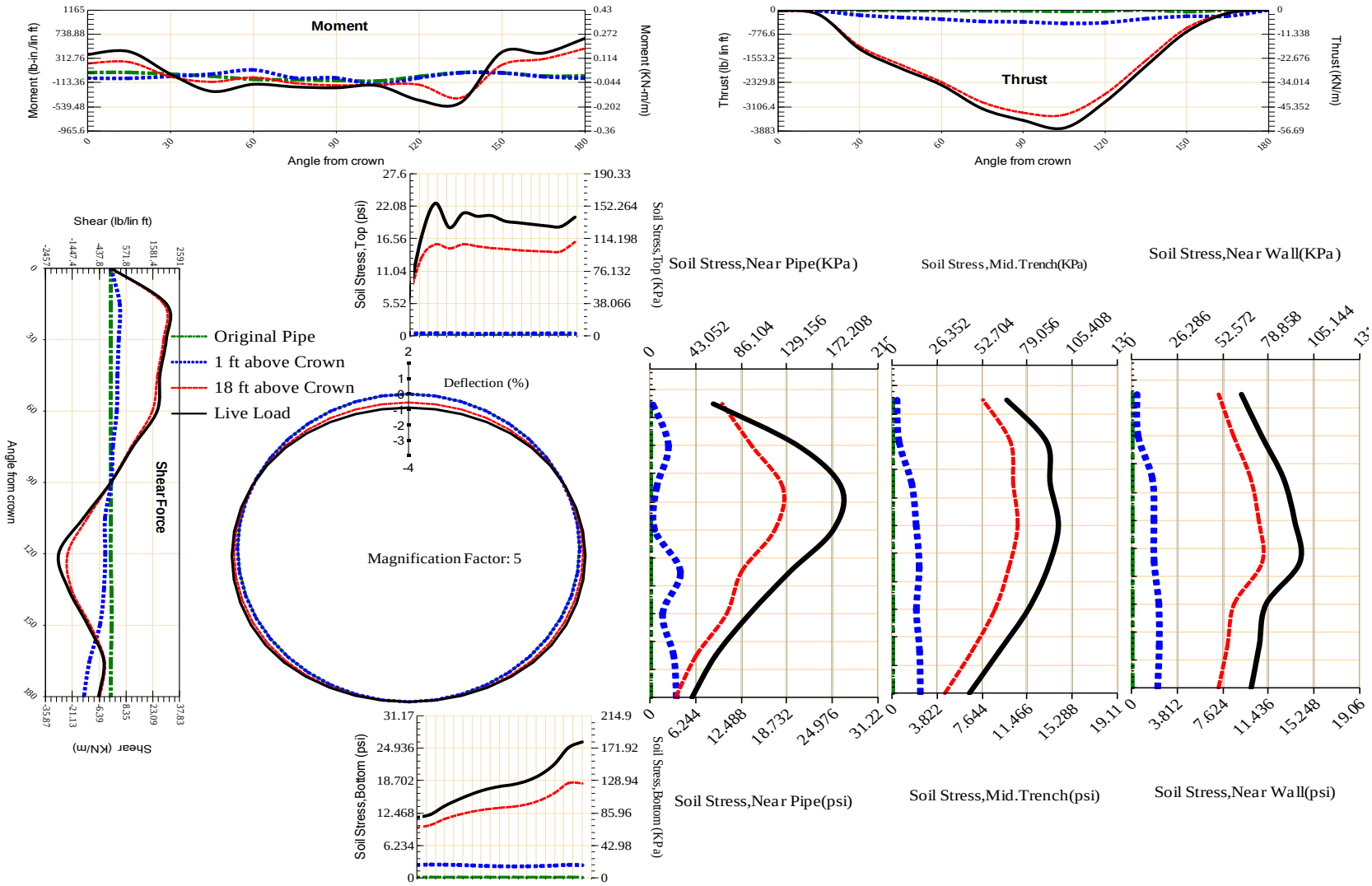

Figure A-226 Param-48-PW200-SF10SF-OD+108-EW10-H18-LiveLoad

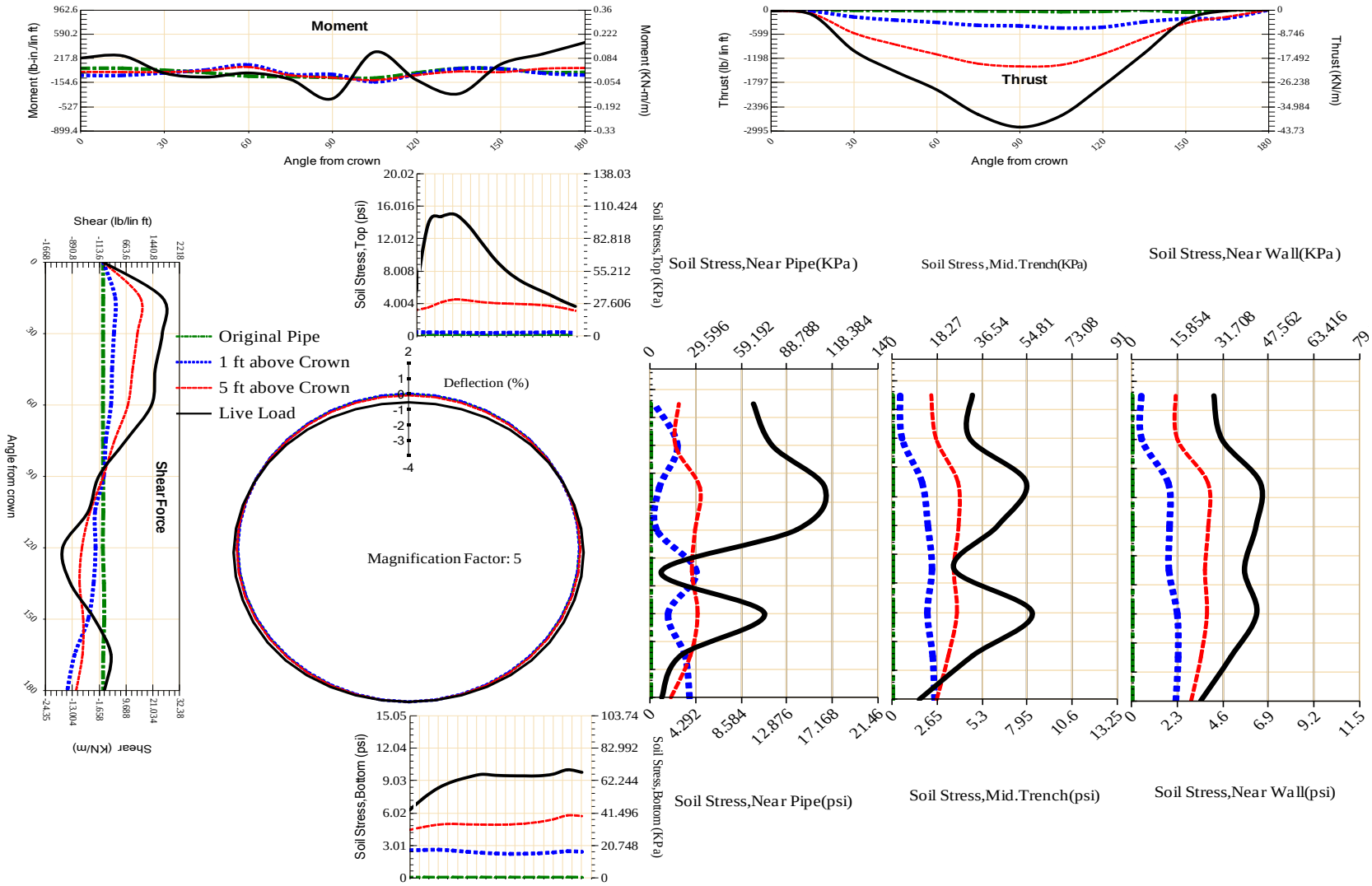

Figure A-227 Param-48-PW200-SF10SF-OD+108-EW10-H5-LiveLoad

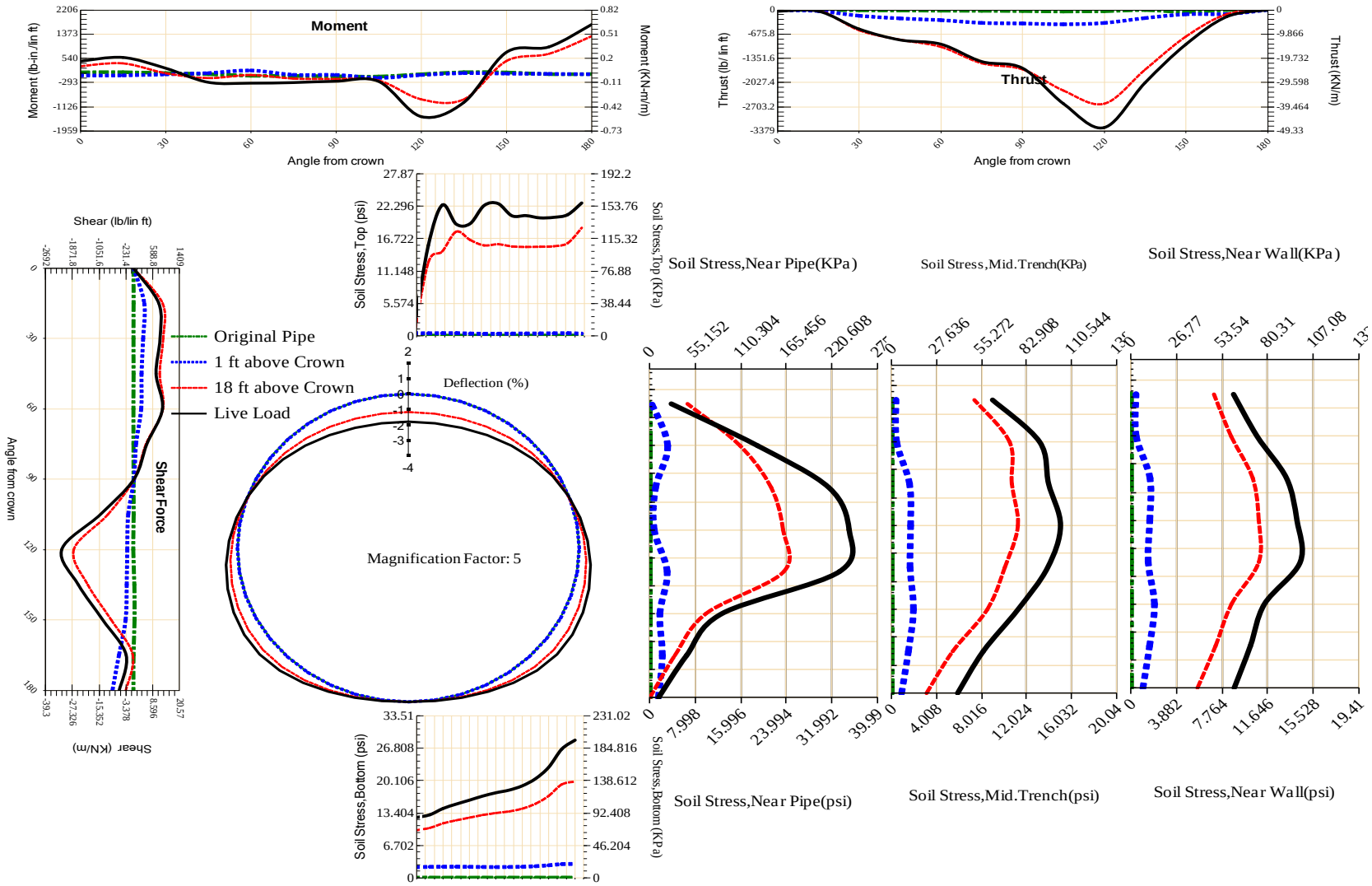

Figure A-228 Param-48-PW200-SF10SF-OD+108-EW3-H18-LiveLoad

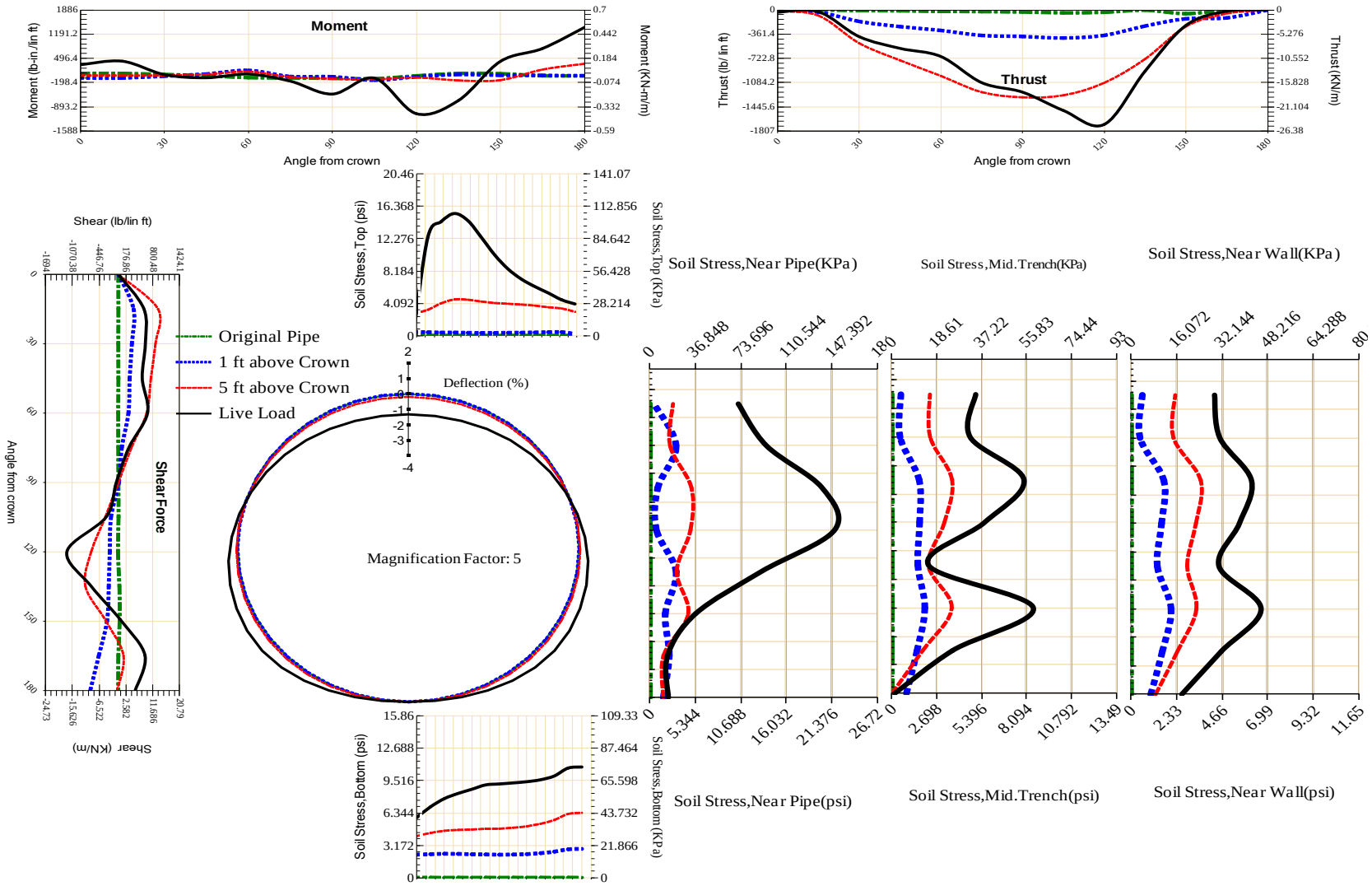

Figure A-229 Param-48-PW200-SF10SF-OD+108-EW3-H5-LiveLoad

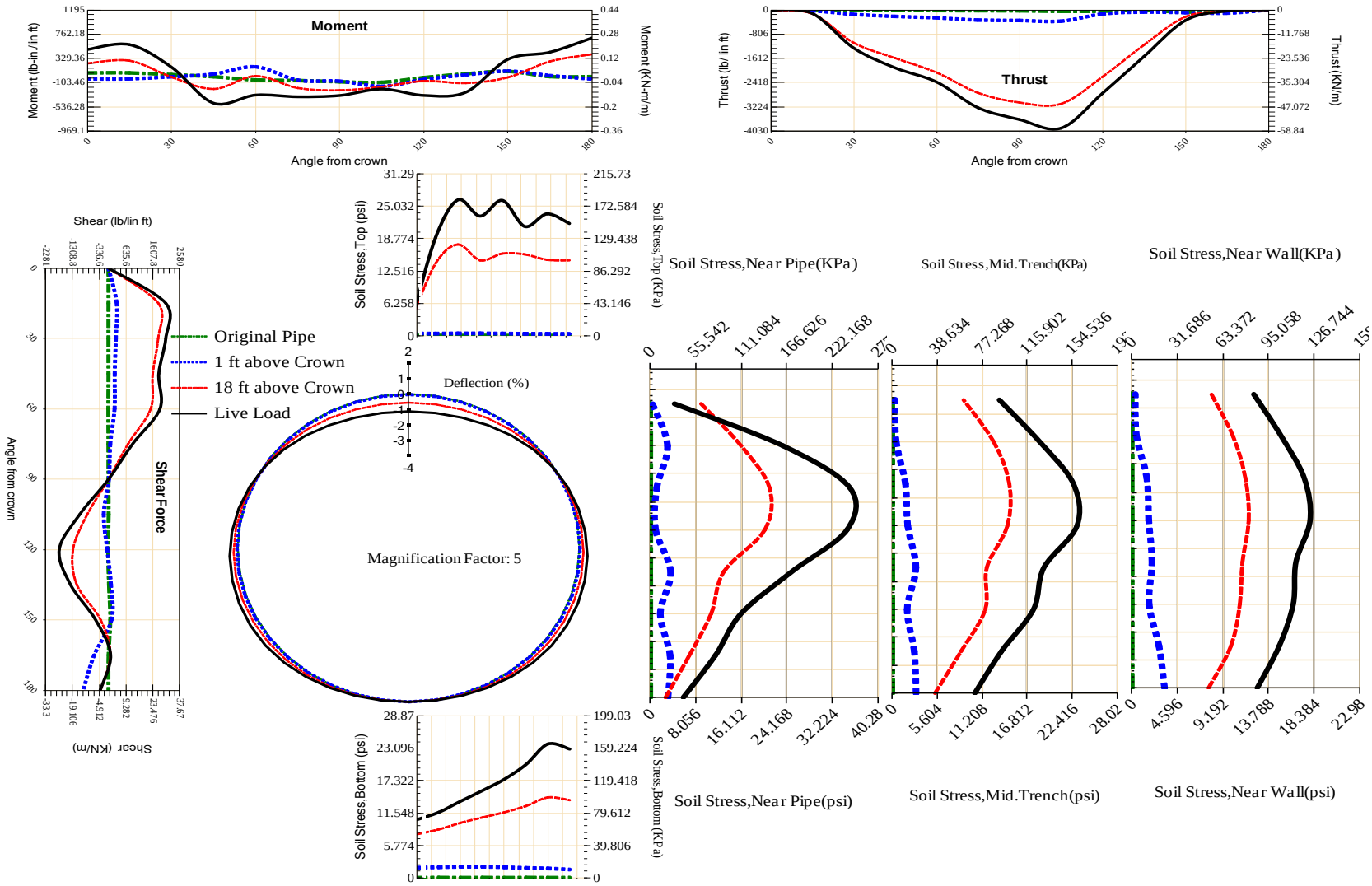

Figure A-230 Param-48-PW200-SF10SF-OD+48-EW10-H18-LiveLoad

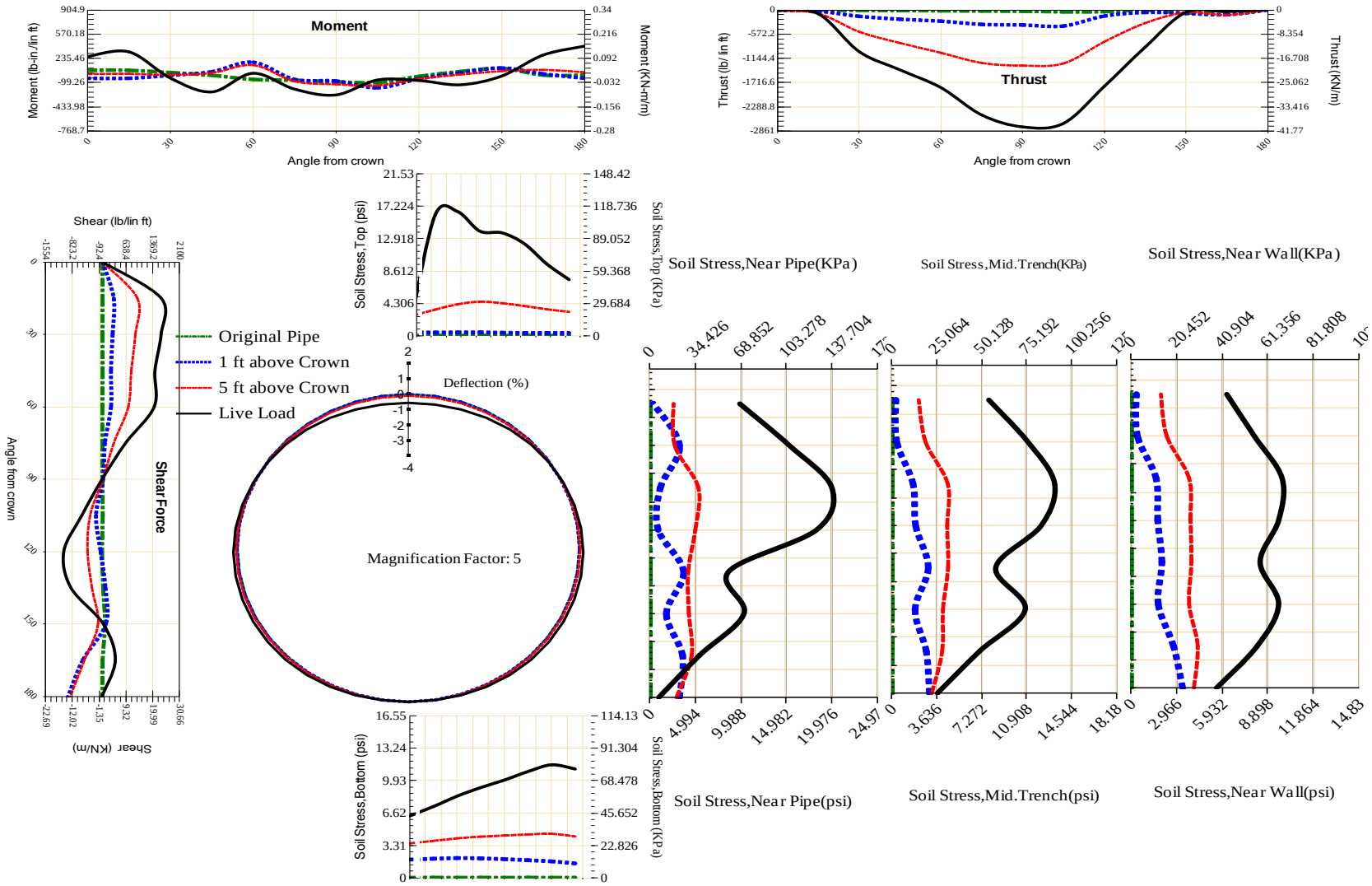

Figure A-231 Param-48-PW200-SF10SF-OD+48-EW10-H5-LiveLoad

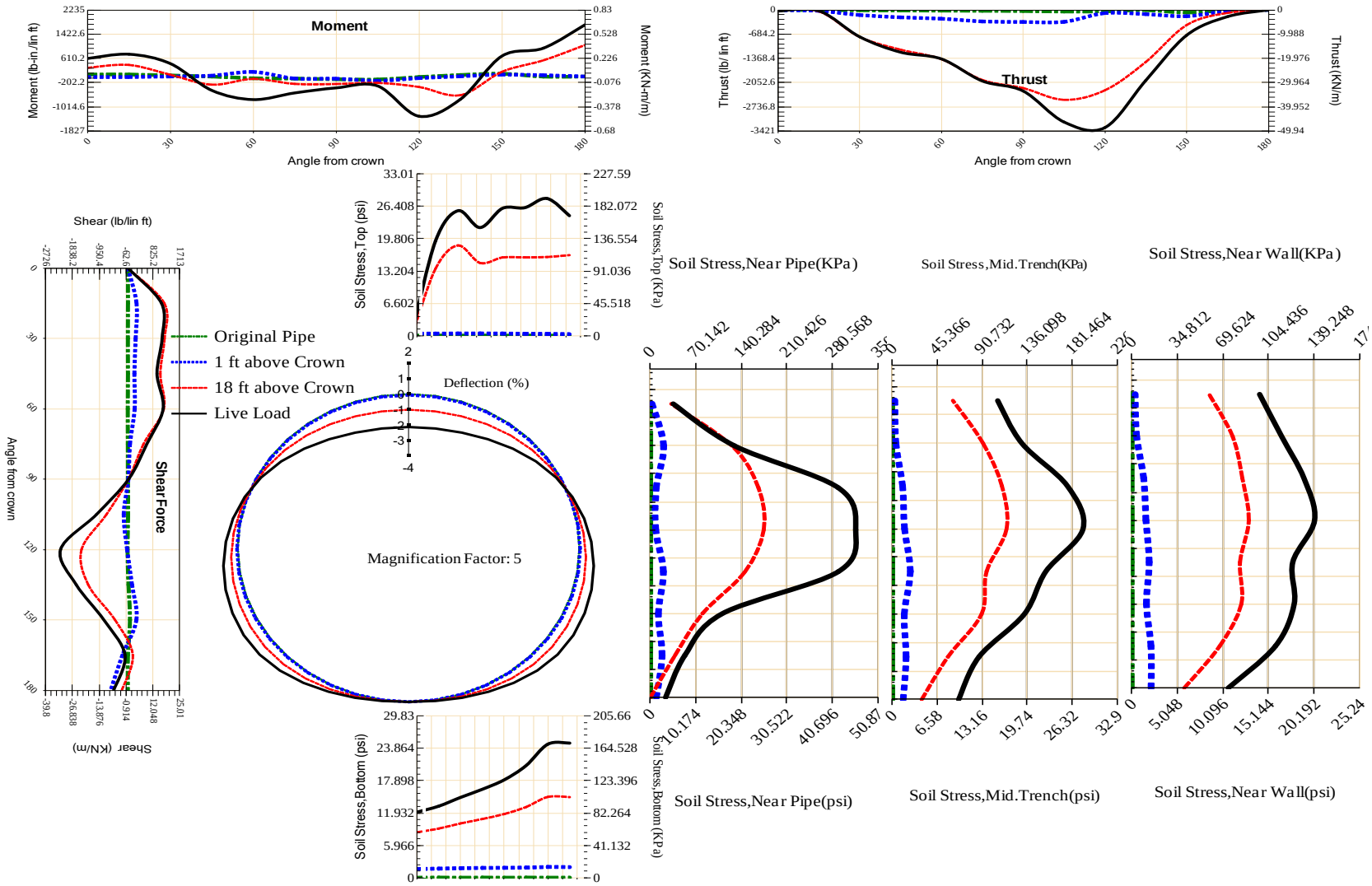

Figure A-232 Param-48-PW200-SF10SF-OD+48-EW3-H18-LiveLoad

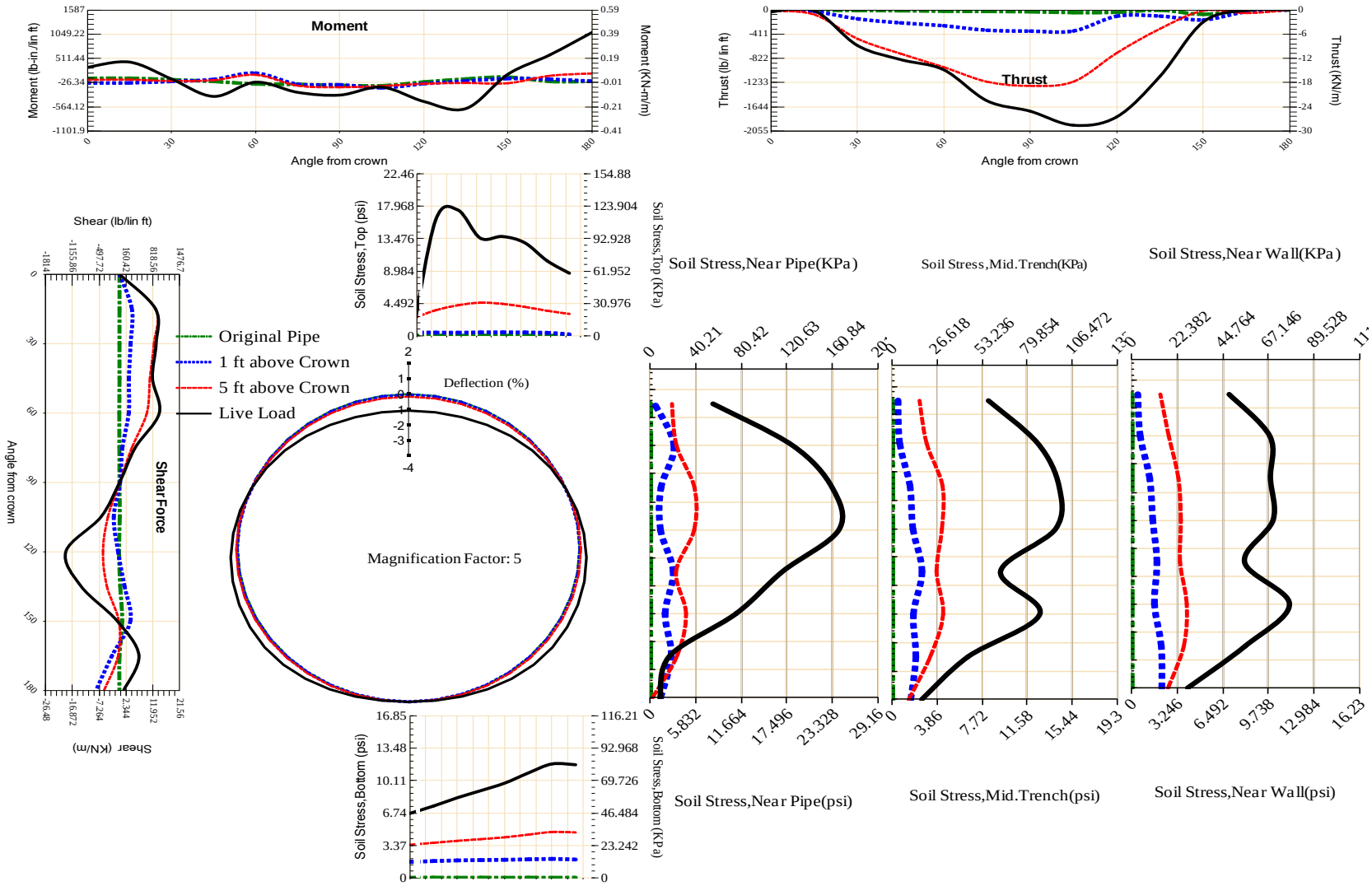

Figure A-233 Param-48-PW200-SF10SF-OD+48-EW3-H5-LiveLoad

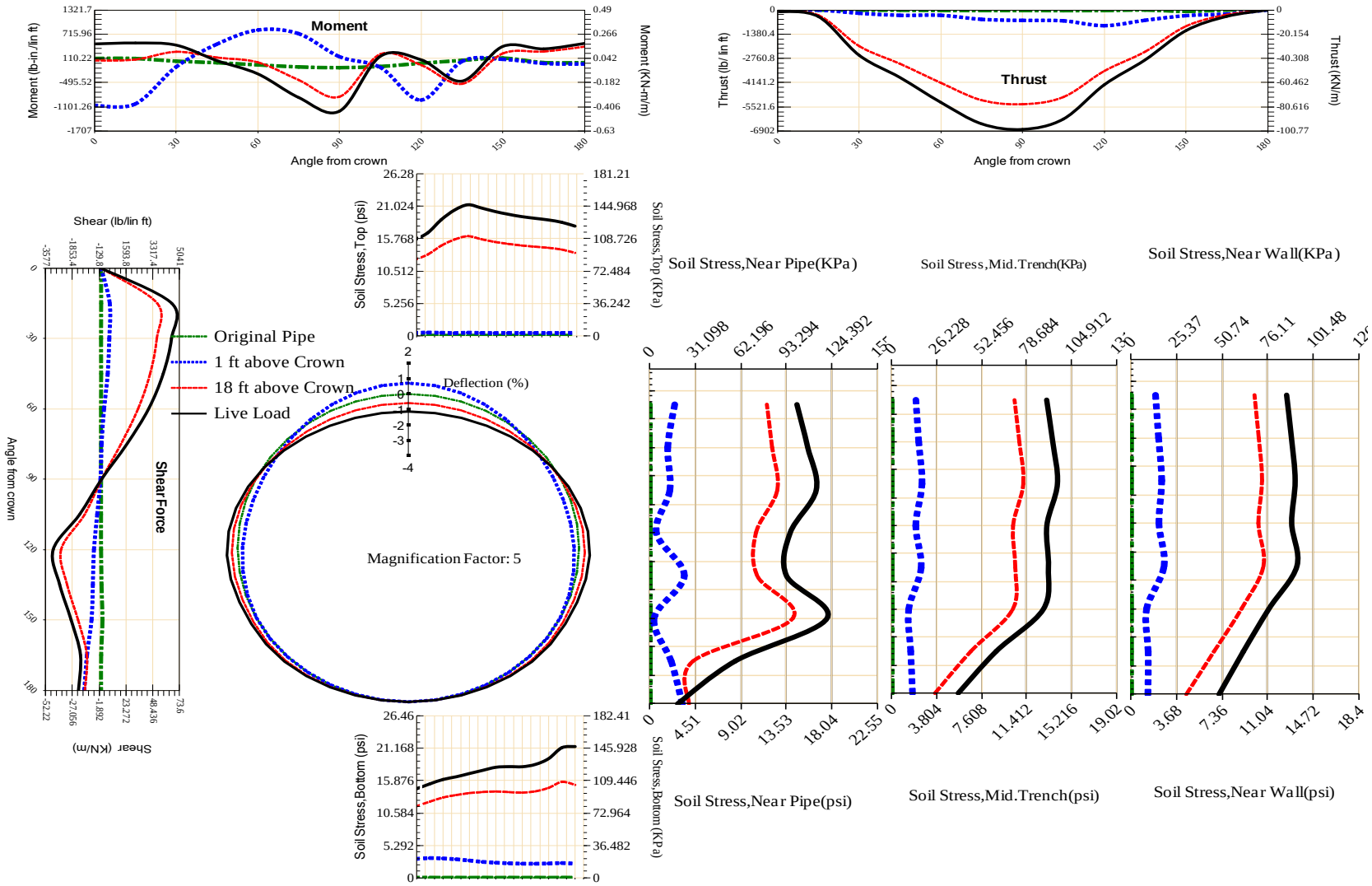

Figure A-234 Param-48-PW200-SF3OR-OD+108-EW10-H18-LiveLoad

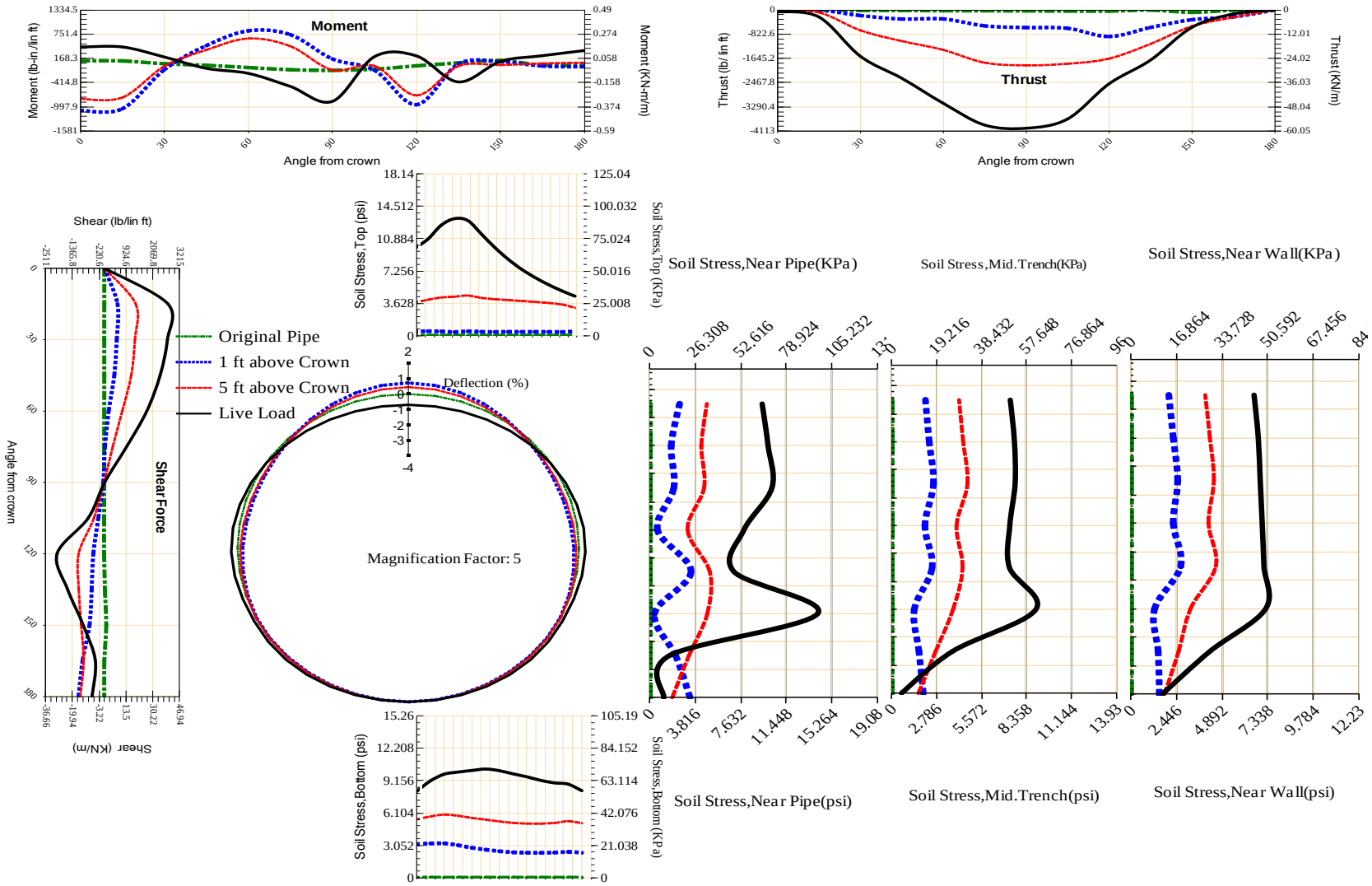

Figure A-235 Param-48-PW200-SF3OR-OD+108-EW10-H5-LiveLoad

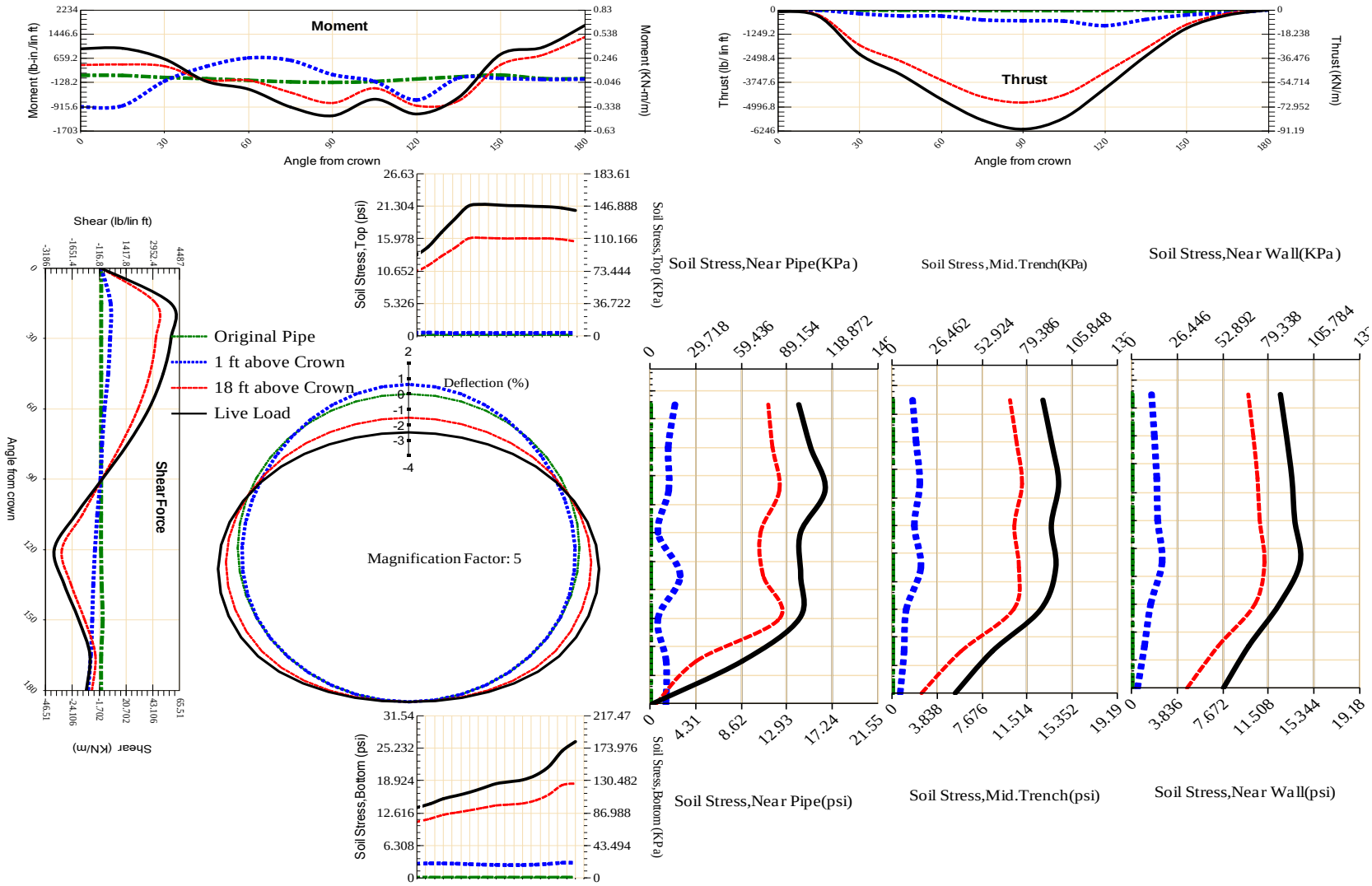

Figure A-236 Param-48-PW200-SF3OR-OD+108-EW3-H18-LiveLoad

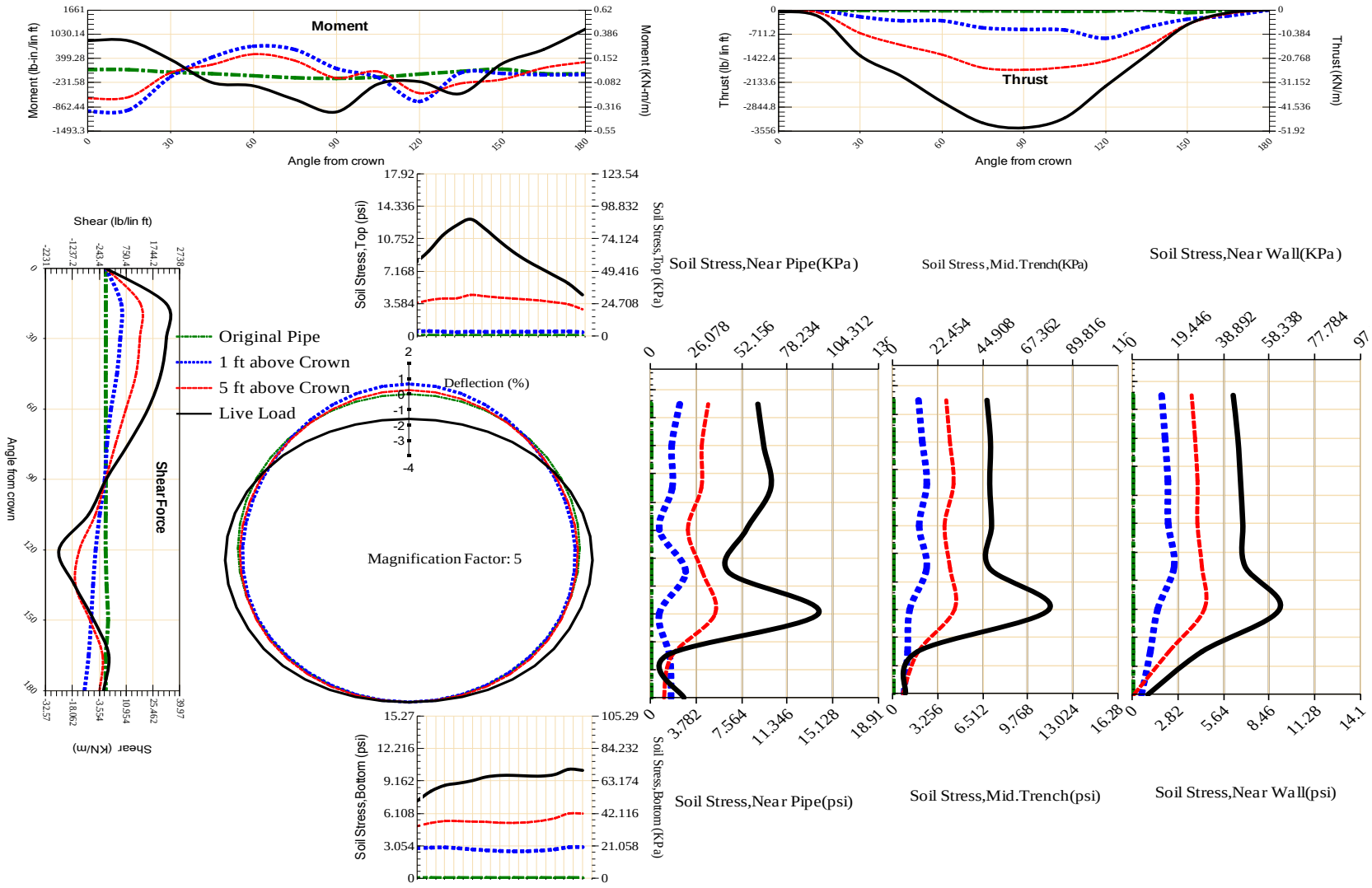

Figure A-237 Param-48-PW200-SF3OR-OD+108-EW3-H5-LiveLoad

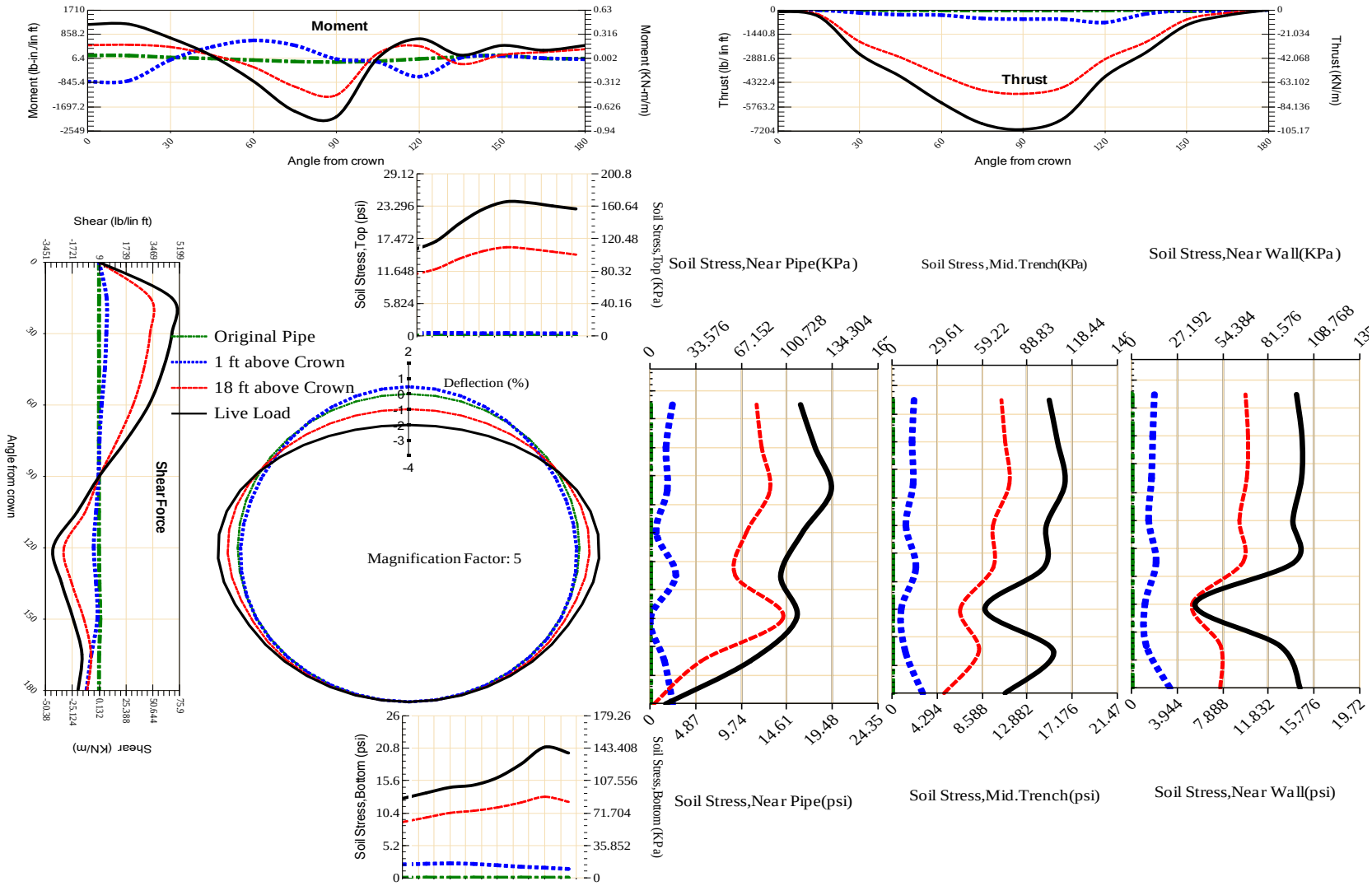

Figure A-238 Param-48-PW200-SF3OR-OD+48-EW10-H18-LiveLoad

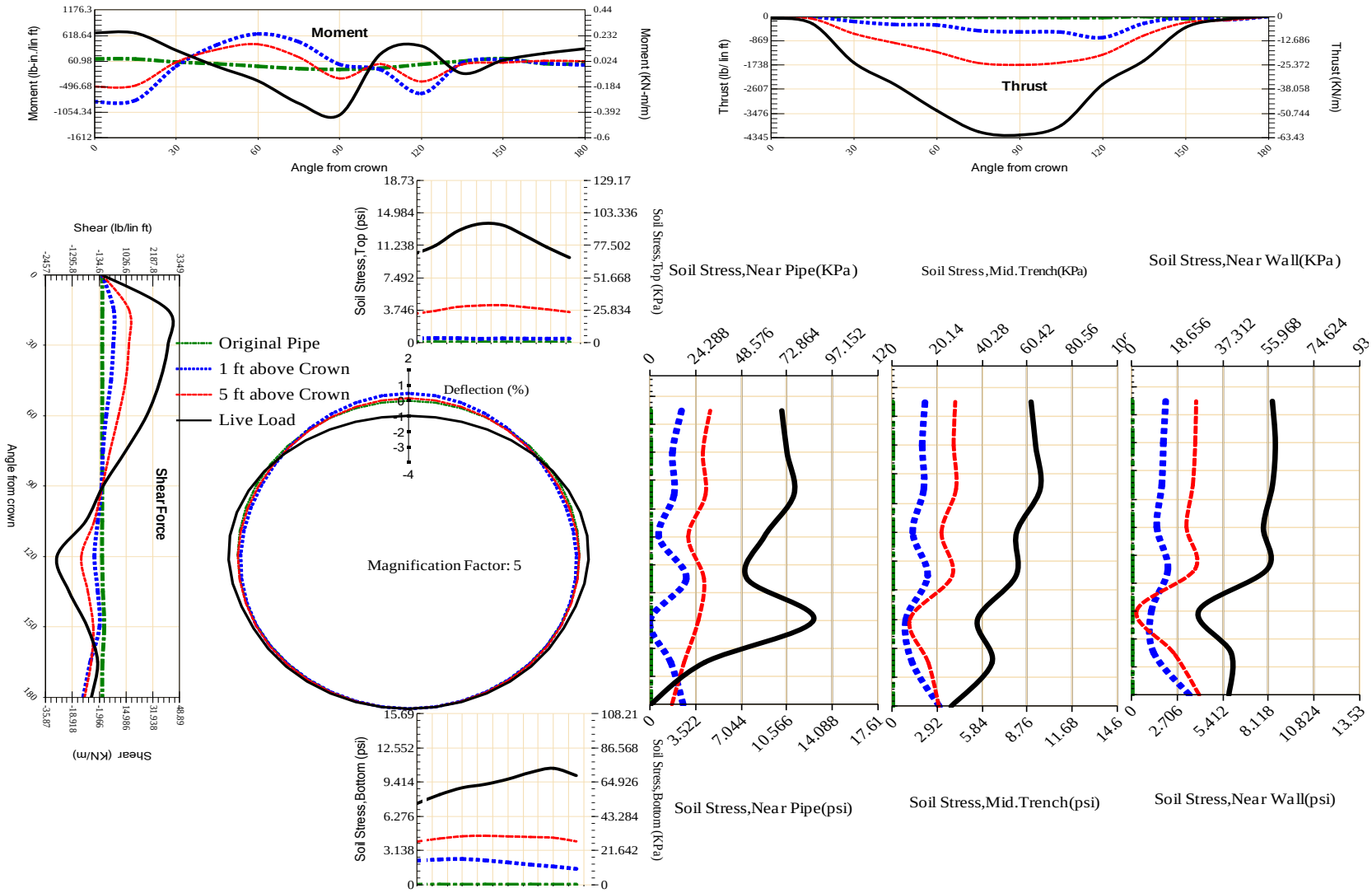

Figure A-239 Param-48-PW200-SF3OR-OD+48-EW10-H5-LiveLoad

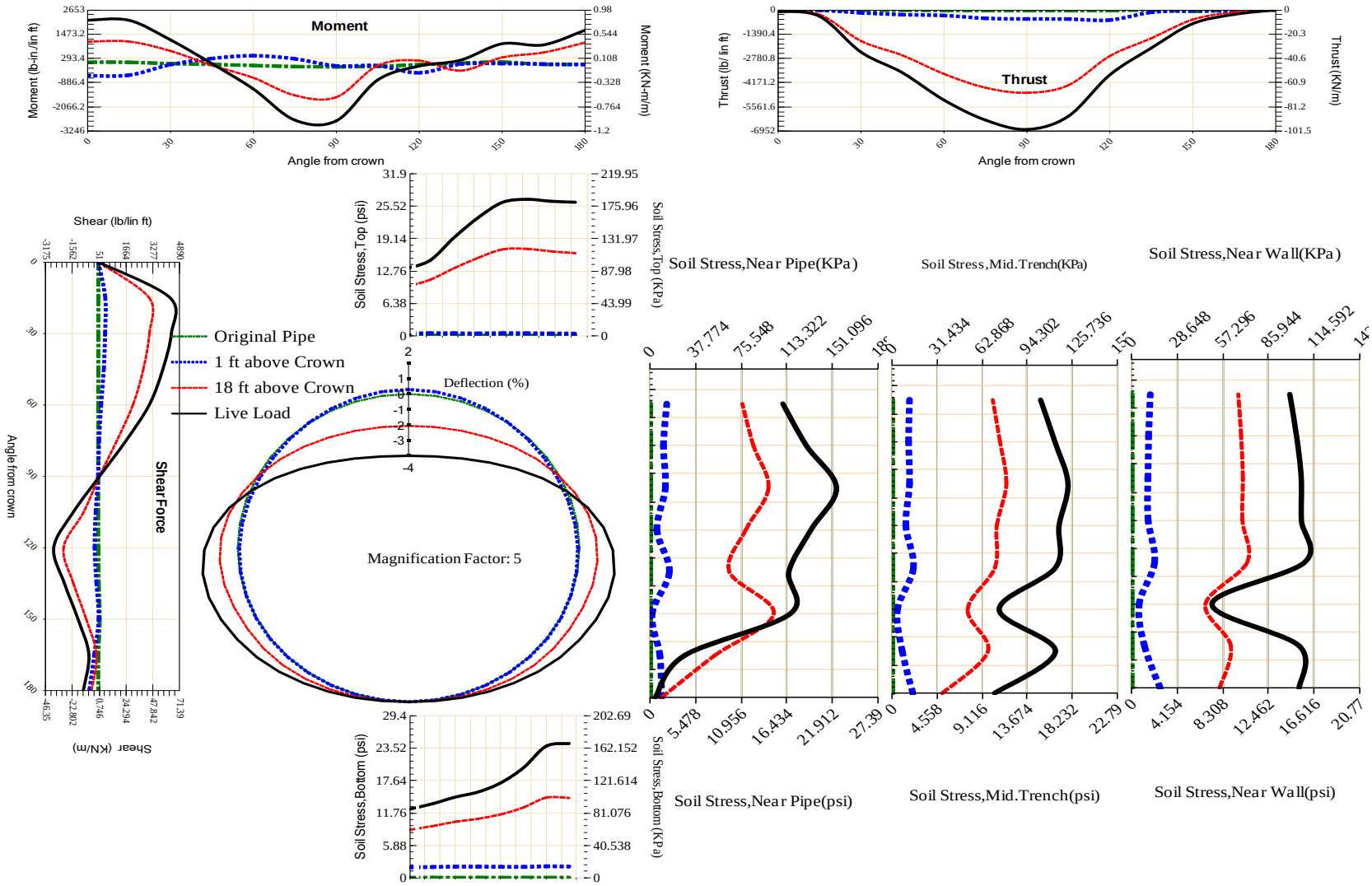

Figure A-240 Param-48-PW200-SF3OR-OD+48-EW3-H18-LiveLoad

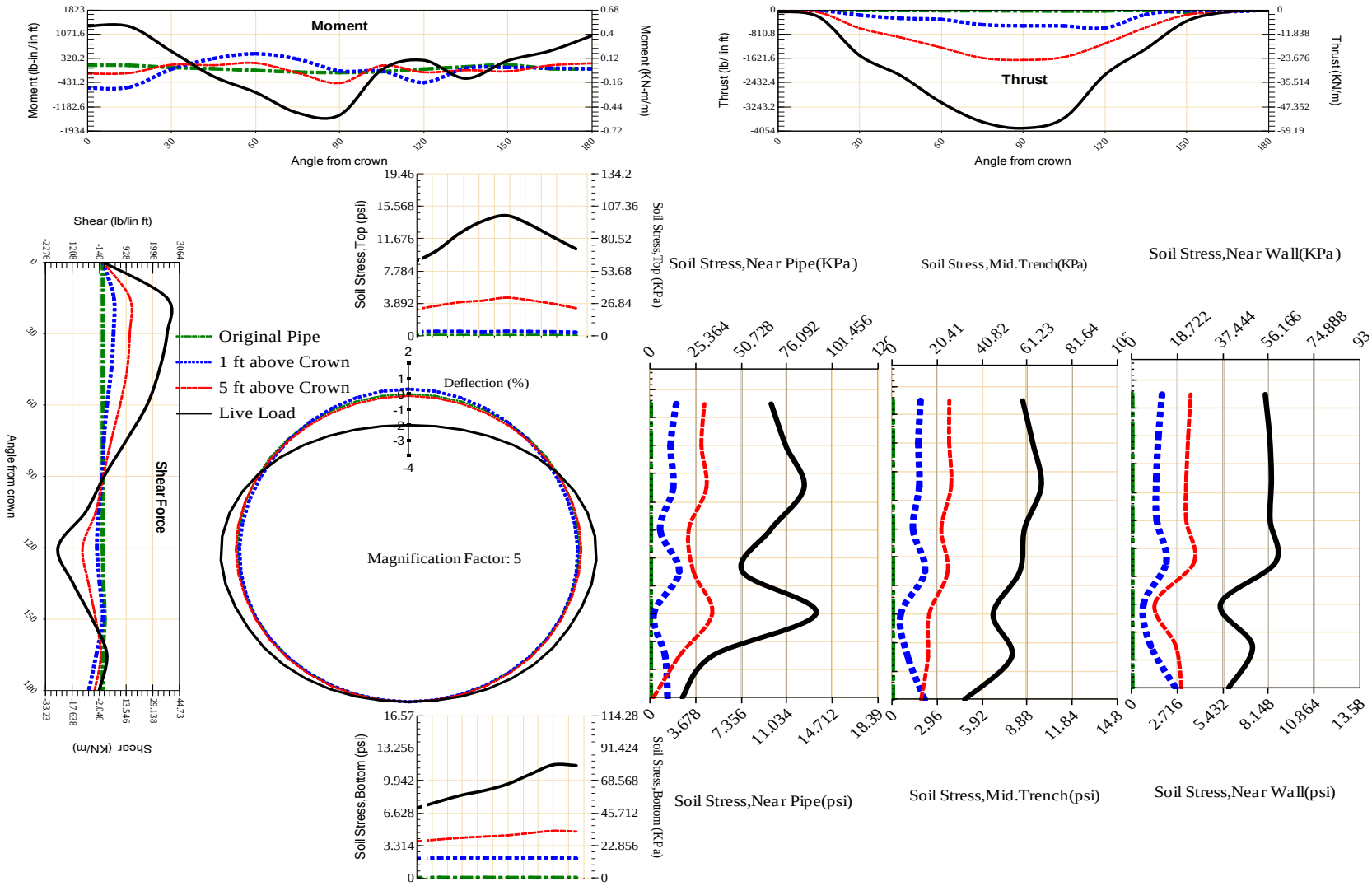

Figure A-241 Param-48-PW200-SF3OR-OD+48-EW3-H5-LiveLoad

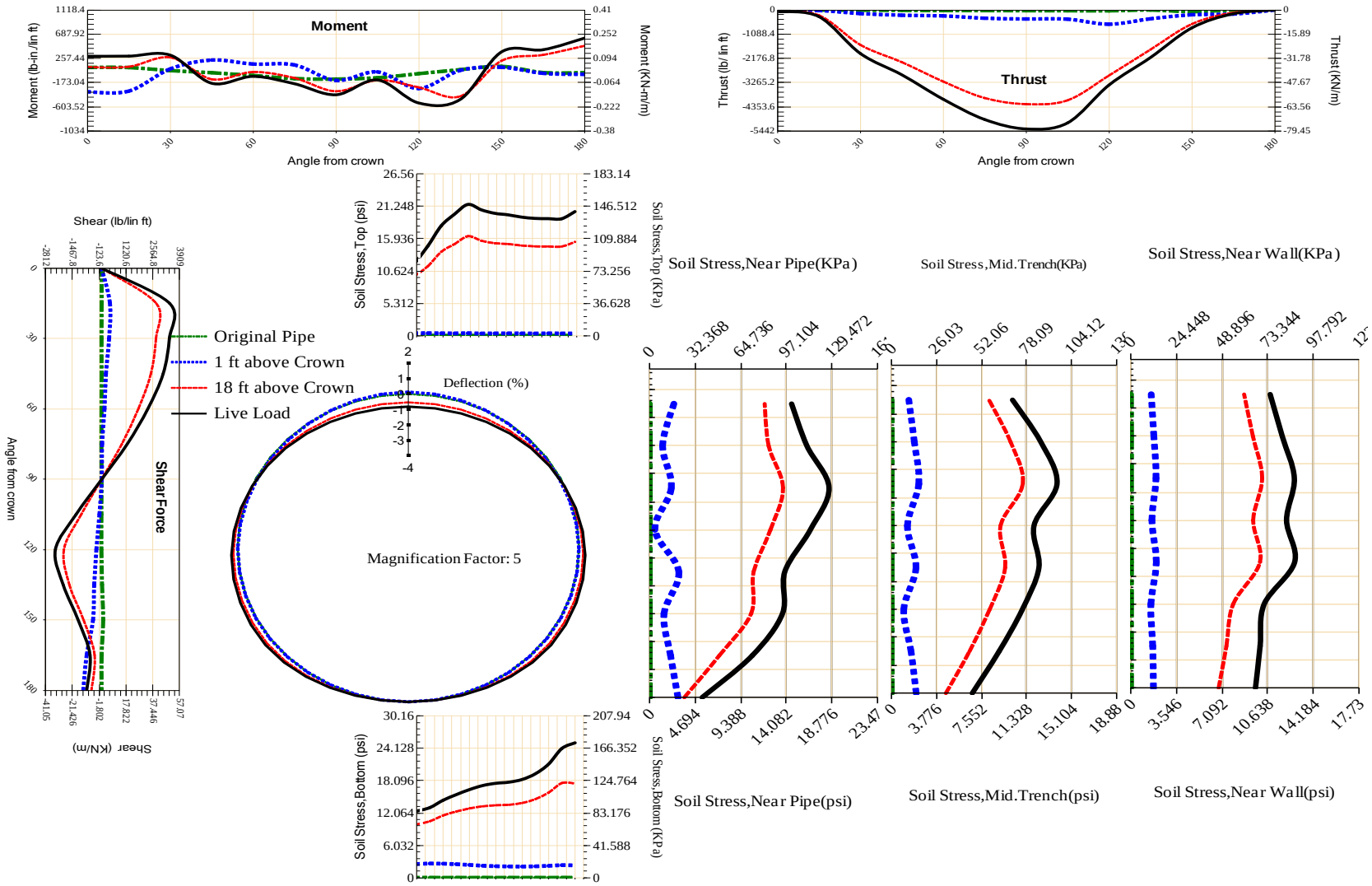

Figure A-242 Param-48-PW200-SF3TR-OD+108-EW10-H18-LiveLoad

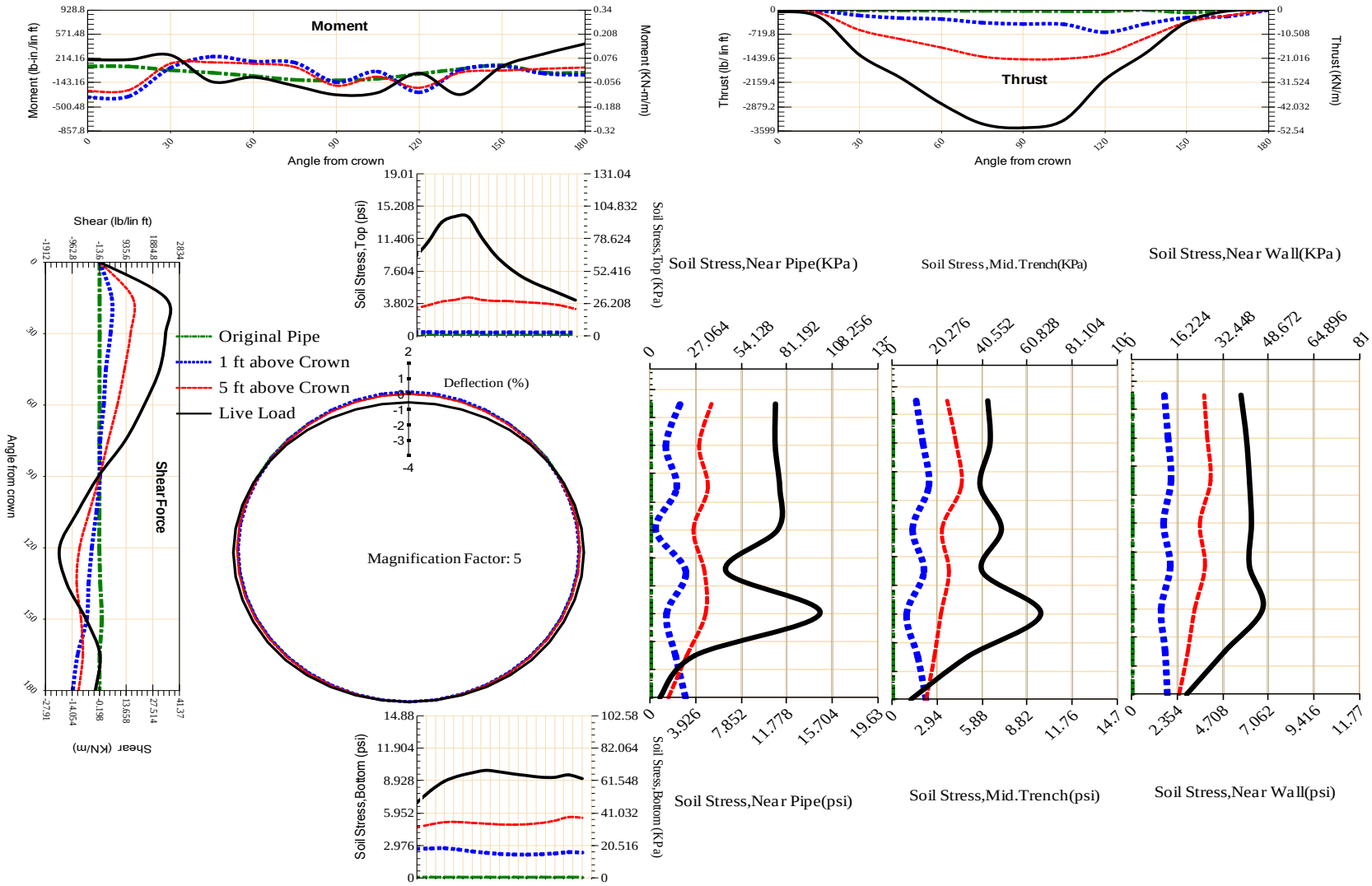

Figure A-243 Param-48-PW200-SF3TR-OD+108-EW10-H5-LiveLoad

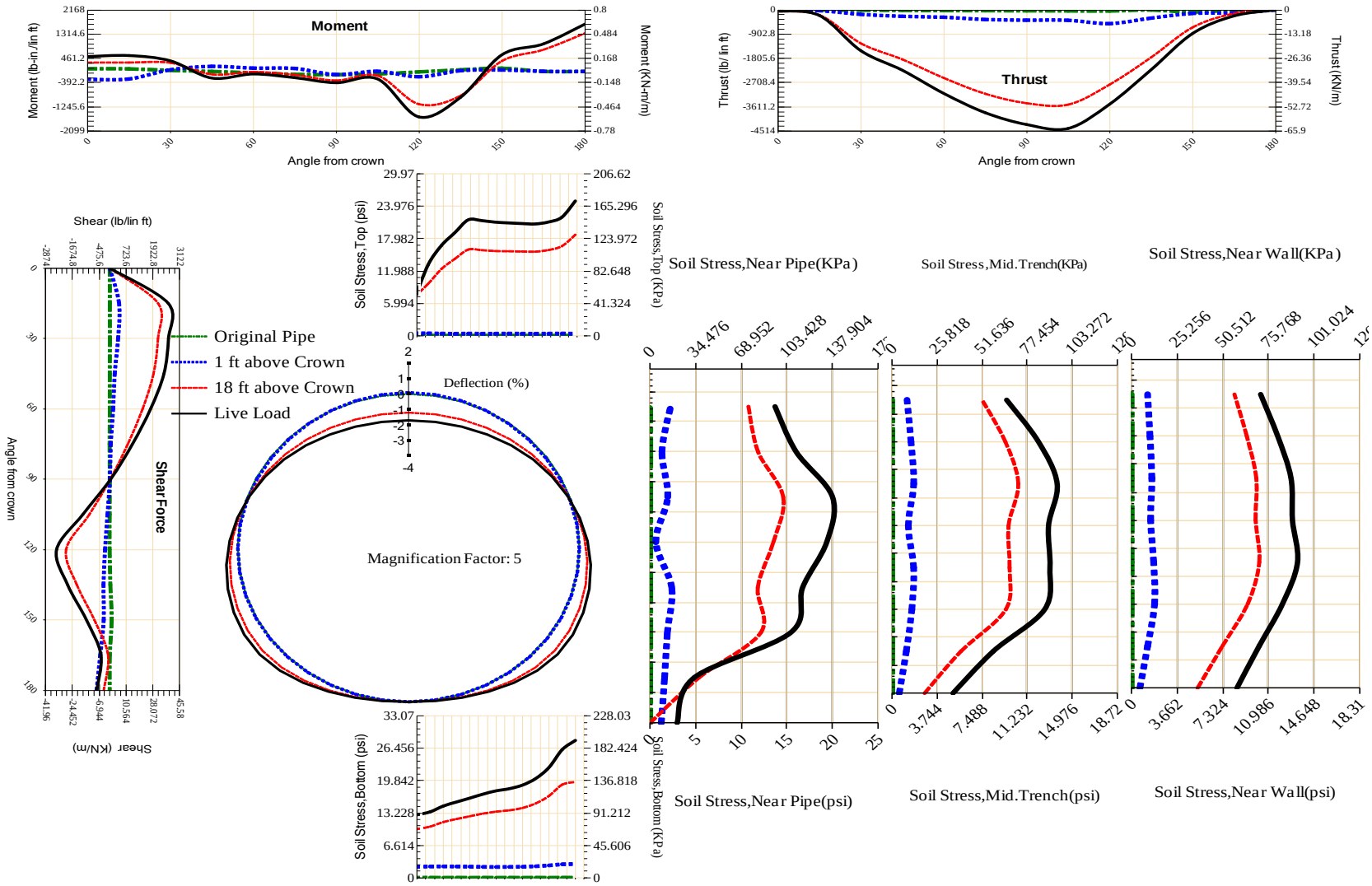

Figure A-244 Param-48-PW200-SF3TR-OD+108-EW3-H18-LiveLoad

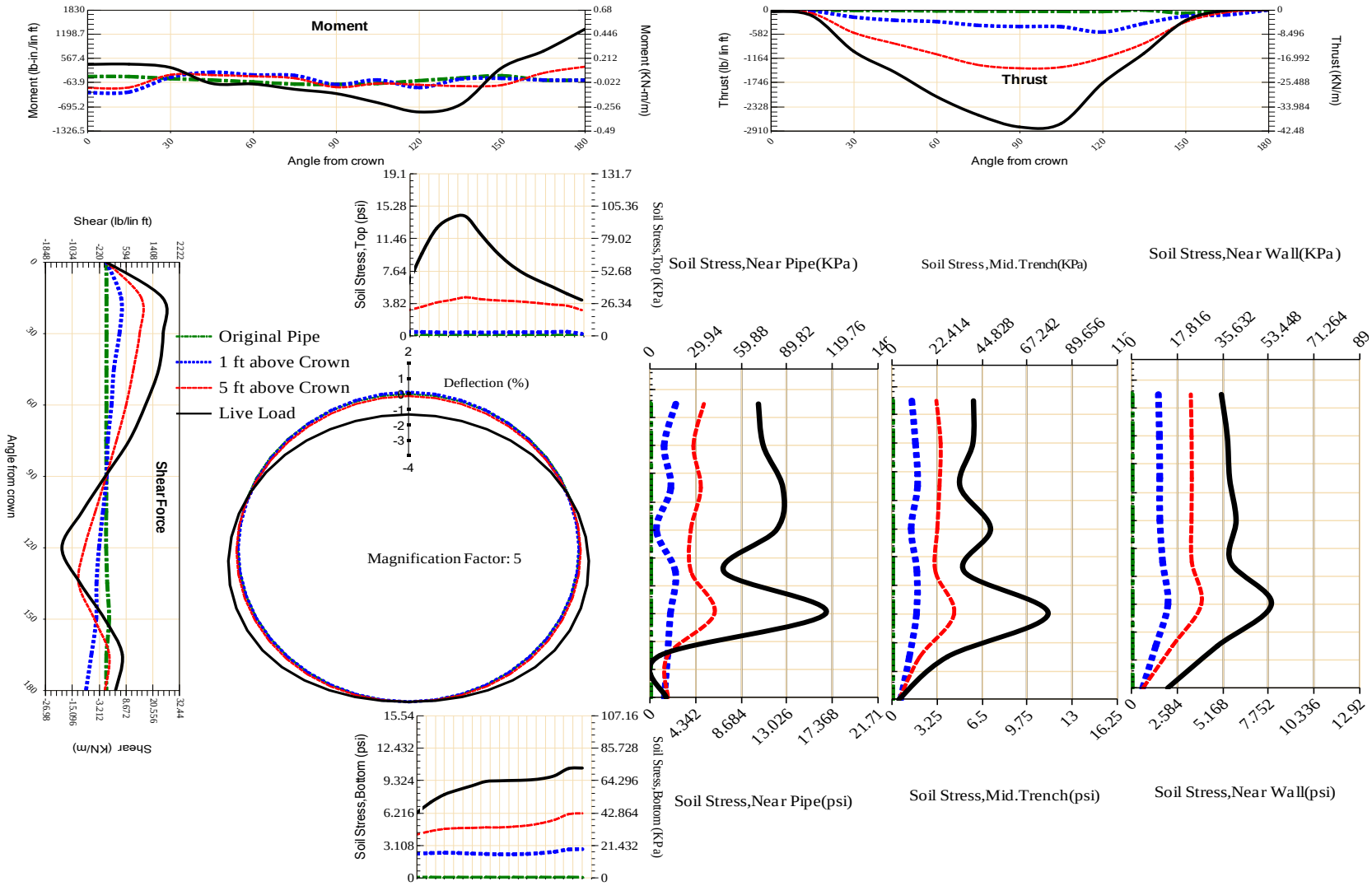

Figure A-245 Param-48-PW200-SF3TR-OD+108-EW3-H5-LiveLoad

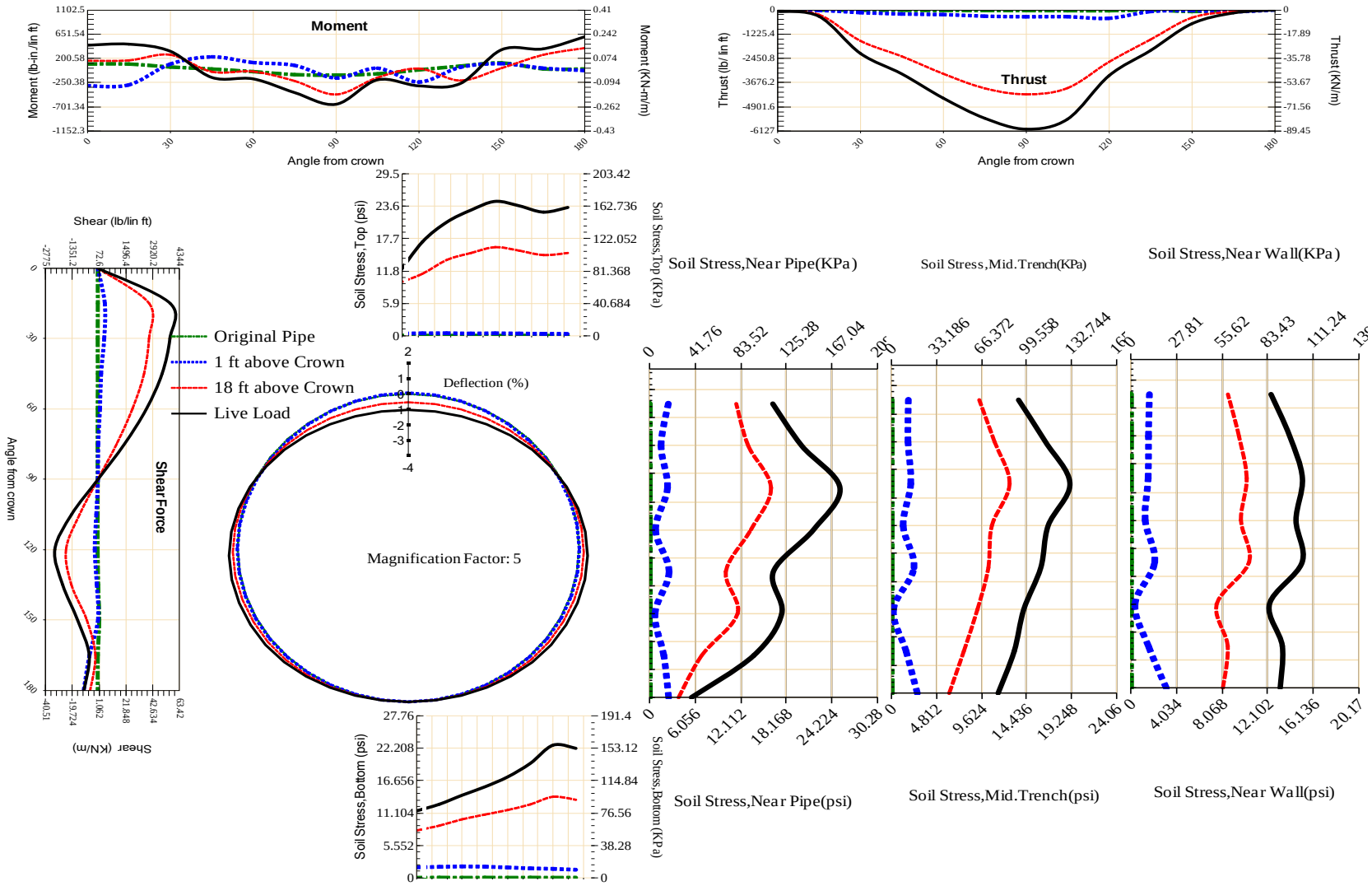

Figure A-246 Param-48-PW200-SF3TR-OD+48-EW10-H18-LiveLoad

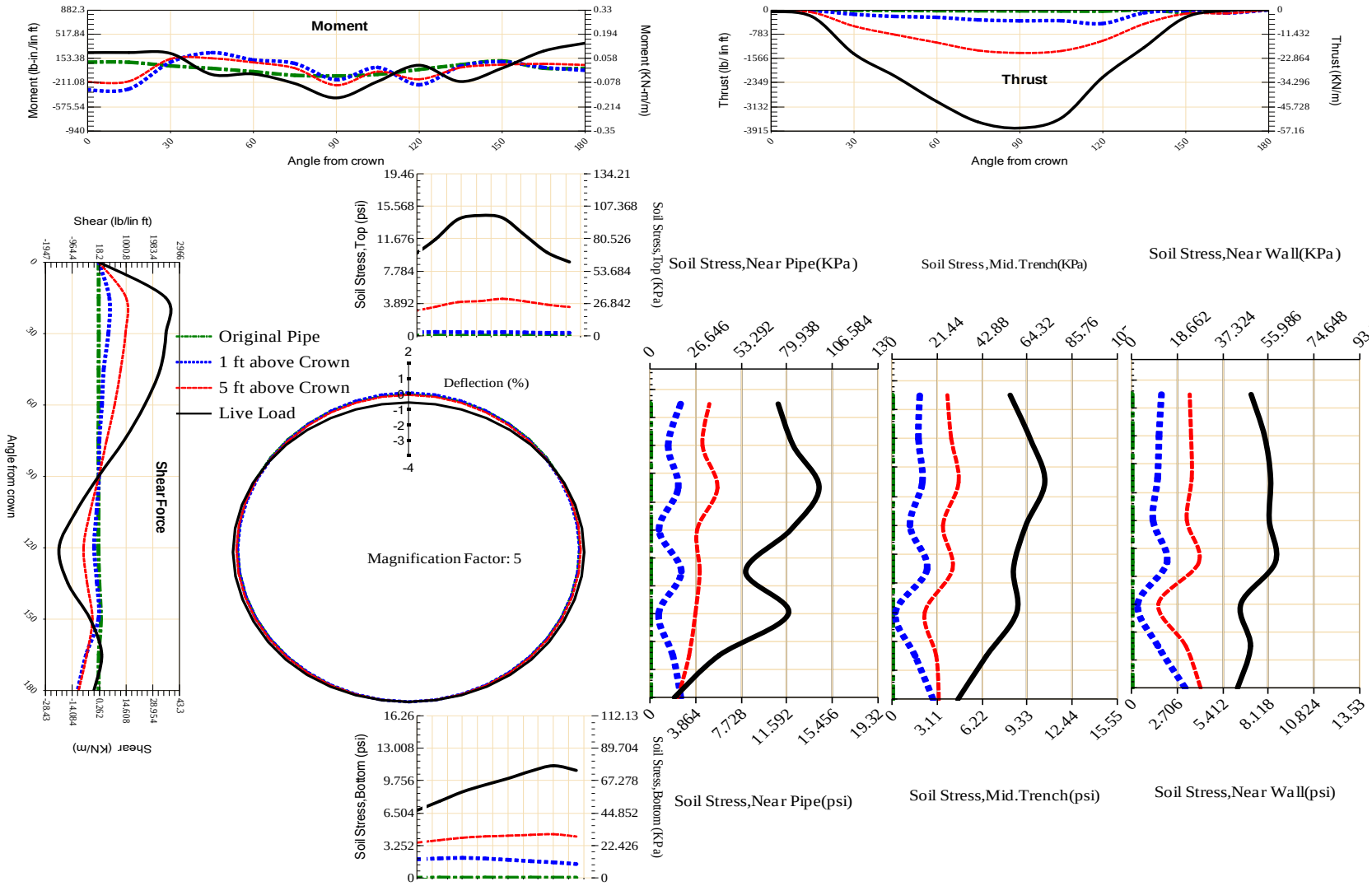

Figure A-247 Param-48-PW200-SF3TR-OD+48-EW10-H5-LiveLoad

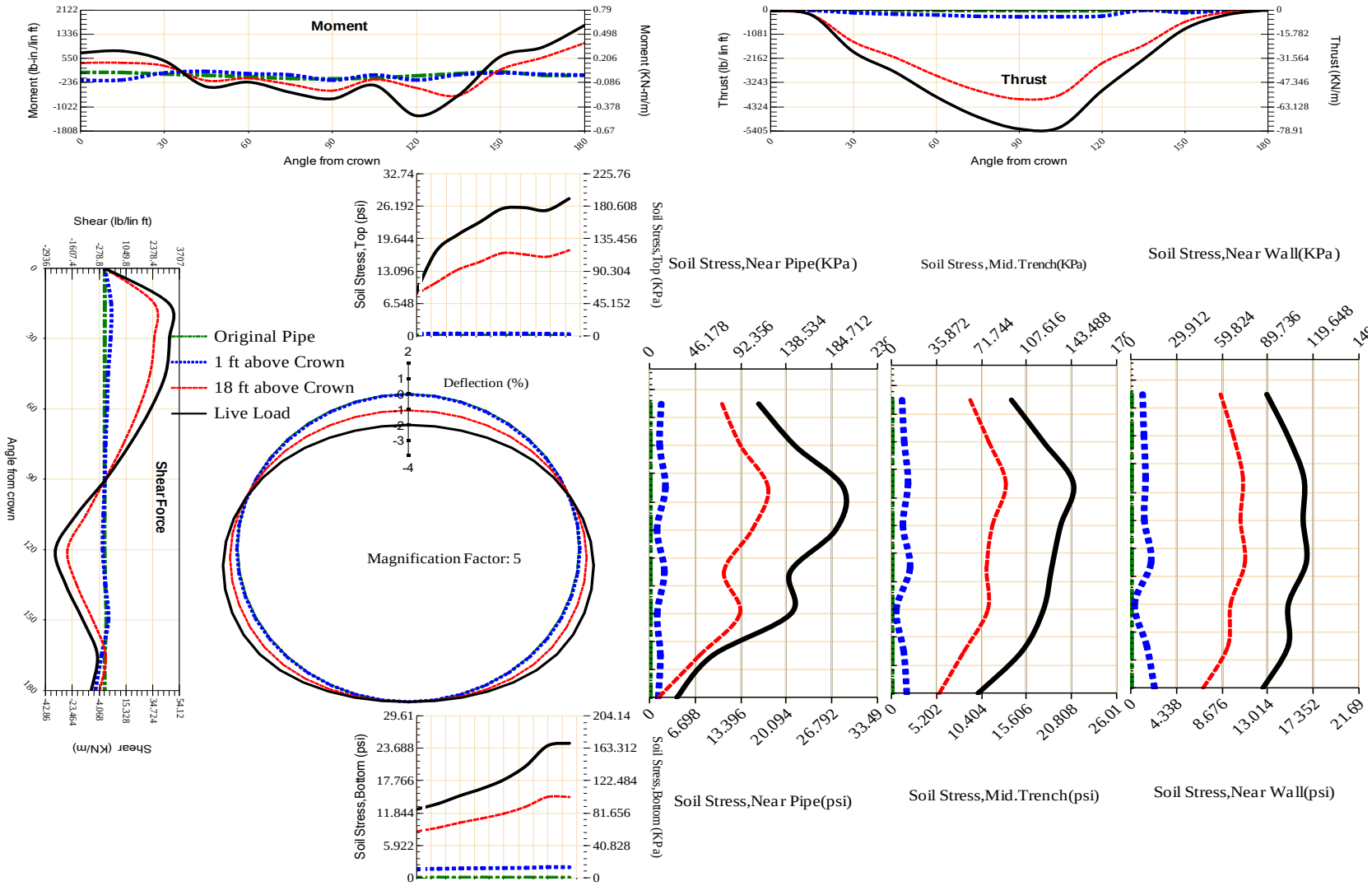

Figure A-248 Param-48-PW200-SF3TR-OD+48-EW3-H18-LiveLoad

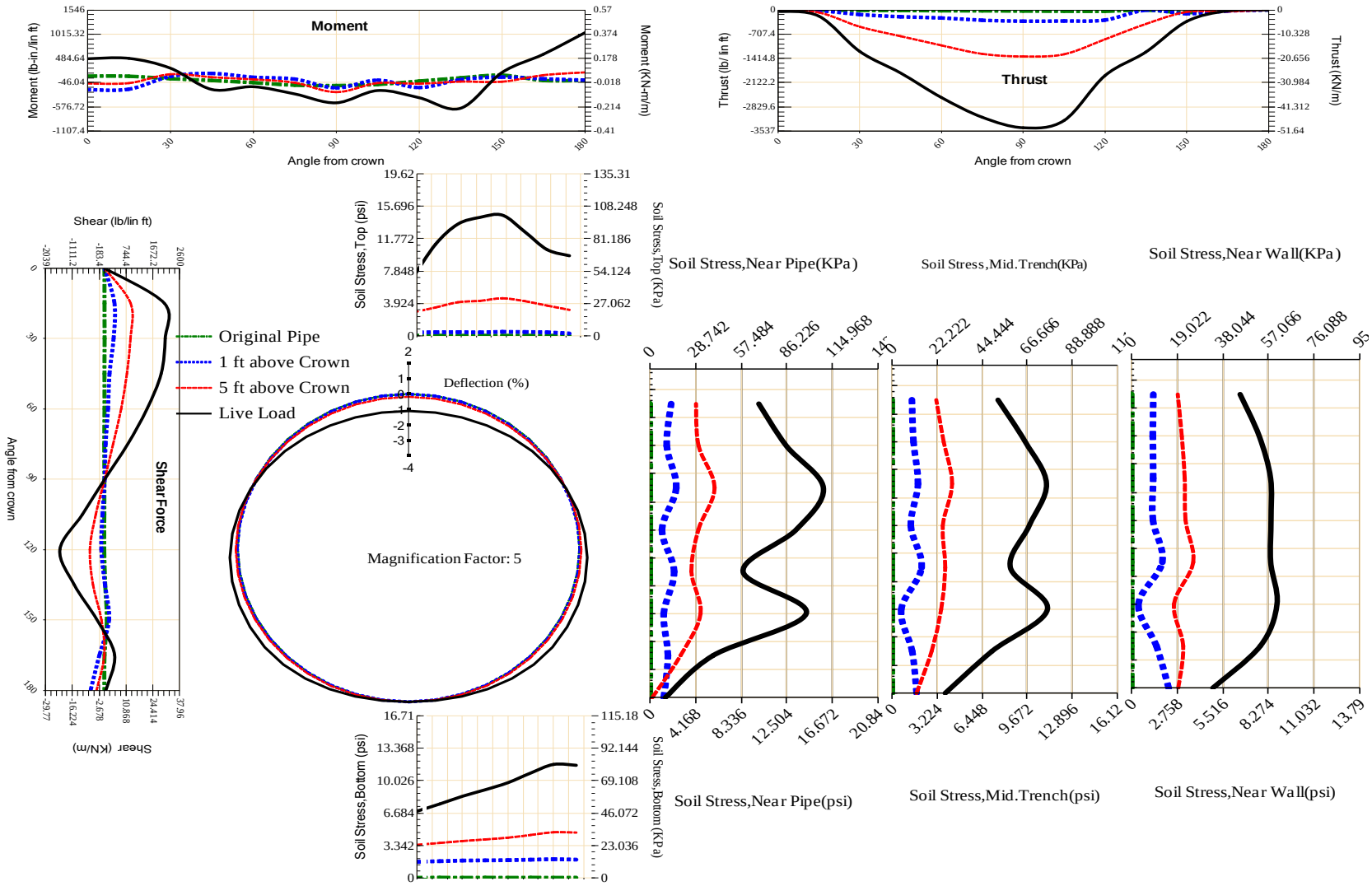

Figure A-249 Param-48-PW200-SF3TR-OD+48-EW3-H5-LiveLoad

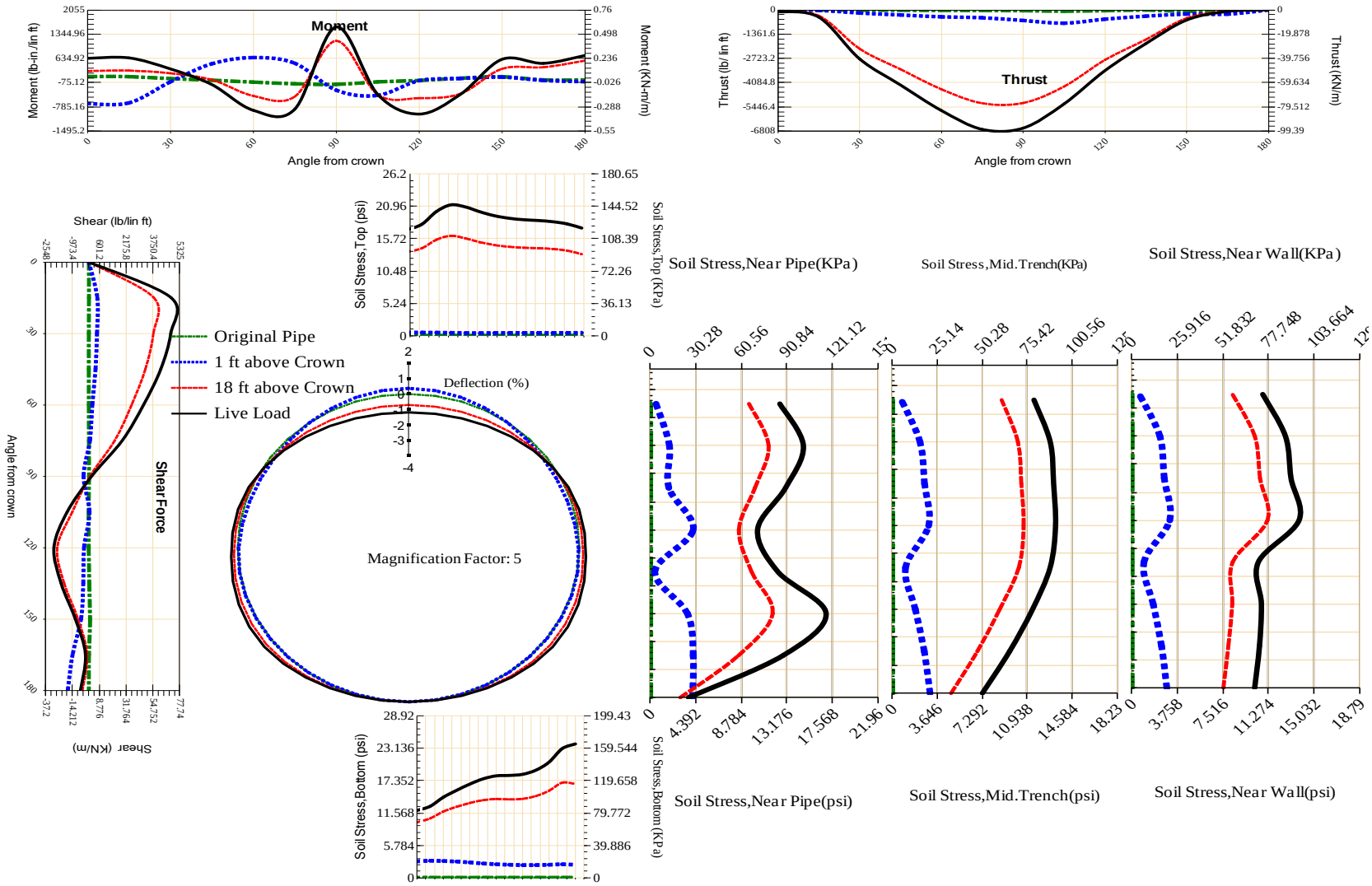

Figure A-250 Param-48-PW200-SF5OR-OD+108-EW10-H18-LiveLoad

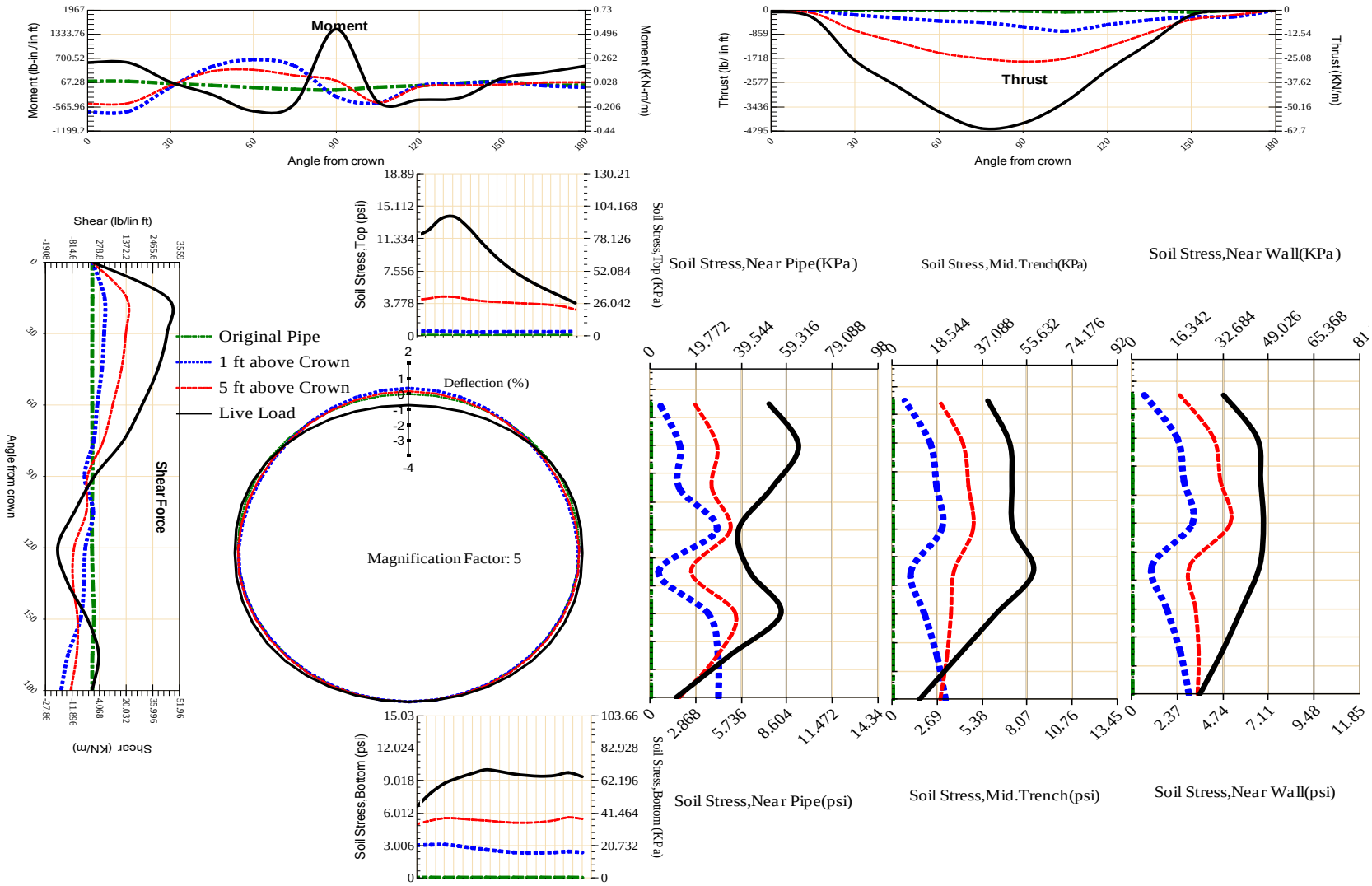

Figure A-251 Param-48-PW200-SF5OR-OD+108-EW10-H5-LiveLoad

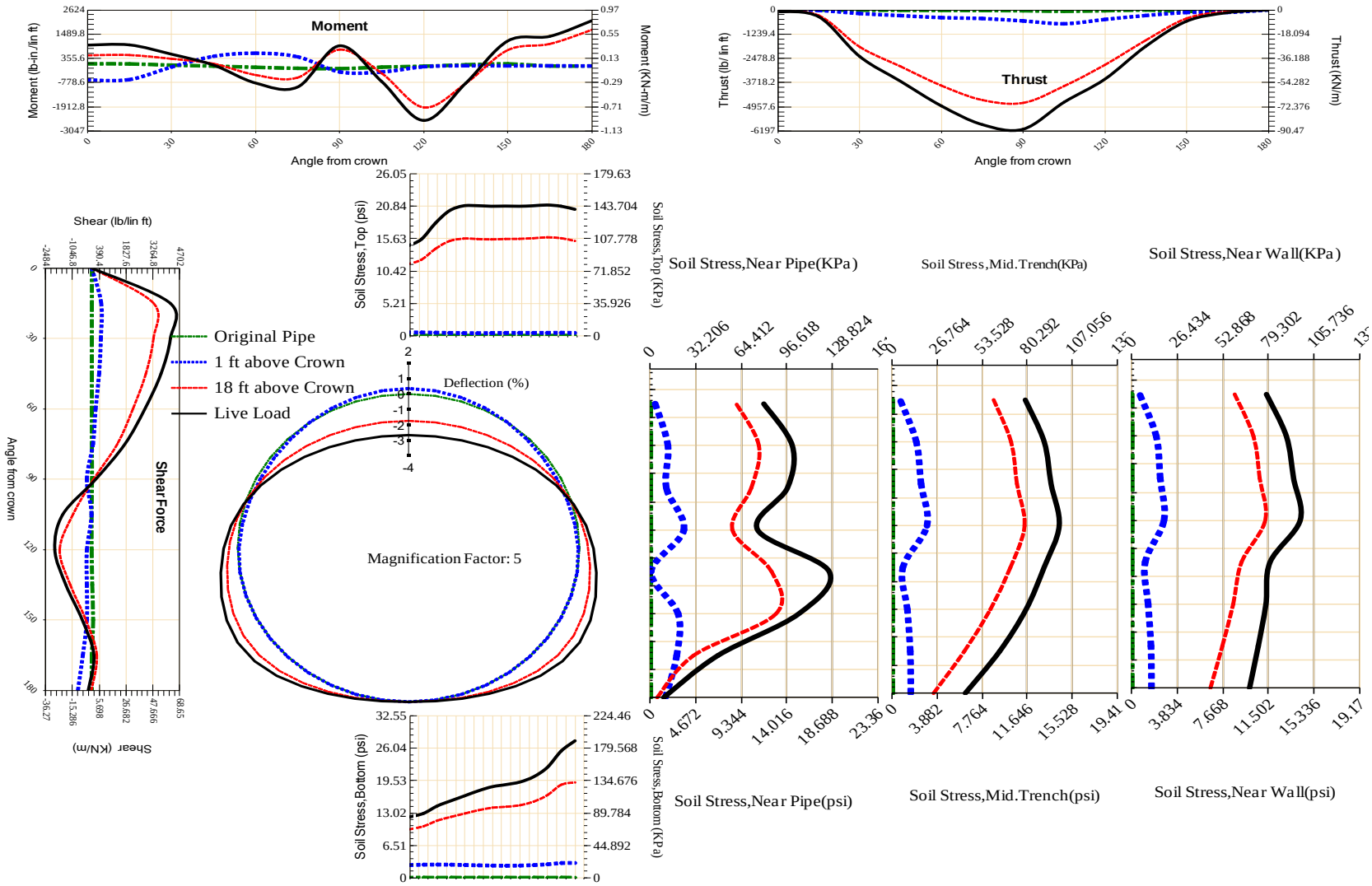

Figure A-252 Param-48-PW200-SF5OR-OD+108-EW3-H18-LiveLoad

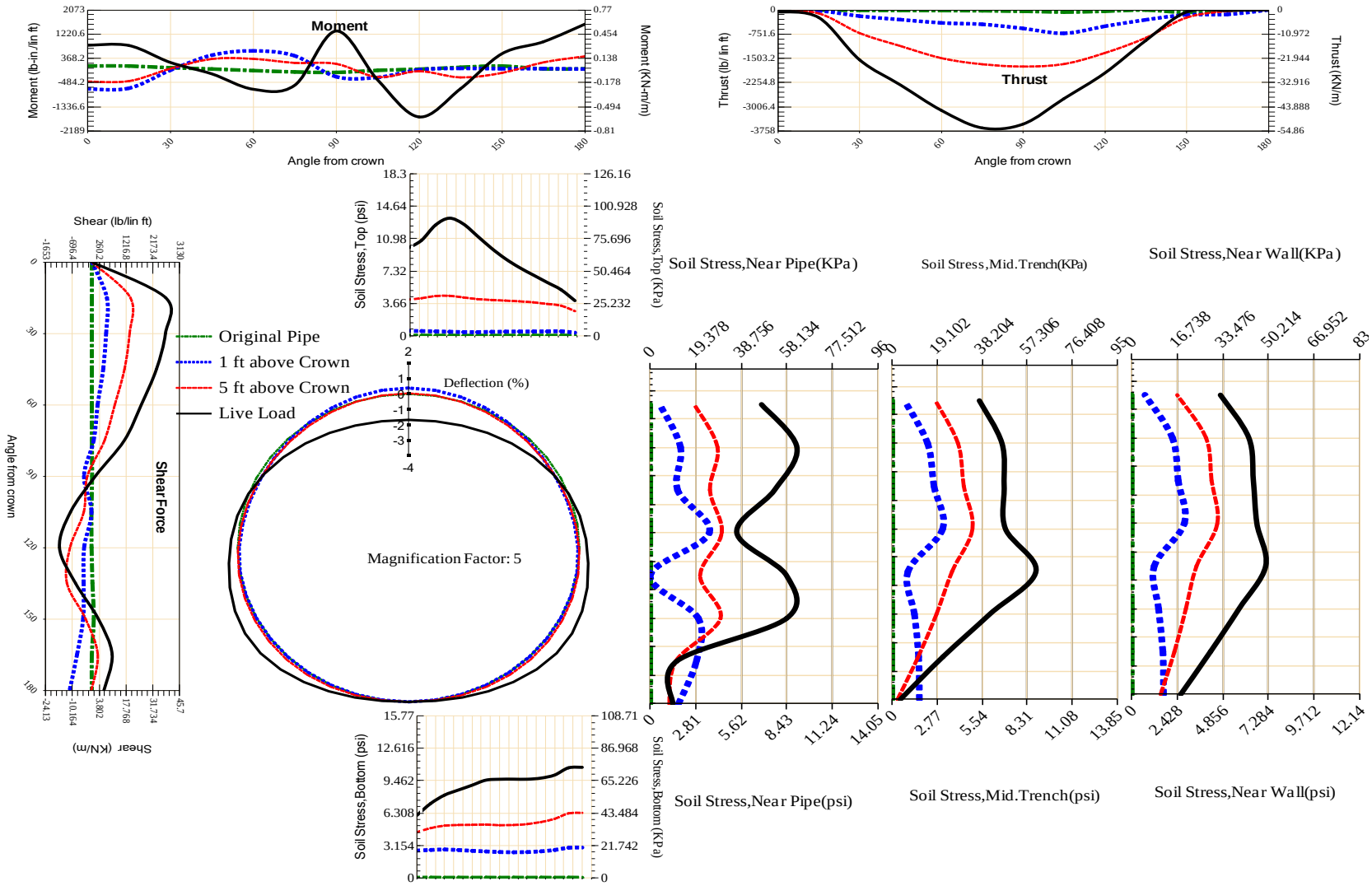

Figure A-253 Param-48-PW200-SF5OR-OD+108-EW3-H5-LiveLoad

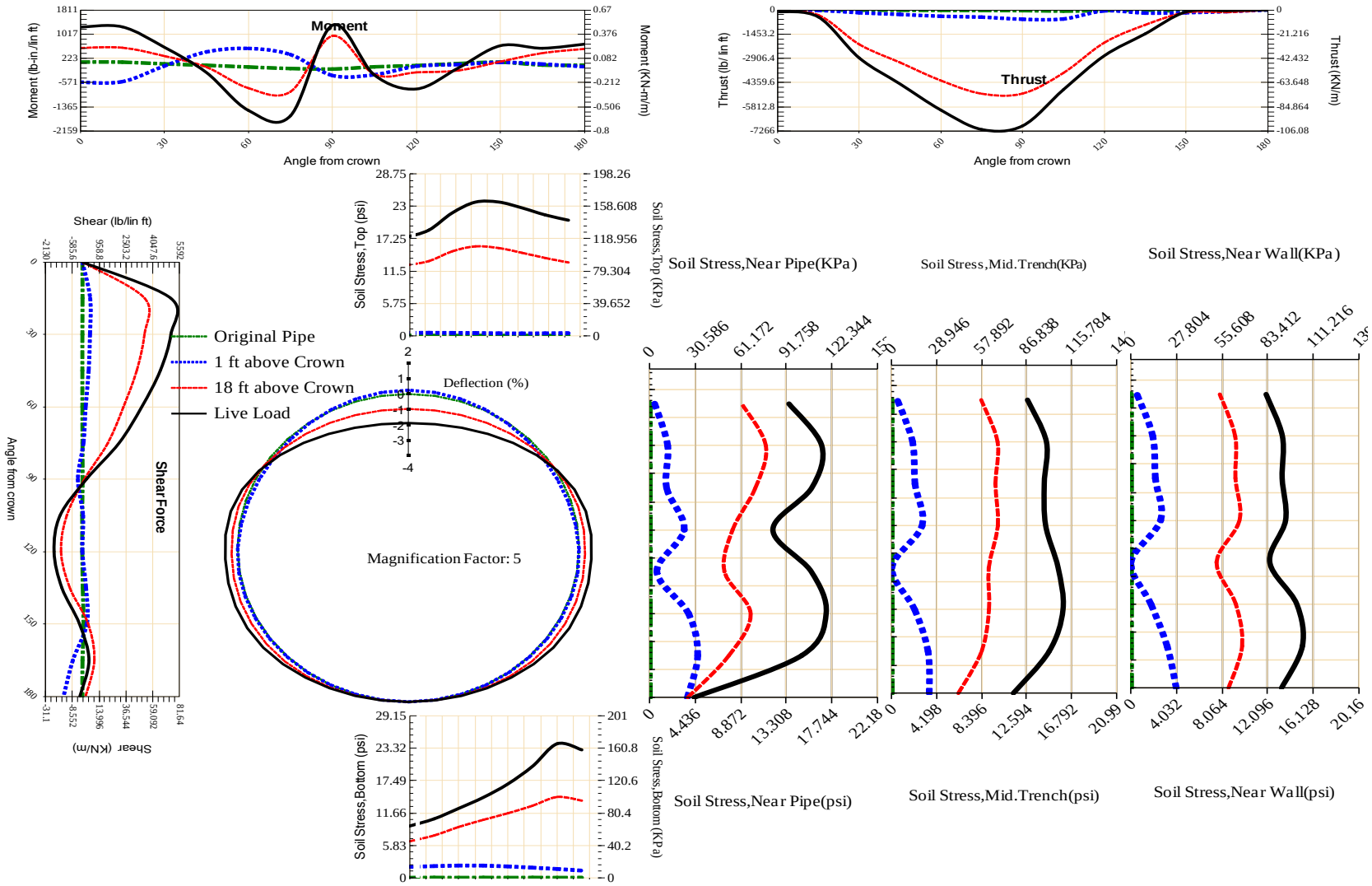

Figure A-254 Param-48-PW200-SF5OR-OD+48-EW10-H18-LiveLoad

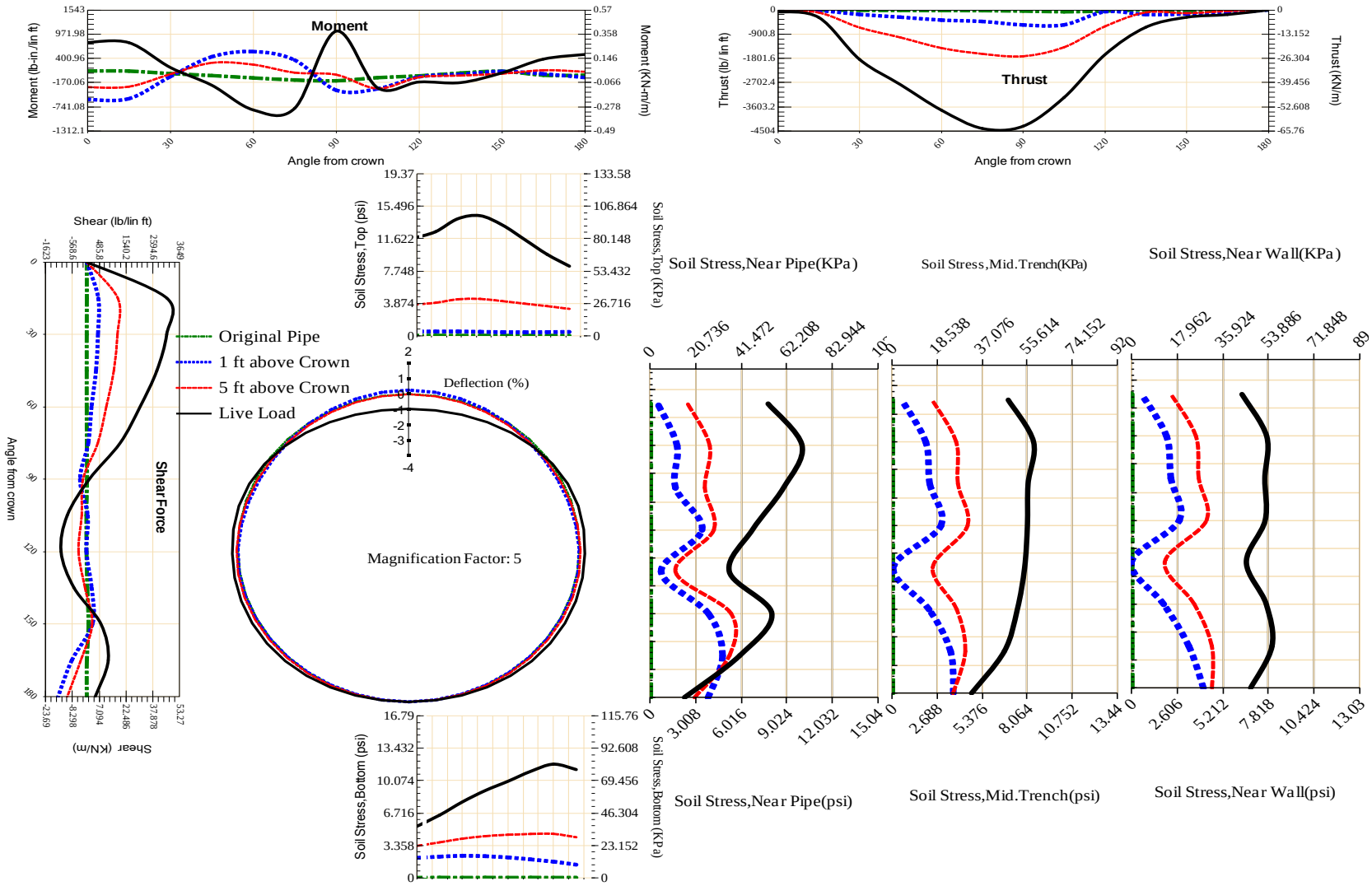

Figure A-255 Param-48-PW200-SF5OR-OD+48-EW10-H5-LiveLoad

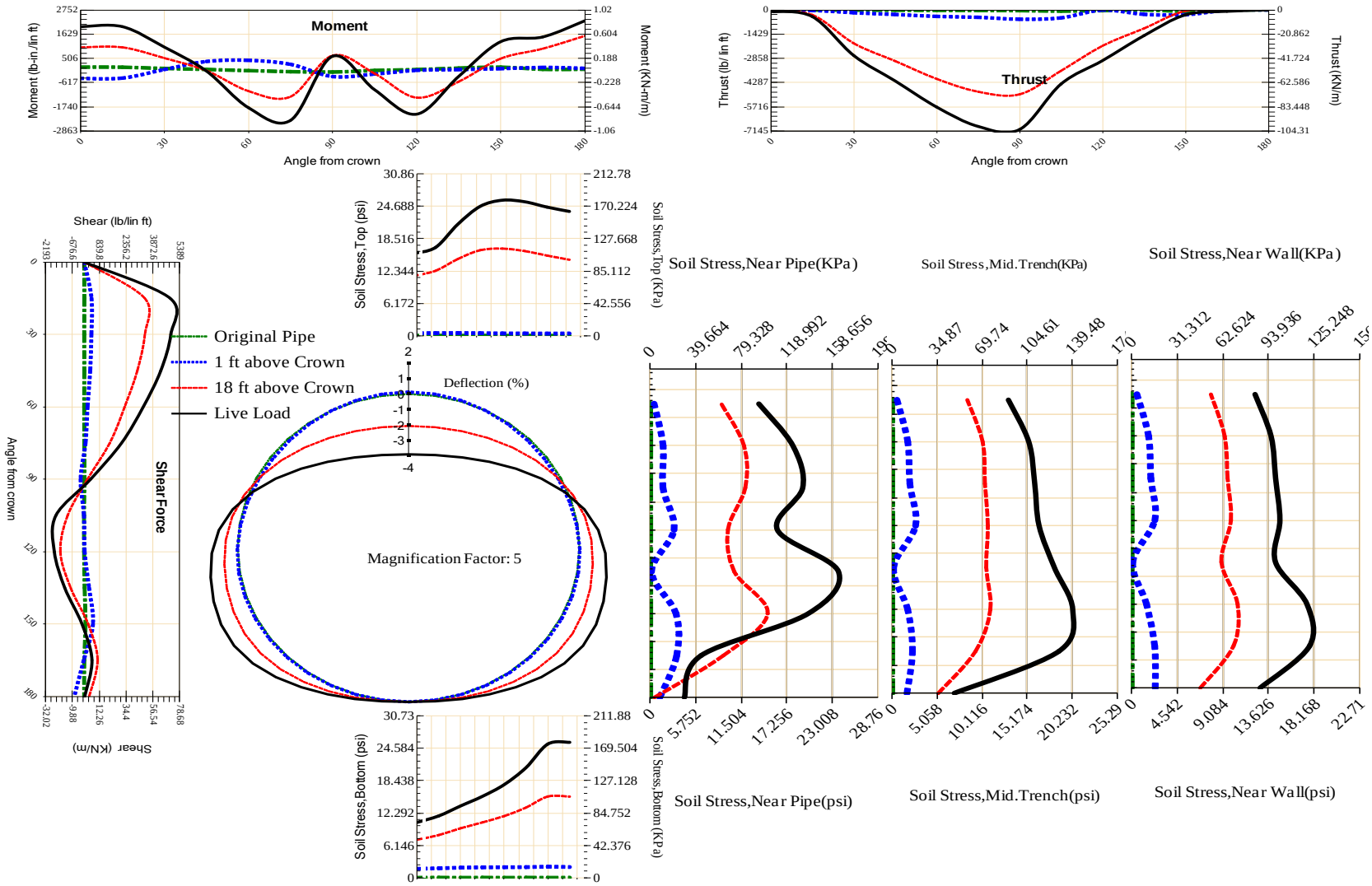

Figure A-256 Param-48-PW200-SF5OR-OD+48-EW3-H18-LiveLoad

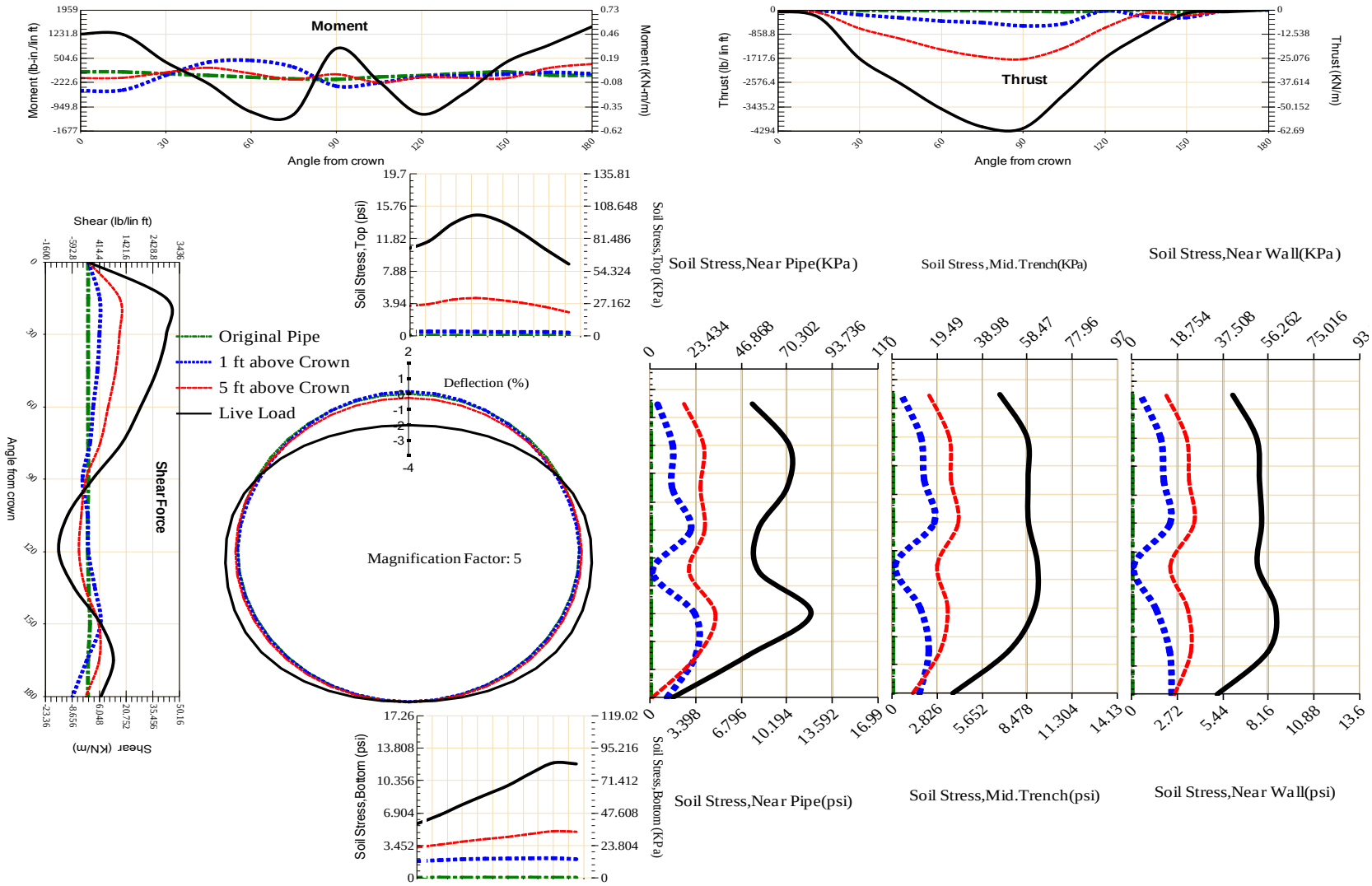

Figure A-257 Param-48-PW200-SF5OR-OD+48-EW3-H5-LiveLoad

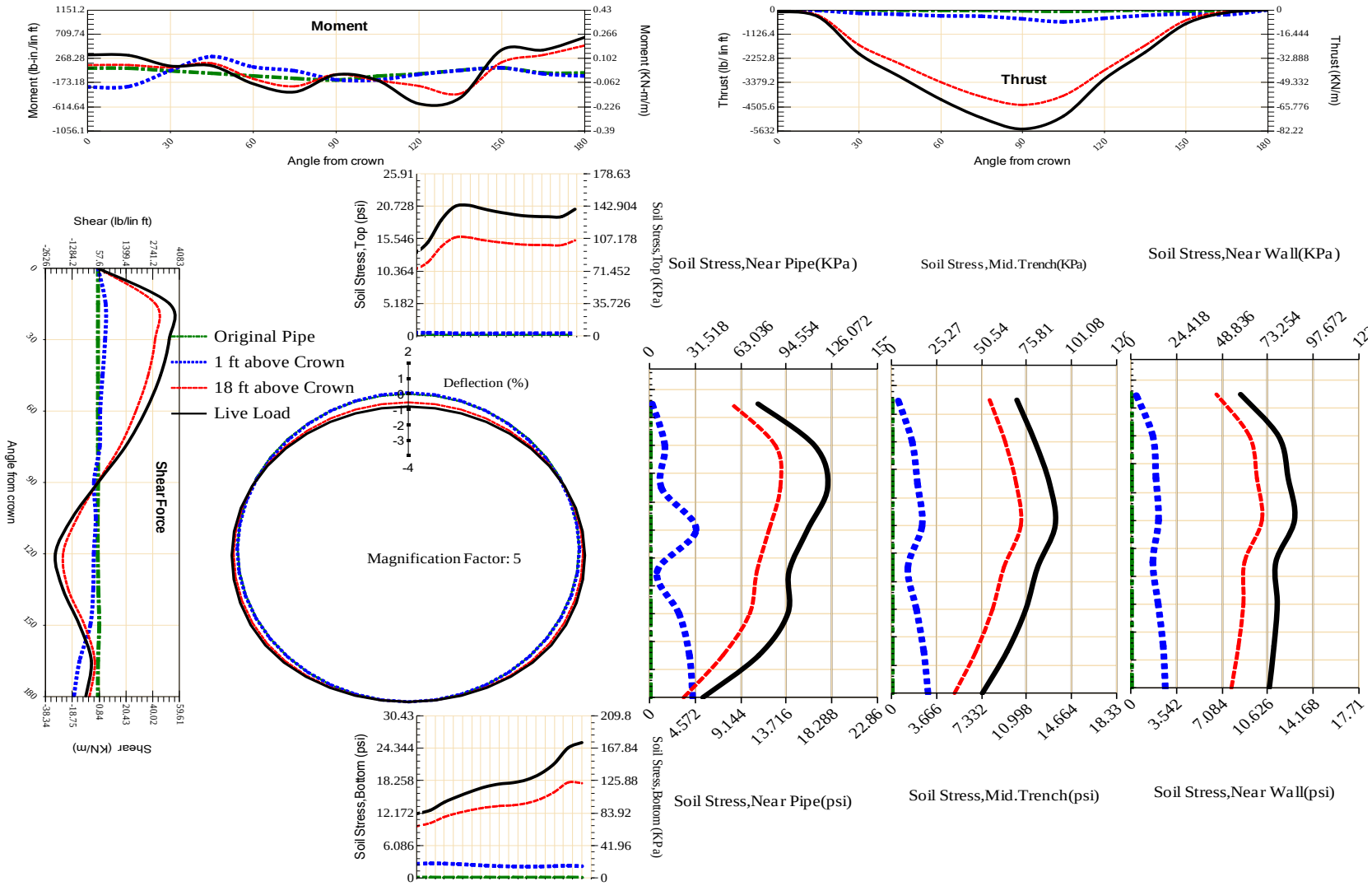

Figure A-258 Param-48-PW200-SF5TR-OD+108-EW10-H18-LiveLoad

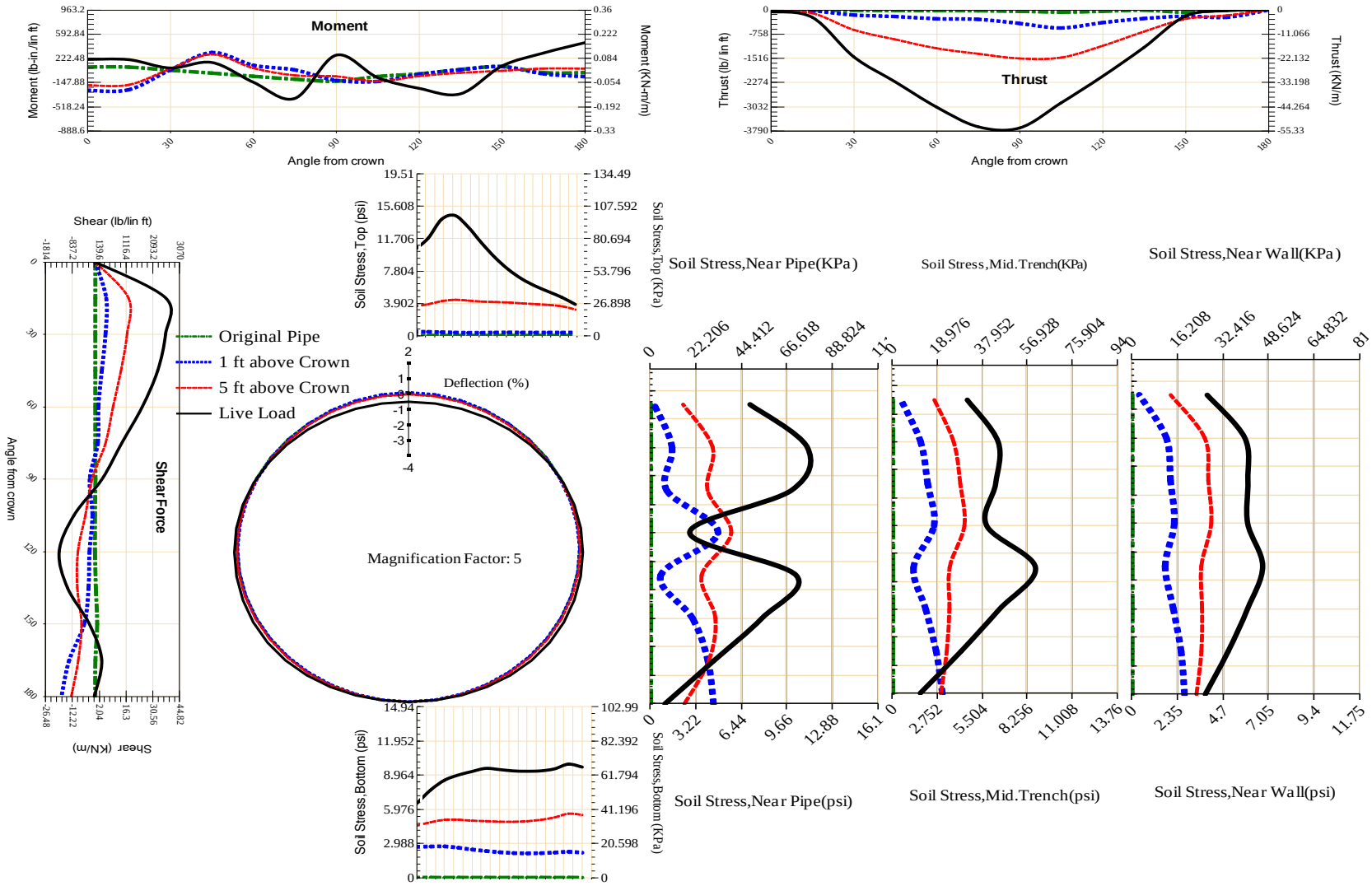

Figure A-259 Param-48-PW200-SF5TR-OD+108-EW10-H5-LiveLoad

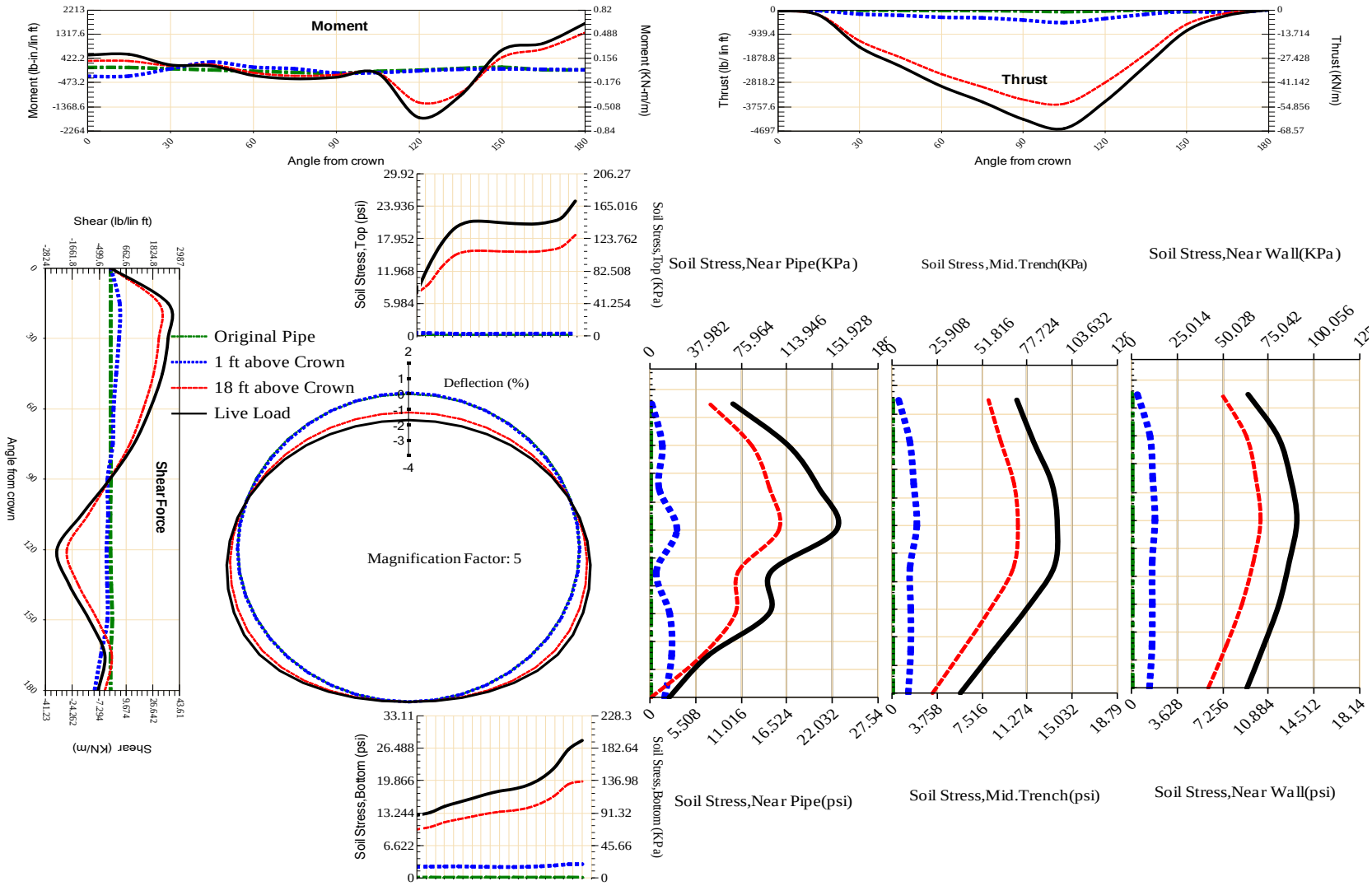

Figure A-260 Param-48-PW200-SF5TR-OD+108-EW3-H18-LiveLoad

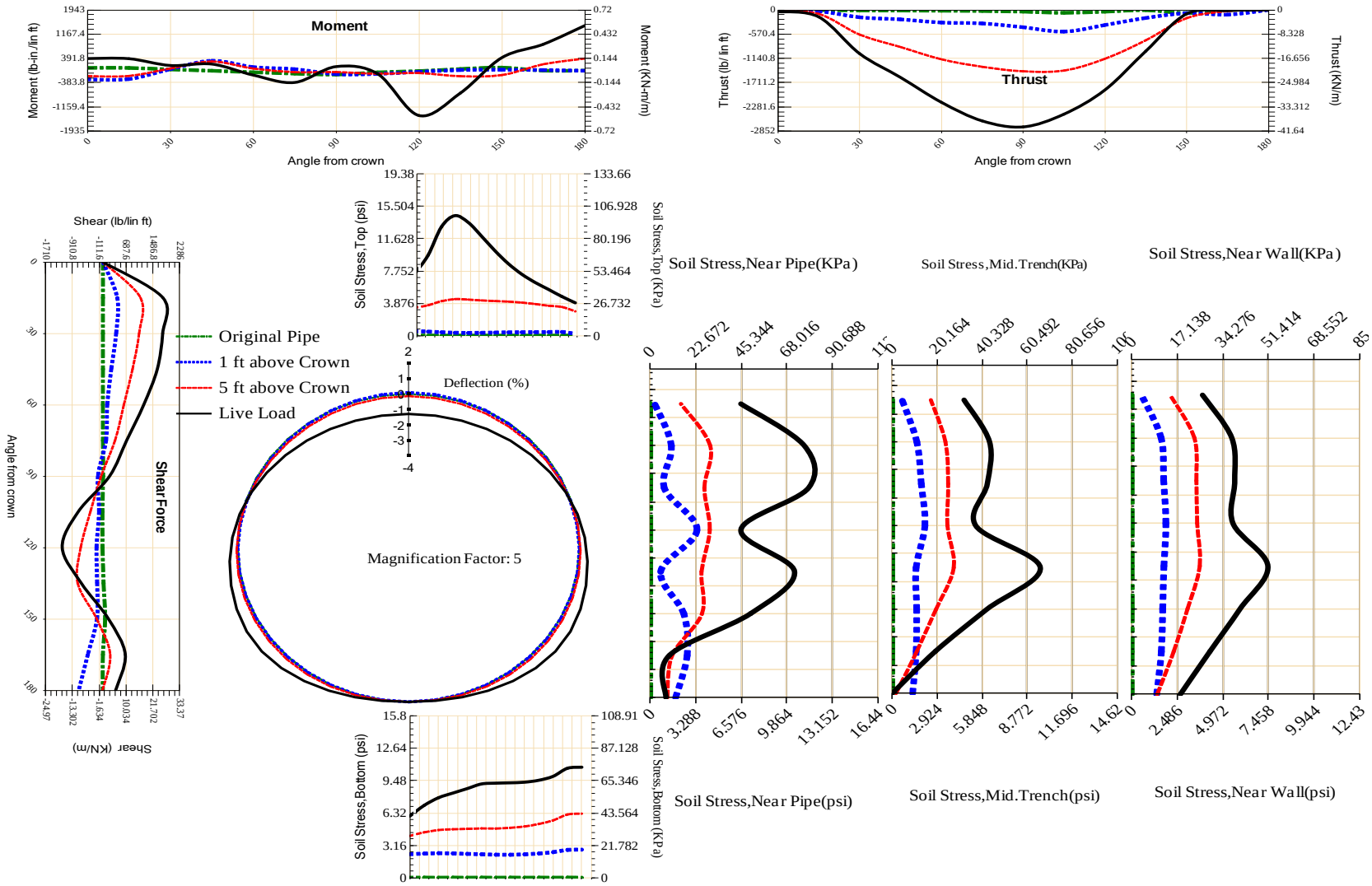

Figure A-261 Param-48-PW200-SF5TR-OD+108-EW3-H5-LiveLoad

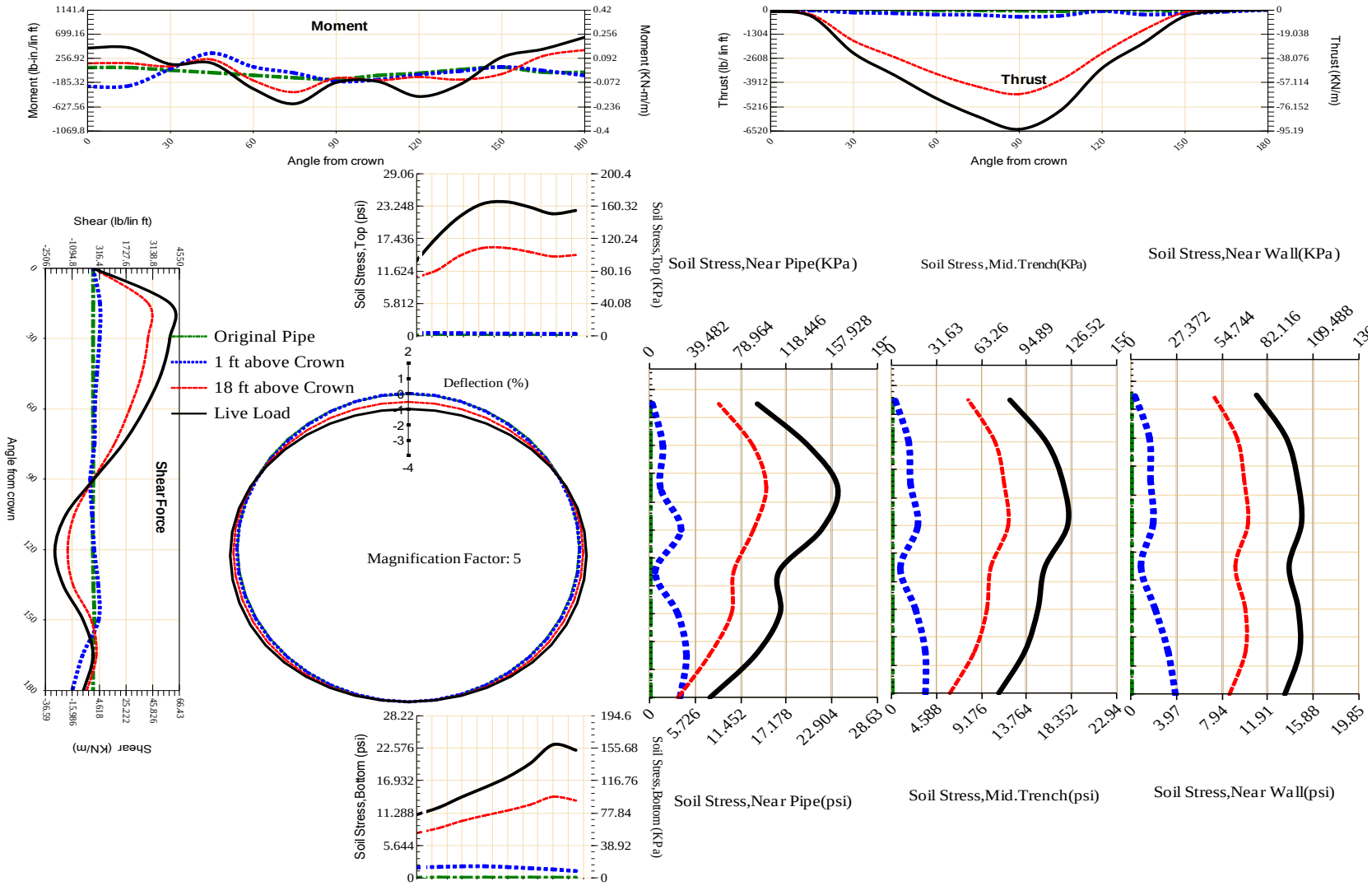

Figure A-262 Param-48-PW200-SF5TR-OD+48-EW10-H18-LiveLoad

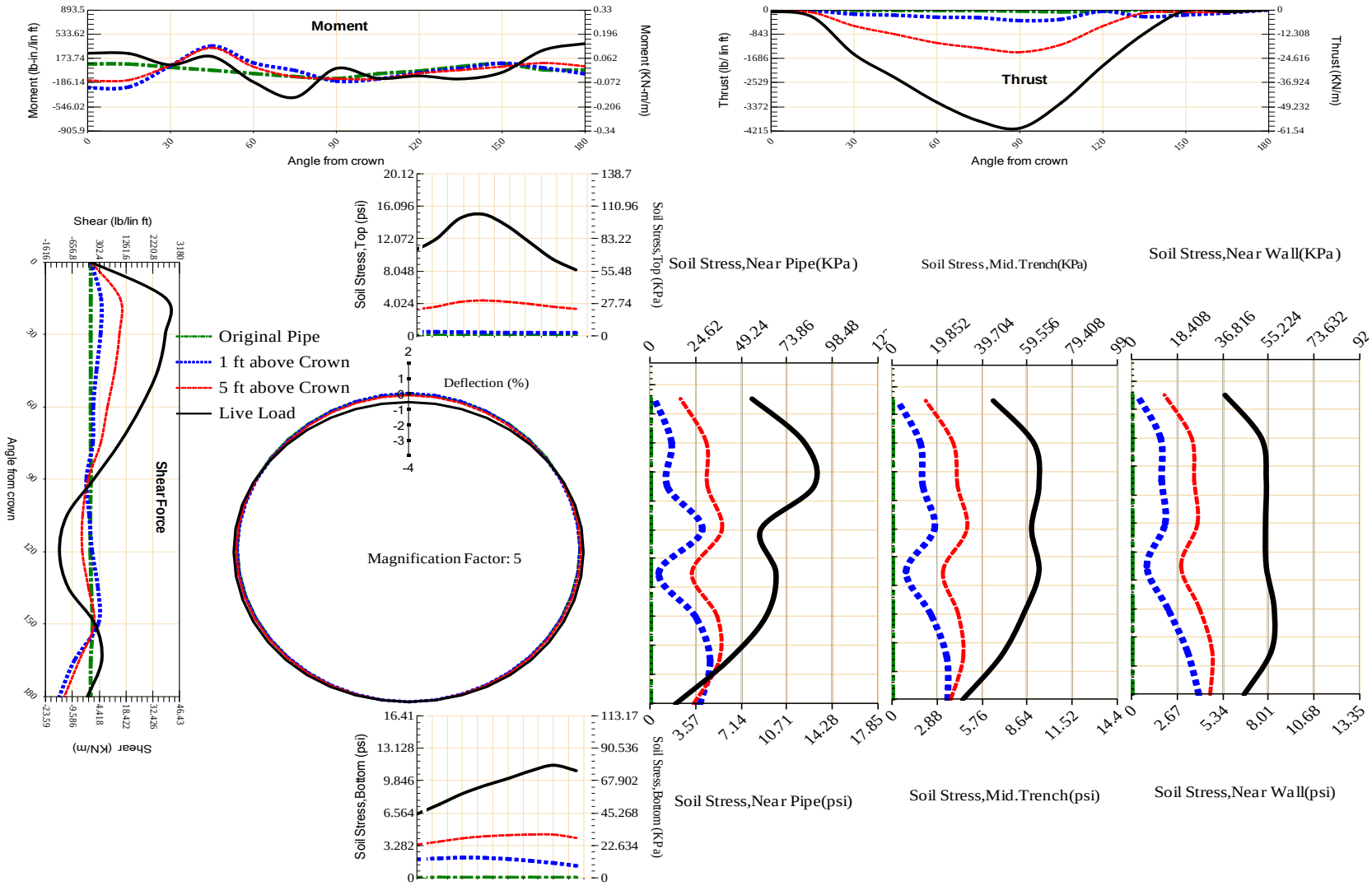

Figure A-263 Param-48-PW200-SF5TR-OD+48-EW10-H5-LiveLoad

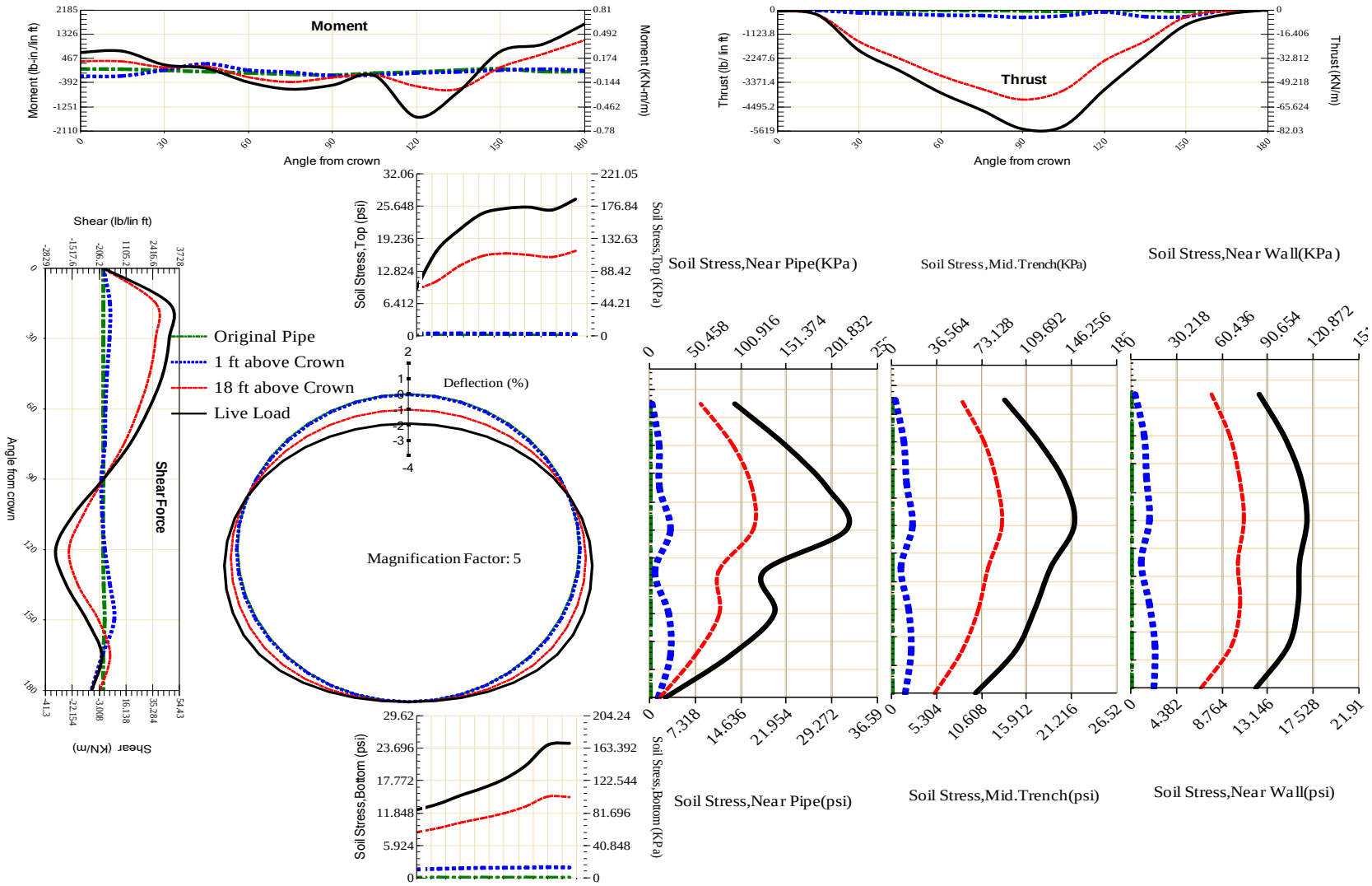

Figure A-264 Param-48-PW200-SF5TR-OD+48-EW3-H18-LiveLoad

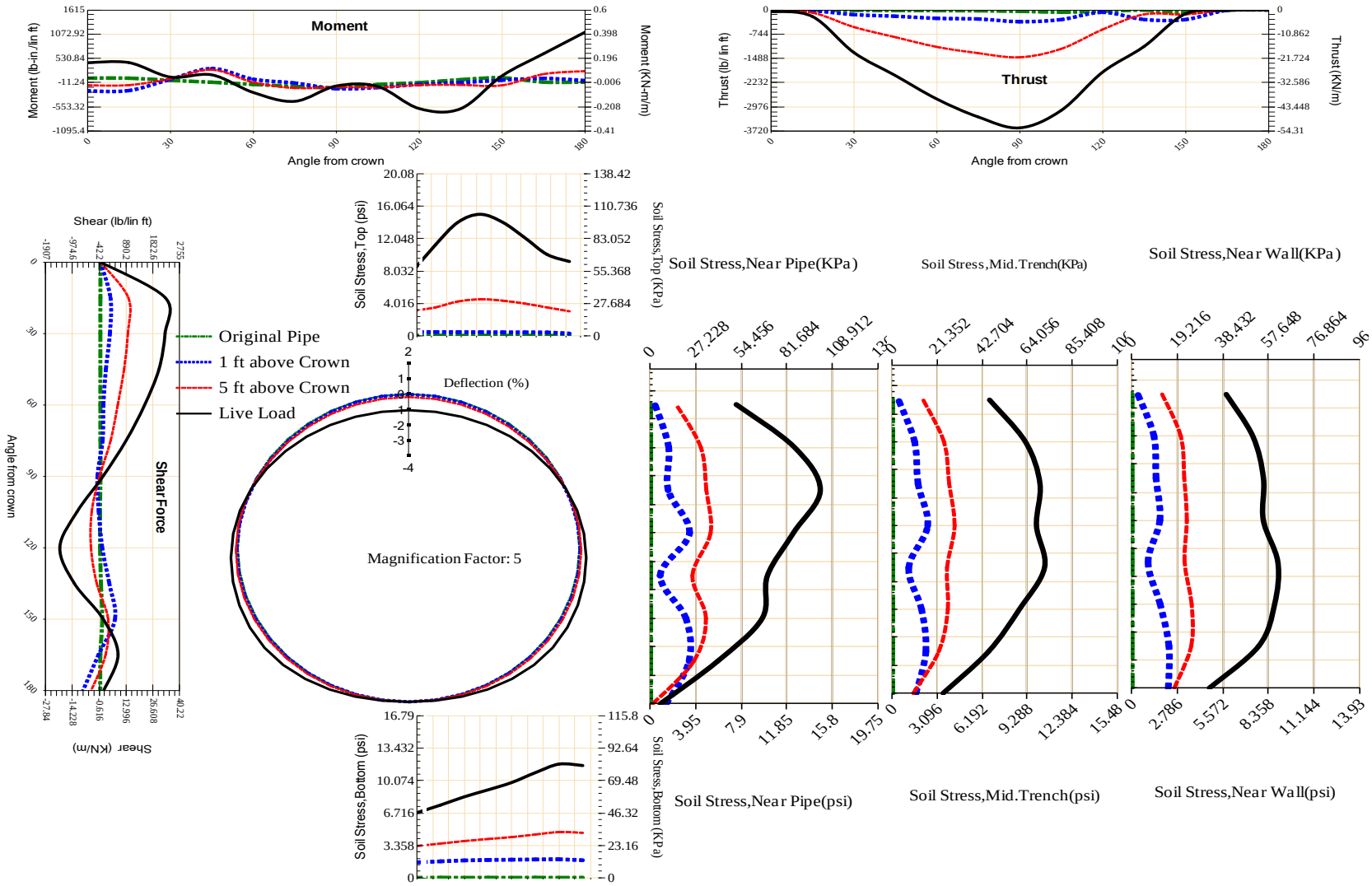

Figure A-265 Param-48-PW200-SF5TR-OD+48-EW3-H5-LiveLoad

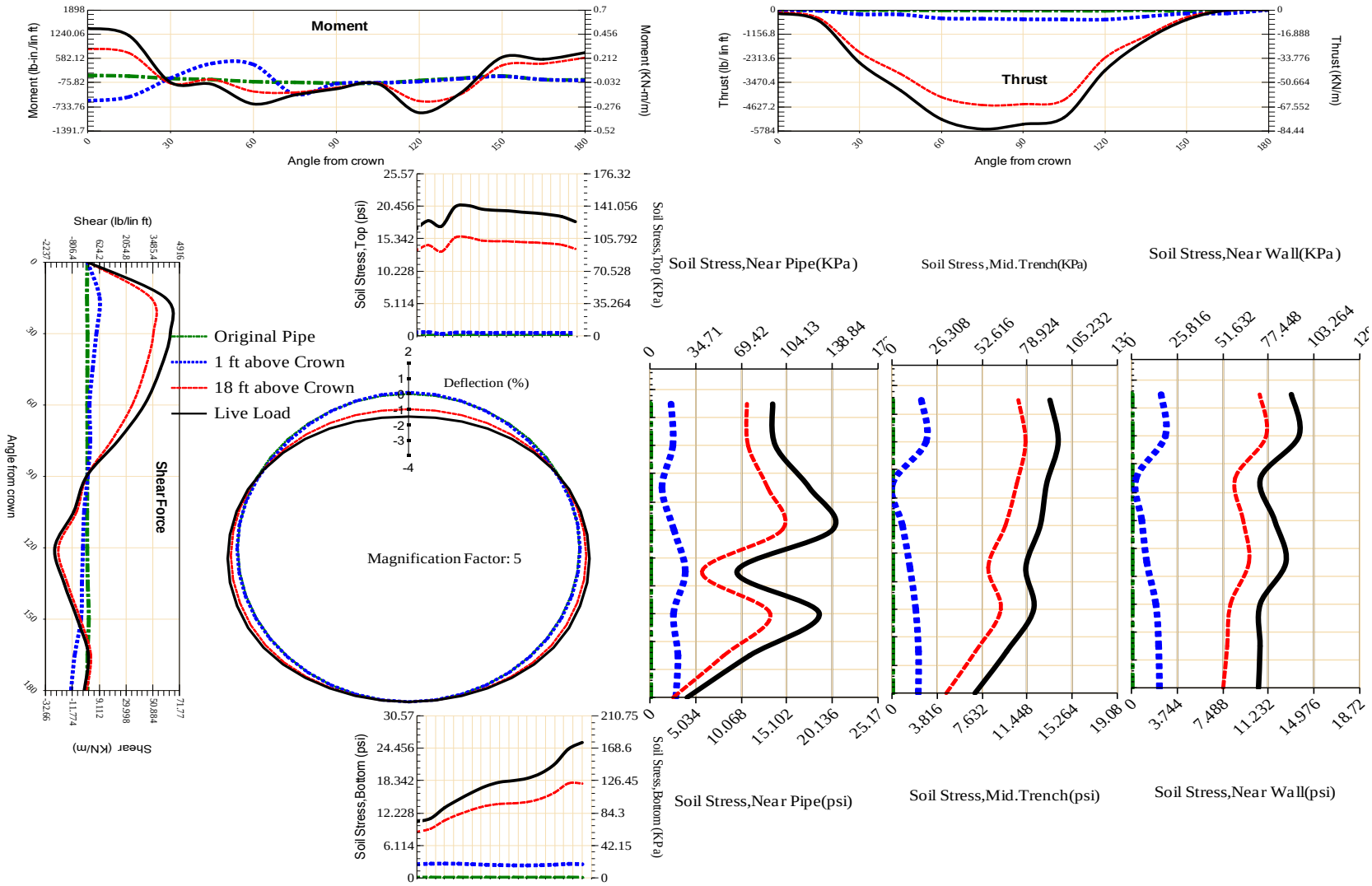

Figure A-266 Param-48-PW200-SF7OR-OD+108-EW10-H18-LiveLoad

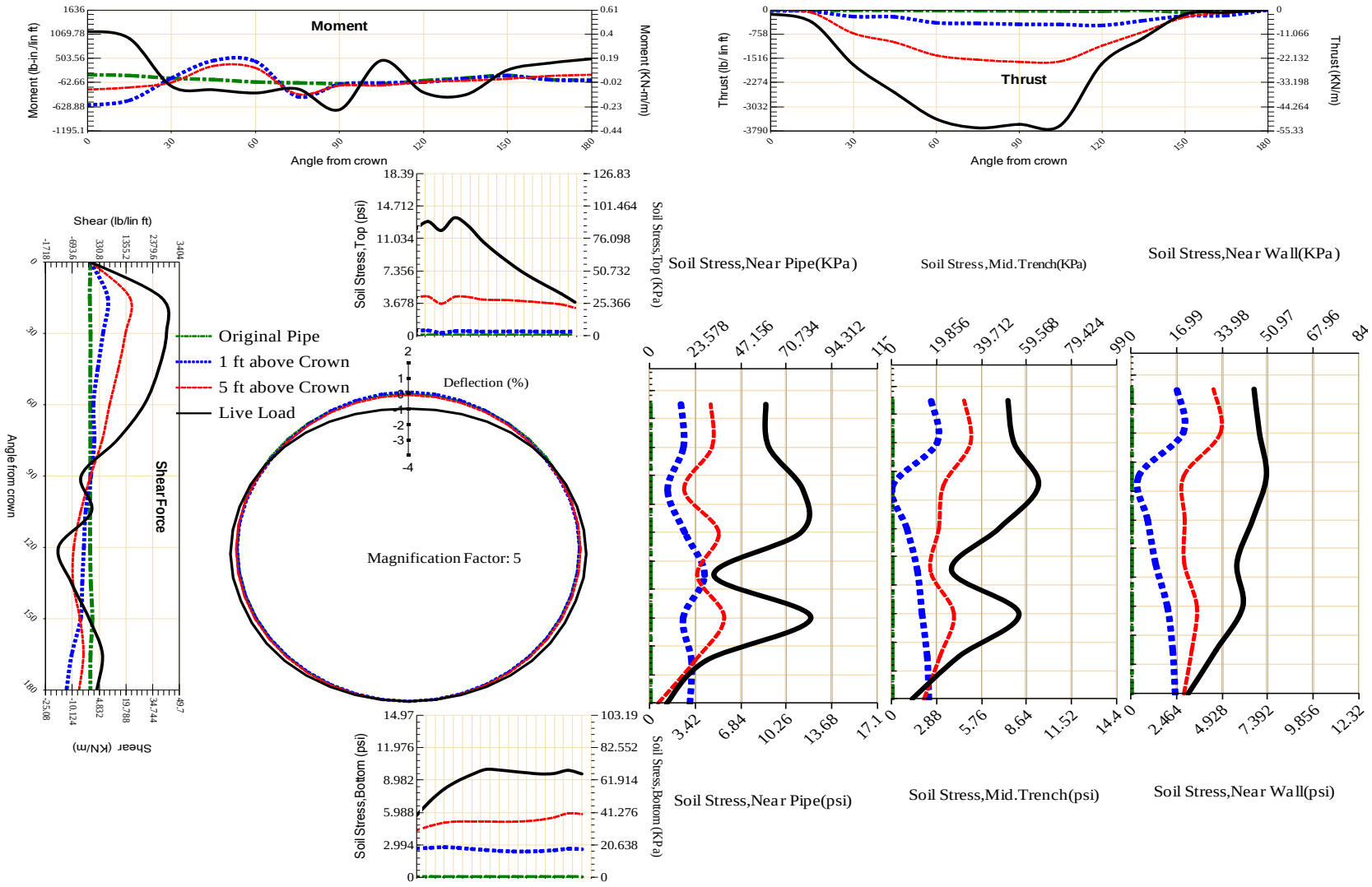

Figure A-267 Param-48-PW200-SF7OR-OD+108-EW10-H5-LiveLoad

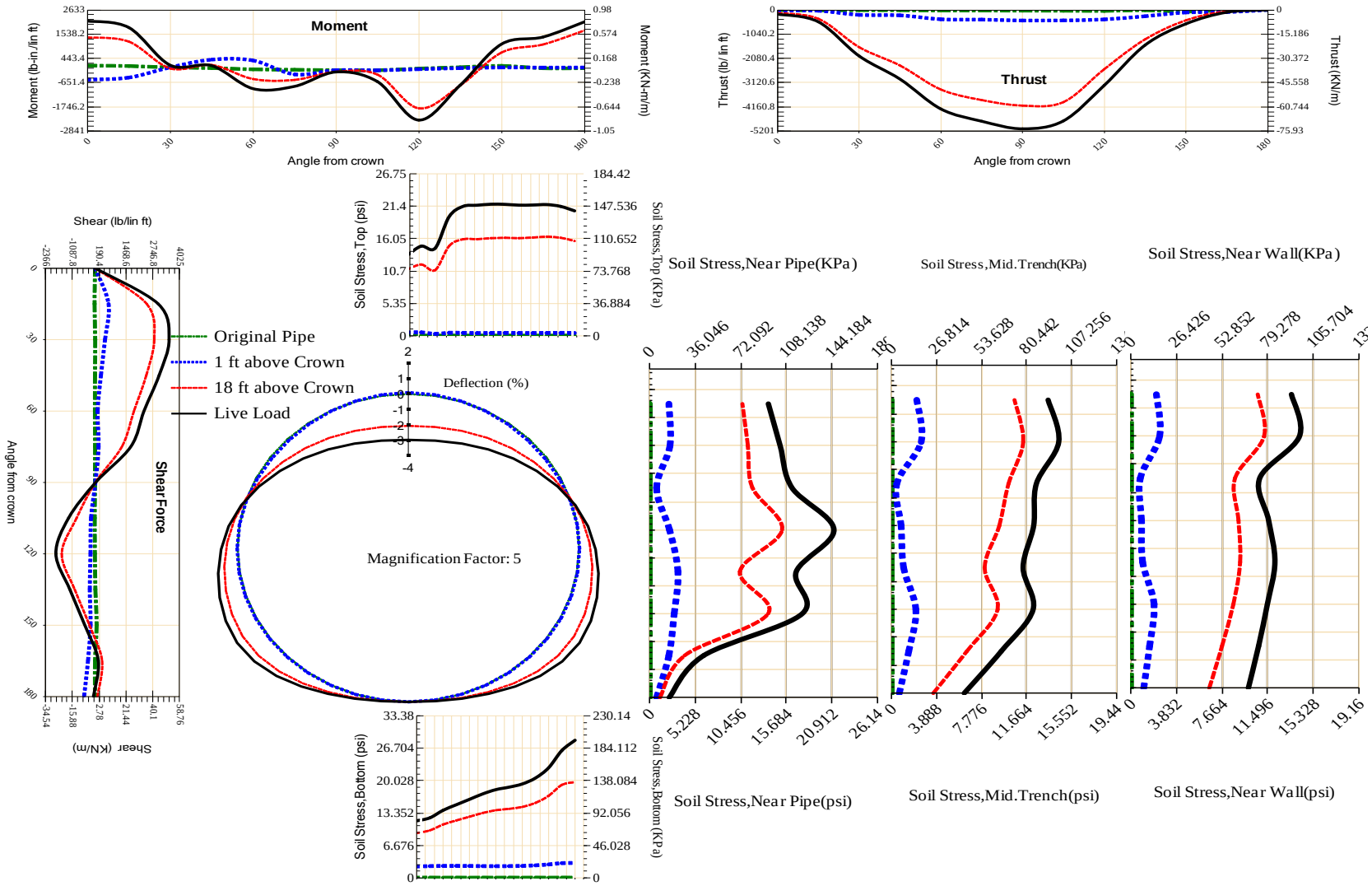

Figure A-268 Param-48-PW200-SF7OR-OD+108-EW3-H18-LiveLoad

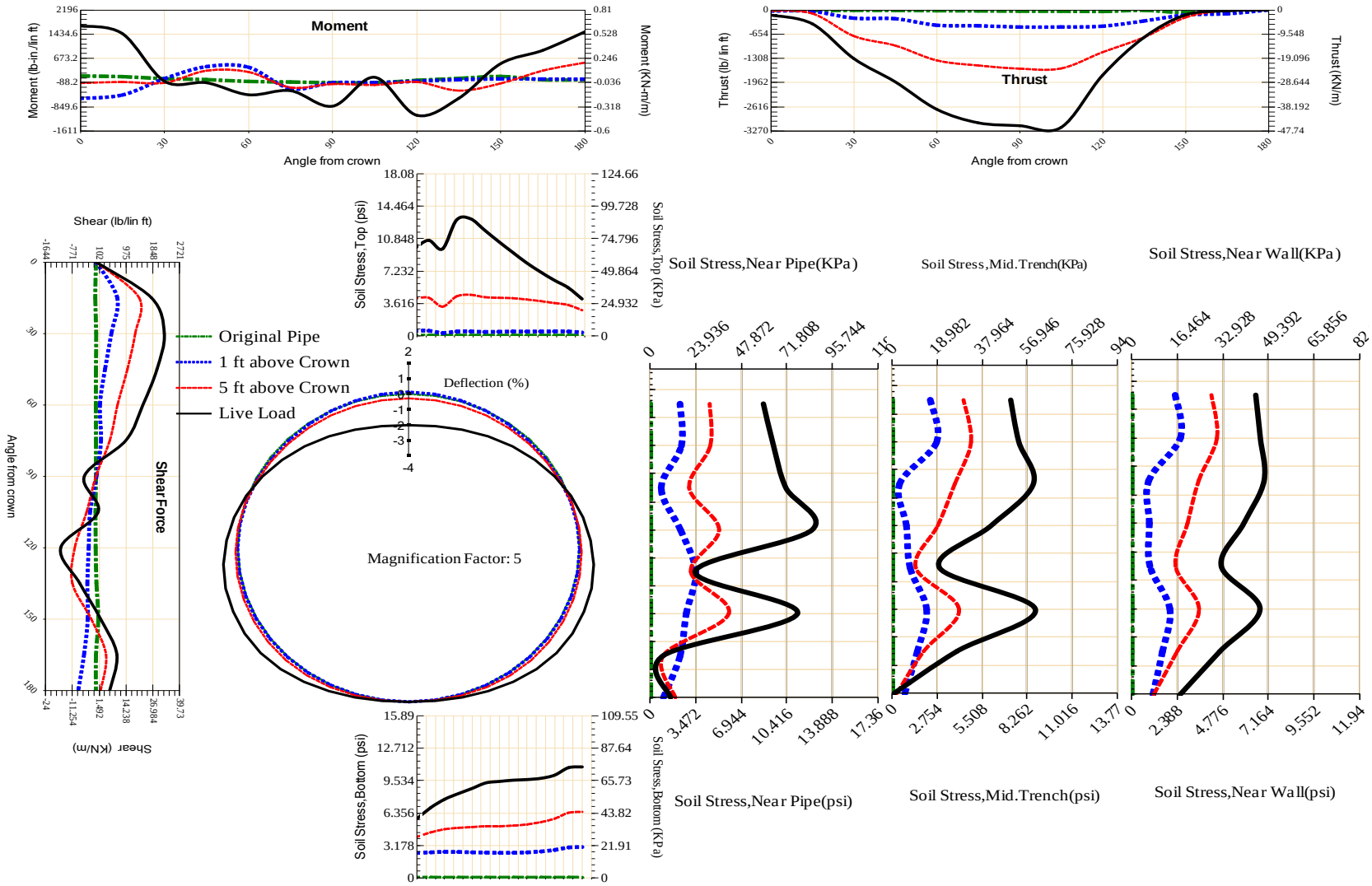

Figure A-269 Param-48-PW200-SF7OR-OD+108-EW3-H5-LiveLoad

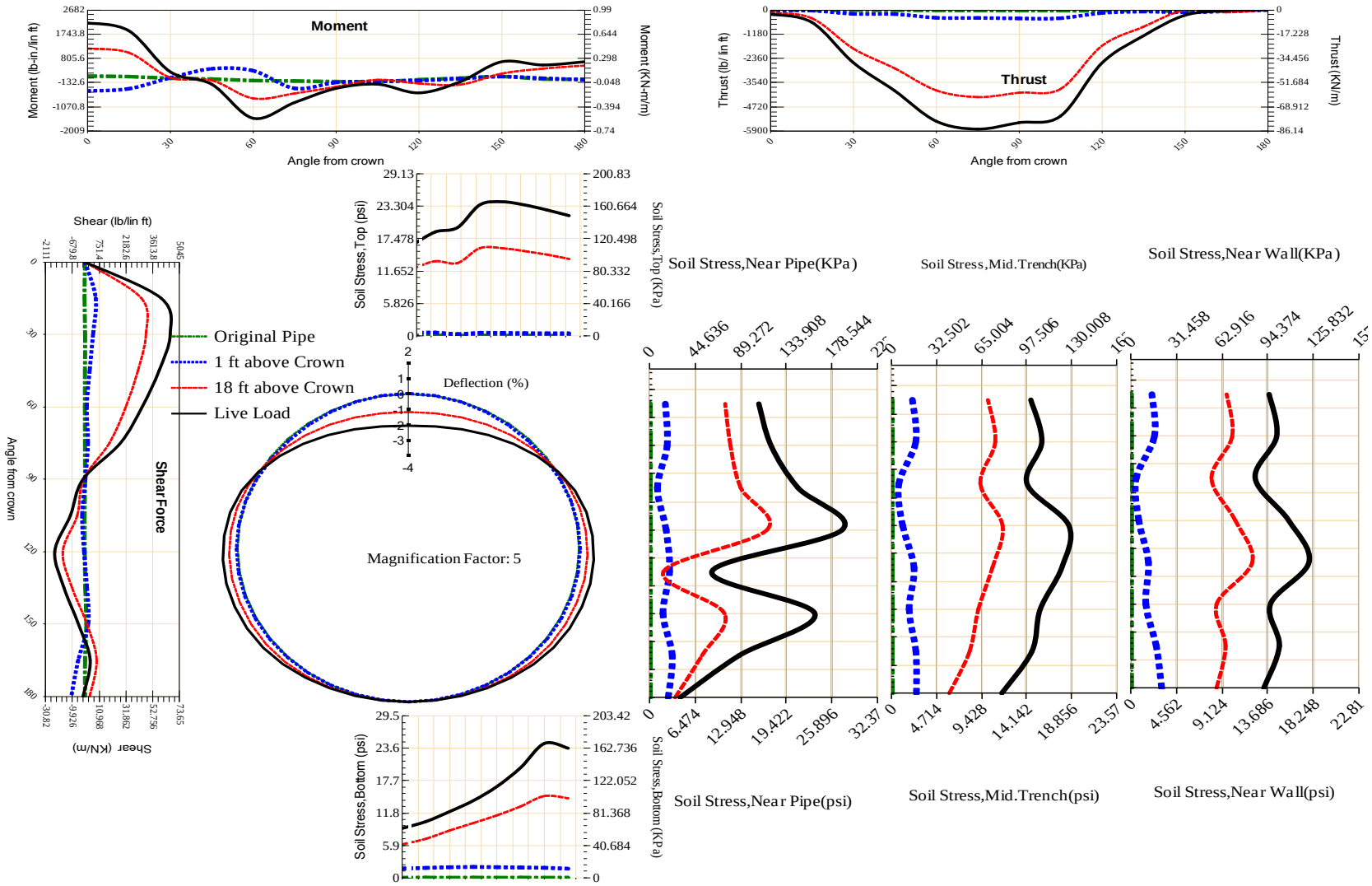

Figure A-270 Param-48-PW200-SF7OR-OD+48-EW10-H18-LiveLoad

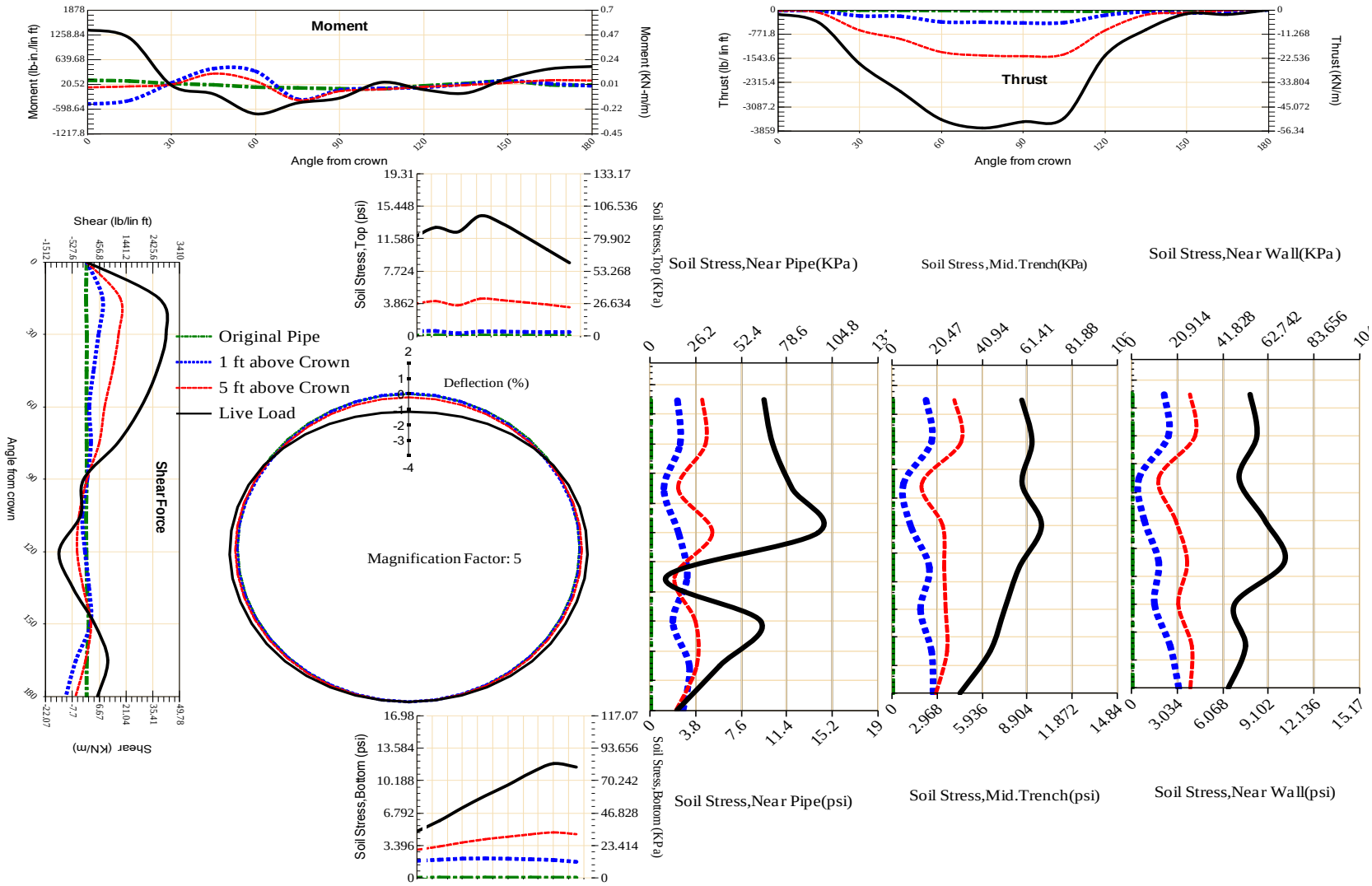

Figure A-271 Param-48-PW200-SF7OR-OD+48-EW10-H5-LiveLoad

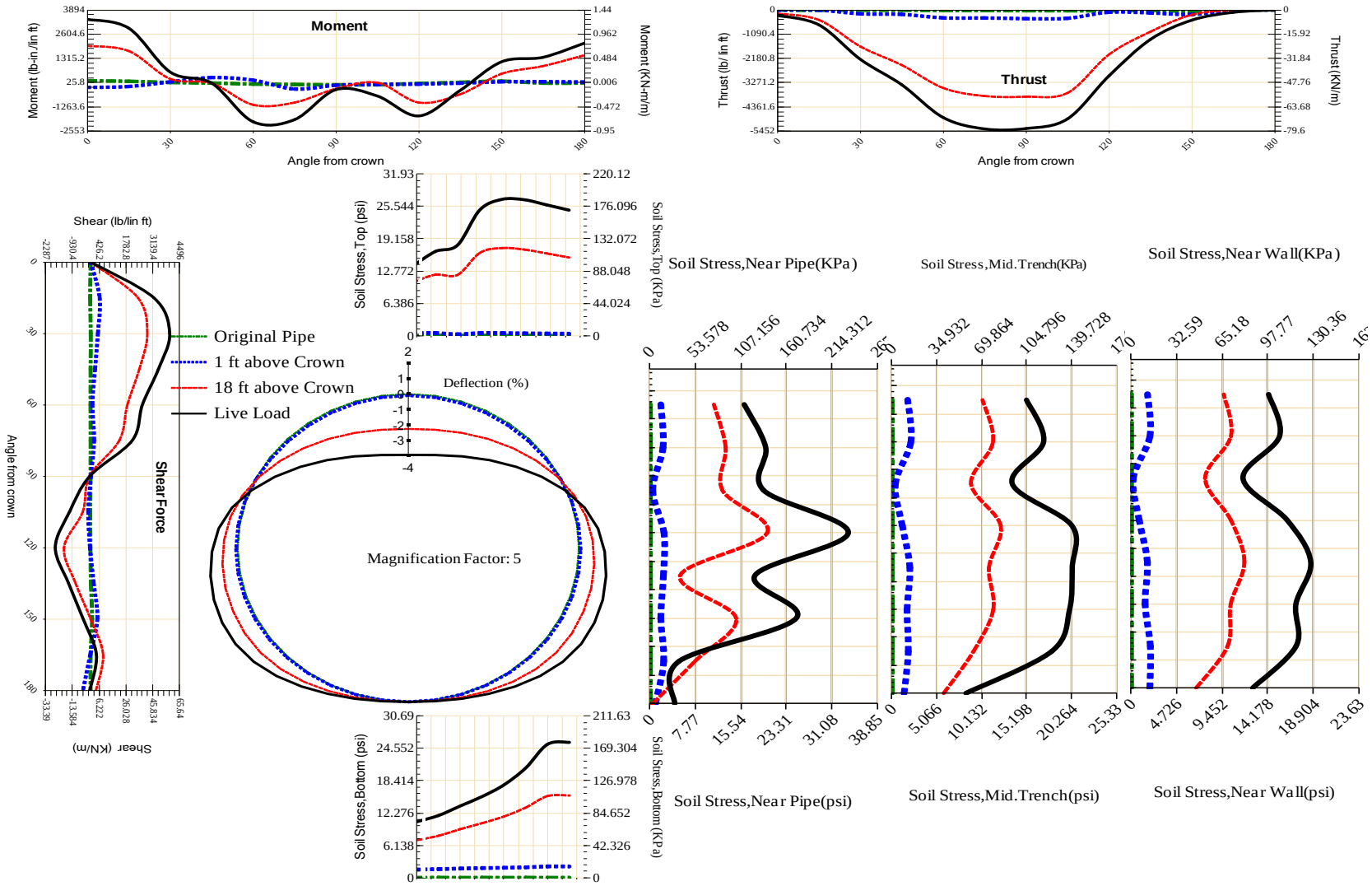

Figure A-272 Param-48-PW200-SF7OR-OD+48-EW3-H18-LiveLoad

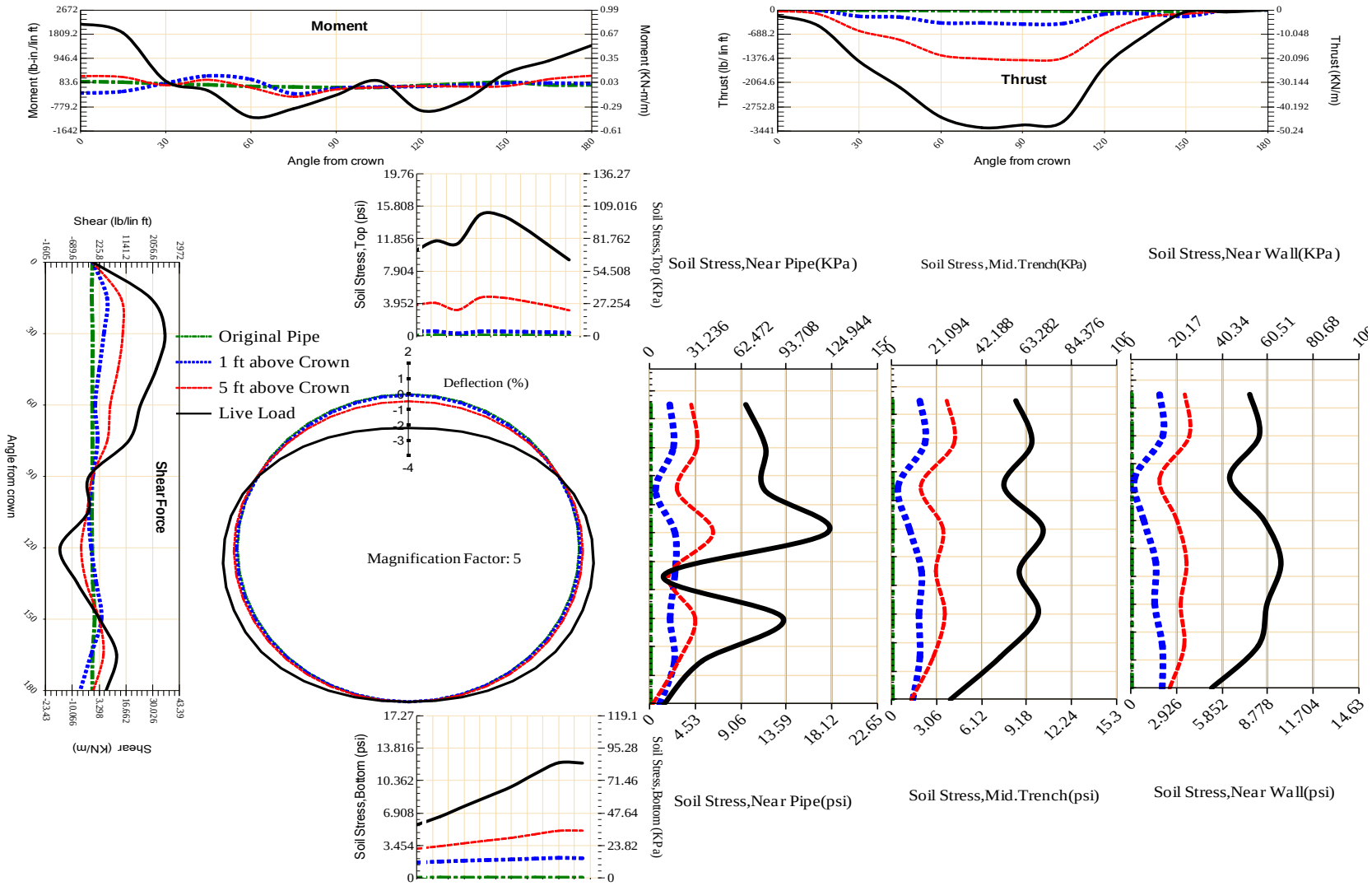

Figure A-273 Param-48-PW200-SF7OR-OD+48-EW3-H5-LiveLoad

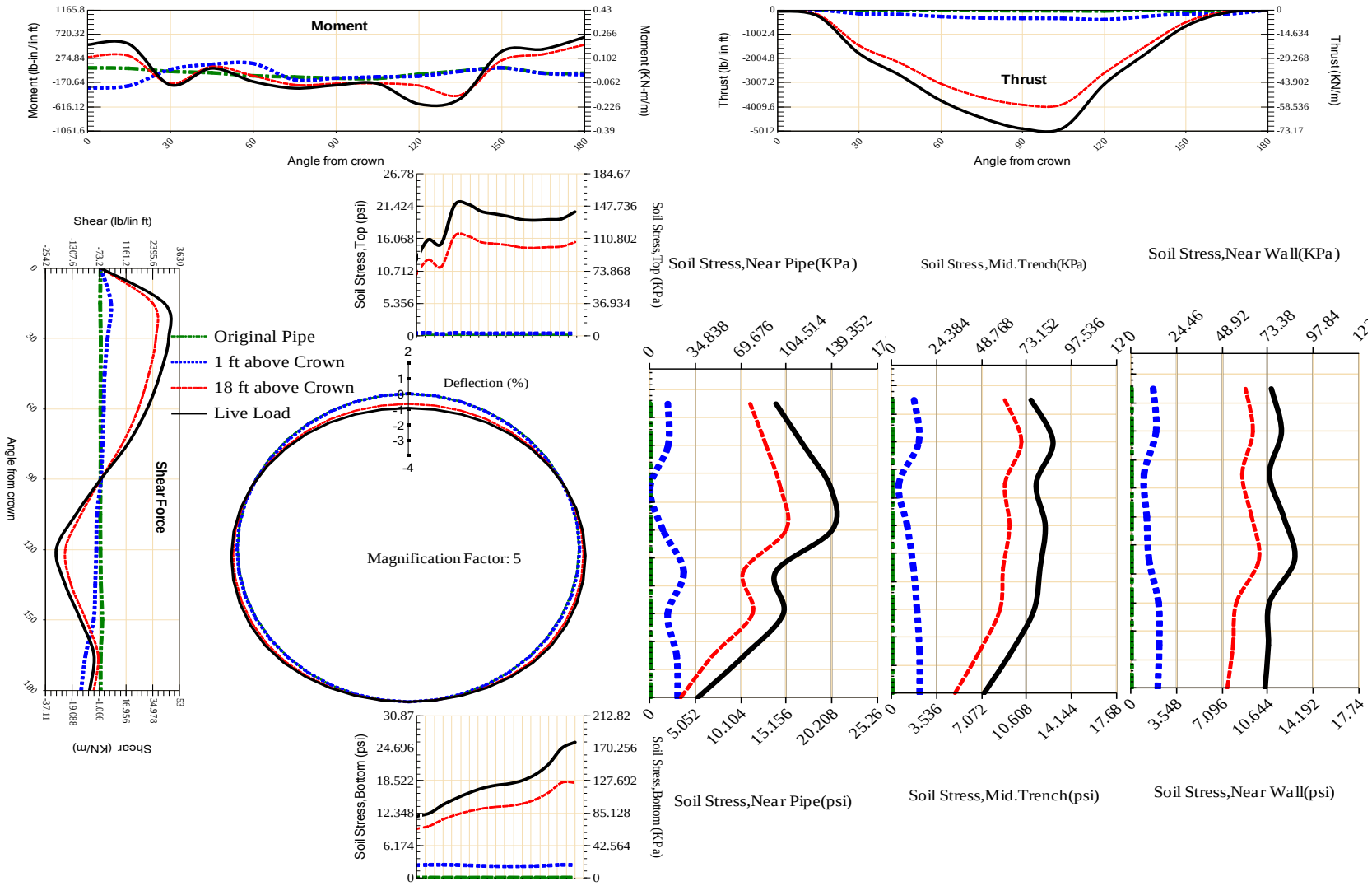

Figure A-274 Param-48-PW200-SF7TR-OD+108-EW10-H18-LiveLoad

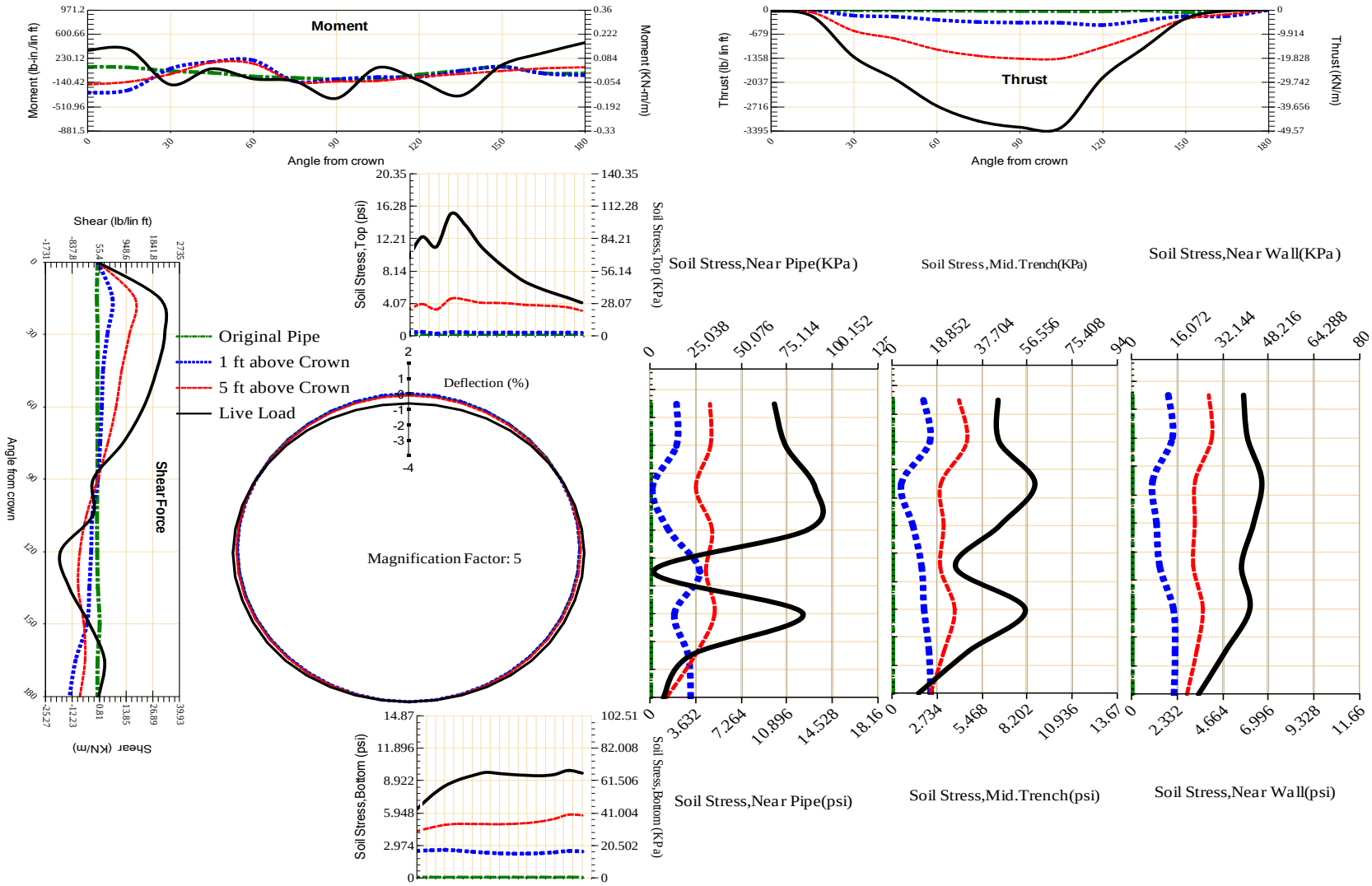

Figure A-275 Param-48-PW200-SF7TR-OD+108-EW10-H5-LiveLoad

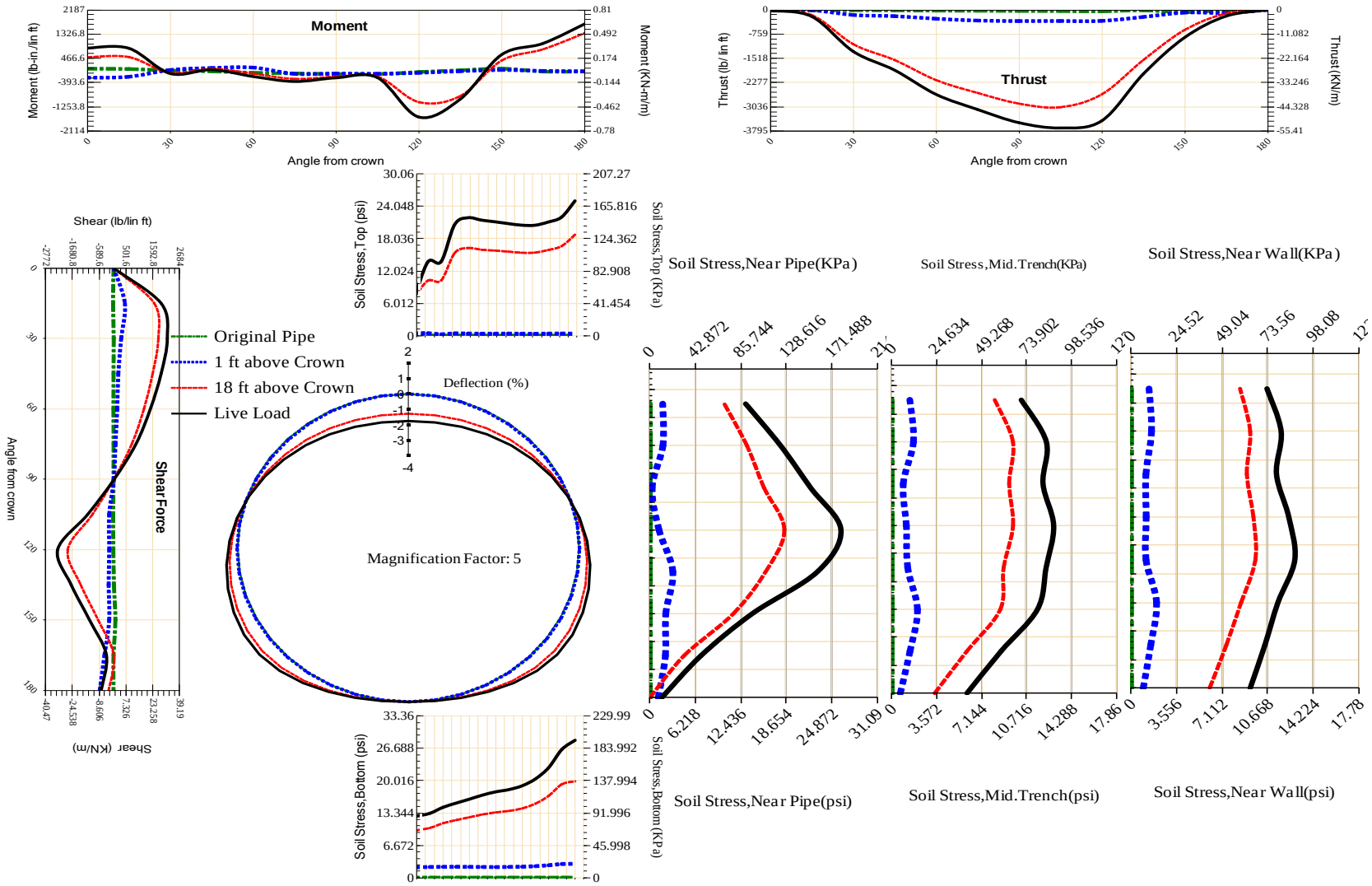

Figure A-276 Param-48-PW200-SF7TR-OD+108-EW3-H18-LiveLoad

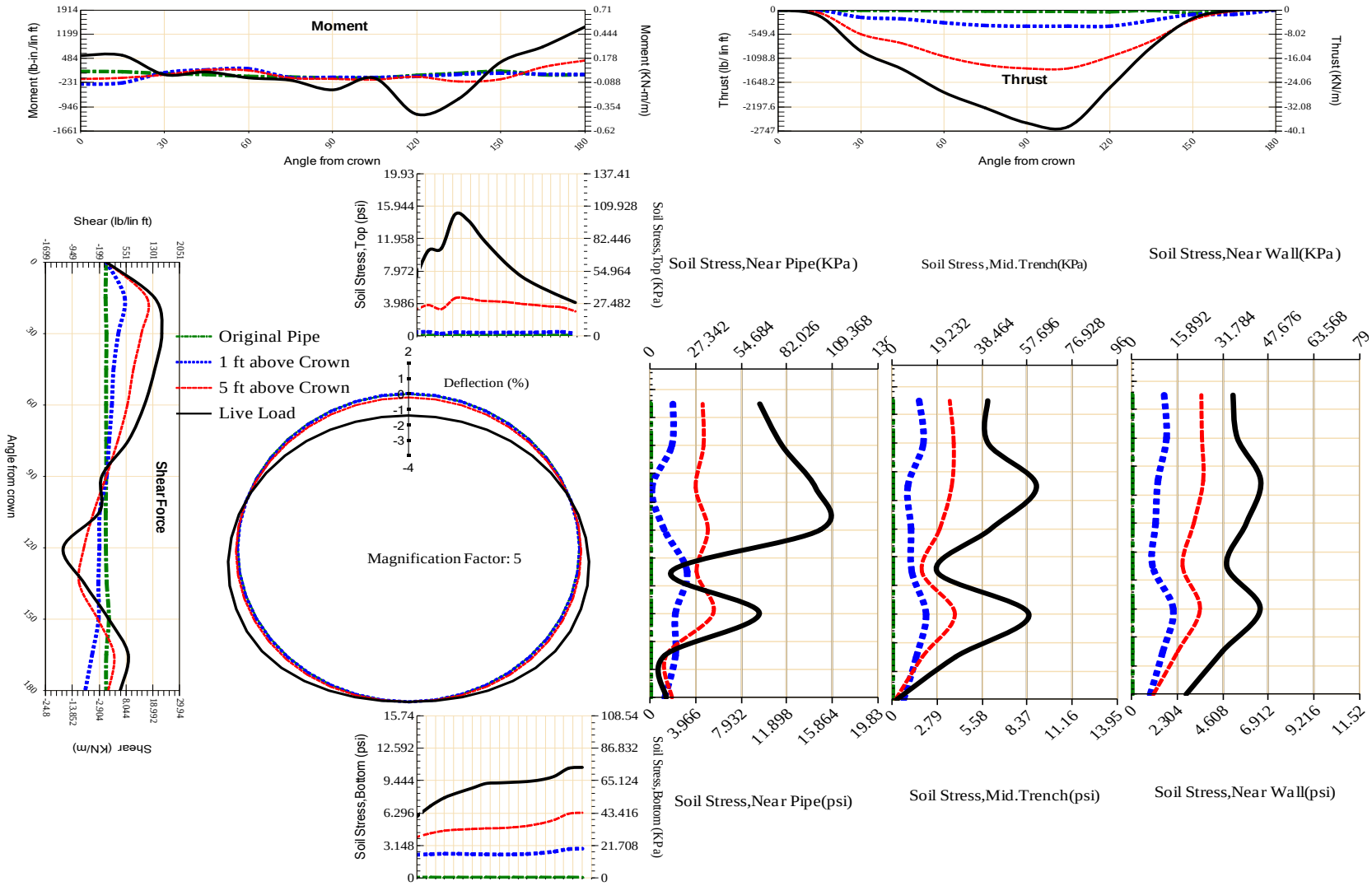

Figure A-277 Param-48-PW200-SF7TR-OD+108-EW3-H5-LiveLoad

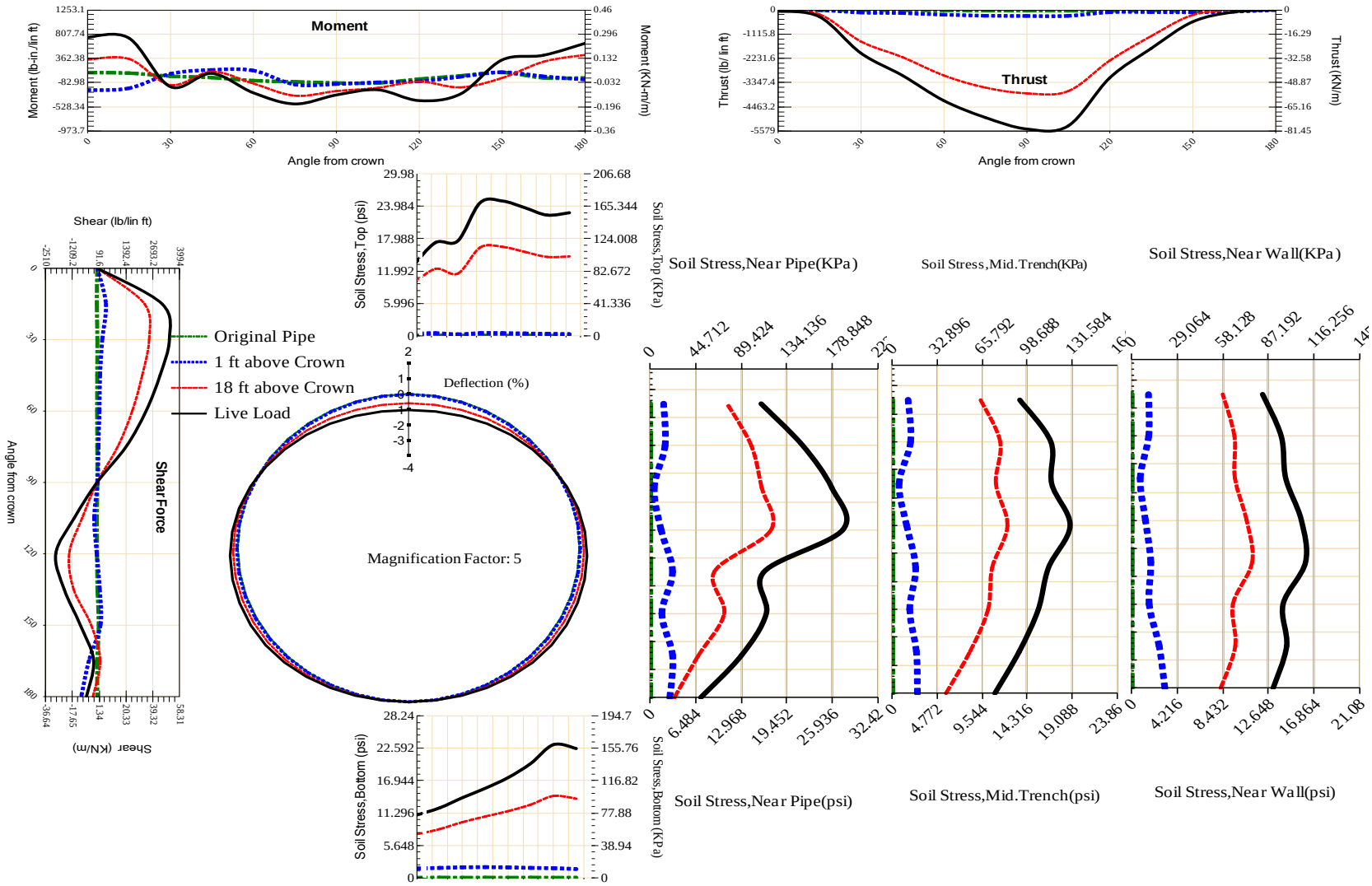

Figure A-278 Param-48-PW200-SF7TR-OD+48-EW10-H18-LiveLoad

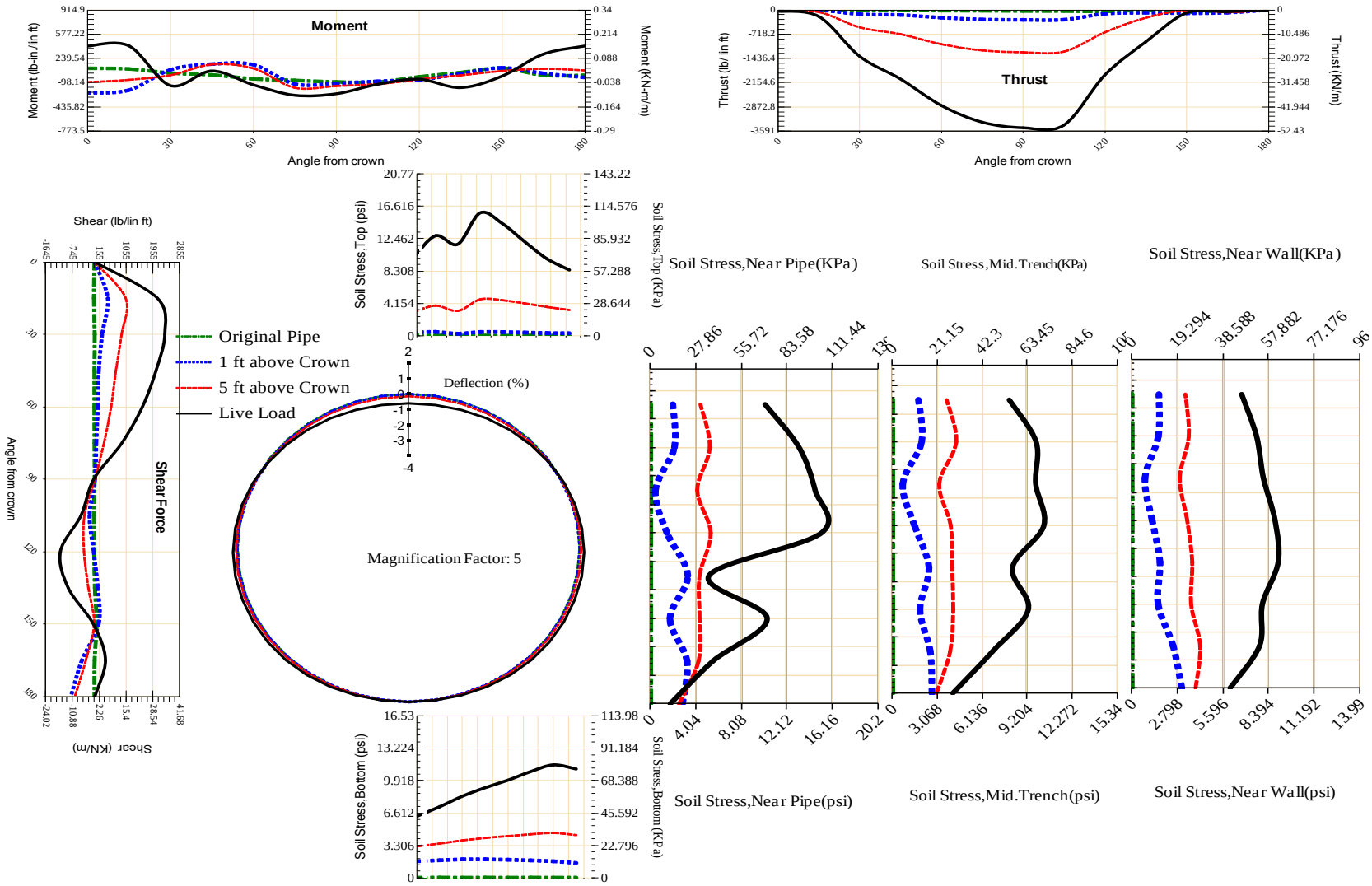

Figure A-279 Param-48-PW200-SF7TR-OD+48-EW10-H5-LiveLoad

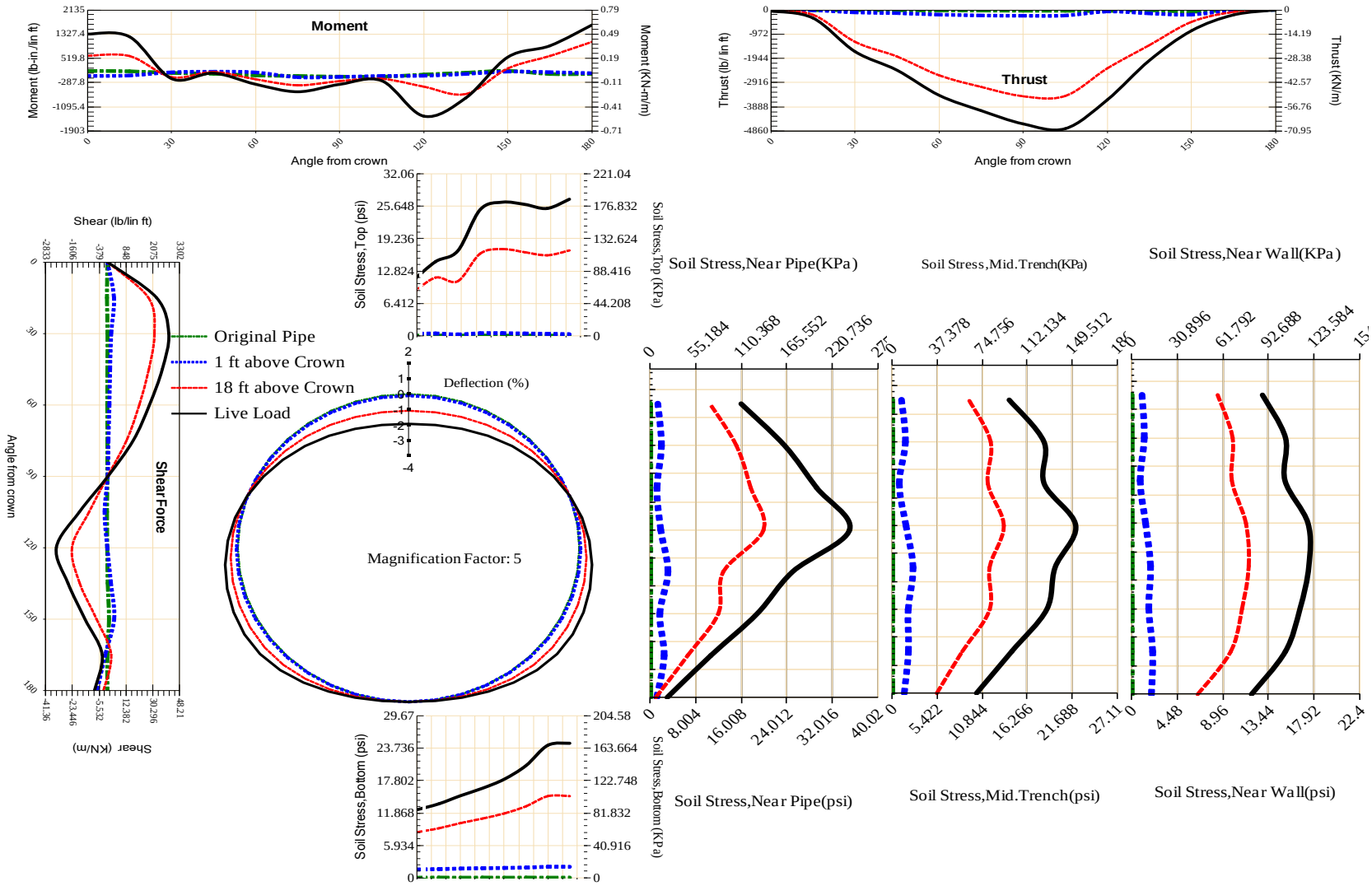

Figure A-280 Param-48-PW200-SF7TR-OD+48-EW3-H18-LiveLoad

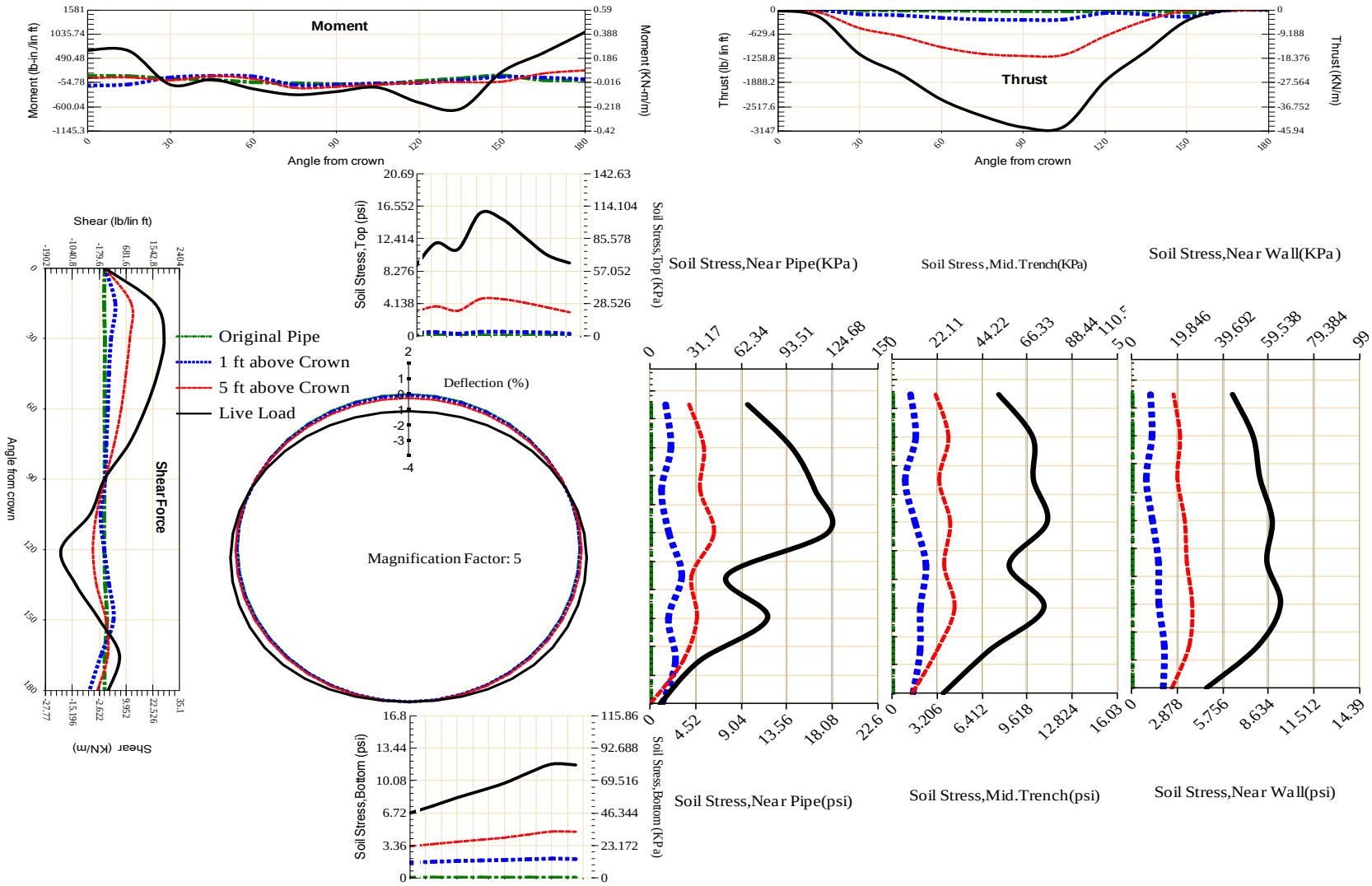

Figure A-281 Param-48-PW200-SF7TR-OD+48-EW3-H5-LiveLoad

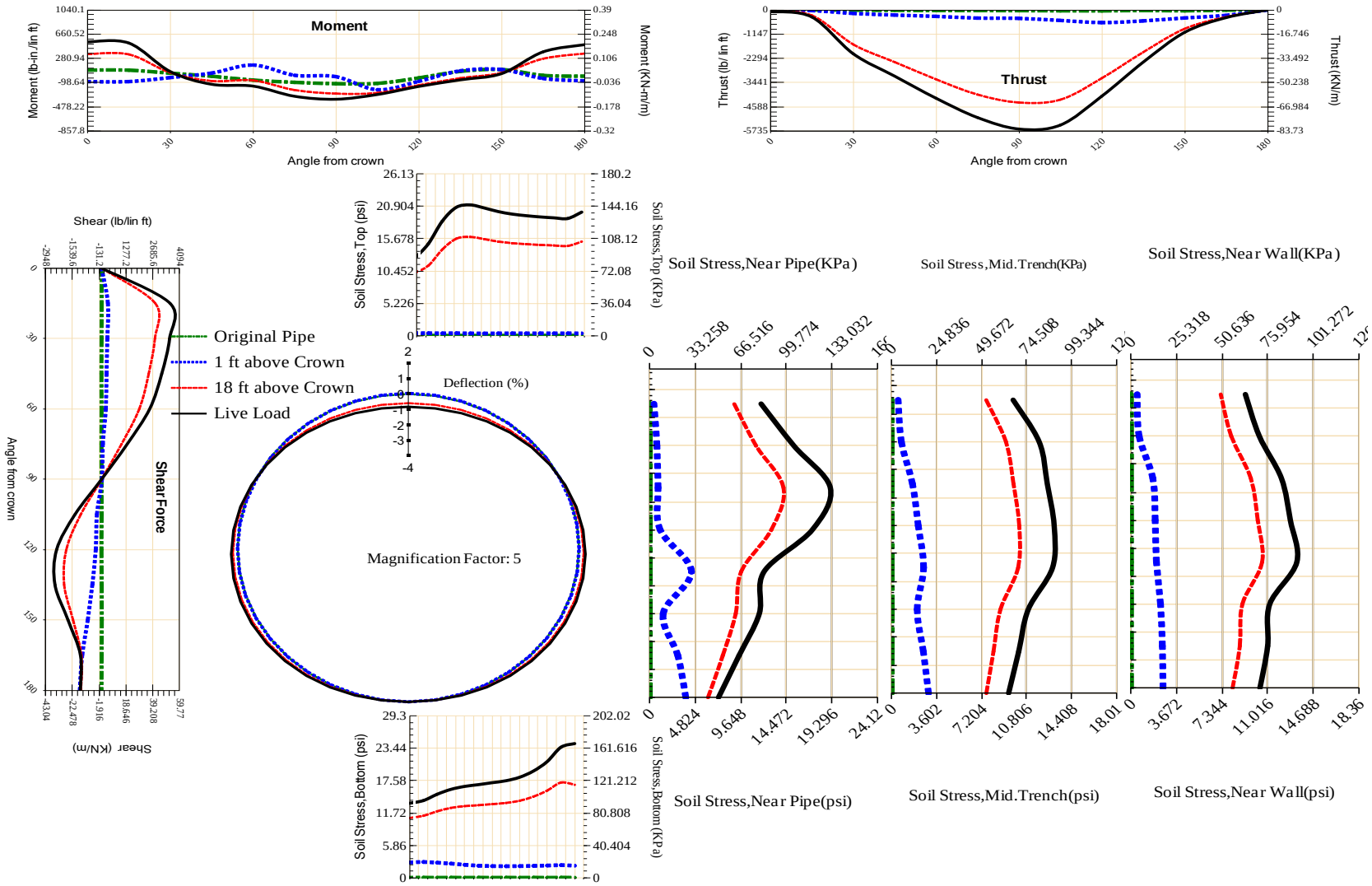

Figure A-282 Param-48-PW200-TR10TR-OD+108-EW10-H18-LiveLoad

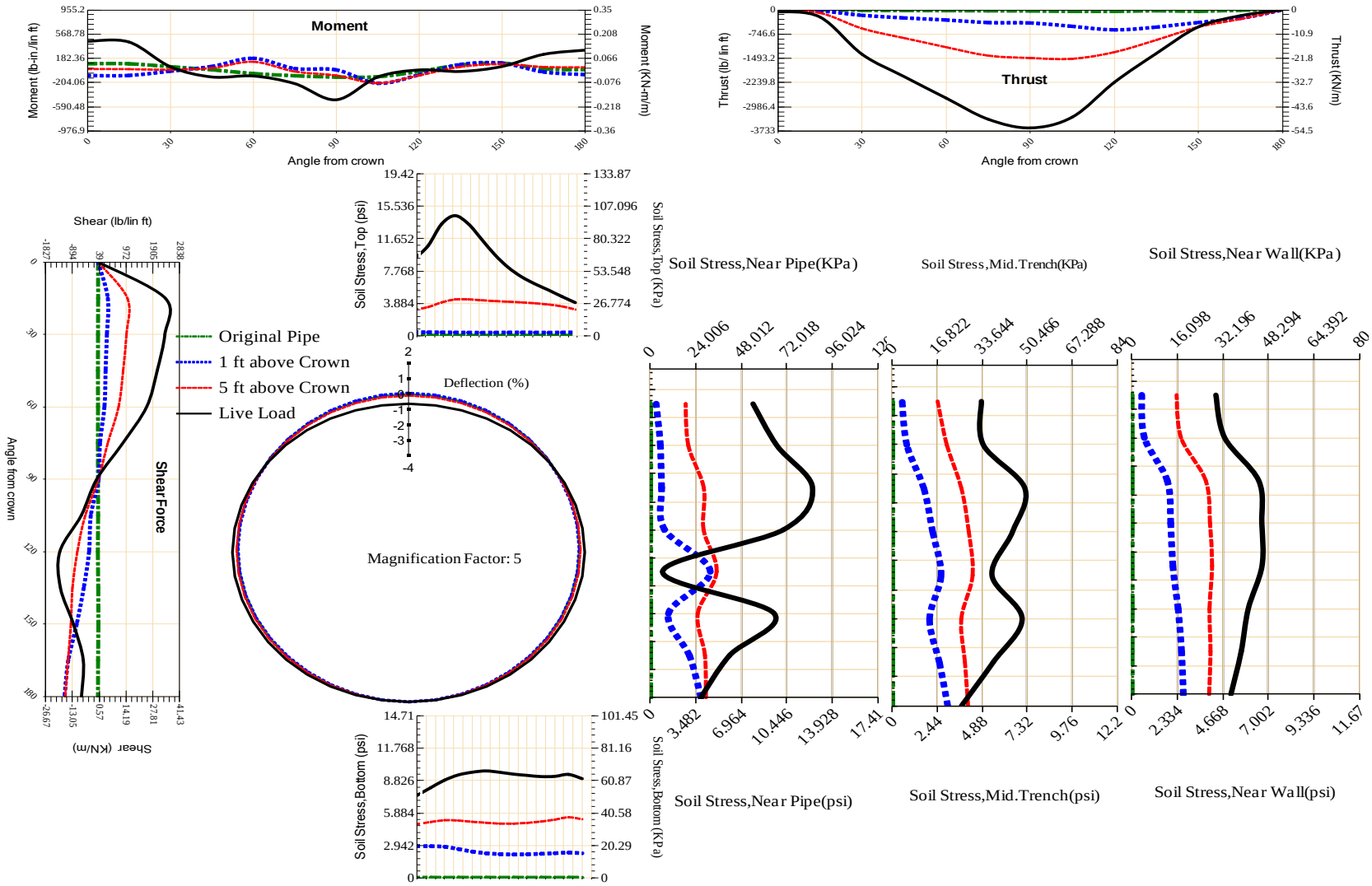

Figure A-283 Param-48-PW200-TR10TR-OD+108-EW10-H5-LiveLoad

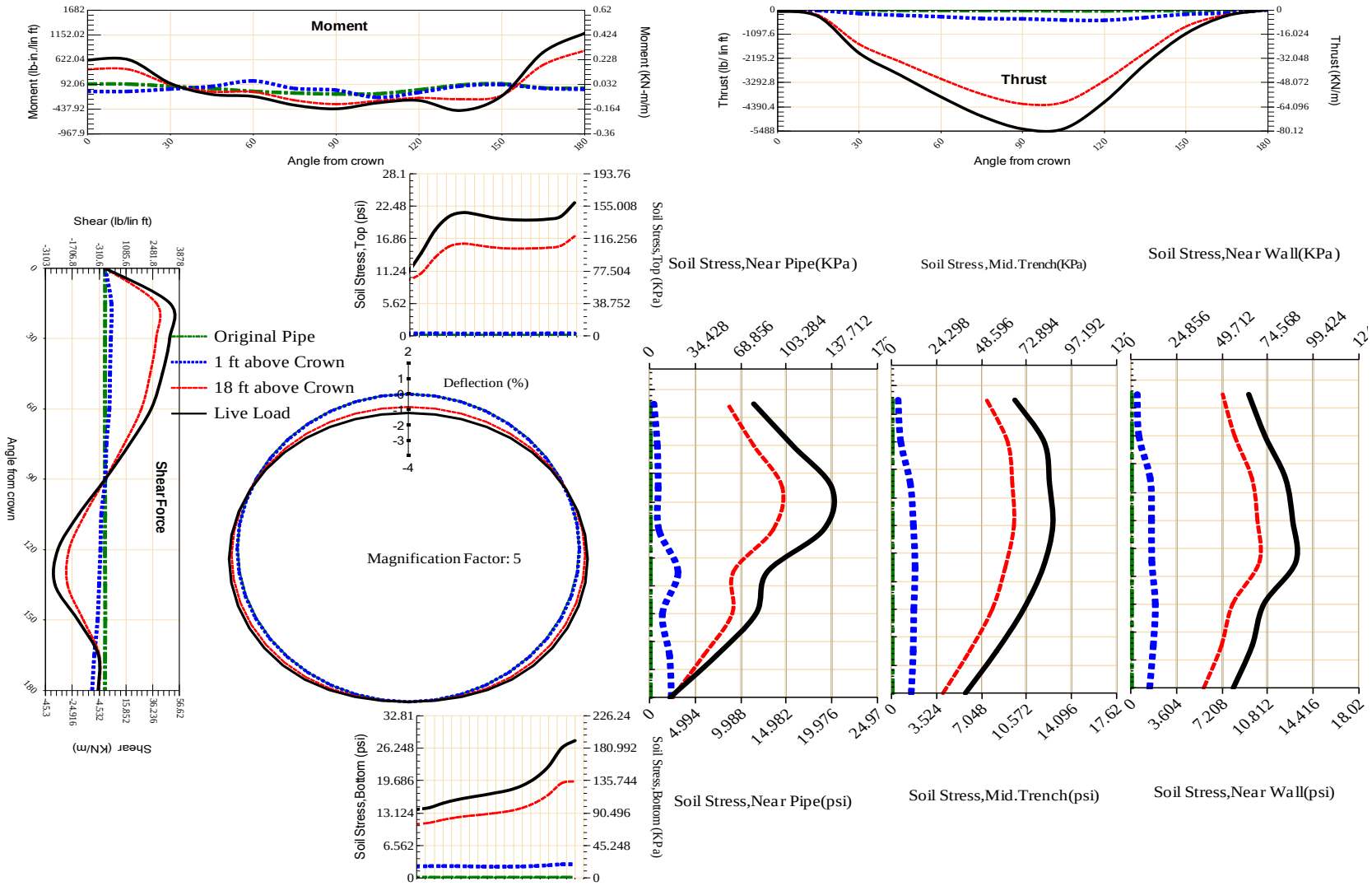

Figure A-284 Param-48-PW200-TR10TR-OD+108-EW3-H18-LiveLoad

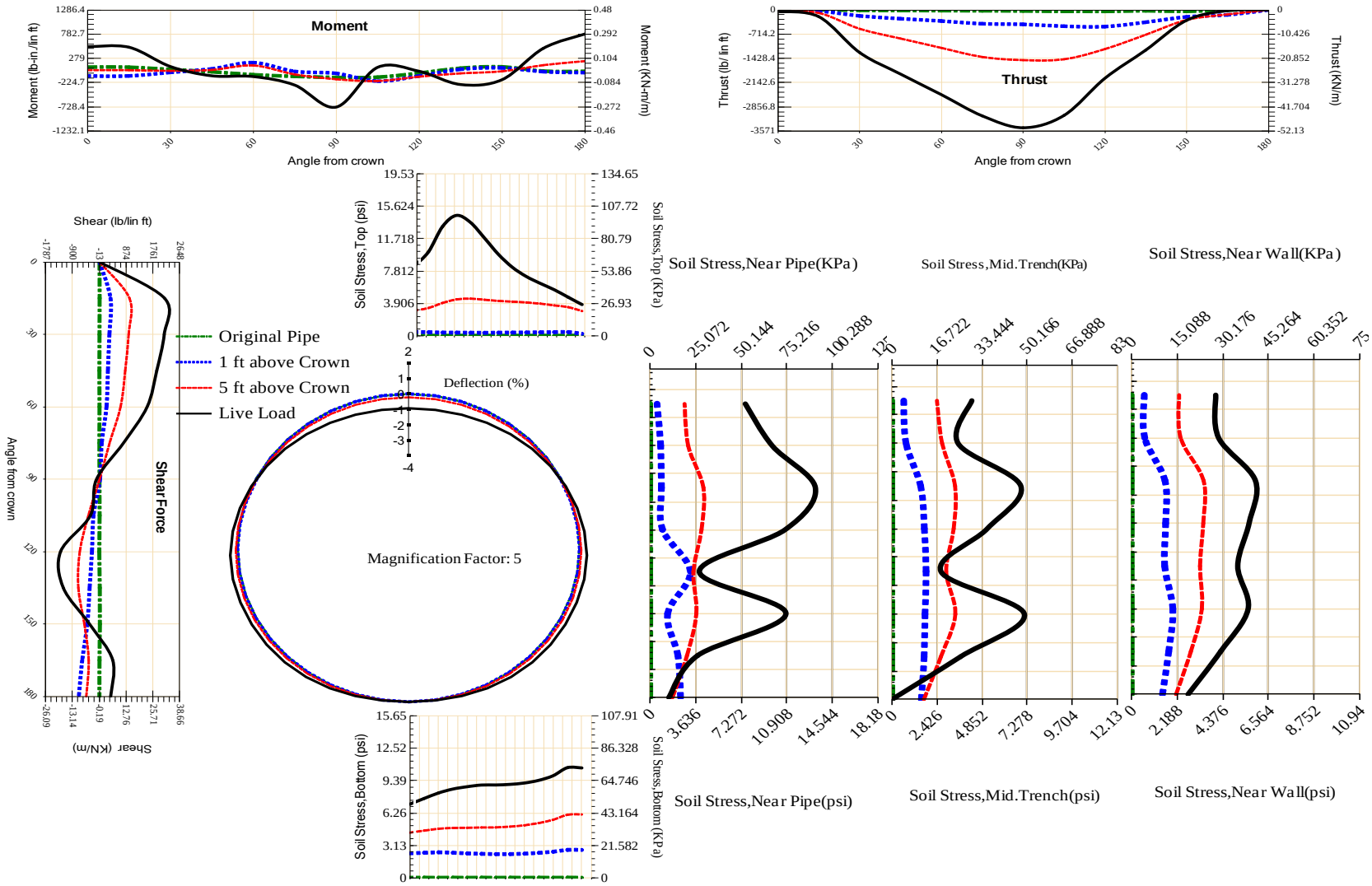

Figure A-285 Param-48-PW200-TR10TR-OD+108-EW3-H5-LiveLoad

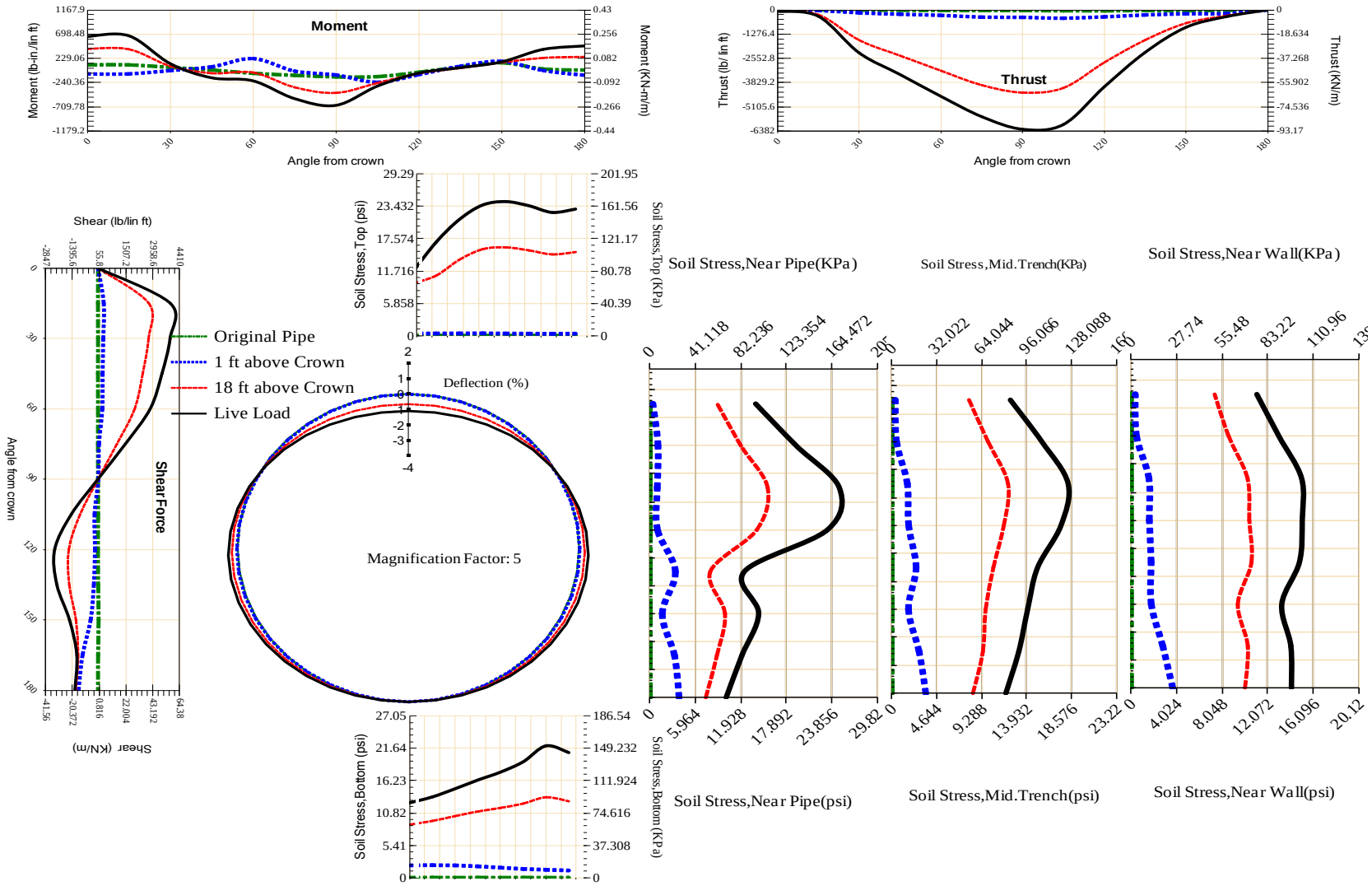

Figure A-286 Param-48-PW200-TR10TR-OD+48-EW10-H18-LiveLoad

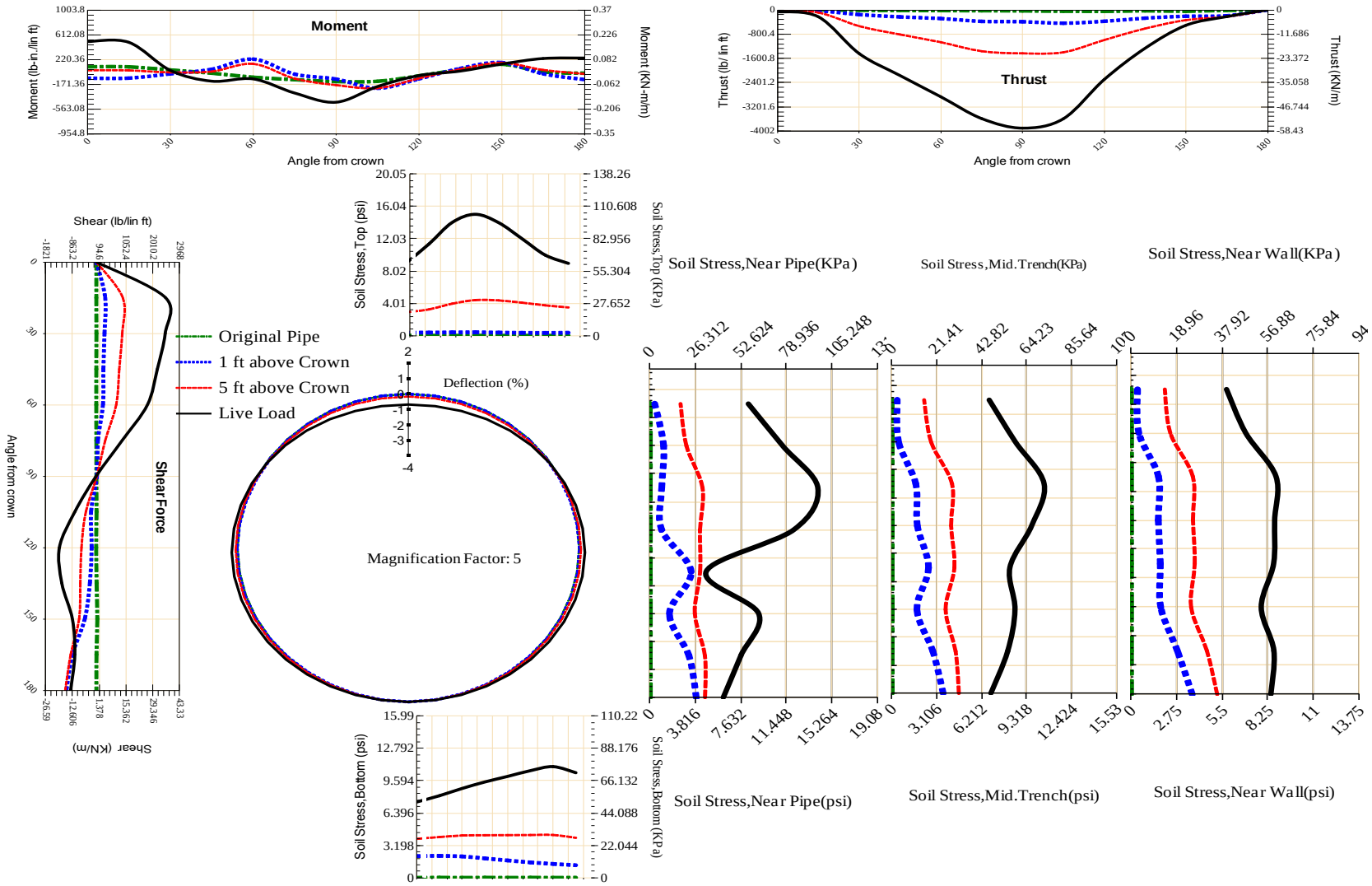

Figure A-287 Param-48-PW200-TR10TR-OD+48-EW10-H5-LiveLoad

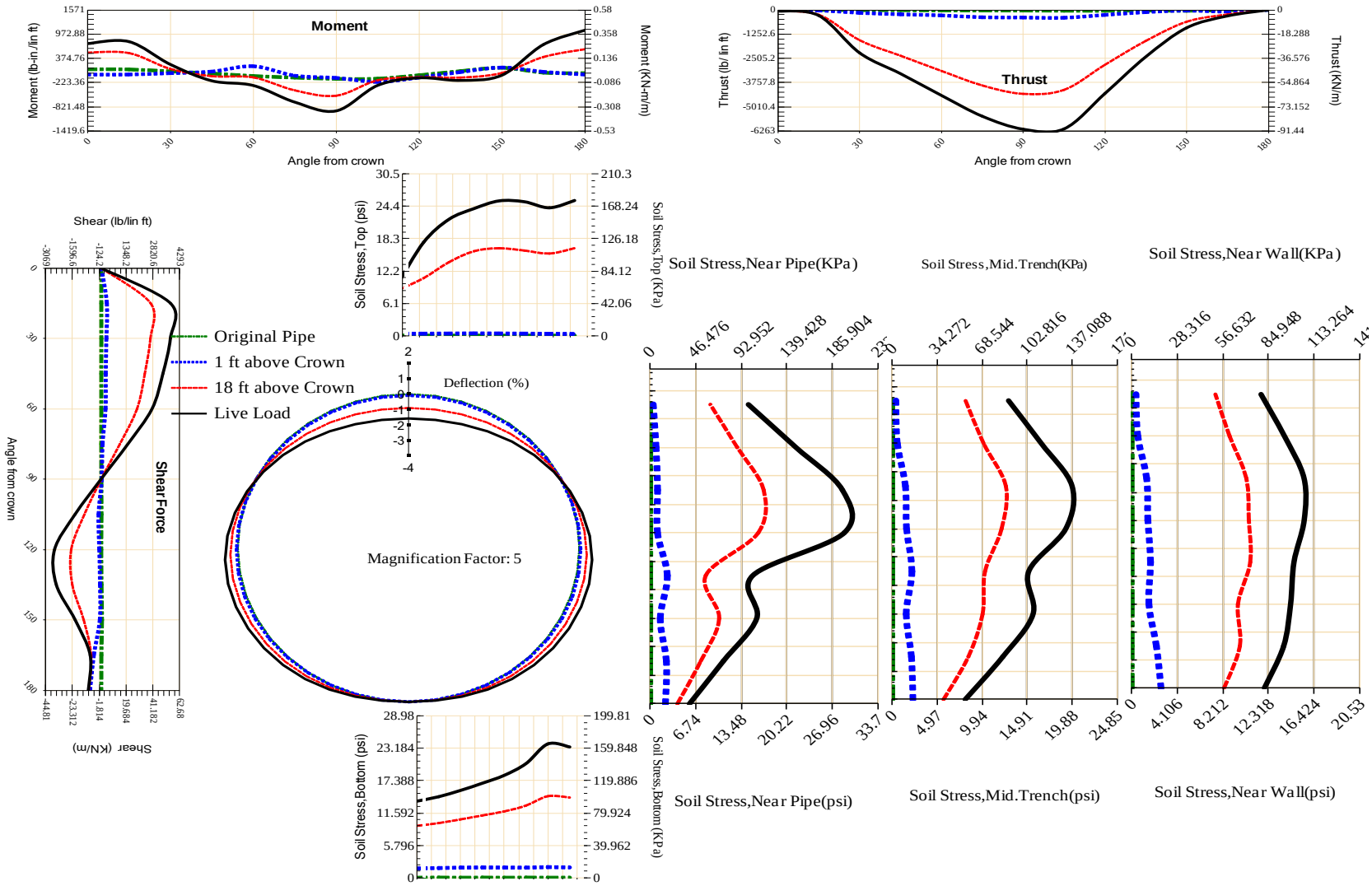

Figure A-288 Param-48-PW200-TR10TR-OD+48-EW3-H18-LiveLoad

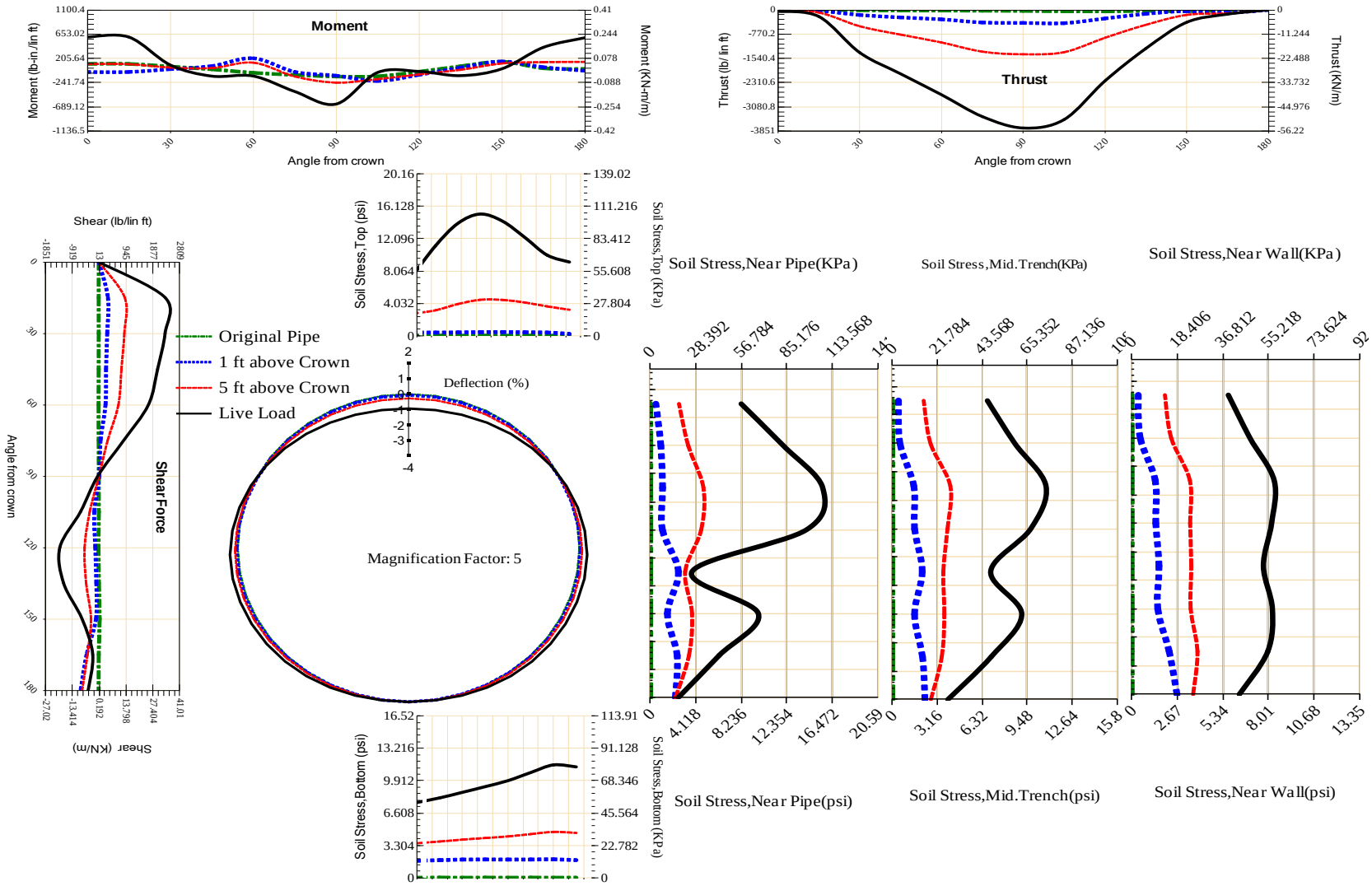

Figure A-289 Param-48-PW200-TR10TR-OD+48-EW3-H5-LiveLoad

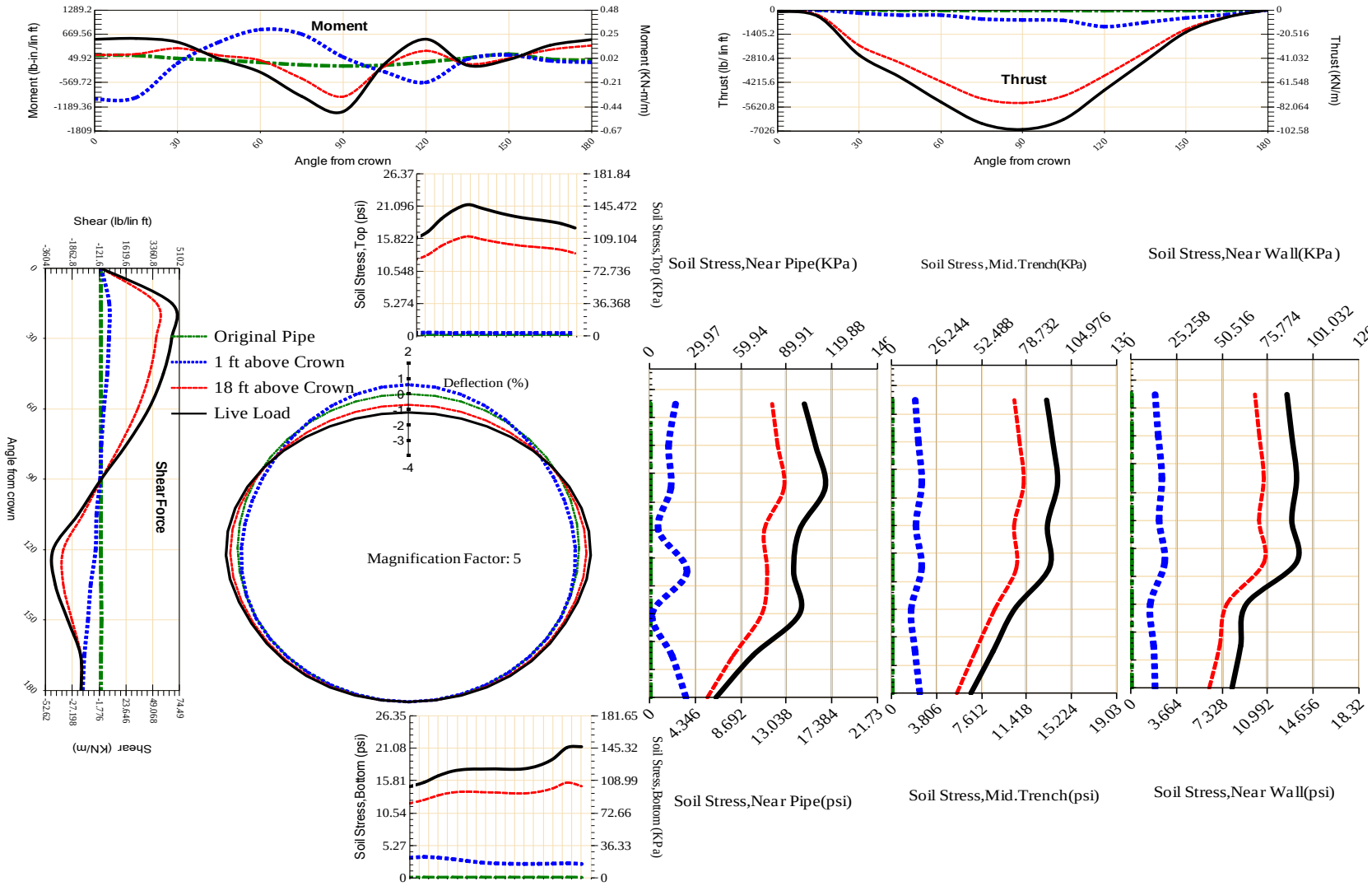

Figure A-290 Param-48-PW200-TR3OR-OD+108-EW10-H18-LiveLoad

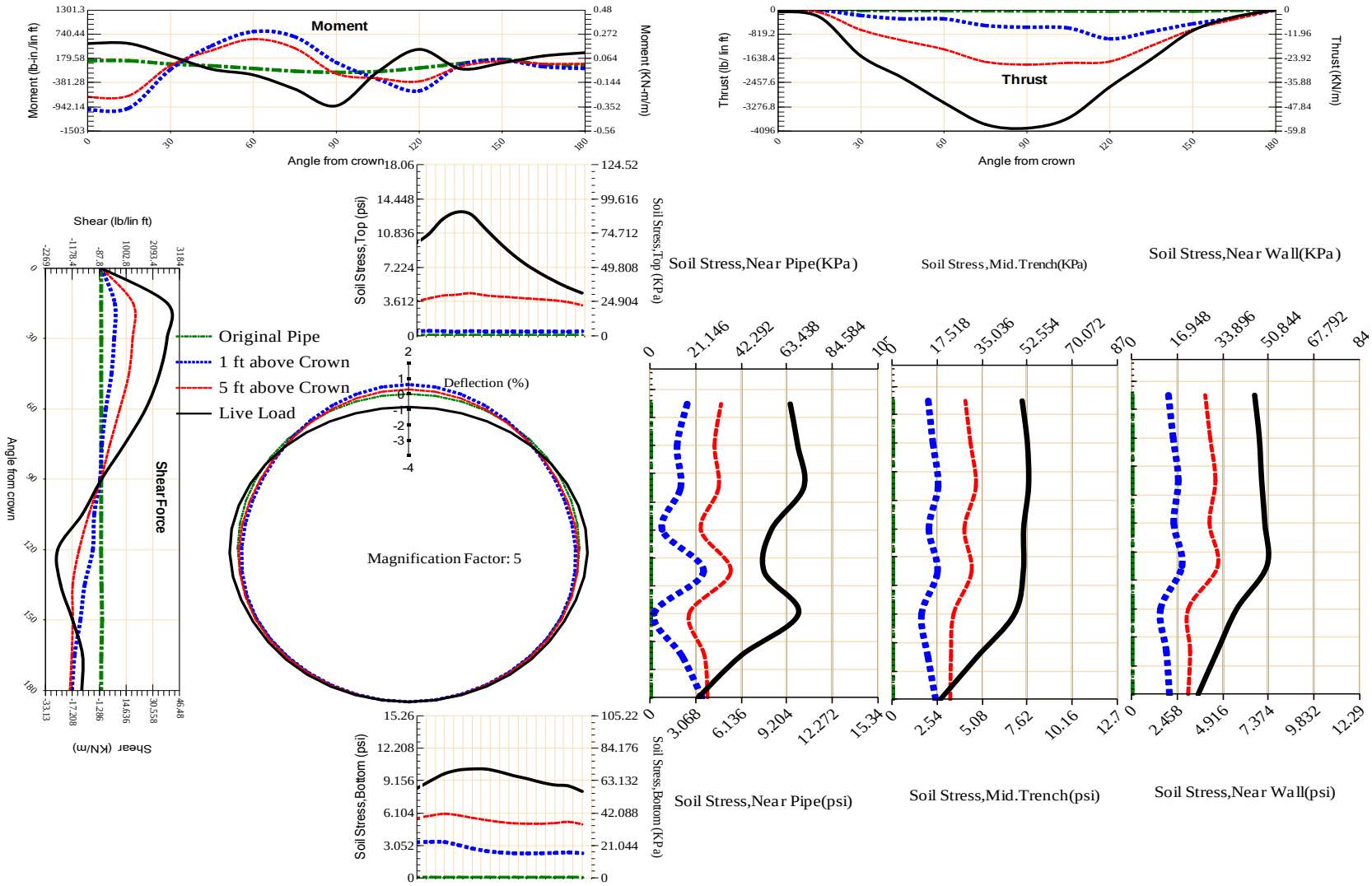

Figure A-291 Param-48-PW200-TR3OR-OD+108-EW10-H5-LiveLoad

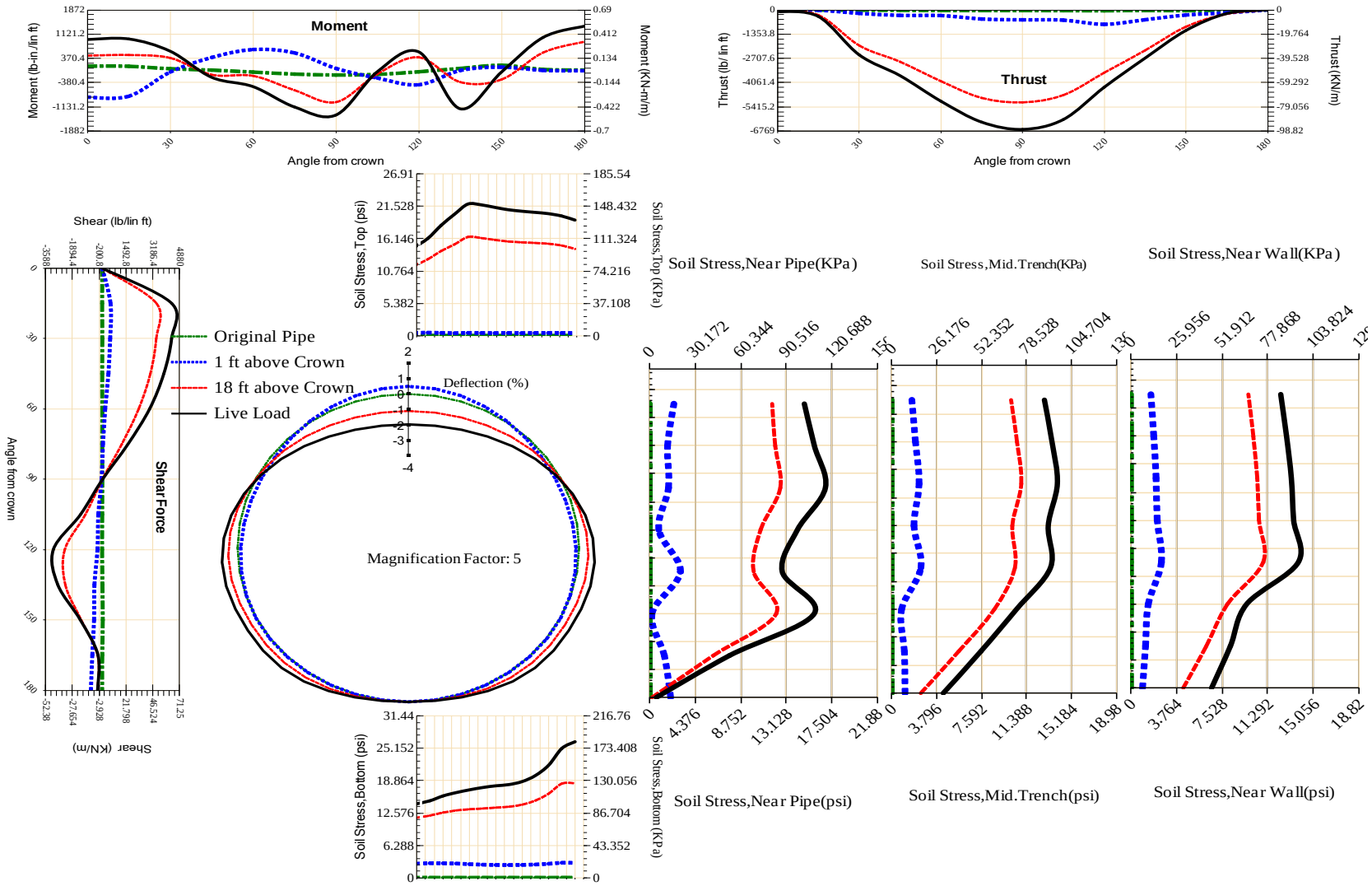

Figure A-292 Param-48-PW200-TR3OR-OD+108-EW3-H18-LiveLoad

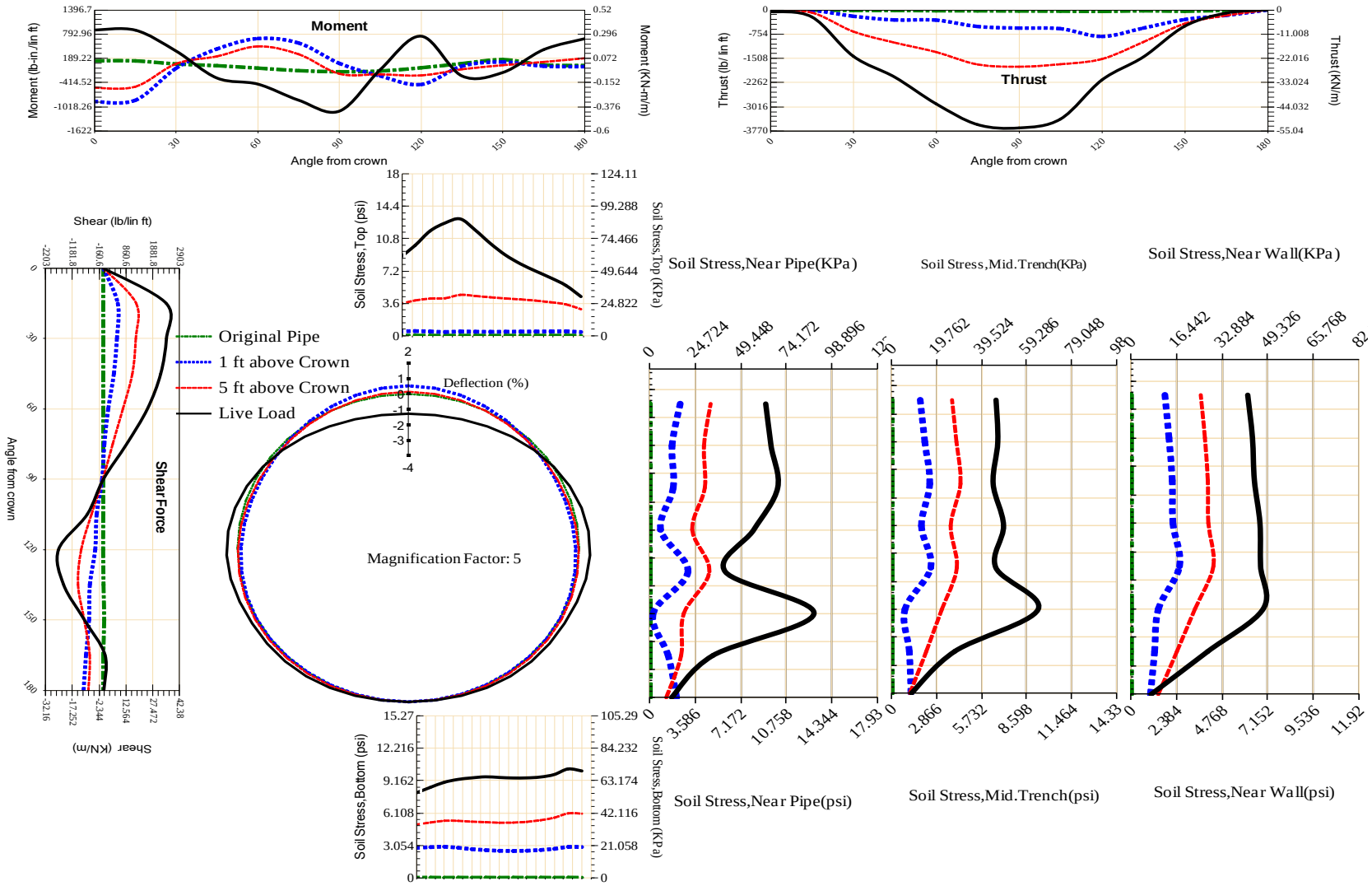

Figure A-293 Param-48-PW200-TR3OR-OD+108-EW3-H5-LiveLoad

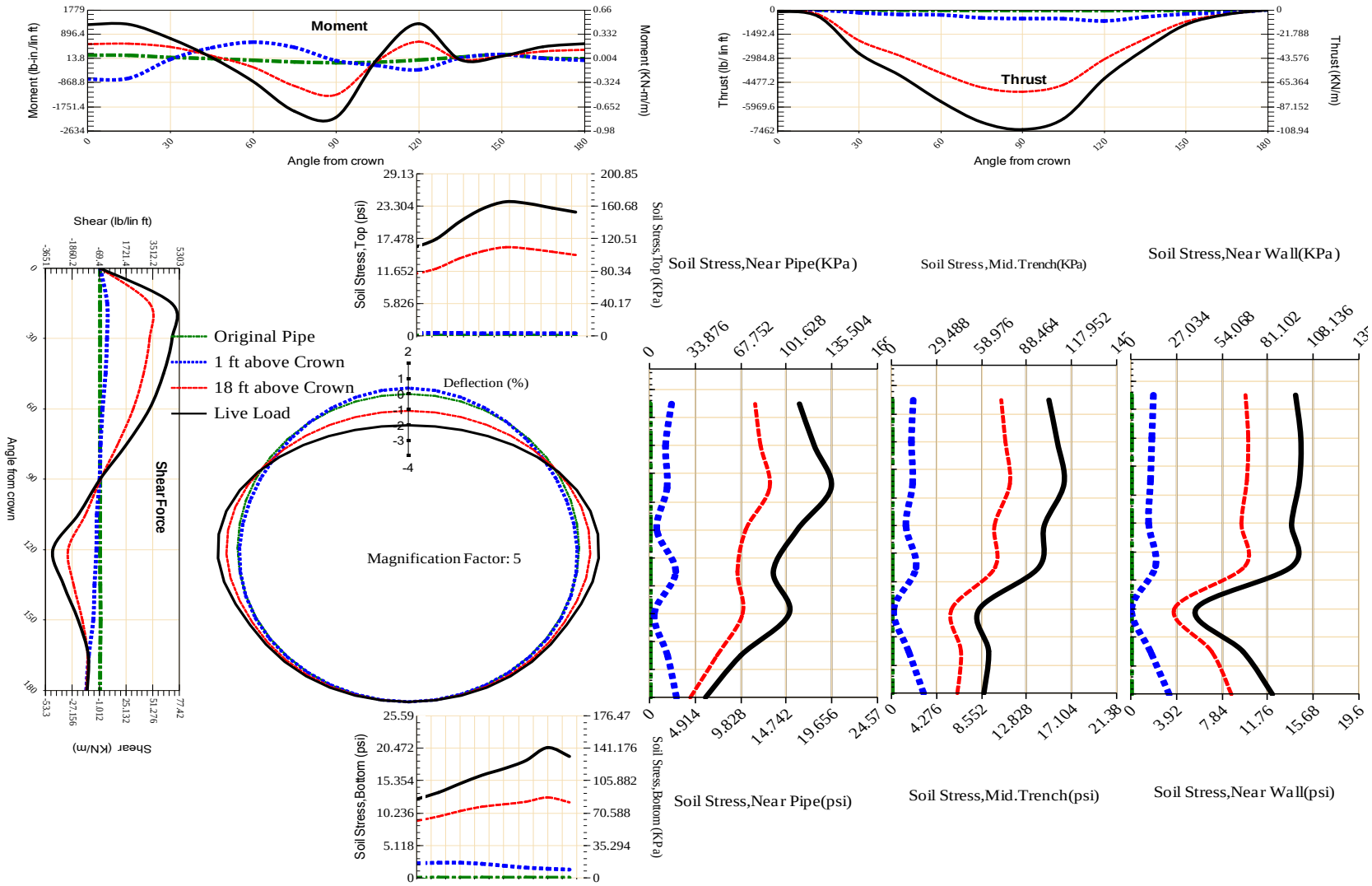

Figure A-294 Param-48-PW200-TR3OR-OD+48-EW10-H18-LiveLoad

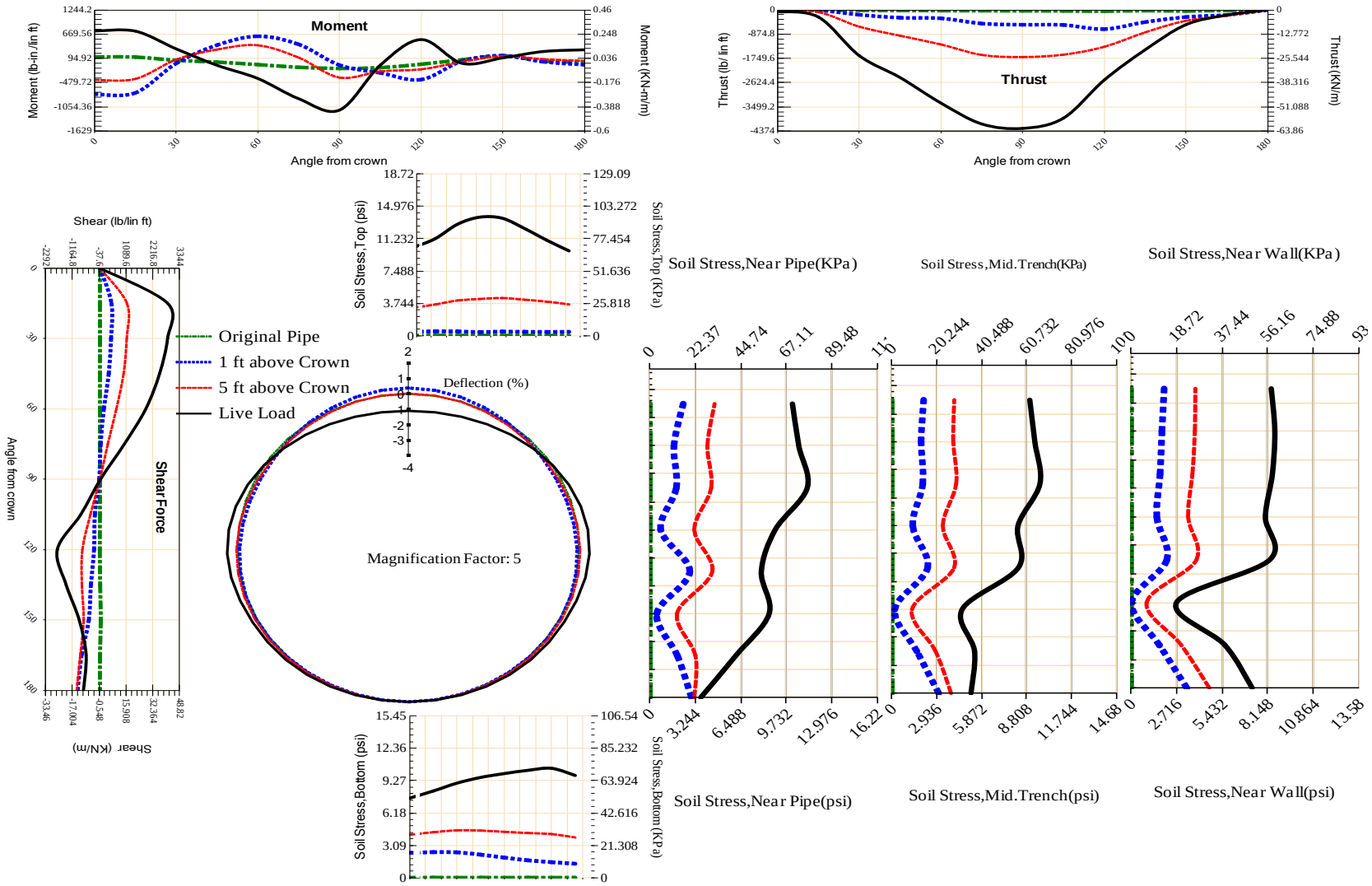

Figure A-295 Param-48-PW200-TR3OR-OD+48-EW10-H5-LiveLoad

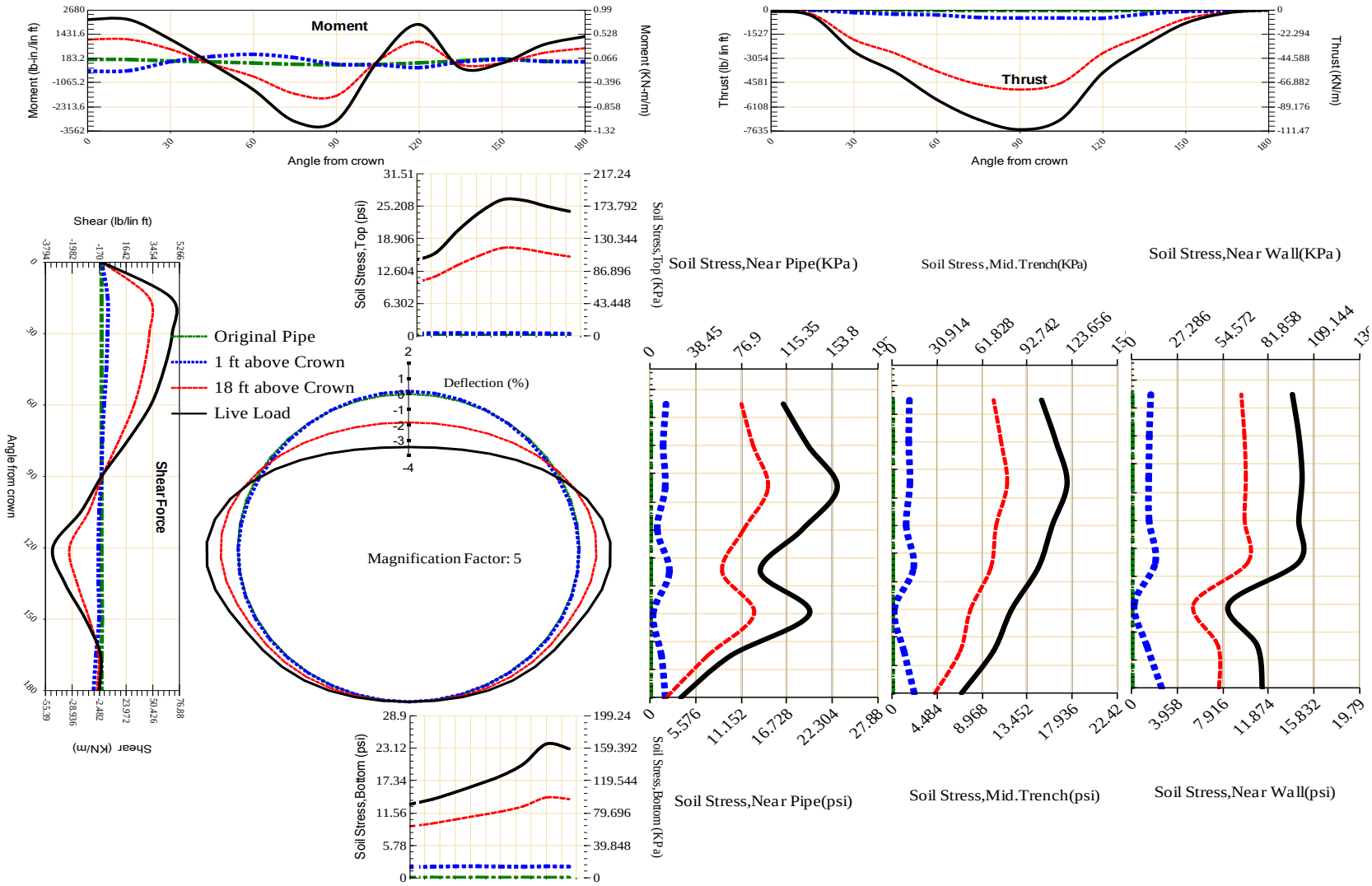

Figure A-296 Param-48-PW200-TR3OR-OD+48-EW3-H18-LiveLoad

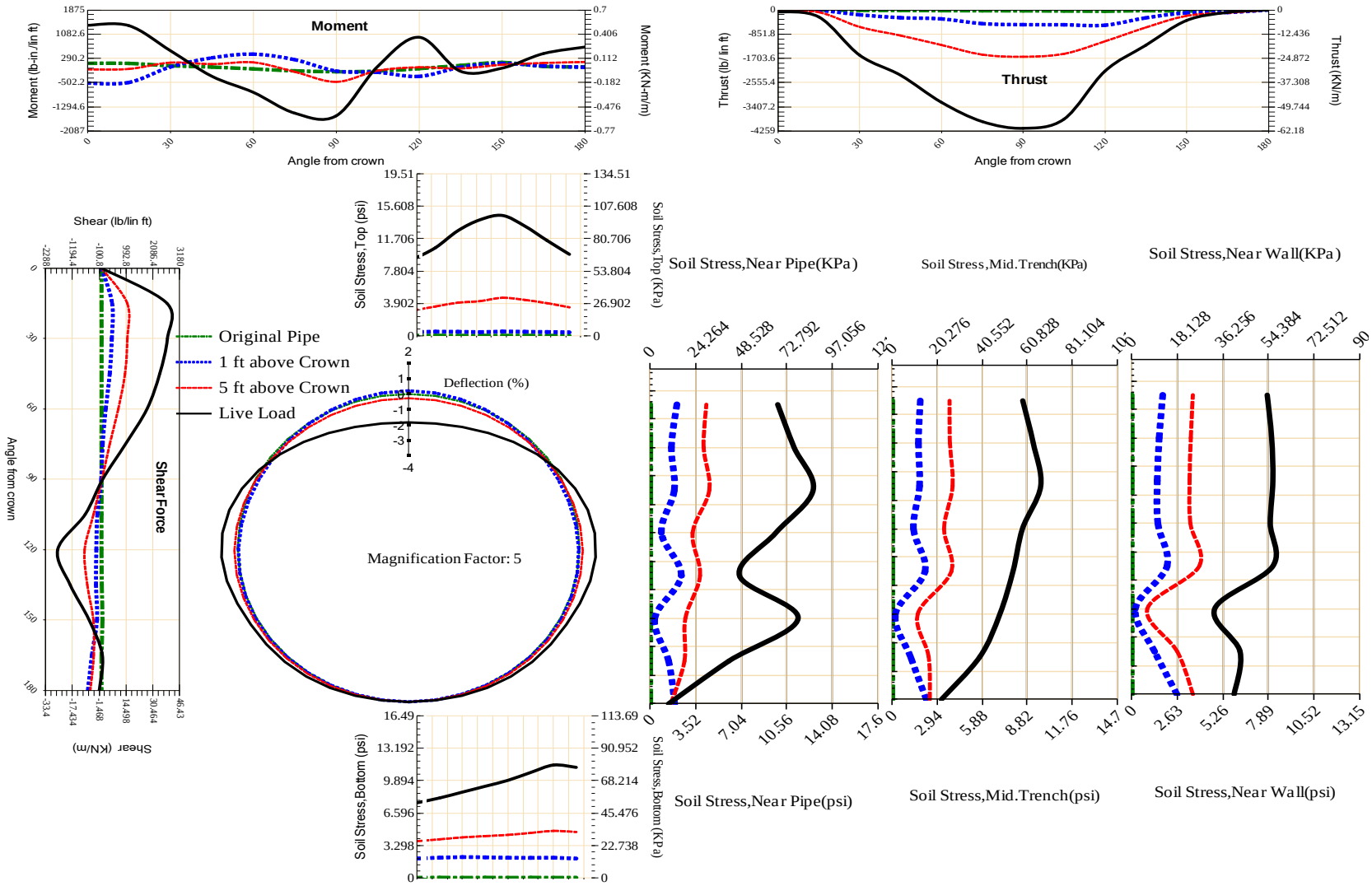

Figure A-297 Param-48-PW200-TR3OR-OD+48-EW3-H5-LiveLoad

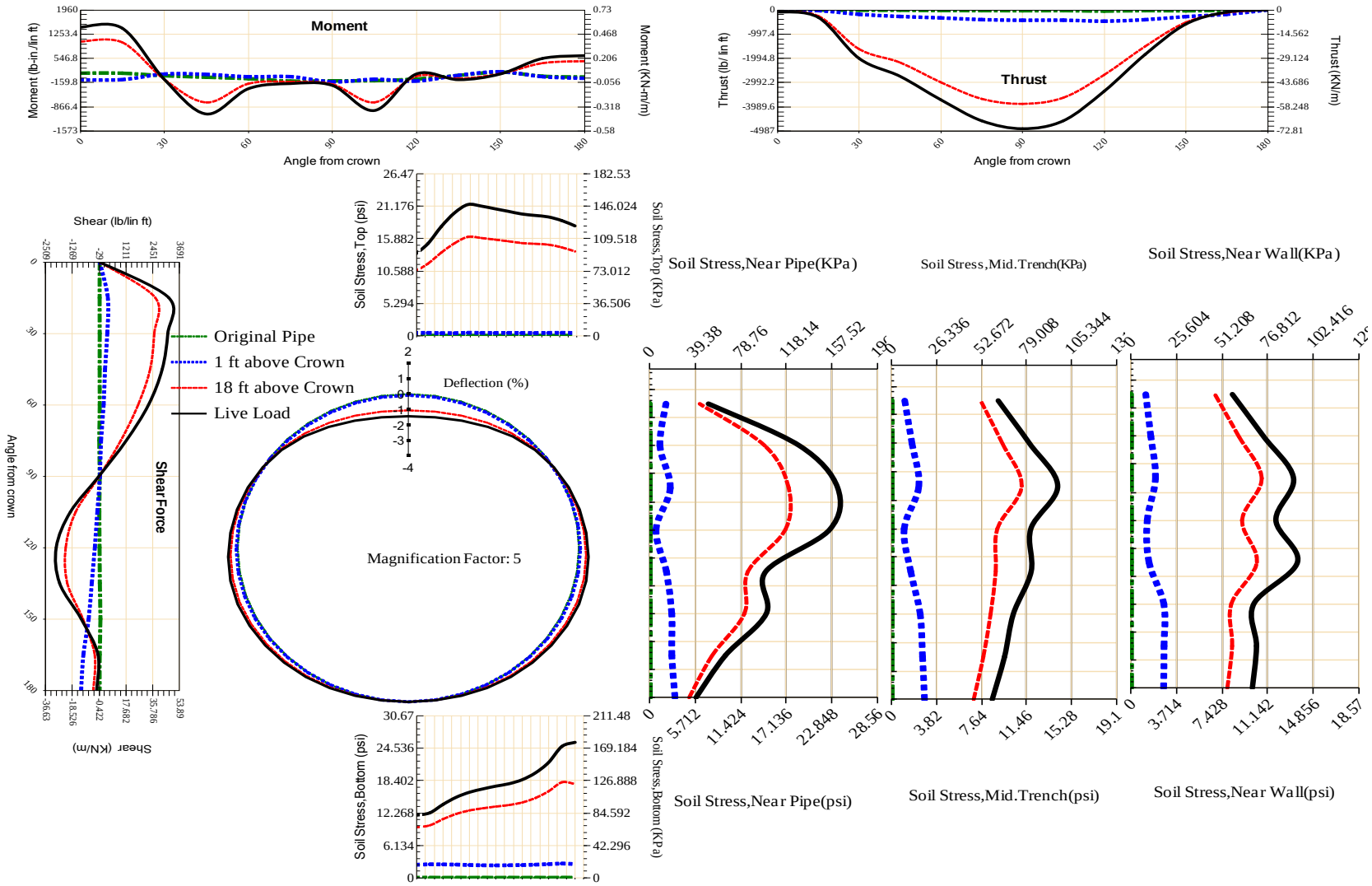

Figure A-298 Param-48-PW200-TR3SF-OD+108-EW10-H18-LiveLoad

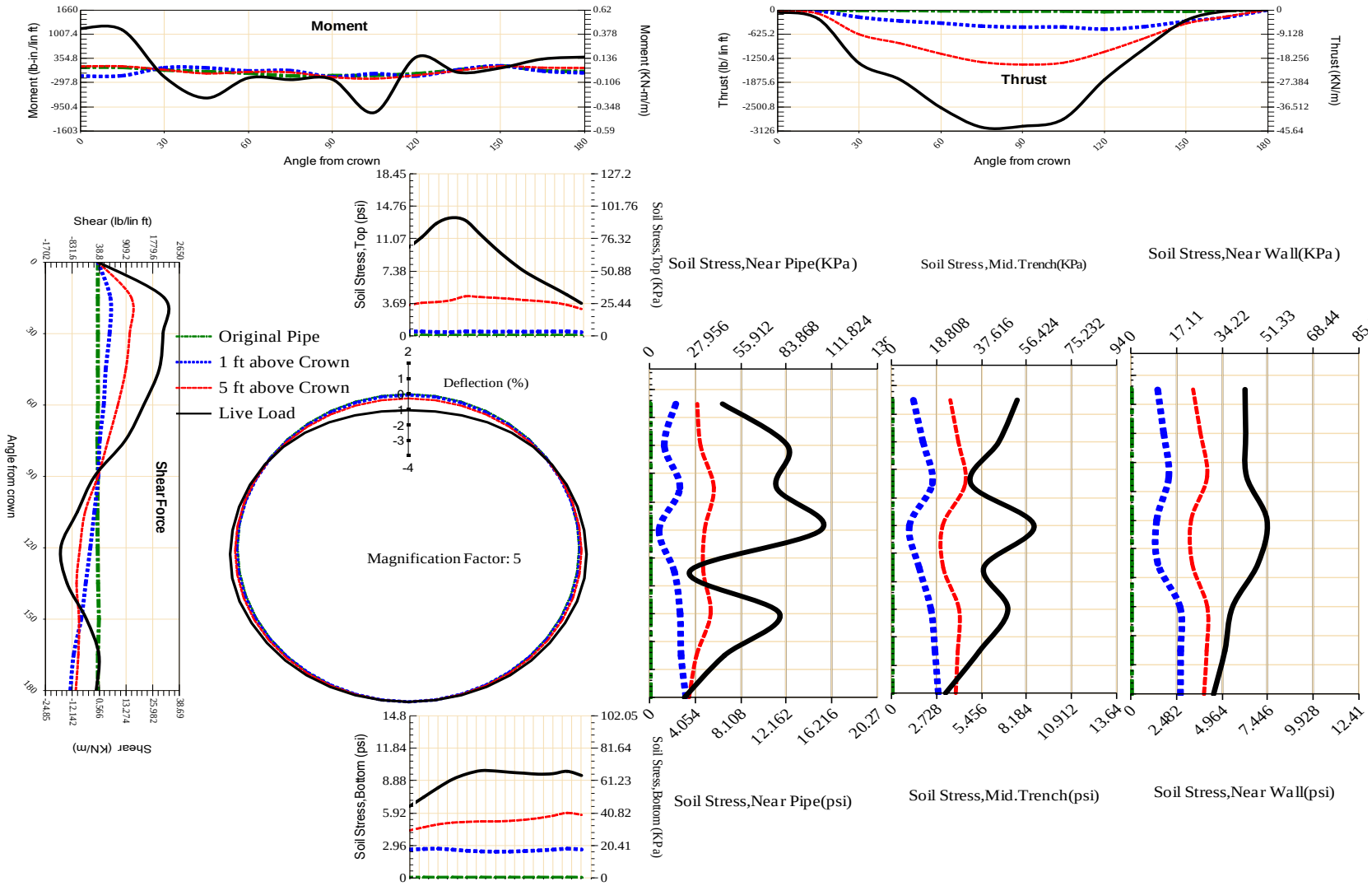

Figure A-299 Param-48-PW200-TR3SF-OD+108-EW10-H5-LiveLoad

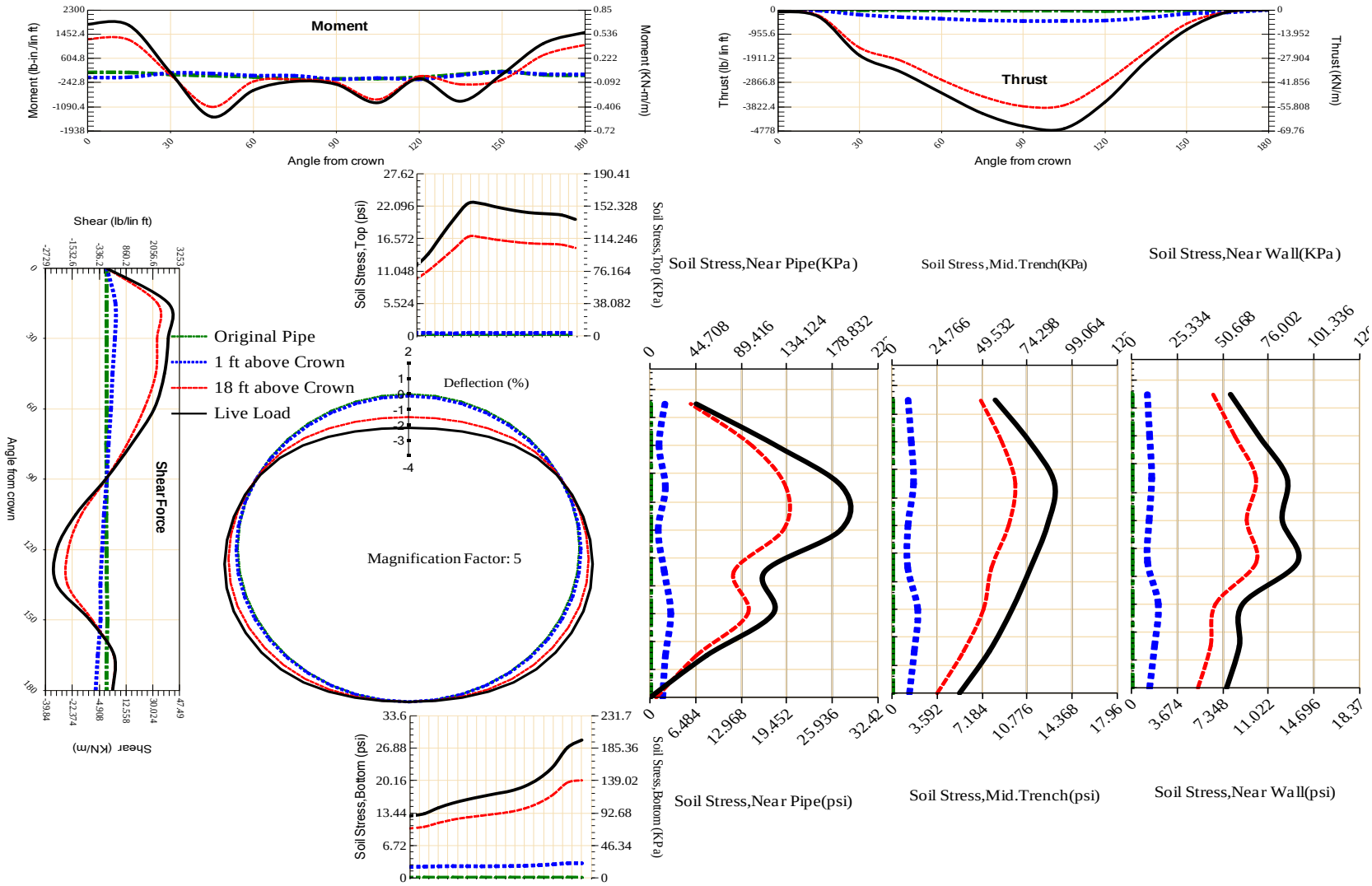

Figure A-300 Param-48-PW200-TR3SF-OD+108-EW3-H18-LiveLoad

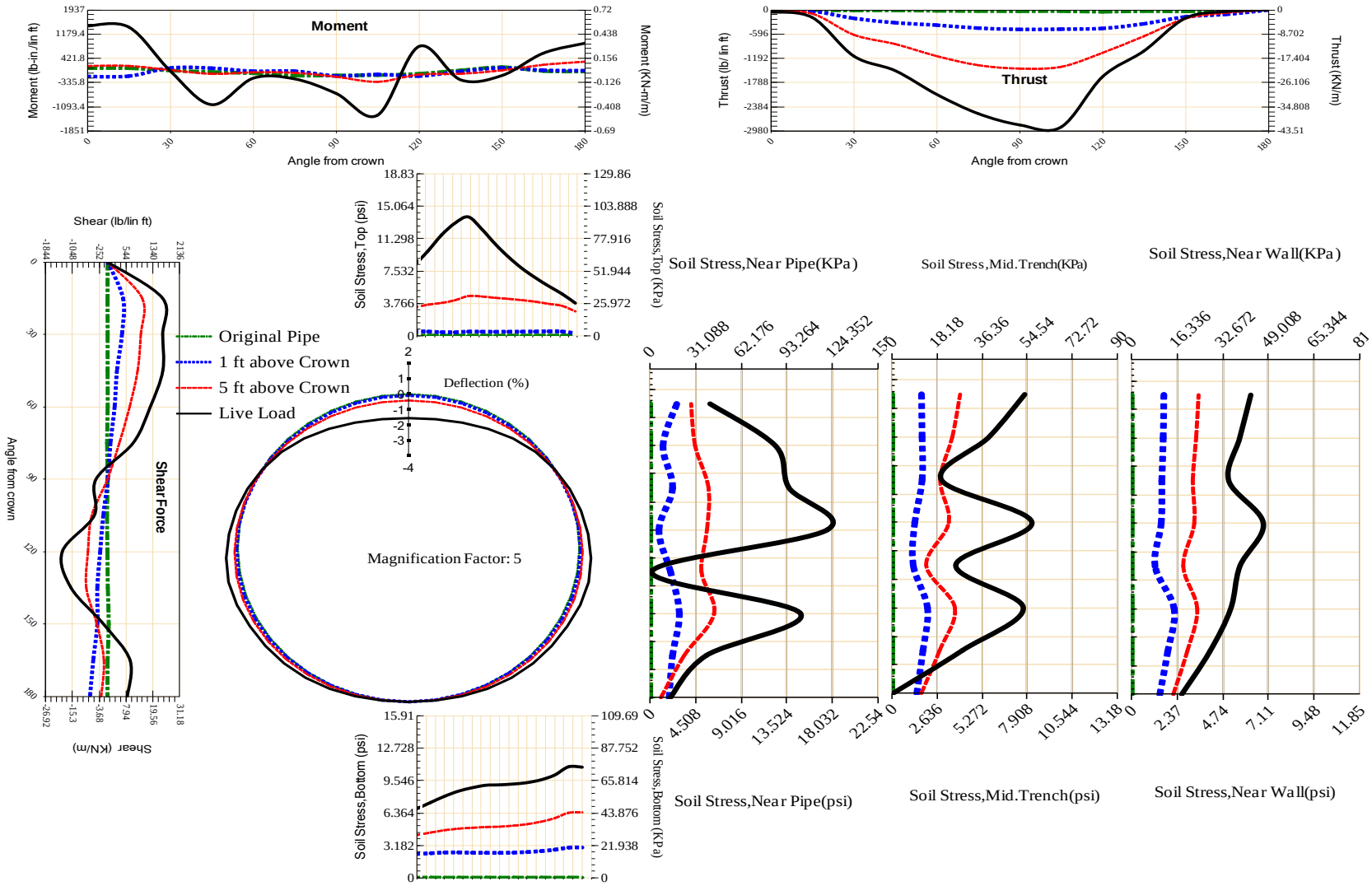

Figure A-301 Param-48-PW200-TR3SF-OD+108-EW3-H5-LiveLoad

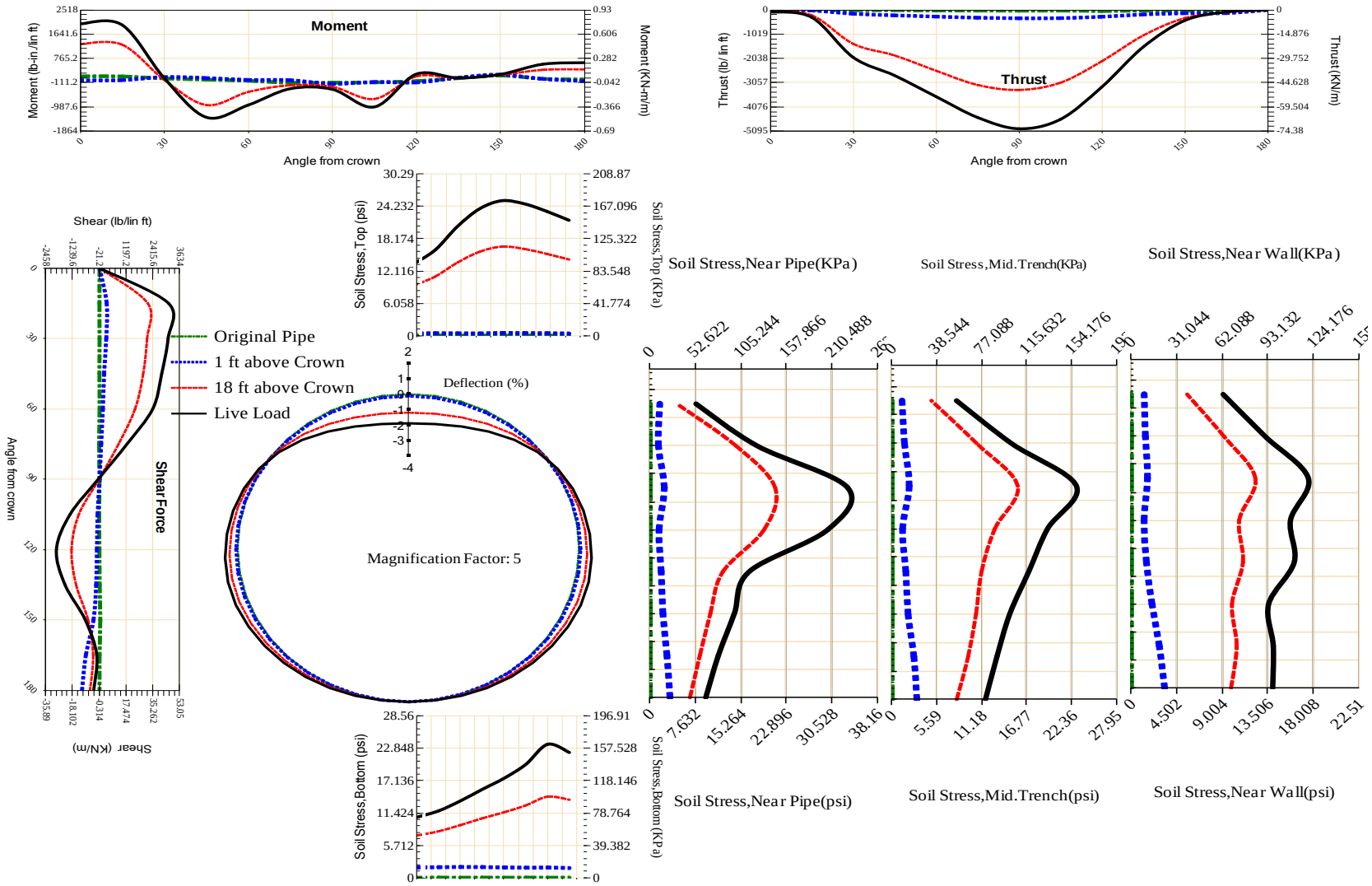

Figure A-302 Param-48-PW200-TR3SF-OD+48-EW10-H18-LiveLoad

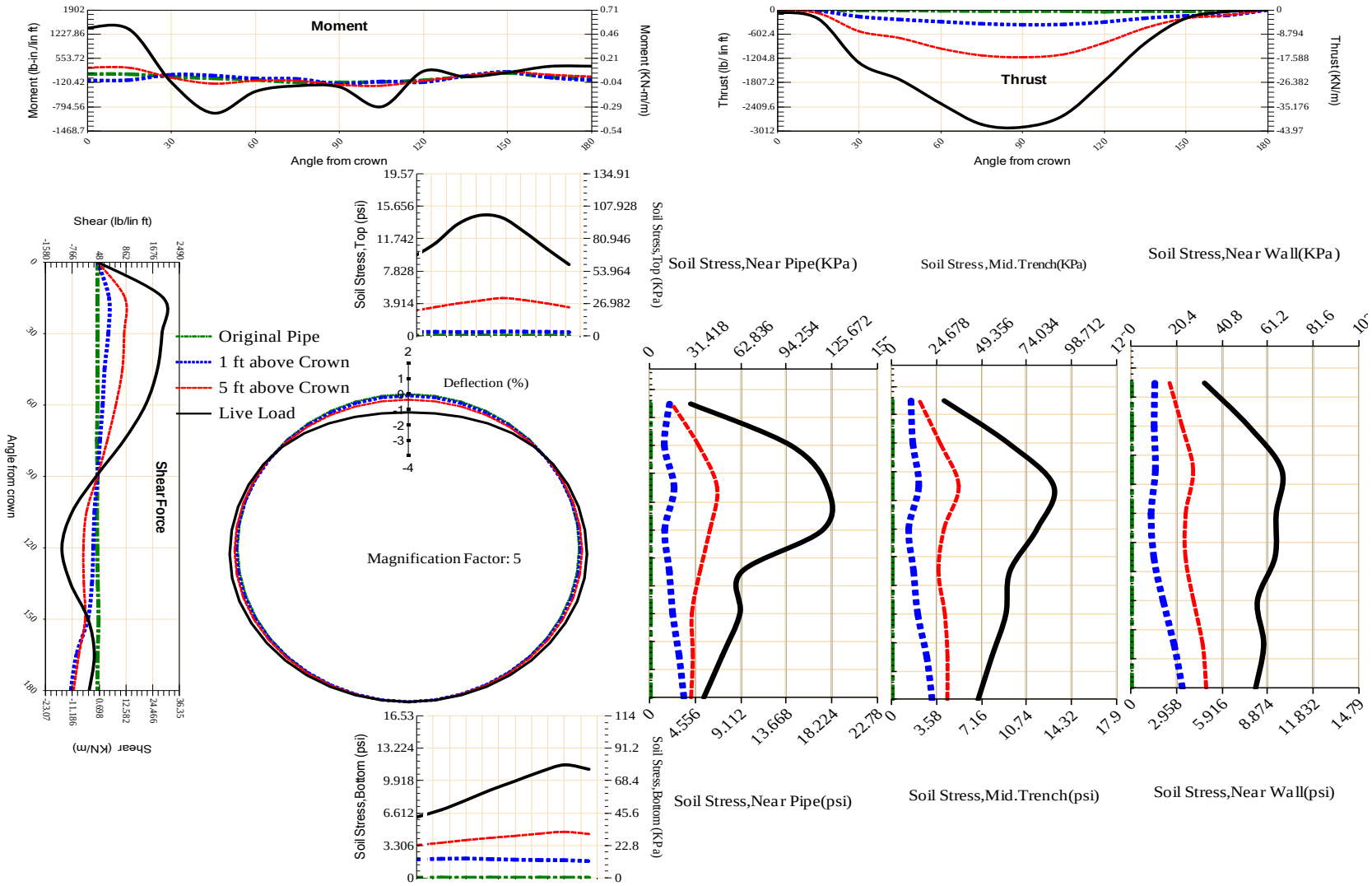

Figure A-303 Param-48-PW200-TR3SF-OD+48-EW10-H5-LiveLoad

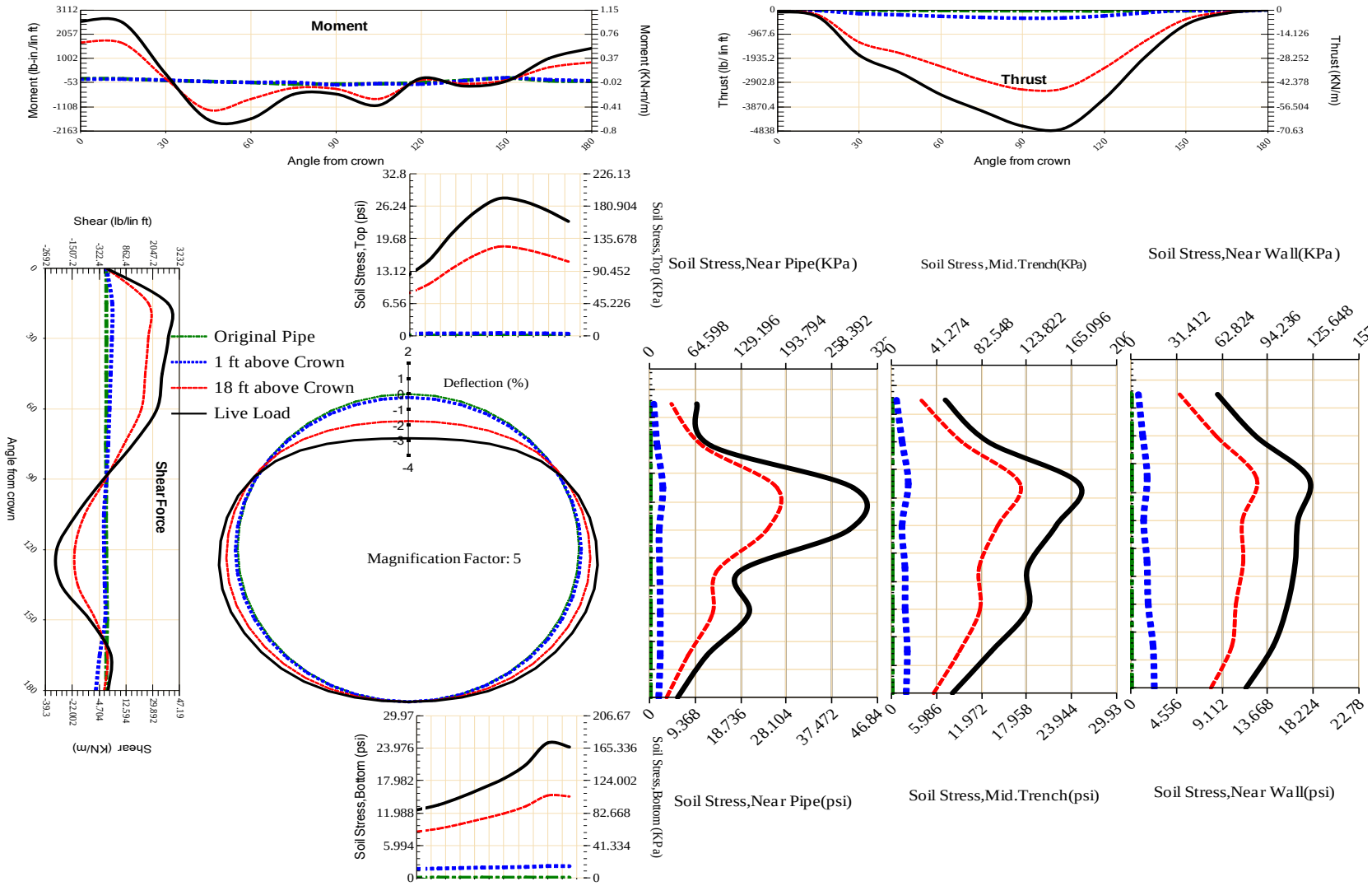

Figure A-304 Param-48-PW200-TR3SF-OD+48-EW3-H18-LiveLoad

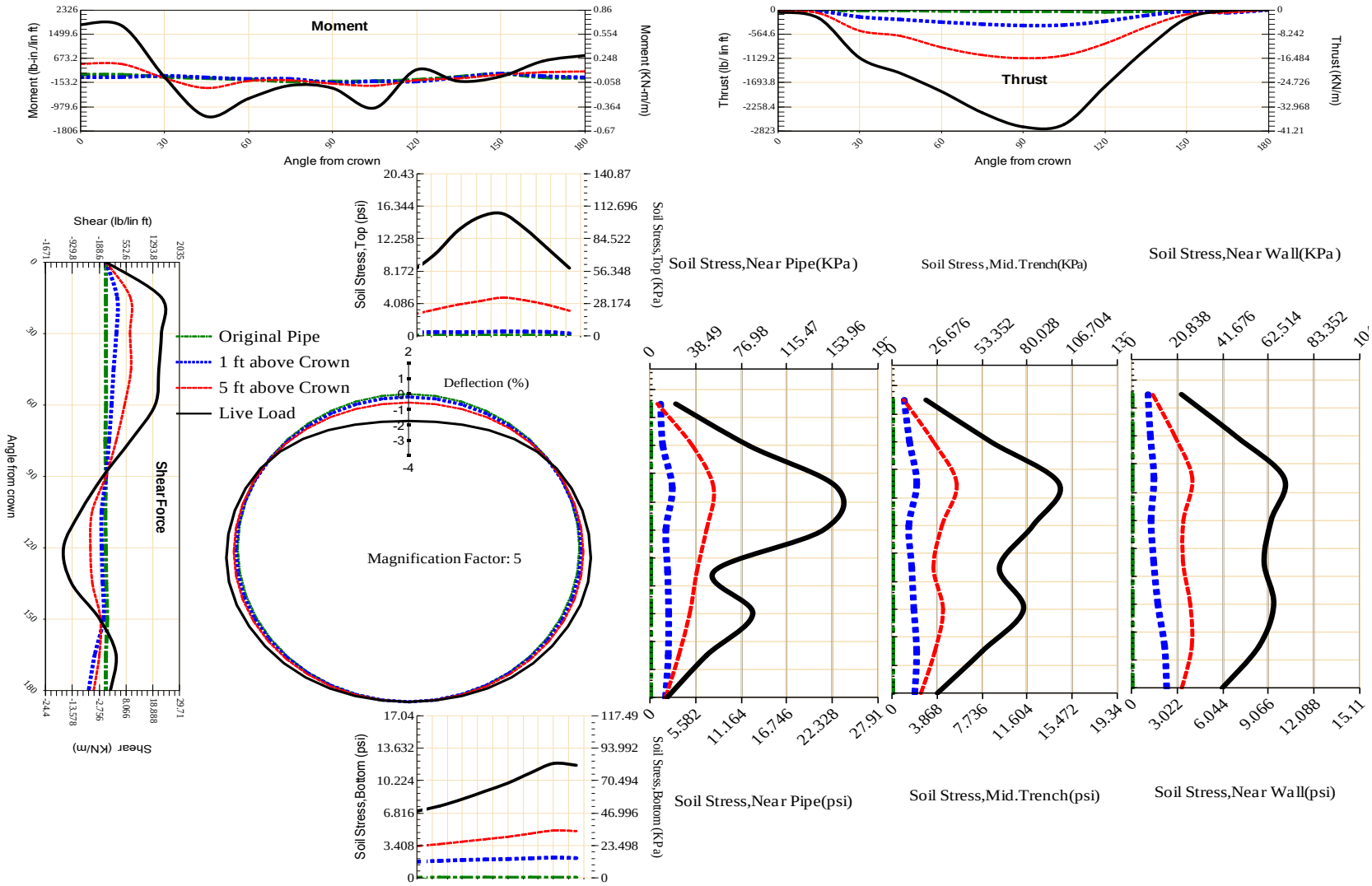

Figure A-305 Param-48-PW200-TR3SF-OD+48-EW3-H5-LiveLoad

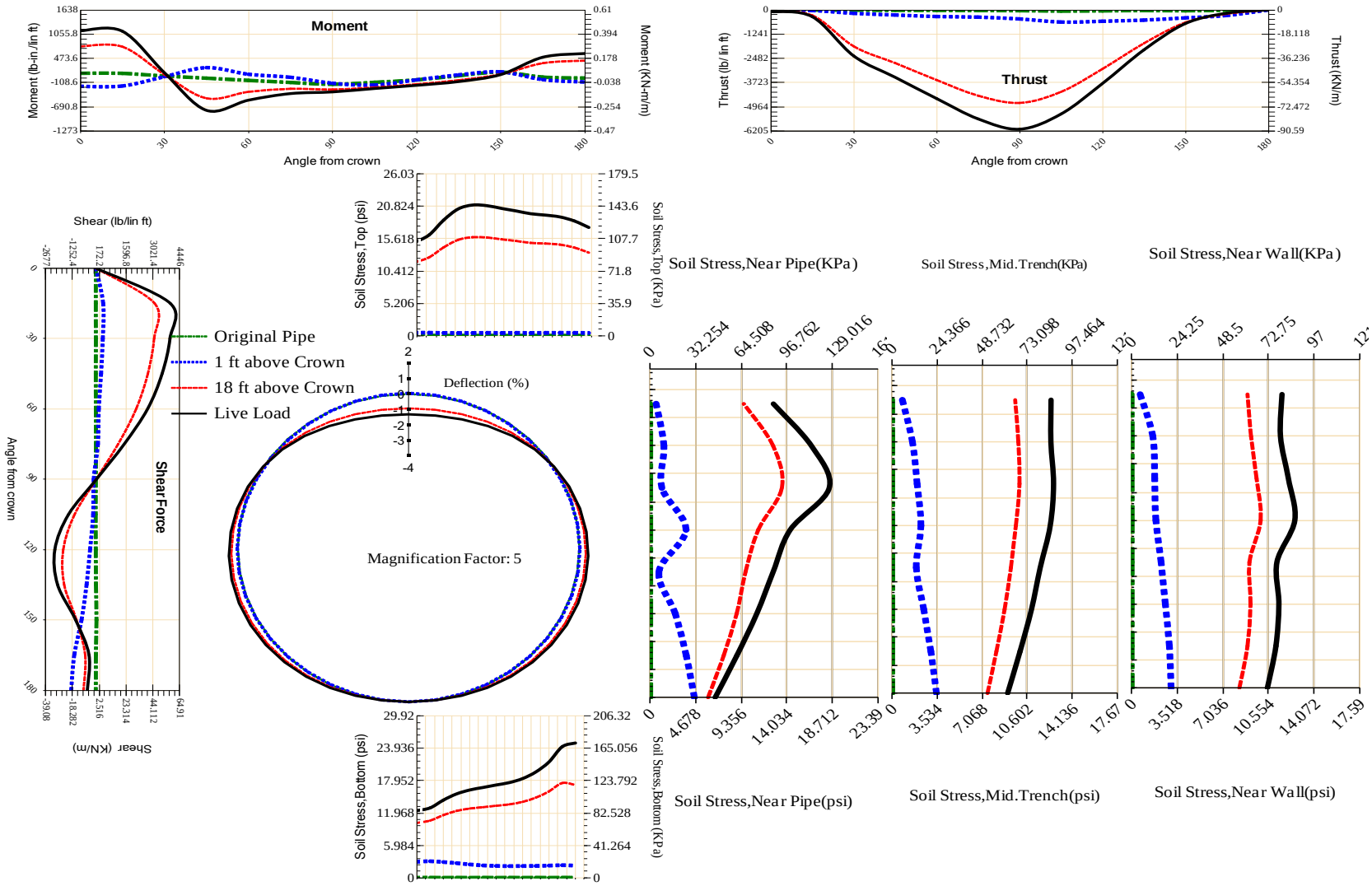

Figure A-306 Param-48-PW200-TR5OR-OD+108-EW10-H18-LiveLoad

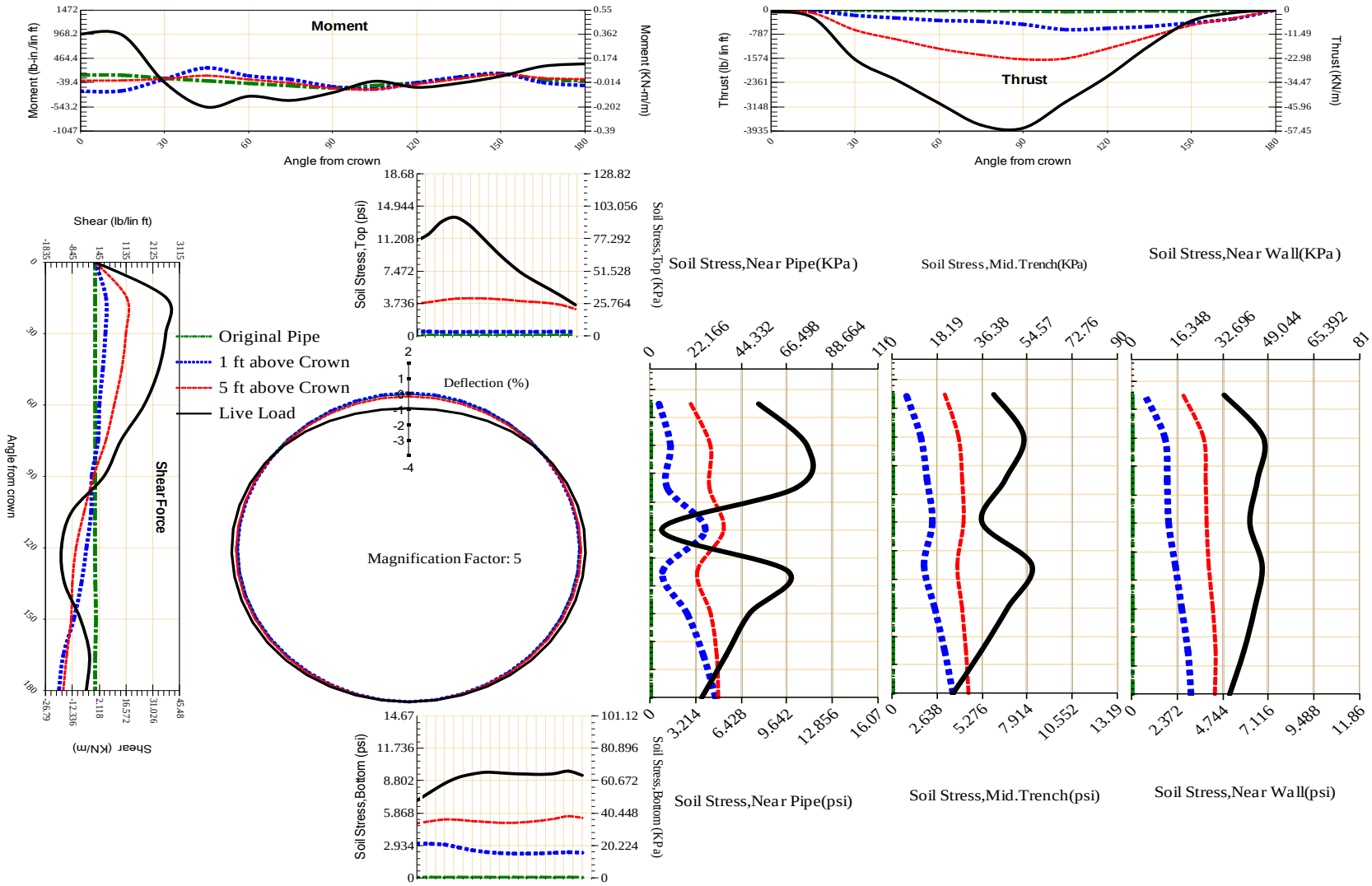

Figure A-307 Param-48-PW200-TR5OR-OD+108-EW10-H5-LiveLoad

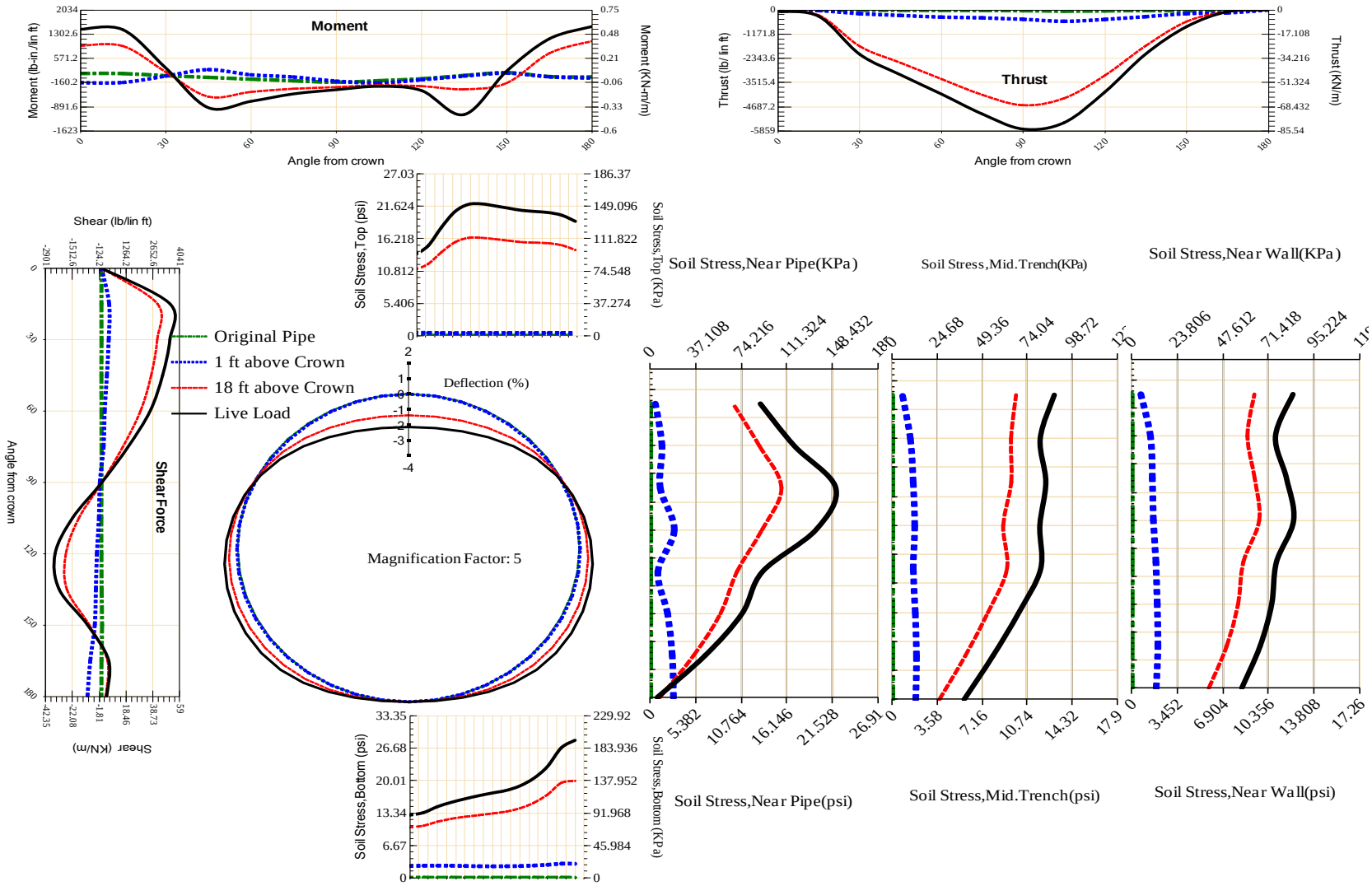

Figure A-308 Param-48-PW200-TR5OR-OD+108-EW3-H18-LiveLoad

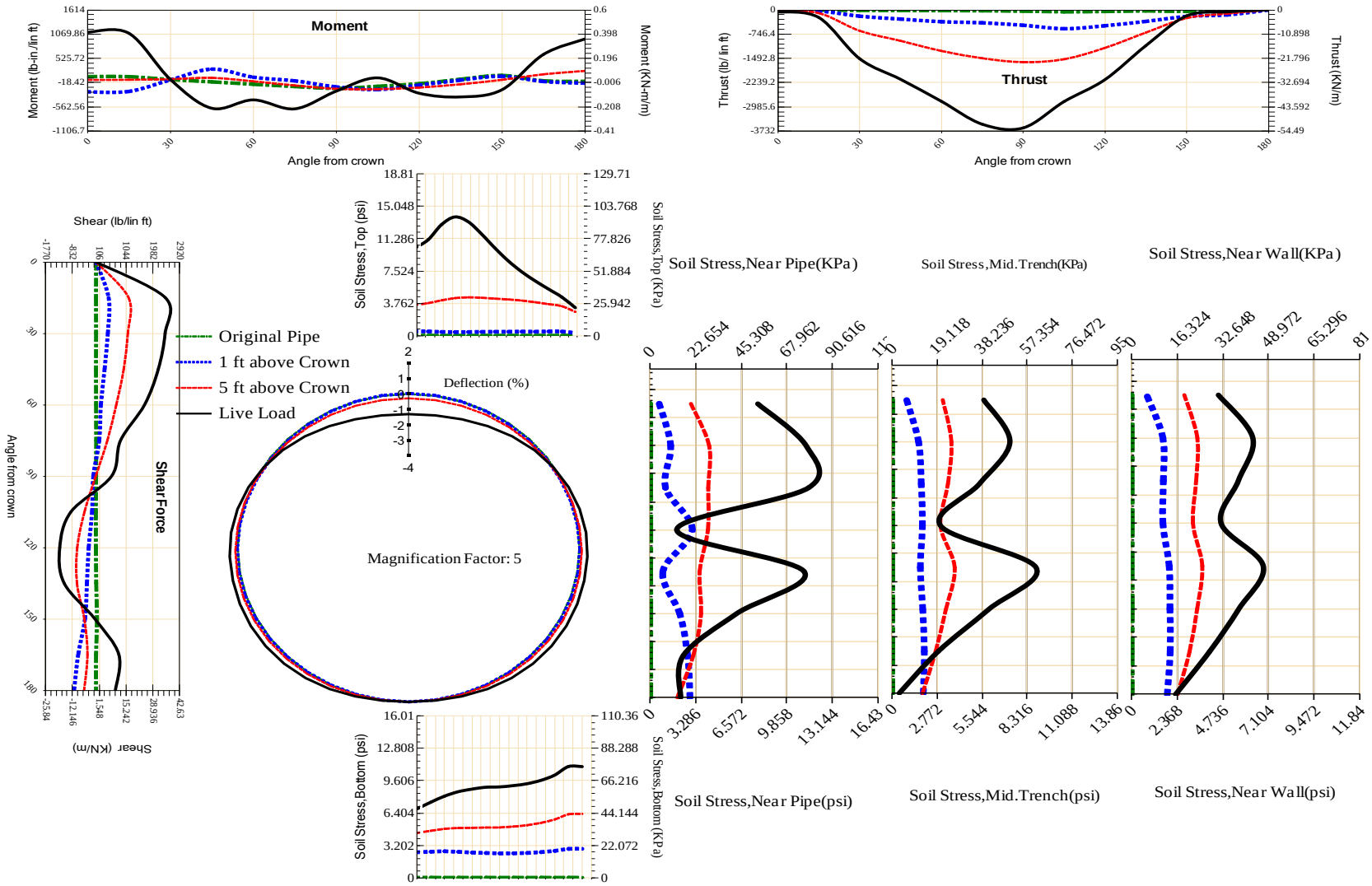

Figure A-309 Param-48-PW200-TR5OR-OD+108-EW3-H5-LiveLoad

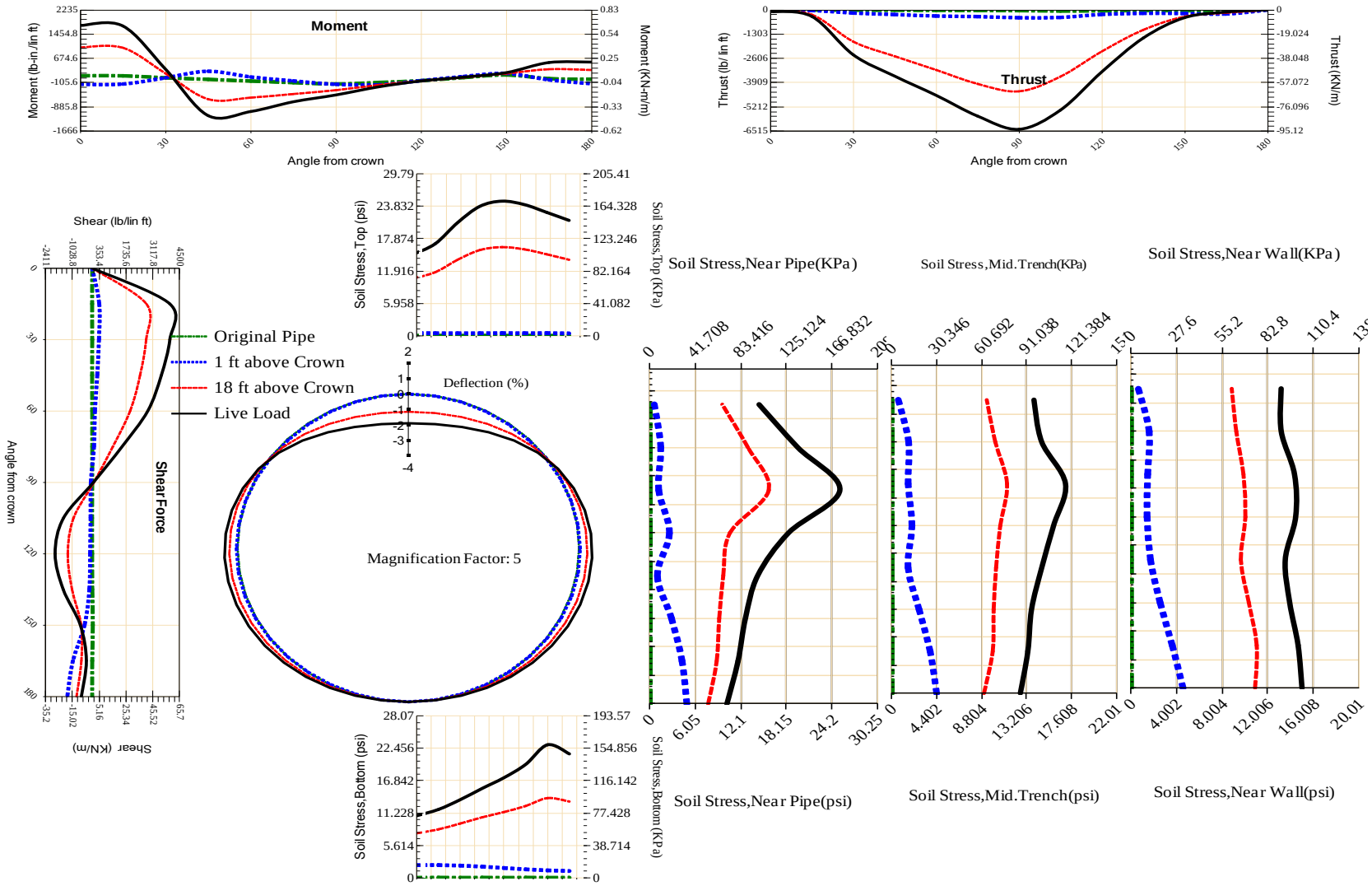

Figure A-310 Param-48-PW200-TR5OR-OD+48-EW10-H18-LiveLoad

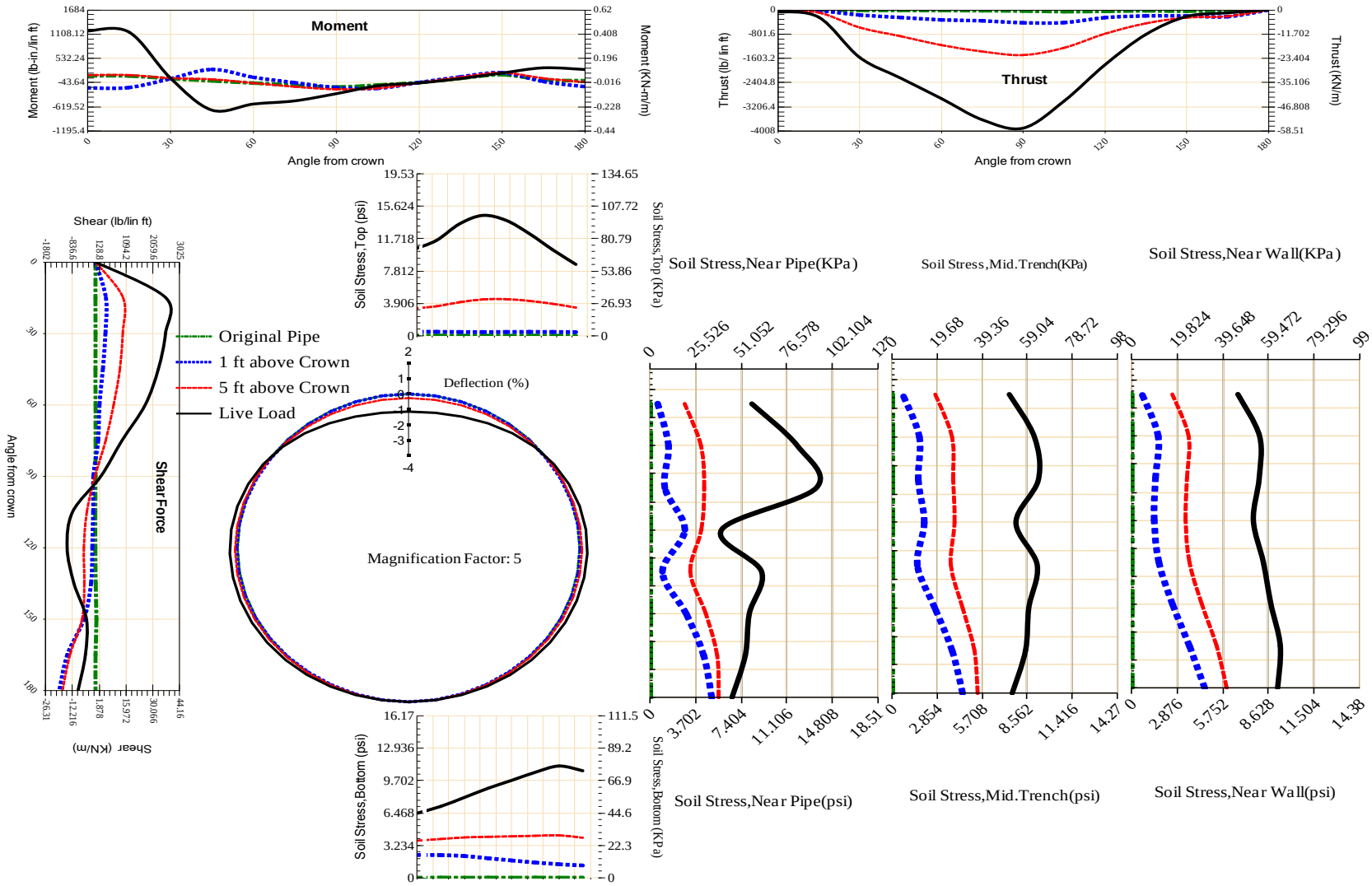

Figure A-311 Param-48-PW200-TR5OR-OD+48-EW10-H5-LiveLoad

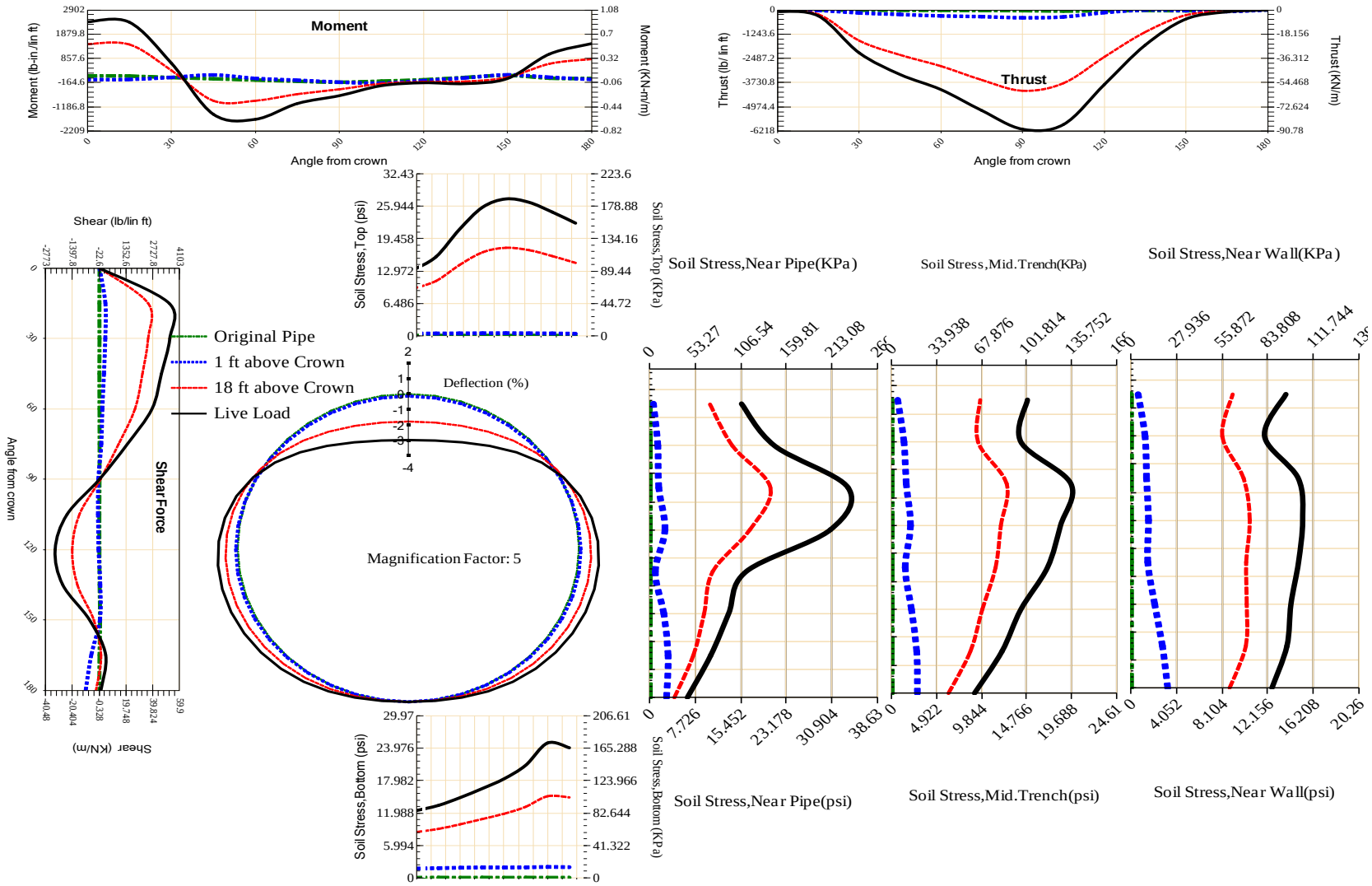

Figure A-312 Param-48-PW200-TR5OR-OD+48-EW3-H18-LiveLoad

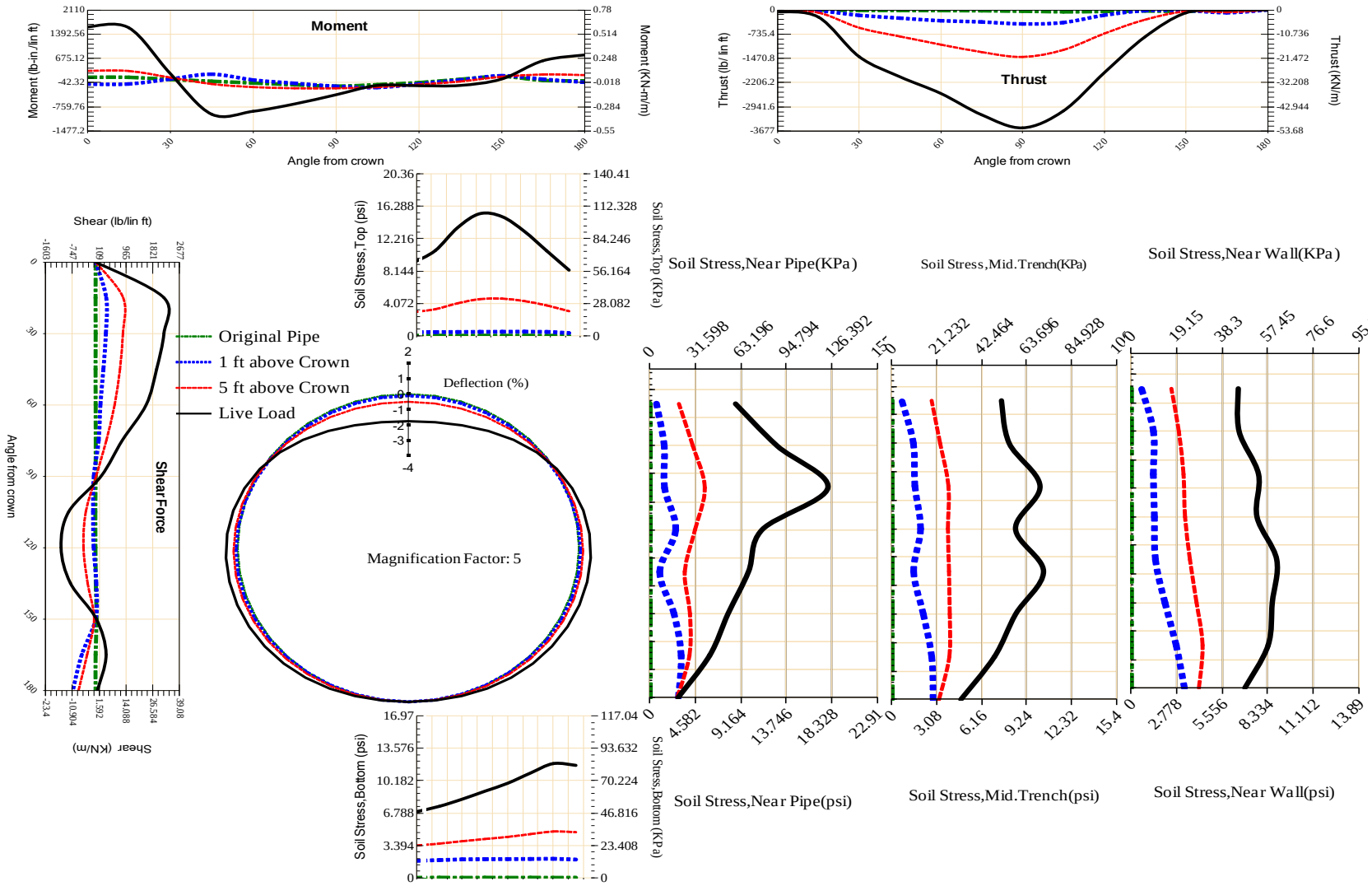

Figure A-313 Param-48-PW200-TR5OR-OD+48-EW3-H5-LiveLoad

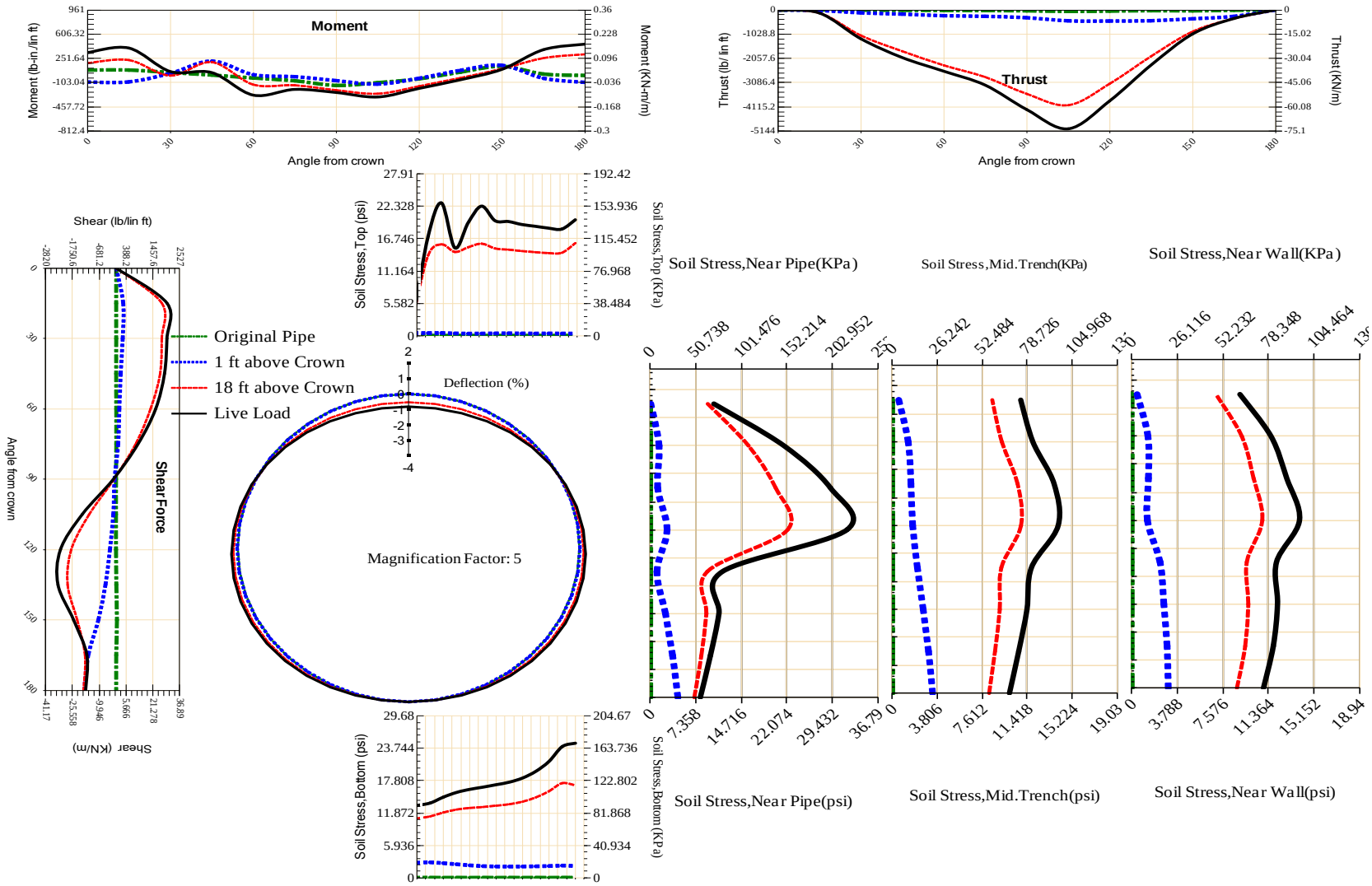

Figure A-314 Param-48-PW200-TR5SF-OD+108-EW10-H18-LiveLoad

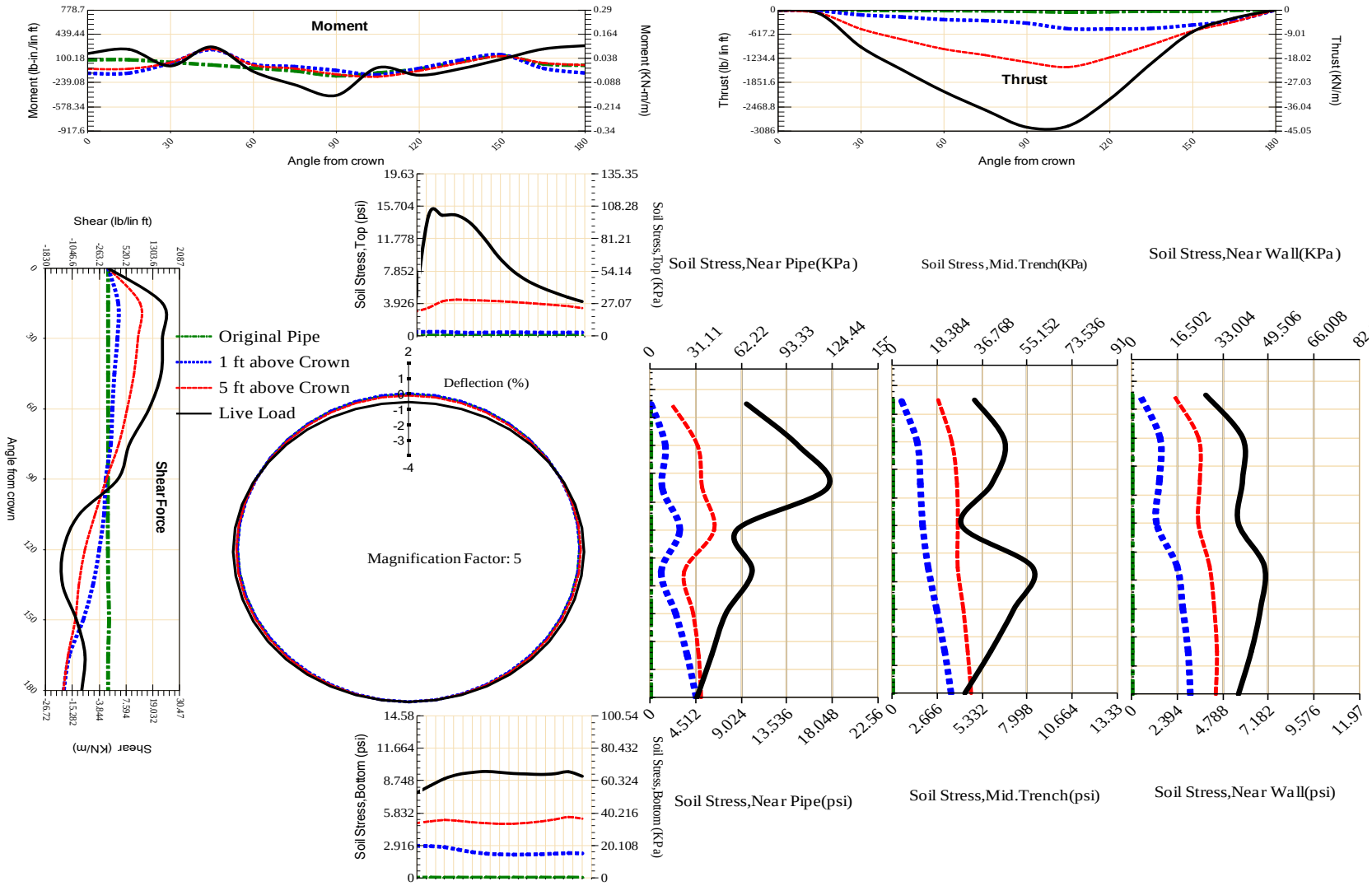

Figure A-315 Param-48-PW200-TR5SF-OD+108-EW10-H5-LiveLoad

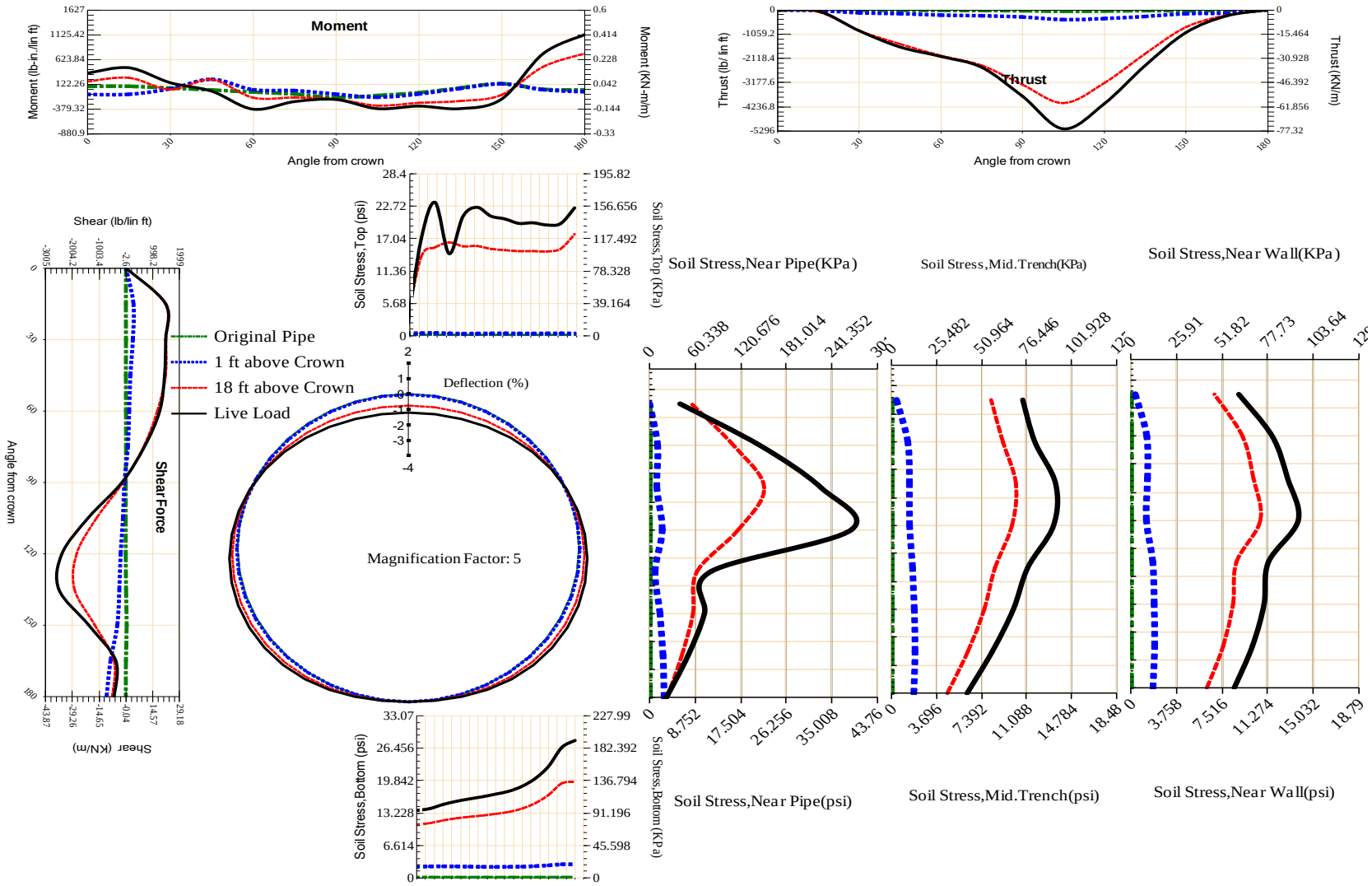

Figure A-316 Param-48-PW200-TR5SF-OD+108-EW3-H18-LiveLoad

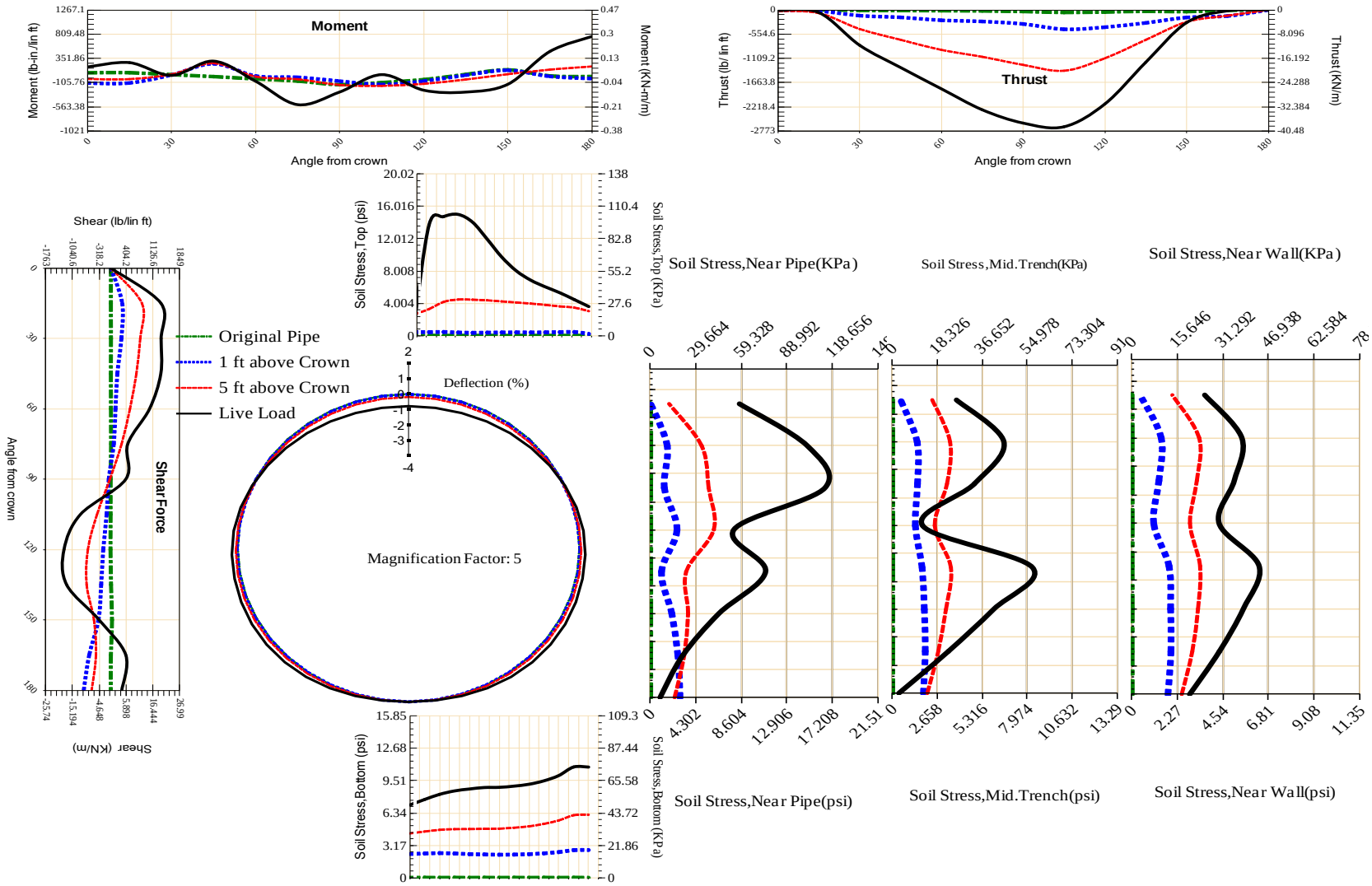

Figure A-317 Param-48-PW200-TR5SF-OD+108-EW3-H5-LiveLoad

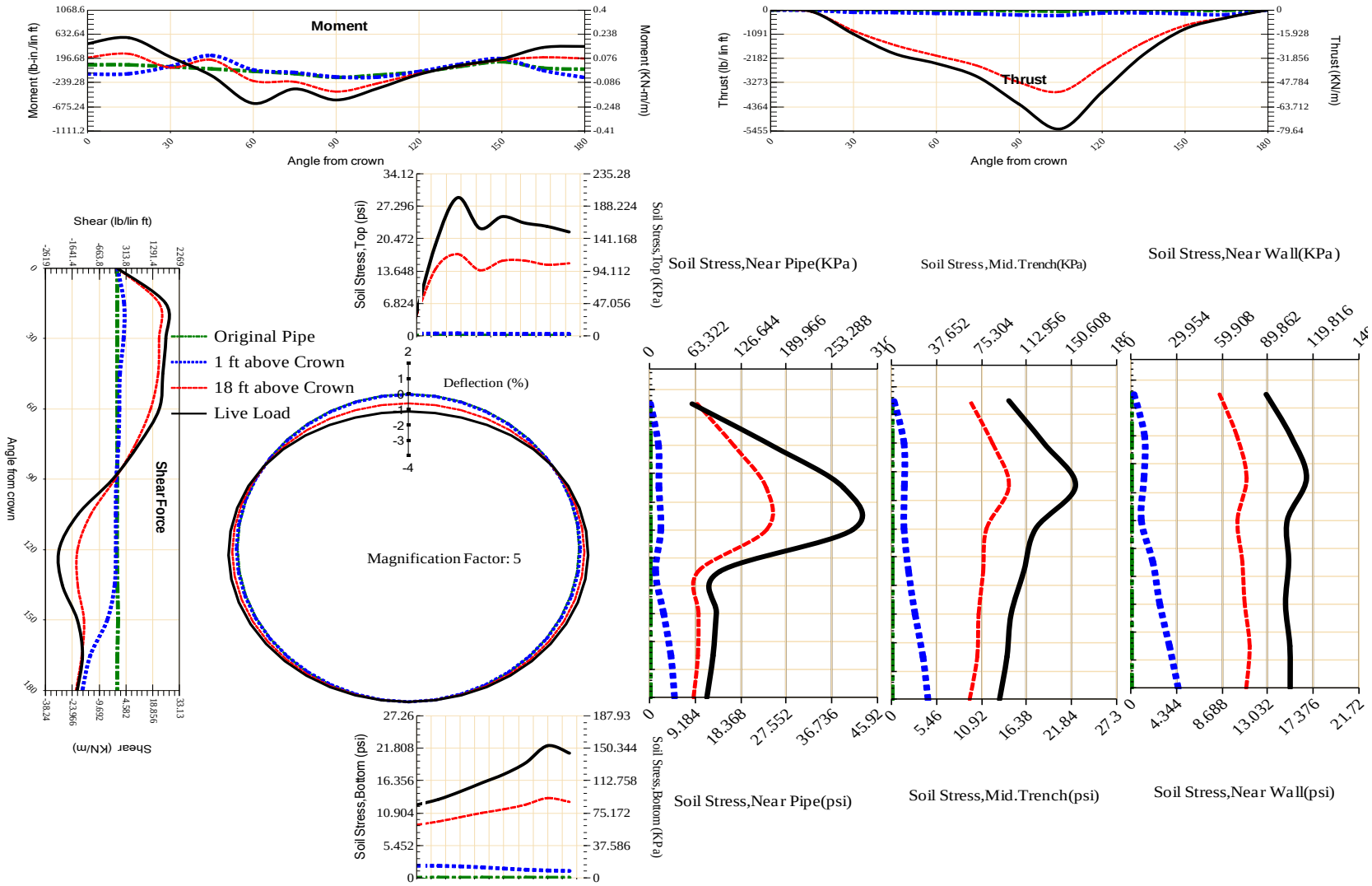

Figure A-318 Param-48-PW200-TR5SF-OD+48-EW10-H18-LiveLoad

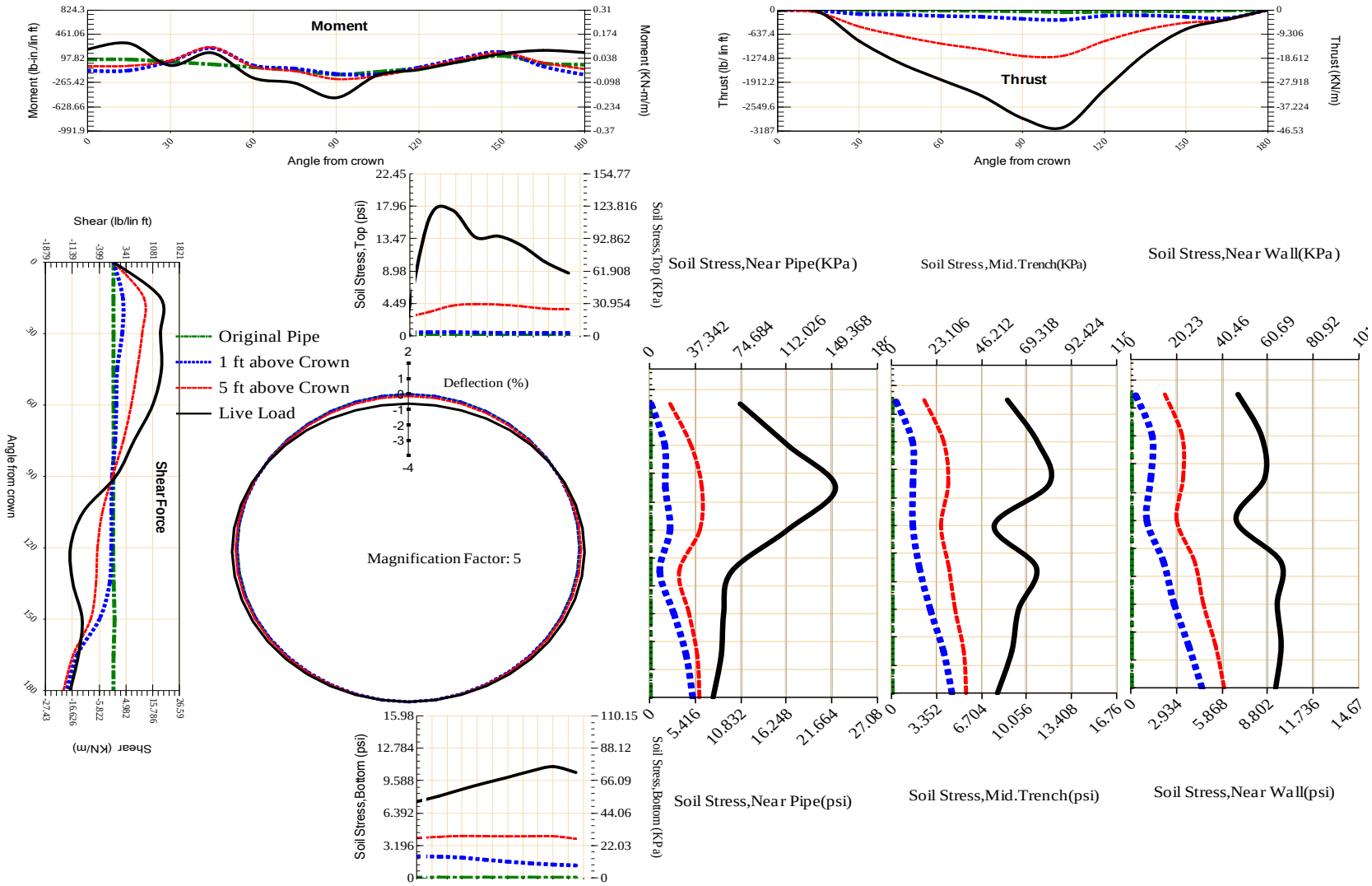

Figure A-319 Param-48-PW200-TR5SF-OD+48-EW10-H5-LiveLoad

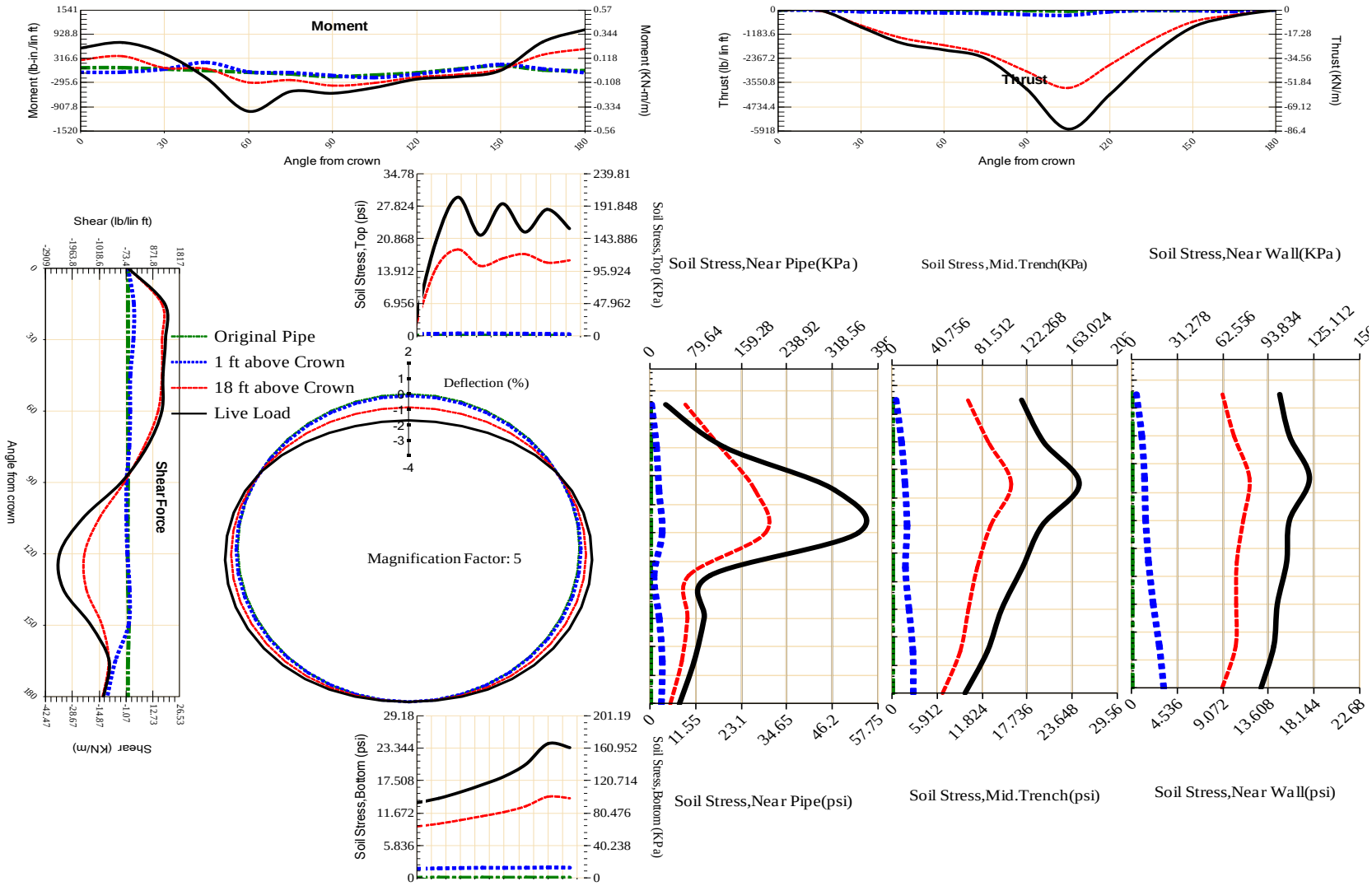

Figure A-320 Param-48-PW200-TR5SF-OD+48-EW3-H18-LiveLoad

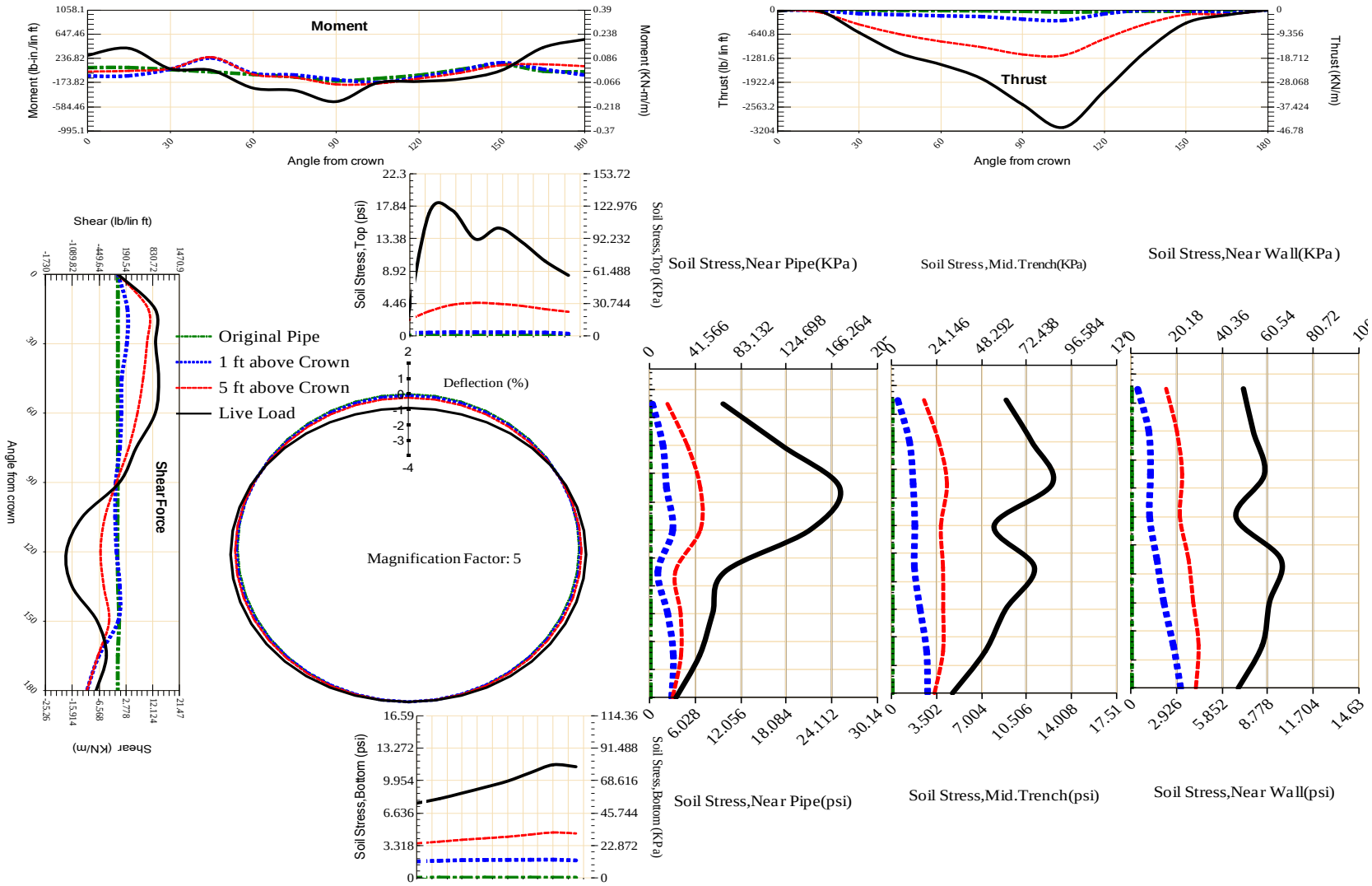

Figure A-321 Param-48-PW200-TR5SF-OD+48-EW3-H5-LiveLoad

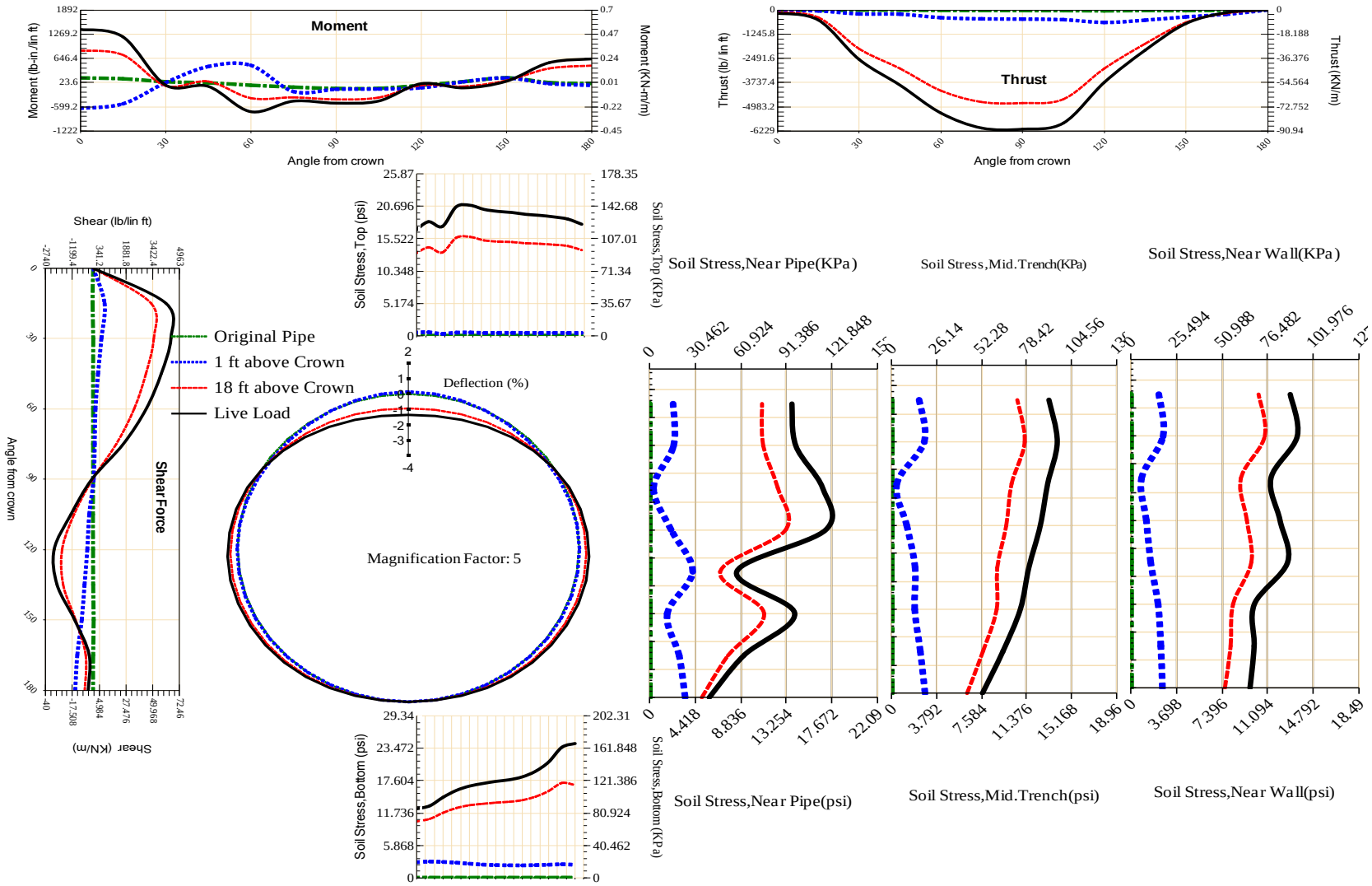

Figure A-322 Param-48-PW200-TR7OR-OD+108-EW10-H18-LiveLoad

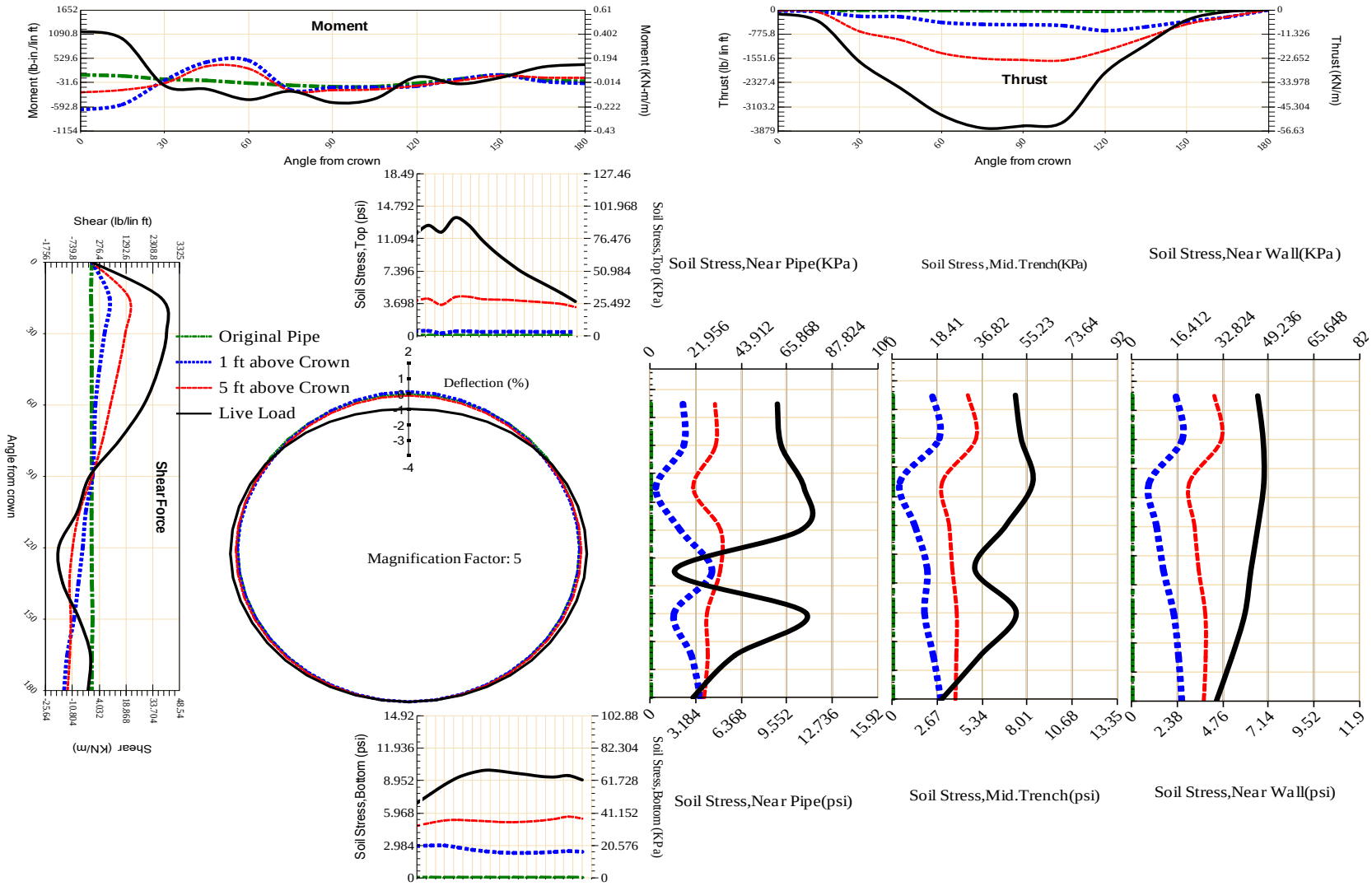

Figure A-323 Param-48-PW200-TR7OR-OD+108-EW10-H5-LiveLoad

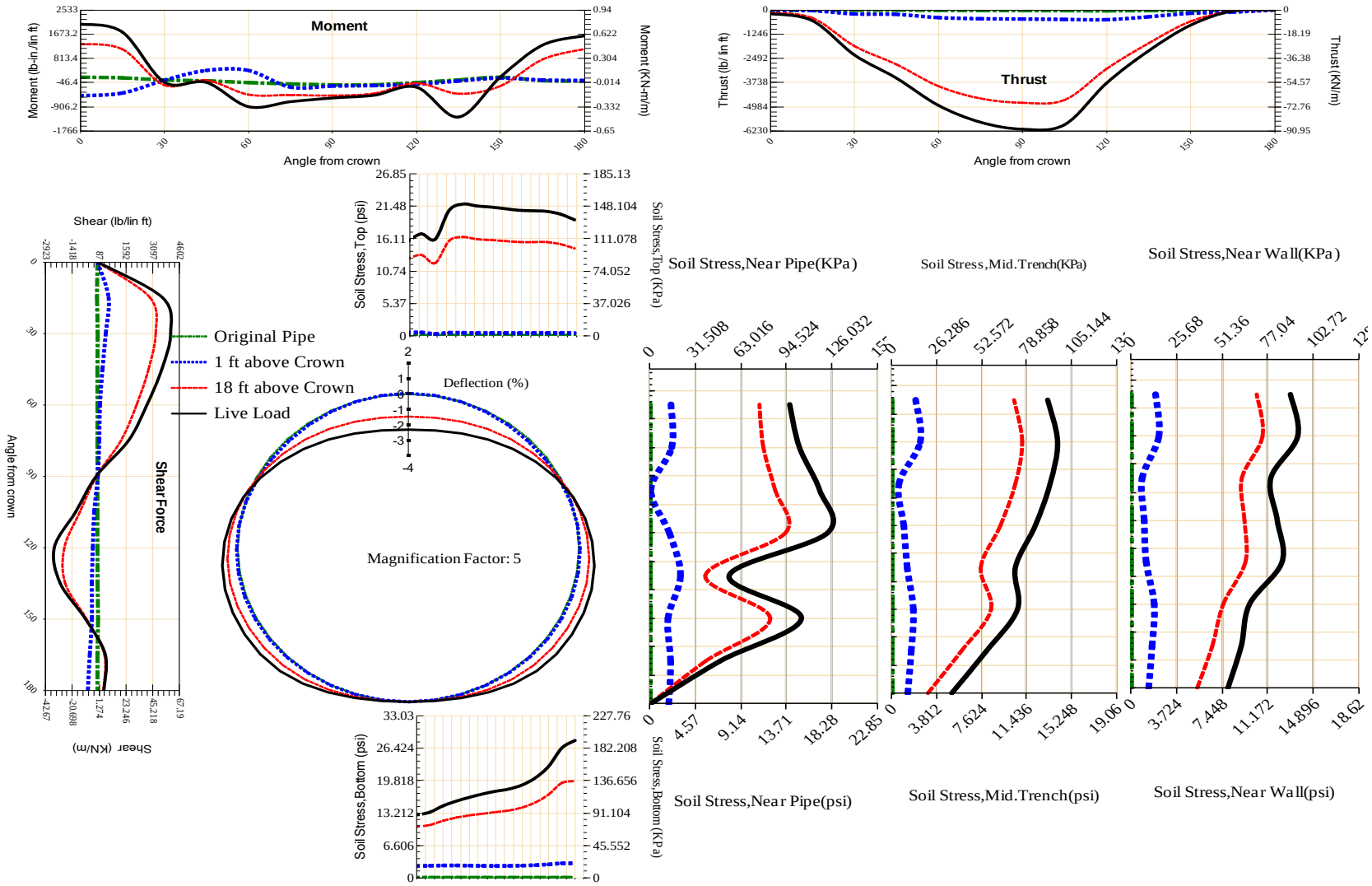

Figure A-324 Param-48-PW200-TR7OR-OD+108-EW3-H18-LiveLoad

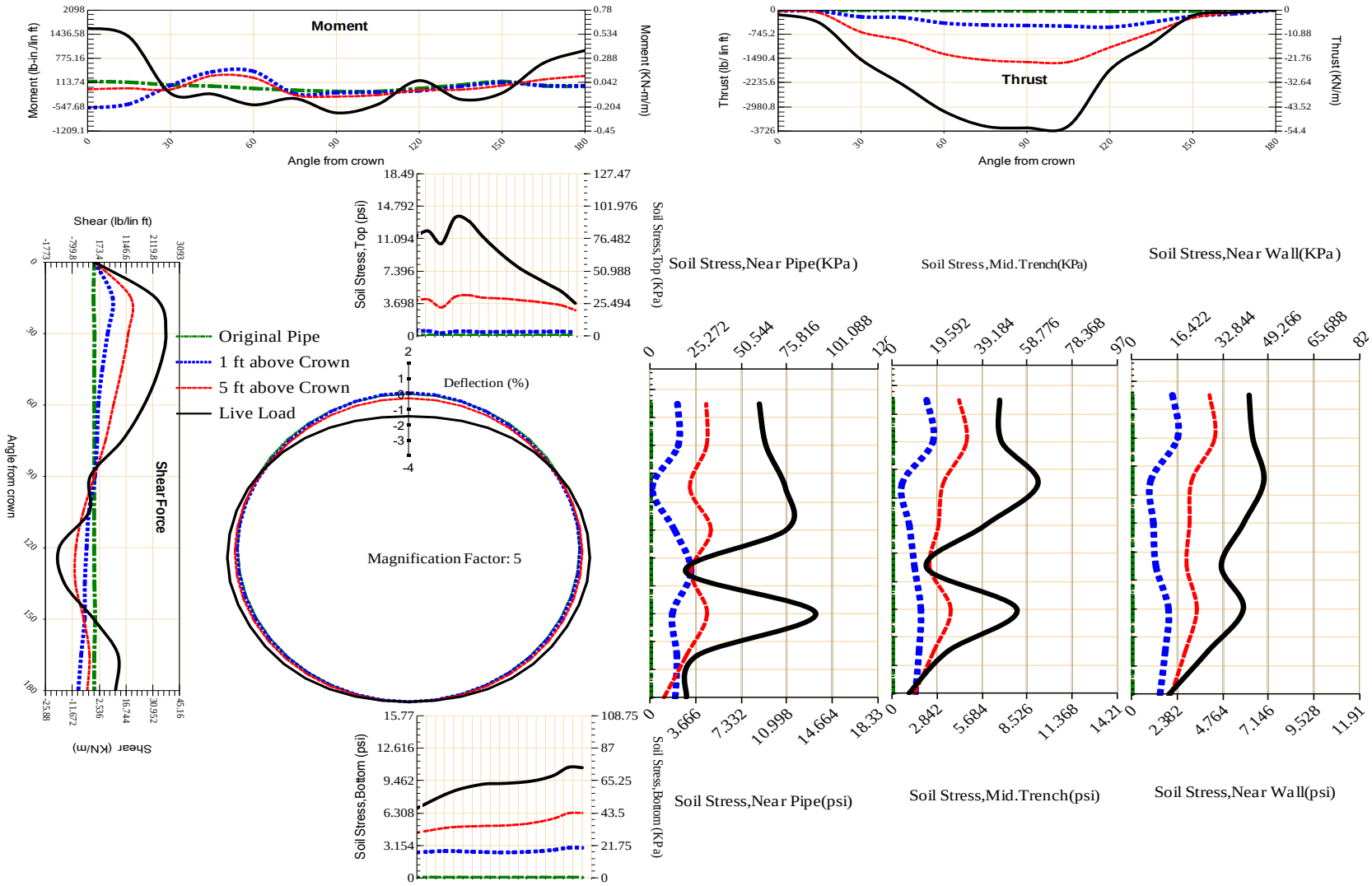

Figure A-325 Param-48-PW200-TR7OR-OD+108-EW3-H5-LiveLoad

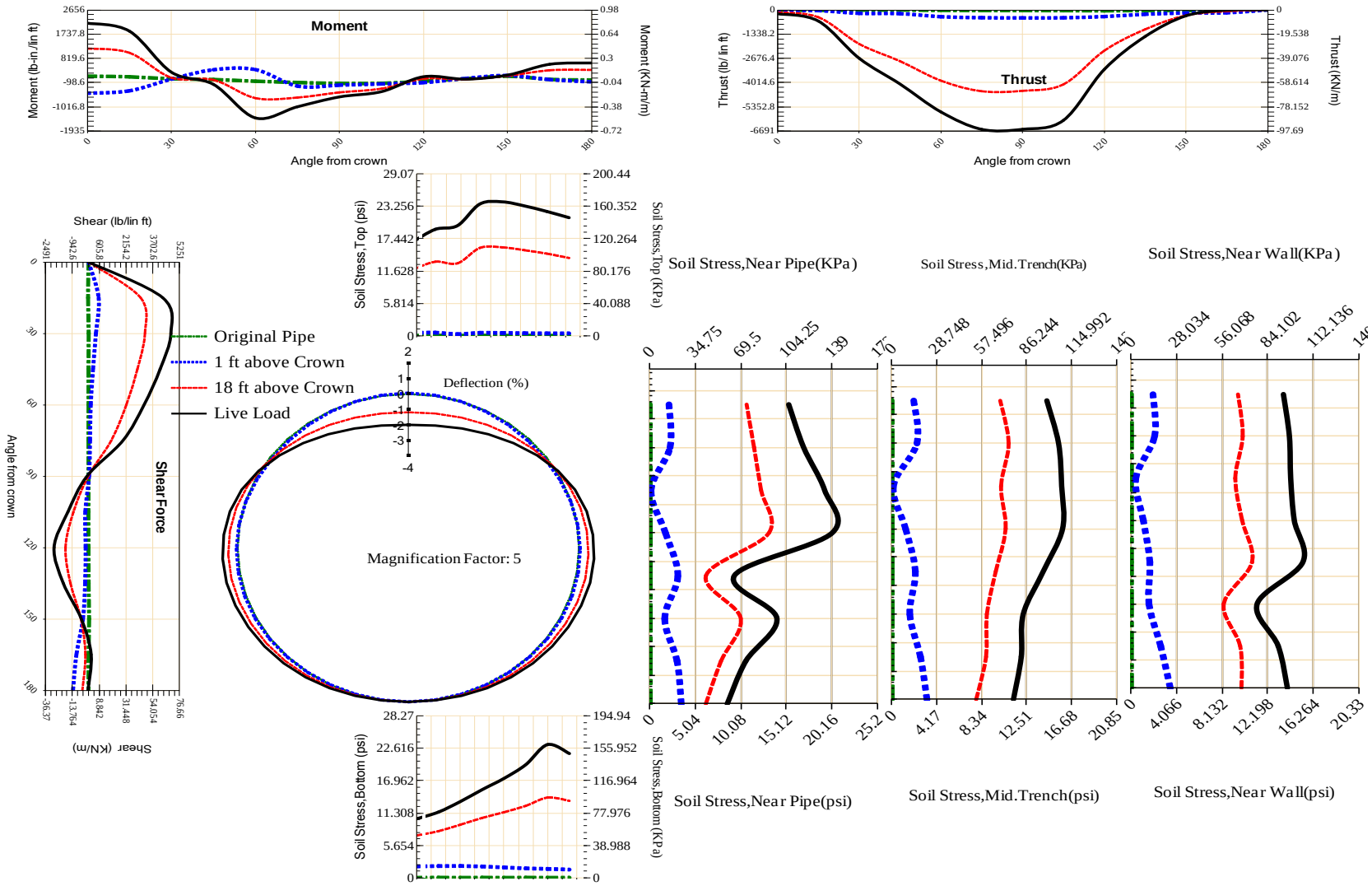

Figure A-326 Param-48-PW200-TR7OR-OD+48-EW10-H18-LiveLoad

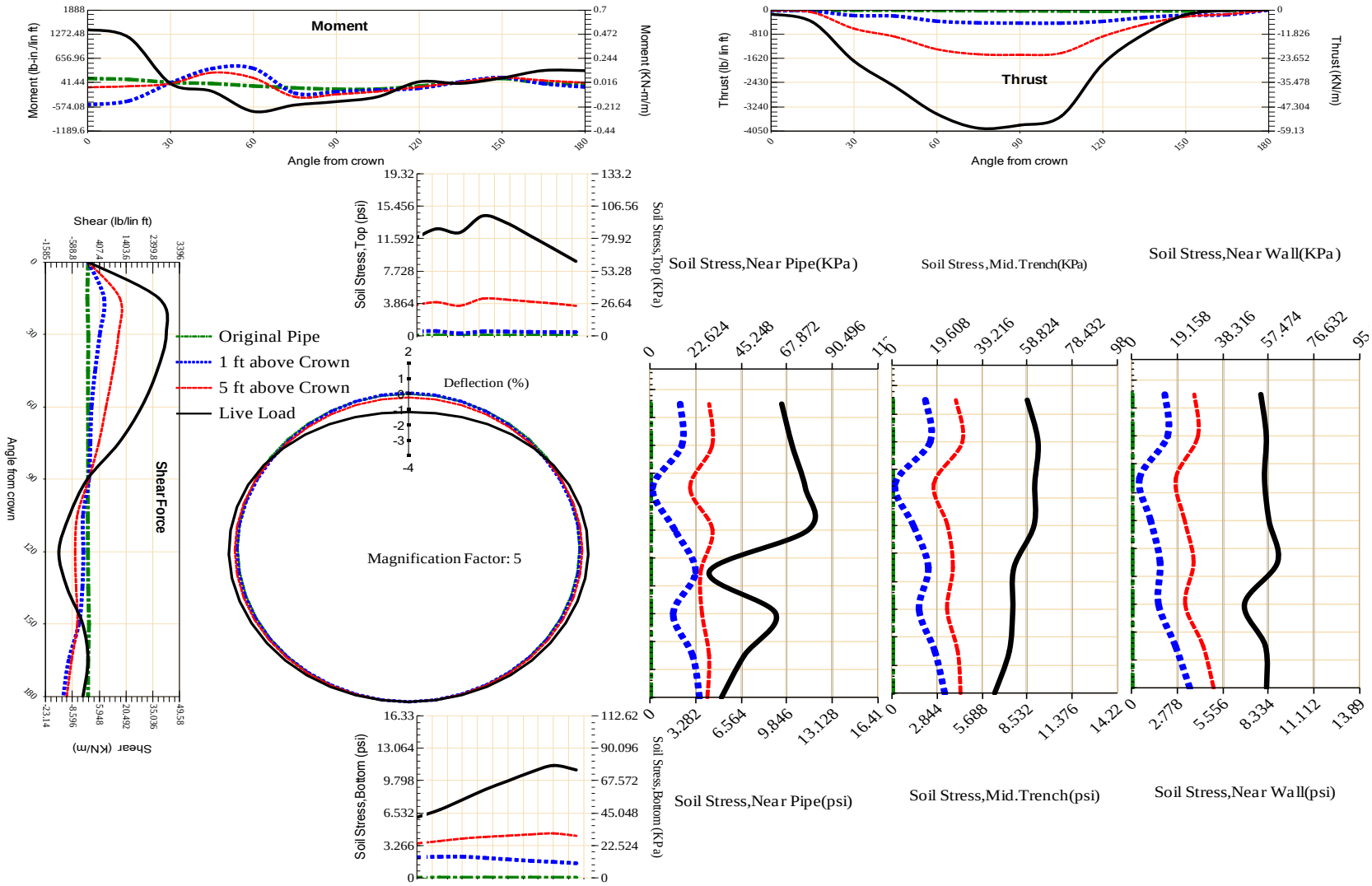

Figure A-327 Param-48-PW200-TR7OR-OD+48-EW10-H5-LiveLoad

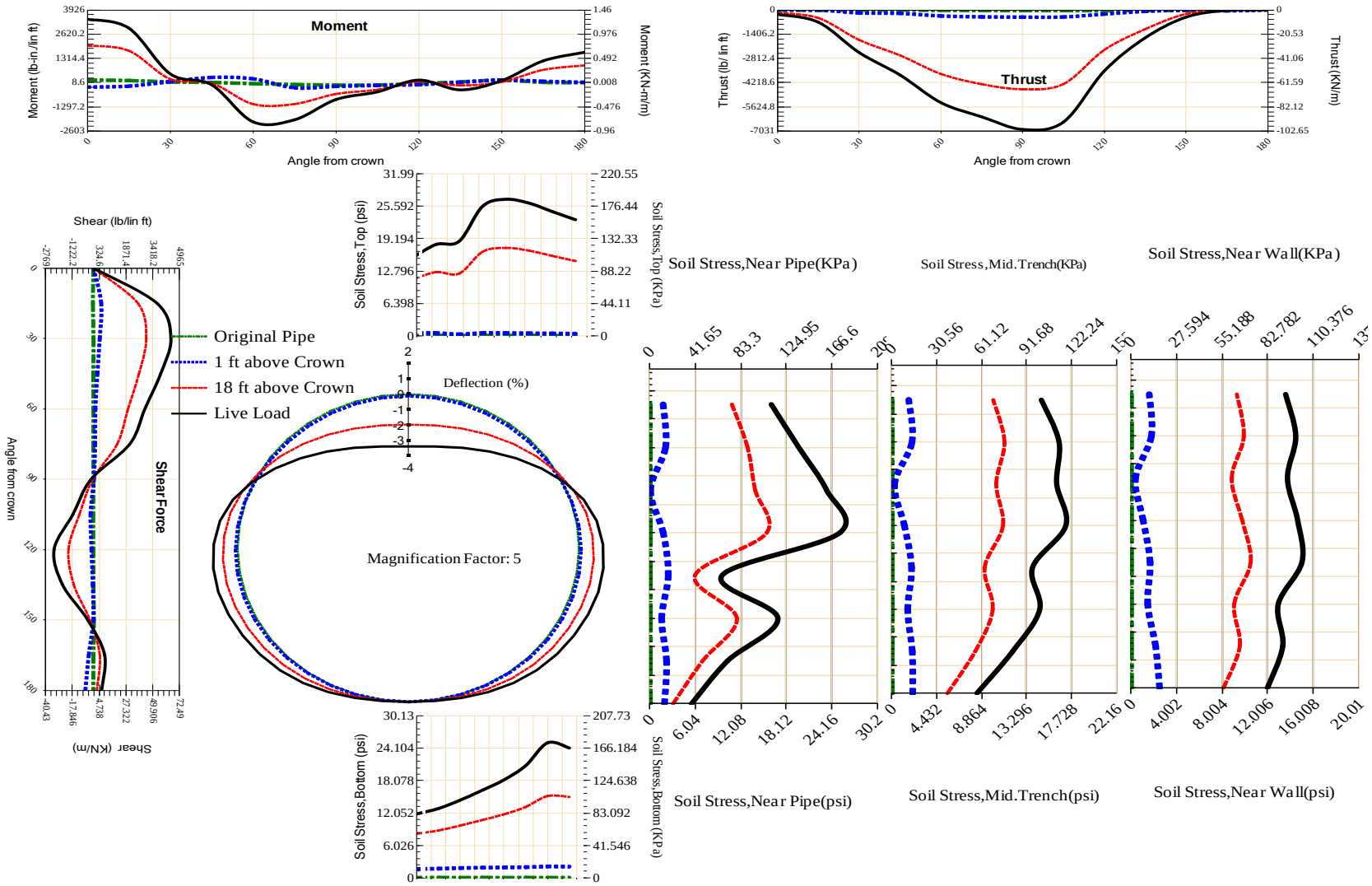

Figure A-328 Param-48-PW200-TR7OR-OD+48-EW3-H18-LiveLoad

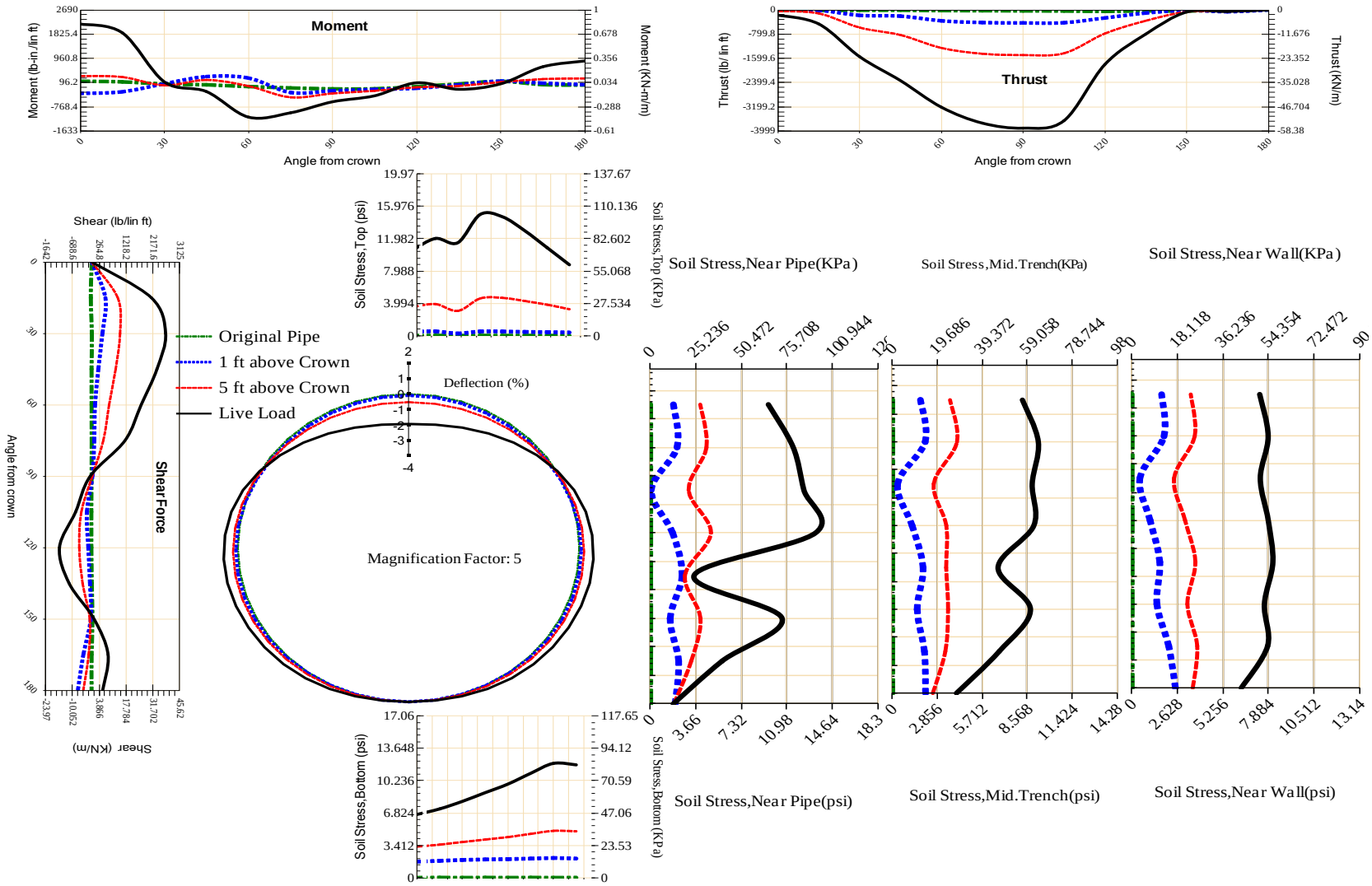

Figure A-329 Param-48-PW200-TR7OR-OD+48-EW3-H5-LiveLoad

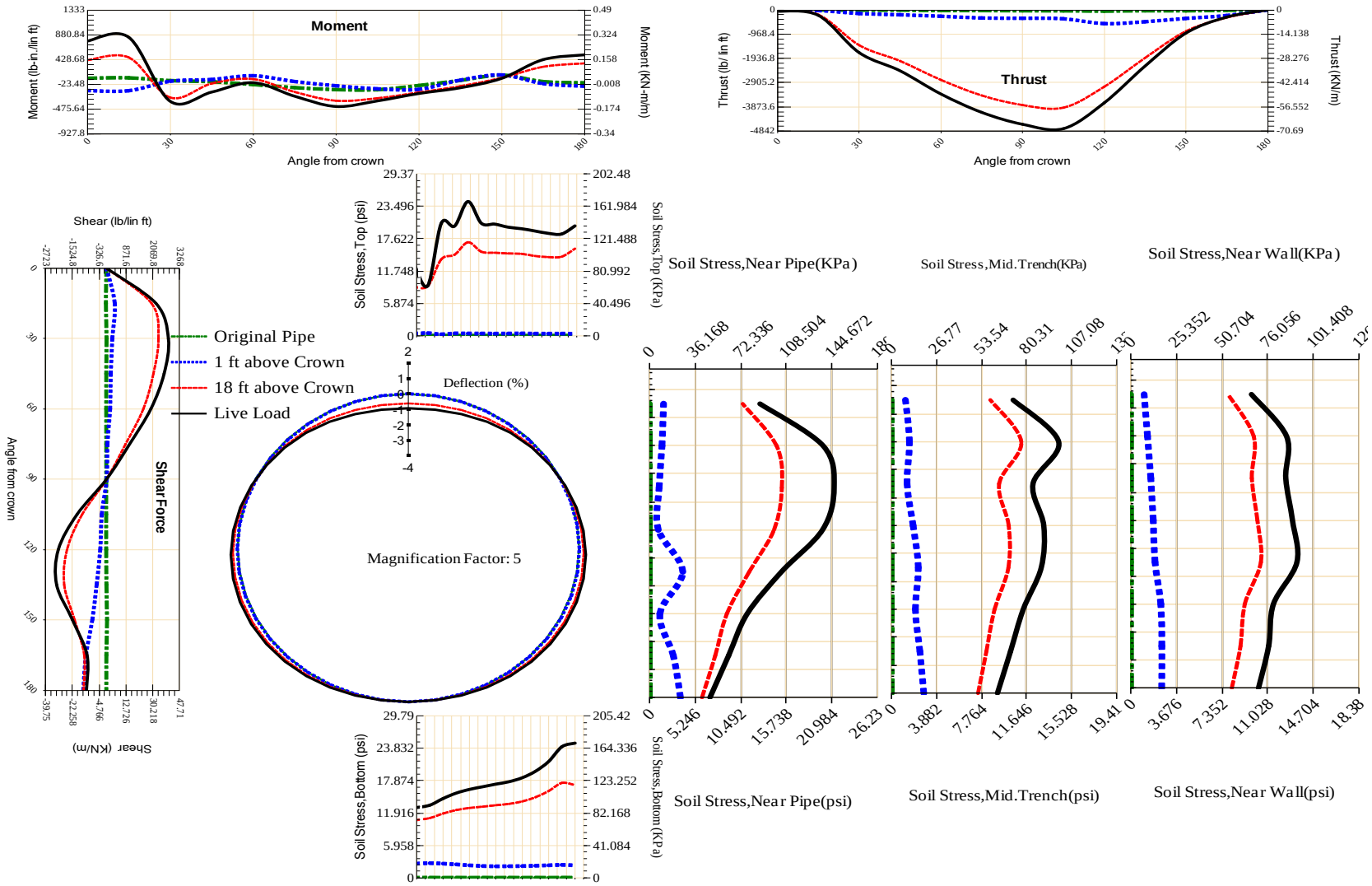

Figure A-330 Param-48-PW200-TR7SF-OD+108-EW10-H18-LiveLoad

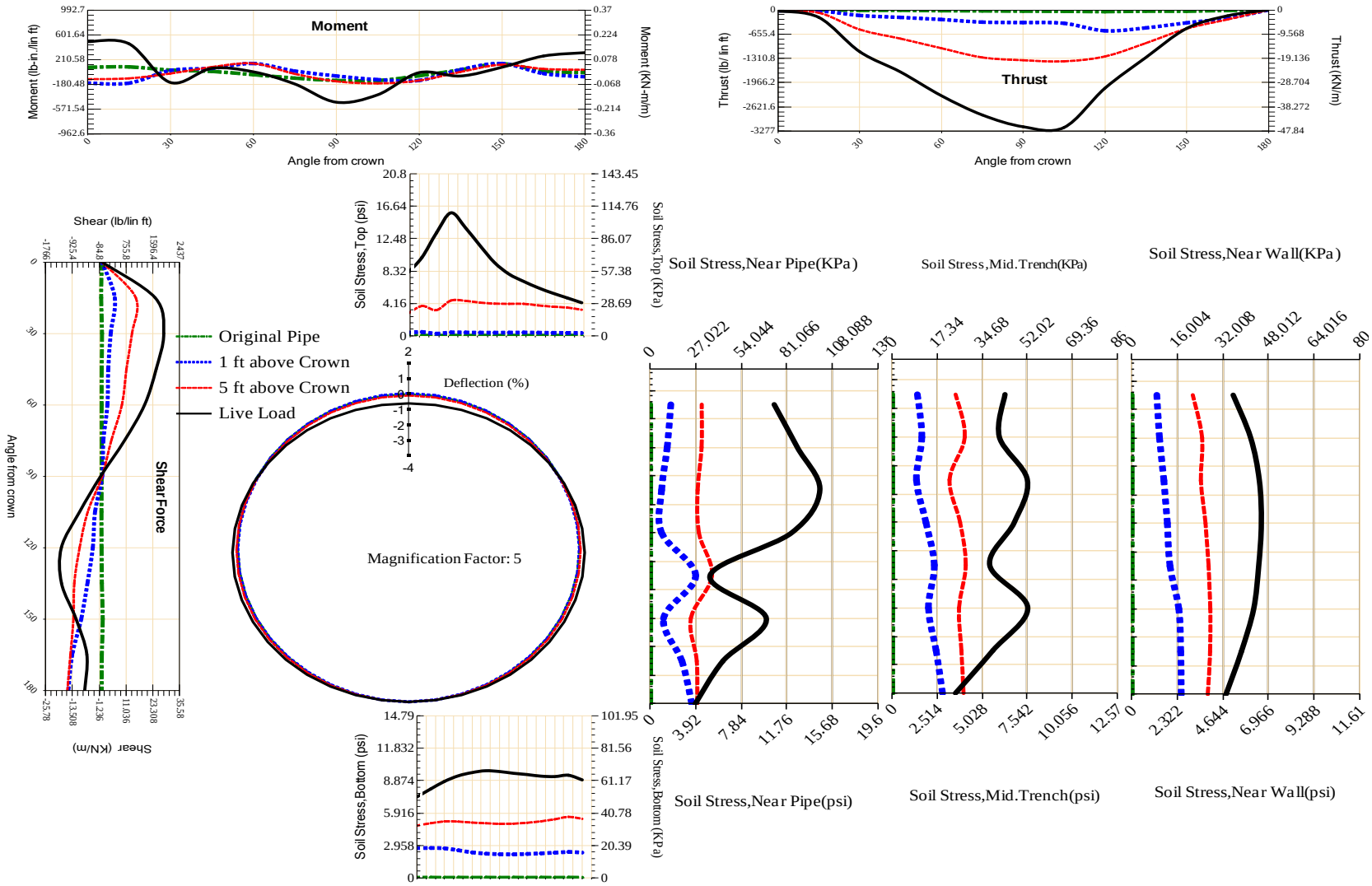

Figure A-331 Param-48-PW200-TR7SF-OD+108-EW10-H5-LiveLoad

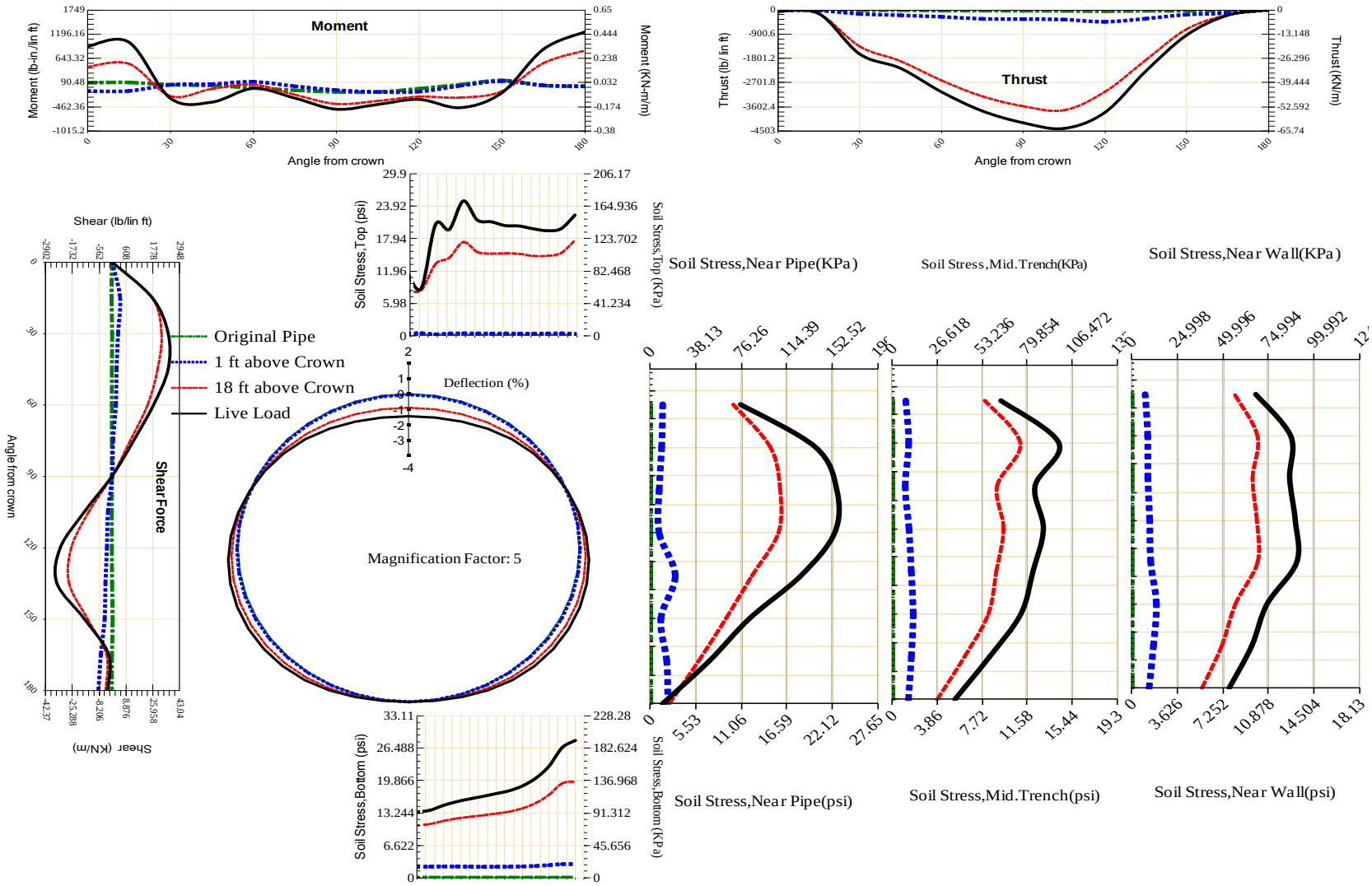

Figure A-332 Param-48-PW200-TR7SF-OD+108-EW3-H18-LiveLoad

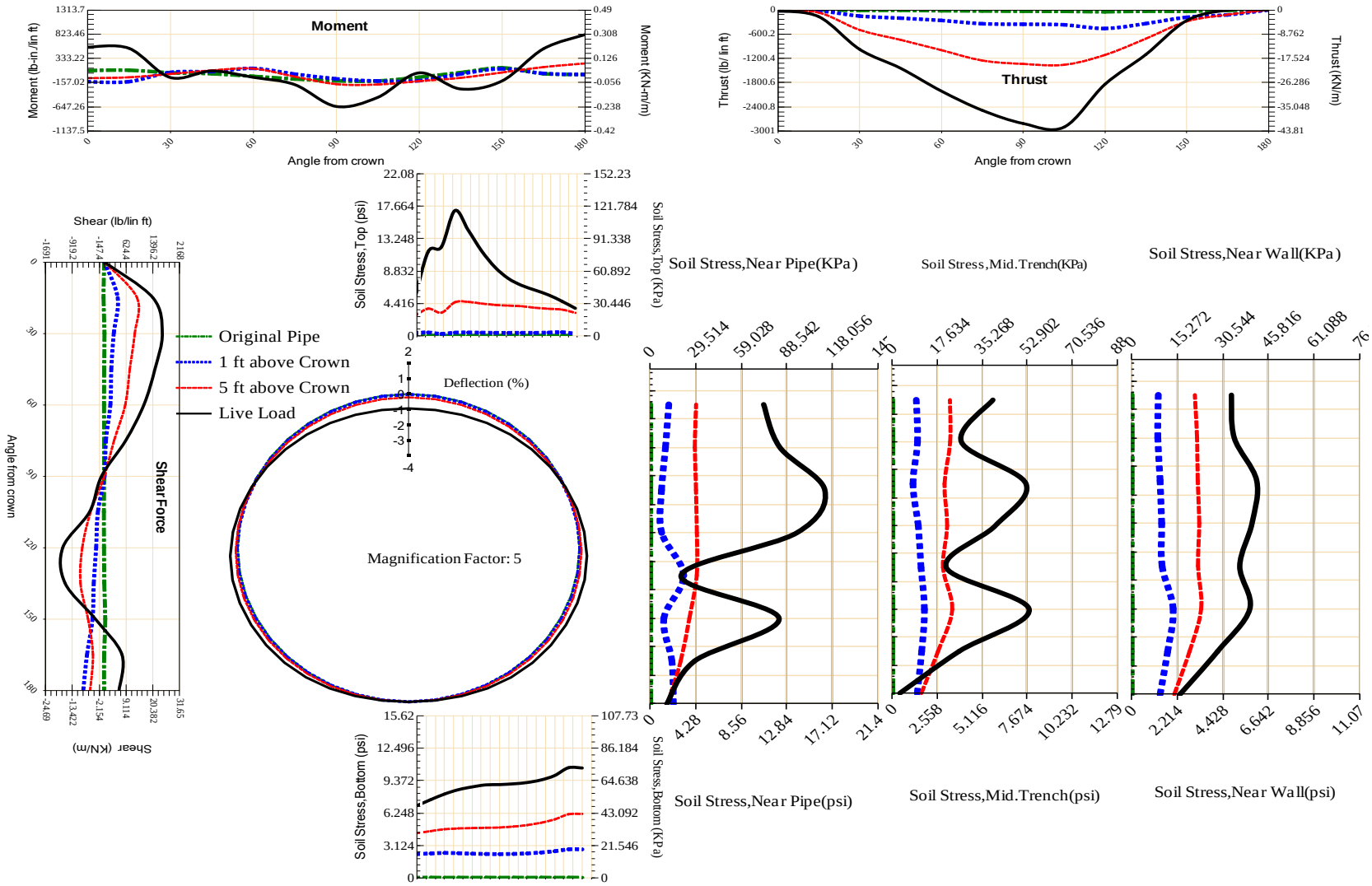

Figure A-333 Param-48-PW200-TR7SF-OD+108-EW3-H5-LiveLoad

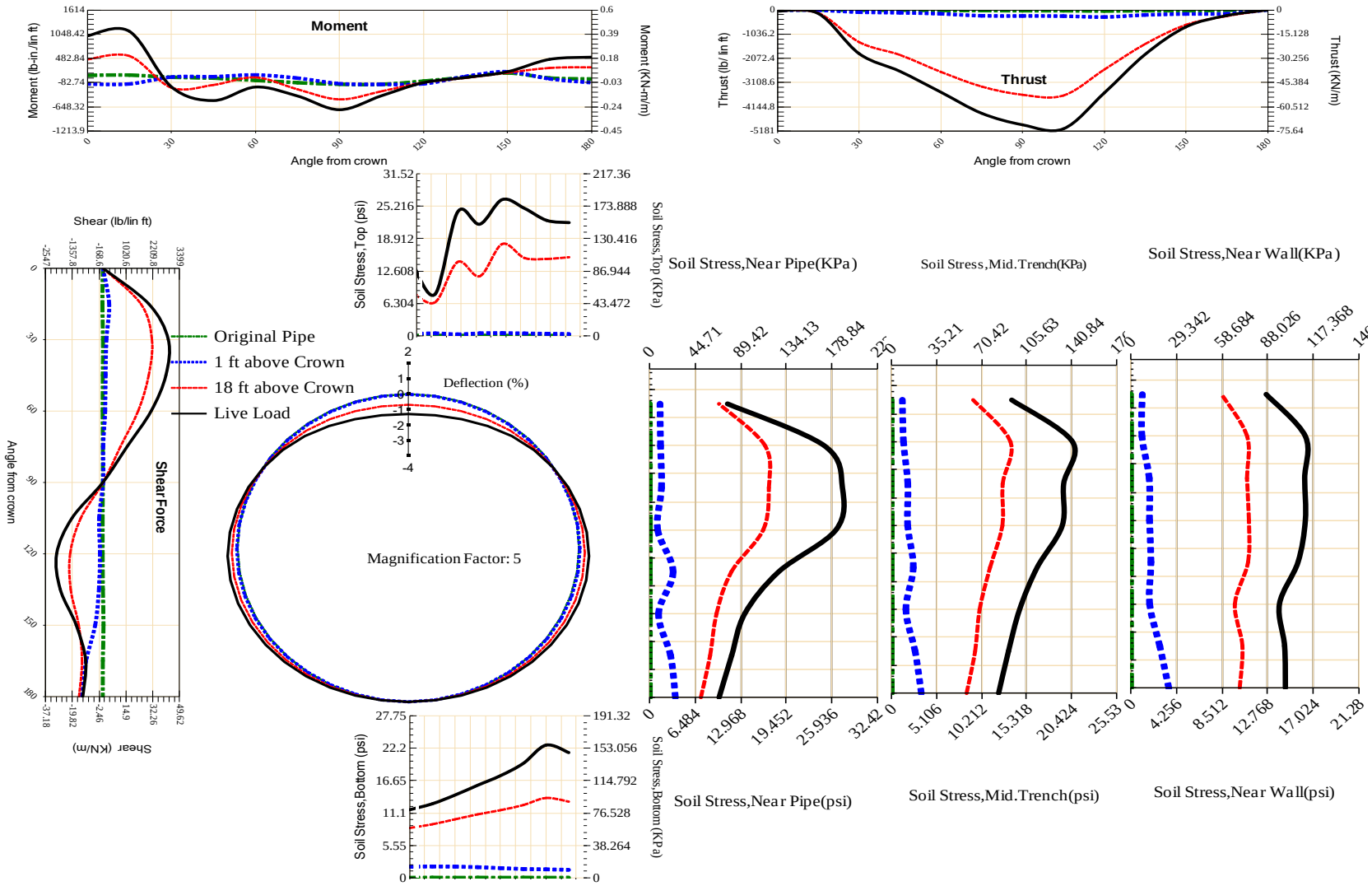

Figure A-334 Param-48-PW200-TR7SF-OD+48-EW10-H18-LiveLoad

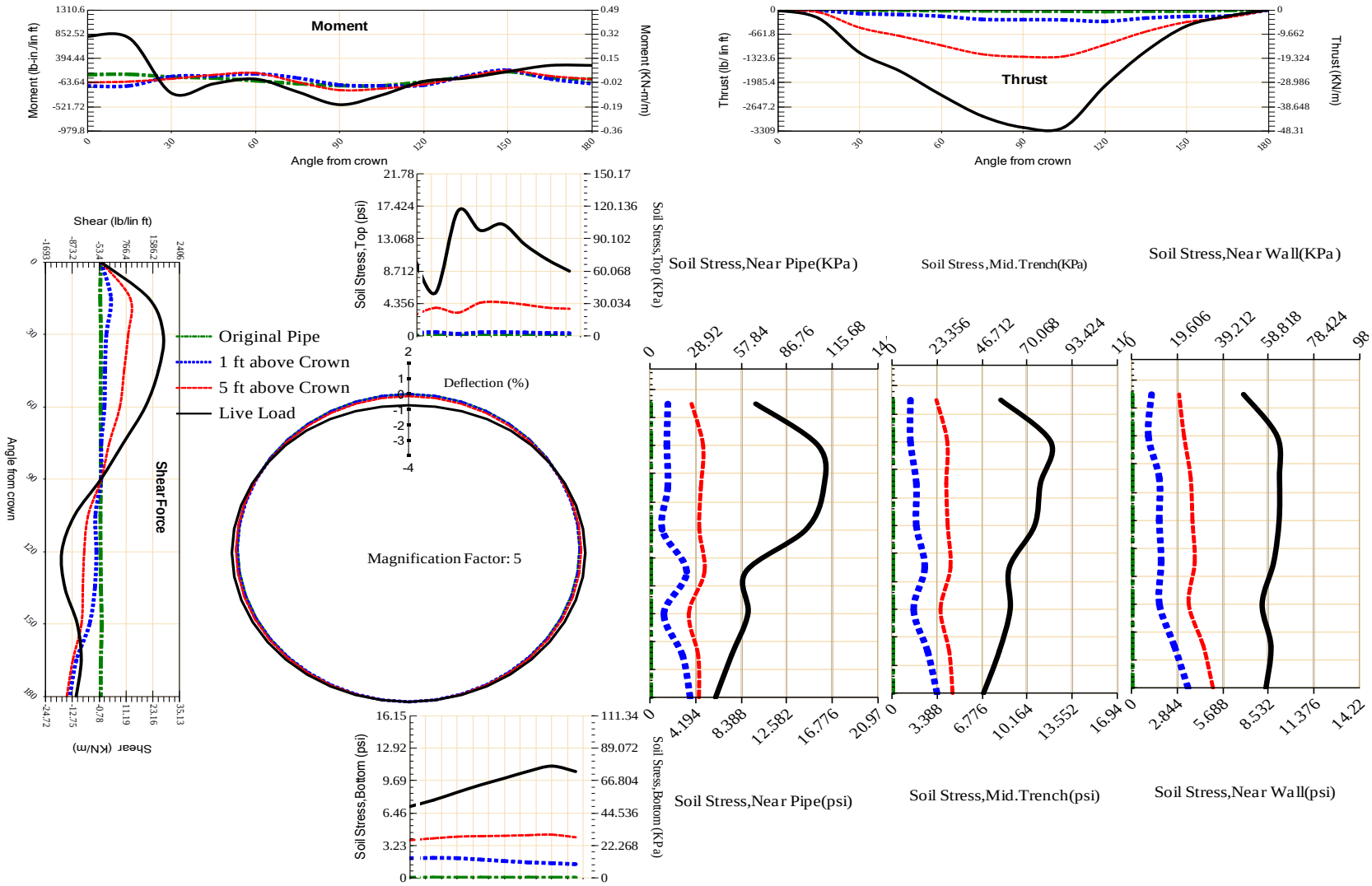

Figure A-335 Param-48-PW200-TR7SF-OD+48-EW10-H5-LiveLoad

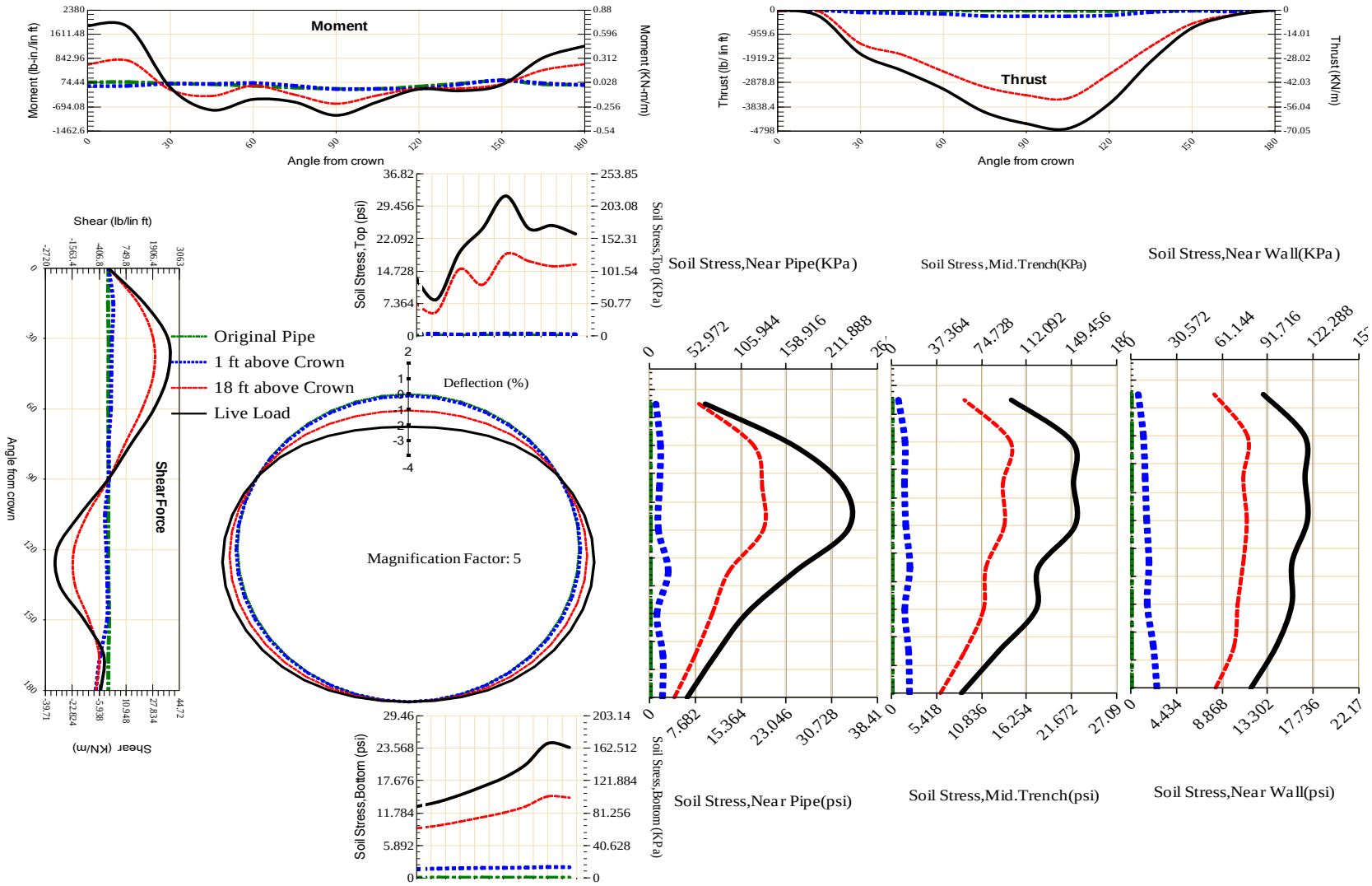

Figure A-336 Param-48-PW200-TR7SF-OD+48-EW3-H18-LiveLoad

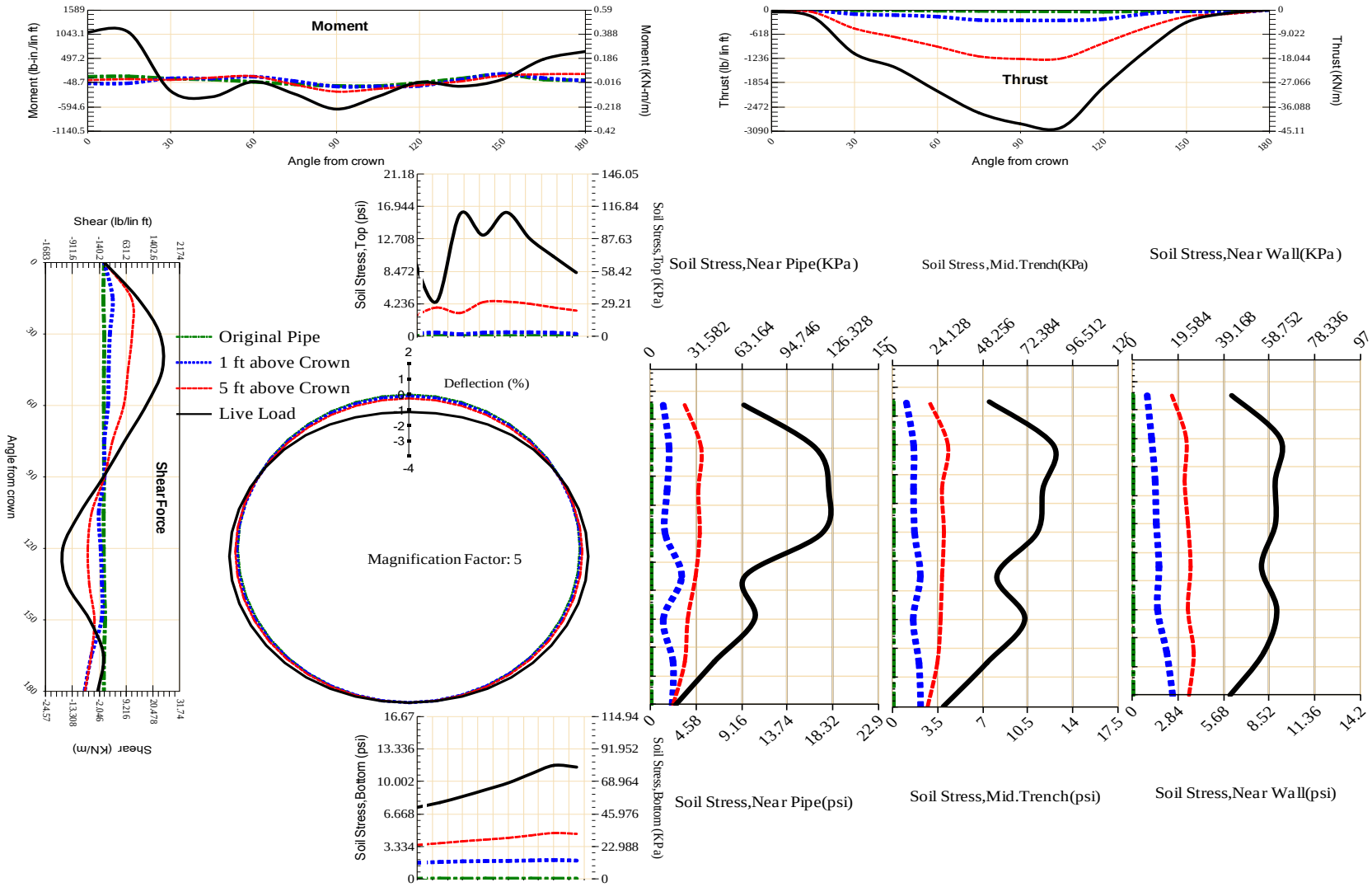

Figure A-337 Param-48-PW200-TR7SF-OD+48-EW3-H5-LiveLoad

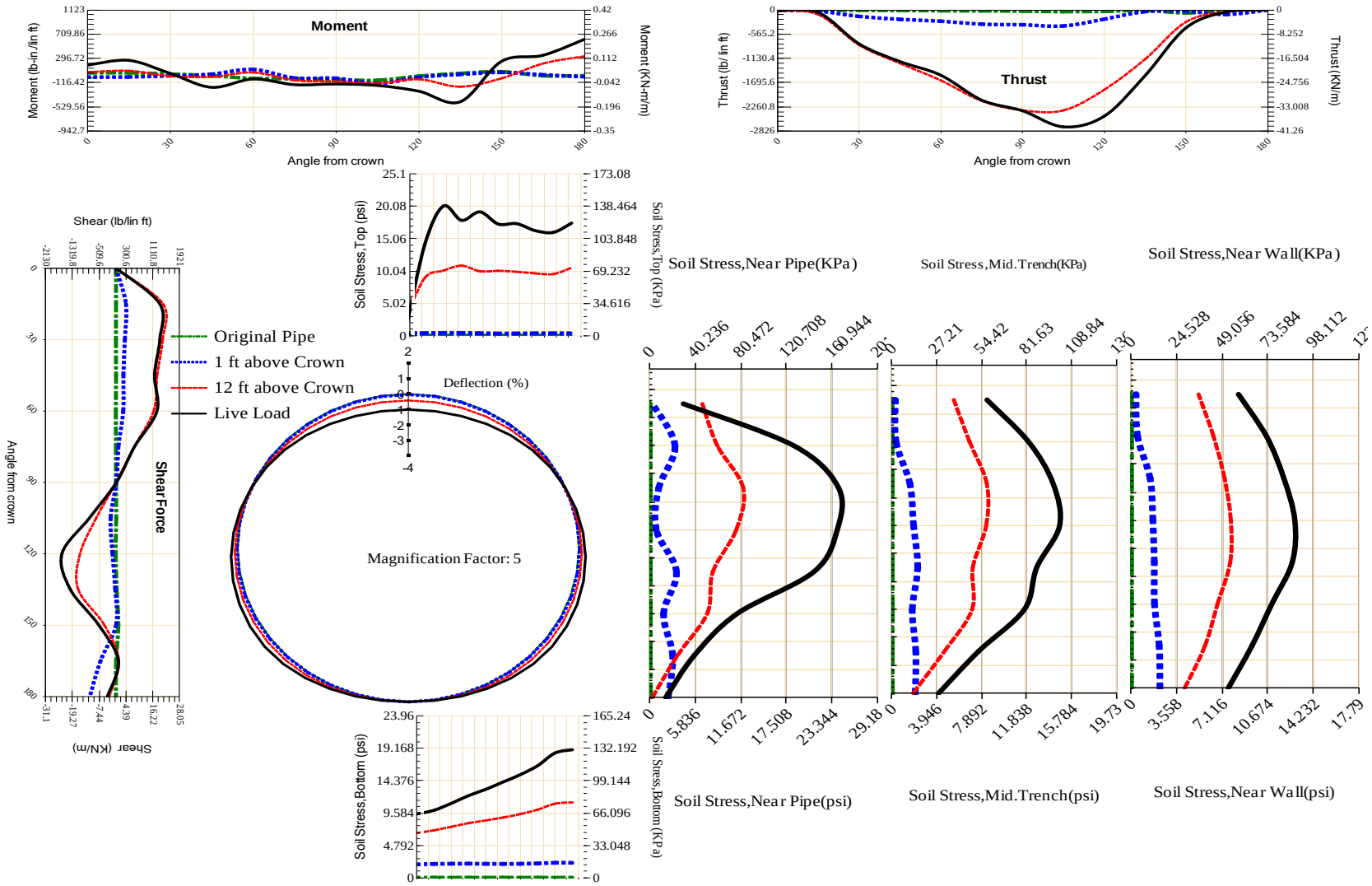

Figure A-338 Param-48-PW230-SF10SF-OD+72-EW5-H12-LiveLoad

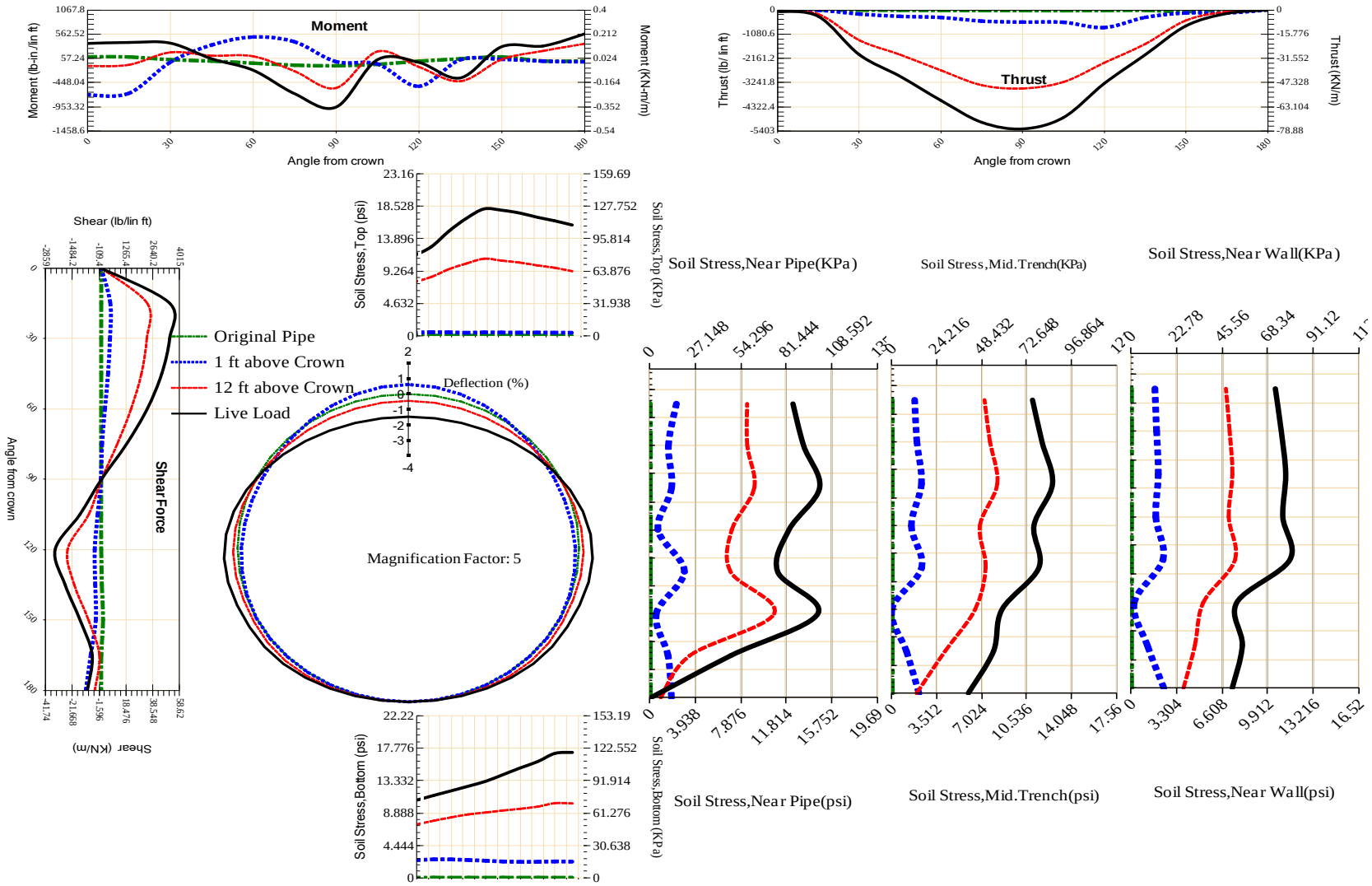

Figure A-339 Param-48-PW230-SF3OR-OD+72-EW5-H12-LiveLoad

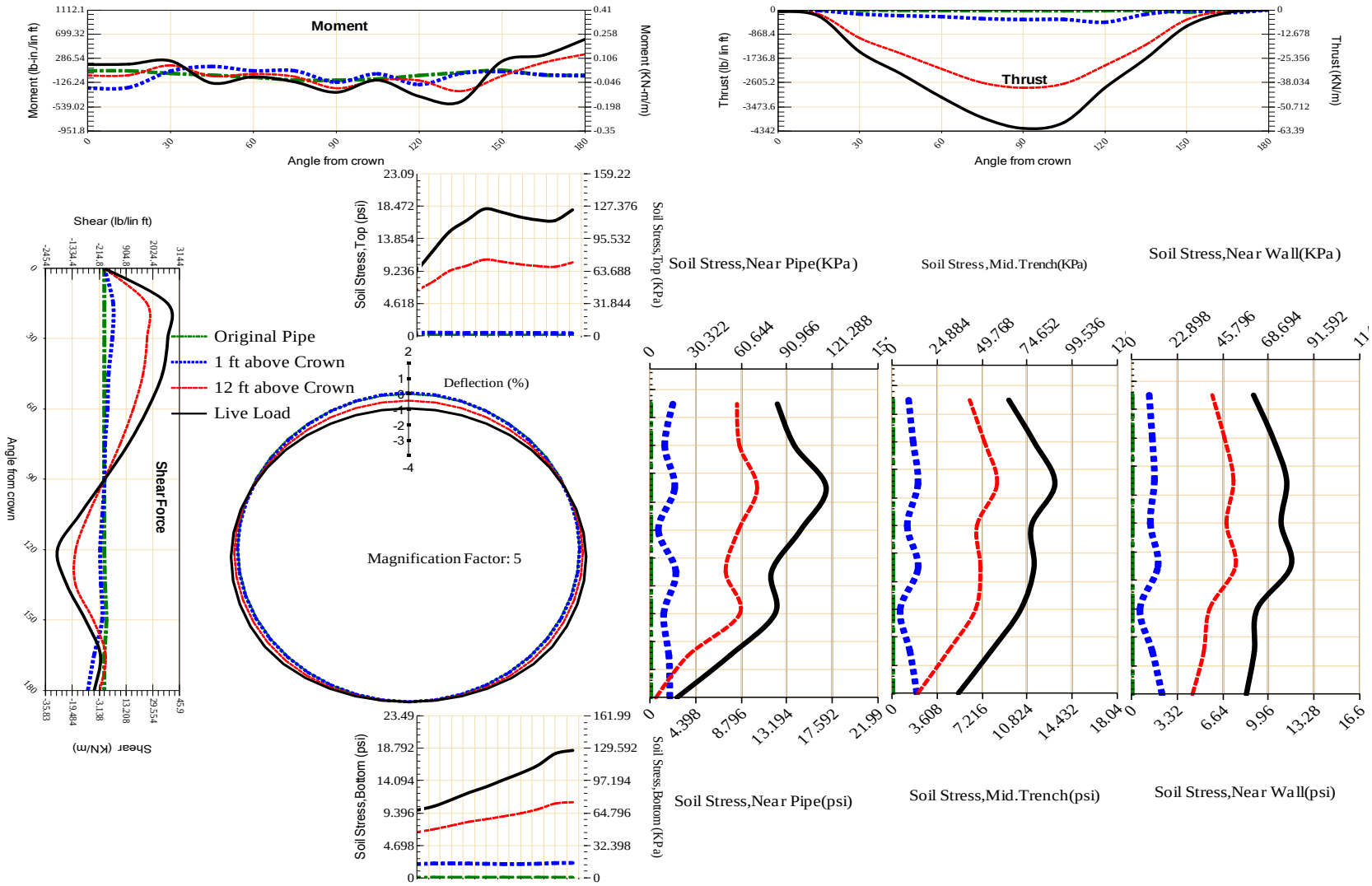

Figure A-340 Param-48-PW230-SF3TR-OD+72-EW5-H12-LiveLoad

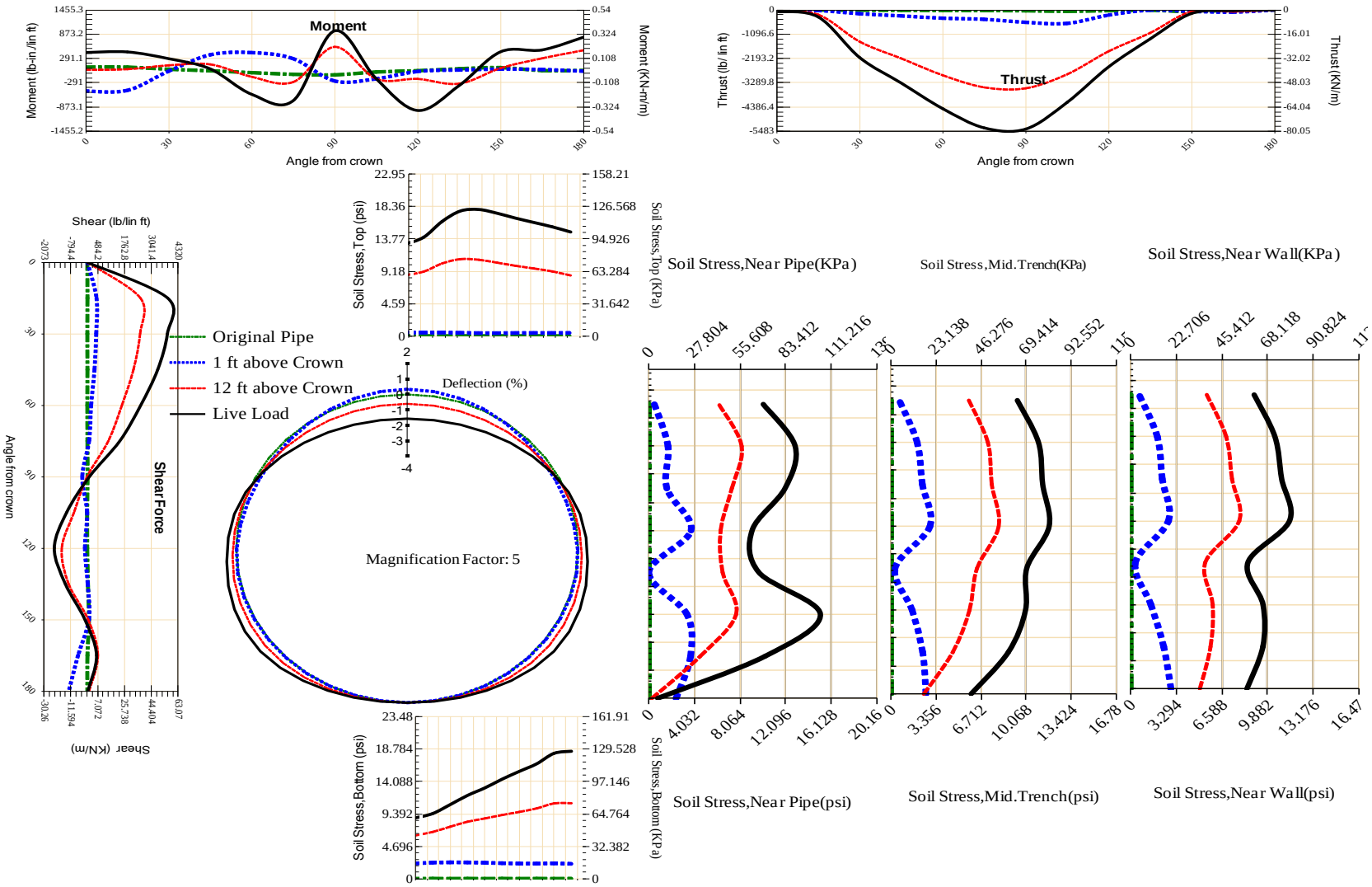

Figure A-341 Param-48-PW230-SF5OR-OD+72-EW5-H12-LiveLoad

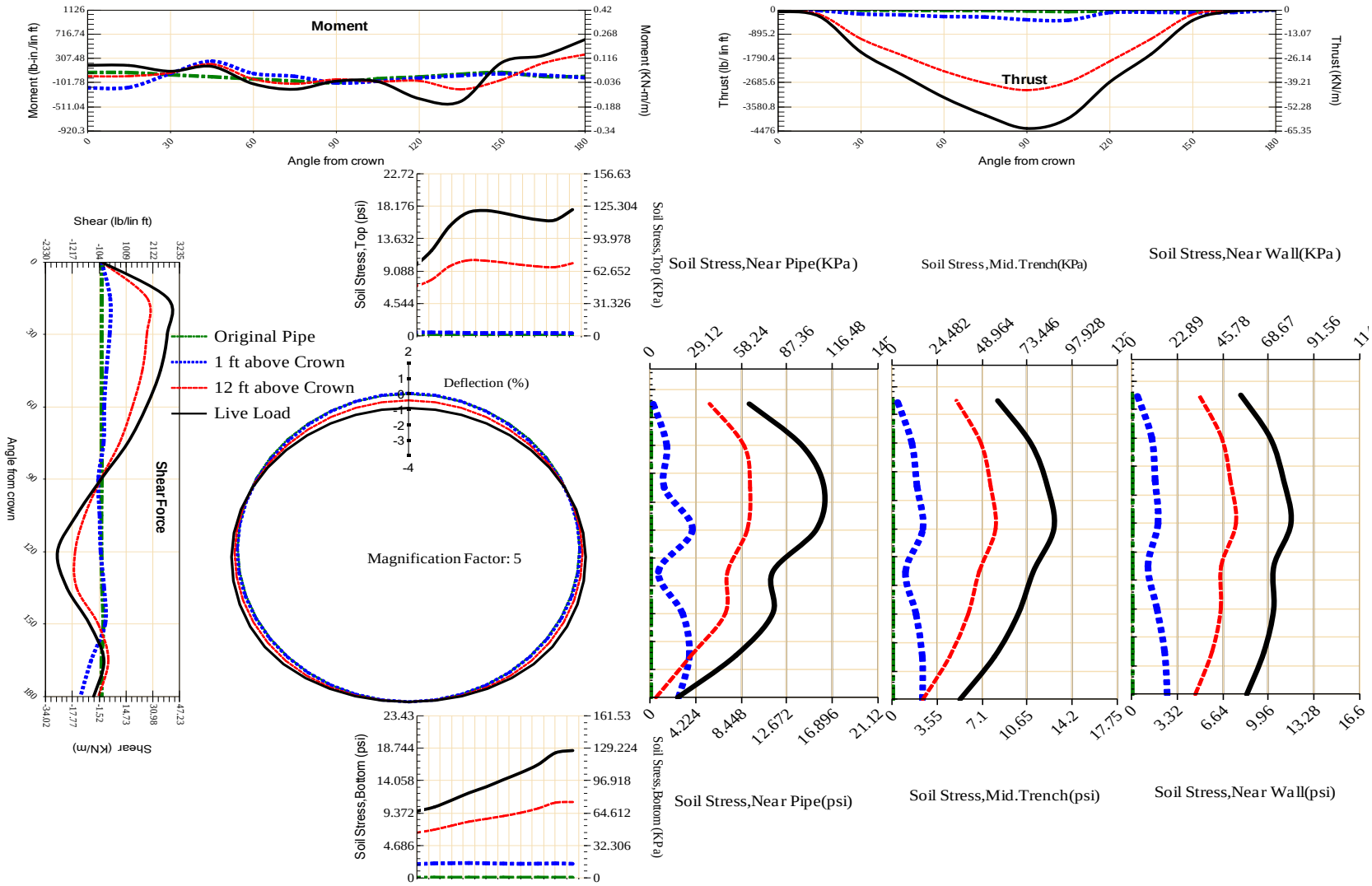

Figure A-342 Param-48-PW230-SF5TR-OD+72-EW5-H12-LiveLoad

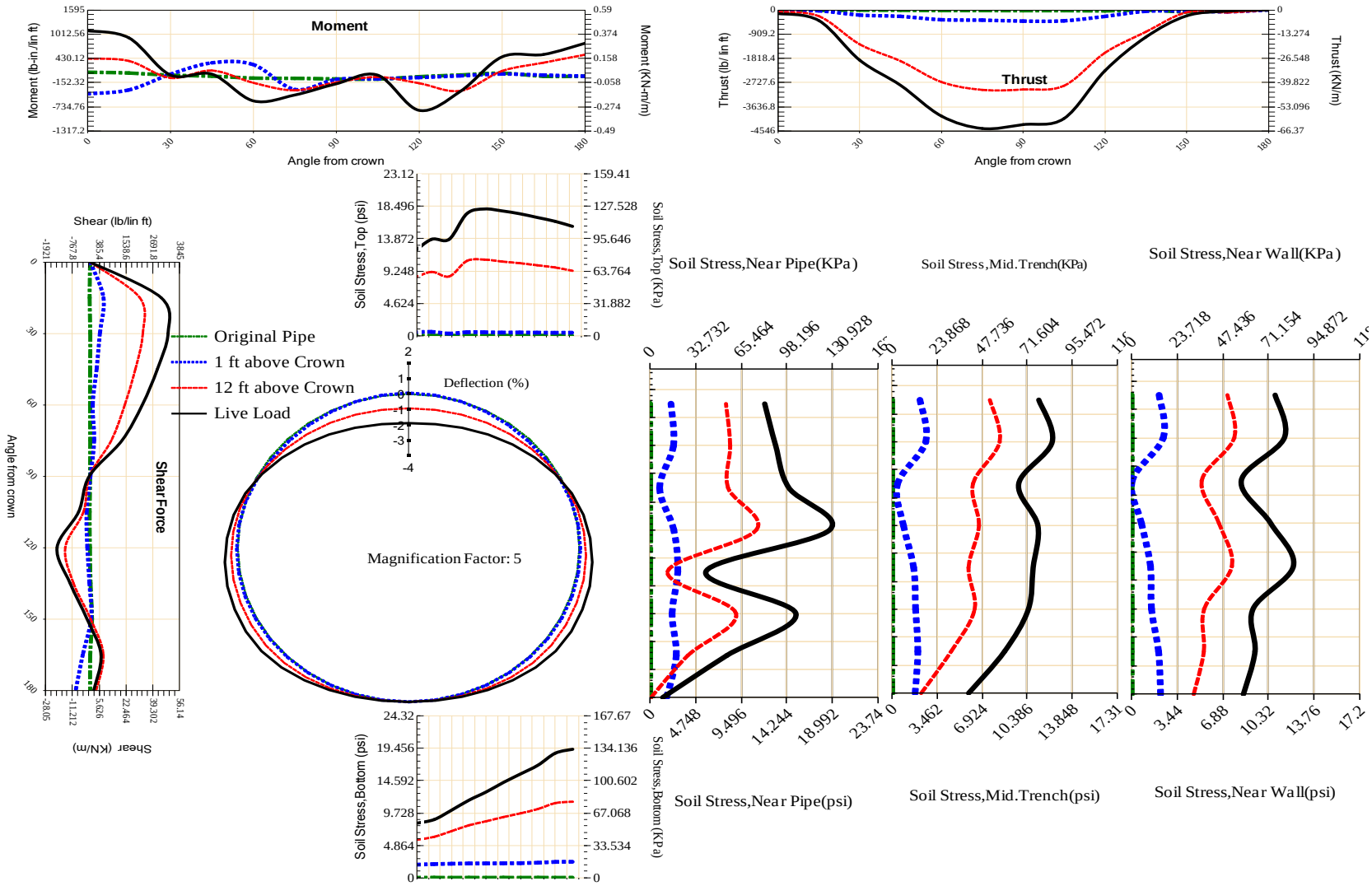

Figure A-343 Param-48-PW230-SF7OR-OD+72-EW5-H12-LiveLoad

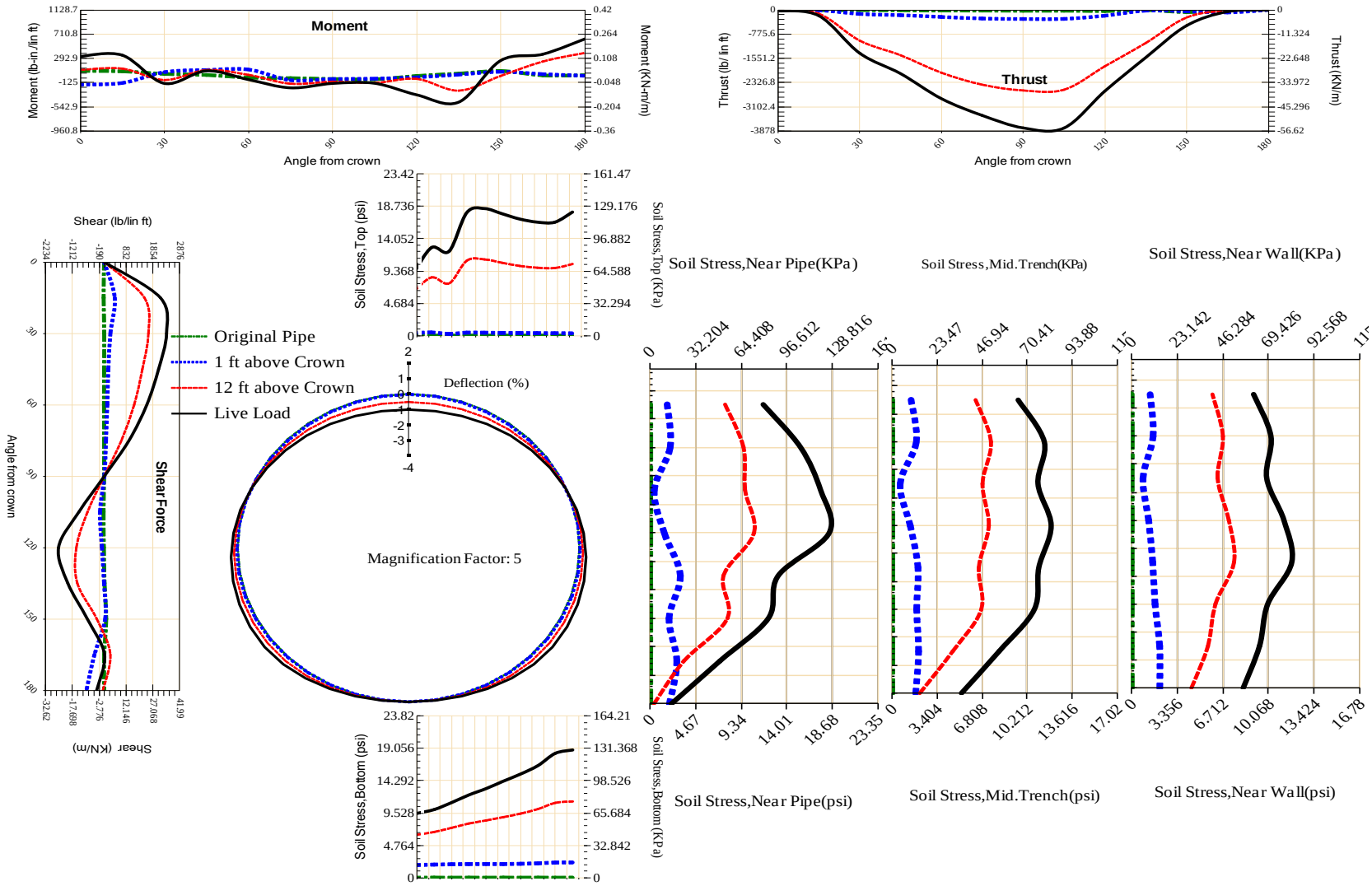

Figure A-344 Param-48-PW230-SF7TR-OD+72-EW5-H12-LiveLoad

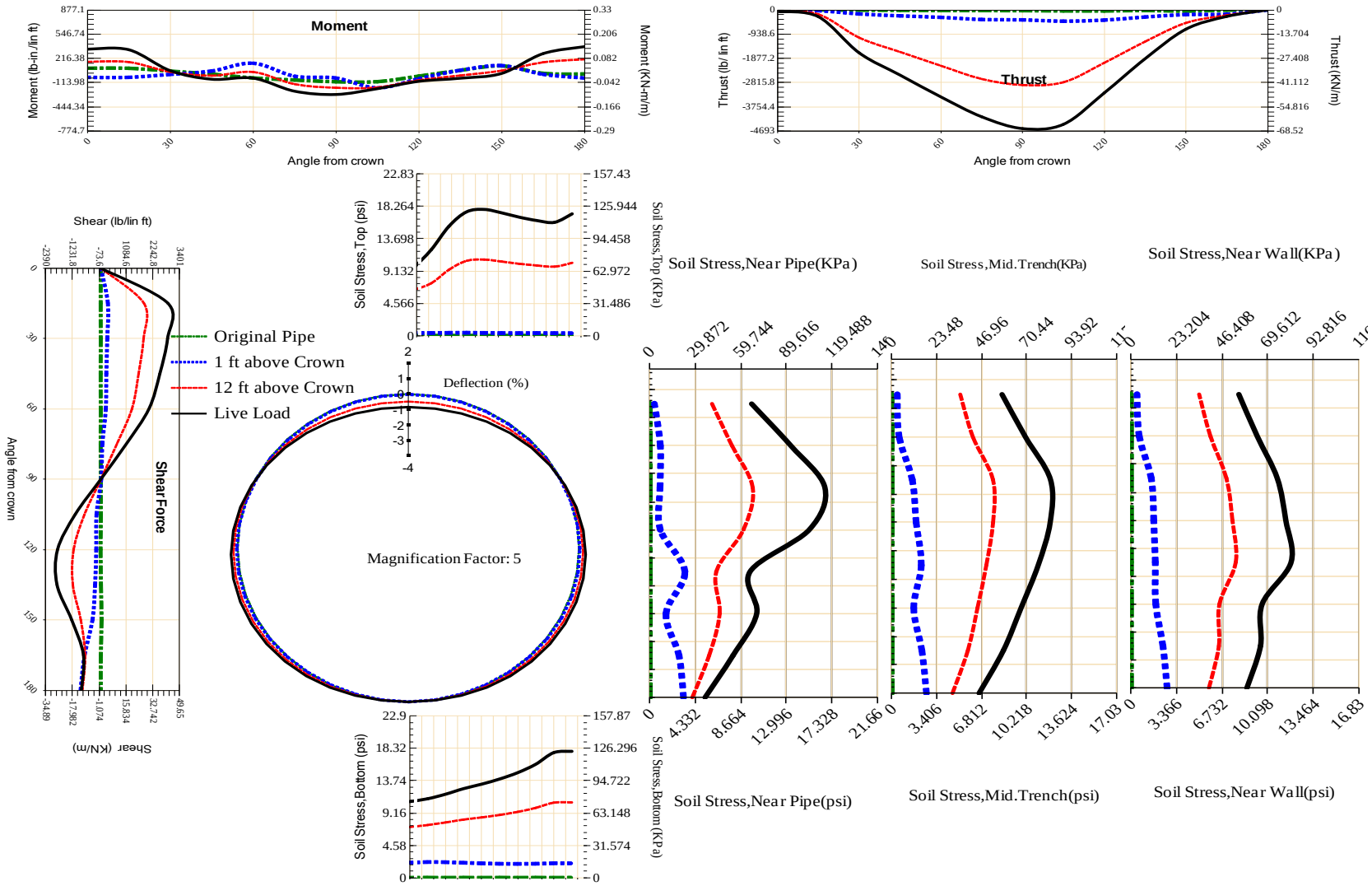

Figure A-345 Param-48-PW230-TR10TR-OD+72-EW5-H12-LiveLoad

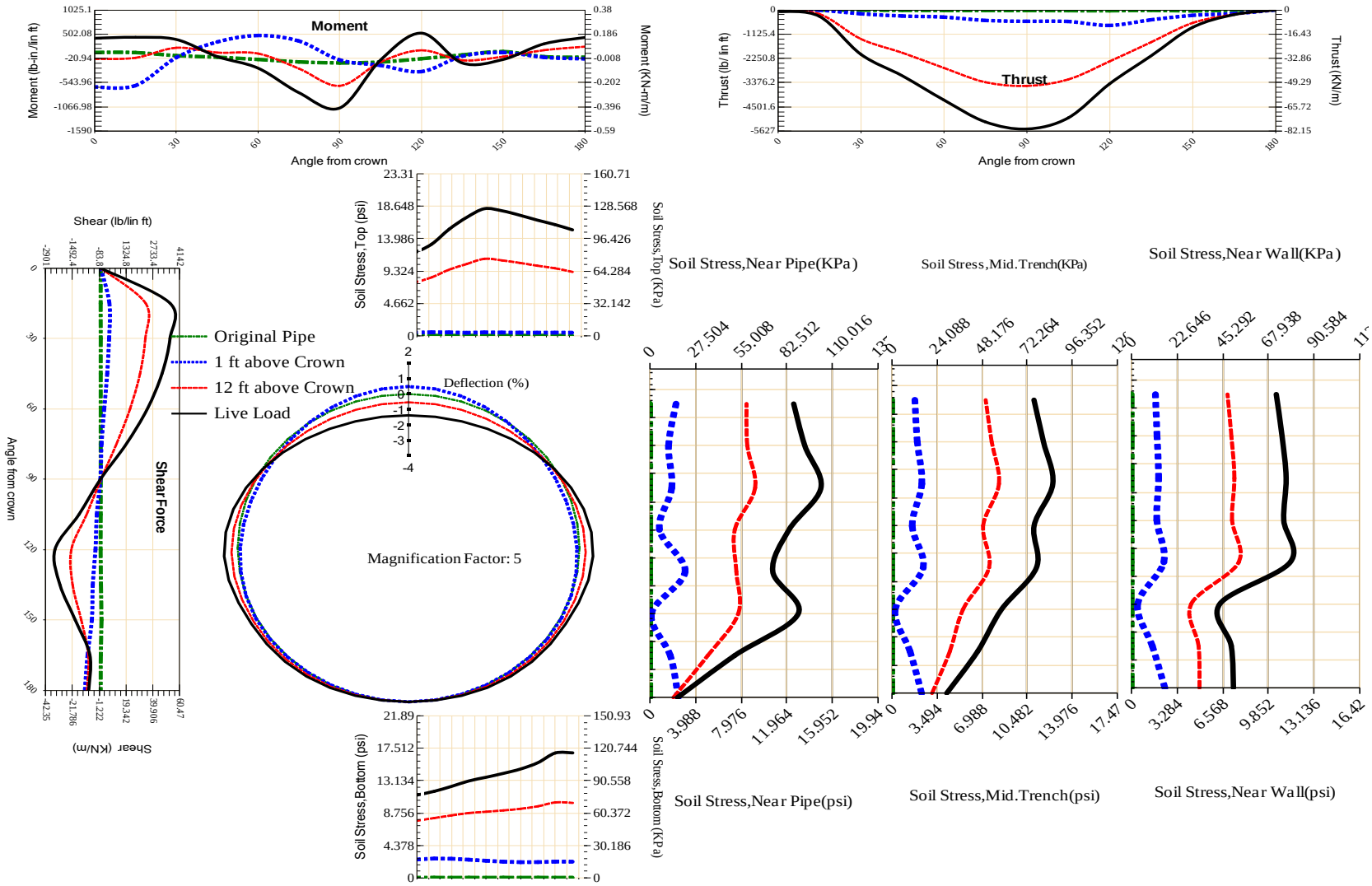

Figure A-346 Param-48-PW230-TR3OR-OD+72-EW5-H12-LiveLoad

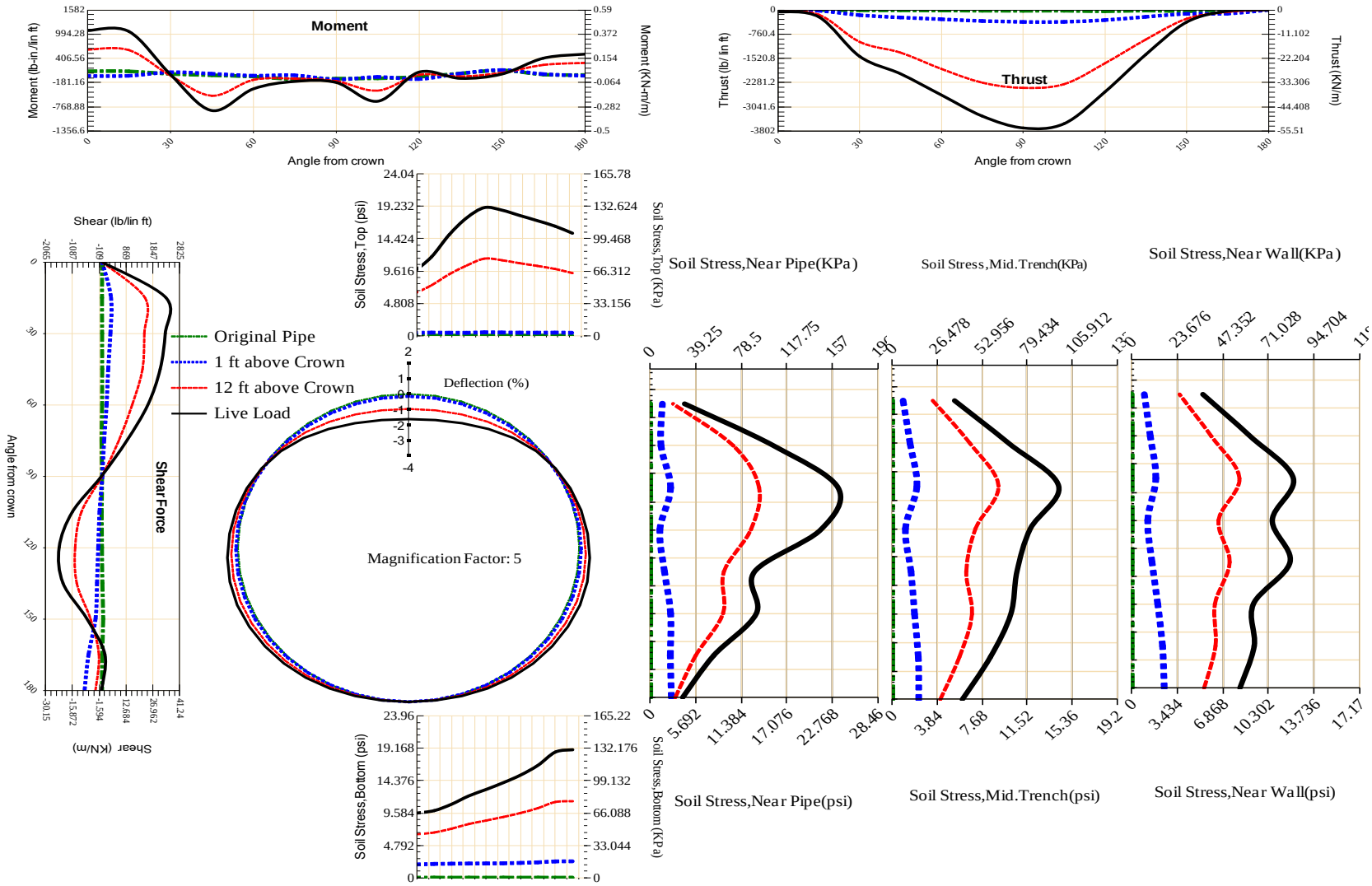

Figure A-347 Param-48-PW230-TR3SF-OD+72-EW5-H12-LiveLoad

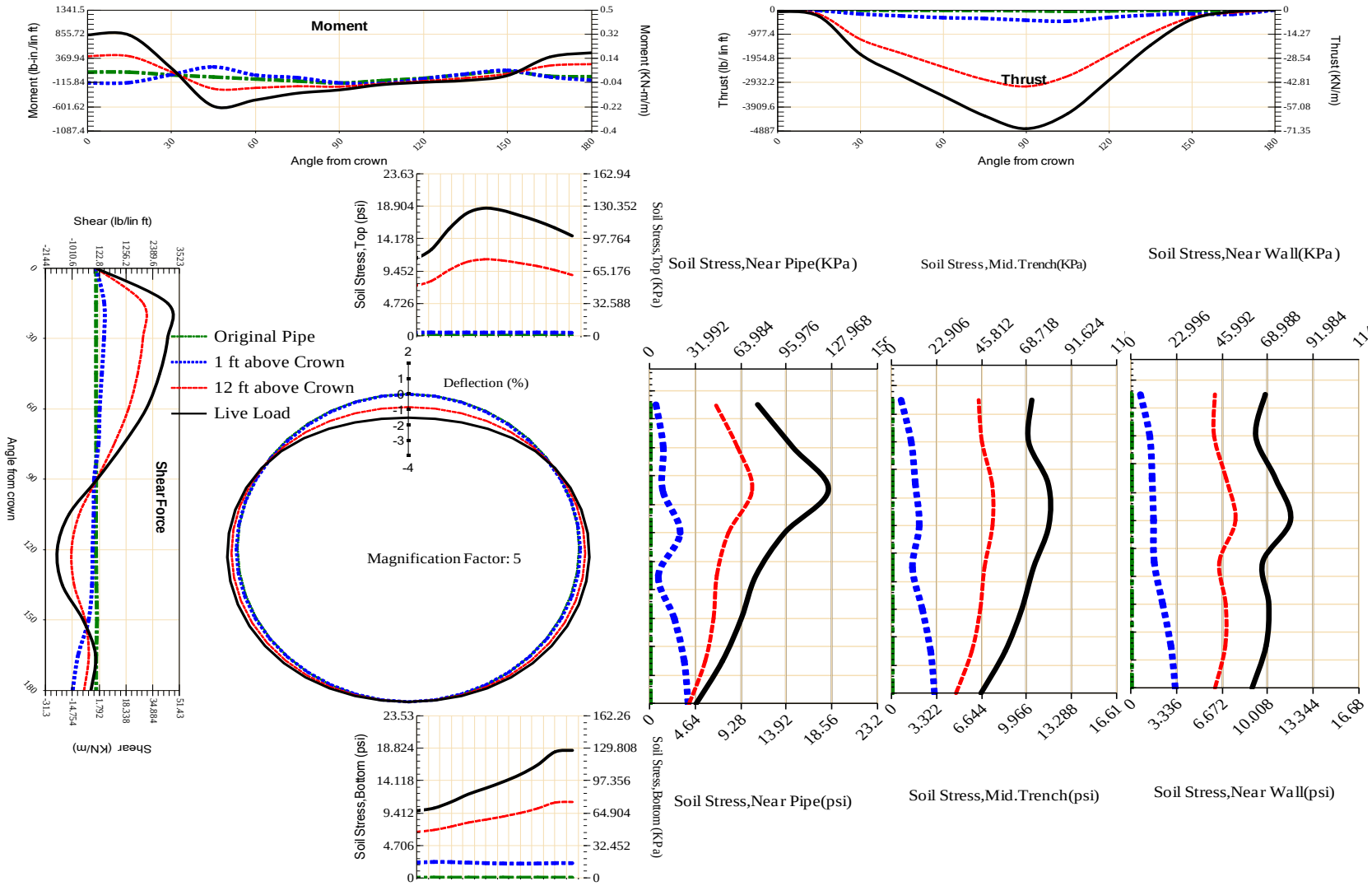

Figure A-348 Param-48-PW230-TR5OR-OD+72-EW5-H12-LiveLoad

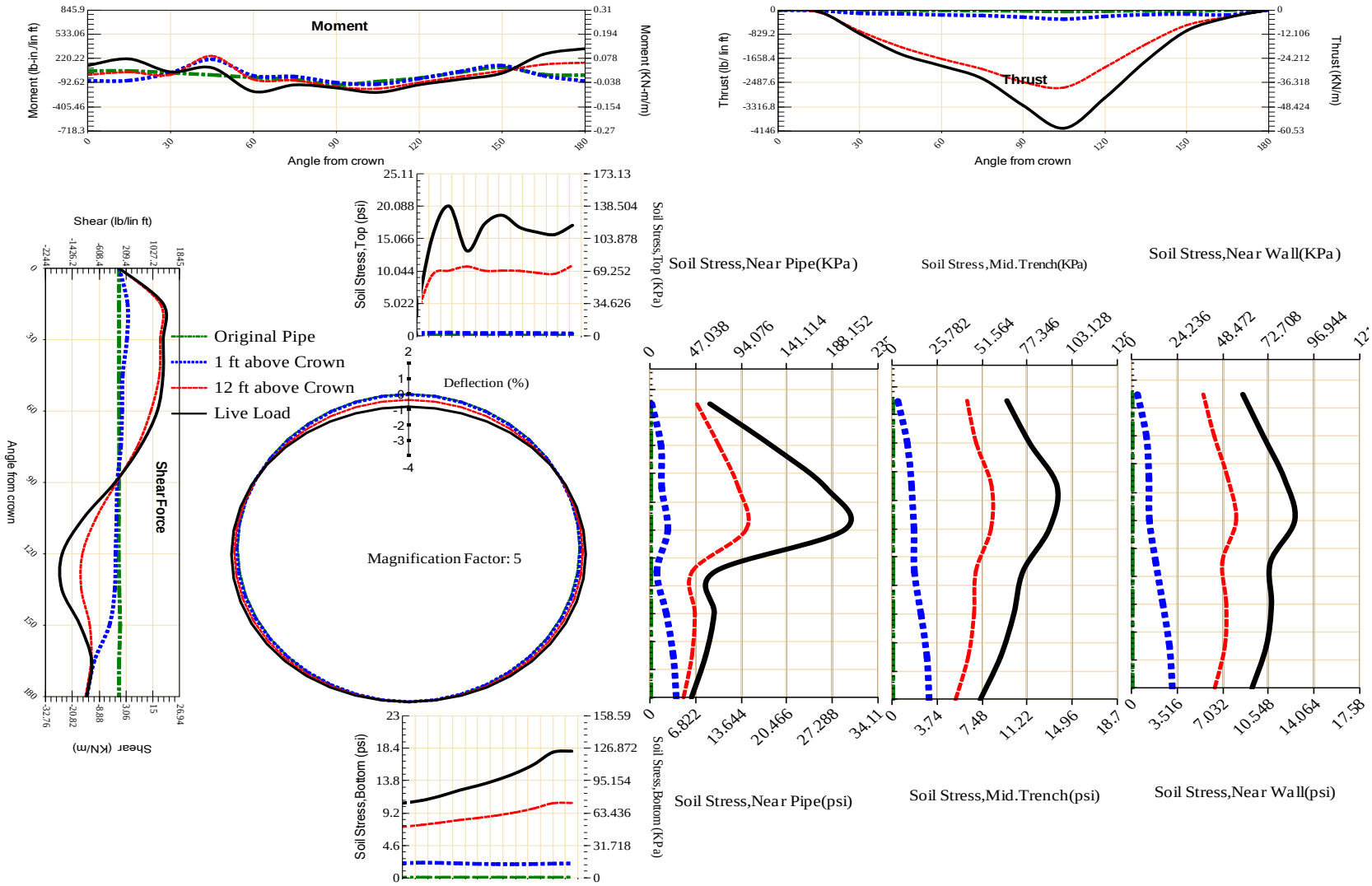

Figure A-349 Param-48-PW230-TR5SF-OD+72-EW5-H12-LiveLoad

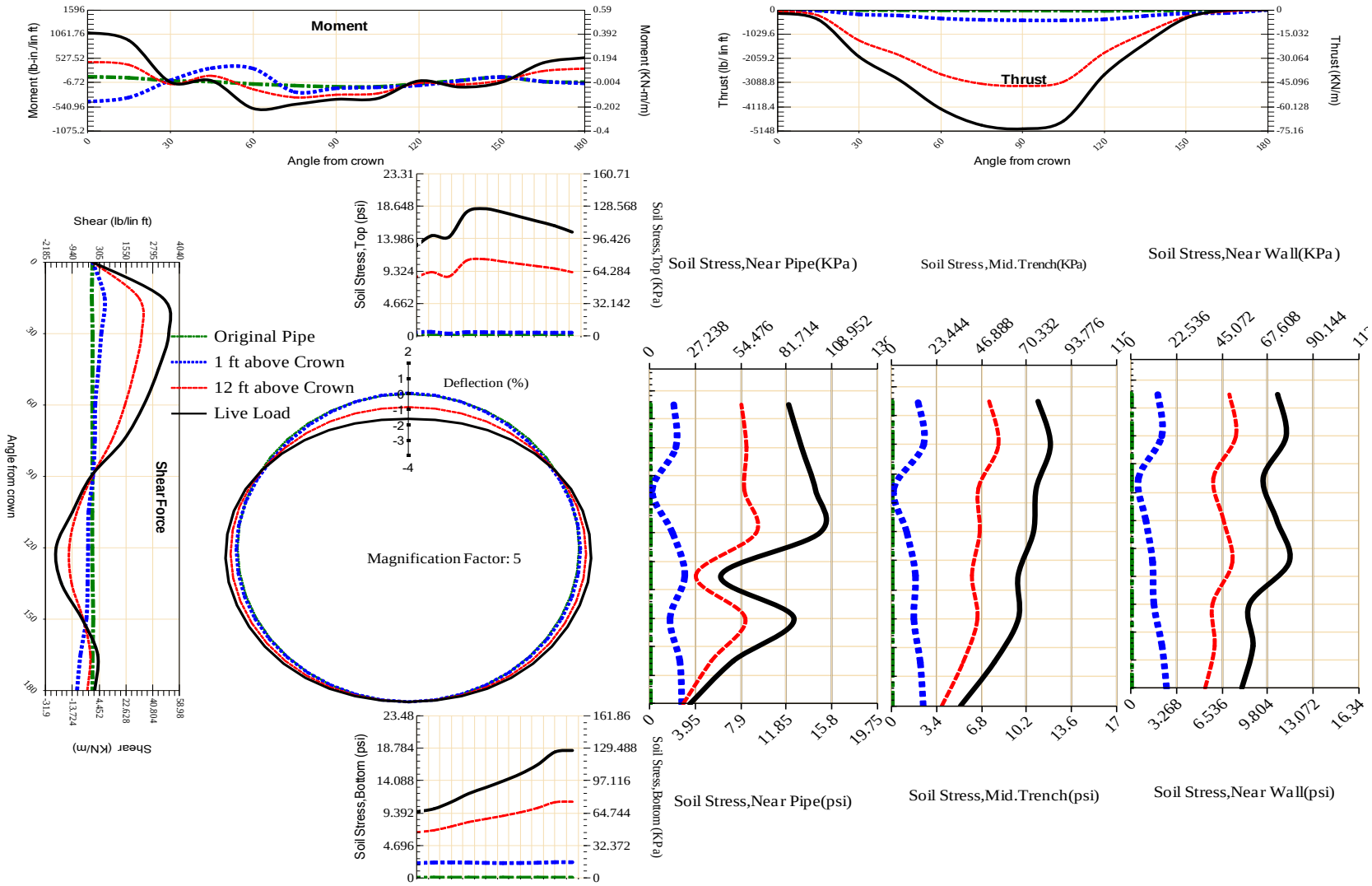

Figure A-350 Param-48-PW230-TR7OR-OD+72-EW5-H12-LiveLoad

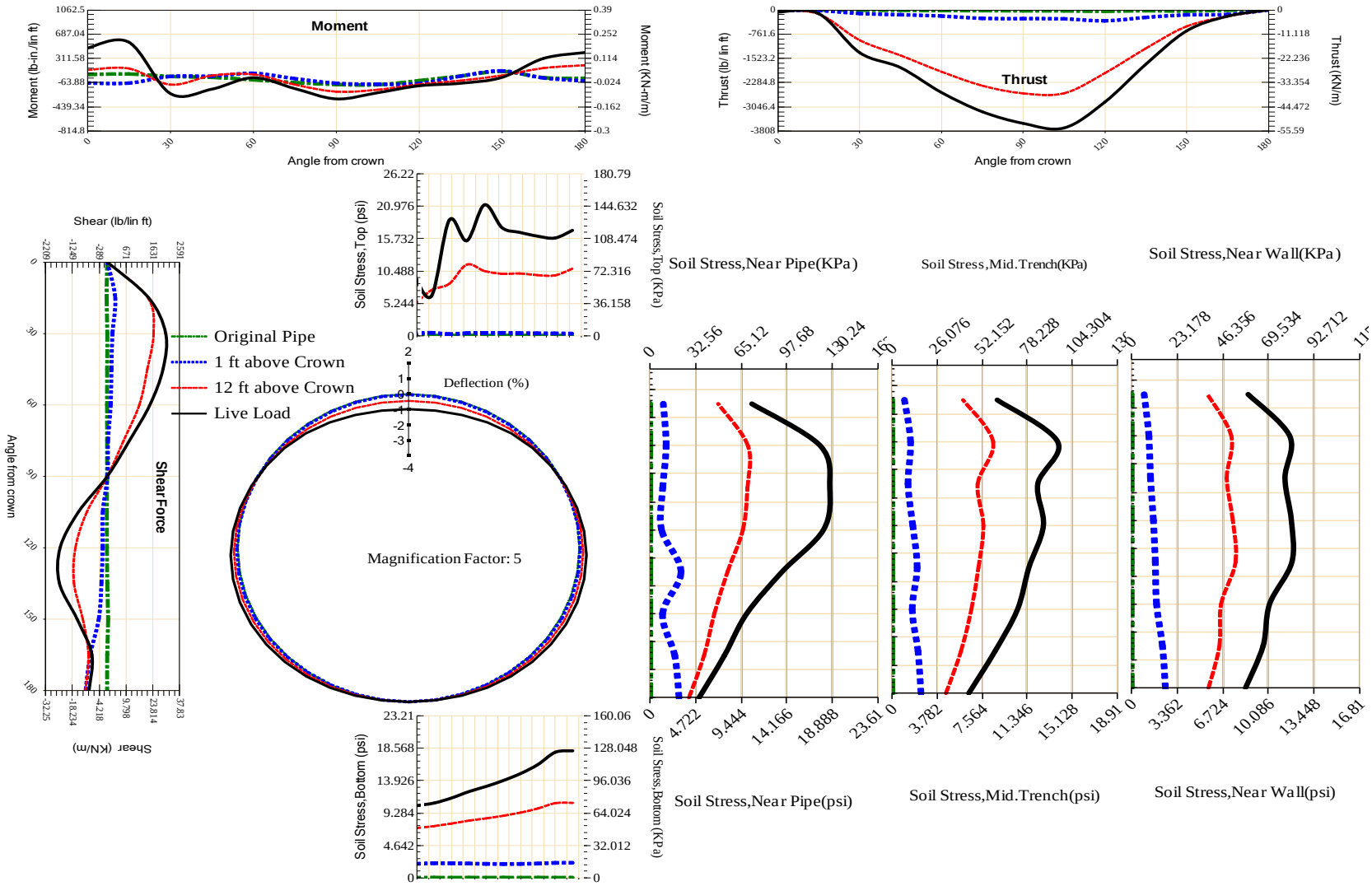

Figure A-351 Param-48-PW230-TR7SF-OD+72-EW5-H12-LiveLoad

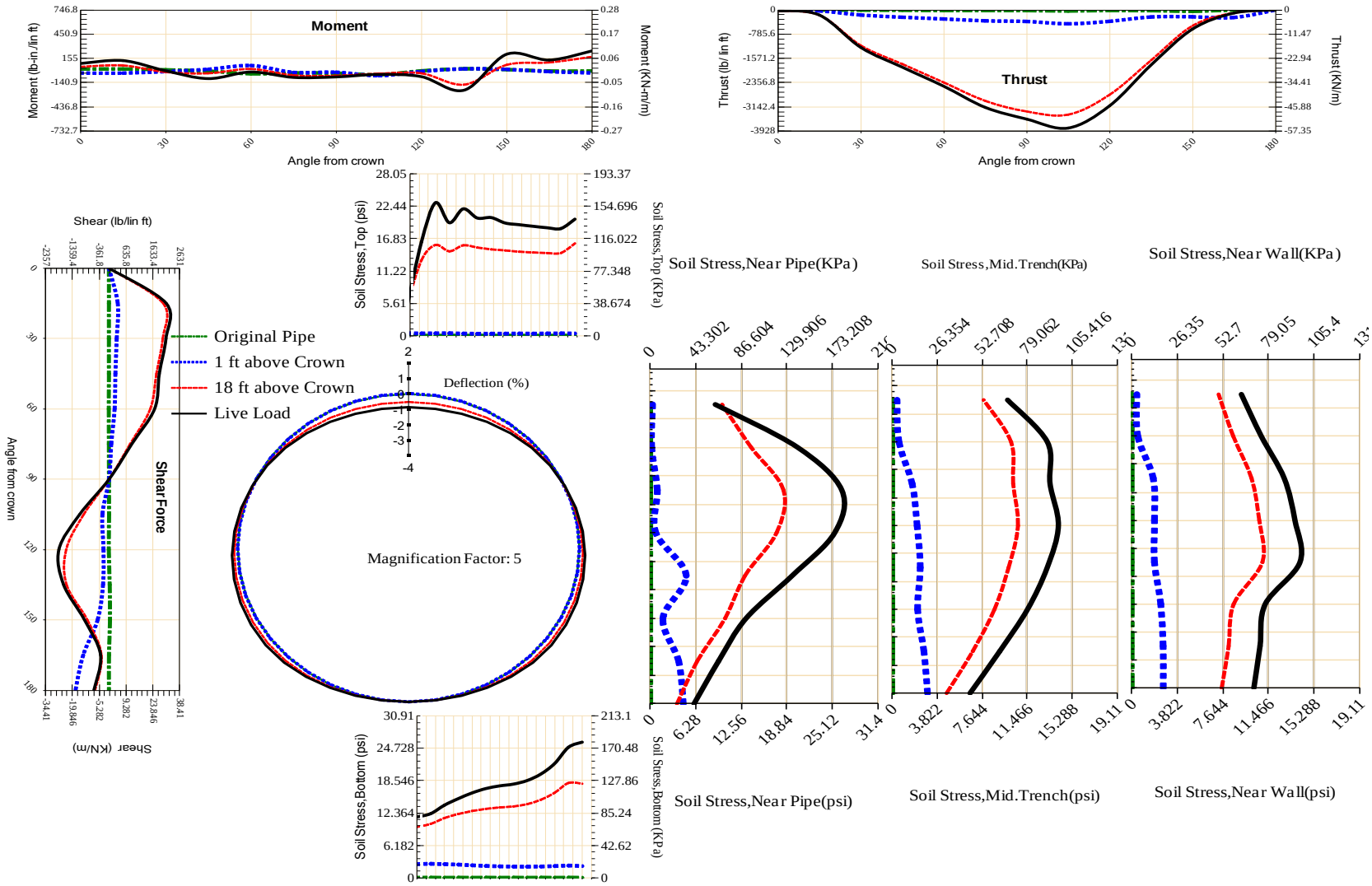

Figure A-352 Param-48-PW288-SF10SF-OD+108-EW10-H18-LiveLoad

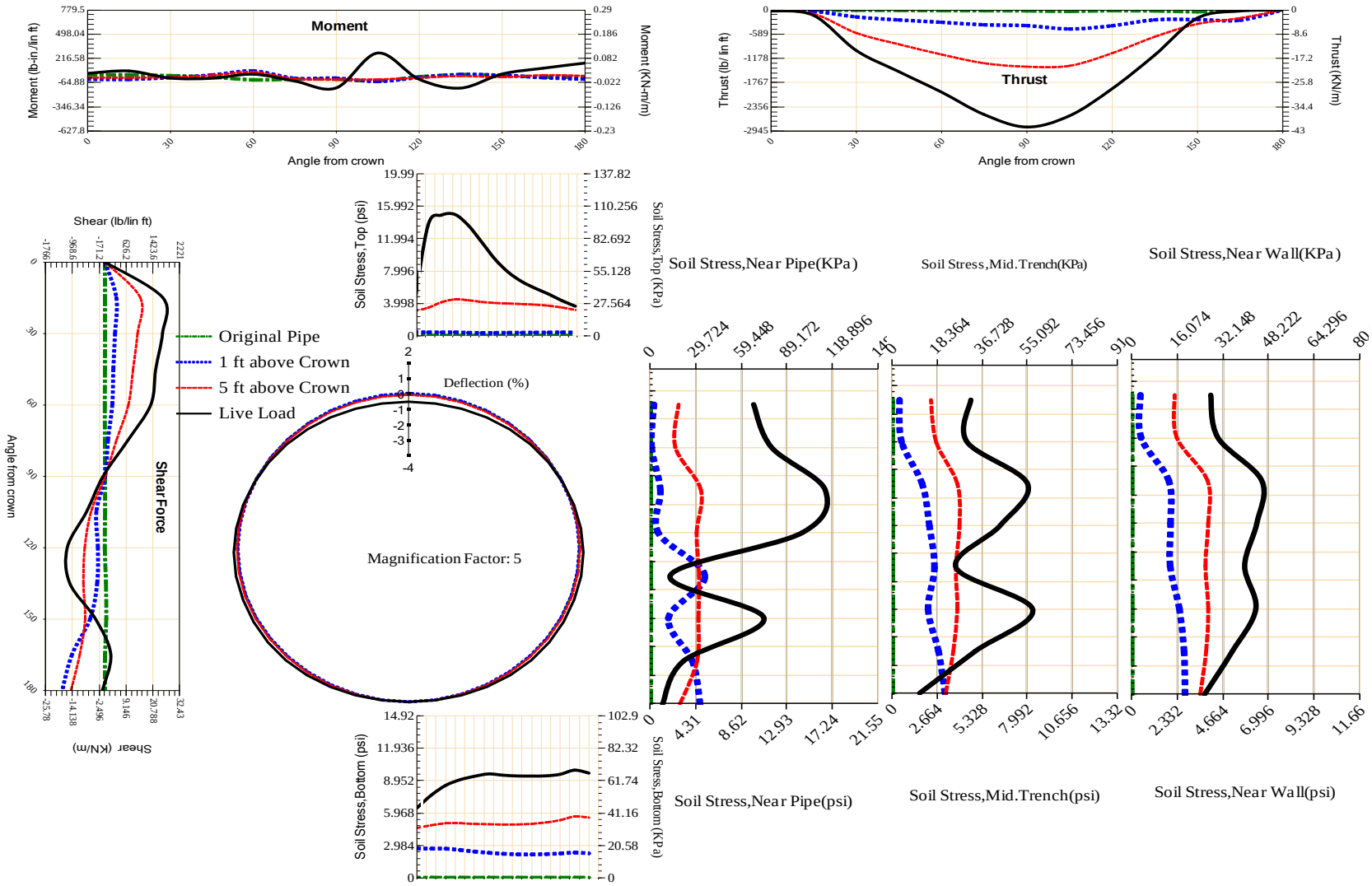

Figure A-353 Param-48-PW288-SF10SF-OD+108-EW10-H5-LiveLoad

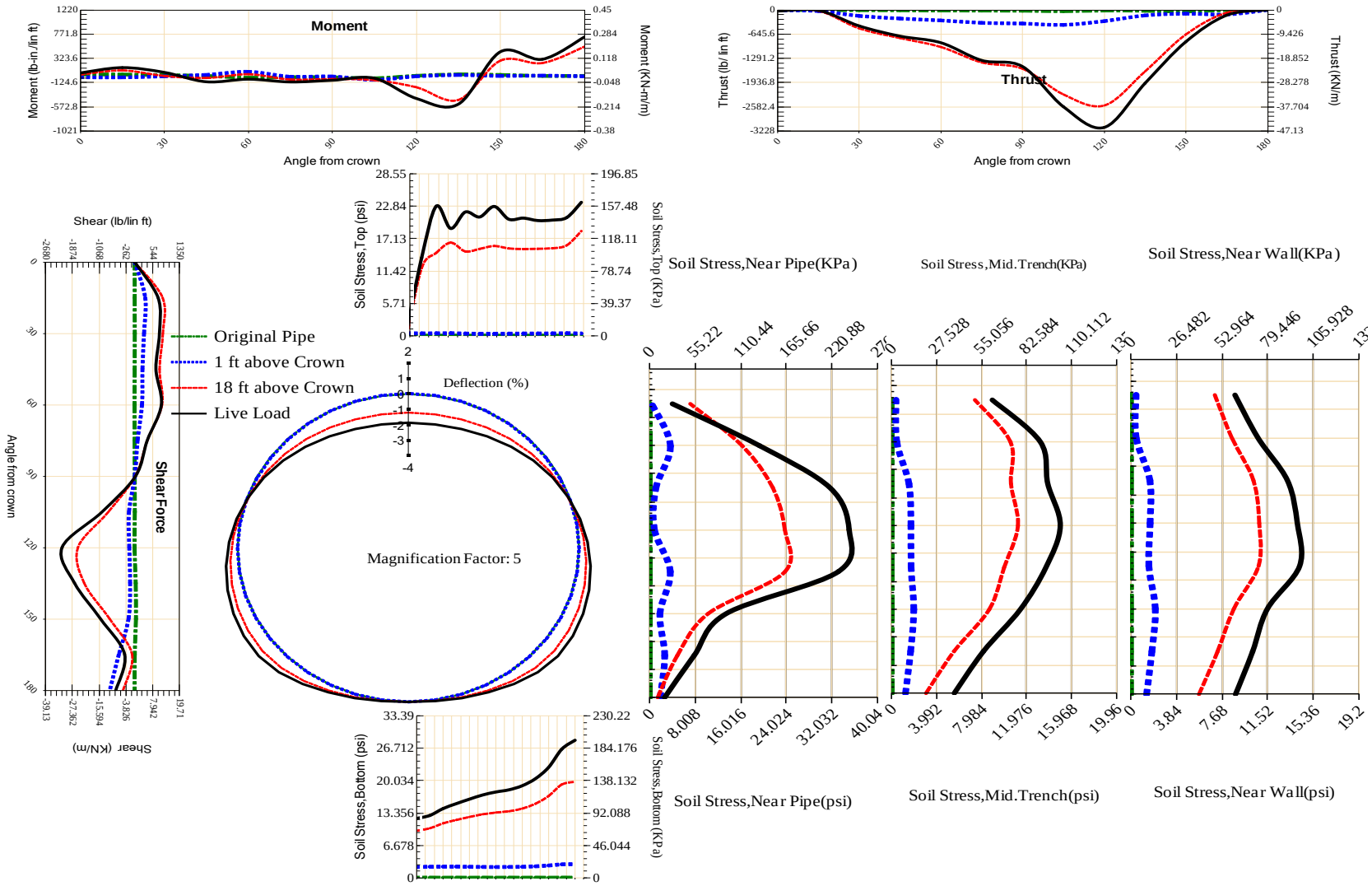

Figure A-354 Param-48-PW288-SF10SF-OD+108-EW3-H18-LiveLoad

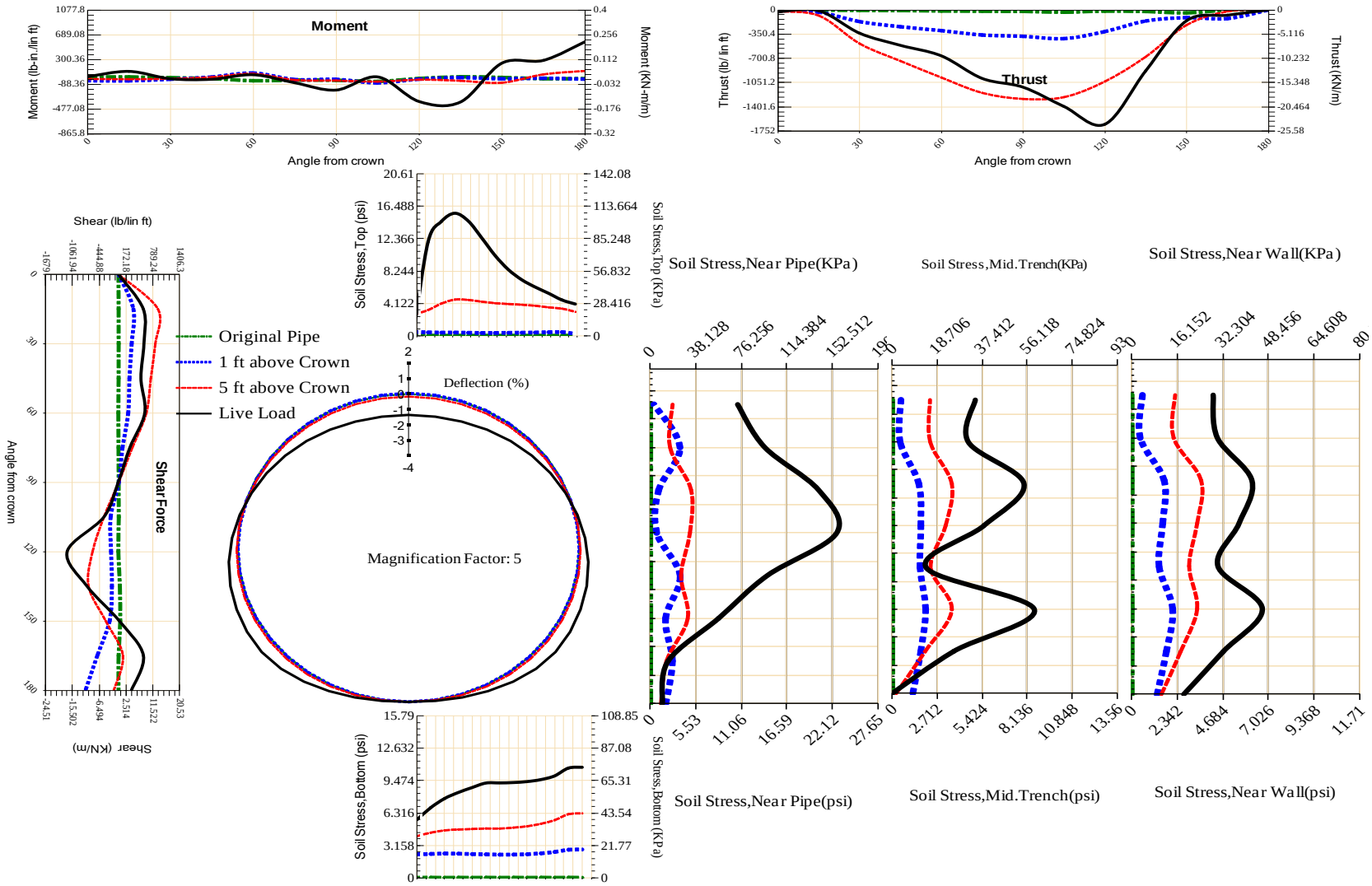

Figure A-355 Param-48-PW288-SF10SF-OD+108-EW3-H5-LiveLoad

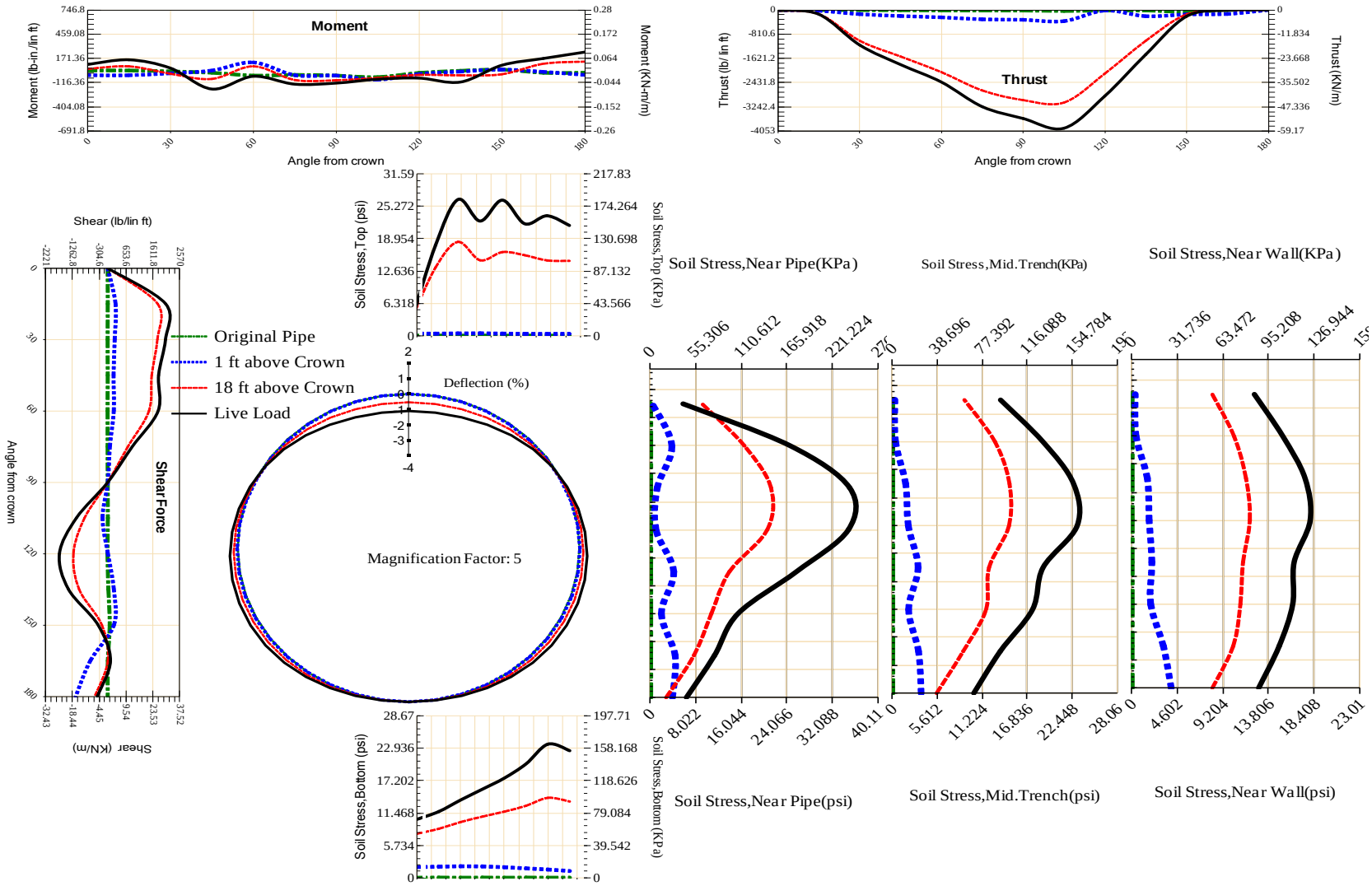

Figure A-356 Param-48-PW288-SF10SF-OD+48-EW10-H18-LiveLoad

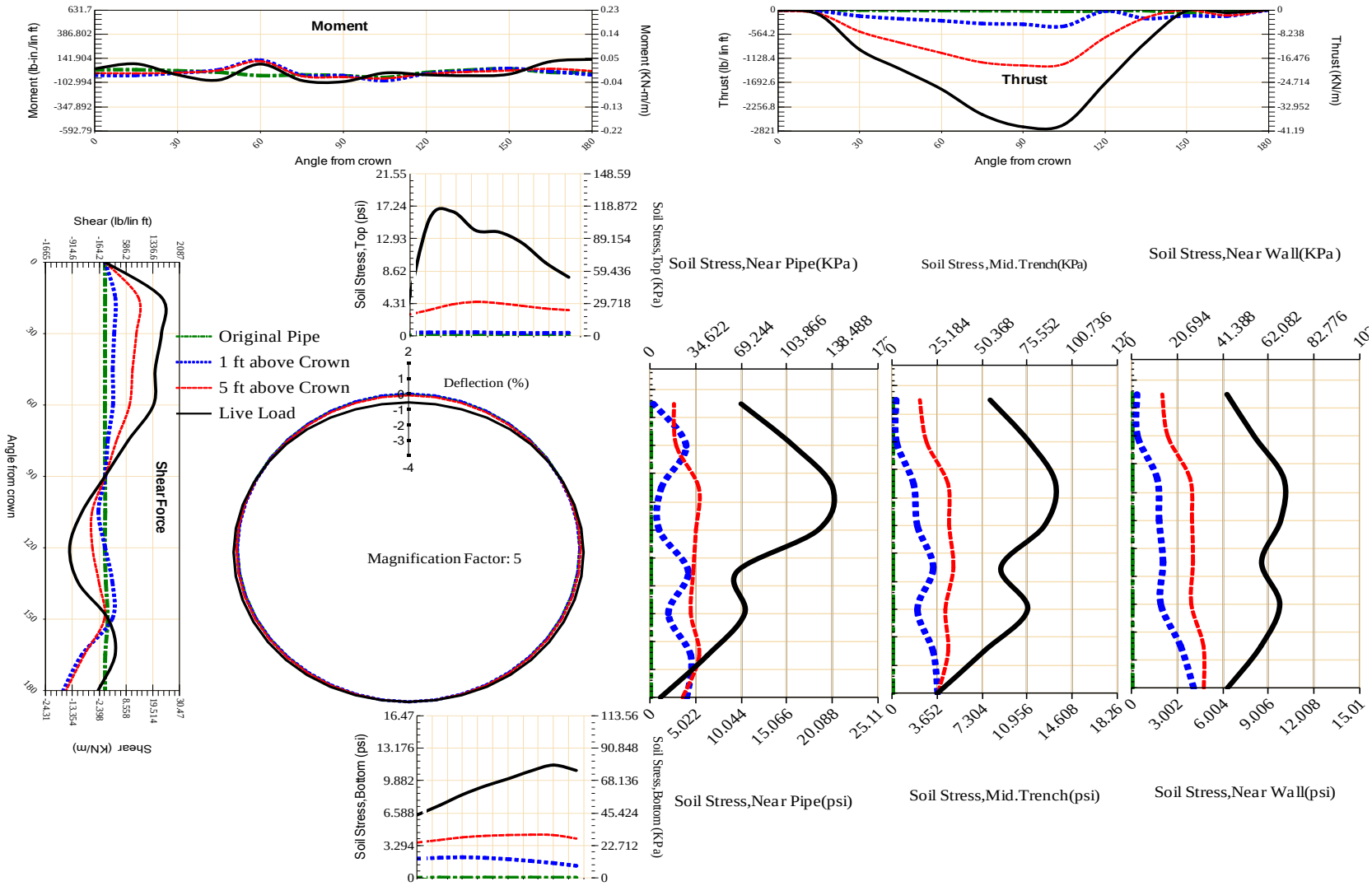

Figure A-357 Param-48-PW288-SF10SF-OD+48-EW10-H5-LiveLoad

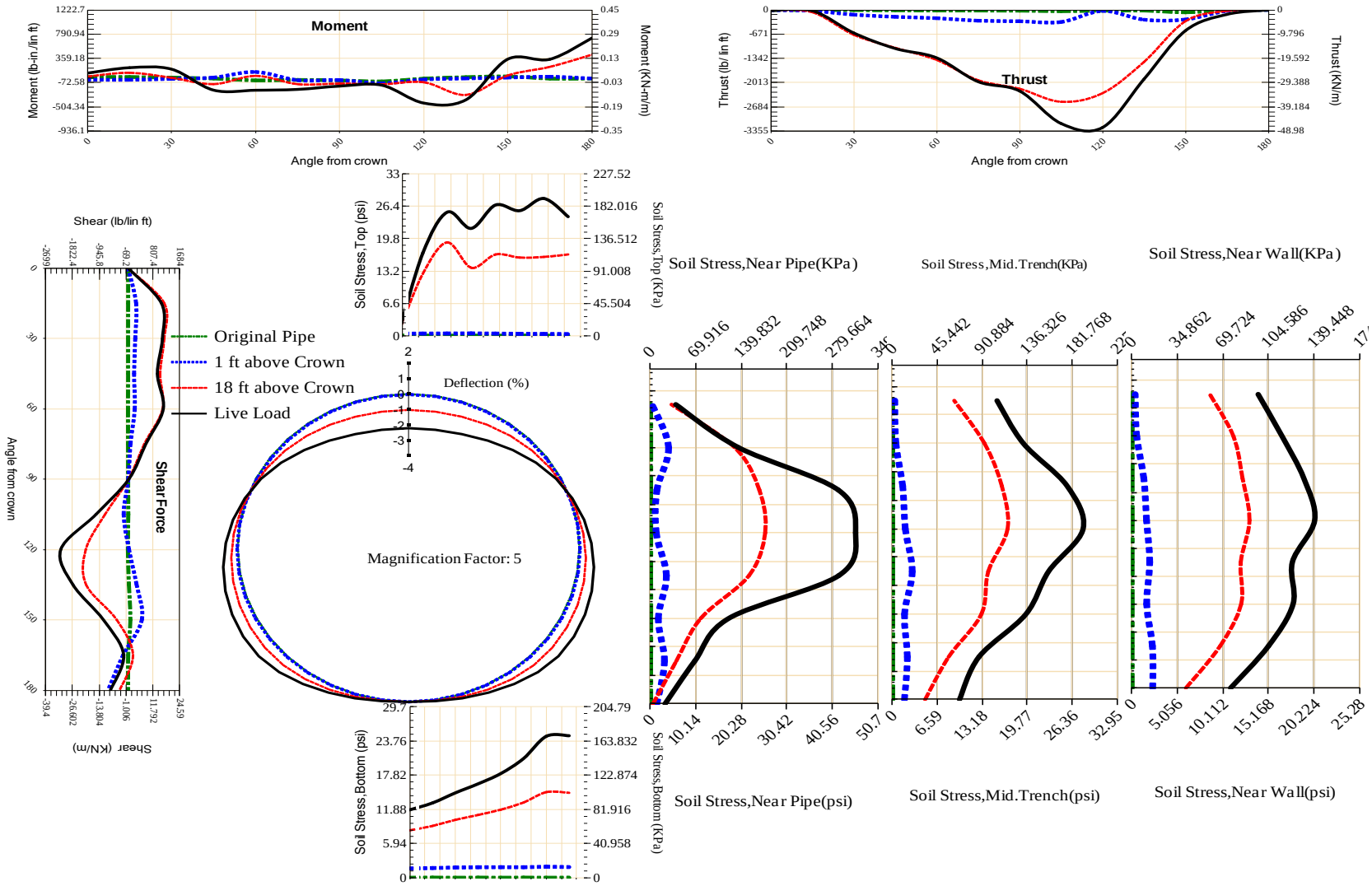

Figure A-358 Param-48-PW288-SF10SF-OD+48-EW3-H18-LiveLoad

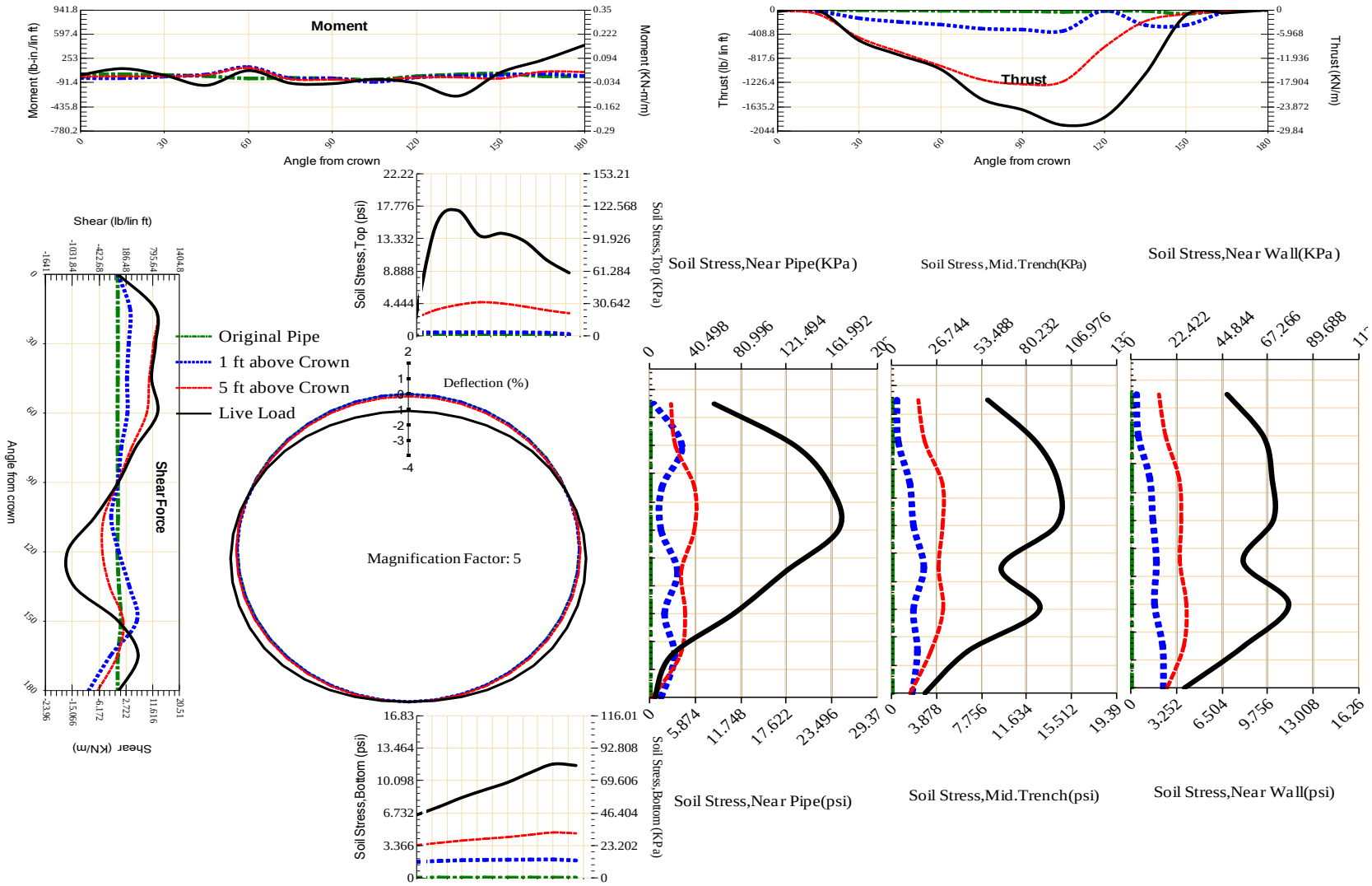

Figure A-359 Param-48-PW288-SF10SF-OD+48-EW3-H5-LiveLoad

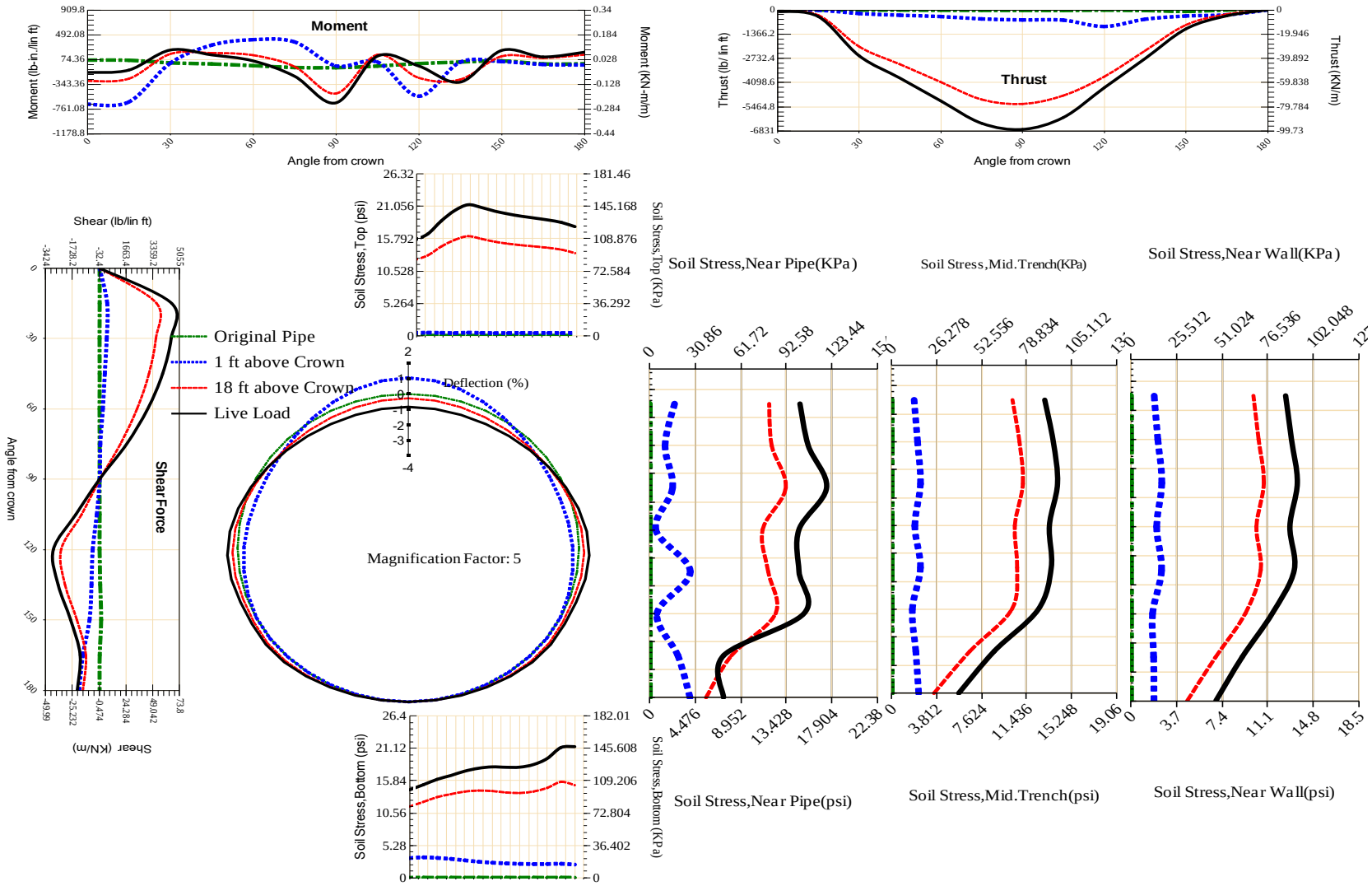

Figure A-360 Param-48-PW288-SF3OR-OD+108-EW10-H18-LiveLoad

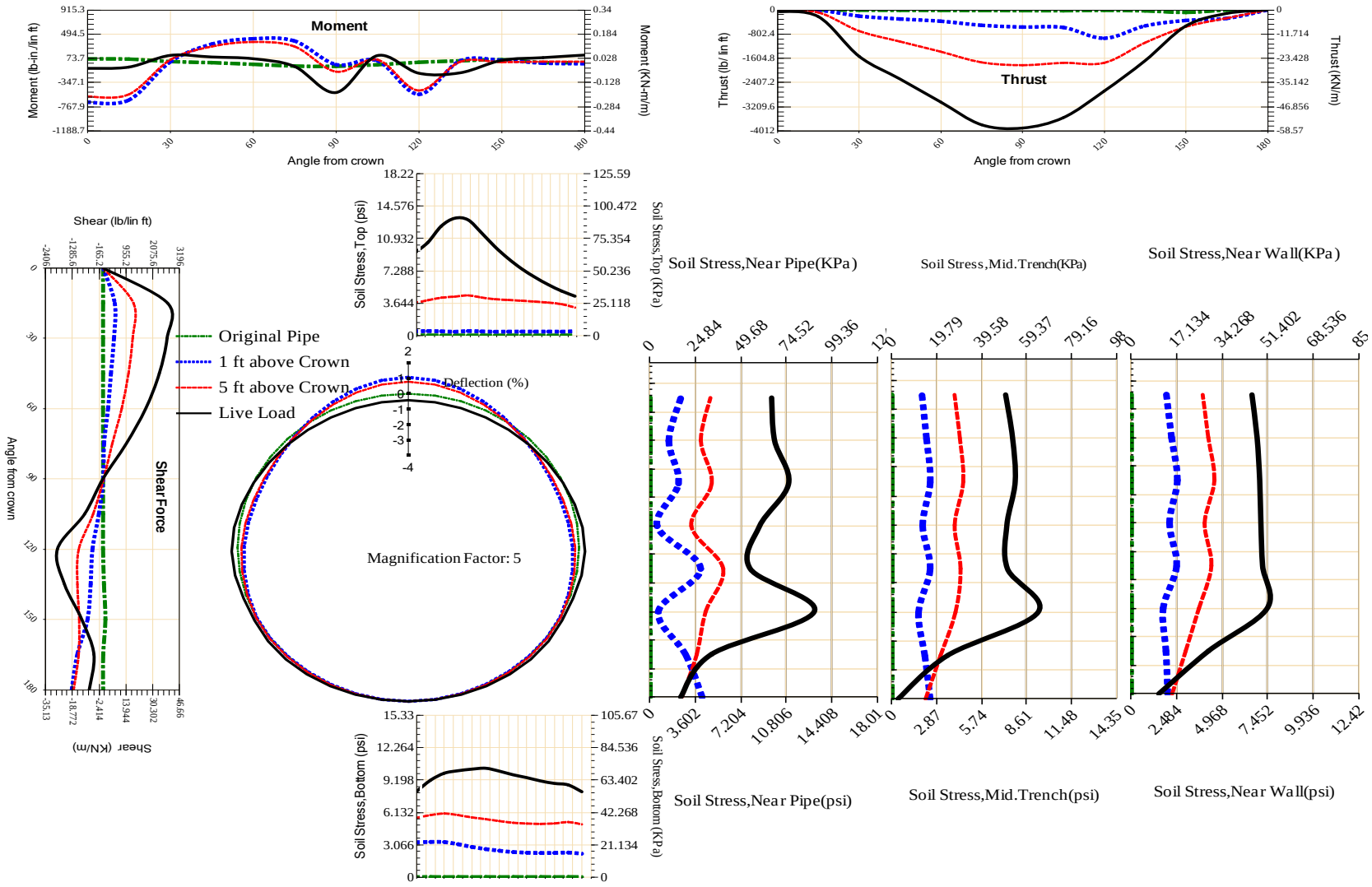

Figure A-361 Param-48-PW288-SF3OR-OD+108-EW10-H5-LiveLoad

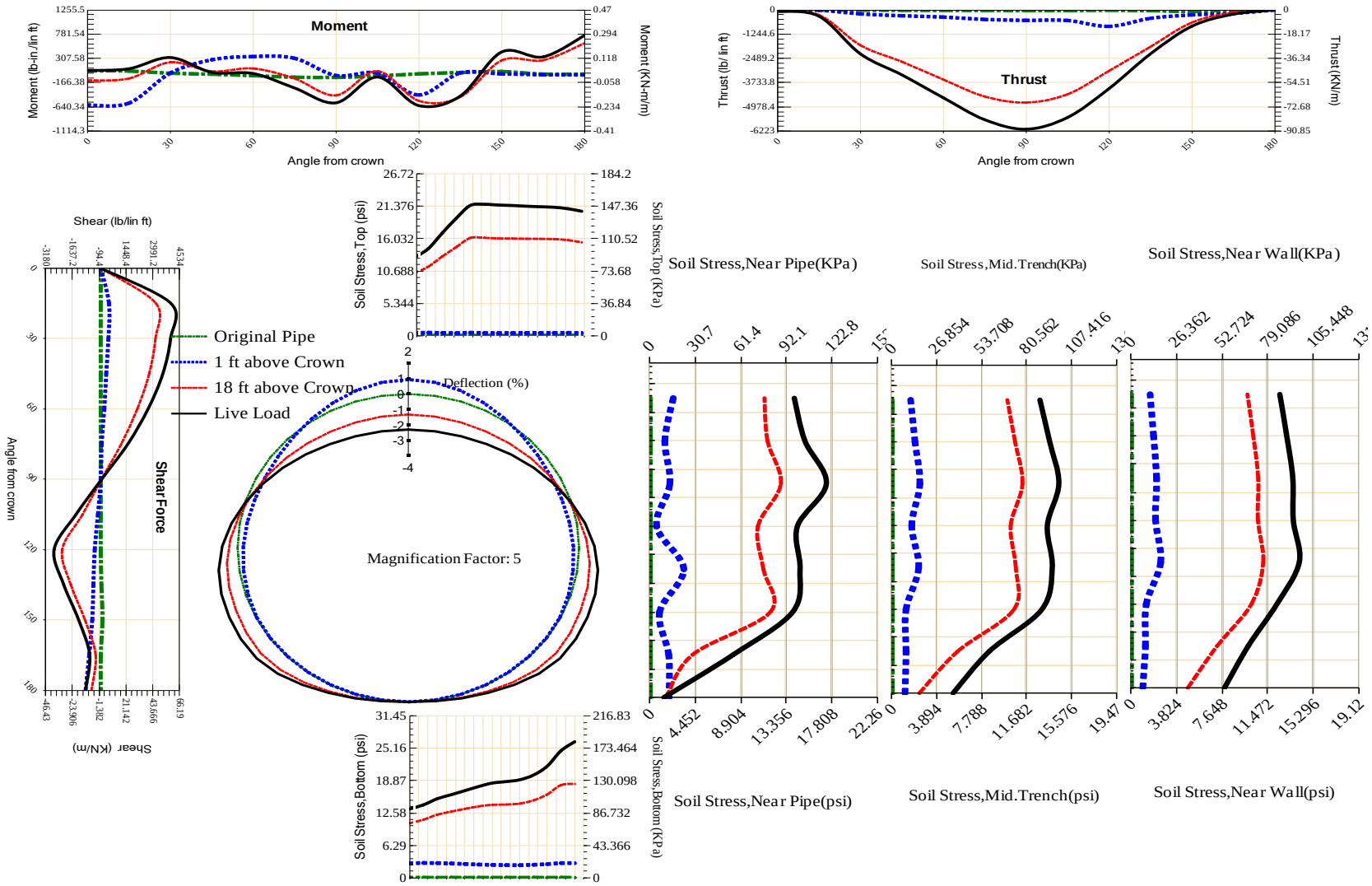

Figure A-362 Param-48-PW288-SF3OR-OD+108-EW3-H18-LiveLoad

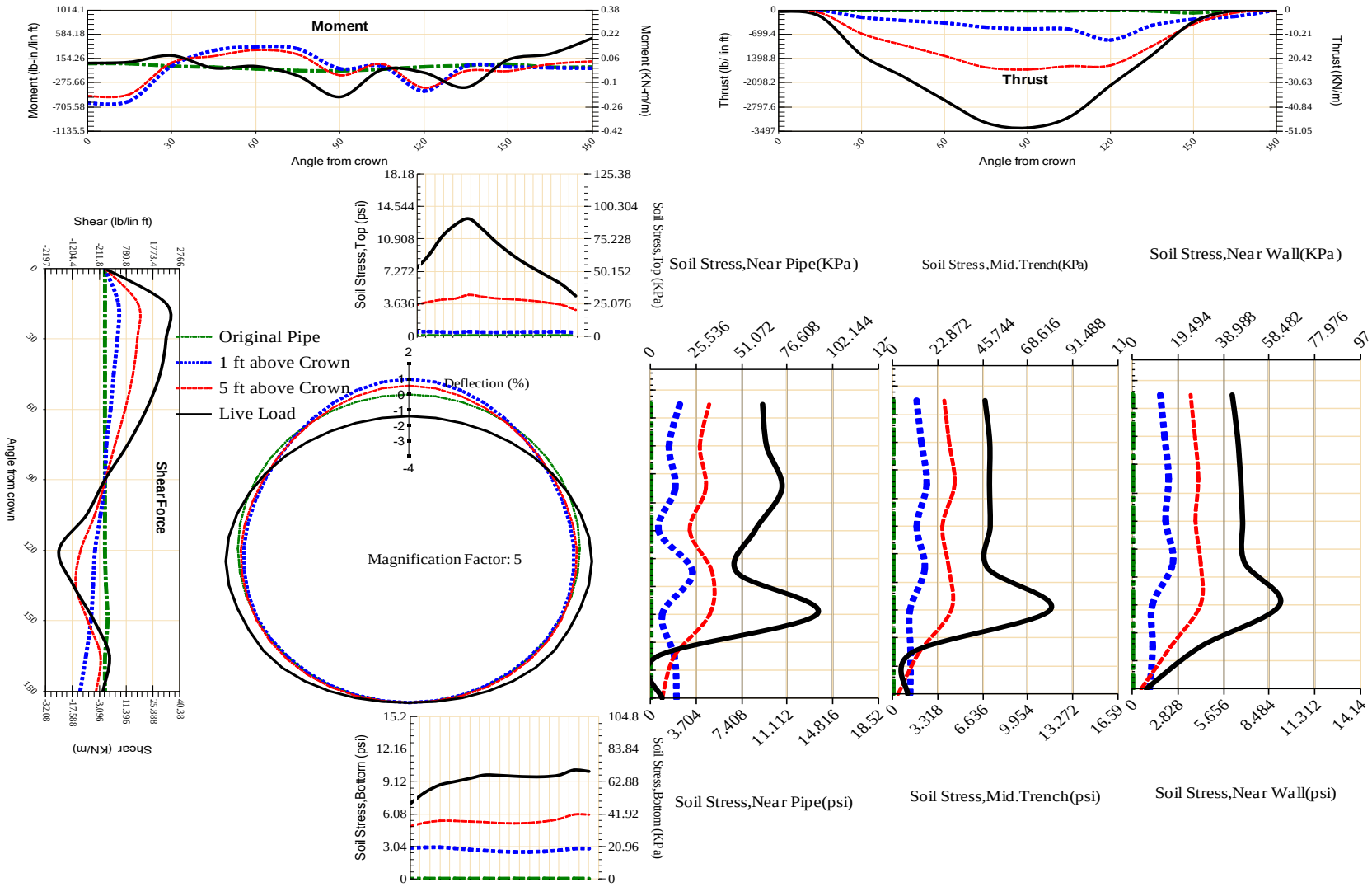

Figure A-363 Param-48-PW288-SF3OR-OD+108-EW3-H5-LiveLoad

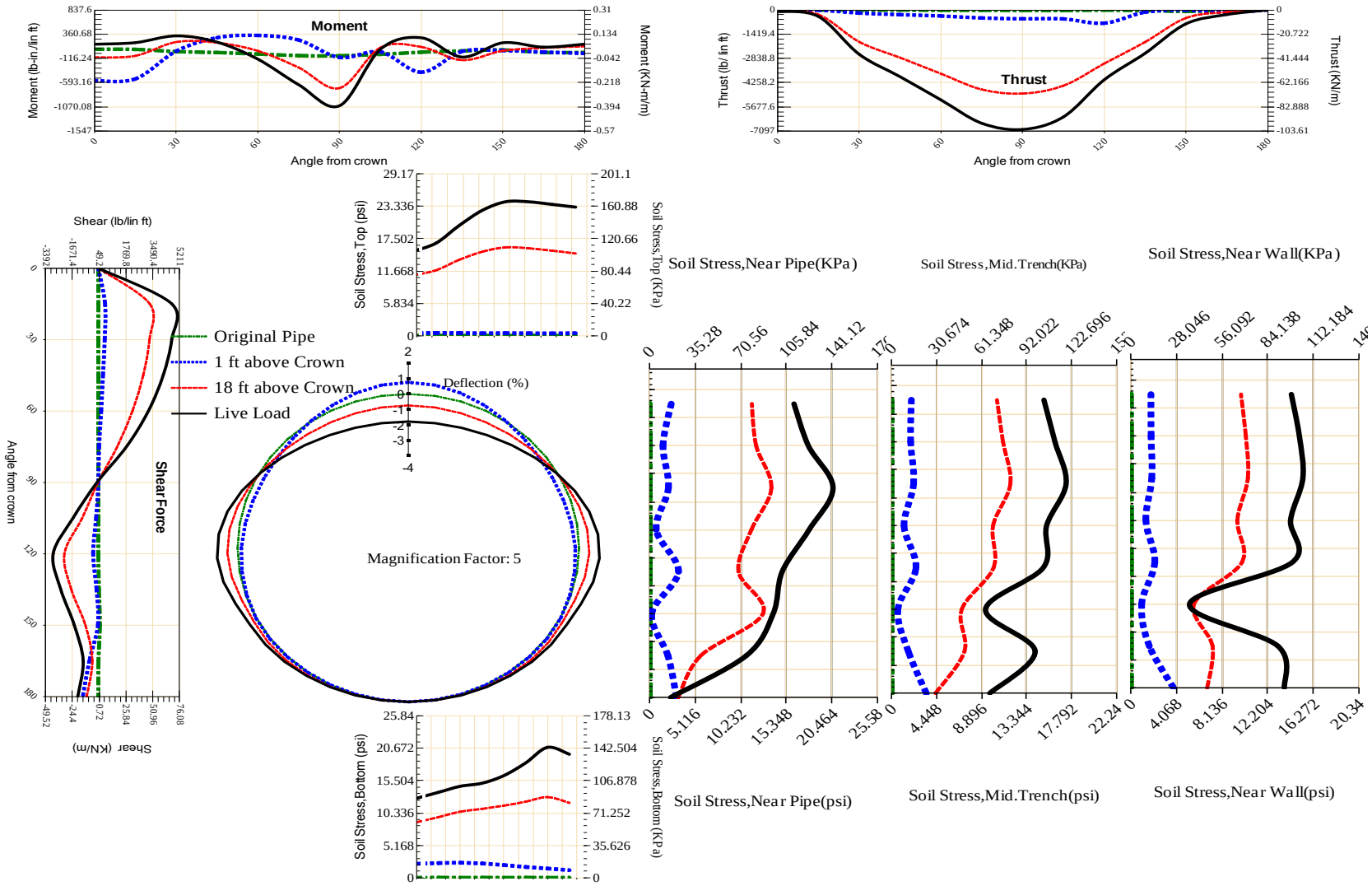

Figure A-364 Param-48-PW288-SF3OR-OD+48-EW10-H18-LiveLoad

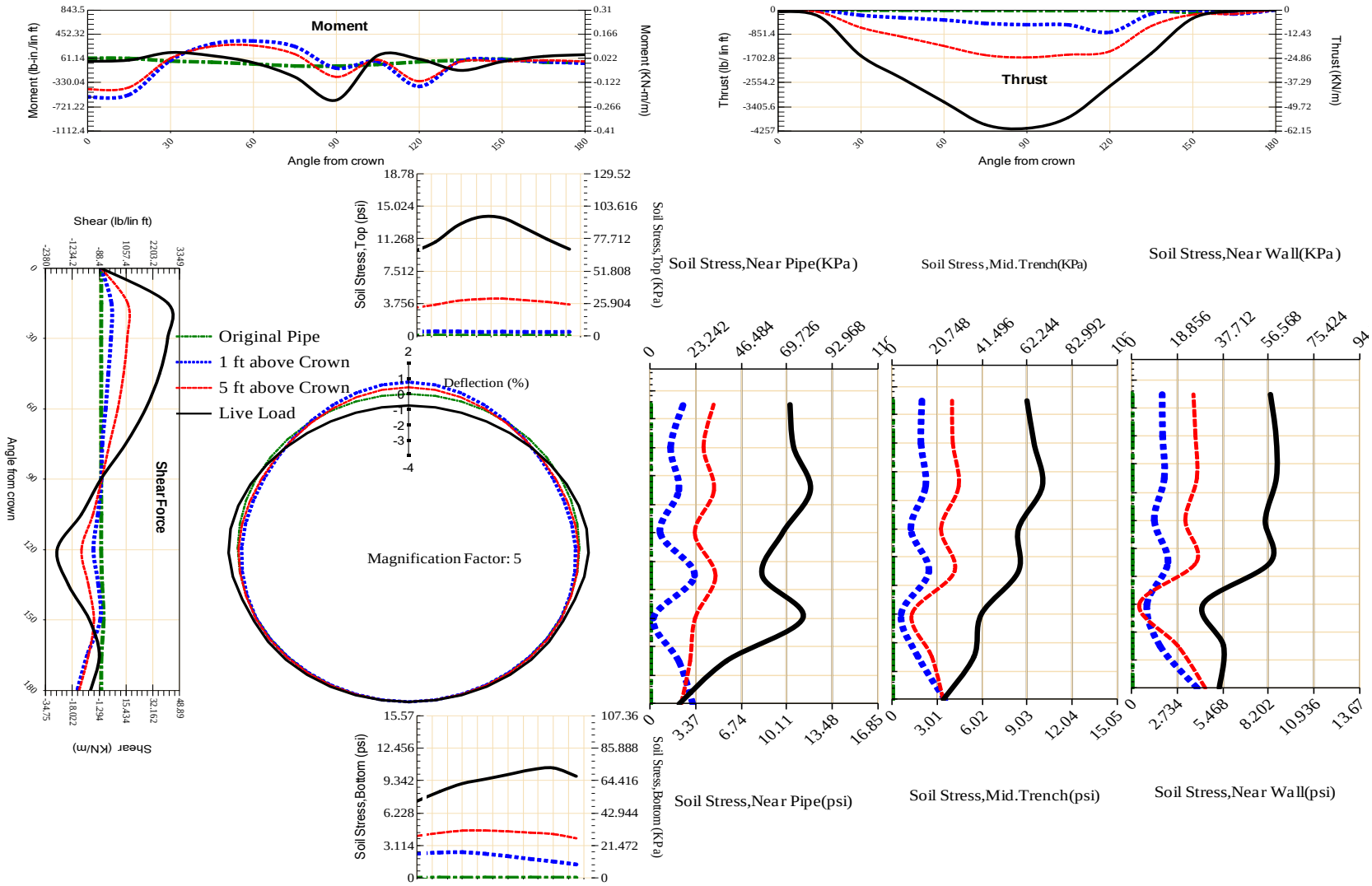

Figure A-365 Param-48-PW288-SF3OR-OD+48-EW10-H5-LiveLoad

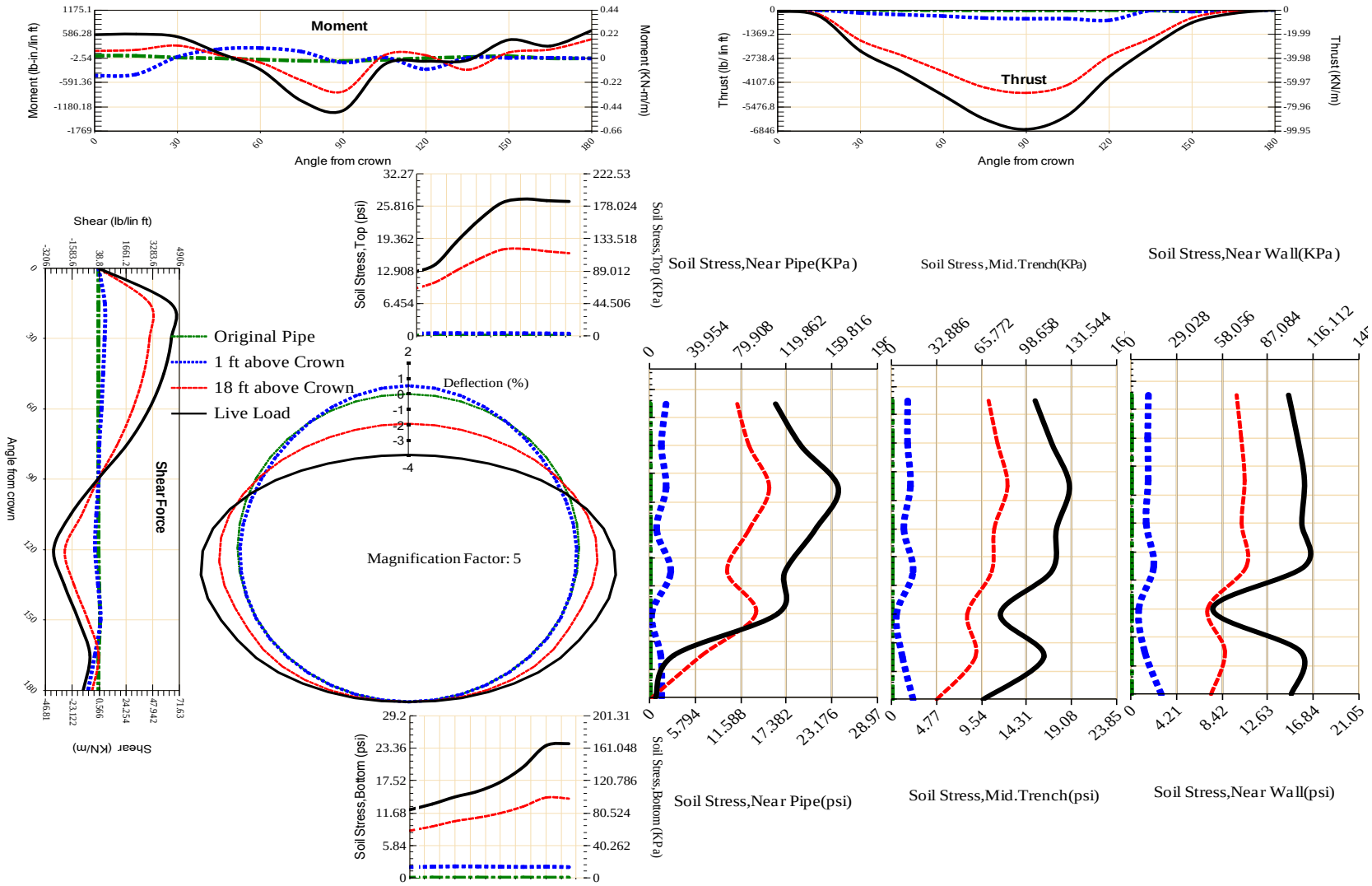

Figure A-366 Param-48-PW288-SF3OR-OD+48-EW3-H18-LiveLoad

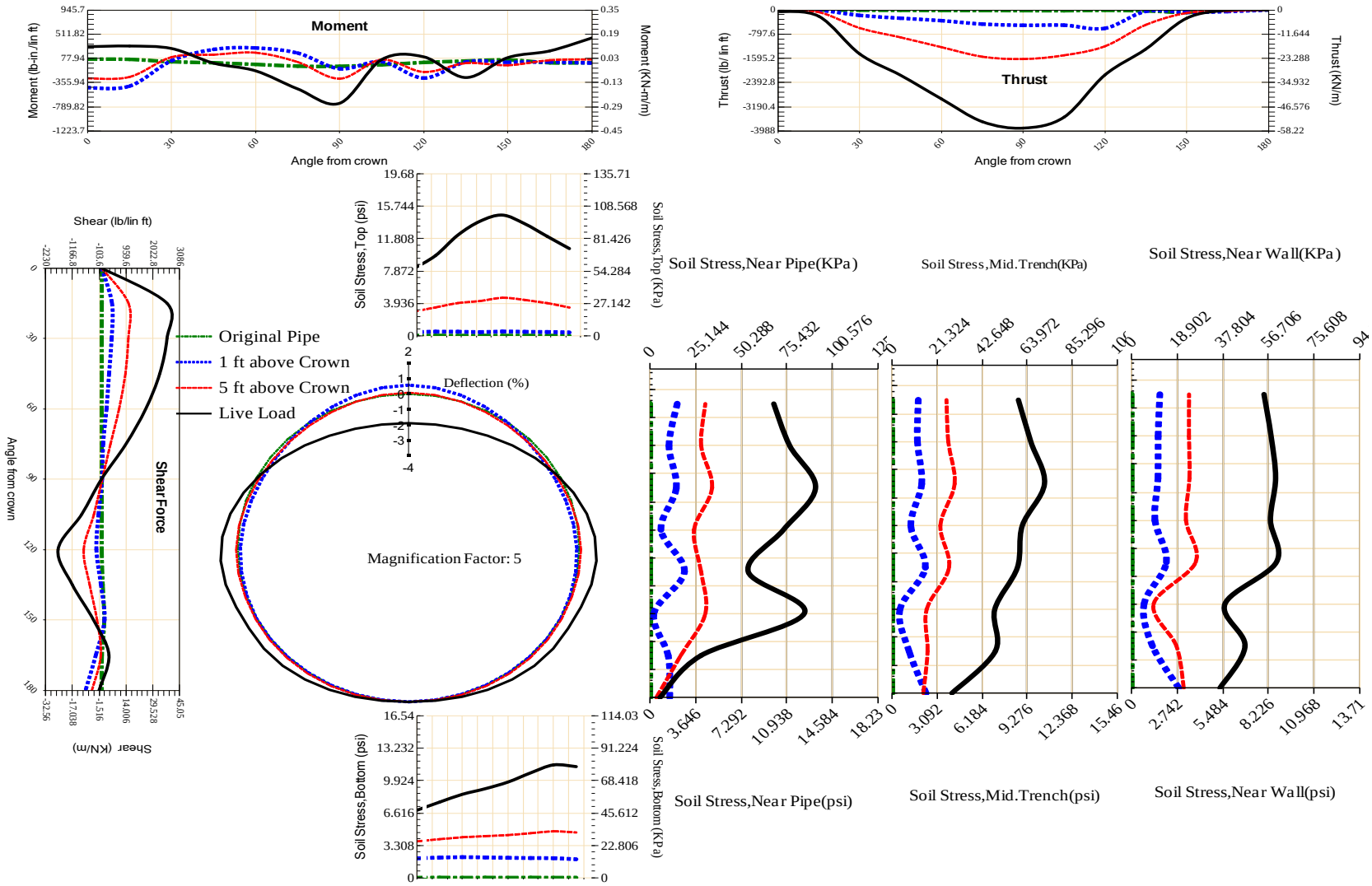

Figure A-367 Param-48-PW288-SF3OR-OD+48-EW3-H5-LiveLoad

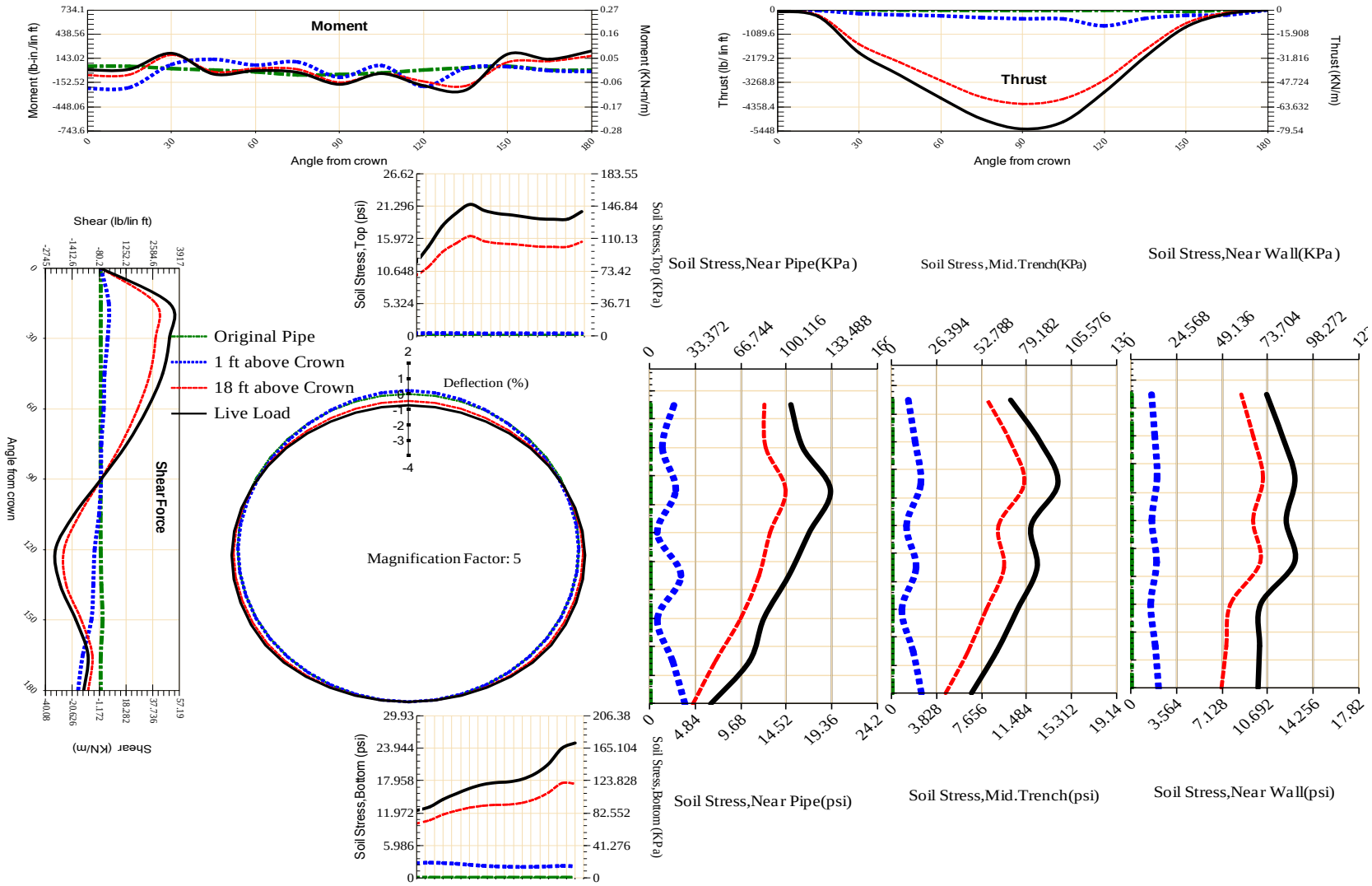

Figure A-368 Param-48-PW288-SF3TR-OD+108-EW10-H18-LiveLoad

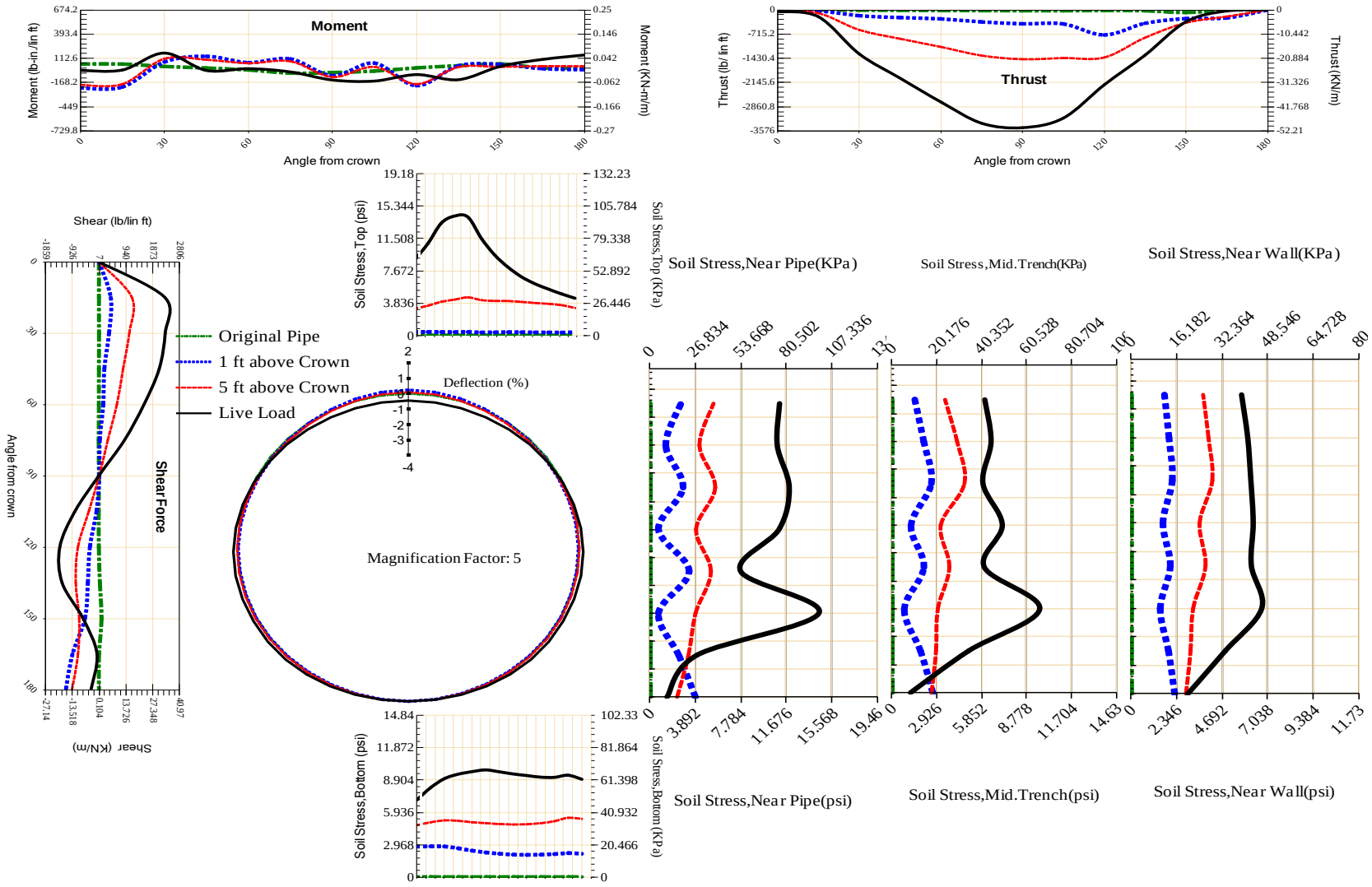

Figure A-369 Param-48-PW288-SF3TR-OD+108-EW10-H5-LiveLoad

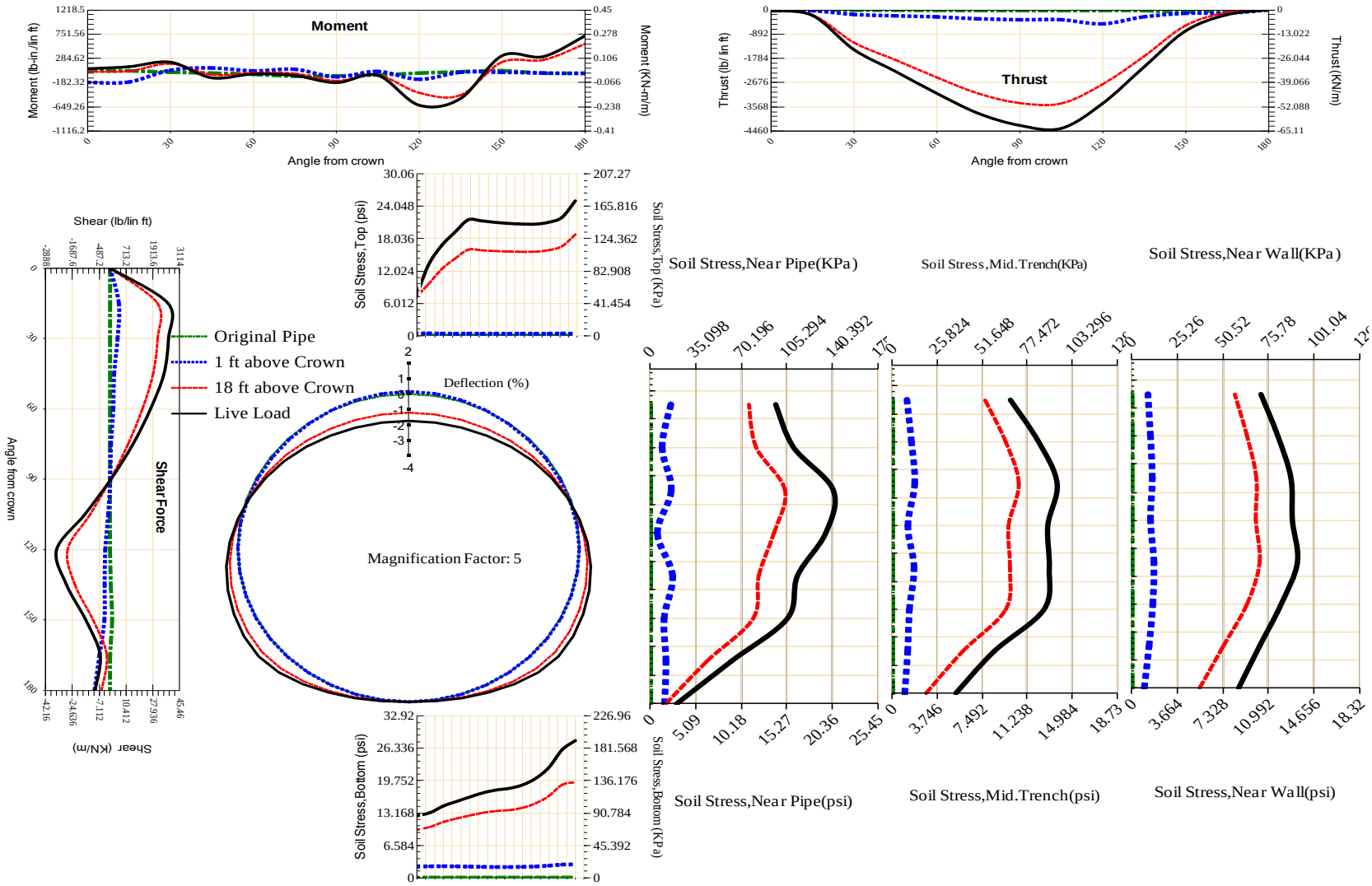

Figure A-370 Param-48-PW288-SF3TR-OD+108-EW3-H18-LiveLoad

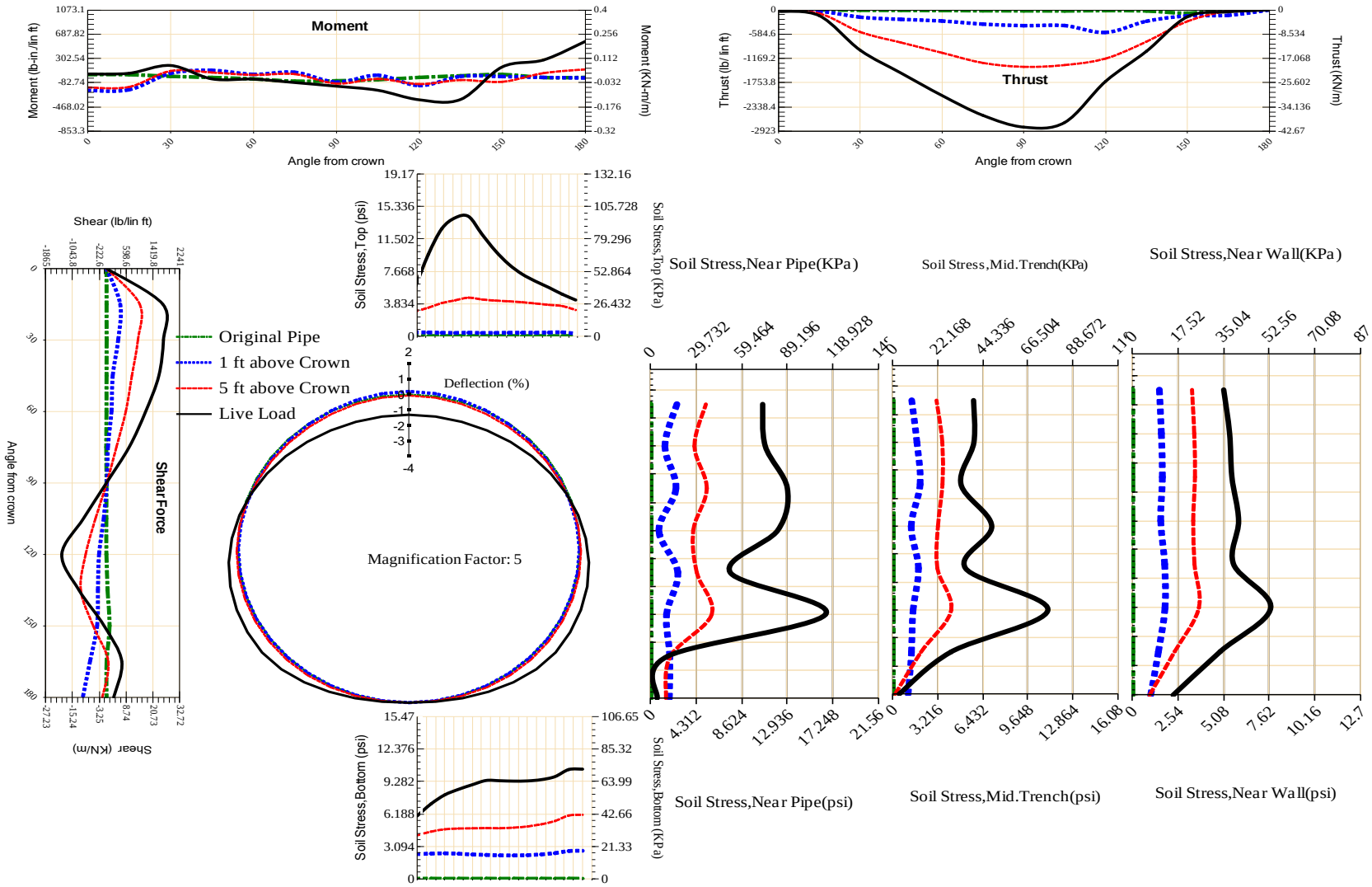

Figure A-371 Param-48-PW288-SF3TR-OD+108-EW3-H5-LiveLoad

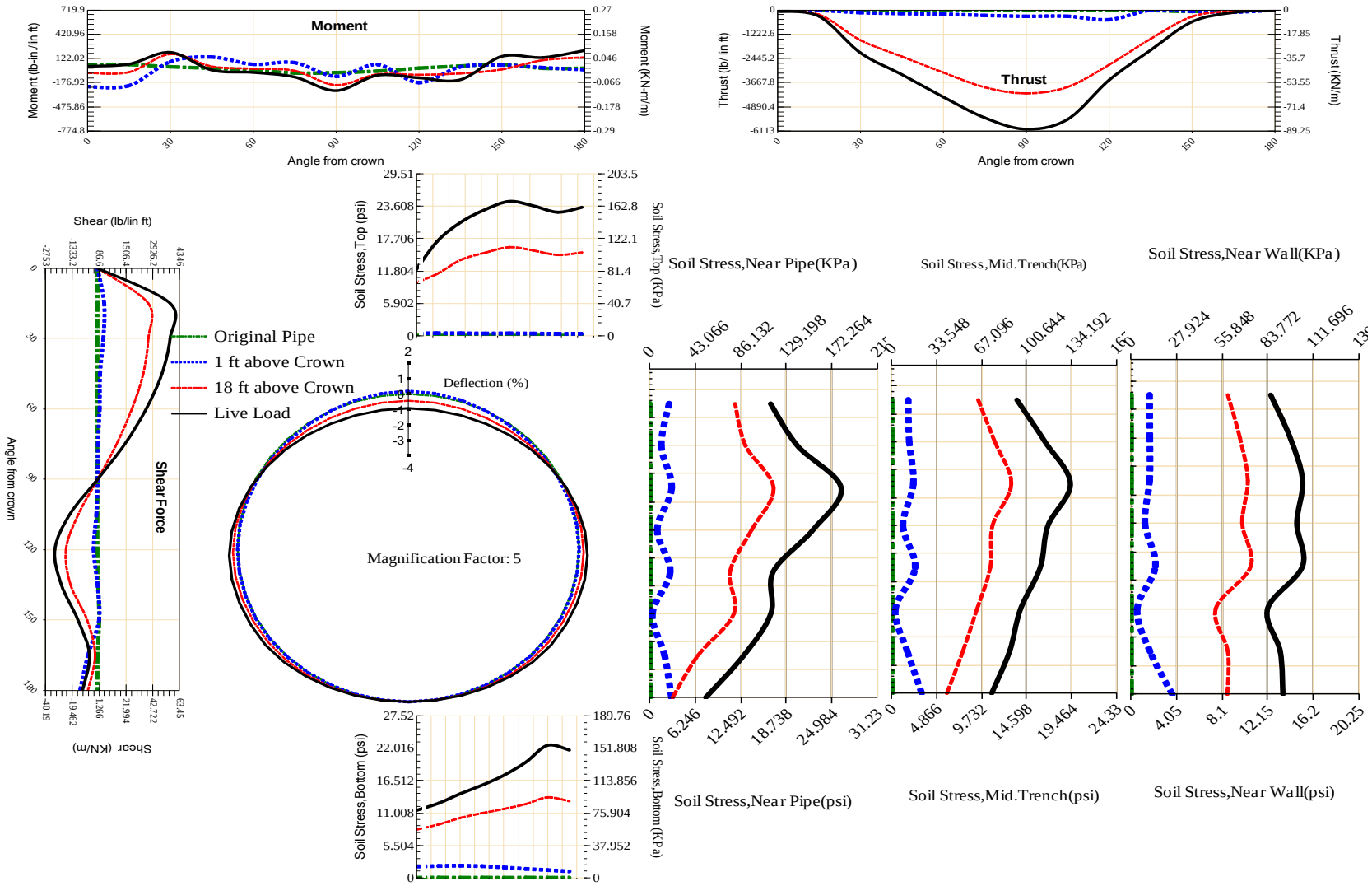

Figure A-372 Param-48-PW288-SF3TR-OD+48-EW10-H18-LiveLoad

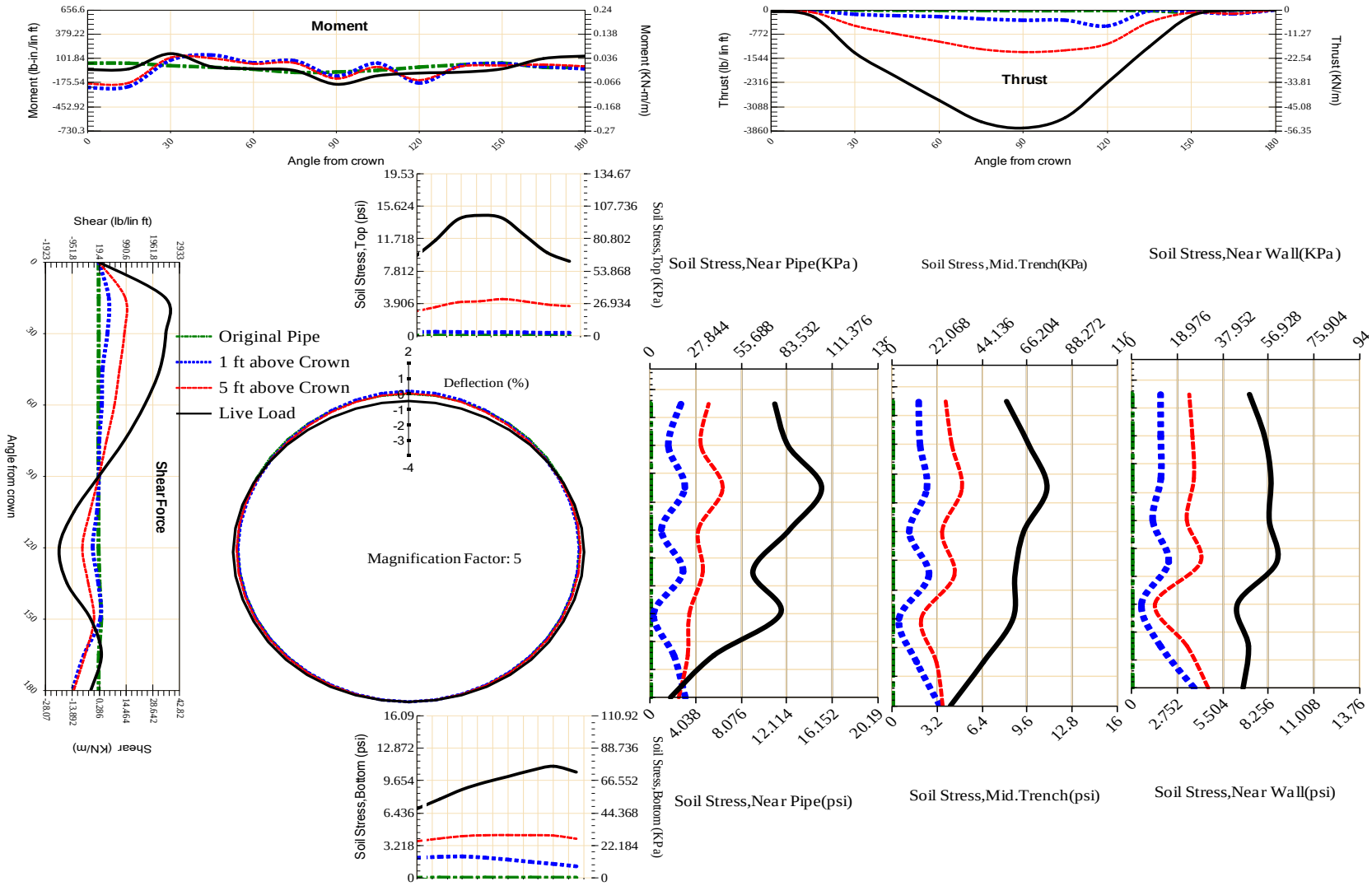

Figure A-373 Param-48-PW288-SF3TR-OD+48-EW10-H5-LiveLoad

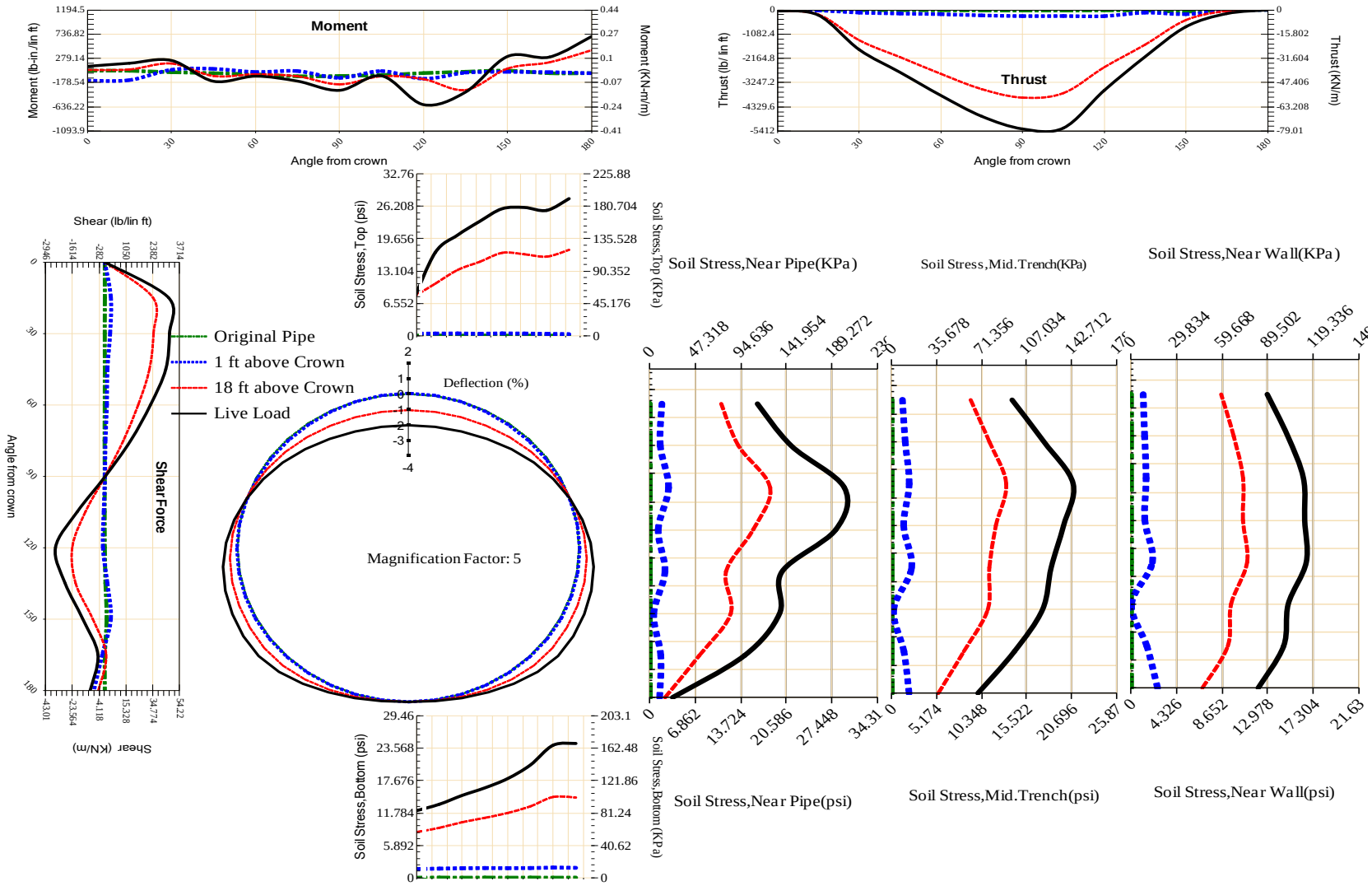

Figure A-374 Param-48-PW288-SF3TR-OD+48-EW3-H18-LiveLoad

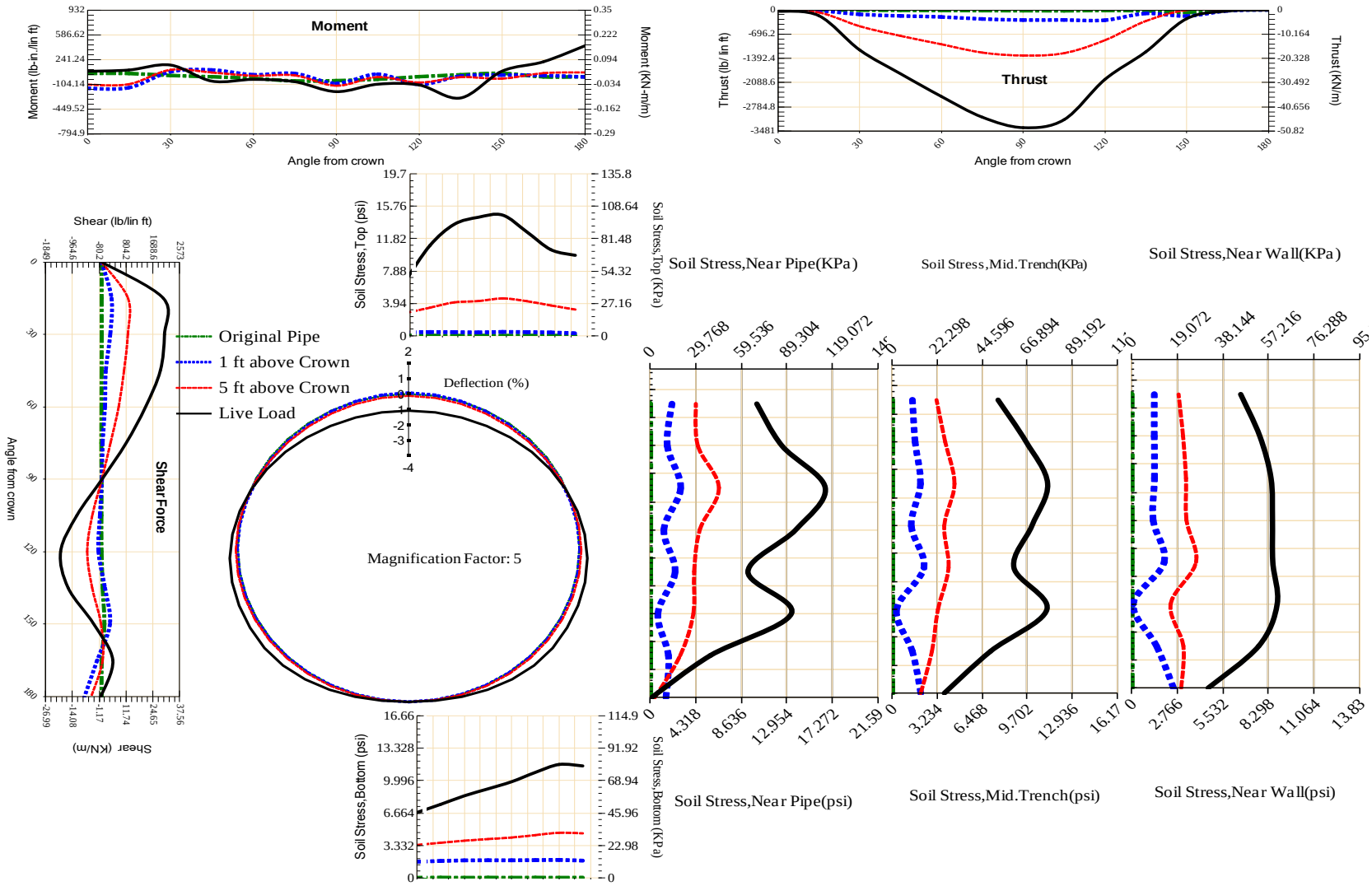

Figure A-375 Param-48-PW288-SF3TR-OD+48-EW3-H5-LiveLoad

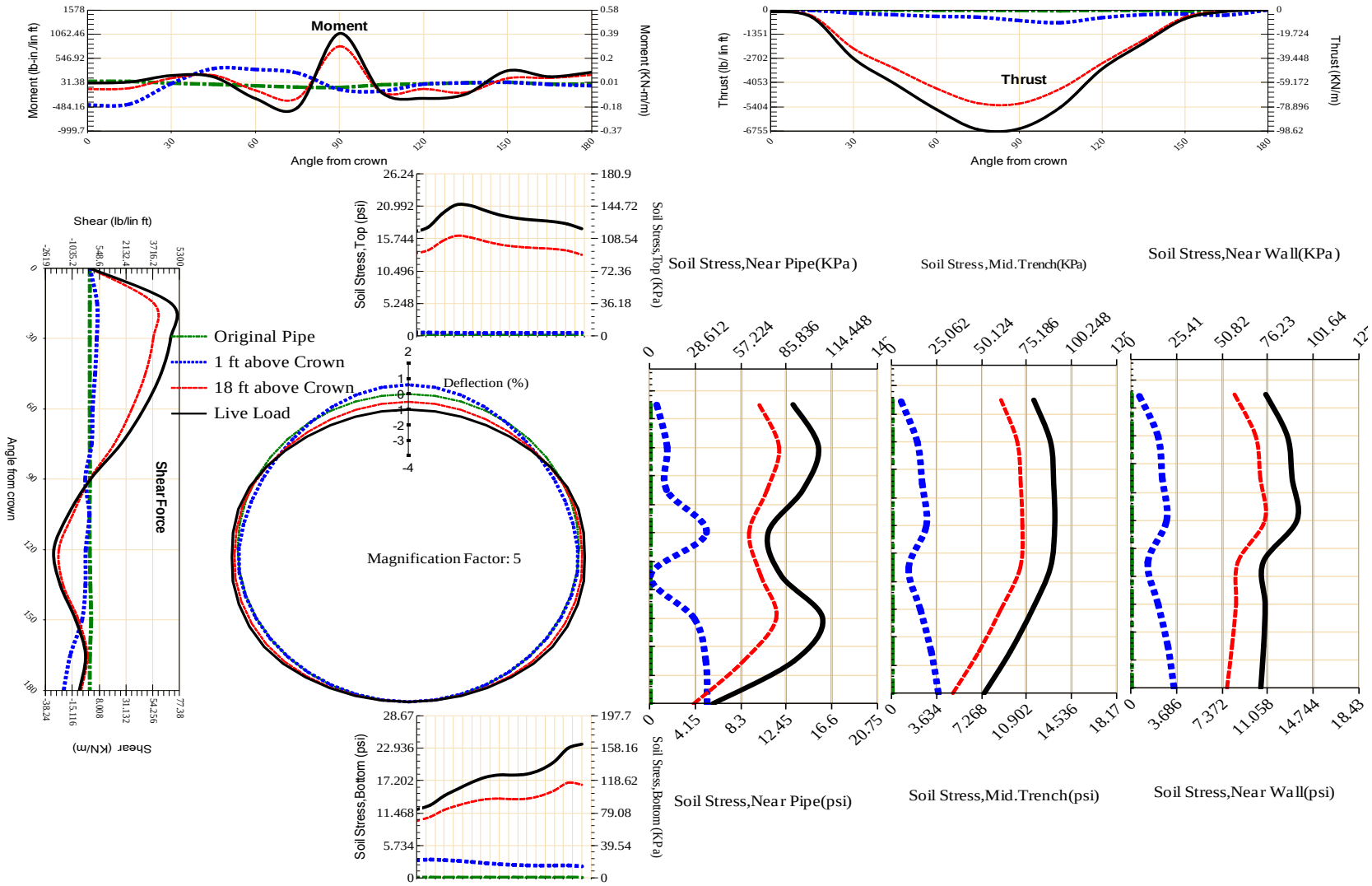

Figure A-376 Param-48-PW288-SF5OR-OD+108-EW10-H18-LiveLoad

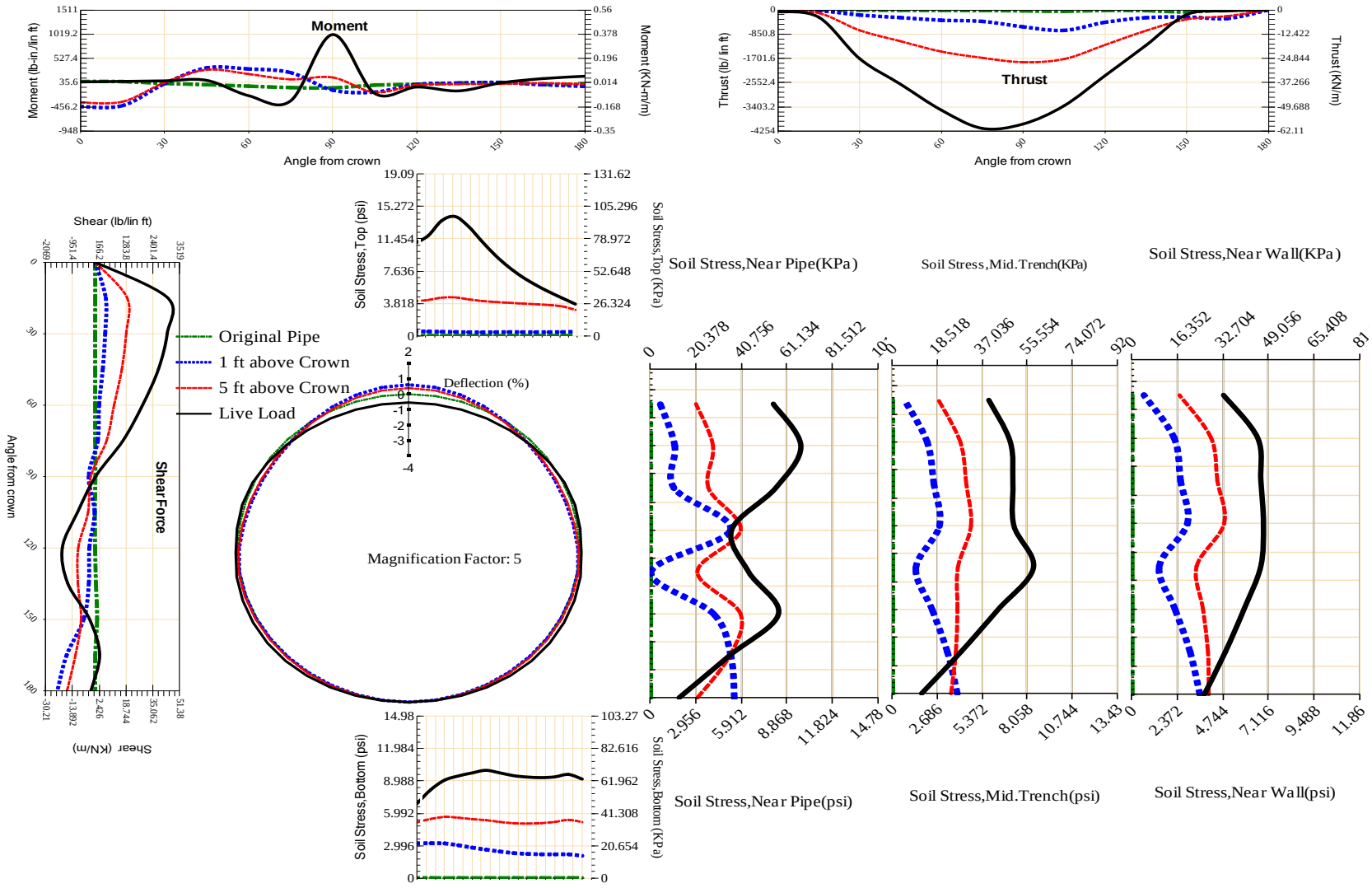

Figure A-377 Param-48-PW288-SF5OR-OD+108-EW10-H5-LiveLoad

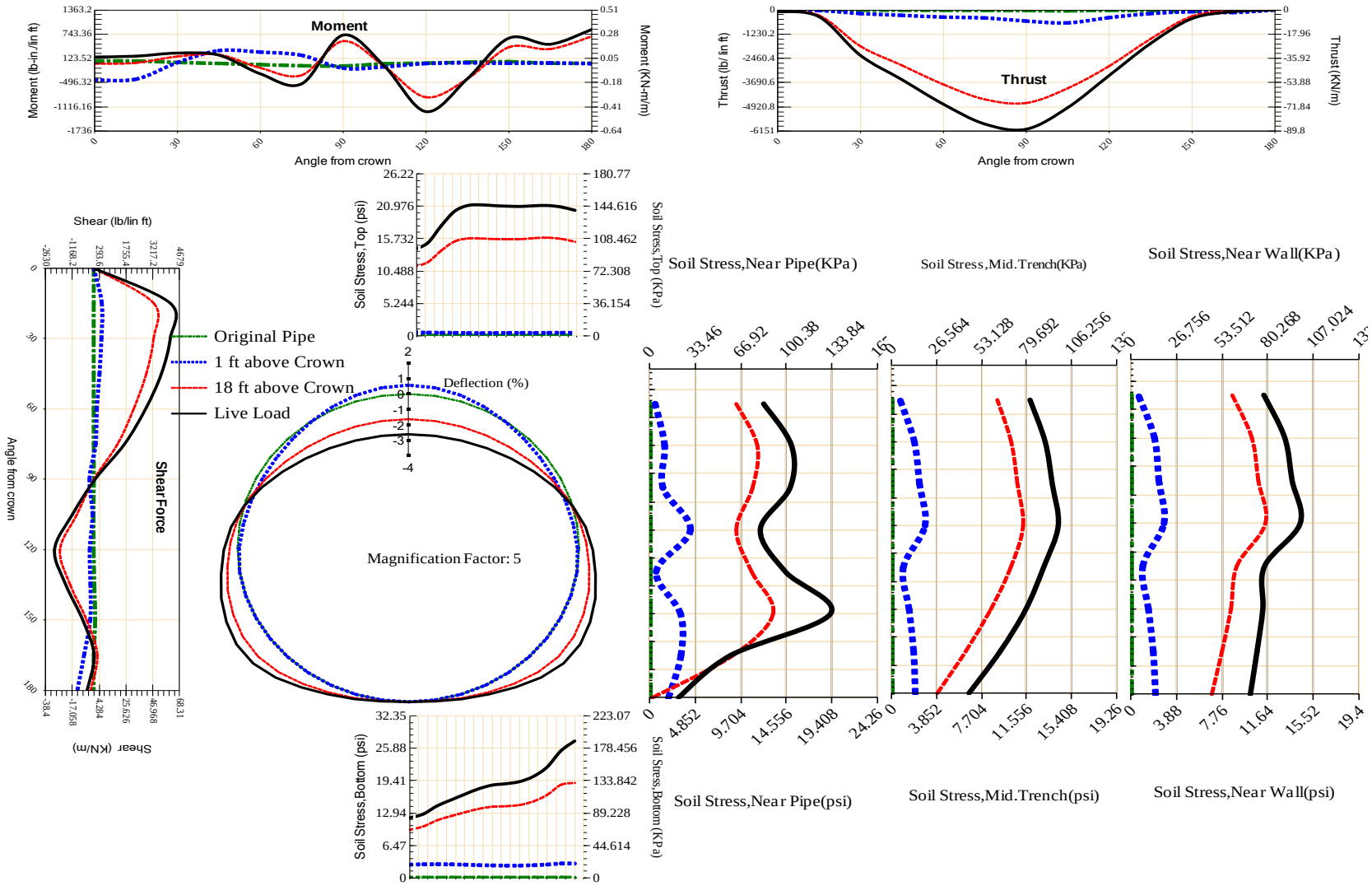

Figure A-378 Param-48-PW288-SF5OR-OD+108-EW3-H18-LiveLoad

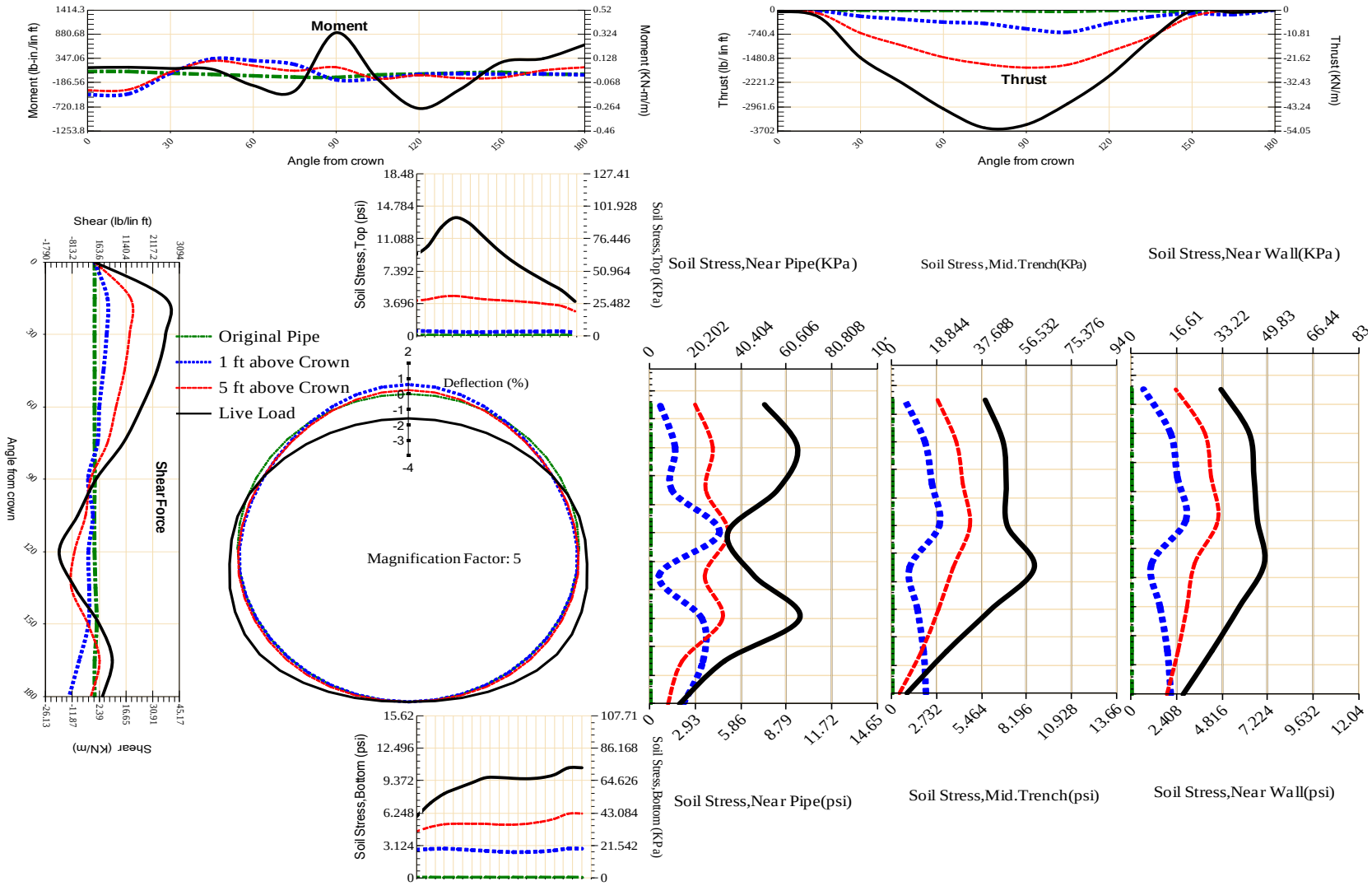

Figure A-379 Param-48-PW288-SF5OR-OD+108-EW3-H5-LiveLoad

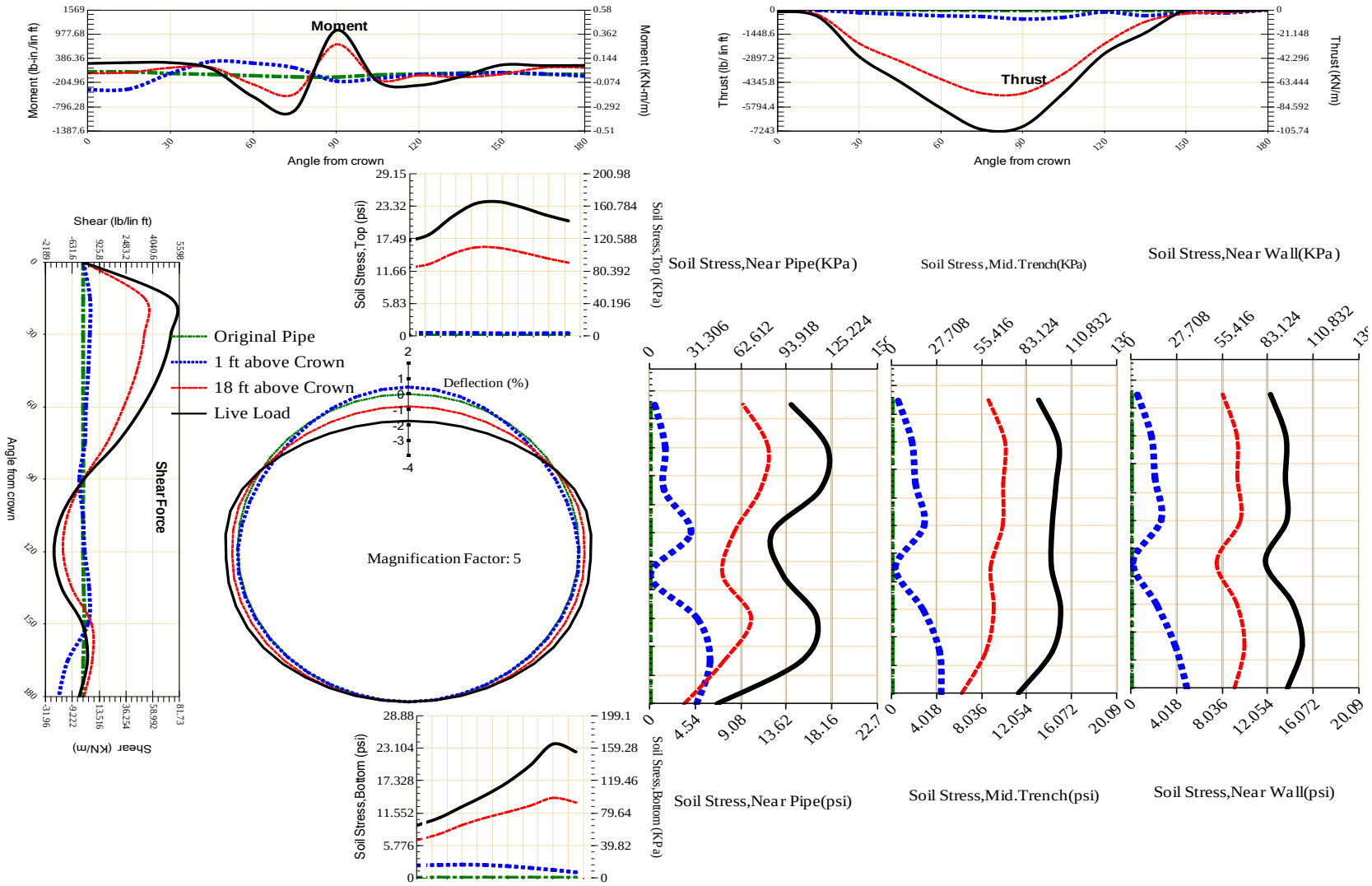

Figure A-380 Param-48-PW288-SF5OR-OD+48-EW10-H18-LiveLoad

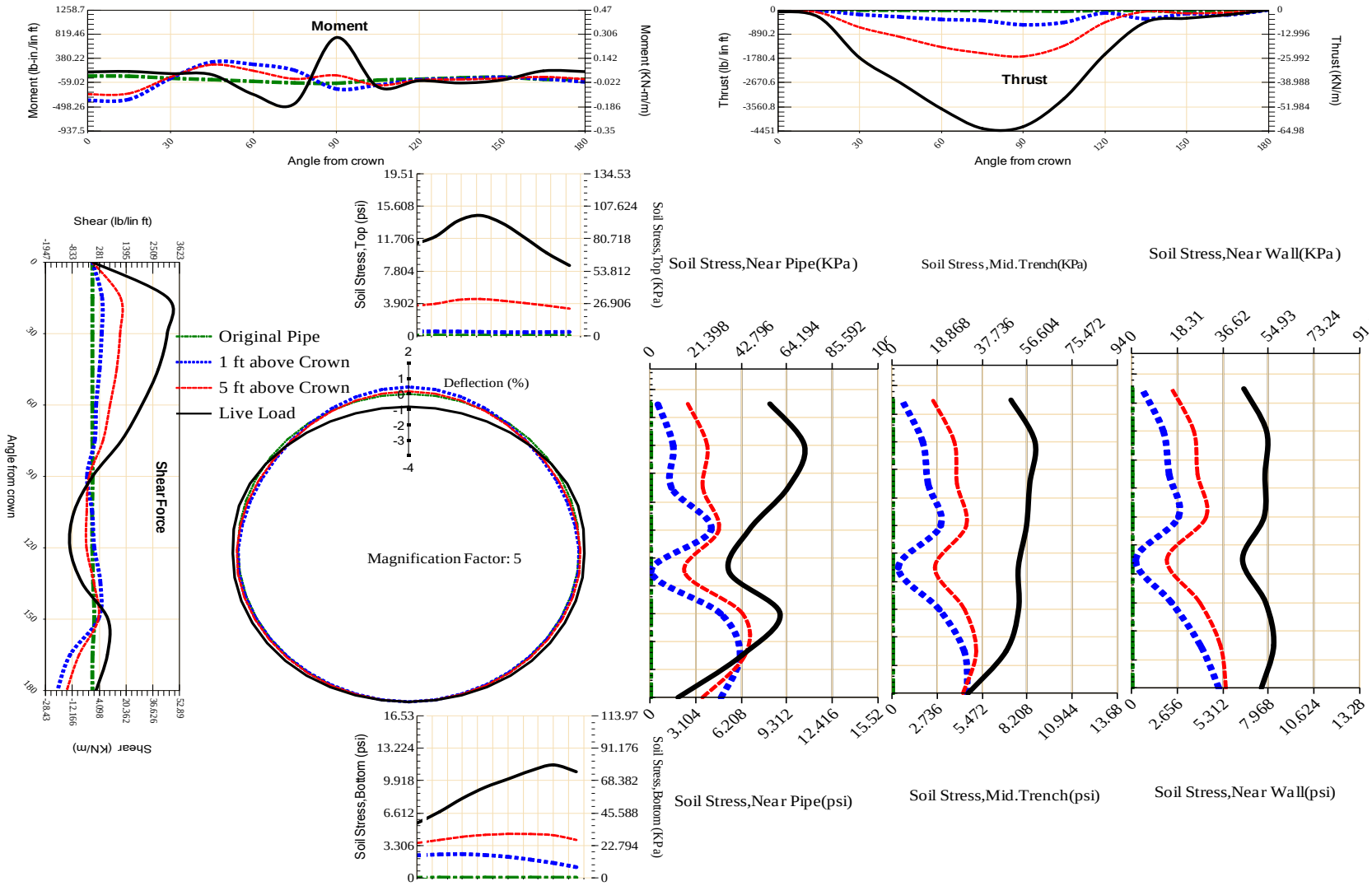

Figure A-381 Param-48-PW288-SF5OR-OD+48-EW10-H5-LiveLoad

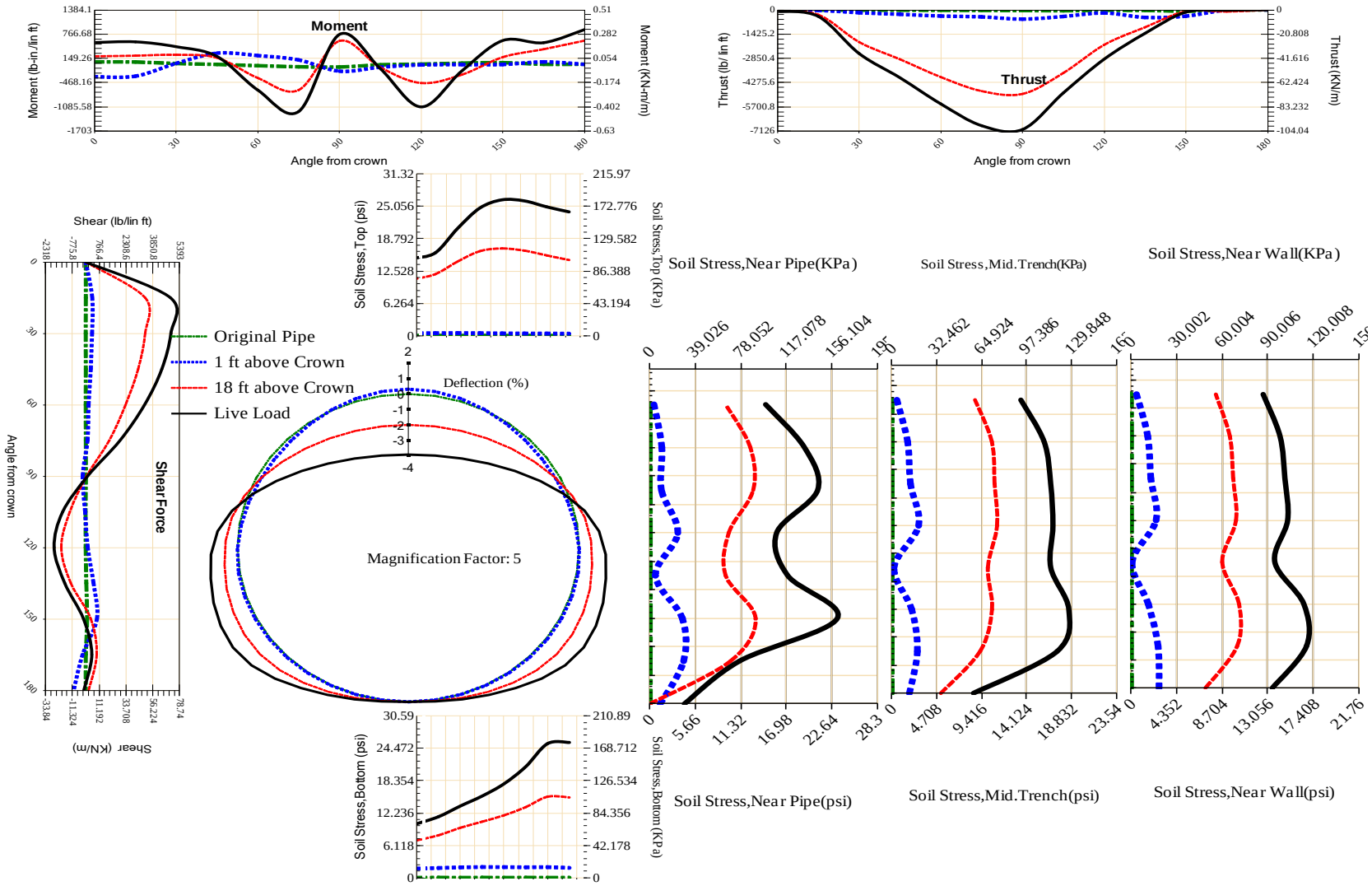

Figure A-382 Param-48-PW288-SF5OR-OD+48-EW3-H18-LiveLoad

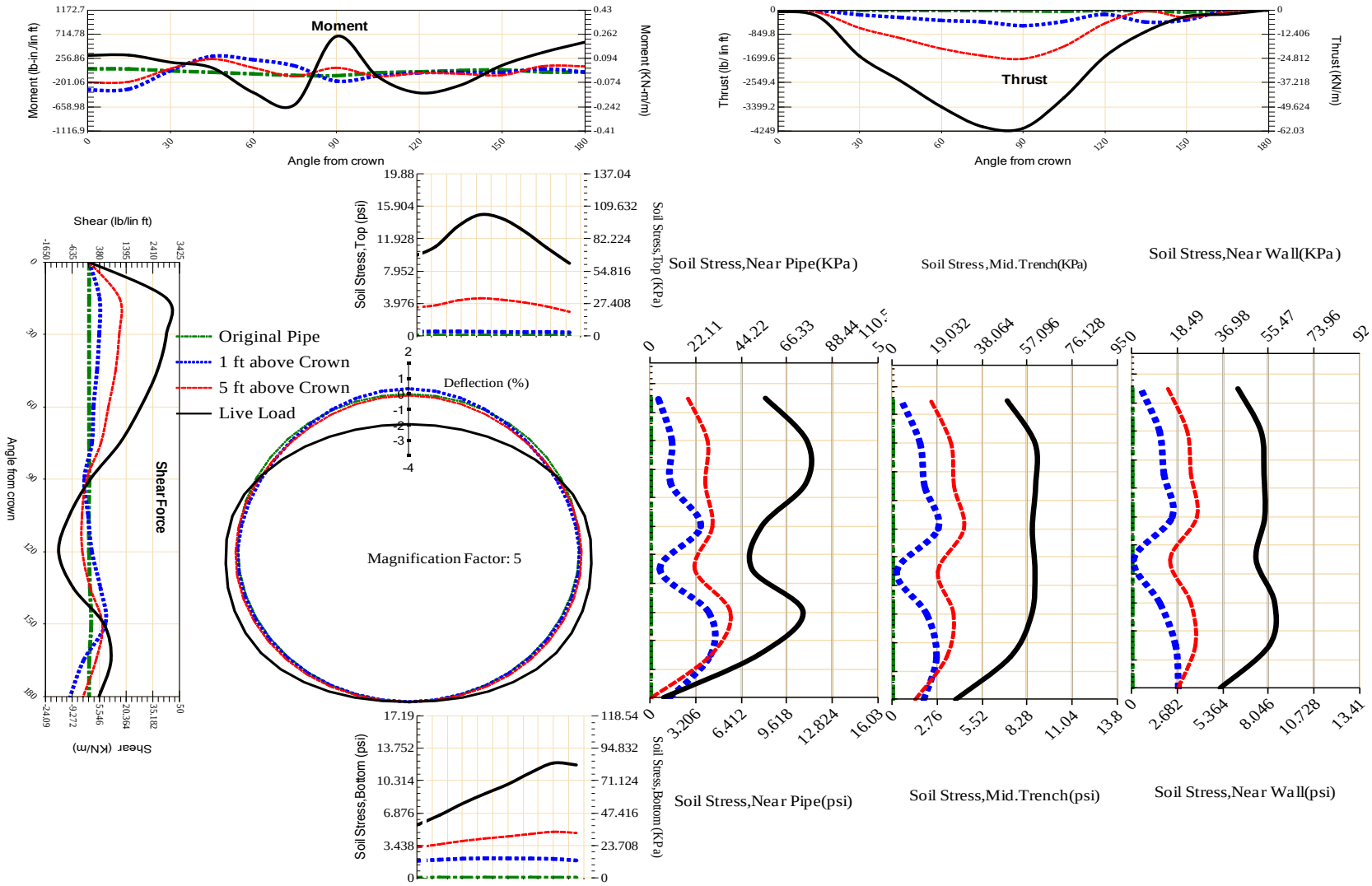

Figure A-383 Param-48-PW288-SF5OR-OD+48-EW3-H5-LiveLoad

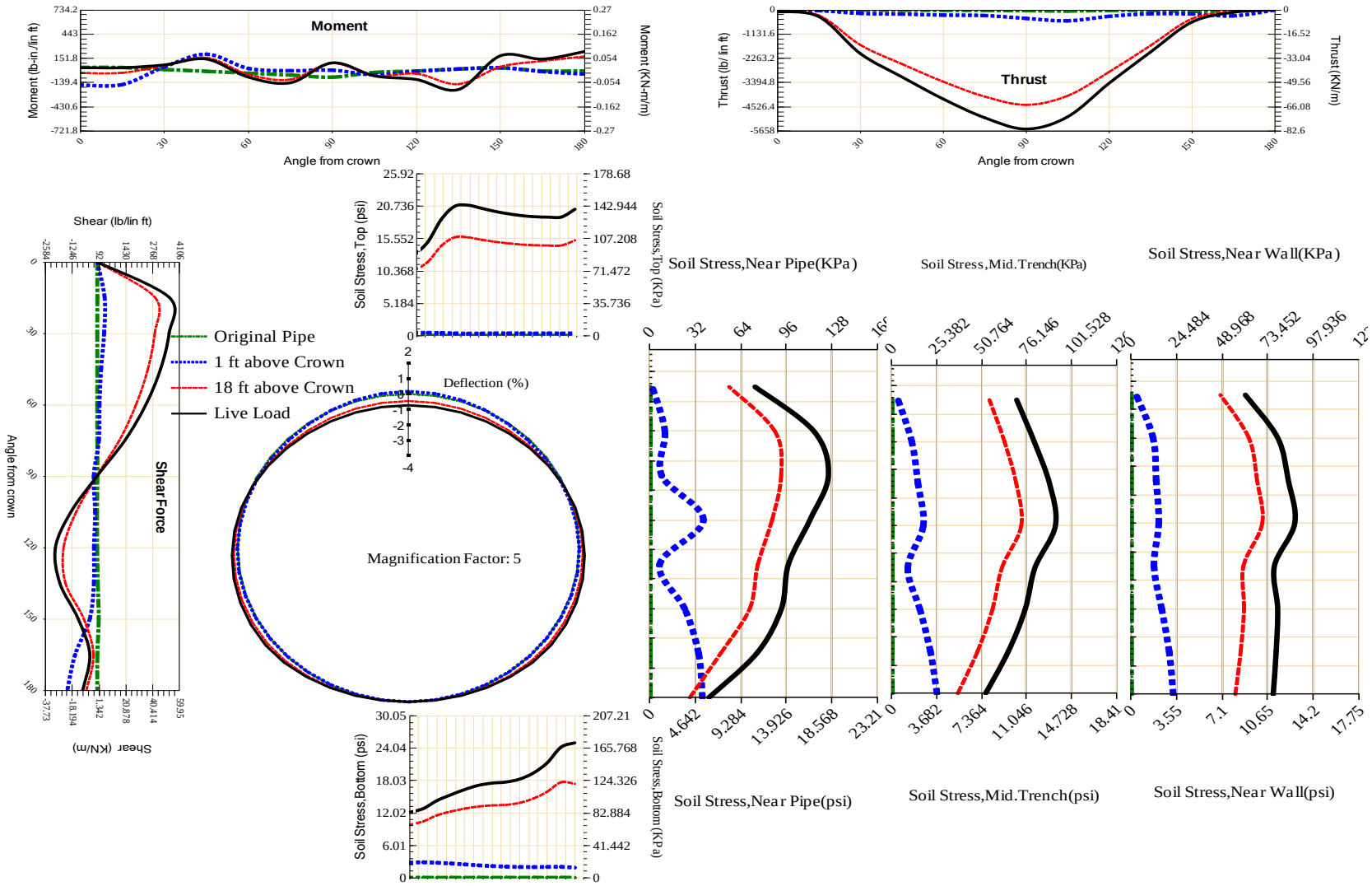

Figure A-384 Param-48-PW288-SF5TR-OD+108-EW10-H18-LiveLoad

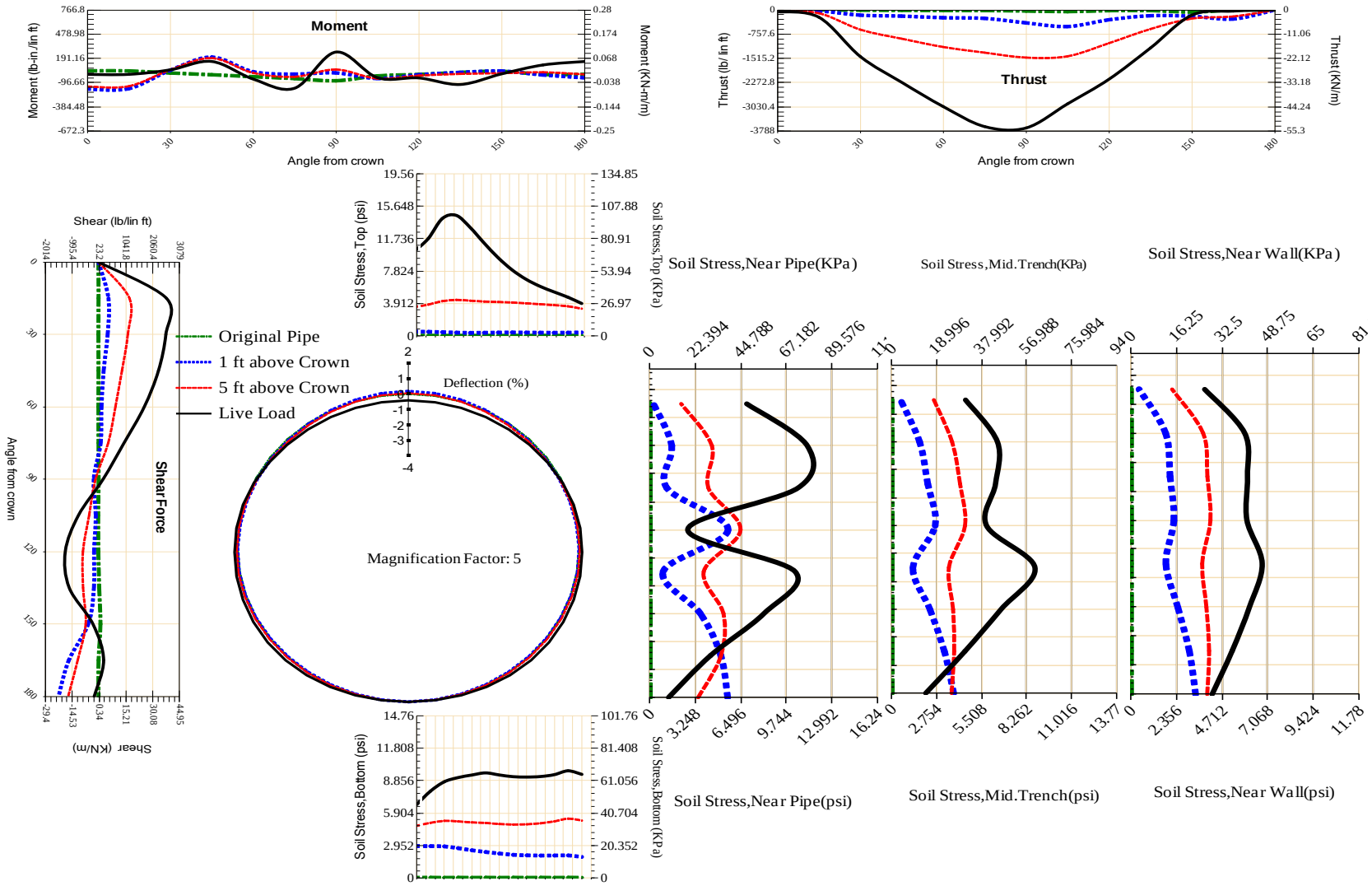

Figure A-385 Param-48-PW288-SF5TR-OD+108-EW10-H5-LiveLoad

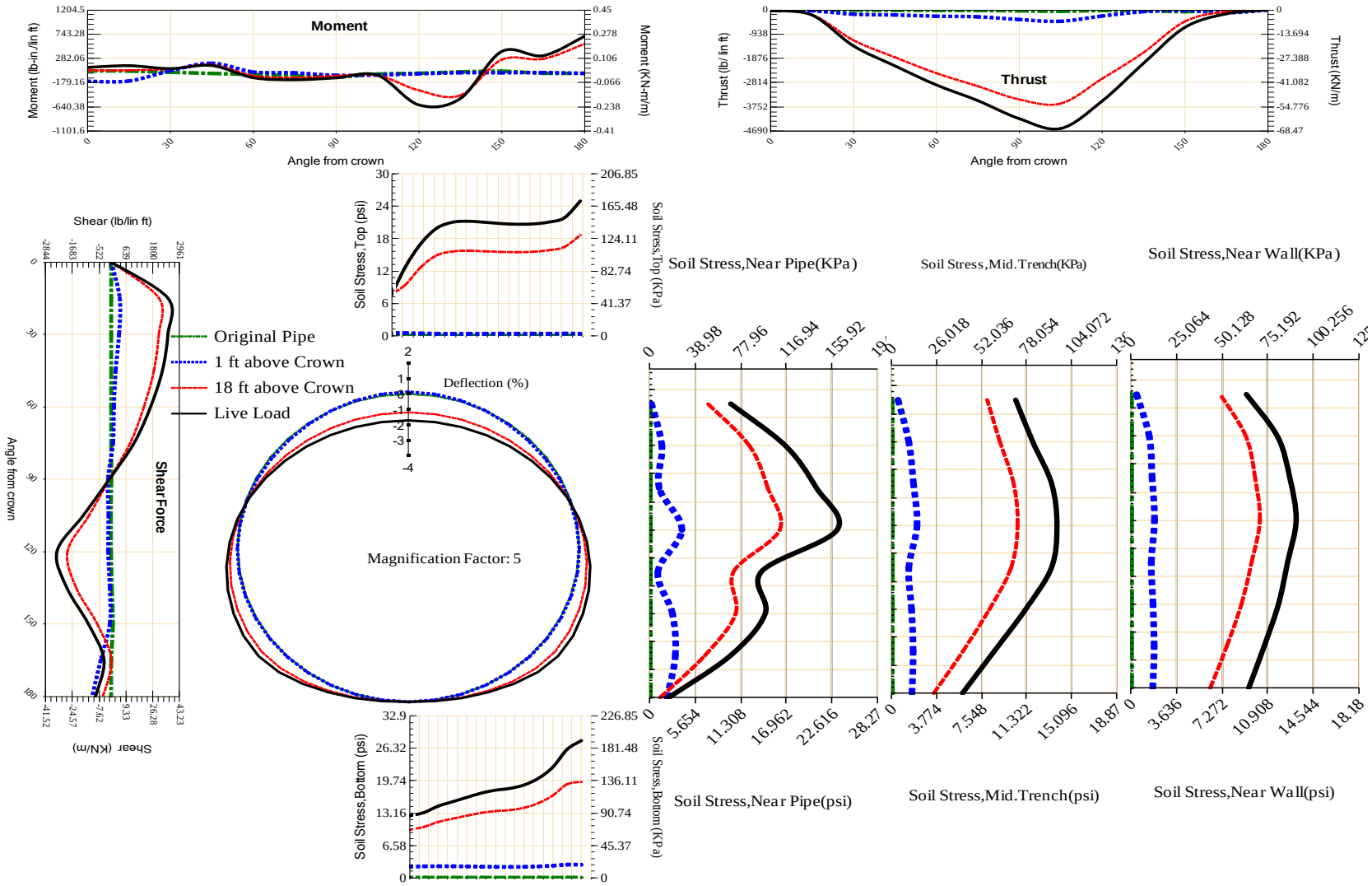

Figure A-386 Param-48-PW288-SF5TR-OD+108-EW3-H18-LiveLoad

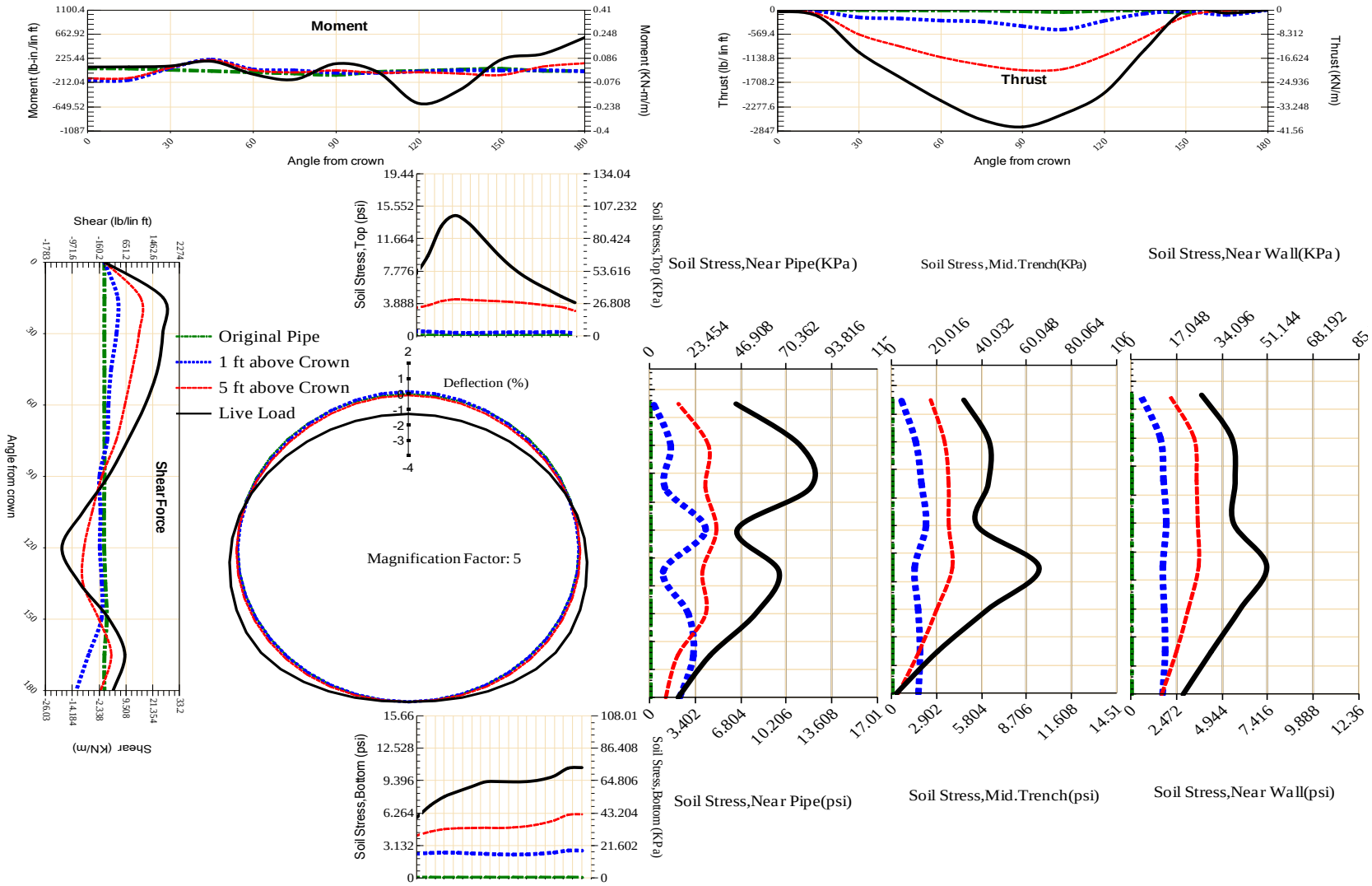

Figure A-387 Param-48-PW288-SF5TR-OD+108-EW3-H5-LiveLoad

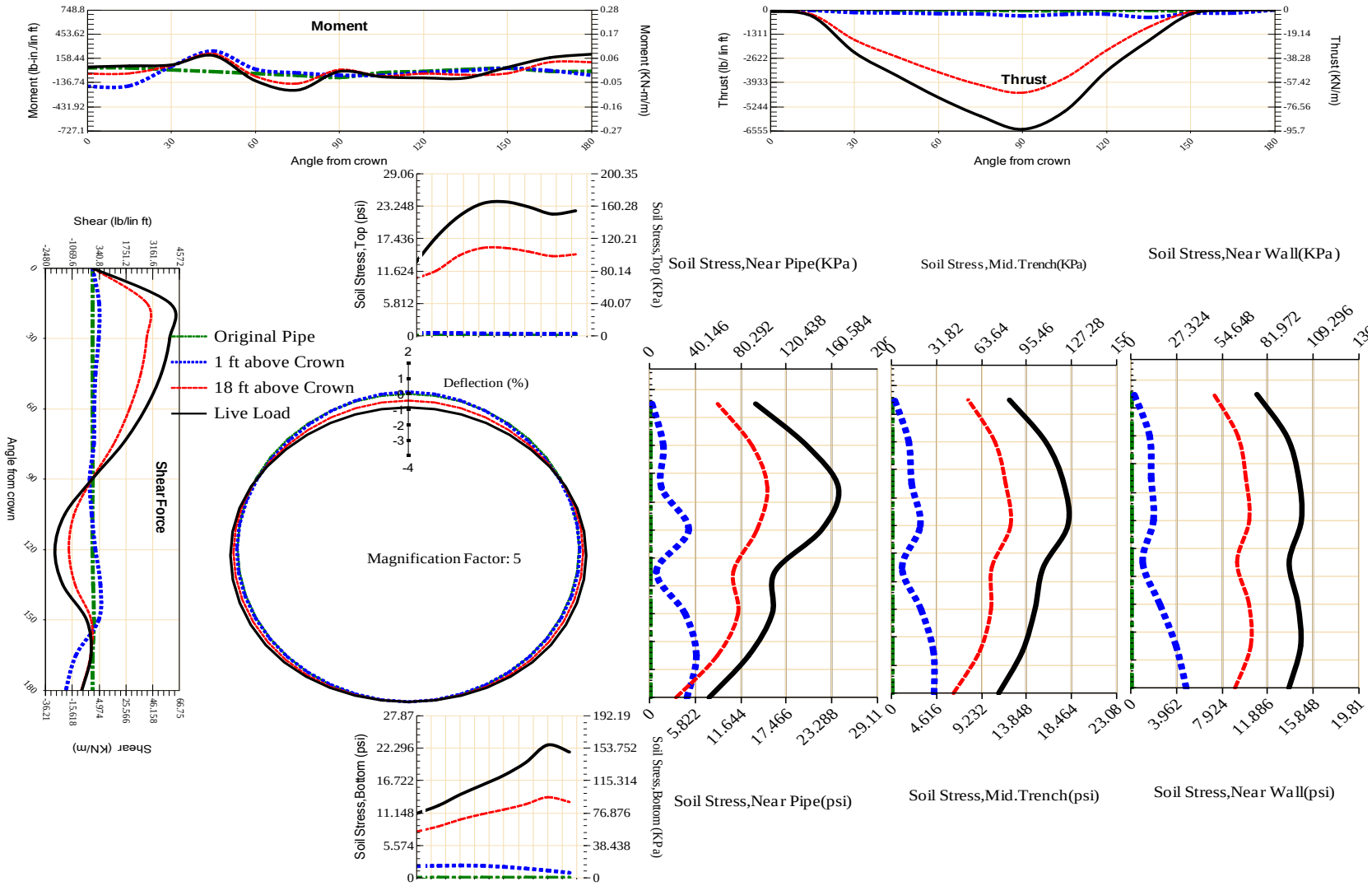

Figure A-388 Param-48-PW288-SF5TR-OD+48-EW10-H18-LiveLoad

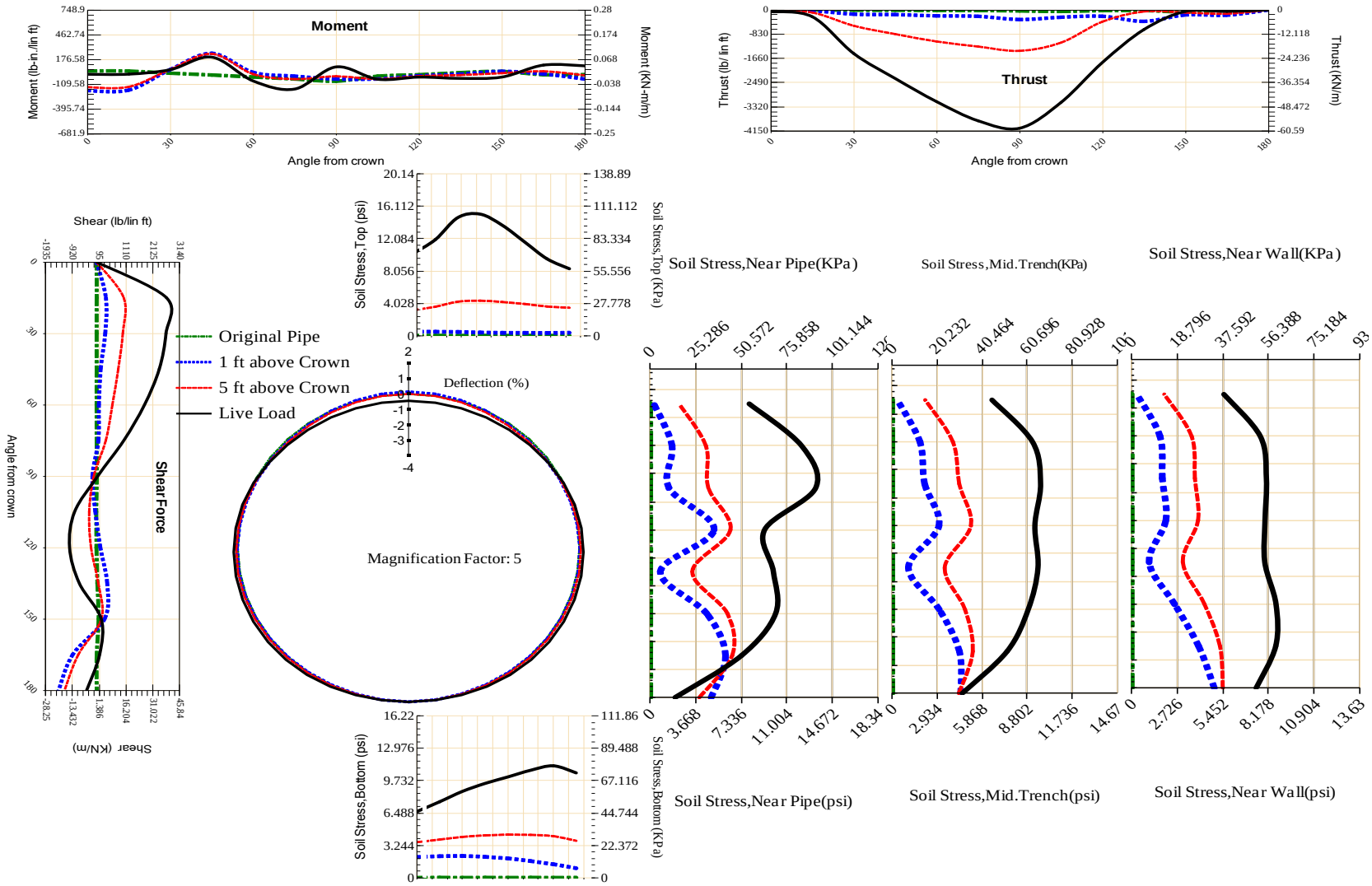

Figure A-389 Param-48-PW288-SF5TR-OD+48-EW10-H5-LiveLoad

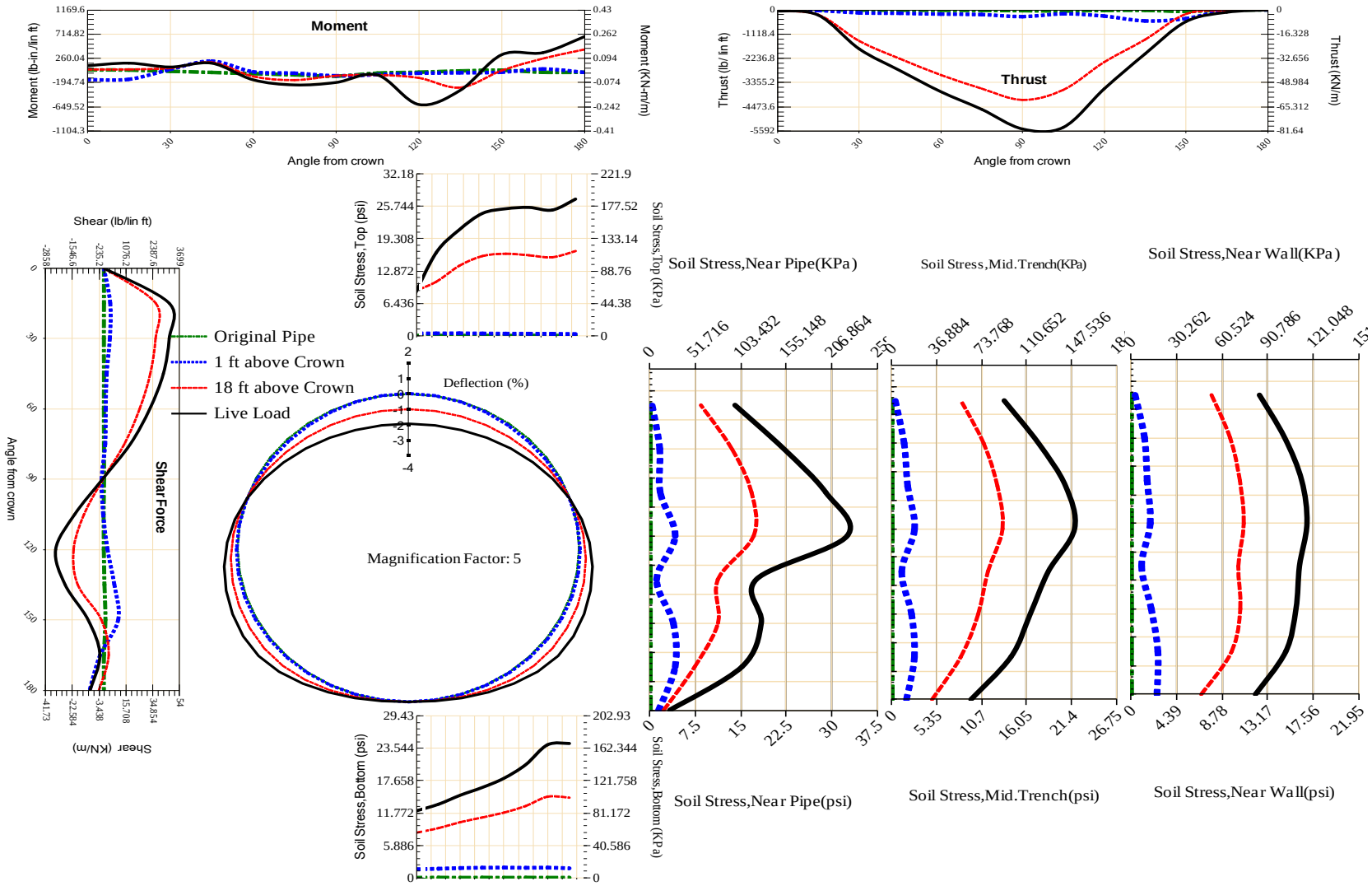

Figure A-390 Param-48-PW288-SF5TR-OD+48-EW3-H18-LiveLoad

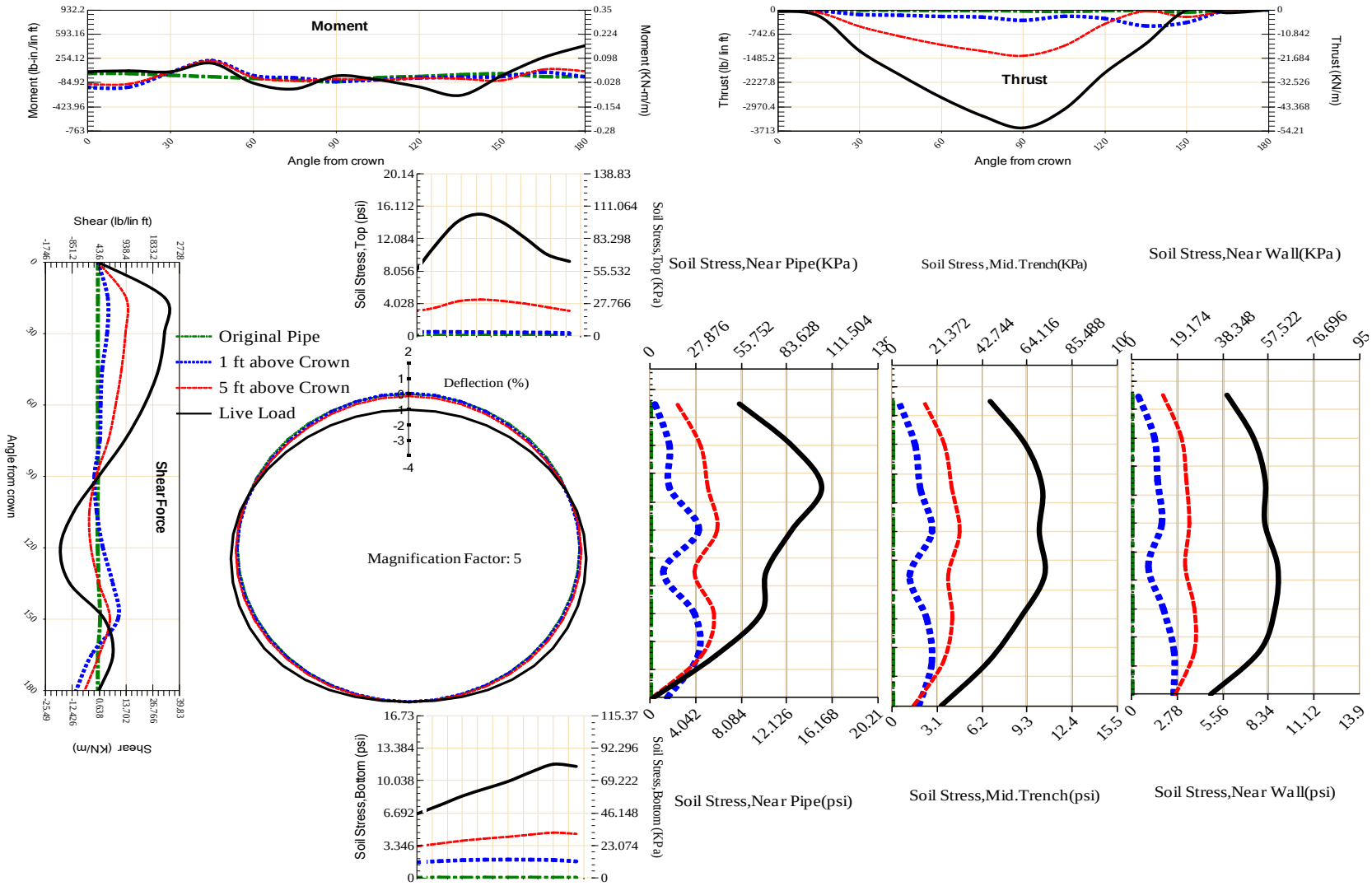

Figure A-391 Param-48-PW288-SF5TR-OD+48-EW3-H5-LiveLoad

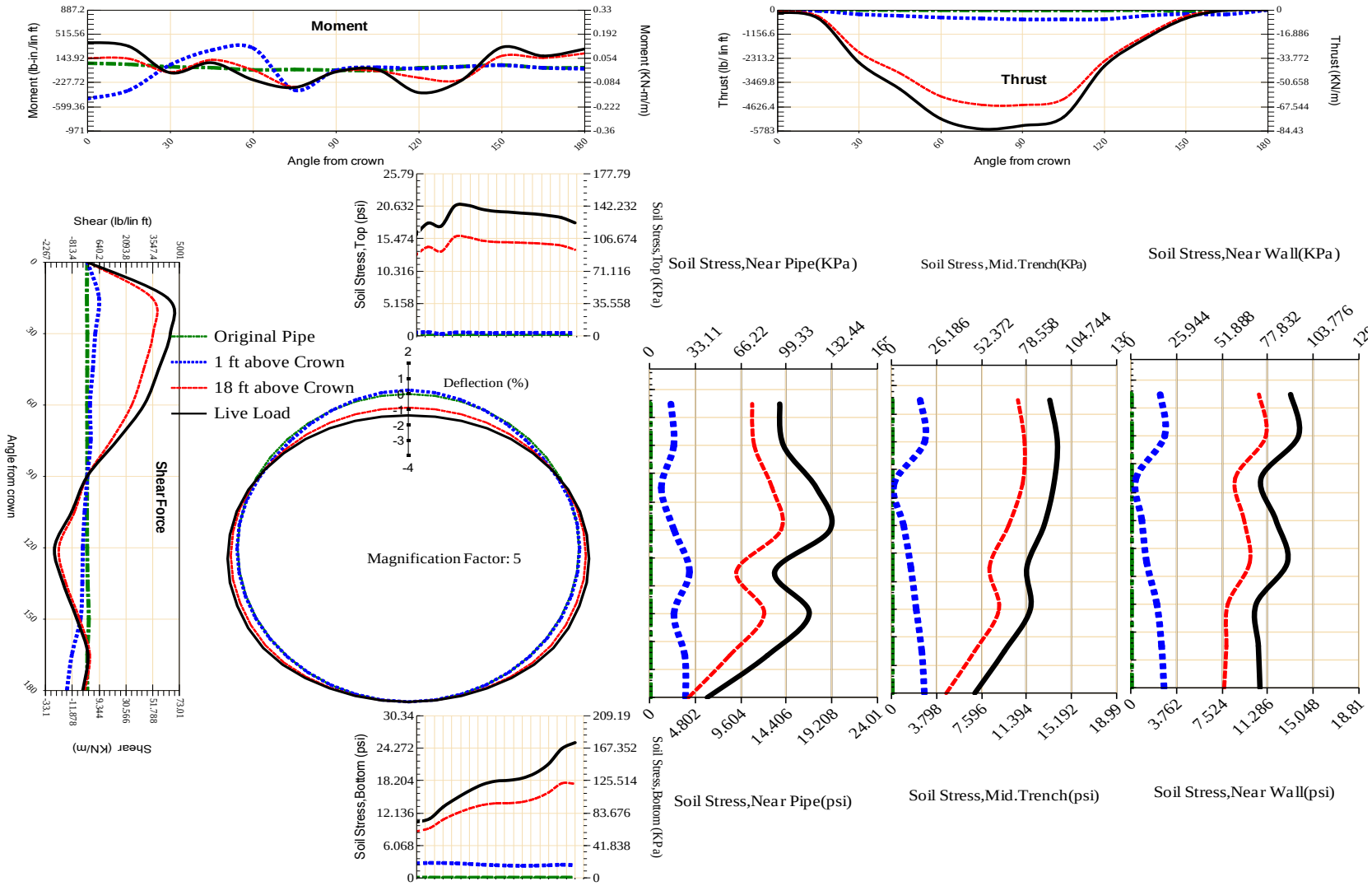

Figure A-392 Param-48-PW288-SF7OR-OD+108-EW10-H18-LiveLoad

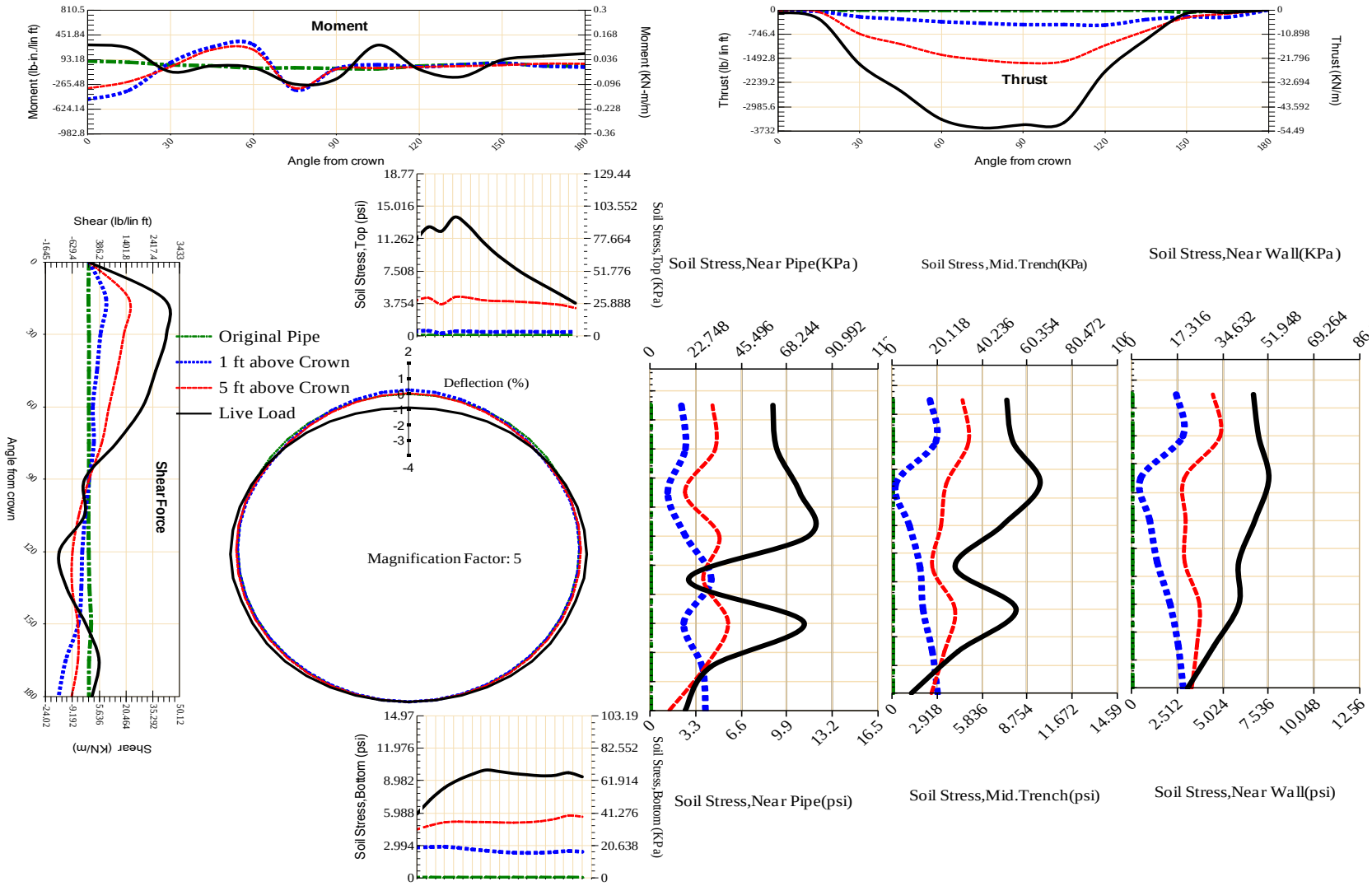

Figure A-393 Param-48-PW288-SF7OR-OD+108-EW10-H5-LiveLoad

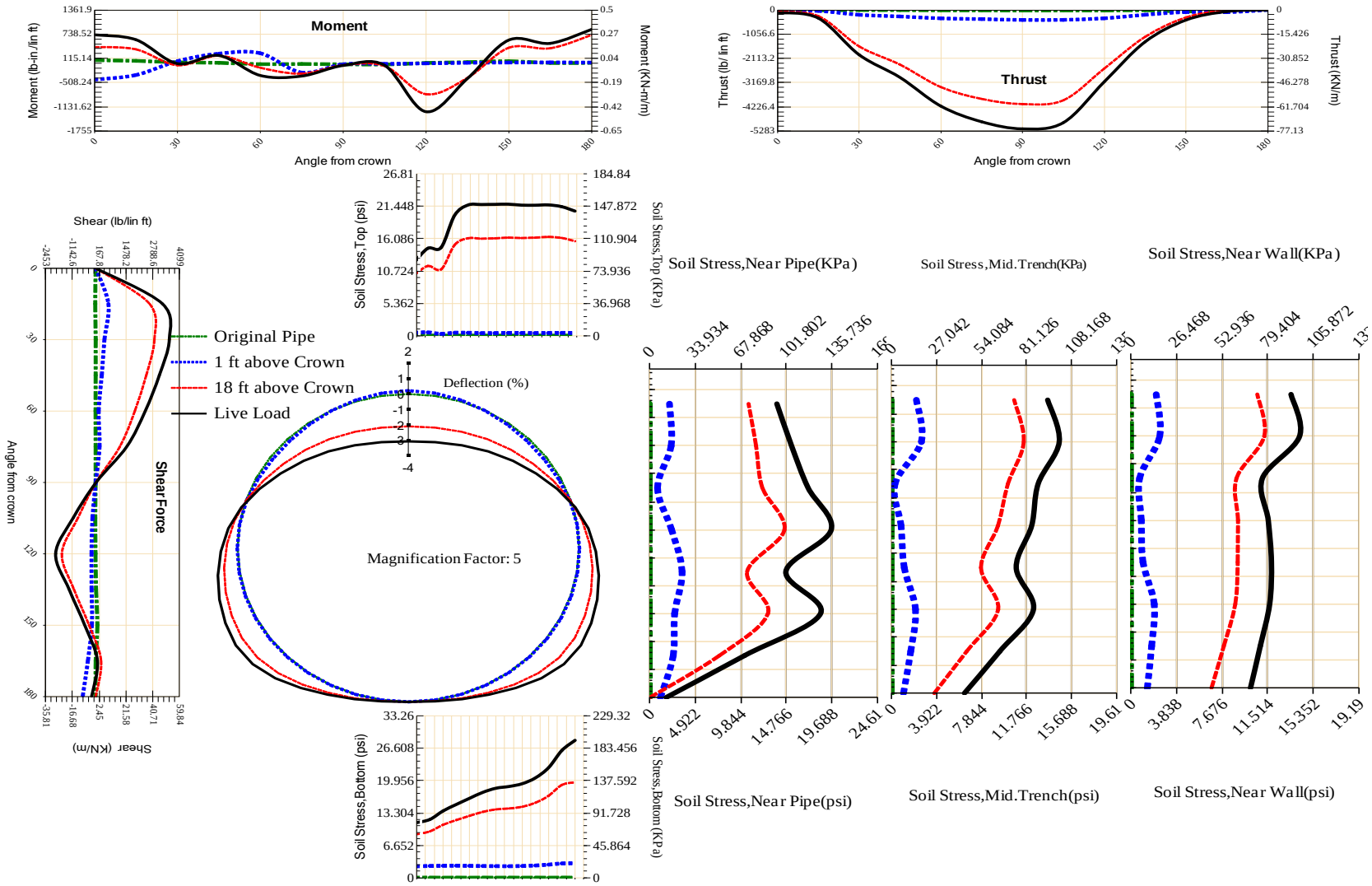

Figure A-394 Param-48-PW288-SF7OR-OD+108-EW3-H18-LiveLoad

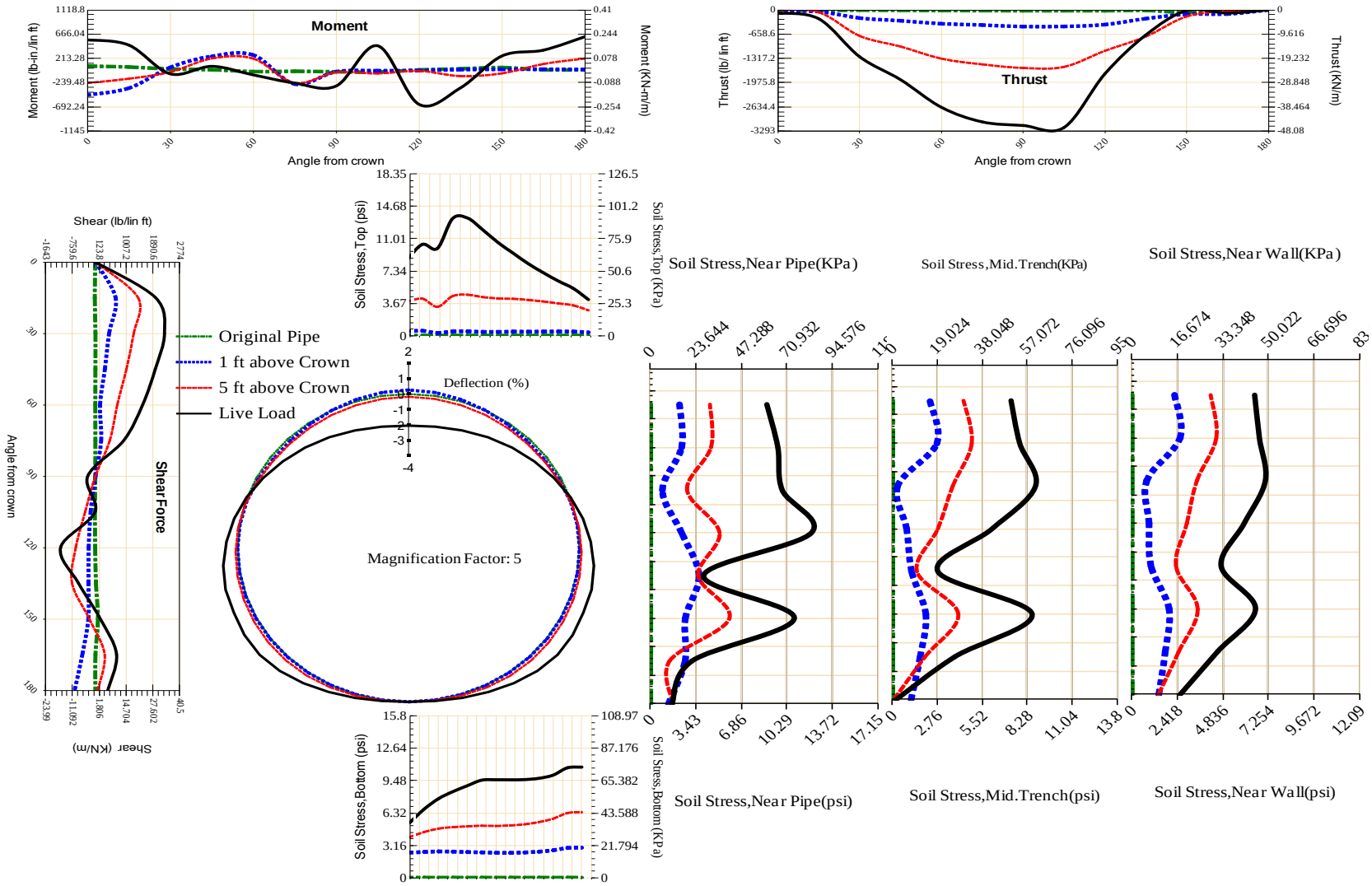

Figure A-395 Param-48-PW288-SF7OR-OD+108-EW3-H5-LiveLoad

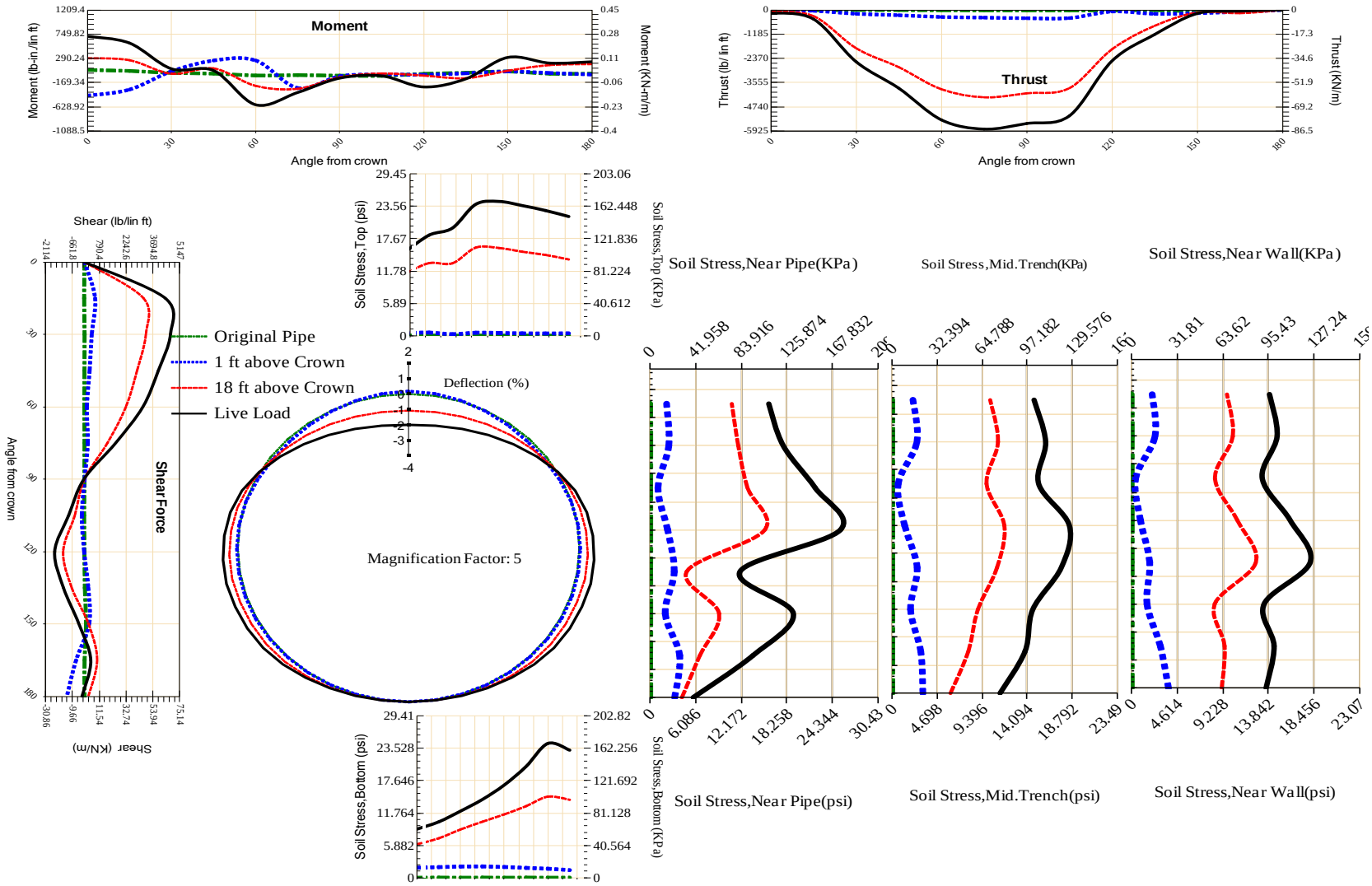

Figure A-396 Param-48-PW288-SF7OR-OD+48-EW10-H18-LiveLoad

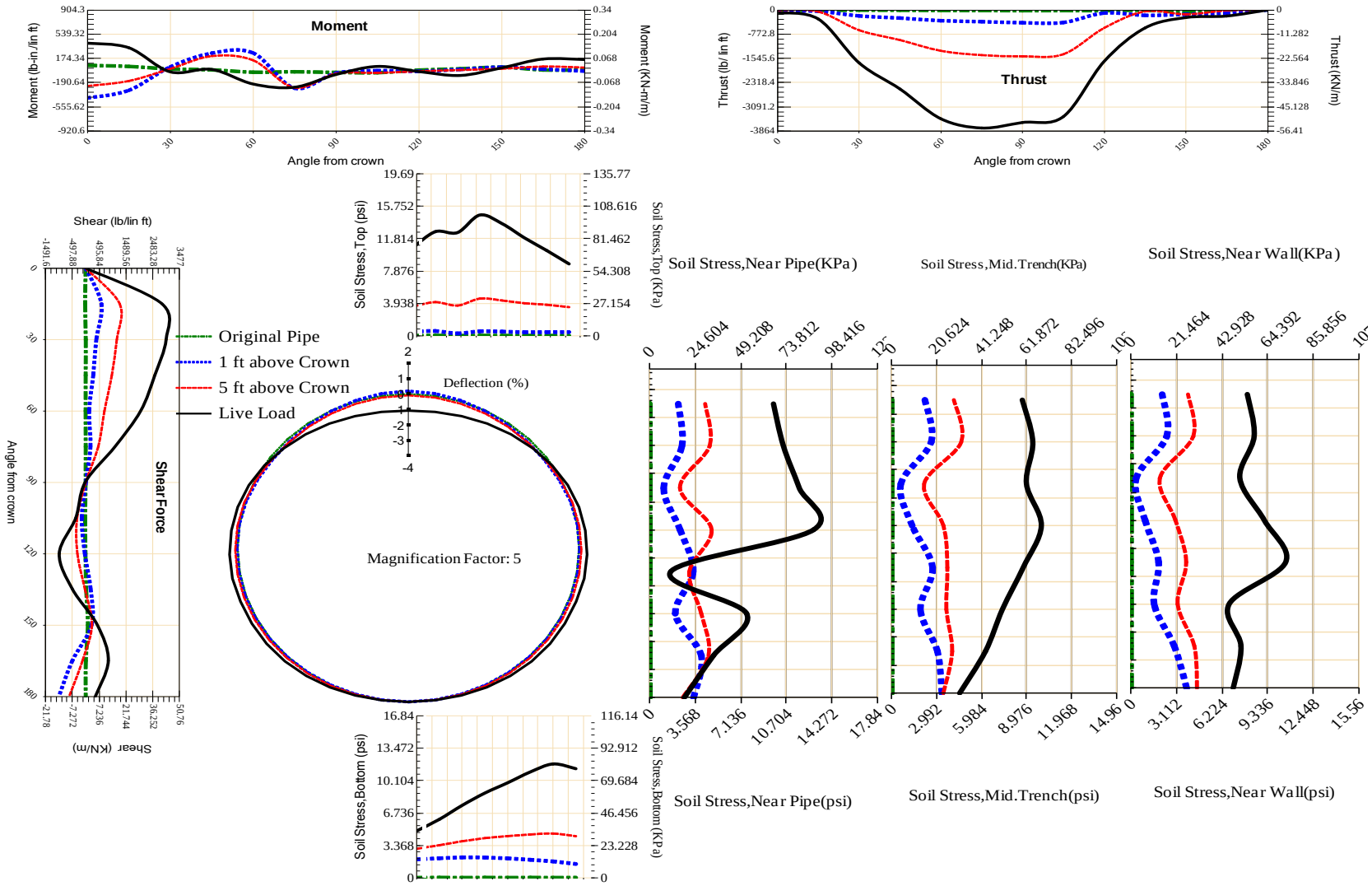

Figure A-397 Param-48-PW288-SF7OR-OD+48-EW10-H5-LiveLoad

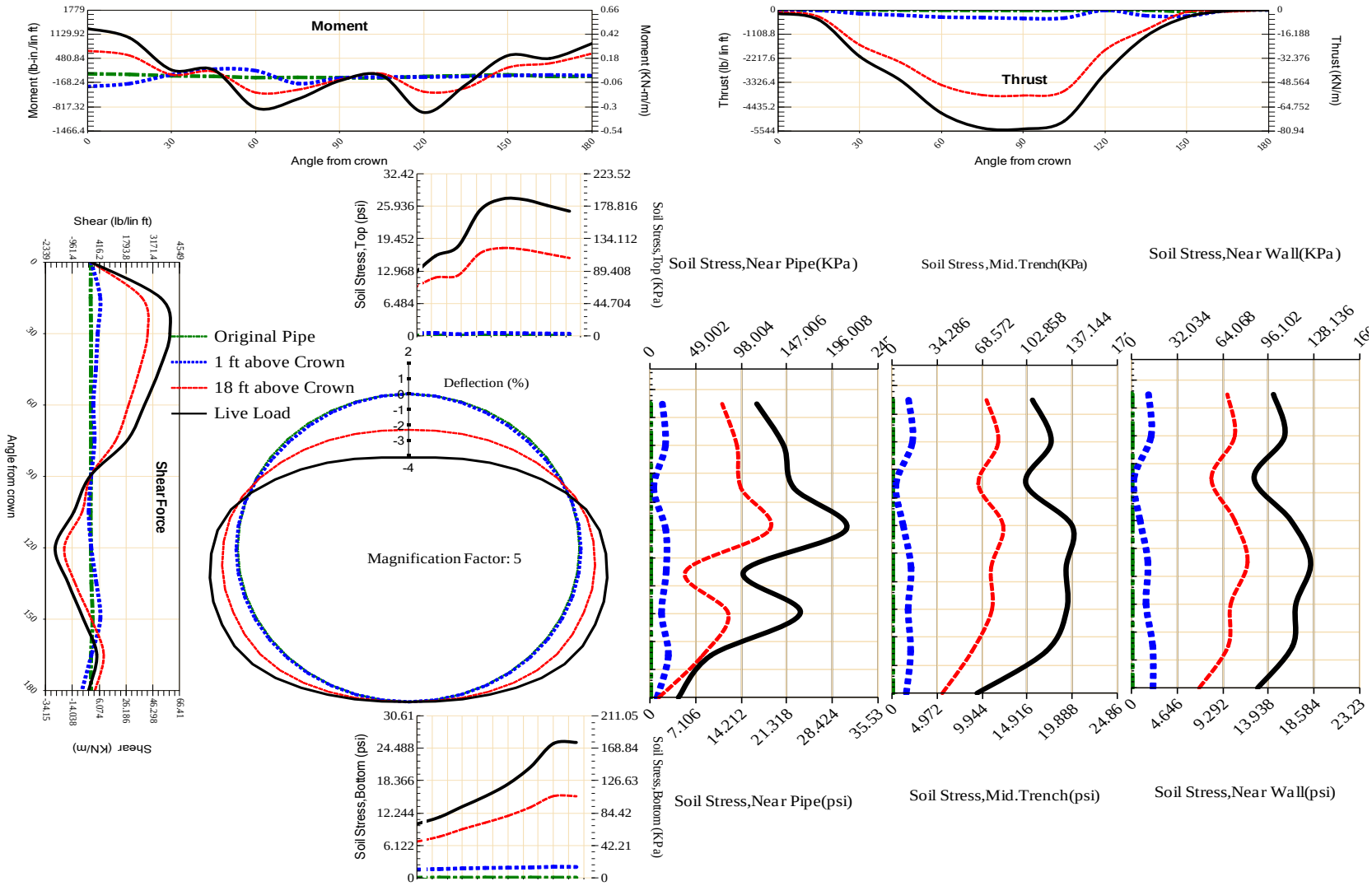

Figure A-398 Param-48-PW288-SF7OR-OD+48-EW3-H18-LiveLoad

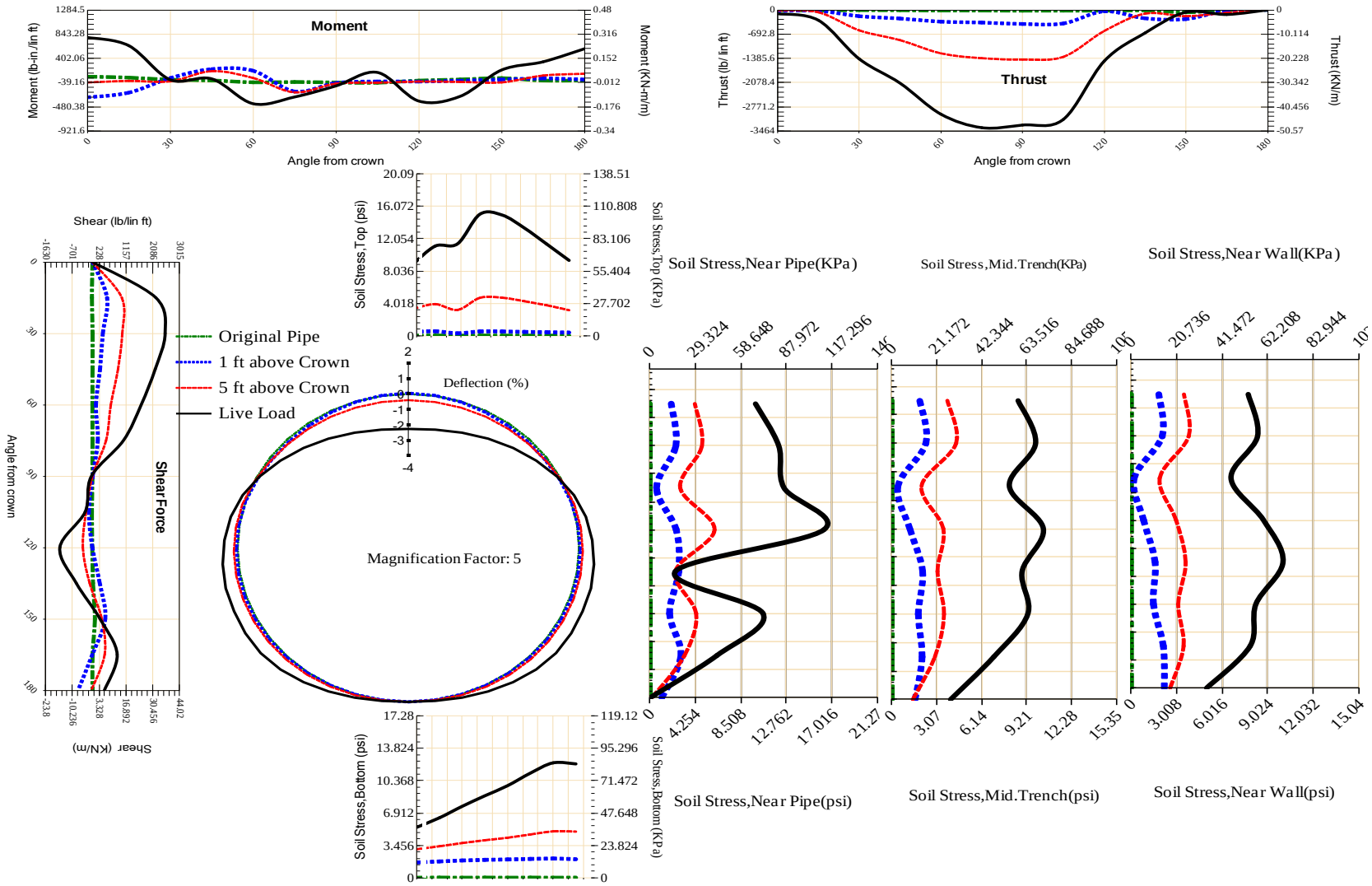

Figure A-399 Param-48-PW288-SF7OR-OD+48-EW3-H5-LiveLoad

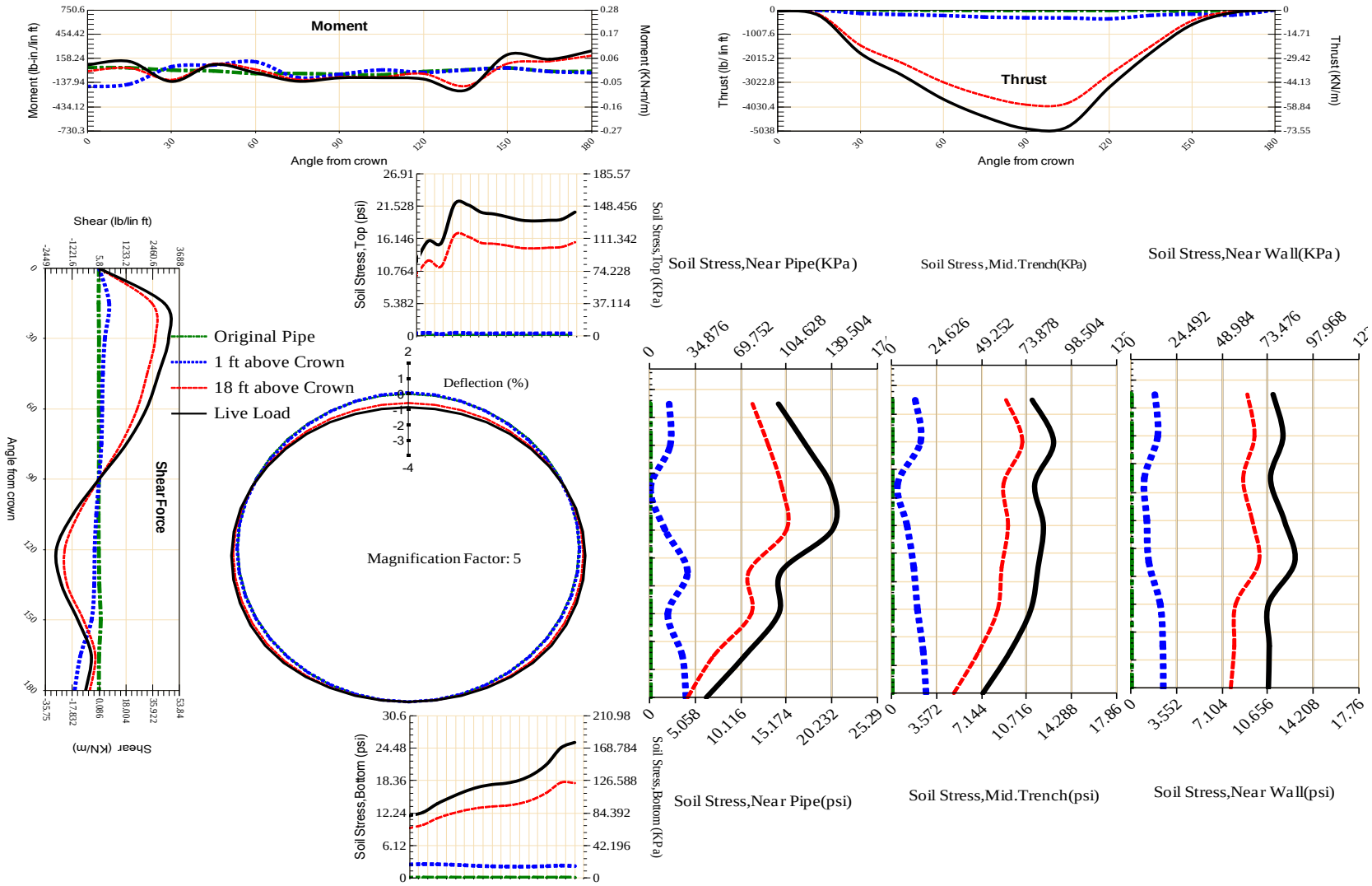

Figure A-400 Param-48-PW288-SF7TR-OD+108-EW10-H18-LiveLoad

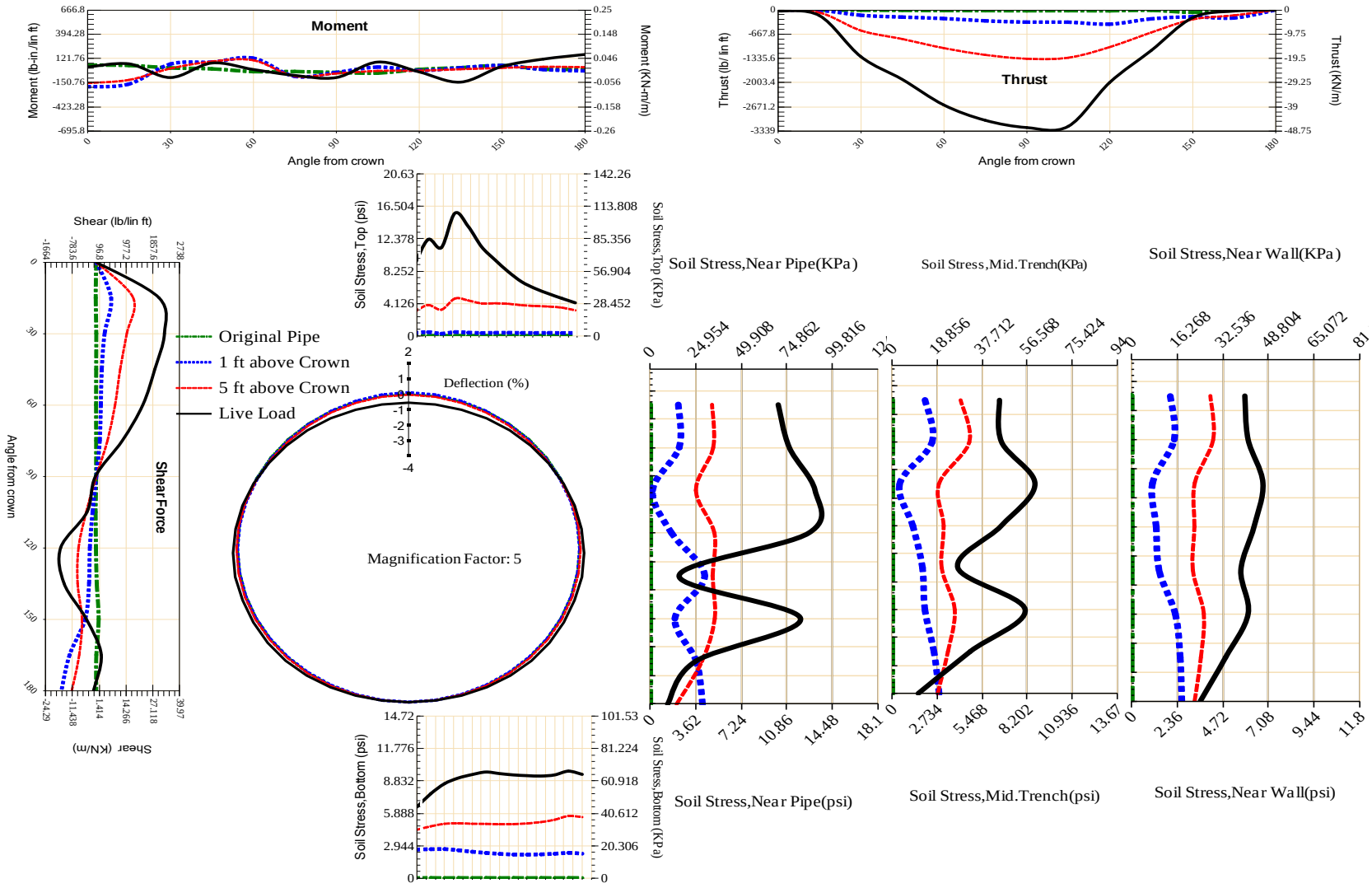

Figure A-401 Param-48-PW288-SF7TR-OD+108-EW10-H5-LiveLoad

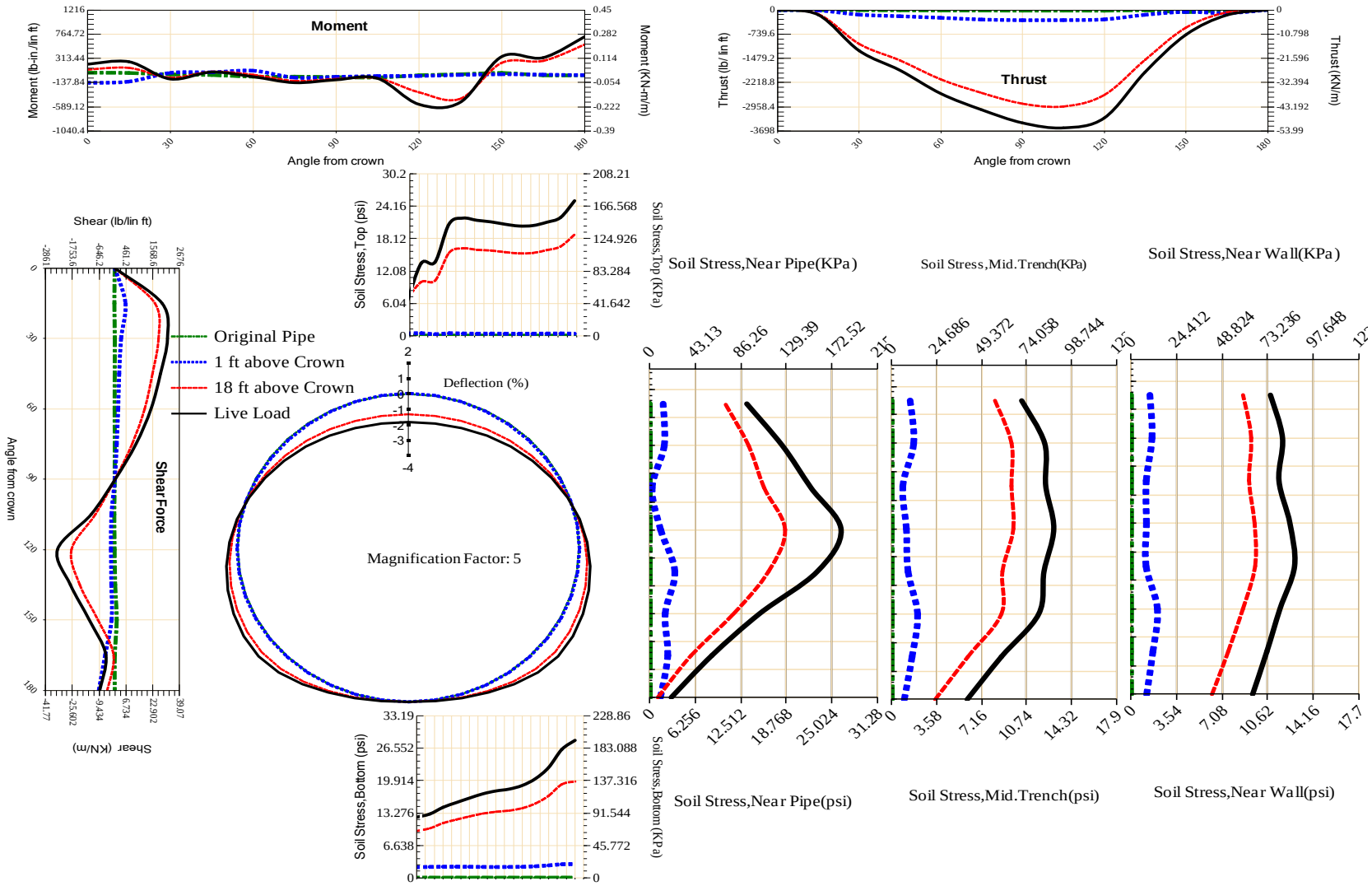

Figure A-402 Param-48-PW288-SF7TR-OD+108-EW3-H18-LiveLoad

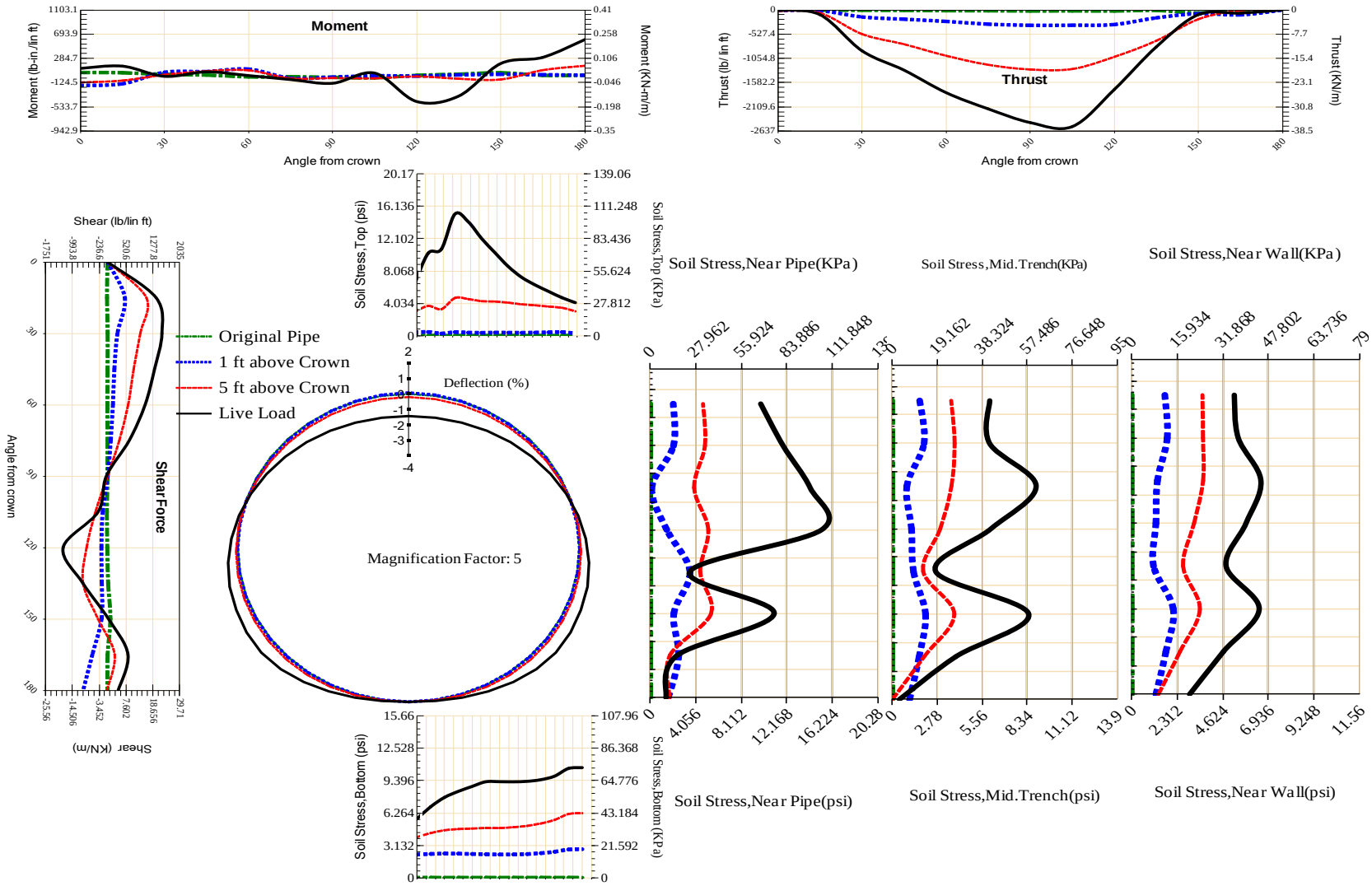

Figure A-403 Param-48-PW288-SF7TR-OD+108-EW3-H5-LiveLoad

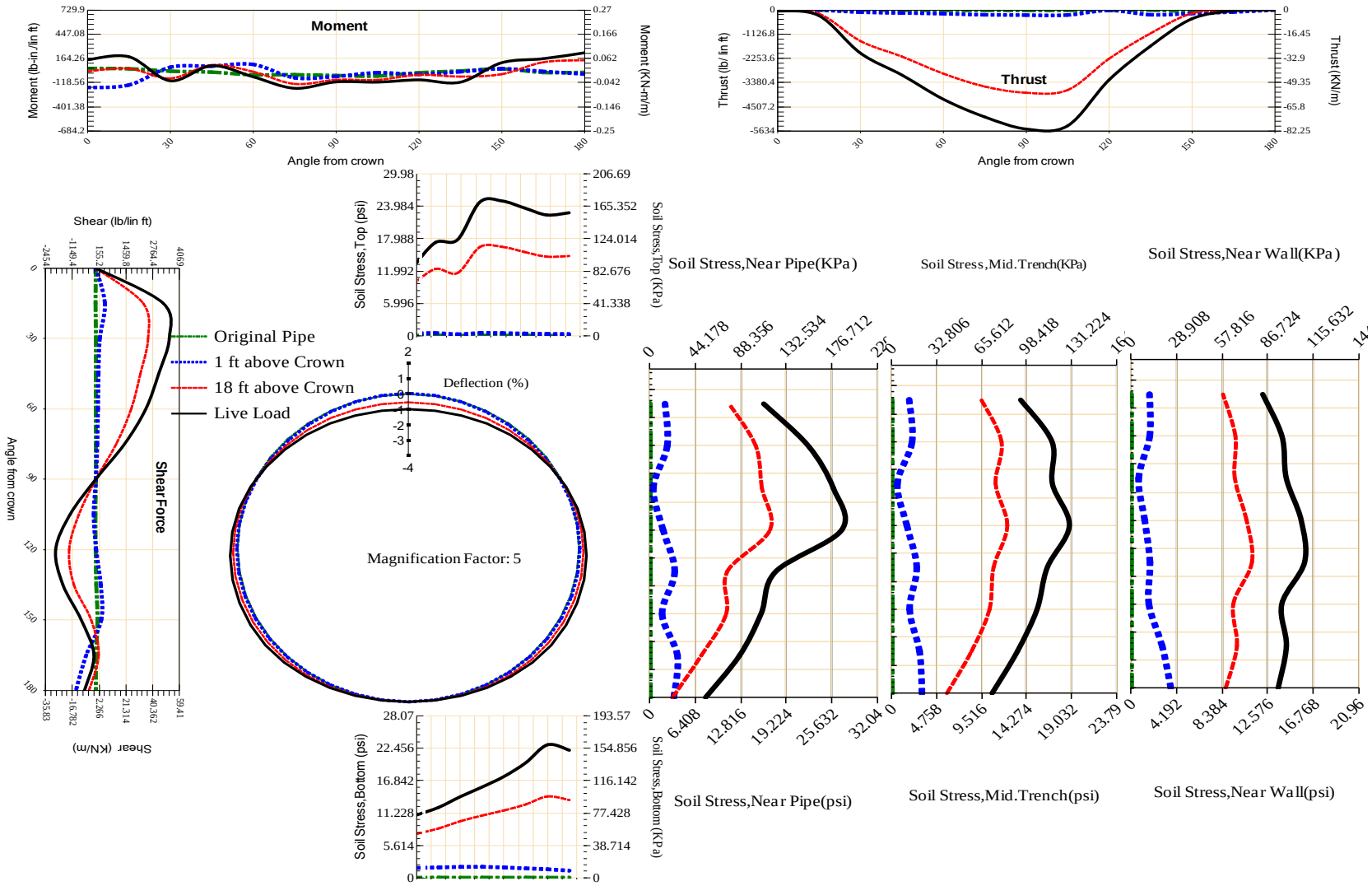

Figure A-404 Param-48-PW288-SF7TR-OD+48-EW10-H18-LiveLoad

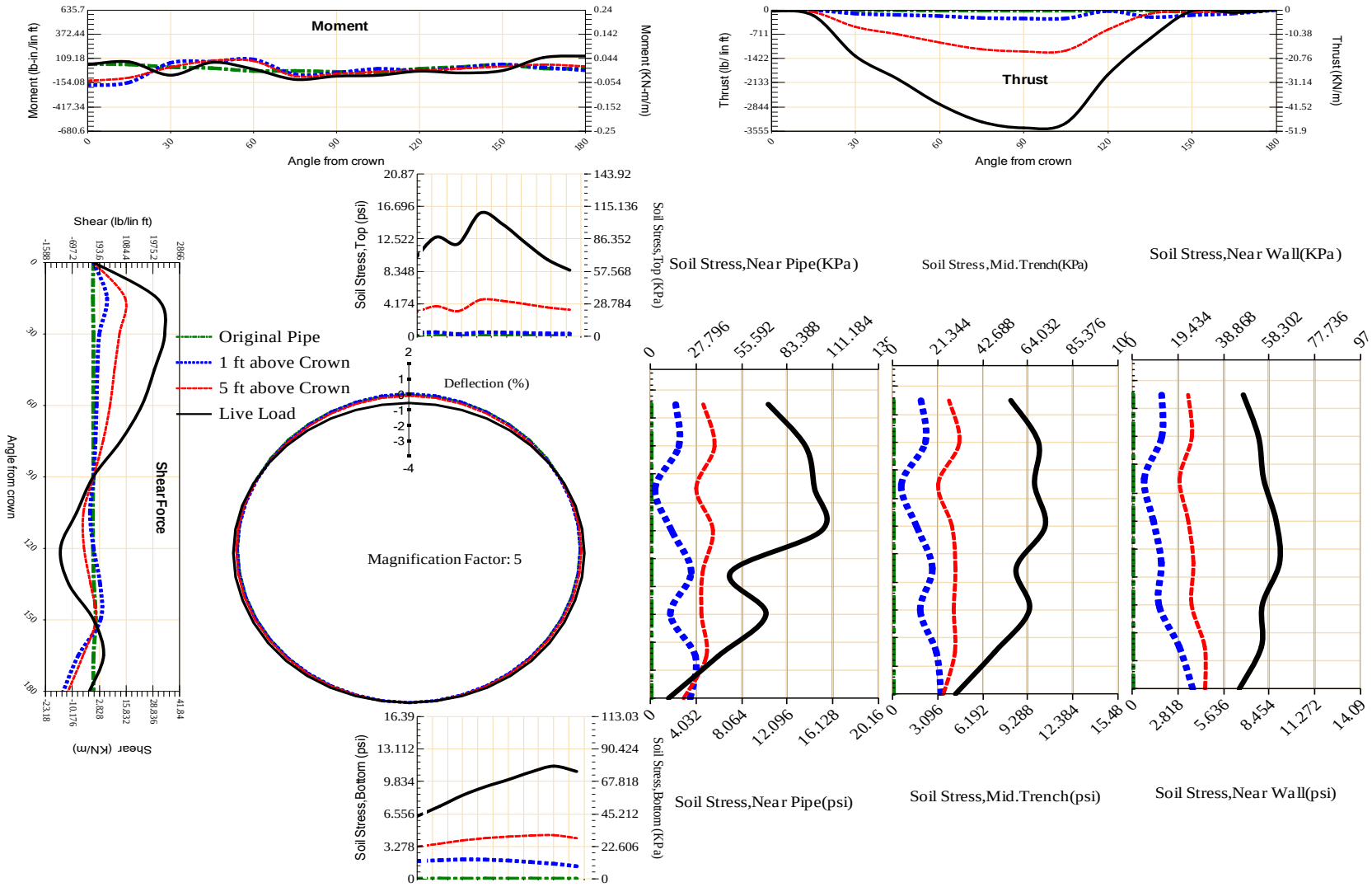

Figure A-405 Param-48-PW288-SF7TR-OD+48-EW10-H5-LiveLoad

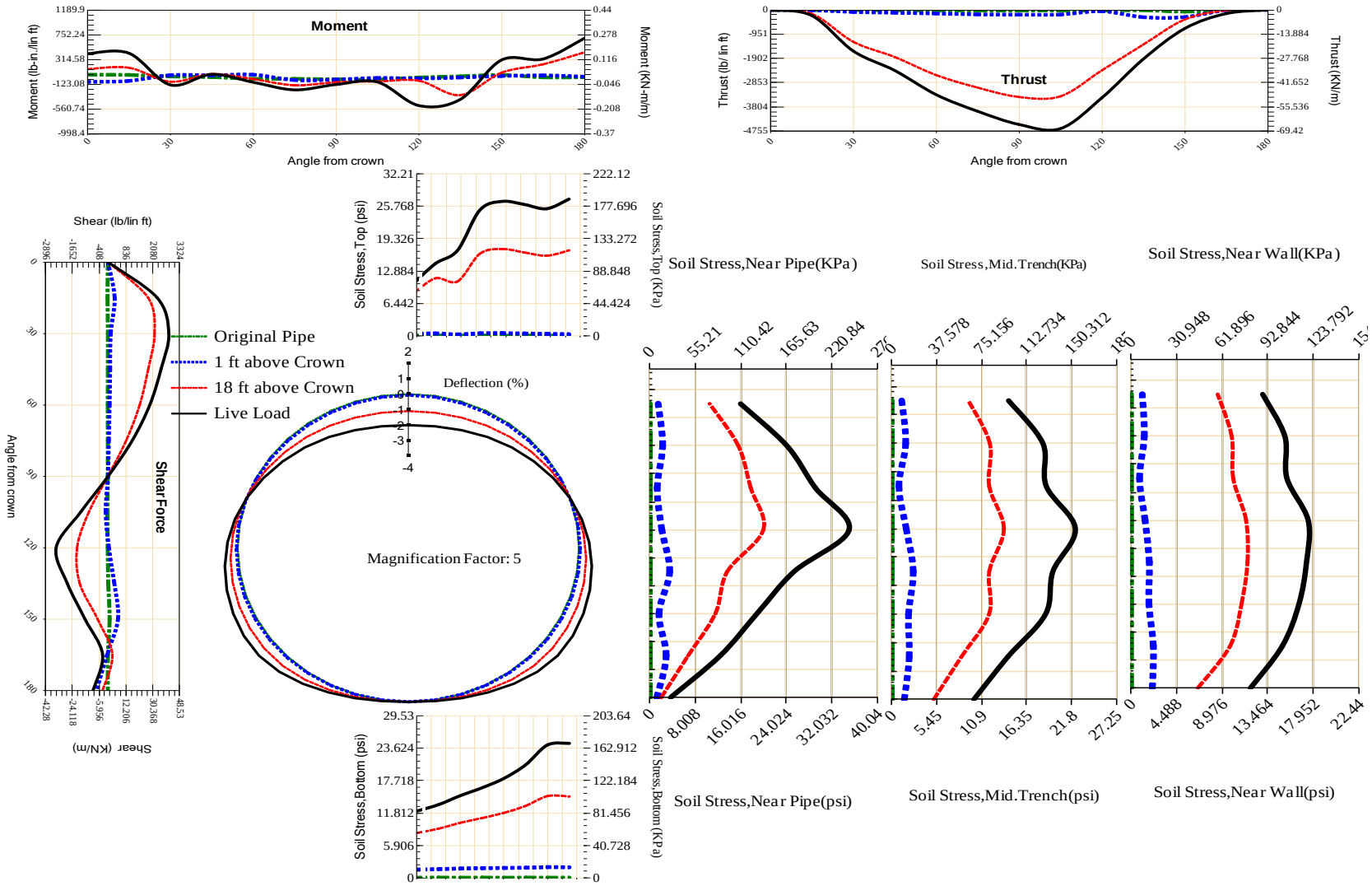

Figure A-406 Param-48-PW288-SF7TR-OD+48-EW3-H18-LiveLoad

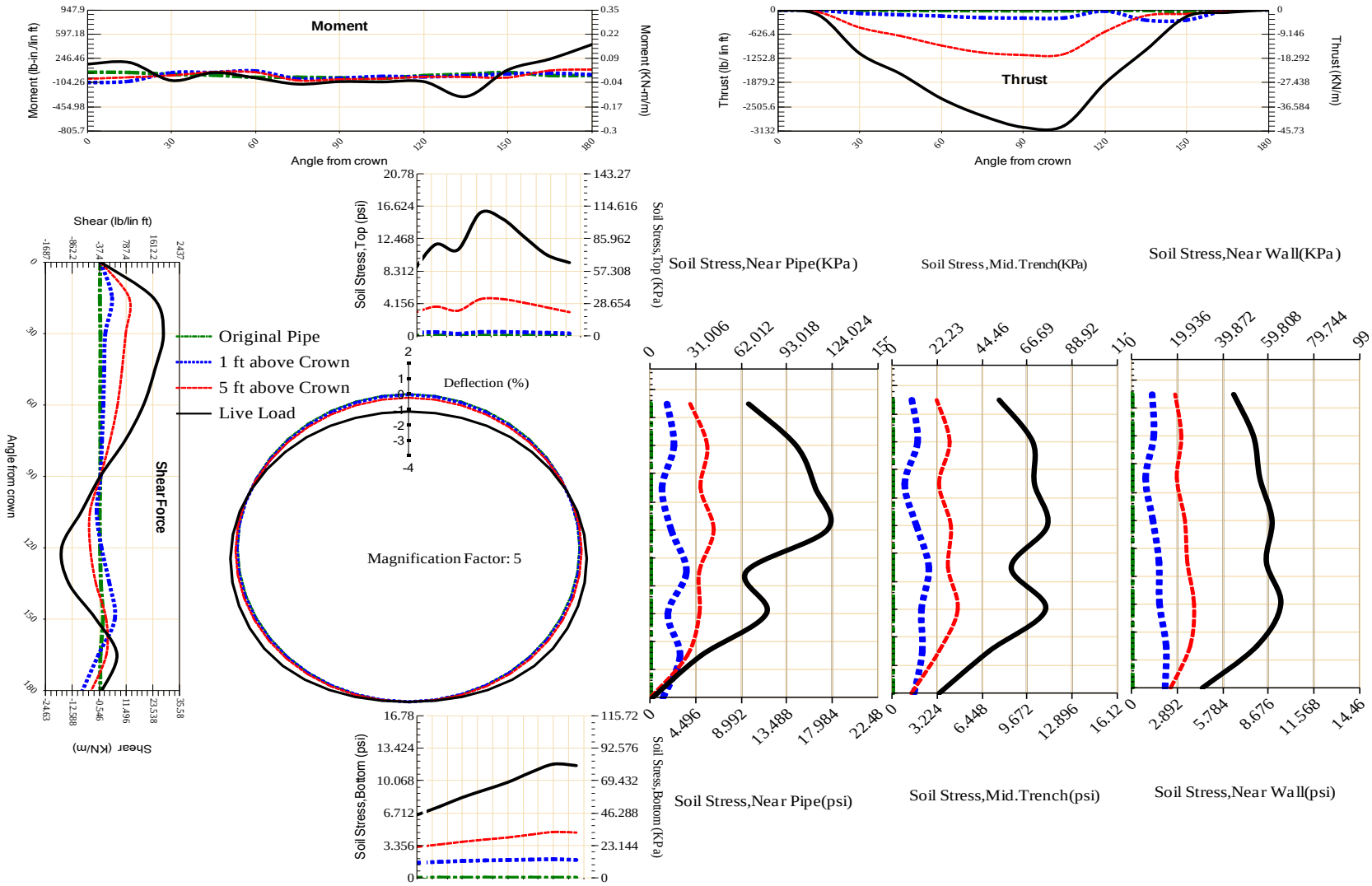

Figure A-407 Param-48-PW288-SF7TR-OD+48-EW3-H5-LiveLoad

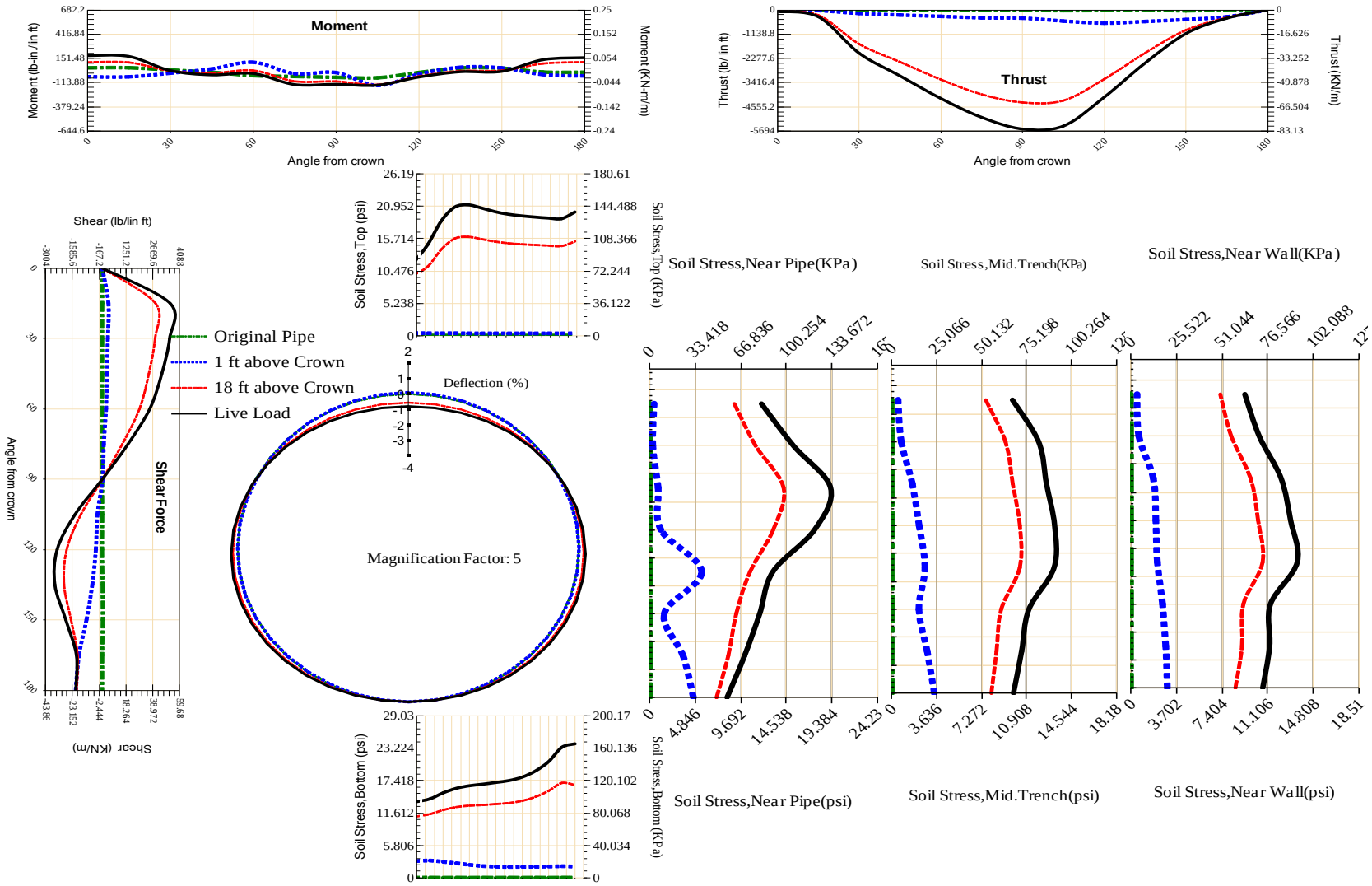

Figure A-408 Param-48-PW288-TR10TR-OD+108-EW10-H18-LiveLoad

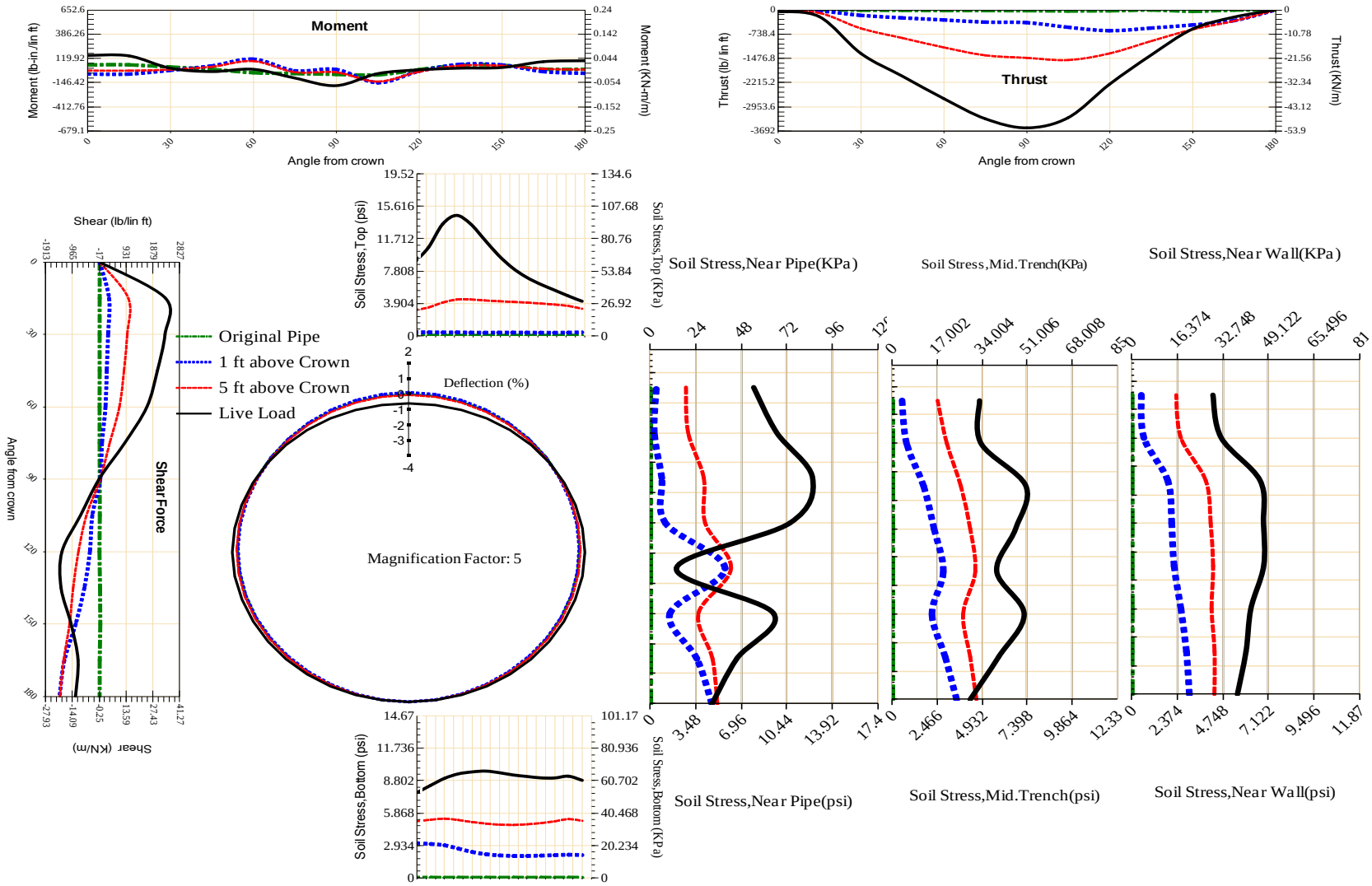

Figure A-409 Param-48-PW288-TR10TR-OD+108-EW10-H5-LiveLoad

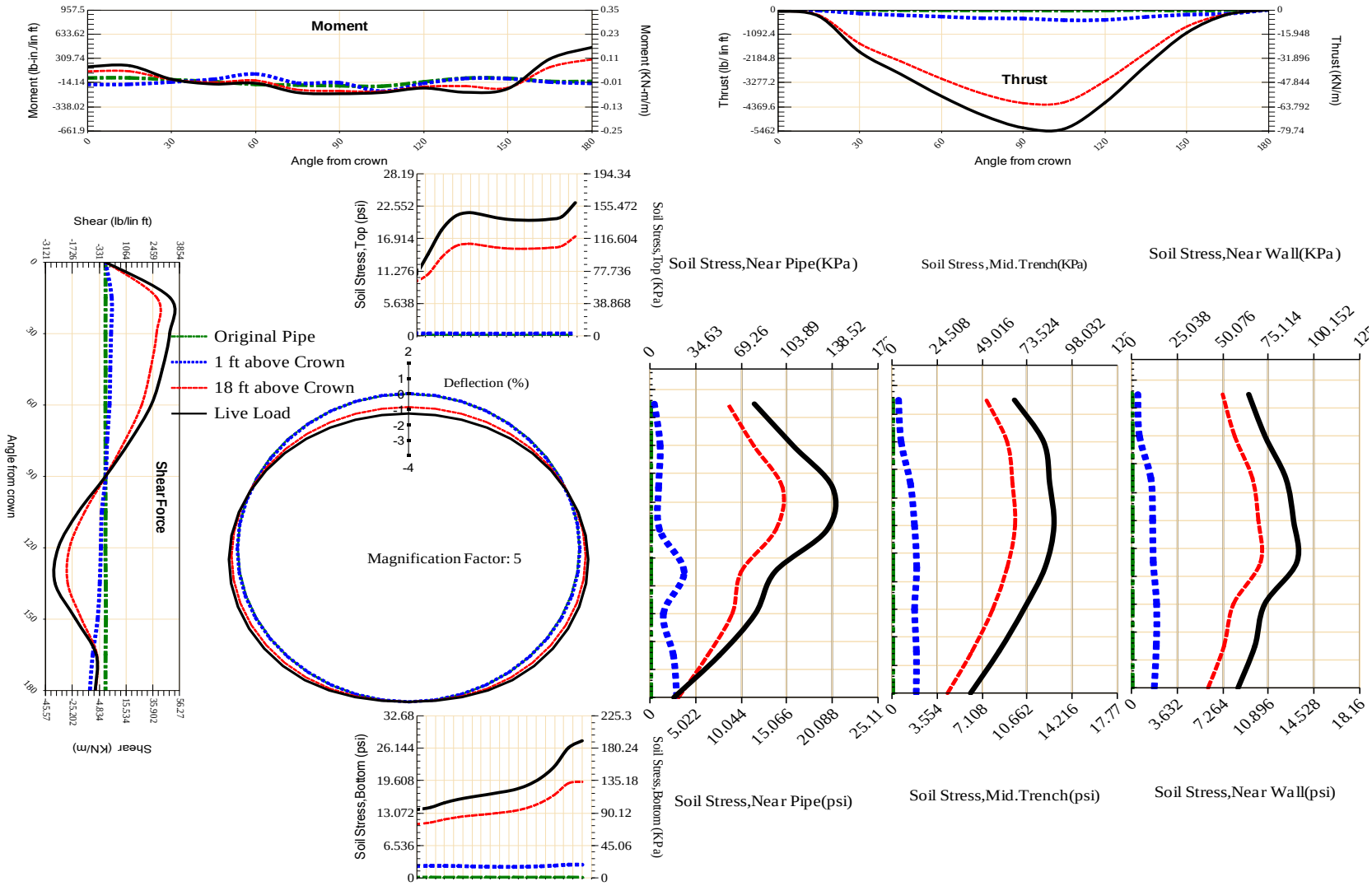

Figure A-410 Param-48-PW288-TR10TR-OD+108-EW3-H18-LiveLoad

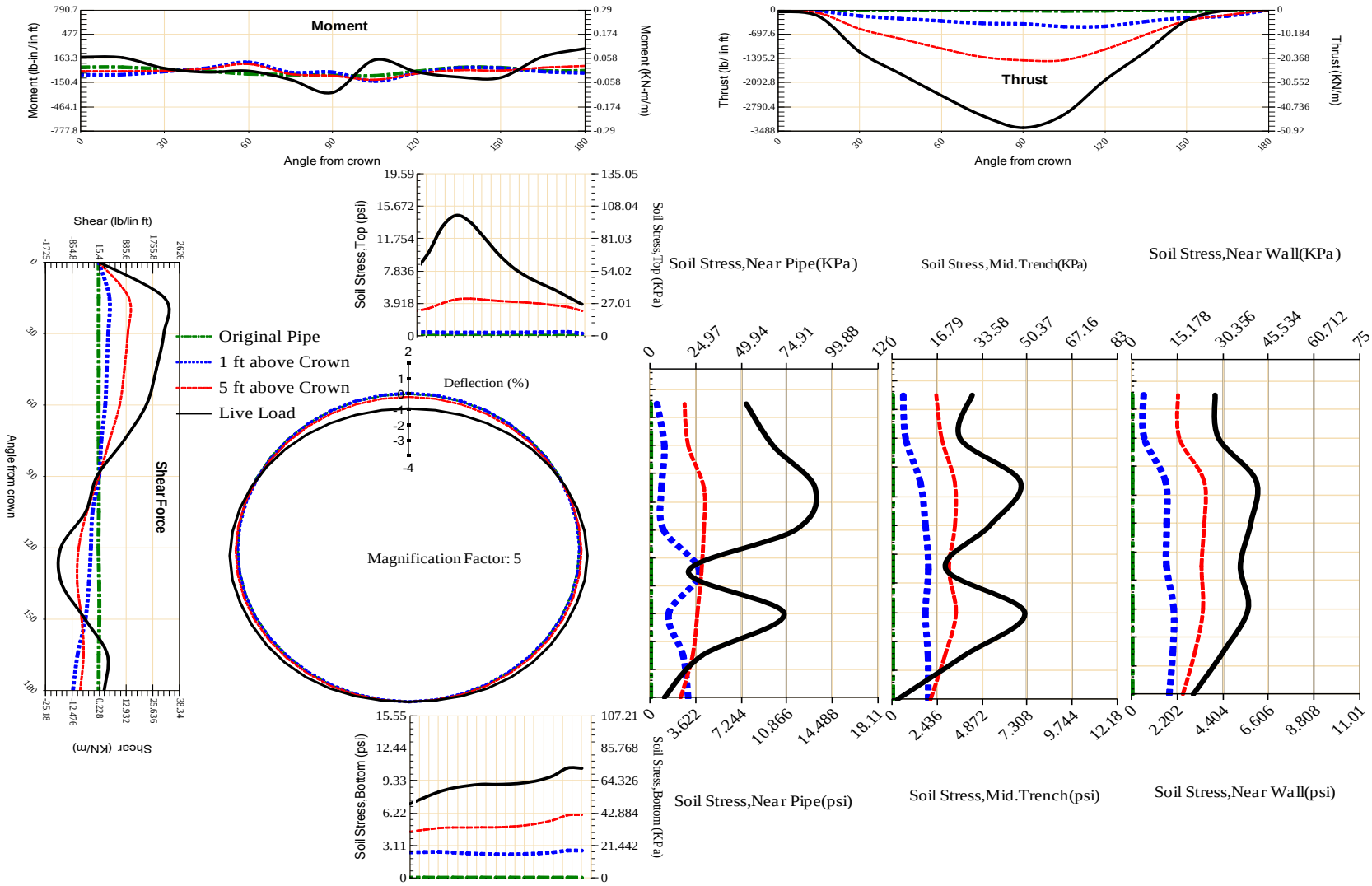

Figure A-411 Param-48-PW288-TR10TR-OD+108-EW3-H5-LiveLoad

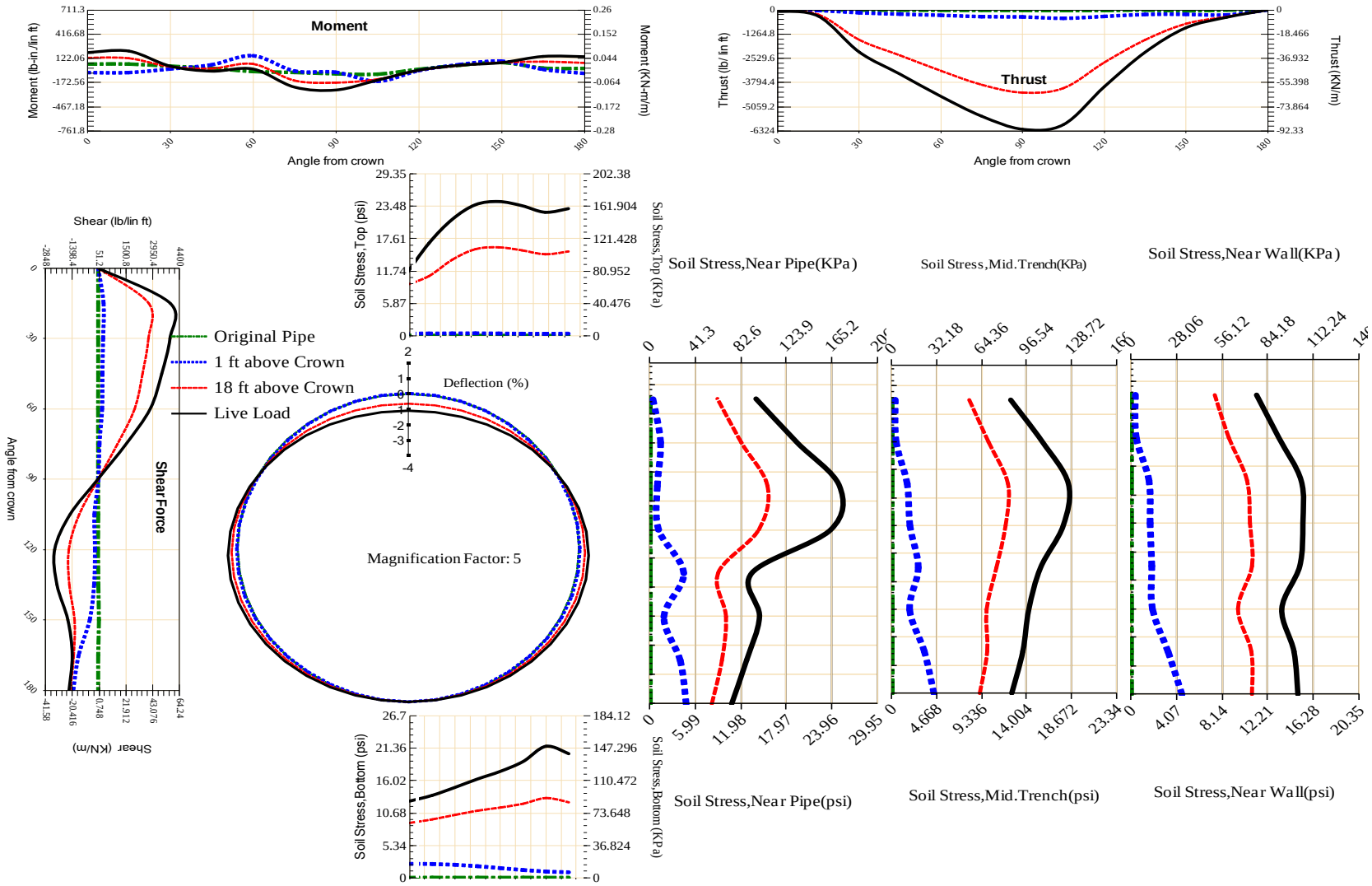

Figure A-412 Param-48-PW288-TR10TR-OD+48-EW10-H18-LiveLoad

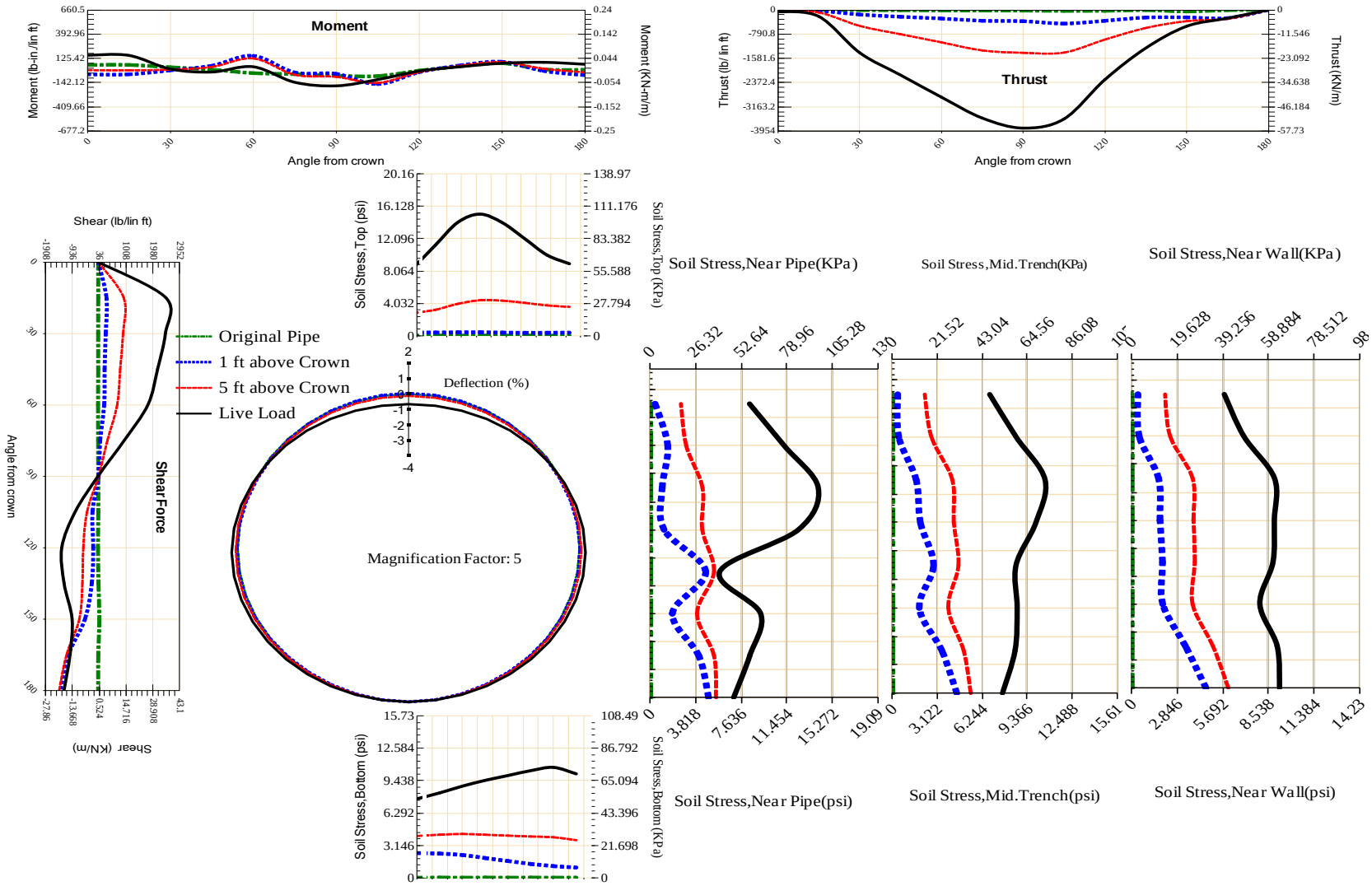

Figure A-413 Param-48-PW288-TR10TR-OD+48-EW10-H5-LiveLoad

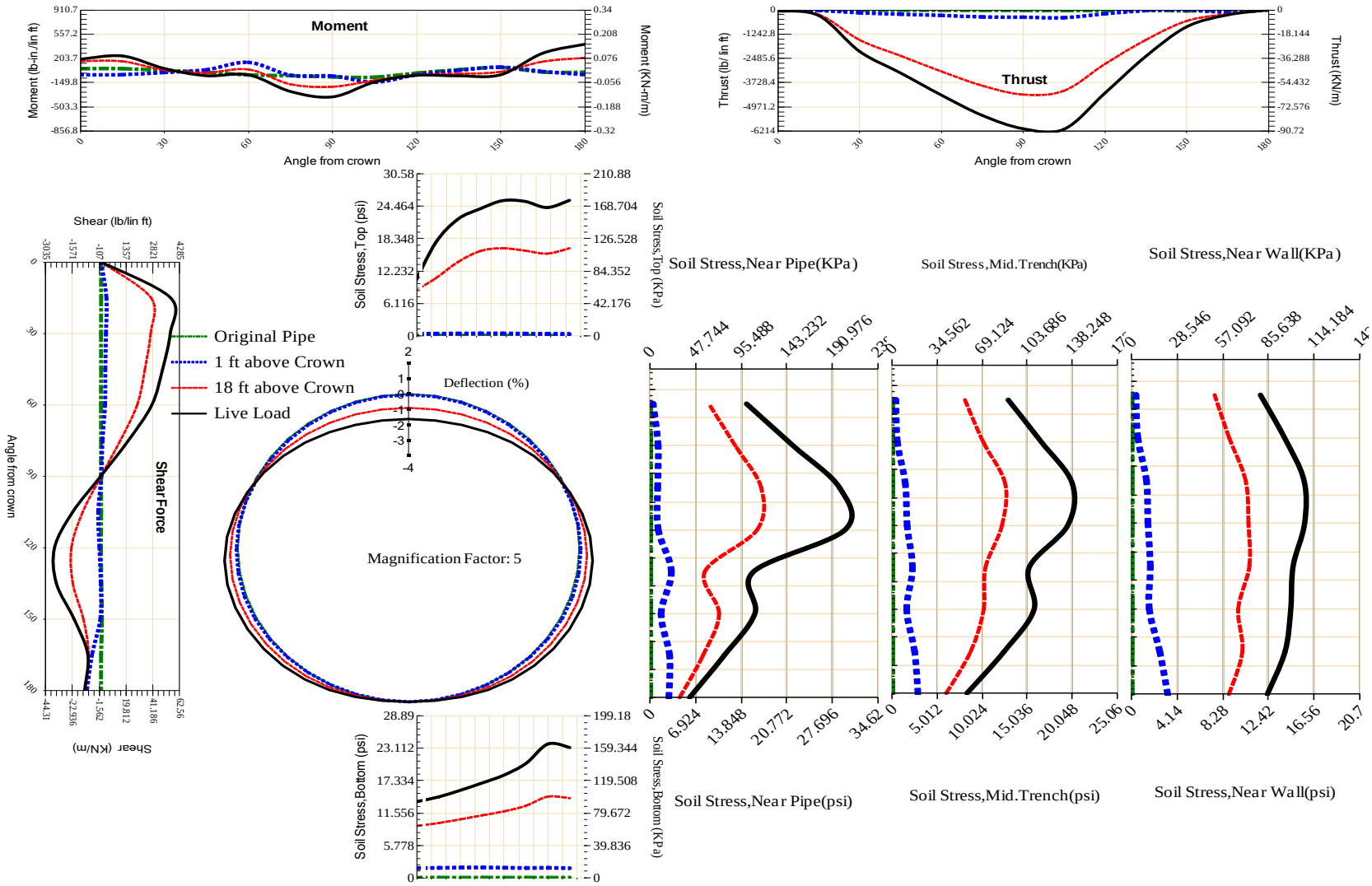

Figure A-414 Param-48-PW288-TR10TR-OD+48-EW3-H18-LiveLoad

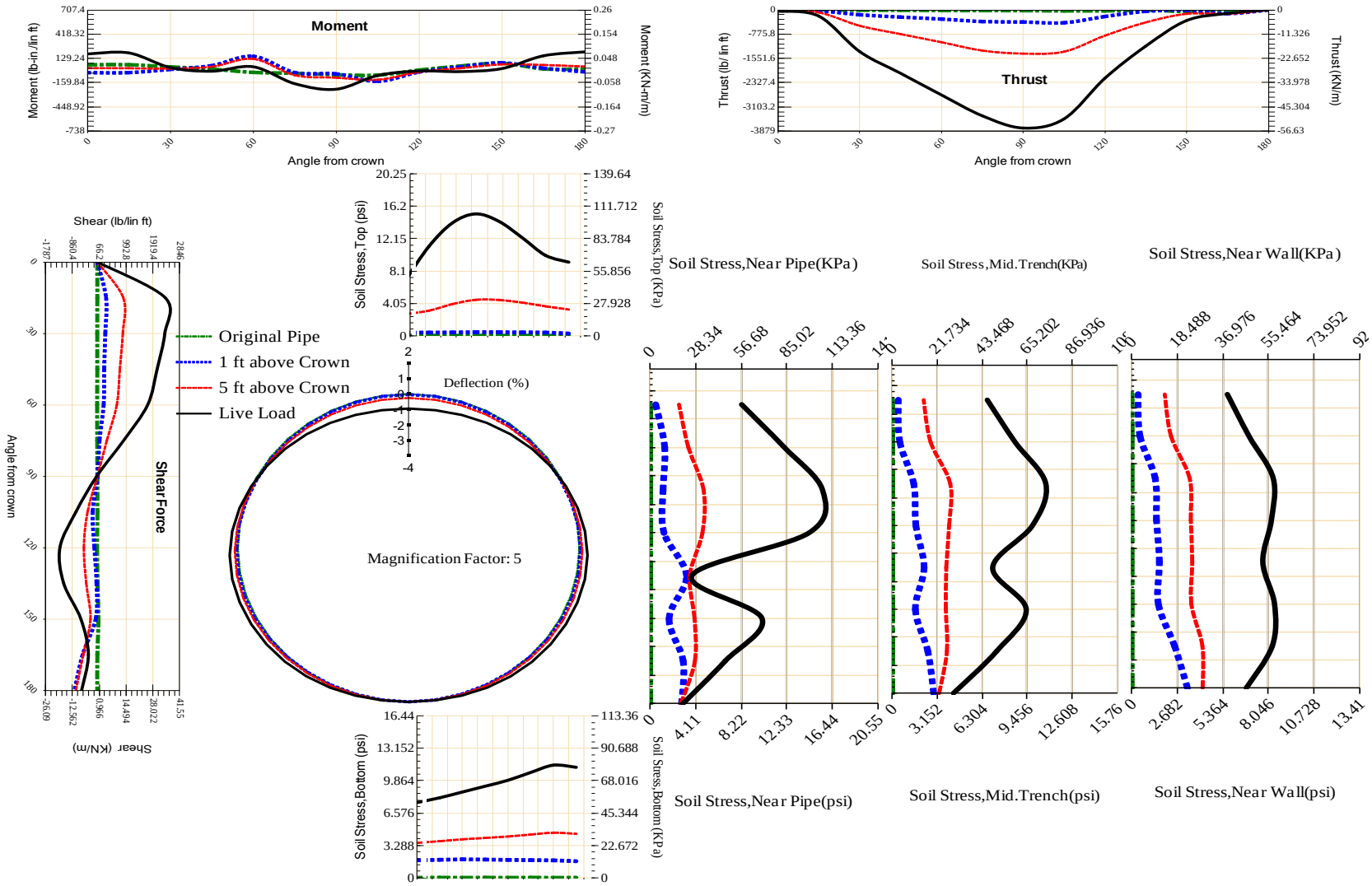

Figure A-415 Param-48-PW288-TR10TR-OD+48-EW3-H5-LiveLoad

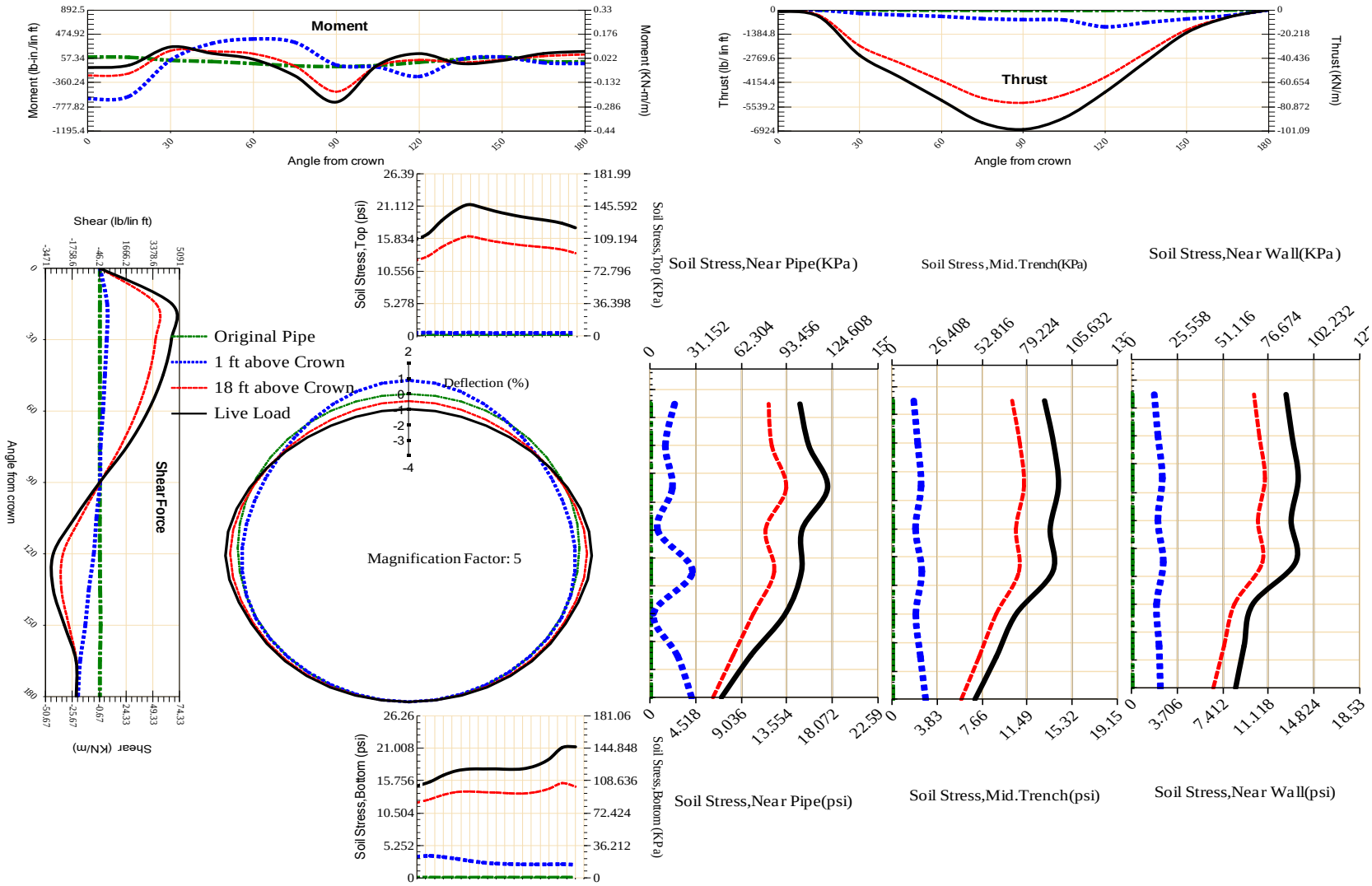

Figure A-416 Param-48-PW288-TR3OR-OD+108-EW10-H18-LiveLoad

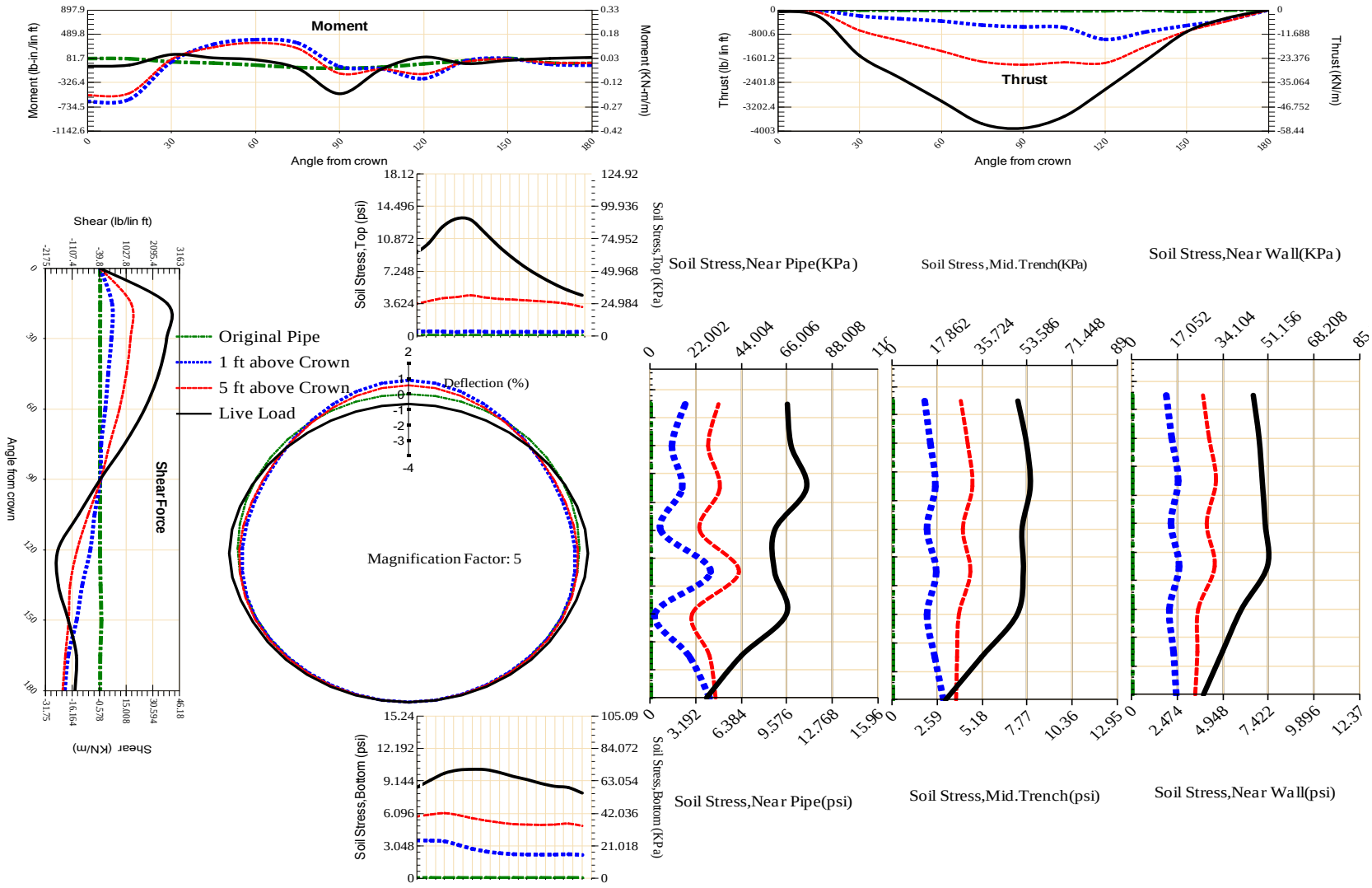

Figure A-417 Param-48-PW288-TR3OR-OD+108-EW10-H5-LiveLoad

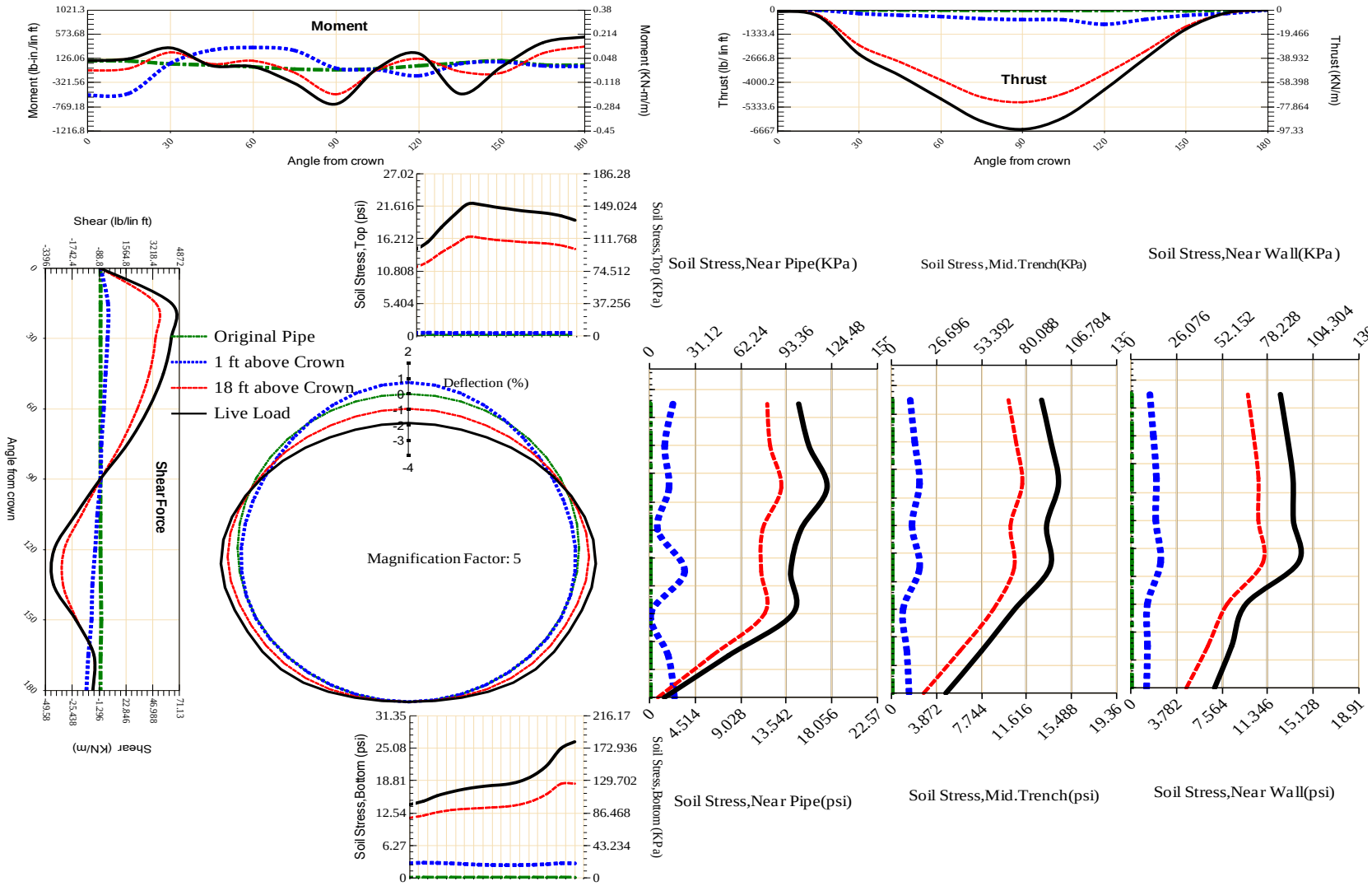

Figure A-418 Param-48-PW288-TR3OR-OD+108-EW3-H18-LiveLoad

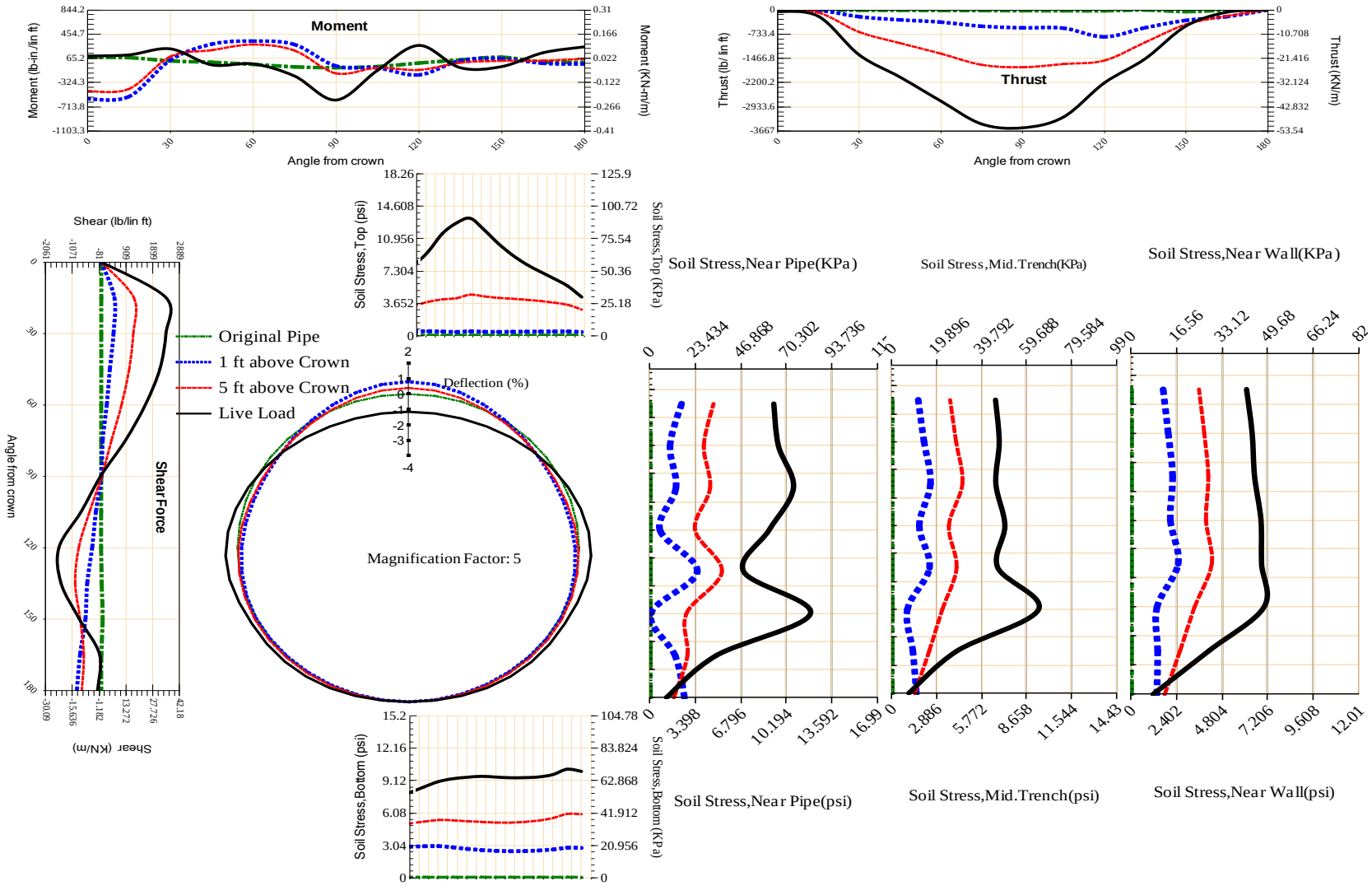

Figure A-419 Param-48-PW288-TR3OR-OD+108-EW3-H5-LiveLoad

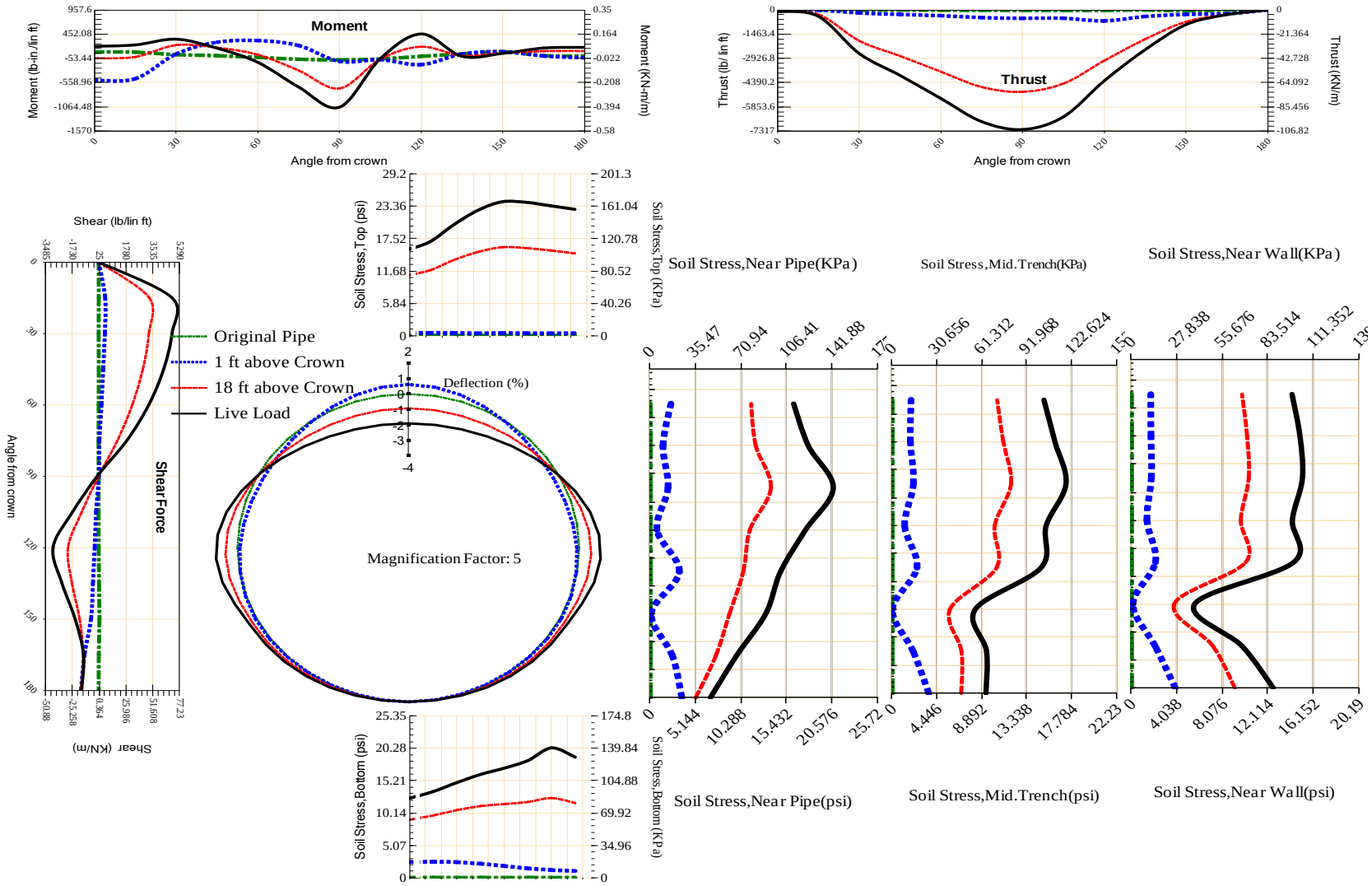

Figure A-420 Param-48-PW288-TR3OR-OD+48-EW10-H18-LiveLoad

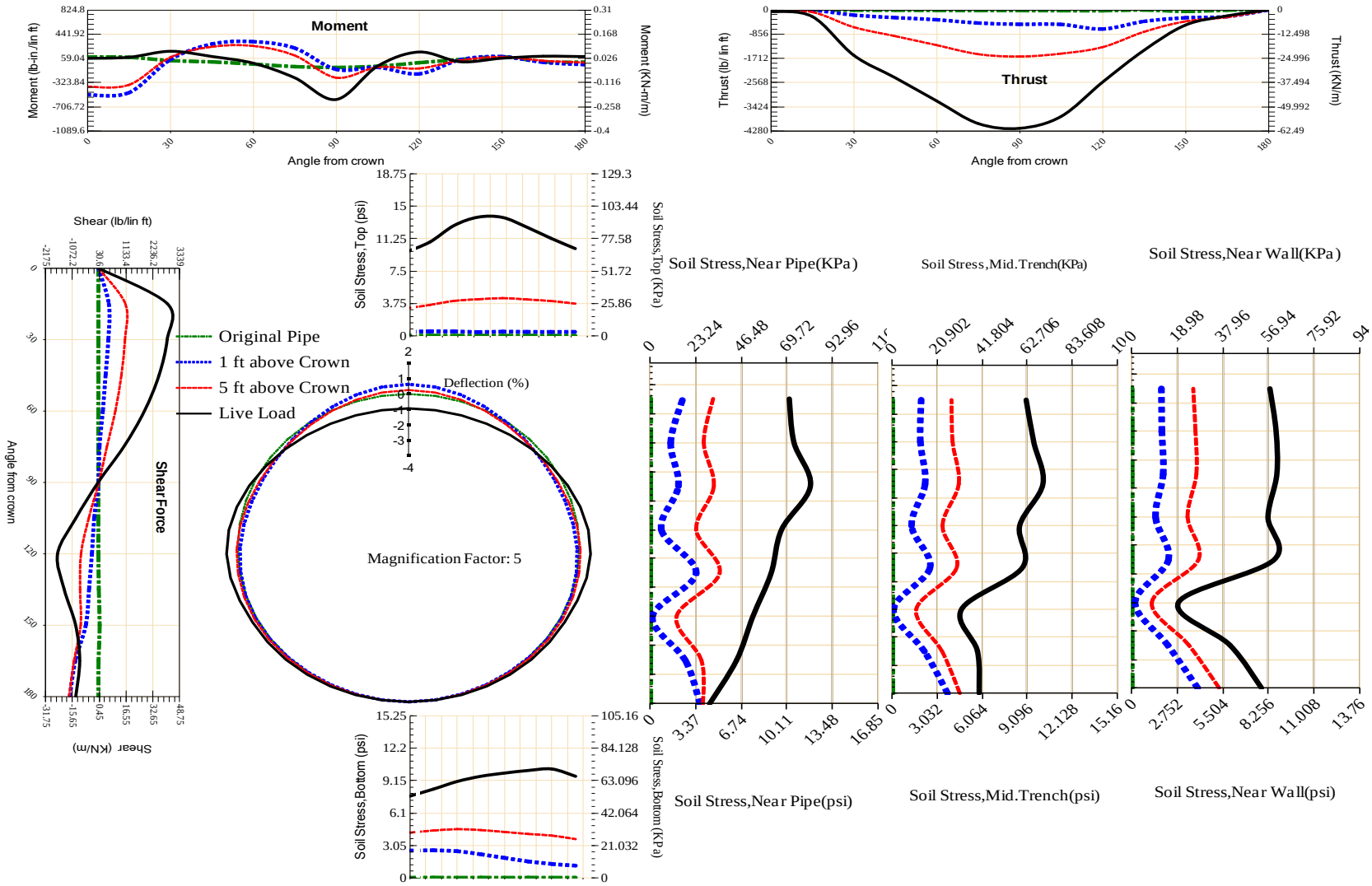

Figure A-421 Param-48-PW288-TR3OR-OD+48-EW10-H5-LiveLoad

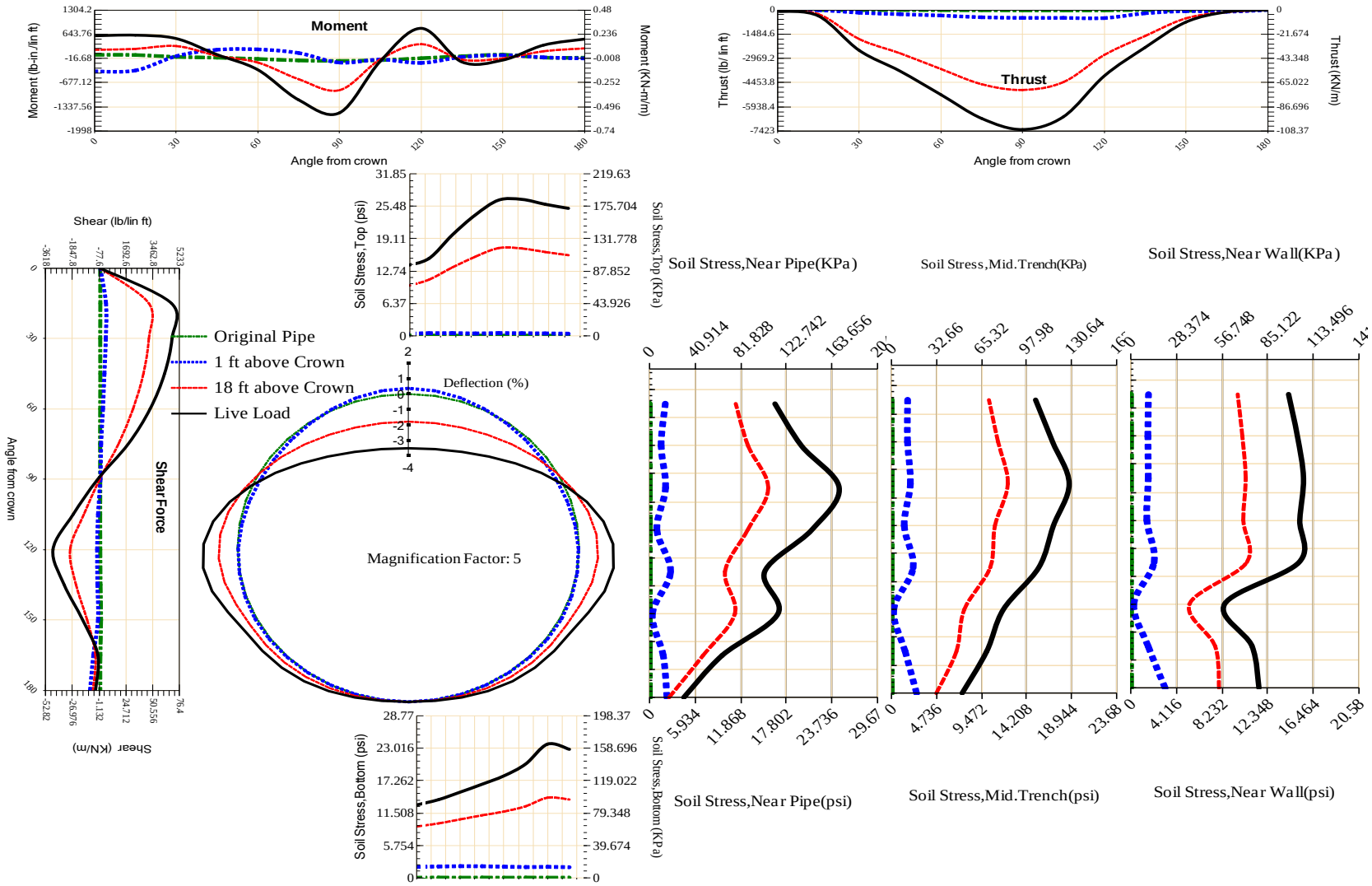

Figure A-422 Param-48-PW288-TR3OR-OD+48-EW3-H18-LiveLoad

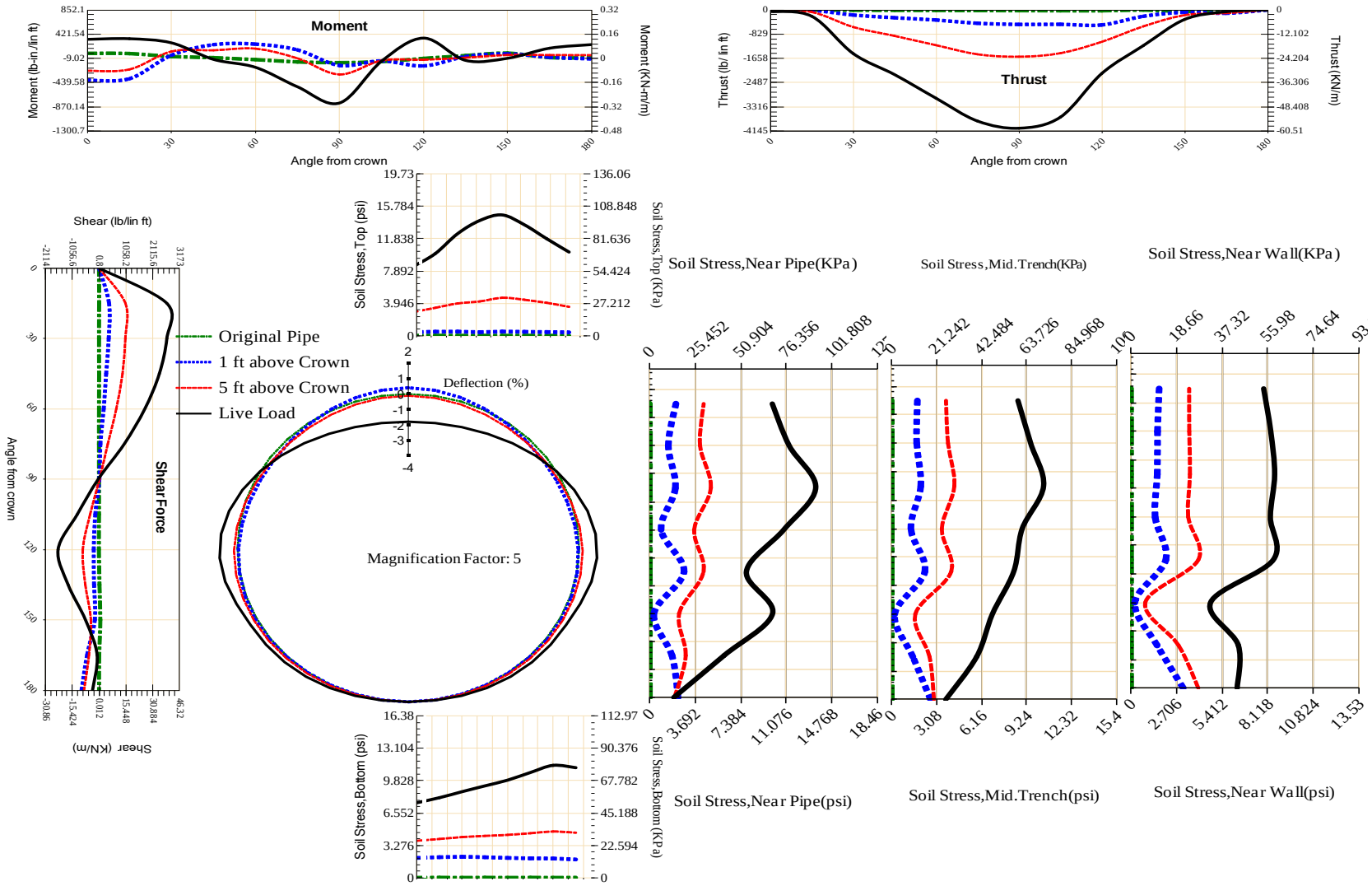

Figure A-423 Param-48-PW288-TR3OR-OD+48-EW3-H5-LiveLoad

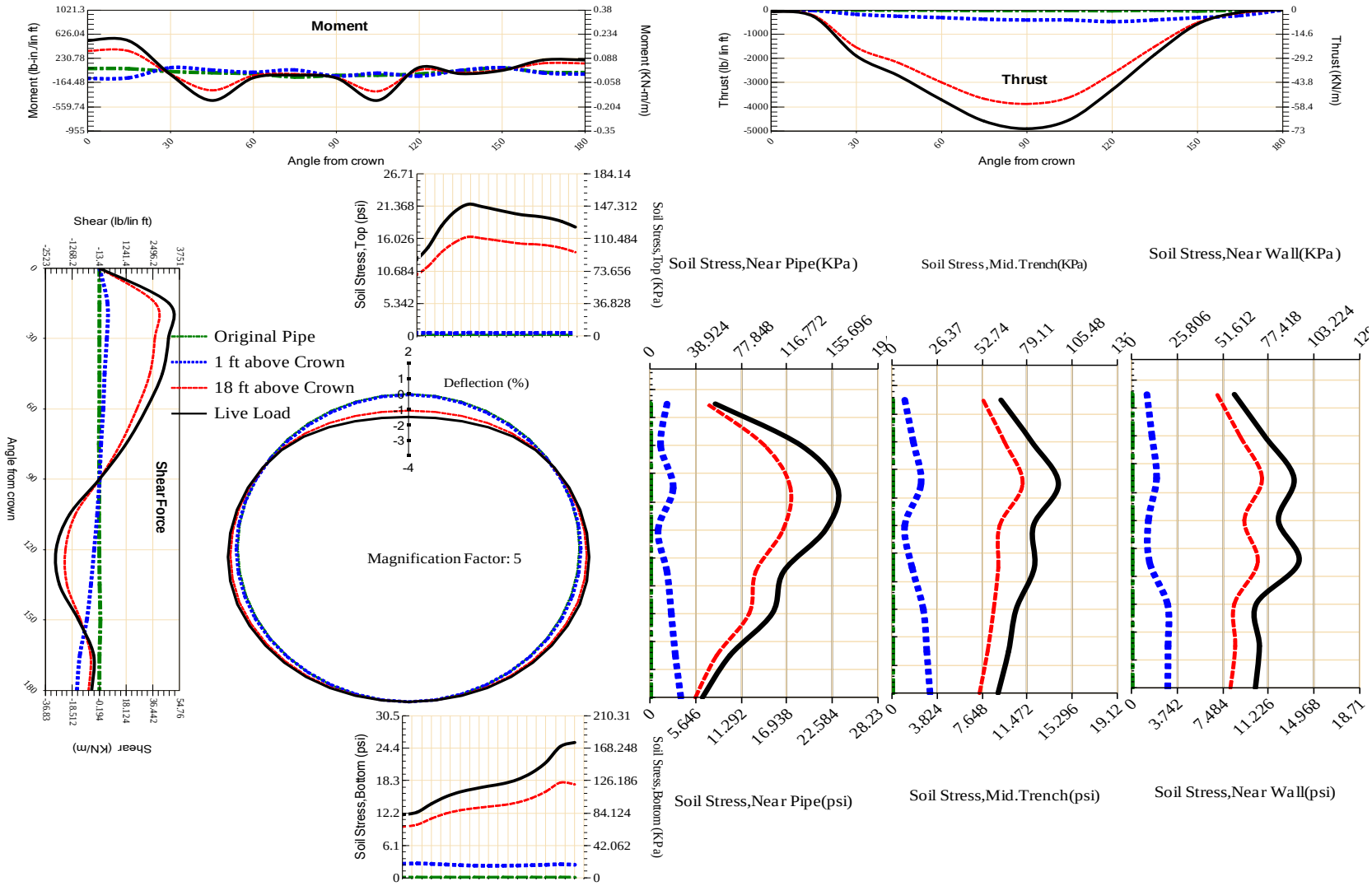

Figure A-424 Param-48-PW288-TR3SF-OD+108-EW10-H18-LiveLoad

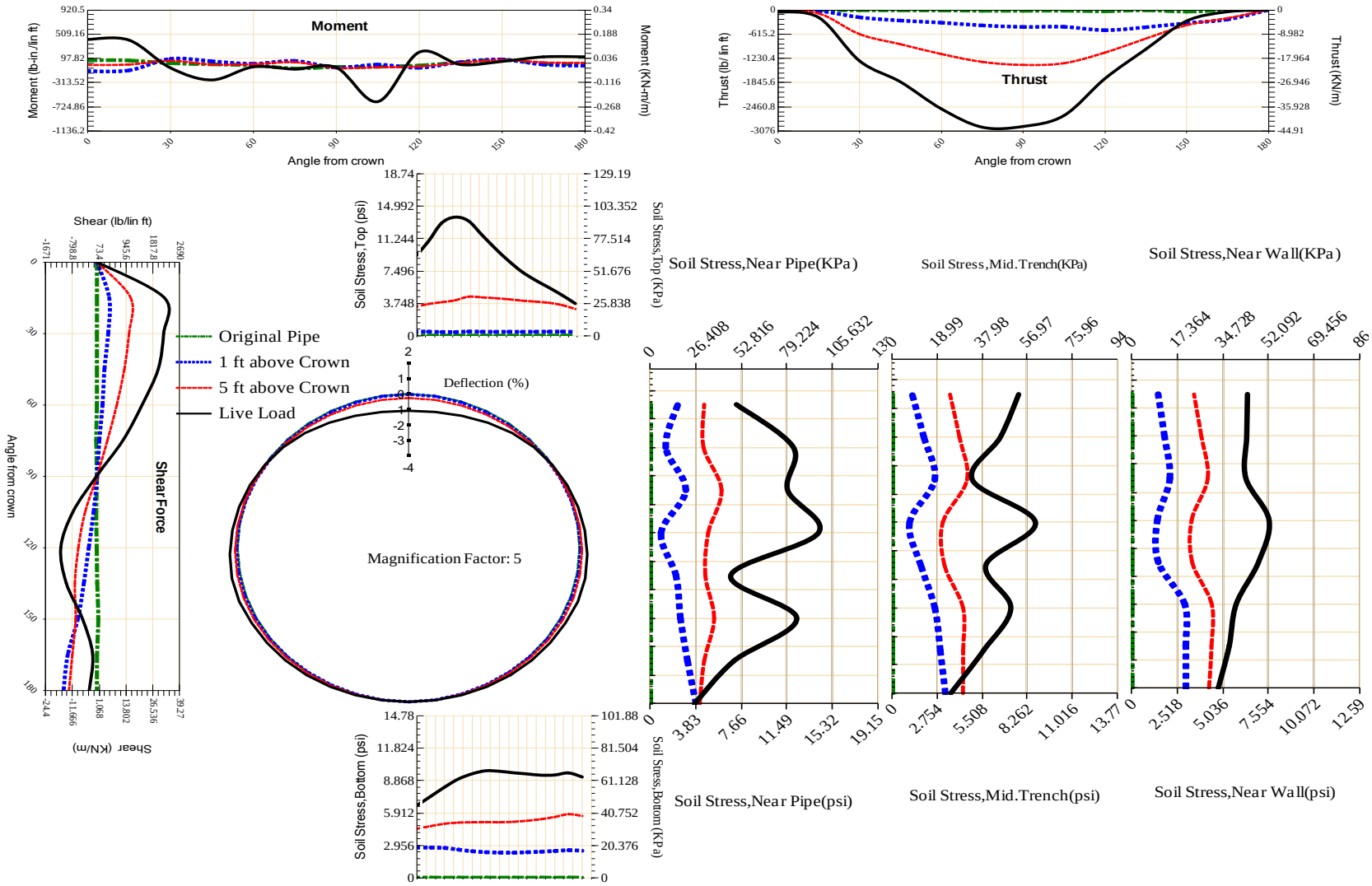

Figure A-425 Param-48-PW288-TR3SF-OD+108-EW10-H5-LiveLoad

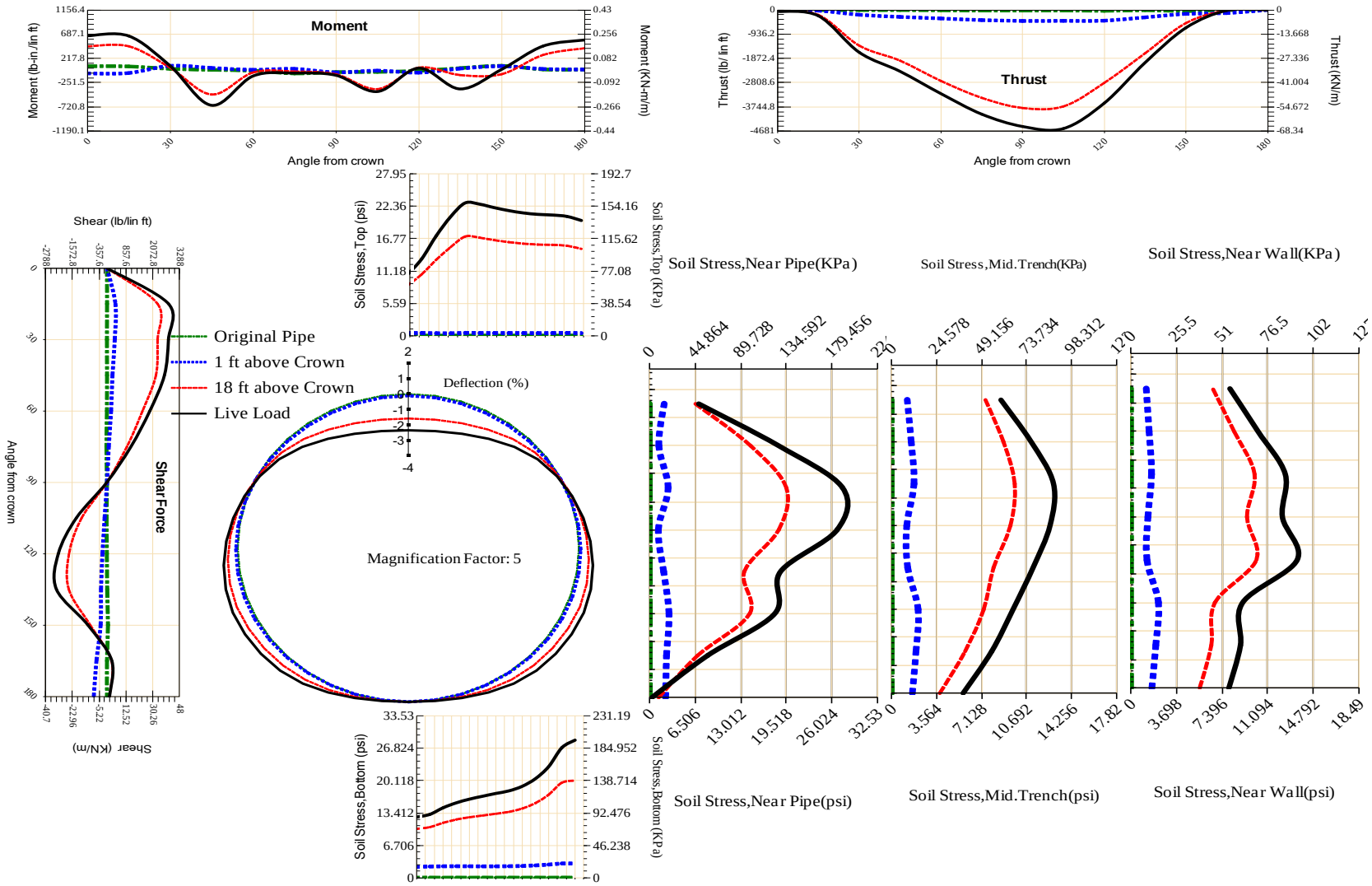

Figure A-426 Param-48-PW288-TR3SF-OD+108-EW3-H18-LiveLoad

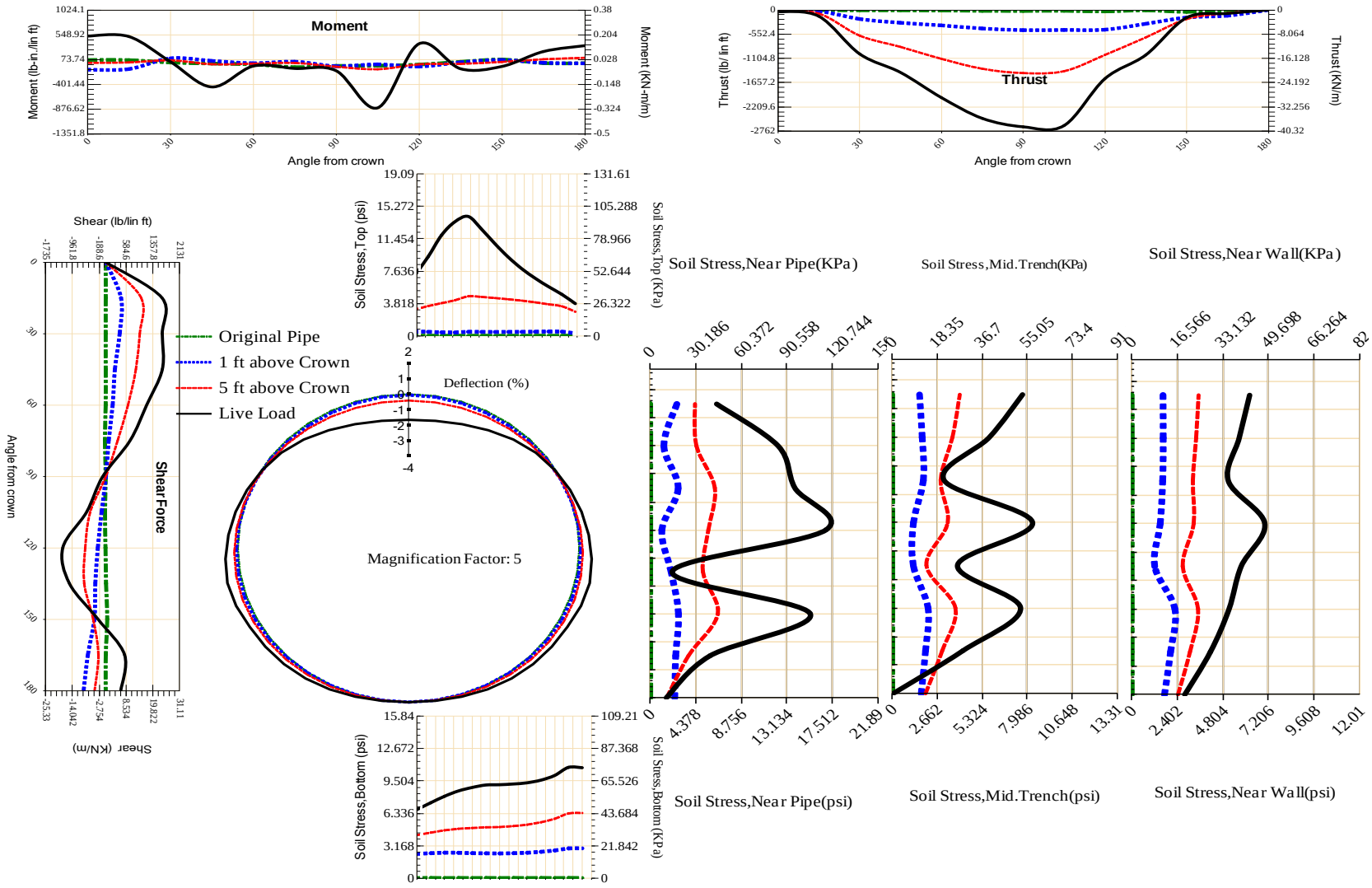

Figure A-427 Param-48-PW288-TR3SF-OD+108-EW3-H5-LiveLoad

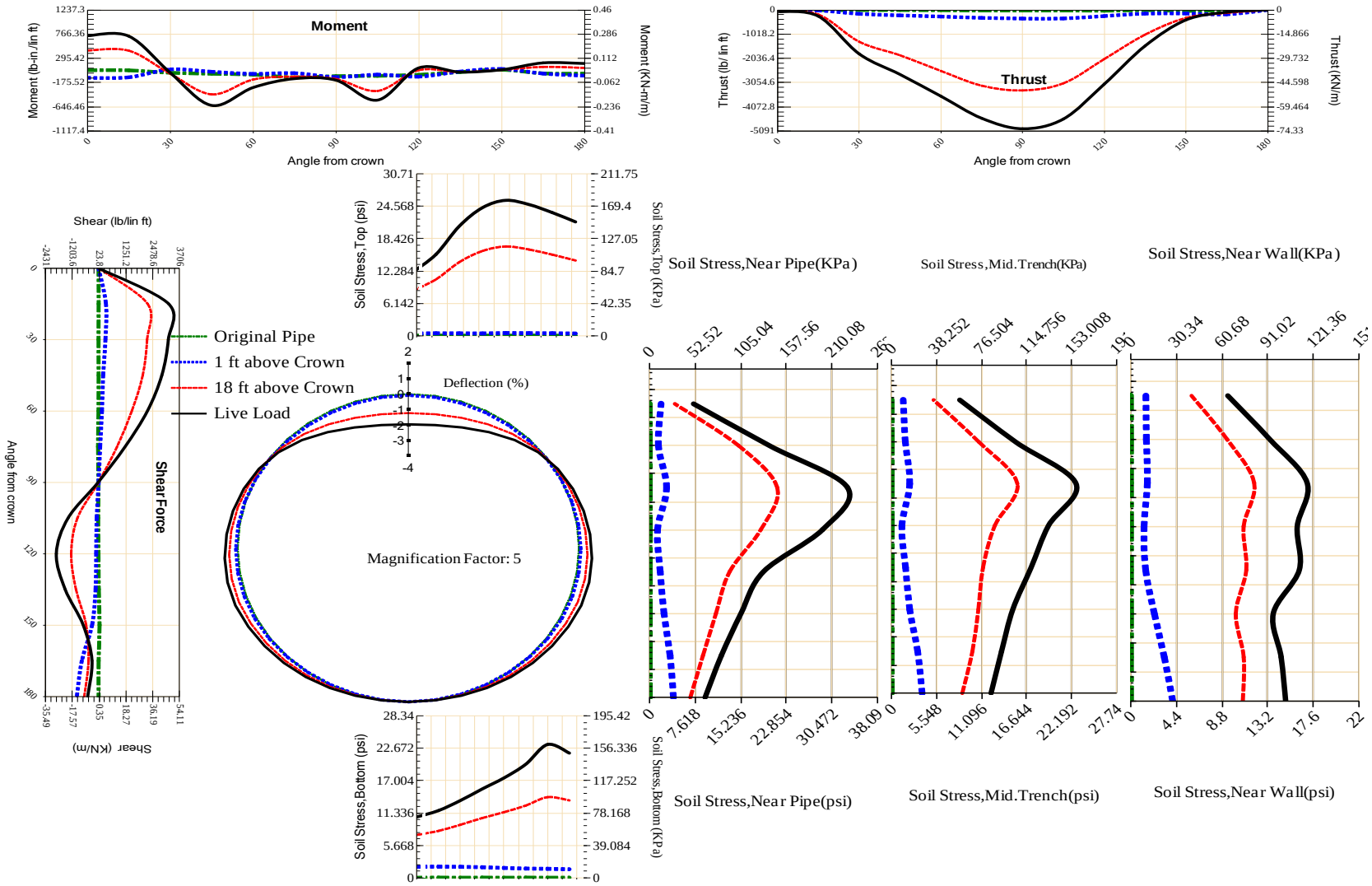

Figure A-428 Param-48-PW288-TR3SF-OD+48-EW10-H18-LiveLoad

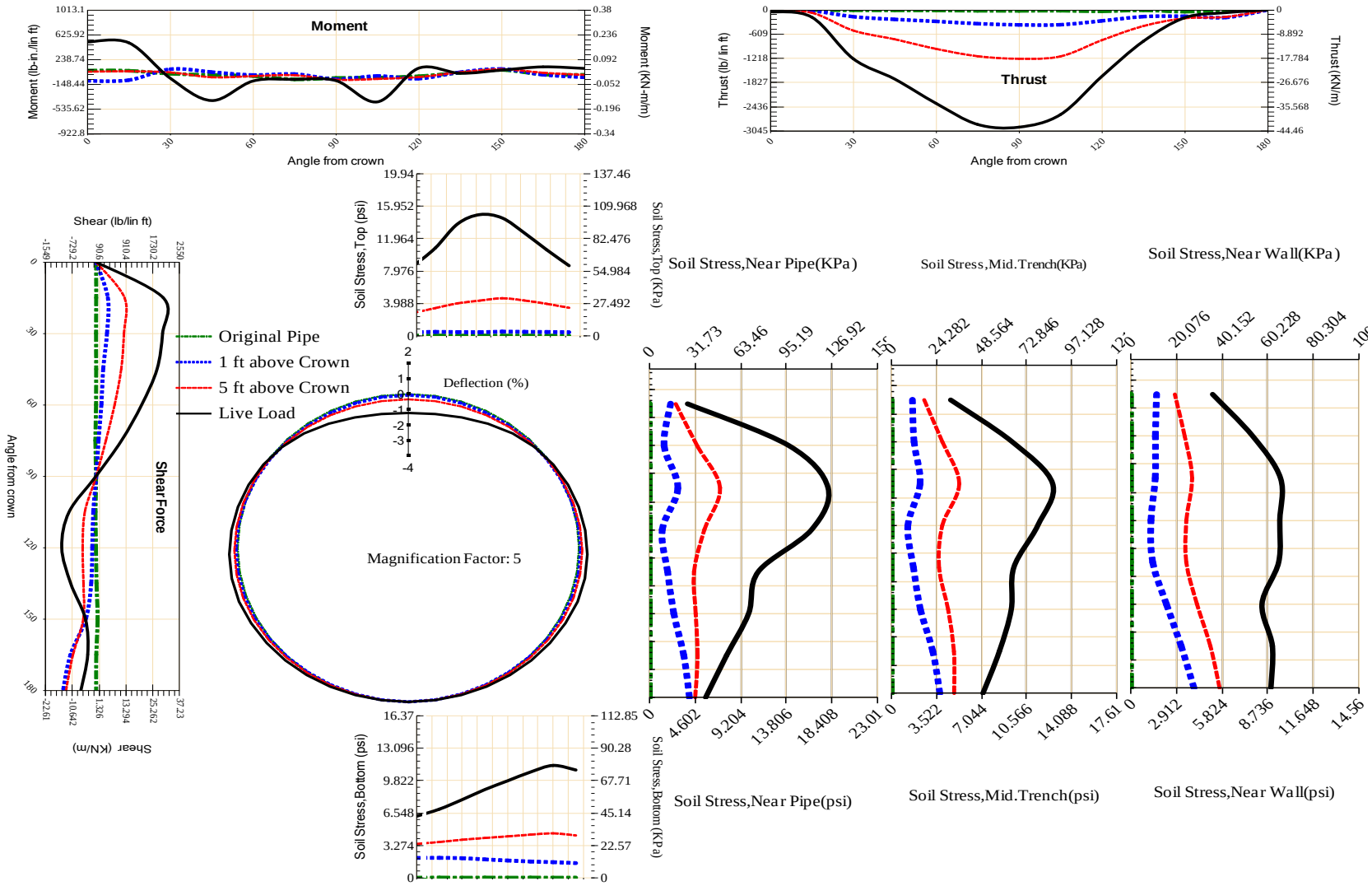

Figure A-429 Param-48-PW288-TR3SF-OD+48-EW10-H5-LiveLoad

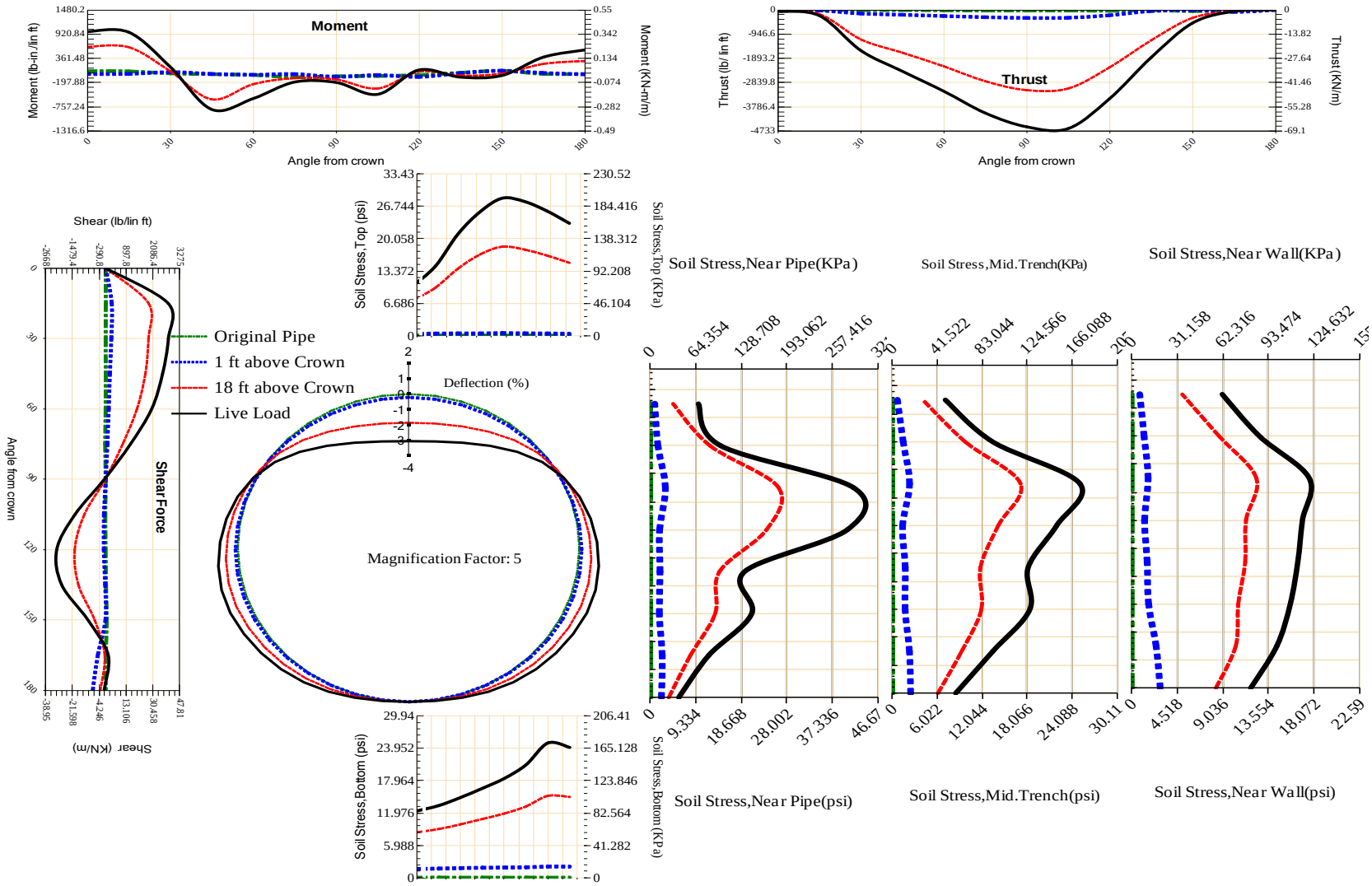

Figure A-430 Param-48-PW288-TR3SF-OD+48-EW3-H18-LiveLoad

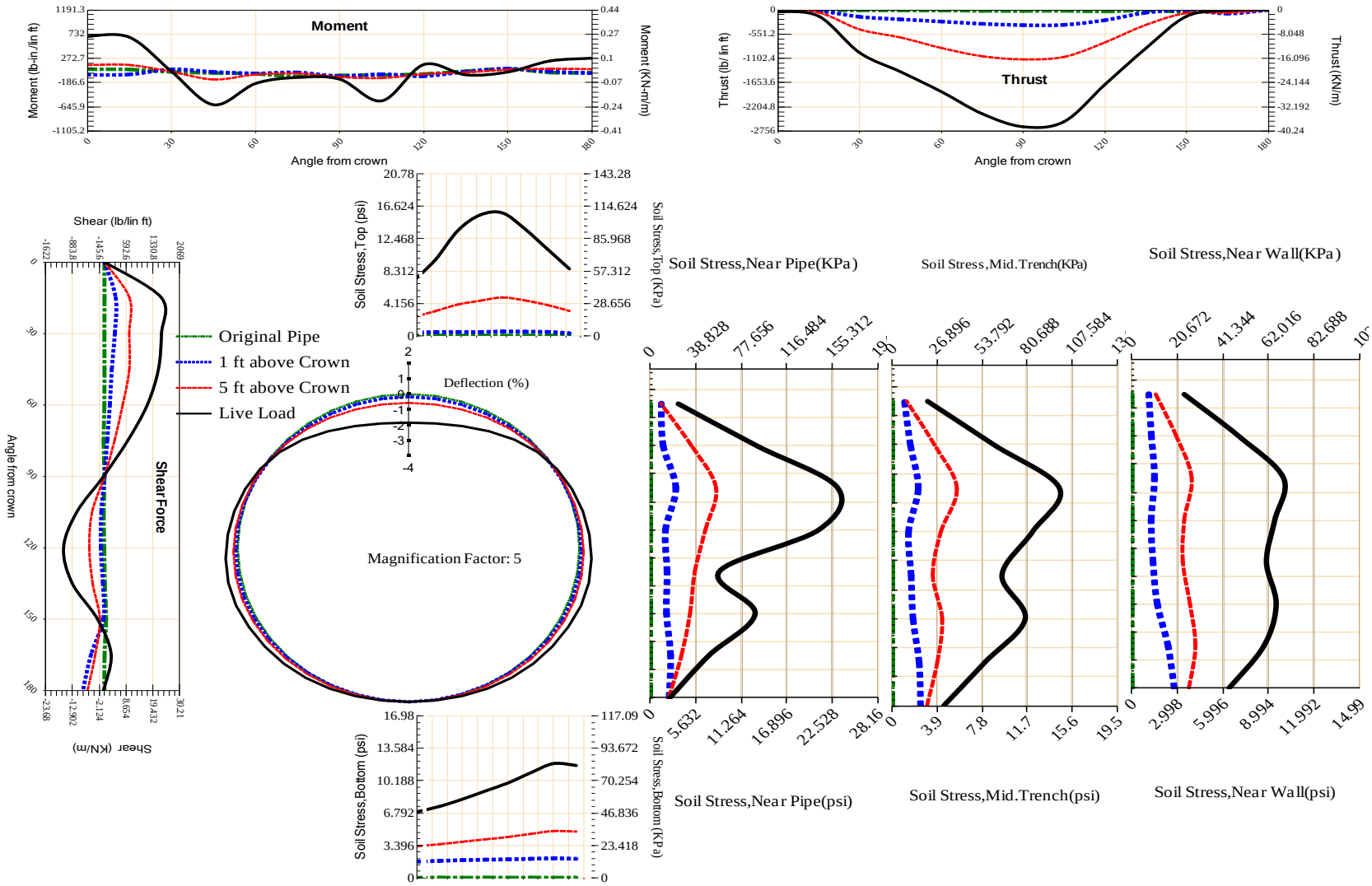

Figure A-431 Param-48-PW288-TR3SF-OD+48-EW3-H5-LiveLoad

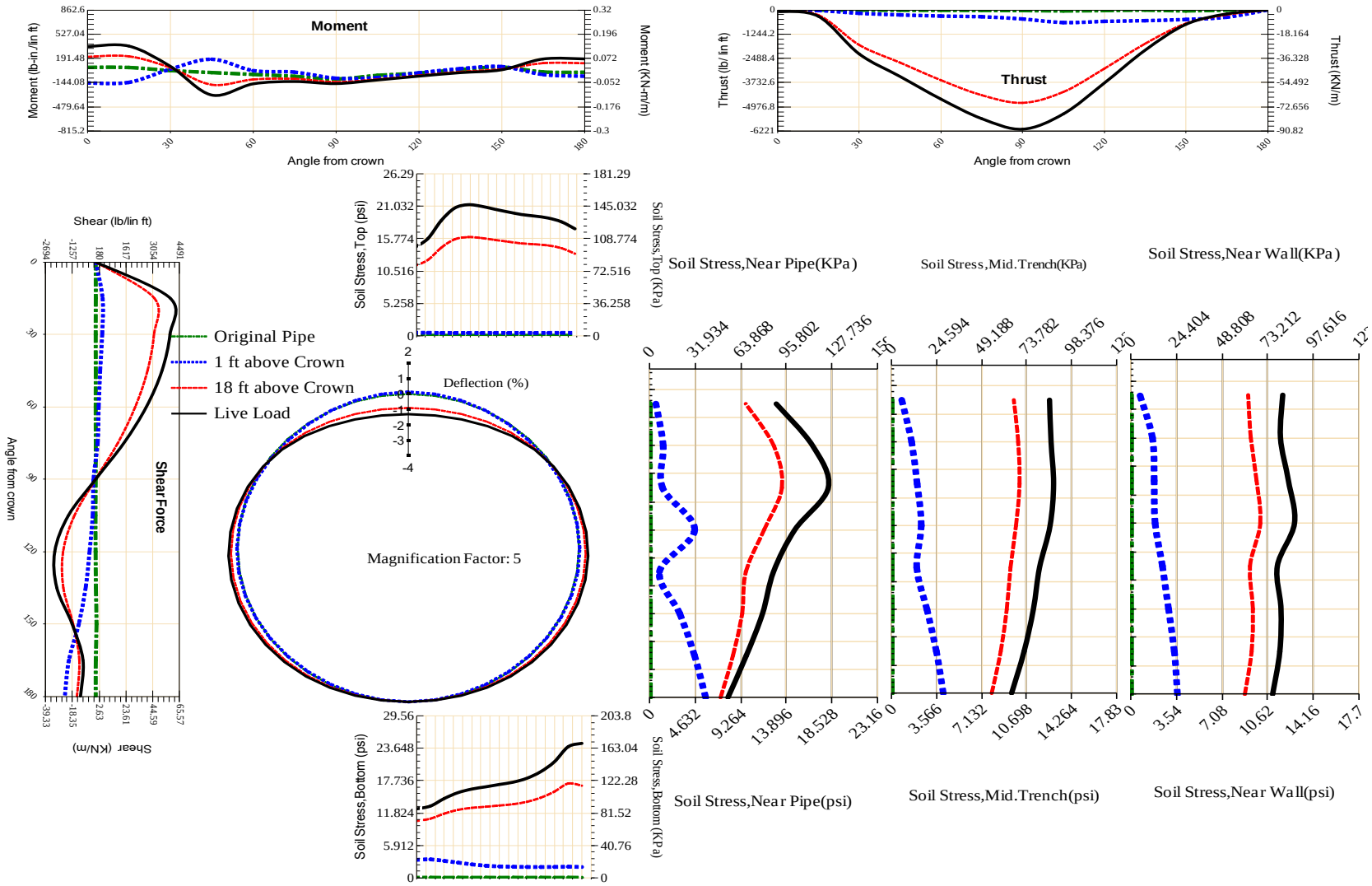

Figure A-432 Param-48-PW288-TR5OR-OD+108-EW10-H18-LiveLoad

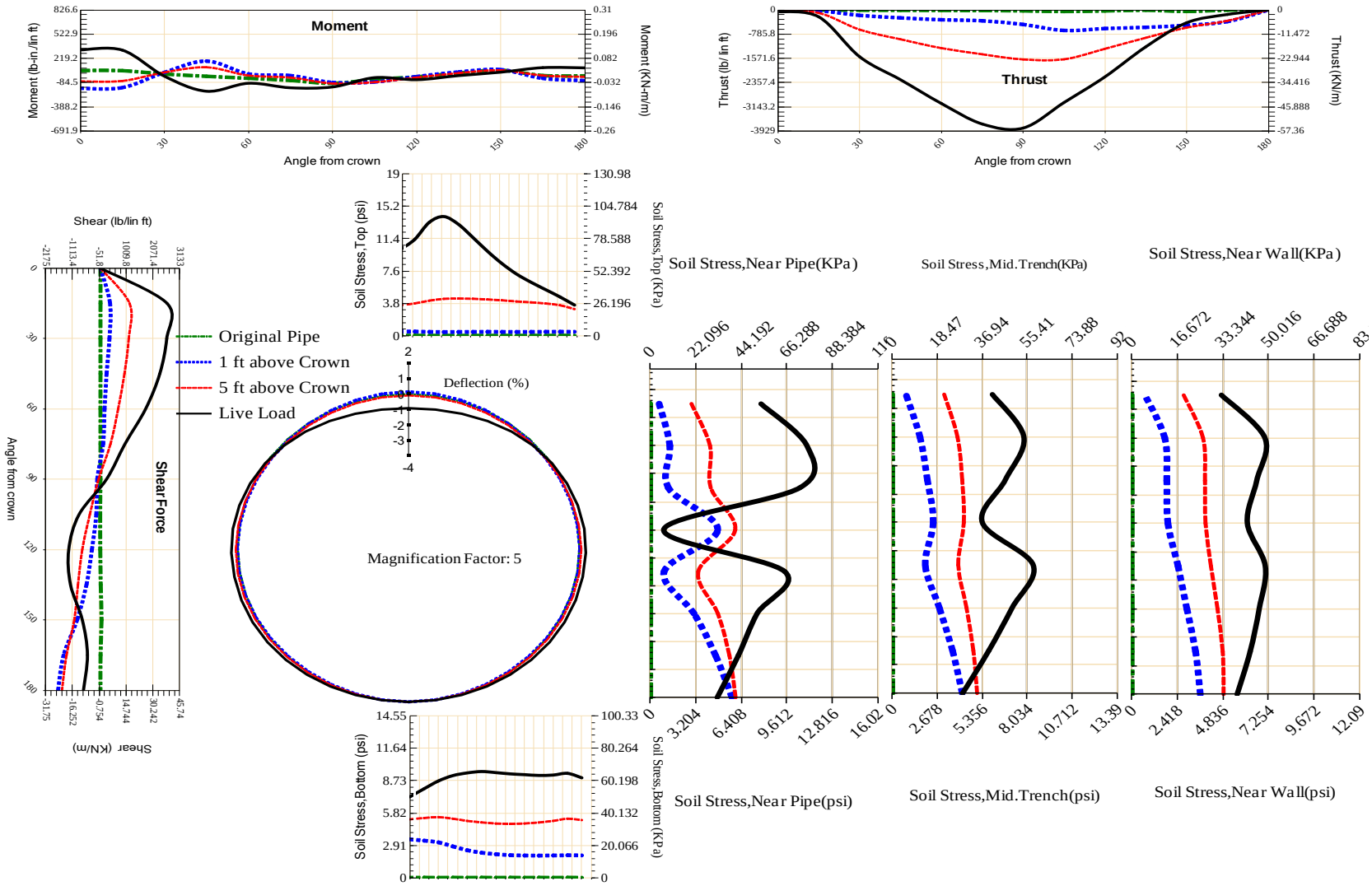

Figure A-433 Param-48-PW288-TR5OR-OD+108-EW10-H5-LiveLoad

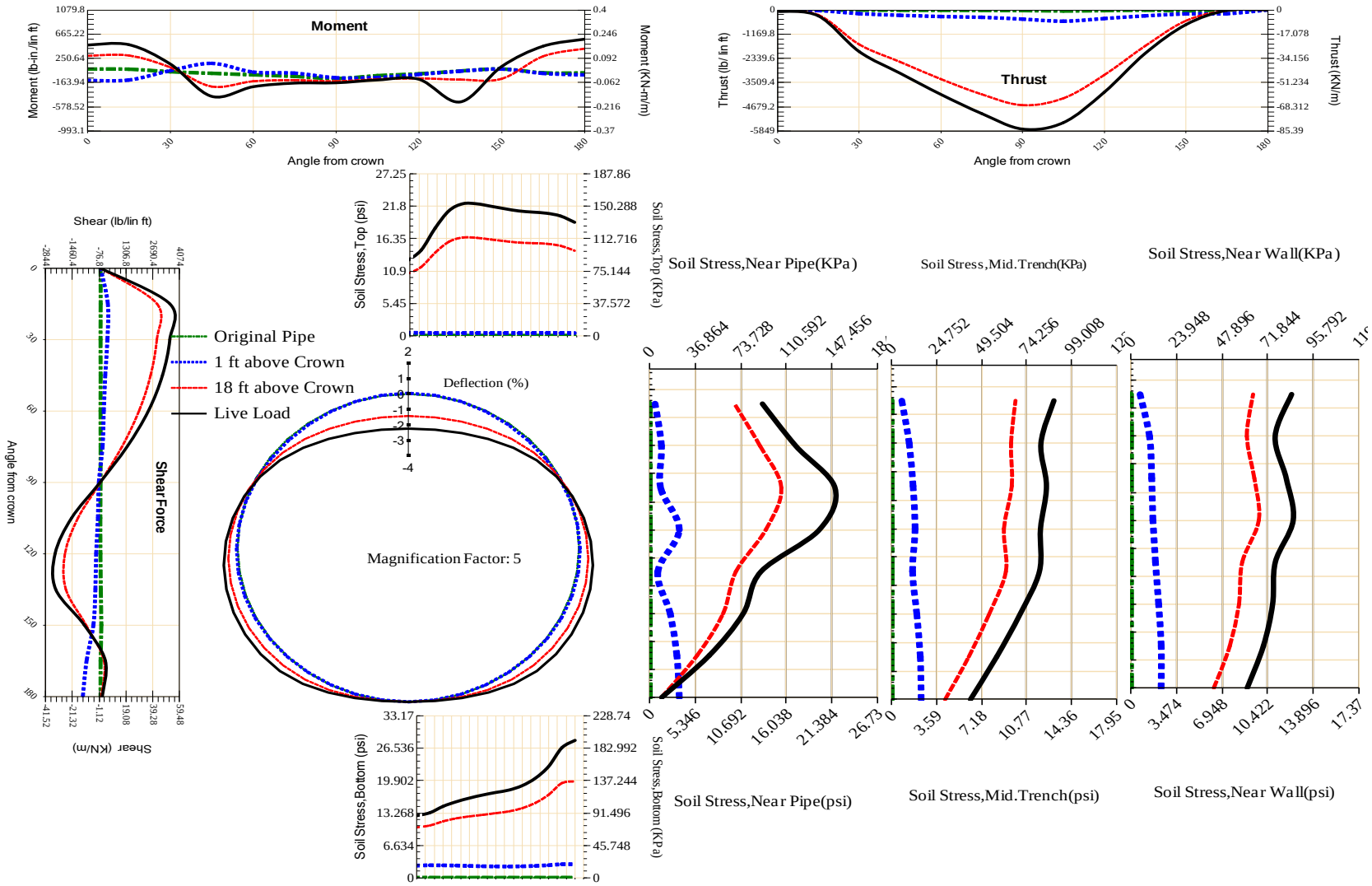

Figure A-434 Param-48-PW288-TR5OR-OD+108-EW3-H18-LiveLoad

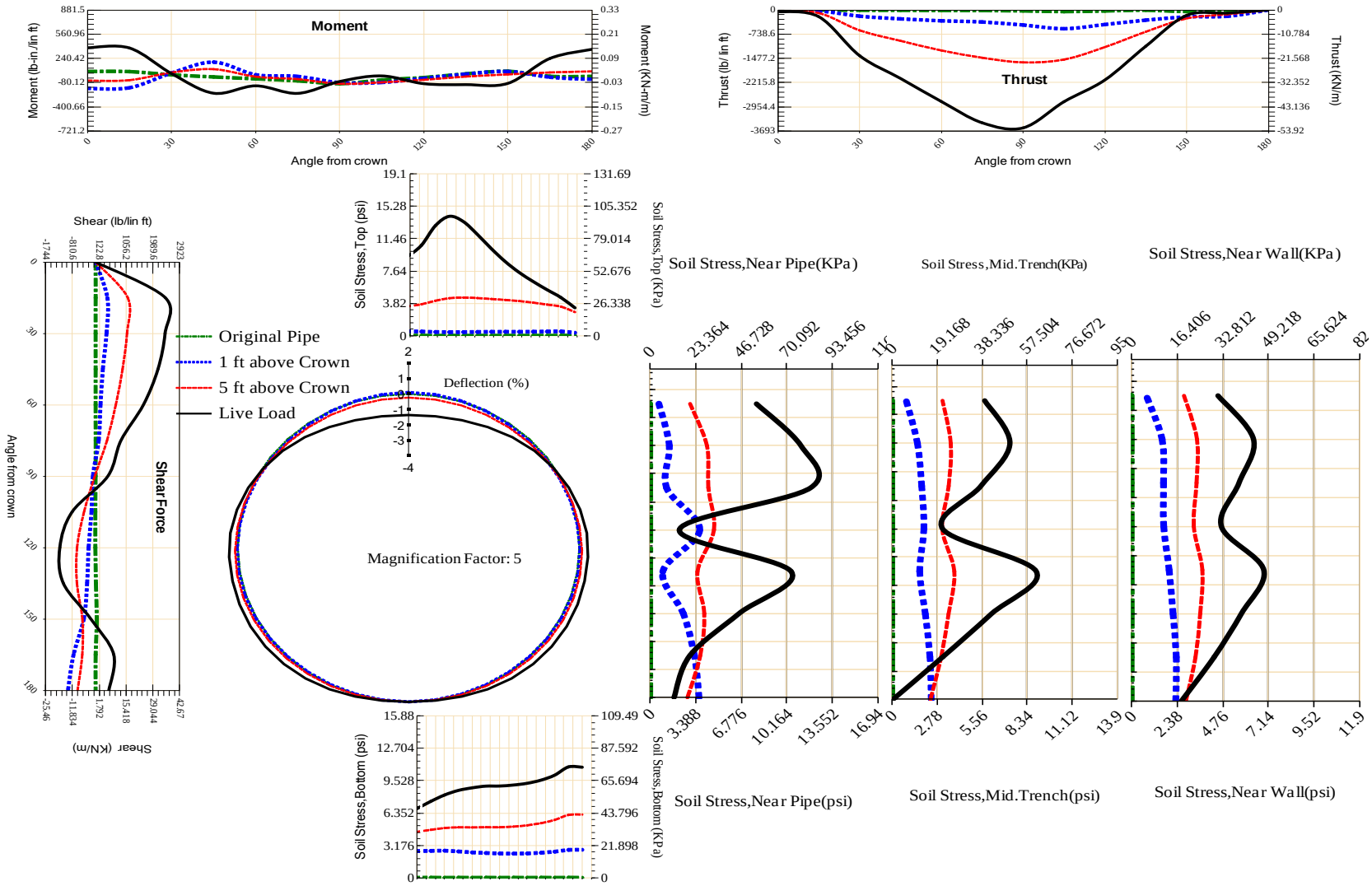

Figure A-435 Param-48-PW288-TR5OR-OD+108-EW3-H5-LiveLoad

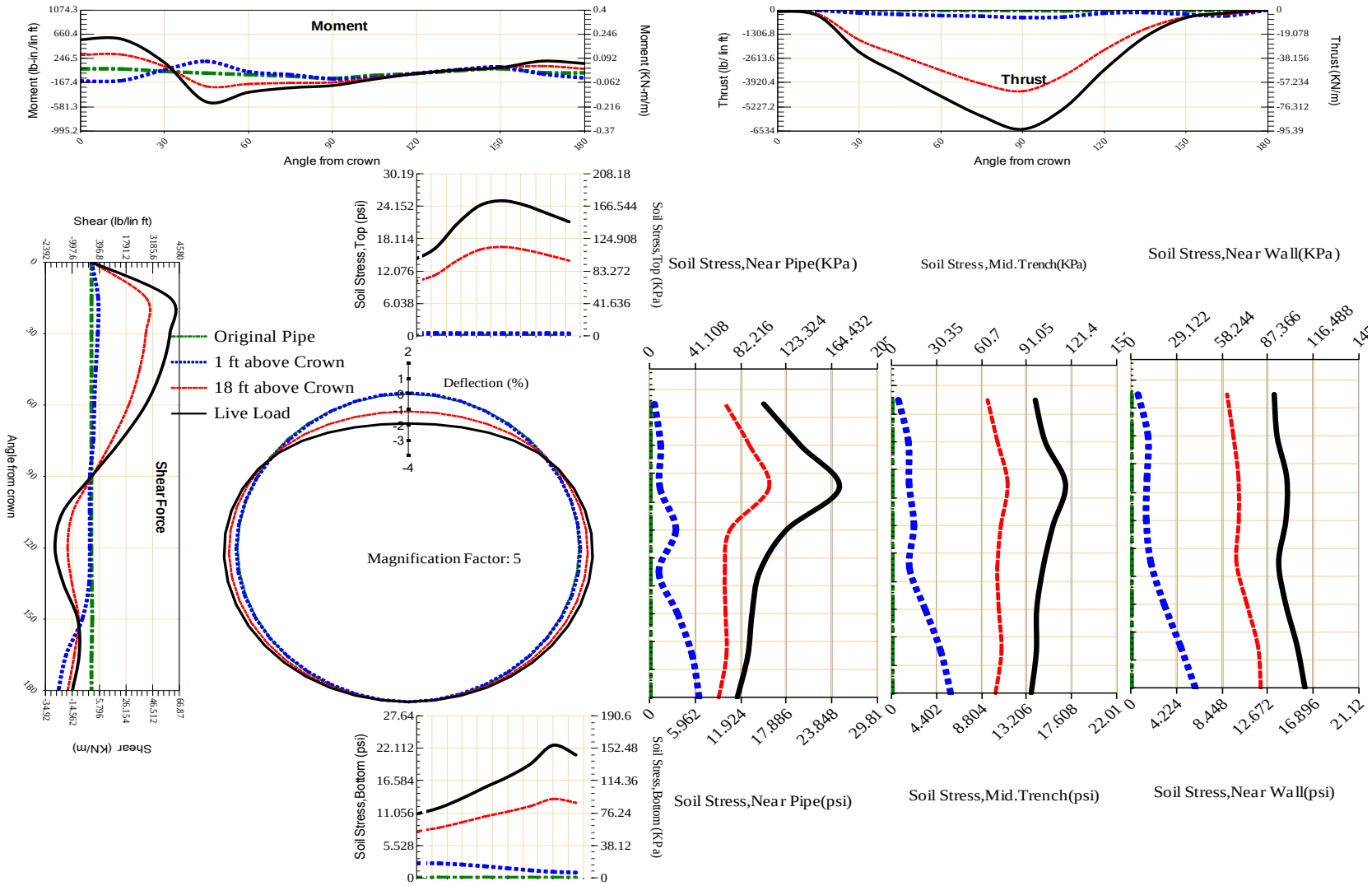

Figure A-436 Param-48-PW288-TR5OR-OD+48-EW10-H18-LiveLoad

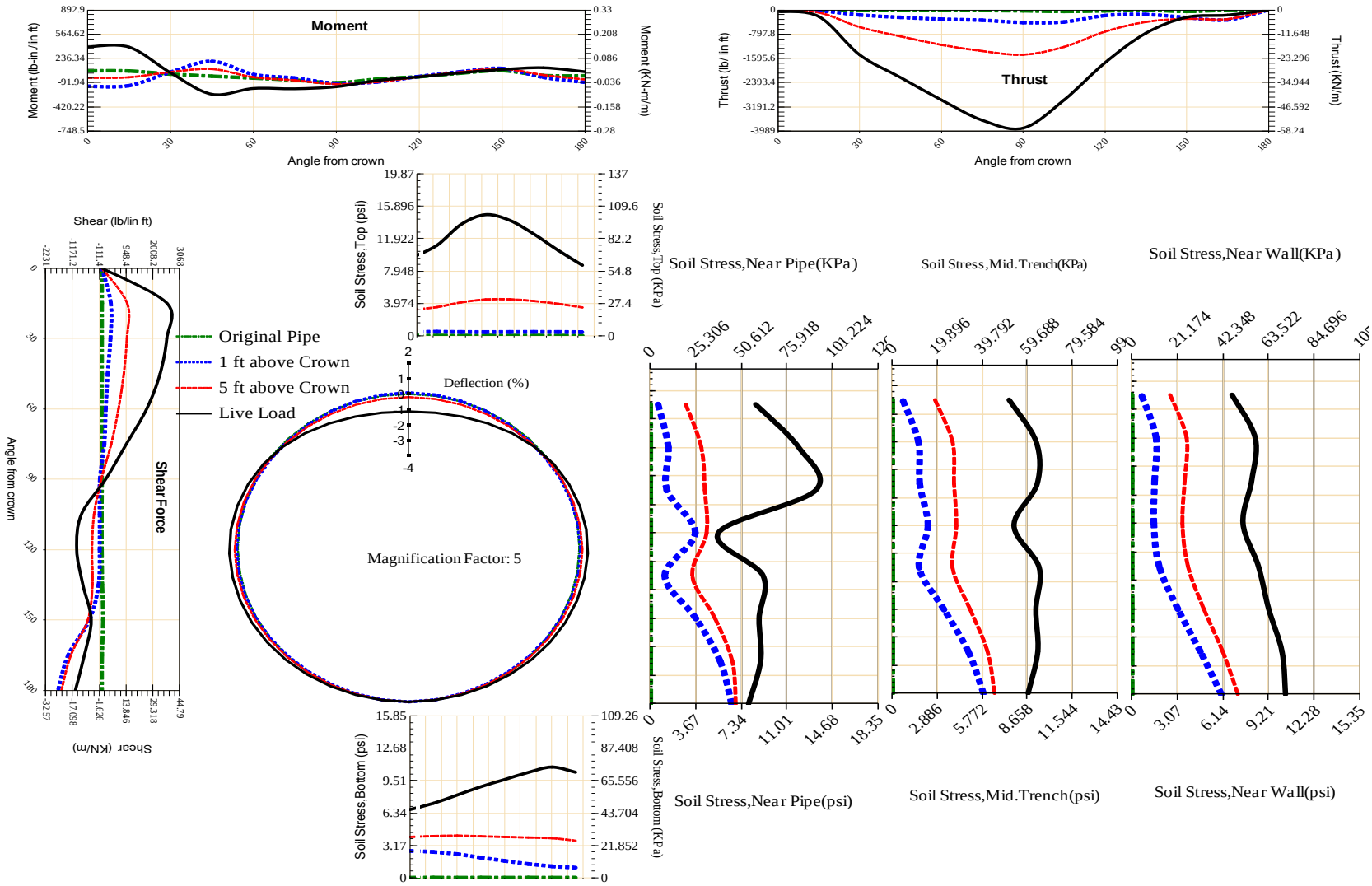

Figure A-437 Param-48-PW288-TR5OR-OD+48-EW10-H5-LiveLoad

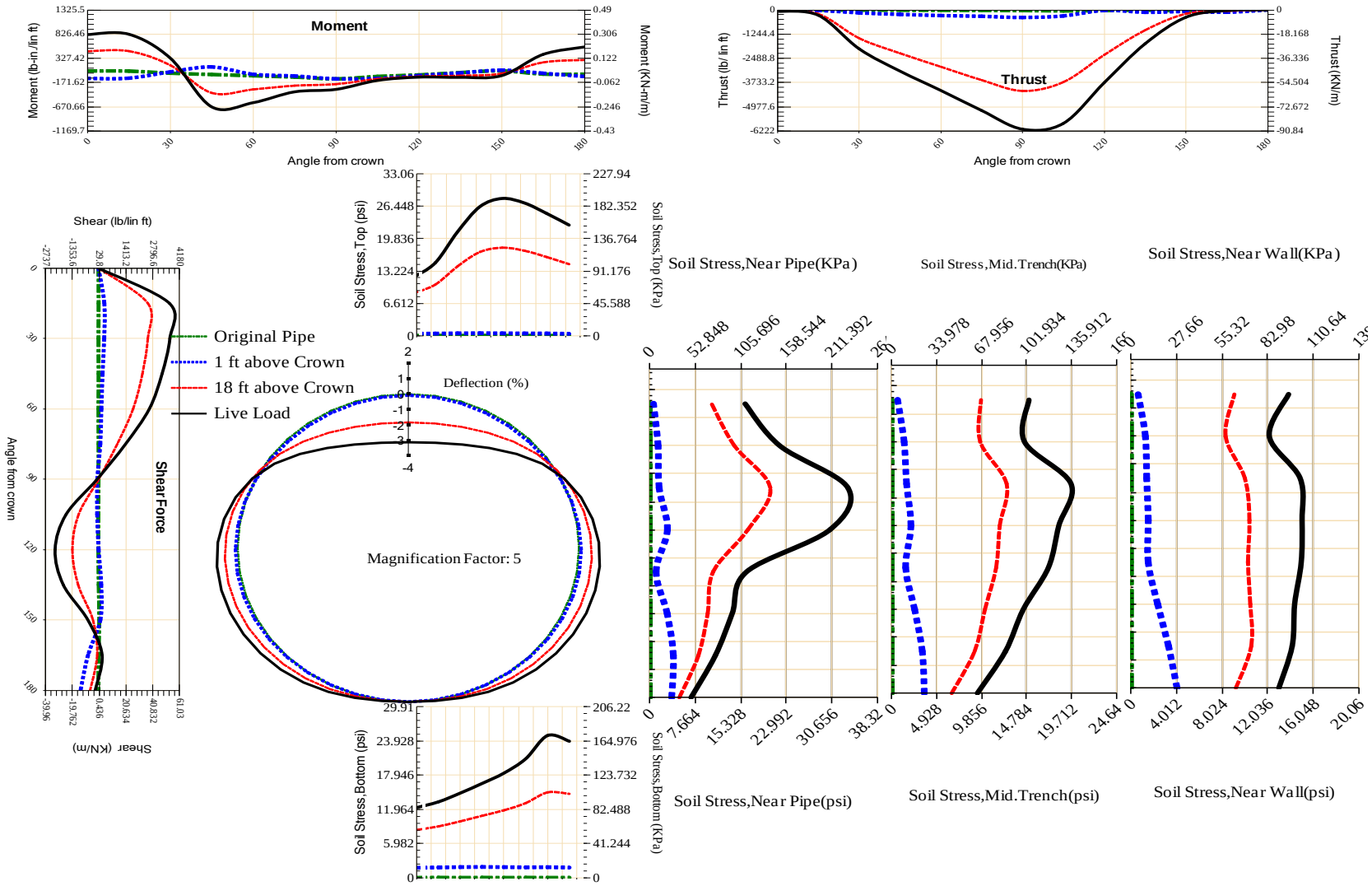

Figure A-438 Param-48-PW288-TR5OR-OD+48-EW3-H18-LiveLoad

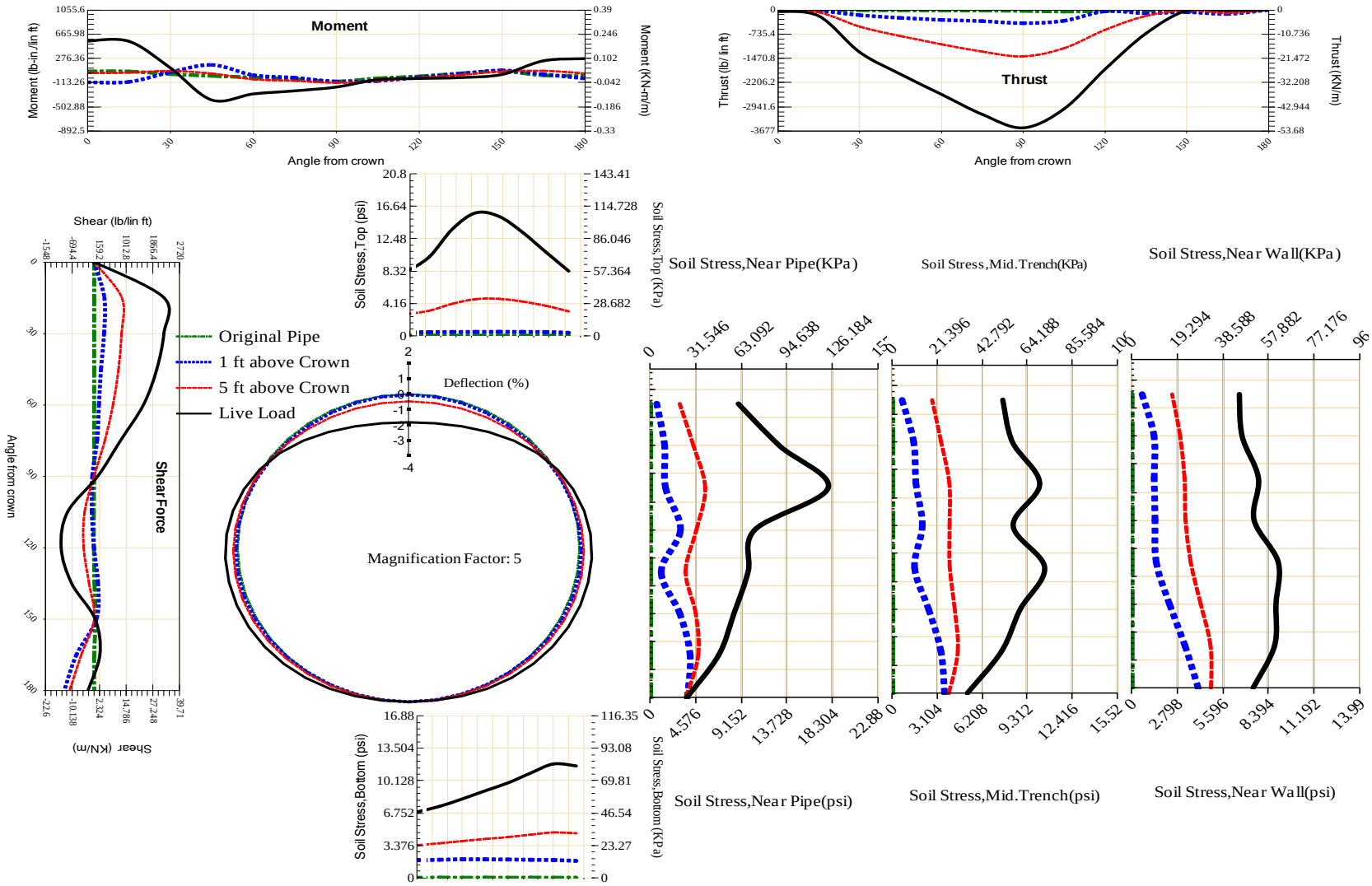

Figure A-439 Param-48-PW288-TR5OR-OD+48-EW3-H5-LiveLoad

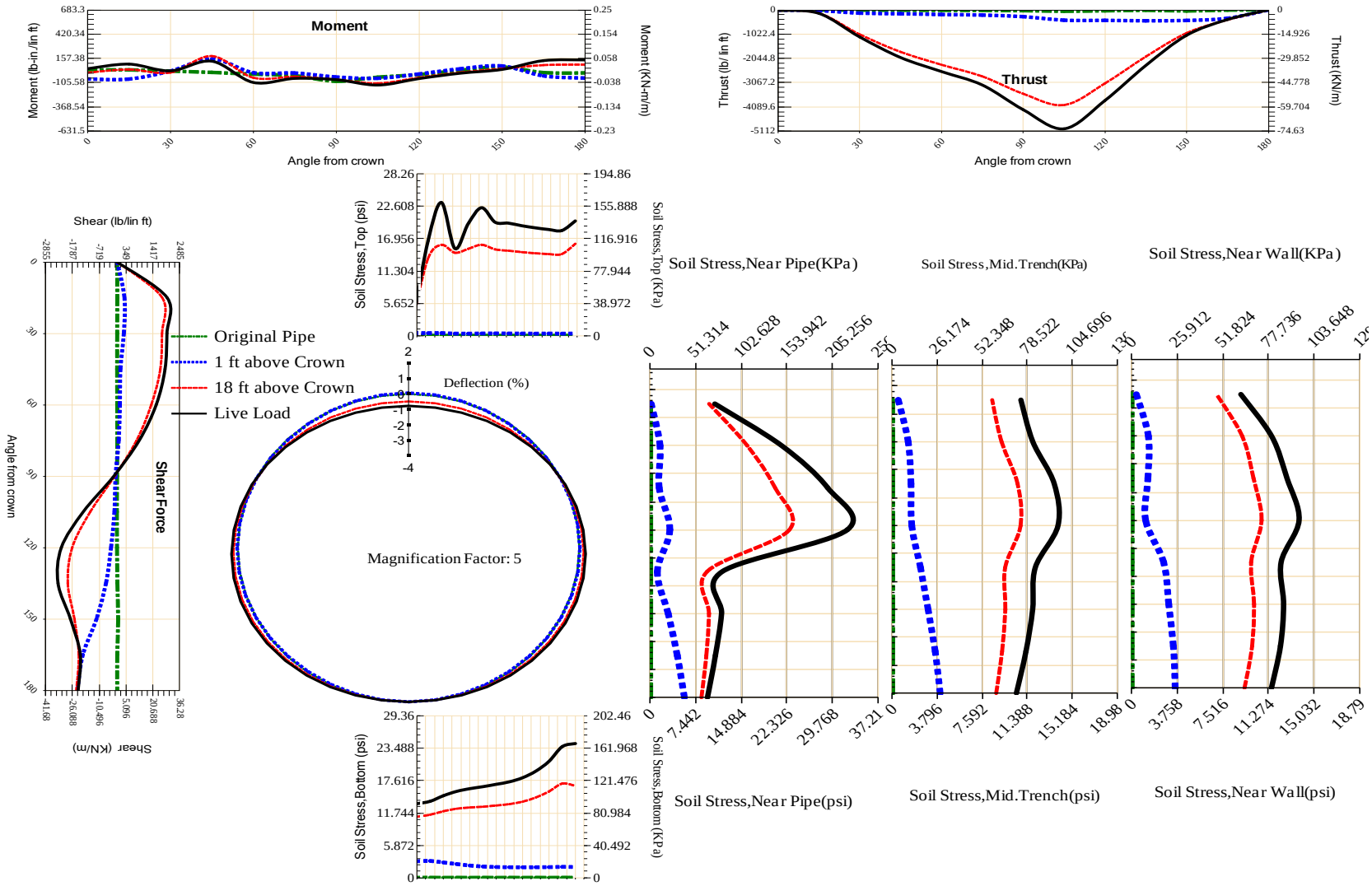

Figure A-440 Param-48-PW288-TR5SF-OD+108-EW10-H18-LiveLoad

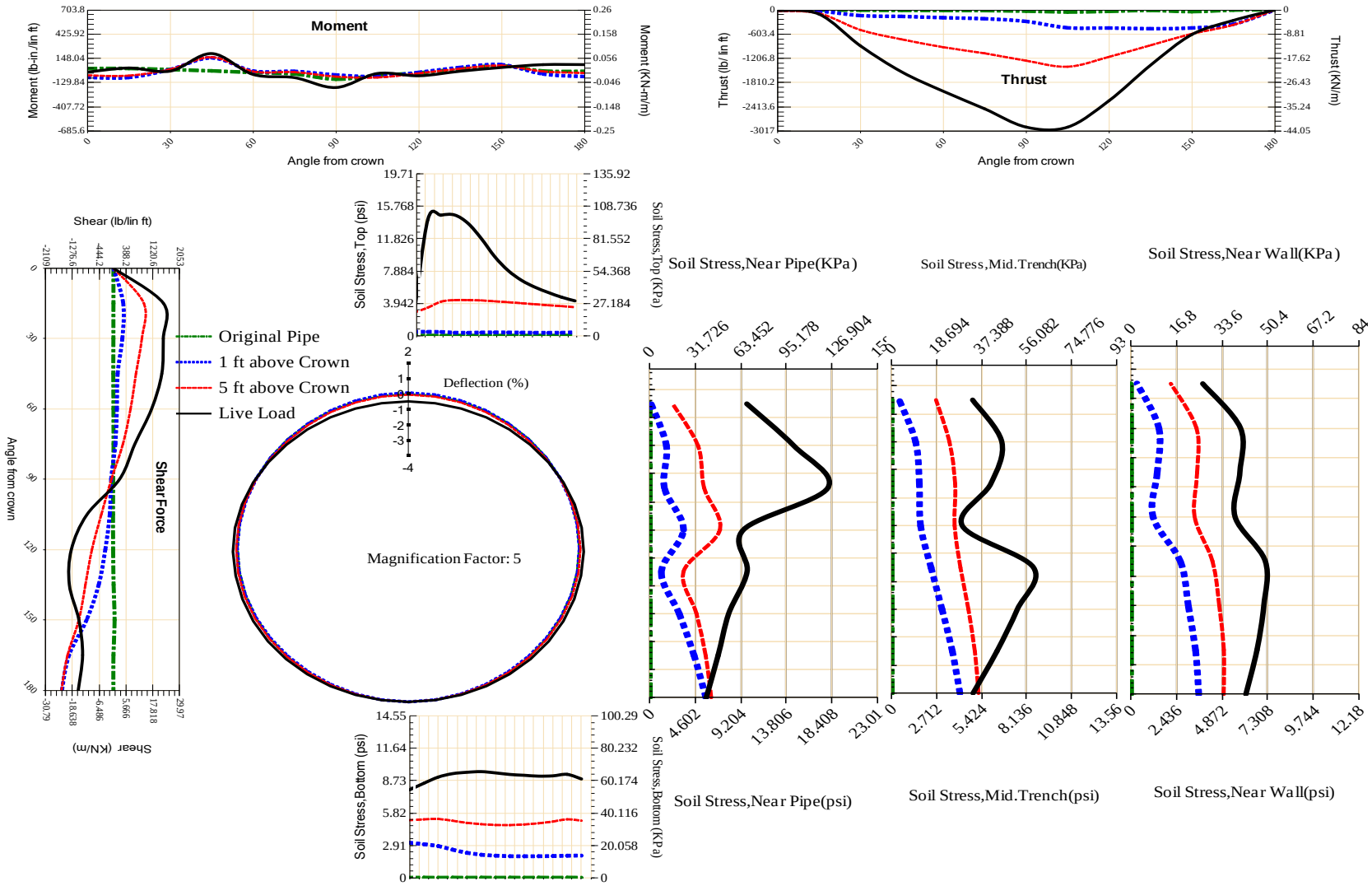

Figure A-441 Param-48-PW288-TR5SF-OD+108-EW10-H5-LiveLoad

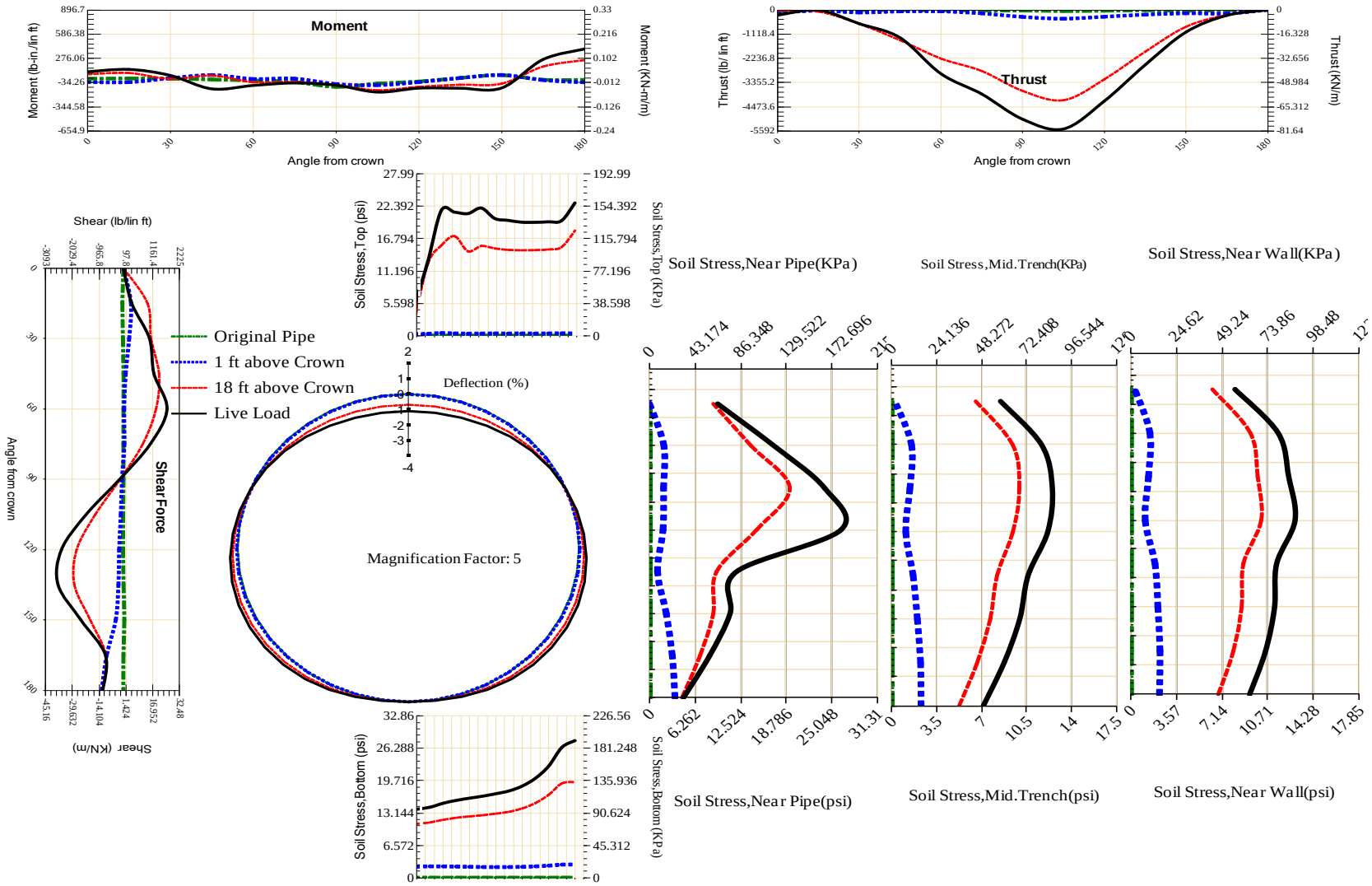

Figure A-442 Param-48-PW288-TR5SF-OD+108-EW3-H18-LiveLoad

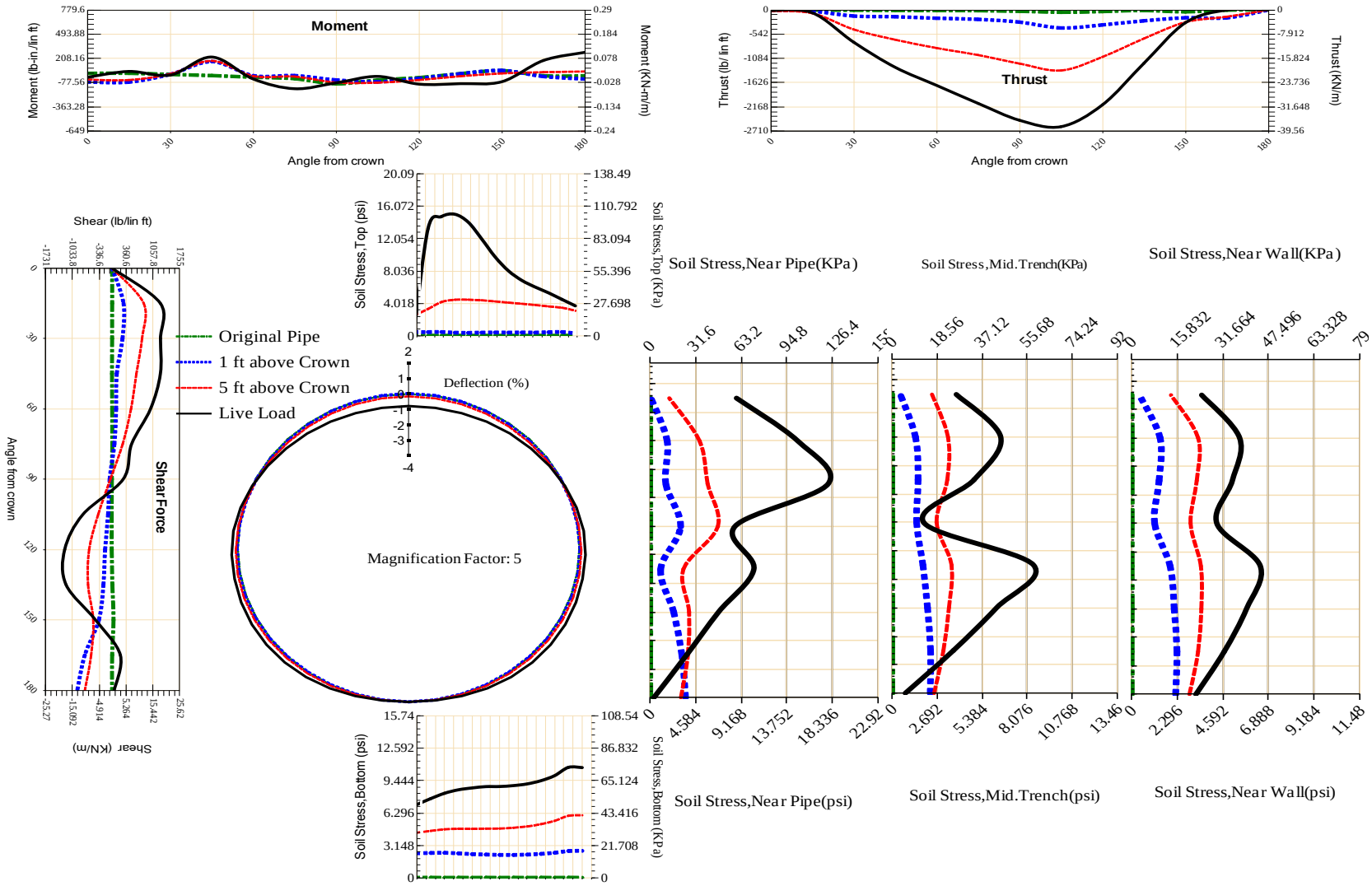

Figure A-443 Param-48-PW288-TR5SF-OD+108-EW3-H5-LiveLoad

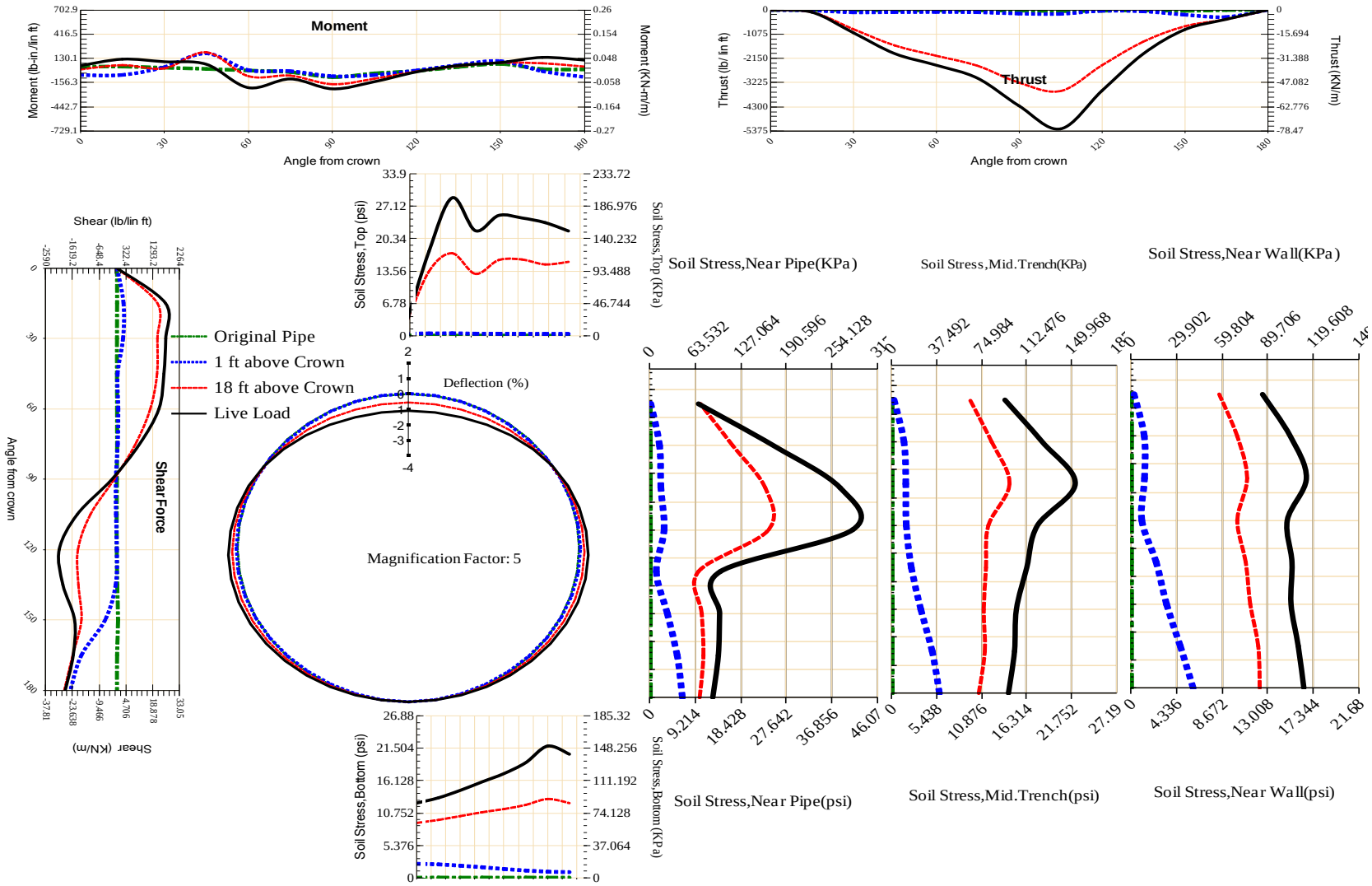

Figure A-444 Param-48-PW288-TR5SF-OD+48-EW10-H18-LiveLoad

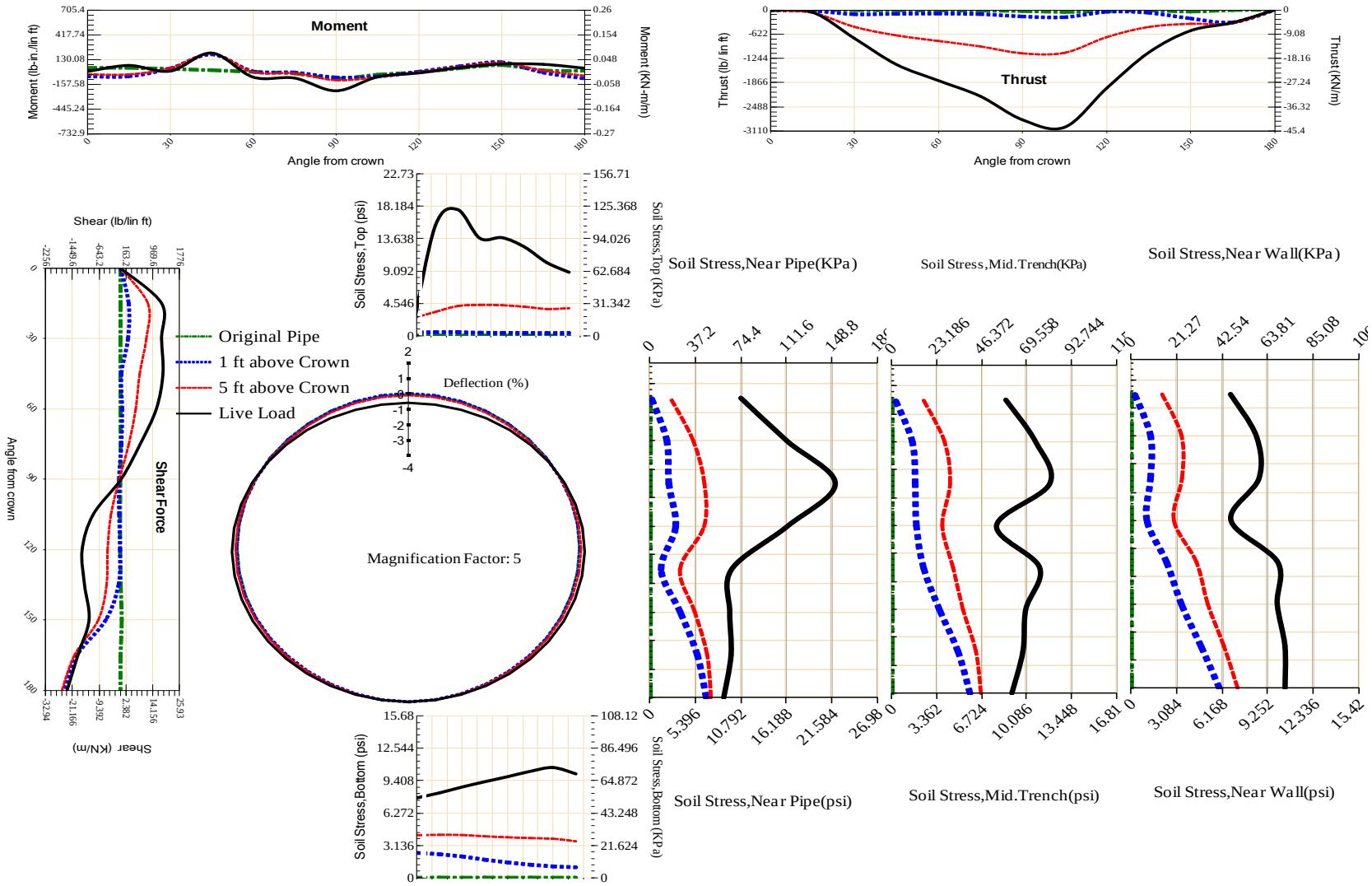

Figure A-445 Param-48-PW288-TR5SF-OD+48-EW10-H5-LiveLoad

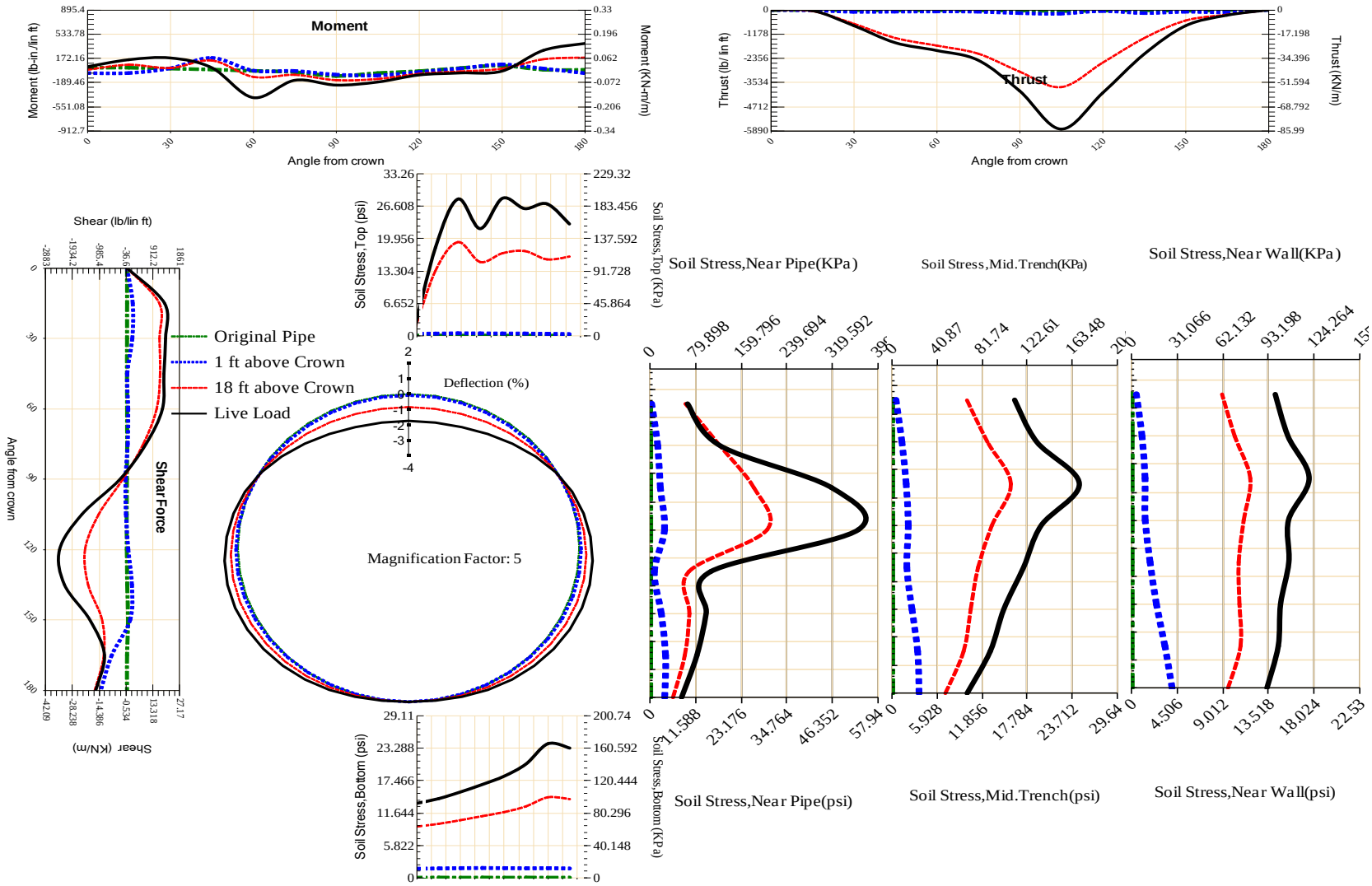

Figure A-446 Param-48-PW288-TR5SF-OD+48-EW3-H18-LiveLoad

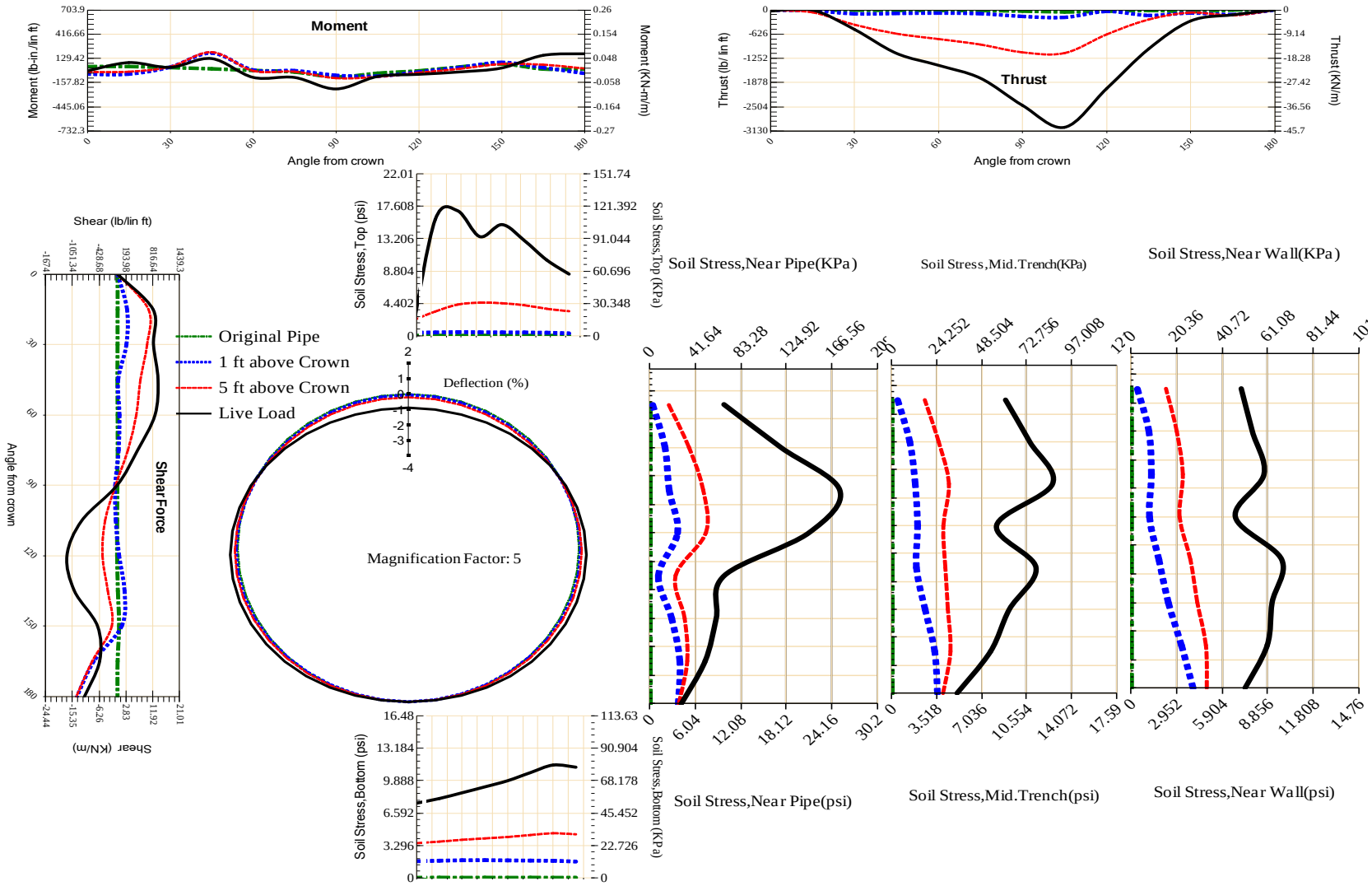

Figure A-447 Param-48-PW288-TR5SF-OD+48-EW3-H5-LiveLoad

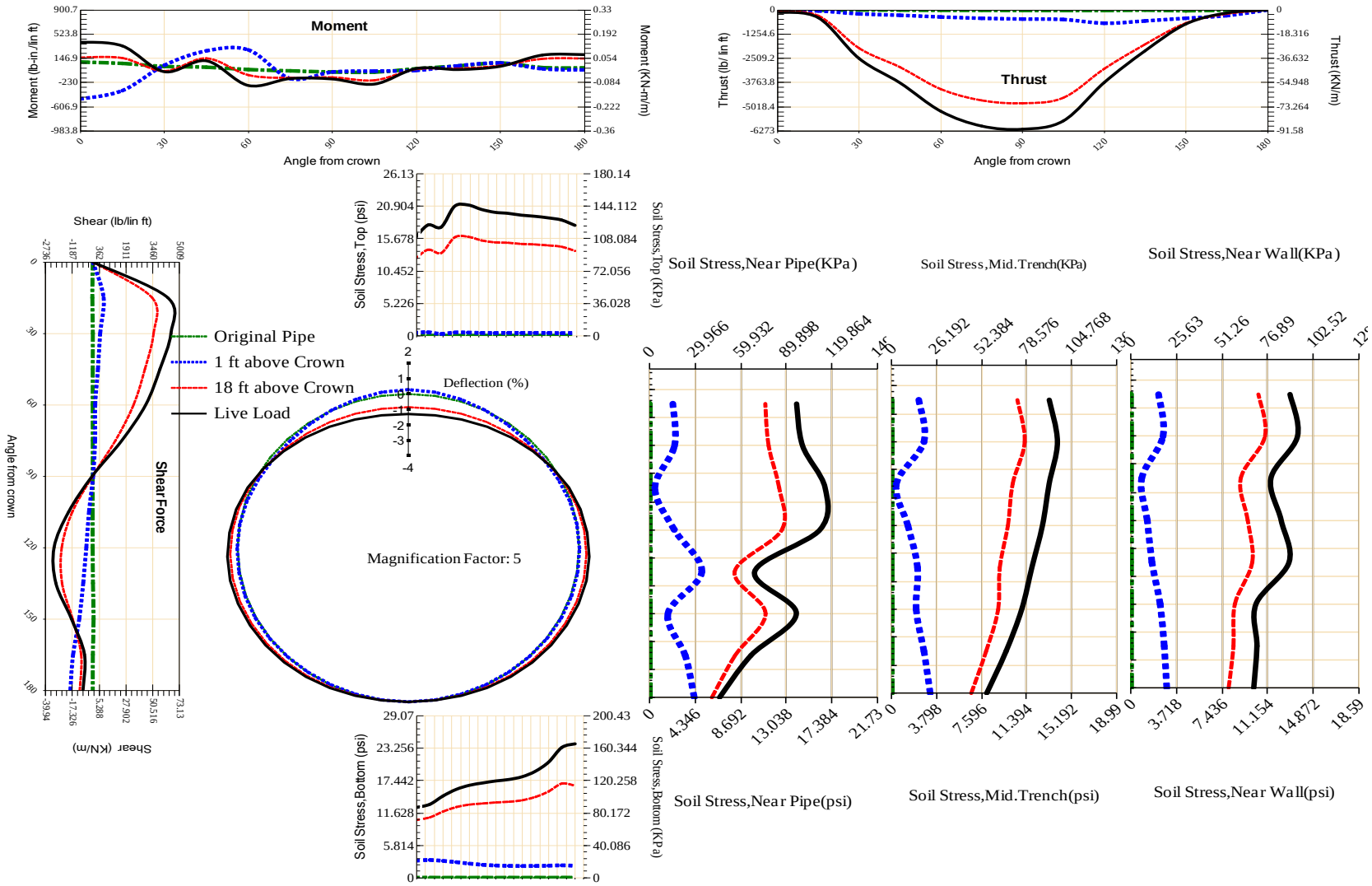

Figure A-448 Param-48-PW288-TR7OR-OD+108-EW10-H18-LiveLoad

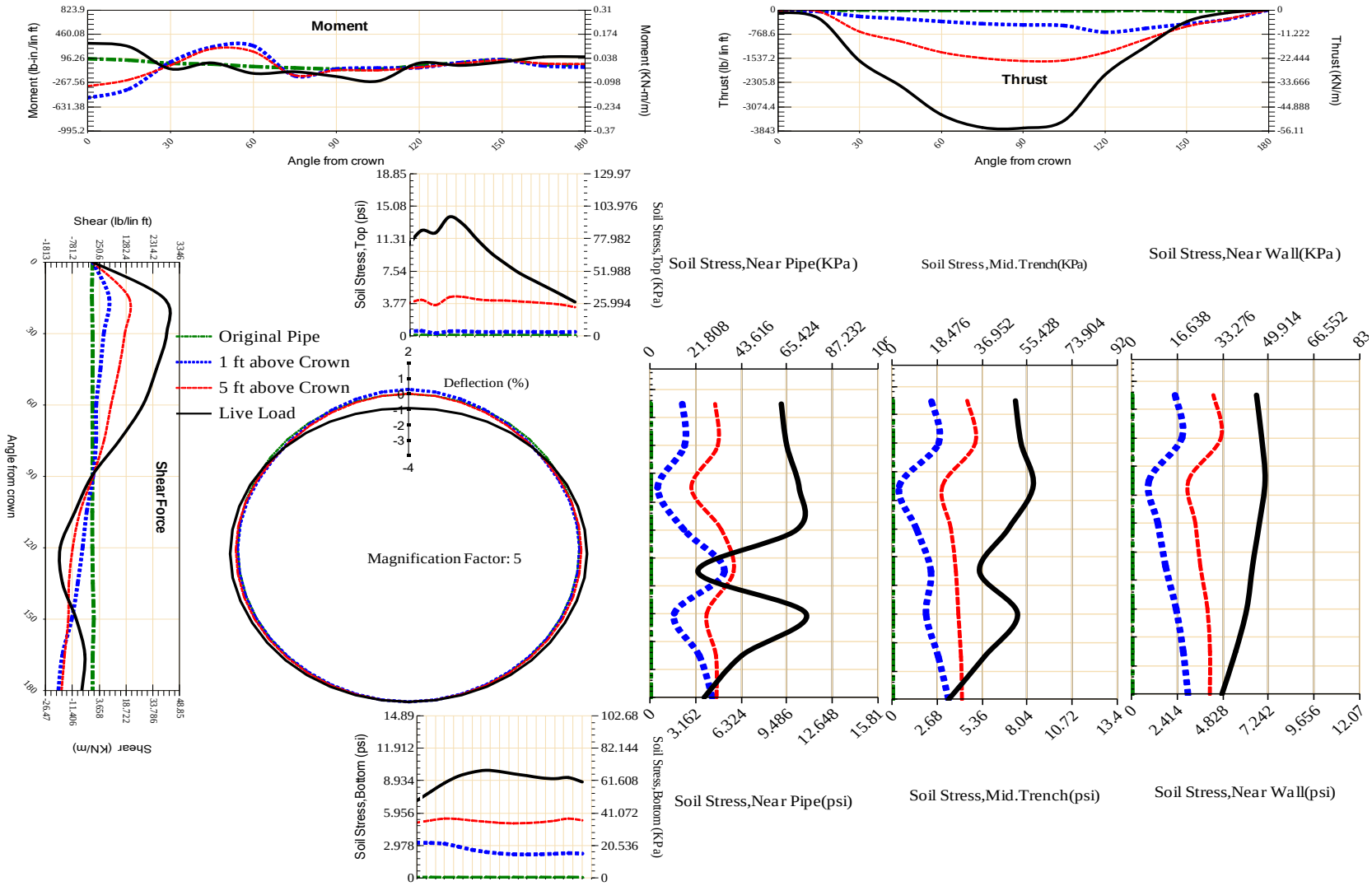

Figure A-449 Param-48-PW288-TR7OR-OD+108-EW10-H5-LiveLoad

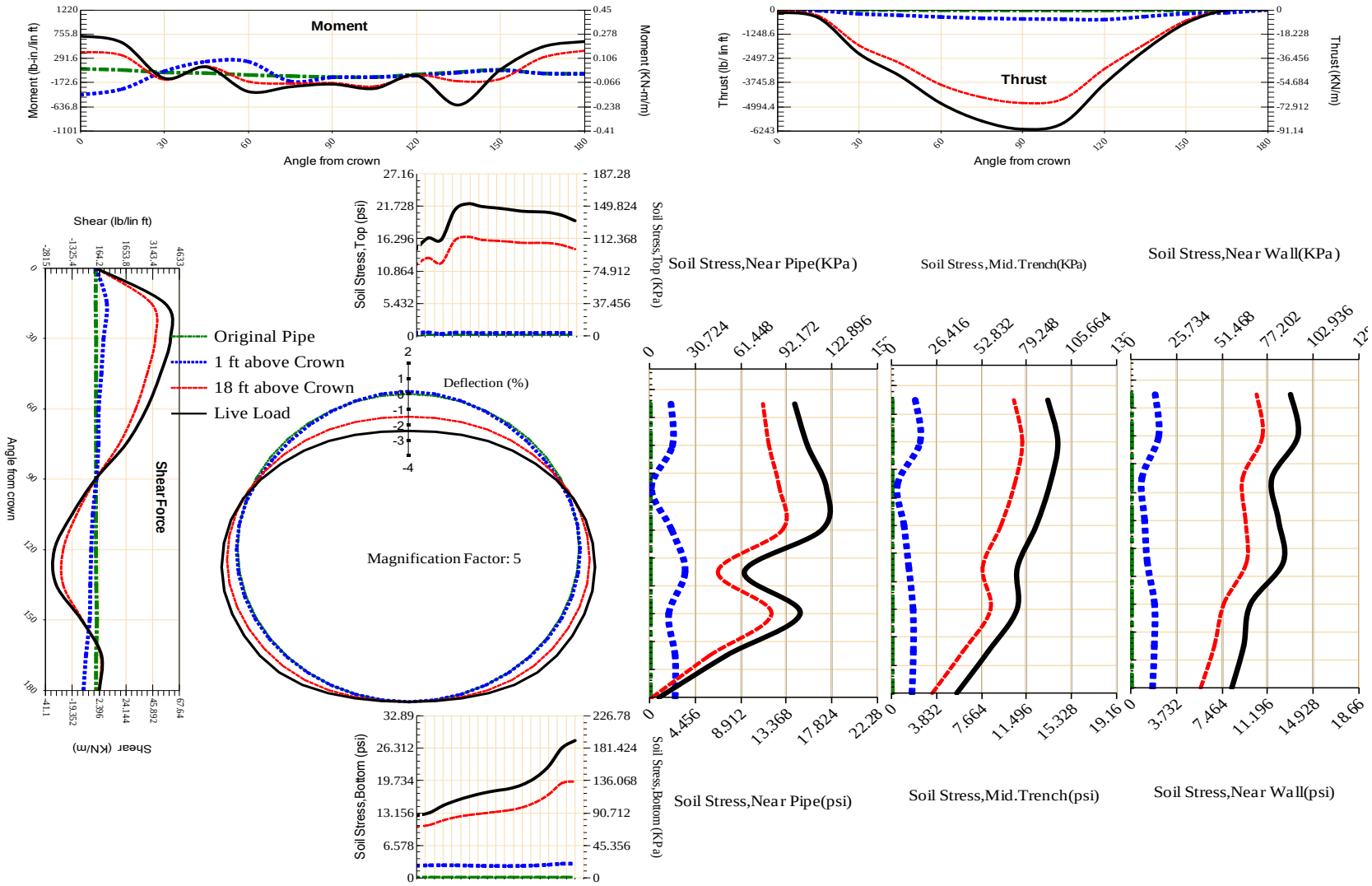

Figure A-450 Param-48-PW288-TR7OR-OD+108-EW3-H18-LiveLoad

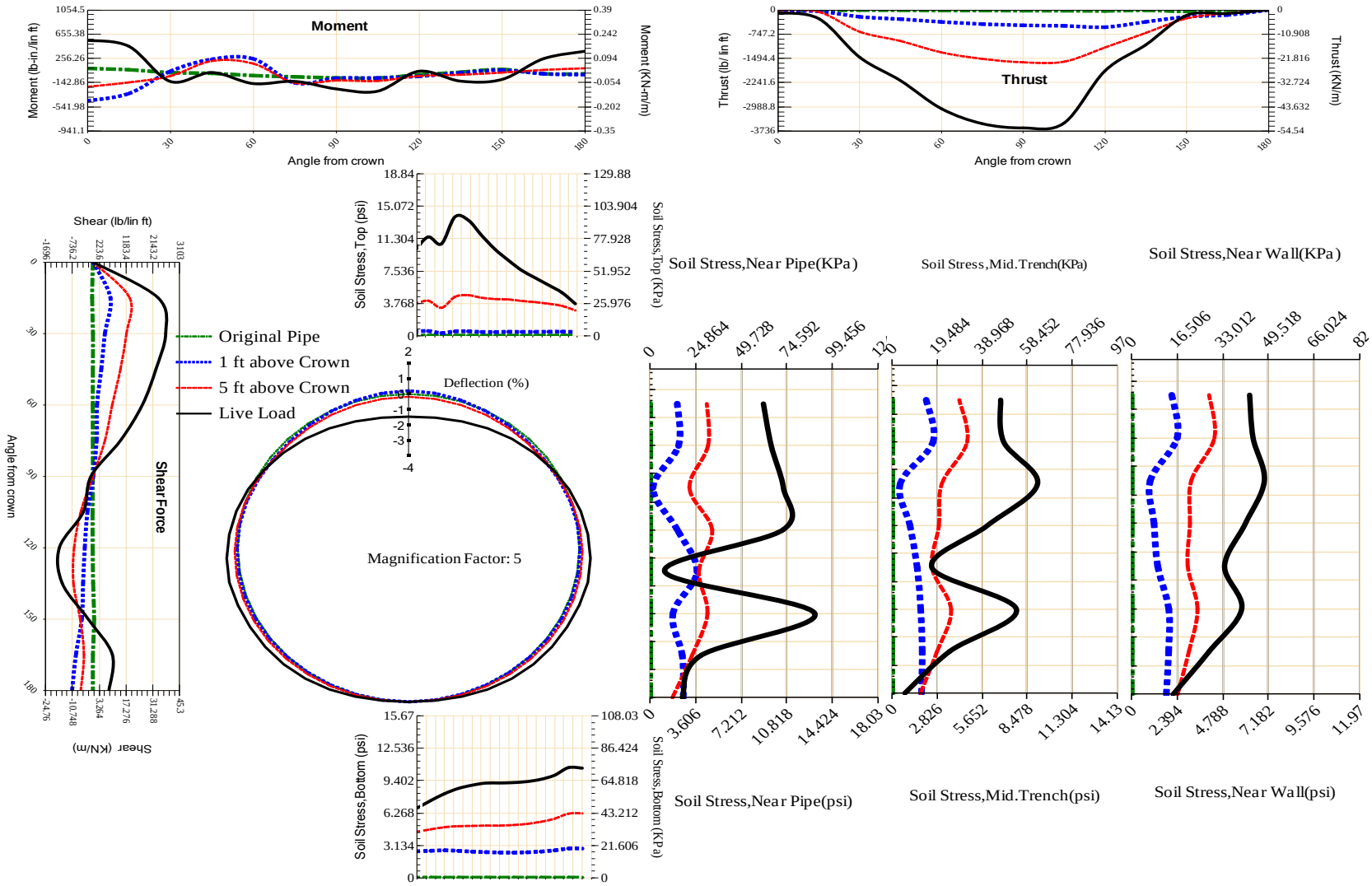

Figure A-451 Param-48-PW288-TR7OR-OD+108-EW3-H5-LiveLoad

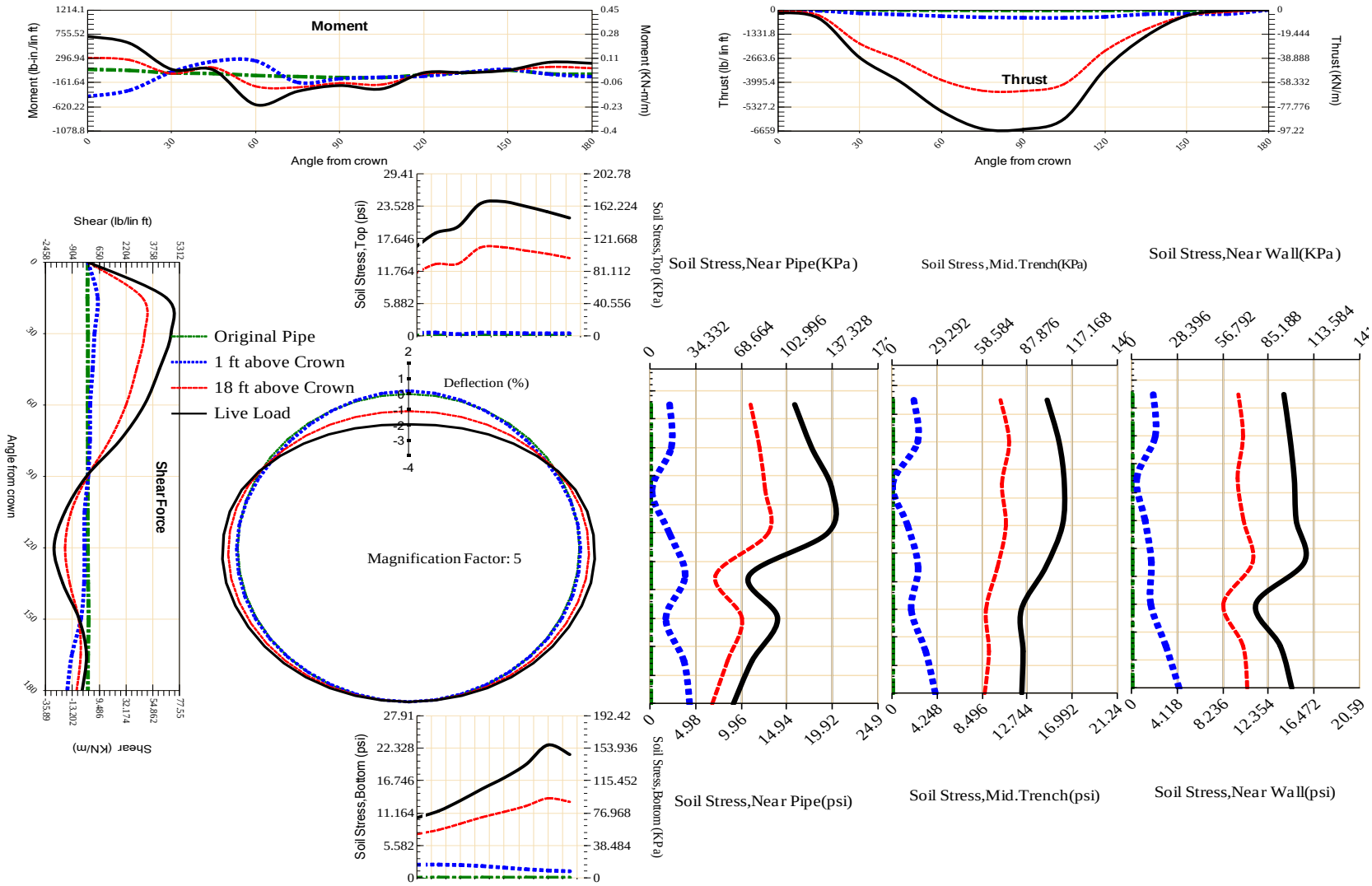

Figure A-452 Param-48-PW288-TR7OR-OD+48-EW10-H18-LiveLoad

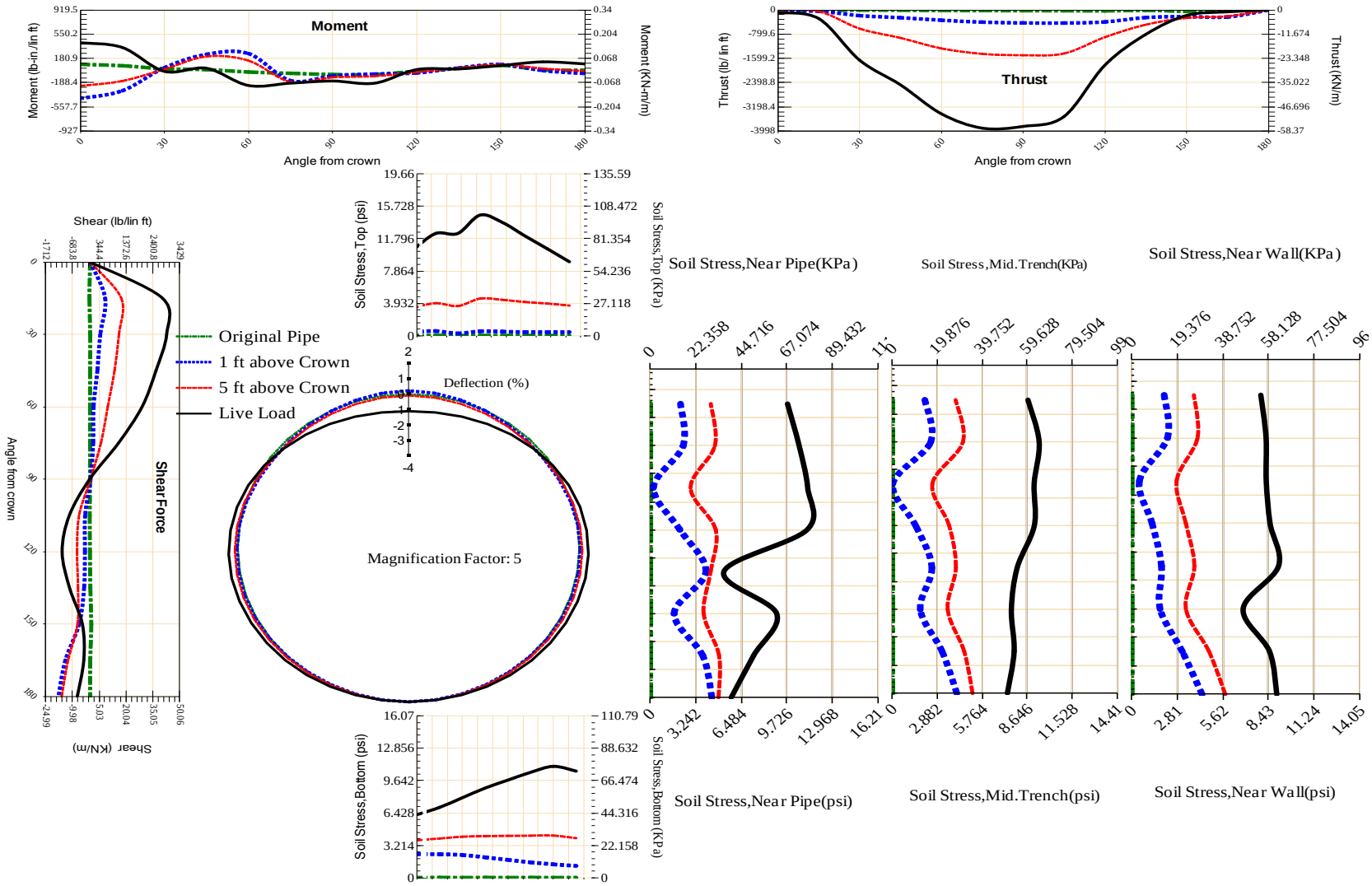

Figure A-453 Param-48-PW288-TR7OR-OD+48-EW10-H5-LiveLoad

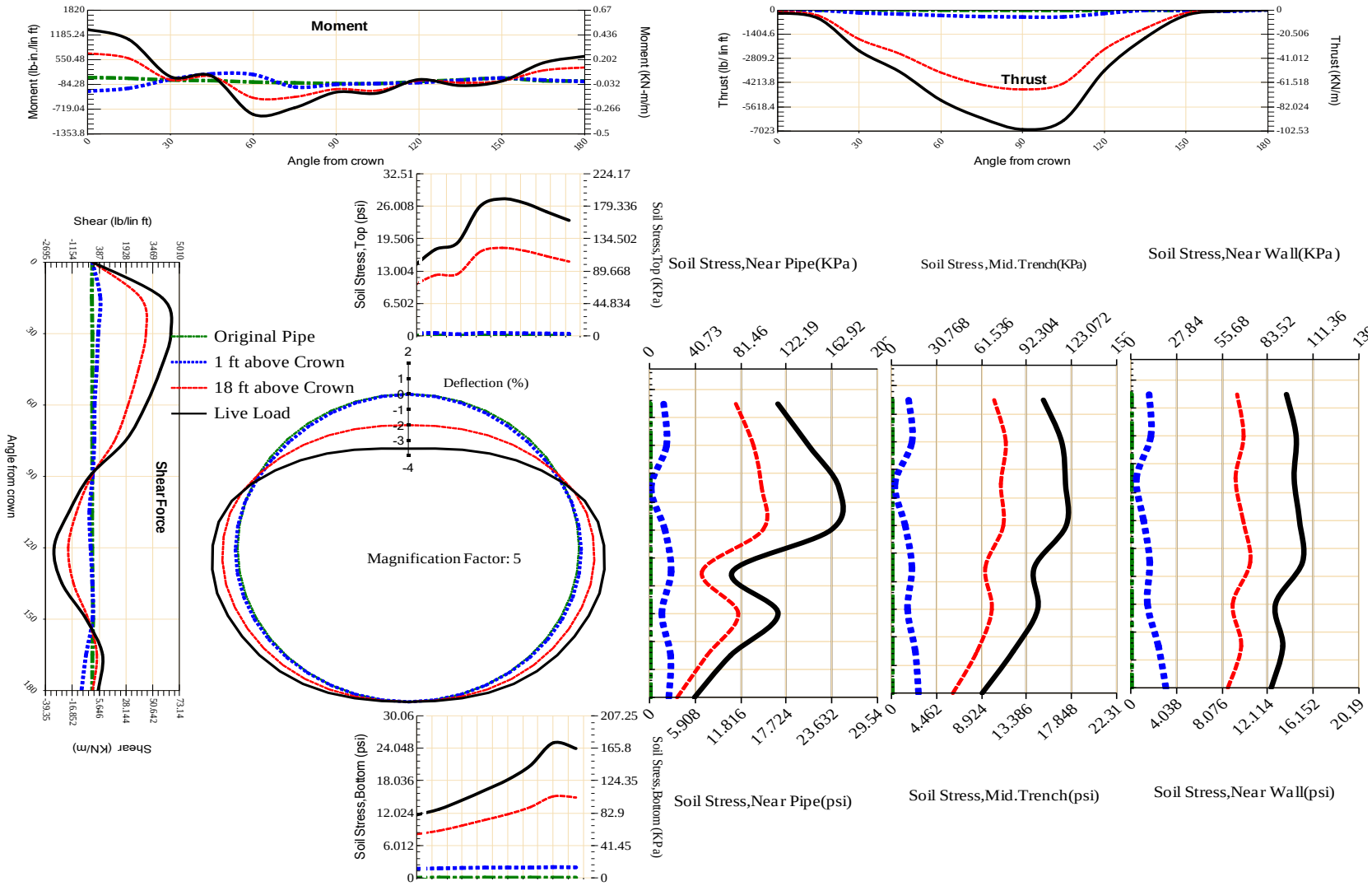

Figure A-454 Param-48-PW288-TR7OR-OD+48-EW3-H18-LiveLoad

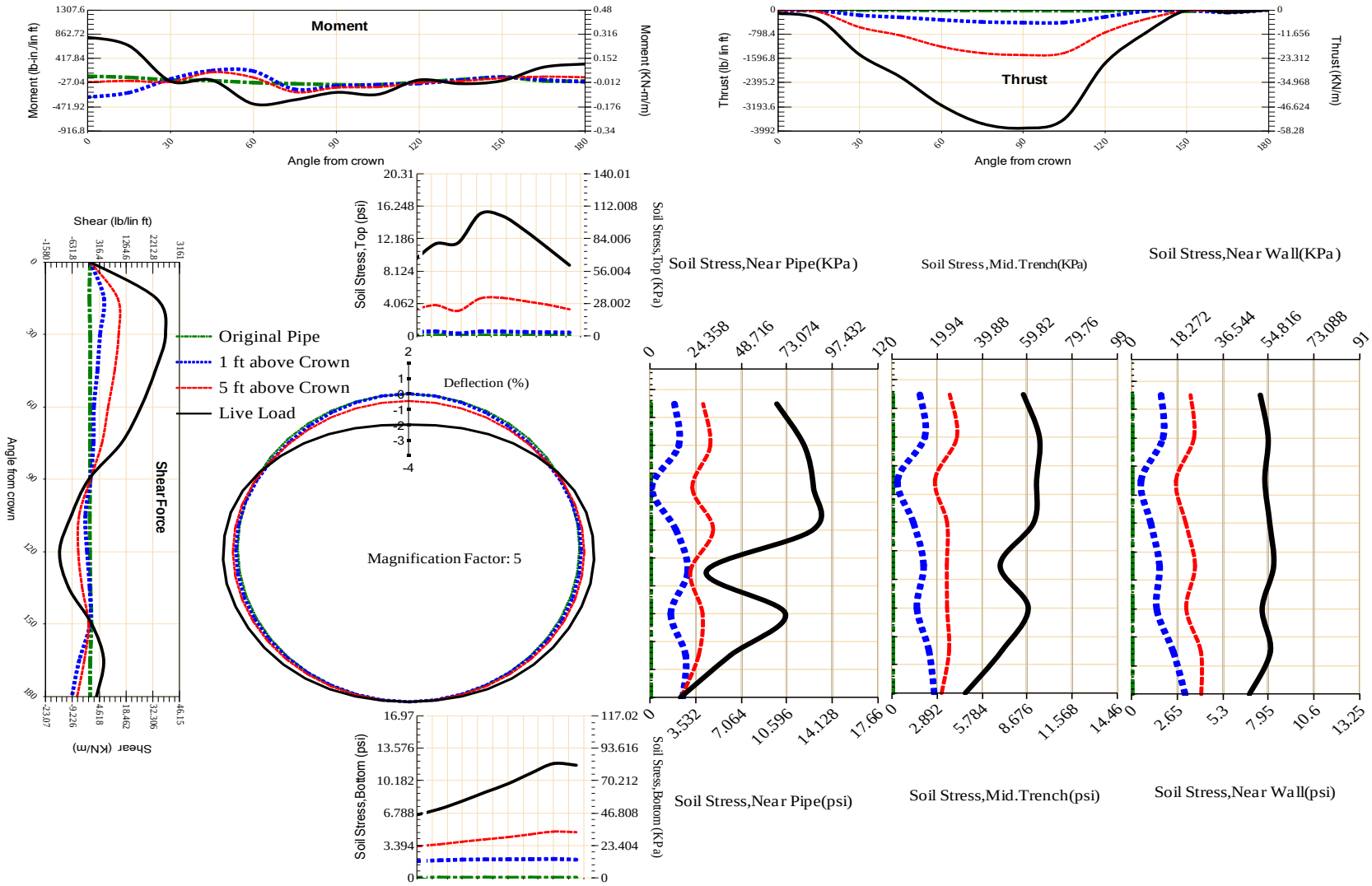

Figure A-455 Param-48-PW288-TR7OR-OD+48-EW3-H5-LiveLoad

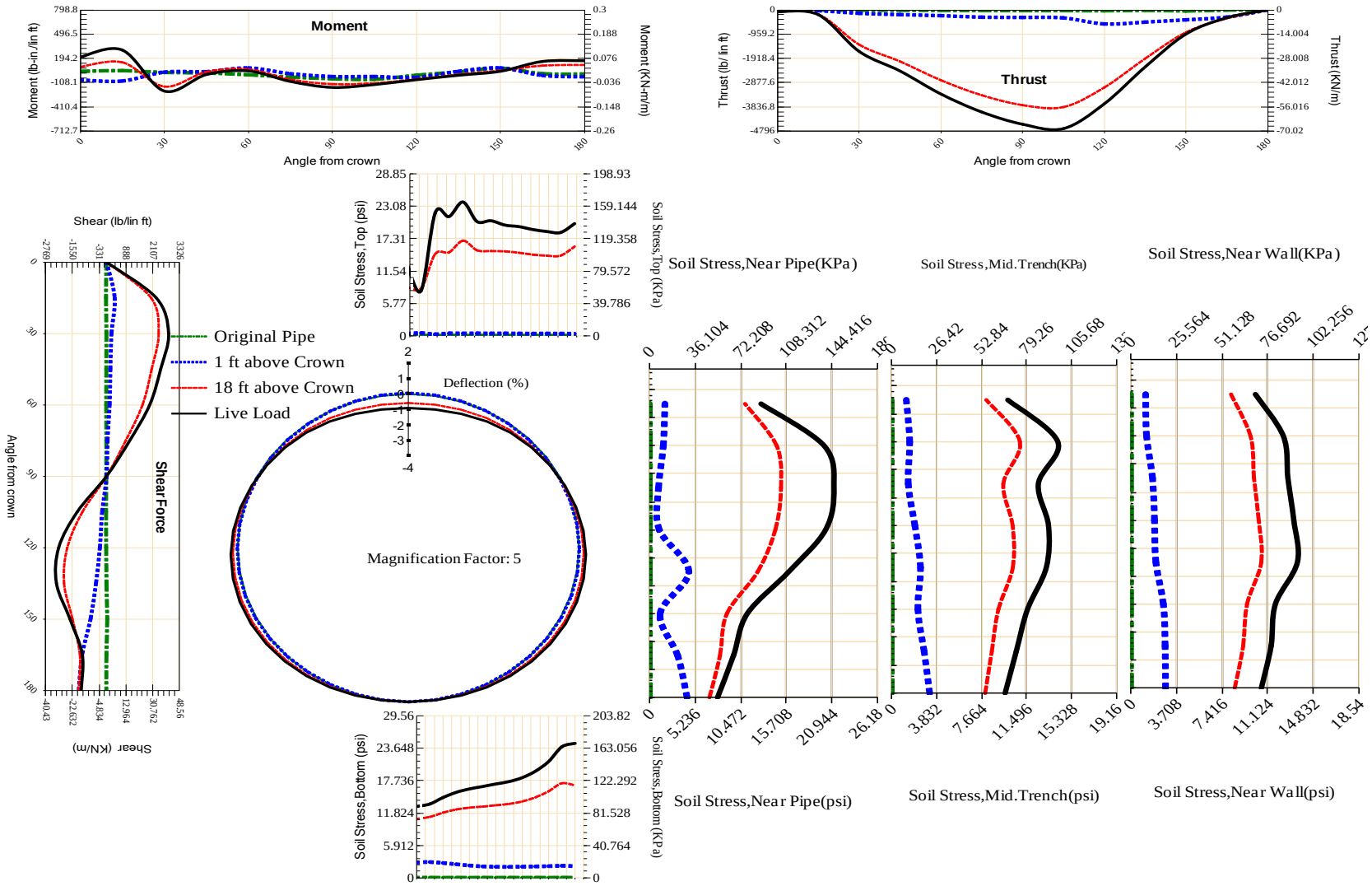

Figure A-456 Param-48-PW288-TR7SF-OD+108-EW10-H18-LiveLoad

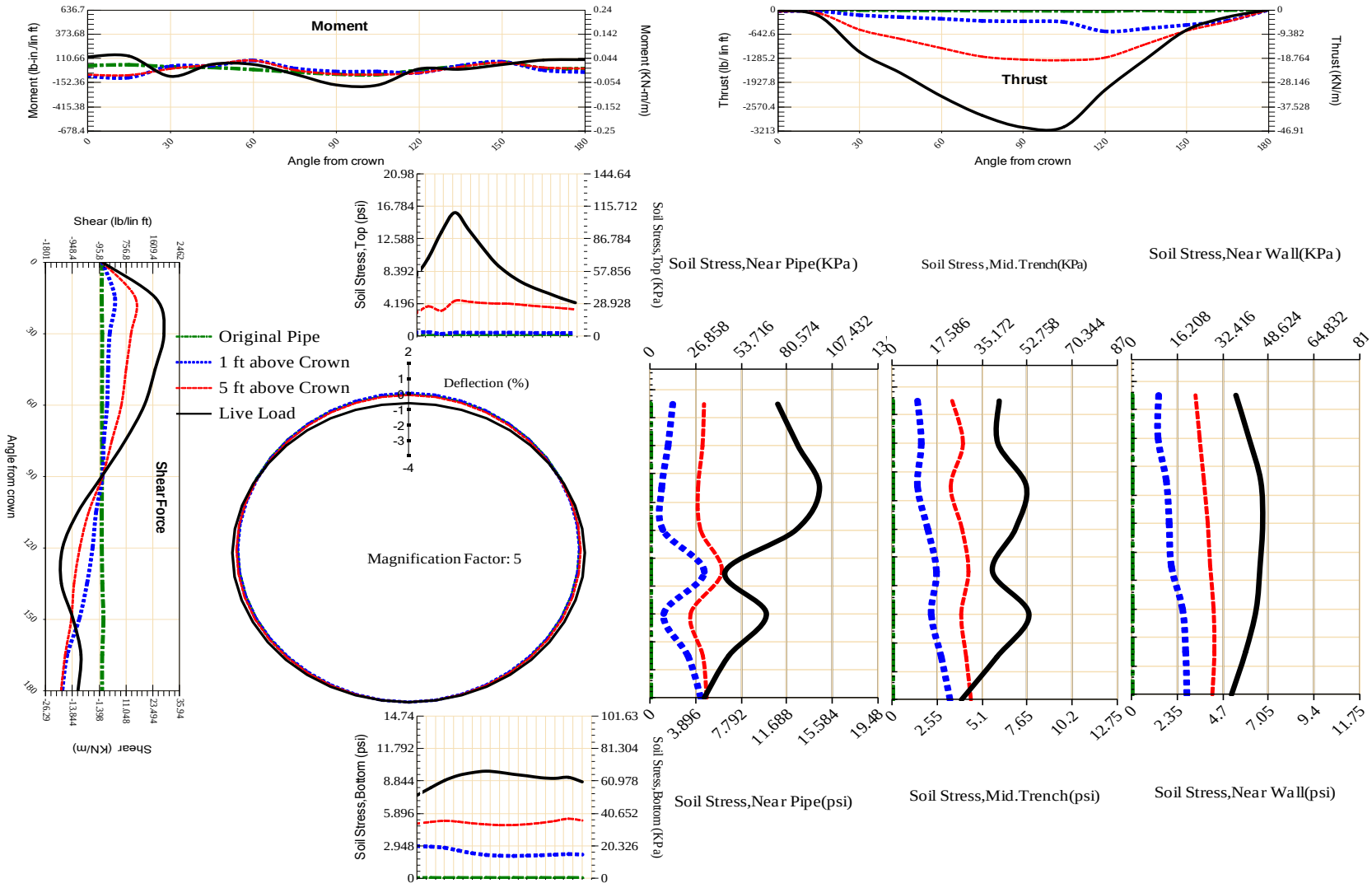

Figure A-457 Param-48-PW288-TR7SF-OD+108-EW10-H5-LiveLoad

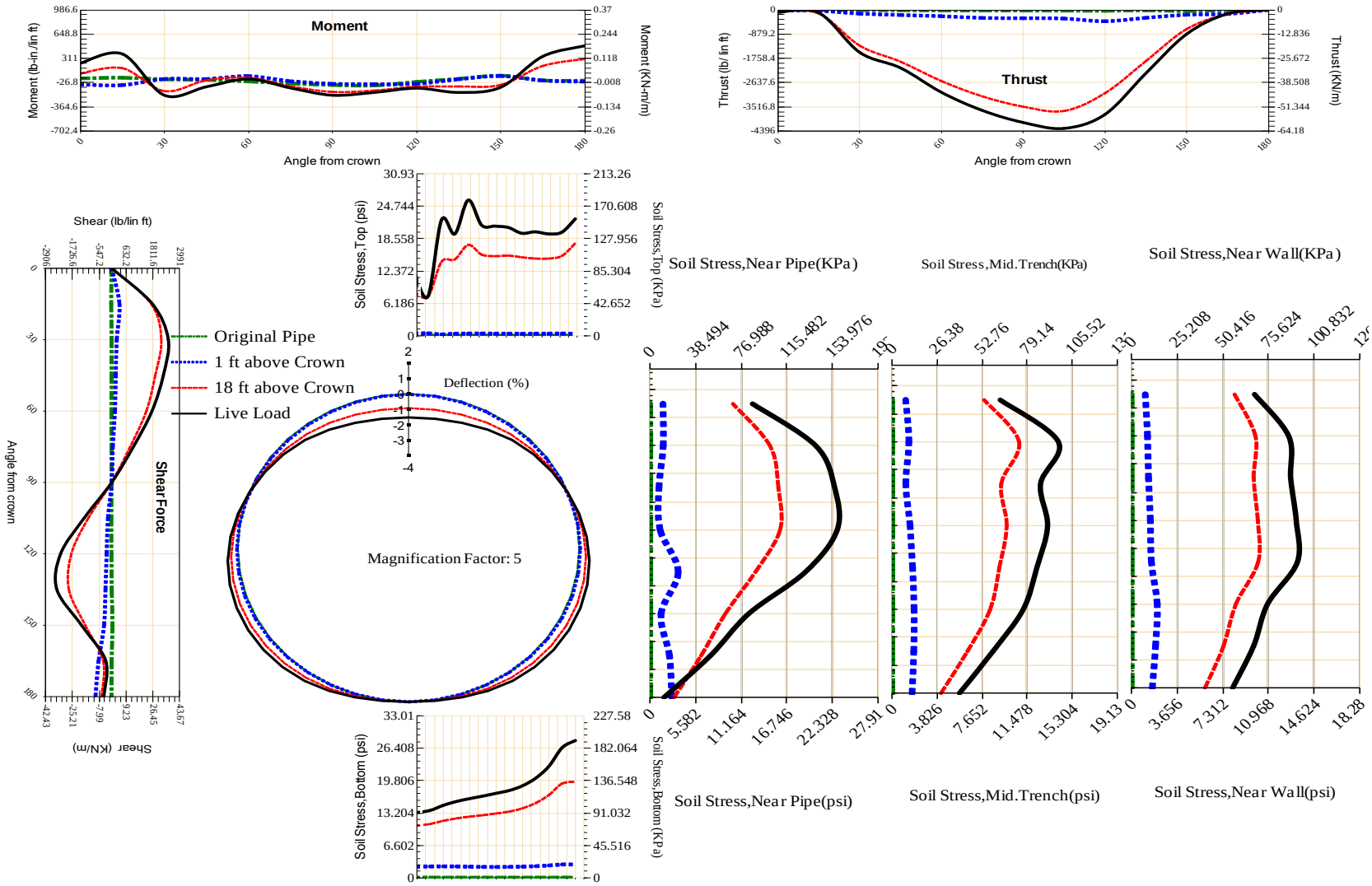

Figure A-458 Param-48-PW288-TR7SF-OD+108-EW3-H18-LiveLoad

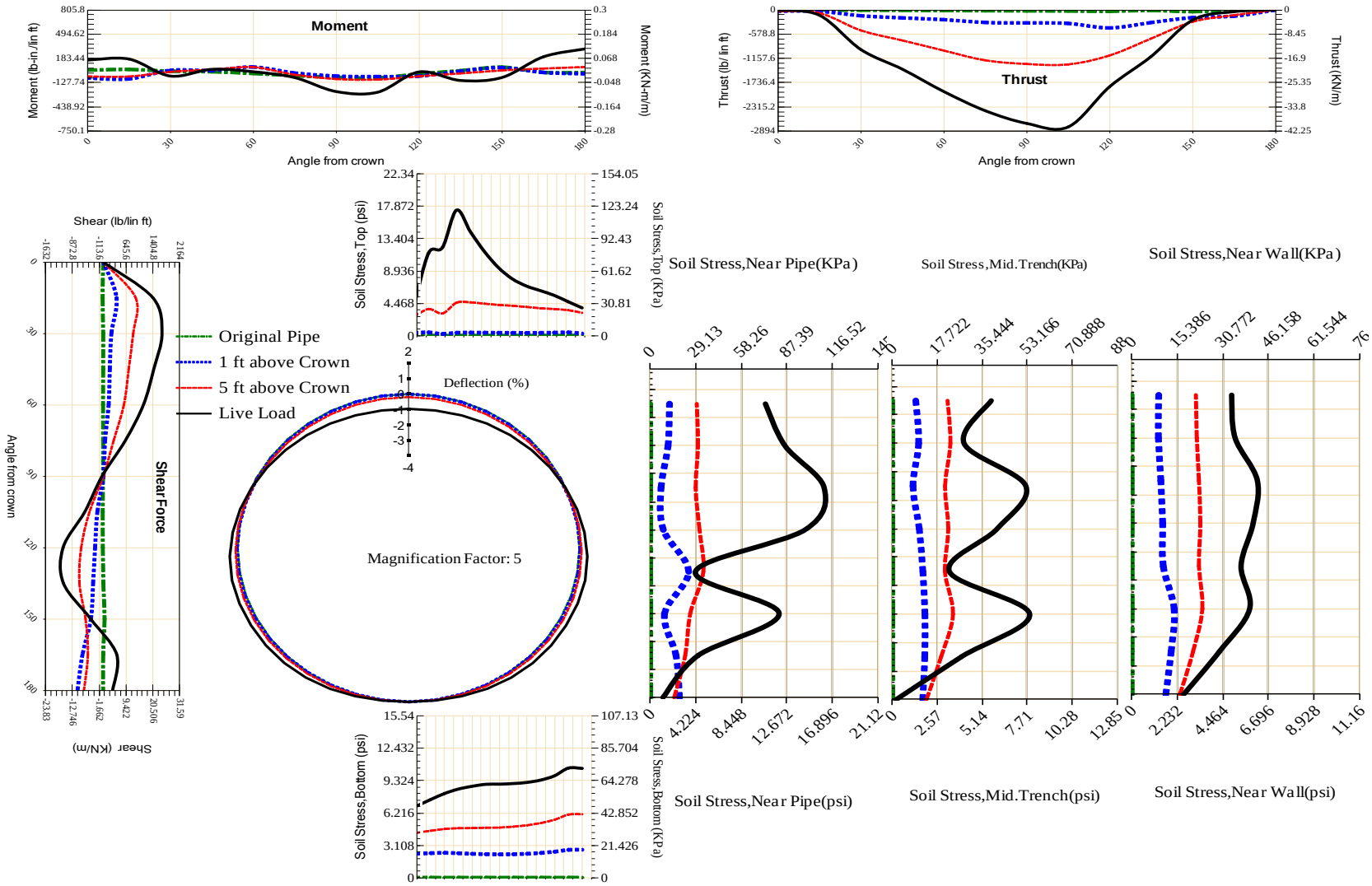

Figure A-459 Param-48-PW288-TR7SF-OD+108-EW3-H5-LiveLoad

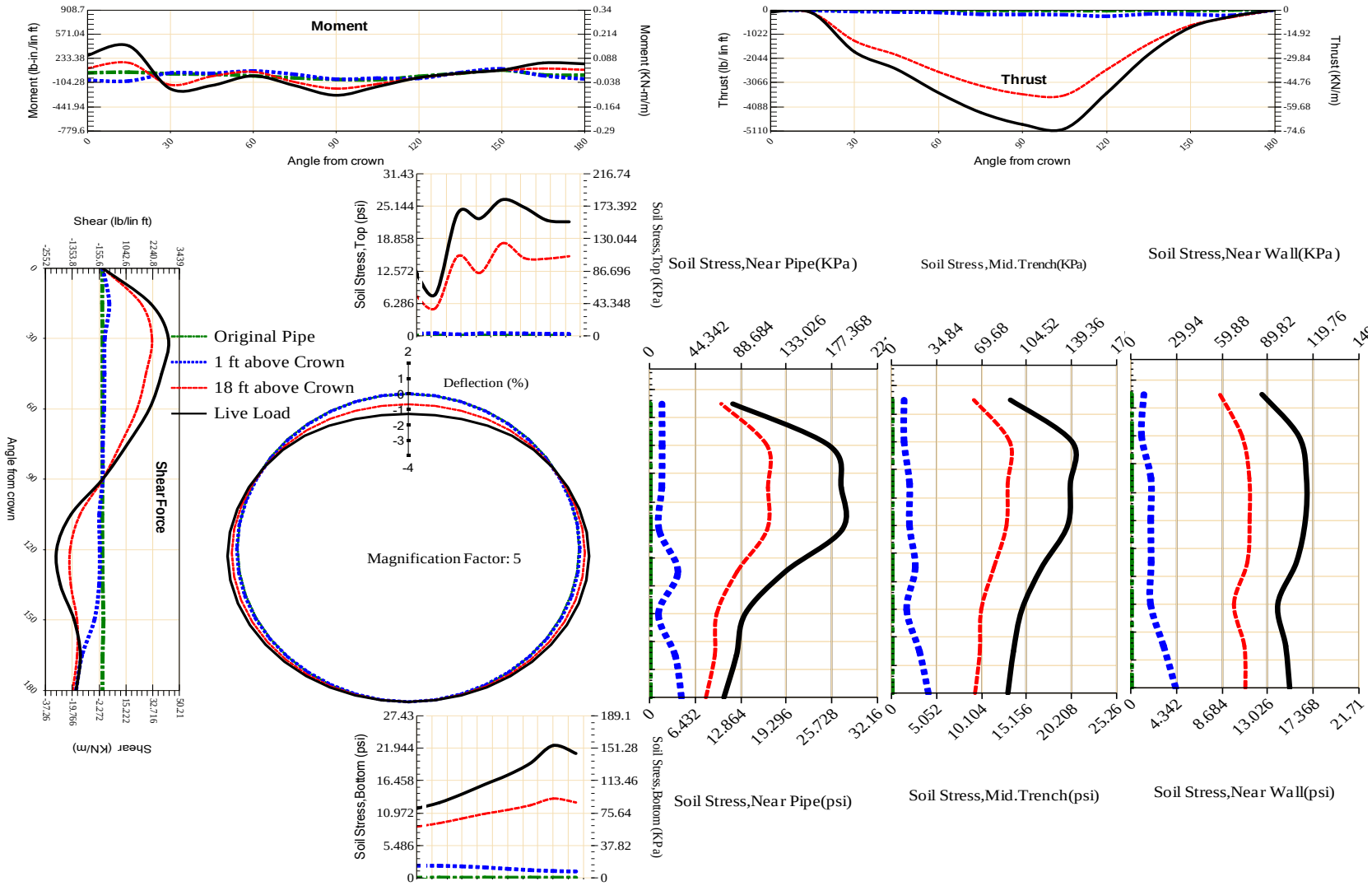

Figure A-460 Param-48-PW288-TR7SF-OD+48-EW10-H18-LiveLoad

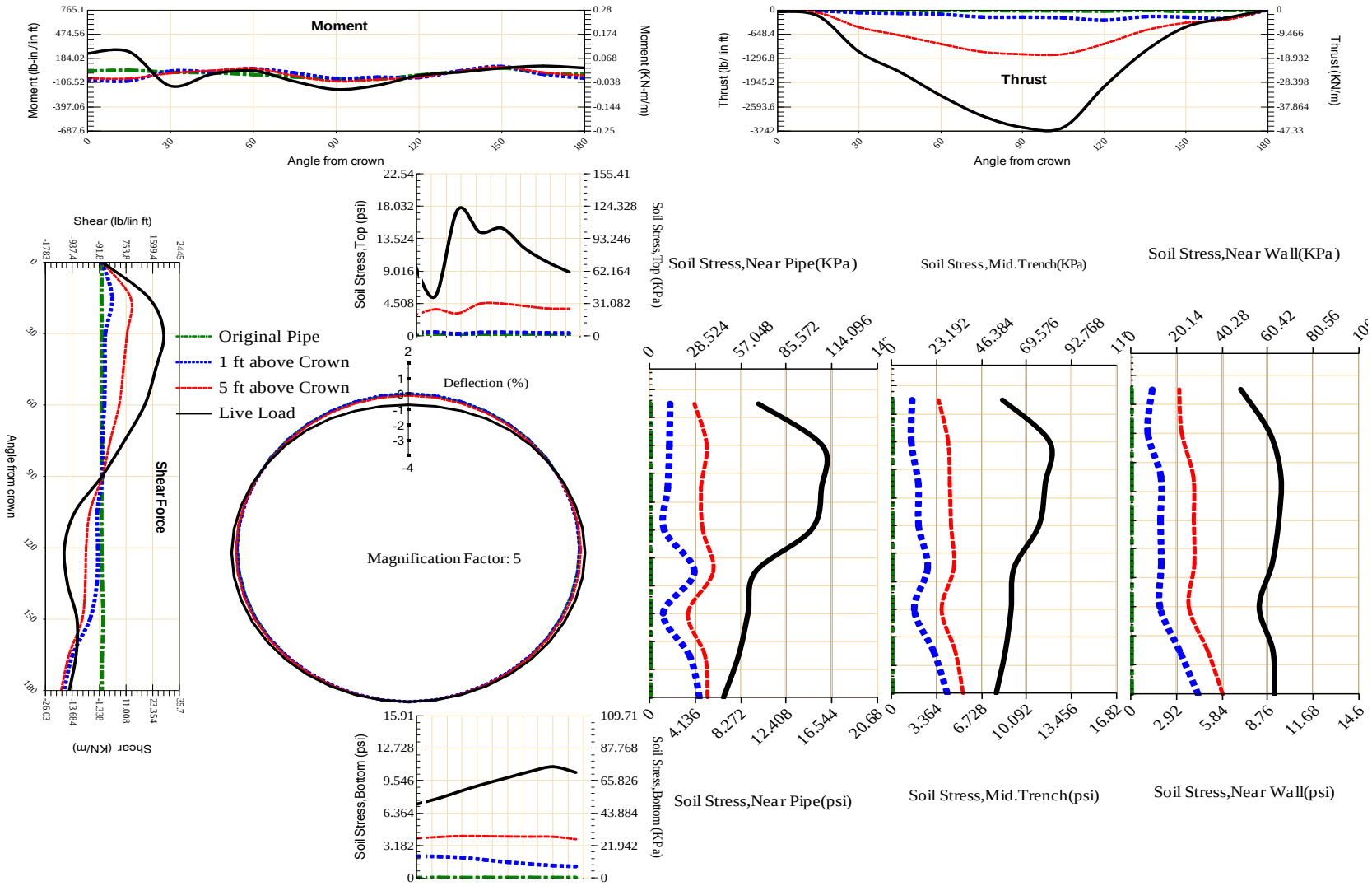

Figure A-461 Param-48-PW288-TR7SF-OD+48-EW10-H5-LiveLoad

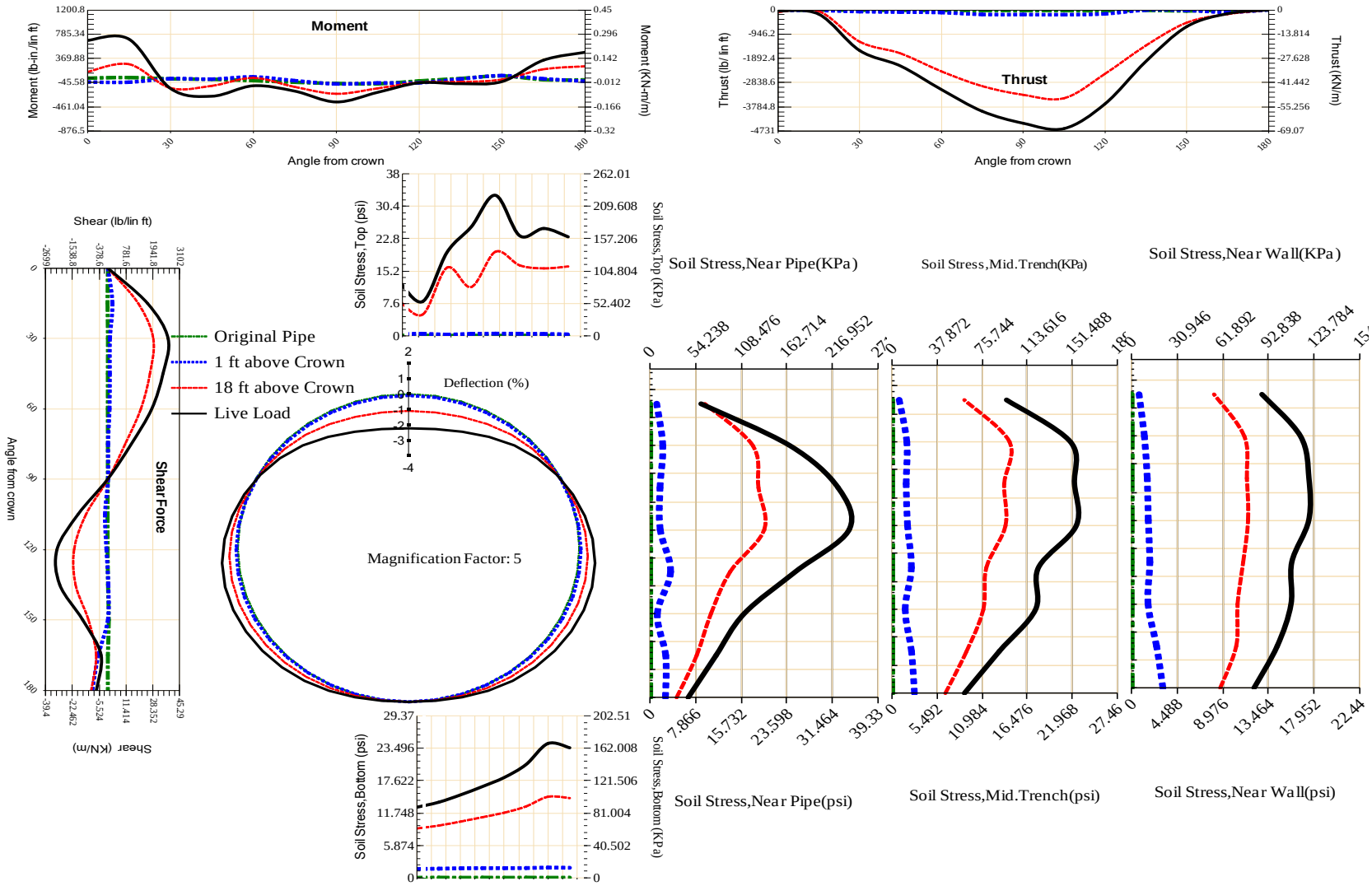

Figure A-462 Param-48-PW288-TR7SF-OD+48-EW3-H18-LiveLoad

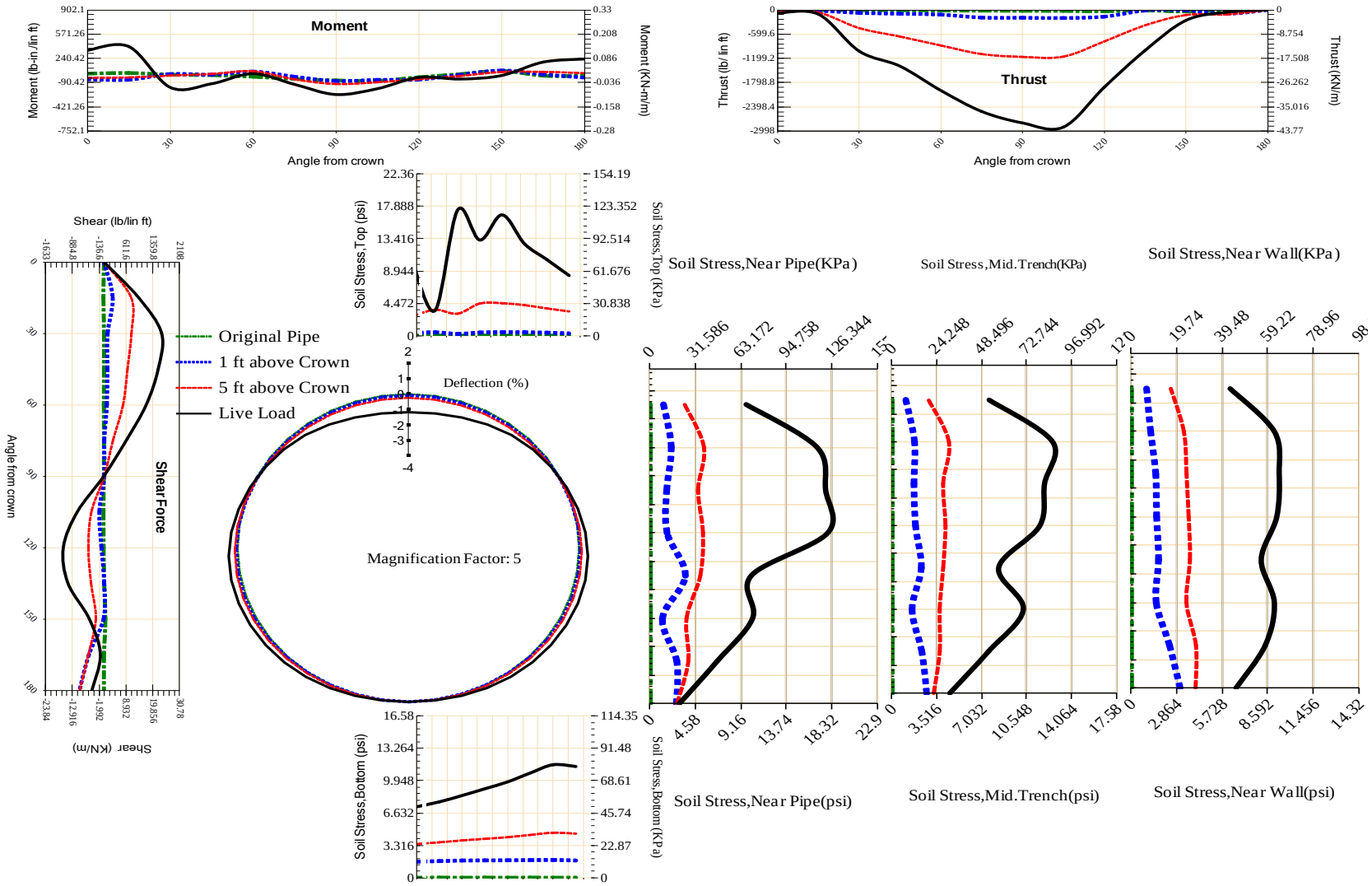

Figure A-463 Param-48-PW288-TR7SF-OD+48-EW3-H5-LiveLoad

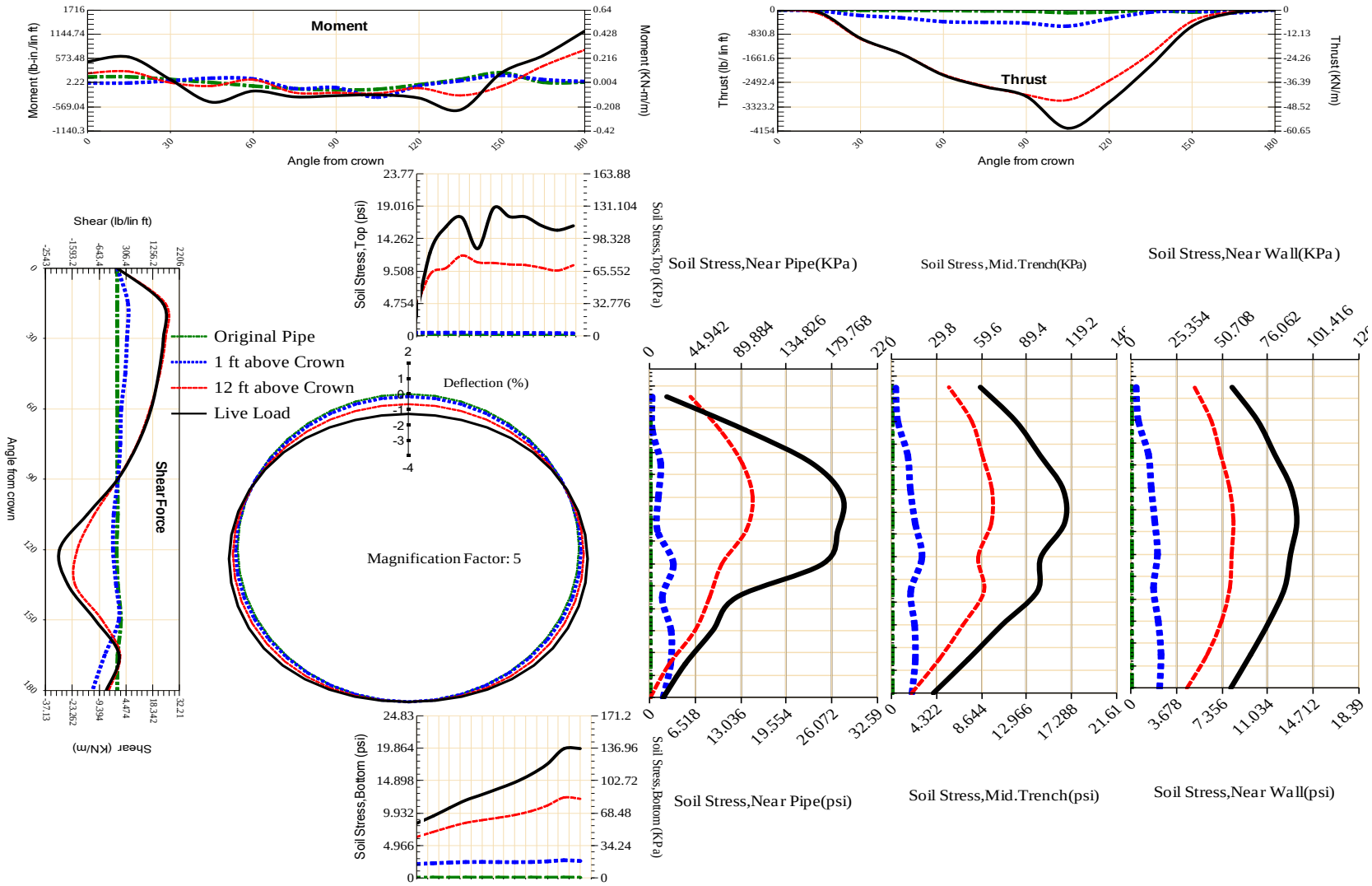

Figure A-464 Param-60-PW230-SF10SF-OD+72-EW5-H12-LiveLoad

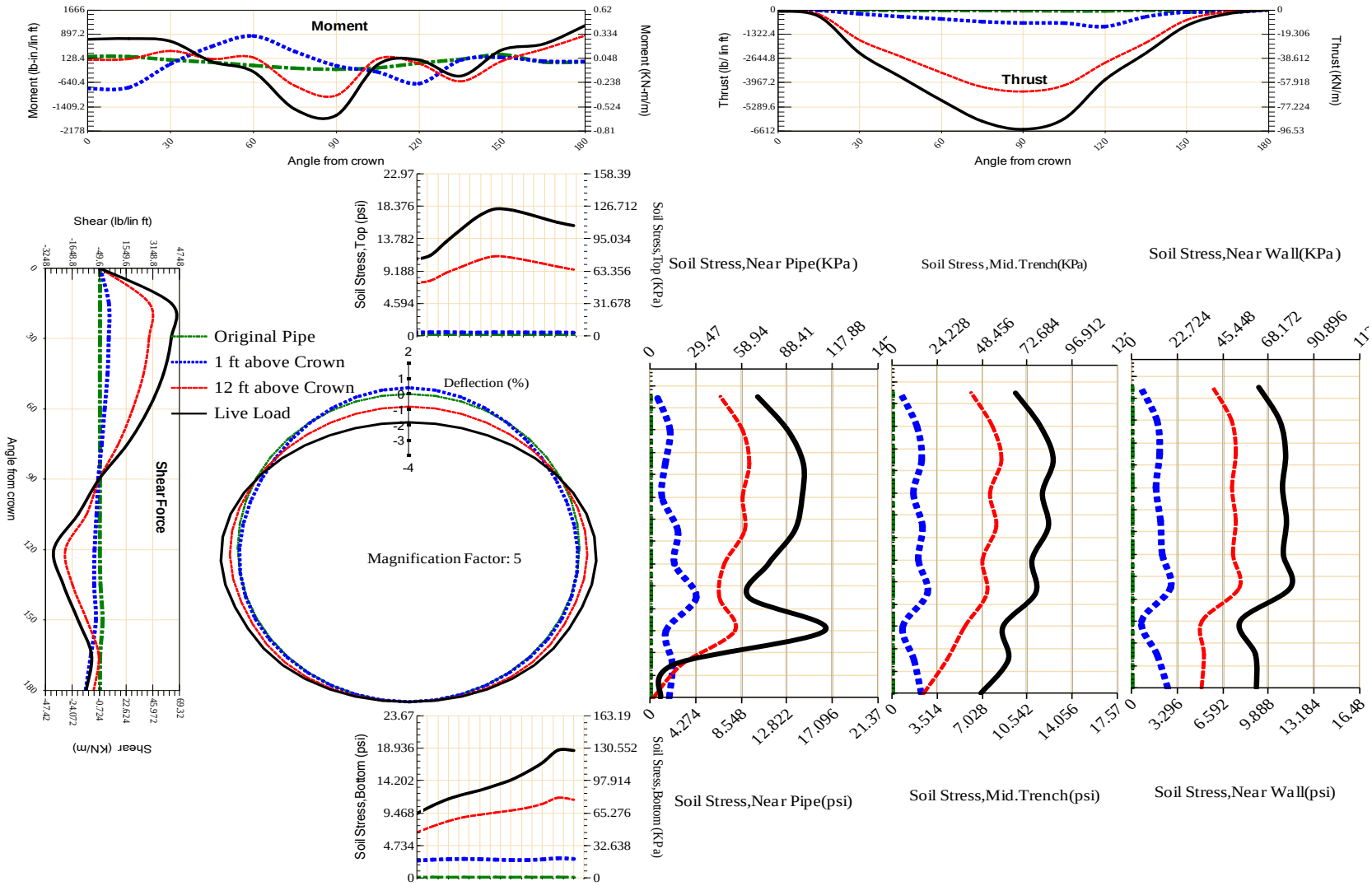

Figure A-465 Param-60-PW230-SF3OR-OD+72-EW5-H12-LiveLoad

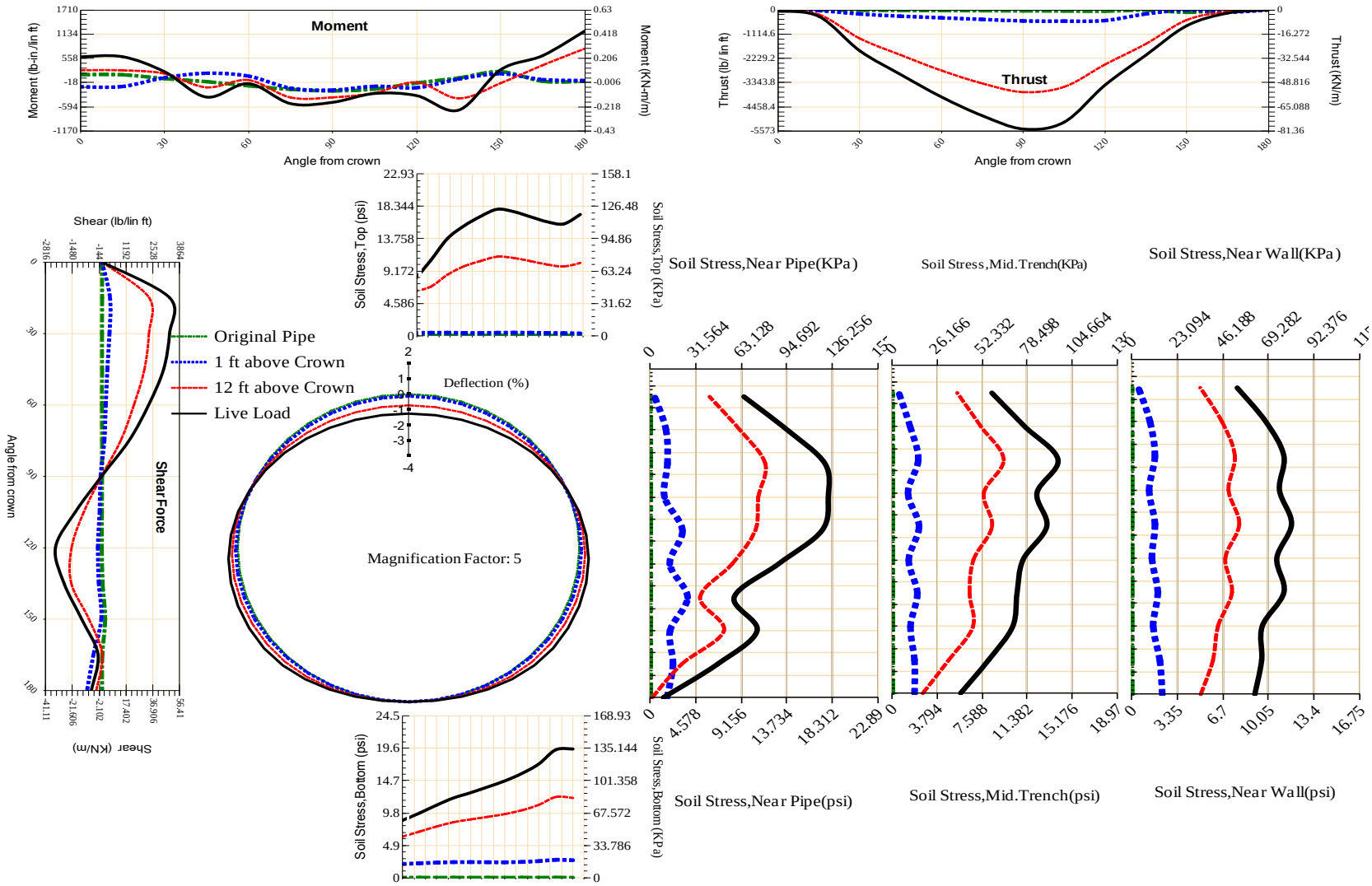

Figure A-466 Param-60-PW230-SF3TR-OD+72-EW5-H12-LiveLoad

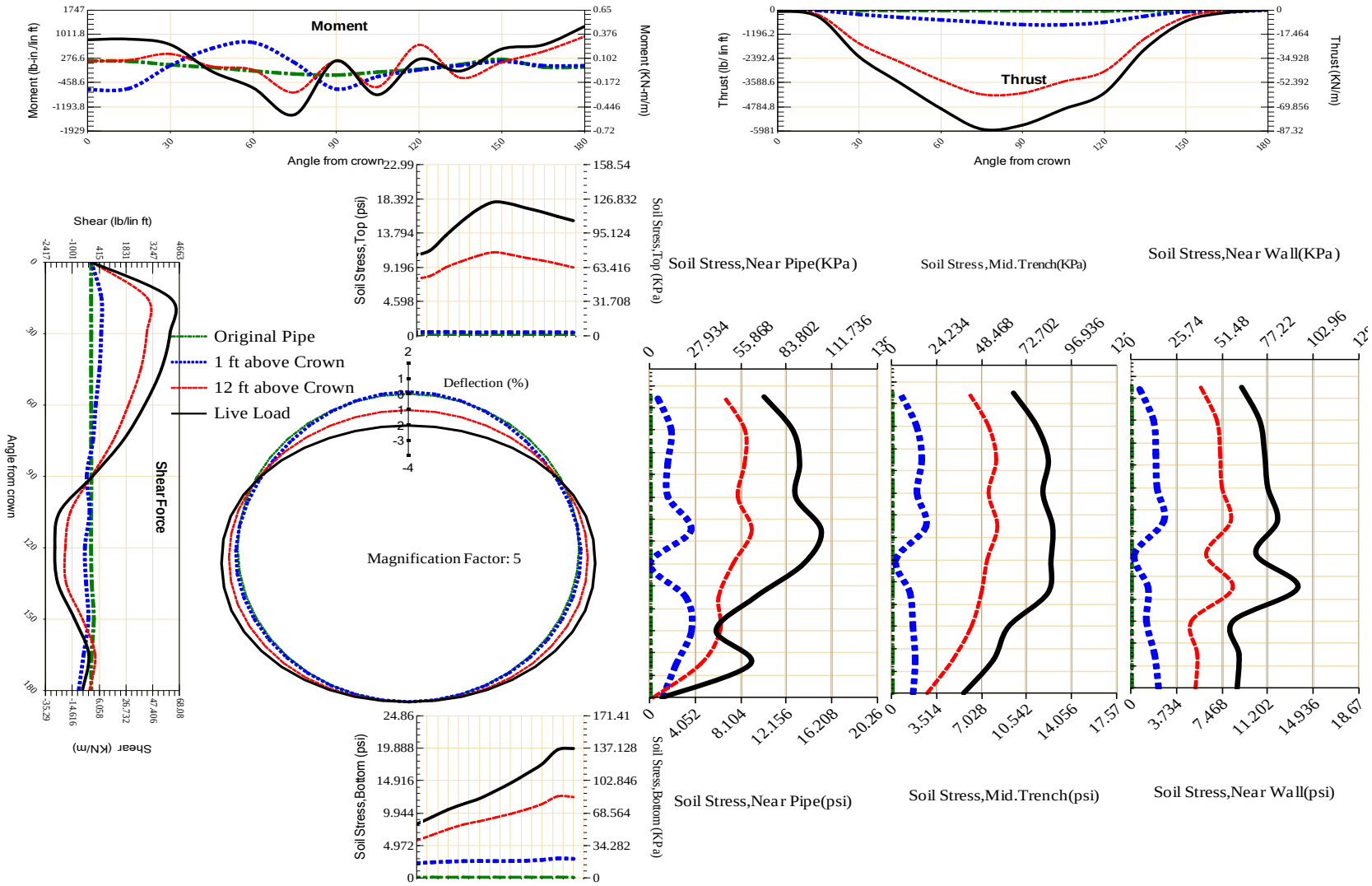

Figure A-467 Param-60-PW230-SF5OR-OD+72-EW5-H12-LiveLoad

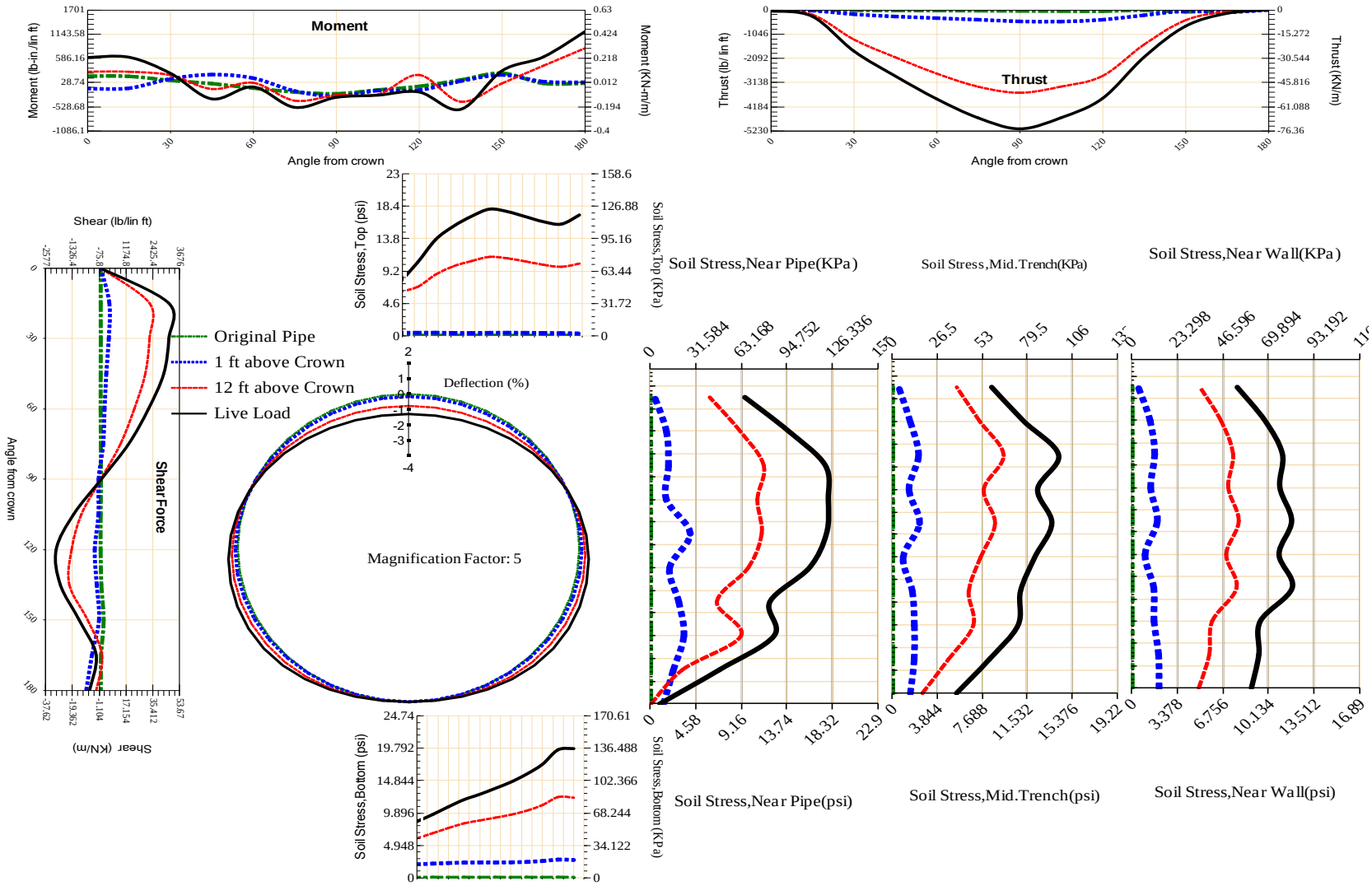

Figure A-468 Param-60-PW230-SF5TR-OD+72-EW5-H12-LiveLoad

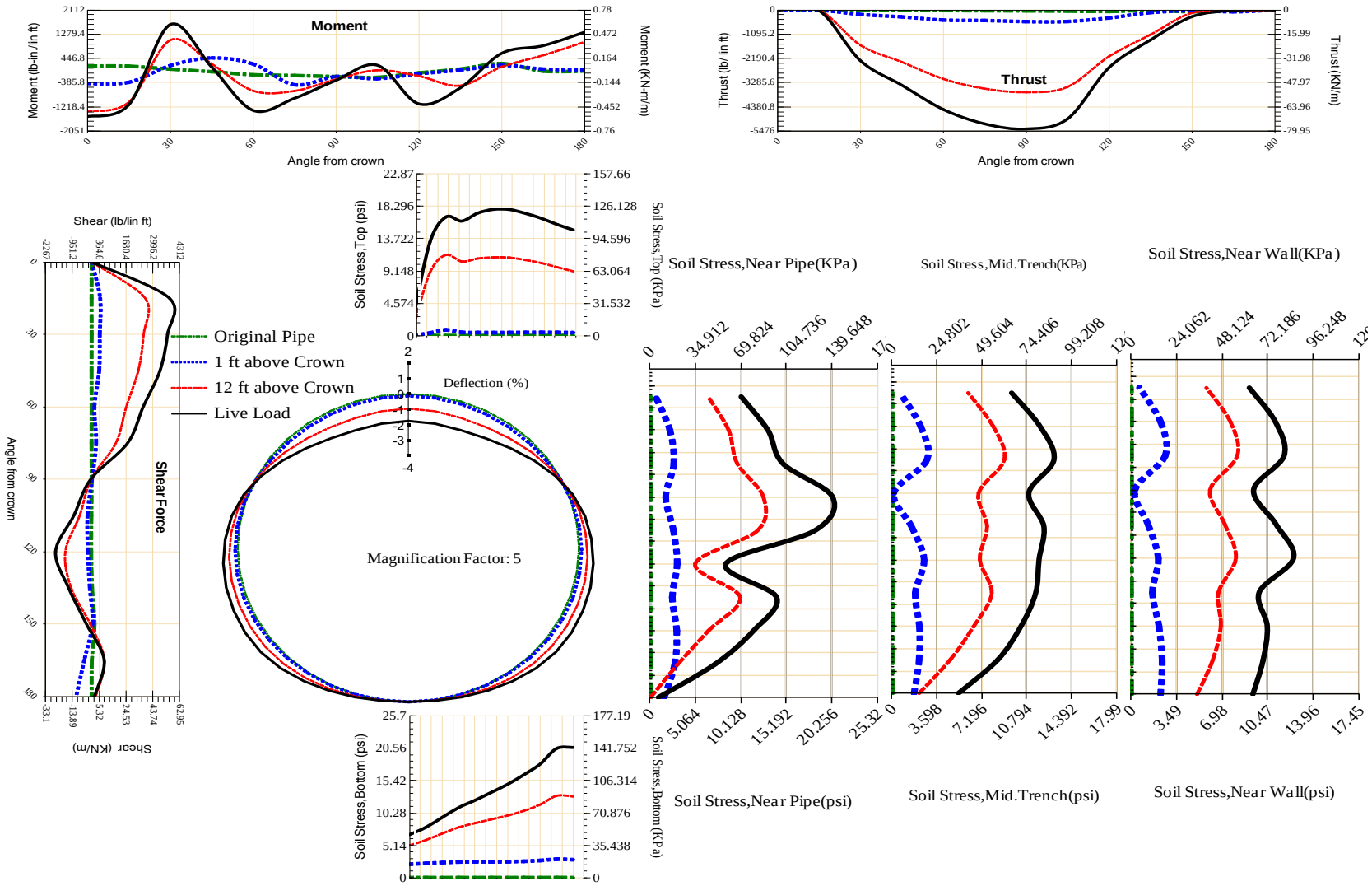

Figure A-469 Param-60-PW230-SF7OR-OD+72-EW5-H12-LiveLoad

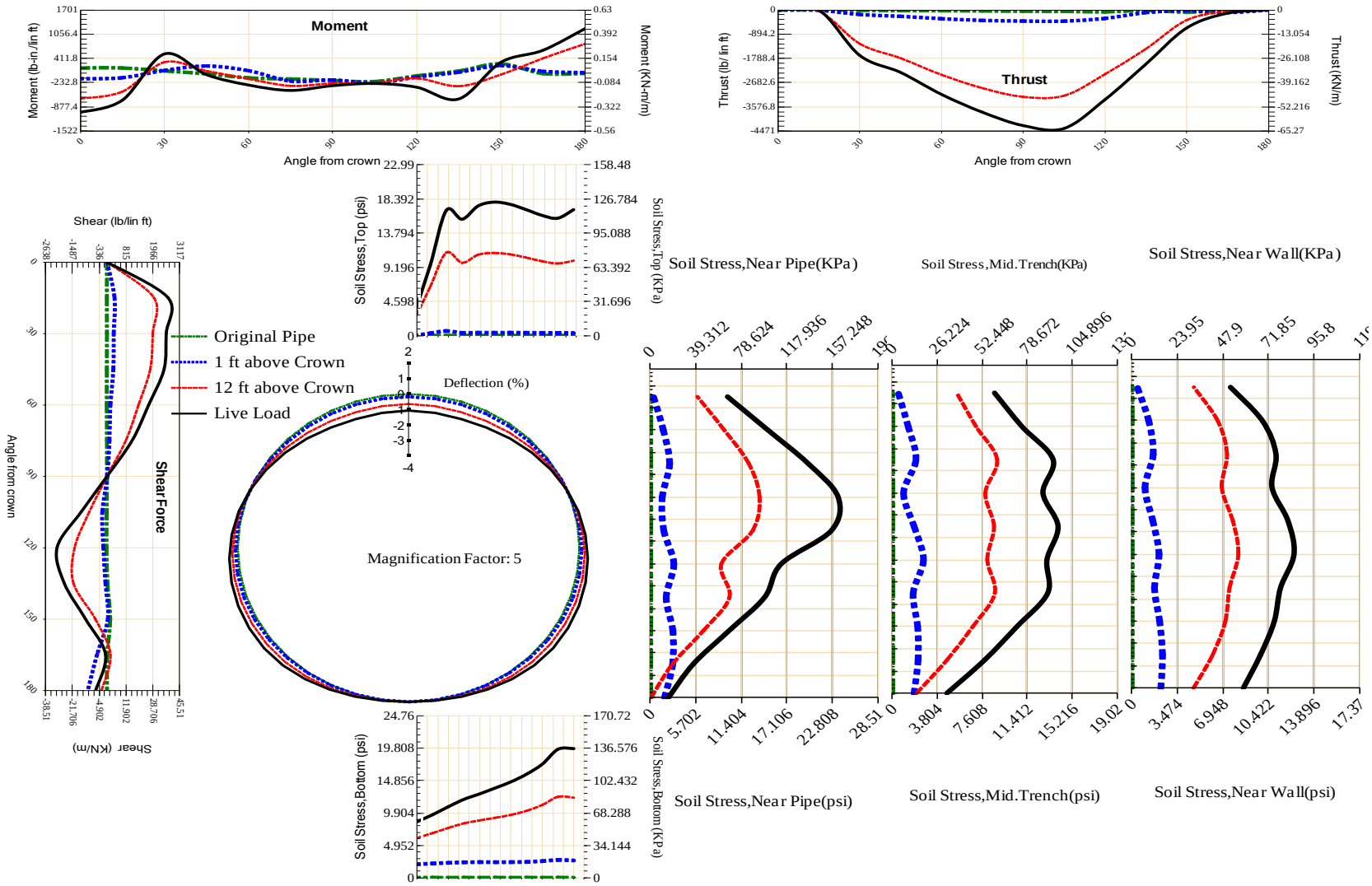

Figure A-470 Param-60-PW230-SF7TR-OD+72-EW5-H12-LiveLoad

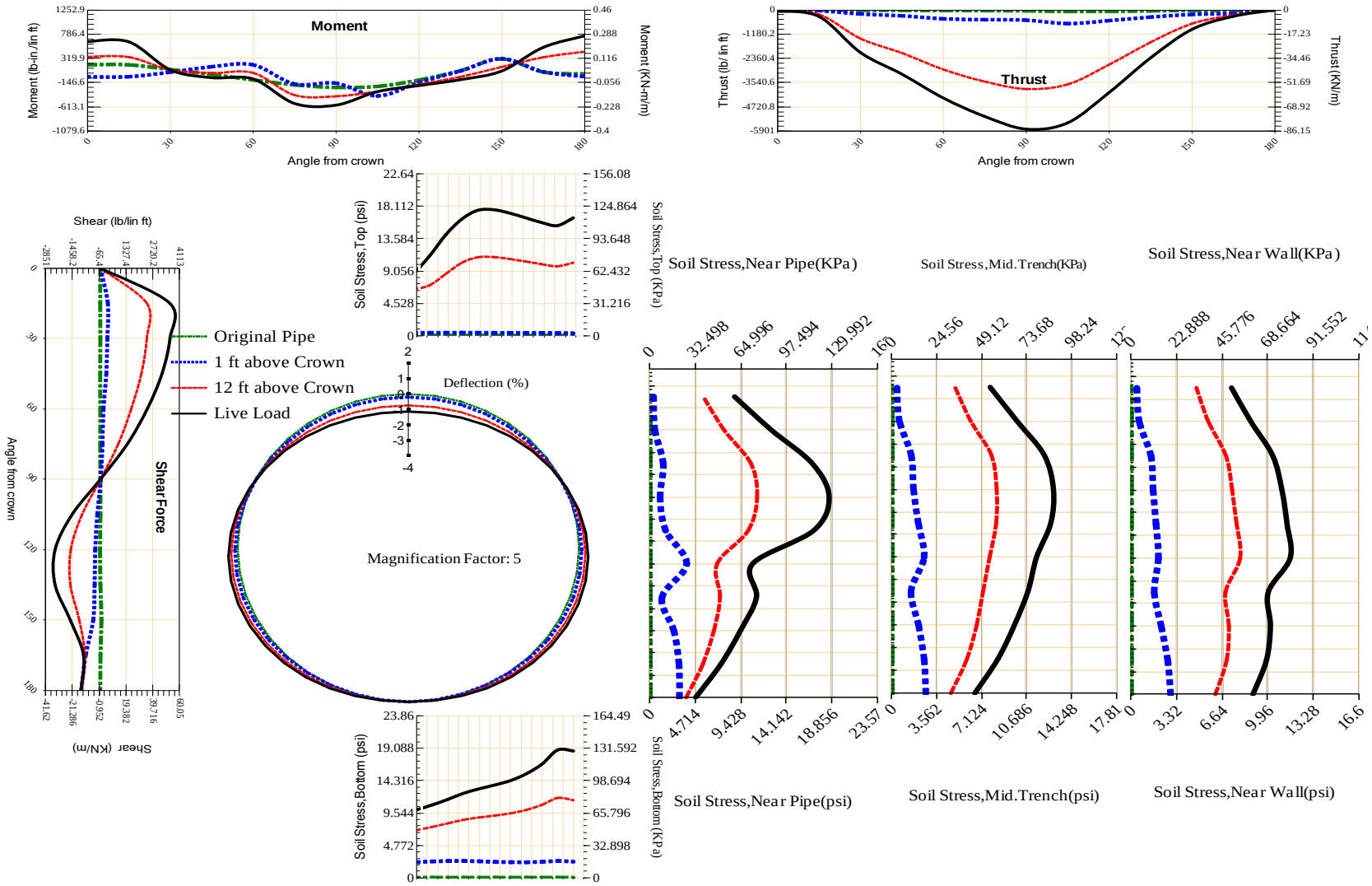

Figure A-471 Param-60-PW230-TR10TR-OD+72-EW5-H12-LiveLoad

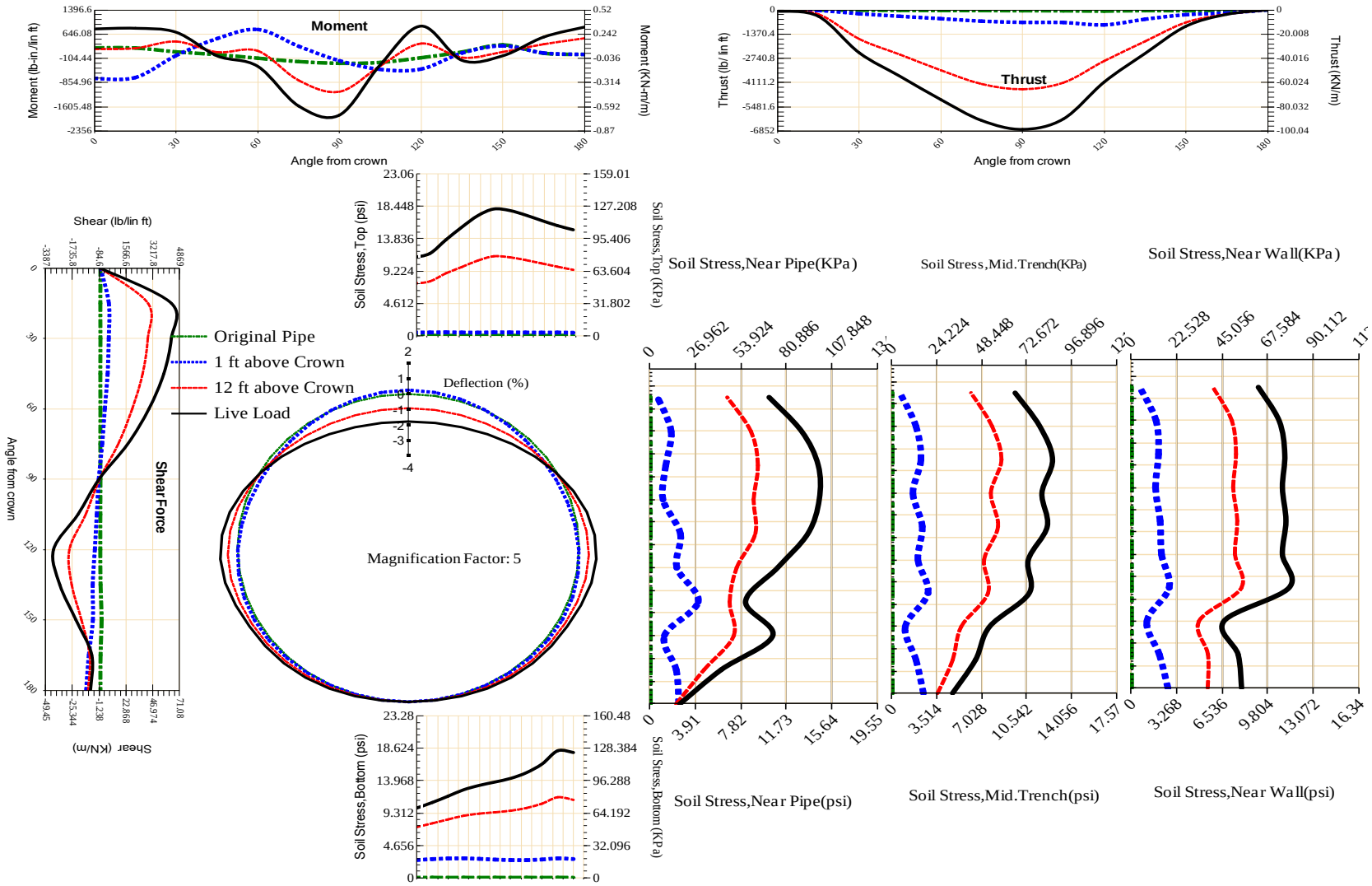

Figure A-472 Param-60-PW230-TR3OR-OD+72-EW5-H12-LiveLoad

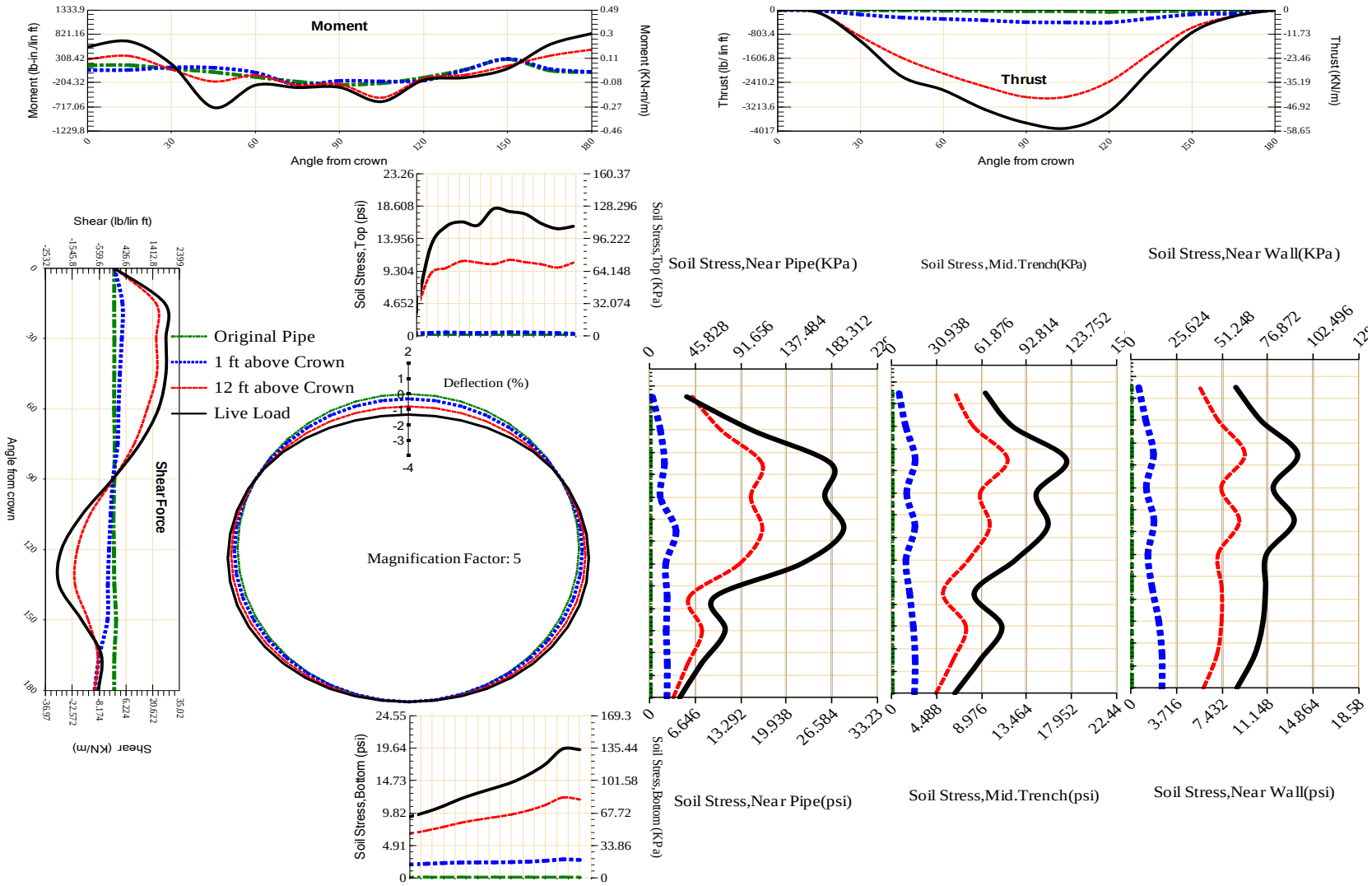

Figure A-473 Param-60-PW230-TR3SF-OD+72-EW5-H12-LiveLoad

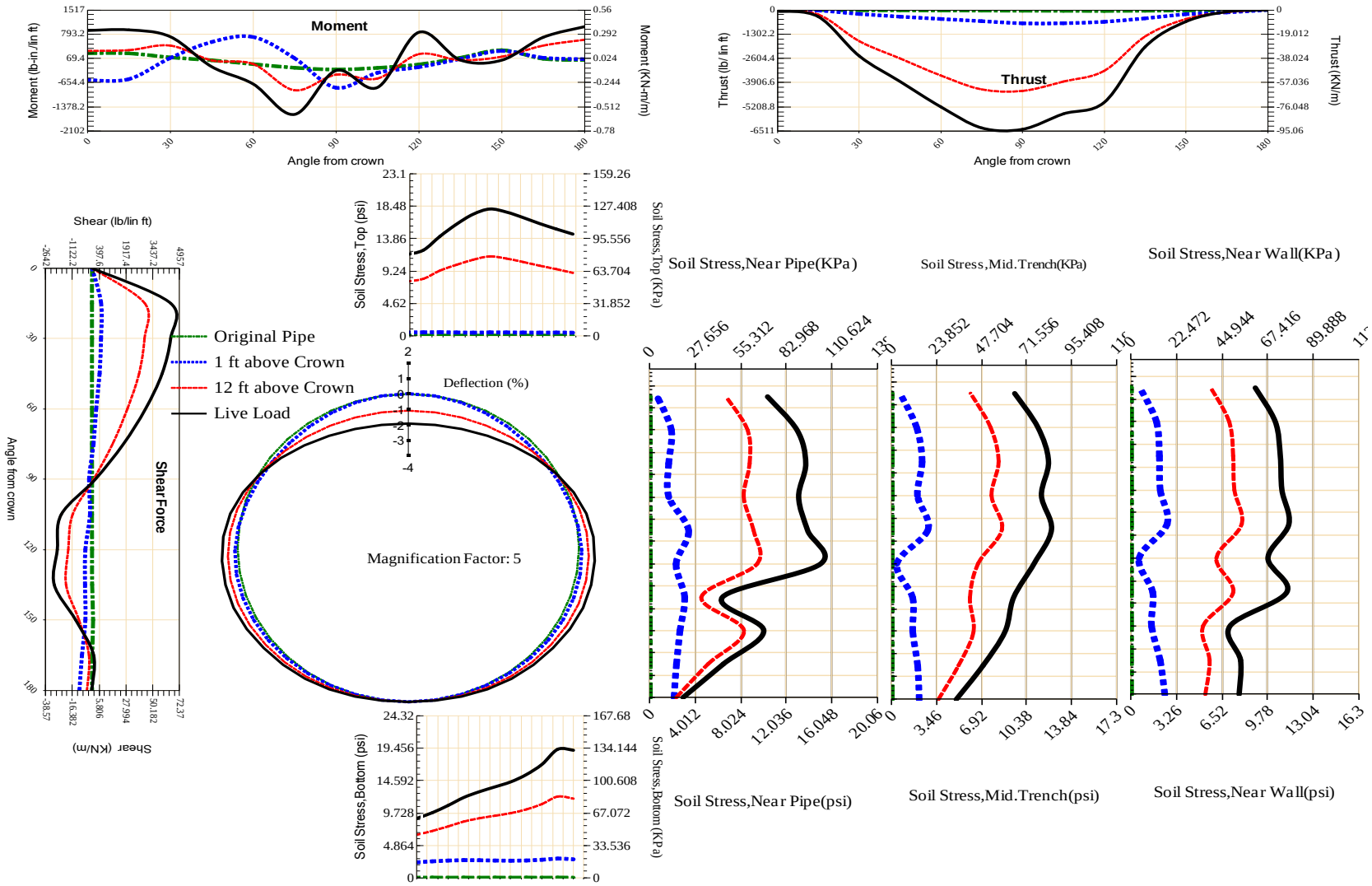

Figure A-474 Param-60-PW230-TR5OR-OD+72-EW5-H12-LiveLoad

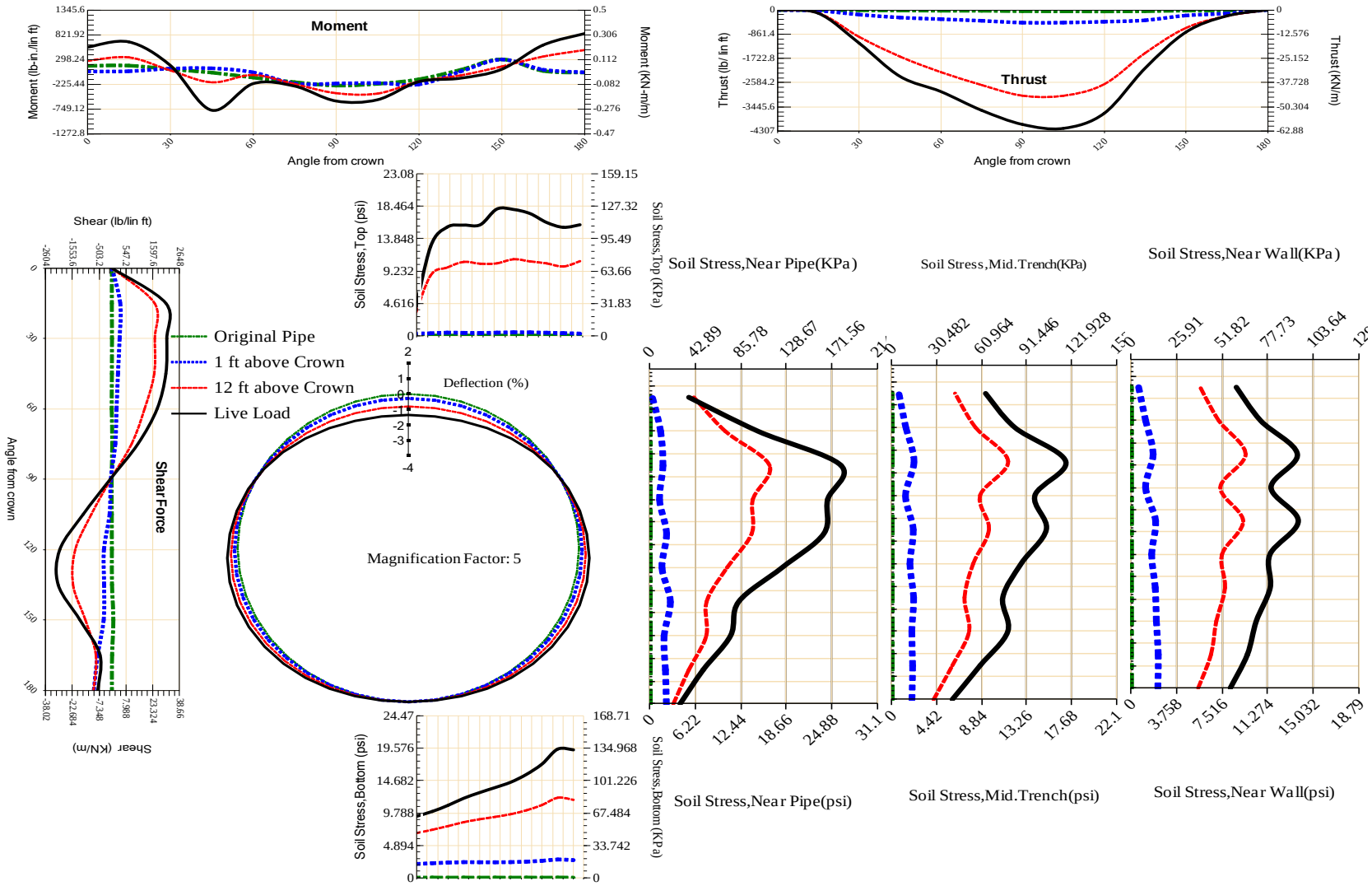

Figure A-475 Param-60-PW230-TR5SF-OD+72-EW5-H12-LiveLoad

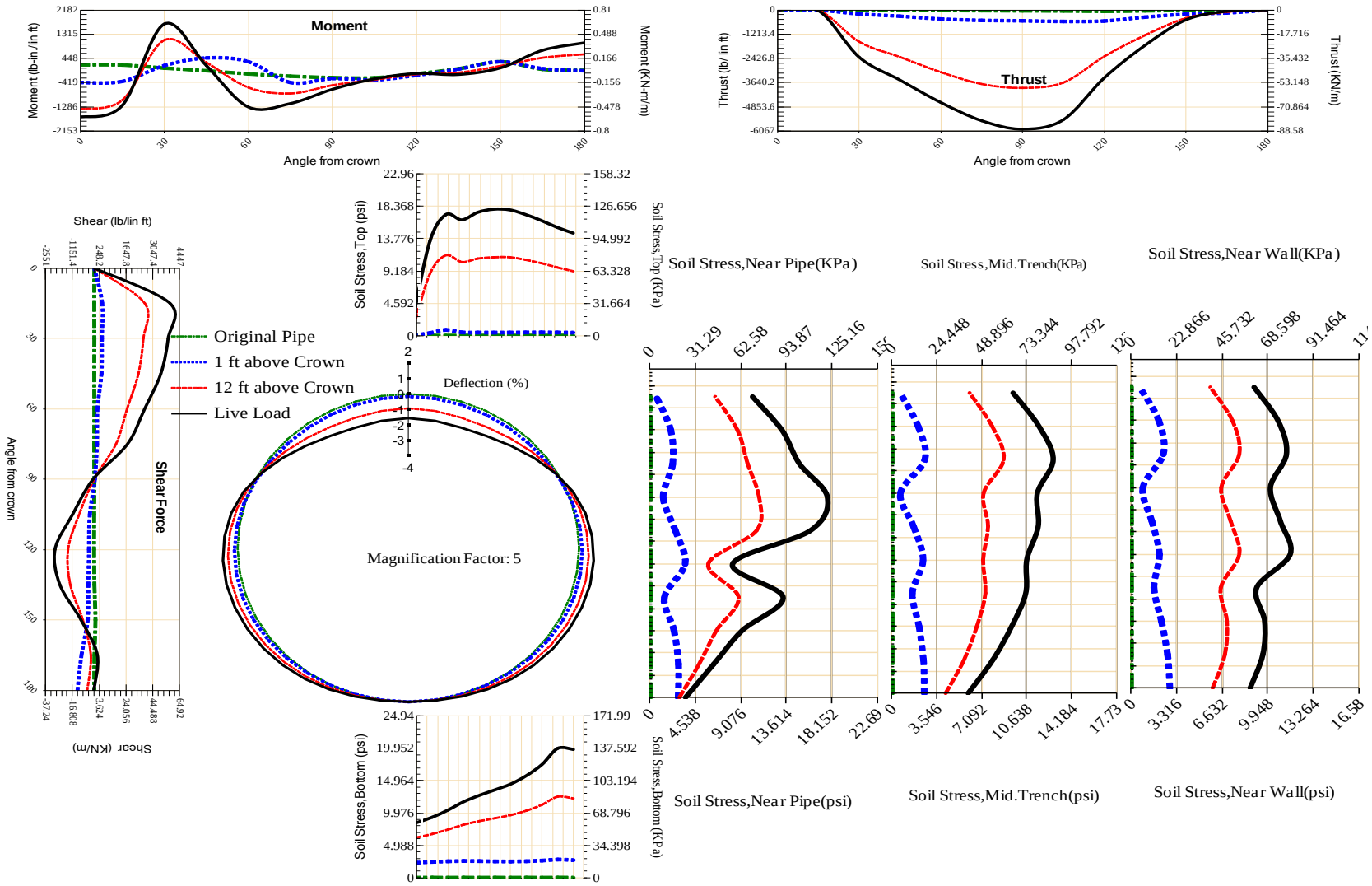

Figure A-476 Param-60-PW230-TR7OR-OD+72-EW5-H12-LiveLoad

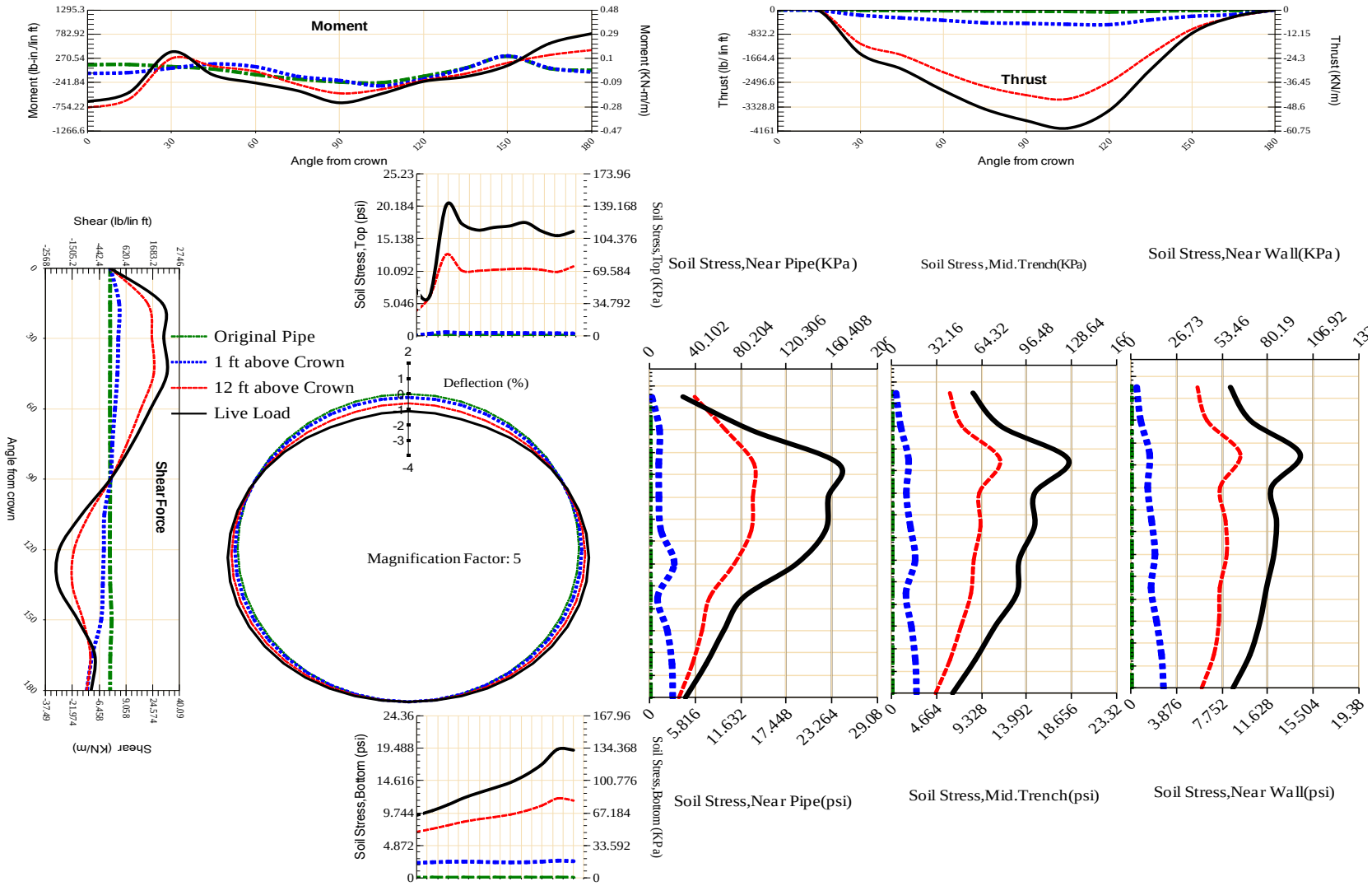

Figure A-477 Param-60-PW230-TR7SF-OD+72-EW5-H12-LiveLoad

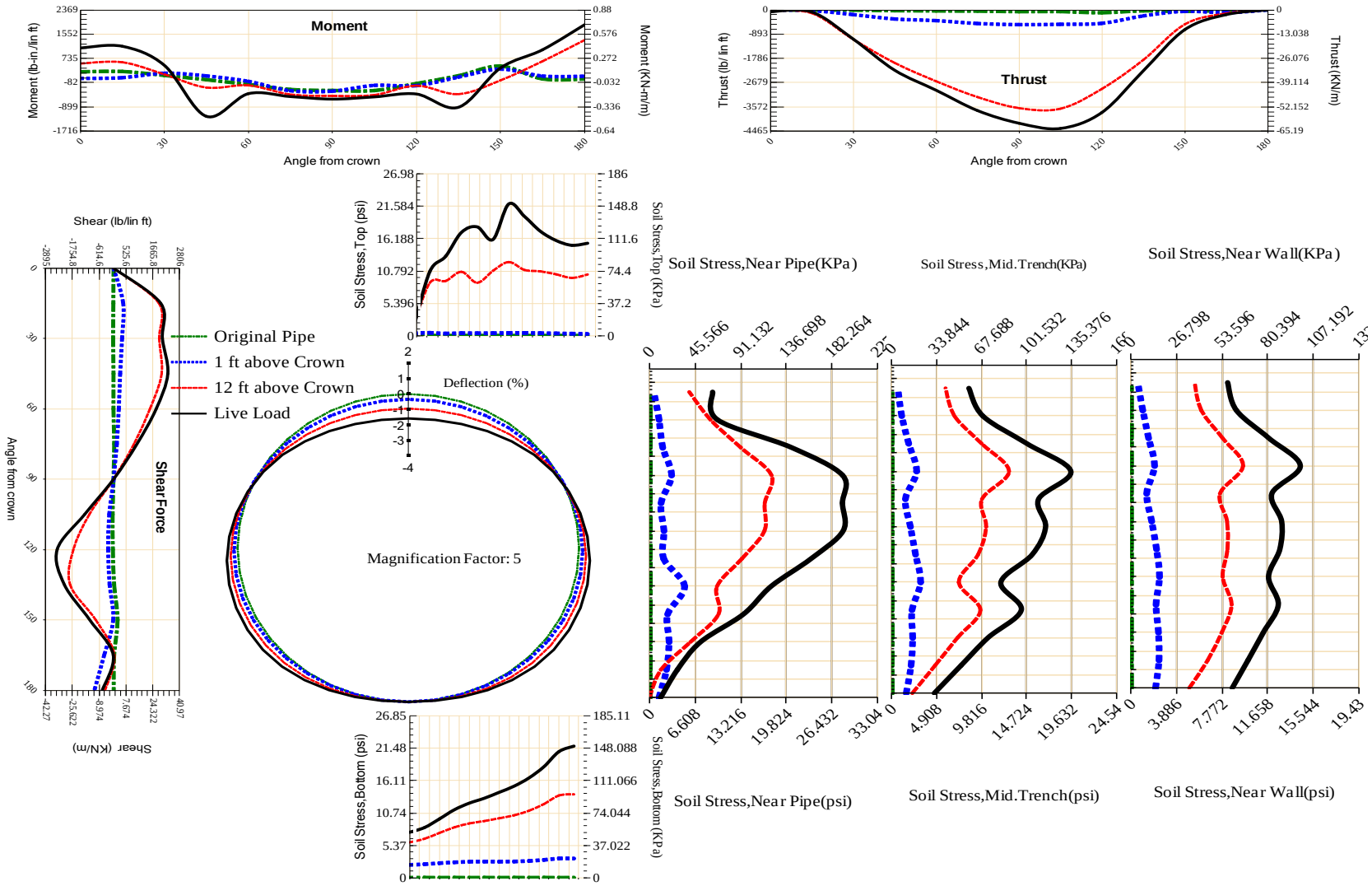

Figure A-478 Param-72-PW230-SF10SF-OD+72-EW5-H12-LiveLoad

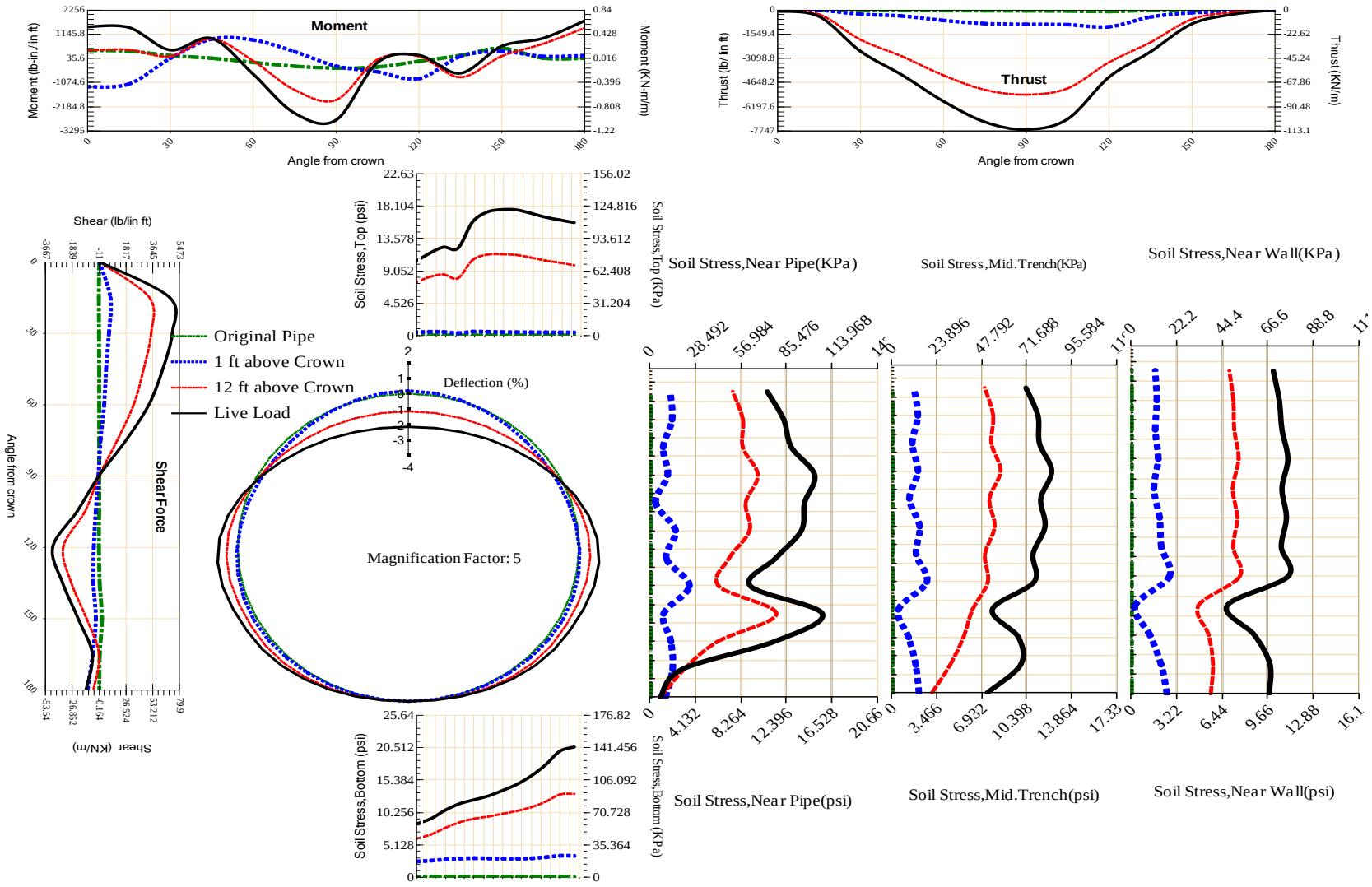

Figure A-479 Param-72-PW230-SF3OR-OD+72-EW5-H12-LiveLoad

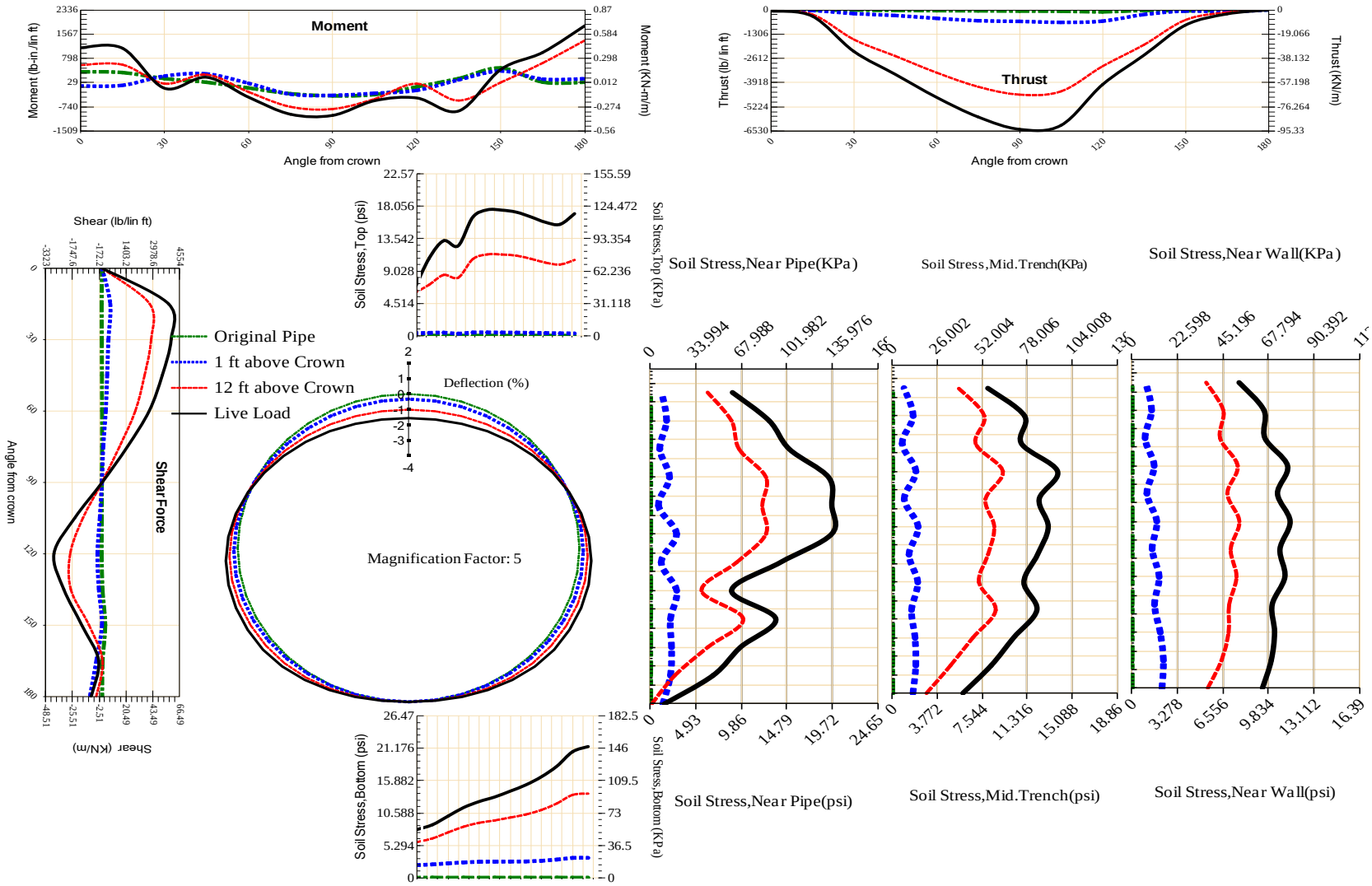

Figure A-480 Param-72-PW230-SF3TR-OD+72-EW5-H12-LiveLoad

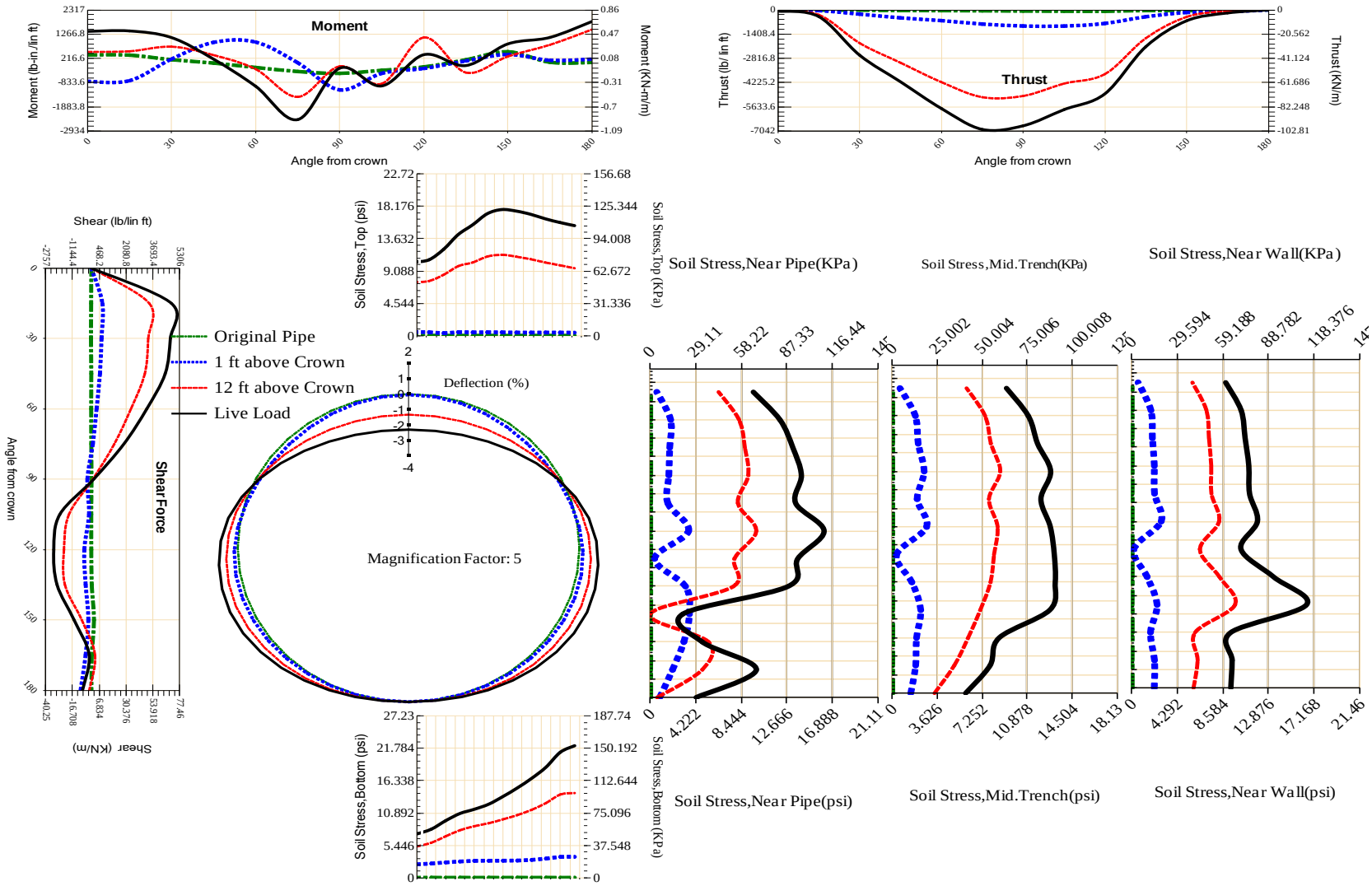

Figure A-481 Param-72-PW230-SF5OR-OD+72-EW5-H12-LiveLoad

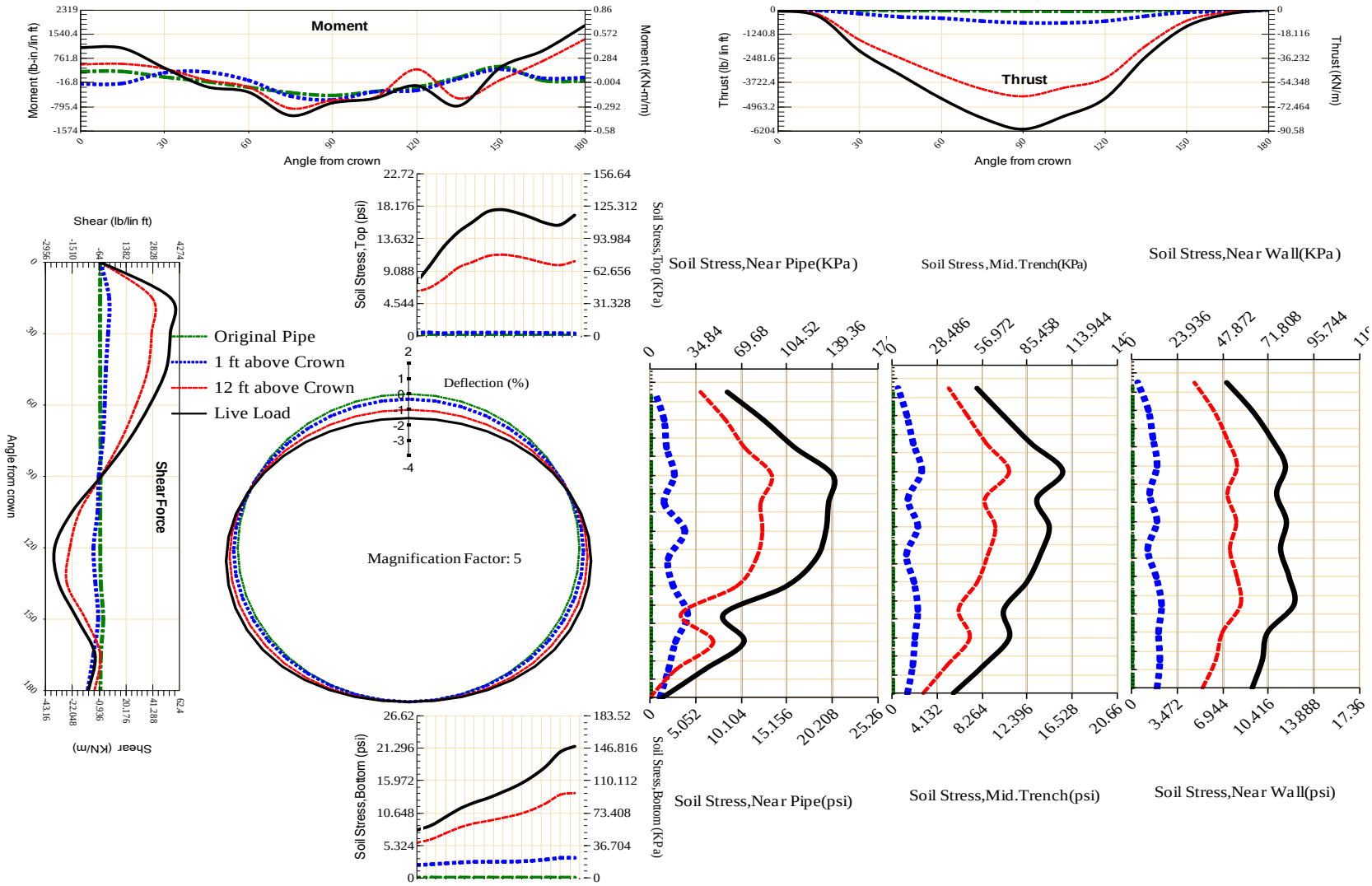

Figure A-482 Param-72-PW230-SF5TR-OD+72-EW5-H12-LiveLoad

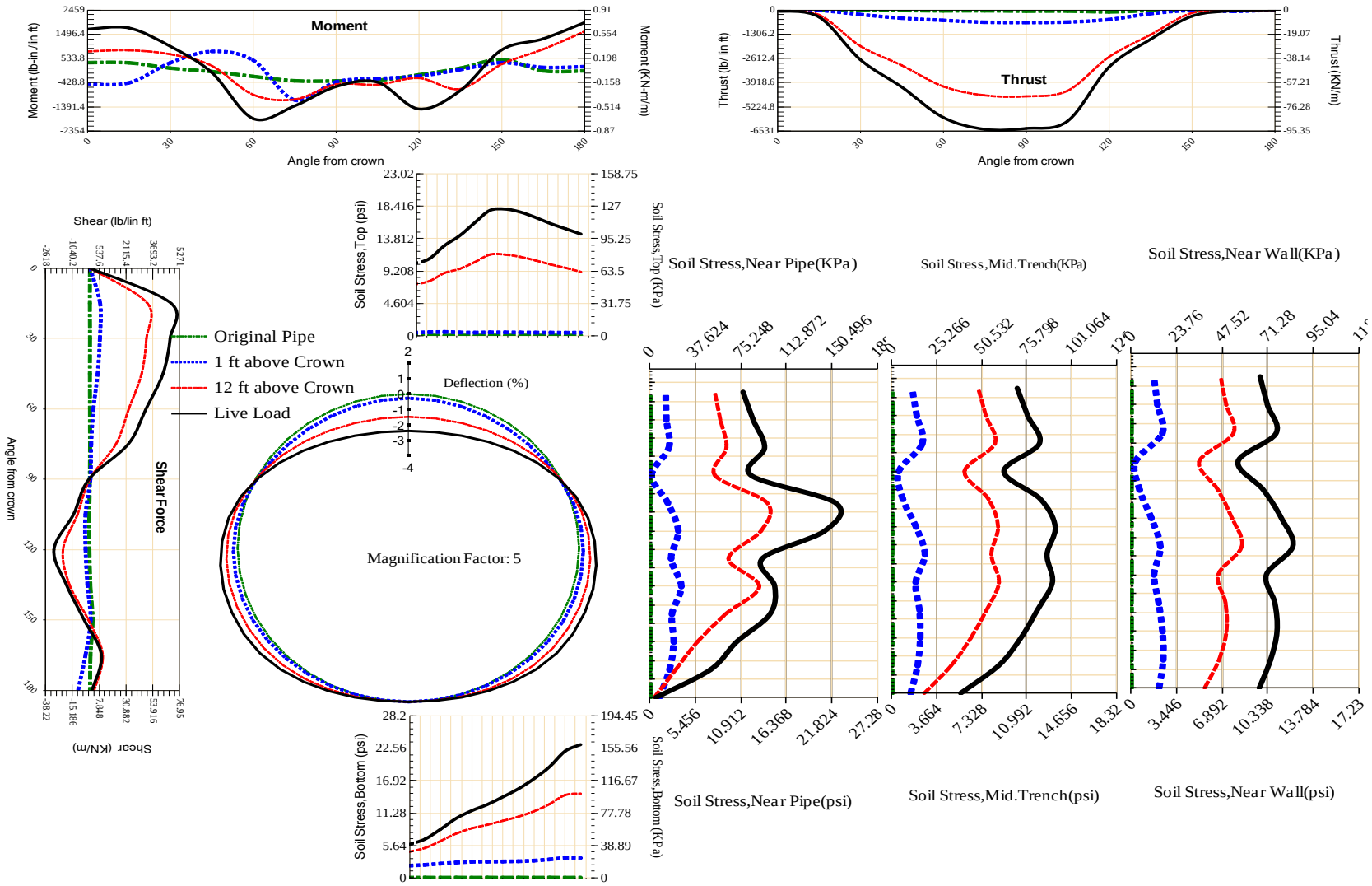

Figure A-483 Param-72-PW230-SF7OR-OD+72-EW5-H12-LiveLoad

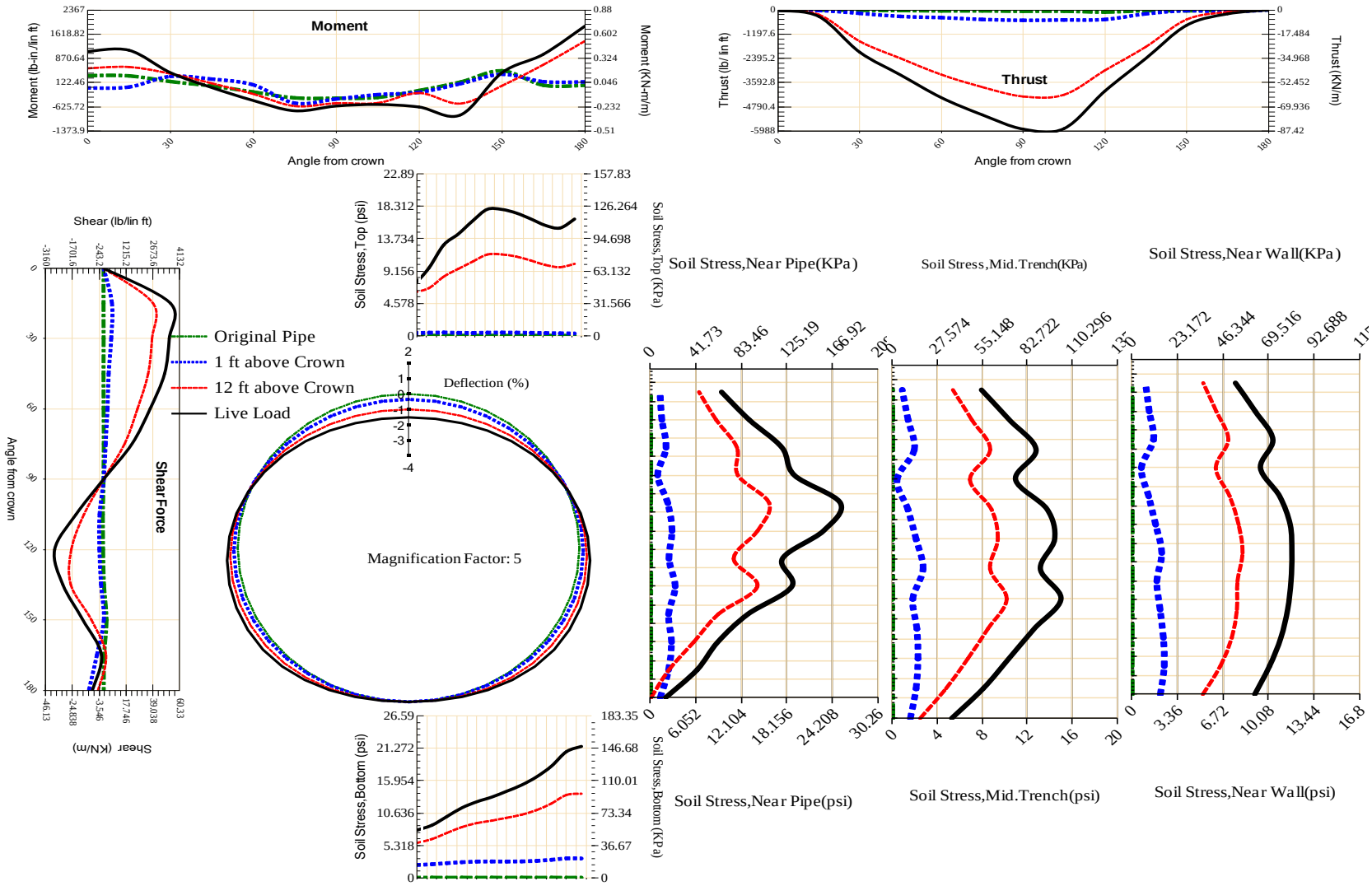

Figure A-484 Param-72-PW230-SF7TR-OD+72-EW5-H12-LiveLoad

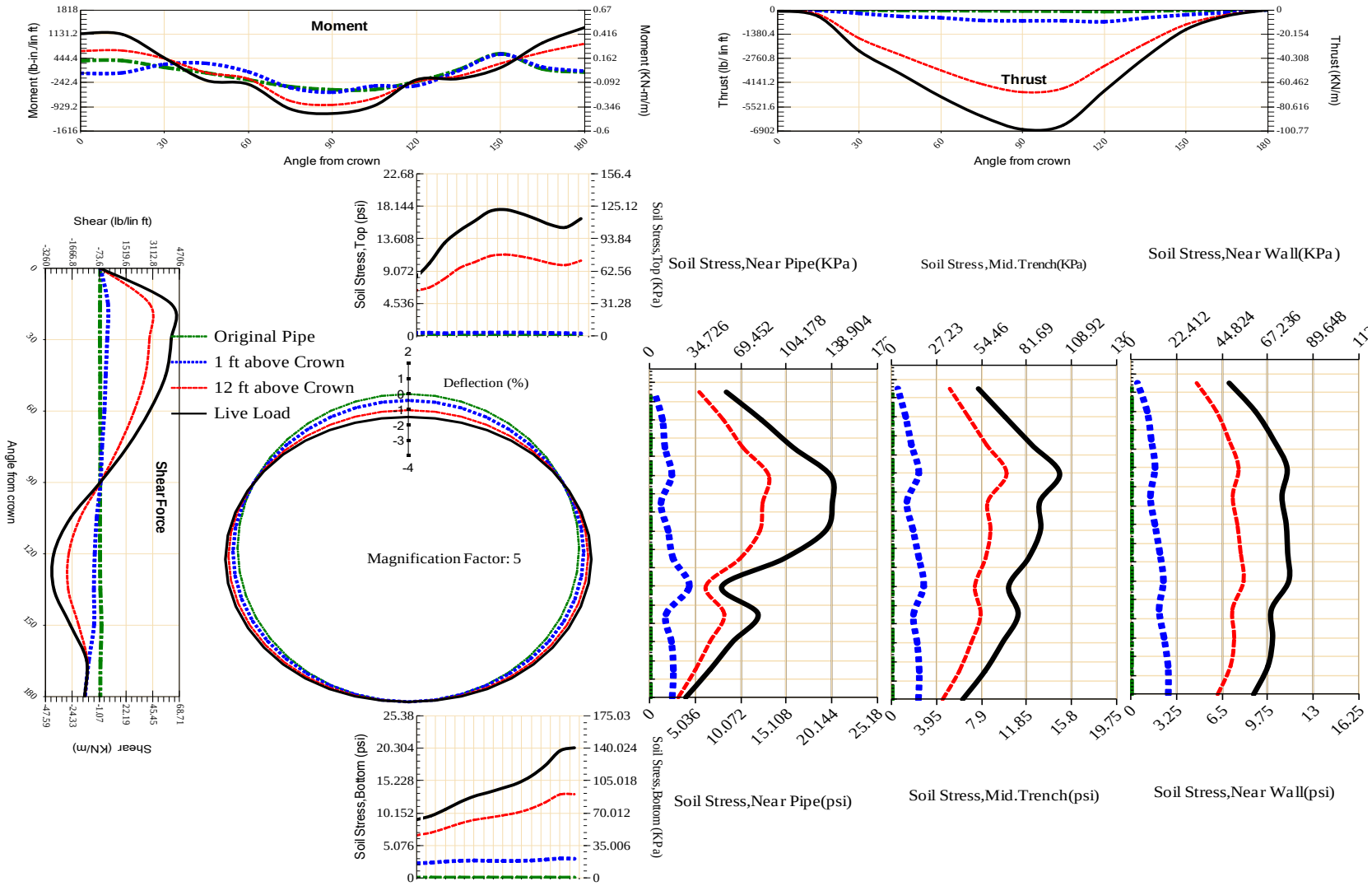

Figure A-485 Param-72-PW230-TR10TR-OD+72-EW5-H12-LiveLoad

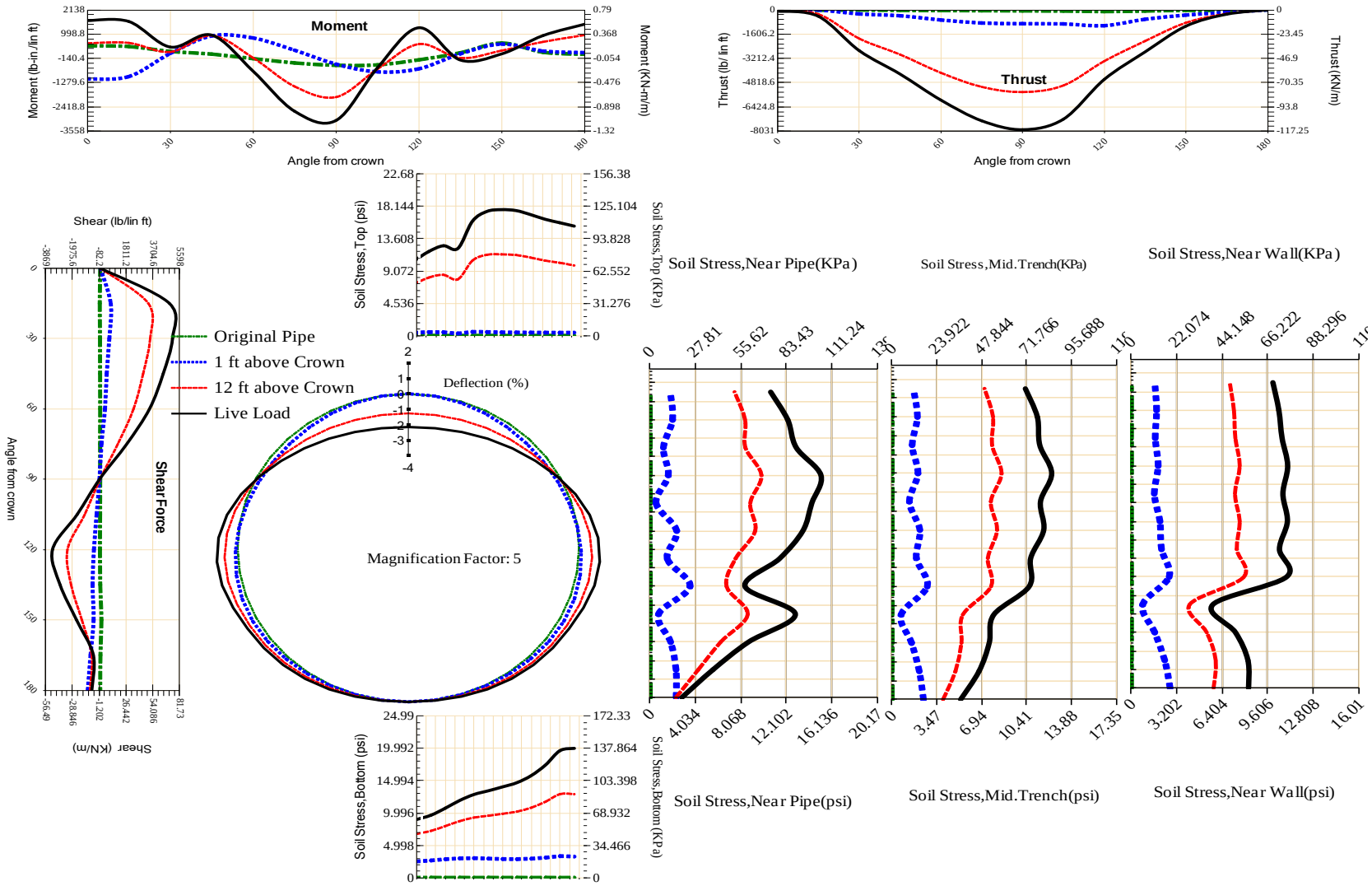

Figure A-486 Param-72-PW230-TR3OR-OD+72-EW5-H12-LiveLoad

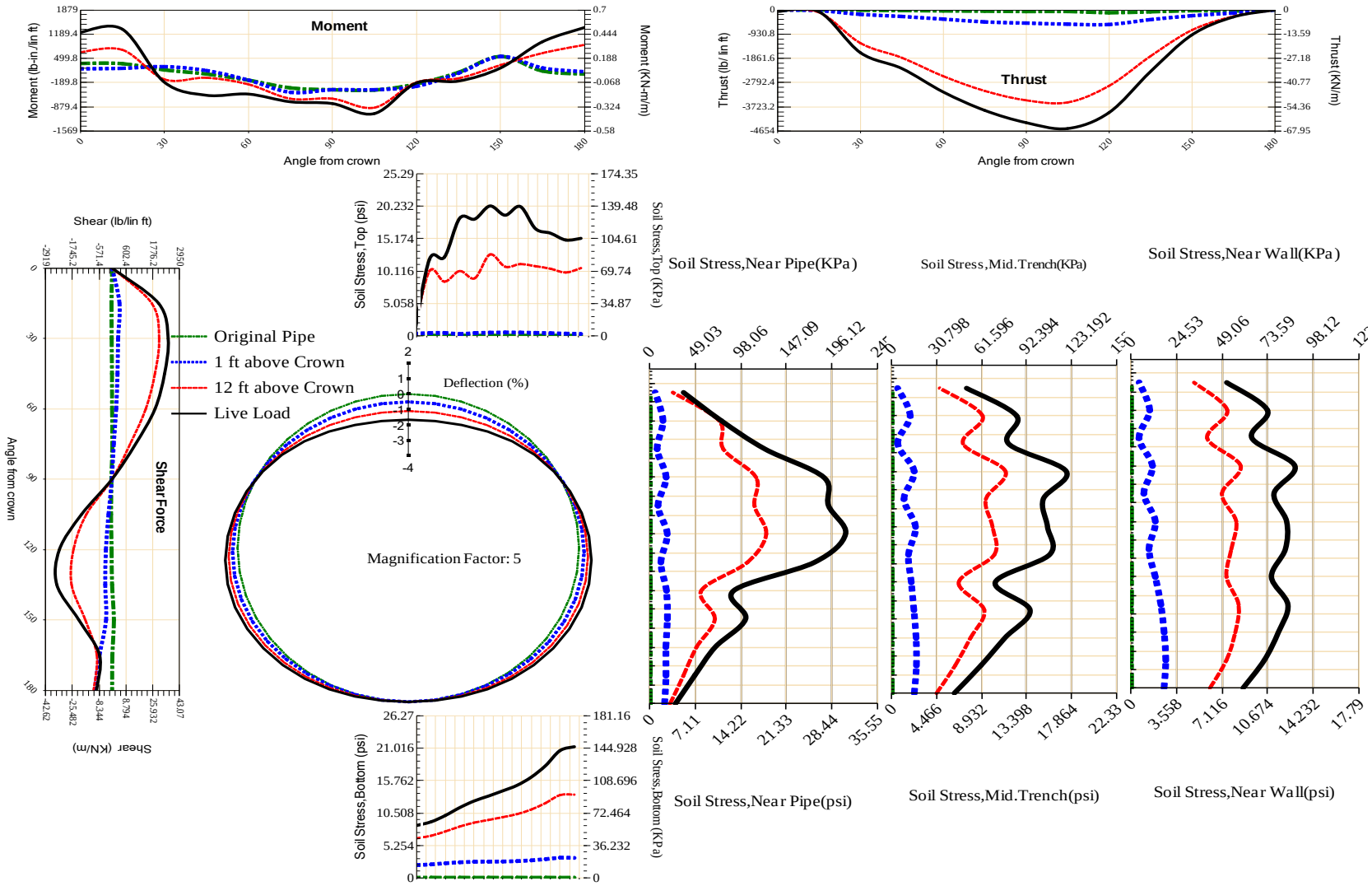

Figure A-487 Param-72-PW230-TR3SF-OD+72-EW5-H12-LiveLoad

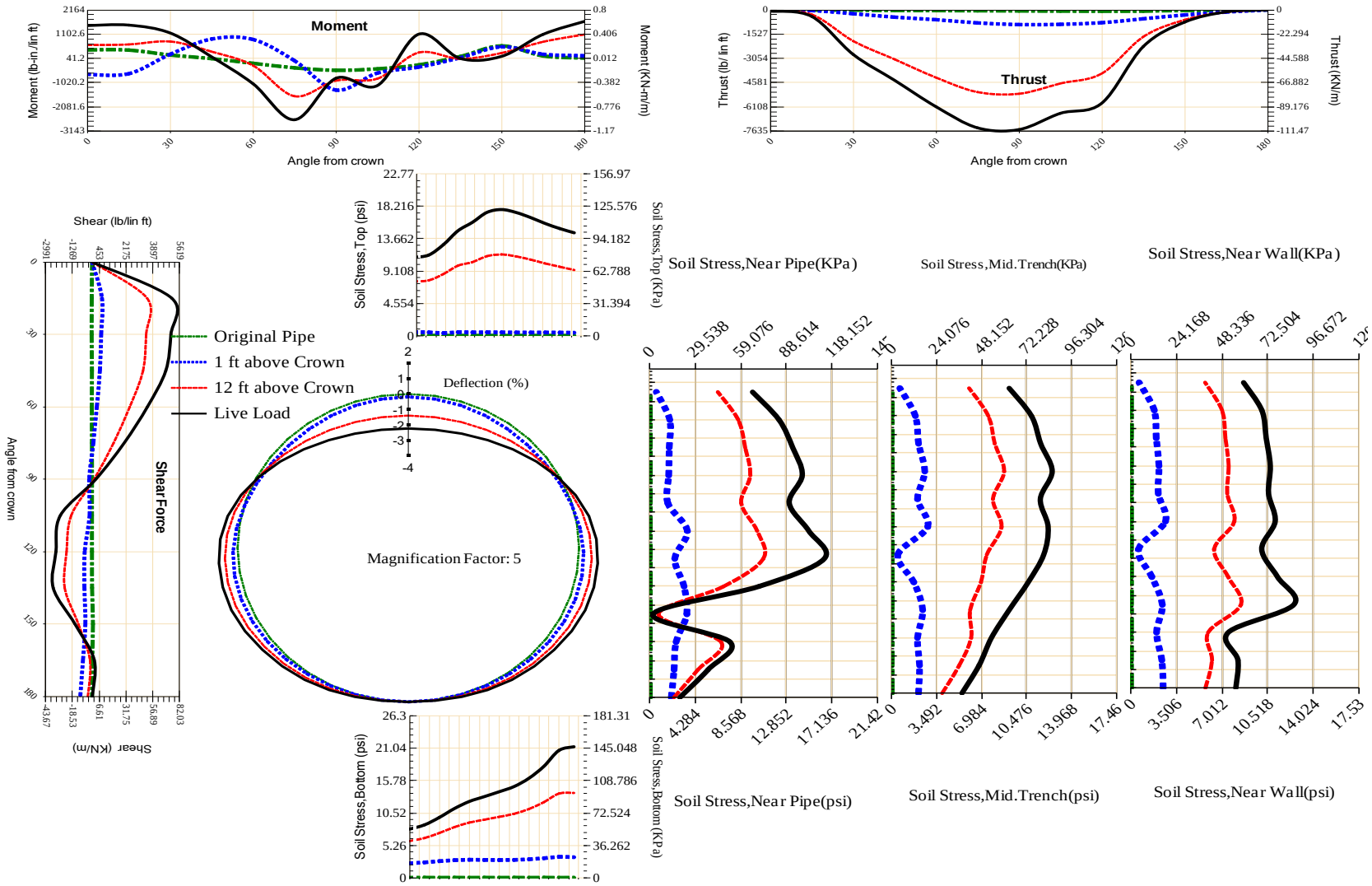

Figure A-488 Param-72-PW230-TR5OR-OD+72-EW5-H12-LiveLoad

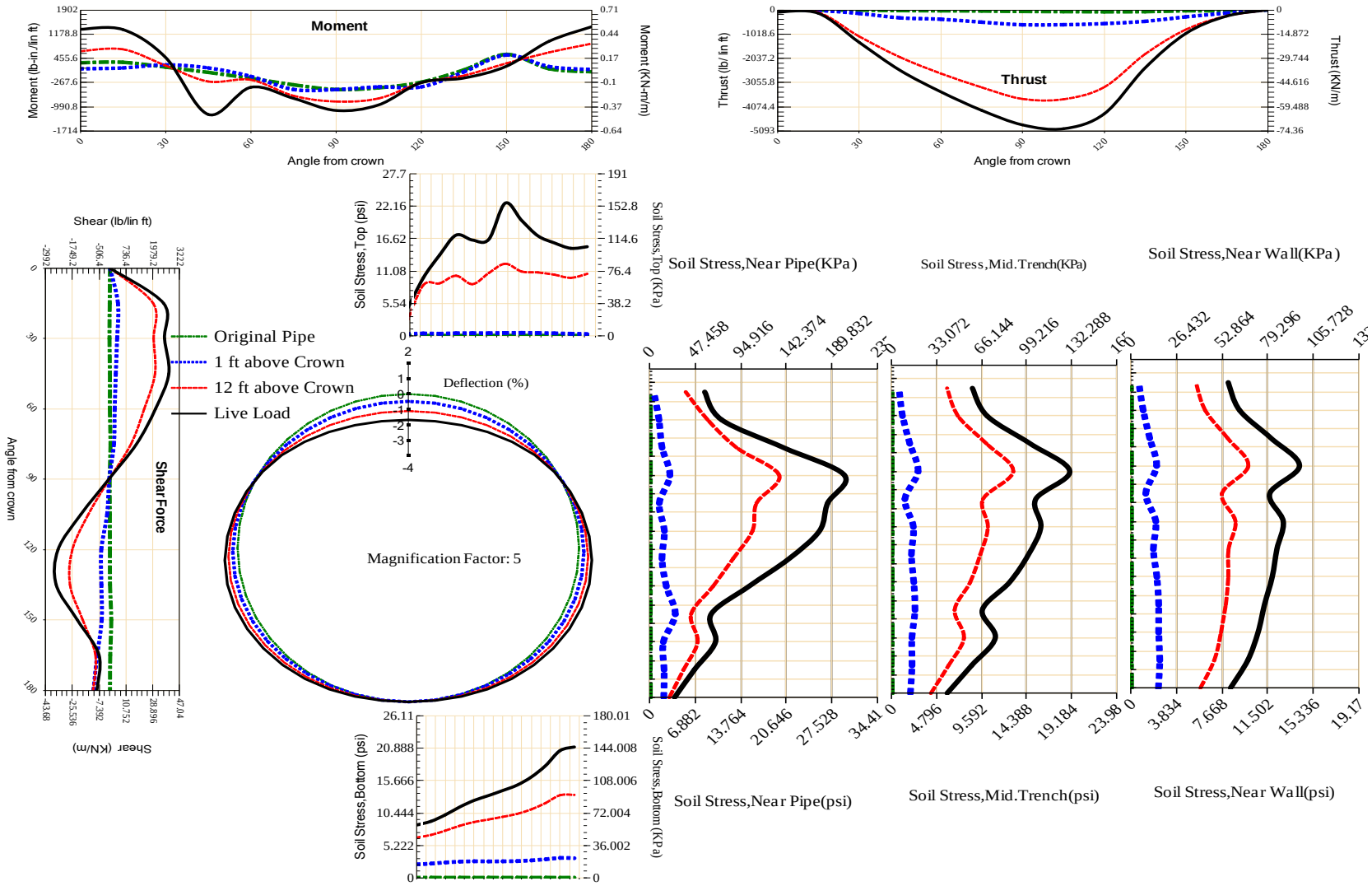

Figure A-489 Param-72-PW230-TR5SF-OD+72-EW5-H12-LiveLoad

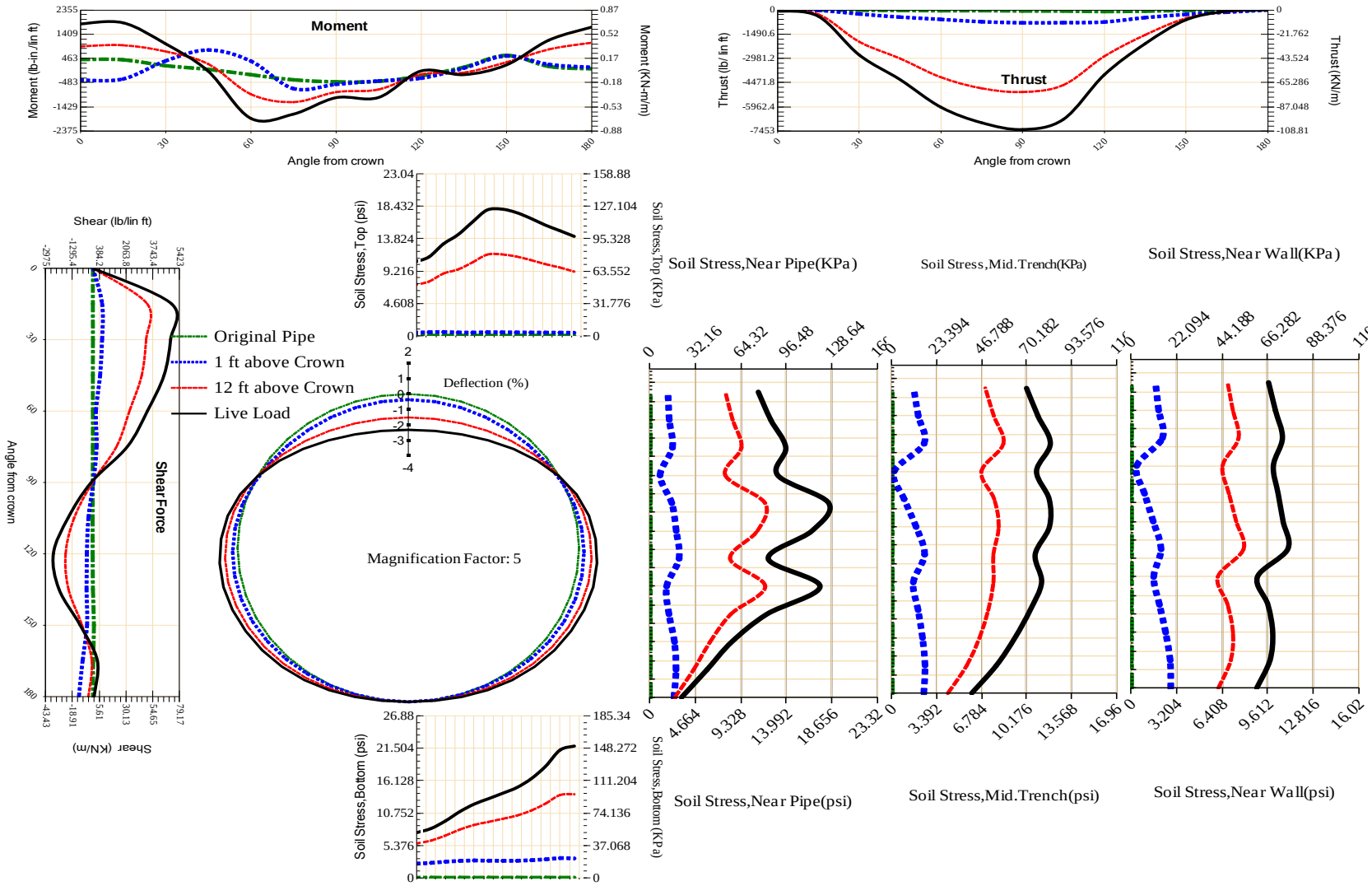

Figure A-490 Param-72-PW230-TR7OR-OD+72-EW5-H12-LiveLoad

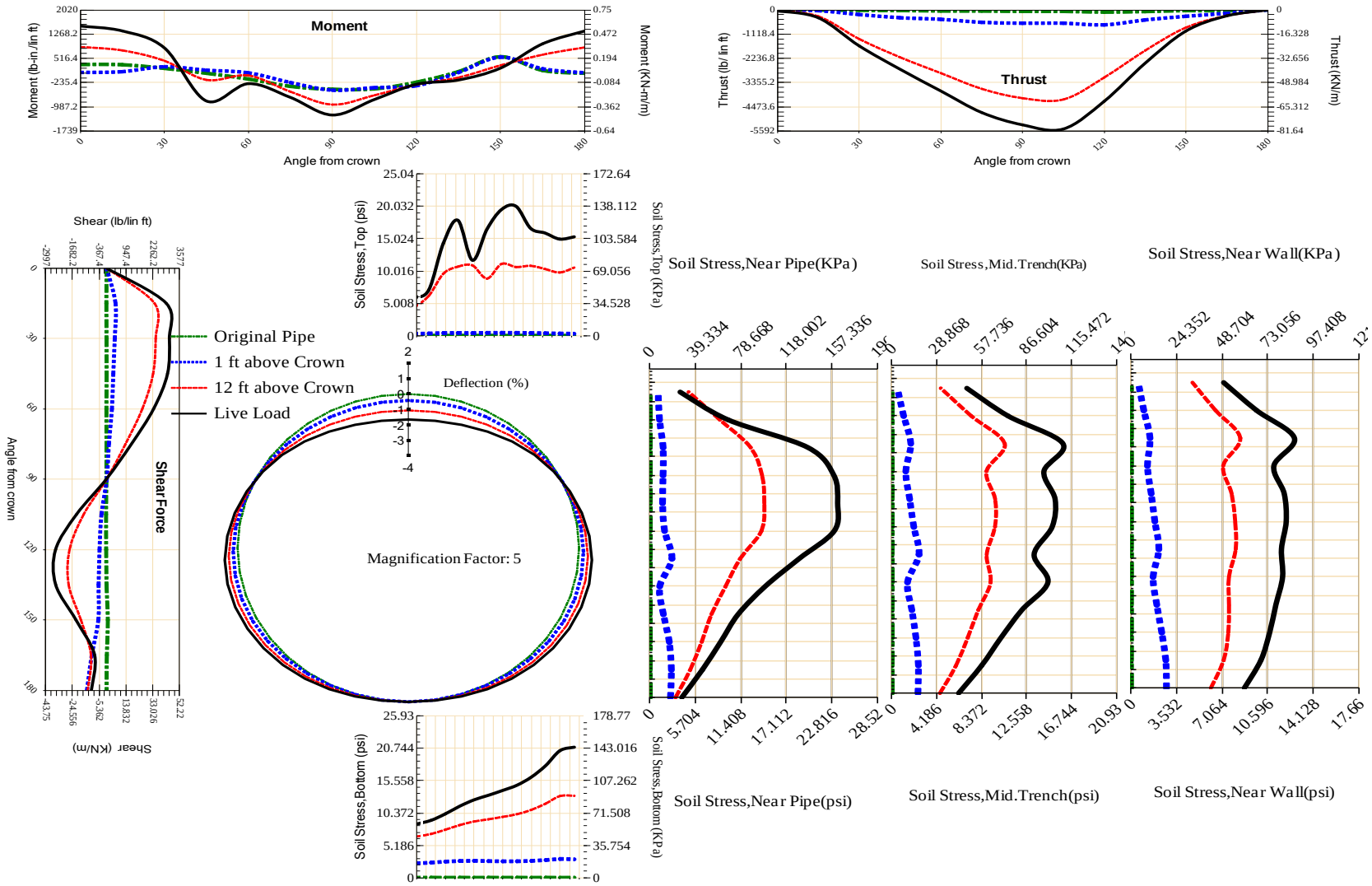

Figure A-491 Param-72-PW230-TR7SF-OD+72-EW5-H12-LiveLoad

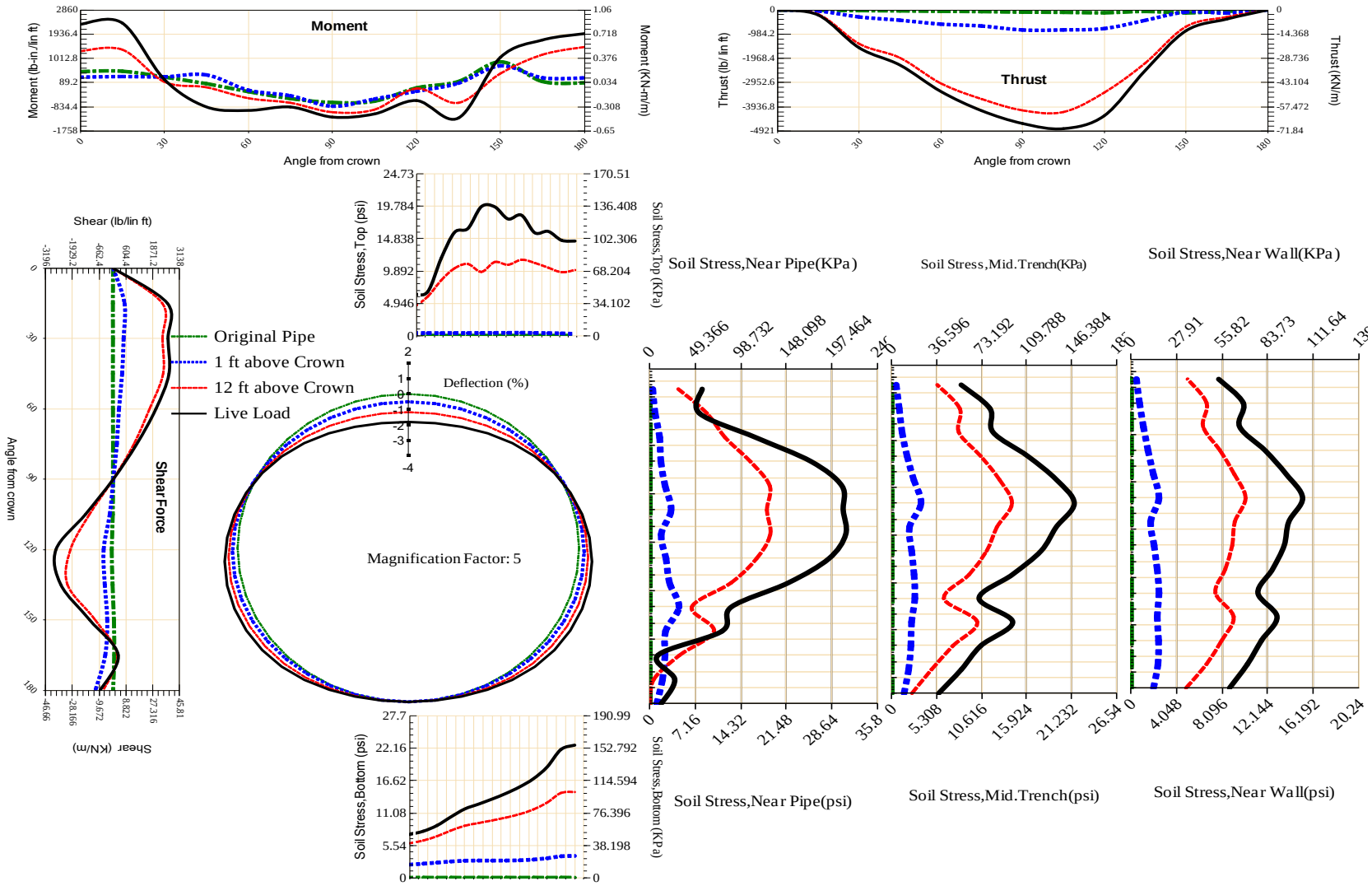

Figure A-492 Param-84-PW230-SF10SF-OD+72-EW5-H12-LiveLoad

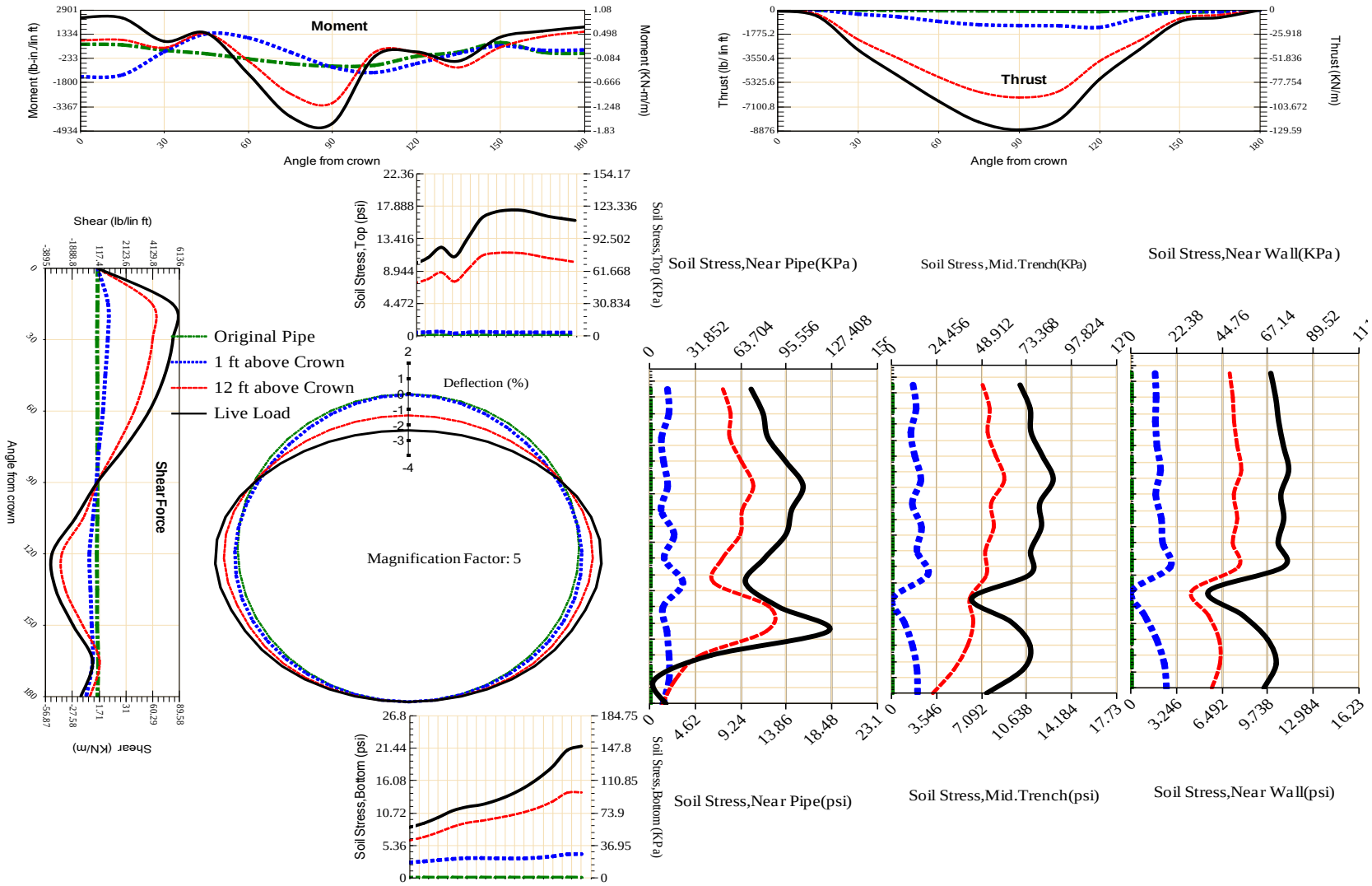

Figure A-493 Param-84-PW230-SF3OR-OD+72-EW5-H12-LiveLoad

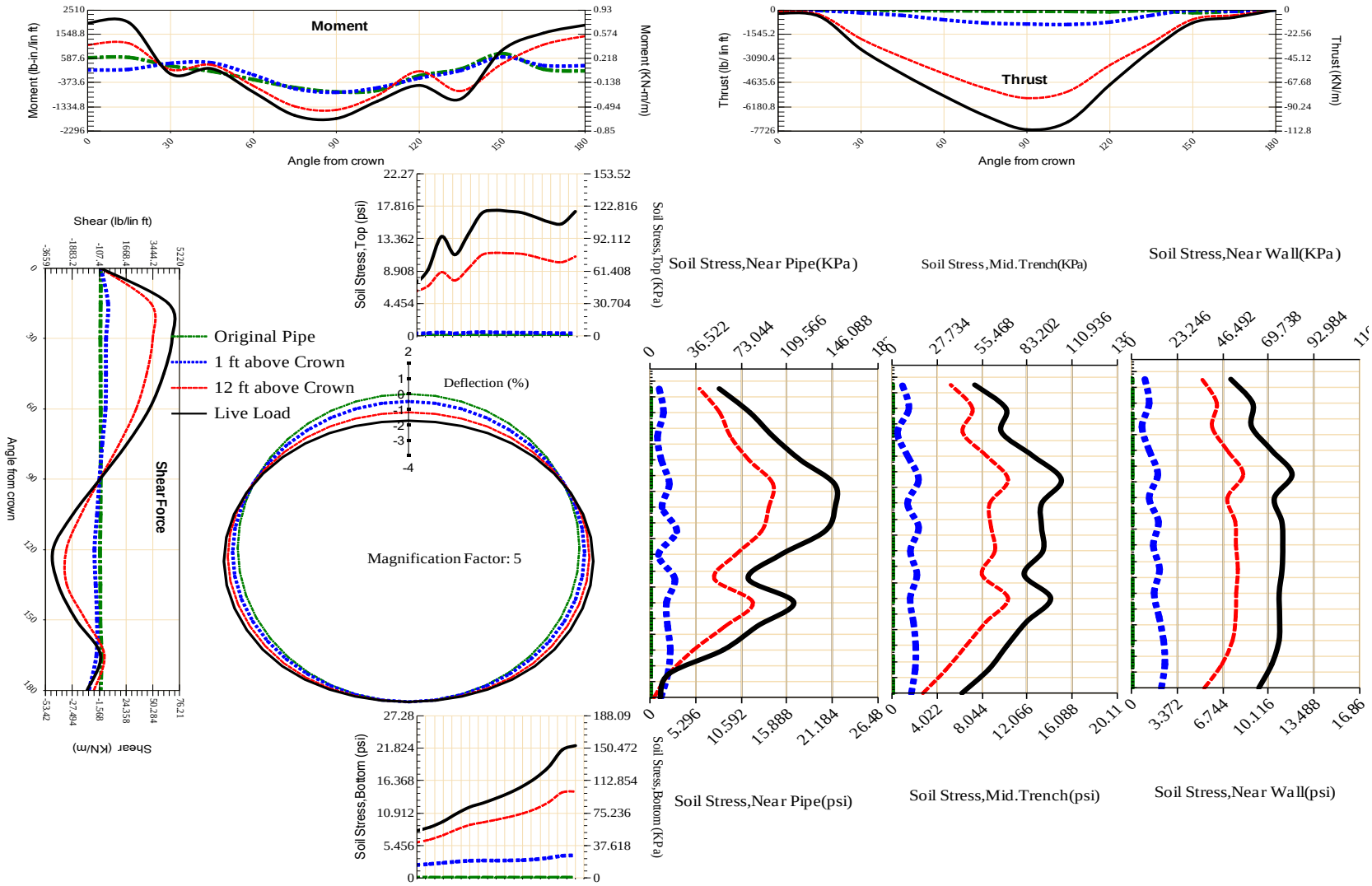

Figure A-494 Param-84-PW230-SF3TR-OD+72-EW5-H12-LiveLoad

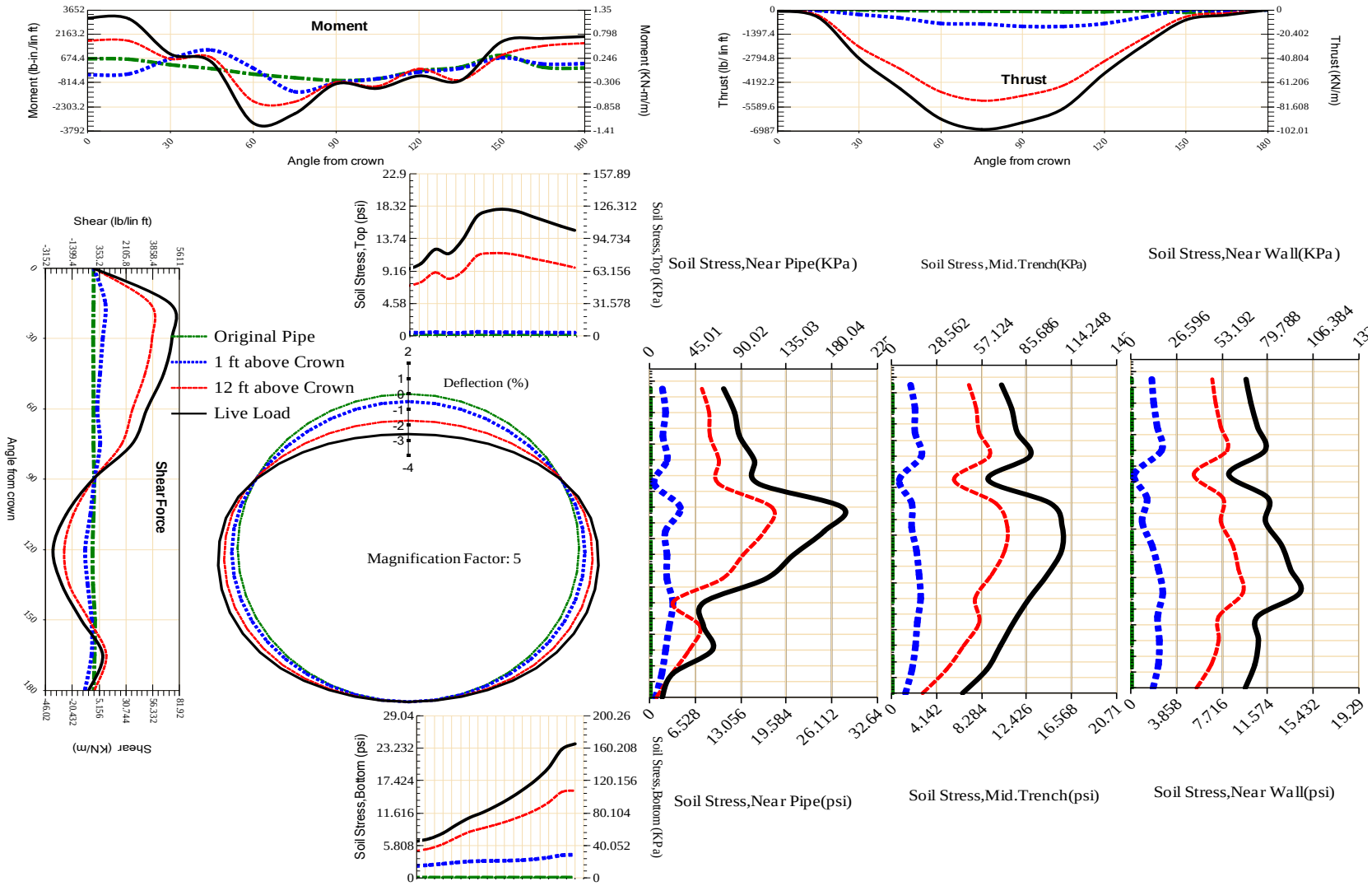

Figure A-495 Param-84-PW230-SF7OR-OD+72-EW5-H12-LiveLoad

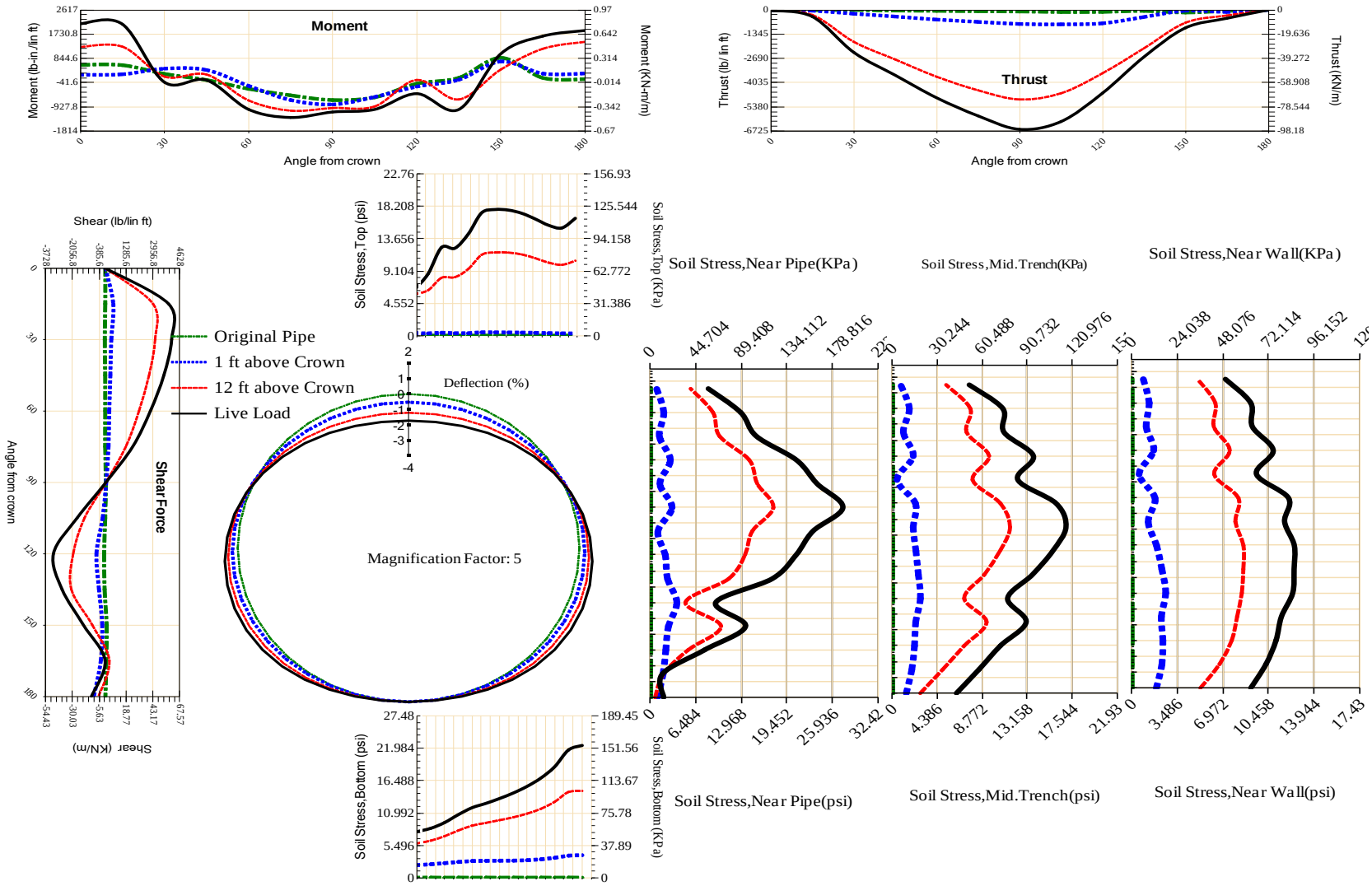

Figure A-496 Param-84-PW230-SF7TR-OD+72-EW5-H12-LiveLoad

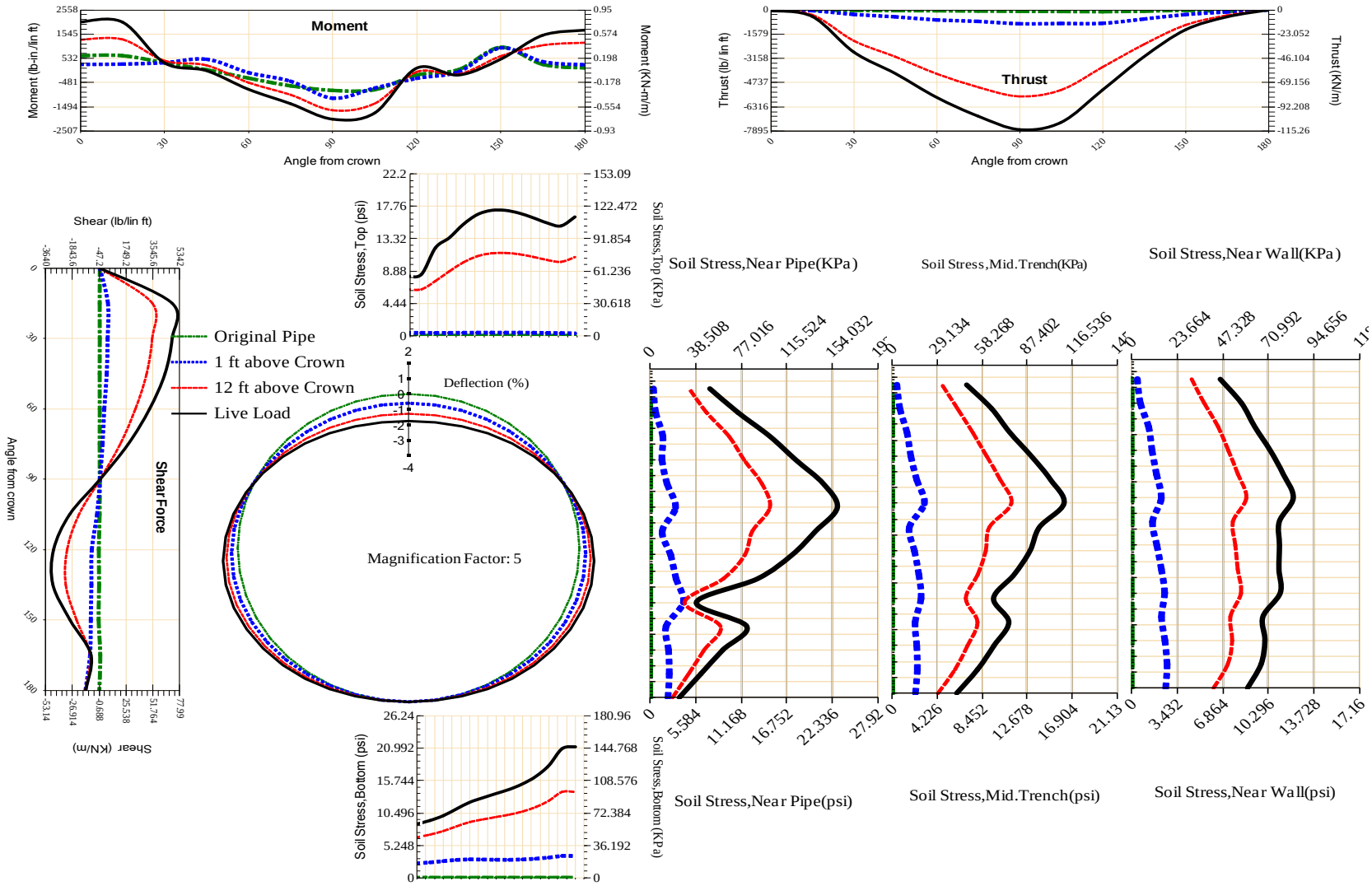

Figure A-497 Param-84-PW230-TR10TR-OD+72-EW5-H12-LiveLoad

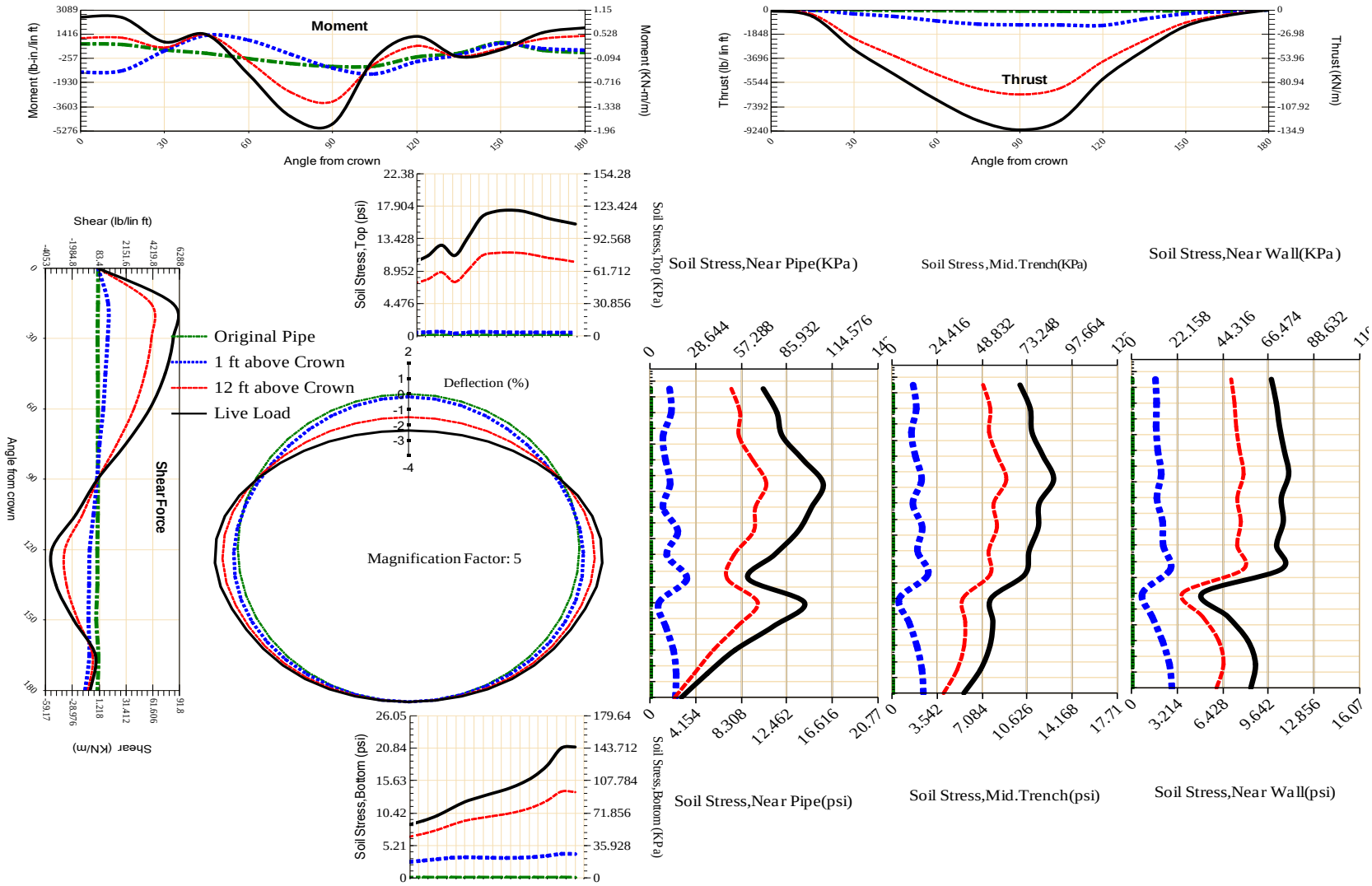

Figure A-498 Param-84-PW230-TR3OR-OD+72-EW5-H12-LiveLoad

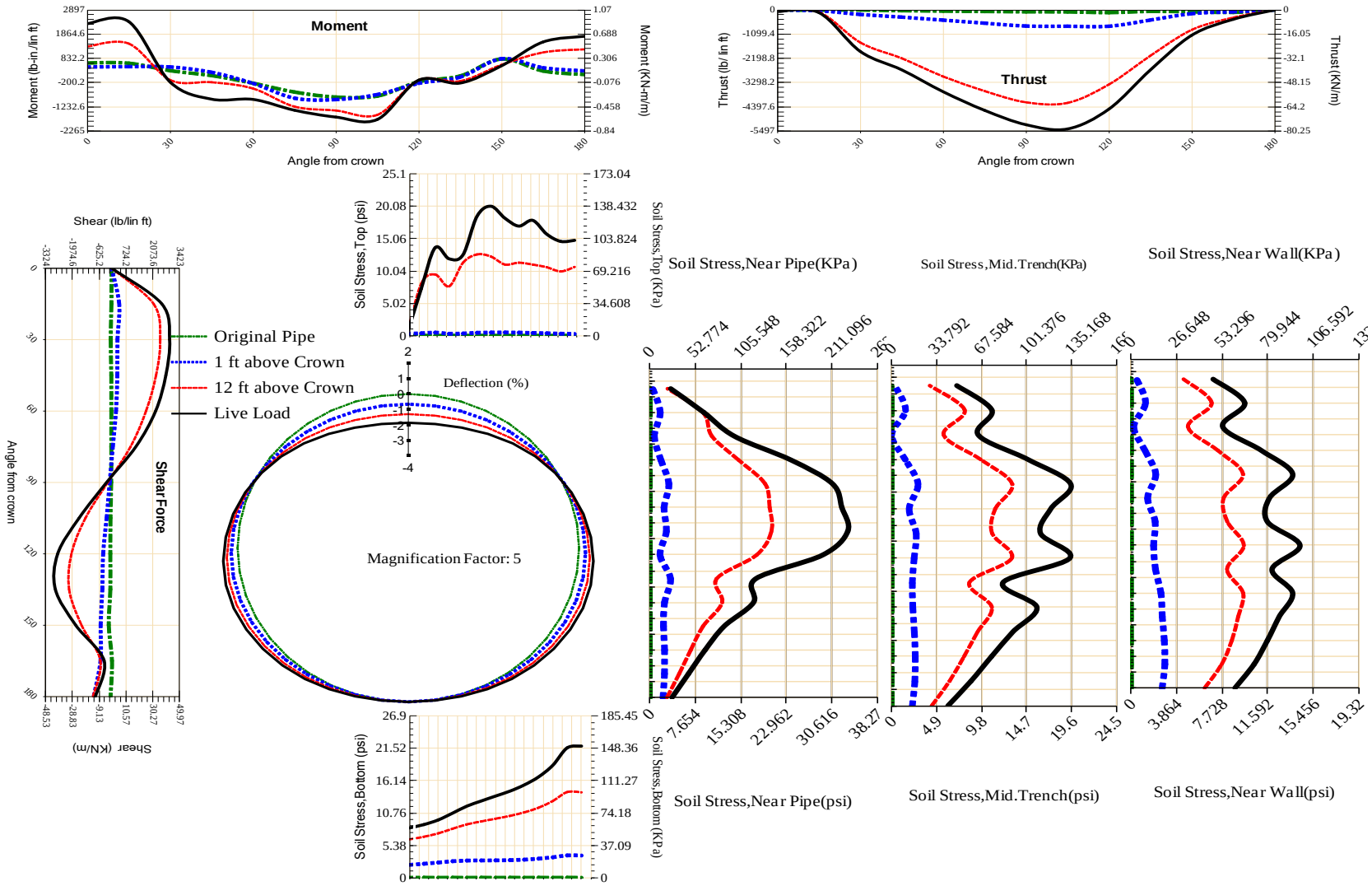

Figure A-499 Param-84-PW230-TR3SF-OD+72-EW5-H12-LiveLoad

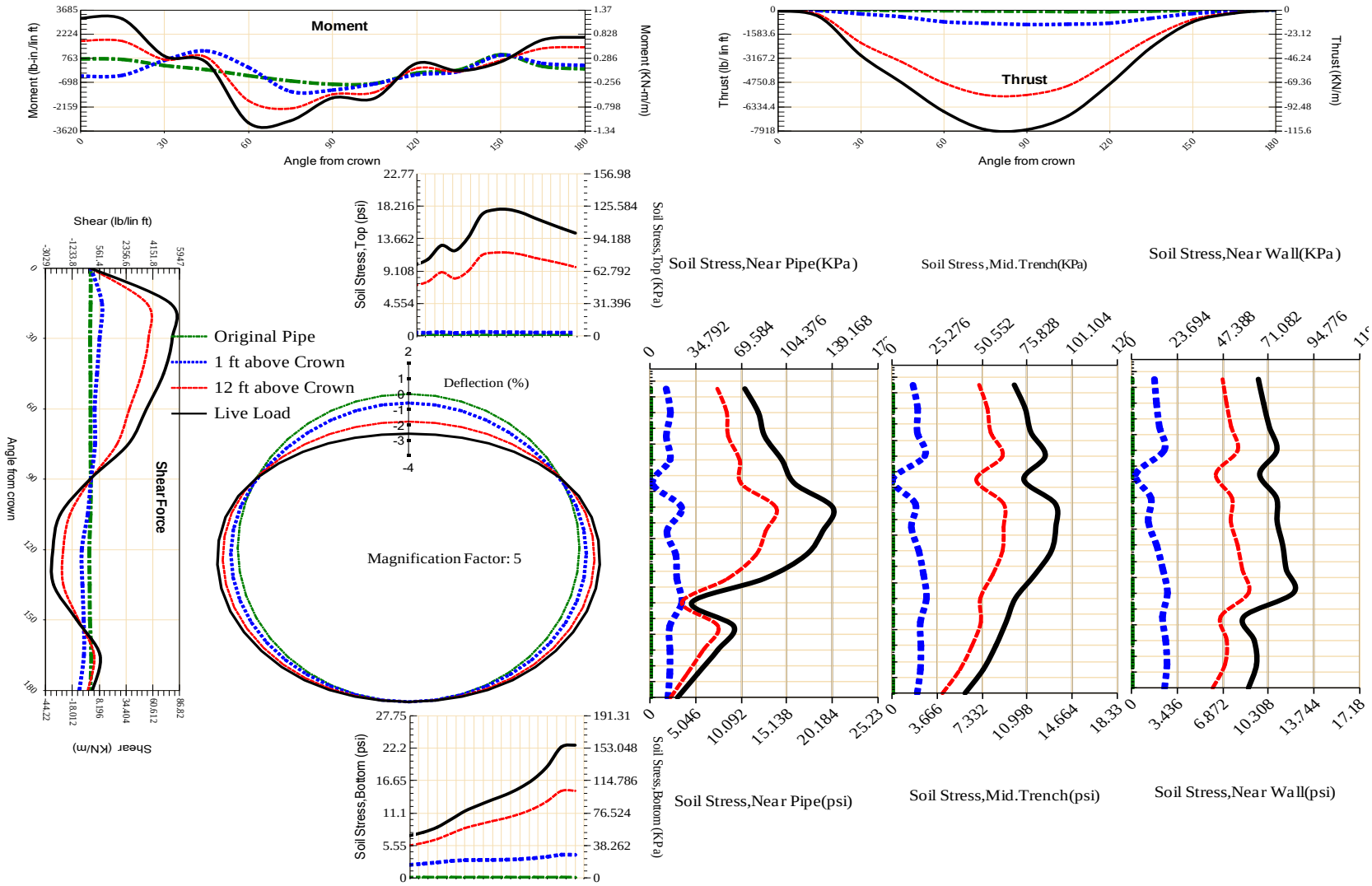

Figure A-500 Param-84-PW230-TR7OR-OD+72-EW5-H12-LiveLoad

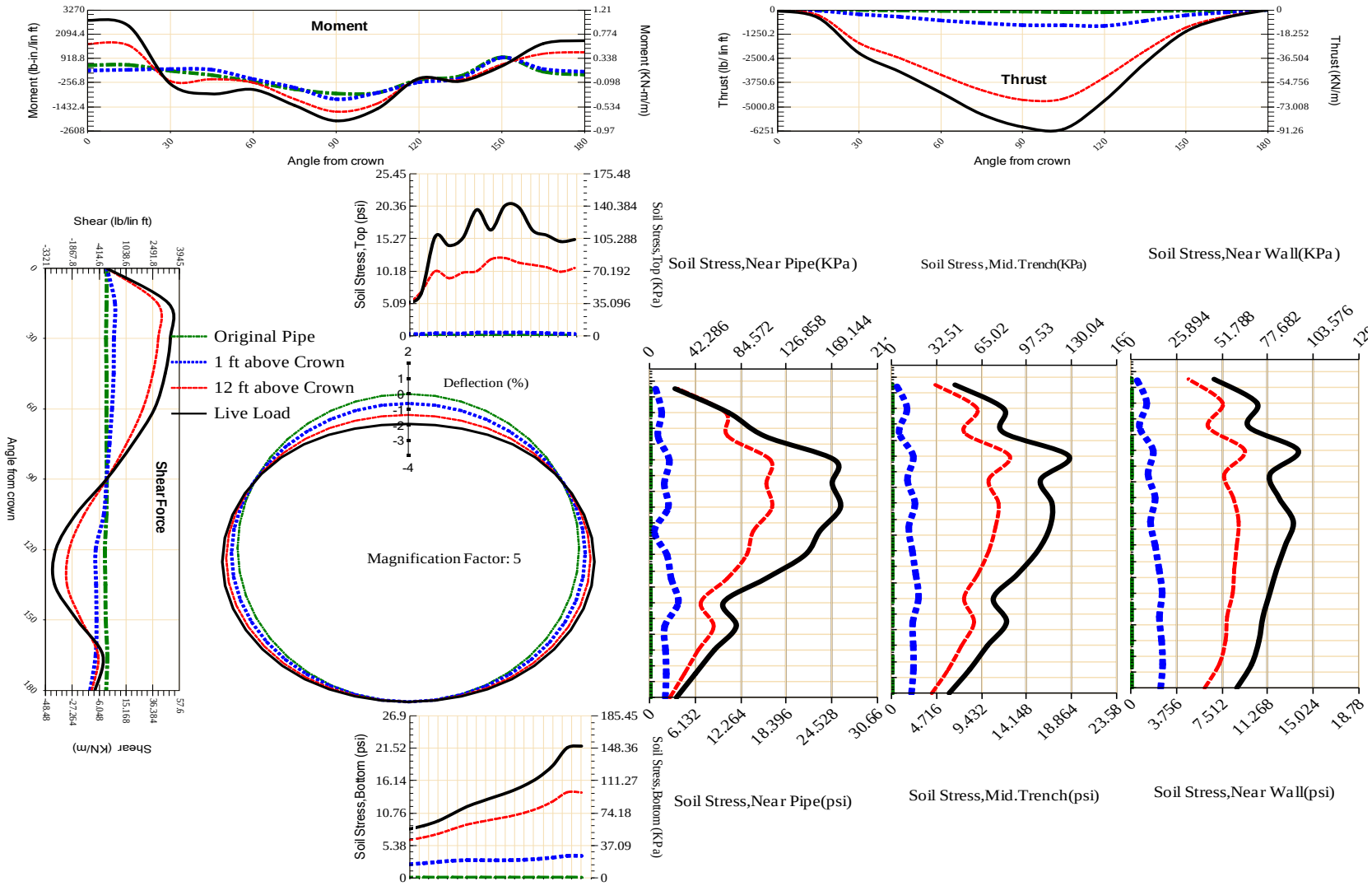

Figure A-501 Param-84-PW230-TR7SF-OD+72-EW5-H12-LiveLoad

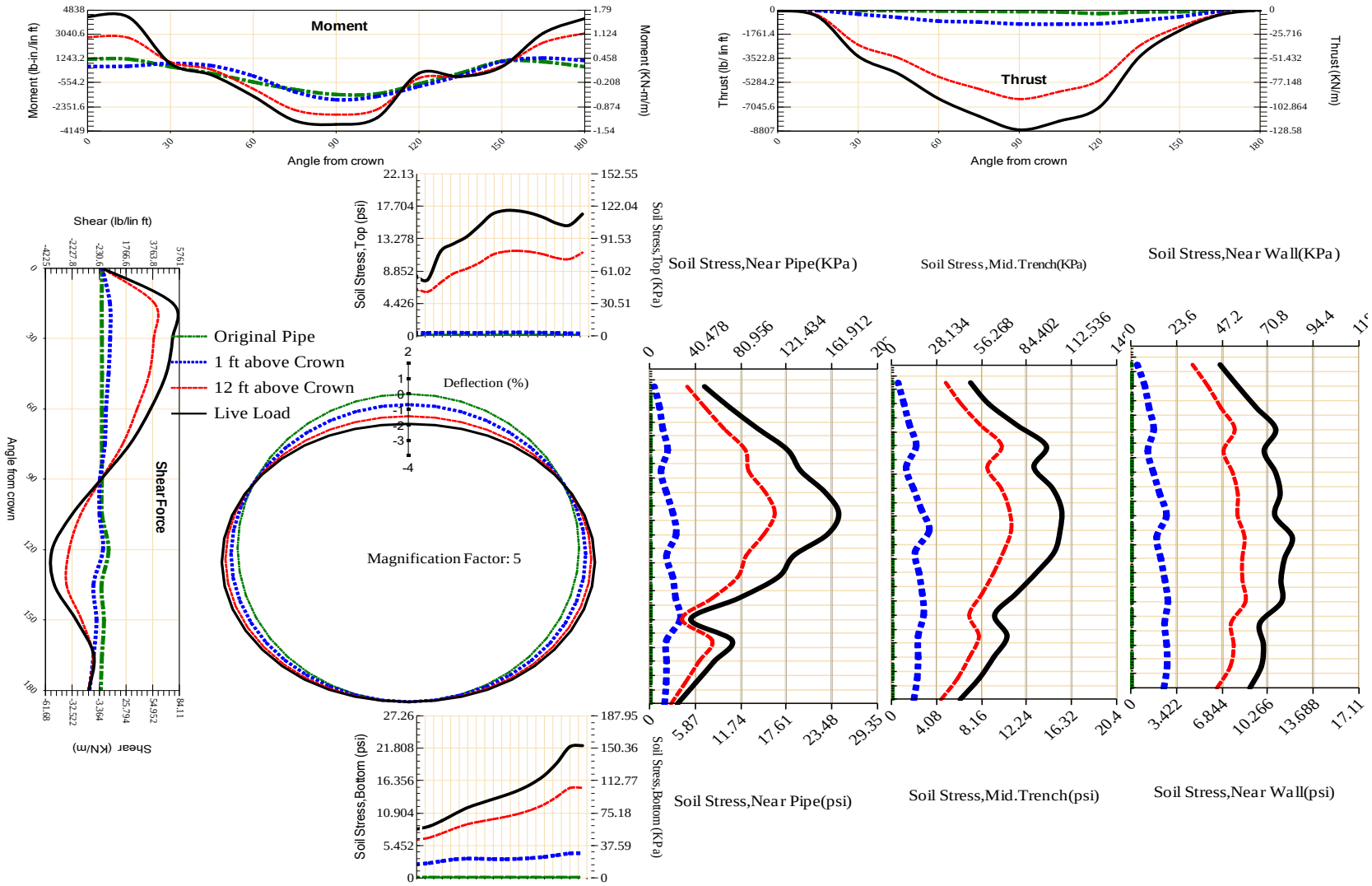

Figure A-502 Param-96-PW200-SF10TR-OD+72-EW5-H12-LiveLoad

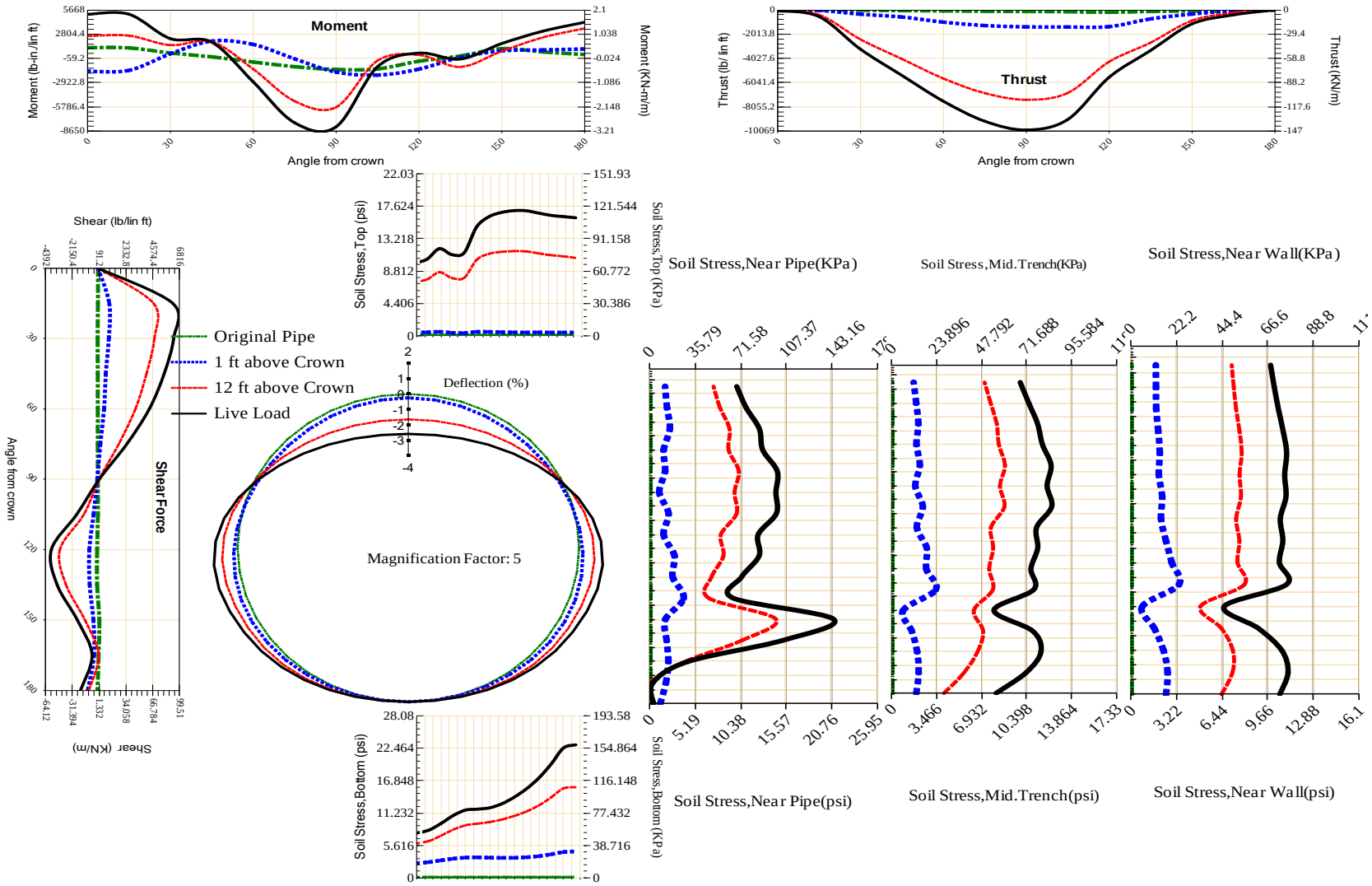

Figure A-503 Param-96-PW200-SF3OR-OD+72-EW5-H12-LiveLoad

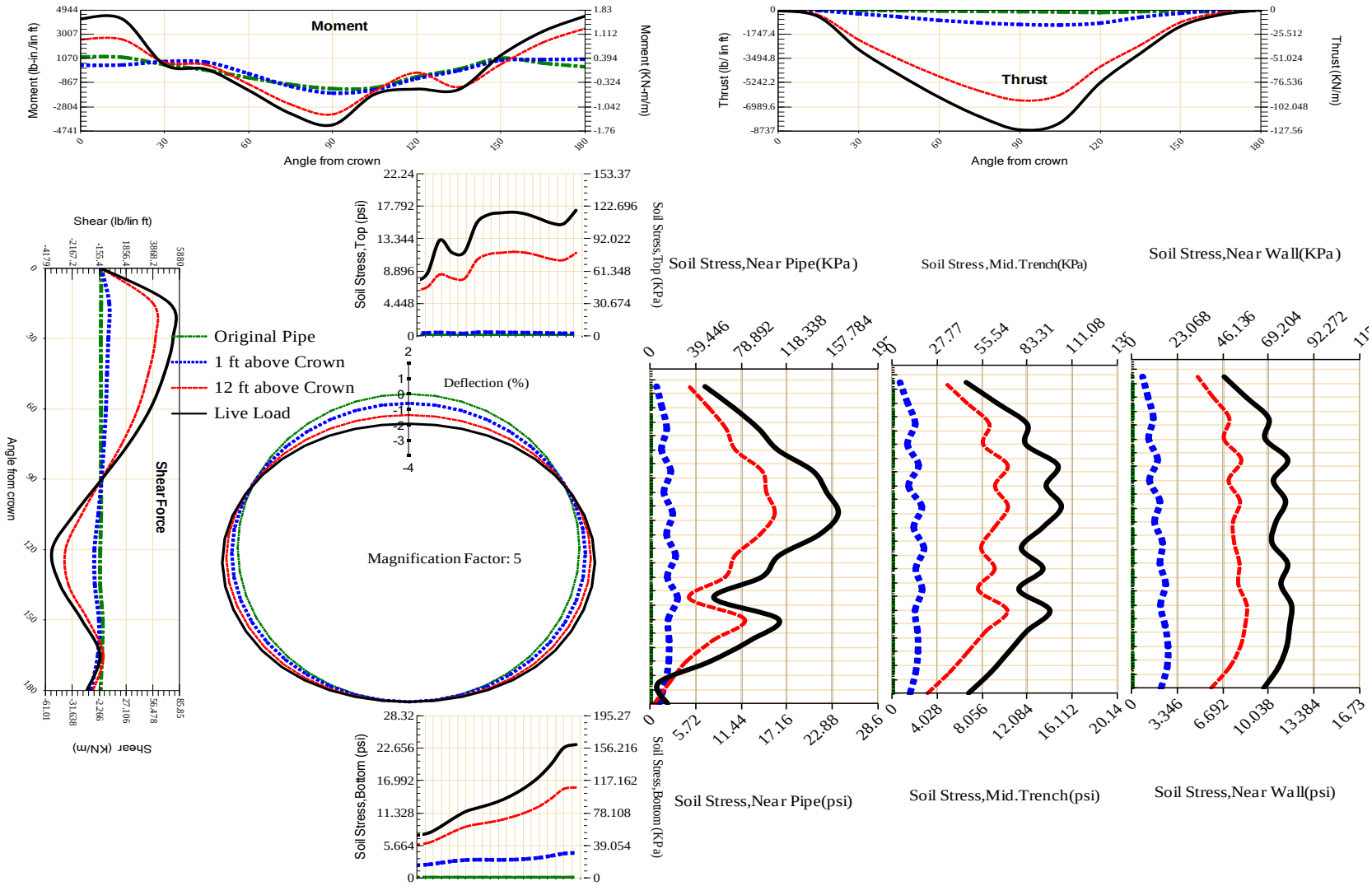

Figure A-504 Param-96-PW200-SF3TR-OD+72-EW5-H12-LiveLoad

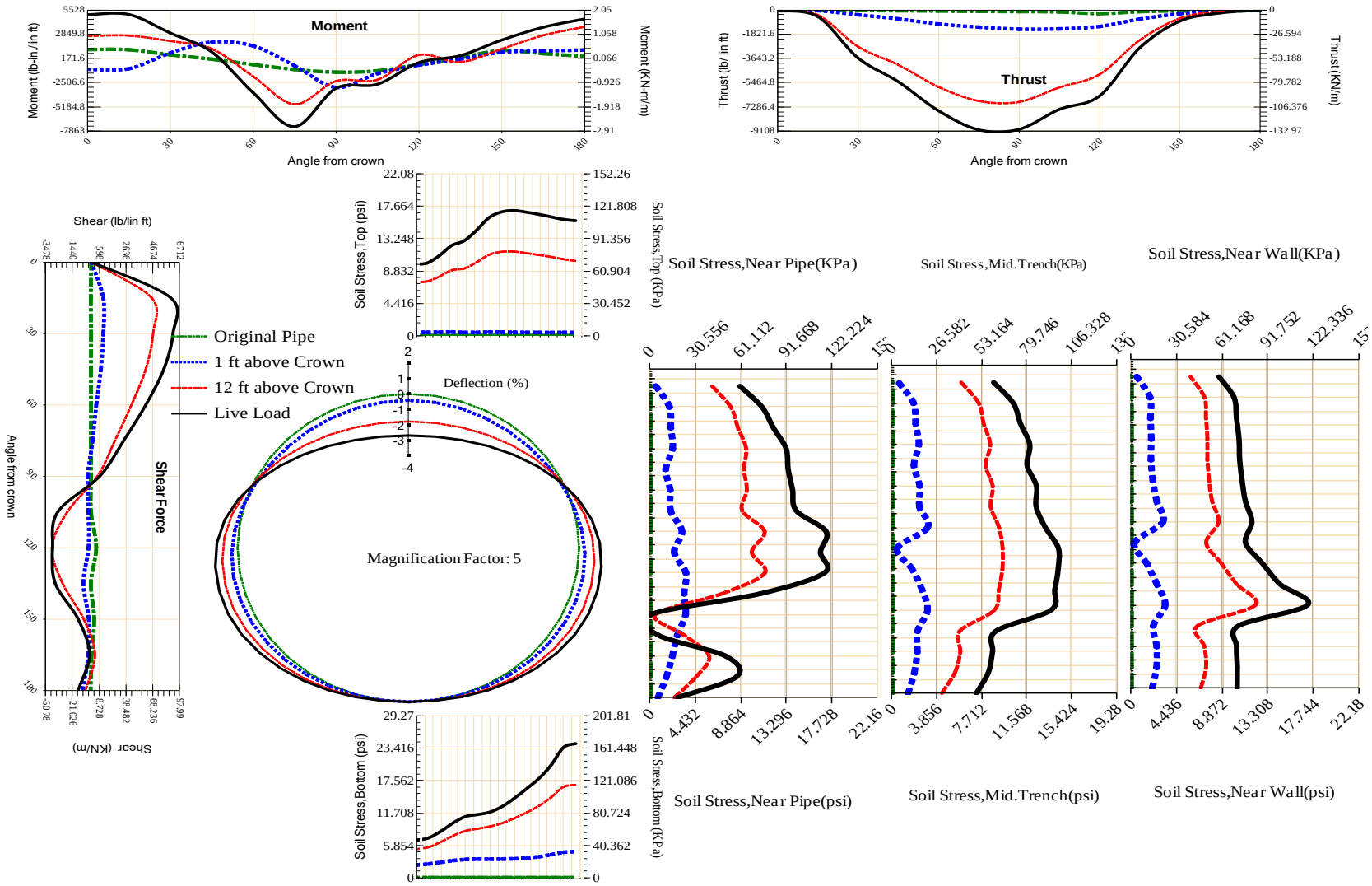

Figure A-505 Param-96-PW200-SF5OR-OD+72-EW5-H12-LiveLoad

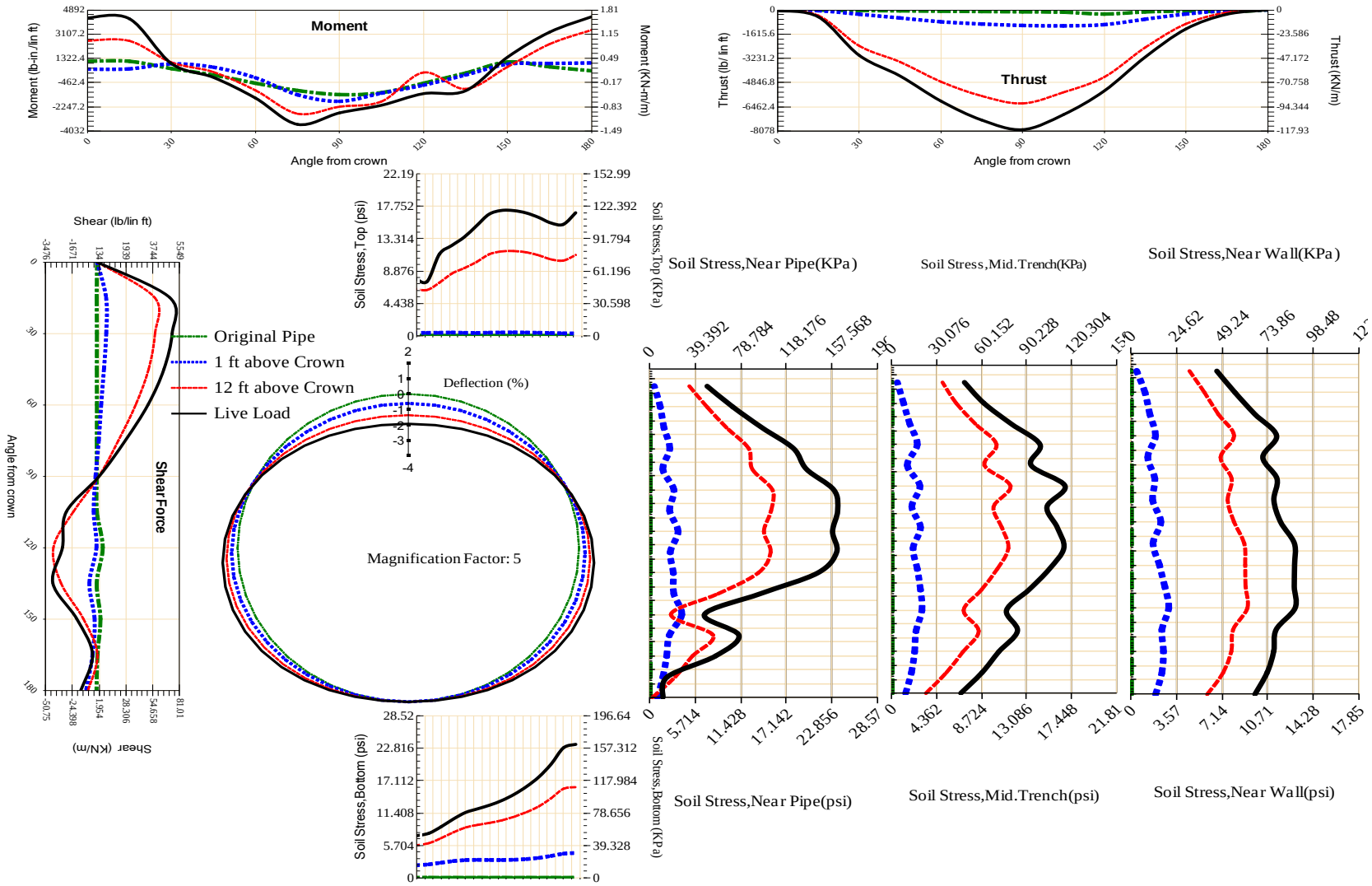

Figure A-506 Param-96-PW200-SF5TR-OD+72-EW5-H12-LiveLoad

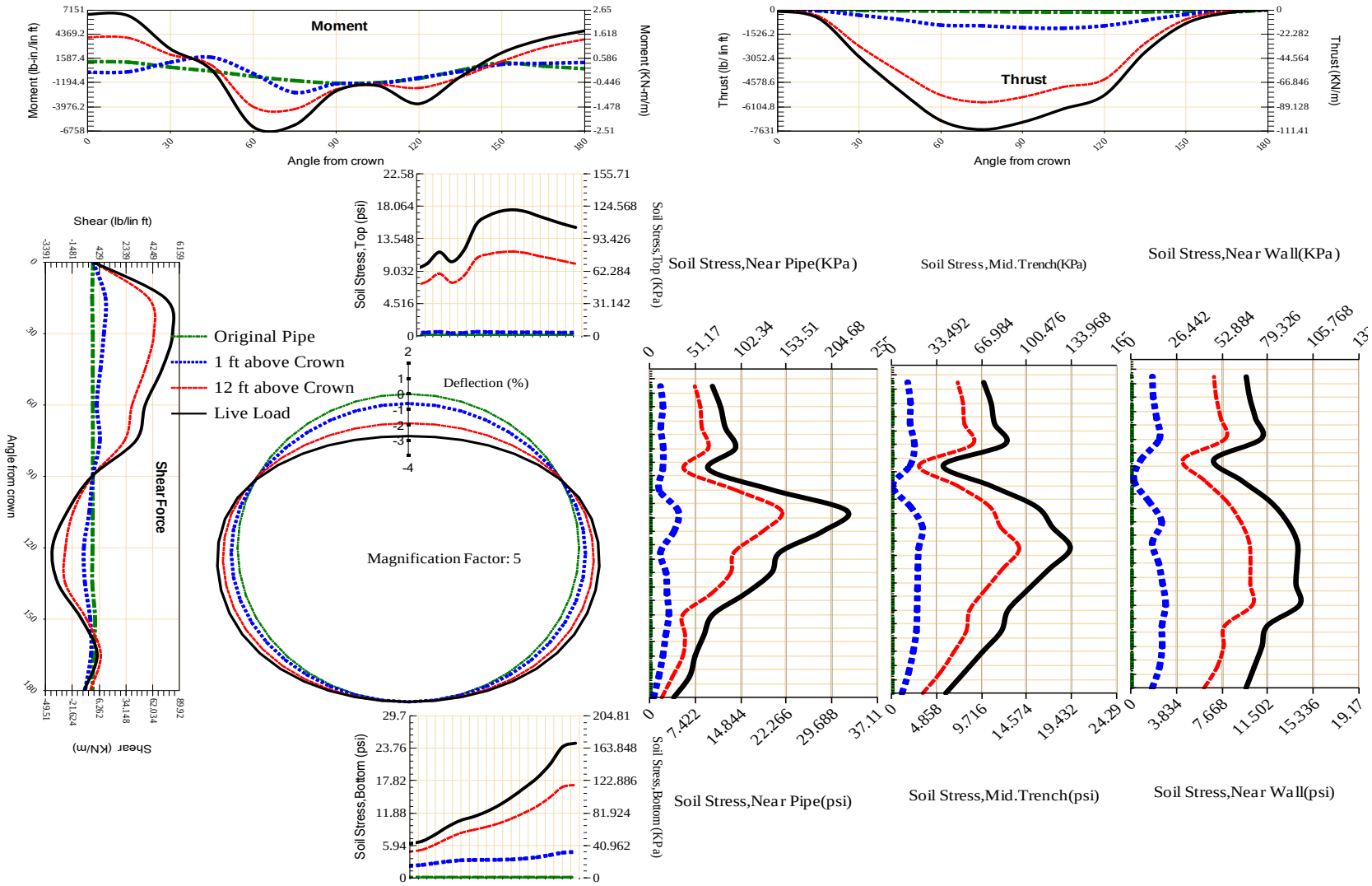

Figure A-507 Param-96-PW200-SF7OR-OD+72-EW5-H12-LiveLoad

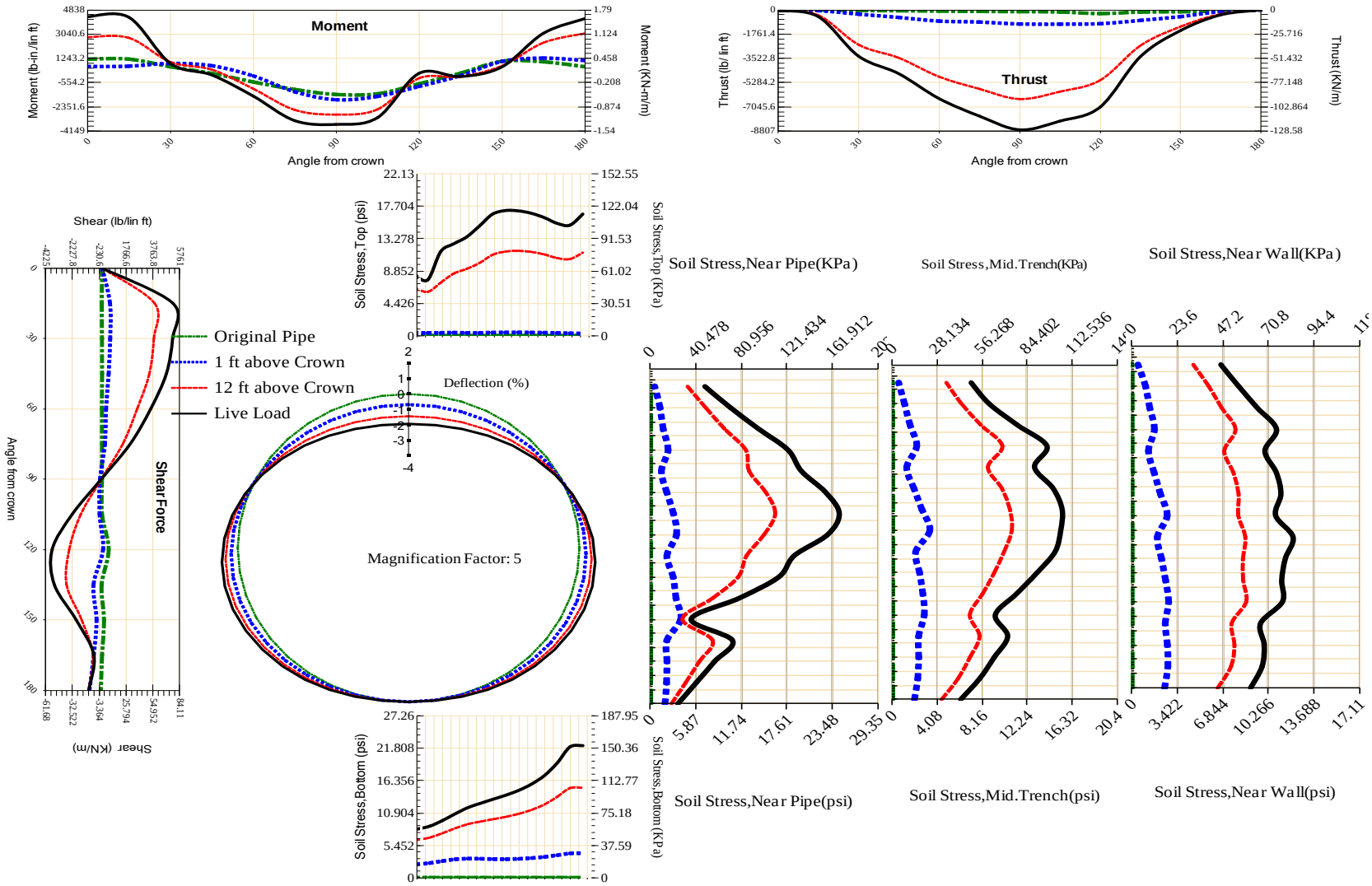

Figure A-508 Param-96-PW200-TR10TR-OD+72-EW5-H12-LiveLoad

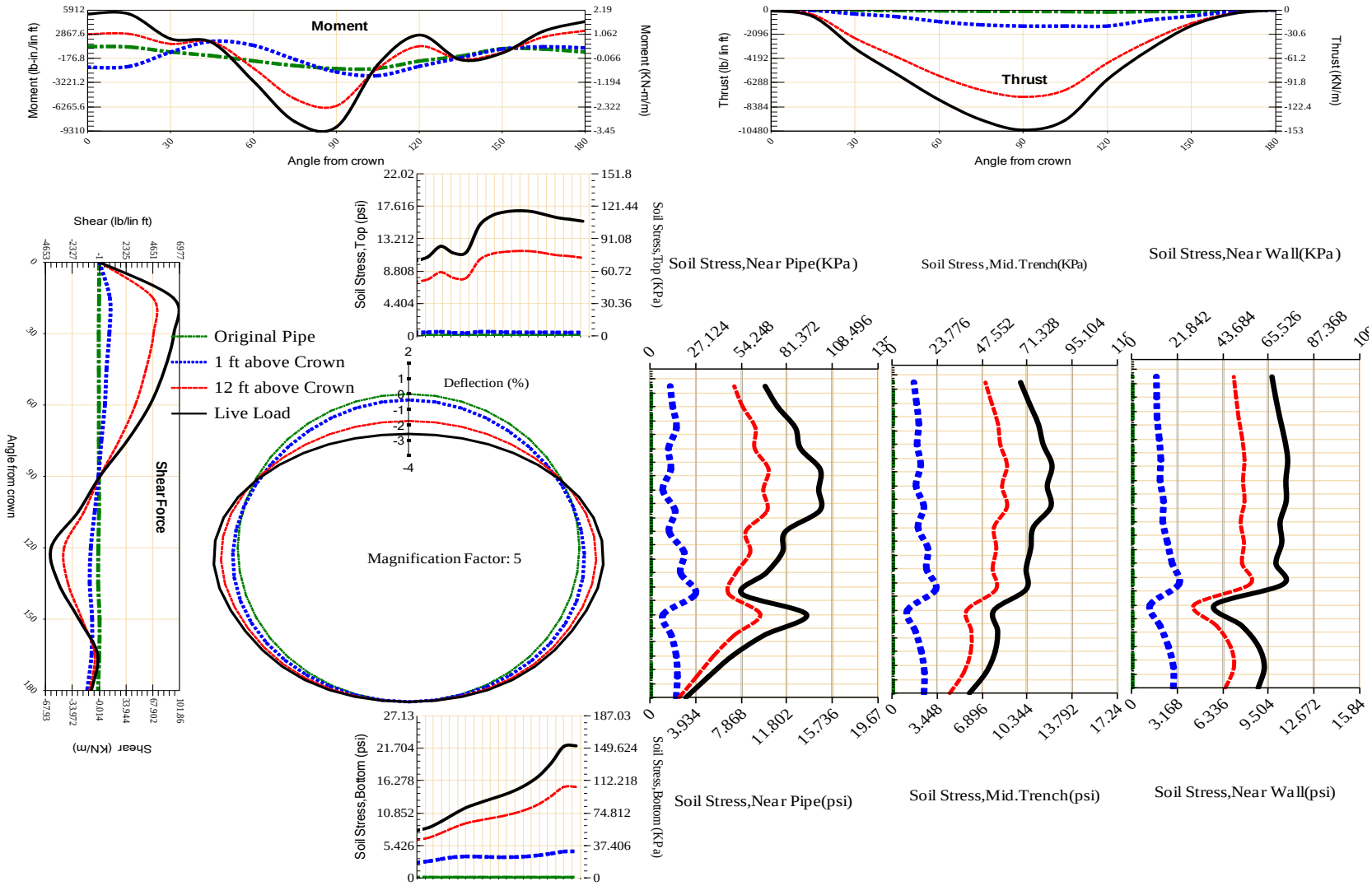

Figure A-509 Param-96-PW200-TR3OR-OD+72-EW5-H12-LiveLoad

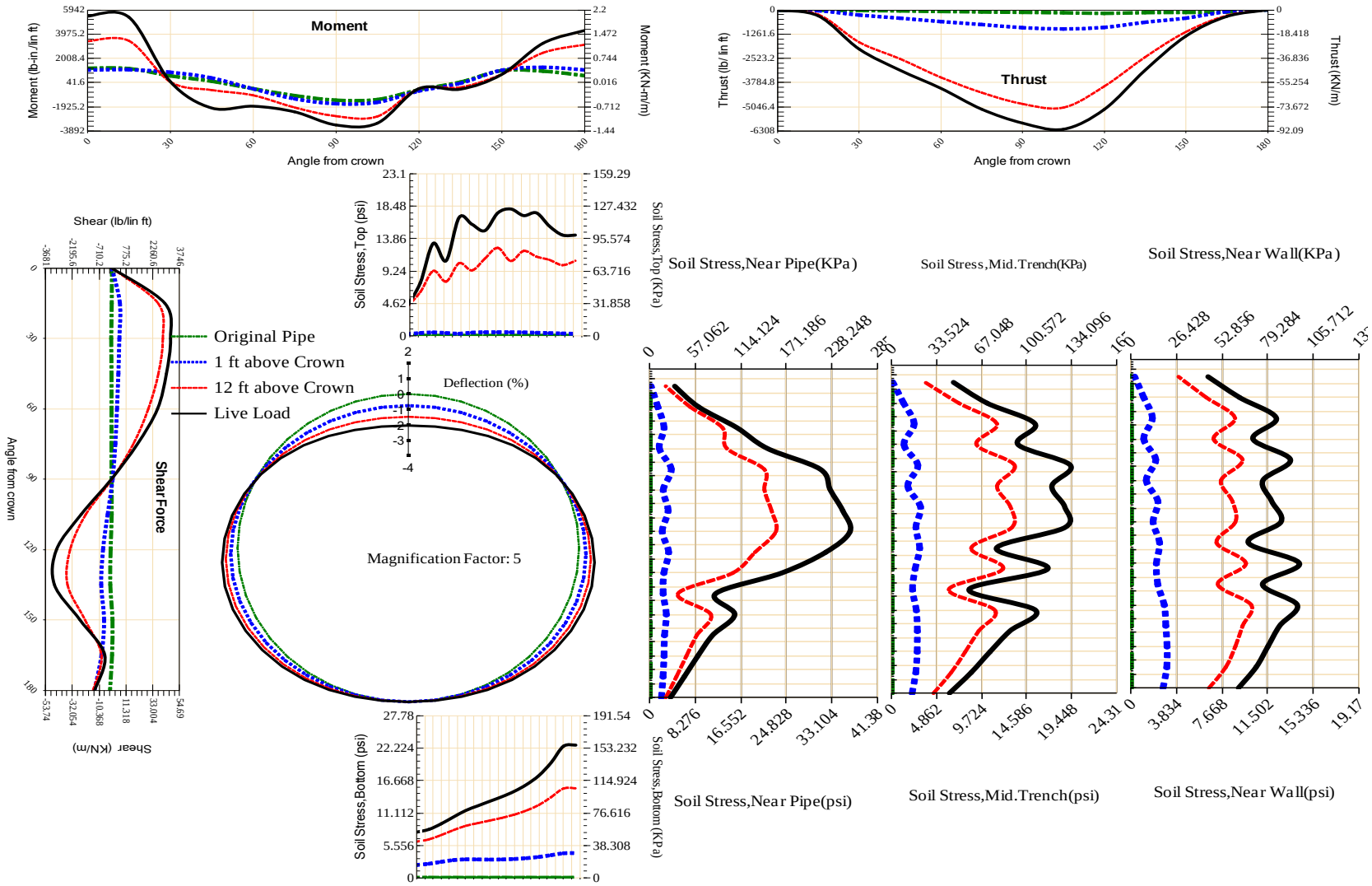

Figure A-510 Param-96-PW200-TR3SF-OD+72-EW5-H12-LiveLoad

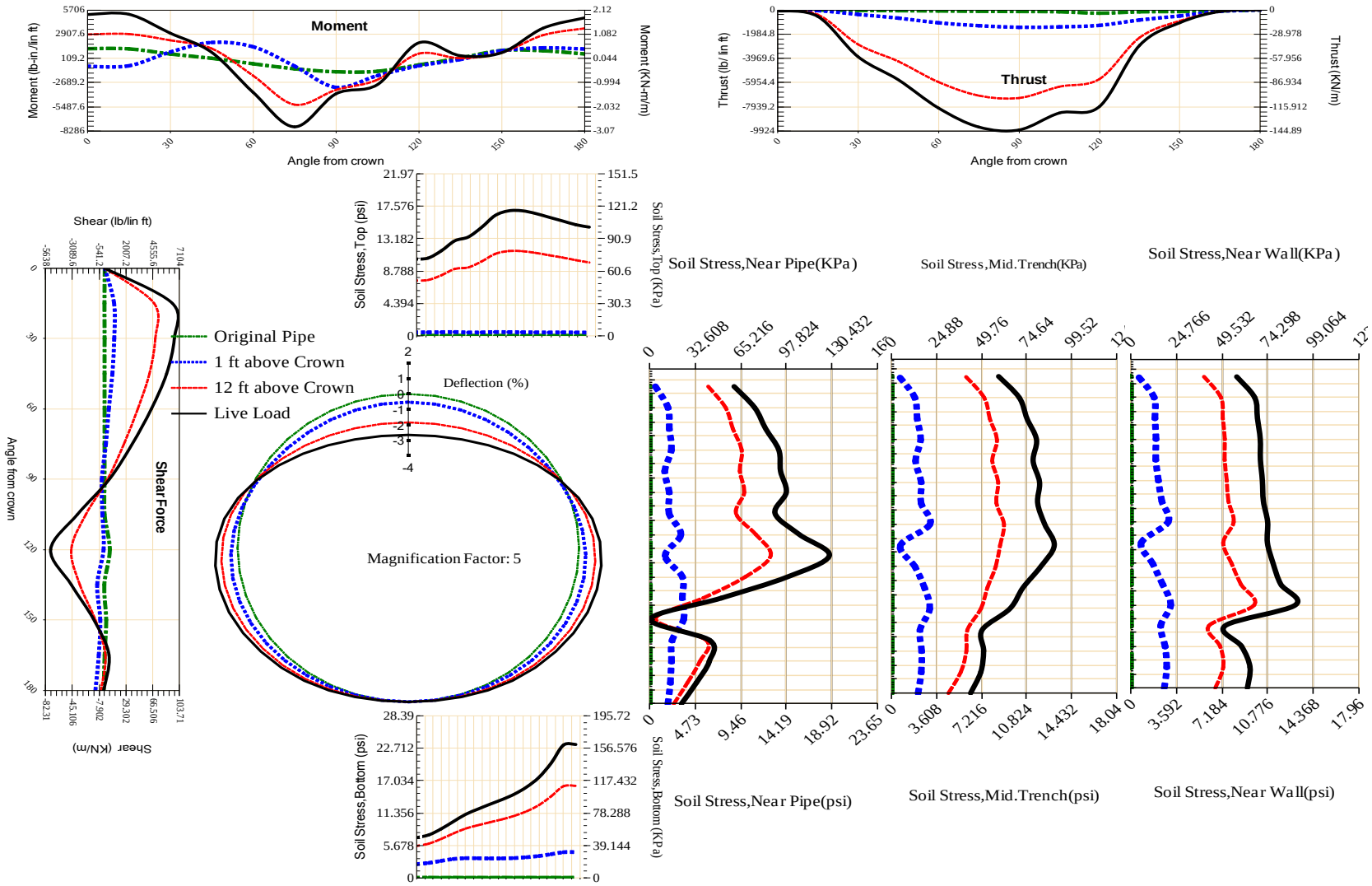

Figure A-511 Param-96-PW200-TR5OR-OD+72-EW5-H12-LiveLoad

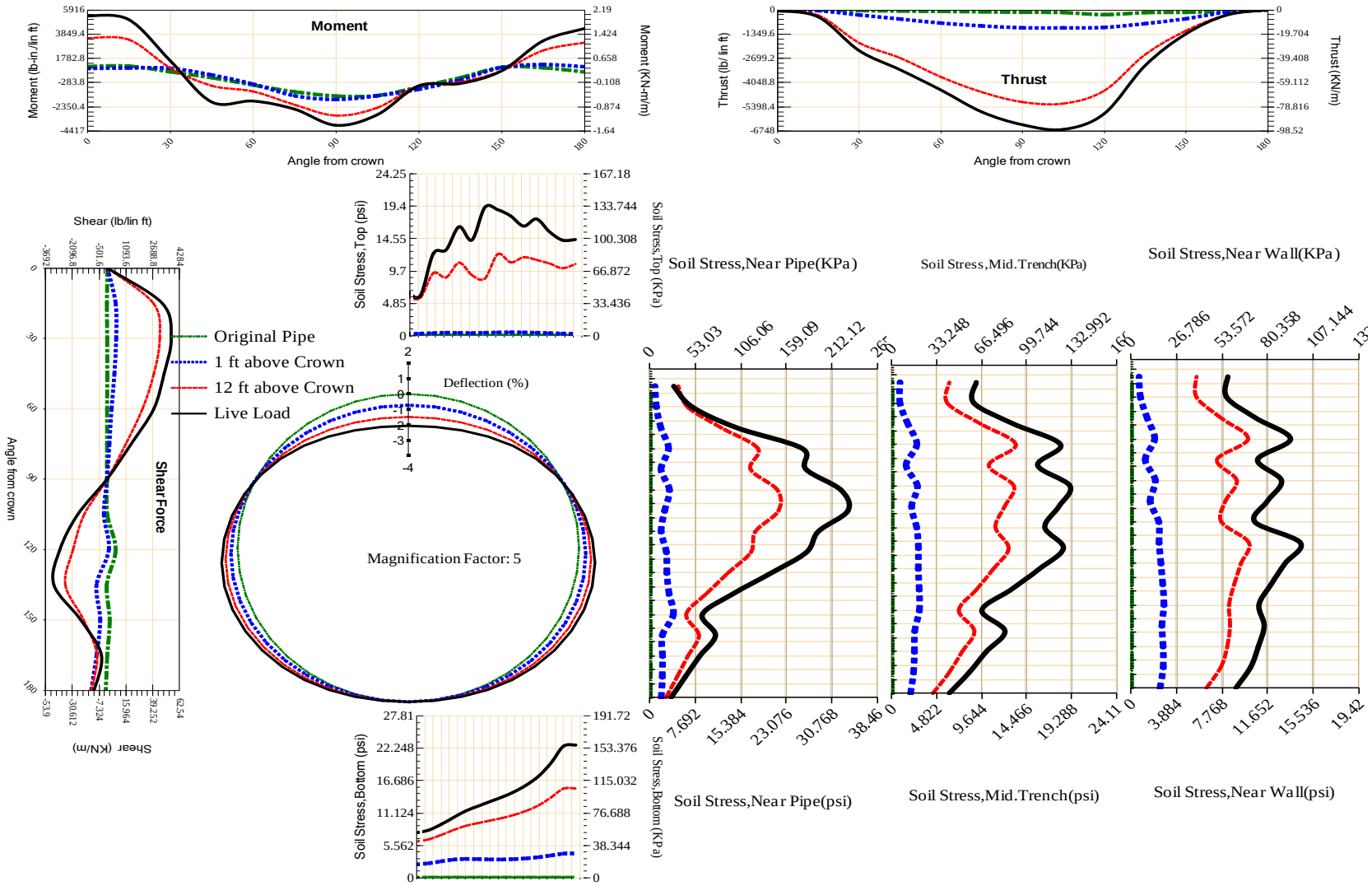

Figure A-512 Param-96-PW200-TR5SF-OD+72-EW5-H12-LiveLoad

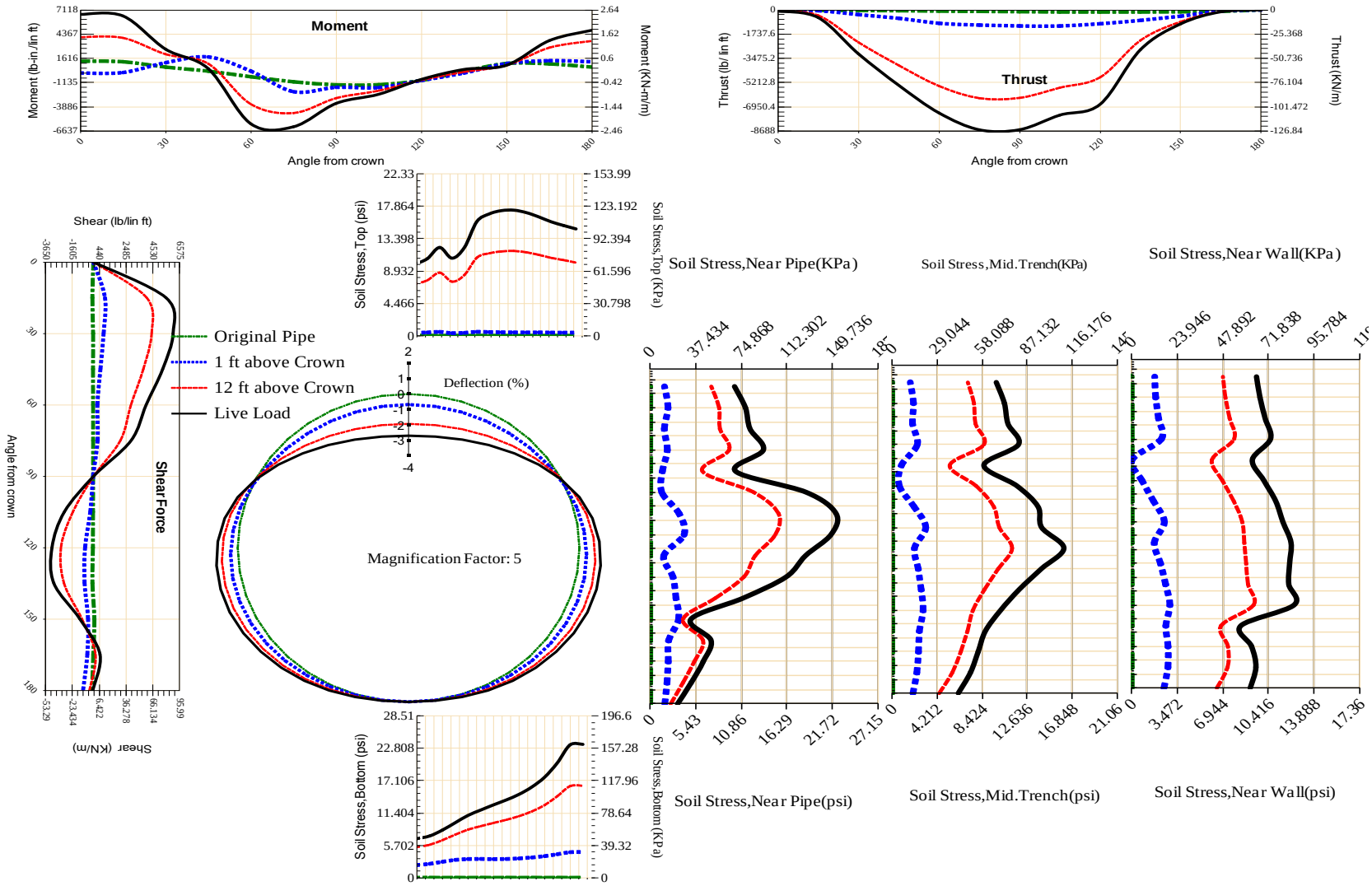

Figure A-513 Param-96-PW200-TR7OR-OD+72-EW5-H12-LiveLoad

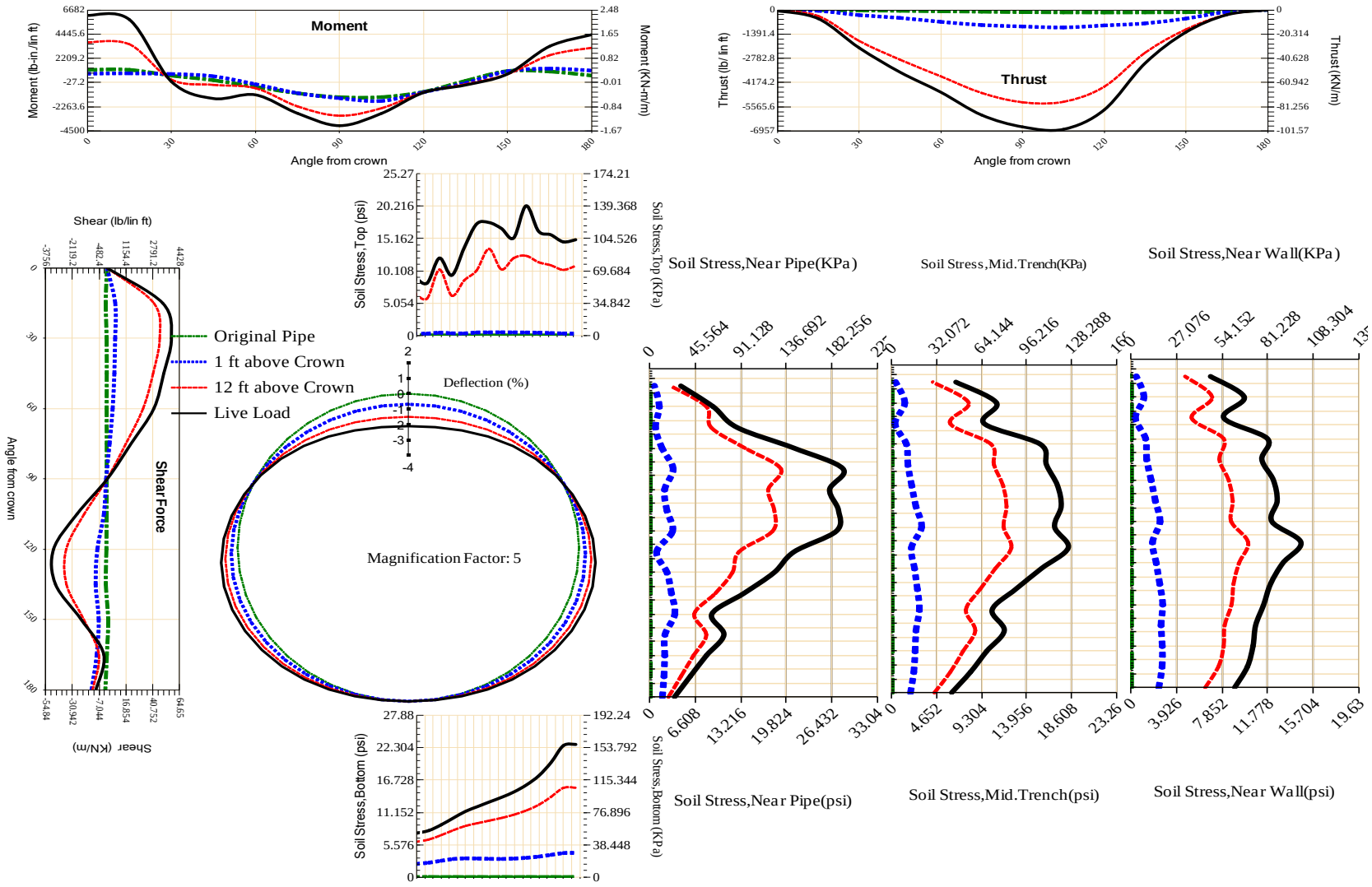

Figure A-514 Param-96-PW200-TR7SF-OD+72-EW5-H12-LiveLoad

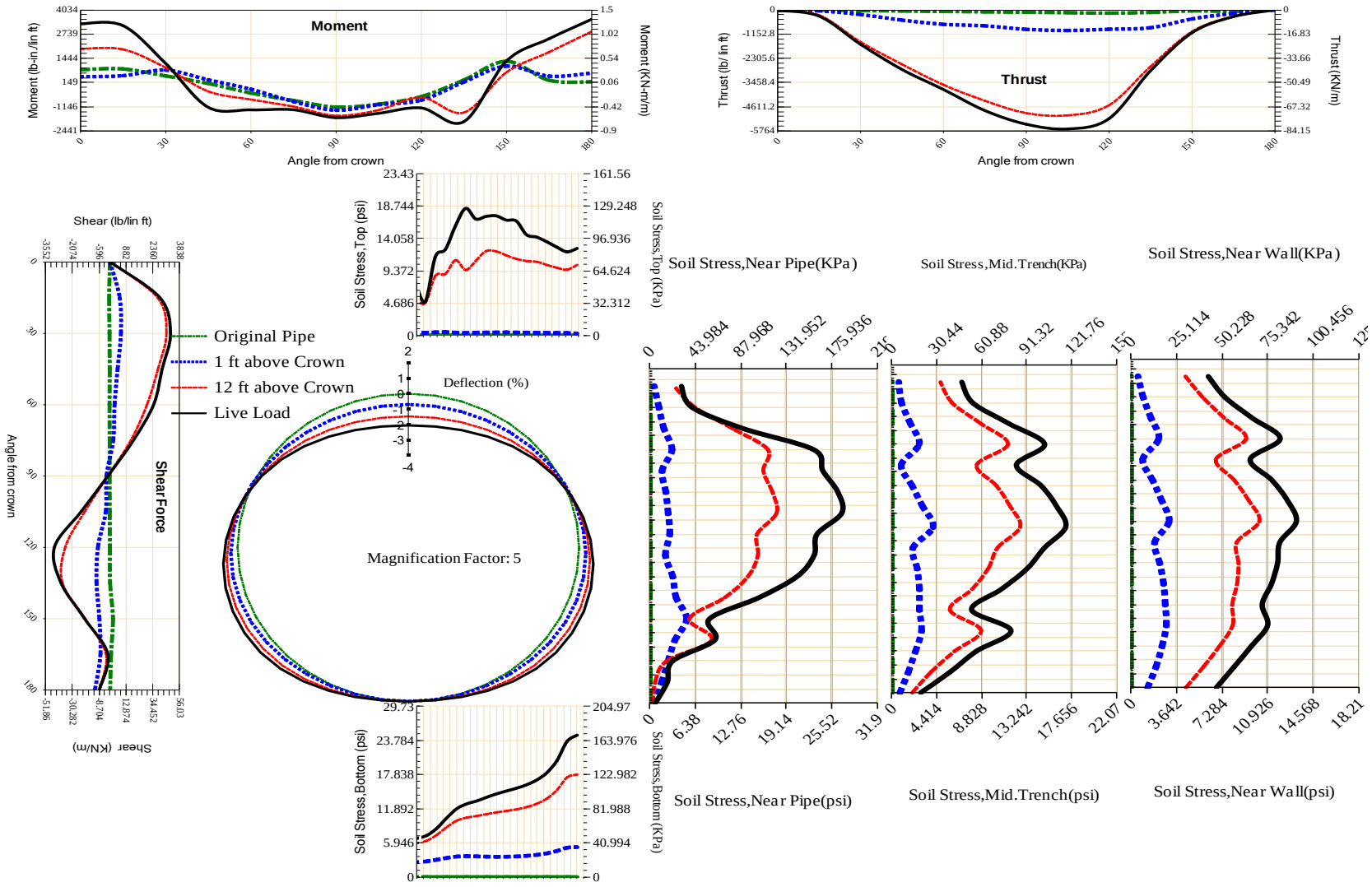

Figure A-515 Param-96-PW230-SF10SF-OD+108-EW5-H12-LiveLoad

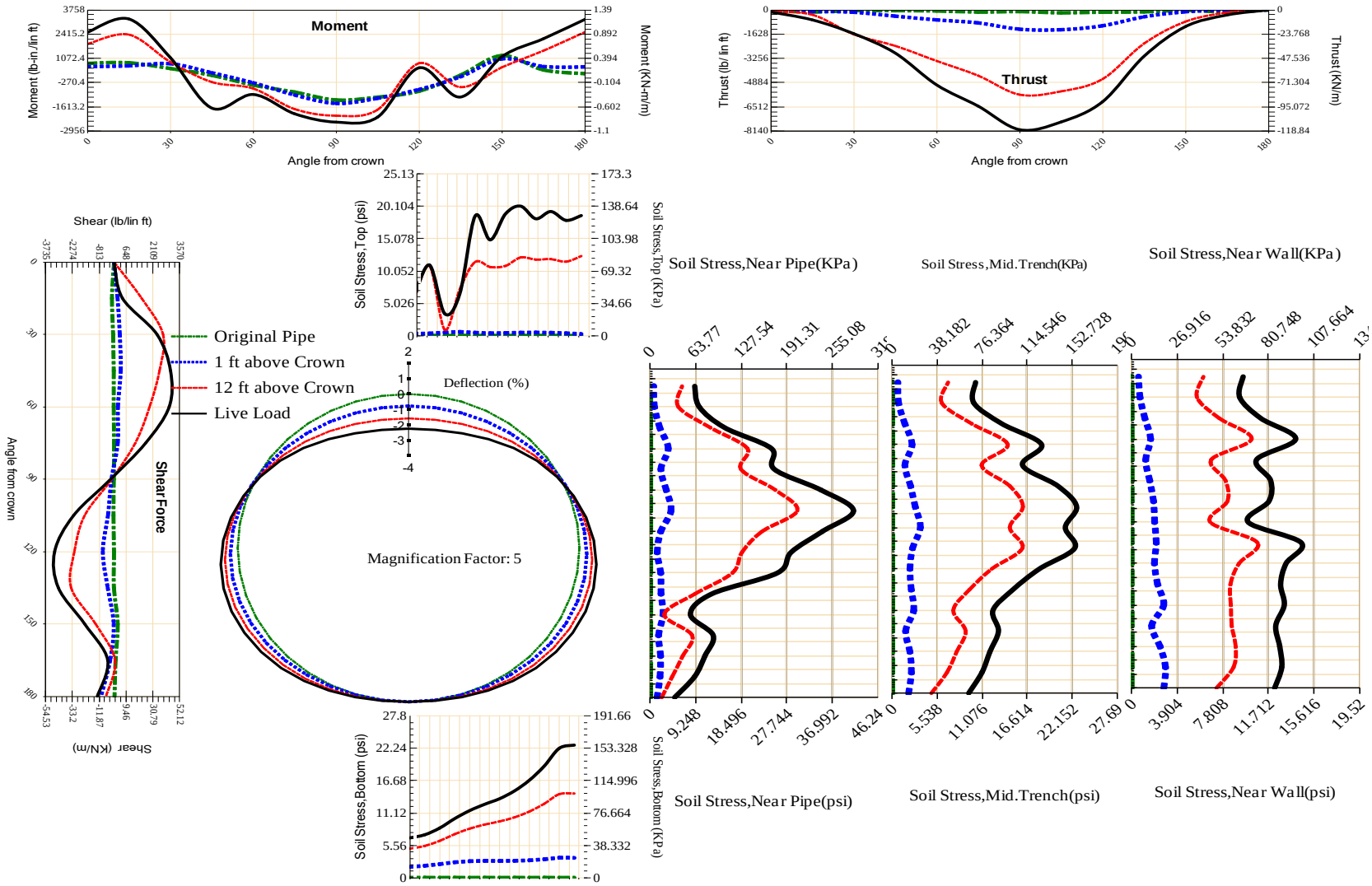

Figure A-516 Param-96-PW230-SF10SF-OD+48-EW5-H12-LiveLoad

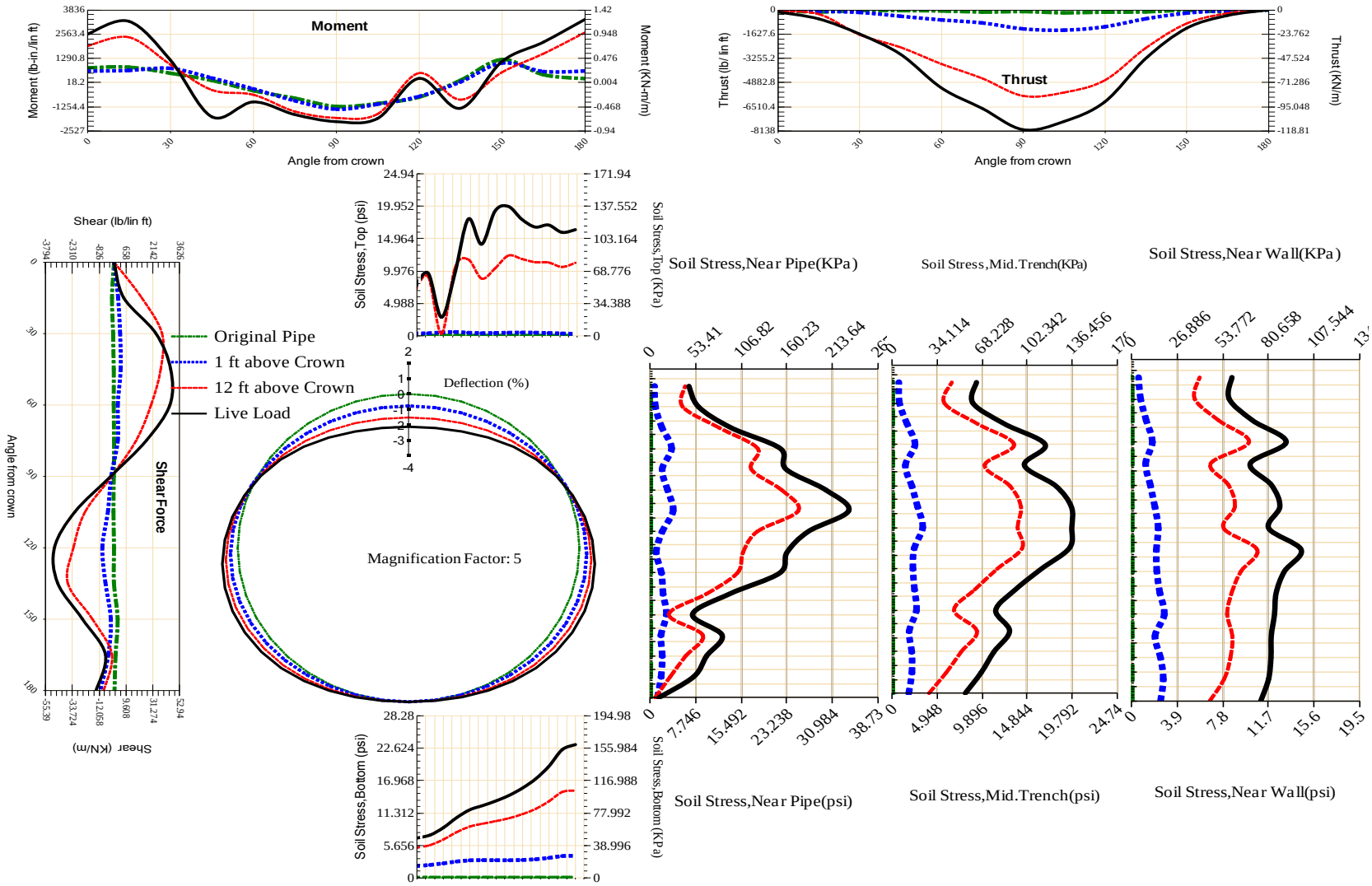

Figure A-517 Param-96-PW230-SF10SF-OD+60-EW5-H12-LiveLoad

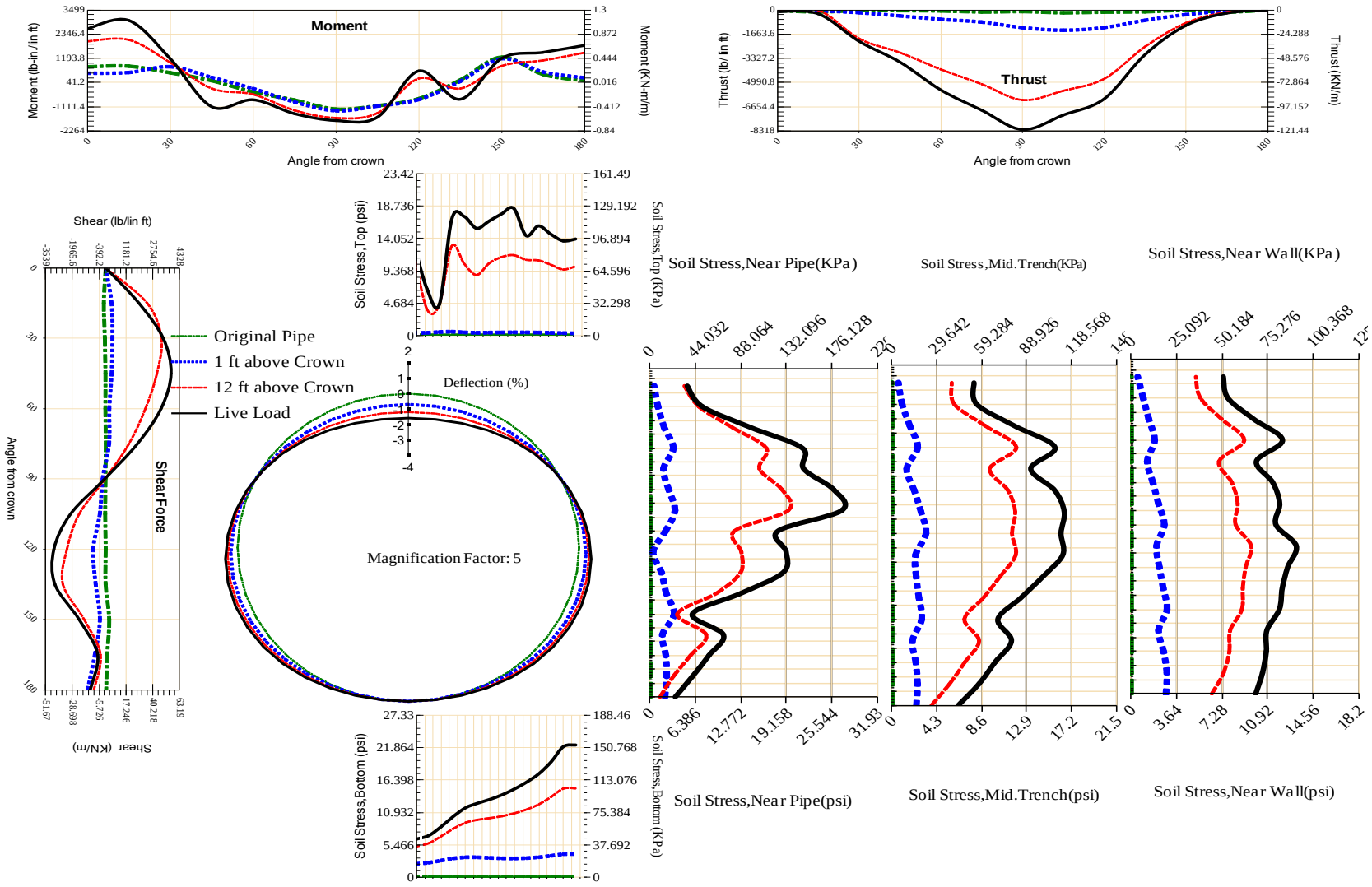

Figure A-518 Param-96-PW230-SF10SF-OD+72-EW10-H12-LiveLoad

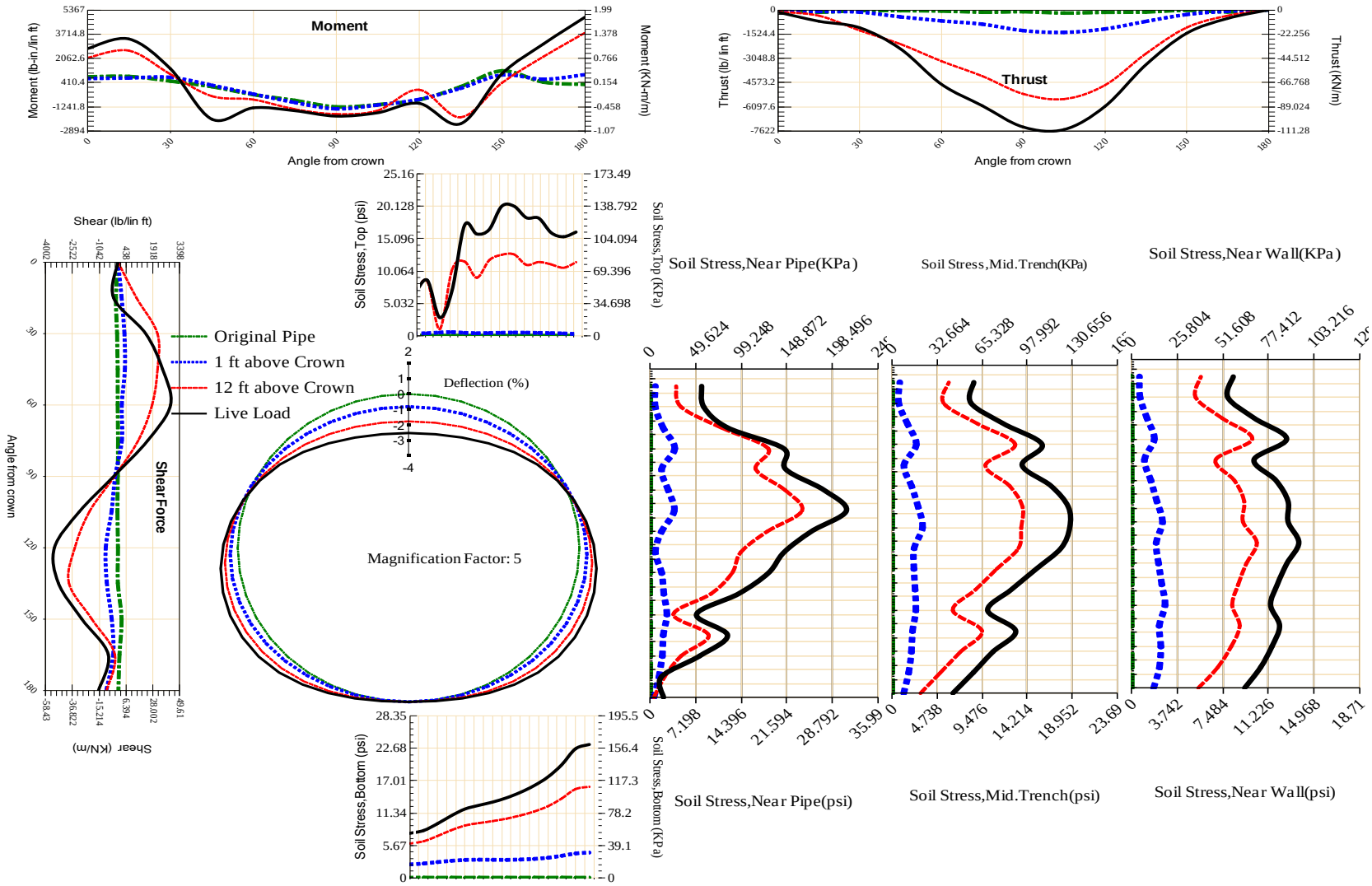

Figure A-519 Param-96-PW230-SF10SF-OD+72-EW3-H12-LiveLoad

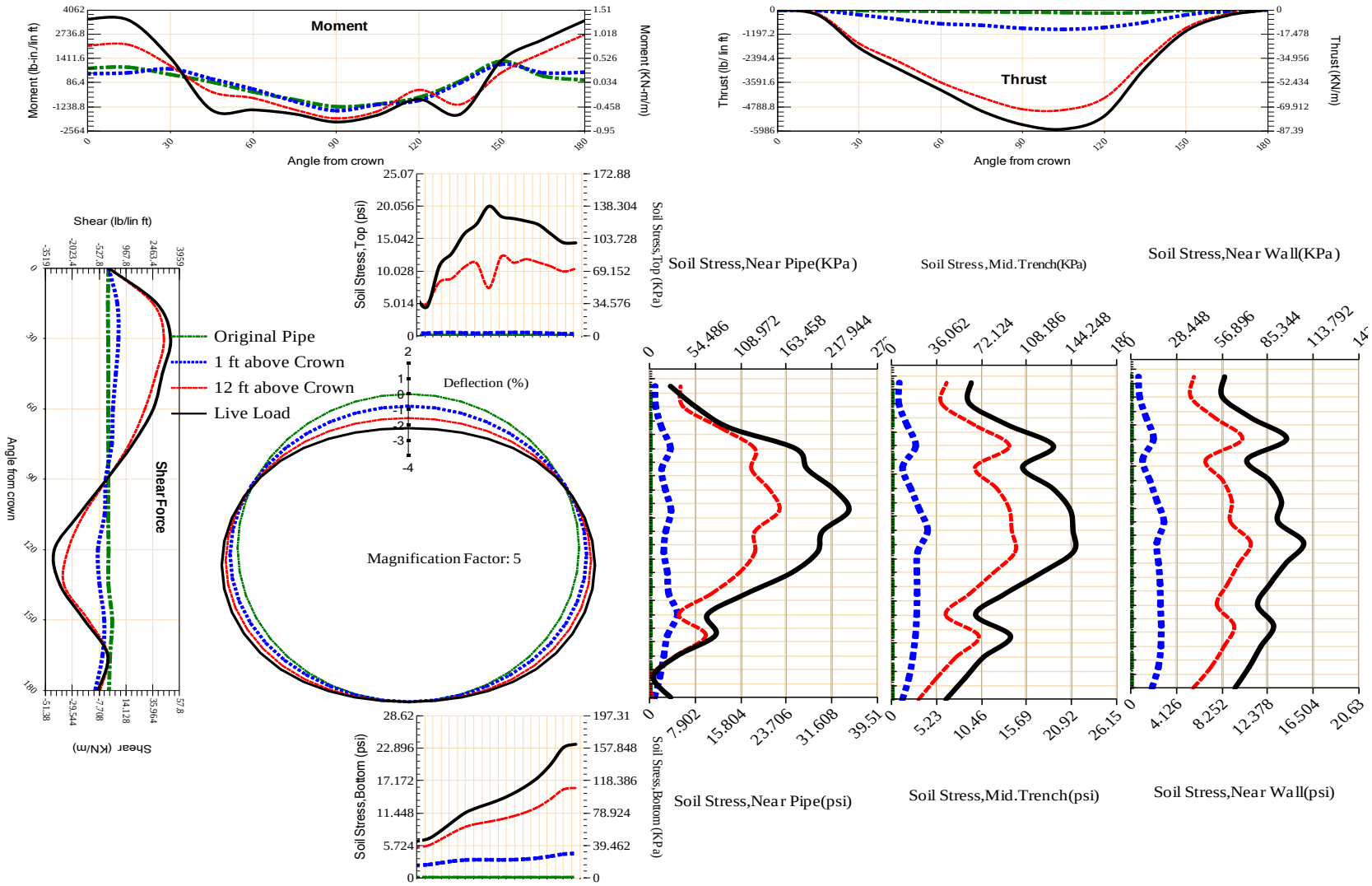

Figure A-520 Param-96-PW230-SF10SF-OD+72-EW5-H12-LiveLoad

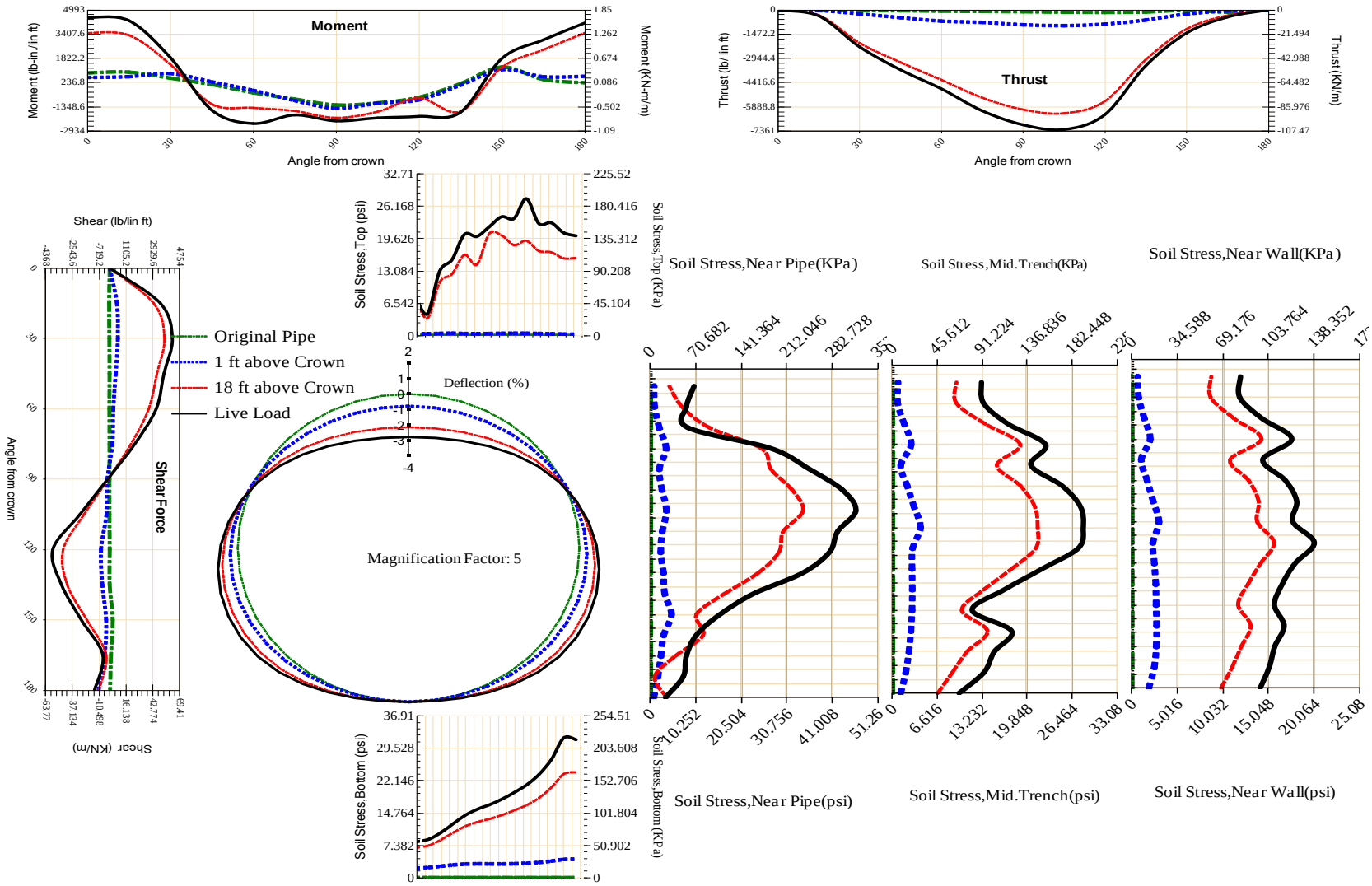

Figure A-521 Param-96-PW230-SF10SF-OD+72-EW5-H18-LiveLoad

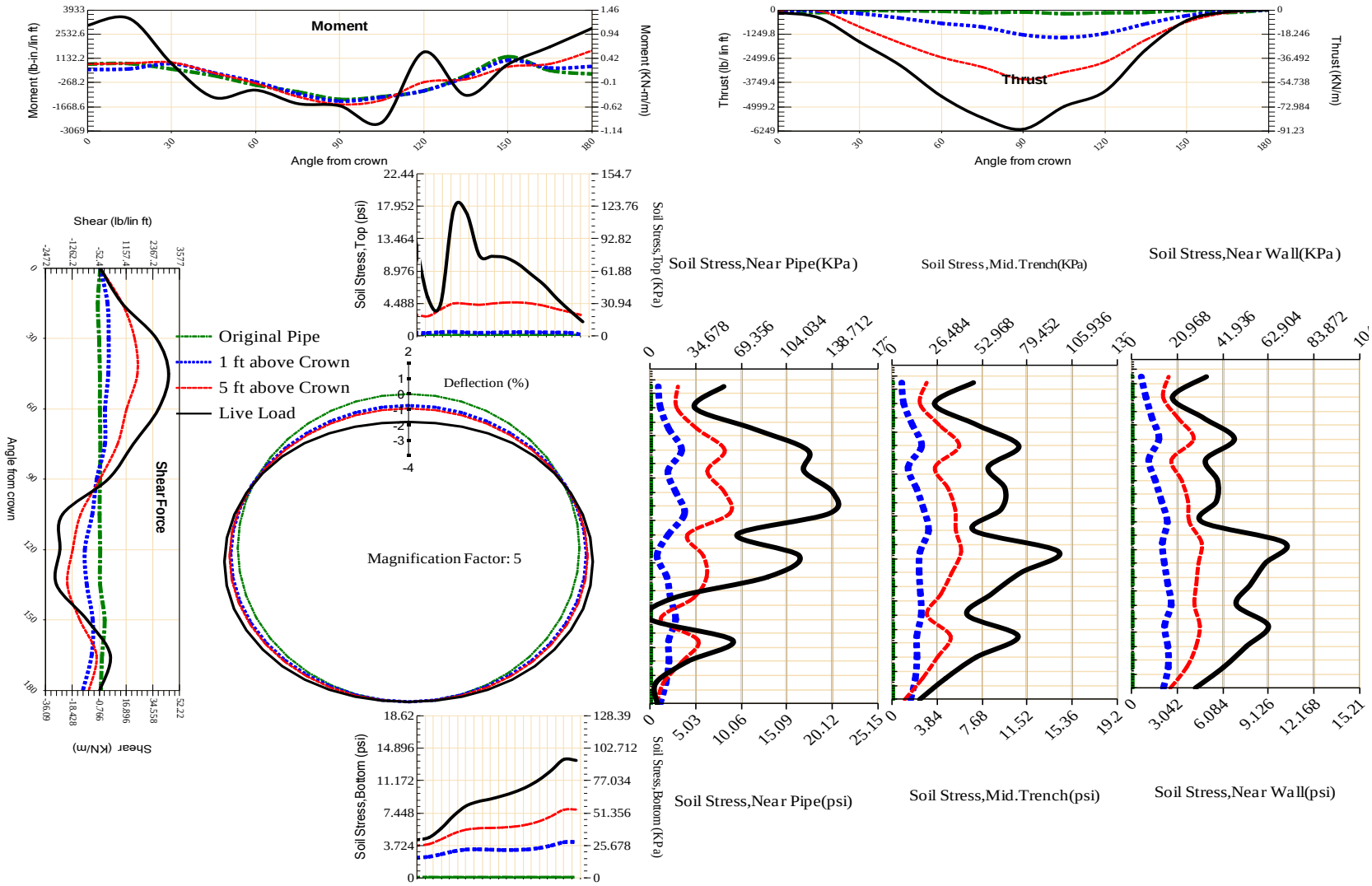

Figure A-522 Param-96-PW230-SF10SF-OD+72-EW5-H5-LiveLoad

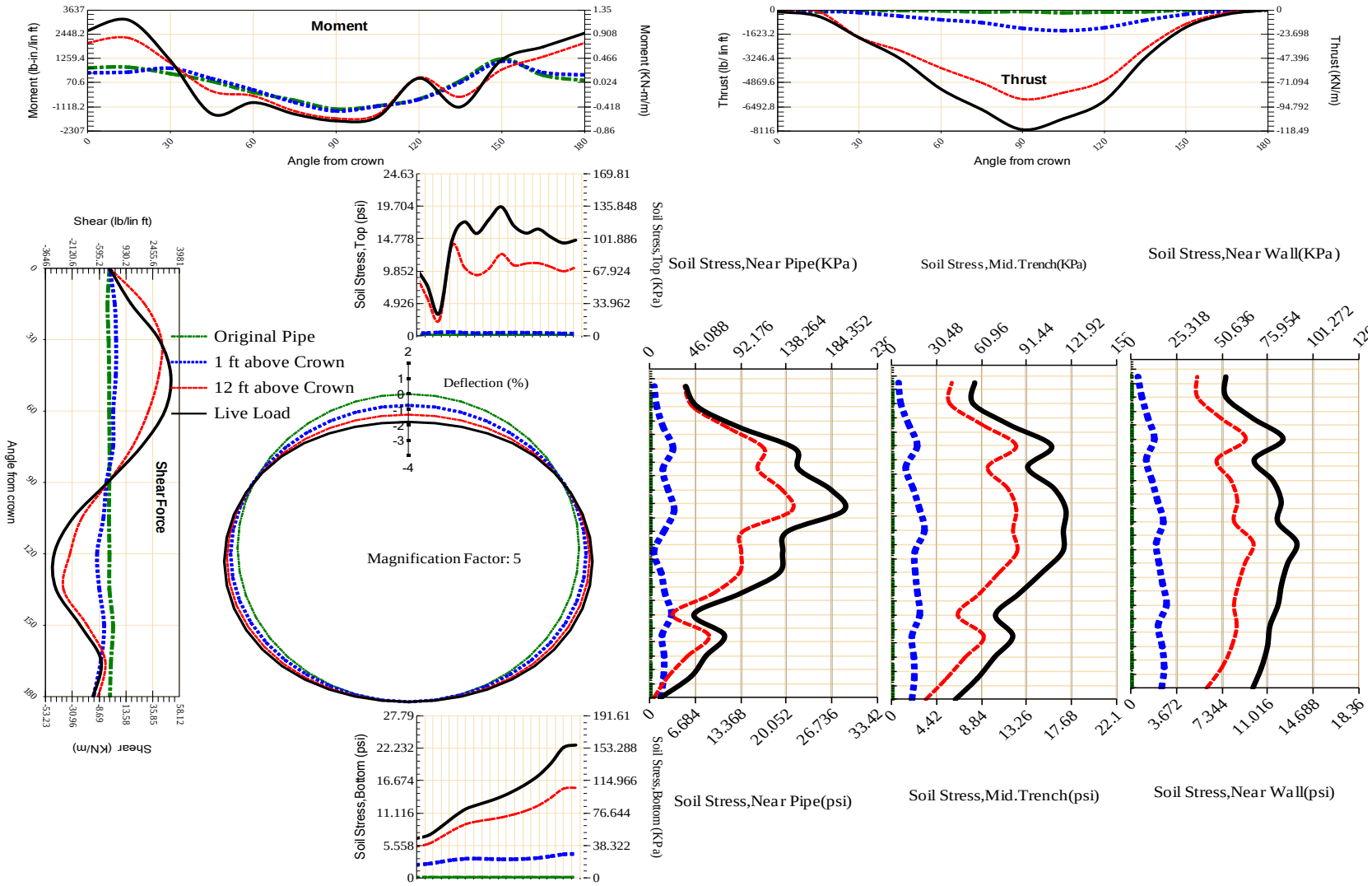

Figure A-523 Param-96-PW230-SF10SF-OD+72-EW7-H12-LiveLoad

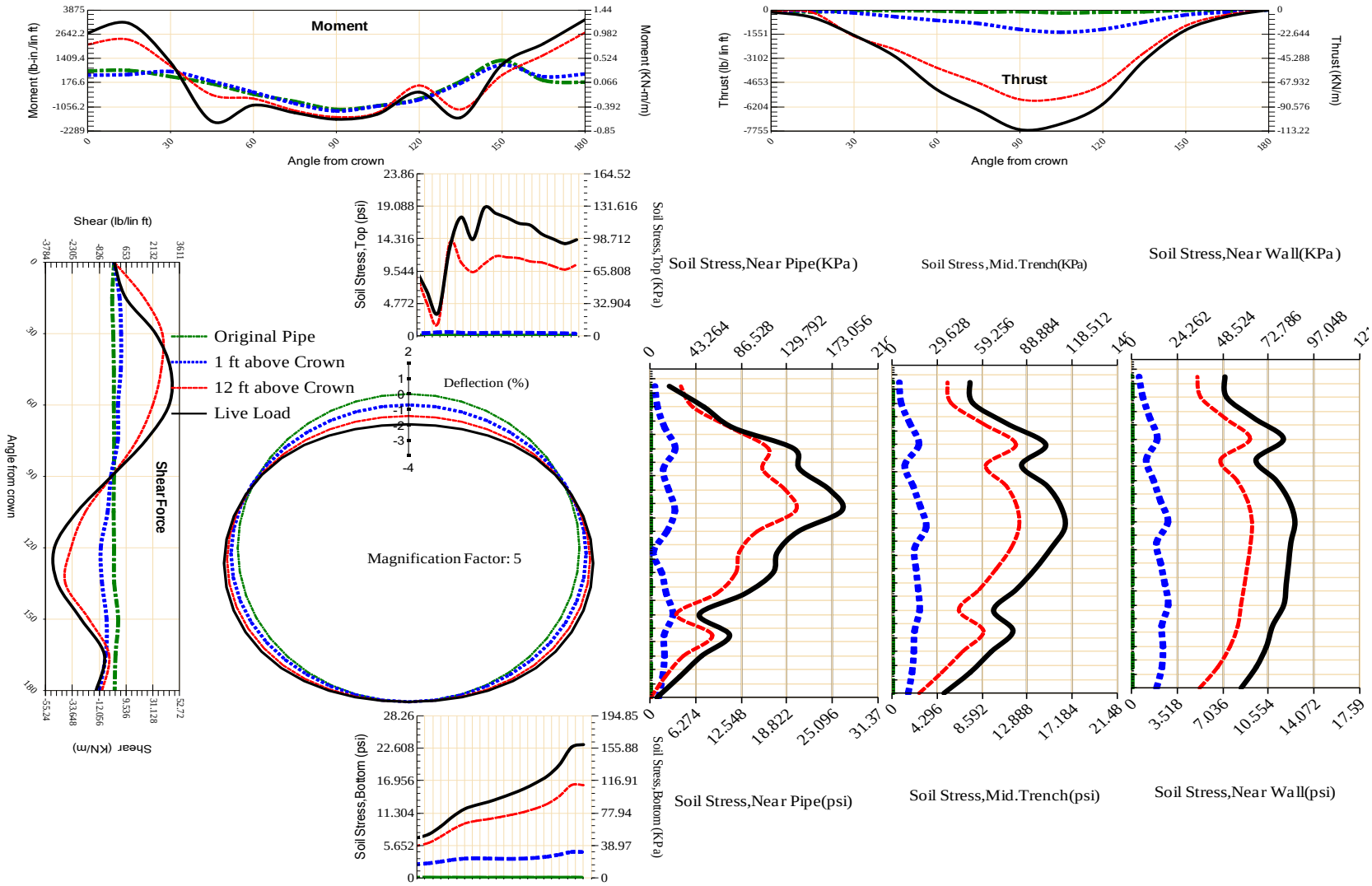

Figure A-524 Param-96-PW230-SF10SF-OD+84-EW5-H12-LiveLoad

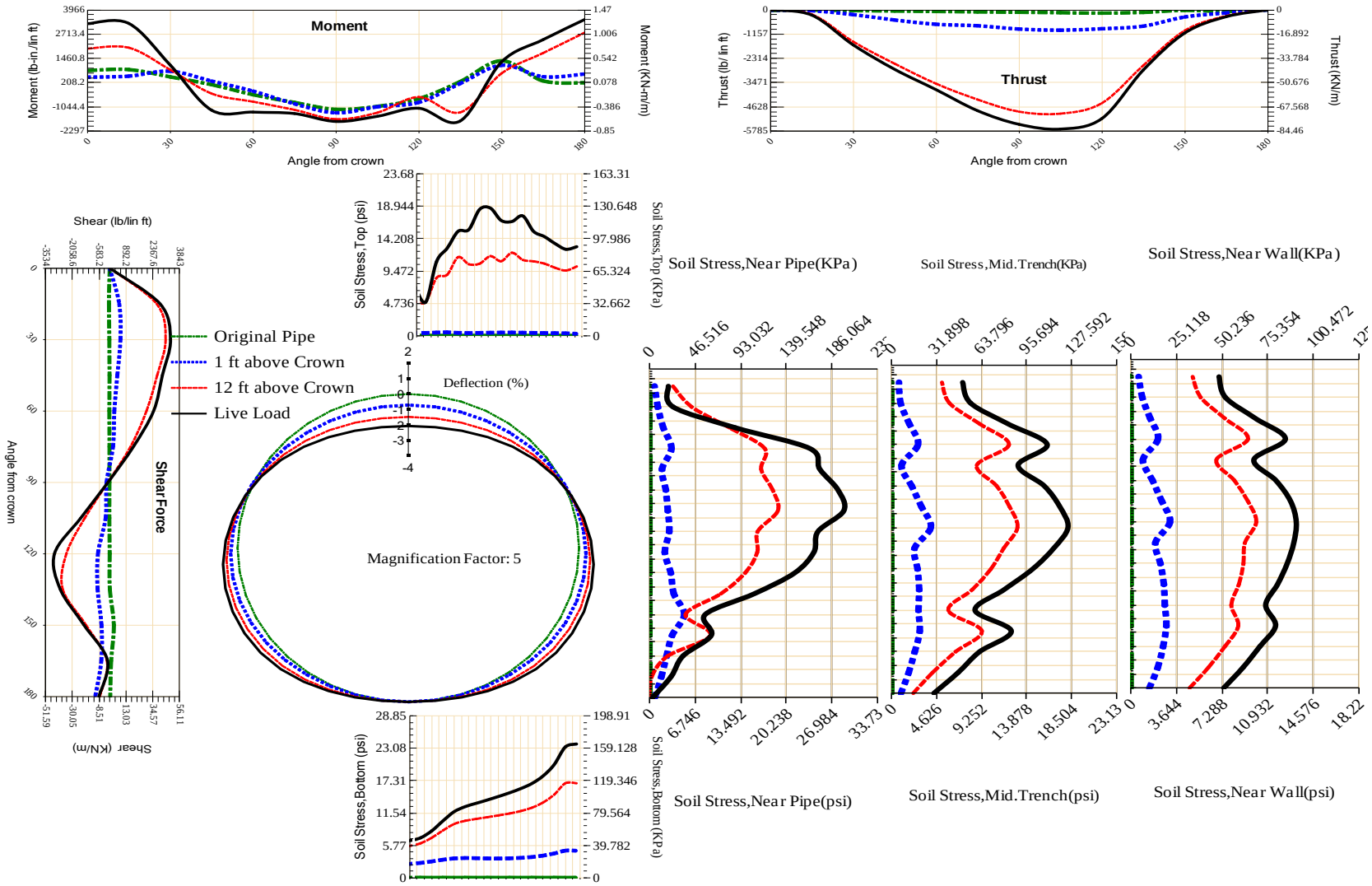

Figure A-525 Param-96-PW230-SF10SF-OD+96-EW5-H12-LiveLoad

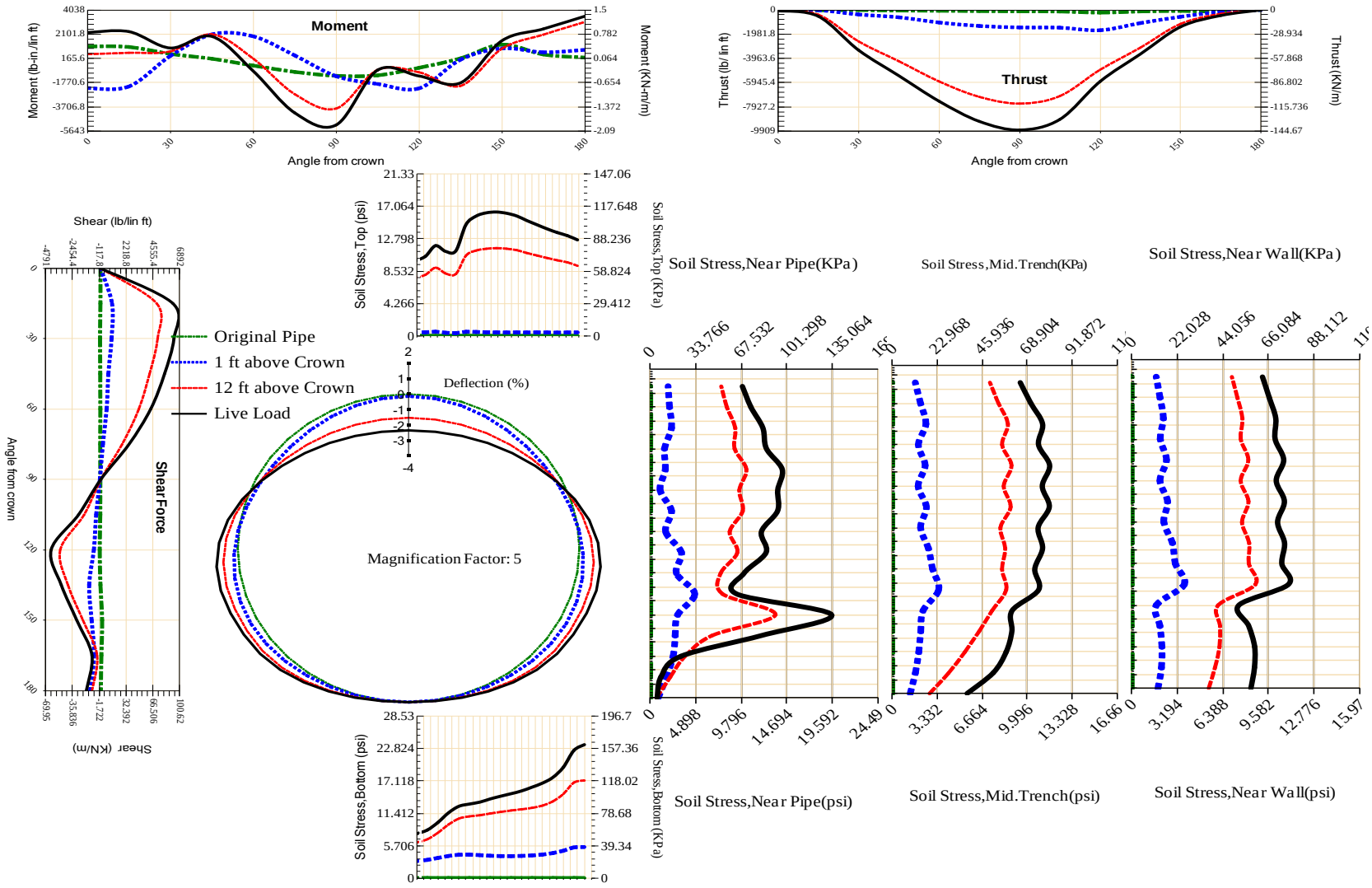

Figure A-526 Param-96-PW230-SF3OR-OD+108-EW5-H12-LiveLoad

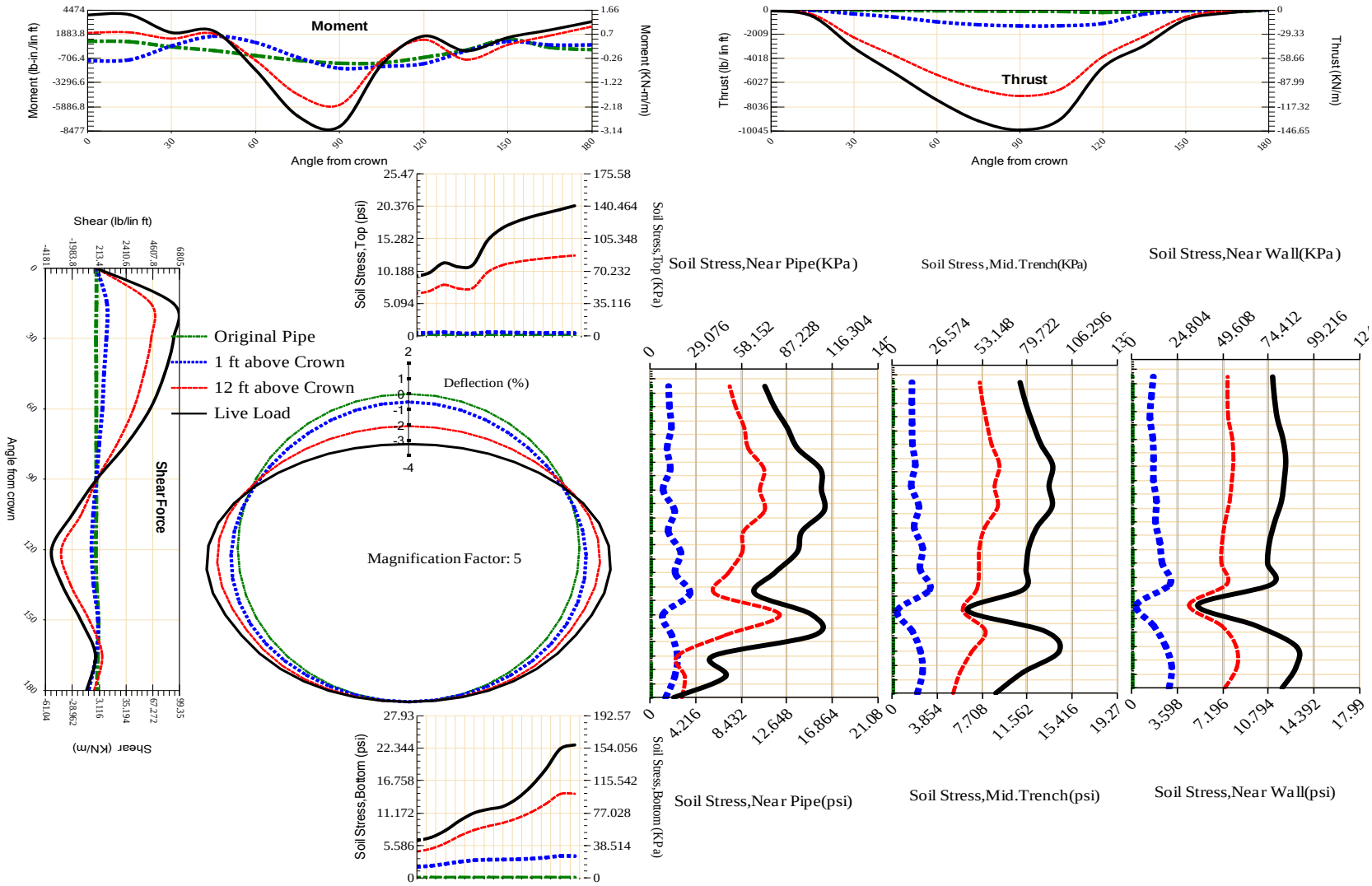

Figure A-527 Param-96-PW230-SF3OR-OD+48-EW5-H12-LiveLoad

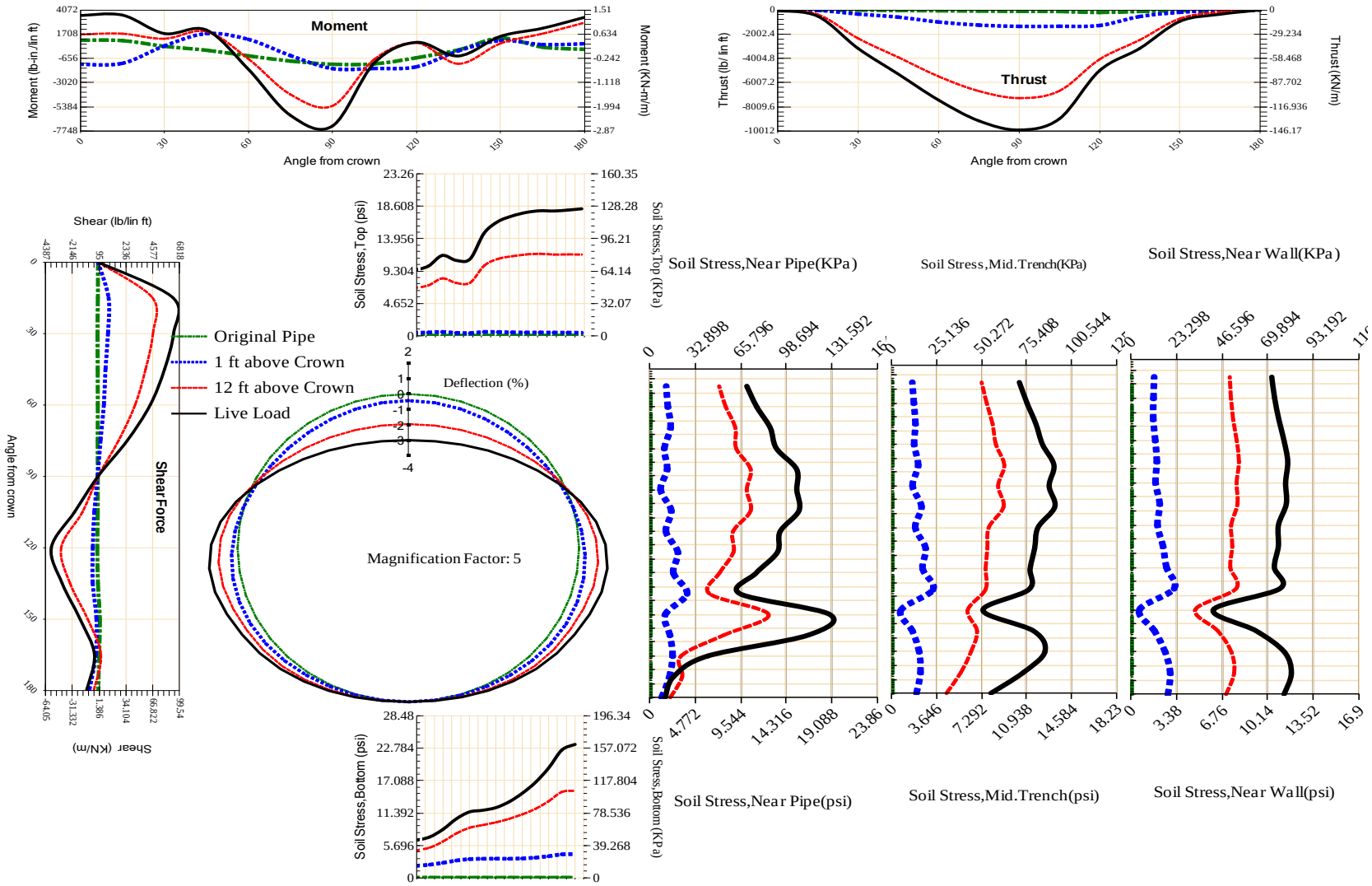

Figure A-528 Param-96-PW230-SF3OR-OD+60-EW5-H12-LiveLoad

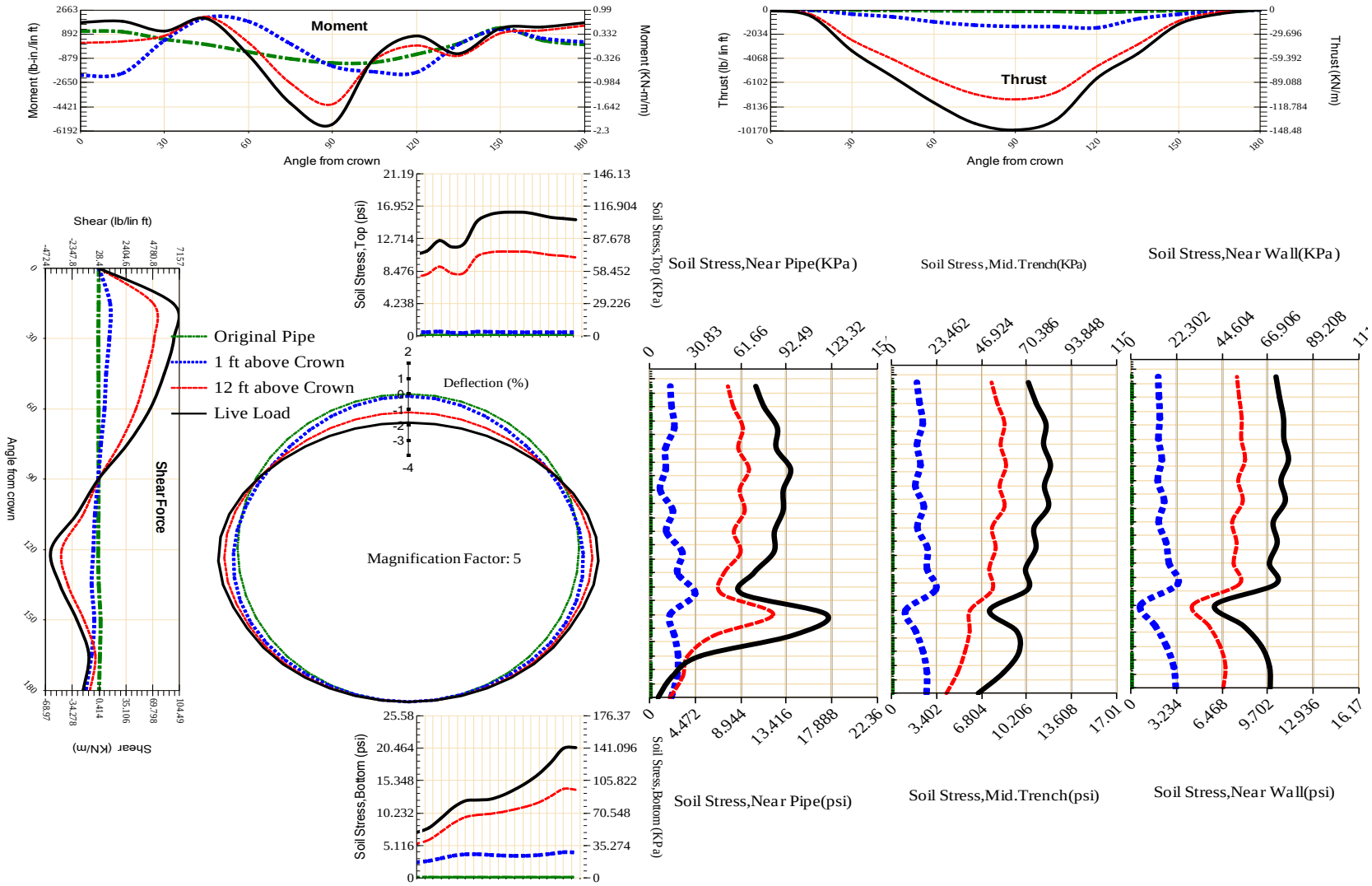

Figure A-529 Param-96-PW230-SF3OR-OD+72-EW10-H12-LiveLoad

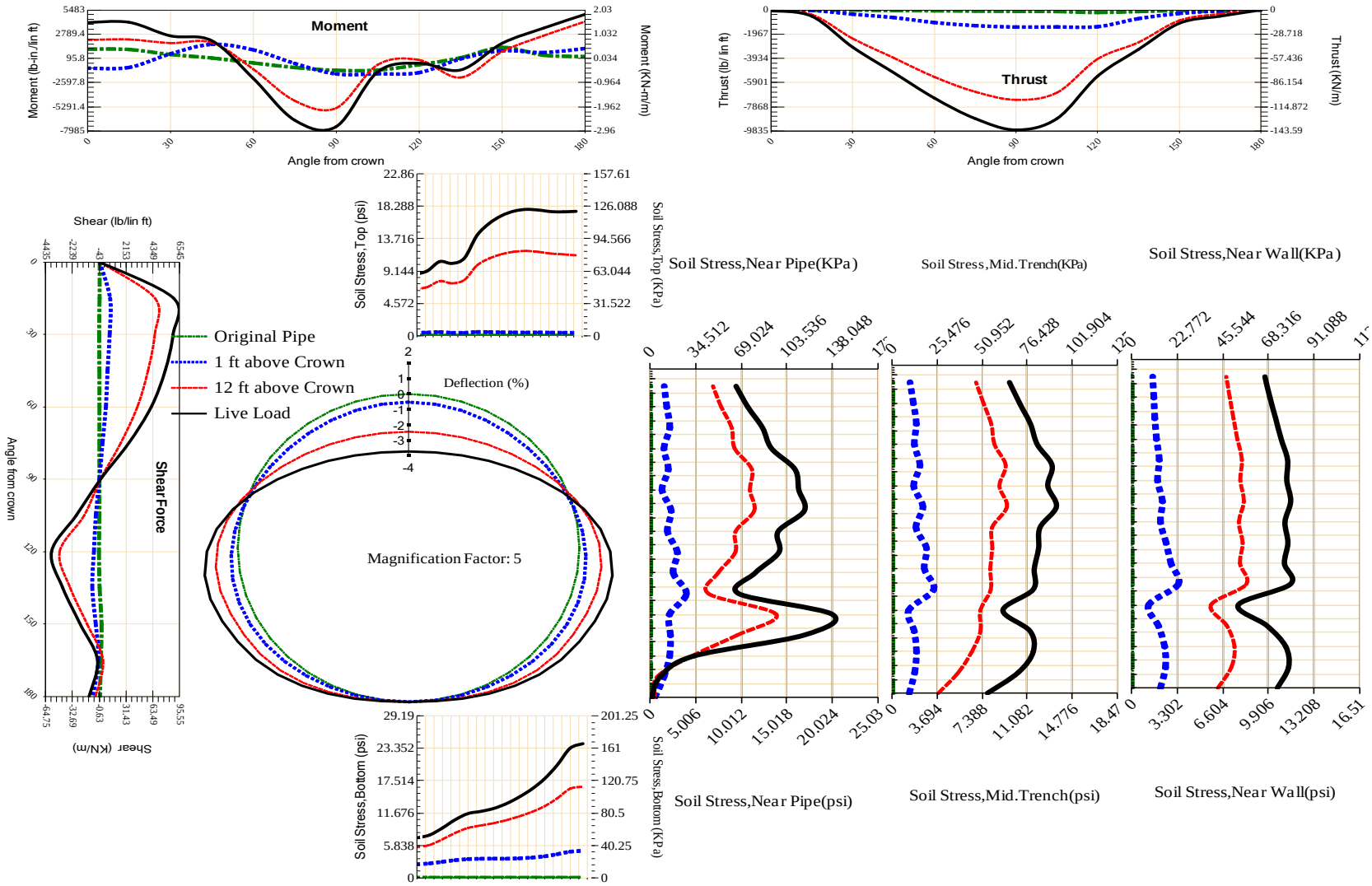

Figure A-530 Param-96-PW230-SF3OR-OD+72-EW3-H12-LiveLoad

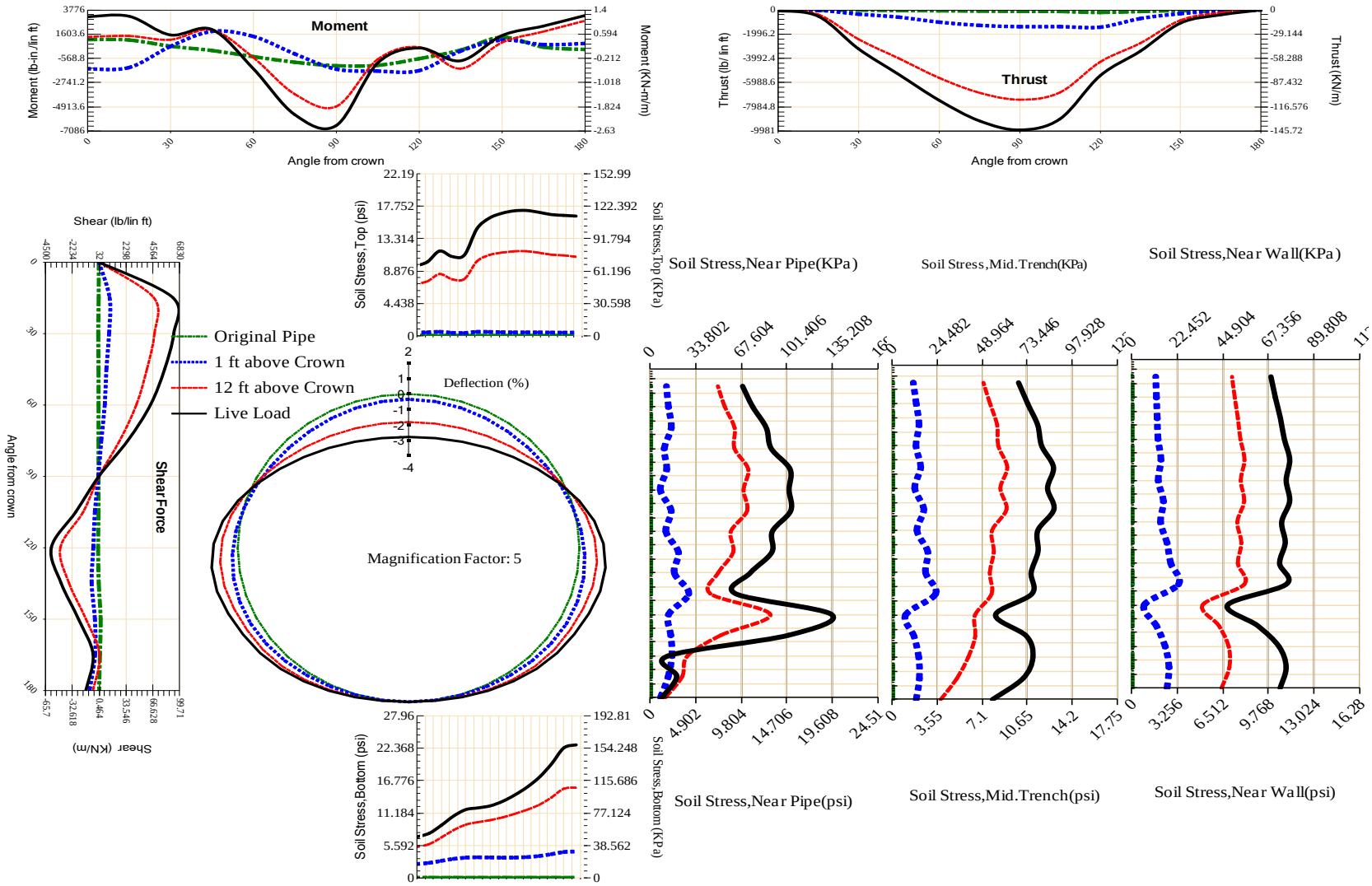

Figure A-531 Param-96-PW230-SF3OR-OD+72-EW5-H12-LiveLoad

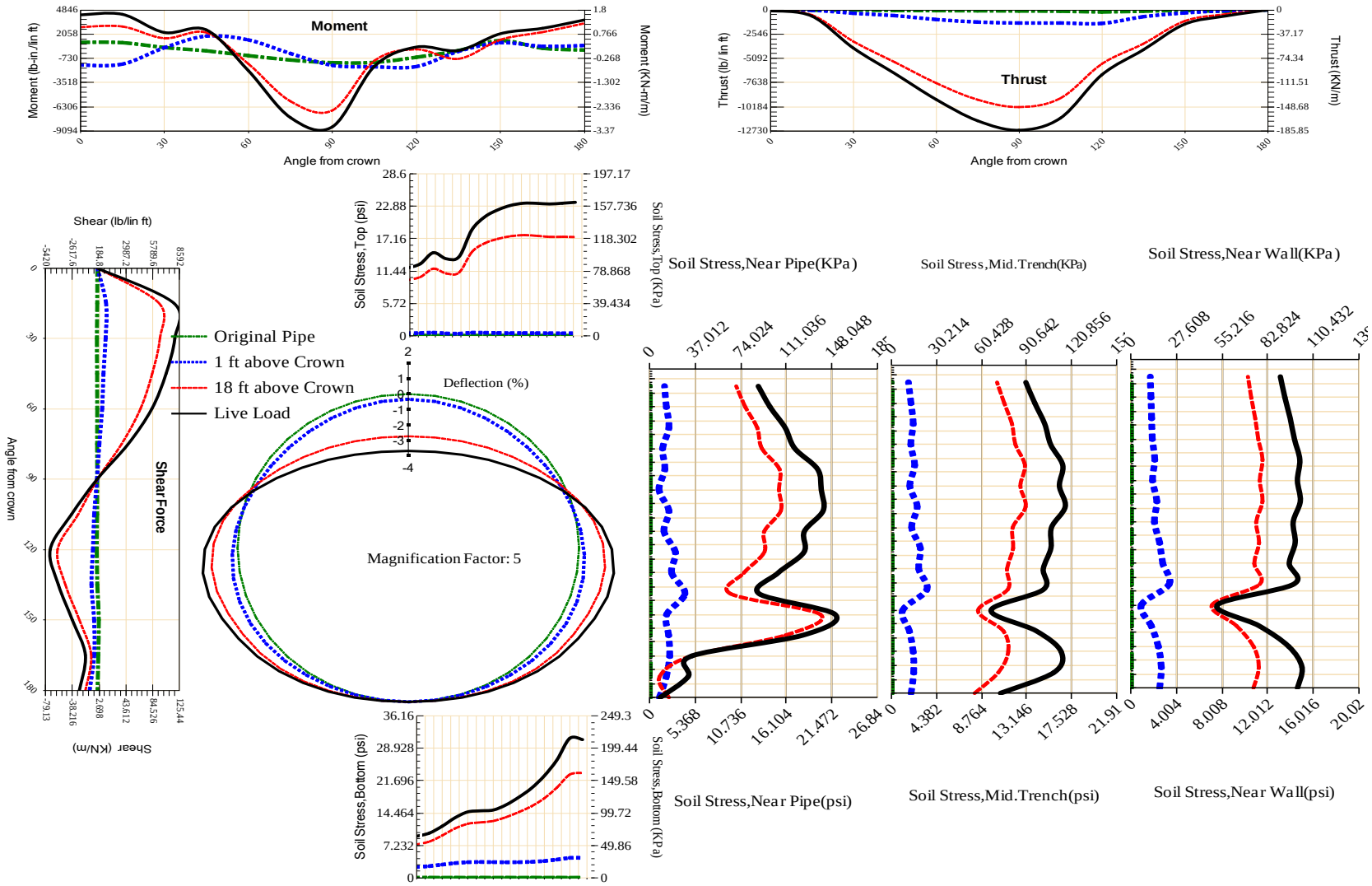

Figure A-532 Param-96-PW230-SF3OR-OD+72-EW5-H18-LiveLoad

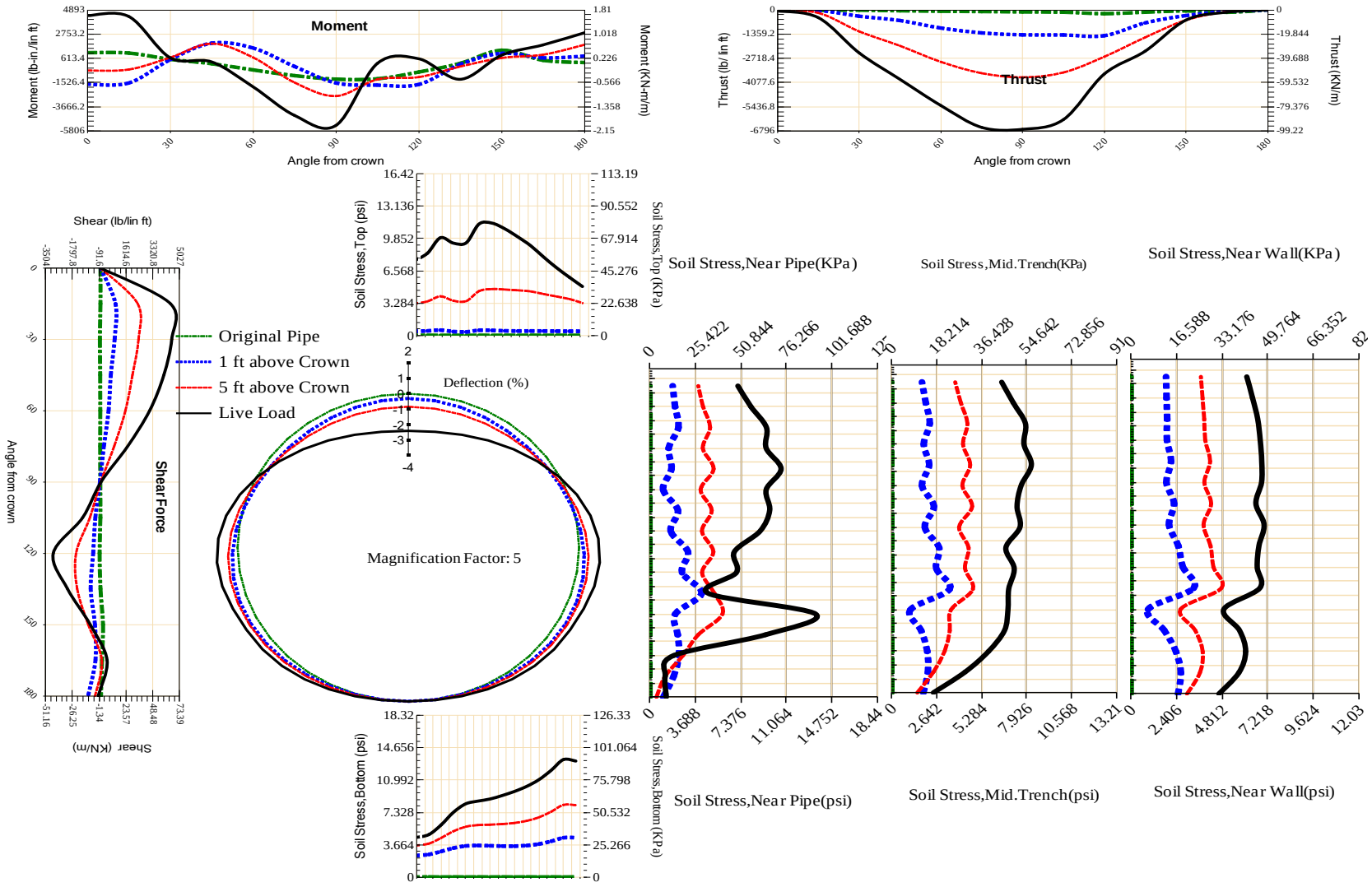

Figure A-533 Param-96-PW230-SF3OR-OD+72-EW5-H5-LiveLoad

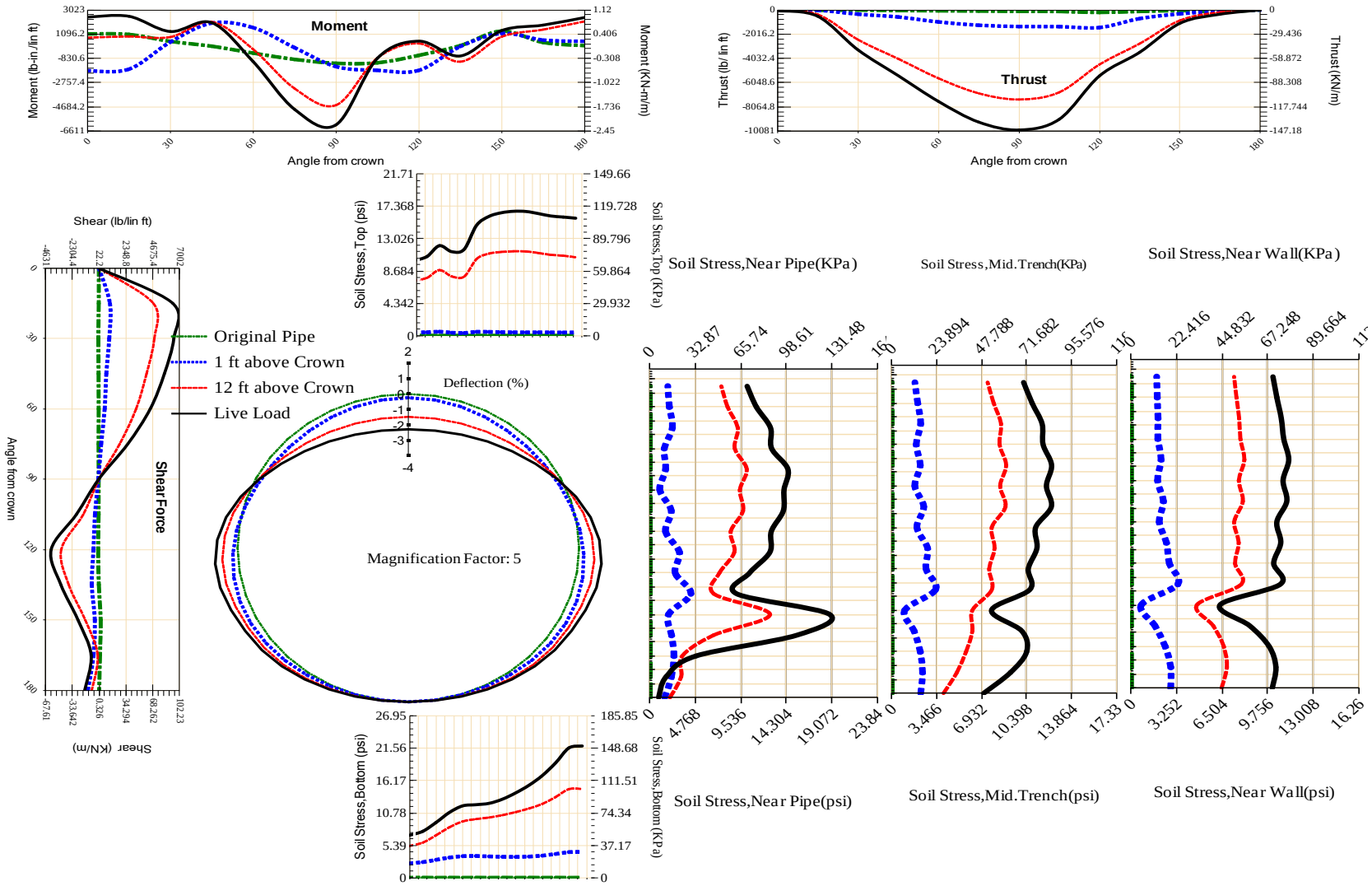

Figure A-534 Param-96-PW230-SF3OR-OD+72-EW7-H12-LiveLoad

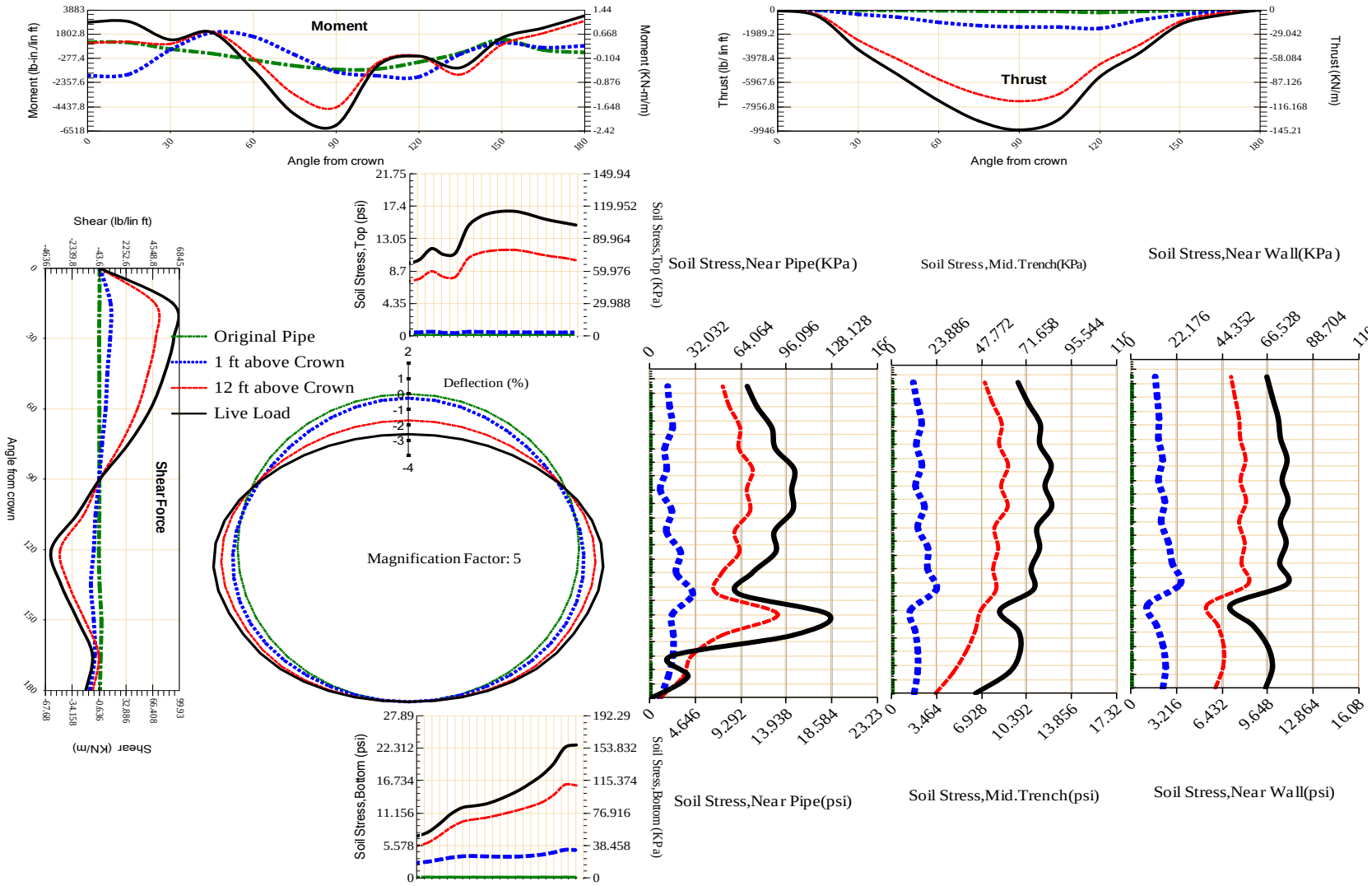

Figure A-535 Param-96-PW230-SF3OR-OD+84-EW5-H12-LiveLoad

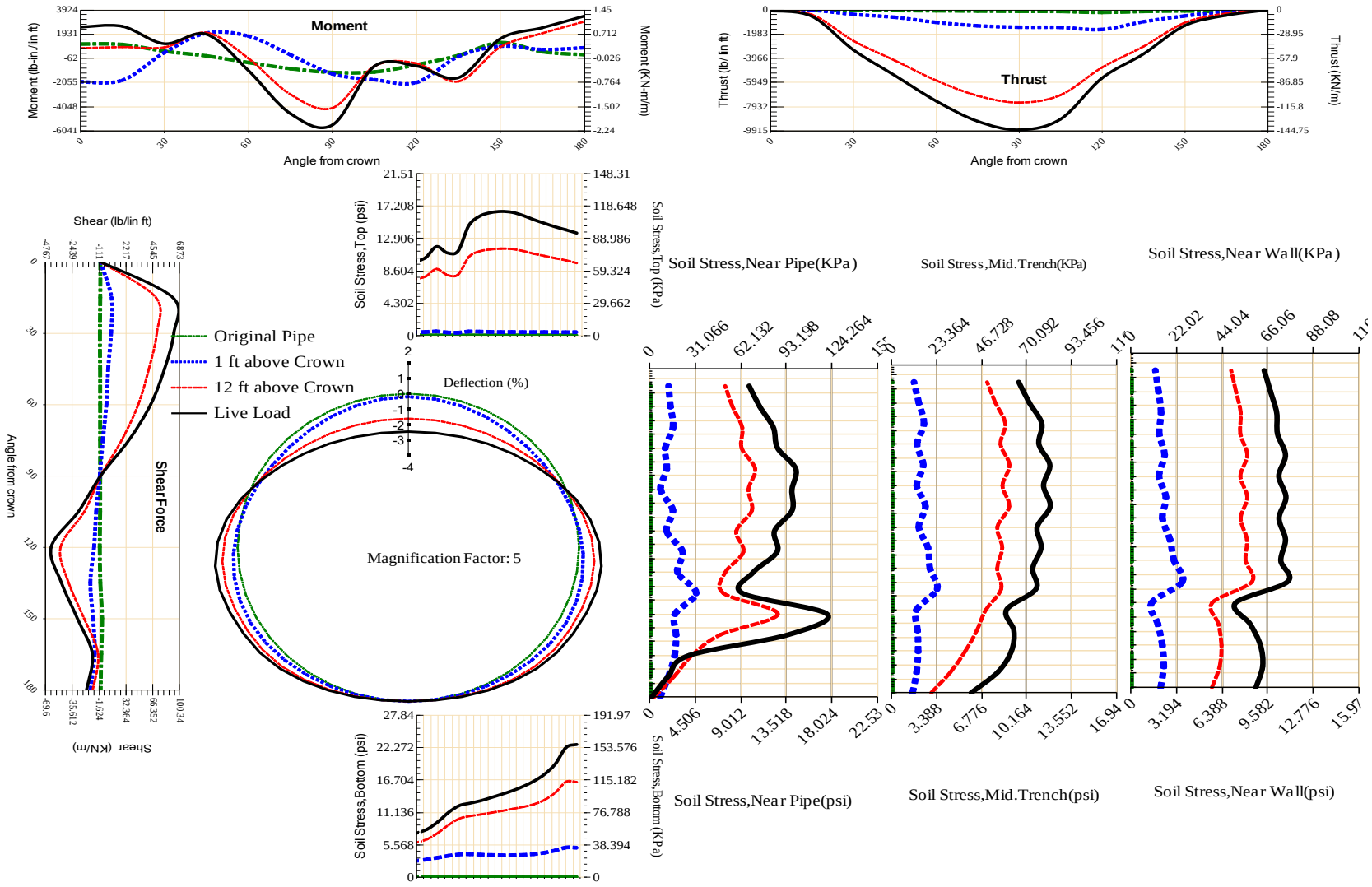

Figure A-536 Param-96-PW230-SF3OR-OD+96-EW5-H12-LiveLoad

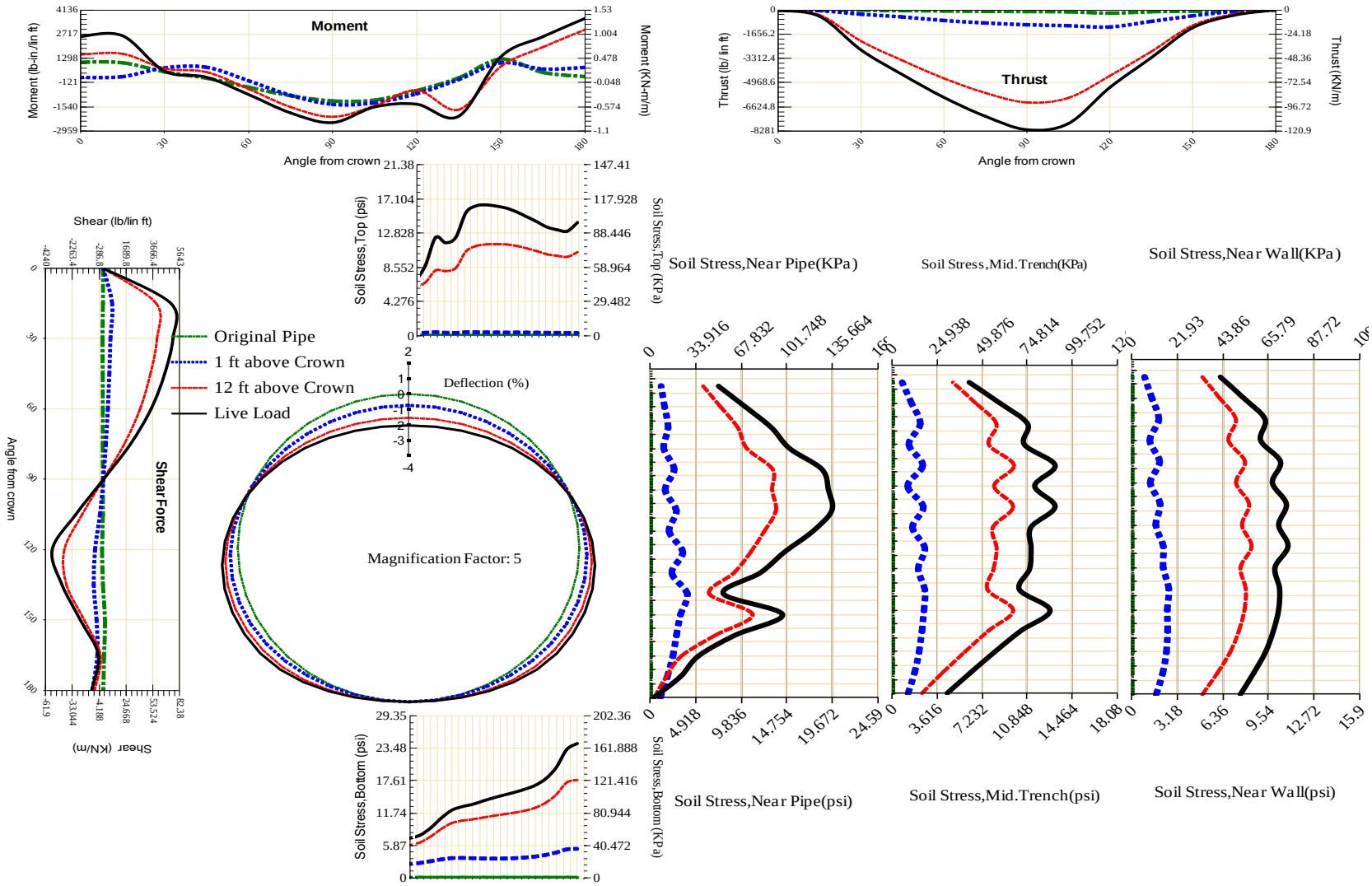

Figure A-537 Param-96-PW230-SF3TR-OD+108-EW5-H12-LiveLoad

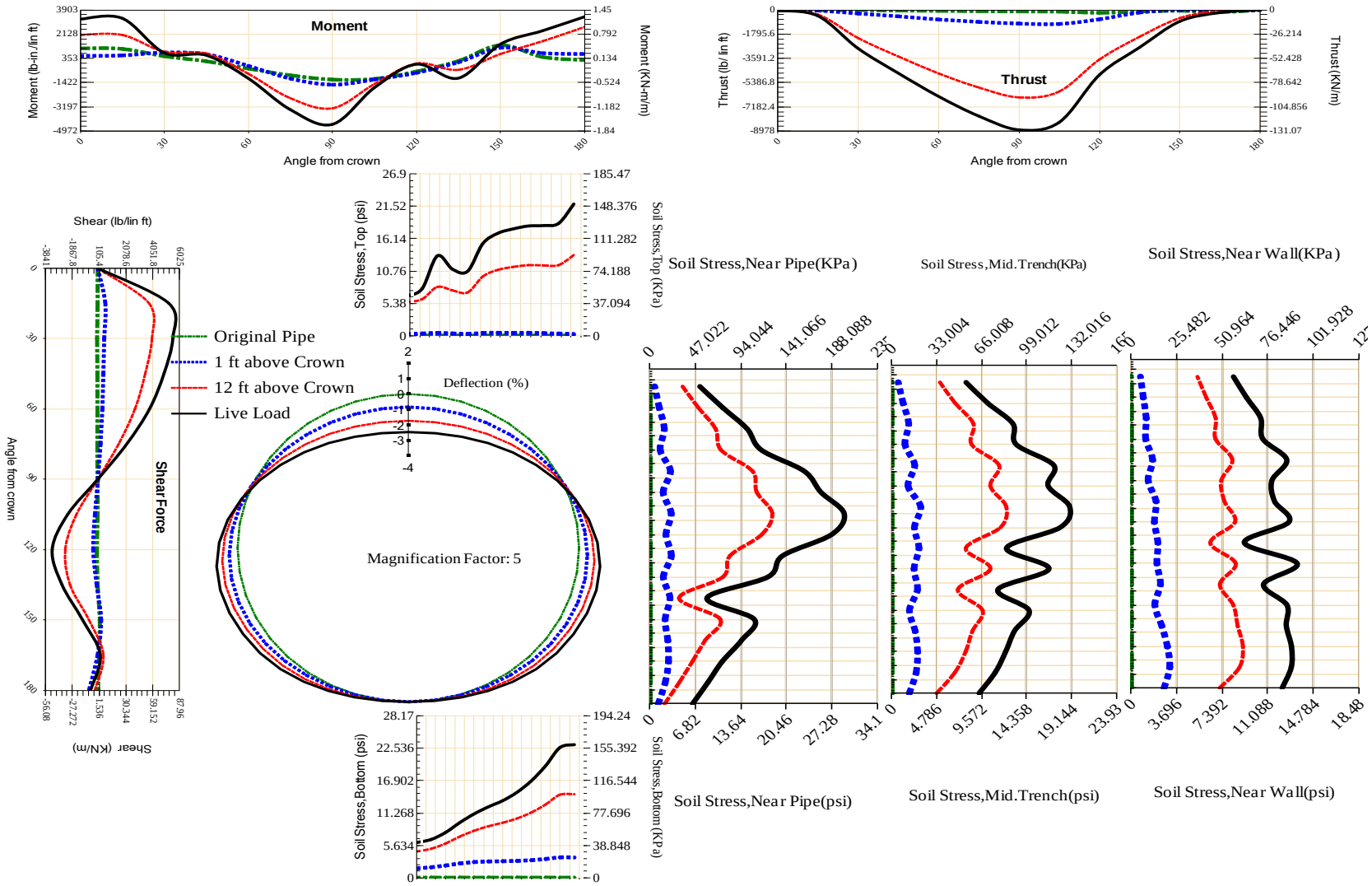

Figure A-538 Param-96-PW230-SF3TR-OD+48-EW5-H12-LiveLoad

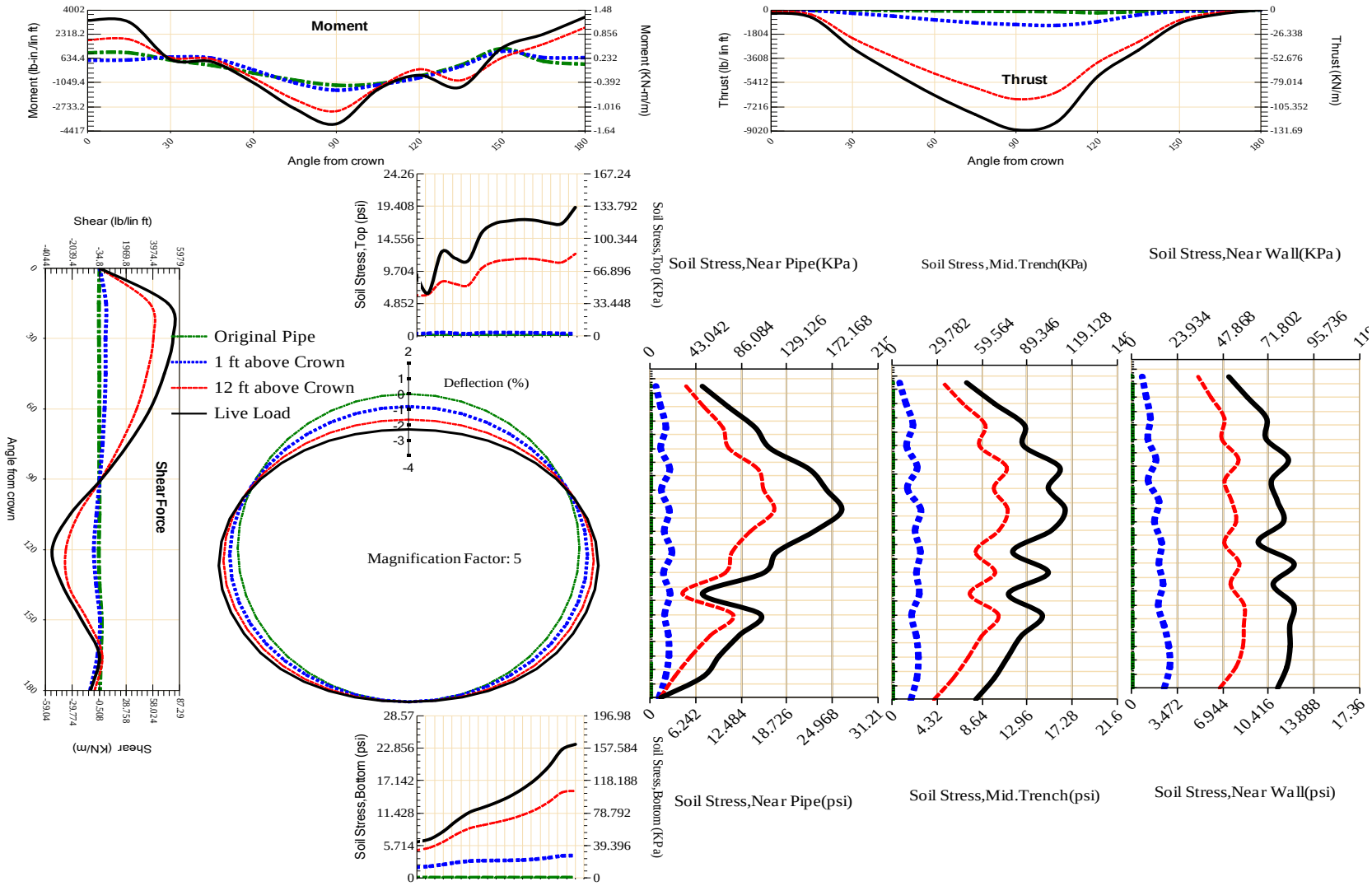

Figure A-539 Param-96-PW230-SF3TR-OD+60-EW5-H12-LiveLoad

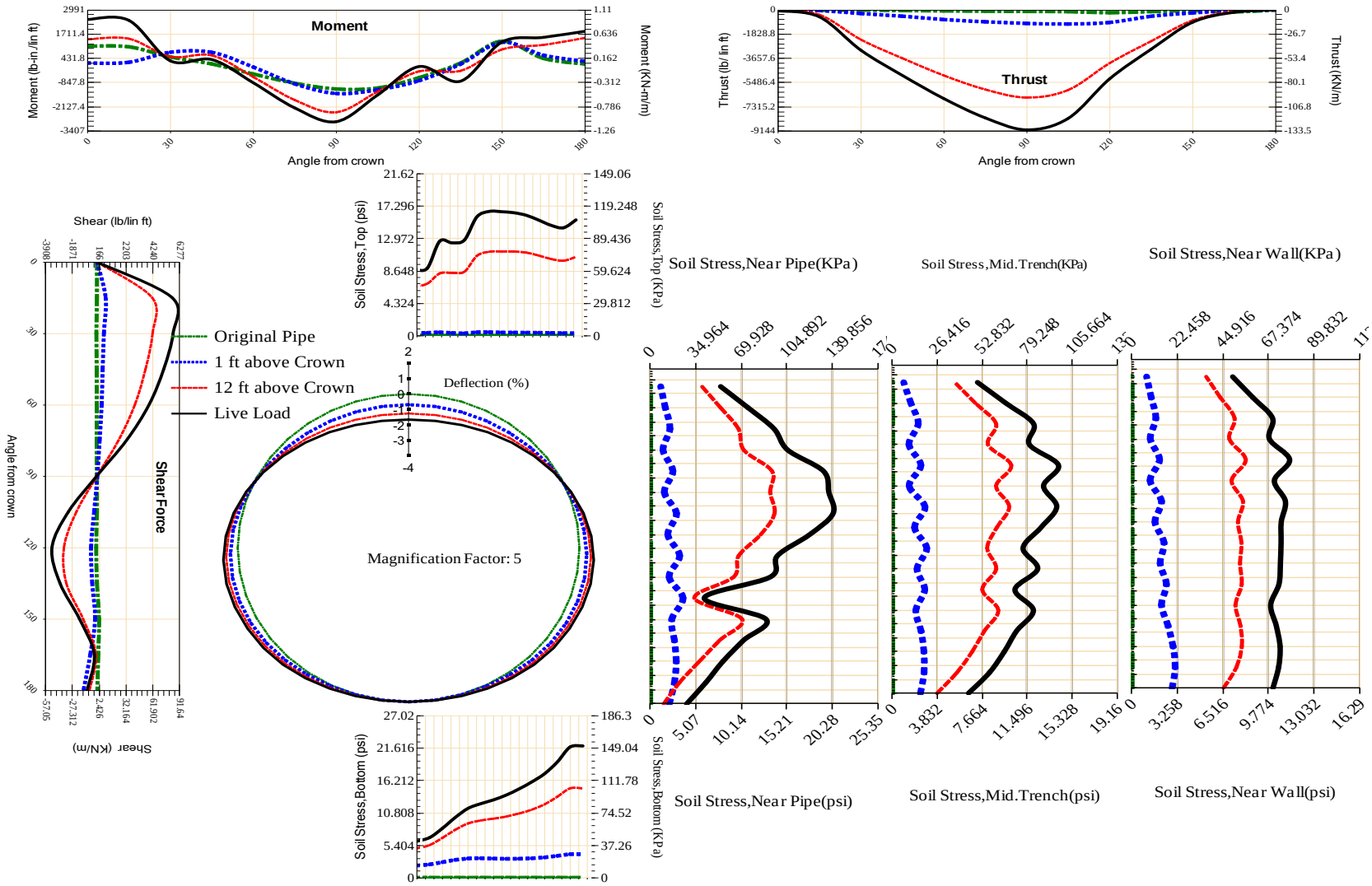

Figure A-540 Param-96-PW230-SF3TR-OD+72-EW10-H12-LiveLoad

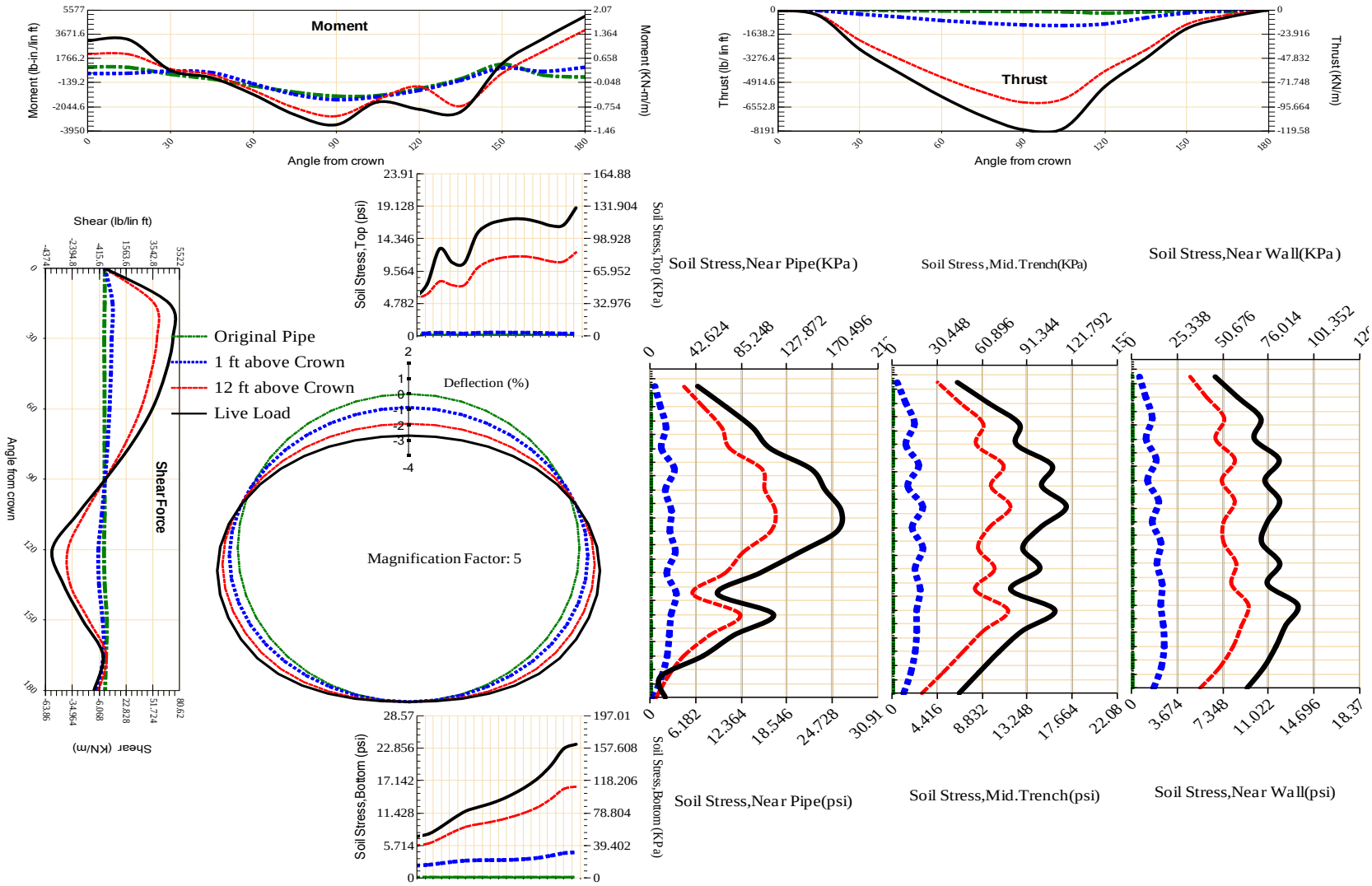

Figure A-541 Param-96-PW230-SF3TR-OD+72-EW3-H12-LiveLoad

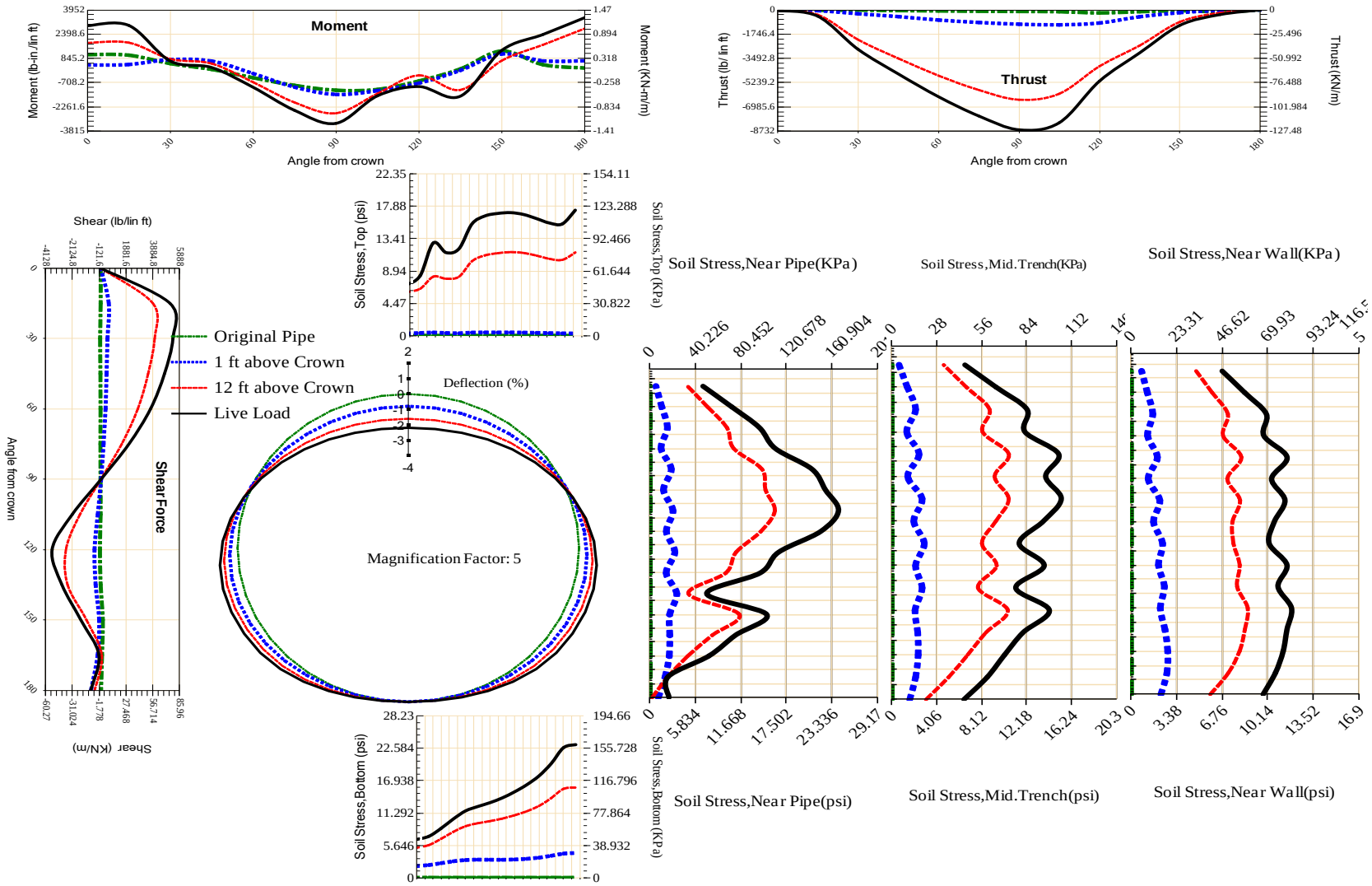

Figure A-542 Param-96-PW230-SF3TR-OD+72-EW5-H12-LiveLoad

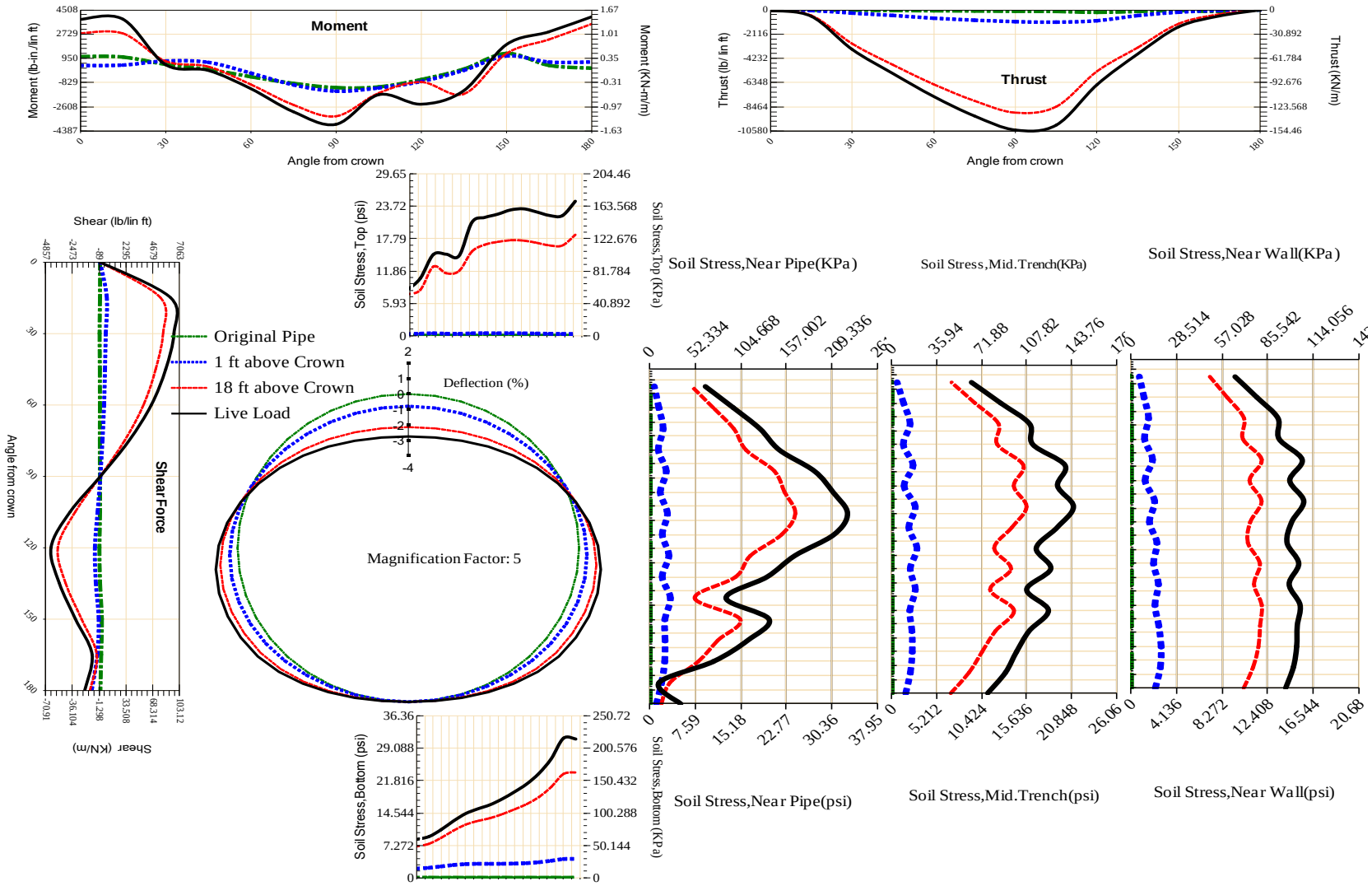

Figure A-543 Param-96-PW230-SF3TR-OD+72-EW5-H18-LiveLoad

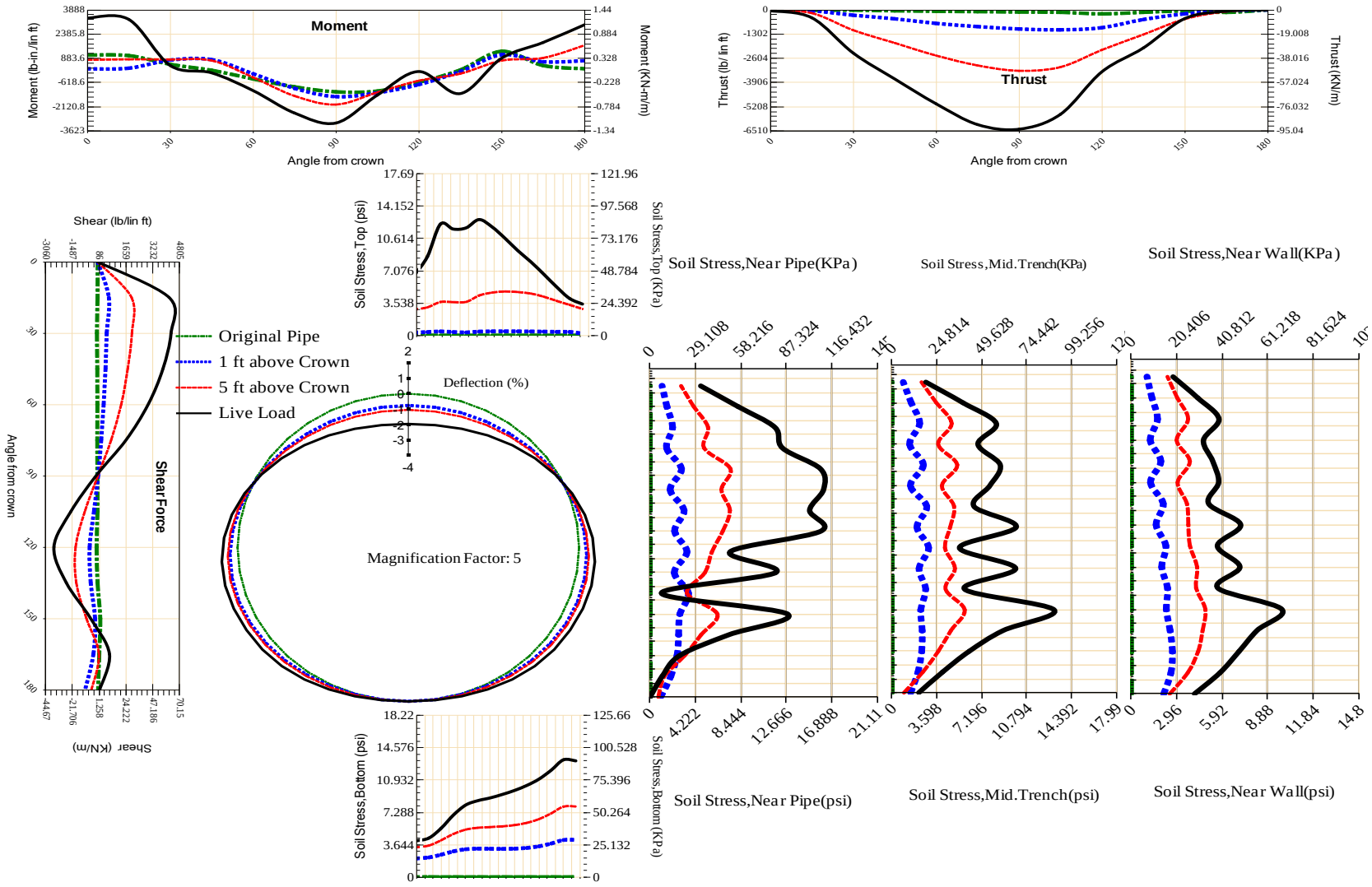

Figure A-544 Param-96-PW230-SF3TR-OD+72-EW5-H5-LiveLoad

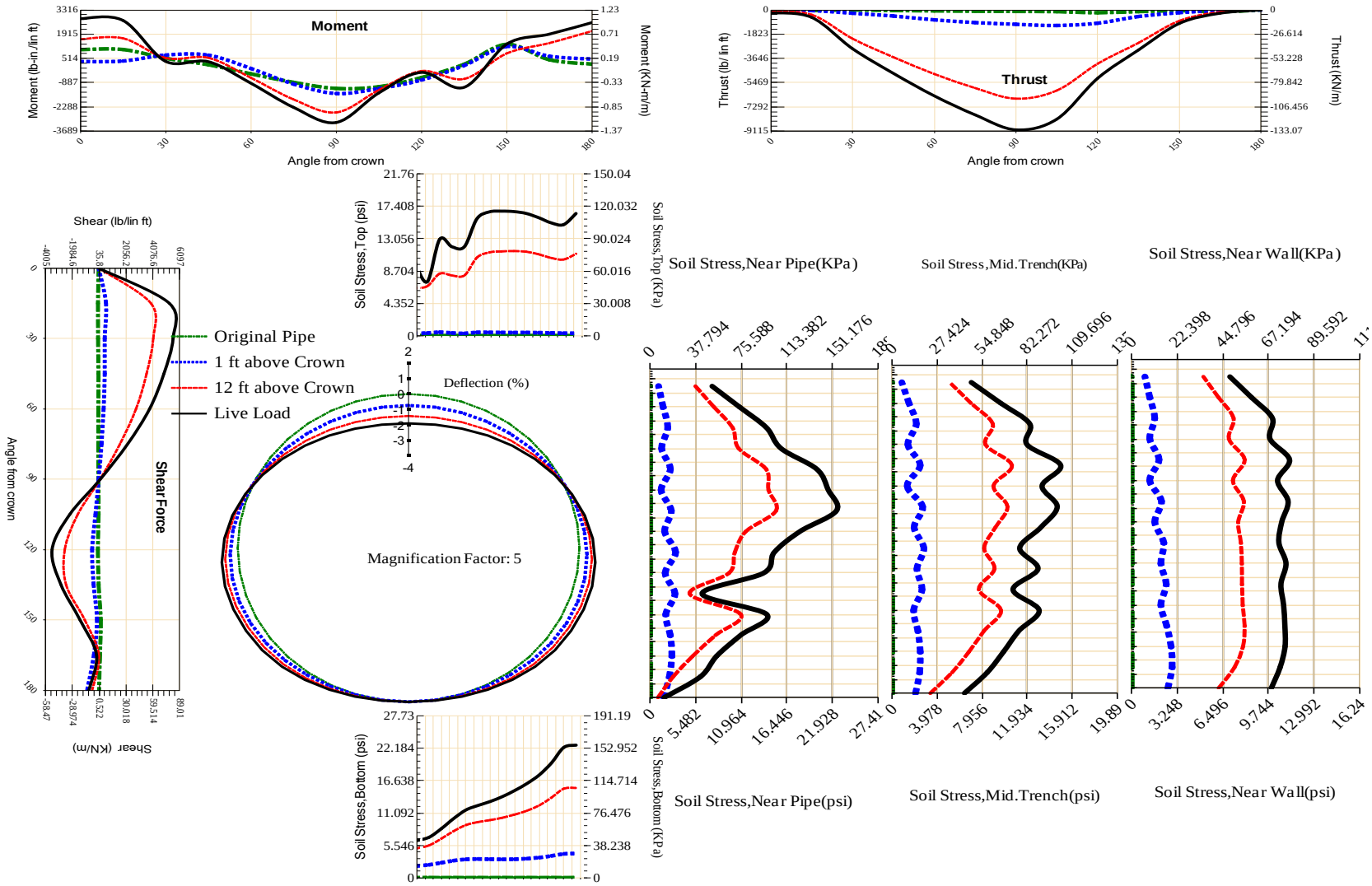

Figure A-545 Param-96-PW230-SF3TR-OD+72-EW7-H12-LiveLoad

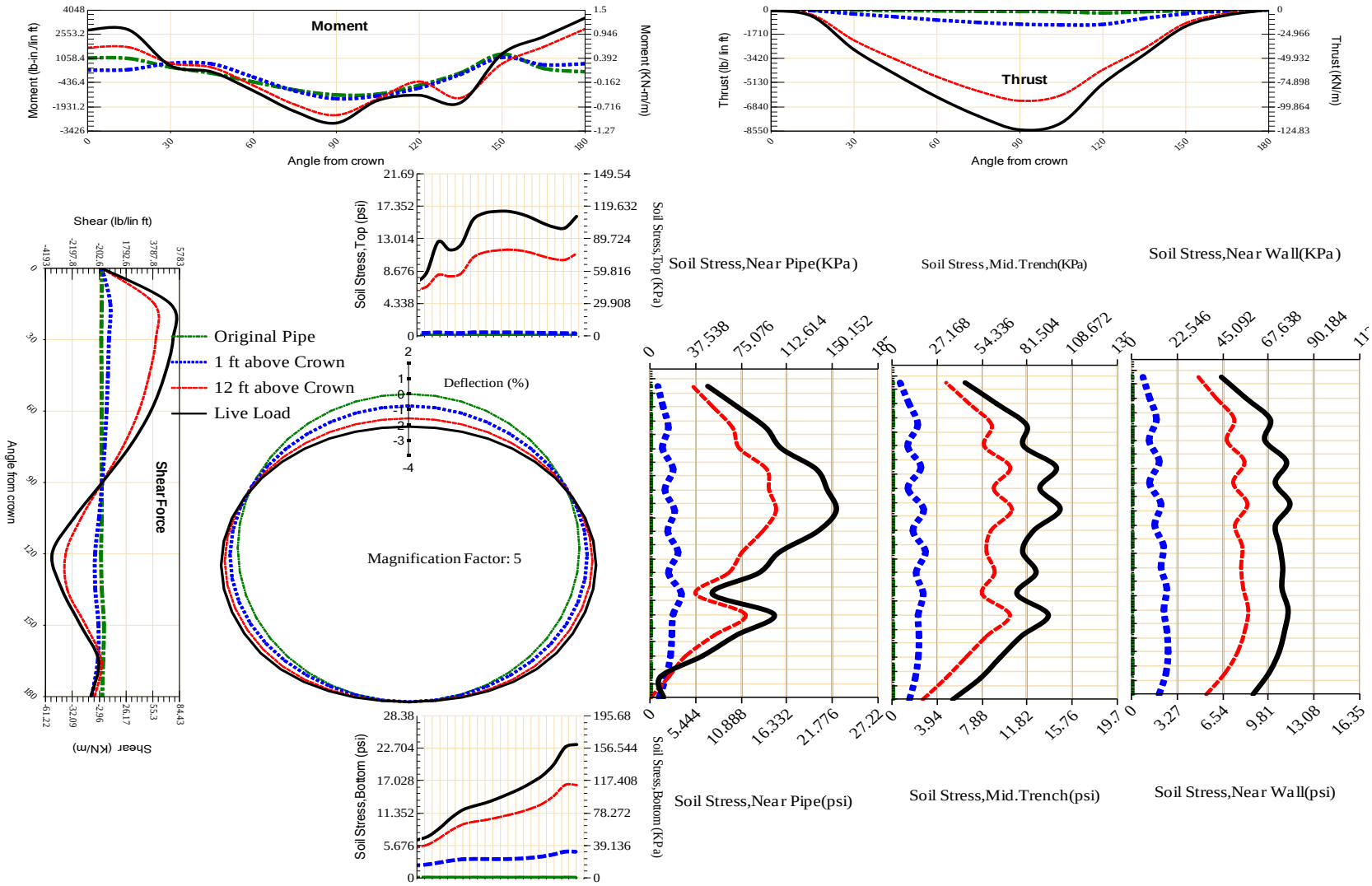

Figure A-546 Param-96-PW230-SF3TR-OD+84-EW5-H12-LiveLoad

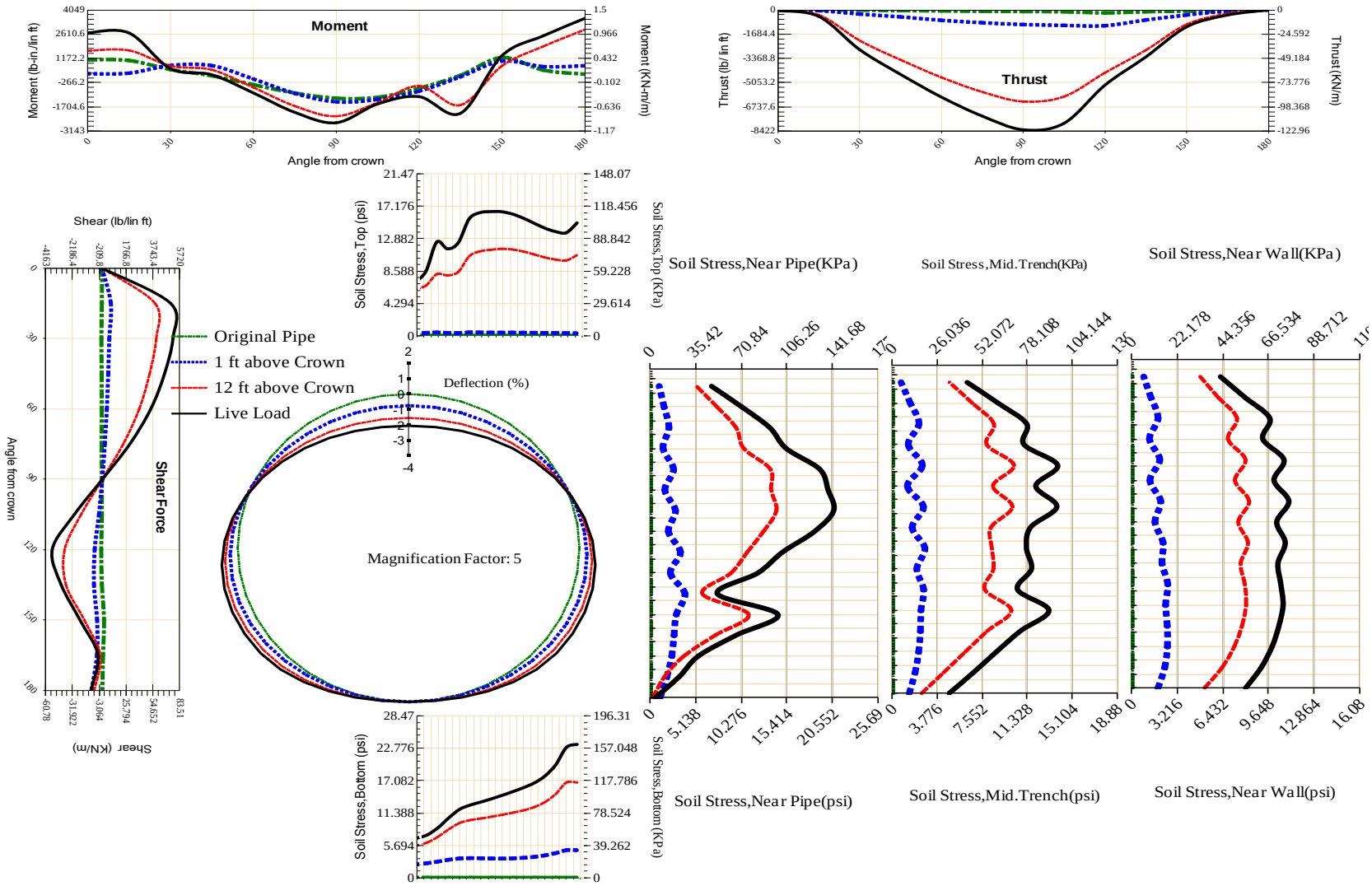

Figure A-547 Param-96-PW230-SF3TR-OD+96-EW5-H12-LiveLoad

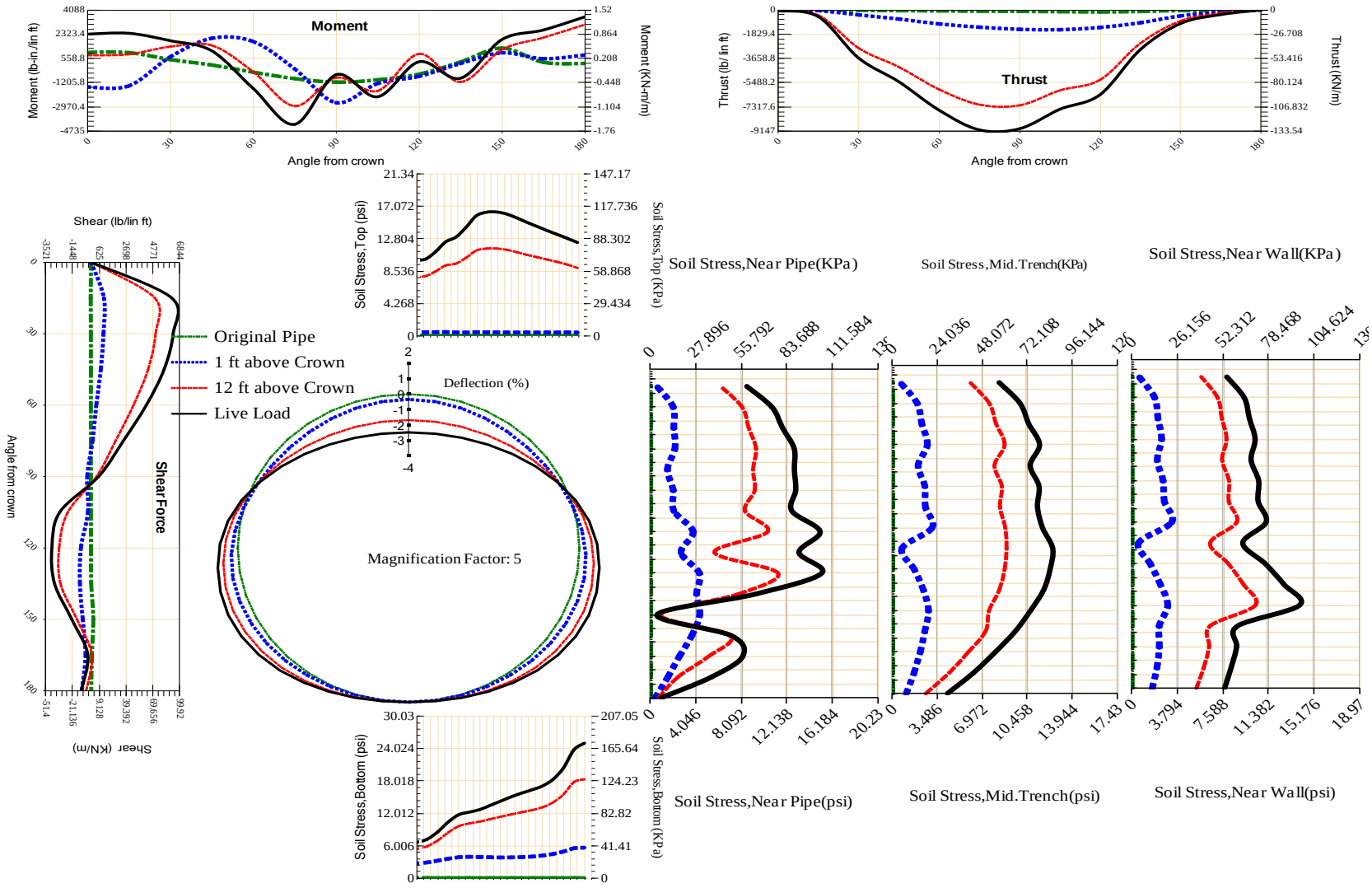

Figure A-548 Param-96-PW230-SF5OR-OD+108-EW5-H12-LiveLoad

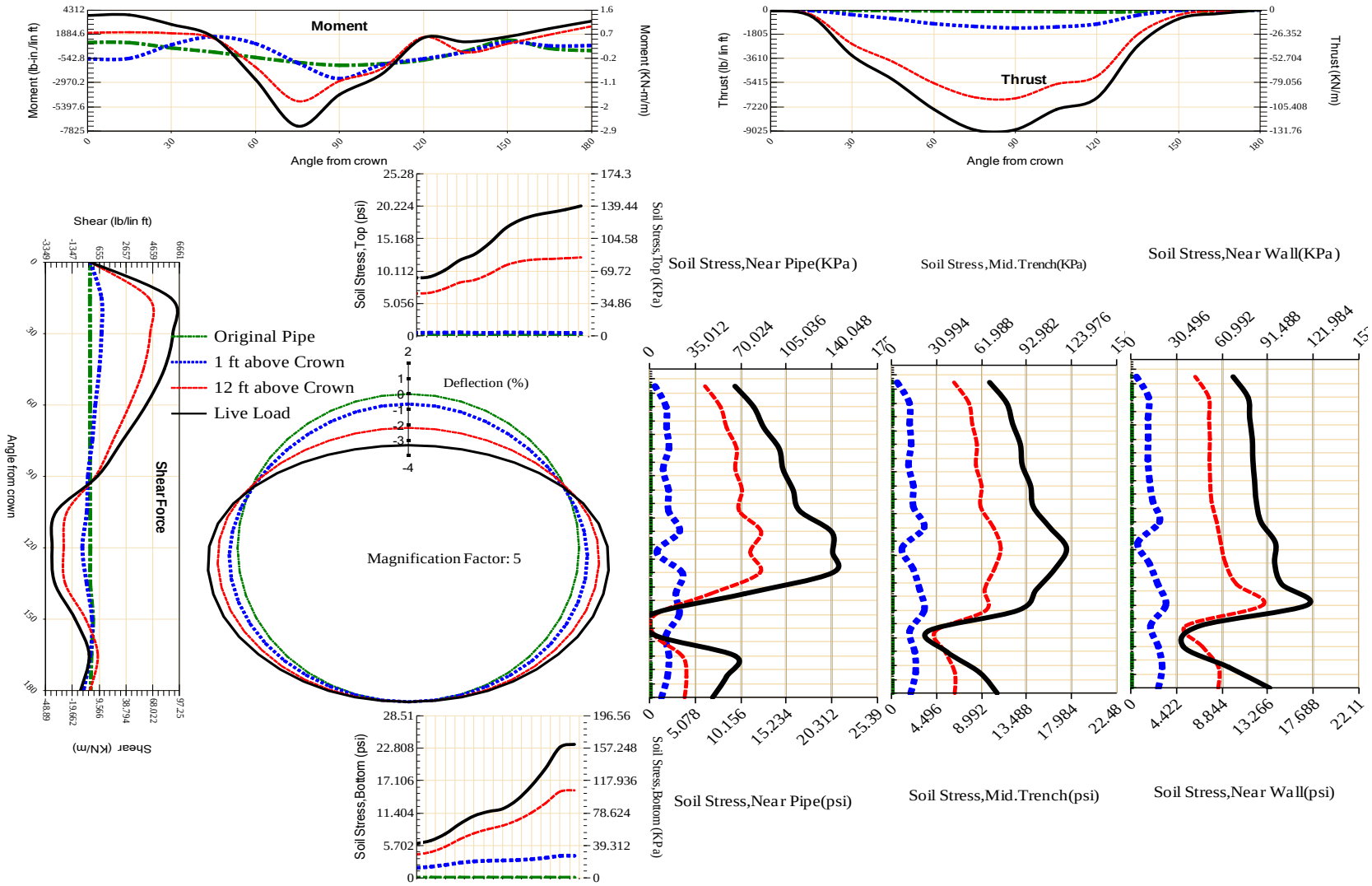

Figure A-549 Param-96-PW230-SF5OR-OD+48-EW5-H12-LiveLoad

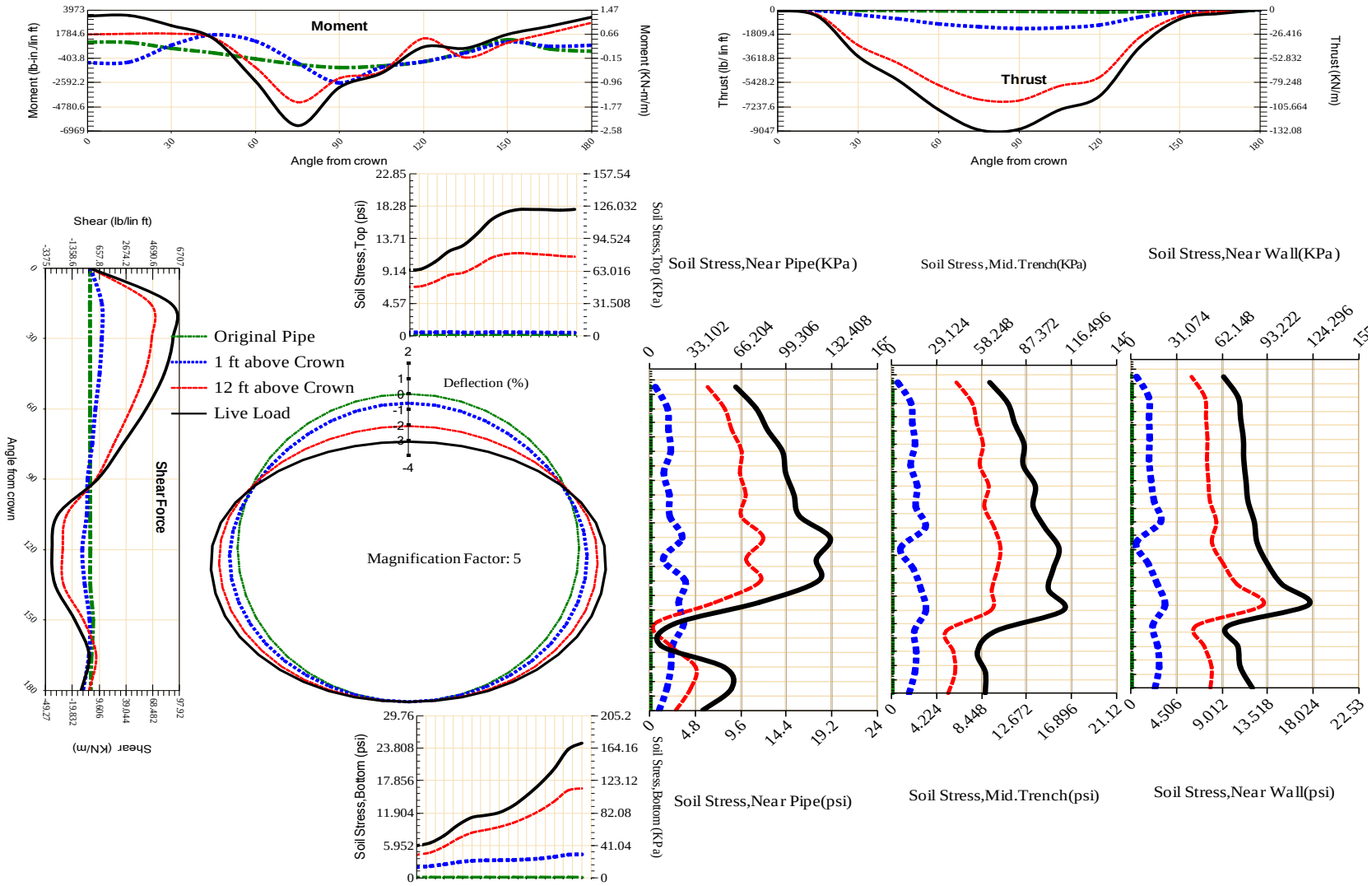

Figure A-550 Param-96-PW230-SF5OR-OD+60-EW5-H12-LiveLoad

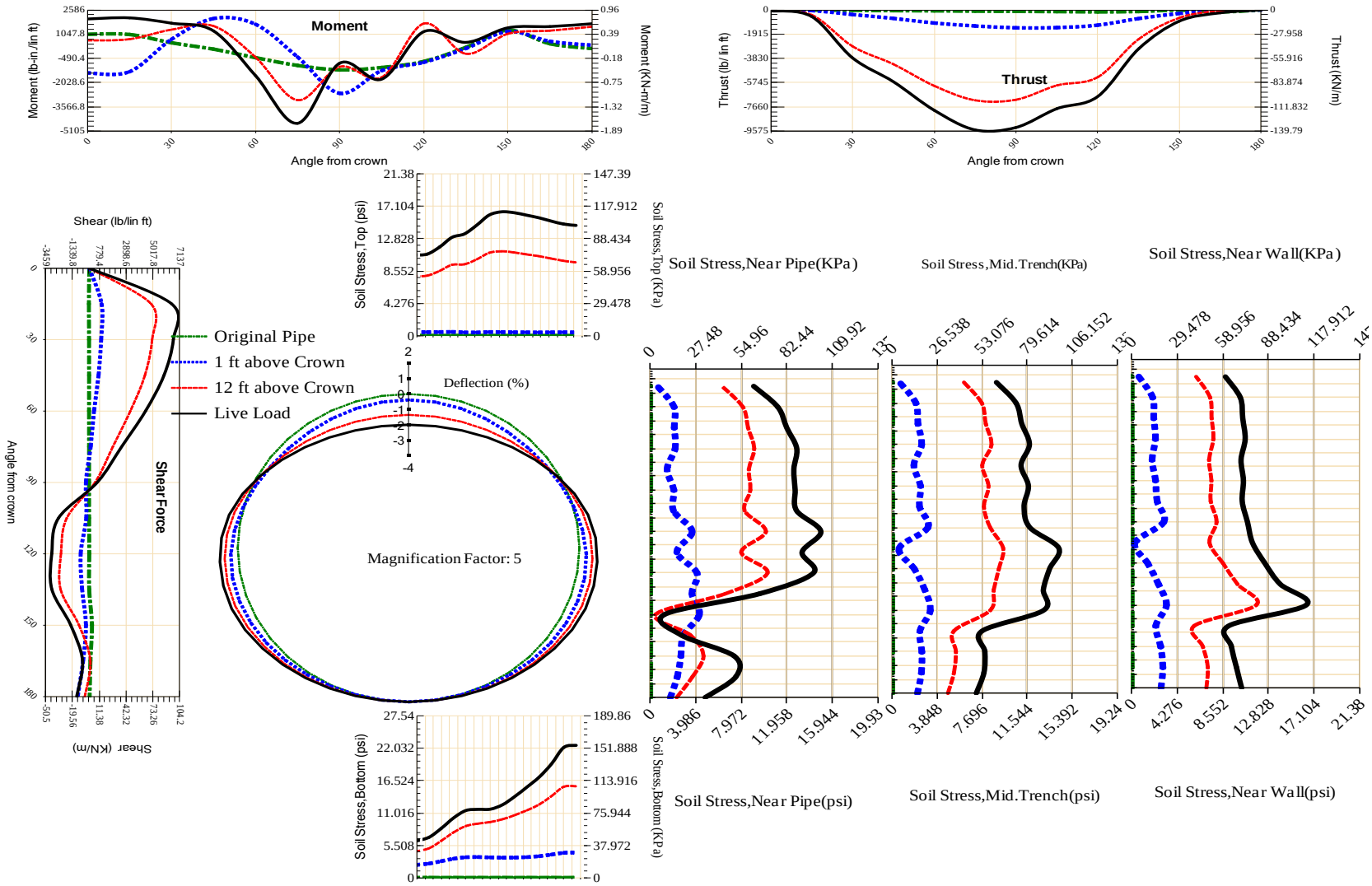

Figure A-551 Param-96-PW230-SF5OR-OD+72-EW10-H12-LiveLoad

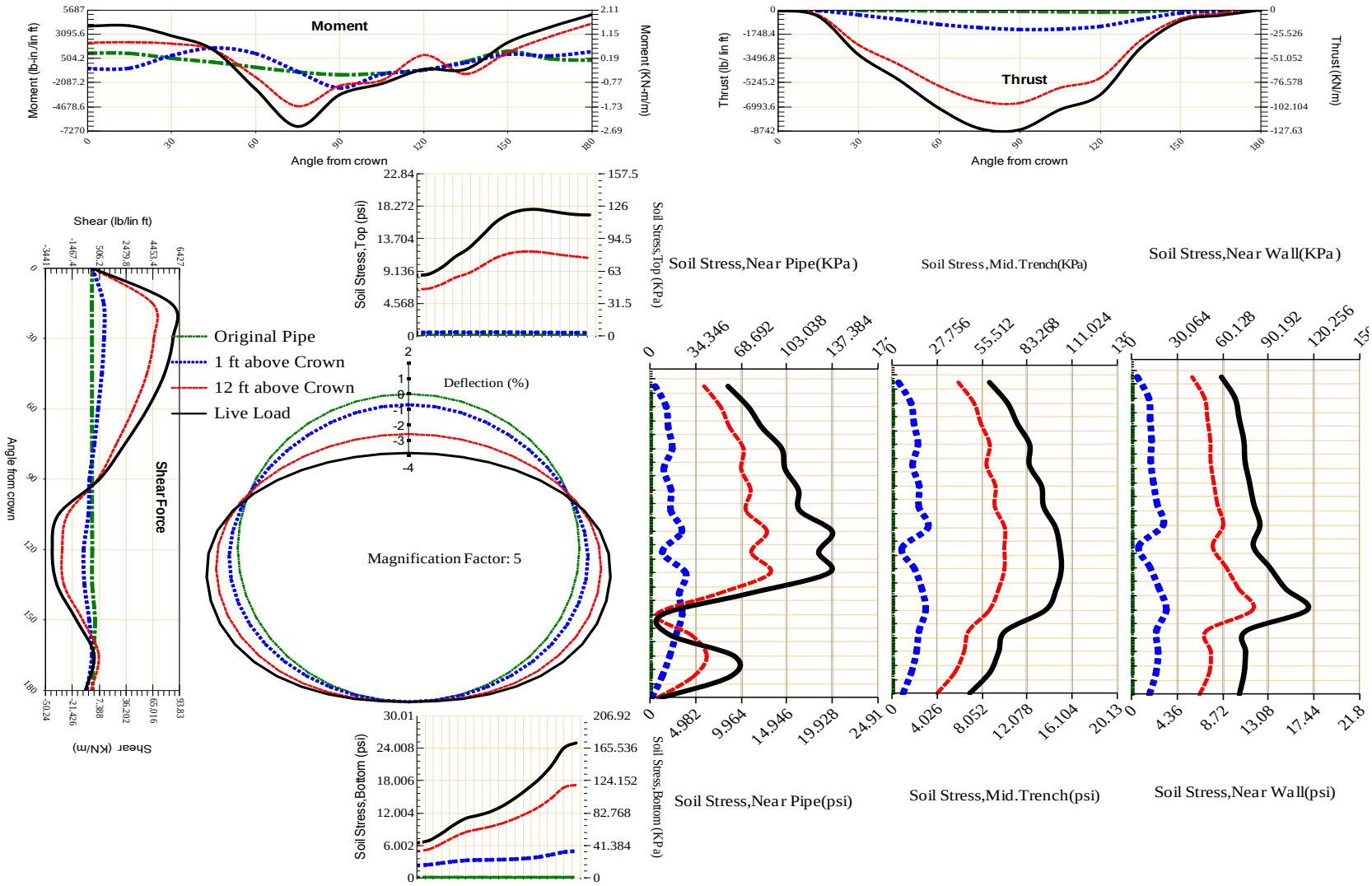

Figure A-552 Param-96-PW230-SF5OR-OD+72-EW3-H12-LiveLoad

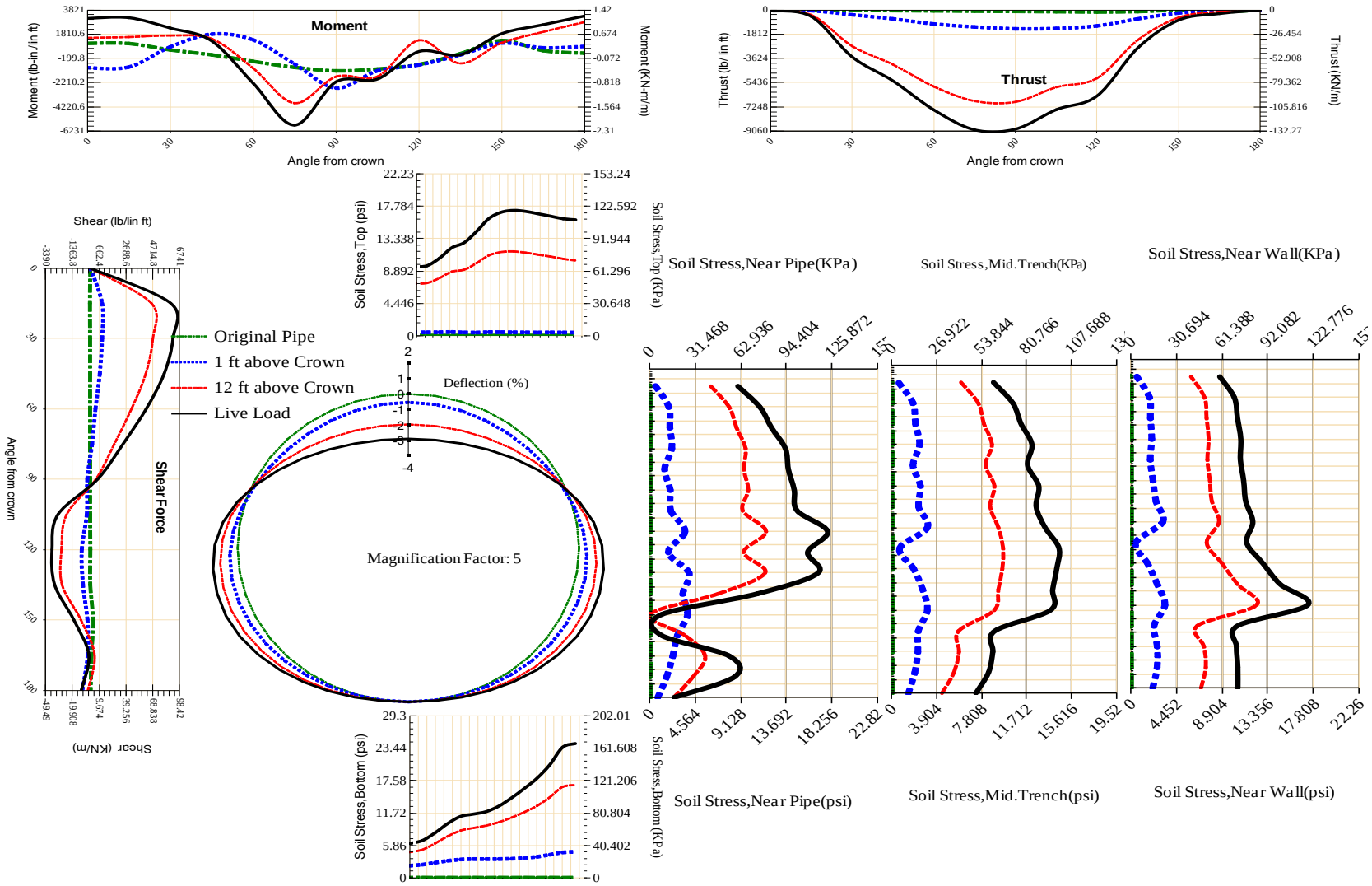

Figure A-553 Param-96-PW230-SF5OR-OD+72-EW5-H12-LiveLoad

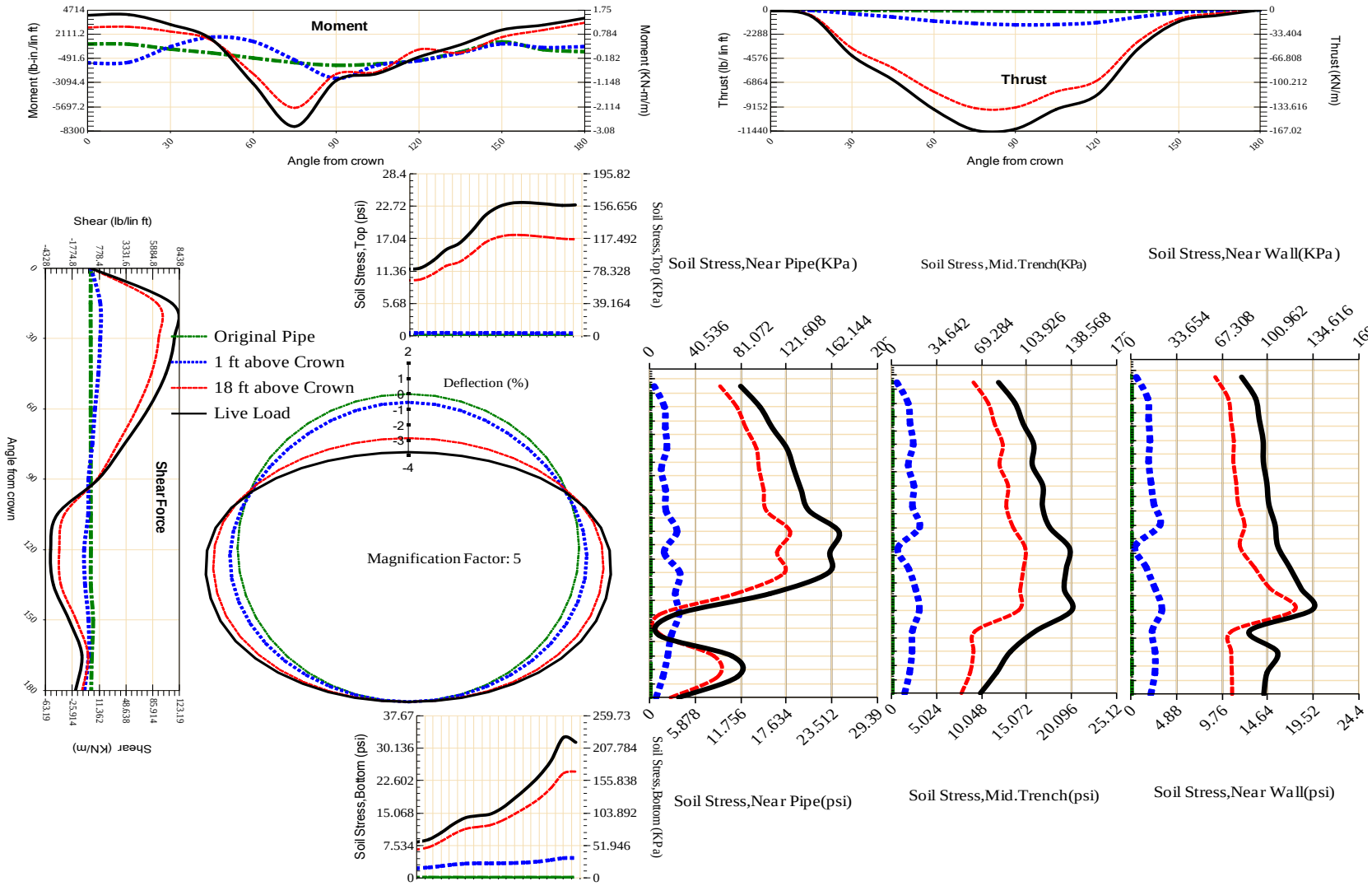

Figure A-554 Param-96-PW230-SF5OR-OD+72-EW5-H18-LiveLoad

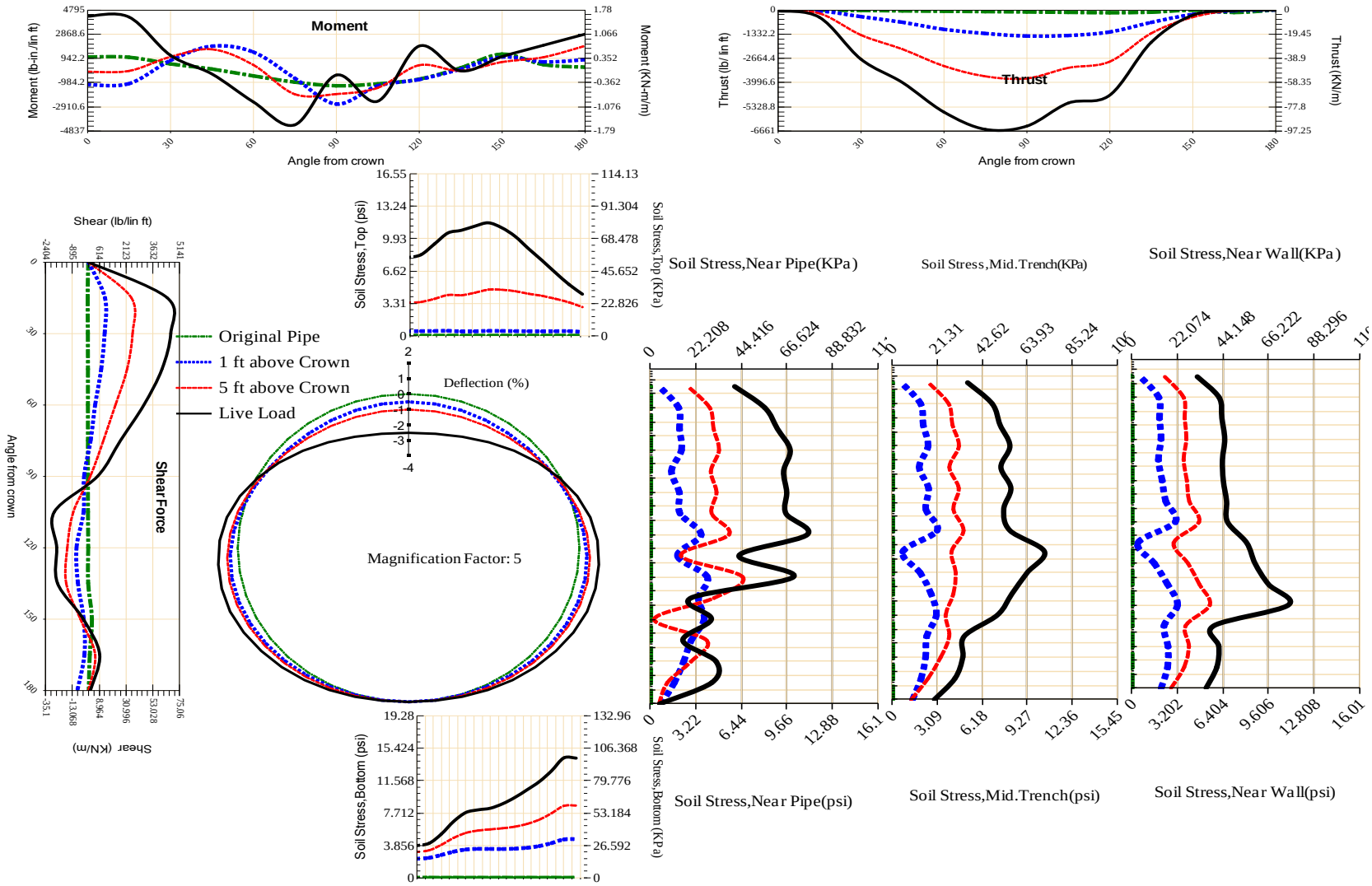

Figure A-555 Param-96-PW230-SF5OR-OD+72-EW5-H5-LiveLoad

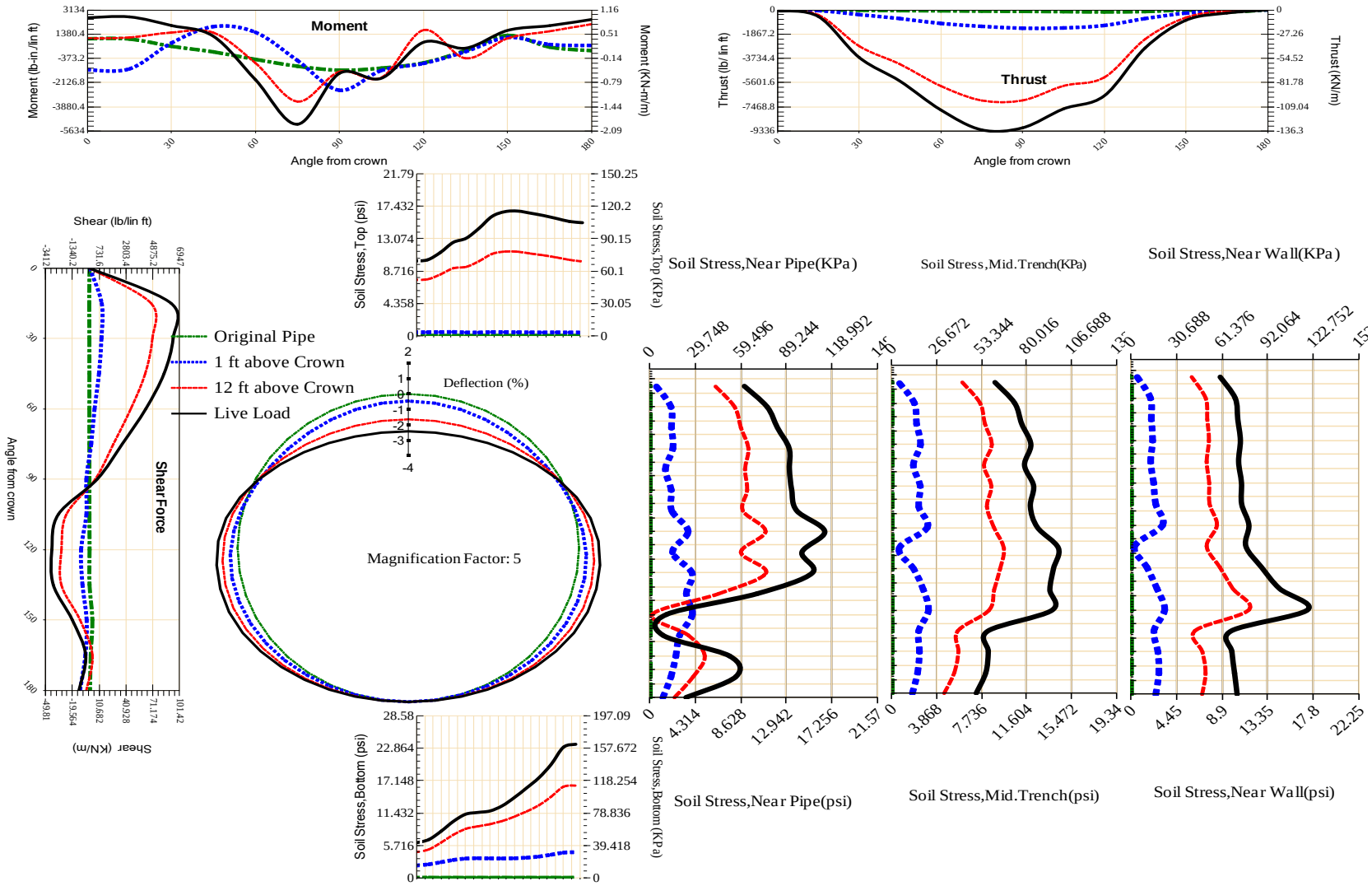

Figure A-556 Param-96-PW230-SF5OR-OD+72-EW7-H12-LiveLoad

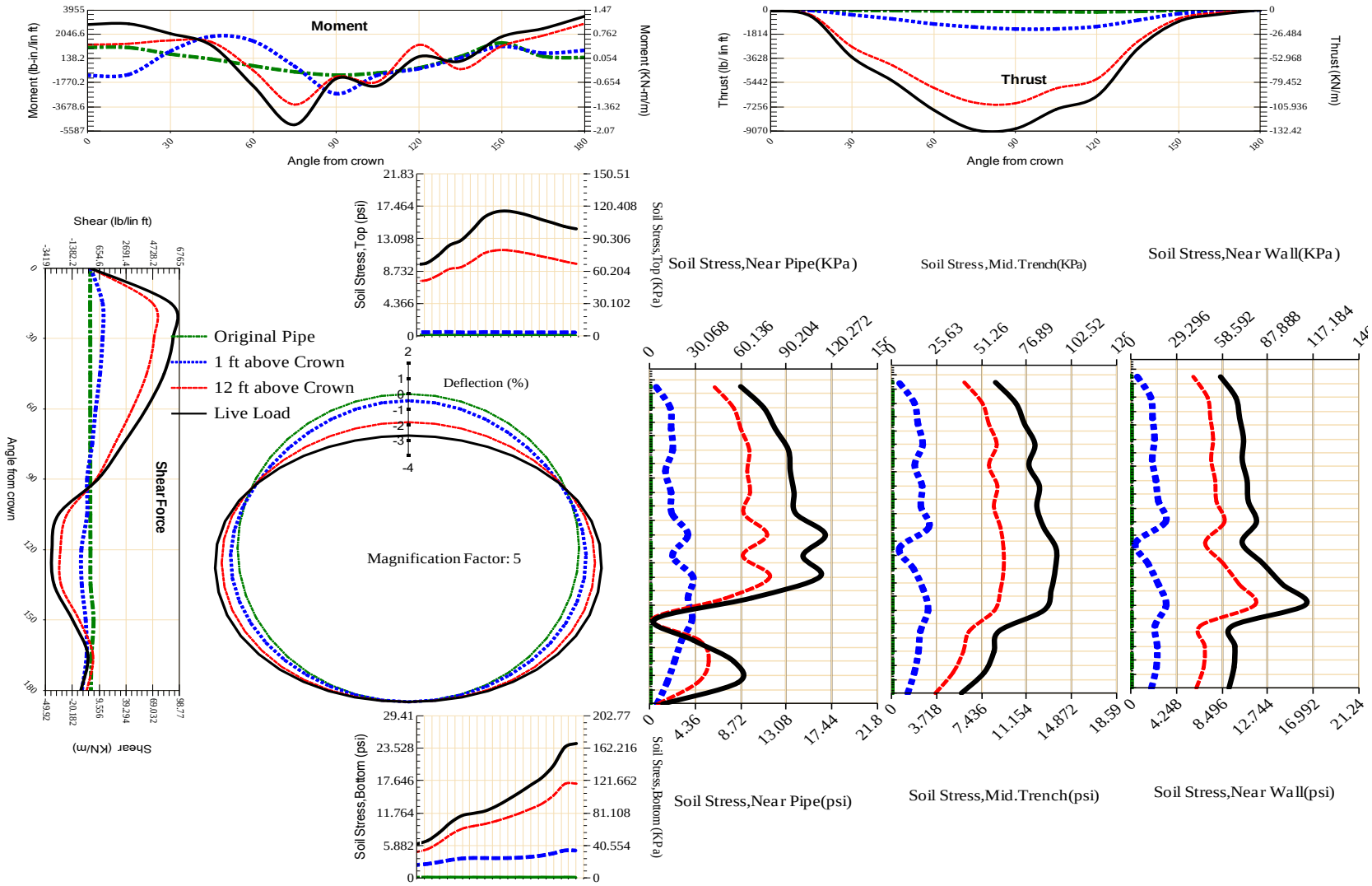

Figure A-557 Param-96-PW230-SF5OR-OD+84-EW5-H12-LiveLoad

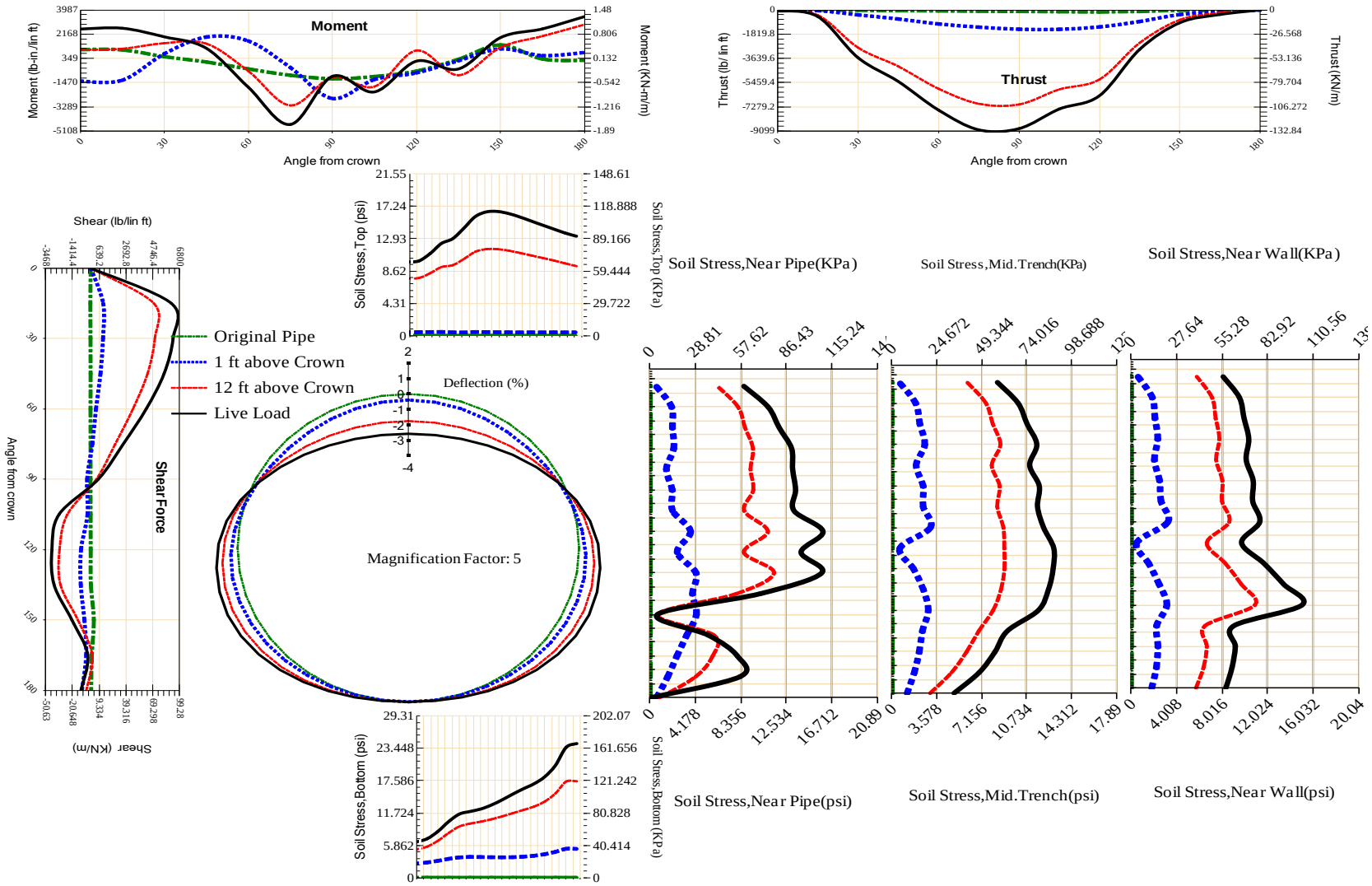

Figure A-558 Param-96-PW230-SF5OR-OD+96-EW5-H12-LiveLoad

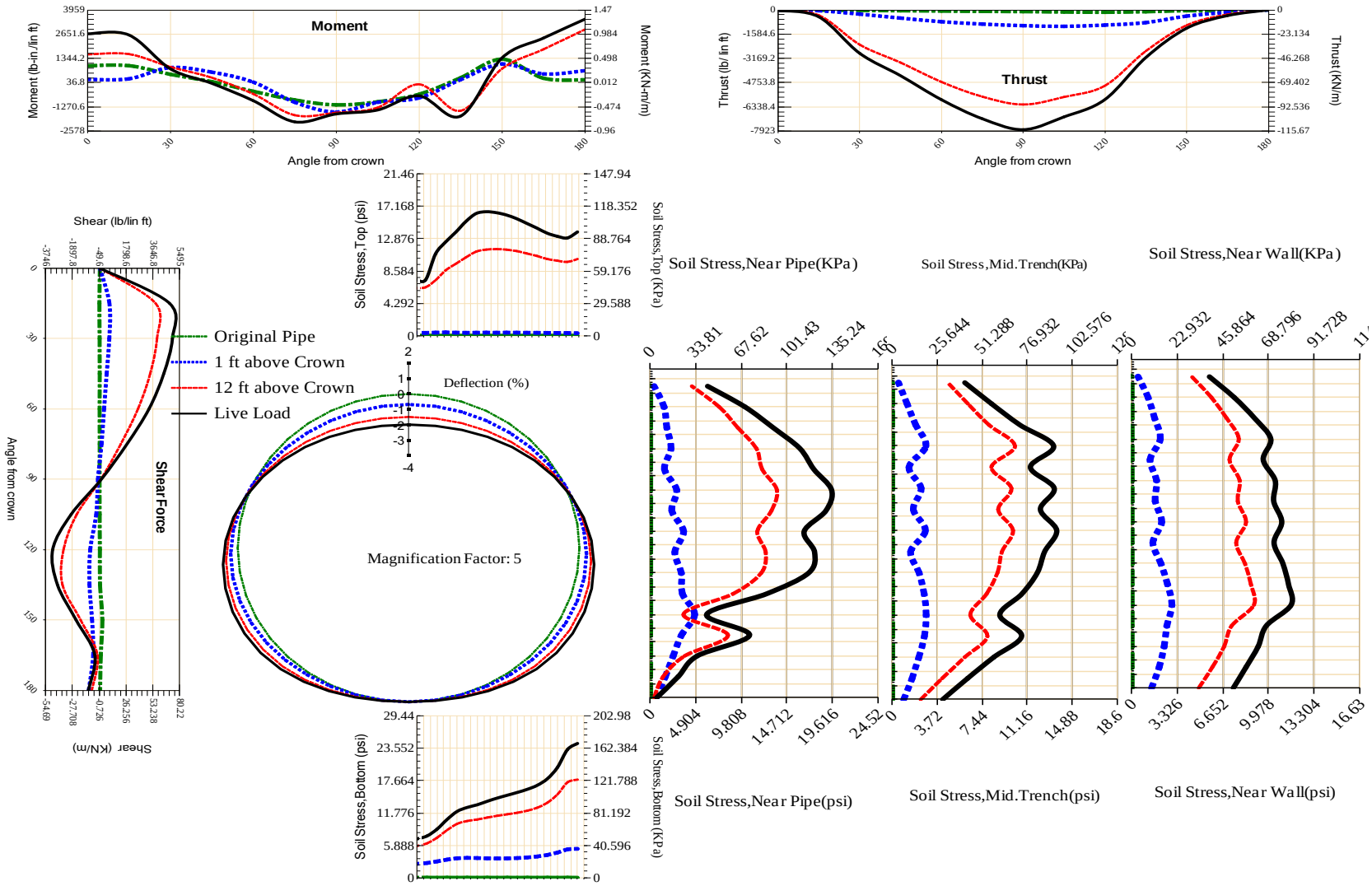

Figure A-559 Param-96-PW230-SF5TR-OD+108-EW5-H12-LiveLoad

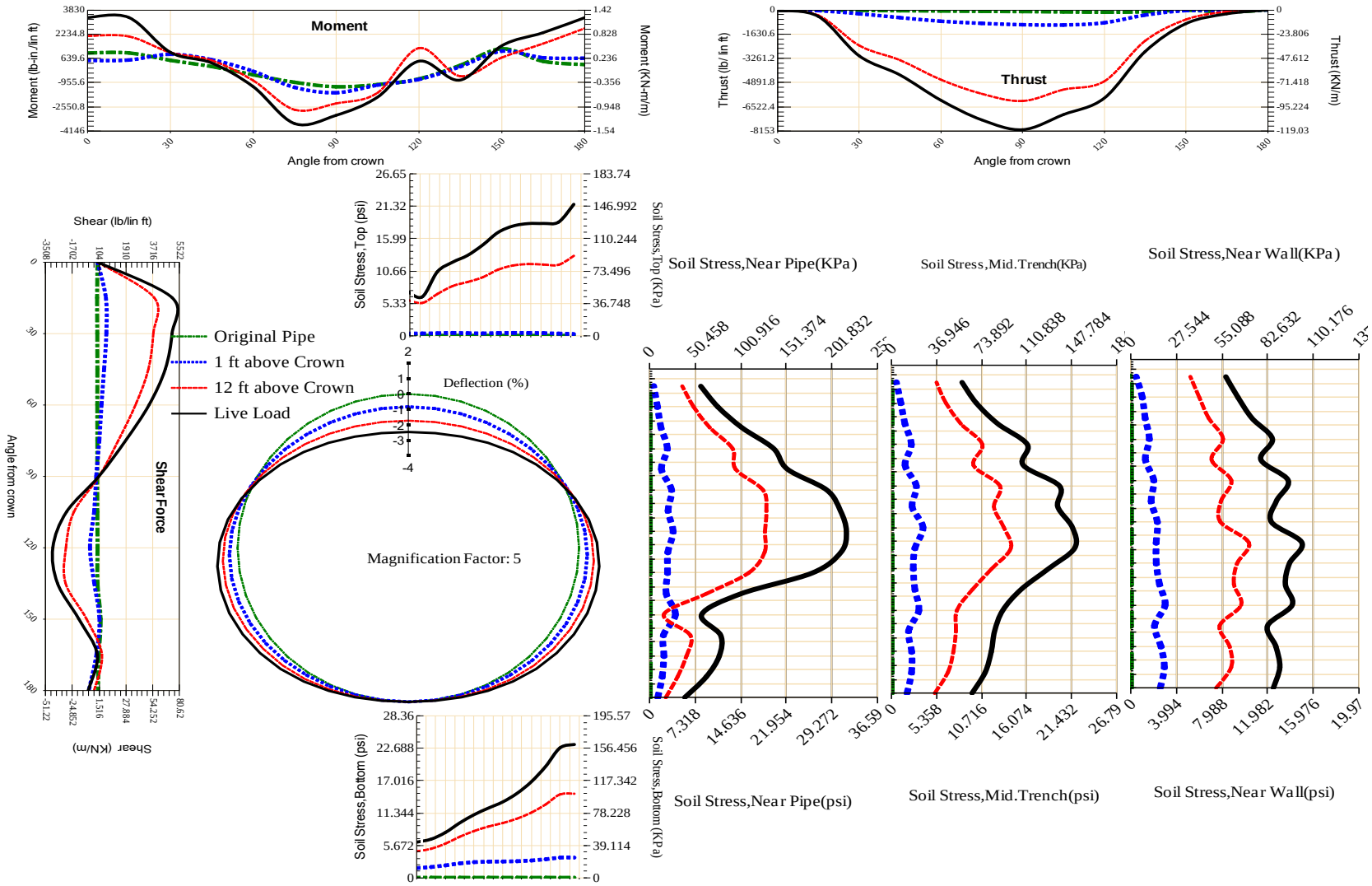

Figure A-560 Param-96-PW230-SF5TR-OD+48-EW5-H12-LiveLoad

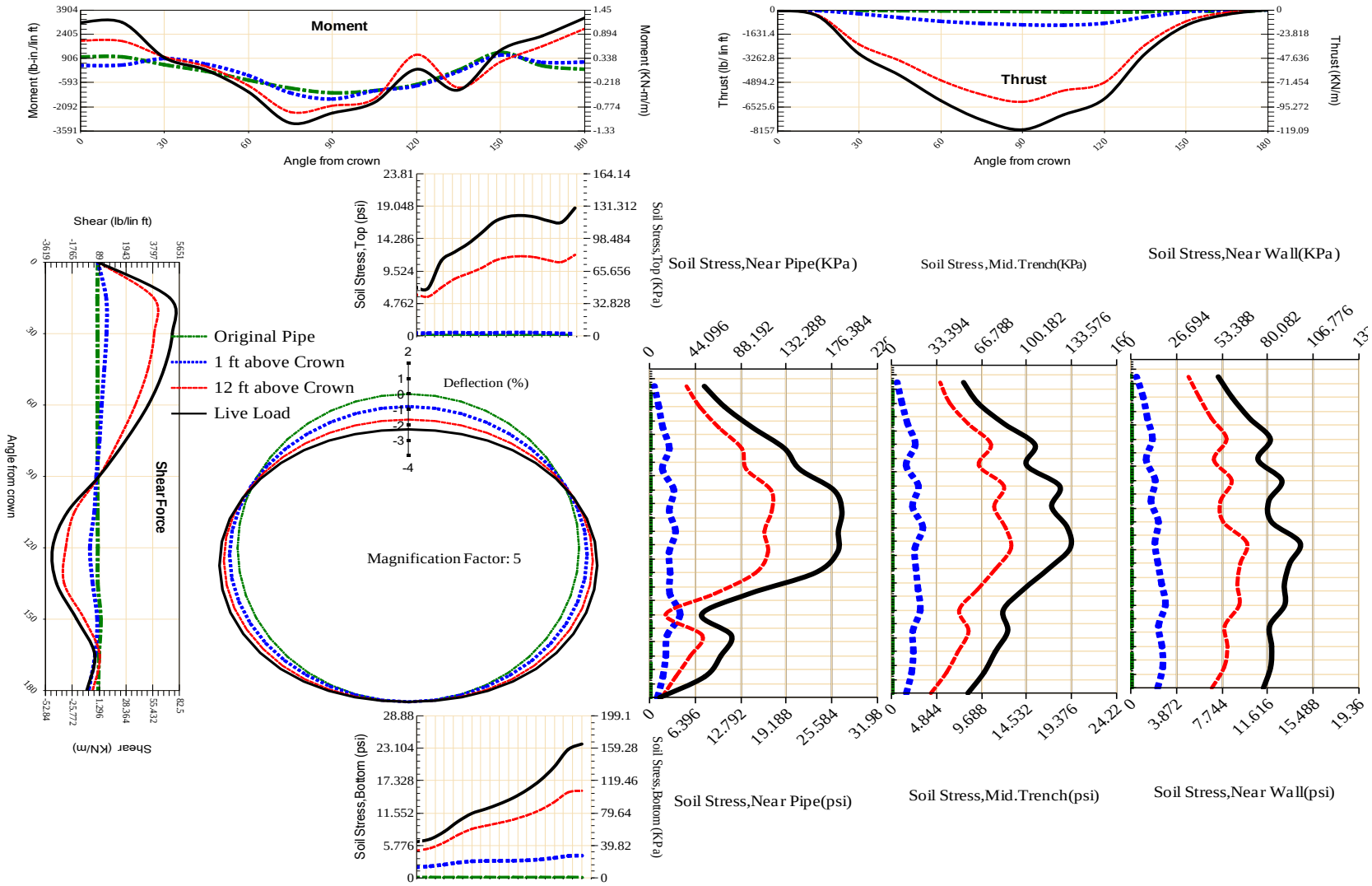

Figure A-561 Param-96-PW230-SF5TR-OD+60-EW5-H12-LiveLoad

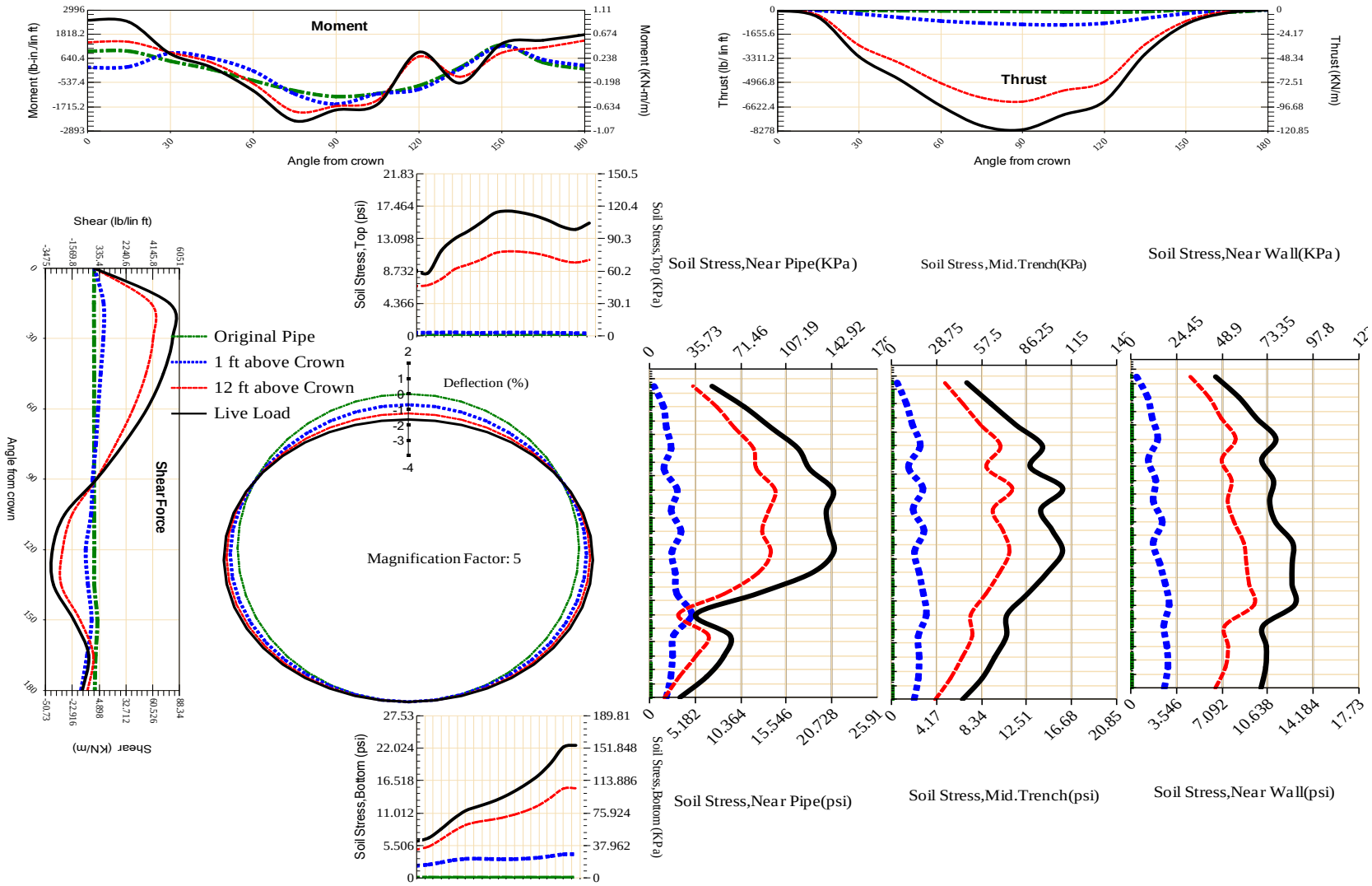

Figure A-562 Param-96-PW230-SF5TR-OD+72-EW10-H12-LiveLoad

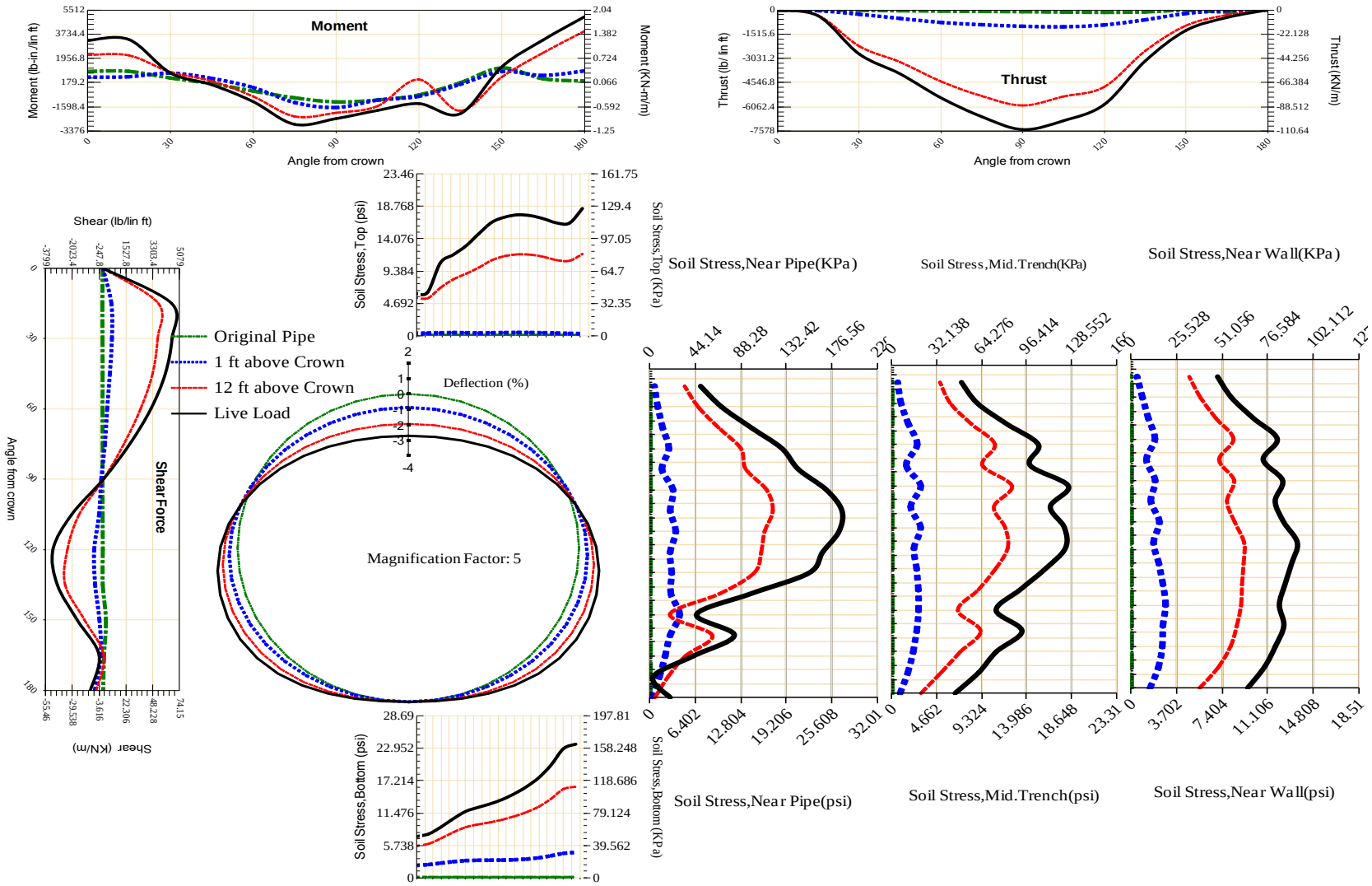

Figure A-563 Param-96-PW230-SF5TR-OD+72-EW3-H12-LiveLoad

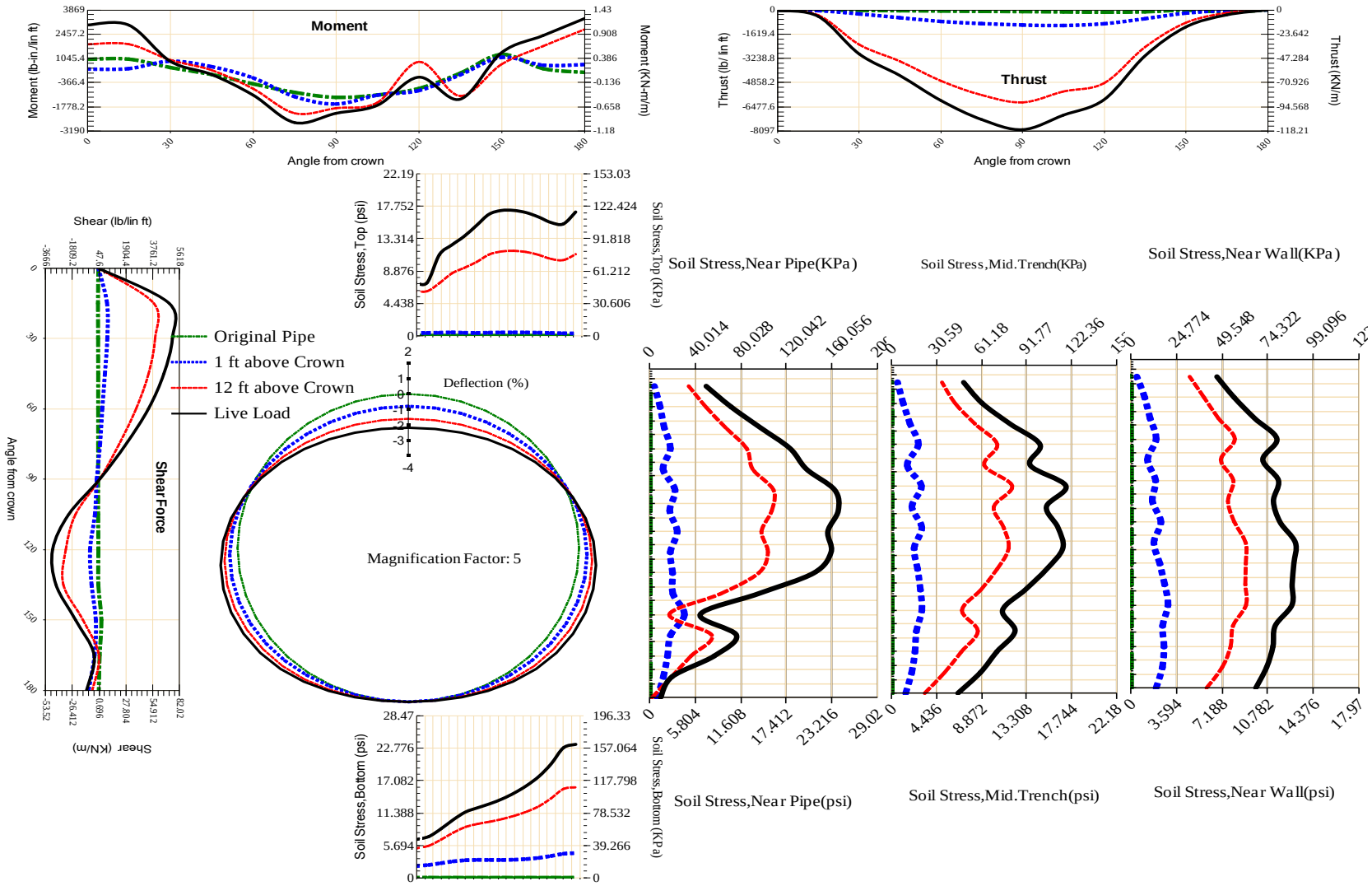

Figure A-564 Param-96-PW230-SF5TR-OD+72-EW5-H12-LiveLoad

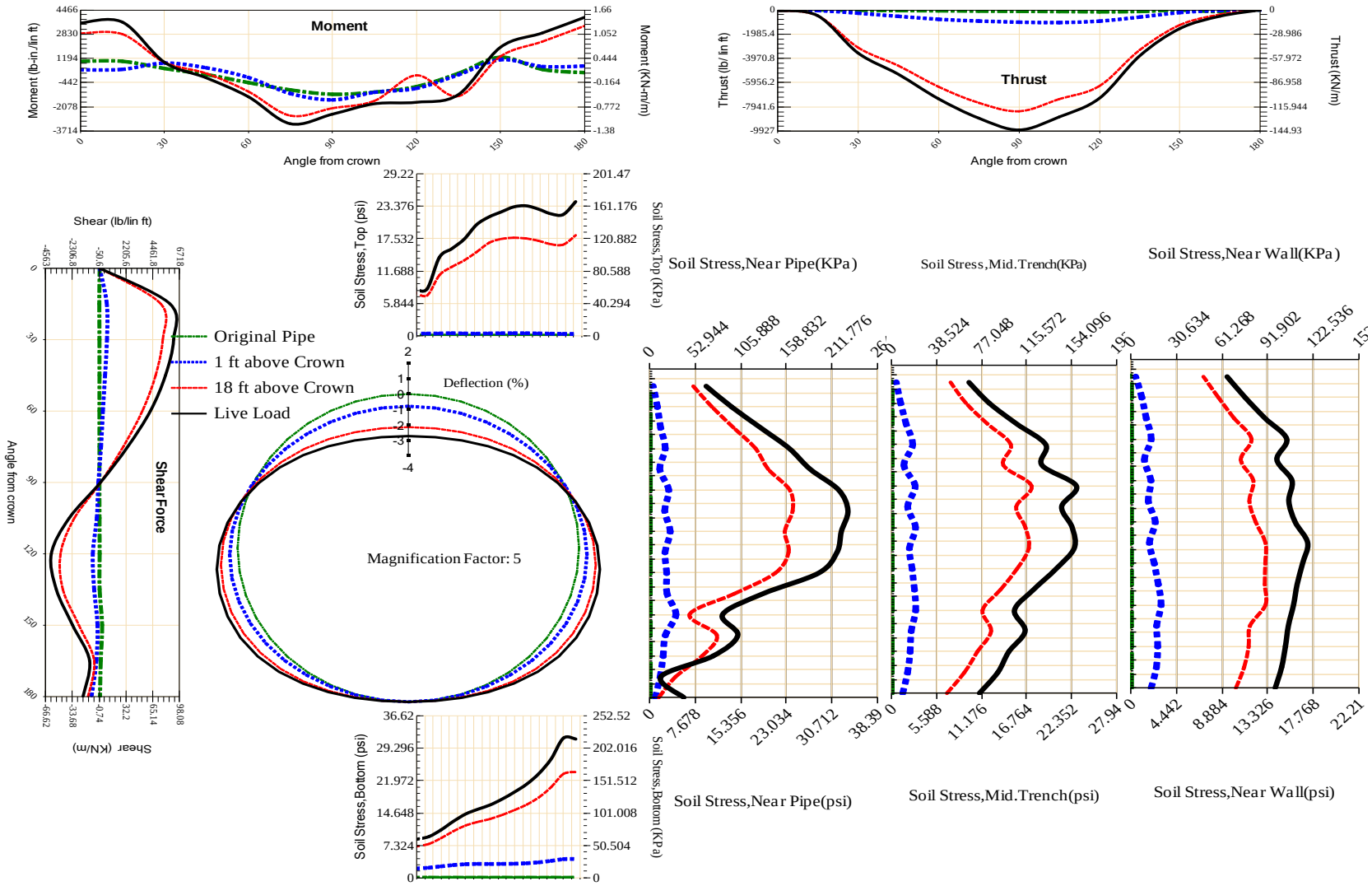

Figure A-565 Param-96-PW230-SF5TR-OD+72-EW5-H18-LiveLoad

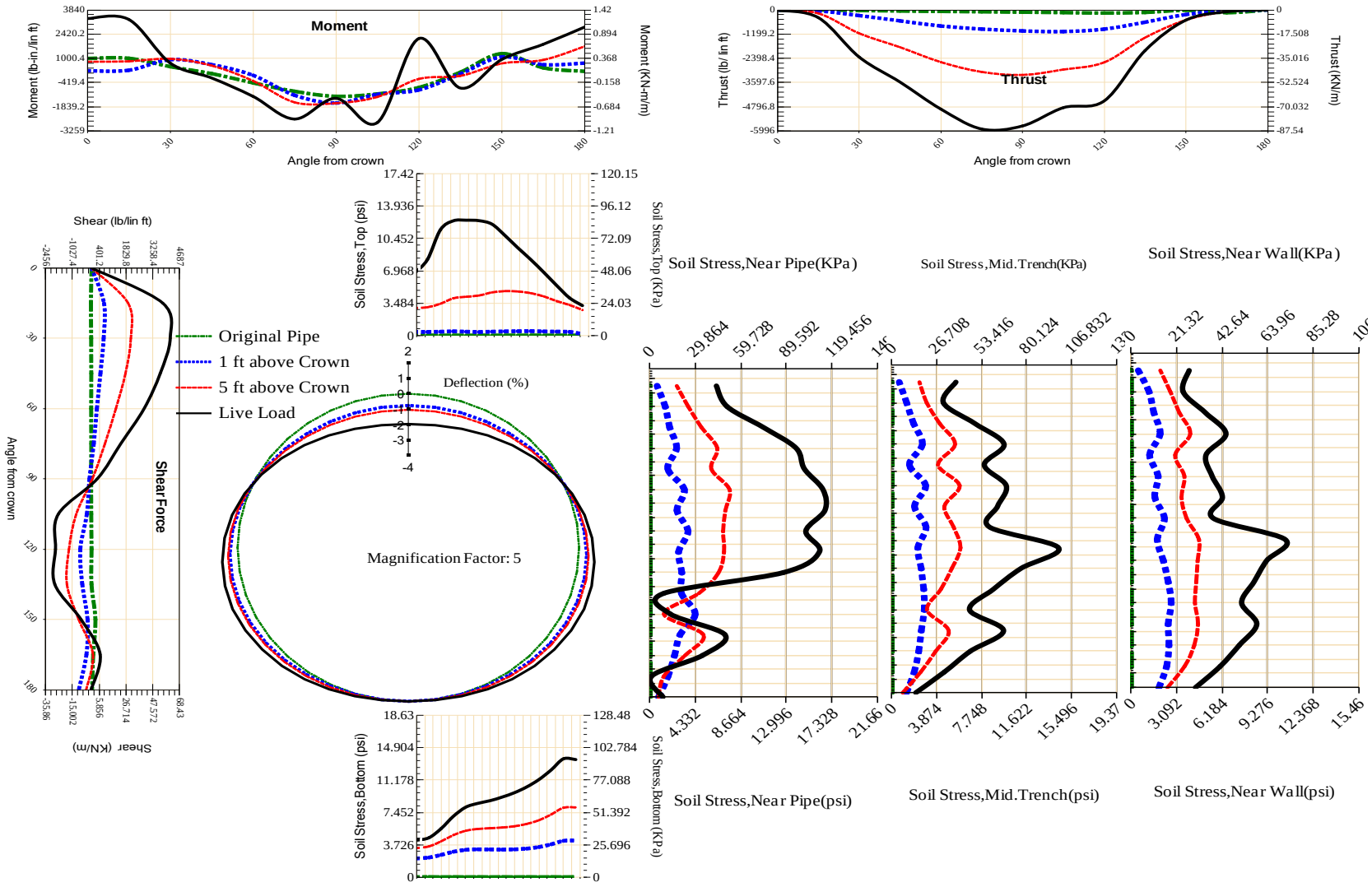

Figure A-566 Param-96-PW230-SF5TR-OD+72-EW5-H5-LiveLoad

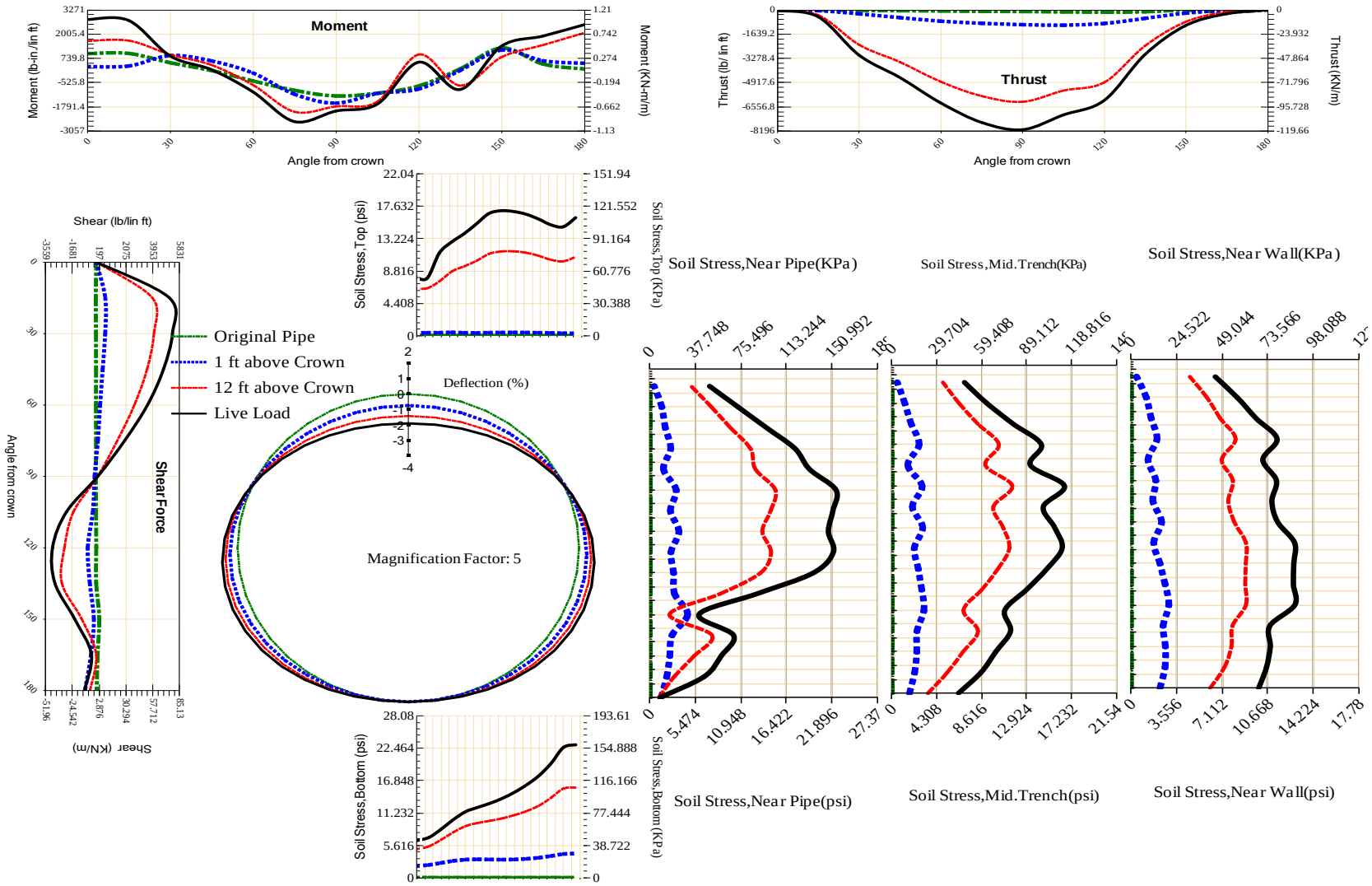

Figure A-567 Param-96-PW230-SF5TR-OD+72-EW7-H12-LiveLoad

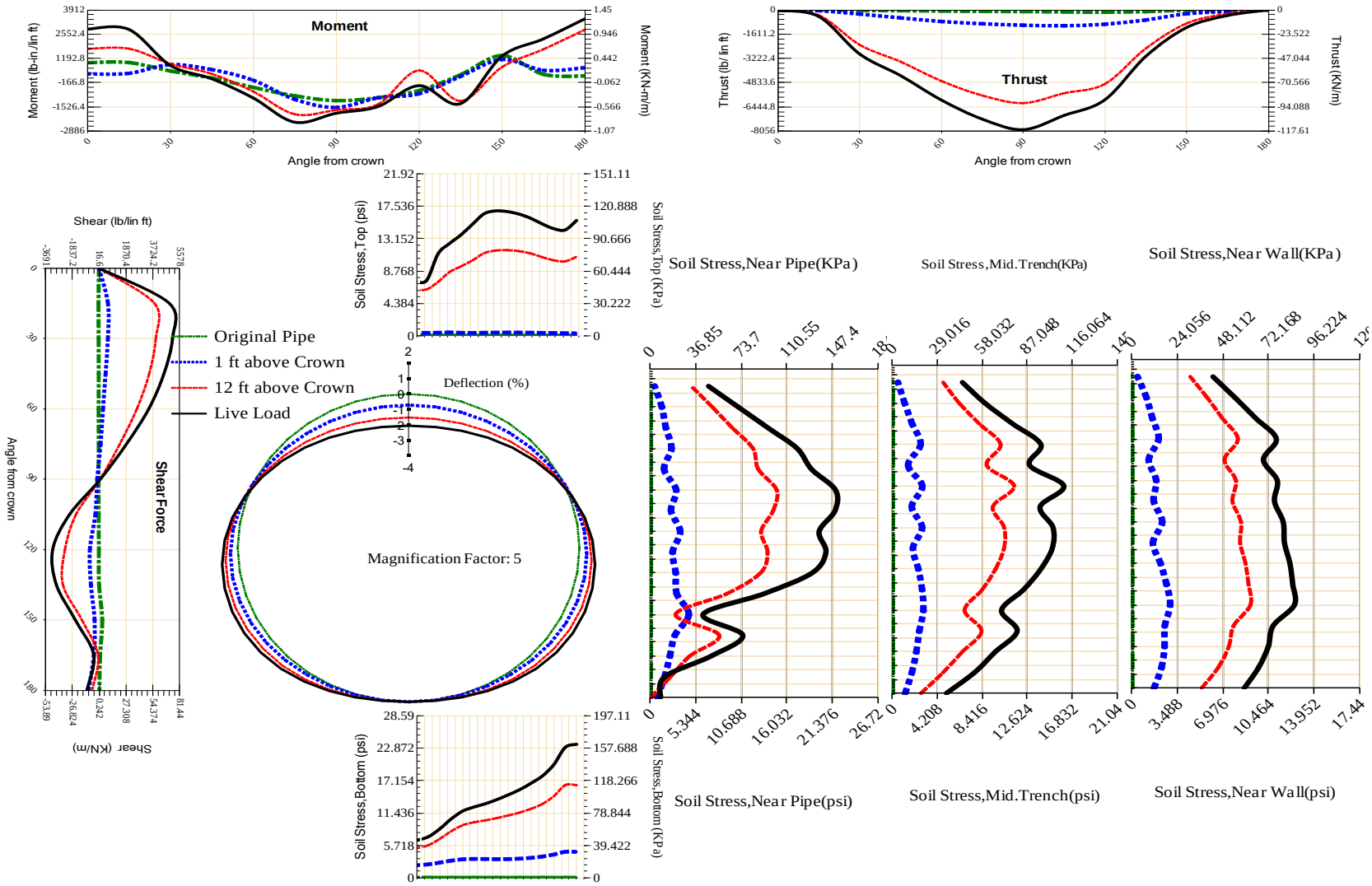

Figure A-568 Param-96-PW230-SF5TR-OD+84-EW5-H12-LiveLoad

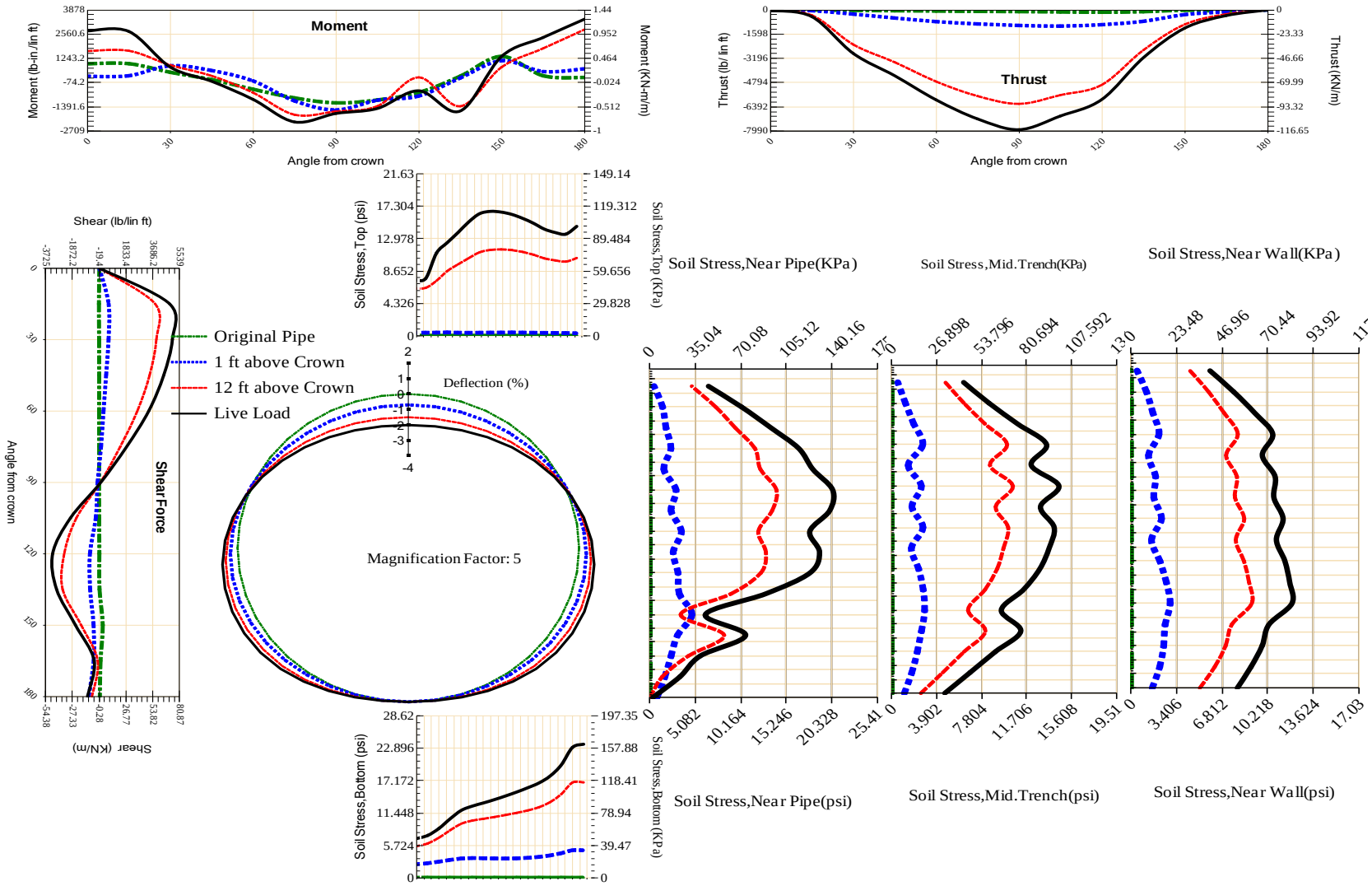

Figure A-569 Param-96-PW230-SF5TR-OD+96-EW5-H12-LiveLoad

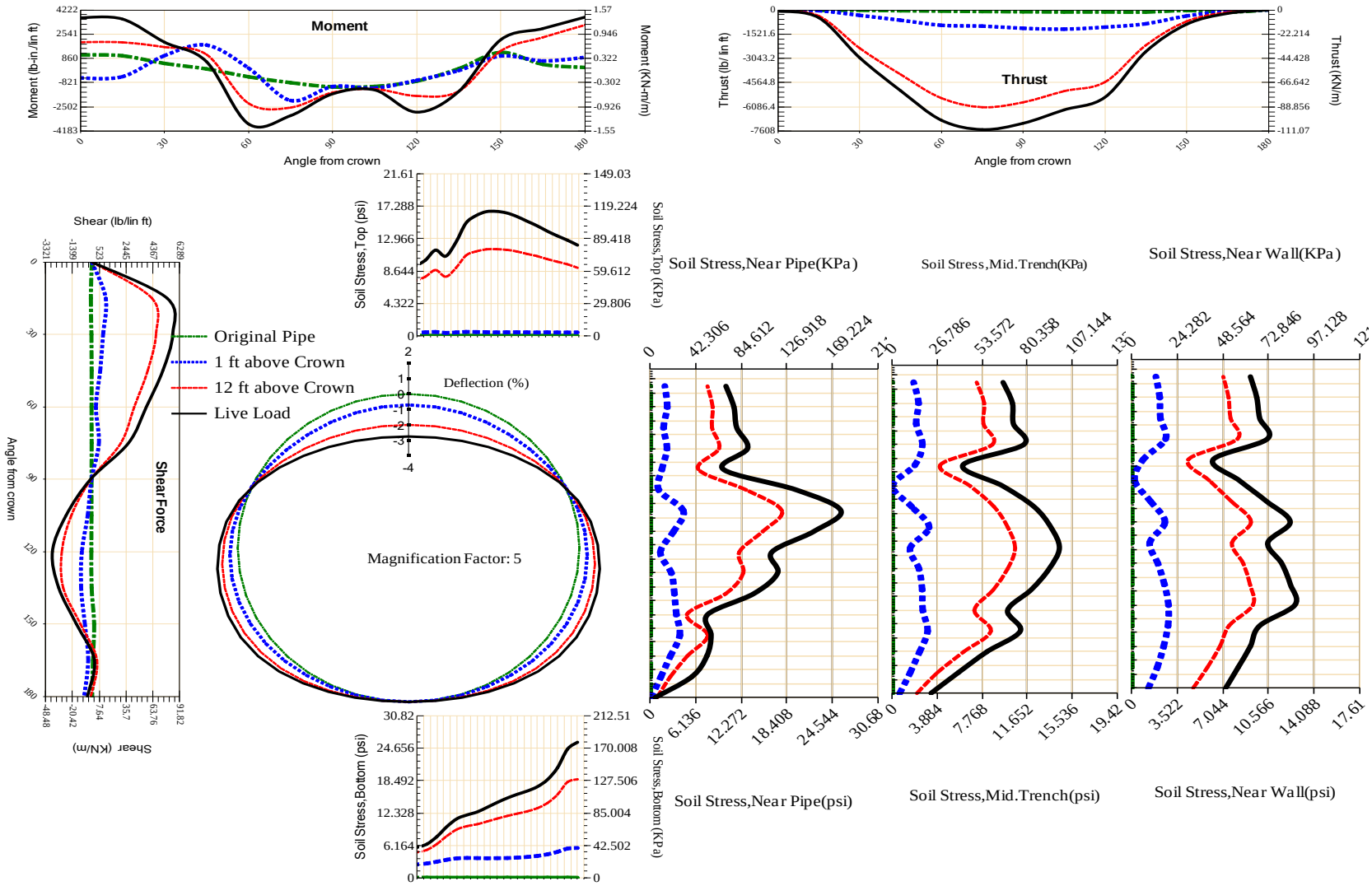

Figure A-570 Param-96-PW230-SF7OR-OD+108-EW5-H12-LiveLoad

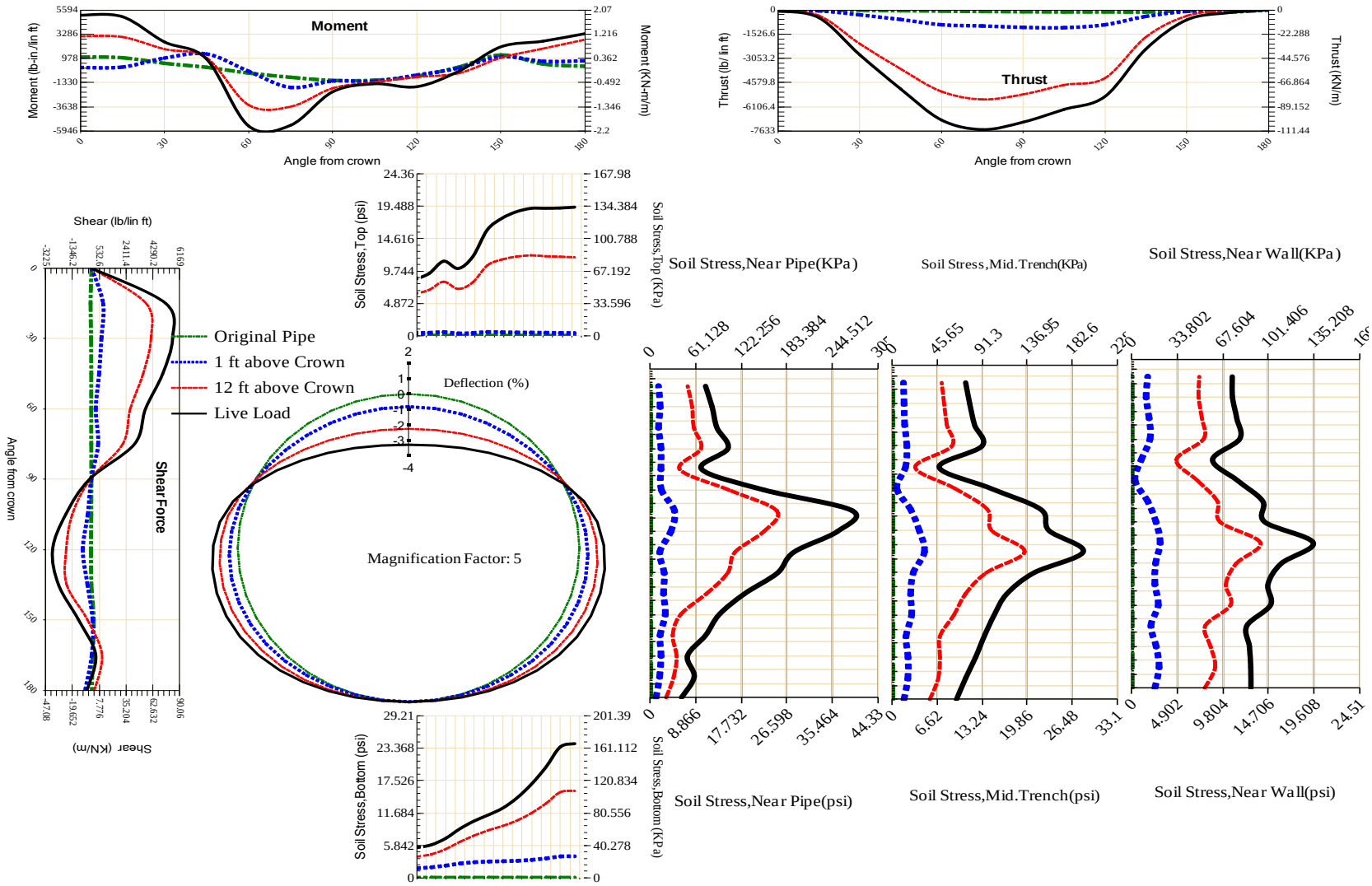

Figure A-571 Param-96-PW230-SF7OR-OD+48-EW5-H12-LiveLoad

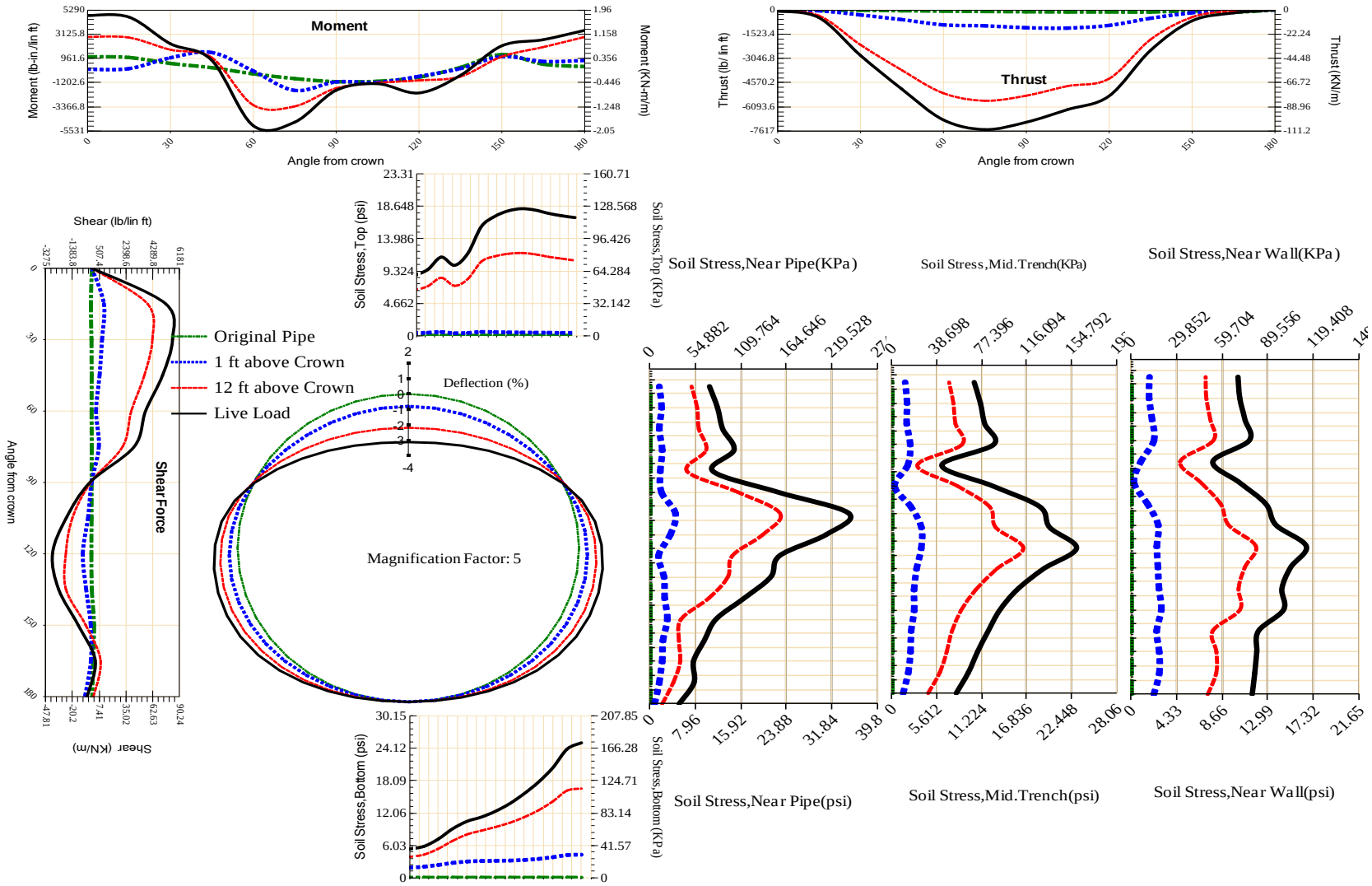

Figure A-572 Param-96-PW230-SF7OR-OD+60-EW5-H12-LiveLoad

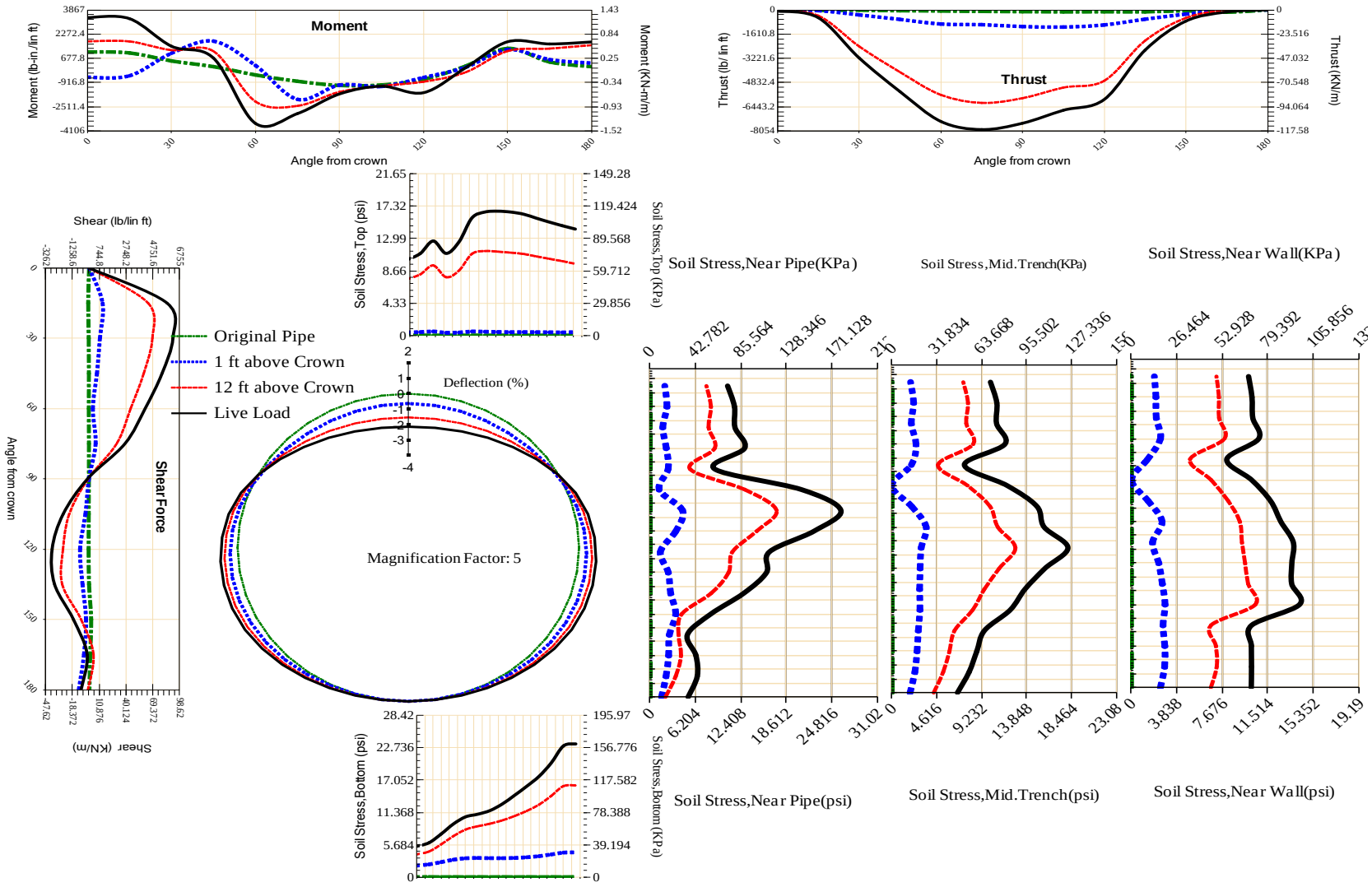

Figure A-573 Param-96-PW230-SF7OR-OD+72-EW10-H12-LiveLoad

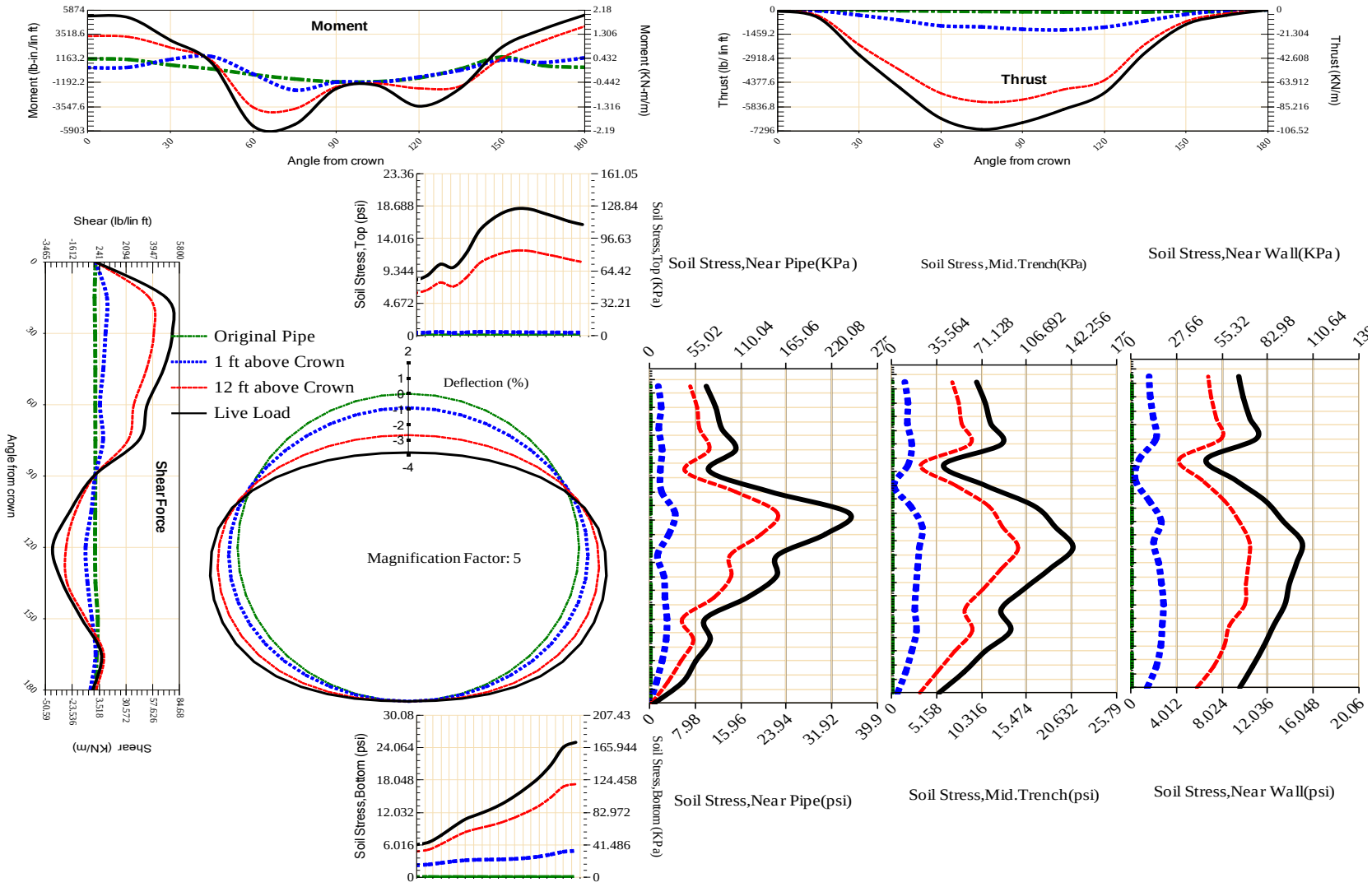

Figure A-574 Param-96-PW230-SF7OR-OD+72-EW3-H12-LiveLoad

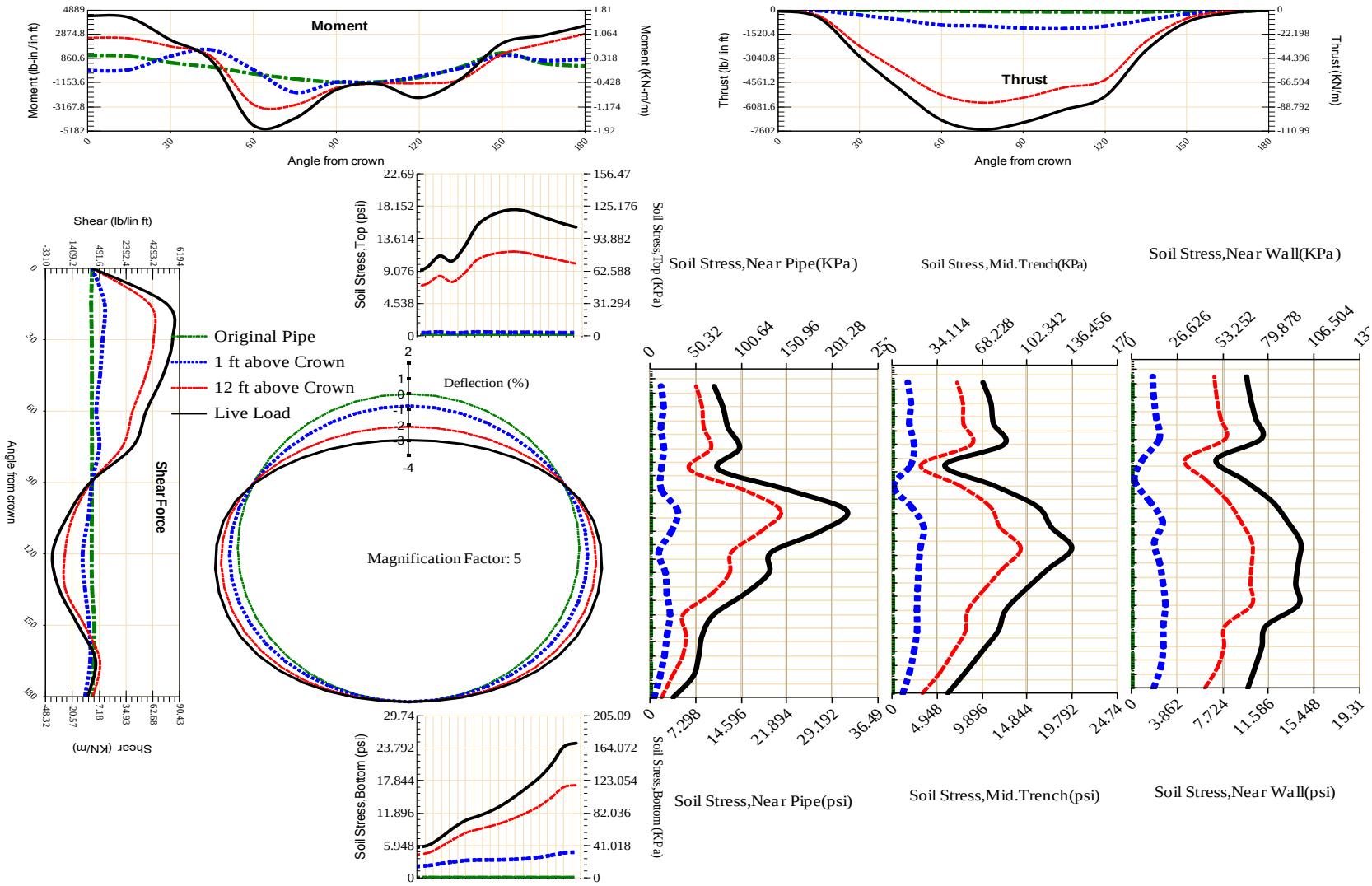

Figure A-575 Param-96-PW230-SF7OR-OD+72-EW5-H12-LiveLoad

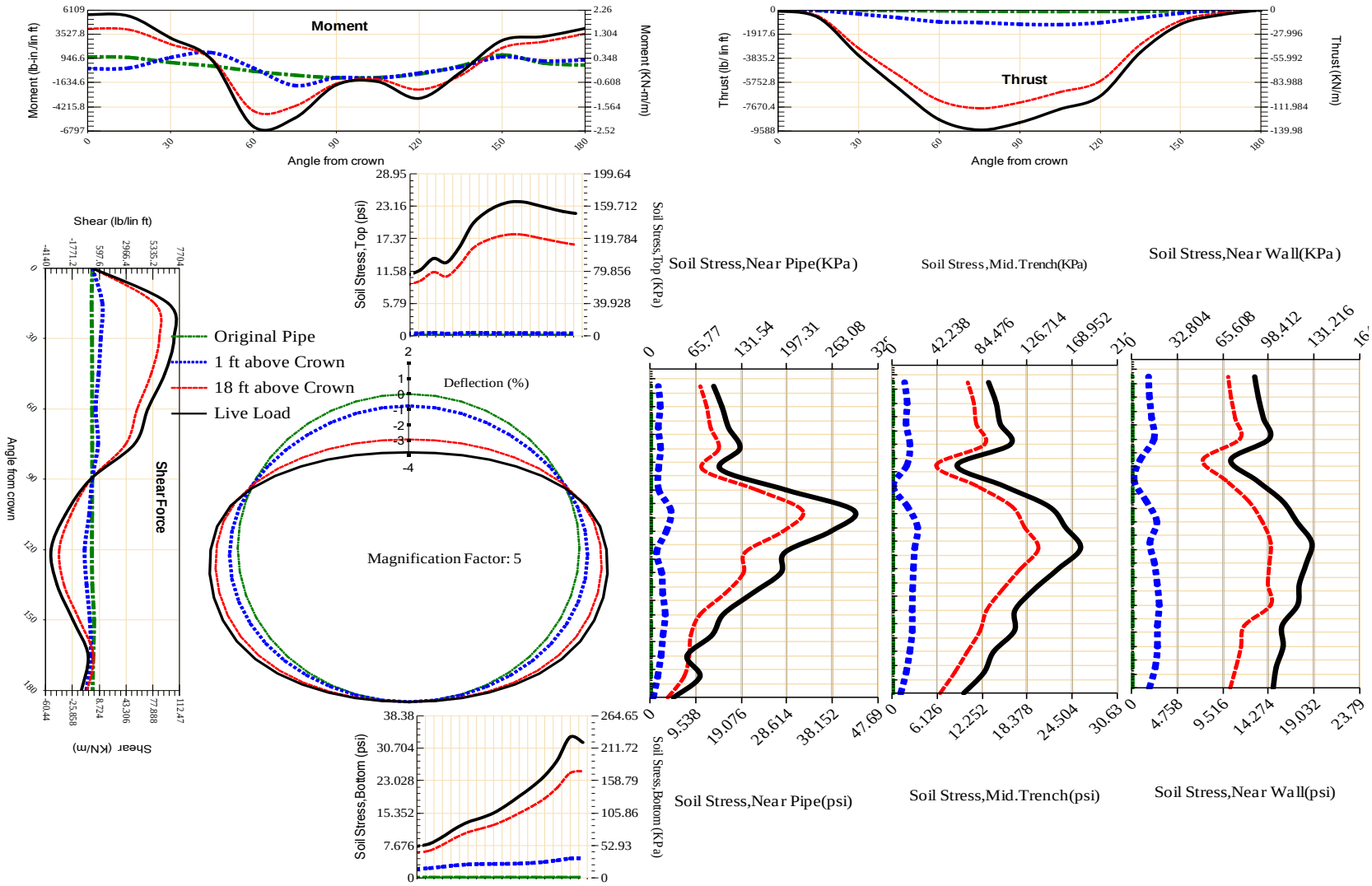

Figure A-576 Param-96-PW230-SF7OR-OD+72-EW5-H18-LiveLoad

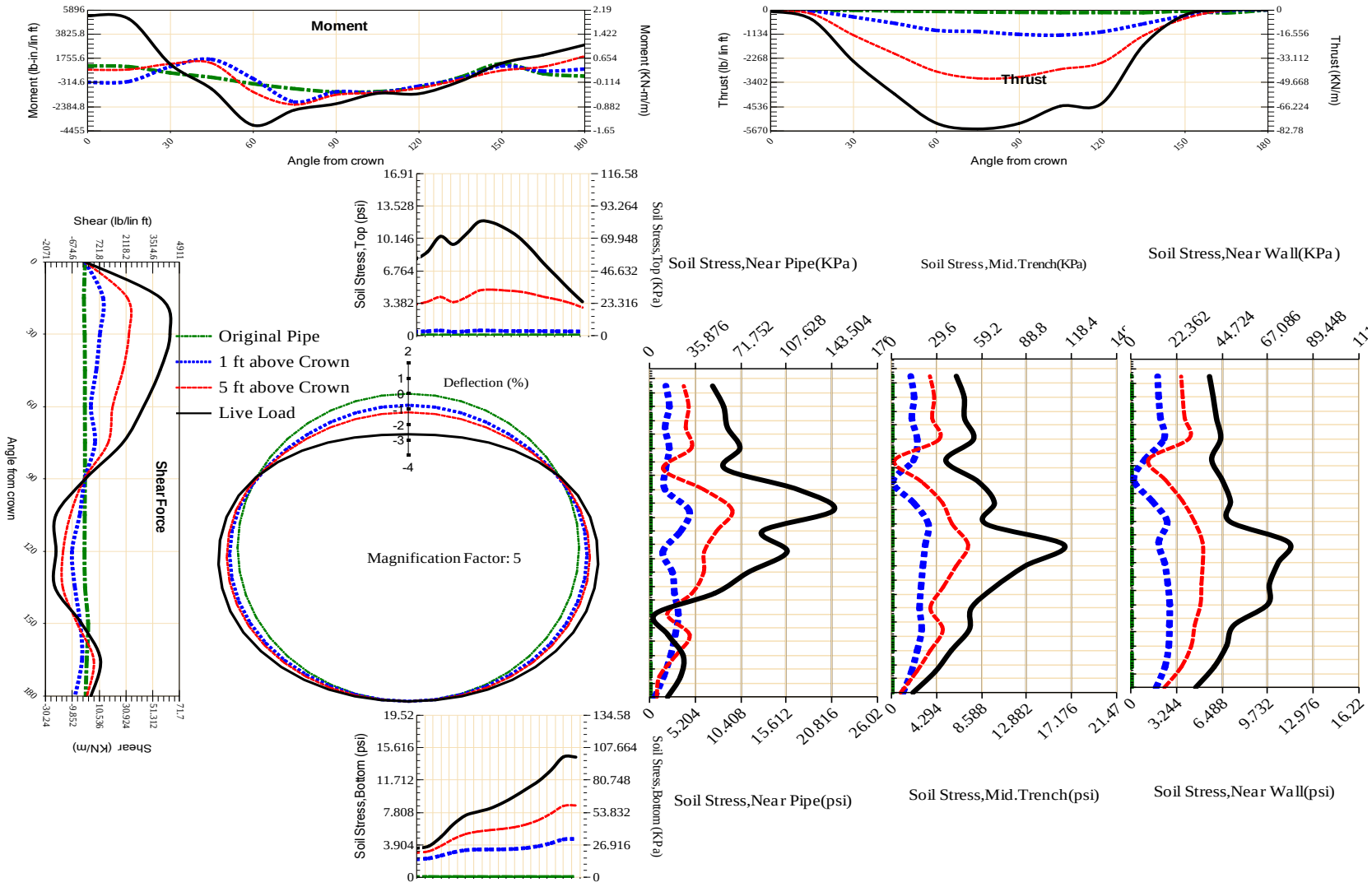

Figure A-577 Param-96-PW230-SF7OR-OD+72-EW5-H5-LiveLoad

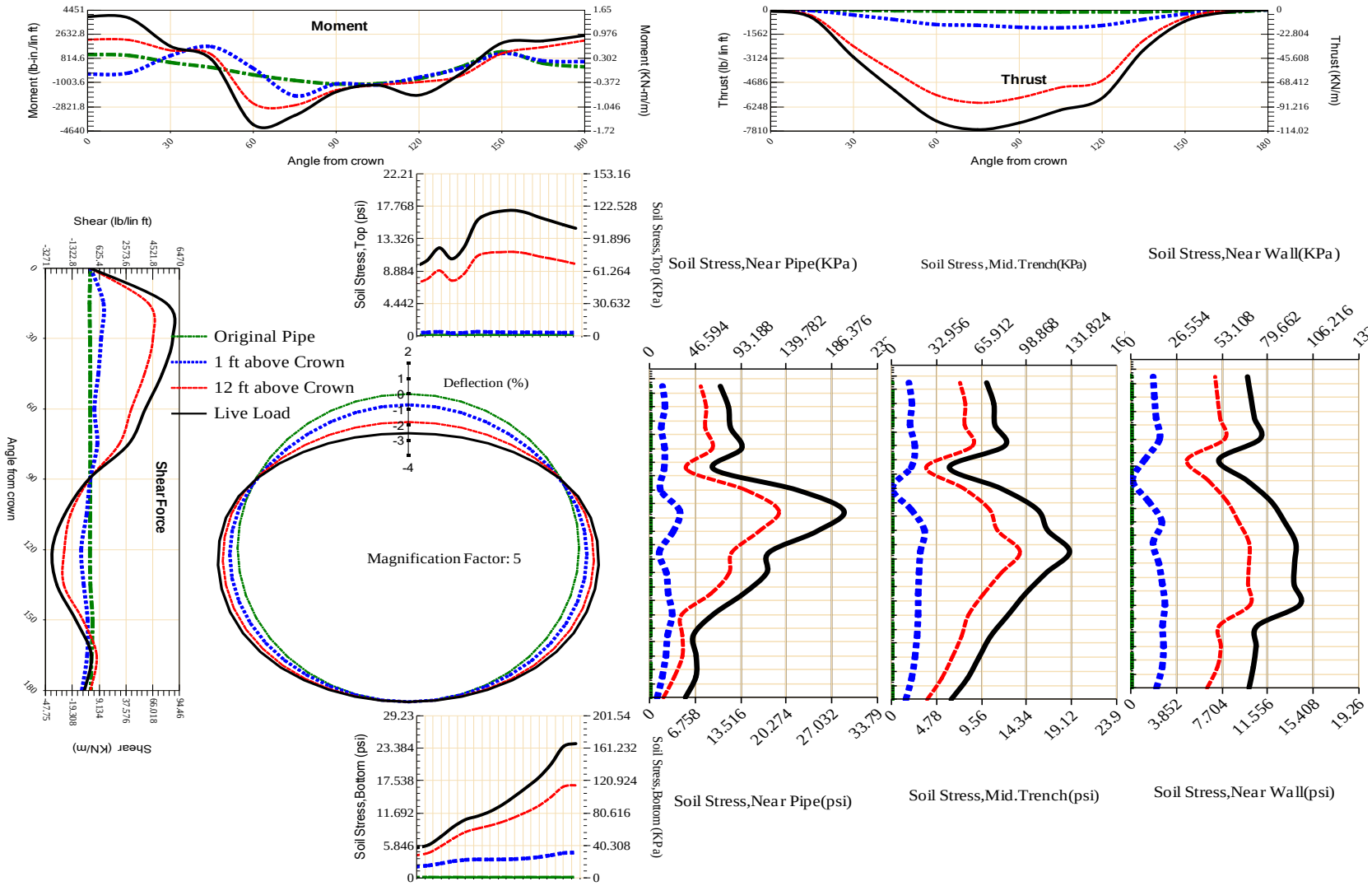

Figure A-578 Param-96-PW230-SF7OR-OD+72-EW7-H12-LiveLoad

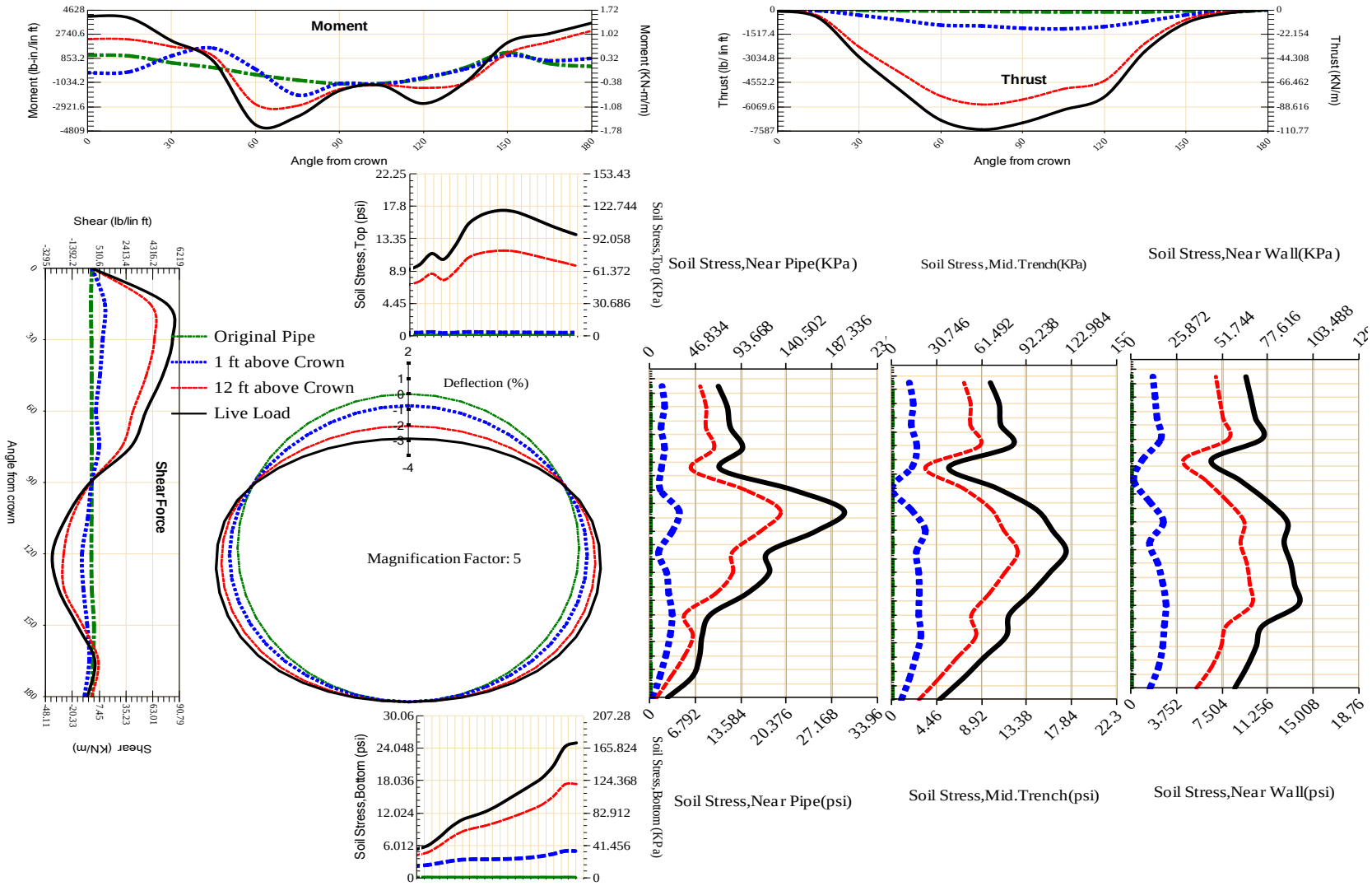

Figure A-579 Param-96-PW230-SF7OR-OD+84-EW5-H12-LiveLoad

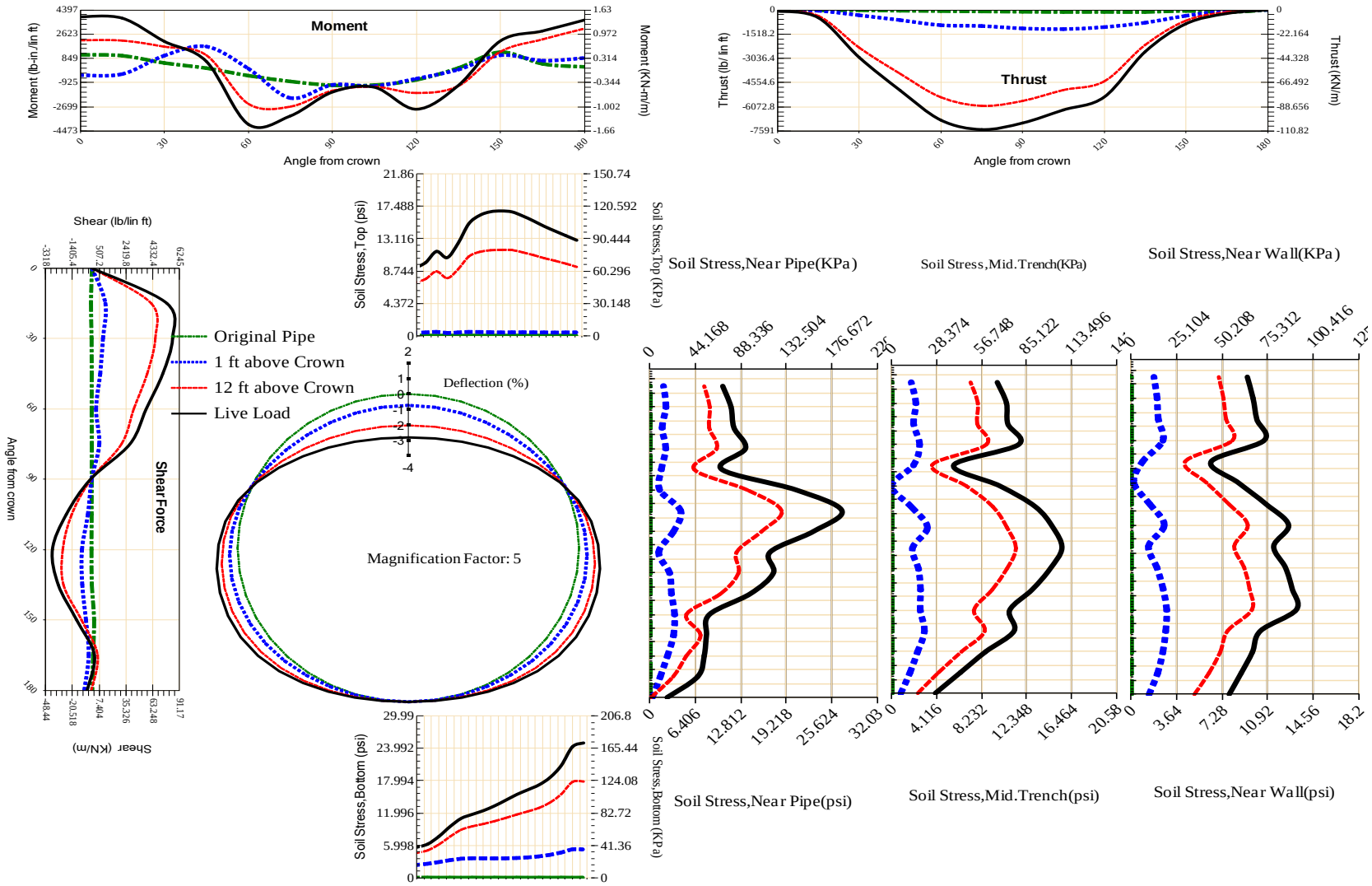

Figure A-580 Param-96-PW230-SF7OR-OD+96-EW5-H12-LiveLoad

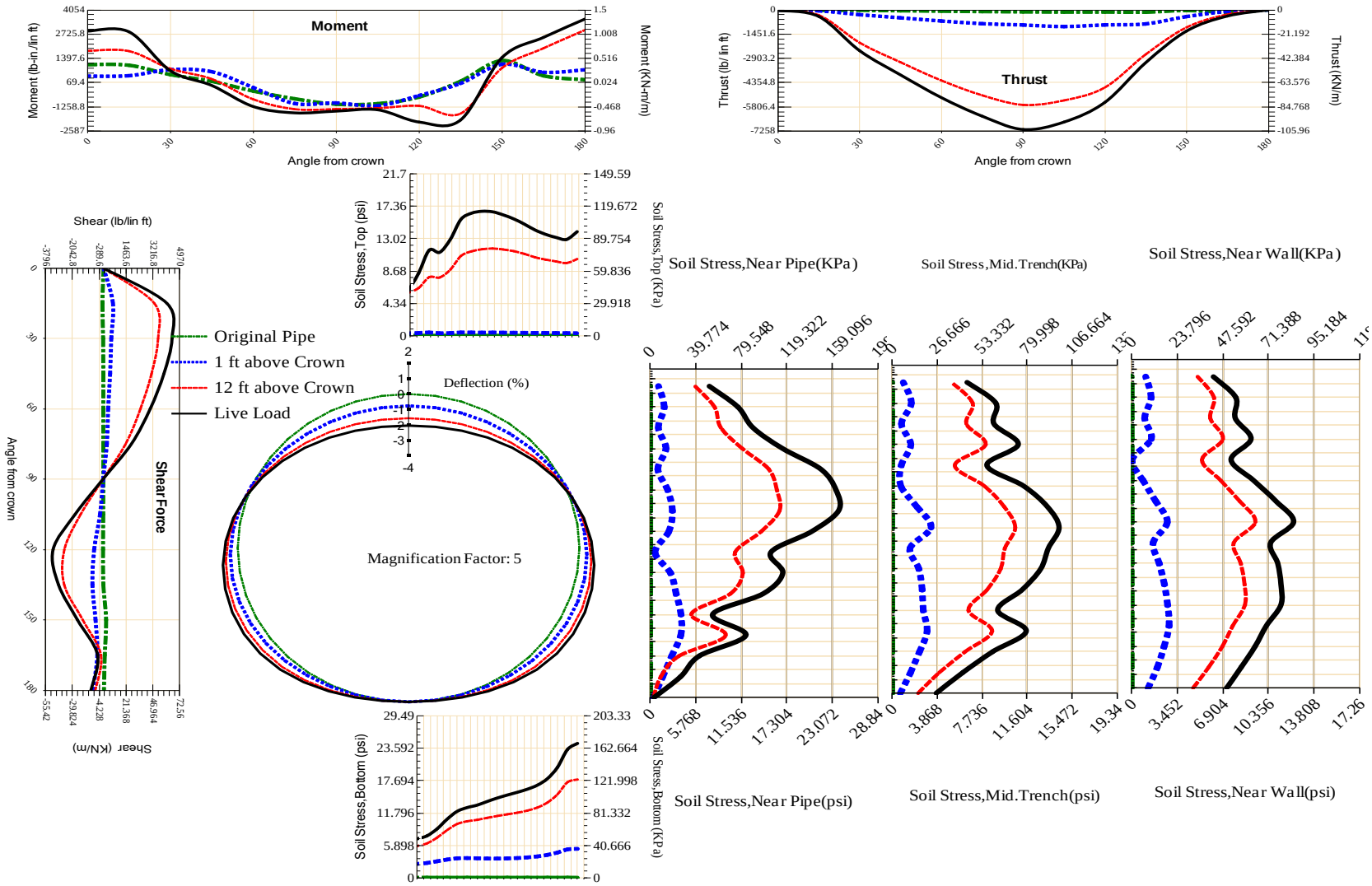

Figure A-581 Param-96-PW230-SF7TR-OD+108-EW5-H12-LiveLoad

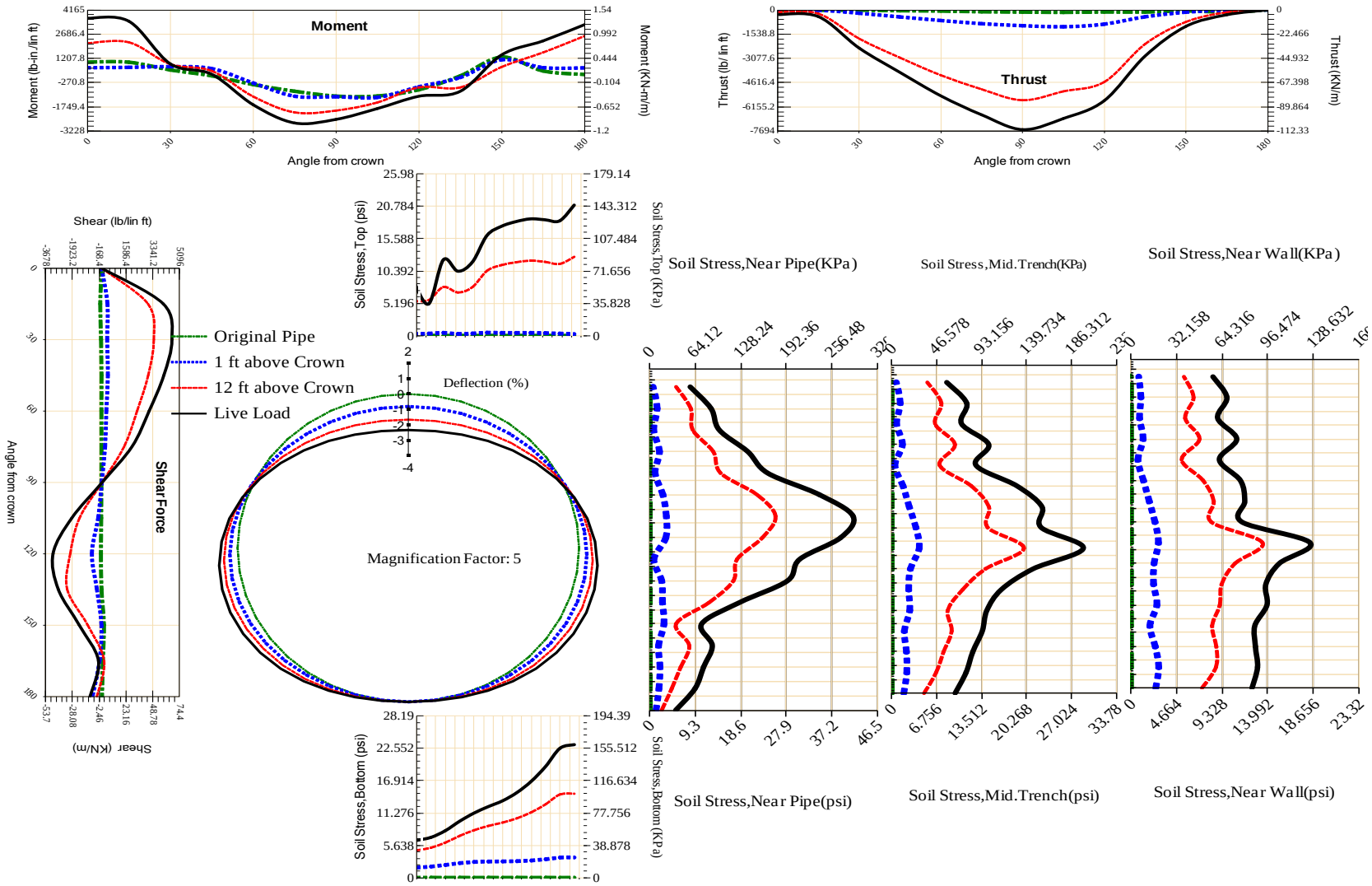

Figure A-582 Param-96-PW230-SF7TR-OD+48-EW5-H12-LiveLoad

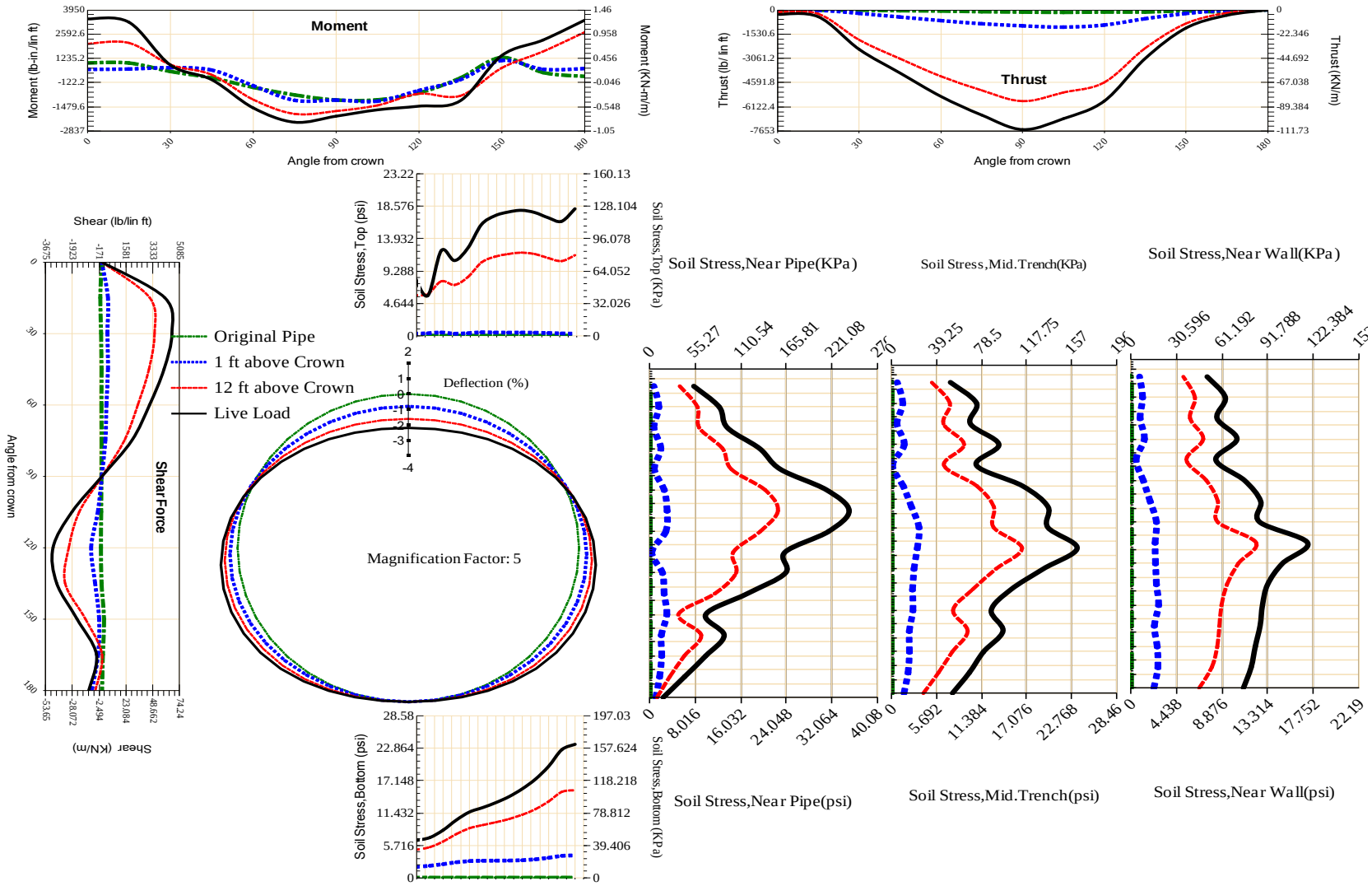

Figure A-583 Param-96-PW230-SF7TR-OD+60-EW5-H12-LiveLoad

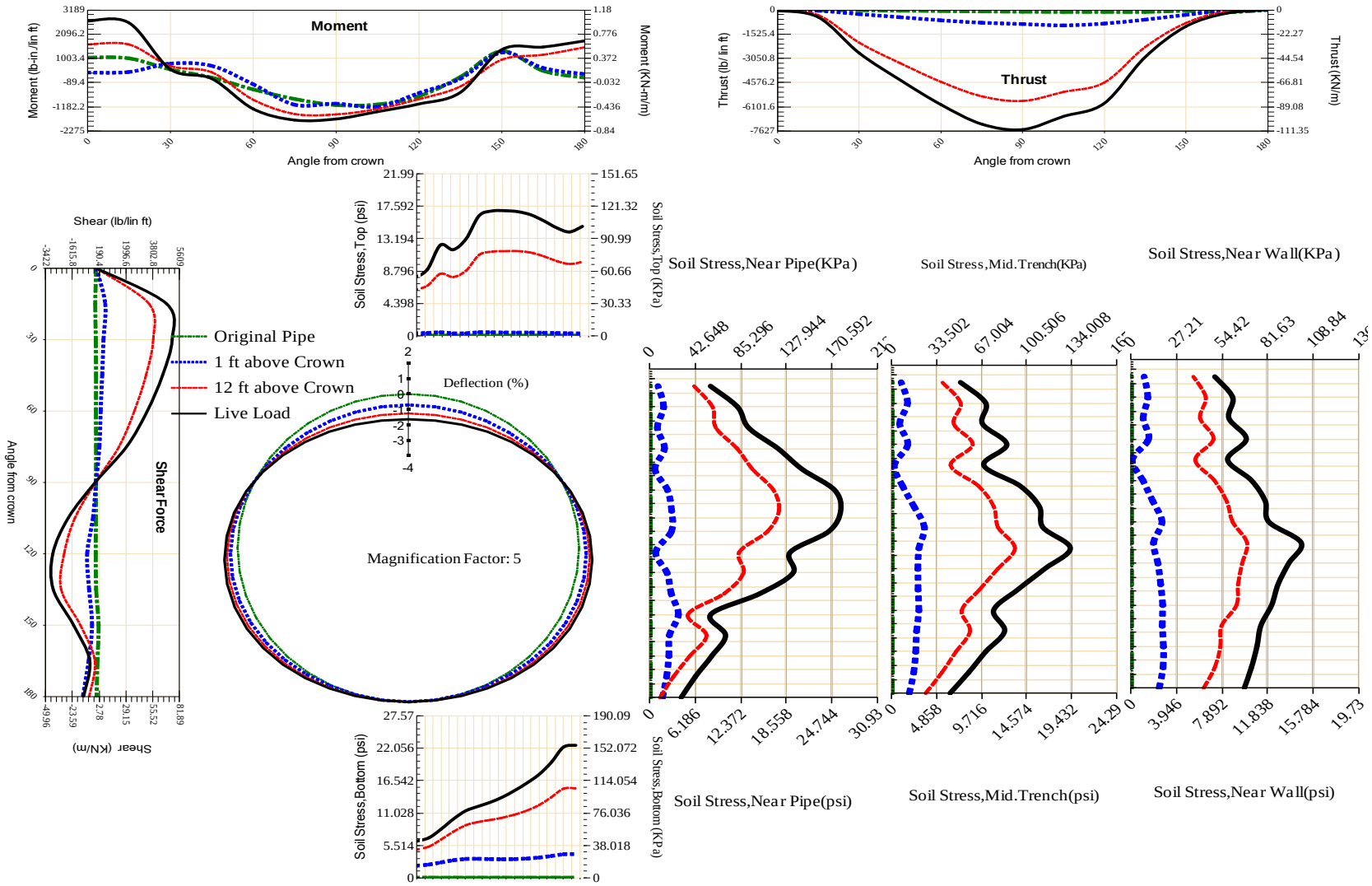

Figure A-584 Param-96-PW230-SF7TR-OD+72-EW10-H12-LiveLoad

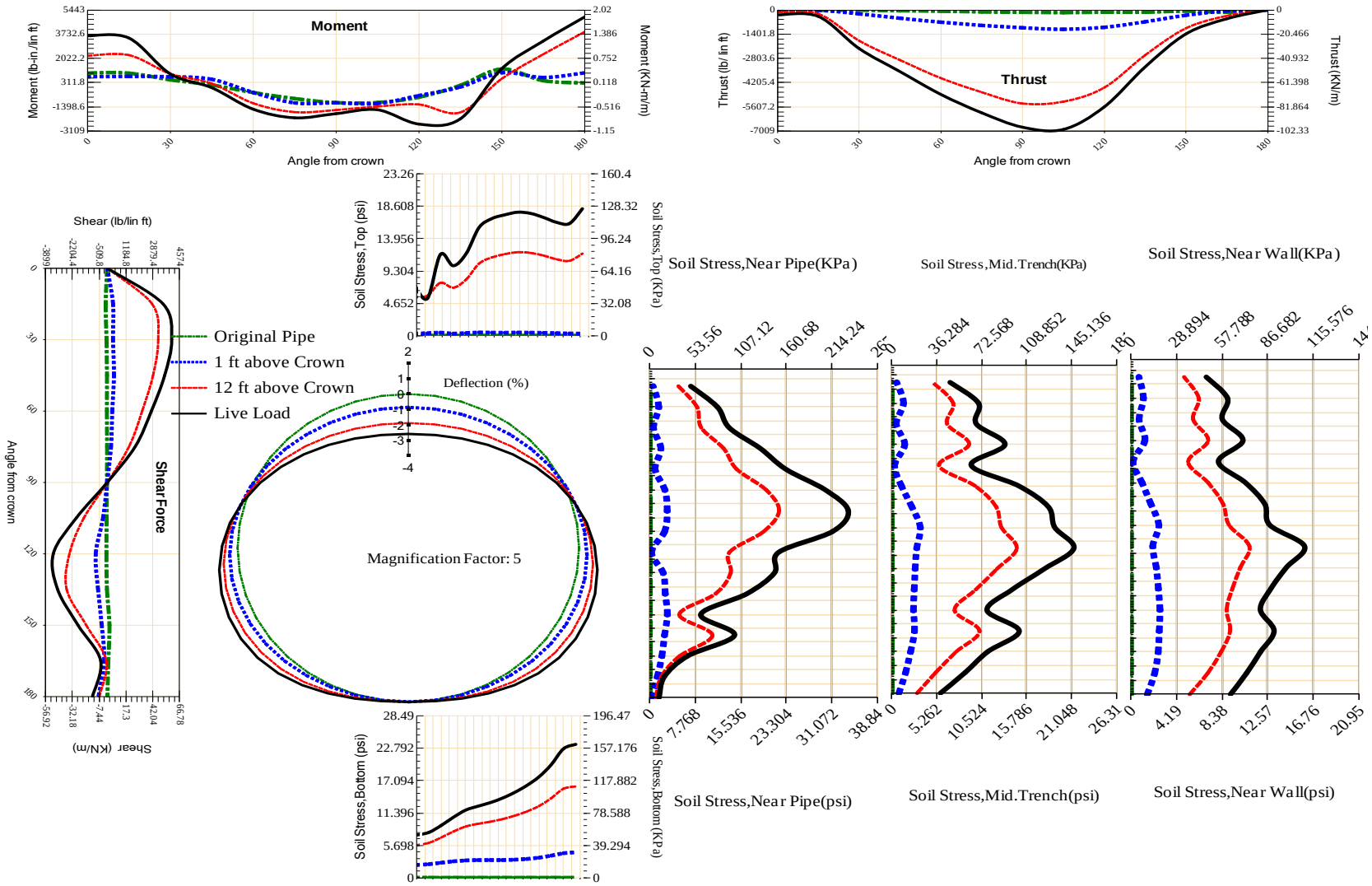

Figure A-585 Param-96-PW230-SF7TR-OD+72-EW3-H12-LiveLoad

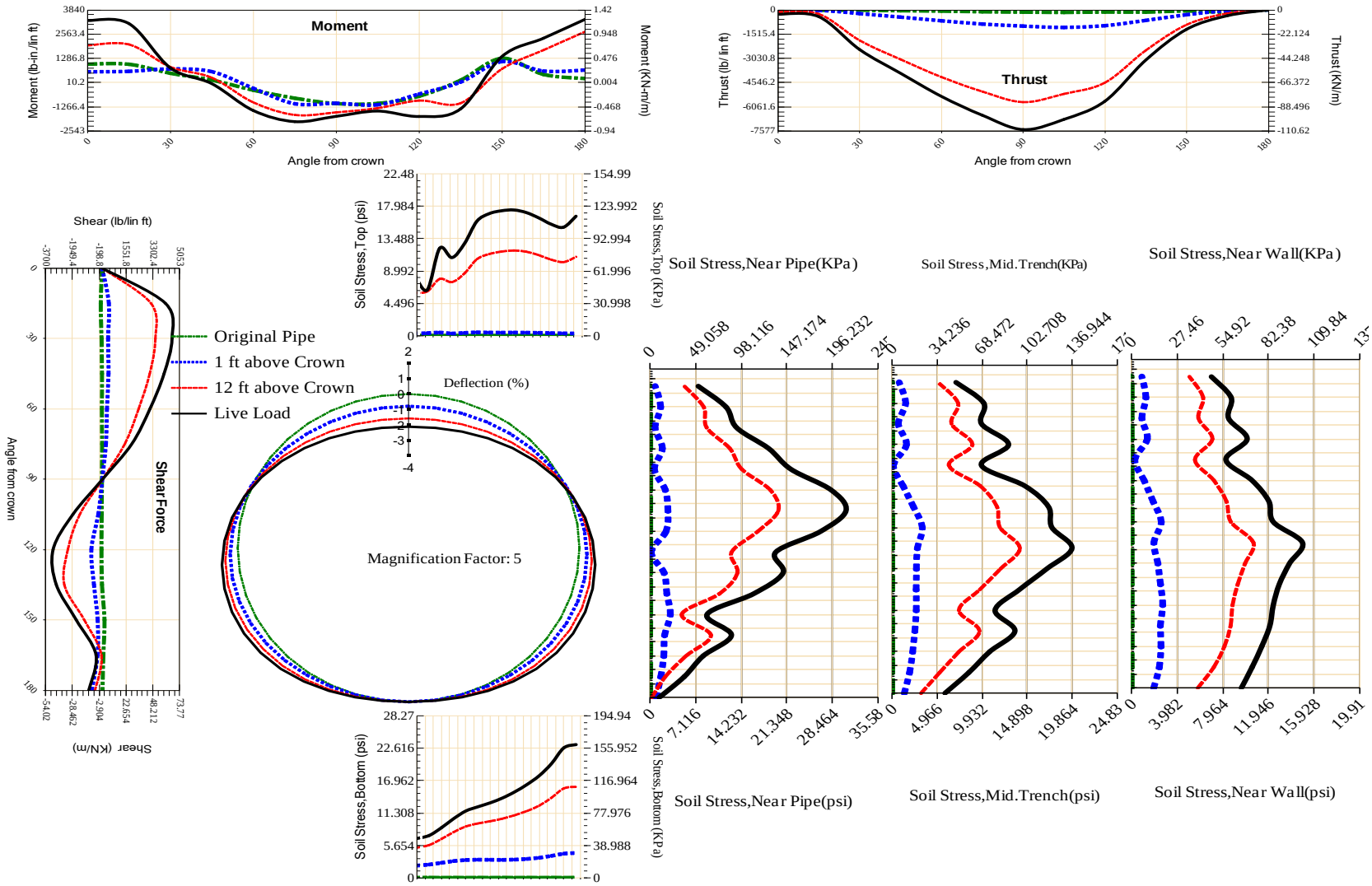

Figure A-586 Param-96-PW230-SF7TR-OD+72-EW5-H12-LiveLoad

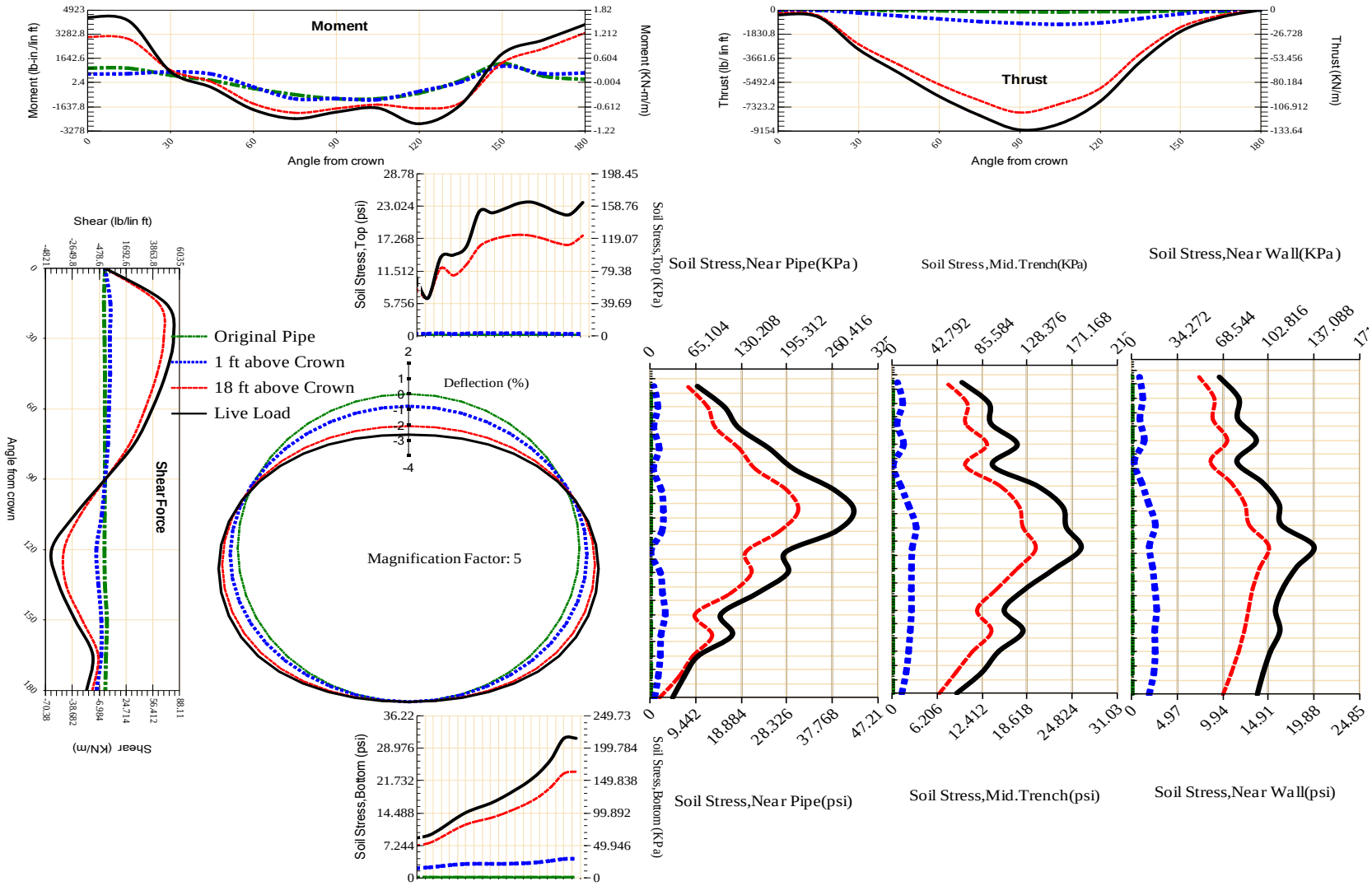

Figure A-587 Param-96-PW230-SF7TR-OD+72-EW5-H18-LiveLoad

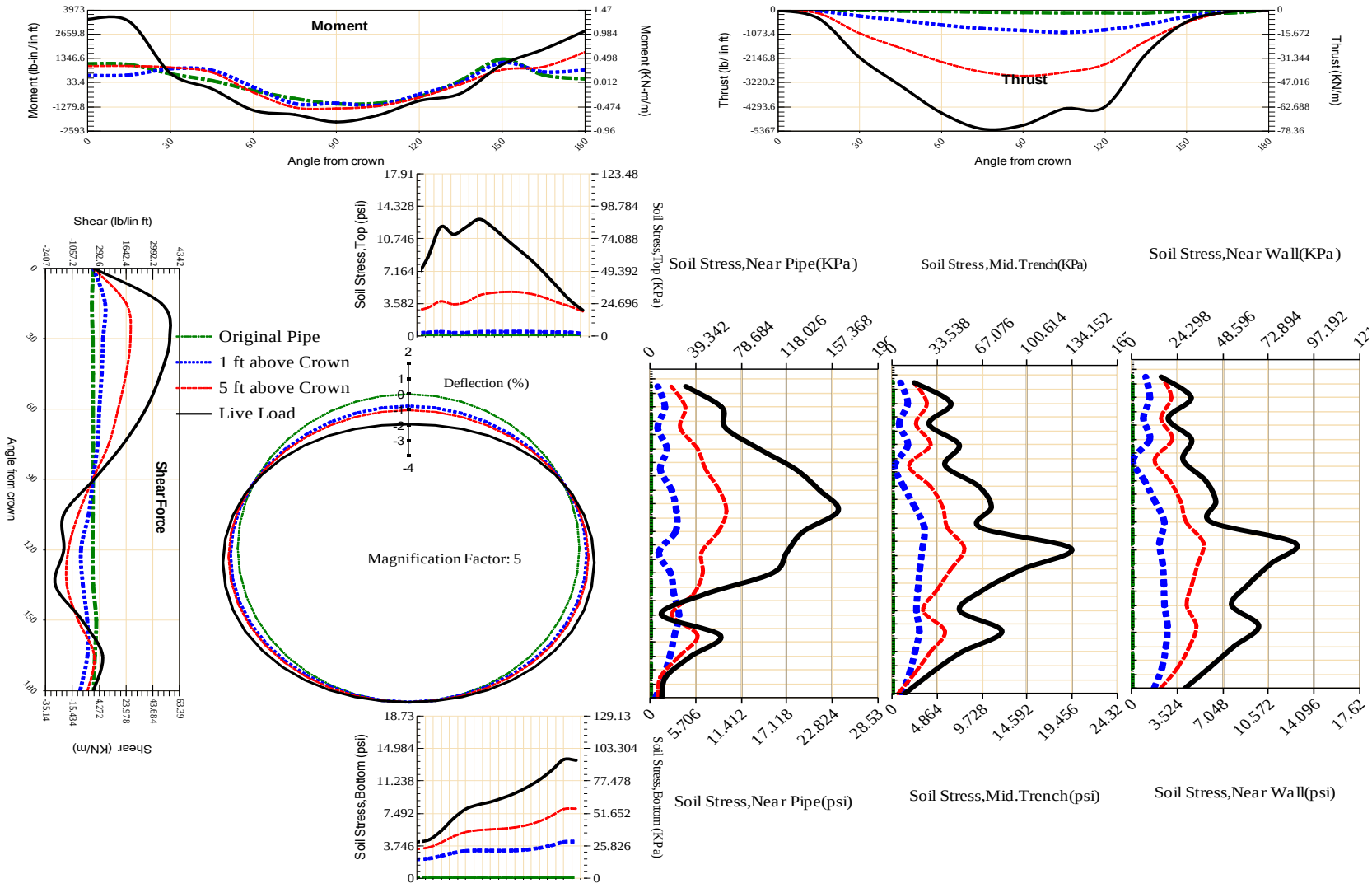

Figure A-588 Param-96-PW230-SF7TR-OD+72-EW5-H5-LiveLoad

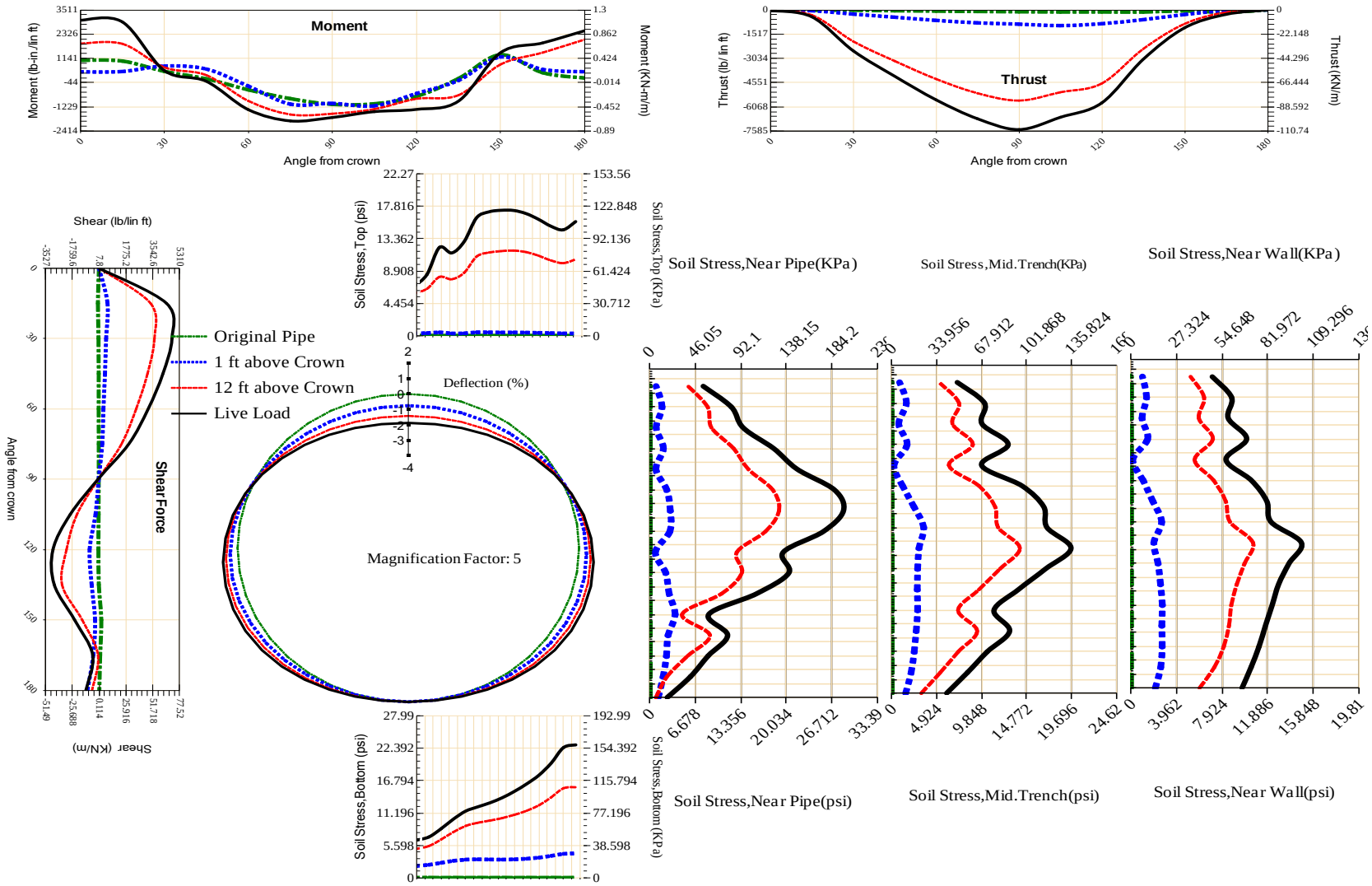

Figure A-589 Param-96-PW230-SF7TR-OD+72-EW7-H12-LiveLoad

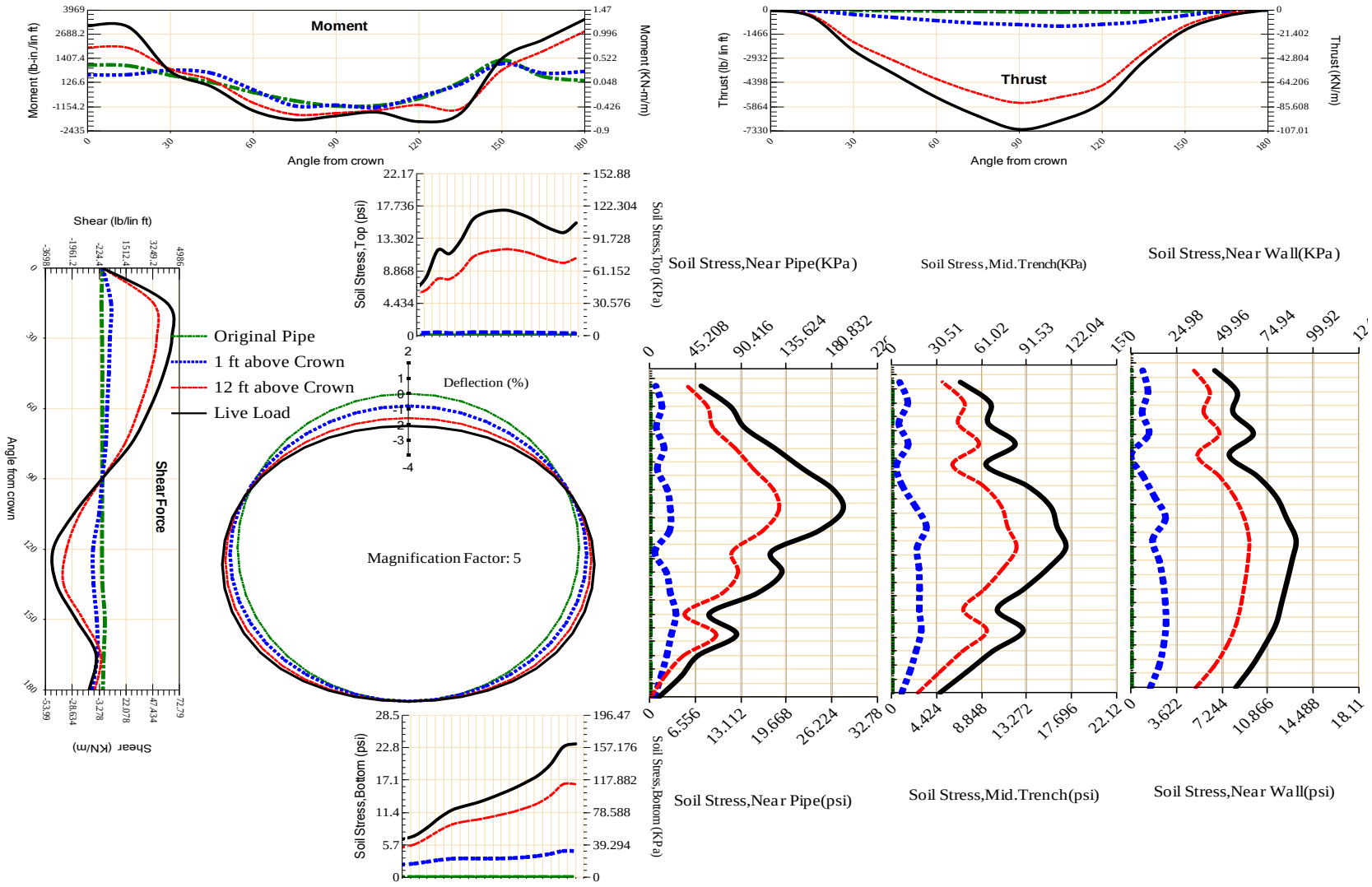

Figure A-590 Param-96-PW230-SF7TR-OD+84-EW5-H12-LiveLoad

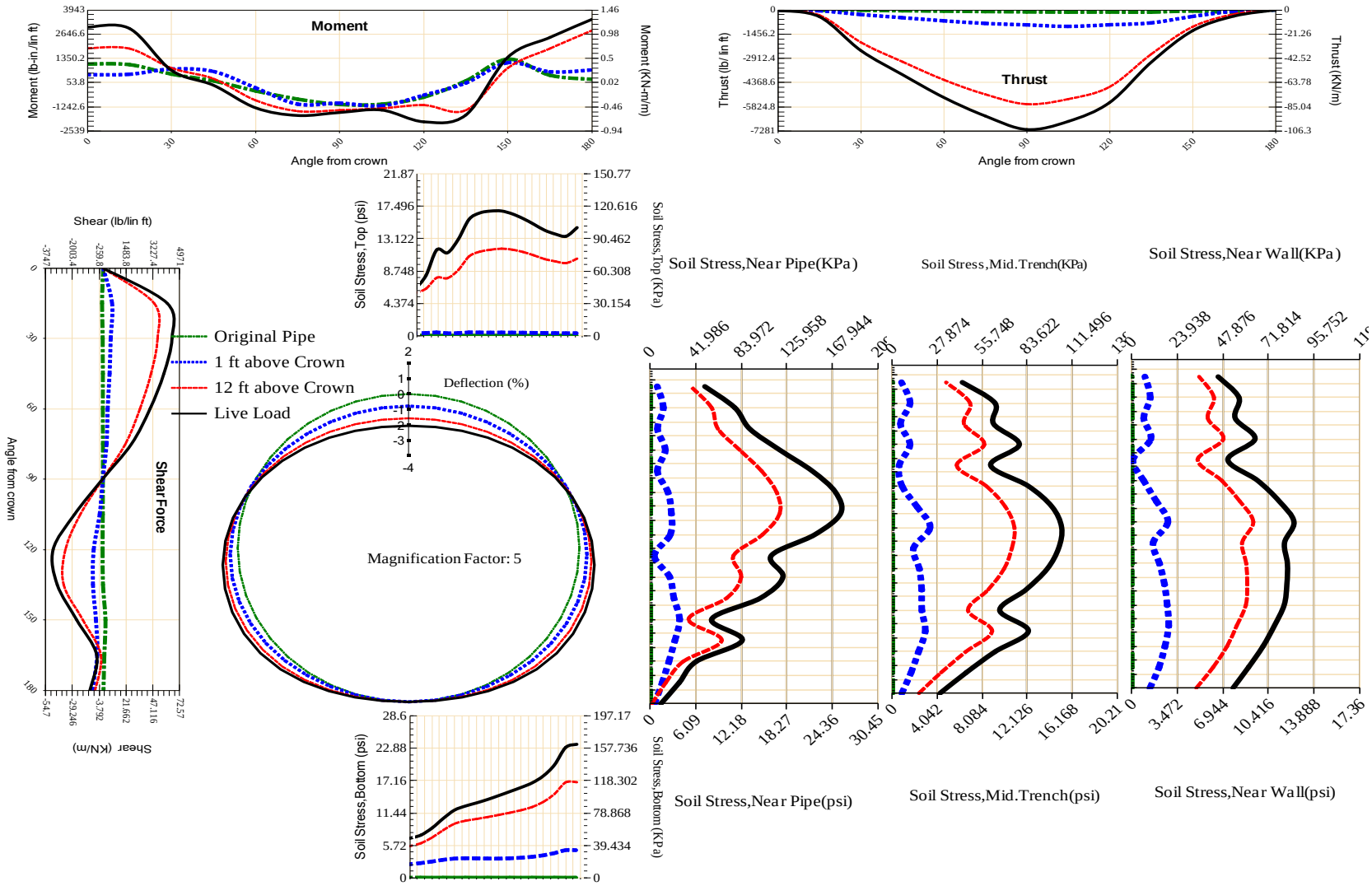

Figure A-591 Param-96-PW230-SF7TR-OD+96-EW5-H12-LiveLoad

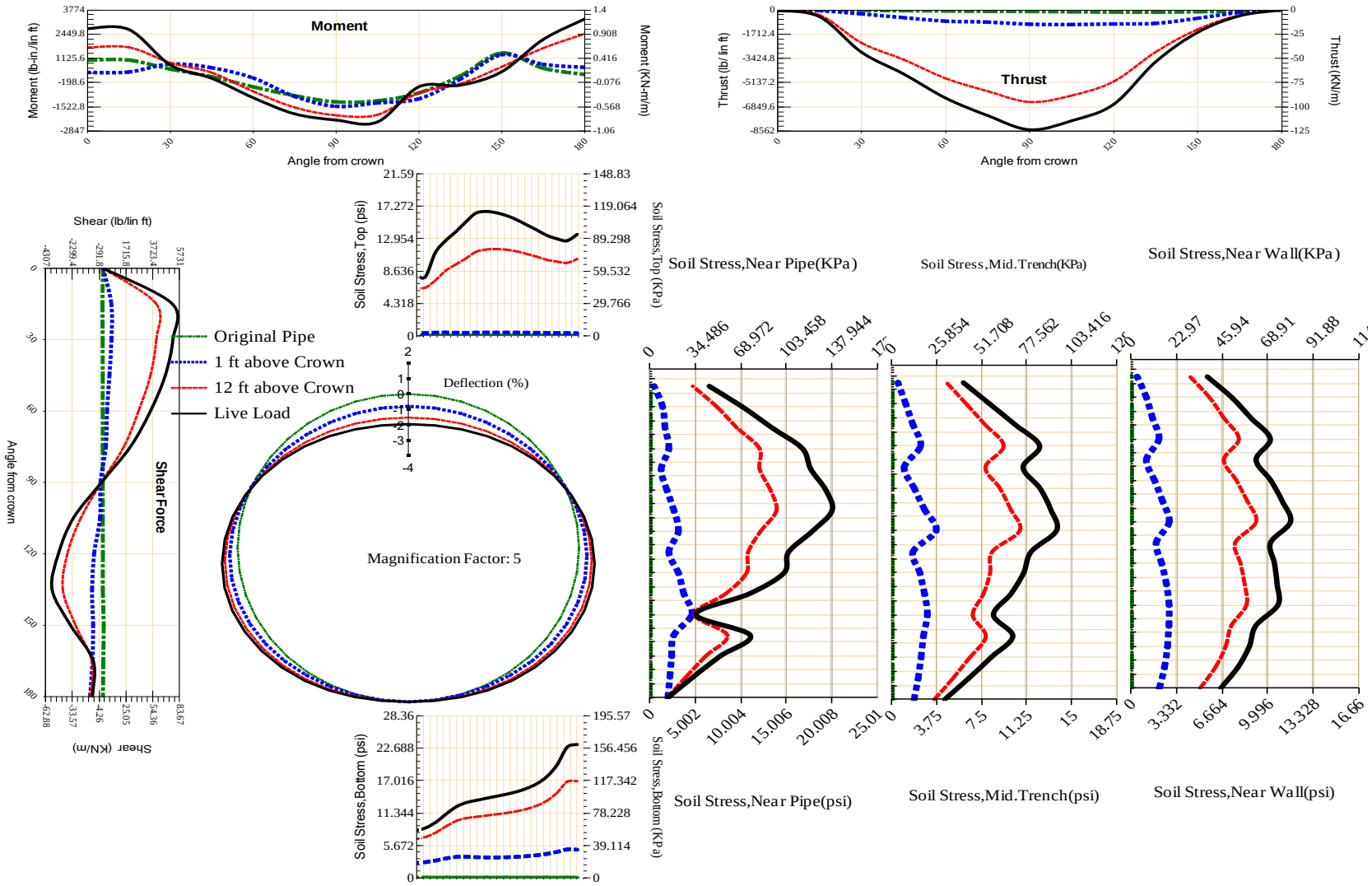

Figure A-592 Param-96-PW230-TR10TR-OD+108-EW5-H12-LiveLoad

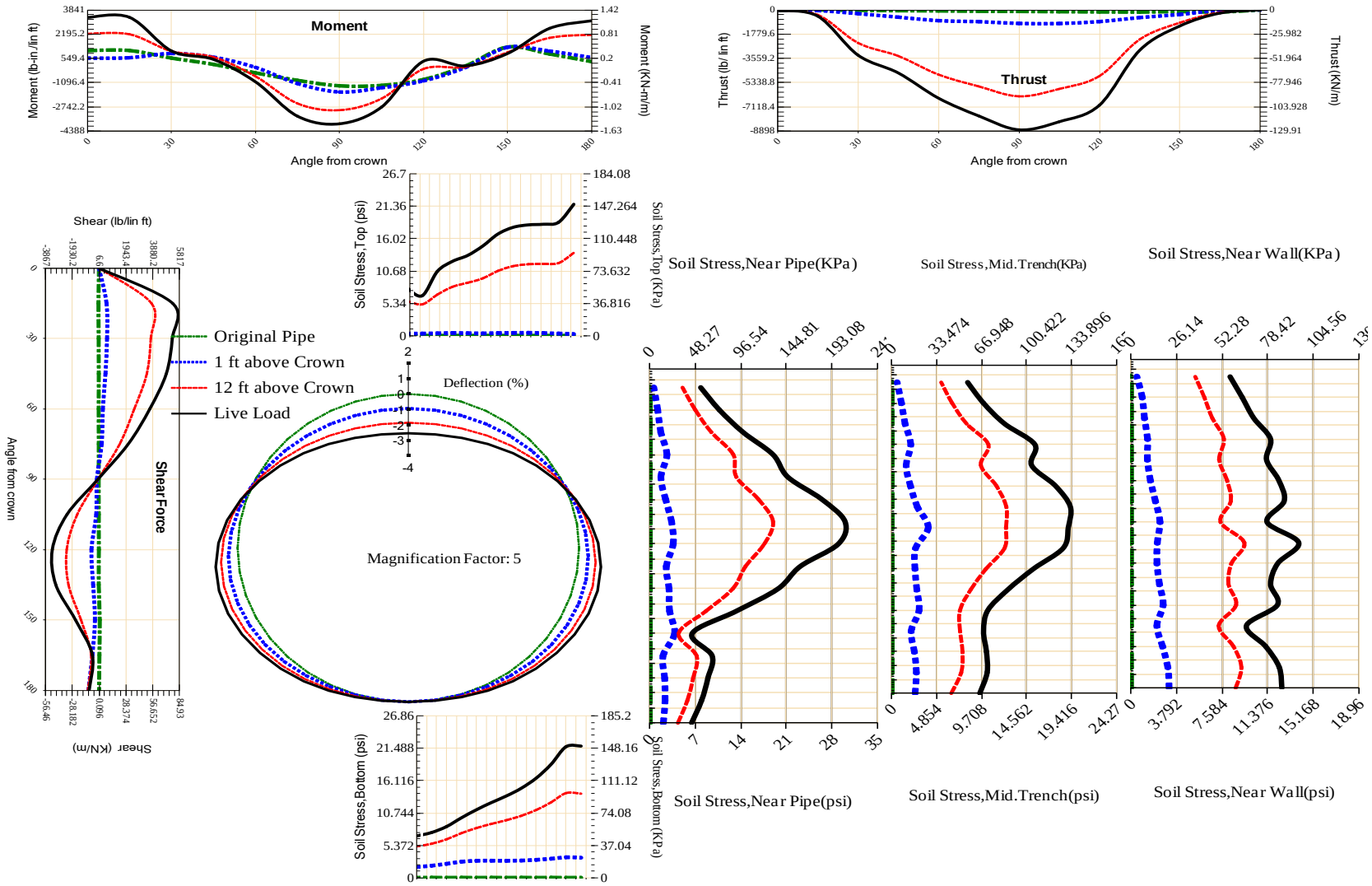

Figure A-593 Param-96-PW230-TR10TR-OD+48-EW5-H12-LiveLoad

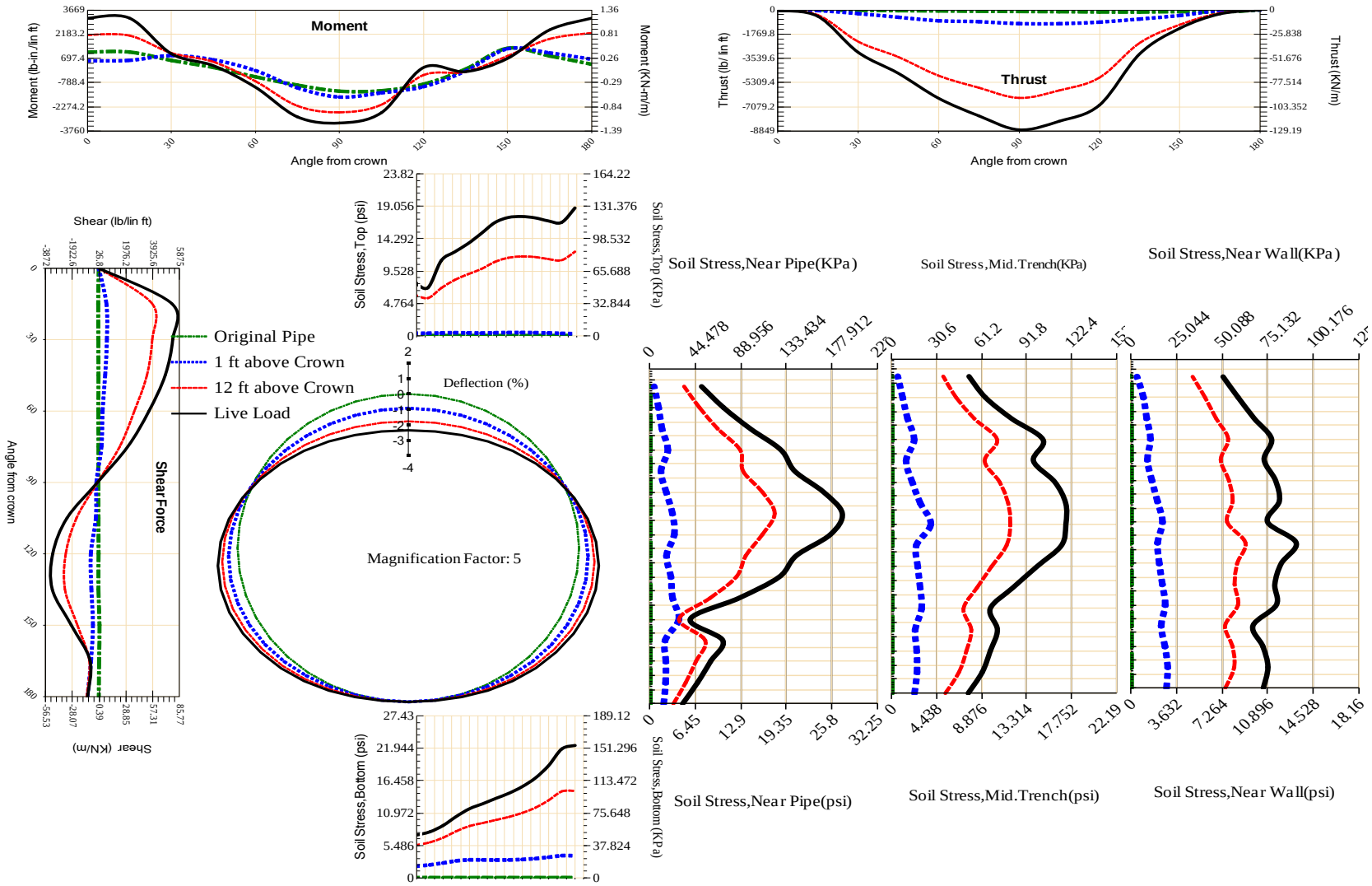

Figure A-594 Param-96-PW230-TR10TR-OD+60-EW5-H12-LiveLoad

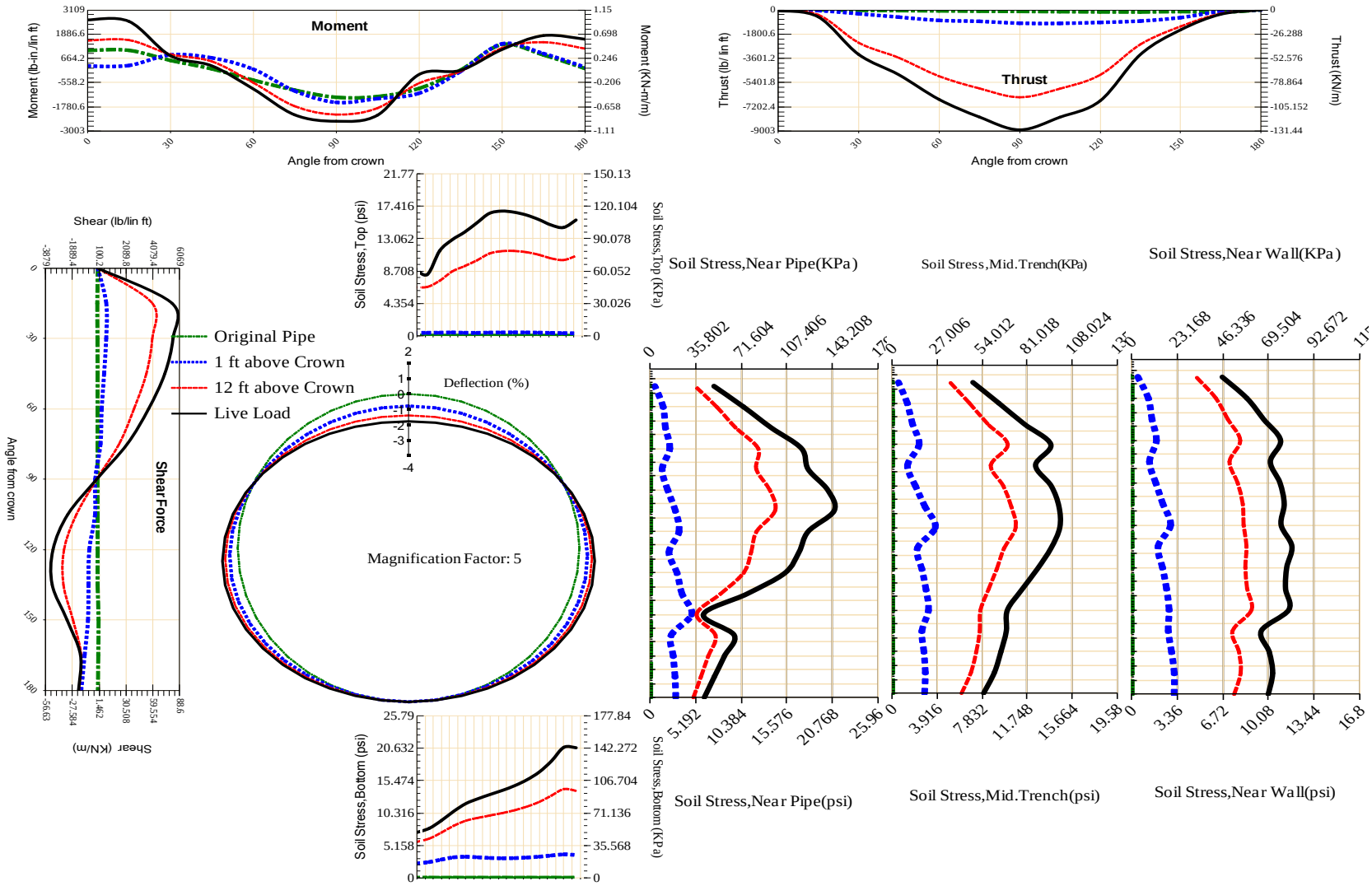

Figure A-595 Param-96-PW230-TR10TR-OD+72-EW10-H12-LiveLoad

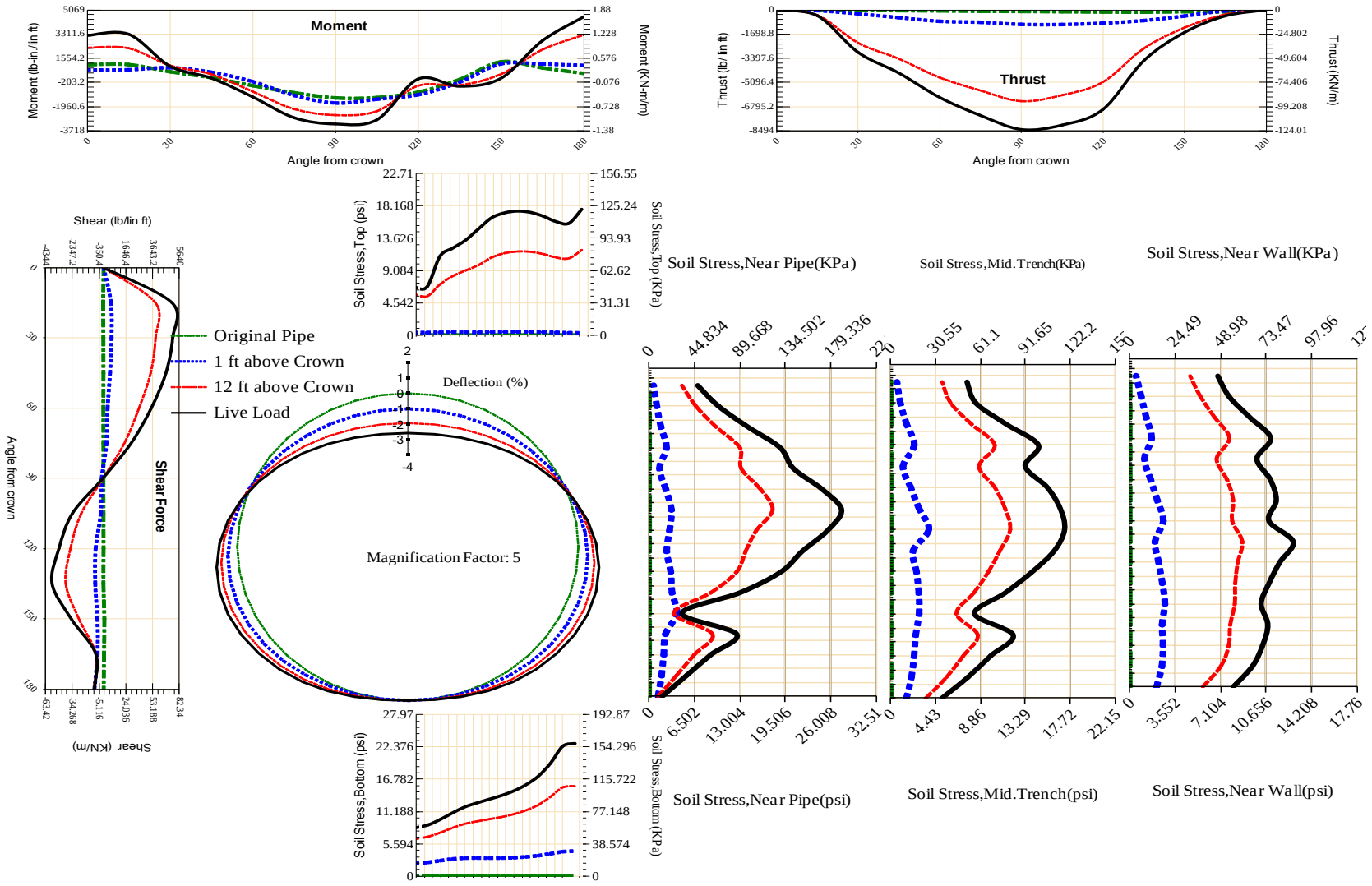

Figure A-596 Param-96-PW230-TR10TR-OD+72-EW3-H12-LiveLoad

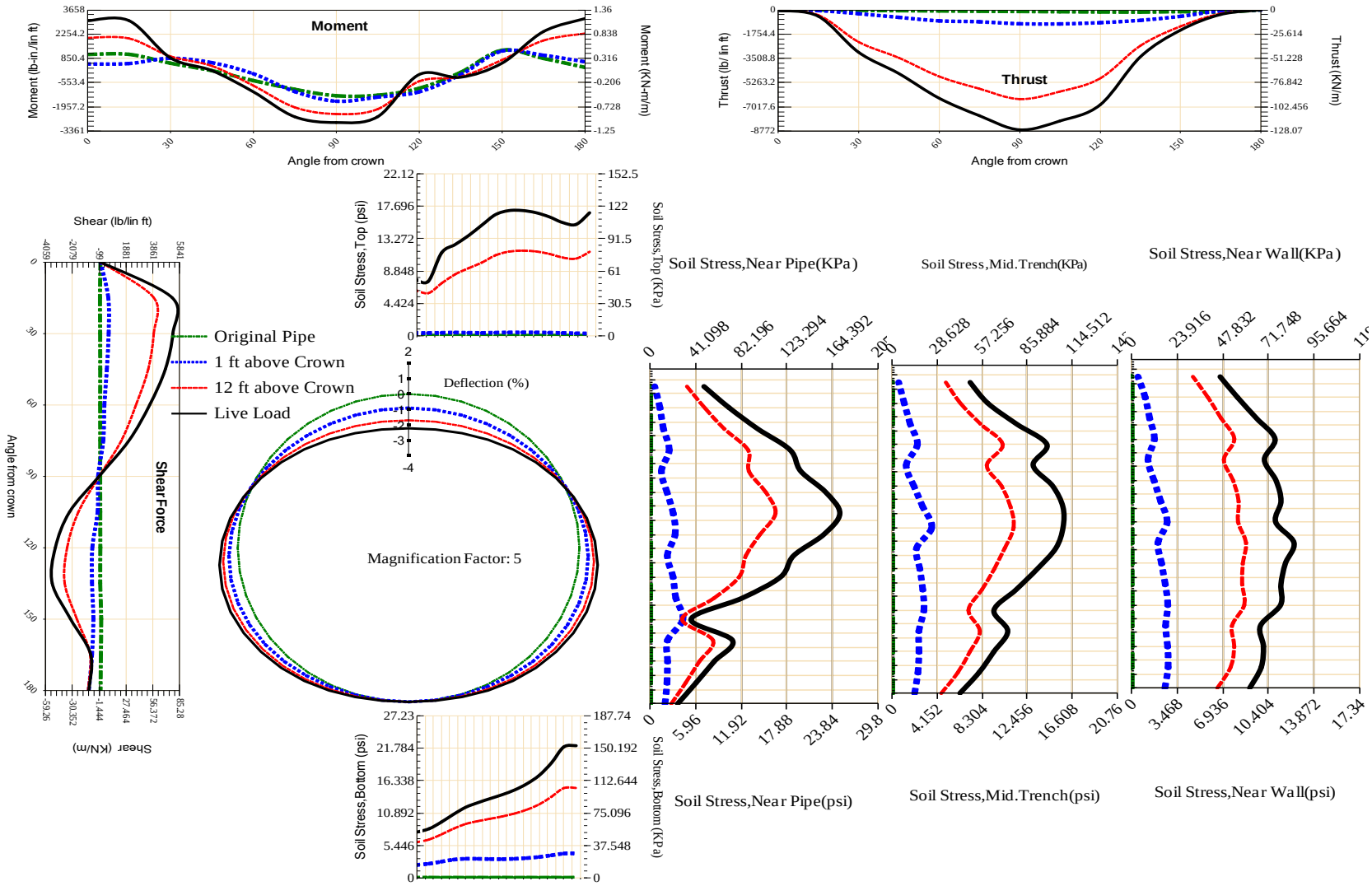

Figure A-597 Param-96-PW230-TR10TR-OD+72-EW5-H12-LiveLoad

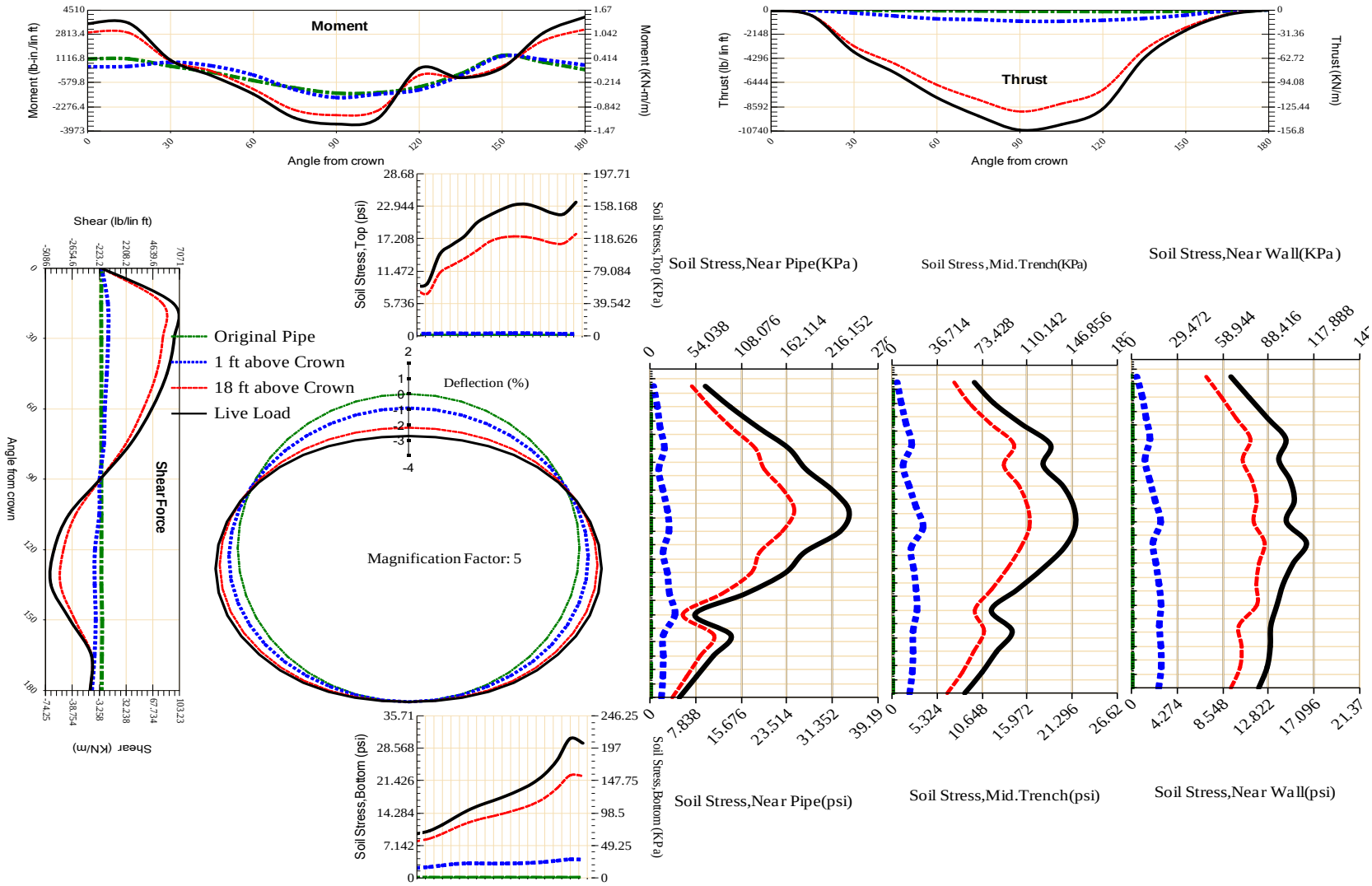

Figure A-598 Param-96-PW230-TR10TR-OD+72-EW5-H18-LiveLoad

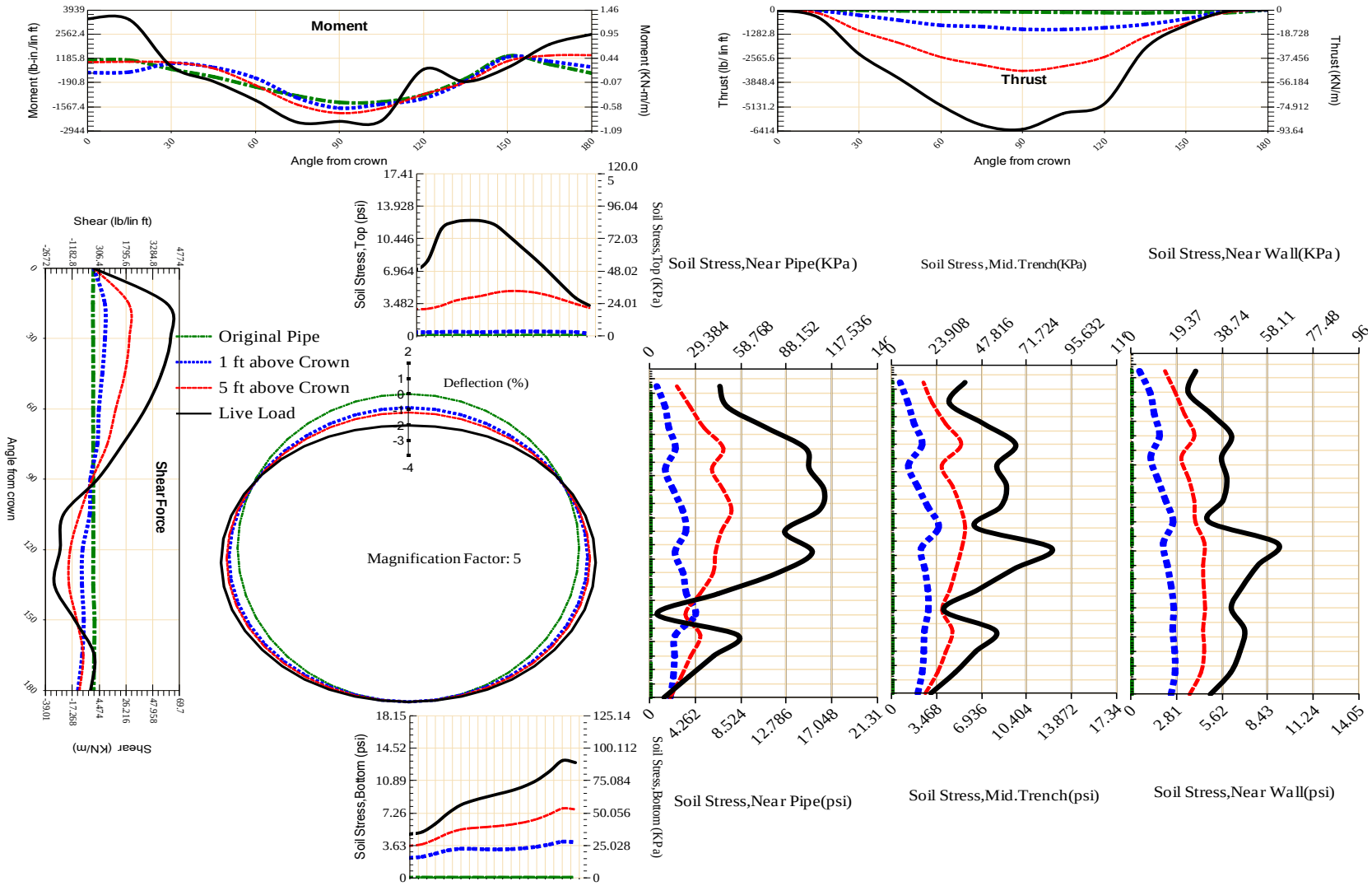

Figure A-599 Param-96-PW230-TR10TR-OD+72-EW5-H5-LiveLoad

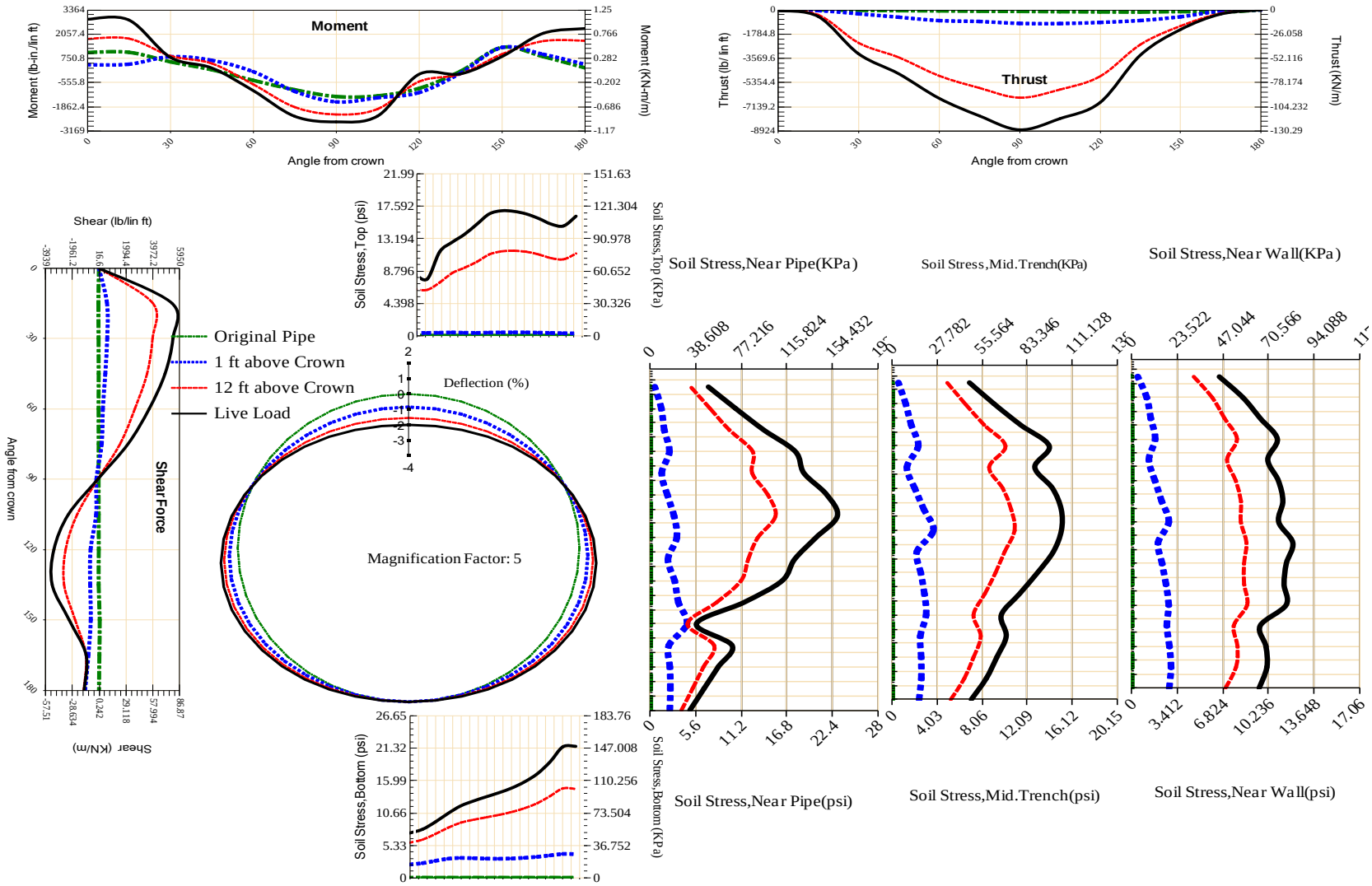

Figure A-600 Param-96-PW230-TR10TR-OD+72-EW7-H12-LiveLoad

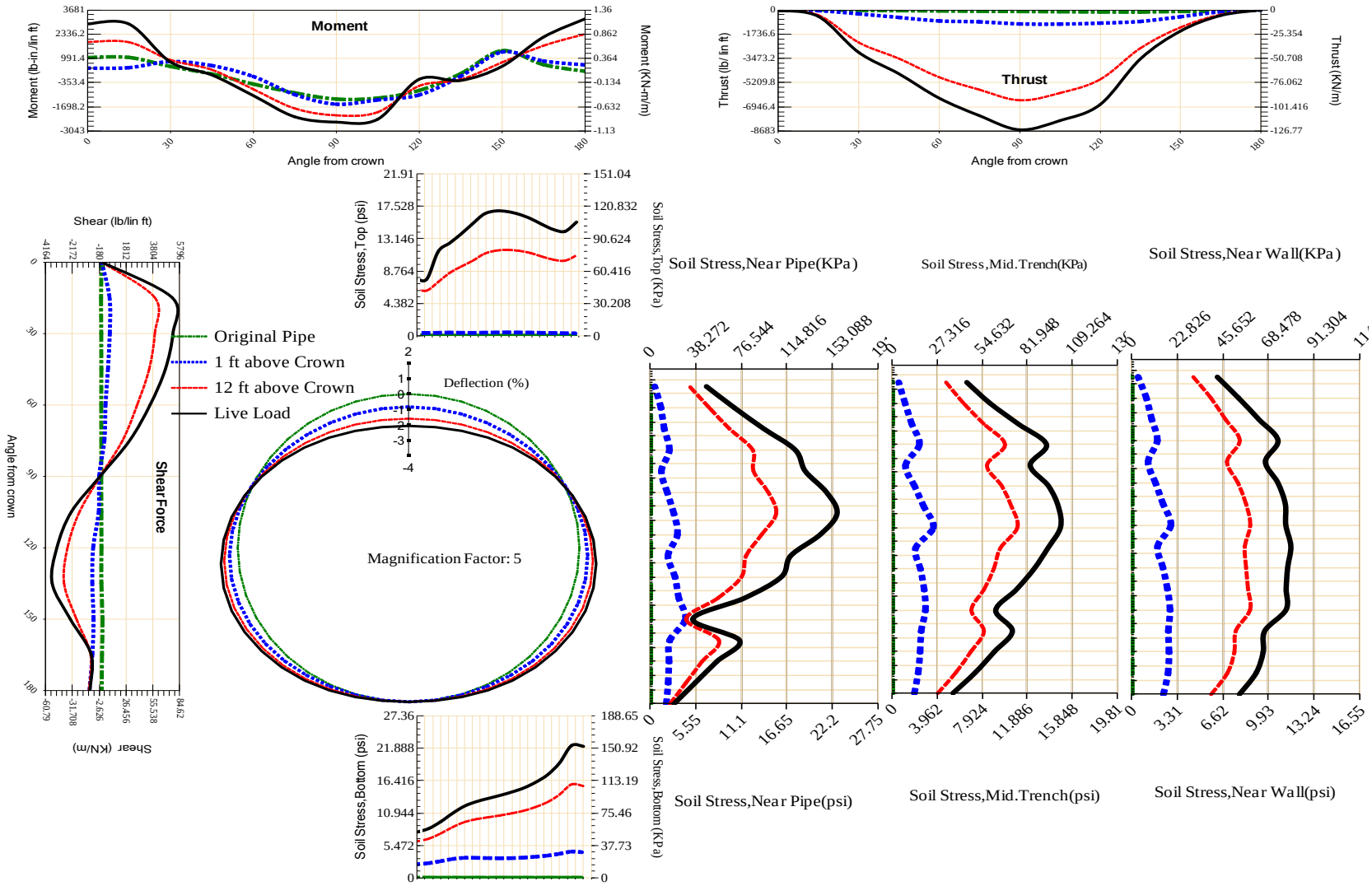

Figure A-601 Param-96-PW230-TR10TR-OD+84-EW5-H12-LiveLoad

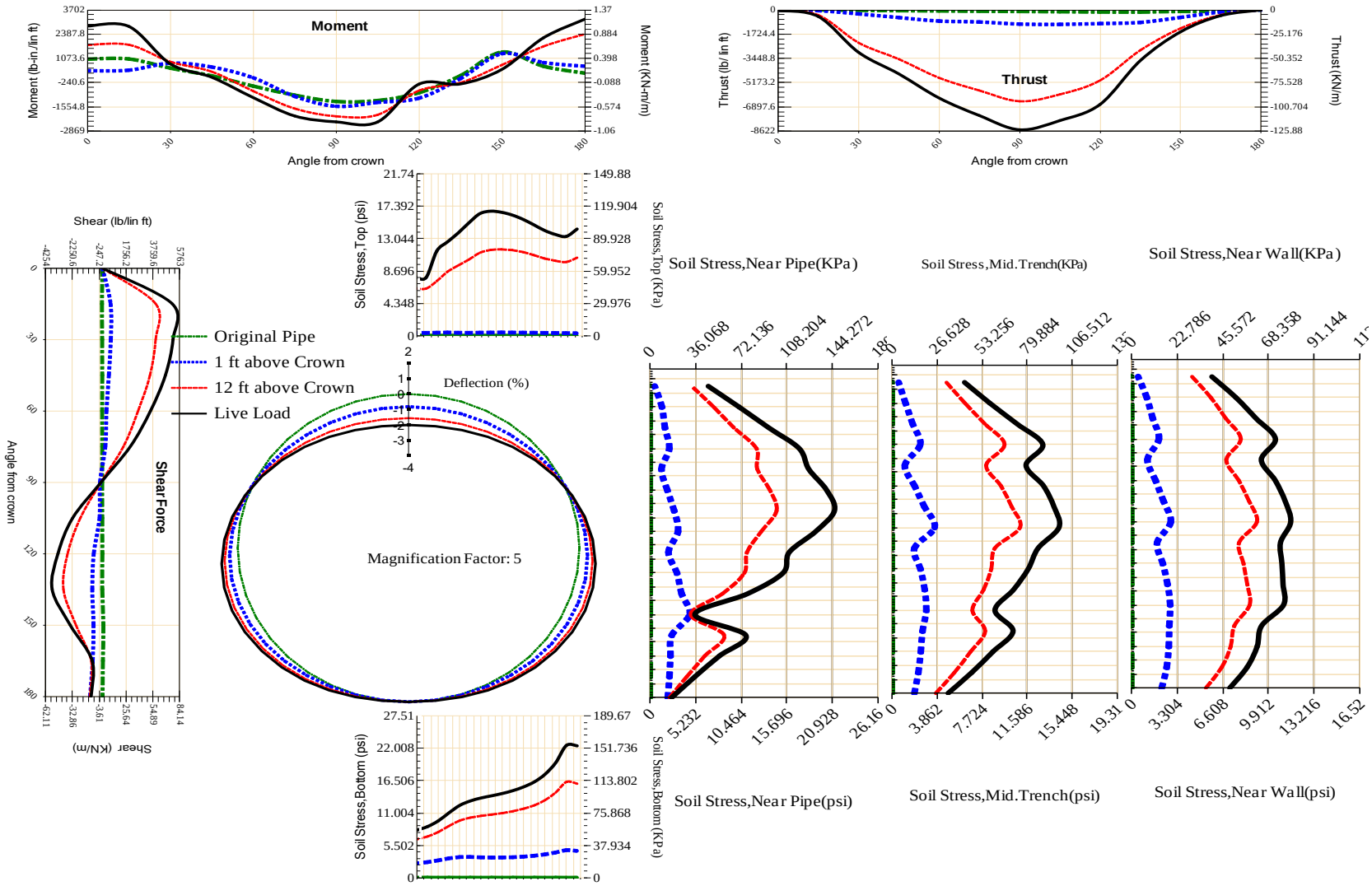

Figure A-602 Param-96-PW230-TR10TR-OD+96-EW5-H12-LiveLoad

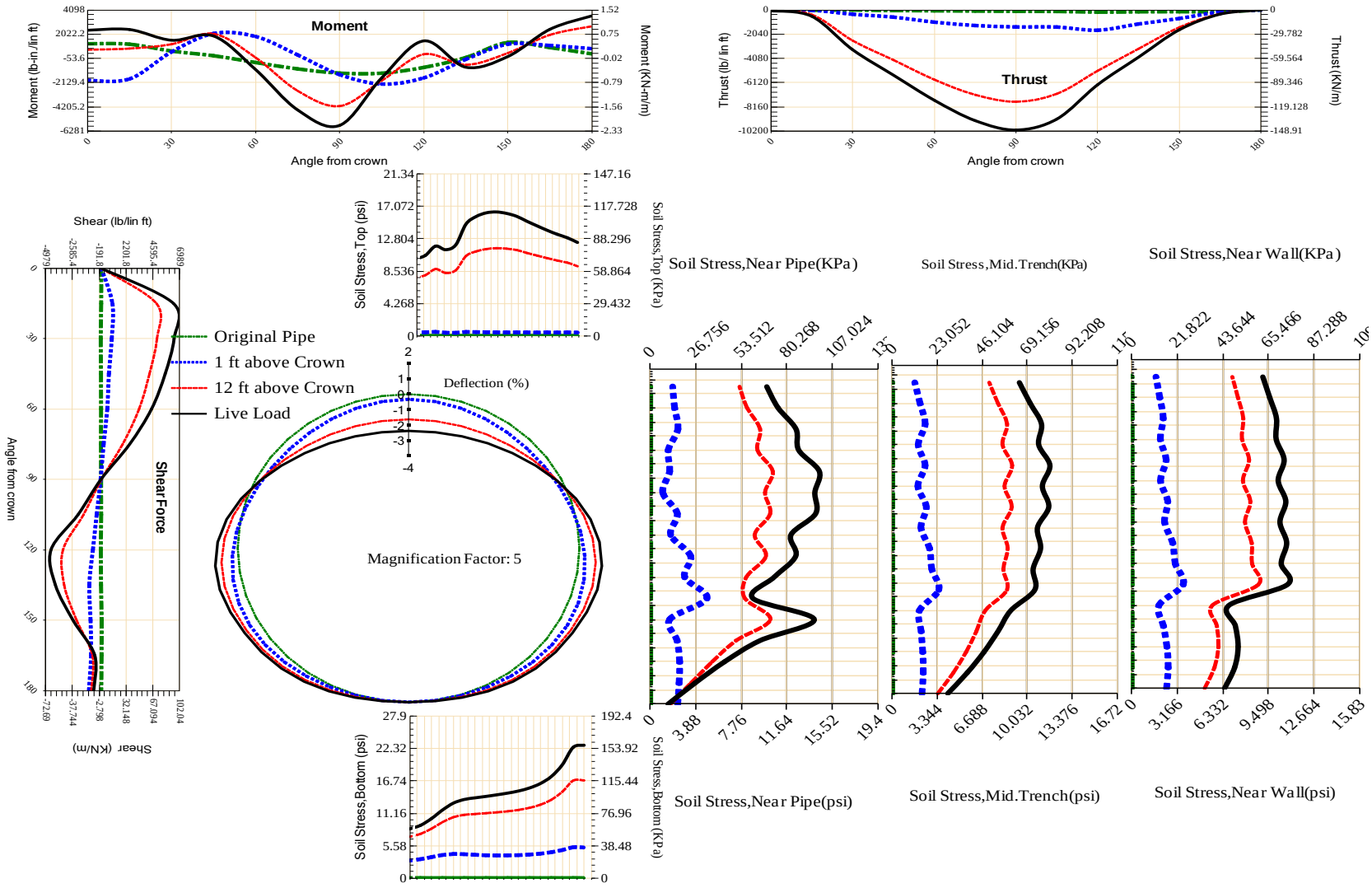

Figure A-603 Param-96-PW230-TR3OR-OD+108-EW5-H12-LiveLoad

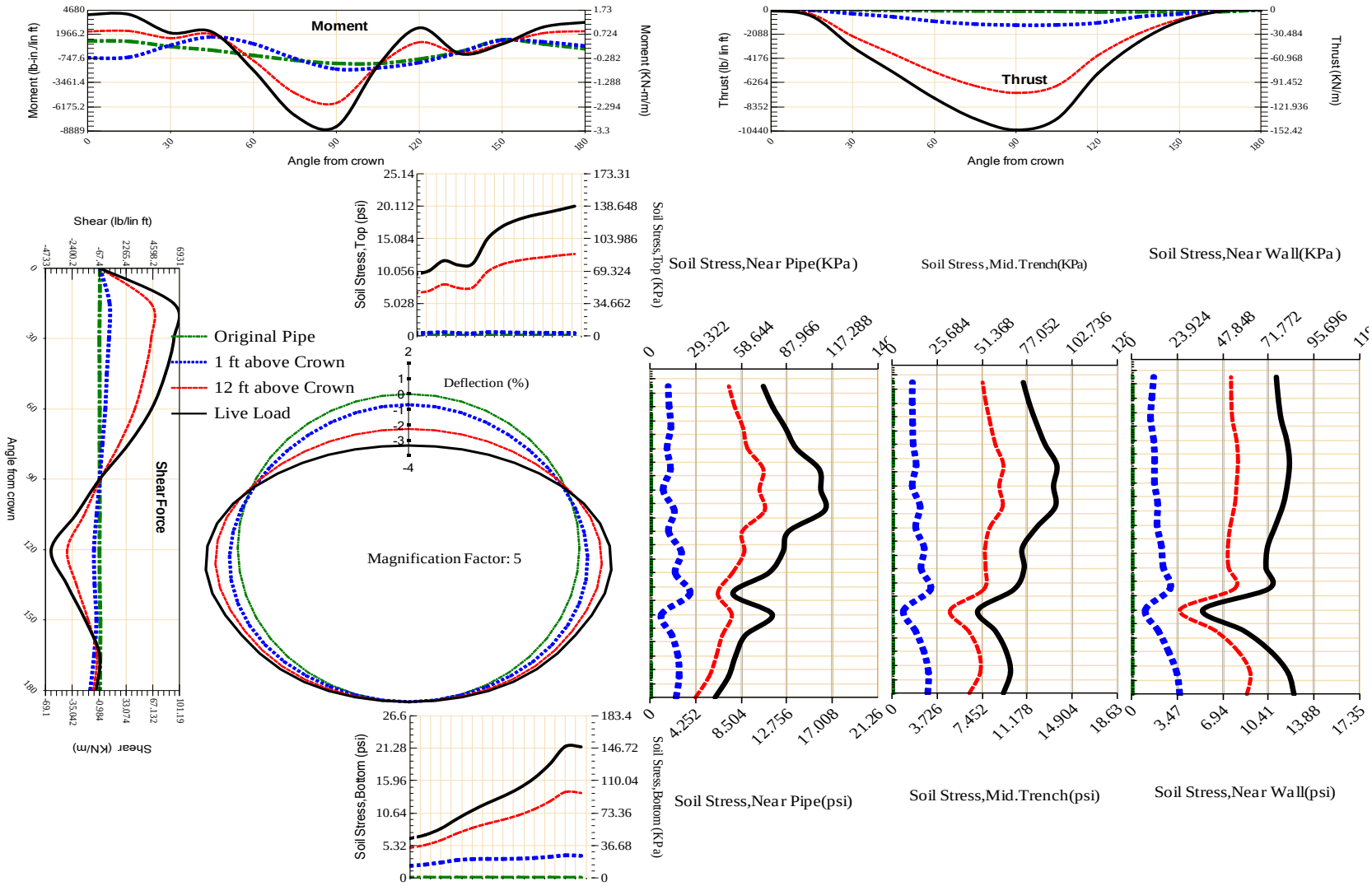

Figure A-604 Param-96-PW230-TR3OR-OD+48-EW5-H12-LiveLoad

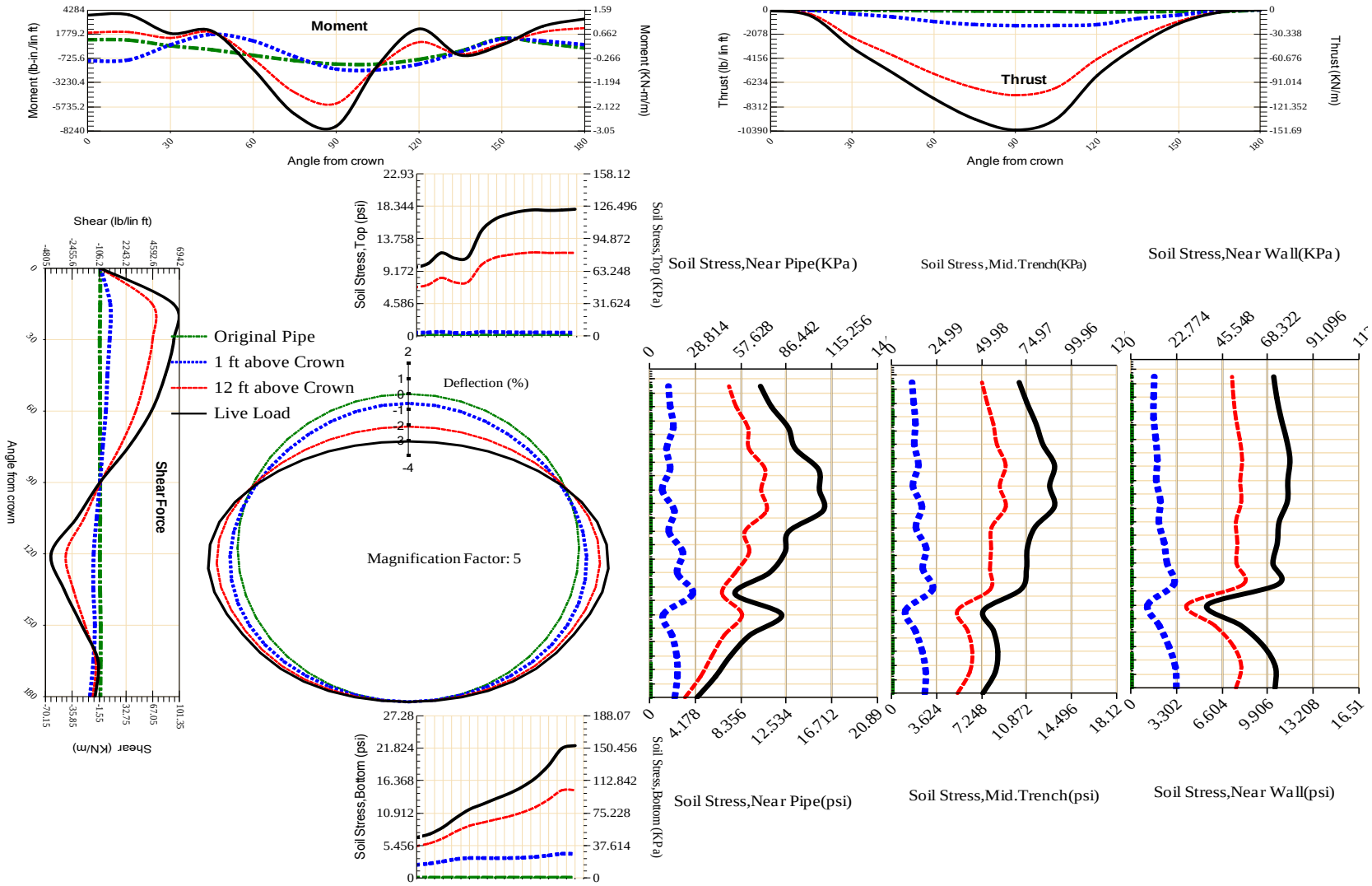

Figure A-605 Param-96-PW230-TR3OR-OD+60-EW5-H12-LiveLoad

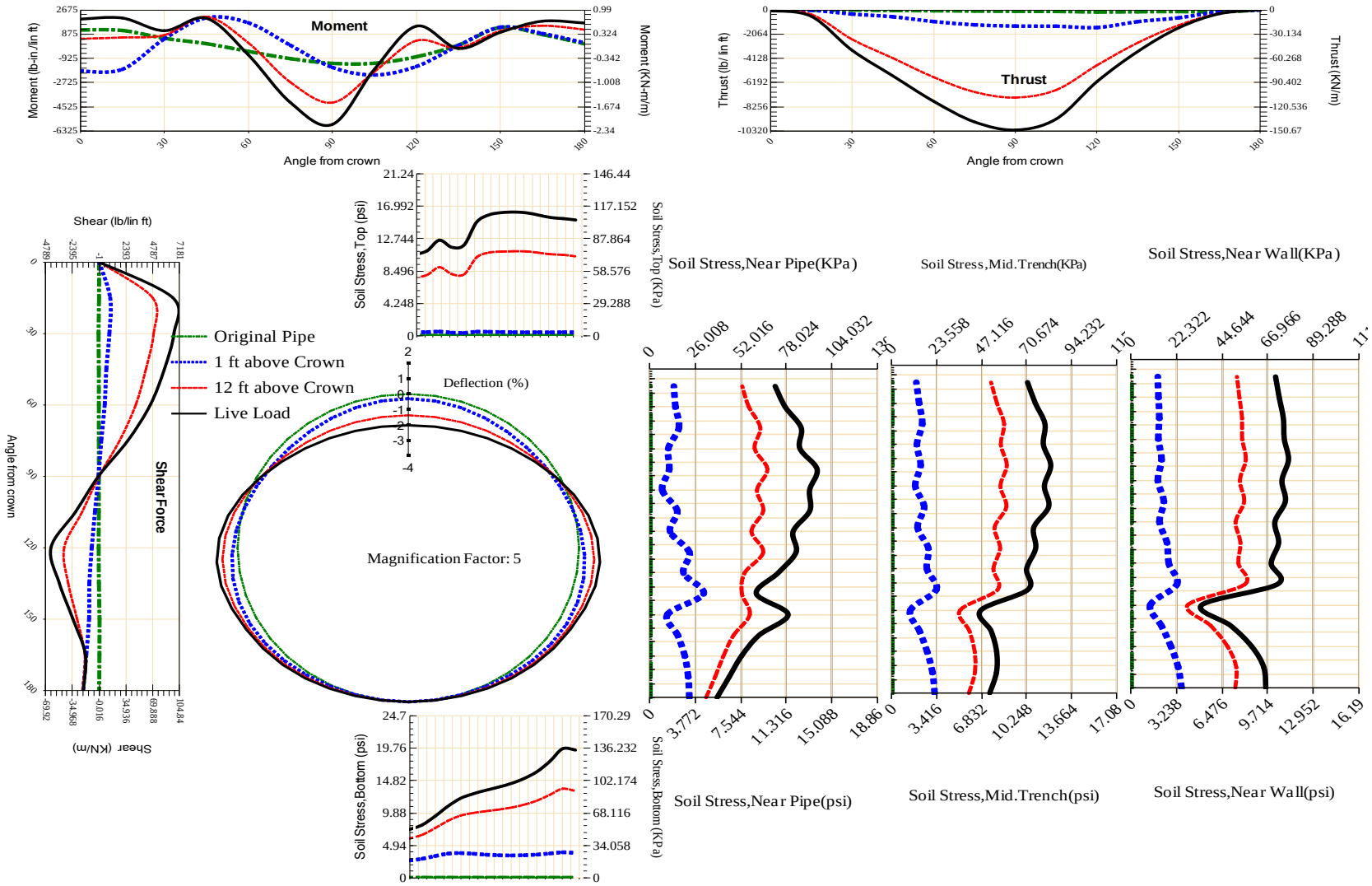

Figure A-606 Param-96-PW230-TR3OR-OD+72-EW10-H12-LiveLoad

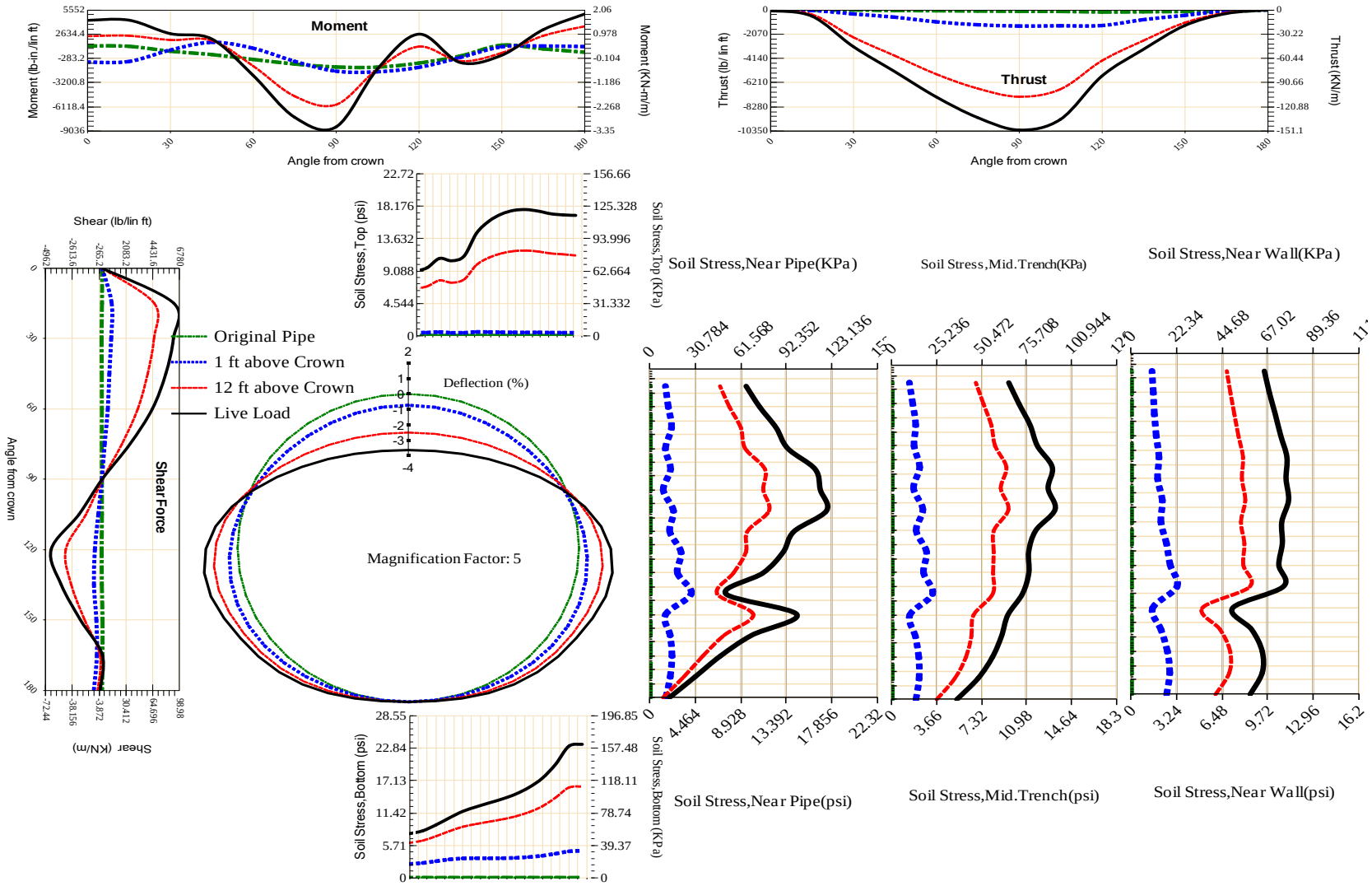

Figure A-607 Param-96-PW230-TR3OR-OD+72-EW3-H12-LiveLoad

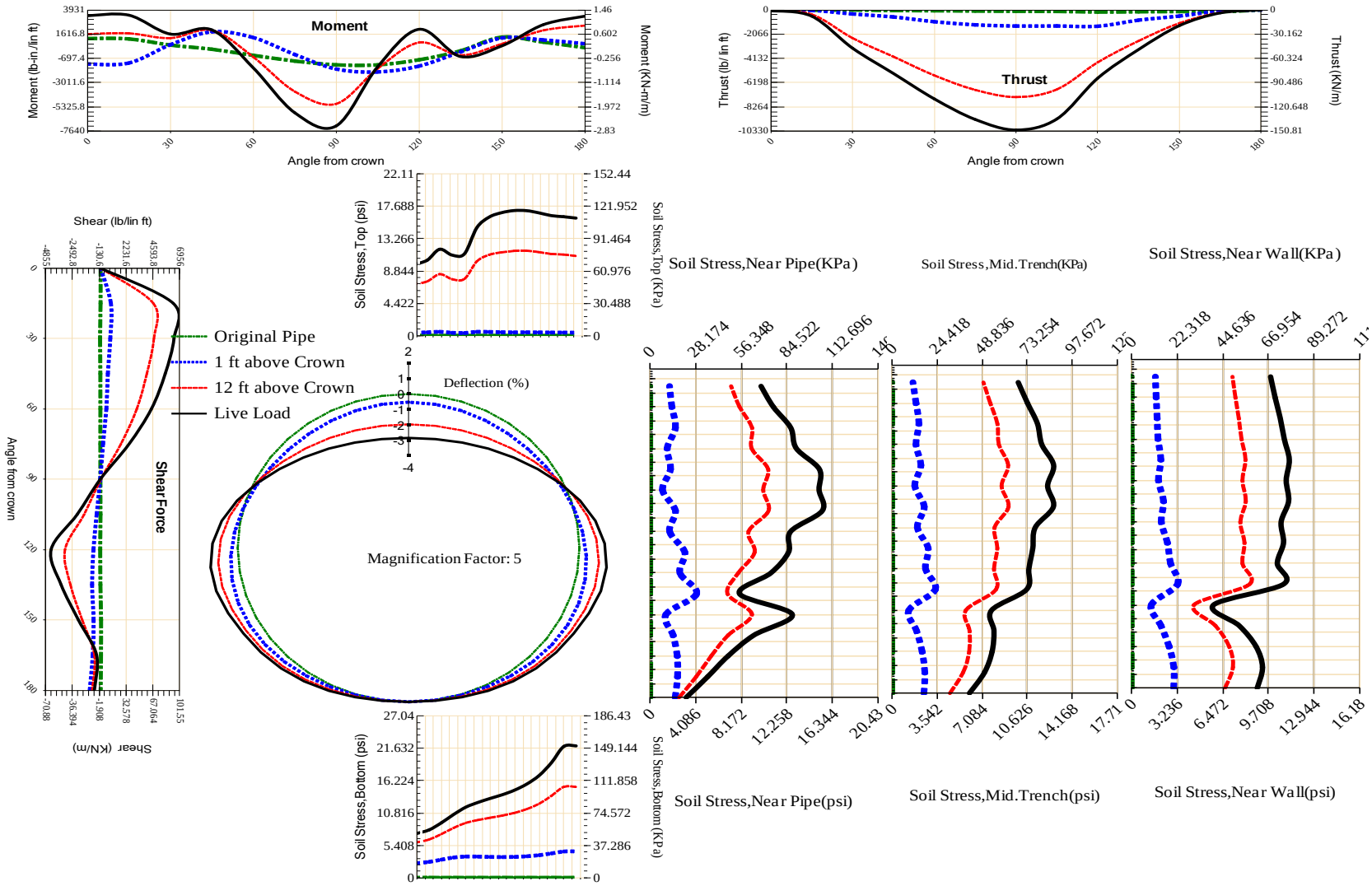

Figure A-608 Param-96-PW230-TR3OR-OD+72-EW5-H12-LiveLoad

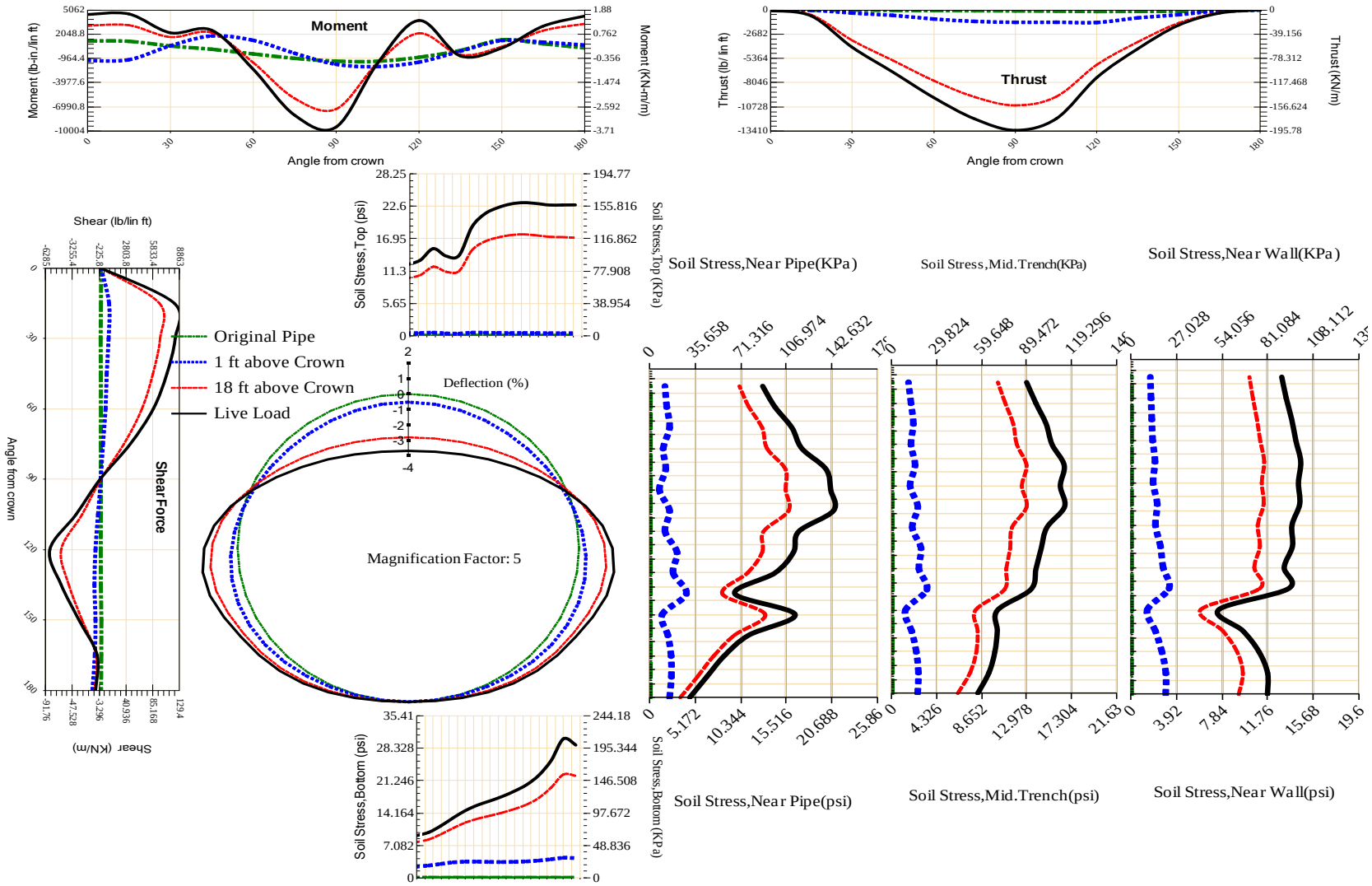

Figure A-609 Param-96-PW230-TR3OR-OD+72-EW5-H18-LiveLoad

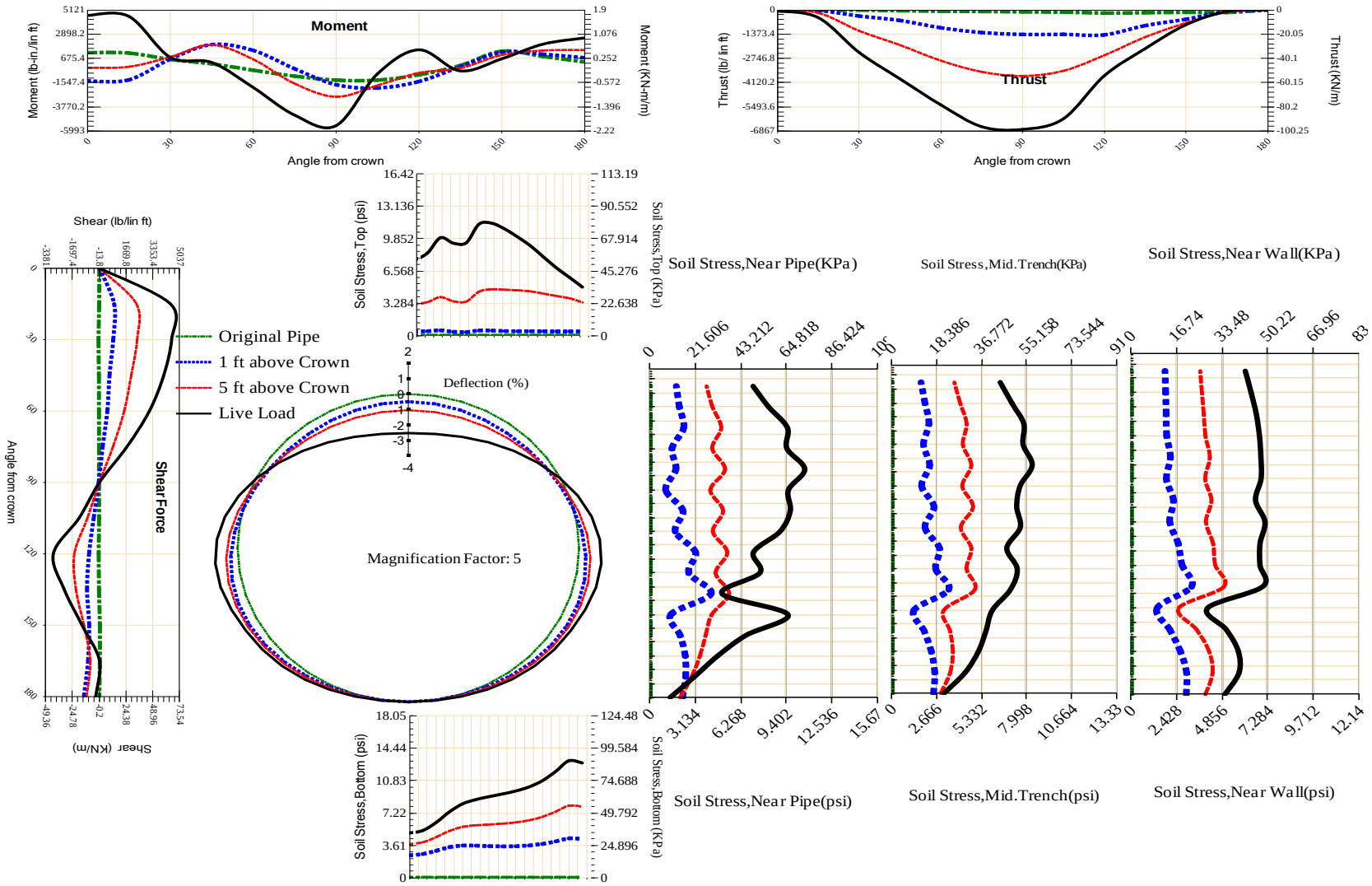

Figure A-610 Param-96-PW230-TR3OR-OD+72-EW5-H5-LiveLoad

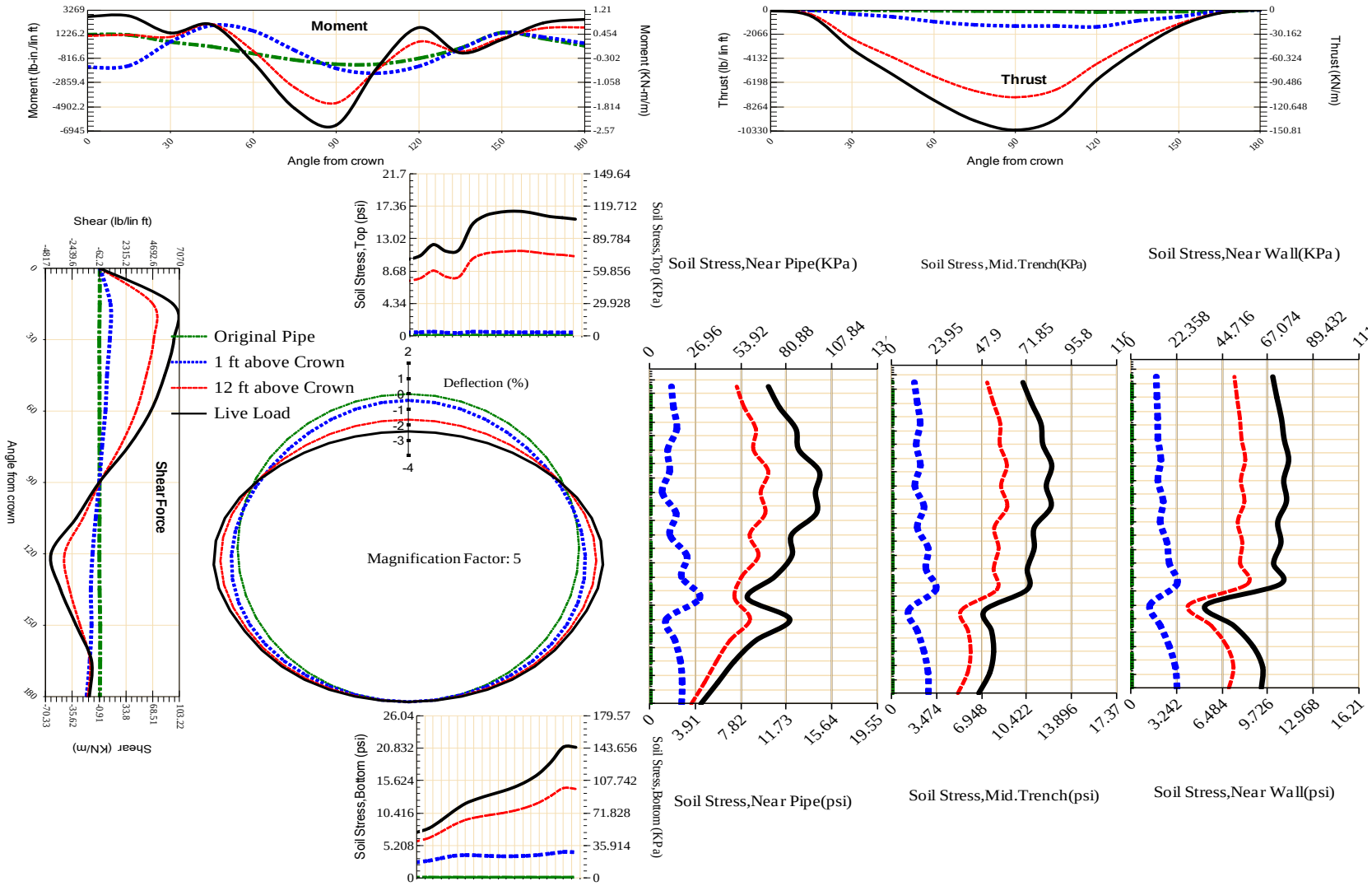

Figure A-611 Param-96-PW230-TR3OR-OD+72-EW7-H12-LiveLoad

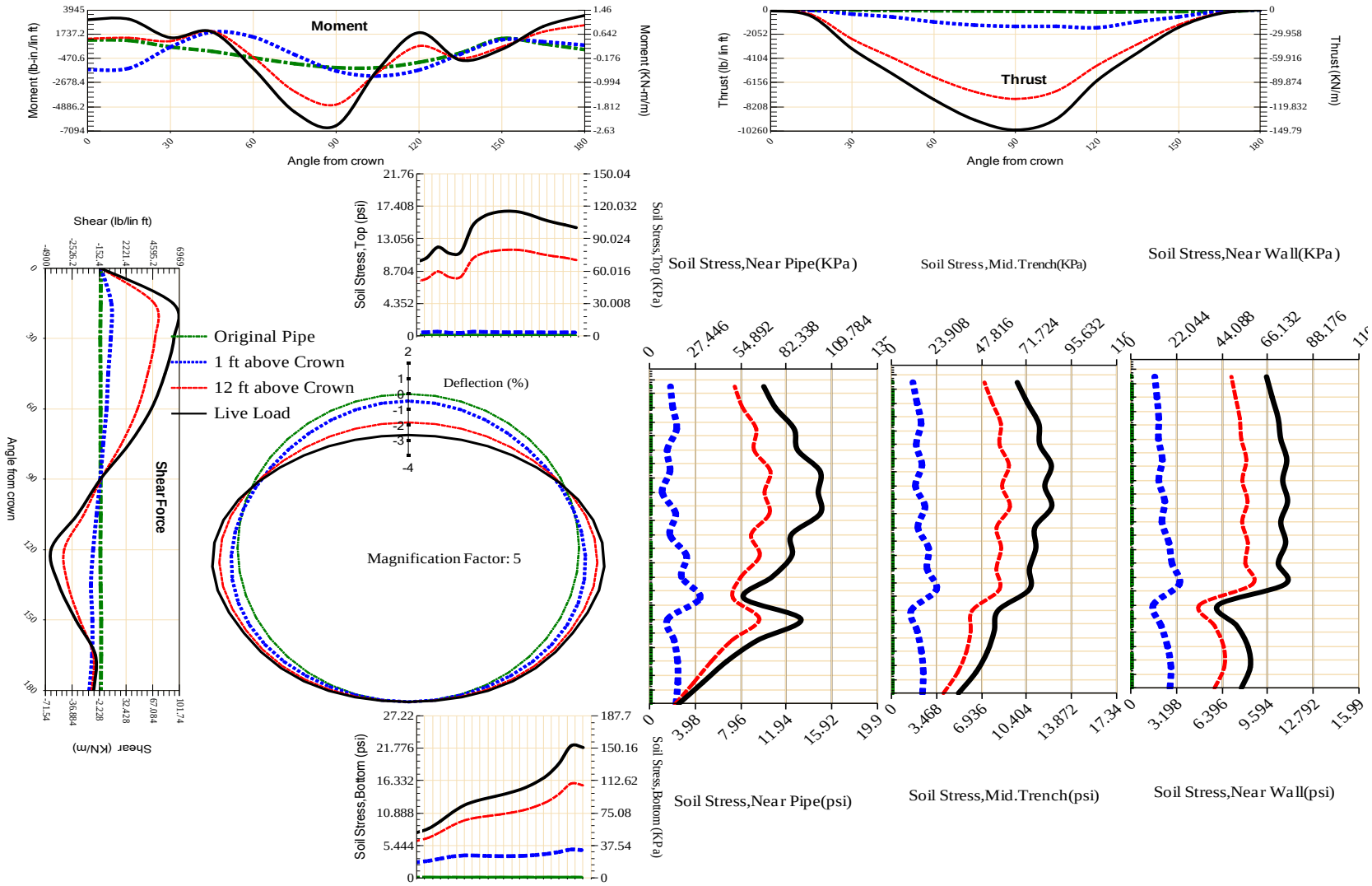

Figure A-612 Param-96-PW230-TR3OR-OD+84-EW5-H12-LiveLoad

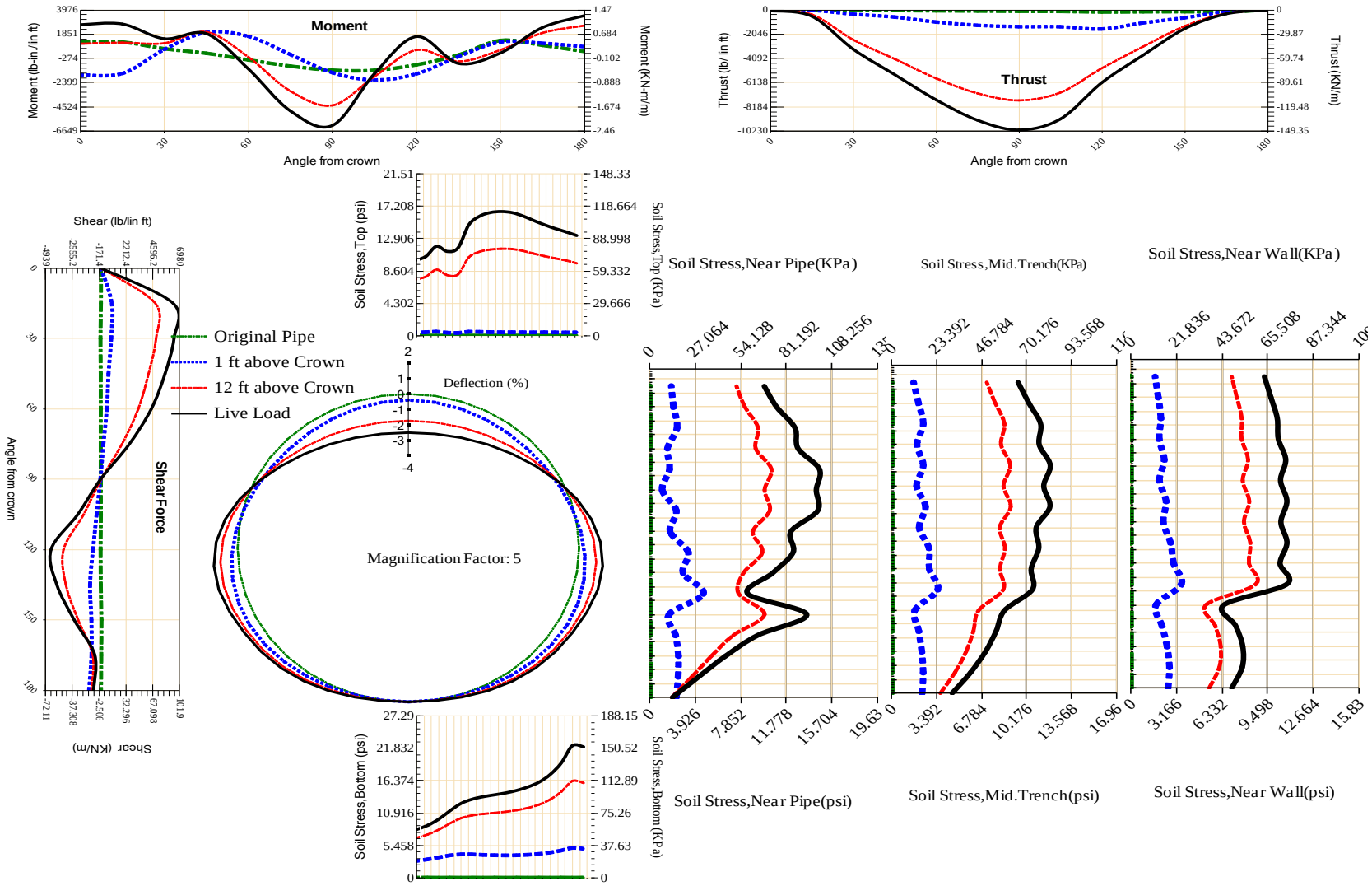

Figure A-613 Param-96-PW230-TR3OR-OD+96-EW5-H12-LiveLoad

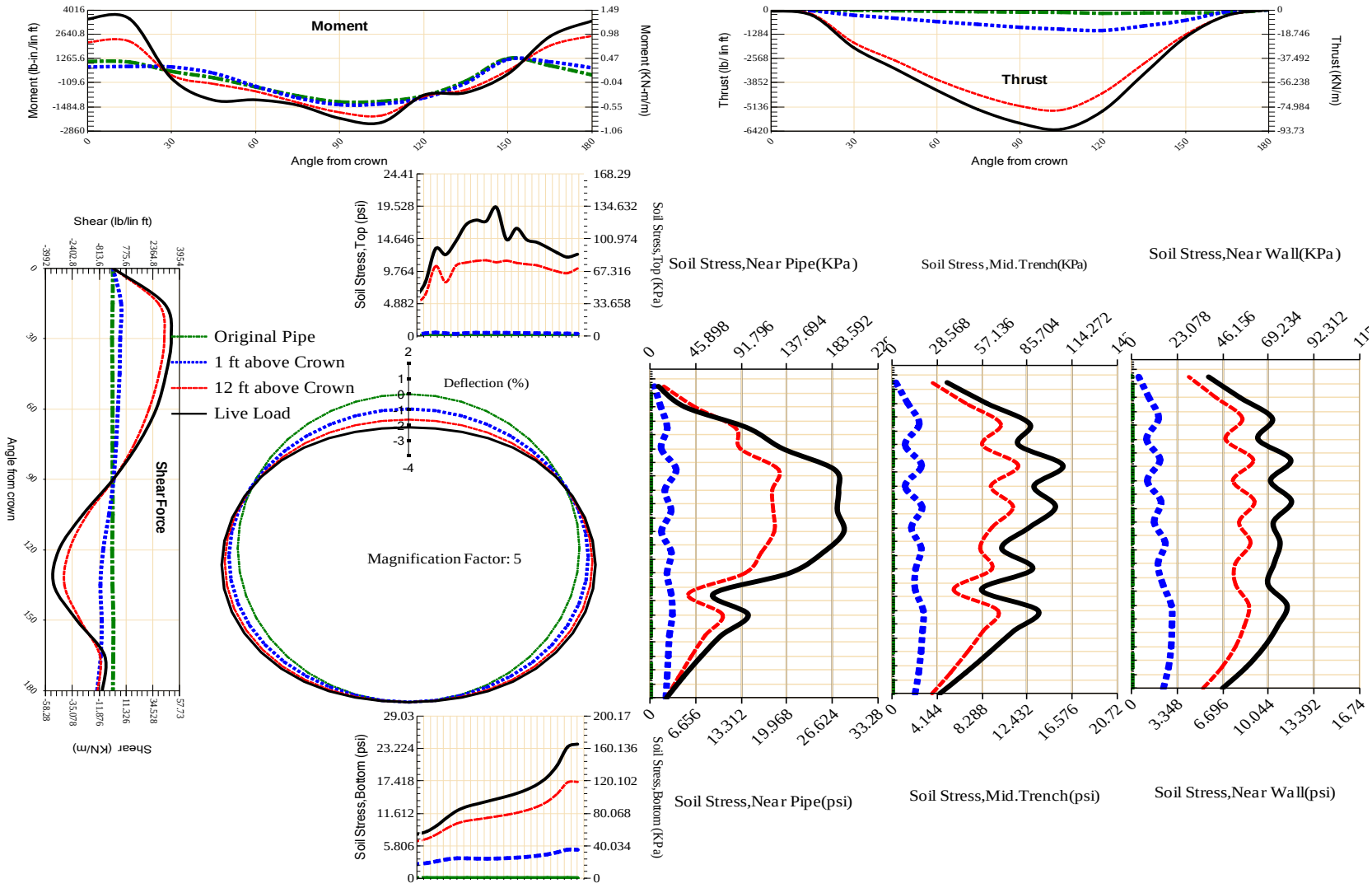

Figure A-614 Param-96-PW230-TR3SF-OD+108-EW5-H12-LiveLoad

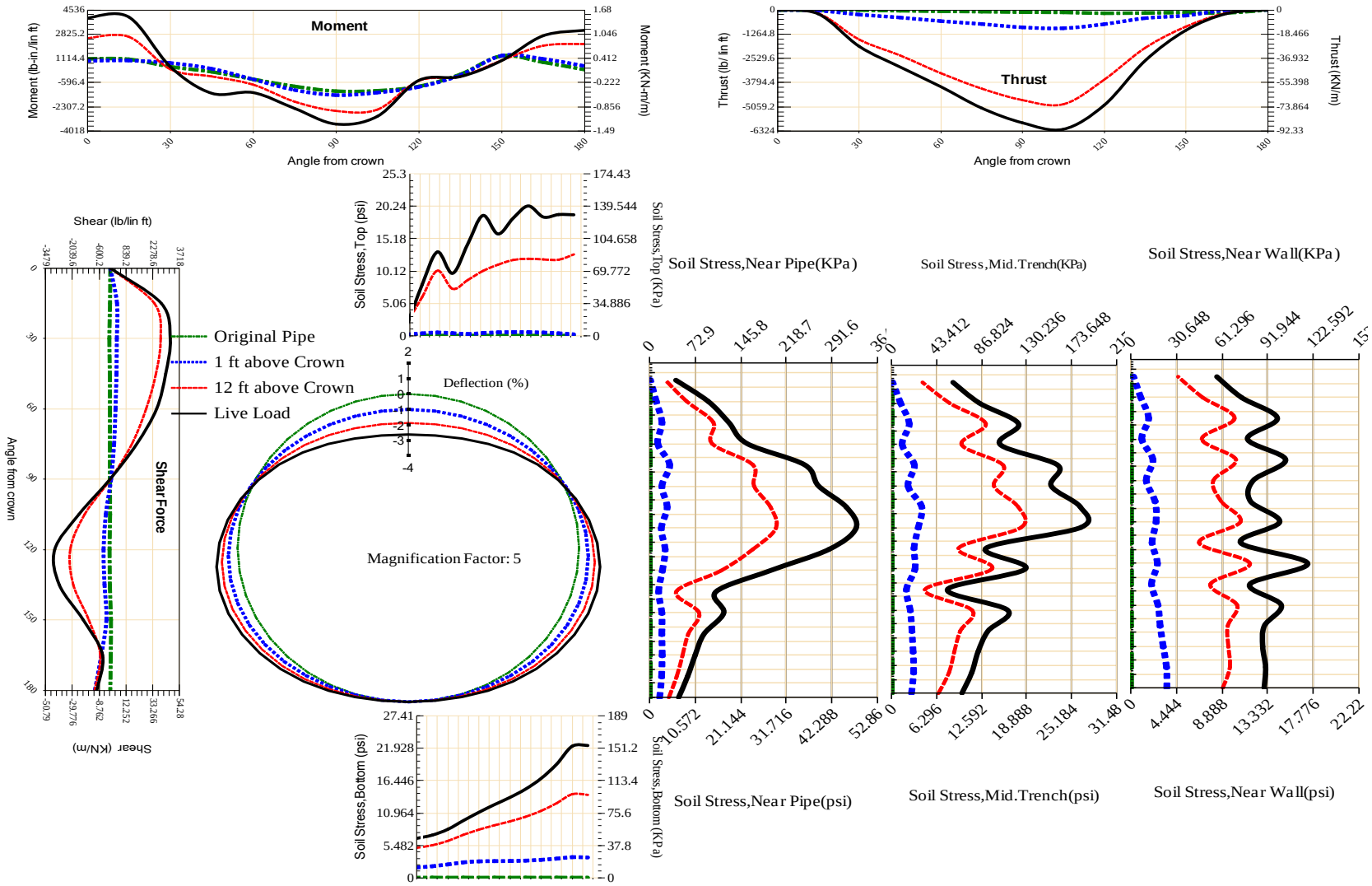

Figure A-615 Param-96-PW230-TR3SF-OD+48-EW5-H12-LiveLoad

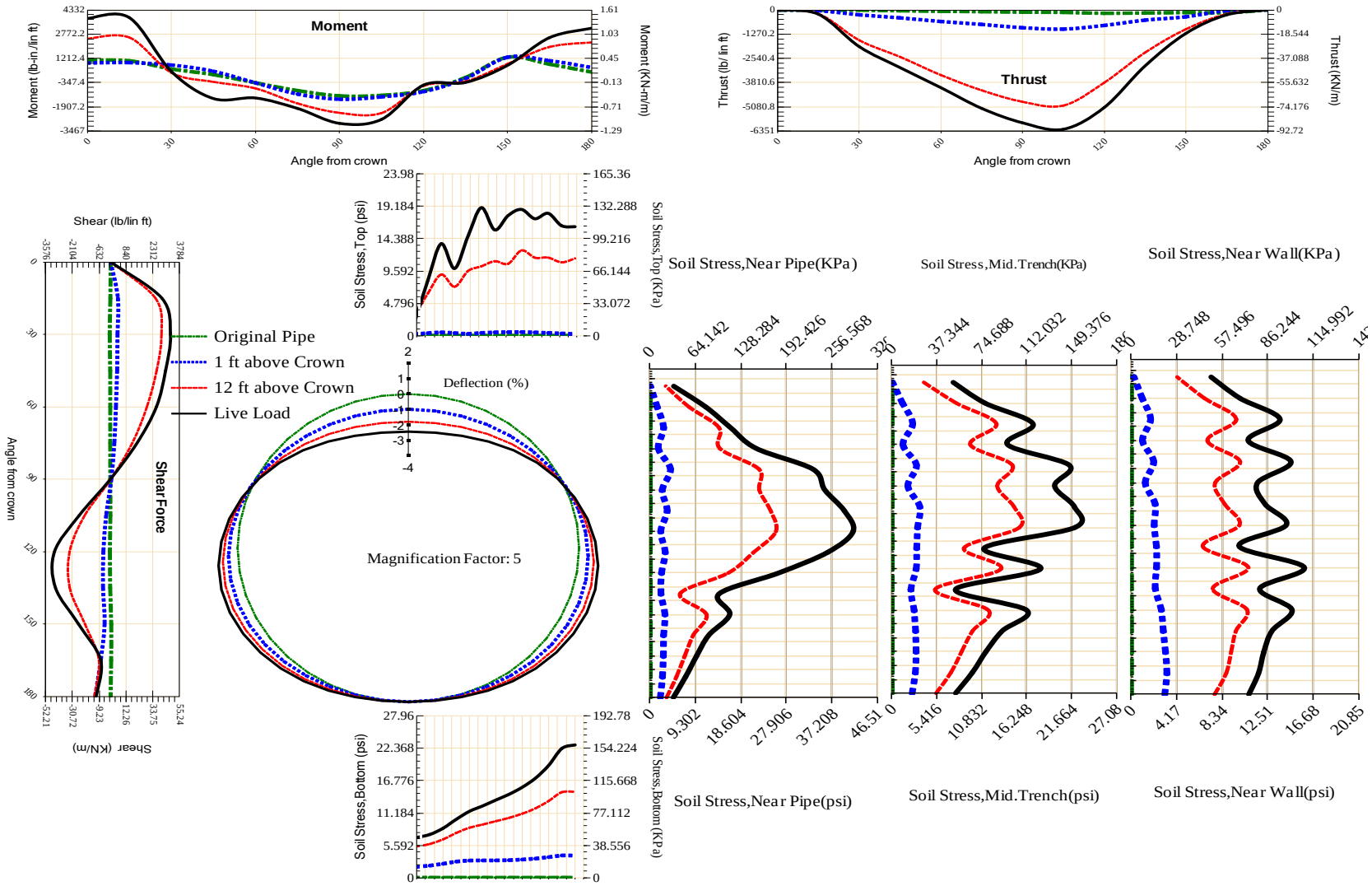

Figure A-616 Param-96-PW230-TR3SF-OD+60-EW5-H12-LiveLoad

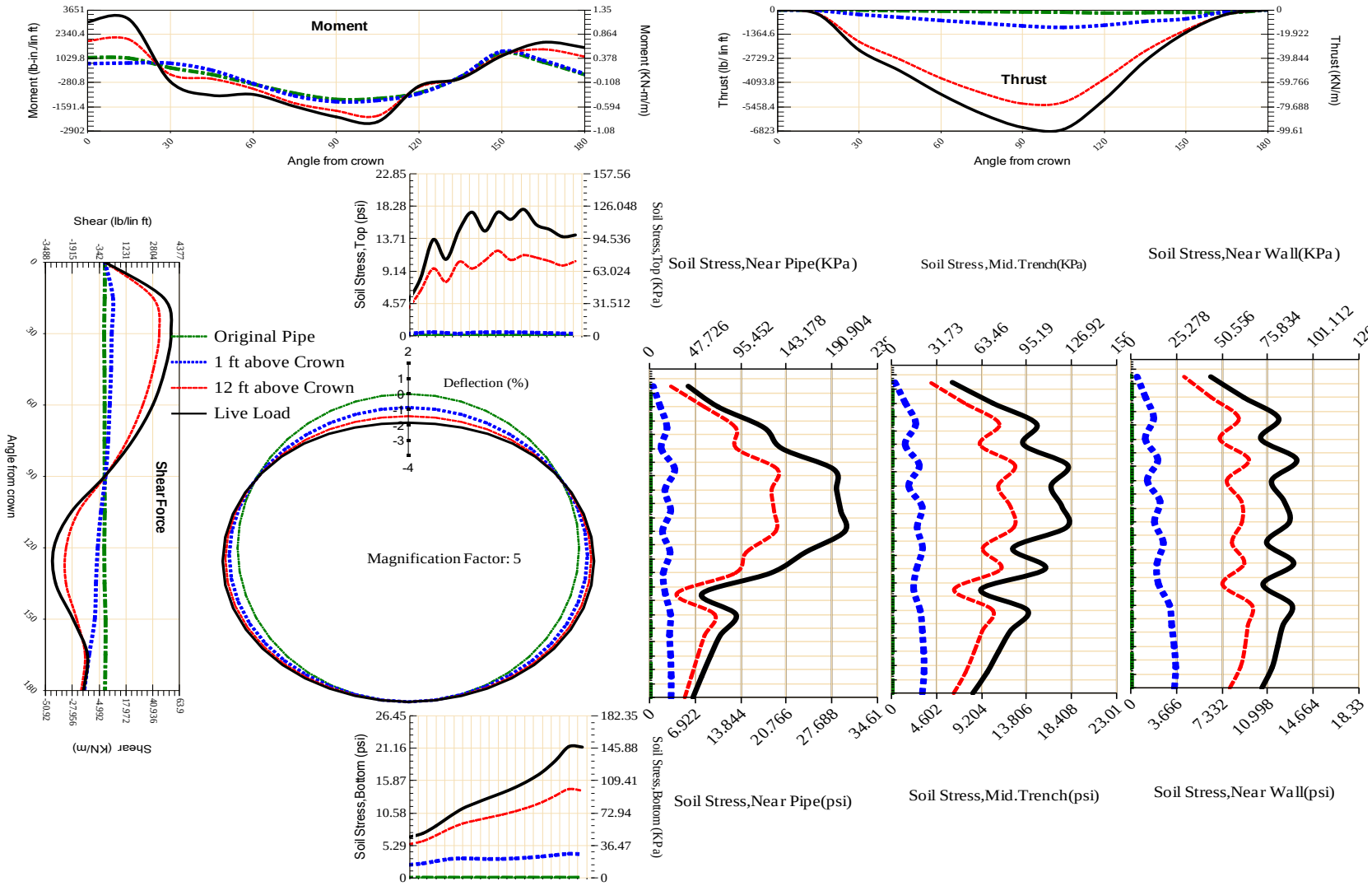

Figure A-617 Param-96-PW230-TR3SF-OD+72-EW10-H12-LiveLoad

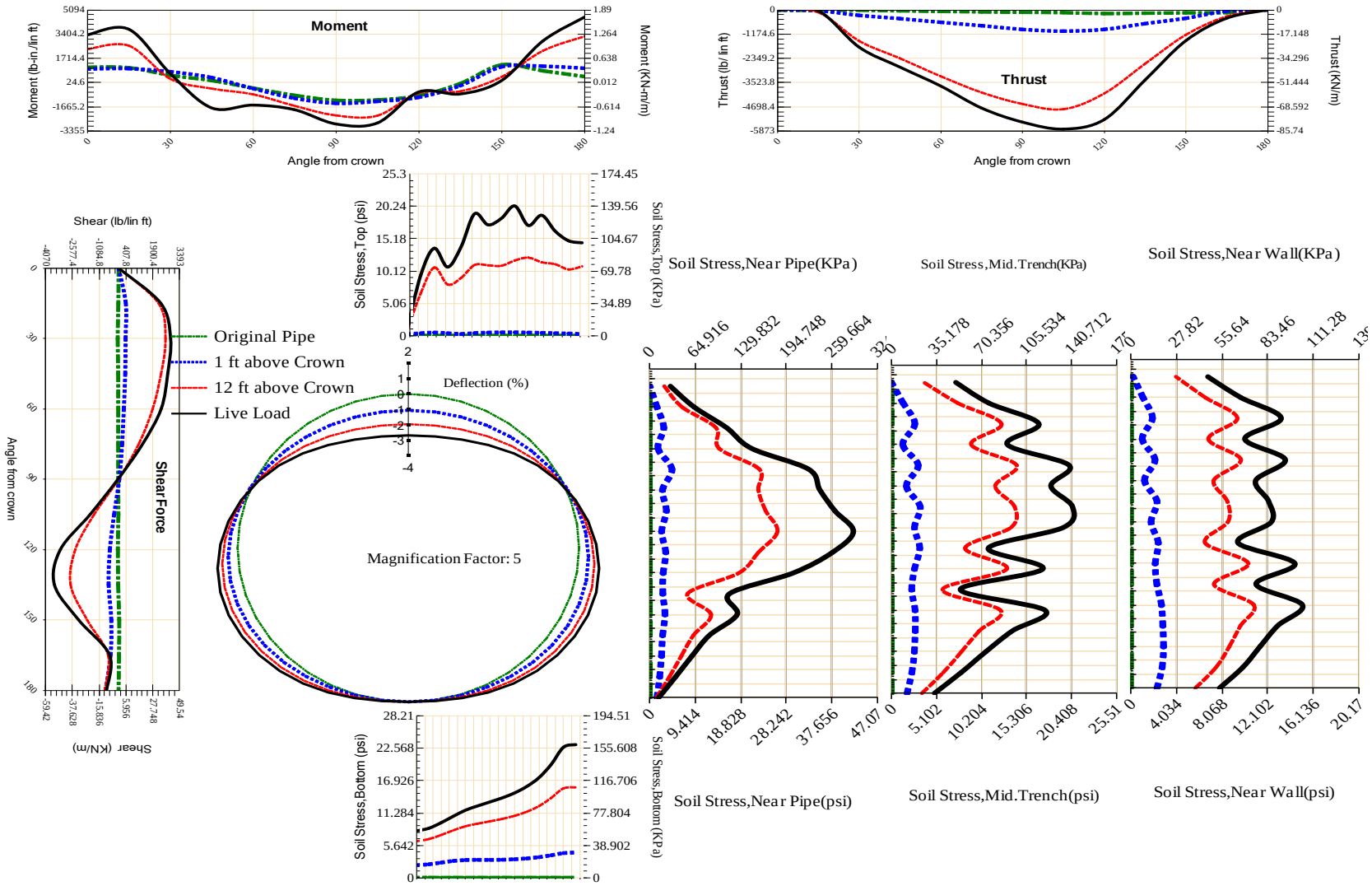

Figure A-618 Param-96-PW230-TR3SF-OD+72-EW3-H12-LiveLoad

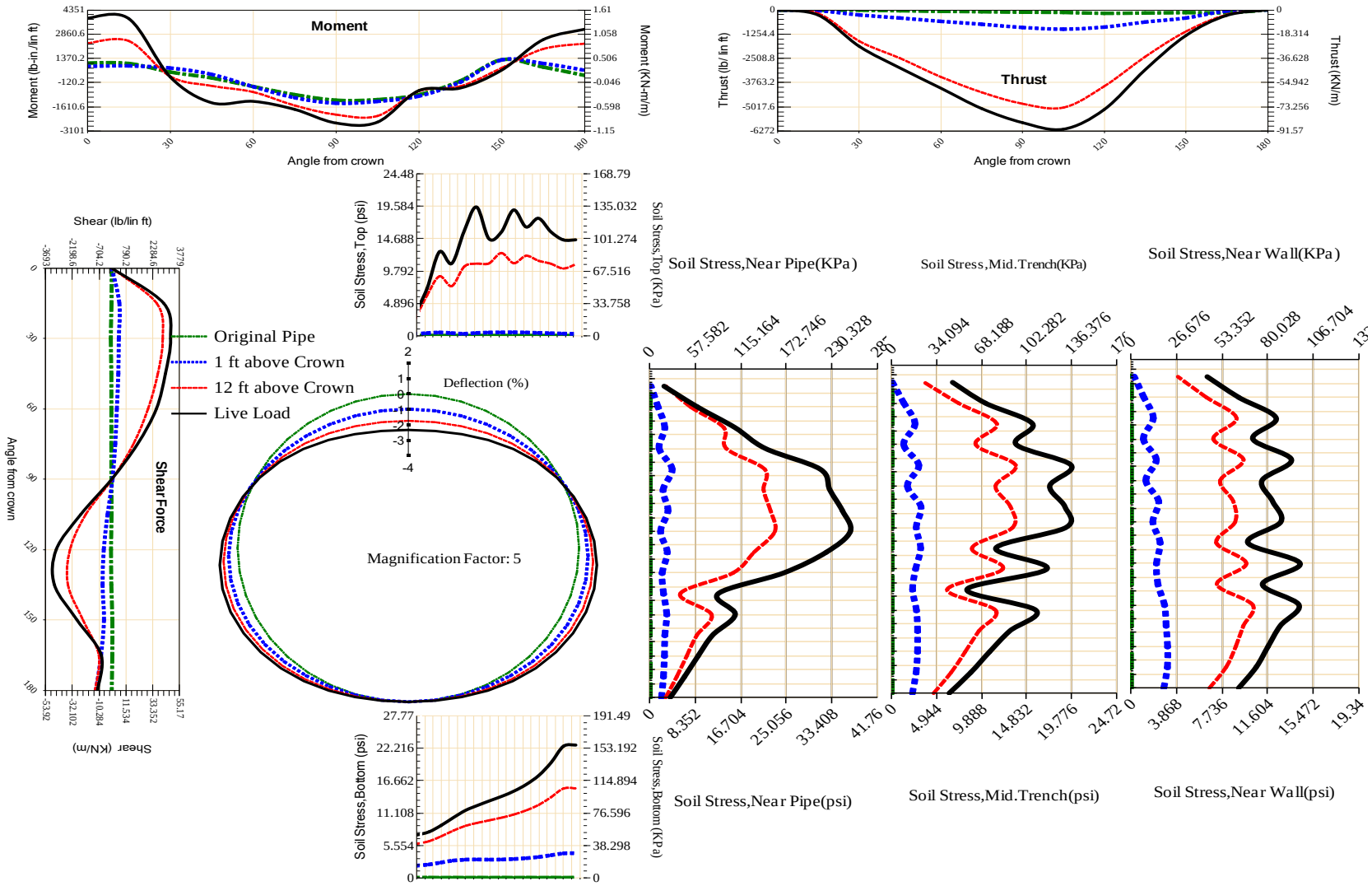

Figure A-619 Param-96-PW230-TR3SF-OD+72-EW5-H12-LiveLoad

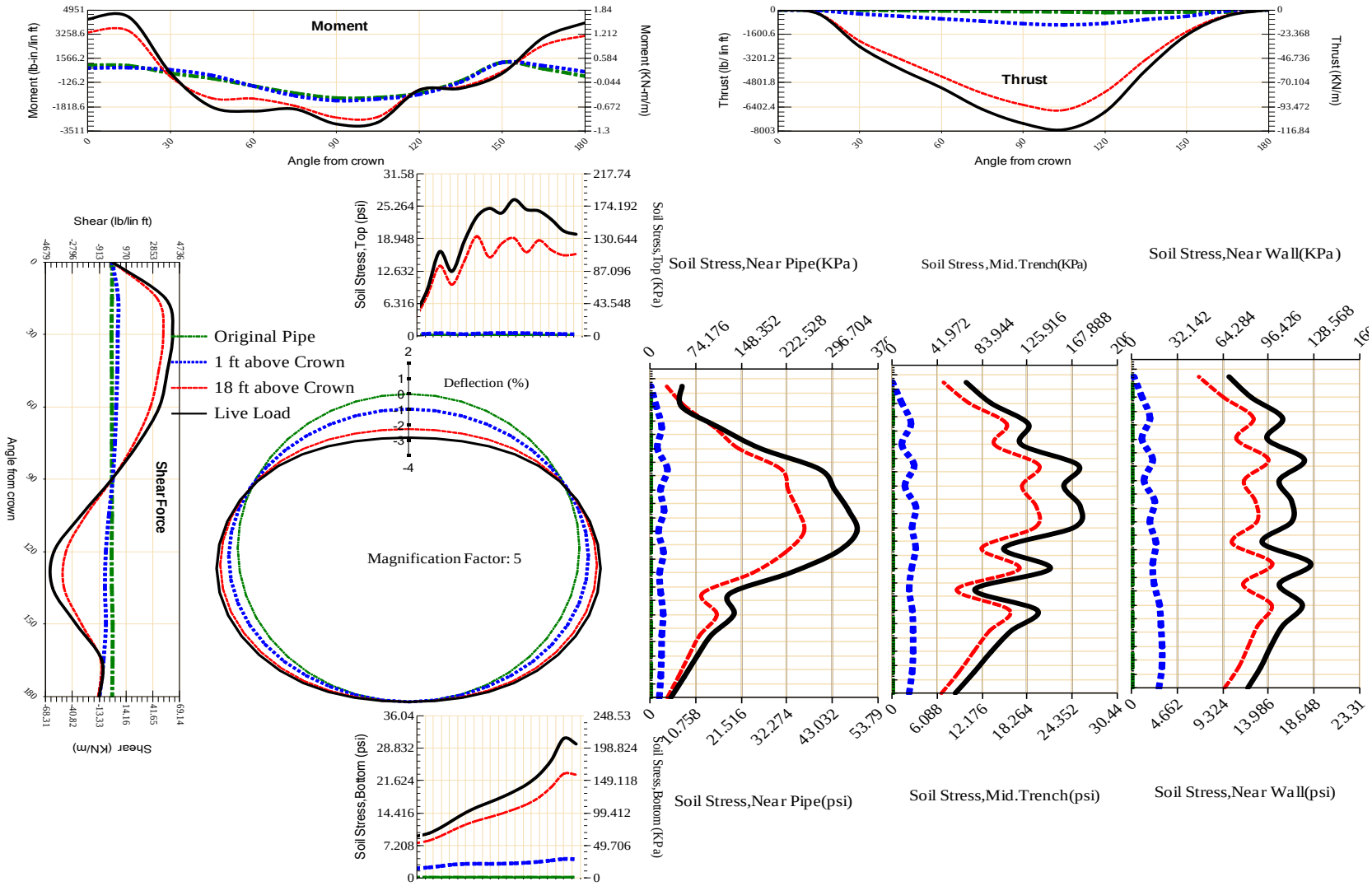

Figure A-620 Param-96-PW230-TR3SF-OD+72-EW5-H18-LiveLoad

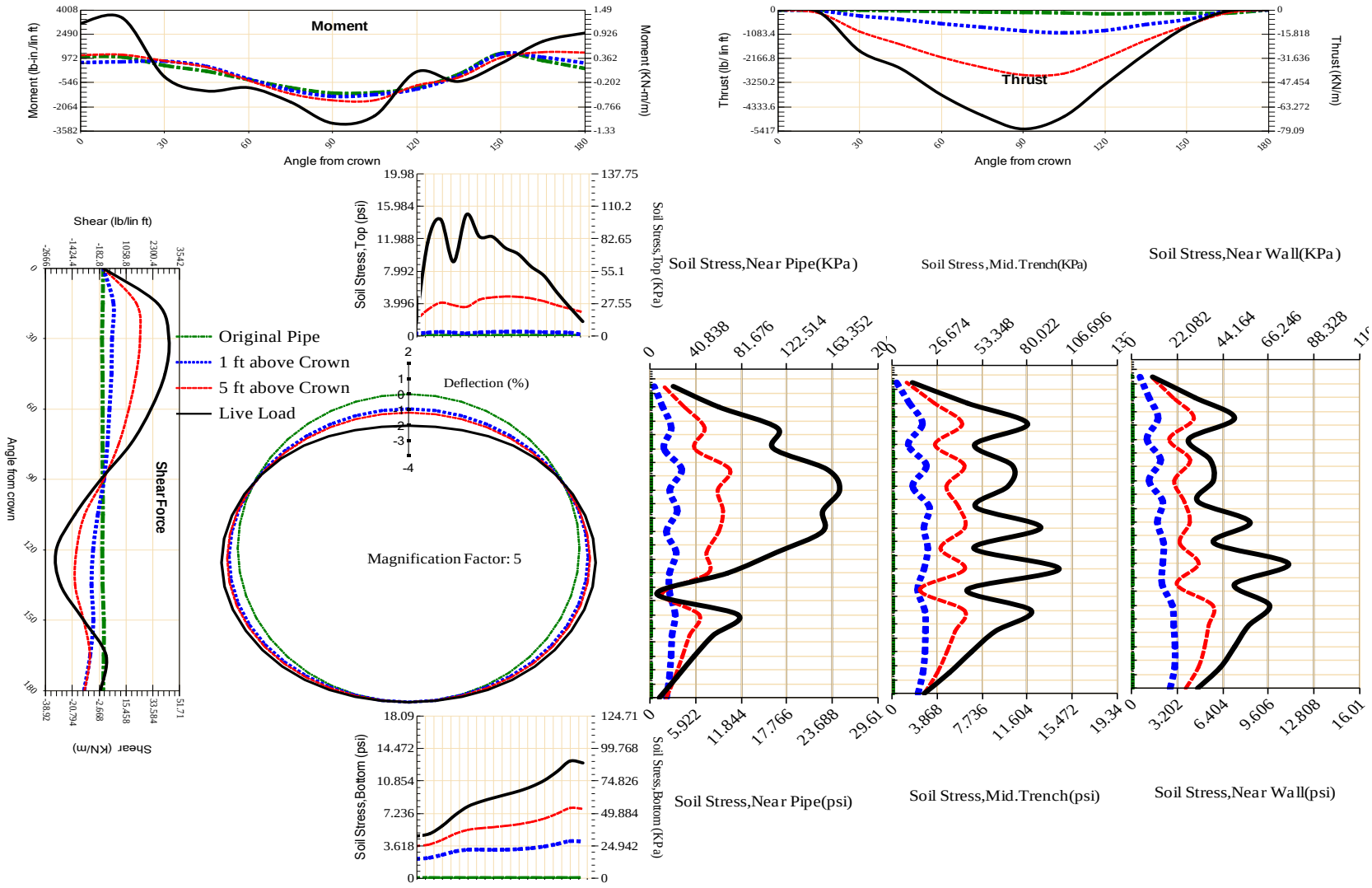

Figure A-621 Param-96-PW230-TR3SF-OD+72-EW5-H5-LiveLoad

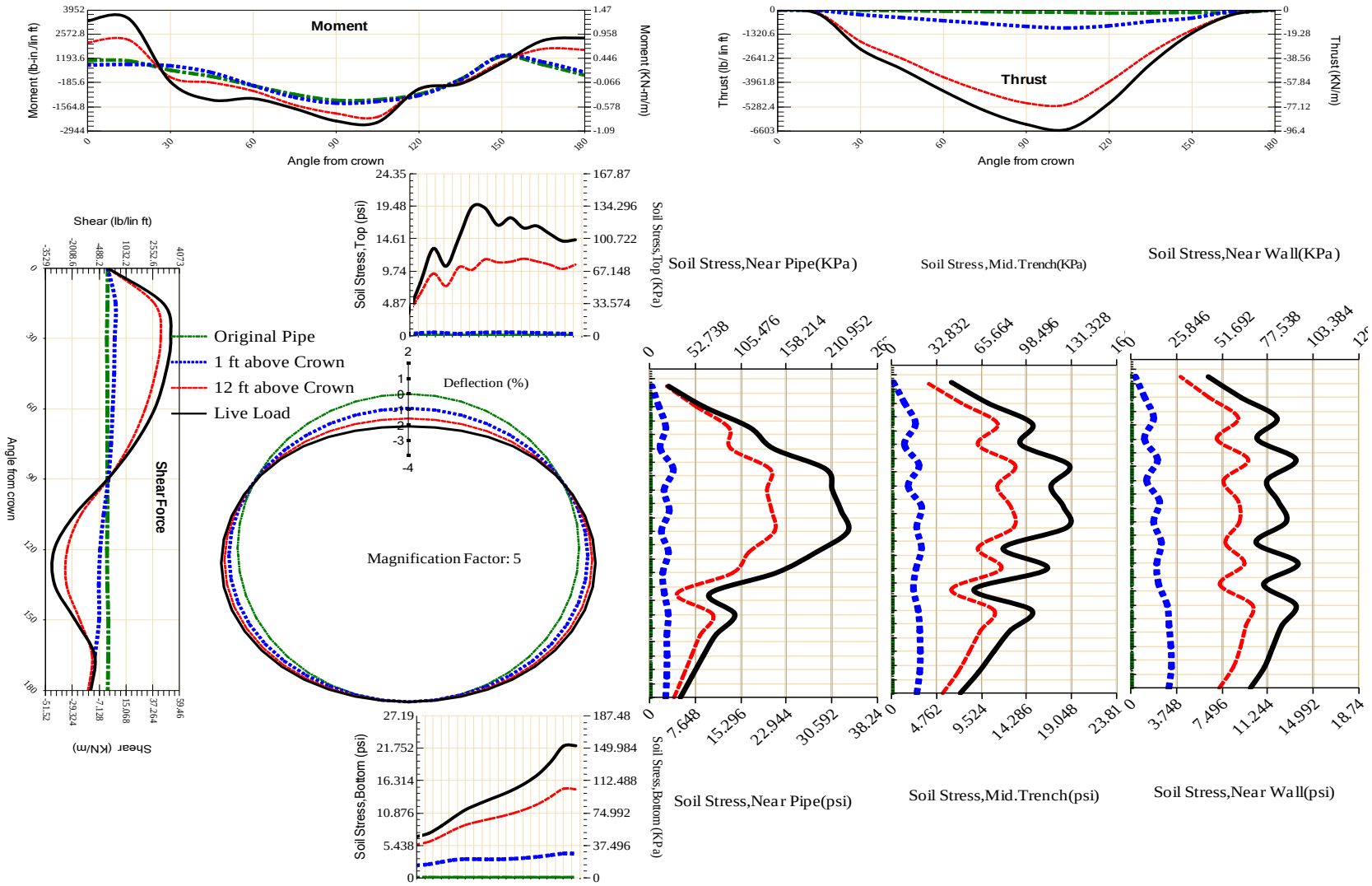

Figure A-622 Param-96-PW230-TR3SF-OD+72-EW7-H12-LiveLoad

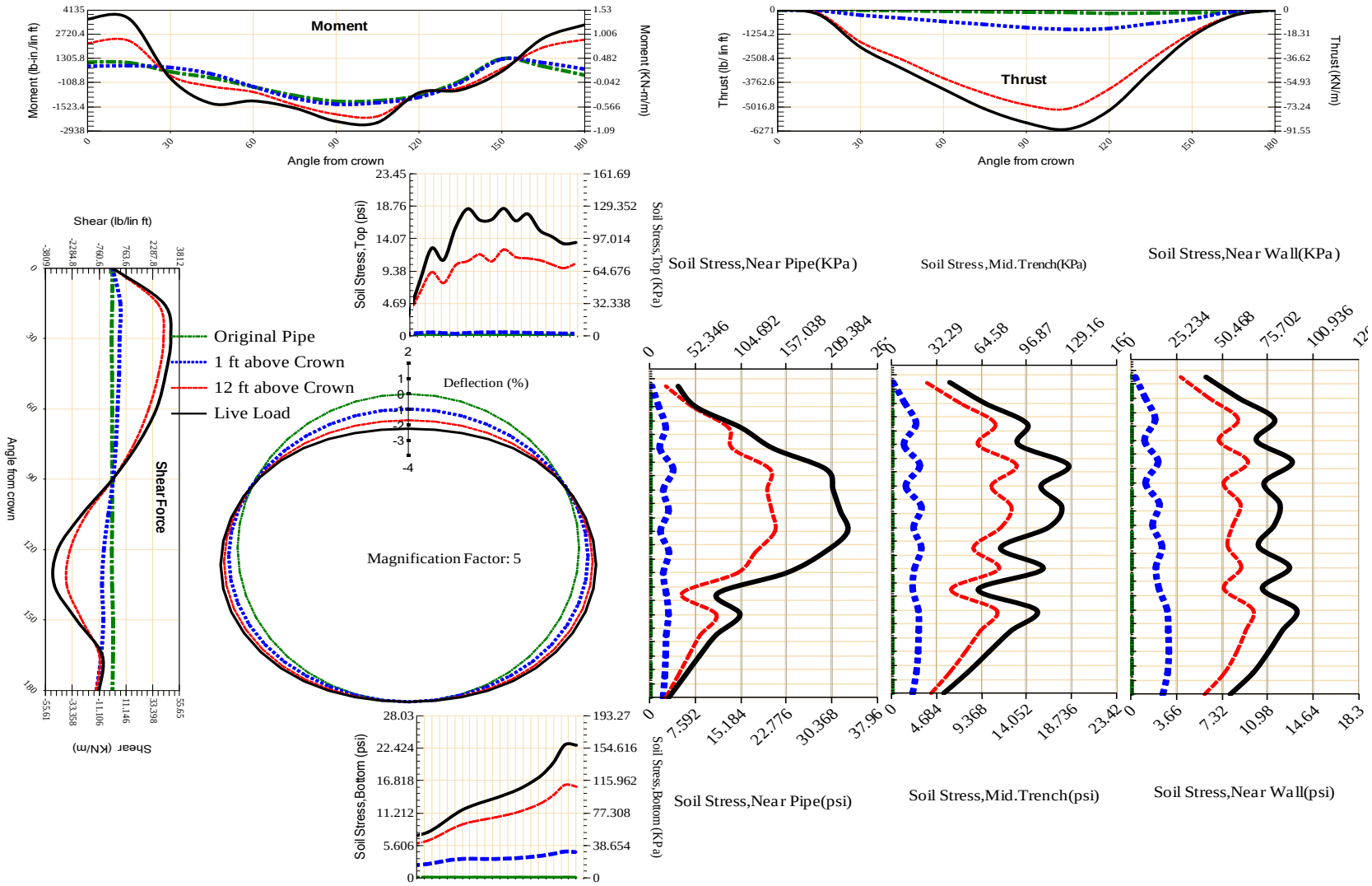

Figure A-623 Param-96-PW230-TR3SF-OD+84-EW5-H12-LiveLoad

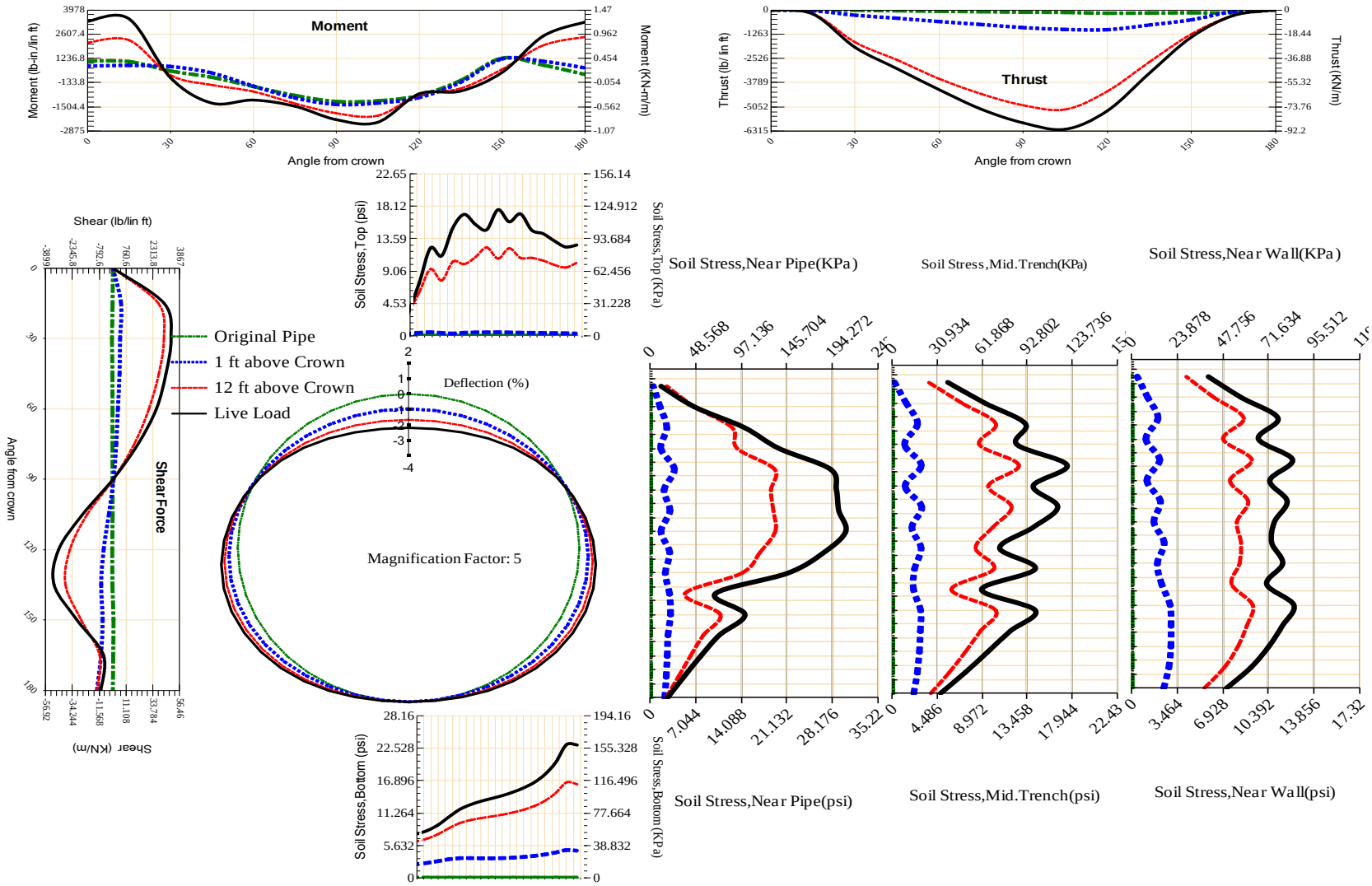

Figure A-624 Param-96-PW230-TR3SF-OD+96-EW5-H12-LiveLoad

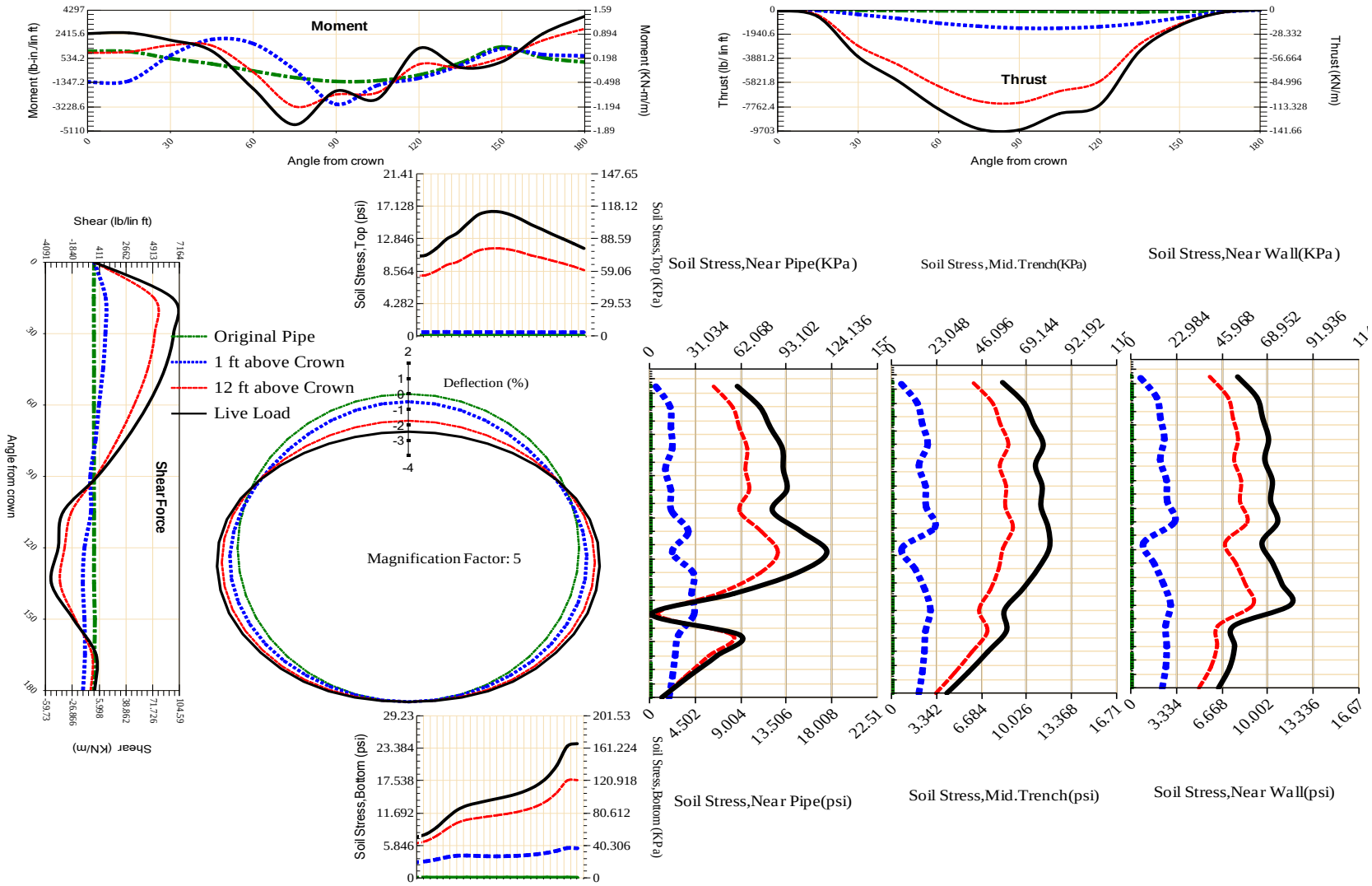

Figure A-625 Param-96-PW230-TR5OR-OD+108-EW5-H12-LiveLoad

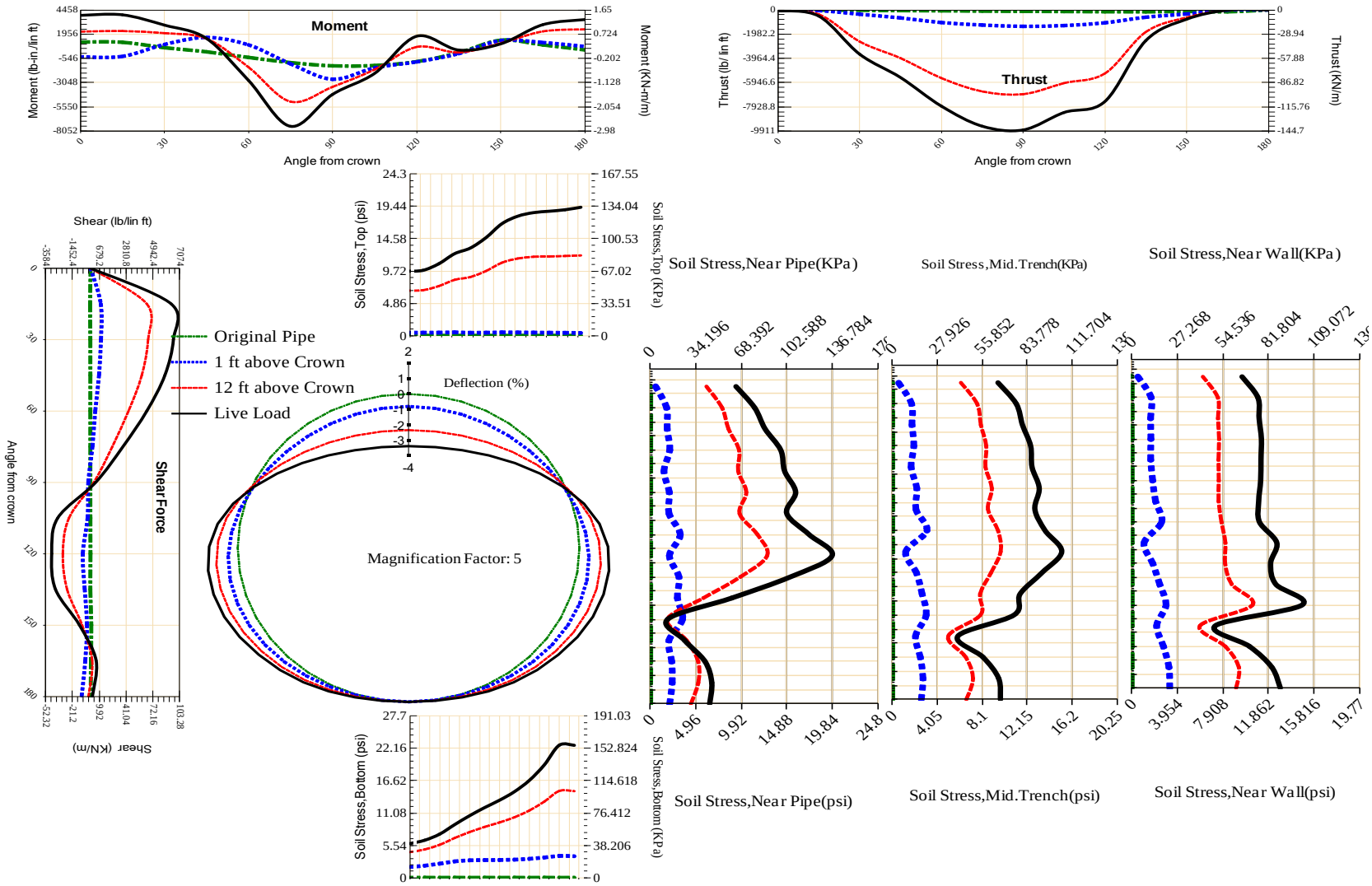

Figure A-626 Param-96-PW230-TR5OR-OD+48-EW5-H12-LiveLoad

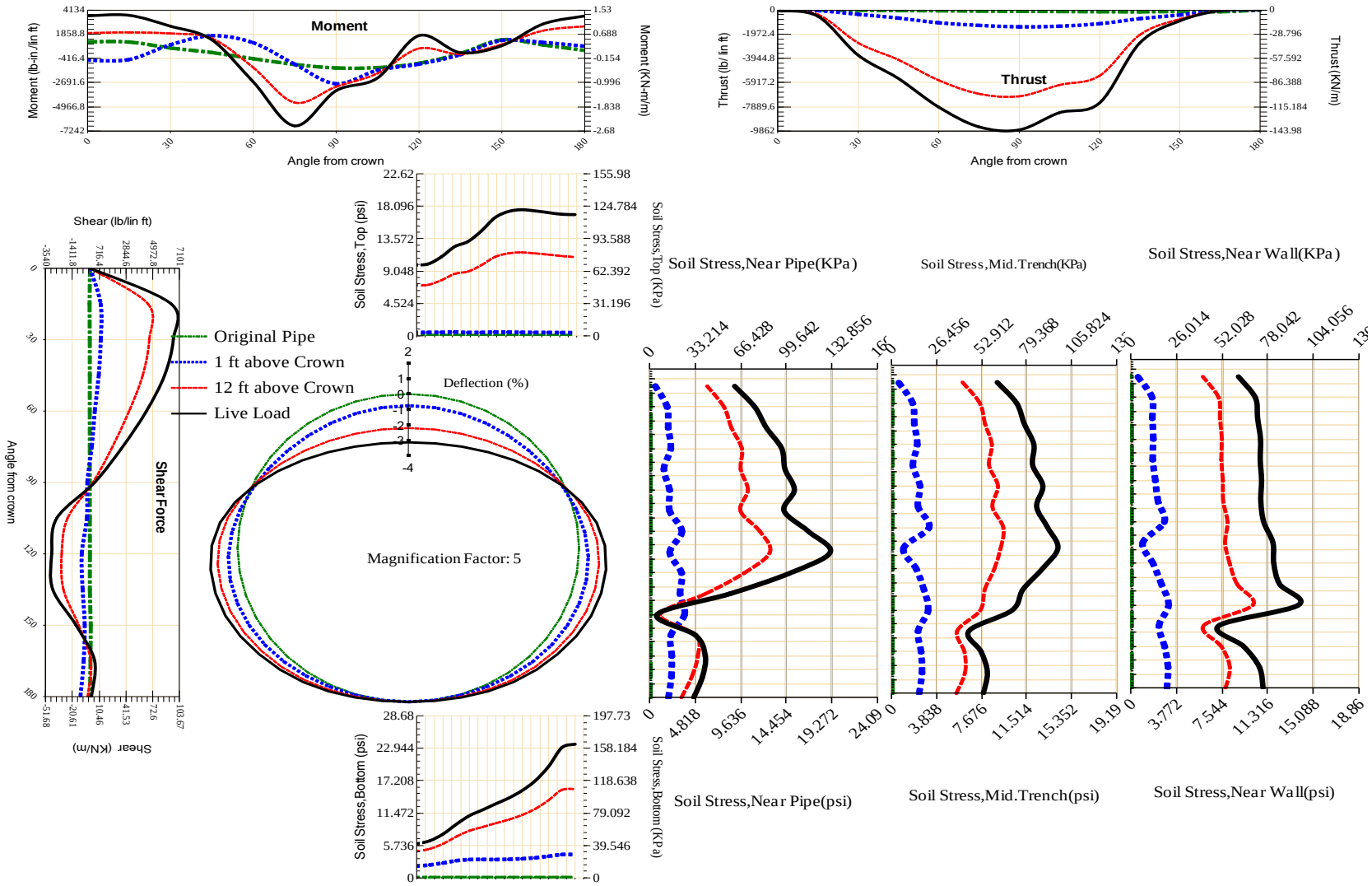

Figure A-627 Param-96-PW230-TR5OR-OD+60-EW5-H12-LiveLoad

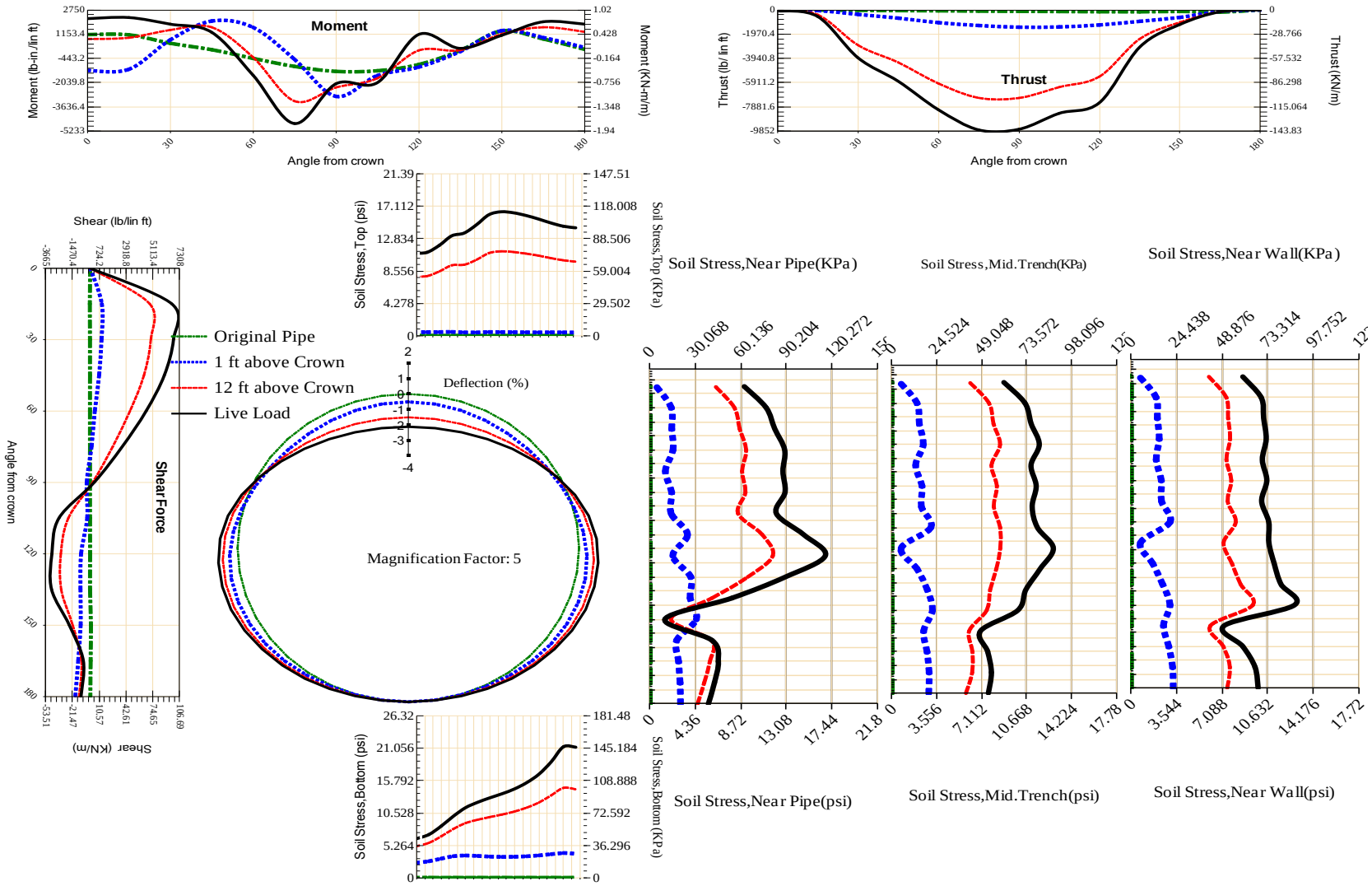

Figure A-628 Param-96-PW230-TR5OR-OD+72-EW10-H12-LiveLoad

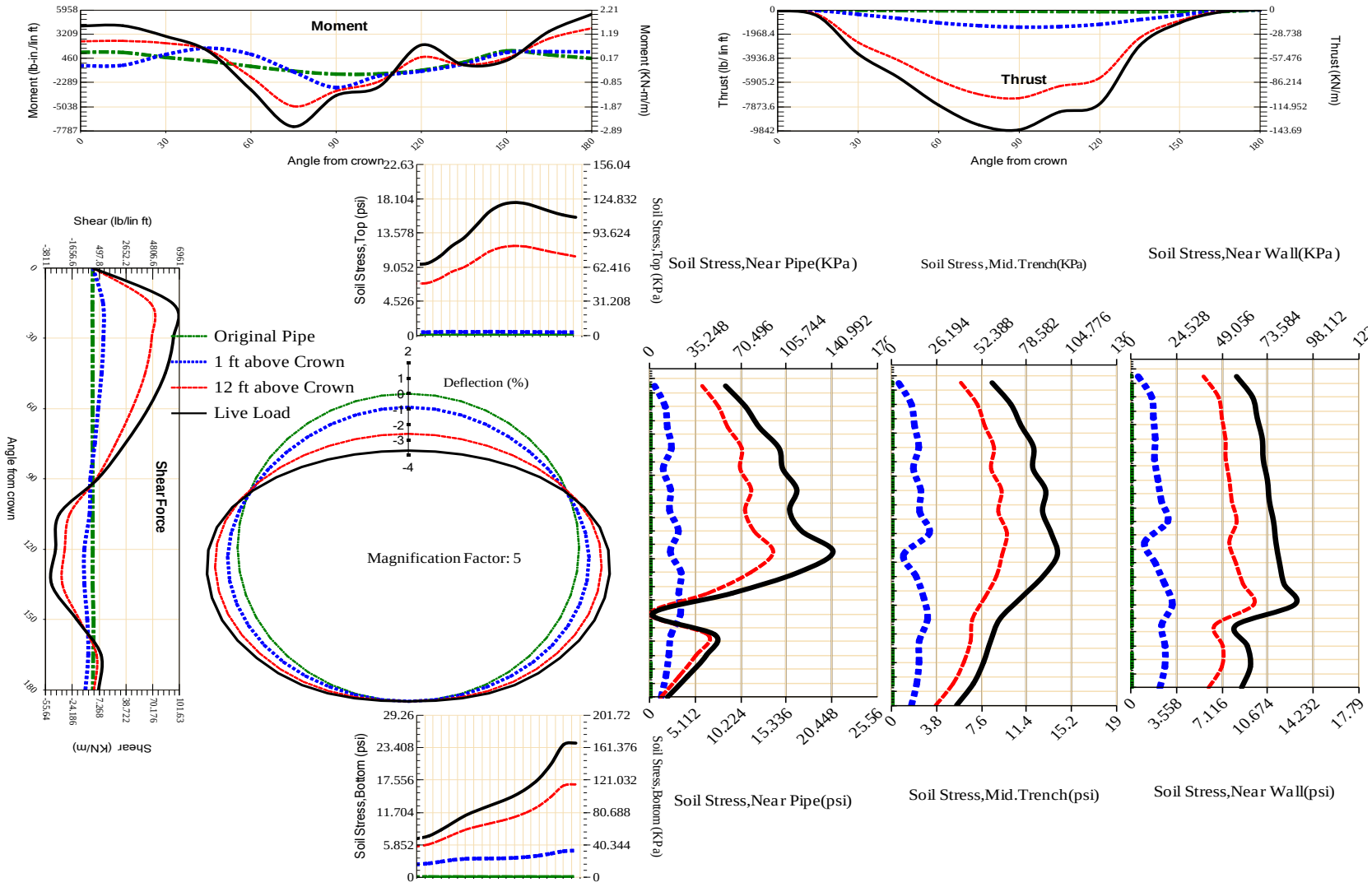

Figure A-629 Param-96-PW230-TR5OR-OD+72-EW3-H12-LiveLoad

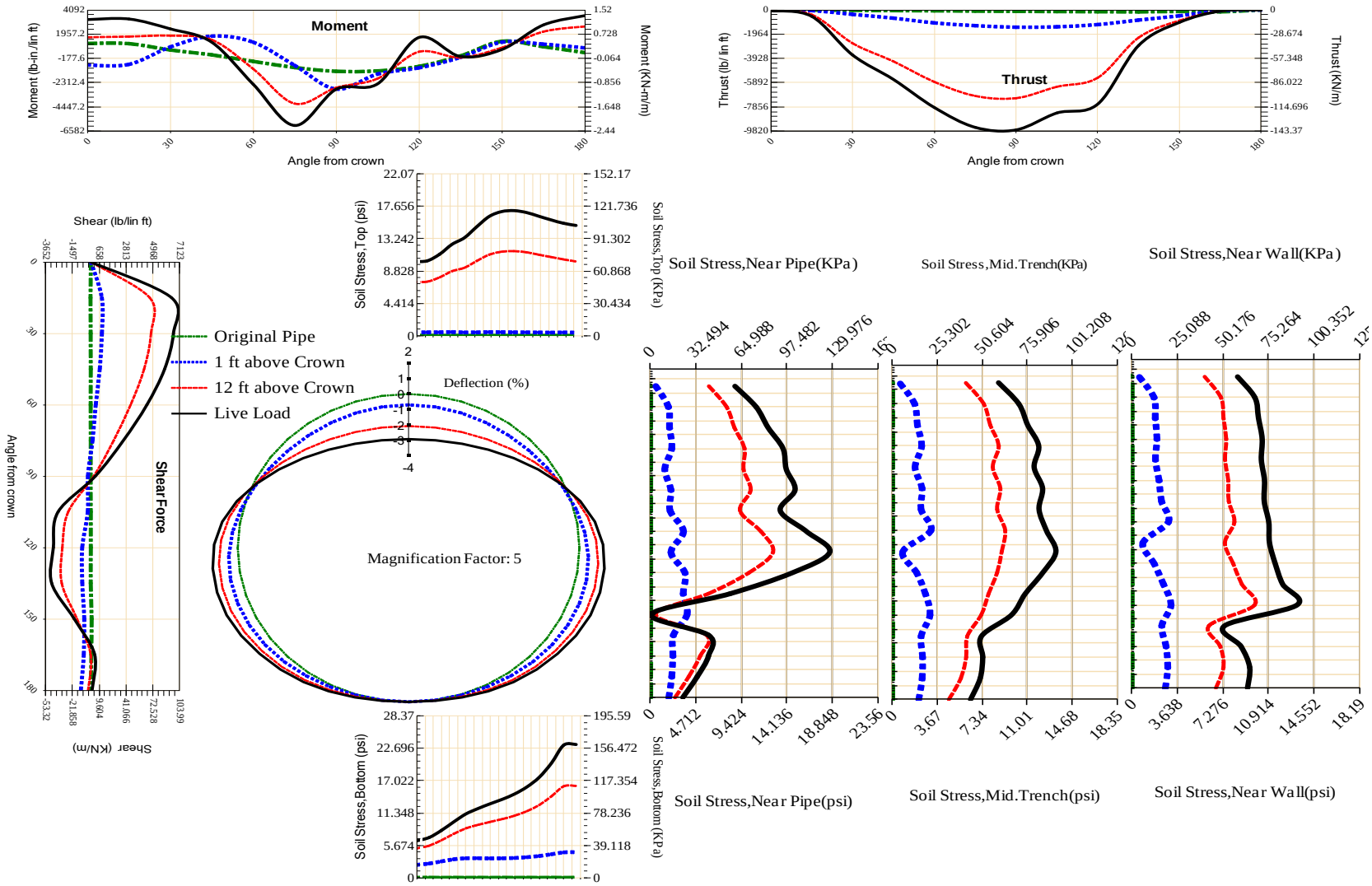

Figure A-630 Param-96-PW230-TR5OR-OD+72-EW5-H12-LiveLoad

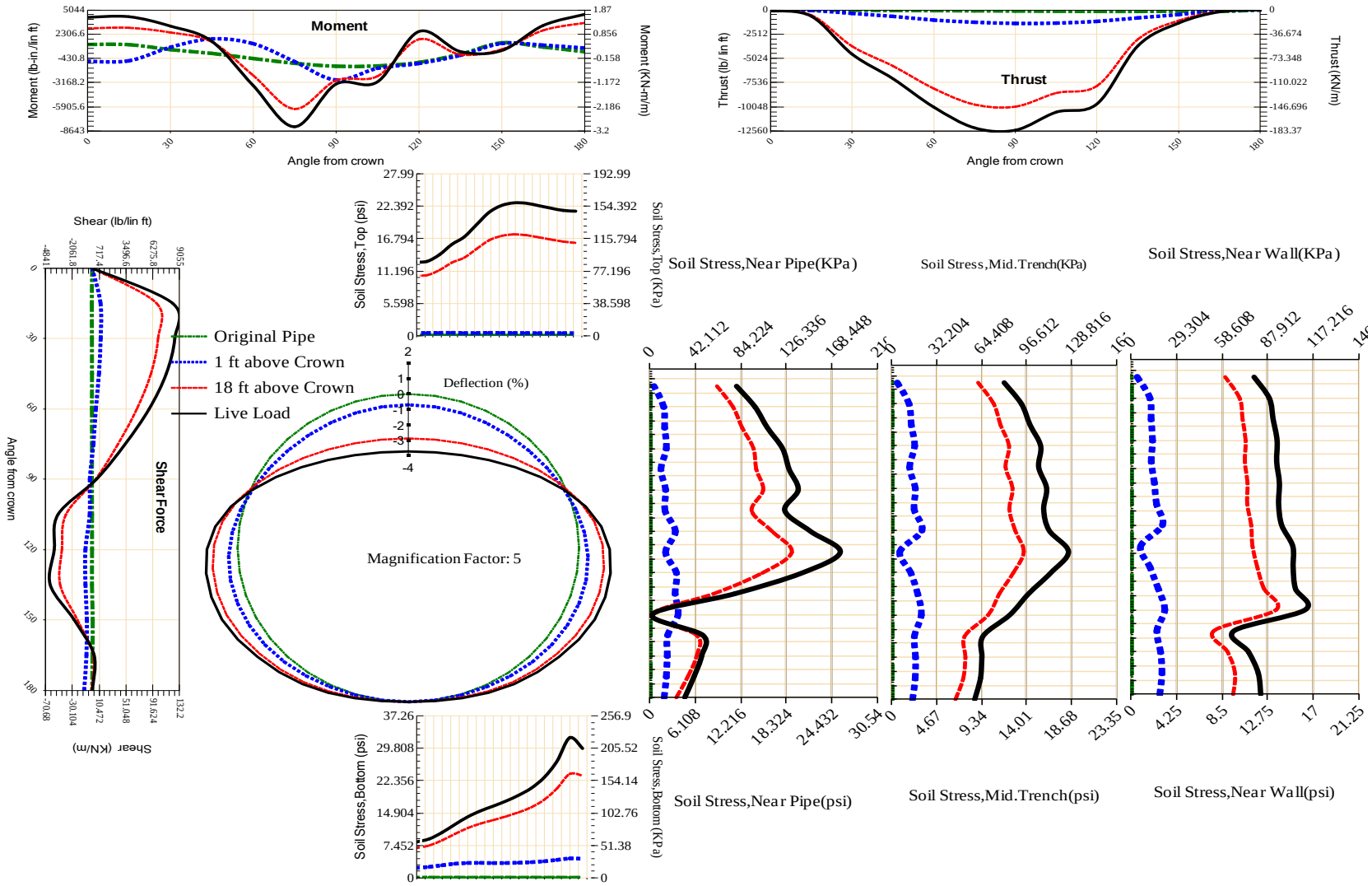

Figure A-631 Param-96-PW230-TR5OR-OD+72-EW5-H18-LiveLoad

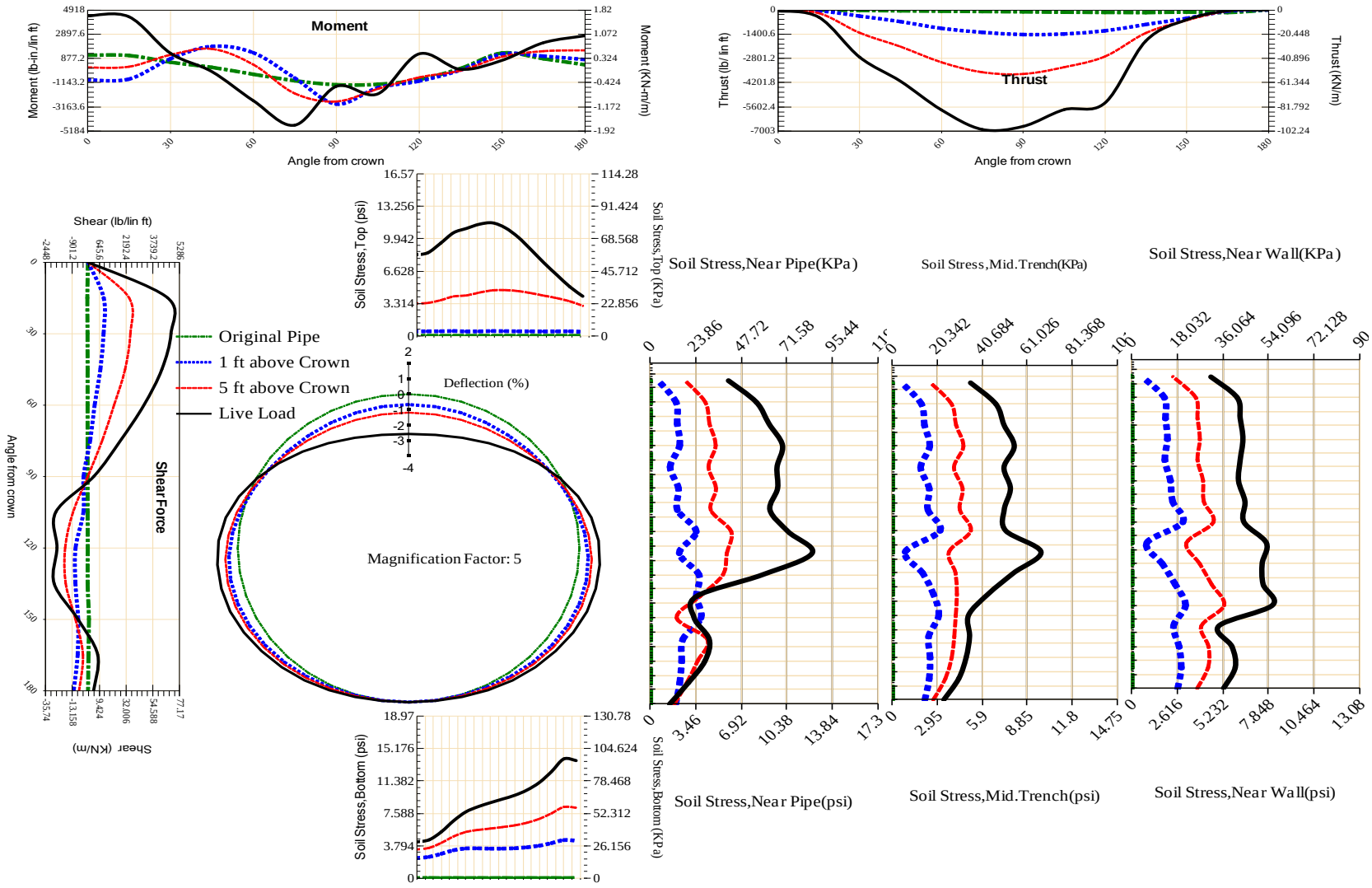

Figure A-632 Param-96-PW230-TR5OR-OD+72-EW5-H5-LiveLoad

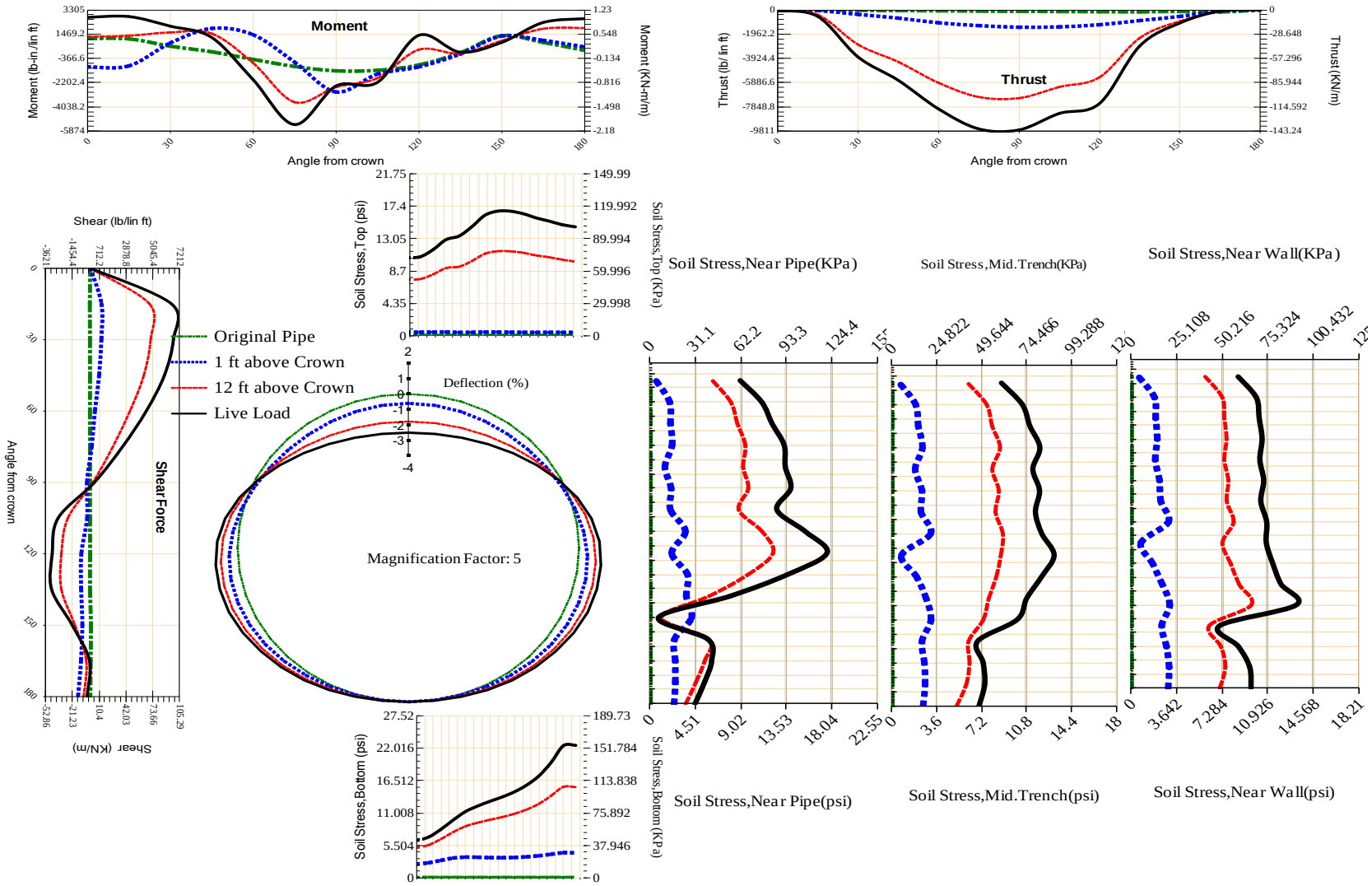

Figure A-633 Param-96-PW230-TR5OR-OD+72-EW7-H12-LiveLoad

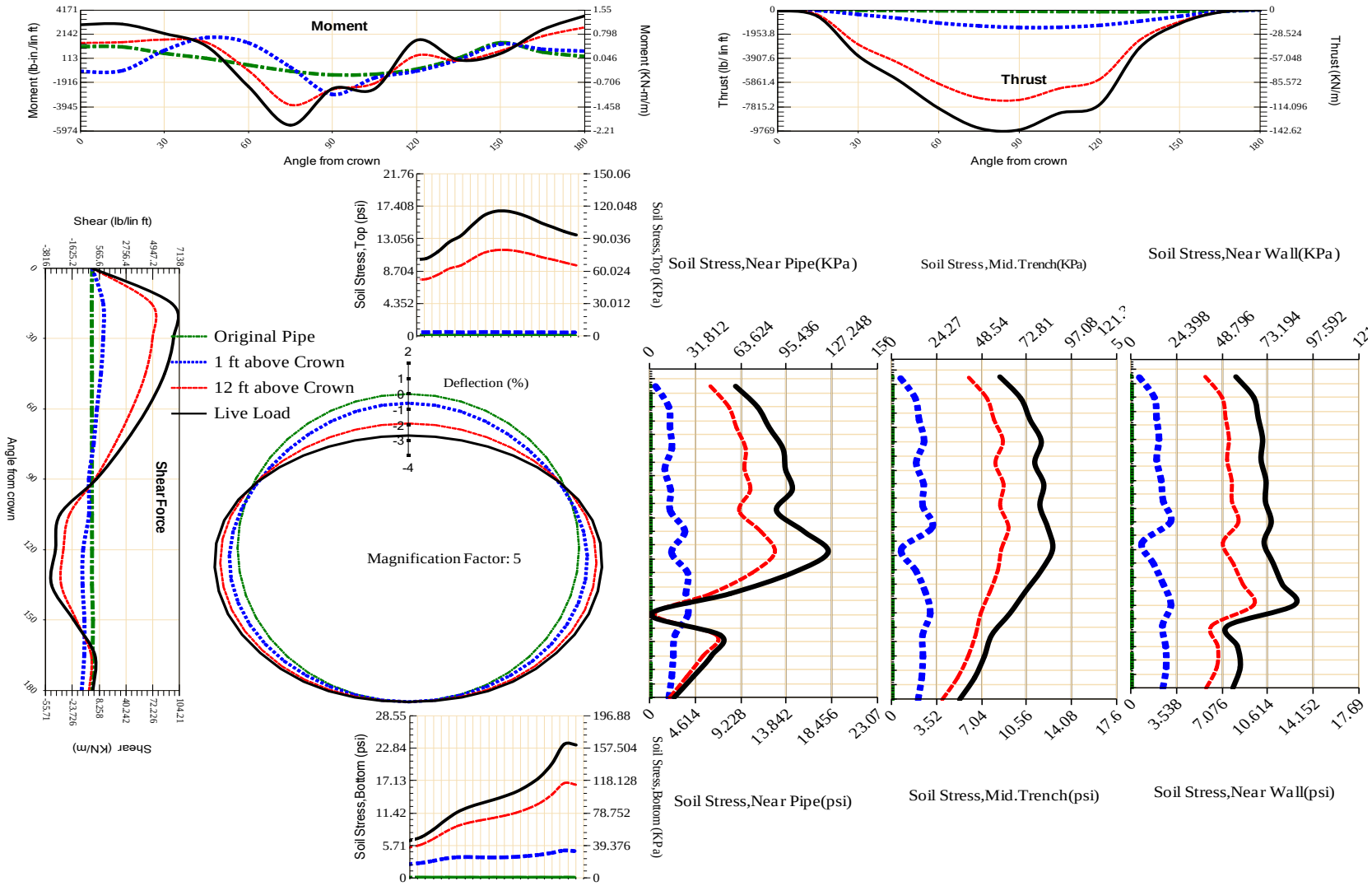

Figure A-634 Param-96-PW230-TR5OR-OD+84-EW5-H12-LiveLoad

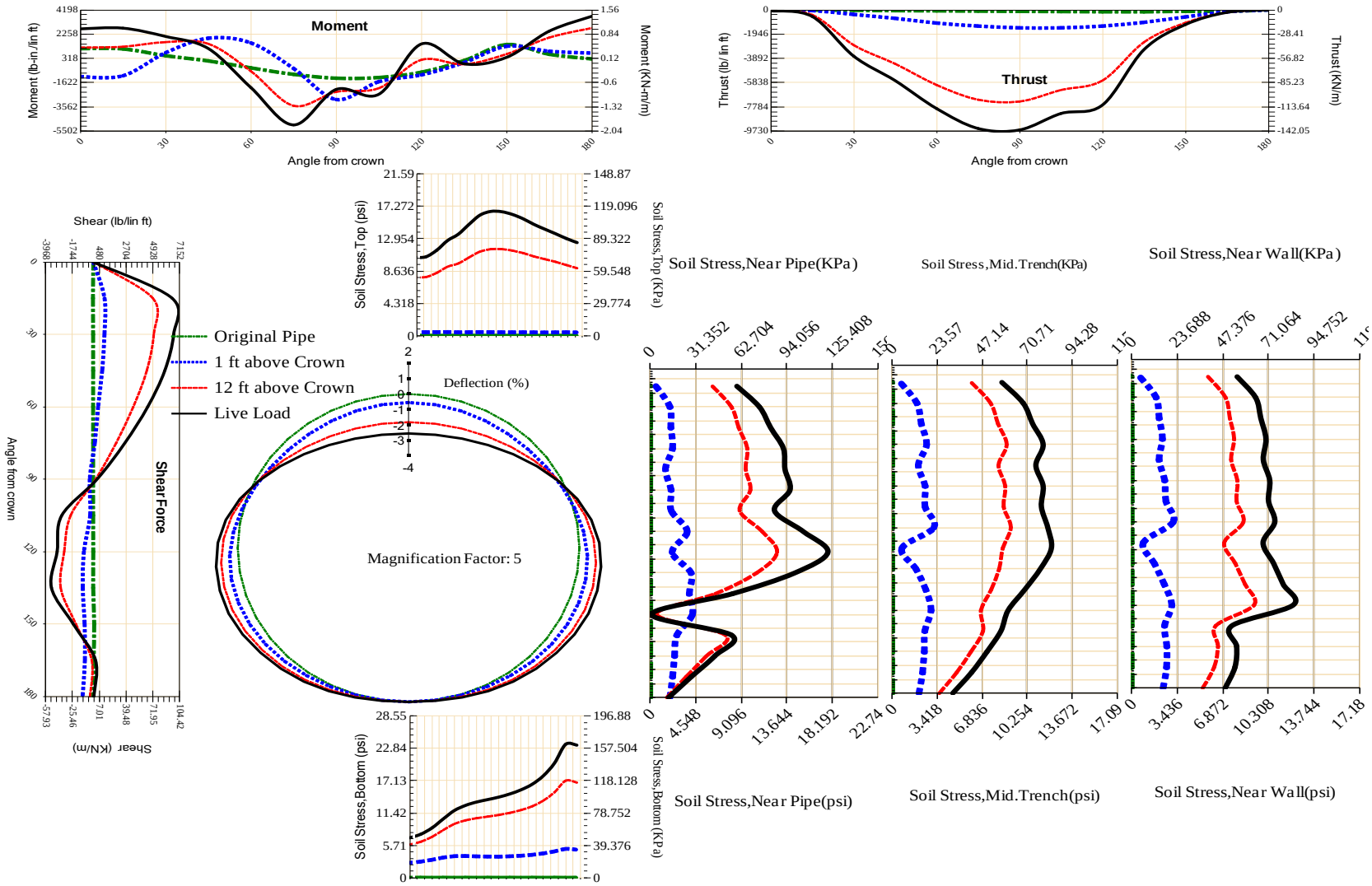

Figure A-635 Param-96-PW230-TR5OR-OD+96-EW5-H12-LiveLoad

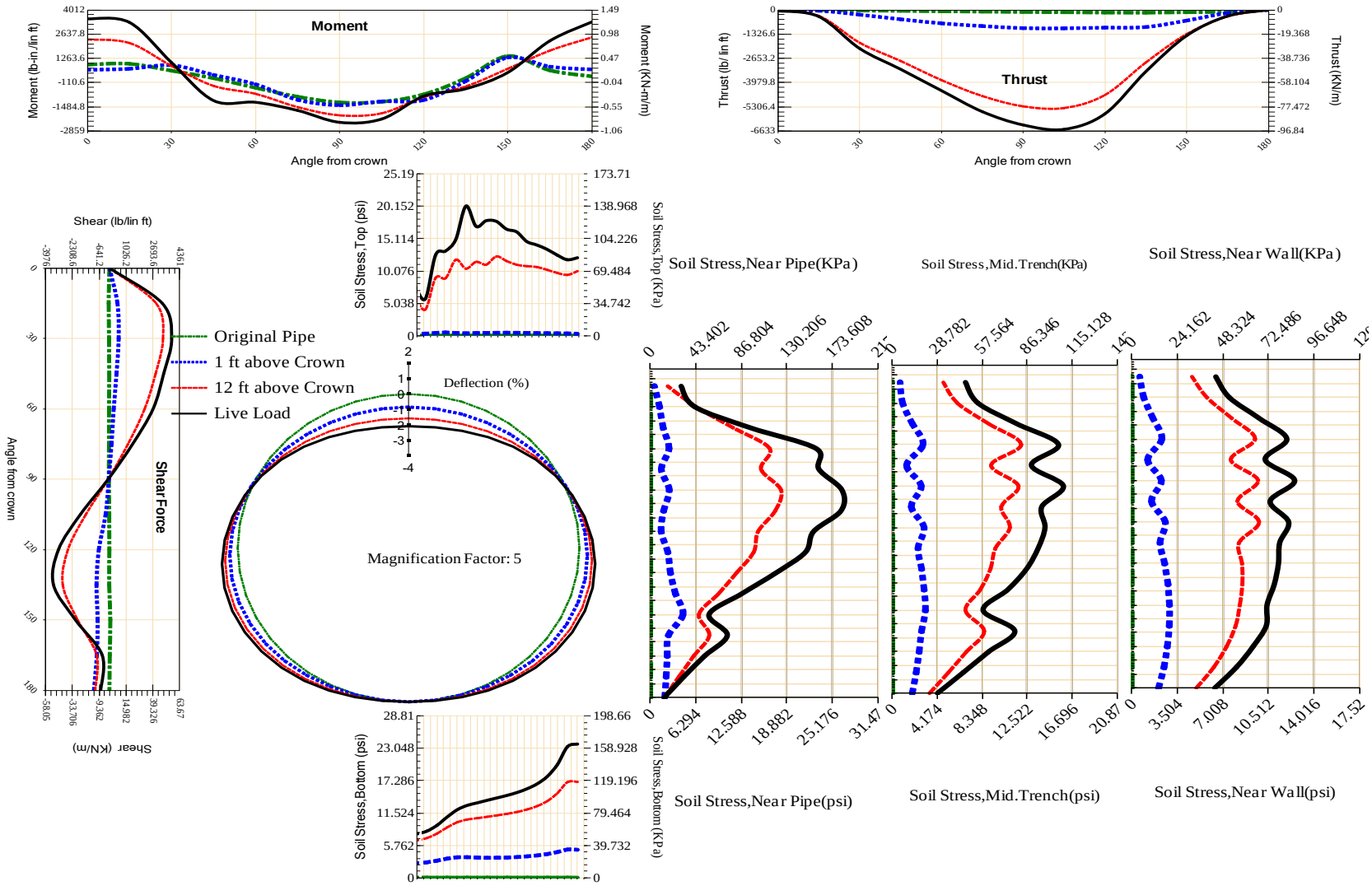

Figure A-636 Param-96-PW230-TR5SF-OD+108-EW5-H12-LiveLoad

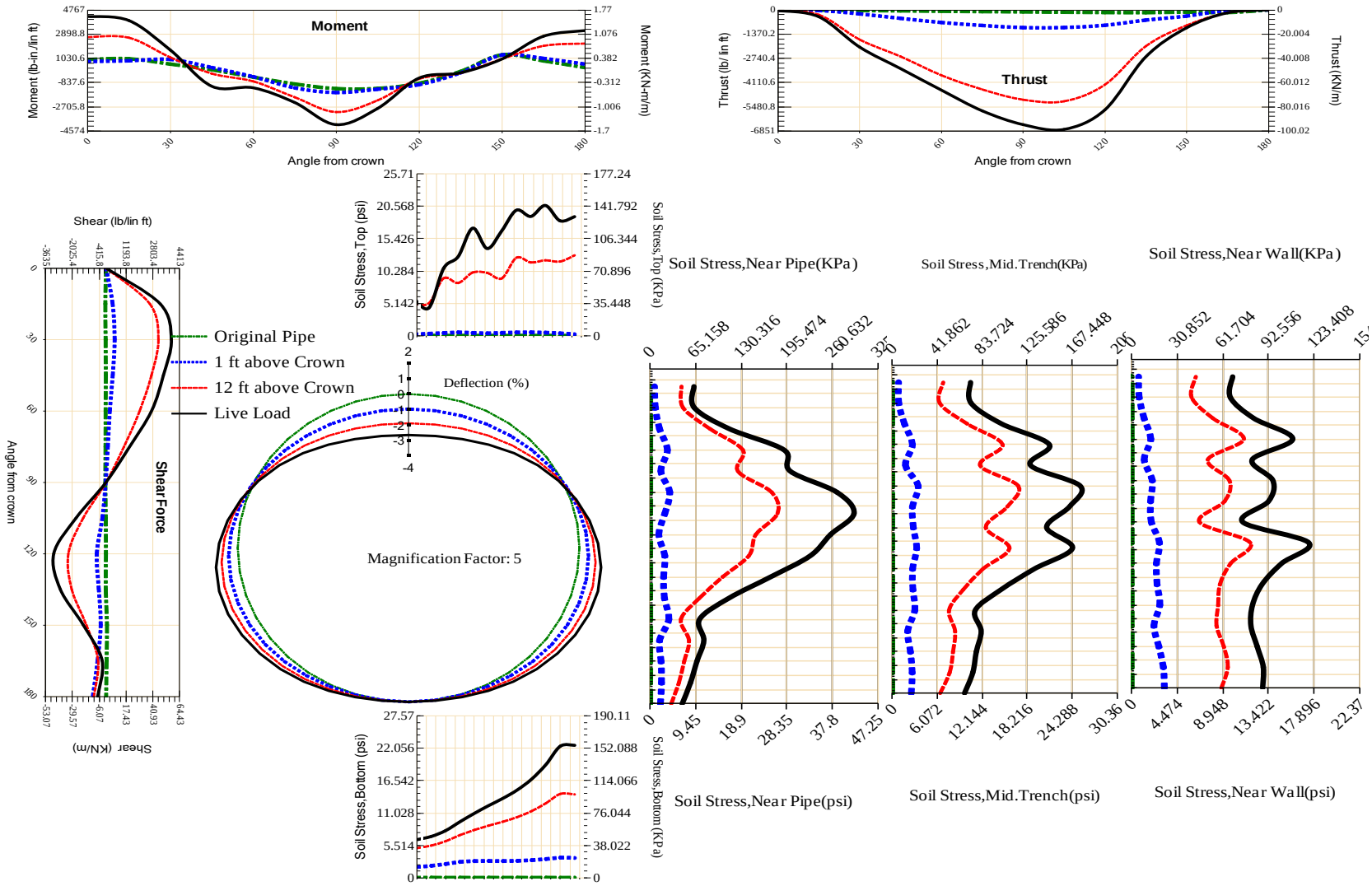

Figure A-637 Param-96-PW230-TR5SF-OD+48-EW5-H12-LiveLoad

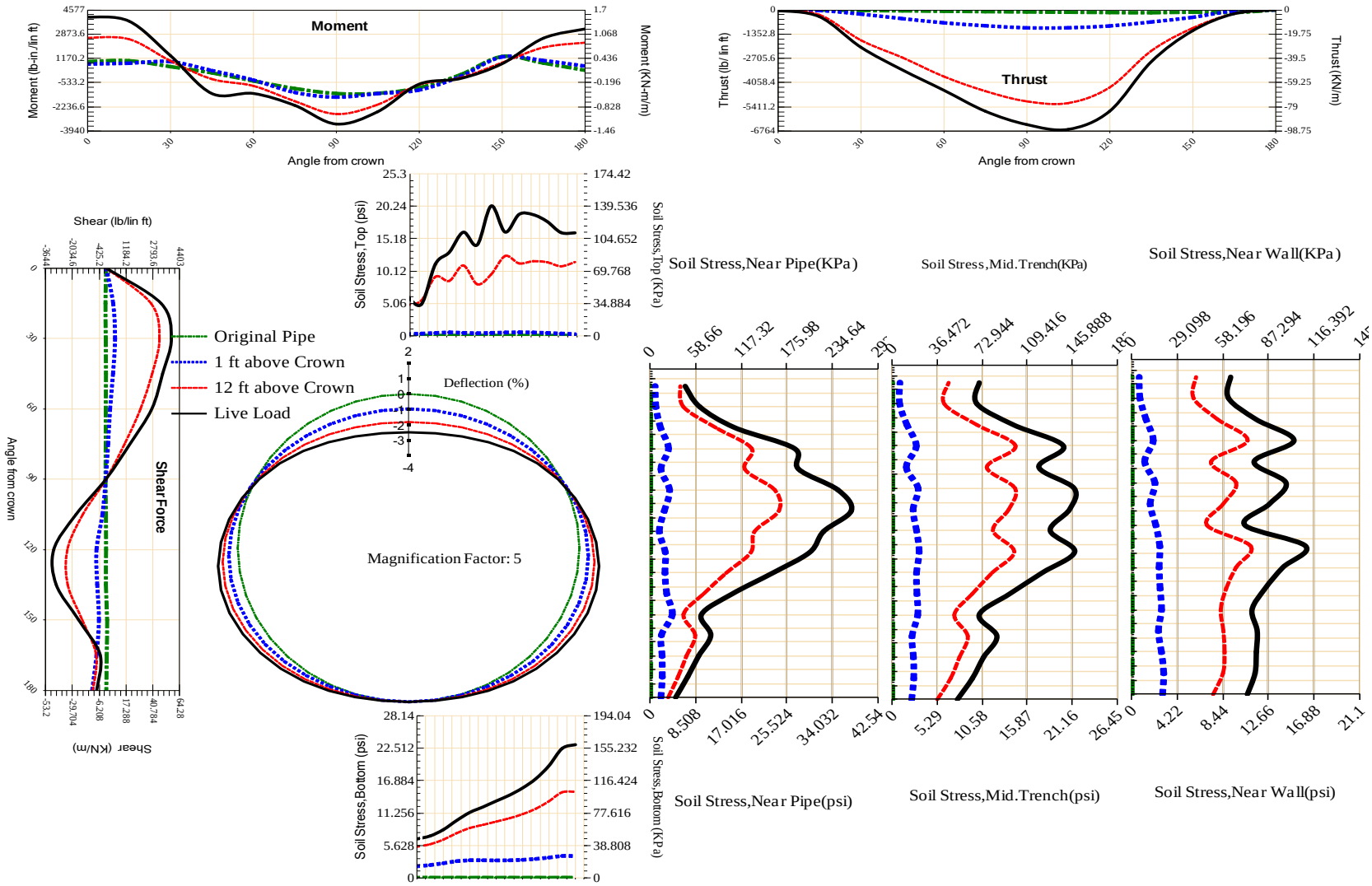

Figure A-638 Param-96-PW230-TR5SF-OD+60-EW5-H12-LiveLoad

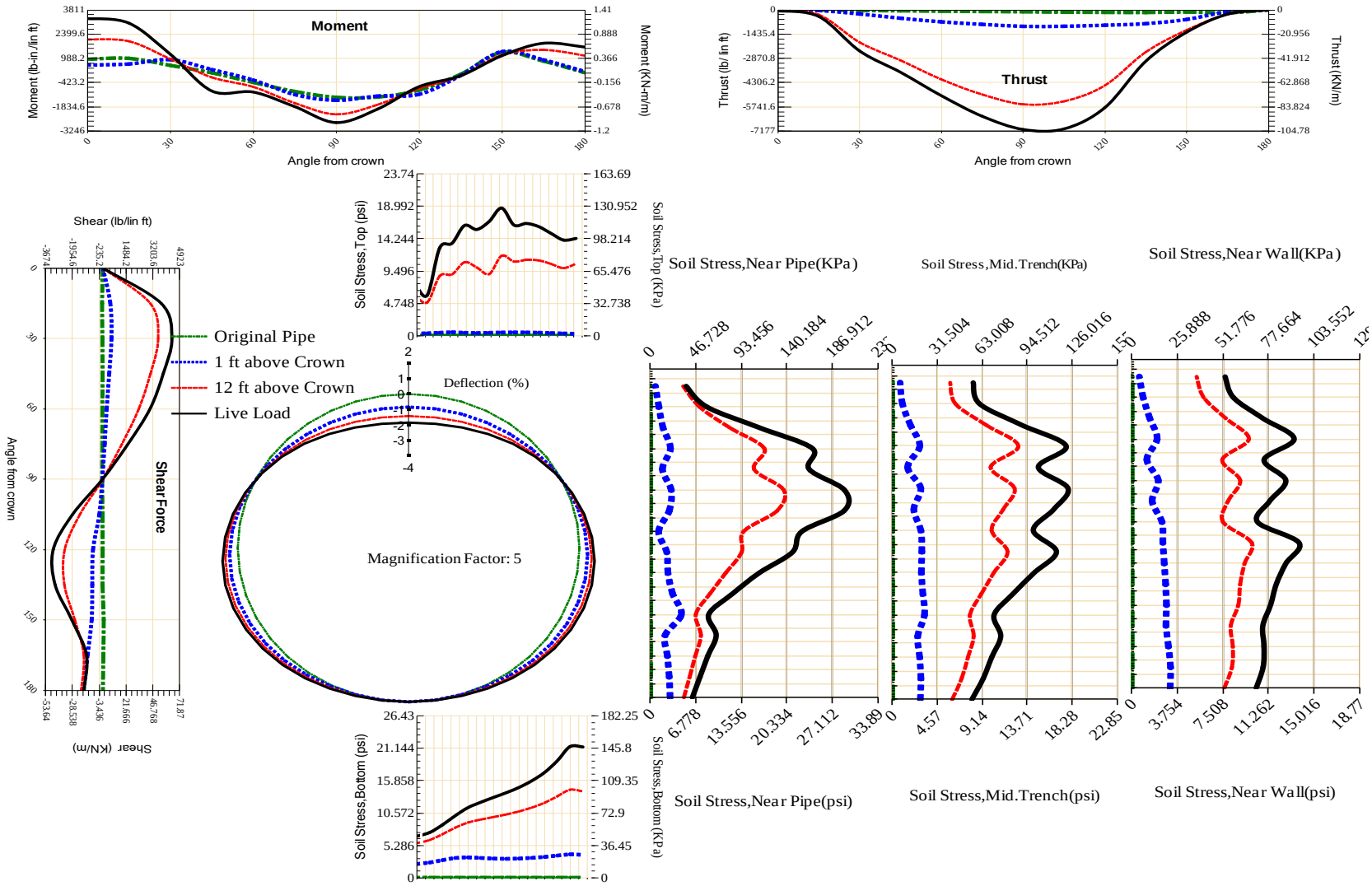

Figure A-639 Param-96-PW230-TR5SF-OD+72-EW10-H12-LiveLoad

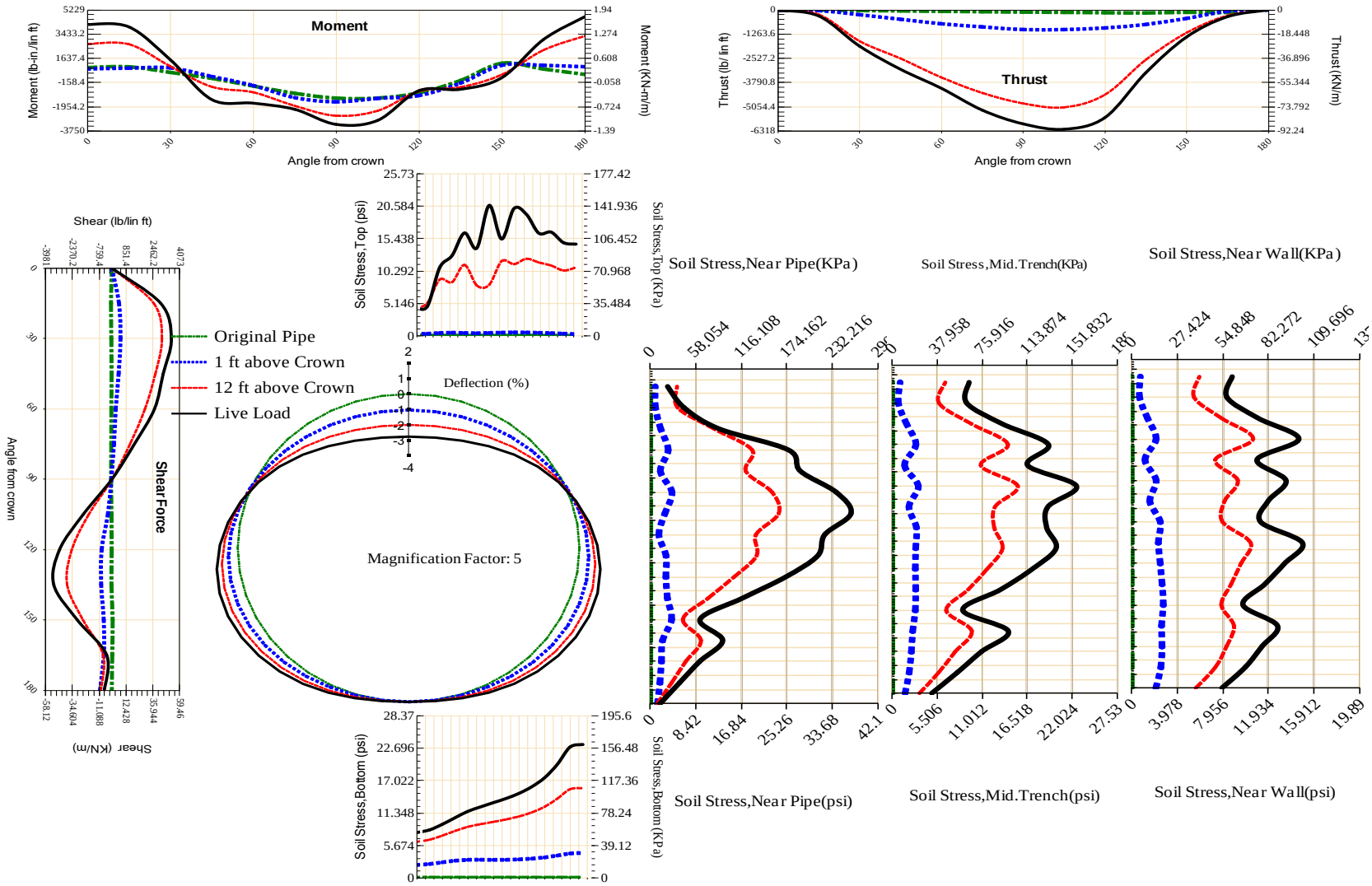

Figure A-640 Param-96-PW230-TR5SF-OD+72-EW3-H12-LiveLoad

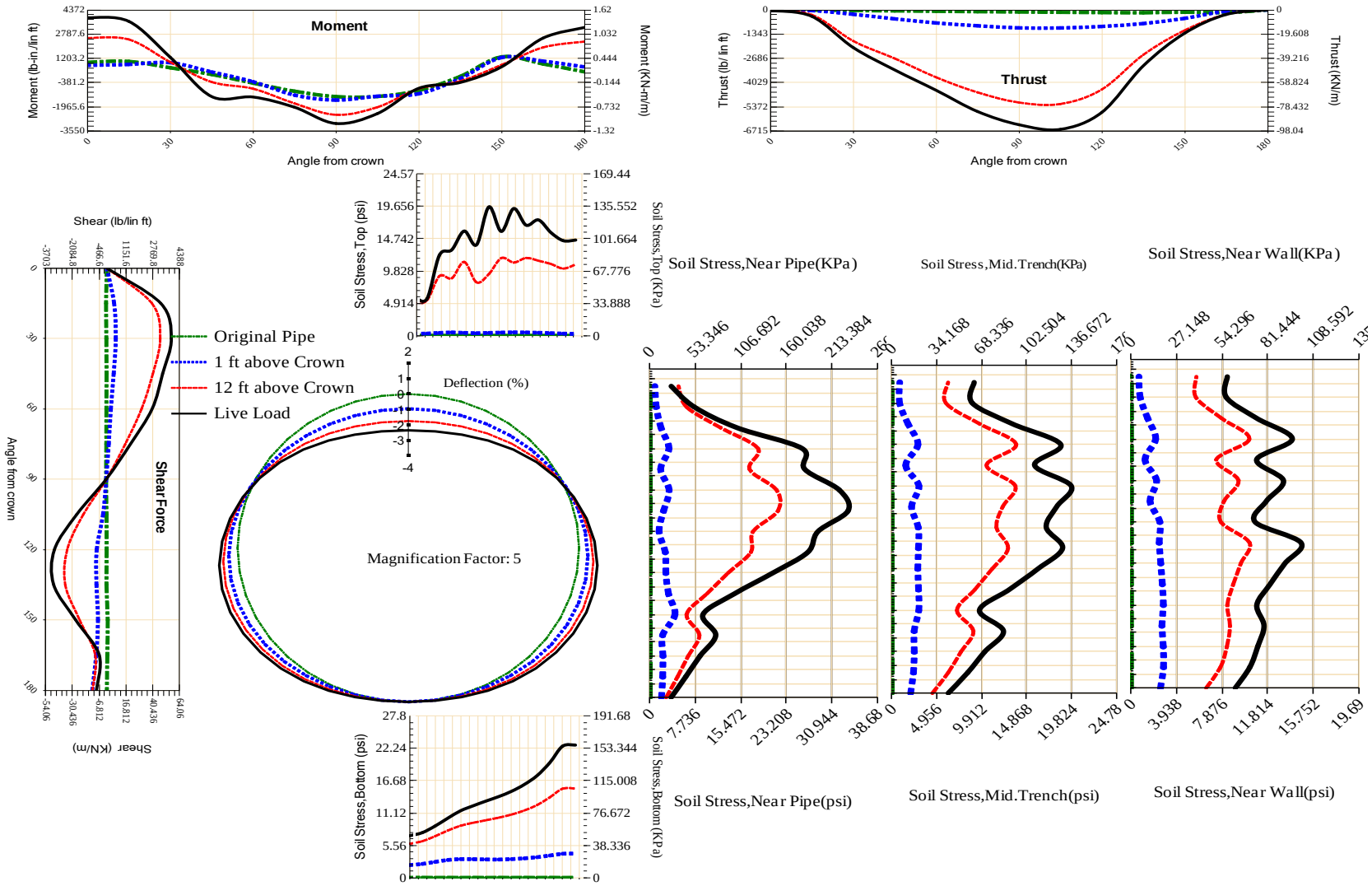

Figure A-641 Param-96-PW230-TR5SF-OD+72-EW5-H12-LiveLoad

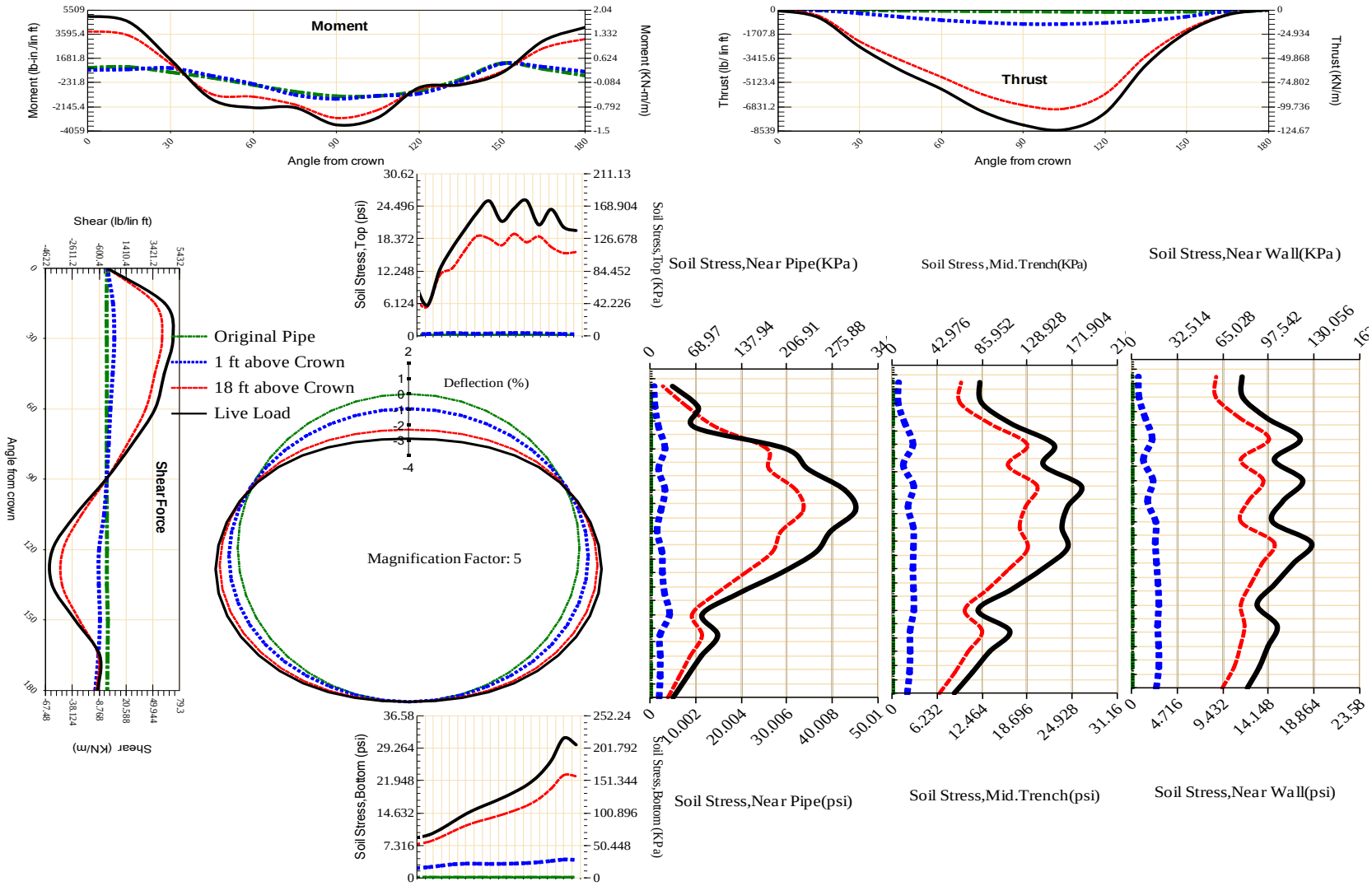

Figure A-642 Param-96-PW230-TR5SF-OD+72-EW5-H18-LiveLoad

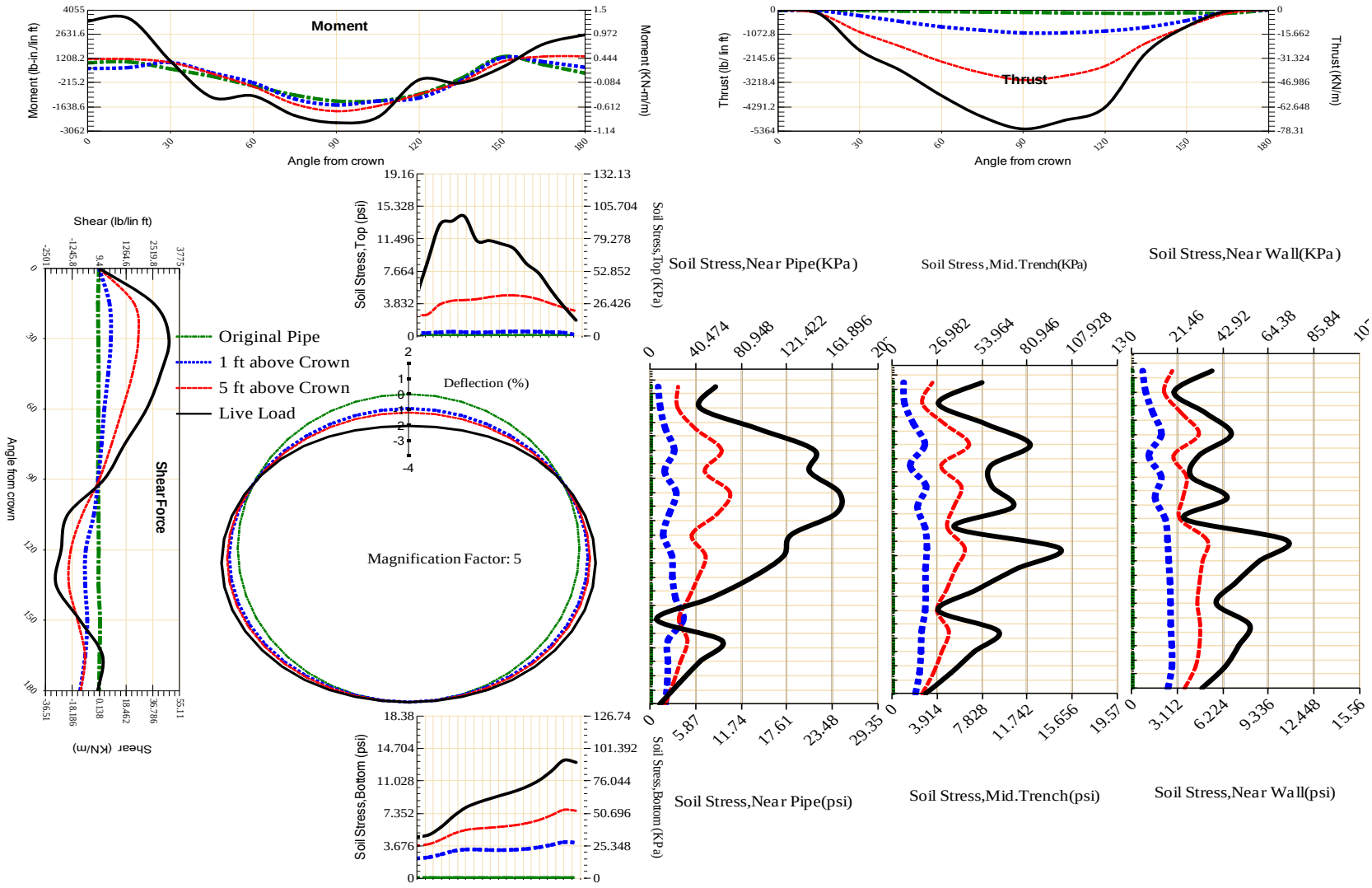

Figure A-643 Param-96-PW230-TR5SF-OD+72-EW5-H5-LiveLoad

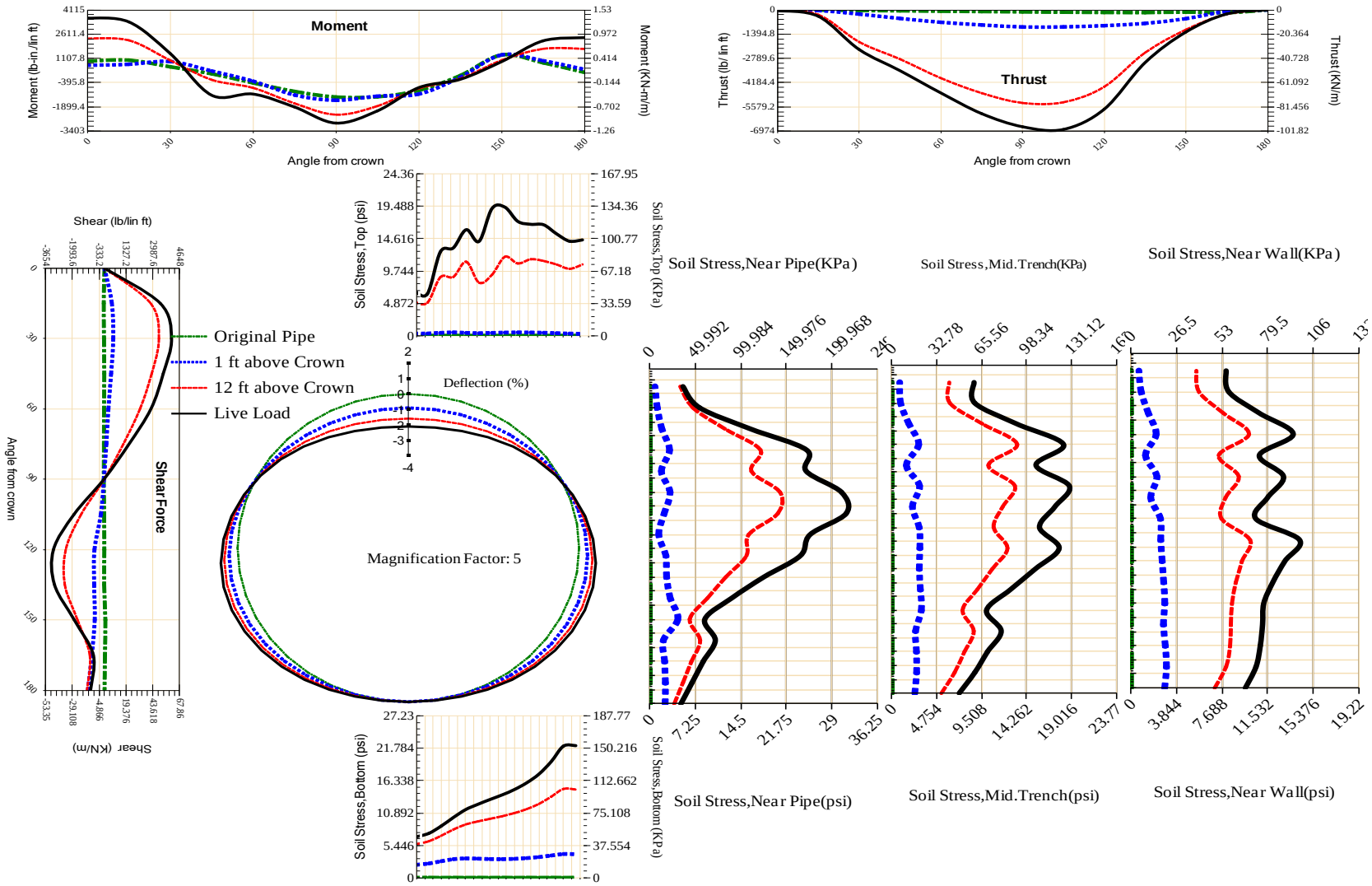

Figure A-644 Param-96-PW230-TR5SF-OD+72-EW7-H12-LiveLoad

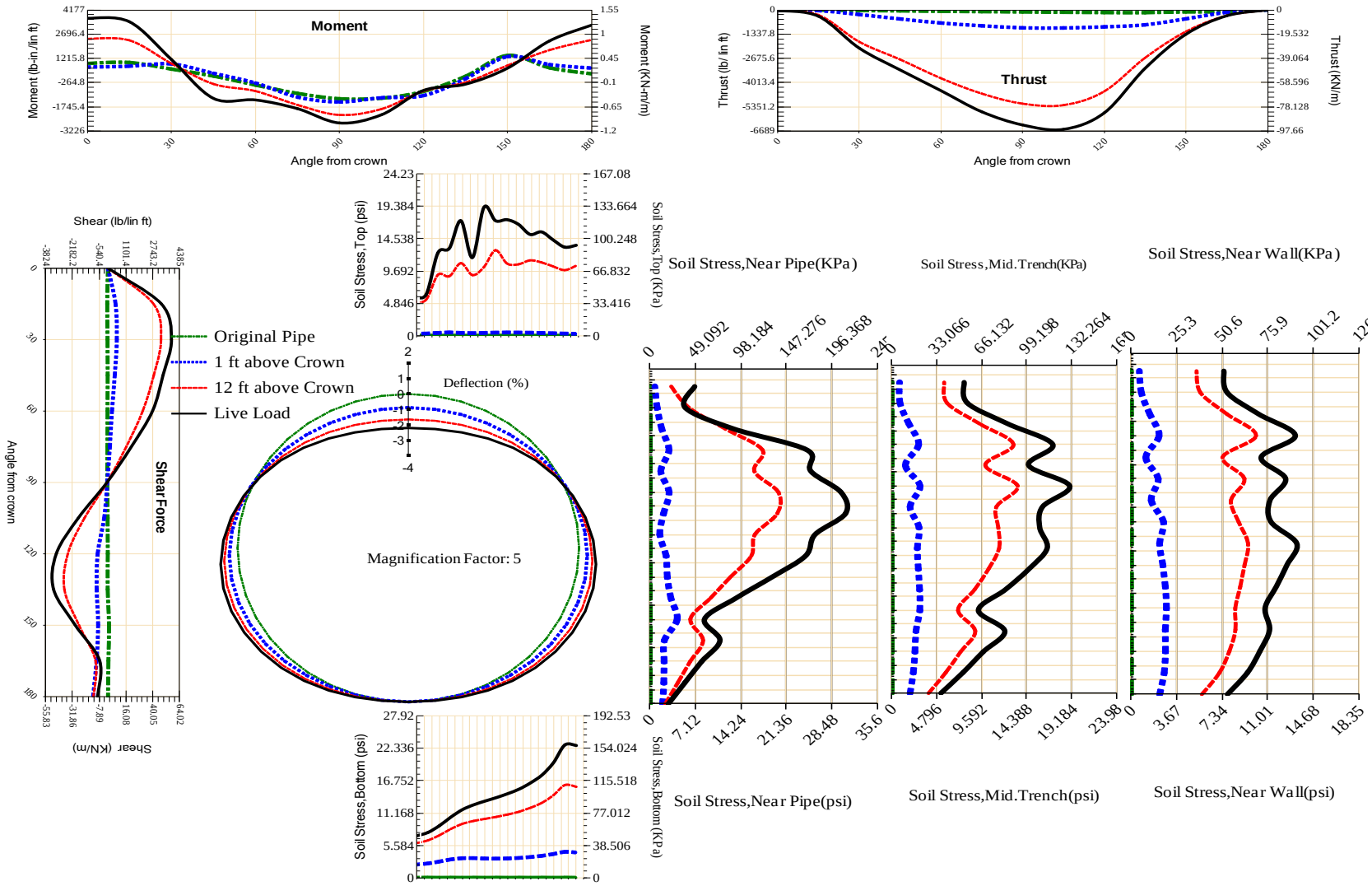

Figure A-645 Param-96-PW230-TR5SF-OD+84-EW5-H12-LiveLoad

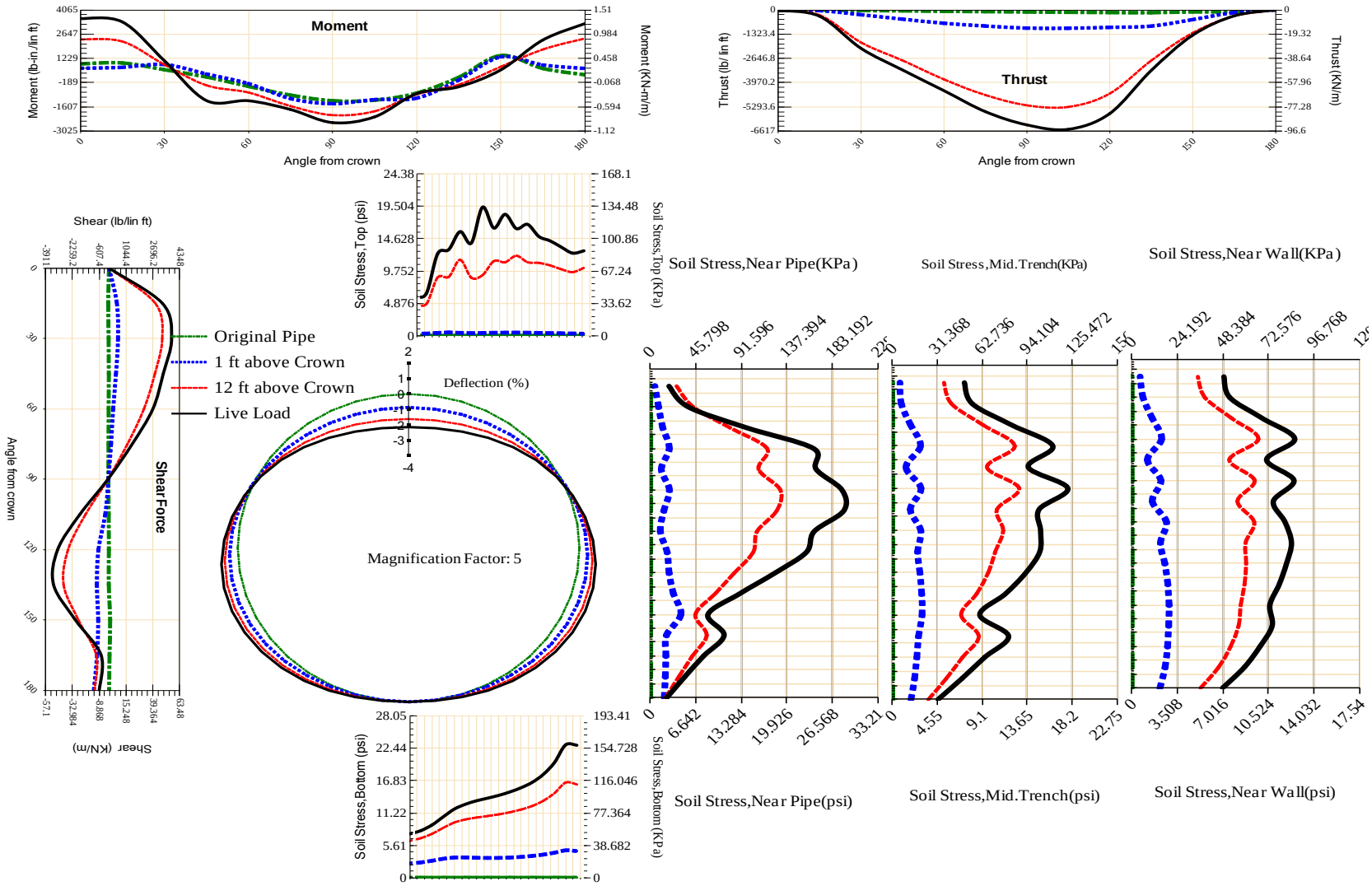

Figure A-646 Param-96-PW230-TR5SF-OD+96-EW5-H12-LiveLoad

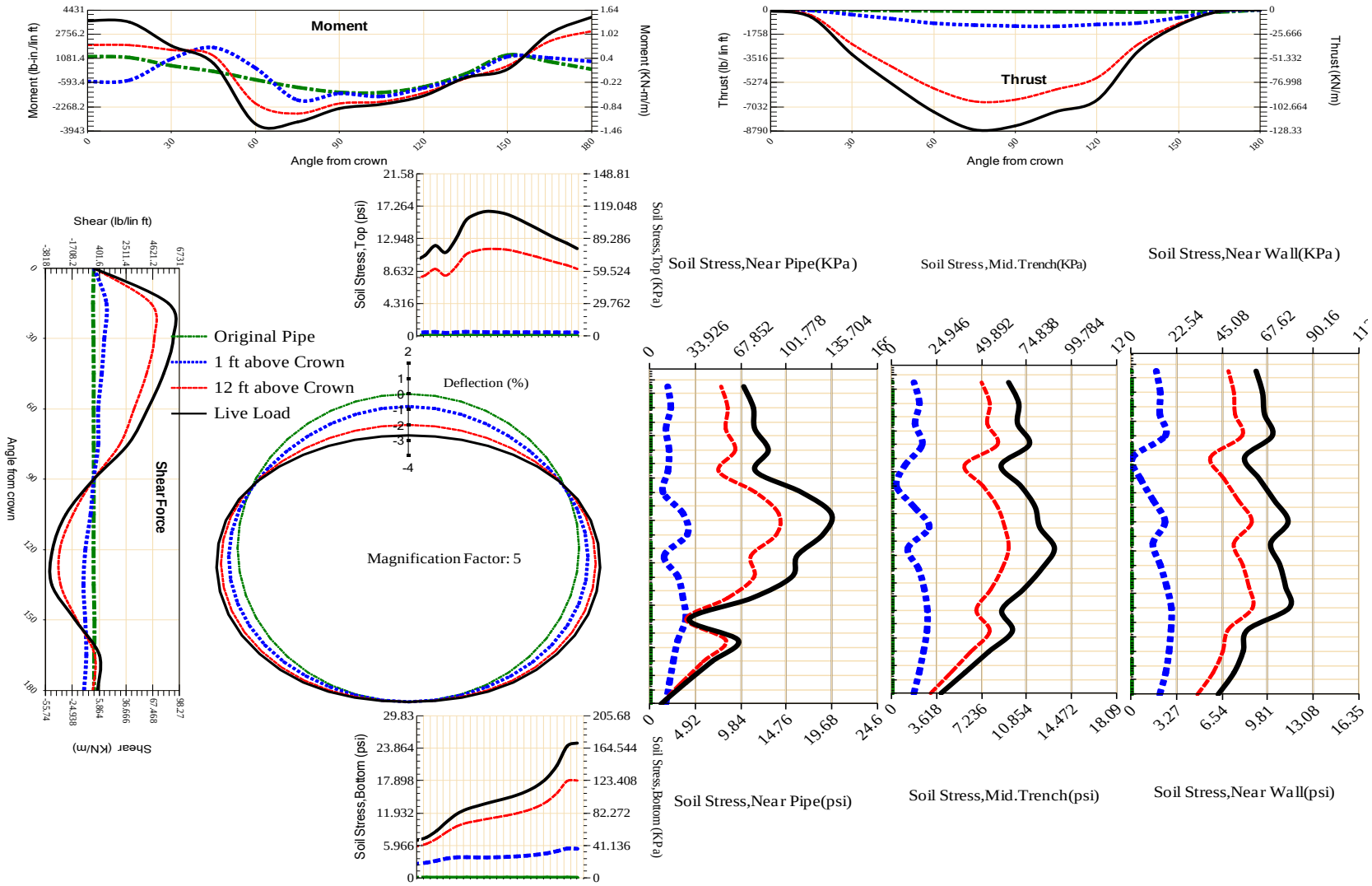

Figure A-647 Param-96-PW230-TR7OR-OD+108-EW5-H12-LiveLoad

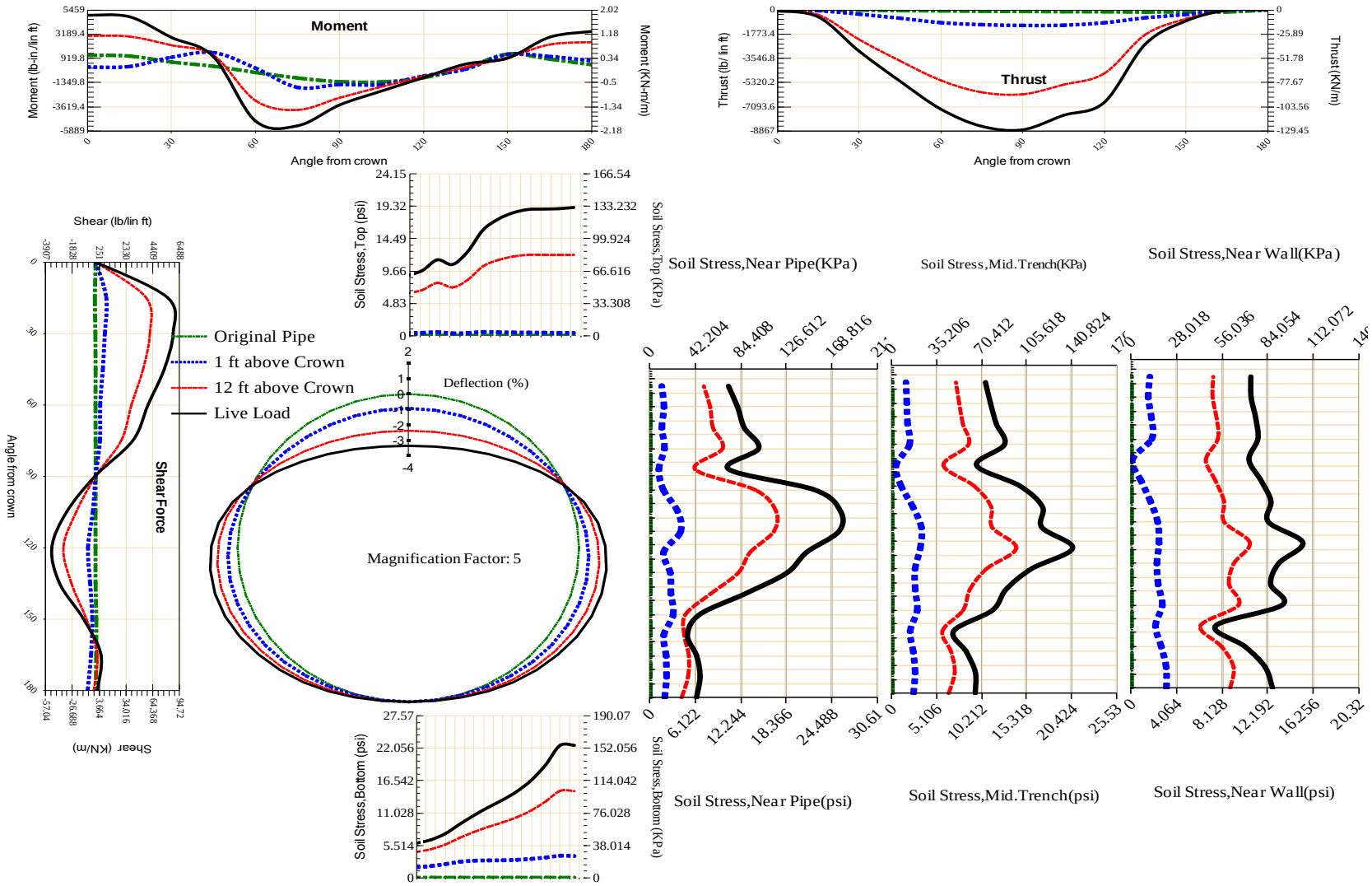

Figure A-648 Param-96-PW230-TR7OR-OD+48-EW5-H12-LiveLoad

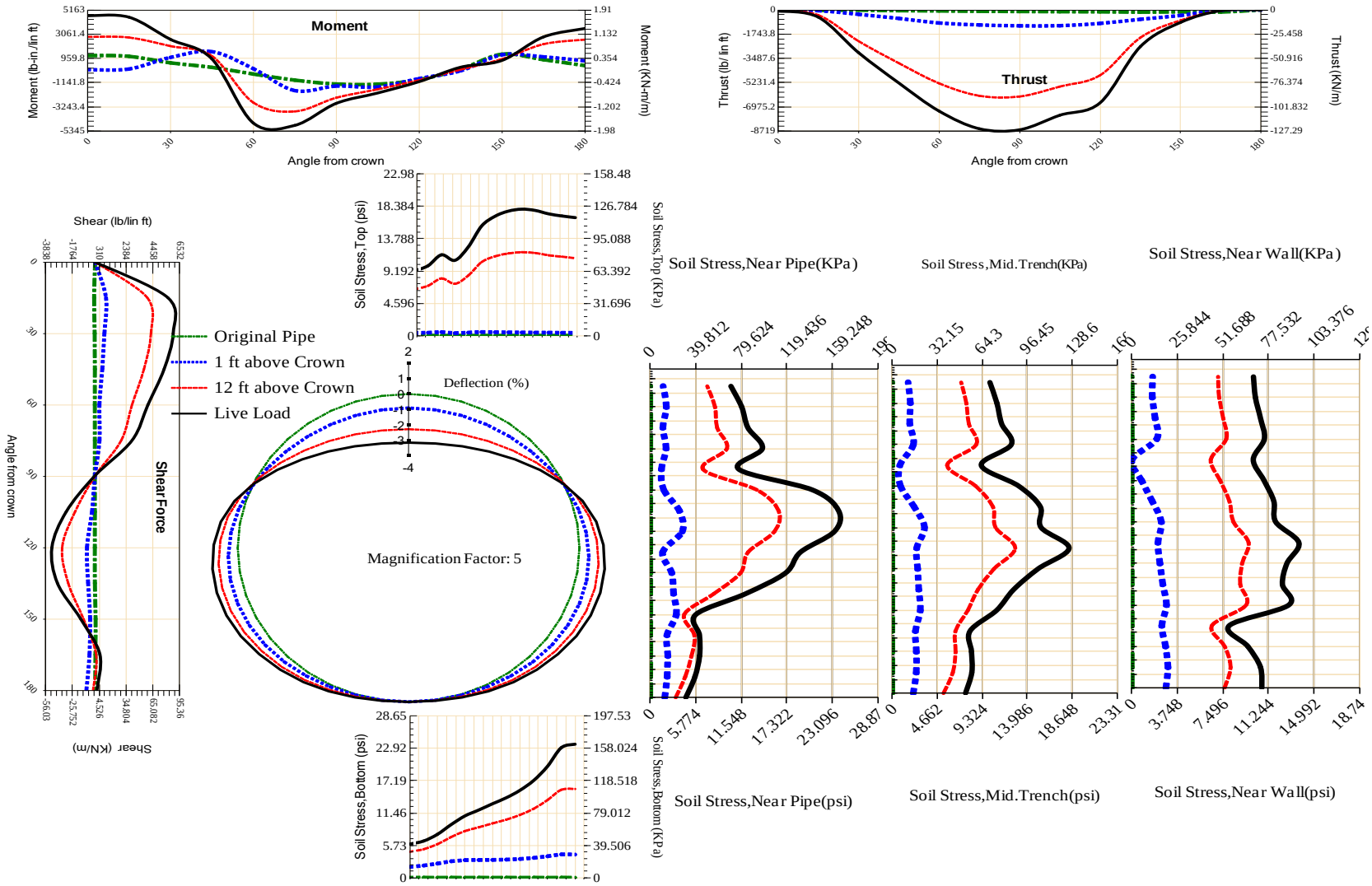

Figure A-649 Param-96-PW230-TR7OR-OD+60-EW5-H12-LiveLoad

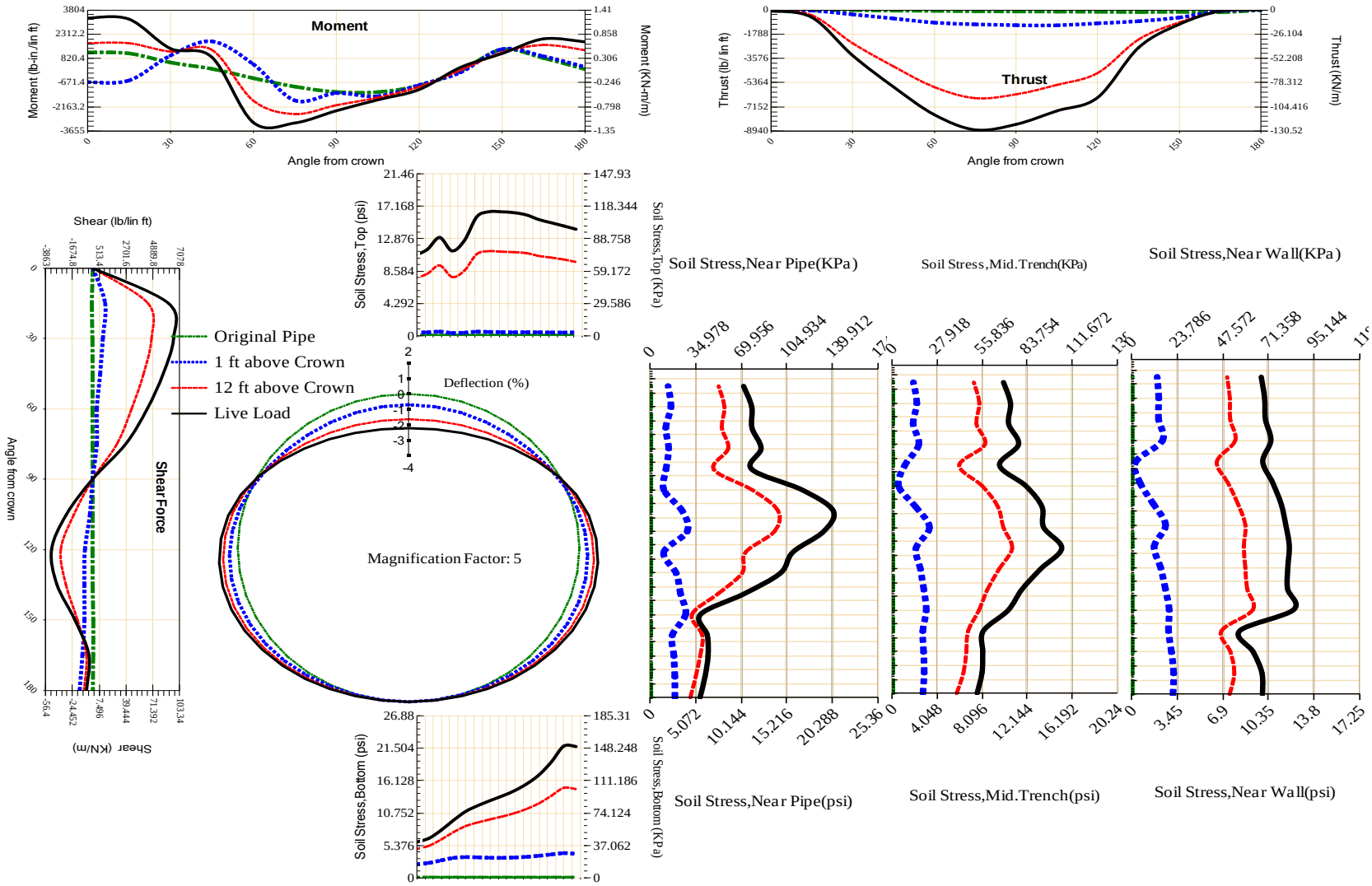

Figure A-650 Param-96-PW230-TR7OR-OD+72-EW10-H12-LiveLoad

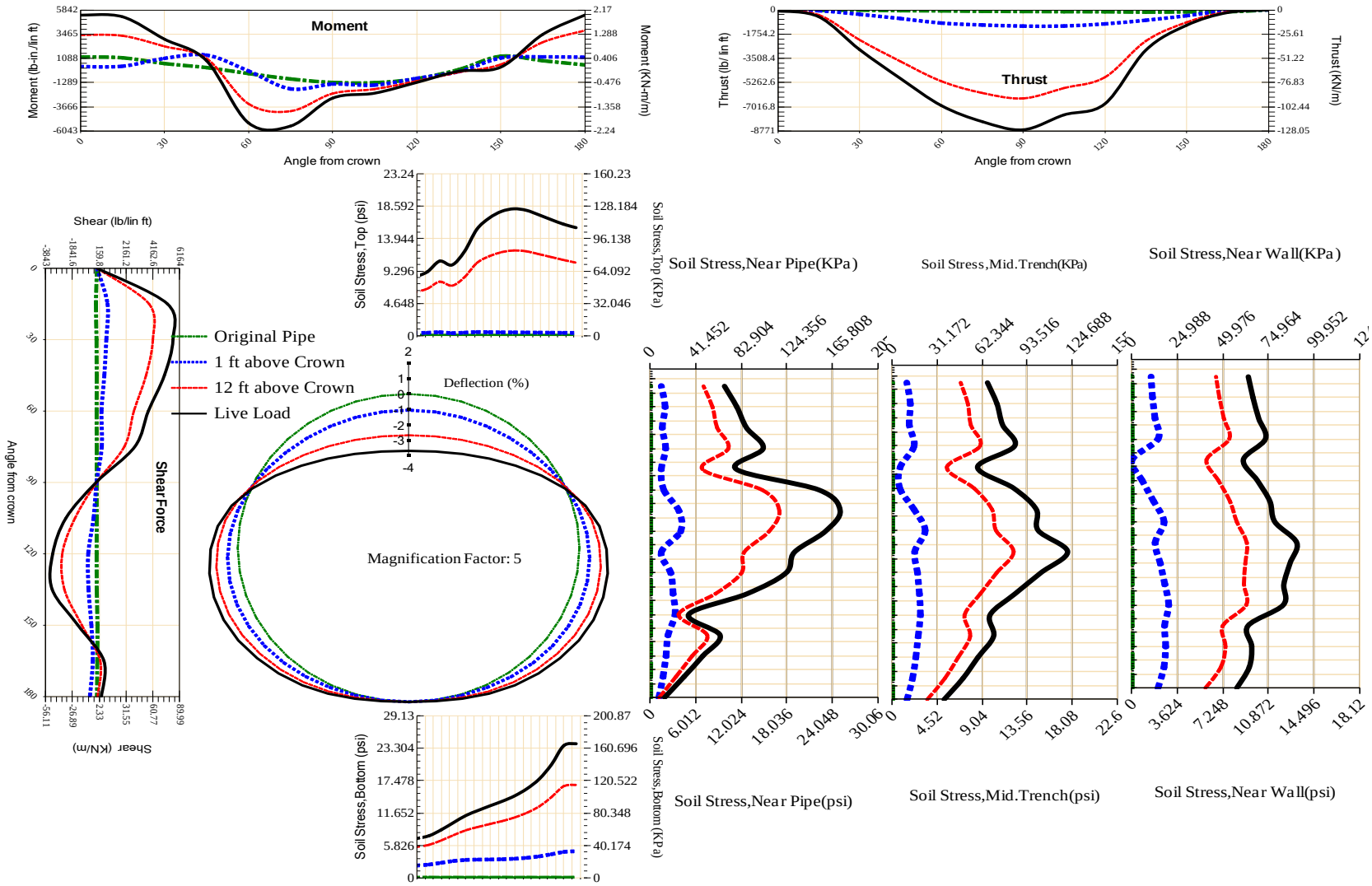

Figure A-651 Param-96-PW230-TR7OR-OD+72-EW3-H12-LiveLoad

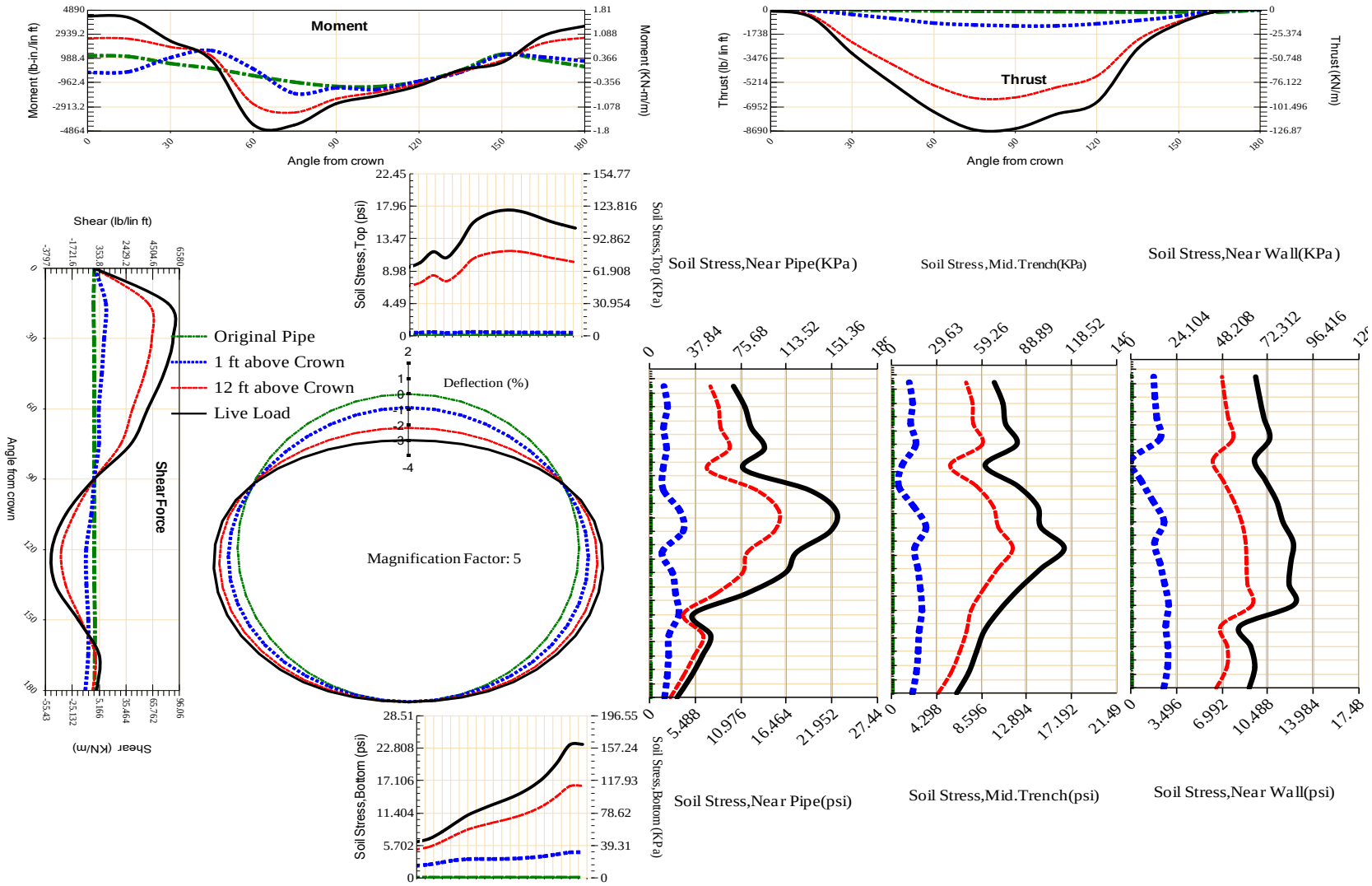

Figure A-652 Param-96-PW230-TR7OR-OD+72-EW5-H12-LiveLoad

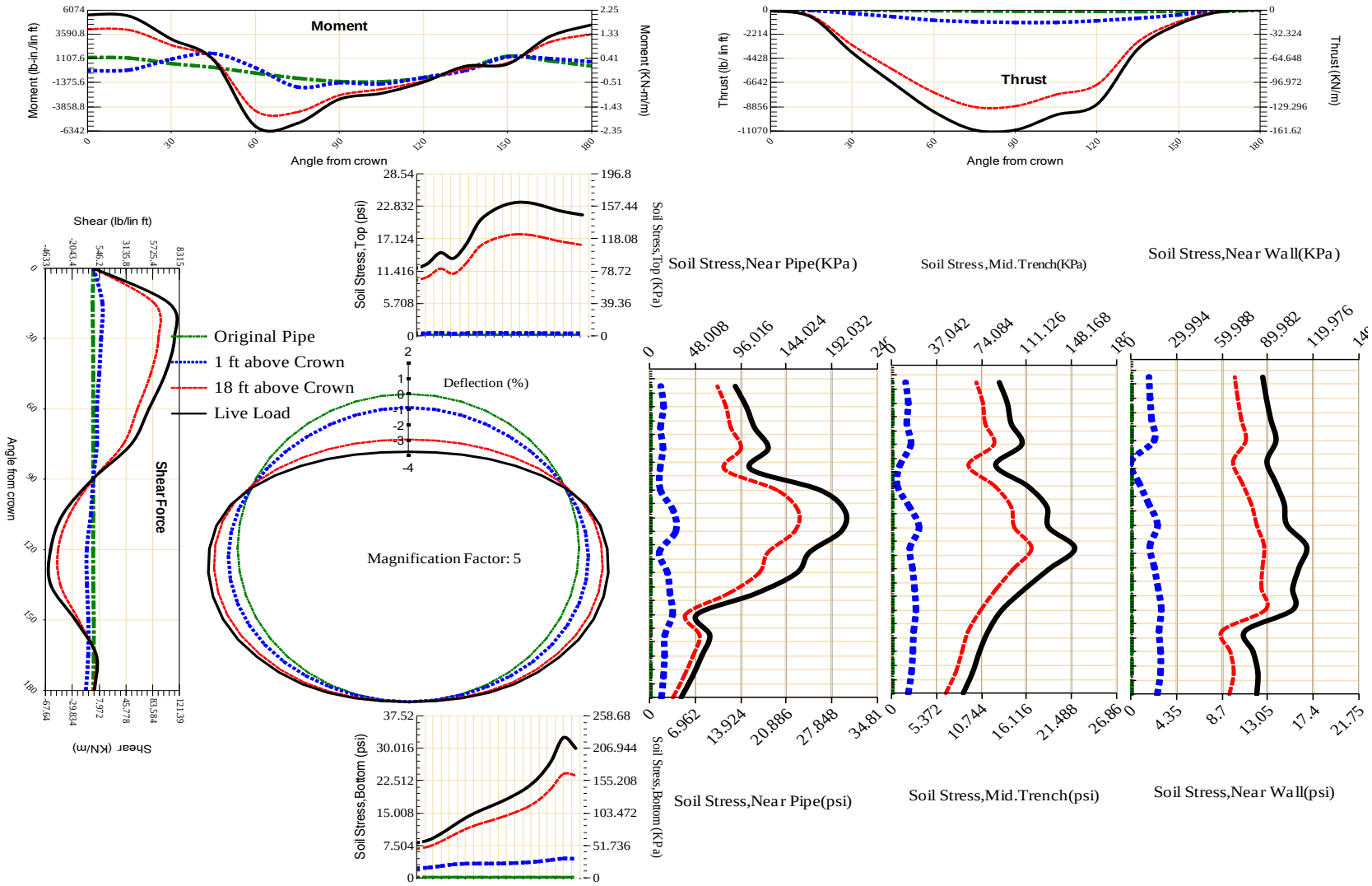

Figure A-653 Param-96-PW230-TR7OR-OD+72-EW5-H18-LiveLoad

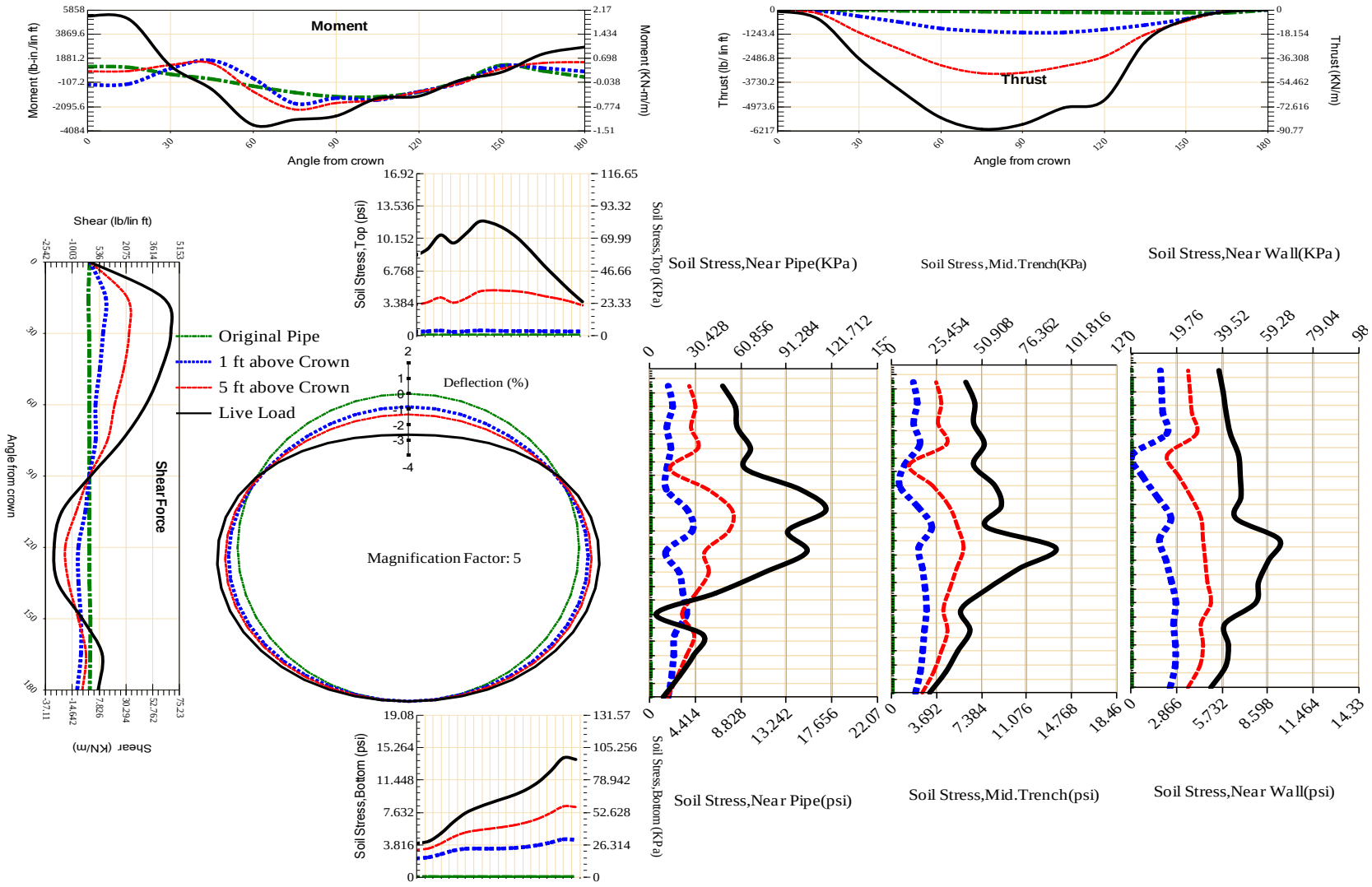

Figure A-654 Param-96-PW230-TR7OR-OD+72-EW5-H5-LiveLoad

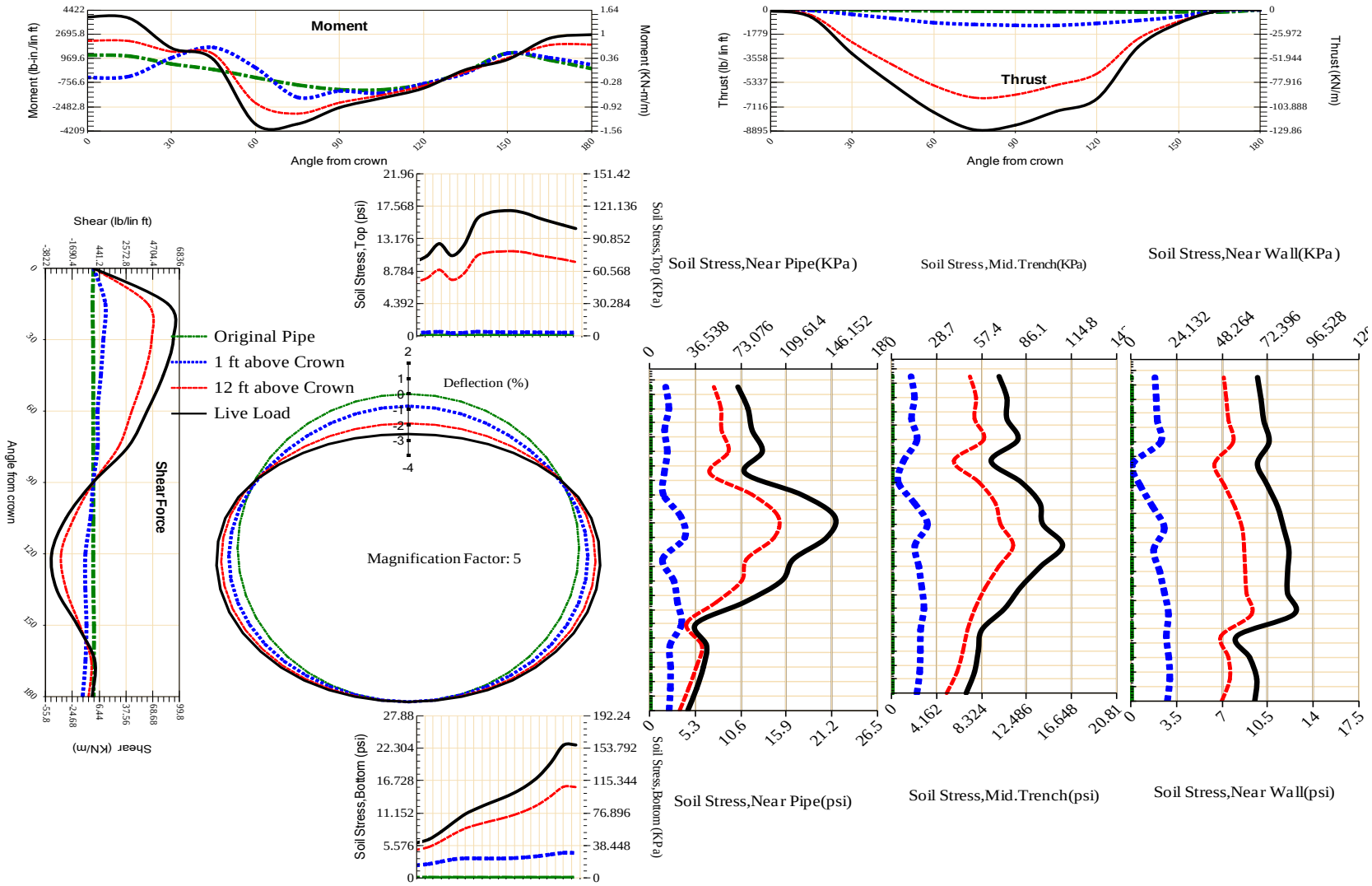

Figure A-655 Param-96-PW230-TR7OR-OD+72-EW7-H12-LiveLoad

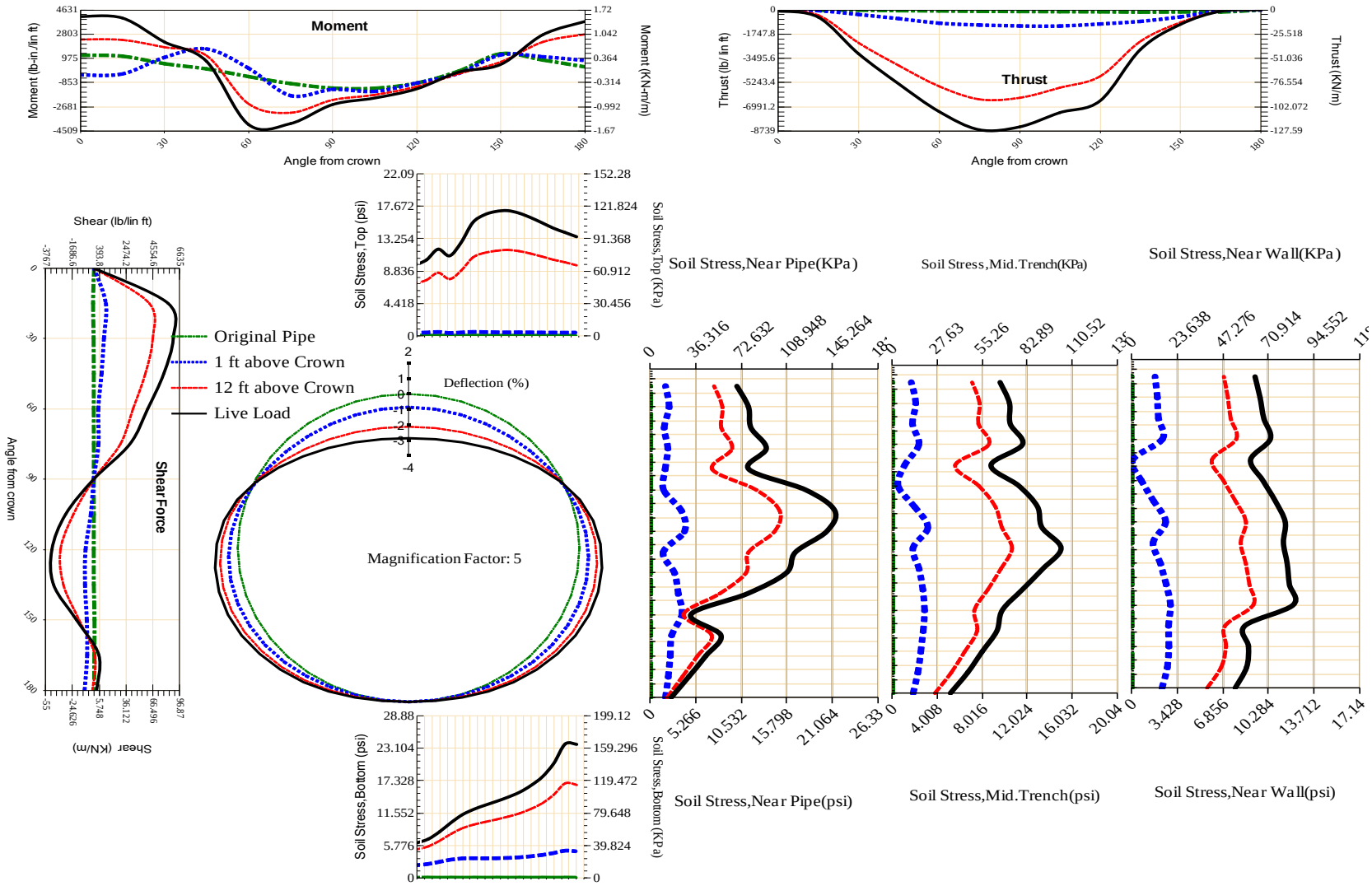

Figure A-656 Param-96-PW230-TR7OR-OD+84-EW5-H12-LiveLoad

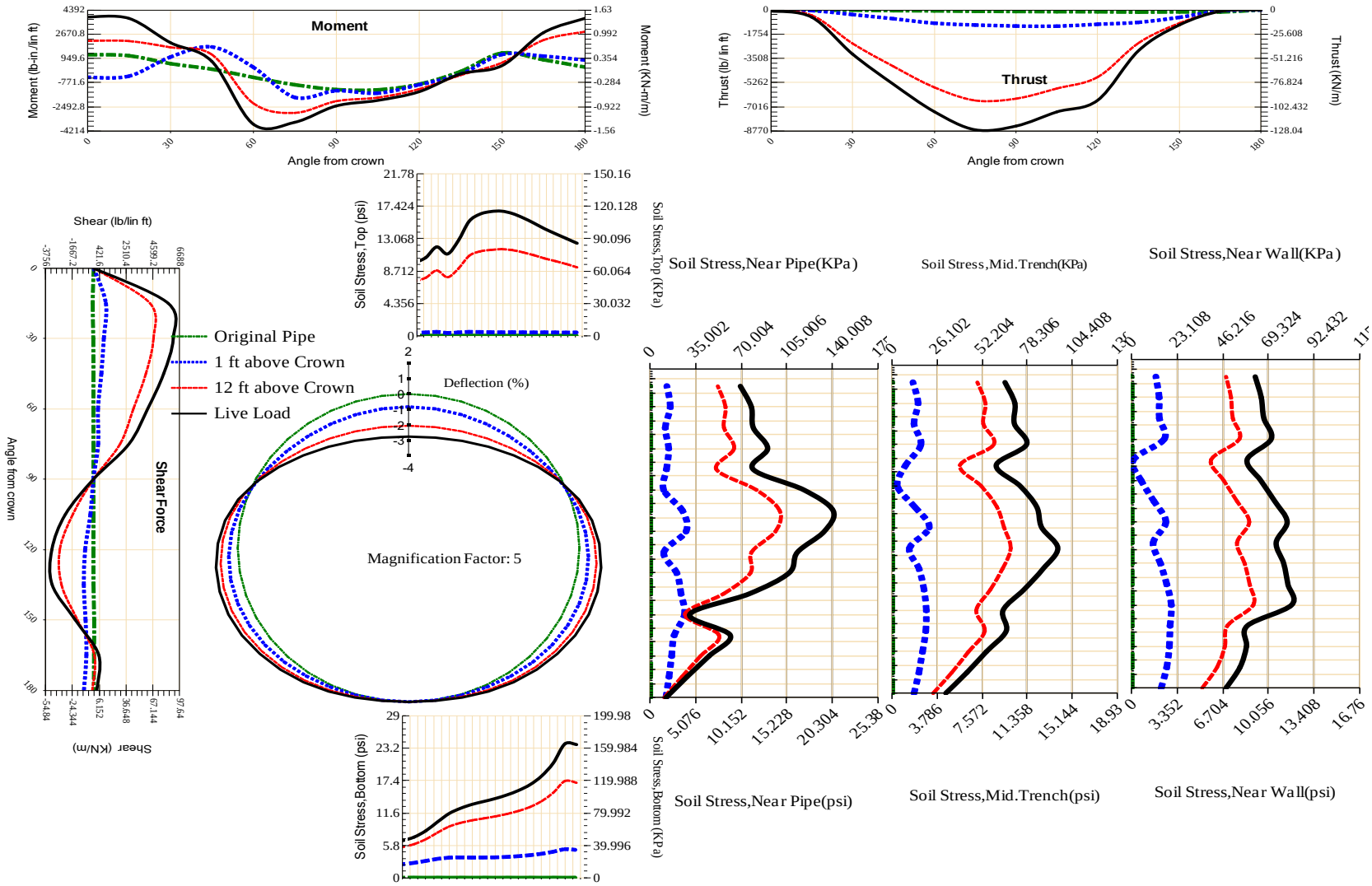

Figure A-657 Param-96-PW230-TR7OR-OD+96-EW5-H12-LiveLoad

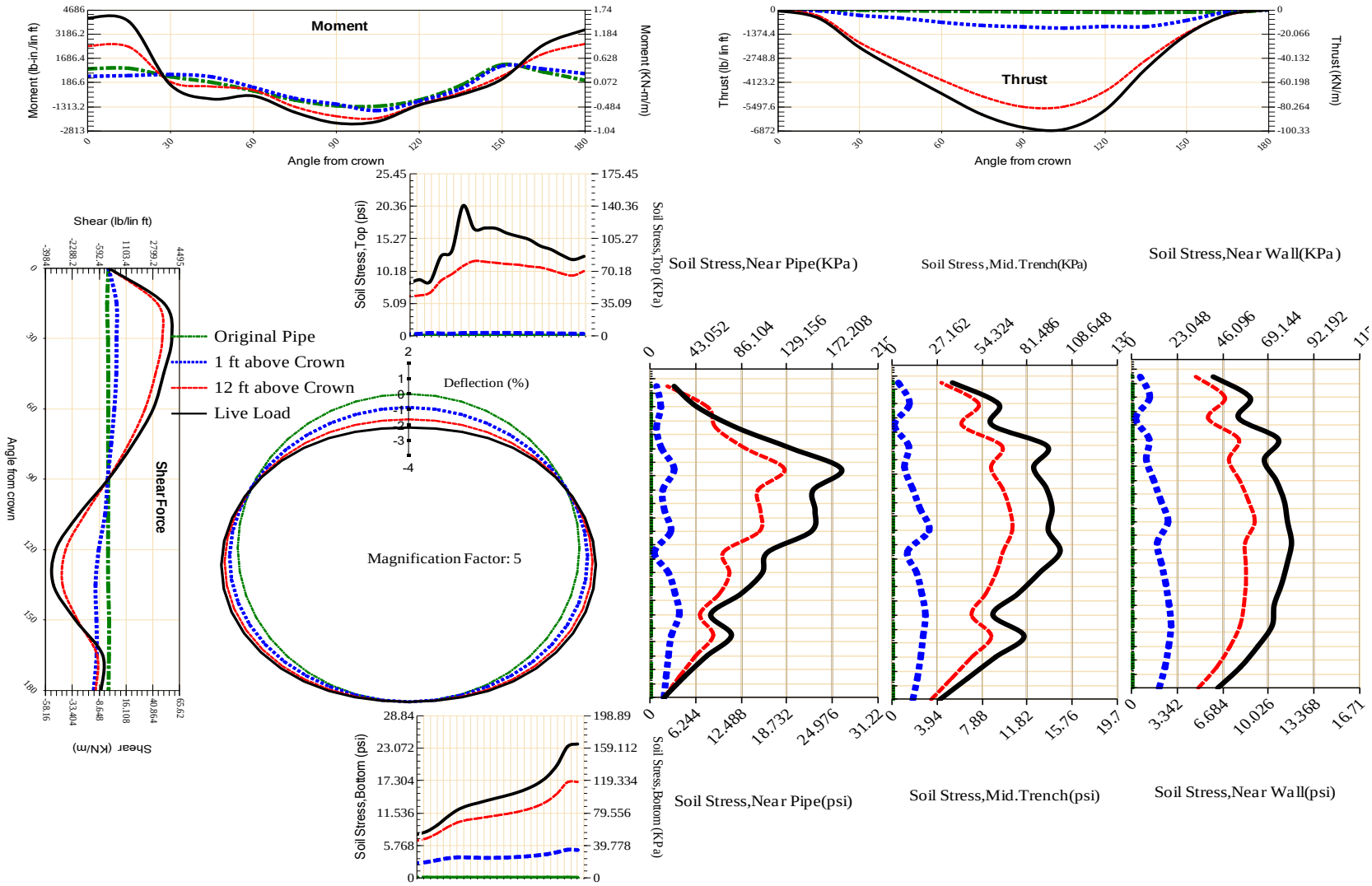

Figure A-658 Param-96-PW230-TR7SF-OD+108-EW5-H12-LiveLoad

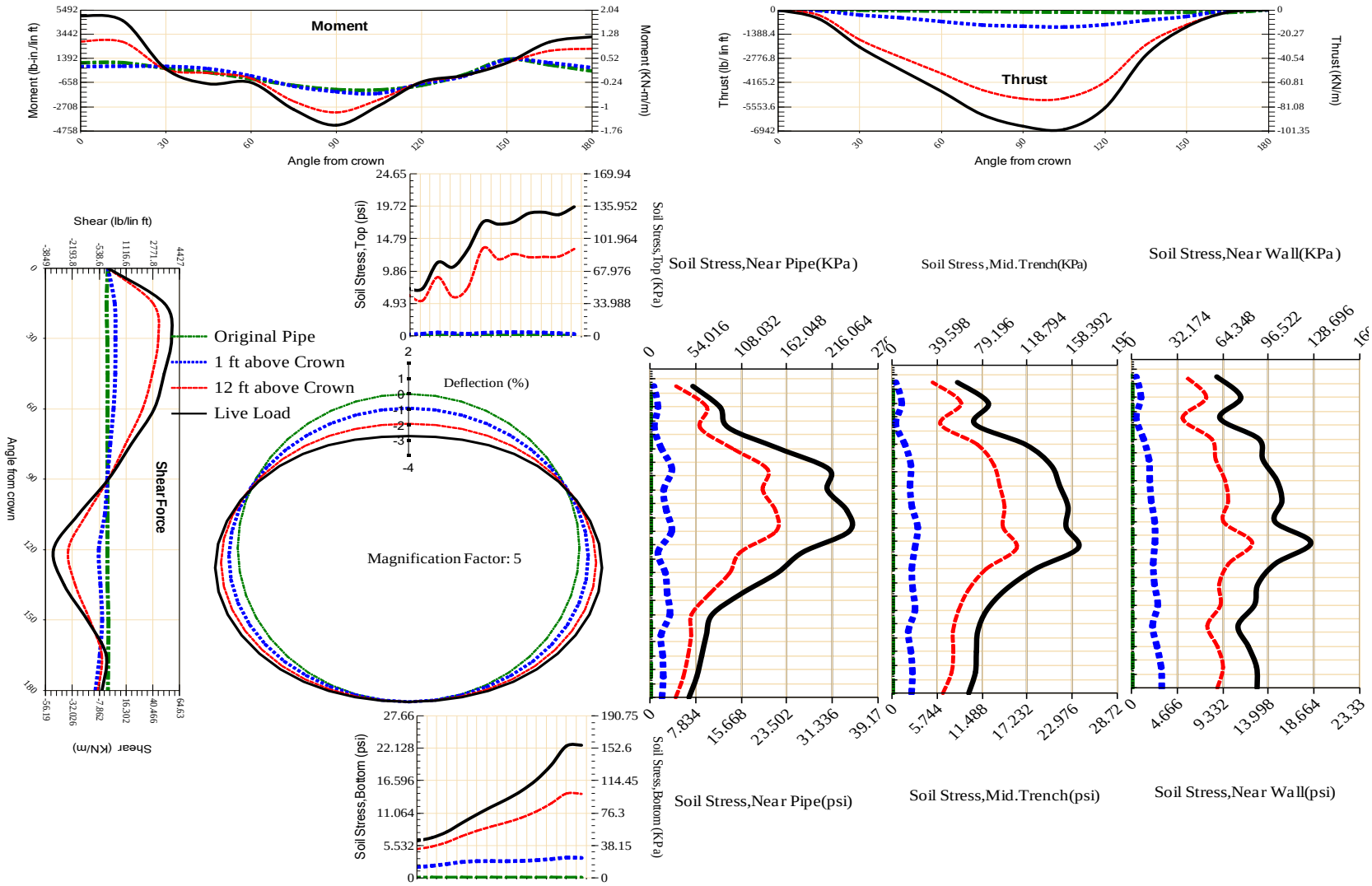

Figure A-659 Param-96-PW230-TR7SF-OD+48-EW5-H12-LiveLoad

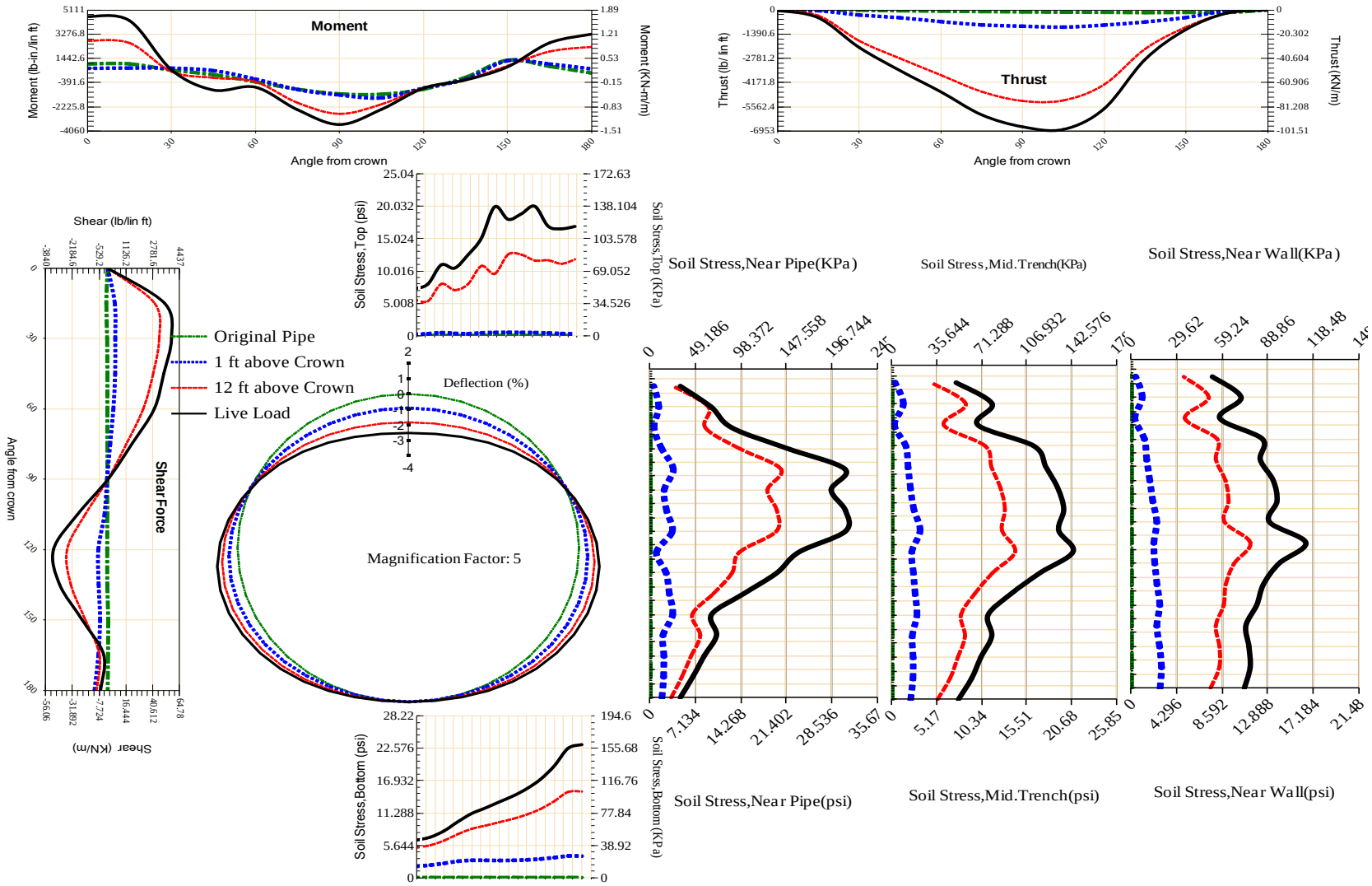

Figure A-660 Param-96-PW230-TR7SF-OD+60-EW5-H12-LiveLoad

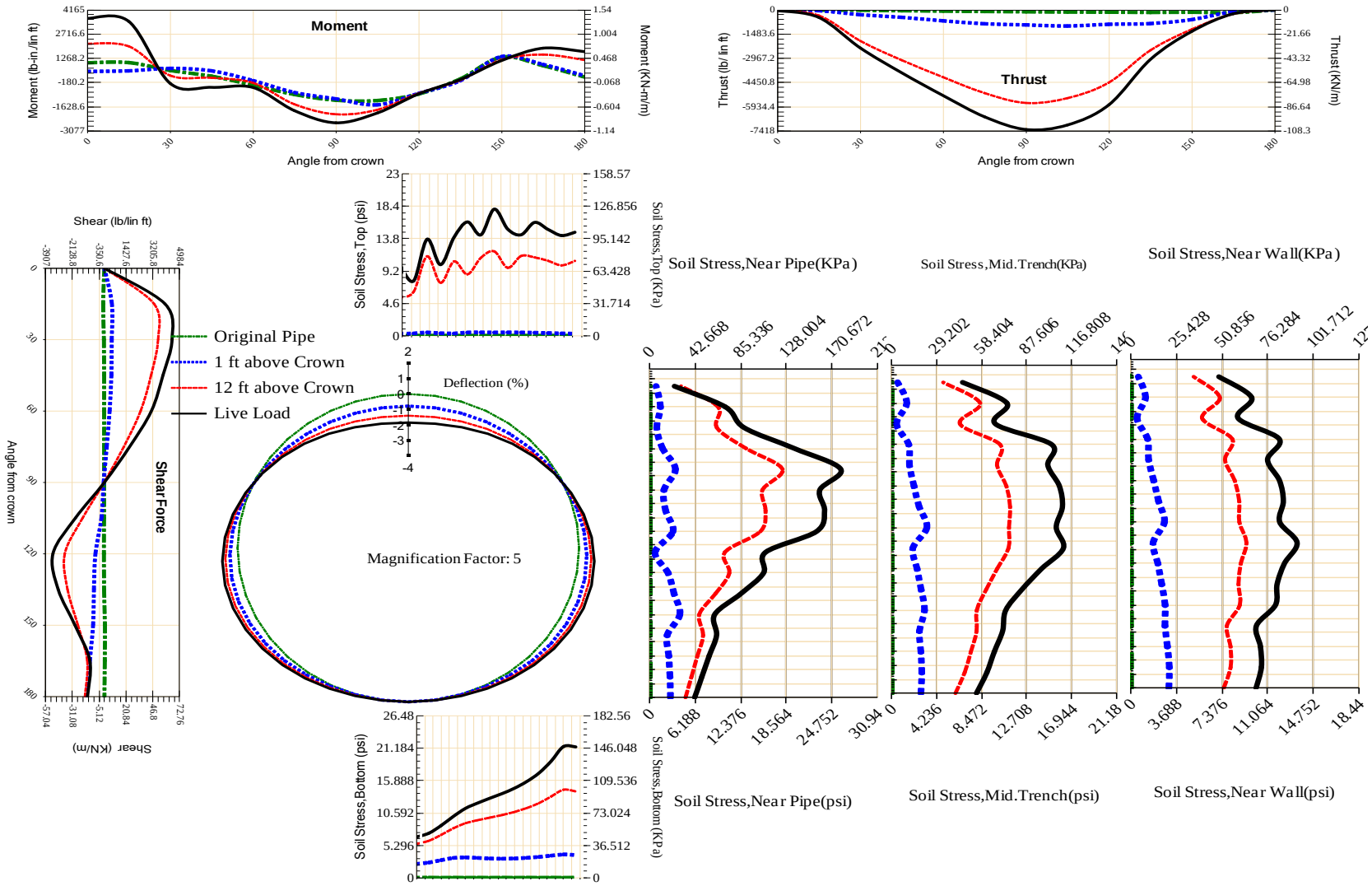

Figure A-661 Param-96-PW230-TR7SF-OD+72-EW10-H12-LiveLoad

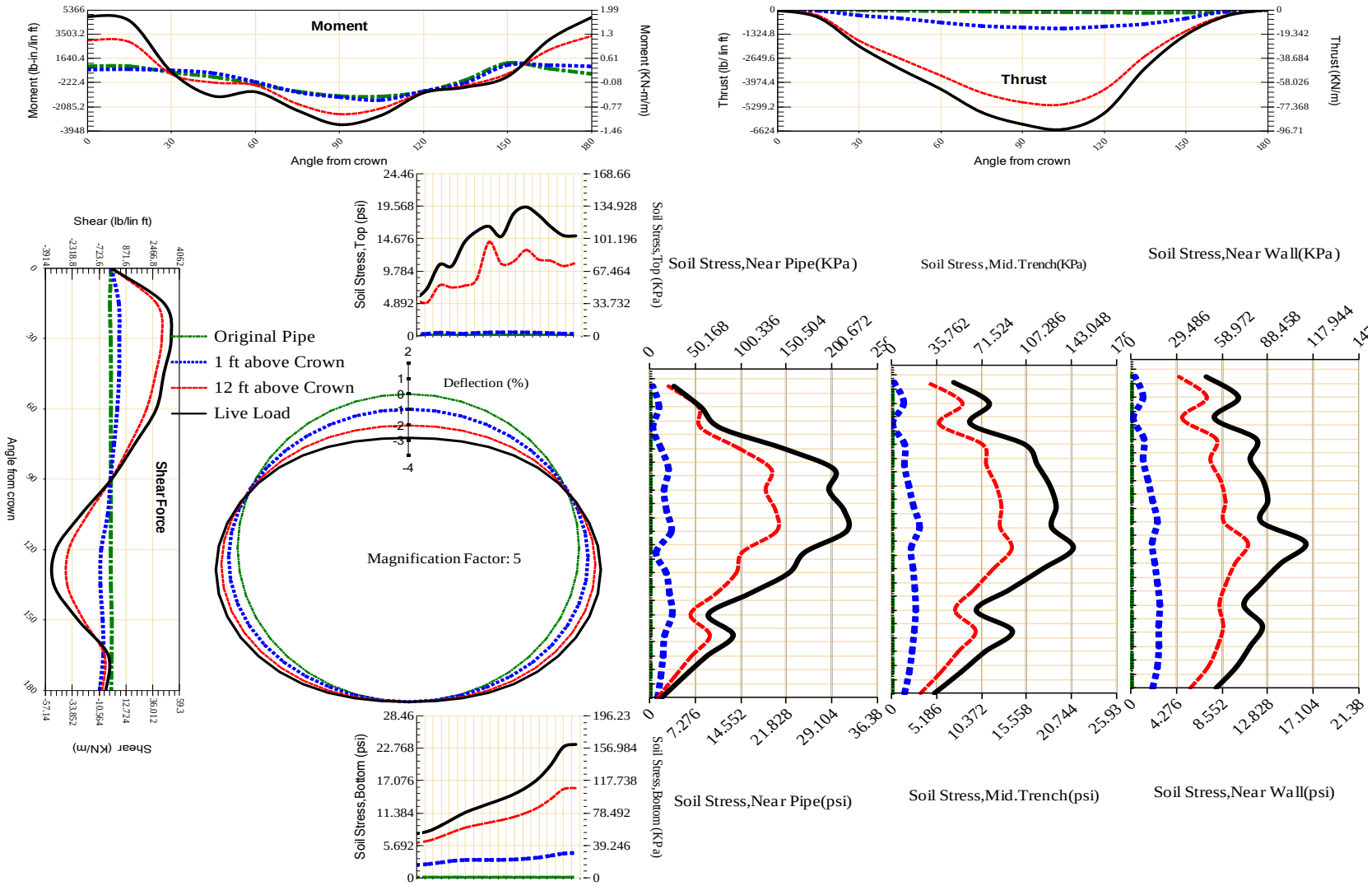

Figure A-662 Param-96-PW230-TR7SF-OD+72-EW3-H12-LiveLoad

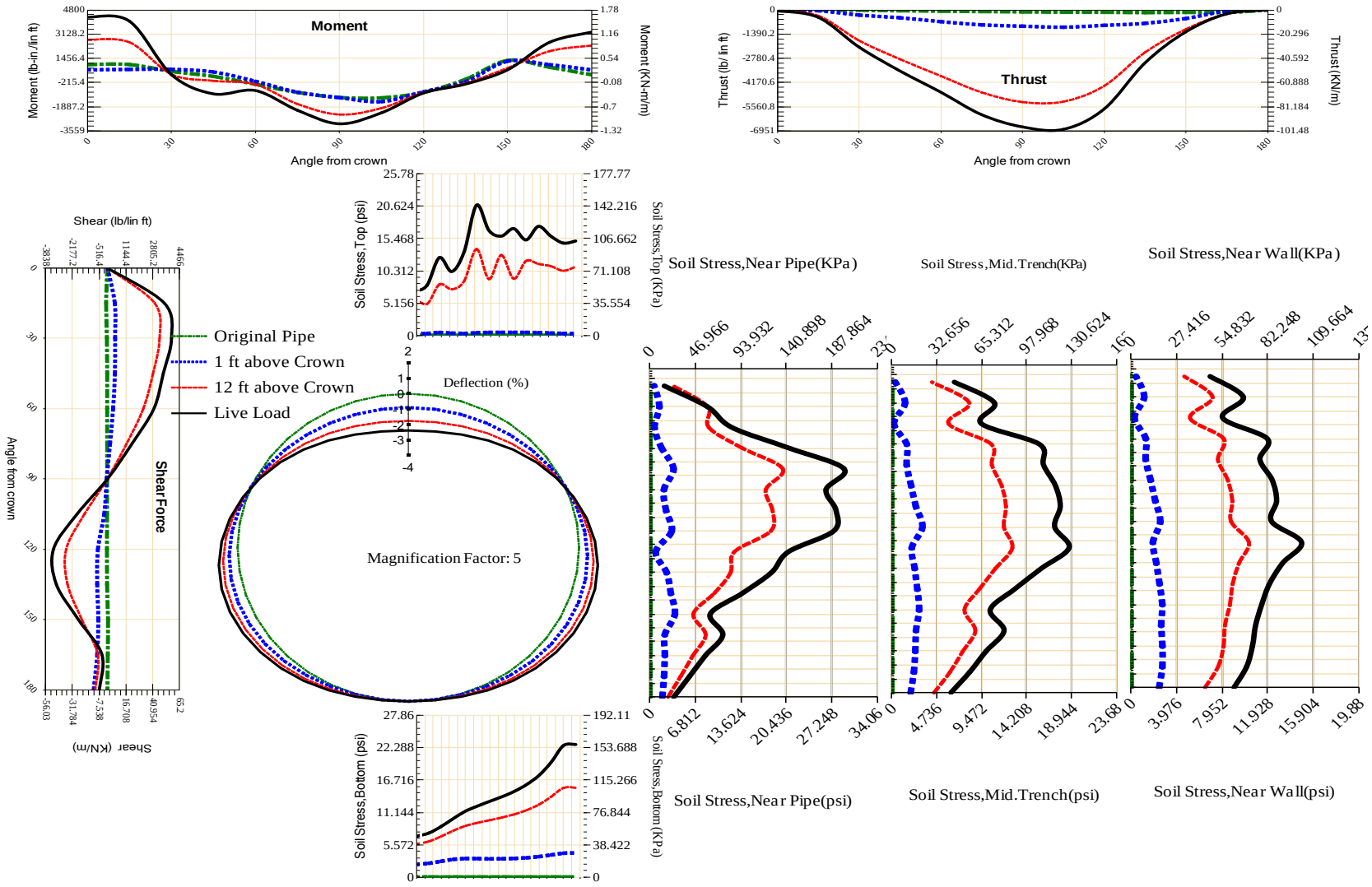

Figure A-663 Param-96-PW230-TR7SF-OD+72-EW5-H12-LiveLoad

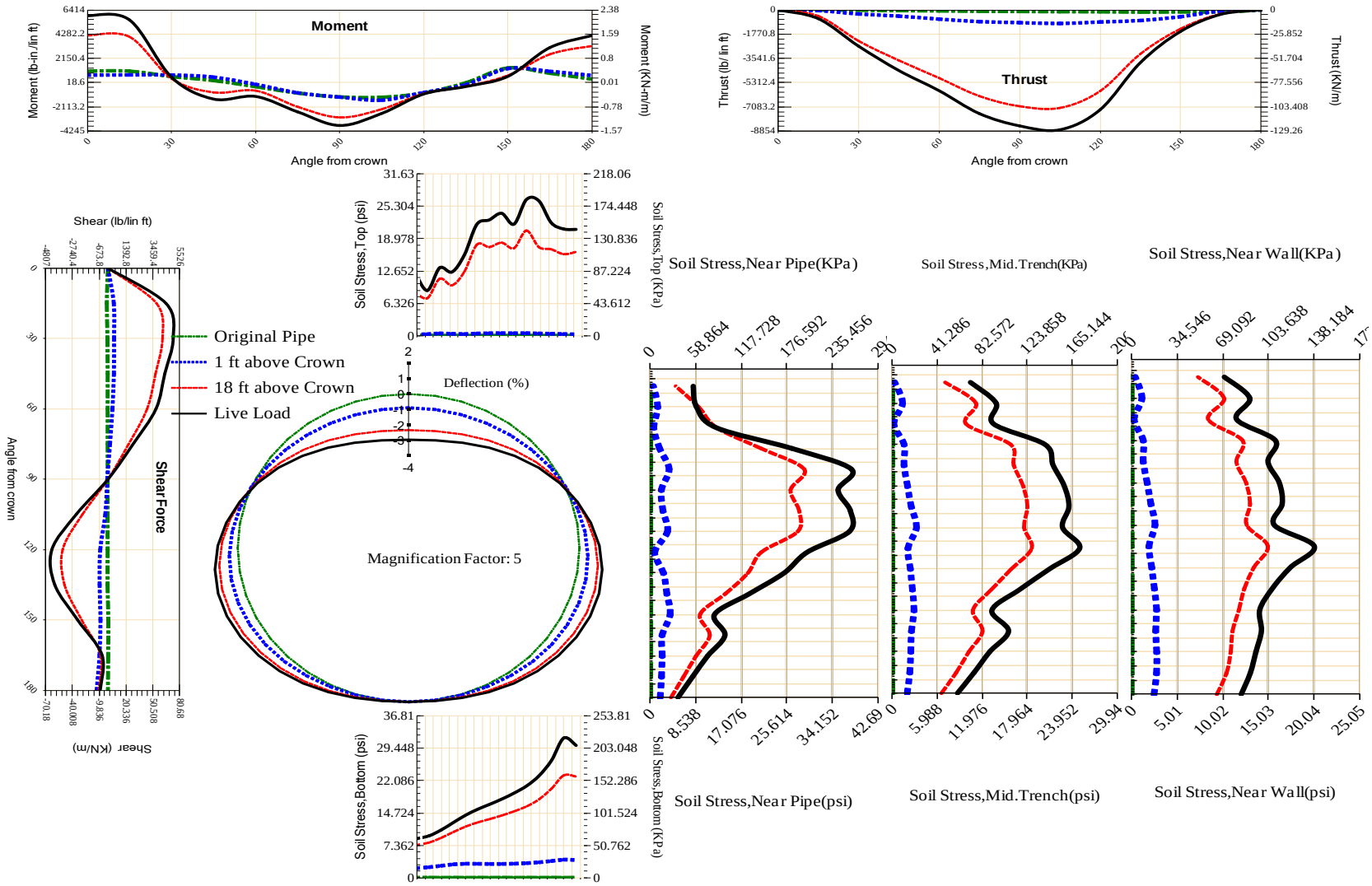

Figure A-664 Param-96-PW230-TR7SF-OD+72-EW5-H18-LiveLoad

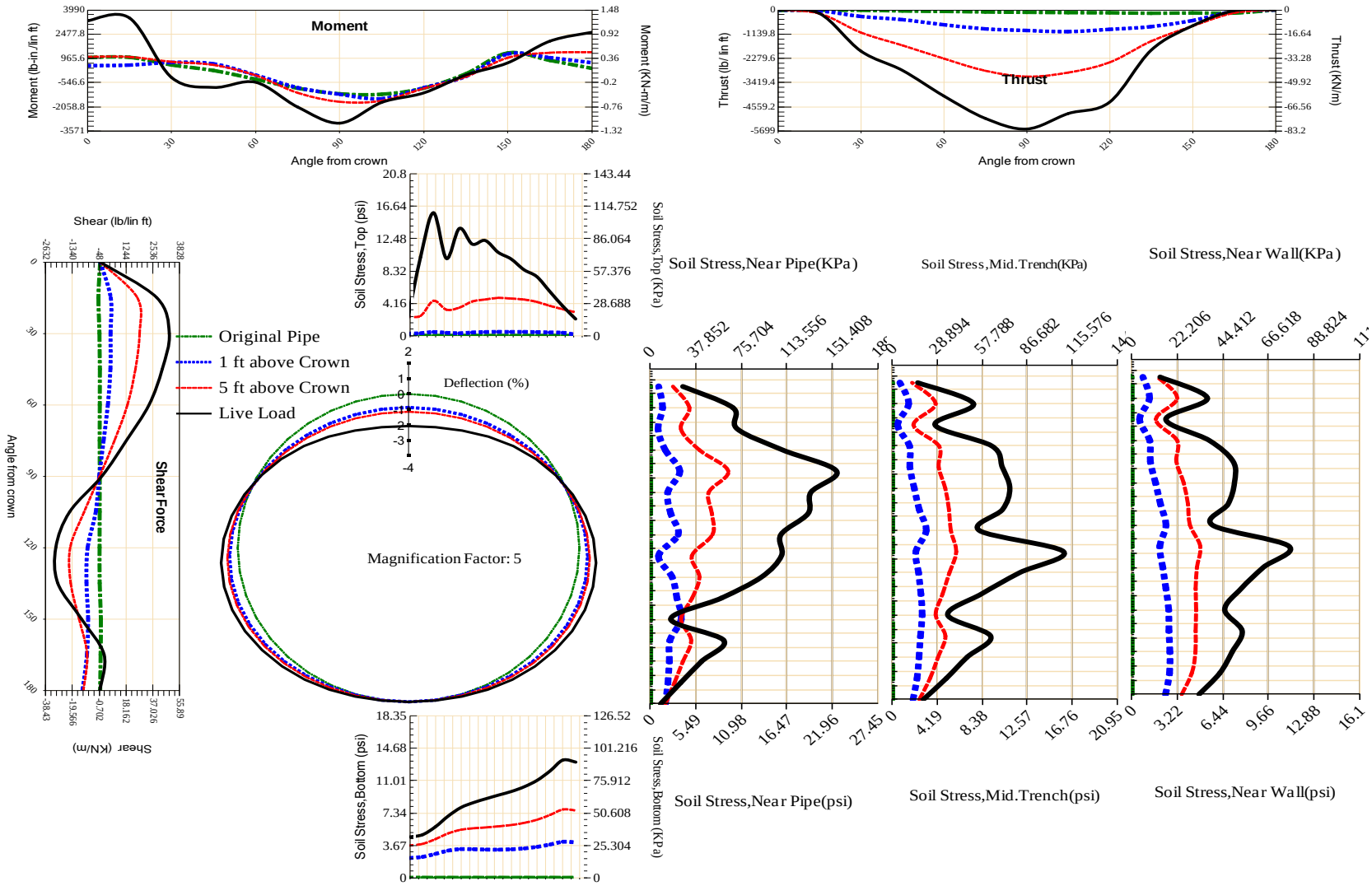

Figure A-665 Param-96-PW230-TR7SF-OD+72-EW5-H5-LiveLoad

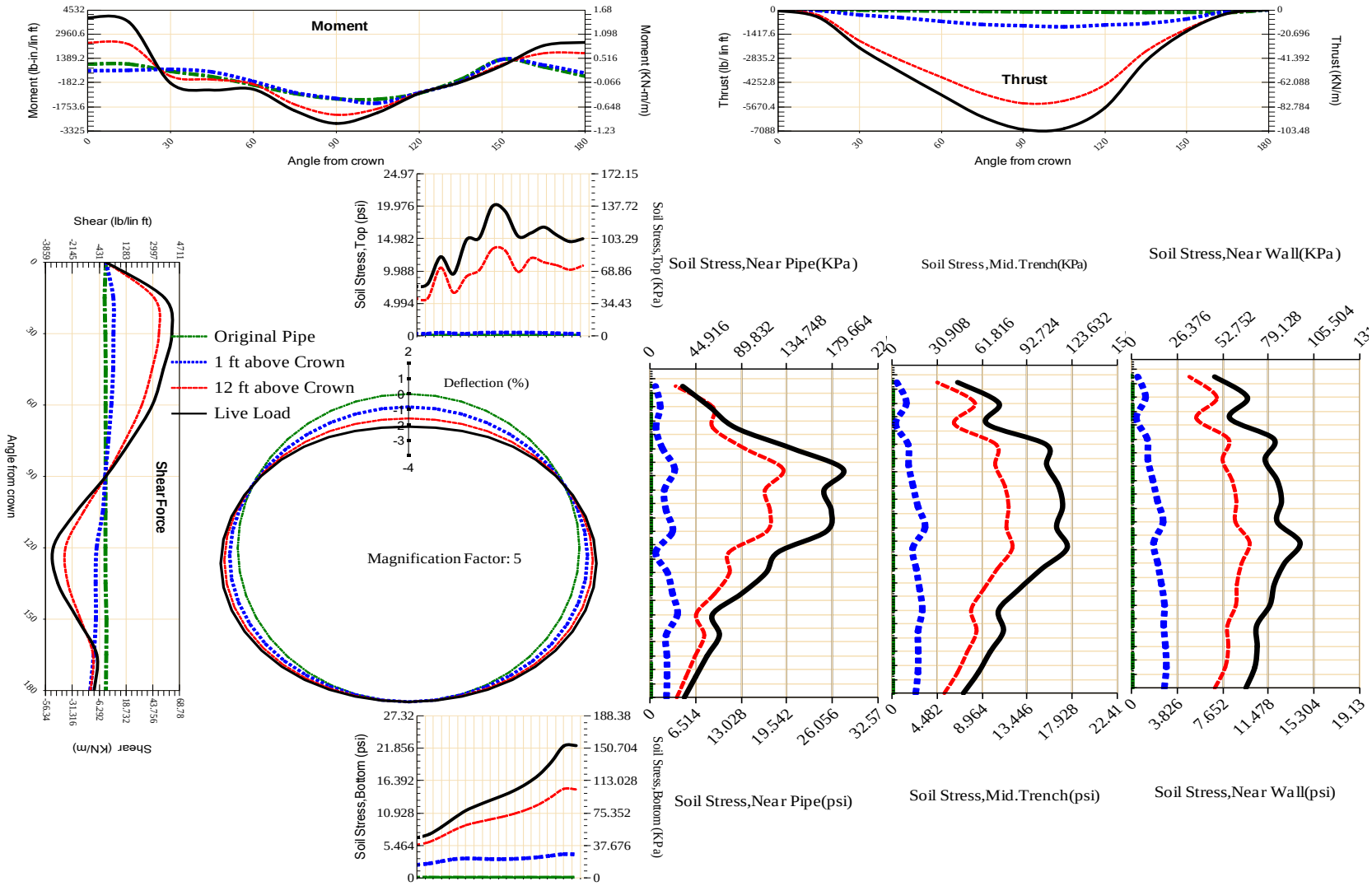

Figure A-666 Param-96-PW230-TR7SF-OD+72-EW7-H12-LiveLoad

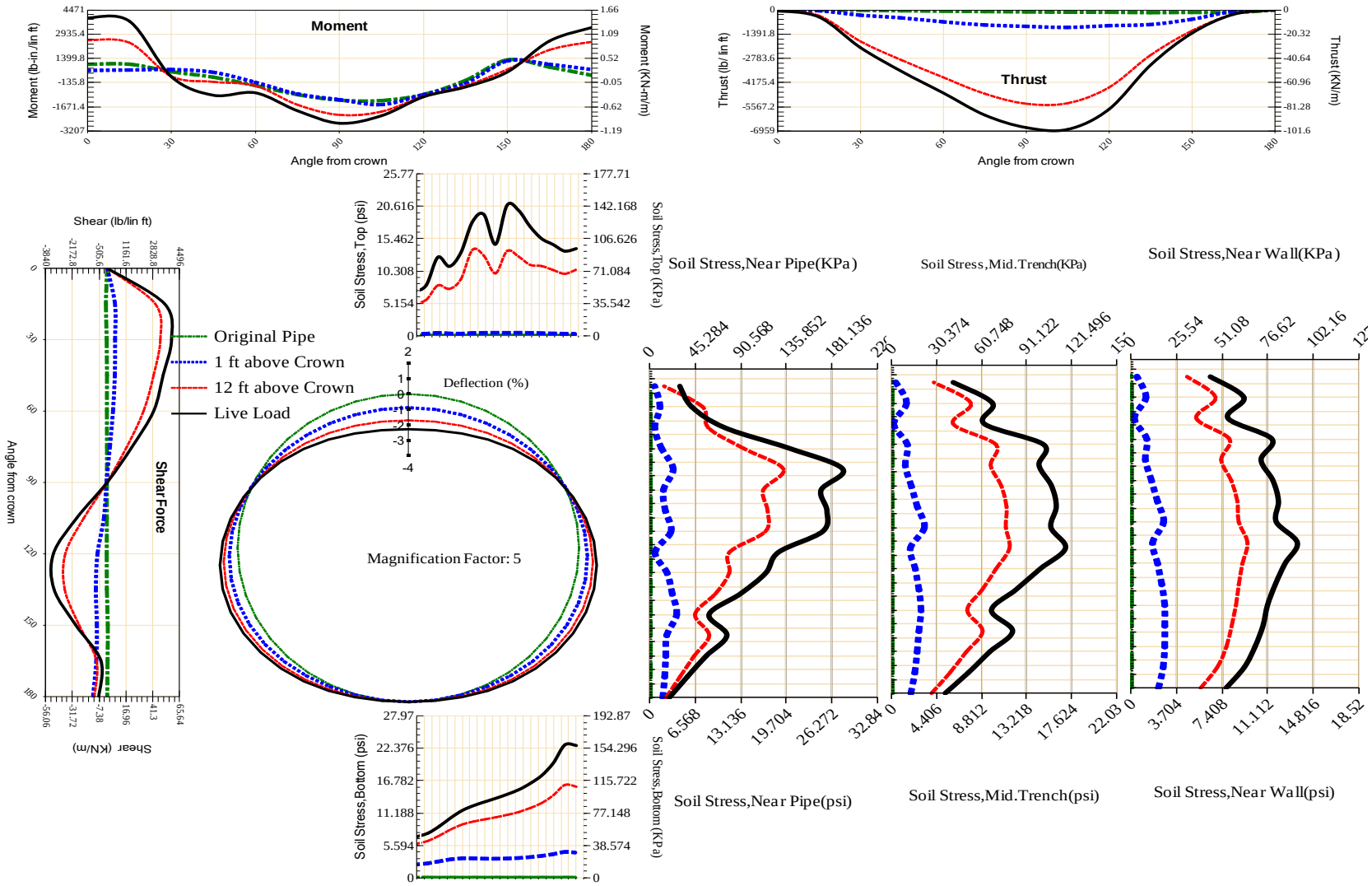

Figure A-667 Param-96-PW230-TR7SF-OD+84-EW5-H12-LiveLoad

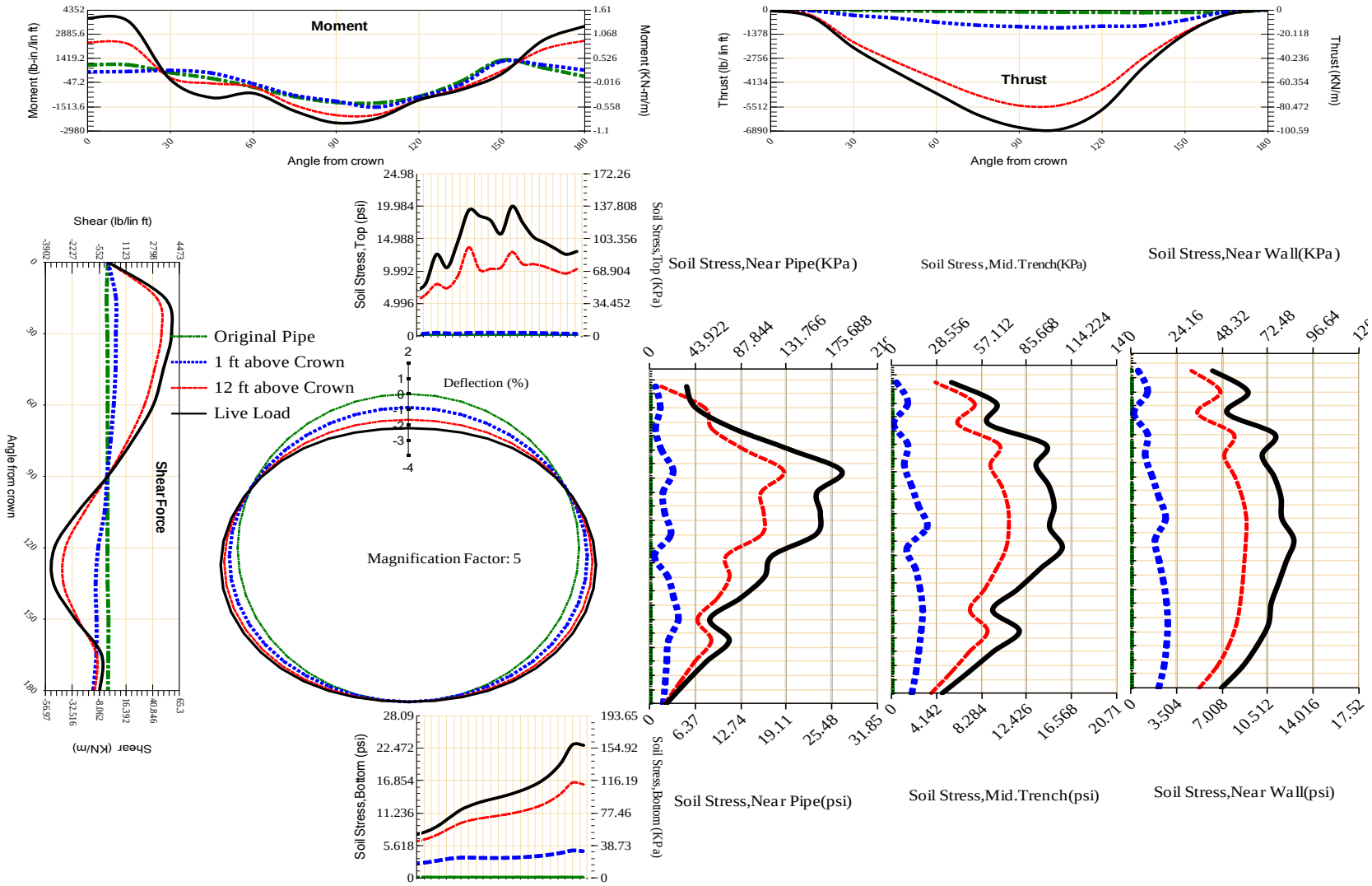

Figure A-668 Param-96-PW230-TR7SF-OD+96-EW5-H12-LiveLoad

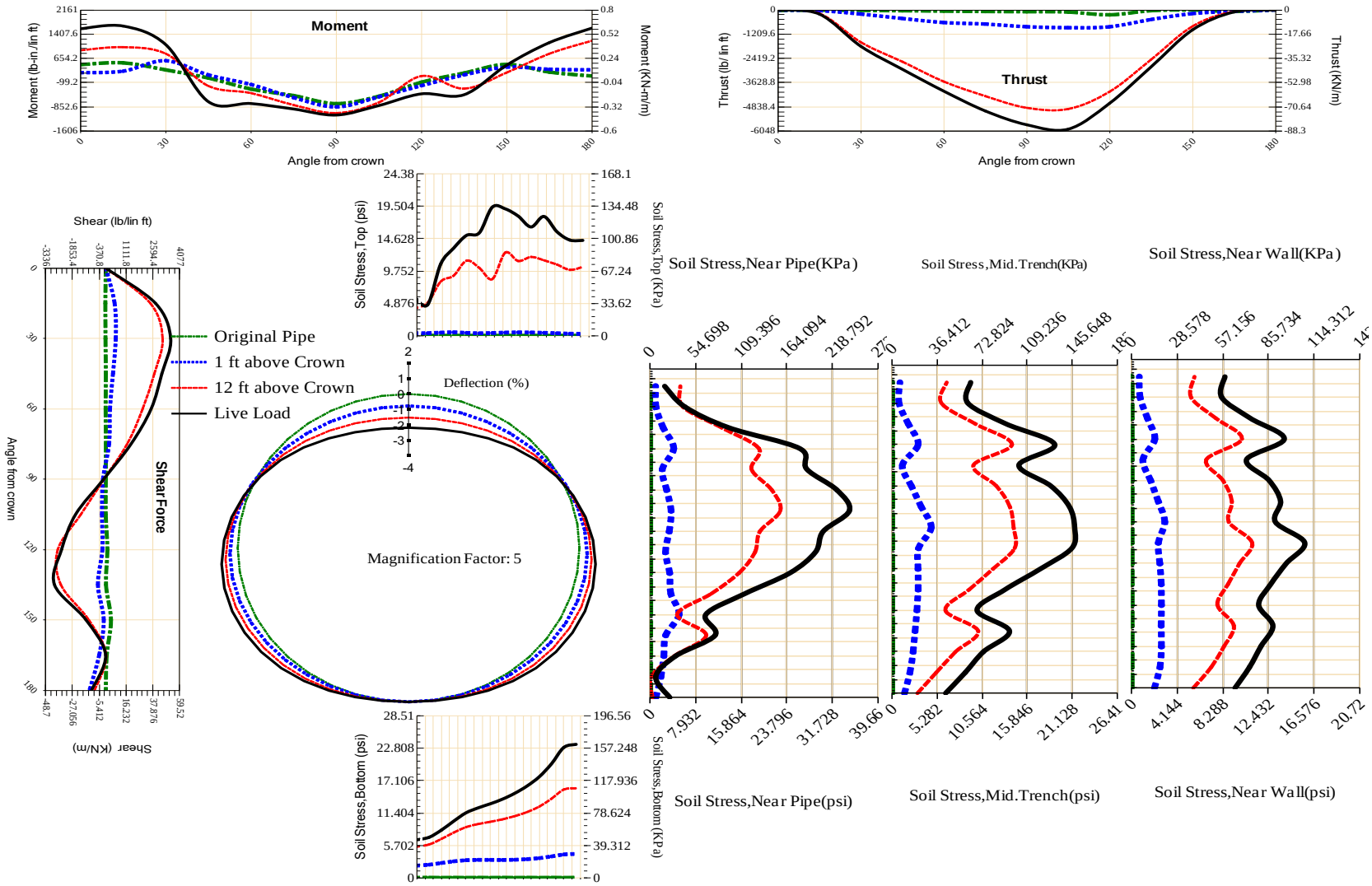

Figure A-669 Param-96-PW288-SF10SF-OD+72-EW5-H12-LiveLoad

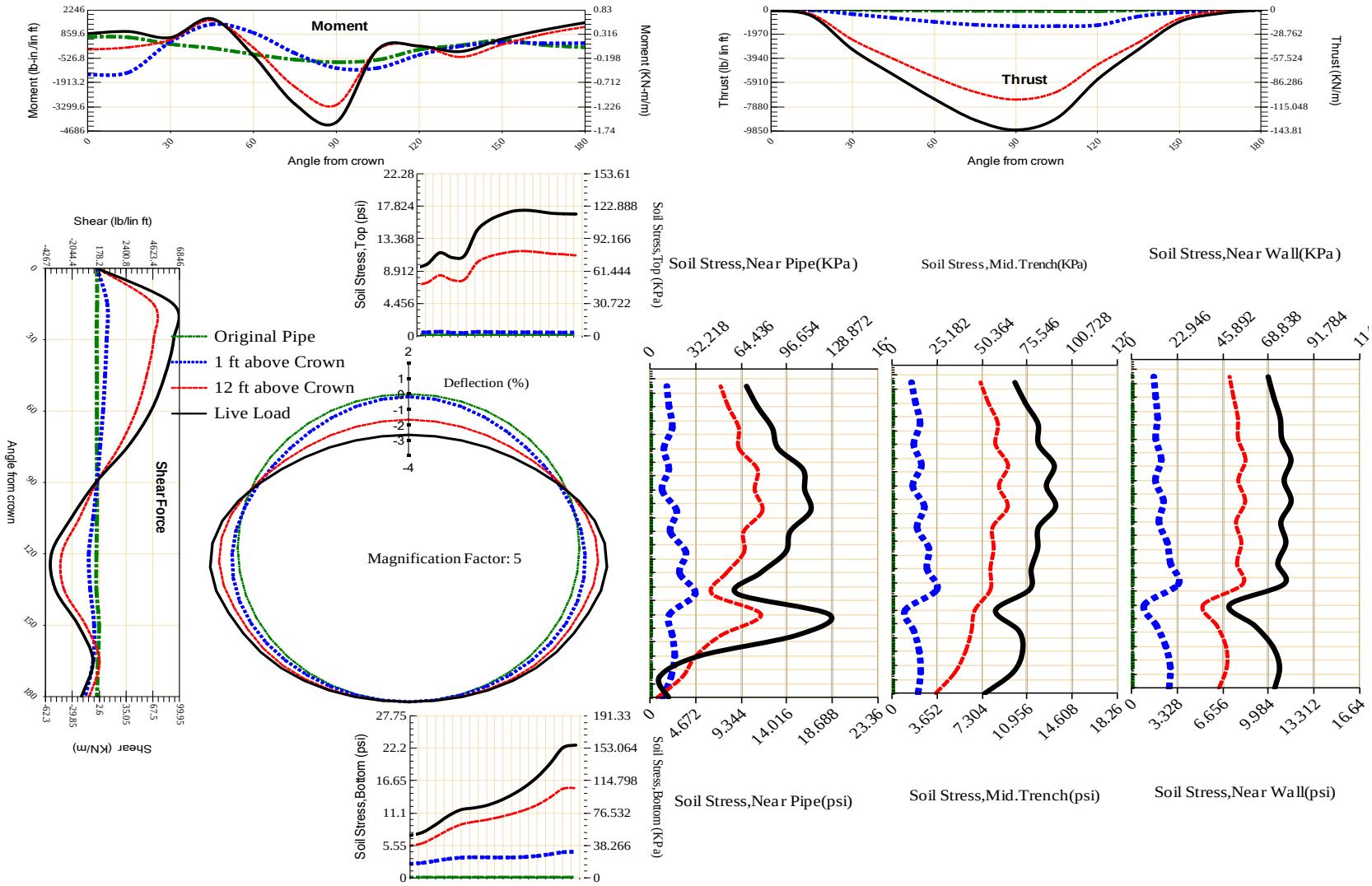

Figure A-670 Param-96-PW288-SF3OR-OD+72-EW5-H12-LiveLoad

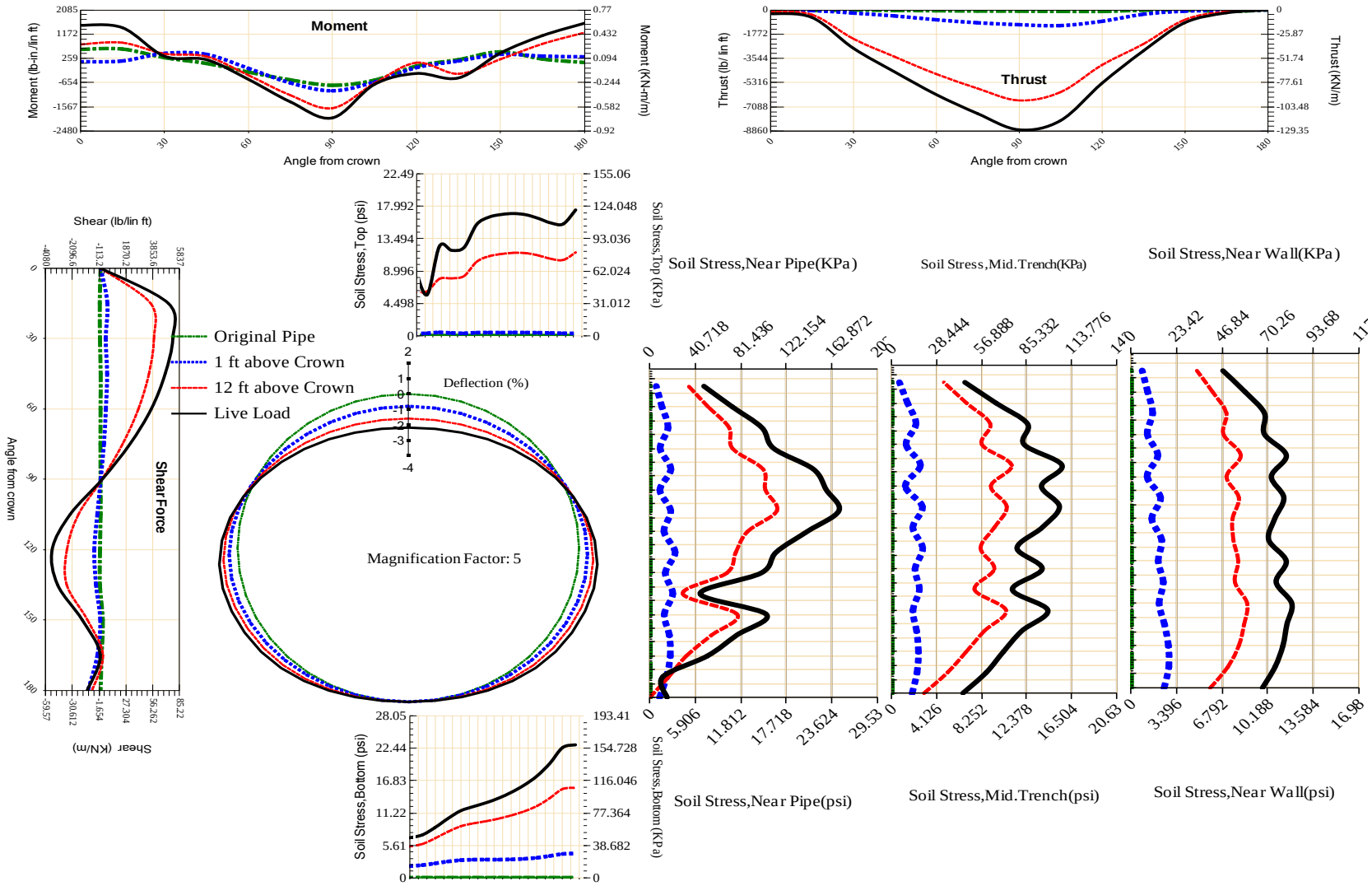

Figure A-671 Param-96-PW288-SF3TR-OD+72-EW5-H12-LiveLoad

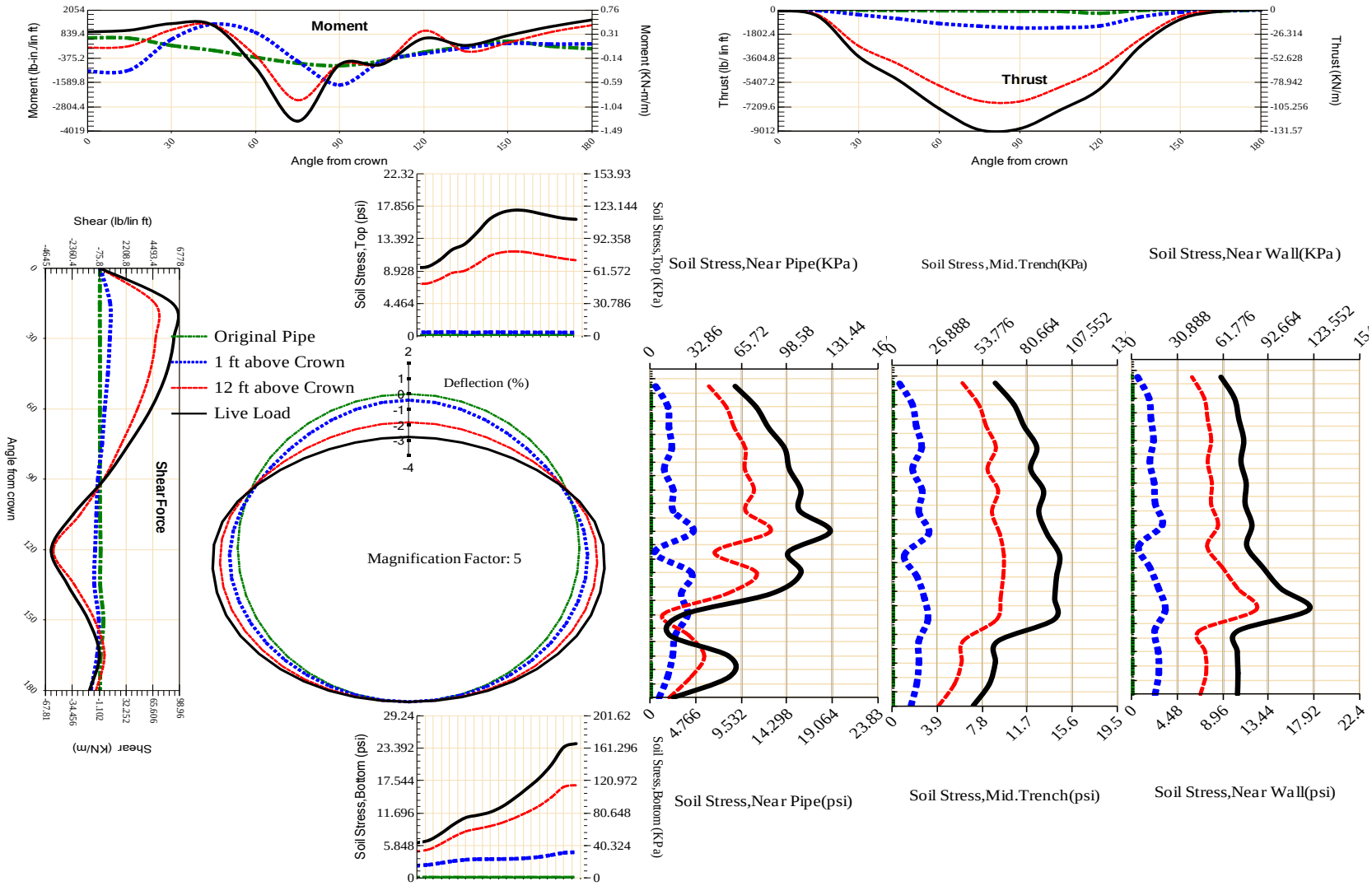

Figure A-672 Param-96-PW288-SF5OR-OD+72-EW5-H12-LiveLoad

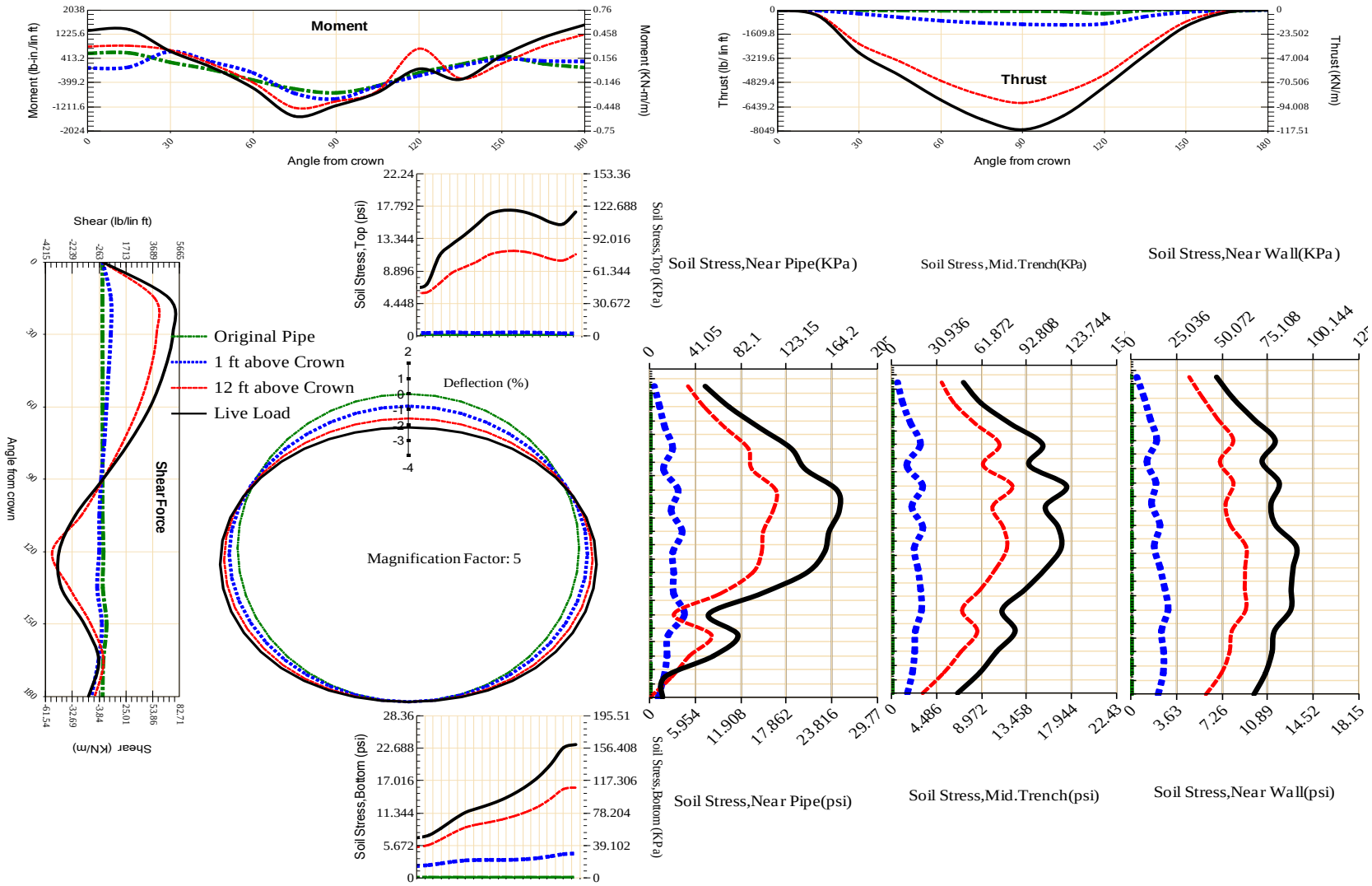

Figure A-673 Param-96-PW288-SF5TR-OD+72-EW5-H12-LiveLoad

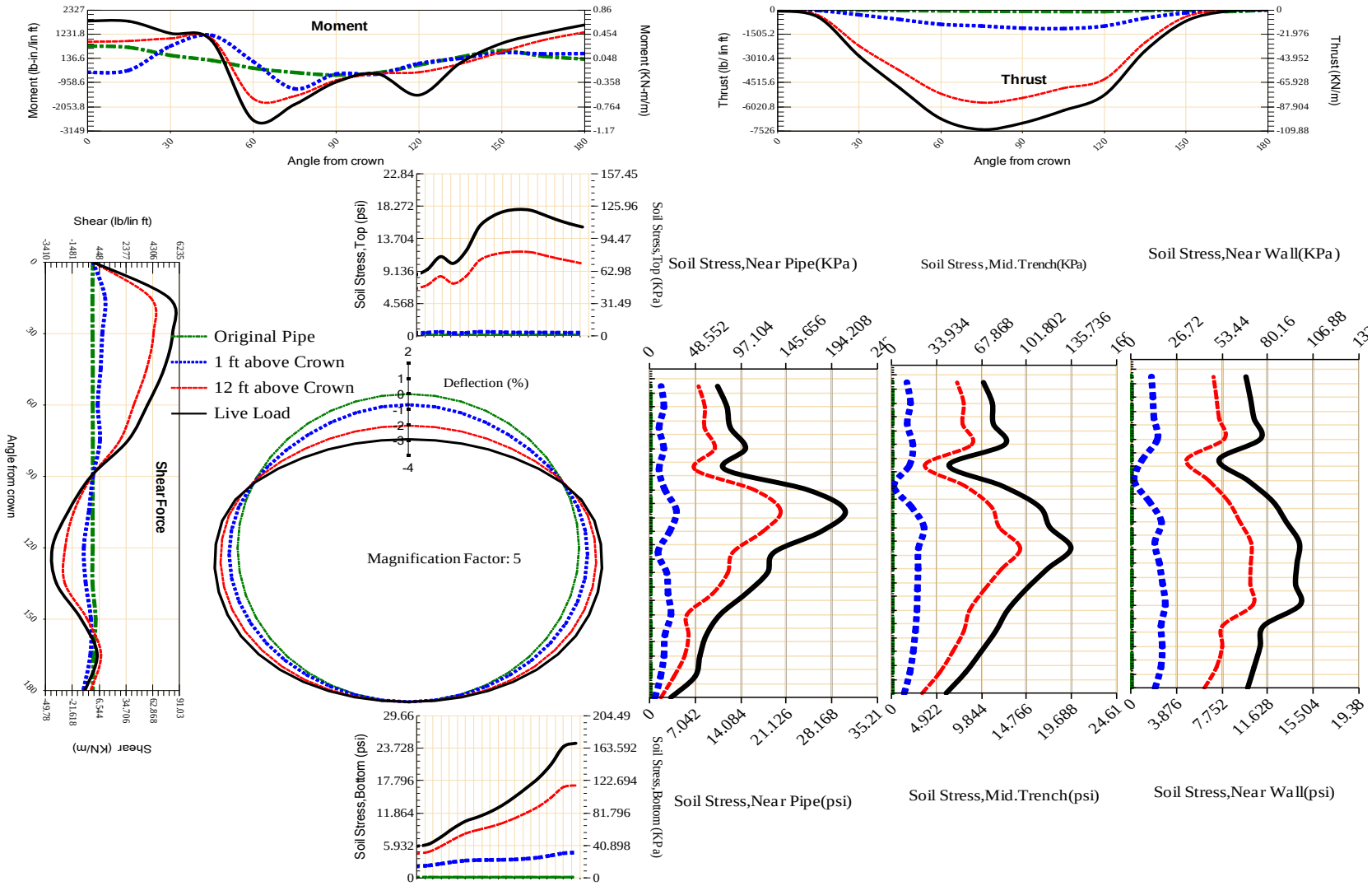

Figure A-674 Param-96-PW288-SF7OR-OD+72-EW5-H12-LiveLoad

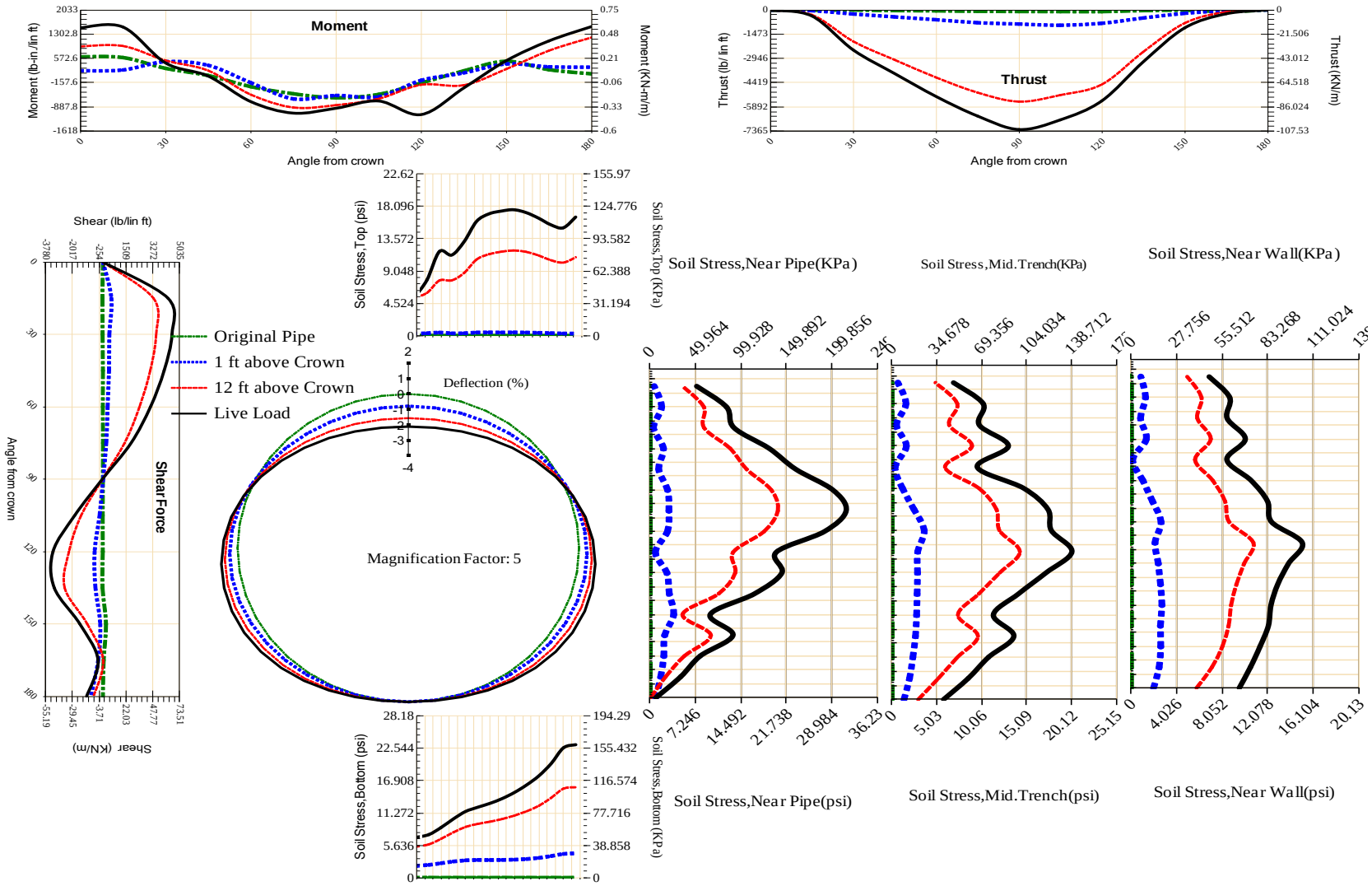

Figure A-675 Param-96-PW288-SF7TR-OD+72-EW5-H12-LiveLoad

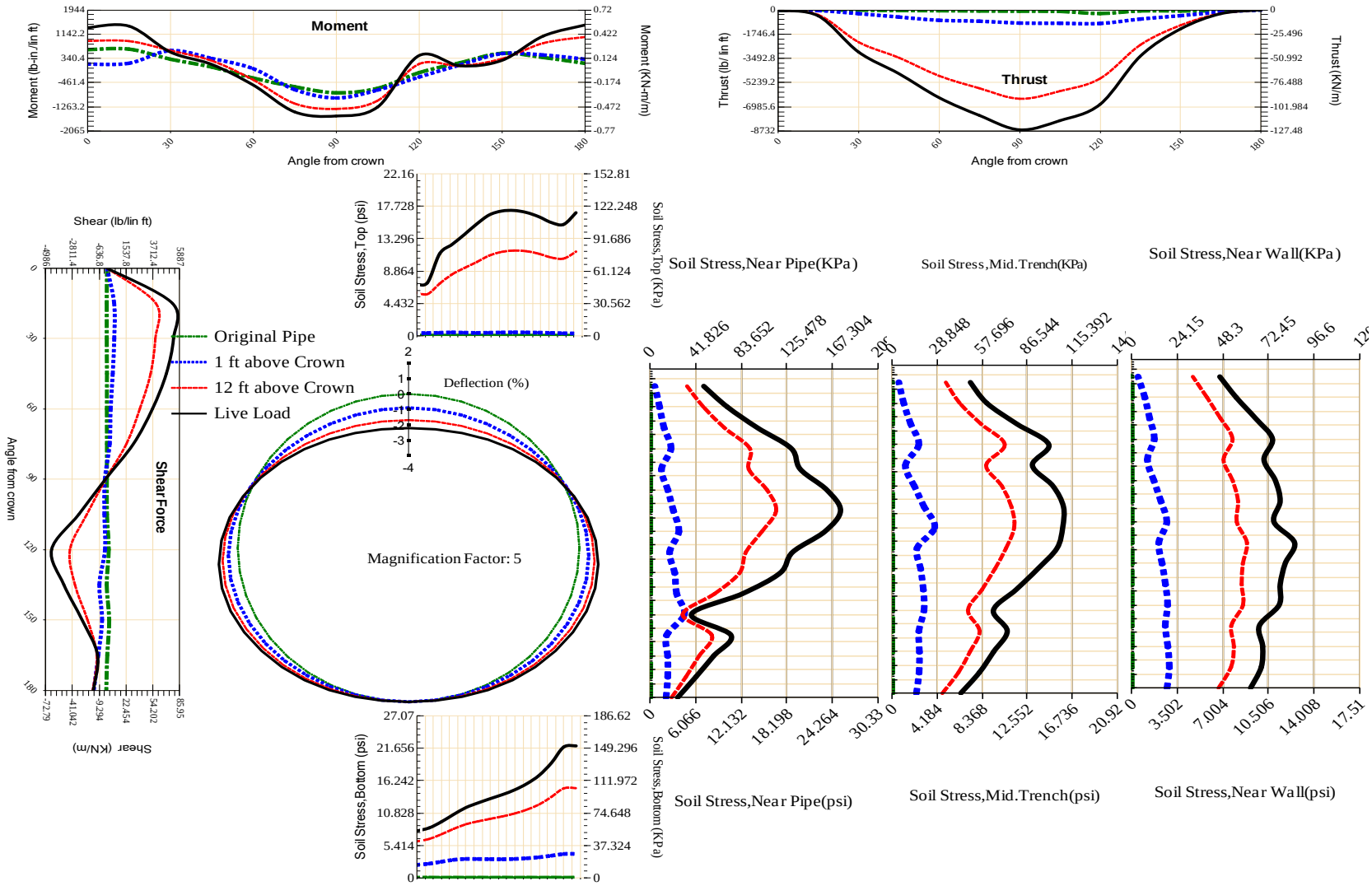

Figure A-676 Param-96-PW288-TR10TR-OD+72-EW5-H12-LiveLoad

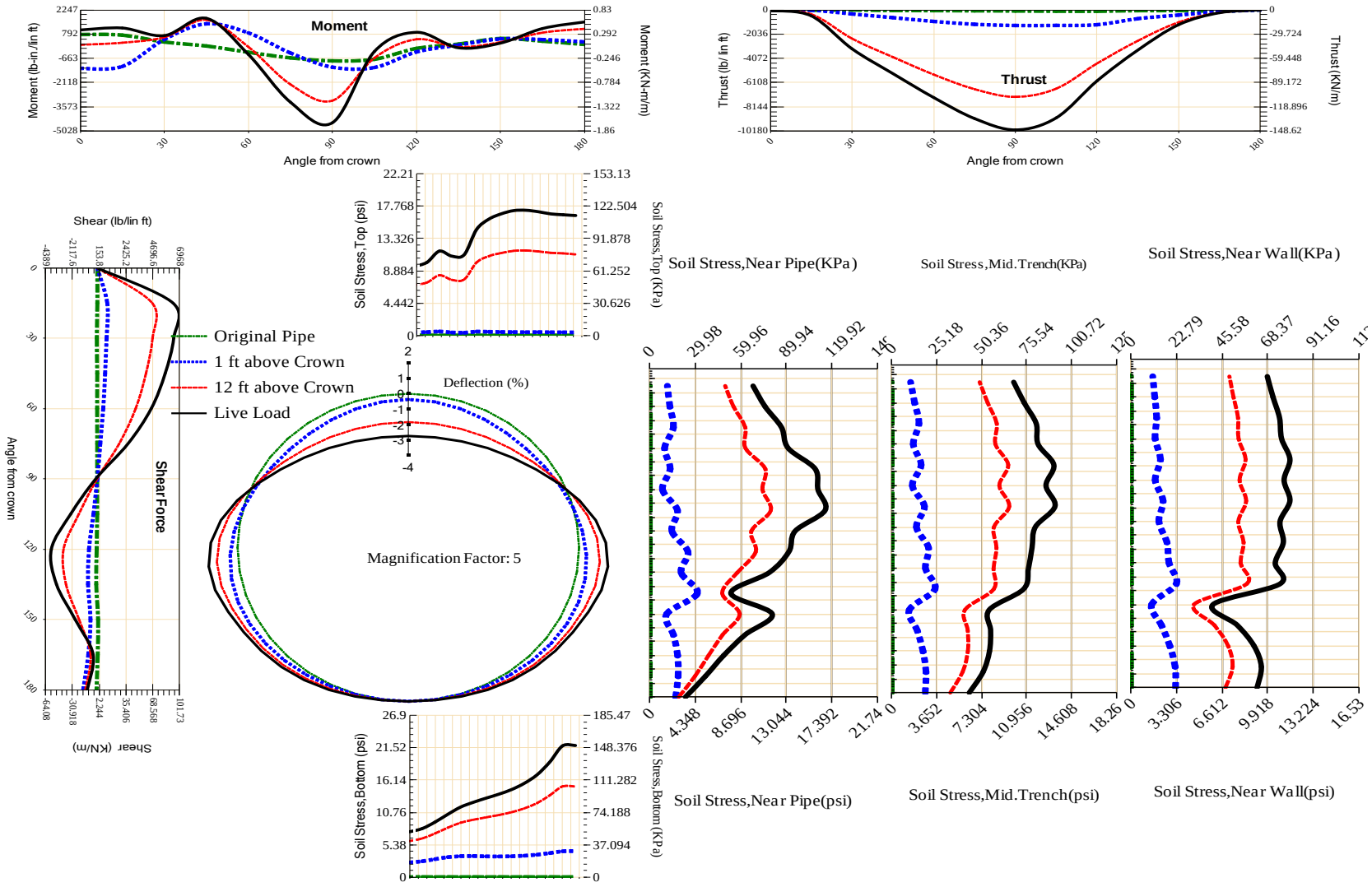

Figure A-677 Param-96-PW288-TR3OR-OD+72-EW5-H12-LiveLoad

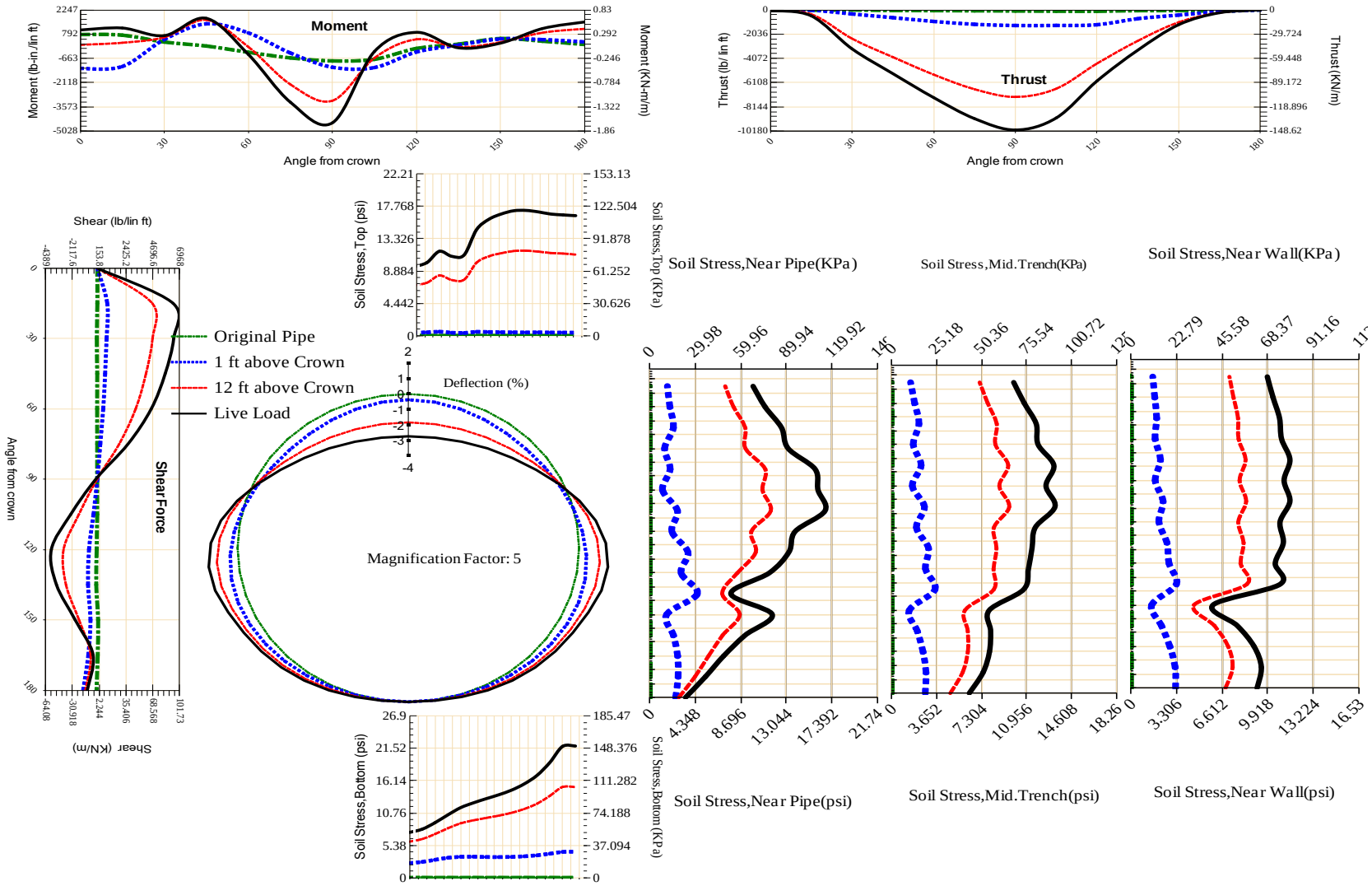

Figure A-677 Param-96-PW288-TR3OR-OD+72-EW5-H12-LiveLoad

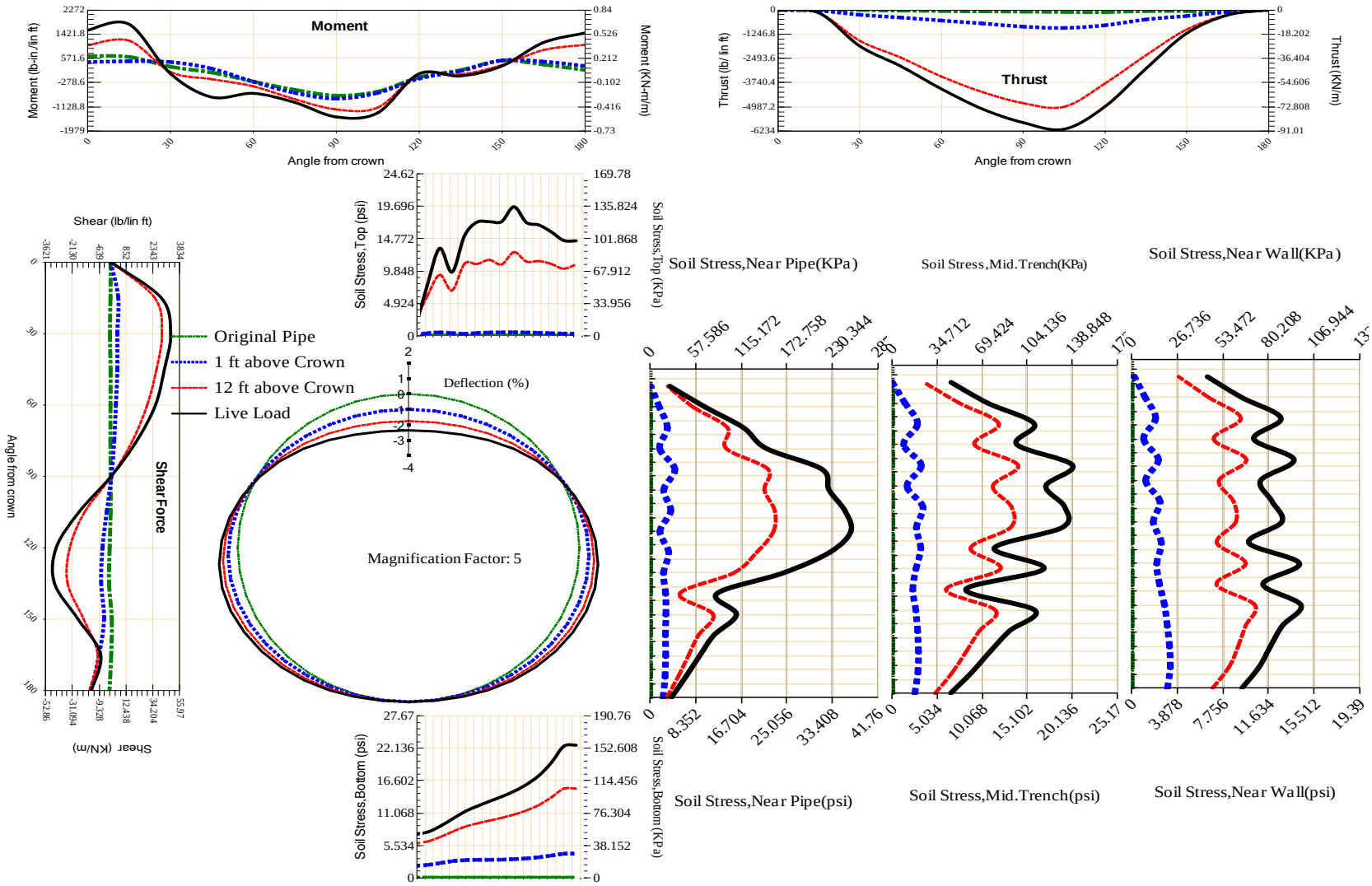

Figure A-678 Param-96-PW288-TR3SF-OD+72-EW5-H12-LiveLoad

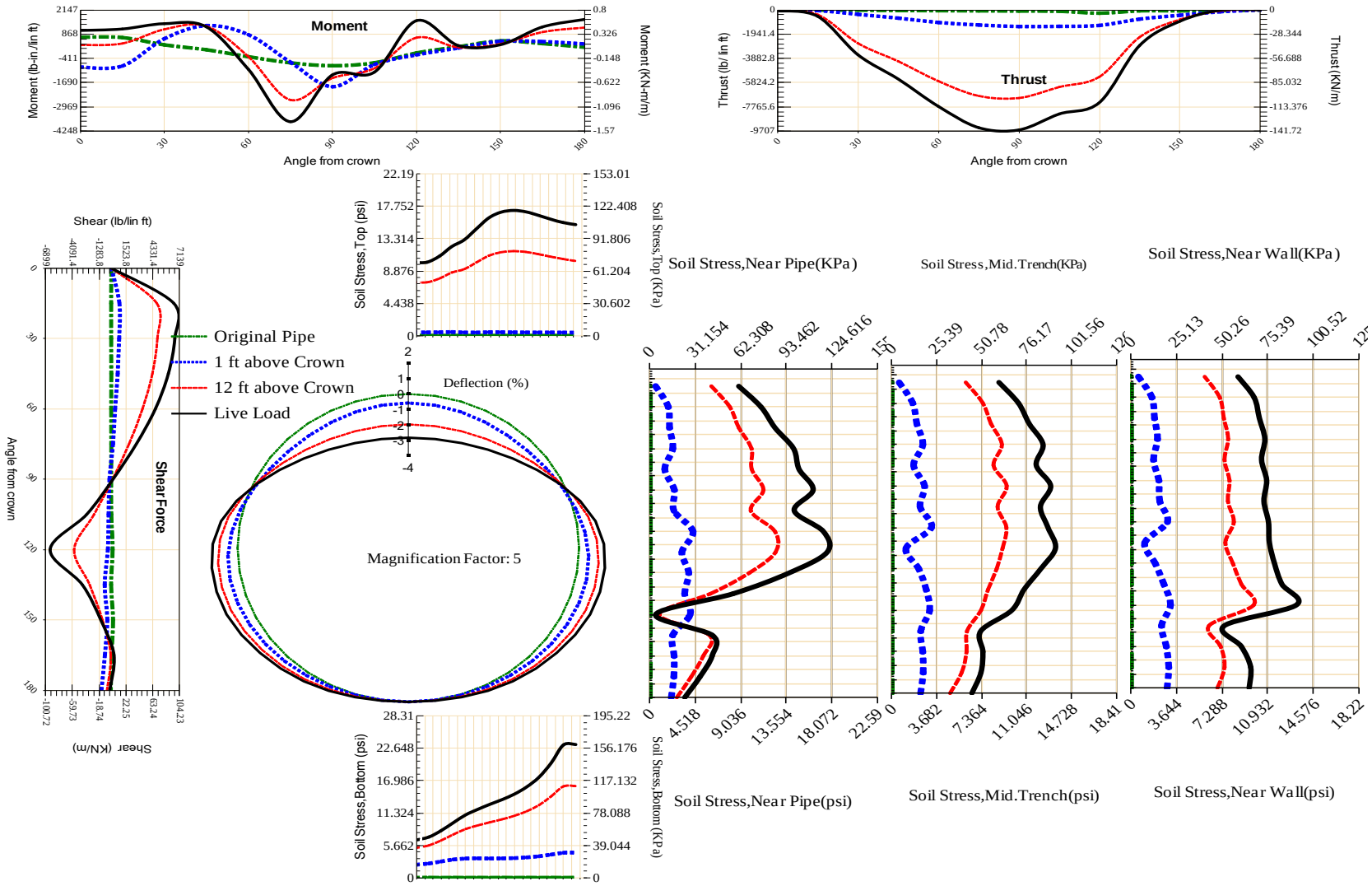

Figure A-679 Param-96-PW288-TR5OR-OD+72-EW5-H12-LiveLoad

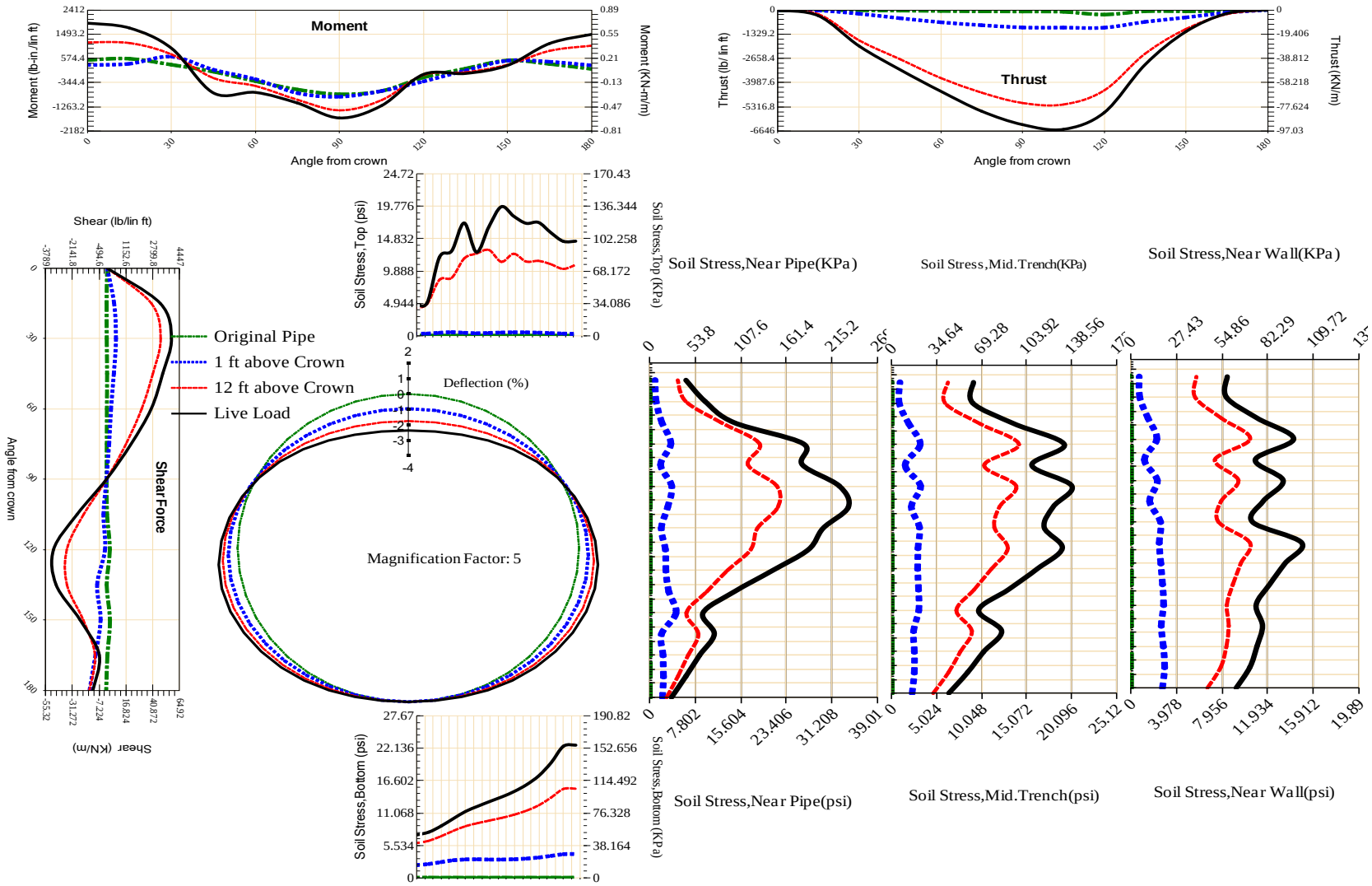

Figure A-680 Param-96-PW288-TR5SF-OD+72-EW5-H12-LiveLoad

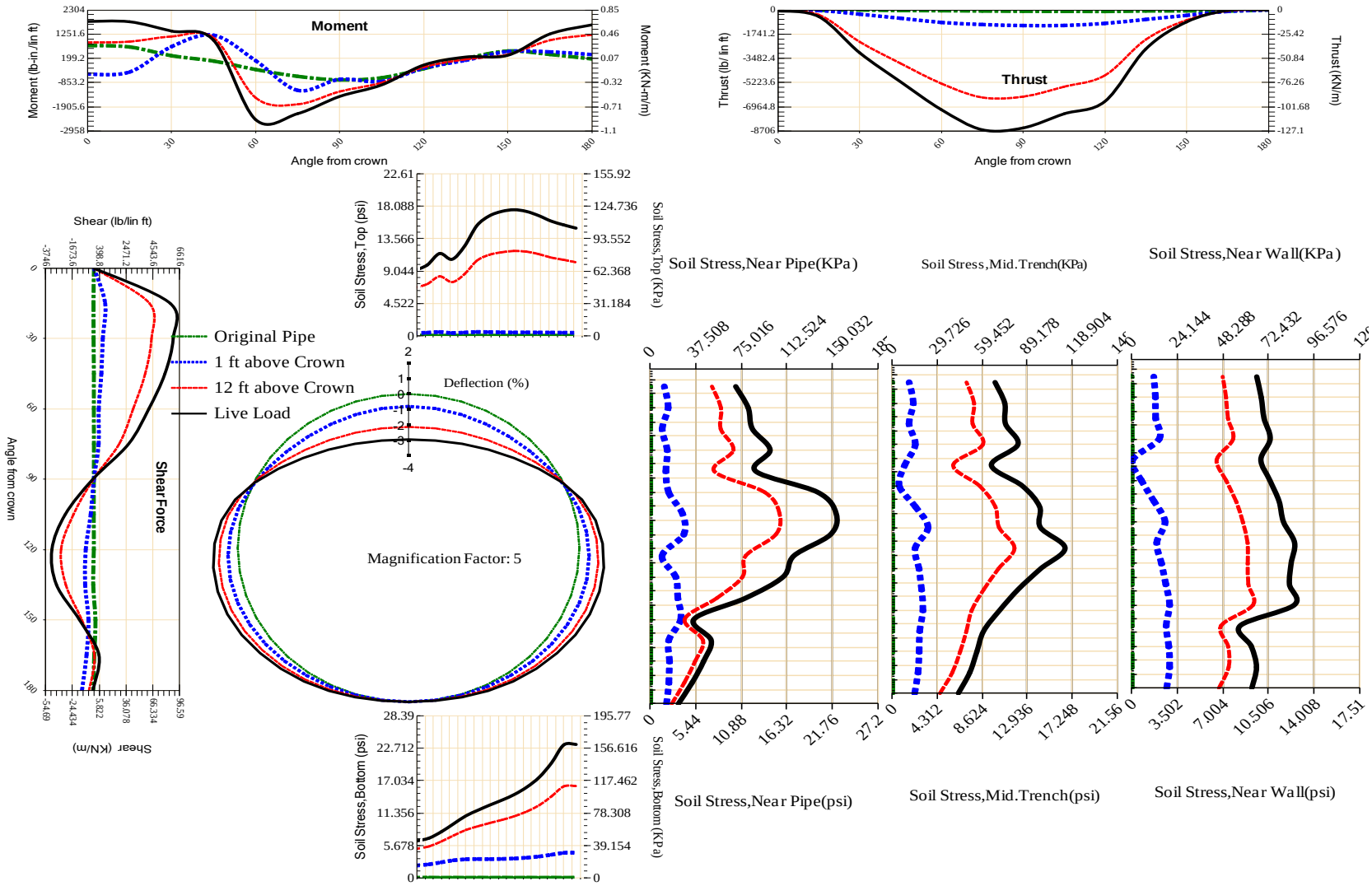

Figure A-681 Param-96-PW288-TR7OR-OD+72-EW5-H12-LiveLoad

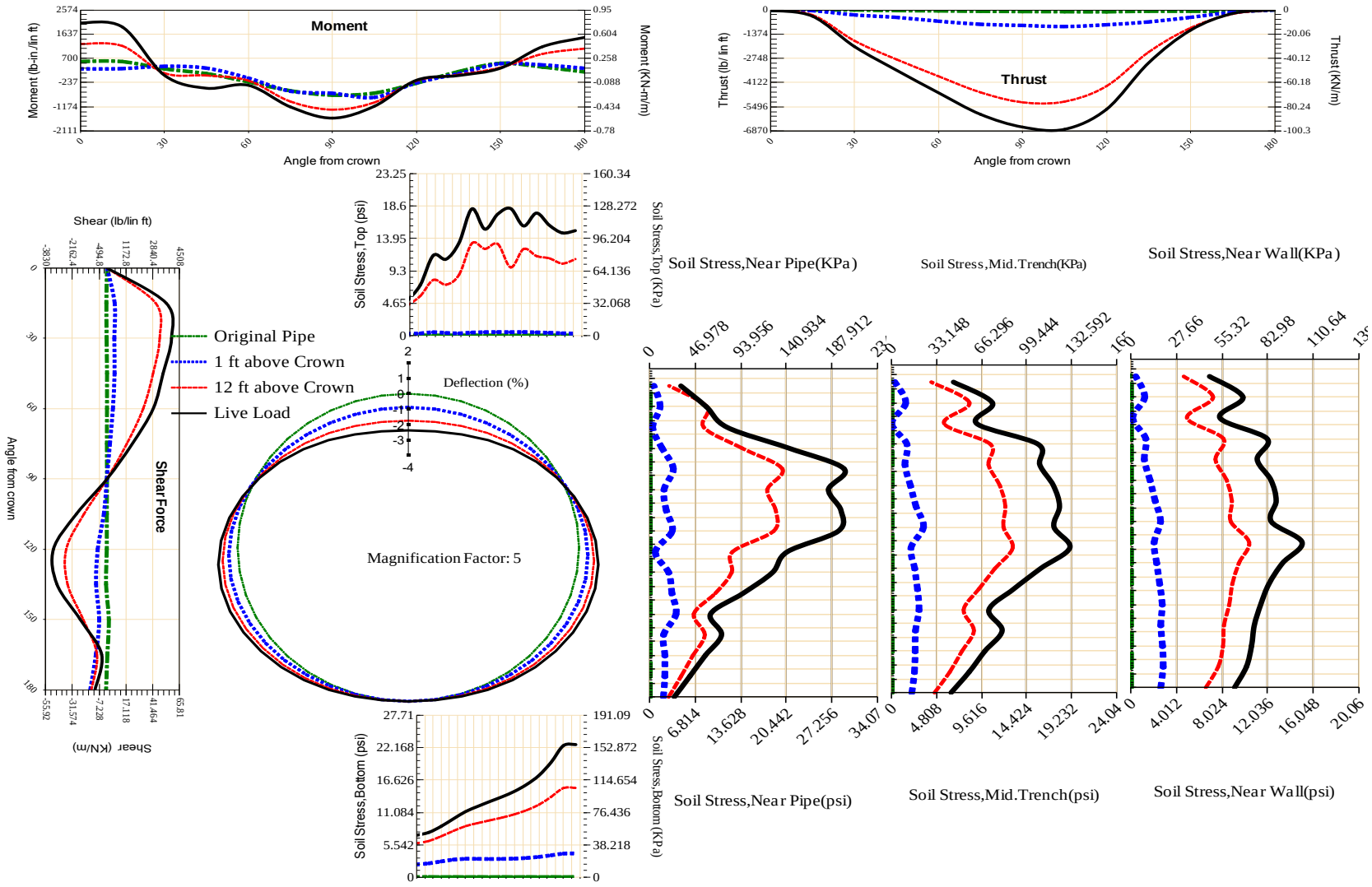

Figure A-682 Param-96-PW288-TR7SF-OD+72-EW5-H12-LiveLoad

References

American Society of Civil Engineers, Buried flexible steel pipe; design and structural analysis, W.R. Whidden (Ed.)ASCE Manual of Practice, MOP (2009).

American Water Works Association (2004), Steel Pipe – A Guide for Design and Installation, AWWA Manual M11, 4th edition, Denver, CO.

Bathe, Klaus-Jürgen. Finite element procedures. Vol. 2. No. 3. Englewood Cliffs: Prentice hall, 1996.

Bellaver, Franciele. “Large Diameter Steel Pipe Field Test Using Controlled Low Strength Material and Staged Construction Modeling Using 3-D Nonlinear Finite Element Analysis,” 2013.

Brinkgreve, Ronald BJ. "Selection of soil models and parameters for geotechnical engineering application." ASCE, (2005.)

Card, Robert J. "Structural Design of Buried Pipes." Pipelines 2012@ sInnovations in Design, Construction, Operations, and Maintenance, Doing More with Less. ASCE, 2012.

Chernoff, Herman, and E. L. Lehmann. "The use of maximum likelihood estimates in χ^2 tests for goodness of fit." The Annals of Mathematical Statistics 25.3 (1954): 579-586.

Clayton, C. R. I. and Symons, I. F., "The pressure of compacted fill on retaining wall." Geotechmique,1992, 42(1), 127-130.

Draper, Norman Richard, Harry Smith, and Elizabeth Pownell. Applied regression analysis. Vol. 3. New York: Wiley, 1966.

Drucker, Daniel Charles, and William Prager. "Soil mechanics and plastic analysis or limit design." Quarterly of applied mathematics 10 (2013).

Duncan, J. M. and Seed, R. B, "Compaction induced lateral earth pressure under Ko conditions." Journal of Geotechnical Engineering, ASCE, 1986, 112(1), 1-22.

Duncan, J.M., "A Design Method for Metal Culvert Structures Based on Finite Element Analyses." Presented at 55th Annual Meeting of the Transportation Research Board, Washington, D.C., 1976.

Duncan, J.M., “Behavior and Design of Long-Span Metal Culverts.” Journal of the Geotechnical Engineering Division, ASCE, Vol. 105, No. GT3, March 1979, pp. 399-418.

El Chazli, G., Hinchberger, S.D., Baumert, M., Allouche, E. , “A medium-scale apparatus and procedure to measure interface shear strength for HDD design,” Proc. 2005 No-Dig Conf., New Orleans, Florida April 24-27, 2005.

Green, Brian H., and Darrel W. Schmitz. "Technical Note: Soil-Based Controlled Low-Strength Materials." *Environmental & Engineering Geoscience*10.2 (2004): 169-174.

Hartley, James D., and James M. Duncan. "E′ and its variation with depth." Journal of transportation engineering 113.5 (1987): 538-553.

Helwany, Sam. Applied soil mechanics with ABAQUS applications. Wiley. com, 2007.

Howard, Amster K. "Modulus of soil reaction values for buried flexible pipe." Journal of the Geotechnical Engineering Division 103.1 (1977): 33-43.

Howard, Amster K. "Pipeline Installation." Relativity publishing, Lakewood, CO. (1996).

Katona, M. G. CANDE, “A Modern Approach for the Structural Design and Analysis of Buried Culverts,” Report FHWA-RD-77-5. FHWA, U.S. Department of Transportation, 1976.

Katona, M. G., M. Mlynarski, and T. J. McGrath. "CANDE-2007 Culvert Analysis and Design Solution Methods and Formulations." (2008): 15-28.

Lade, Poul V. "Overview of constitutive models for soils." ASCE, 2005.

Lamont, Peter A. "Common pipe flow formulas compared with the theory of roughness." *Journal of the American Water Works Association* 73.5 (1981).

McGrath, Timothy J., Ernest T. Selig, and Mark C. Webb. "Instrumentation for monitoring buried pipe behavior during backfilling." ASTM SPECIAL TECHNICAL PUBLICATION 1358 (1999): 101-120.

McGrath, Timothy J. "Pipe-soil interactions during backfill placement," 1998.

McGrath, T. J., and E. T. Selig. "Instrumentation for Investigating Behavior of Pipe and Soil During Backfilling." (1995).

McGrath, Timothy J., Richard E. Chambers, and P. Sharff. "Recent Trends in Installation Standards for Plastic Pipe." Buried Plastic Pipe Technology (1990): 281-293.

Najafi. M., “Testing and Evaluation of the Statically Loaded Large Diameter Steel Pipe with Native Backfill,” Center for Underground Infrastructure Research and Education, 2012.

Neter, John, William Wasserman, and Michael H. Kutner. Applied linear statistical models. Vol. 4. Chicago: Irwin, 1996.

Parmakian, J. "Mínimum Thickness for Handling Steel Pipes." Water Power & Dam Construction, June (1982).

Peaeson, E., and H. Haetlet. "Biometrika tables for statisticians." Biometrika Trust (1976).

Pettibone, H. C., and A. K. Howard. "Distribution of soil pressures on concrete pipe." Am Soc Civil Engr J Pipeline Div (1967).

Potter, John C. "Effects of Vehicles on Buried, High-Pressure Pipe." Journal of Transportation Engineering 111.3 (1985): 224-236.

Sargand, Shad M., and Glenn A. Hazen. Field Verification of Standard Installation Direct Design (SIDD) Method for Concrete Pipe: Final Report. Ohio University, Center for Geotechnical and Environmental Research, 1998.

Selig, Ernest T. "Soil parameters for design of buried pipelines." Pipeline Infrastructure. ASCE, 1988.

Shmulevich, Itzhak, Naftali Galili, and Amnon Foux. "Soil stress distribution around buried pipes." Journal of transportation engineering 112.5 (1986): 481-494.

Spangler, Merlin Grant, and G. E. Shafer. "The structural design of flexible pipe culverts." Highway Research Board Proceedings. 1937.

Srivastava, Amit, Chaitanya R. Goyal, and Abhishek Raghuvanshi. "Load settlement response of footing placed over buried flexible pipe through model plate load test." *International Journal of Geomechanics* (2012).

Suleiman, M.T., R. A. Lohnes, T. J. Wipf, and F. W. Klaiber. “Analysis of Deeply Buried Flexible Pipes.” Transportation Research Record No. 1849. Transportation Research Board, National Research Council, Washington D.C., 2003: 124-133.

Tian, Yinghui, and Mark J. Cassidy. "Modeling of pipe–soil interaction and its application in numerical simulation." *International Journal of Geomechanics* 8.4 (2008): 213-229.

Watkins, Reynold K., and M. G. Spangler. "Some characteristics of the modulus of passive resistance of soil: A study in similitude." Highway Research Board Proceedings. 1958.

Watkins, Reynold King, and L. Loren Runar Anderson. Structural mechanics of buried pipes. CRC Press, 2000.

Wilson, Edwin B., and Margaret M. Hilferty. "The distribution of chi-square." Proceedings of the National Academy of Sciences of the United States of America 17.12 (1931): 684.

Zarghamee, M.S., Tigue, D., “Soil Structure Interaction of Flexible Pipe under Pressure,” Transportation Research Record No. 1087. Transportation Research Board, National Research Council, Washington D.C., 1986: 46-53.

Zhang, J., D. P. Stewart, and M. F. Randolph. "Kinematic hardening model for pipeline-soil interaction under various loading conditions." *The International Journal of Geomechanics* 2.4 (2002): 419-446.

Biographical Information

Mojtaba Salehi Dezfooli received his B.S. Degree in Civil Engineering from University of Tehran, Tehran, Iran, in September 2006 and M.Sc. Degree in Hydraulic Structures from University of Tehran, Tehran, Iran, in September 2009. He completed his Ph.D. Degree in Civil Engineering/Structures at the University of Texas at Arlington in December 2013.

His research interests include nonlinear finite element analysis, behavior of steel and concrete structures including pipes and culverts, nonlinear analysis of structures, and structural stability.